FOSSIL ENERGY

DOE/BC/14885-18
(DE96001257)

DEVELOPMENT OF COST-EFFECTIVE SURFACTANT FLOODING TECHNOLOGY

RECEIVED
NOV 19 1996
OSTI

Final Report

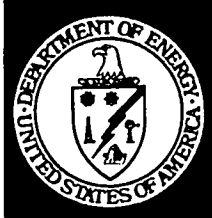
By
Gary A. Pope
Texaco

Kamy Sepehrnoori
NationsBank

November 1996

Performed Under Contract No. DE-AC22-92BC14885

The University of Texas
Center for Petroleum and Geosystems Engineering
Austin, Texas



Bartlesville Project Office
U. S. DEPARTMENT OF ENERGY
Bartlesville, Oklahoma

MASTER

DISTRIBUTION OF THIS DOCUMENT IS UNLIMITED

DISCLAIMER

This report was prepared as an account of work sponsored by an agency of the United States Government. Neither the United States Government nor any agency thereof, nor any of their employees, makes any warranty, expressed or implied, or assumes any legal liability or responsibility for the accuracy, completeness, or usefulness of any information, apparatus, product, or process disclosed, or represents that its use would not infringe privately owned rights. Reference herein to any specific commercial product, process, or service by trade name, trademark, manufacturer, or otherwise does not necessarily constitute or imply its endorsement, recommendation, or favoring by the United States Government or any agency thereof. The views and opinions of authors expressed herein do not necessarily state or reflect those of the United States Government.

This report has been reproduced directly from the best available copy.

Available to DOE and DOE contractors from the Office of Scientific and Technical Information, P.O. Box 62, Oak Ridge, TN 37831; prices available from (615) 576-8401.

Available to the public from the National Technical Information Service, U.S. Department of Commerce, 5285 Port Royal Rd., Springfield VA 22161

DOE/BC/14885-18
Distribution Category UC-122

Development of Cost-Effective Surfactant Flooding Technology

Final Report

By
Gary A. Pope and Kamy Sepehrnoori

November 1996

Work Performed Under Contract No. DE-AC22-92BC14885

Prepared for
U.S. Department of Energy
Assistant Secretary for Fossil Energy

Jerry F. Casteel, Project Manager
Bartlesville Project Office
P.O. Box 1398
Bartlesville, OK 74005

Prepared by
The University of Texas
Center for Petroleum and Geosystems Engineering
Department of Petroleum Engineering
Austin, TX 78712

MASTER

DISTRIBUTION OF THIS DOCUMENT IS UNLIMITED

DISCLAIMER

Portions of this document may be illegible in electronic image products. Images are produced from the best available original document.

ACKNOWLEDGMENTS

We wish to thank Drs. Mojdeh Delshad, Michael G. Edwards, Min T. Lim, and Jianchun Liu and the Graduate Research Assistants Hichem Dakhlia, Khaled Bendakhlia, Hyun-Soo Kim, Sandeep Sinha, Adam Vaskas, Wei-Jr Wu, and Shengyou Xiao for their work in this project. We would also like to thank the participating companies of the Enhanced Oil and Gas Recovery Research Program of the Center for Petroleum and Geosystems Engineering at The University of Texas at Austin for their support of this research. Computing resources for this work were provided by The University of Texas Center for High Performance Computing.

TABLE OF CONTENTS

ACKNOWLEDGMENTS i

TABLE OF CONTENTS ii

ABSTRACT 1

EXECUTIVE SUMMARY 3
UTCHEM Modeling Enhancements 5

TASK 1. HIGH-RESOLUTION, FULLY IMPLICIT, COMPOSITIONAL SIMULATION 7
1. Introduction 7
2. Physical and Mathematical Model 10
2.1 General Description 10
2.2 Basic Assumptions 10
2.3 Mass Conservation Equations 11
2.4 Pressure Equation 12
2.5 Initial and Boundary Conditions 13
2.6 Constitutive Relations 14
3. Numerical Model 16
3.1 Physical-Property Calculations 16
3.1.1 Phase Behavior and Flash Calculations 16
3.1.2 Adsorption 22
3.1.3 Interfacial-Tension Model 23
3.1.4 Relative Permeability and Capillary Desaturation 24
3.1.5 Polymer Viscosity 25
3.1.6 Compositional Phase Viscosity 26
3.1.7 Permeability Reduction 27
3.1.8 Capillary Pressure 28
3.1.9 Phase Density, Gravity and Reservoir Dip 28
3.2 High-Order Temporal Discretization 29
3.3 High-Order Spatial Discretization 29
3.4 TVD Method and Flux Limiter 30
3.5 Governing Equations 31
3.6 Well Models 33
3.6.1 Phase-Productivity Index 34
3.6.2 Gravity Head 34
3.6.3 Bottomhole Pressure for Rate-Constrained Wells 35
3.6.4 Injection Rate 35
3.6.5 Production Rate 35
3.7 Solution of the Nonlinear System of Equations 36
3.8 Timestepping Algorithms 37
4. Simulation Results 41
4.1 One-Dimensional Convection-Diffusion Problem 41
4.1.1 Comparison with Analytical Solutions 41
4.1.2 Comparison with Low-Order Temporal Scheme 41
4.1.3 Comparison with Low-Order Spatial Scheme 41
4.1.4 Comparison with IMPES method 41
4.2 One-Dimensional Waterflood 41
4.2.1 Comparison with Buckley-Leverett Solution 41
4.2.2 Comparison with IMPES method 42

4.2.3 Capillary End Effect 42
4.2.4 Gravity-Inversion Problem 42
4.3 One-Dimensional Polymerflood 42
4.3.1 Comparison with Analytical Solution 43
4.3.2 Comparison with Low-Order Spatial Scheme 43
4.3.3 Comparison with IMPES Method 43
4.3.4 Effect of TVD Flux Limiting 43
4.3.5 Polymer-Property Model Verification 43
4.4 Two-Dimensional Tracer Flood 43
4.4.1 Comparison with Analytical Solution 43
4.4.2 Hydraulic-Fracture Diagnostic Test 43
4.5 Two-Dimensional Waterflood 44
4.5.1 Comparison with IMPES Method 44
4.5.2 Comparison with Low-Order Spatial Scheme 44
4.6 Two-Dimensional Polymerflood 44
4.6.1 Cross-Sectional Simulation 44
4.6.2 Potential Rate Allocation Method 45
4.6.3 Polymer-Property Model Verification 45
4.7 Two-Dimensional Surfactant Flood 45
4.8 Three-Dimensional Tracer Flood 46
4.8.1 Comparison with IMPES Method 46
4.8.2 Comparison with Conventional Schemes 46
4.8.3 Nonuniform Grid Test 46
4.9 Three-Dimensional Polymerflood with Horizontal Wells 47
4.9.1 Horizontal-Well Model Verification 47
4.9.2 Comparison with IMPES method 47
4.10 Computational Efficiency 47
4.10.1 Two-Dimensional Surfactant Flood 47
4.10.2 Three-Dimensional Tracer Flood 47
5. Summary, Conclusions, and Recommendations 80
5.1 Summary and Conclusions 80
5.2 Recommendations 81
5.2.1 Improvements of Physical-Property Models 81
5.2.2 Improvements of Numerical Models 81
6. Nomenclature 83
7. References 86

TASK 2. OPTIMIZATION OF SURFACTANT FLOODING
Part I: Reservoir Modeling Studies 89
1. UTCHEM Modeling Enhancements 89
2. Optimization of Surfactant/Polymer Flooding for Three Reservoirs 91
2.1 Introduction 91
2.2 Optimization Design for Reservoir A 91
2.2.1 Coreflood Simulations 92
2.2.1.1 Descriptions of Coreflood 92
2.2.1.2 Processing Experimental Data to UTCHEM Model 92
2.2.1.3 Simulation of Coreflood 93
2.2.2 2-D Vertical Cross-Sectional Simulation 94
2.2.3 Sensitivity Analyses 95
2.2.3.1 Surfactant Concentration 95
2.2.3.2 Surfactant/Polymer Slug Size 95
2.2.3.3 Polymer Concentration 96
2.2.3.4 Gravity and Buoyancy 96
2.2.3.5 Microemulsion Properties 97

2.2.4 Temperature Effect 98
2.2.4.1 Temperature Effect on Corefloods 98
2.2.4.2 Temperature Effect on 2-D Cross-Sectional Simulations 99
2.2.5 Permeability-Dependent Waterflood Residual Oil Saturation 100
2.2.6 Surfactant/Polymer Interactions 100
2.2.7 A 3-D Simulation 101
2.2.8 Summary and Conclusions for Reservoir A 102
2.3 Optimization Design for Reservoir B 102
2.3.1 Reservoir Description and Injection Scheme 103
2.3.2 Base Case Simulation 103
2.3.2.1 Production Strategies 104
2.3.2.2 Grid Geometry 104
2.3.2.3 Grid Refinement 105
2.3.2.4 Temperature Effect 105
2.3.2.5 Description of Base Case 106
2.3.3 Sensitivity of Starting Time for Chemical Slug 106
2.3.4 Effect of Vertical Permeability 107
2.3.5 Effect of Injection Scheme and Chemical Property 107
2.3.5.1 Amount of Injected Surfactant 107
2.3.5.2 Amount of Injected Polymer 108
2.3.5.3 Surfactant Adsorption 108
2.3.5.4 Surfactant Phase Behavior 108
2.3.5.5 Oil Capillary-Desaturation Curve 108
2.3.6 Permeability-Dependent Waterflood Residual-Oil Saturation 109
2.3.7 Sensitivity Analyses for the New Base Case 110
2.3.7.1 Amount of Surfactant and Slug Size 110
2.3.7.2 Amount of Polymer 111
2.3.8 Polymer/Surfactant Interactions 111
2.3.9 Summary and Conclusions for Reservoir B 111
2.4 Optimized Design for Reservoir C 112
2.4.1 Reservoir Description 112
2.4.2 Base Case for S/P Flooding 112
2.4.3 Salinity-Gradient Design 113
2.4.4 Permeability-Dependent Residual-Oil Saturation 115
2.4.5 Effect of Competitive Adsorption 115
2.4.5.1 New Base Case 116
2.4.5.2 Competitive Adsorption 116
2.4.5.3 Competitive Adsorption with Salinity Gradient .. 116
2.4.6 Optimum Injection Scheme 117
3. Optimization of Alkaline/Surfactant/ Polymer Flooding for Reservoir D 283
3.1 Introduction 283
3.2 ASP Chemicals and Reactions 283
3.3 Core-Flooding History Match 284
3.3.1 History Match of Berea Corefloods 284
3.3.1.1 KMAY7 Type II(-) Phase Behavior 285
3.3.1.2 KMAY7 Type III Phase Behavior 286
3.3.1.3 KMAY7 Salinity-Gradient Case 286
3.3.2 Reservoir Coreflooding Simulations 287
3.4 Field-Scale Simulations 287
3.4.1 Reservoir Characterization 287

3.4.2 Tracer Simulations 288
3.4.3 ASP Simulations 289
3.4.3.1 ASP Field-Scale Simulation - Series I and II 289
3.4.3.2 ASP Field-Scale Simulation - Series III 290
3.4.3.2.1 Amount of Surfactant and ASP Slug Size 291
3.4.3.2.2 Phase Behavior and Chemical Adsorption 292
3.4.3.2.3 Amount of Polymer 292
3.4.4 ASP Simulations Based on Reservoir Coreflood 293
3.5 Summary and Conclusions 293
4. References 295

TASK 2. OPTIMIZATION OF SURFACTANT FLOODING
Part II: Economic Analysis 378
1. Introduction 378
1.1 Background 378
1.2 Research Objective 379
1.3 Overview 379
2. Chemical Flooding Economic Model 380
2.1 Introduction 380
2.2 Chemical Flood Description 380
2.3 Data Acquisition 381
2.4 Predicting After-Tax Cash Flows 381
2.4.1 Revenue 381
2.4.2 Capital Costs 382
2.4.2.1 Workover Costs 382
2.4.2.2 Development Drilling Costs 382
2.4.2.3 Facilities and Equipment Costs 383
2.4.2.4 Leasehold Cost 383
2.4.3 Operating Costs 383
2.4.3.1 Chemical Injection Operating Costs 384
2.4.3.2 Treatment of Produced Fluids 384
2.4.4 Oil and Gas Taxation 384
2.4.4.1 Depreciation 385
2.4.4.2 Depletion 385
2.4.4.3 Treatment of Intangible Drilling Costs 386
2.4.4.4 Severance and Ad Valorem Taxes 386
2.4.4.5 Income Tax 386
2.4.4.6 Tax Credits 386
2.4.5 Adjustments 387
2.5 Discounted Cash Flow Analysis 387
2.5.1 Definition of Economic Limit 387
2.5.2 Selecting a Discount Rate 387
2.5.3 Net Present Value 388
2.5.4 Internal Rate of Return 388
2.5.5 Discounted Return on Investment 388
2.5.6 Investment Efficiency 388
2.5.7 Growth Rate of Return 389
2.5.8 Payback Period 389
2.5.9 Profitability Per Barrel 389
2.6 Chemical Flood Performance 389
2.6.1 Recovery Efficiency 389
2.6.2 Chemical Efficiencies 390
3. Surfactant Flooding Case Studies 396
3.1 Introduction 396

3.2 Onshore Surfactant Flood Case 1 396
3.2.1 Reservoir Description and Simulation 396
3.2.2 Economic Analysis 397
3.3 Onshore Surfactant Flood Case 2 398
3.3.1 Reservoir Description and Simulation 398
3.3.2 Economic Analysis 398
3.4 Conclusions 399
4. Optimization of Surfactant Flooding 407
4.1 Introduction 407
4.2 Evaluating Mutually Exclusive Projects 407
4.3 Selecting a Suitable Profitability Measure 407
4.4 Optimization of Surfactant Flooding 408
4.4.1 Technical Performance 408
4.4.2 Determining the Optimum Design 409
4.4.3 Effect of Oil Price 411
4.4.4 Effect of Profitability Measures 412
4.5 Conclusions 413
5. Evaluating Risk and Uncertainty in Surfactant Flooding 451
5.1 Introduction 451
5.2 Sensitivity Analysis 451
5.2.1 Determining the Strategic Variables 452
5.2.2 Sensitivity to Oil Price and Discount Rate 452
5.2.3 Sensitivity to Chemical Prices 453
5.2.4 Sensitivity to Facilities and Equipment Costs 453
5.2.5 Independent Versus Integrated Producers 453
5.3 Risk Analysis 454
5.3.1 Monte Carlo Simulation 455
5.3.1.1 Selecting Probability Distributions 455
5.3.1.2 Simulation Results 456
5.4 Conclusions 457
6. Conclusions and Recommendations 474
7. References 476

List of Tables

TASK 1. HIGH-RESOLUTION, FULLY IMPLICIT, COMPOSITIONAL SIMULATION

Table 4.1: Input data for Holing's one-dimensional polymerflood.
Table 4.2: Input data for one-dimensional polymerflood for validating polymer properties.
Table 4.3: Input data for two-dimensional polymerflood for validating polymer properties.
Table 4.4: Input data for two-dimensional surfactant flood.

TASK 2. OPTIMIZATION OF SURFACTANT FLOODING
Part I: Reservoir Modeling Studies

Table 2.1: Coreflood data for Reservoir A.
Table 2.2: Input data for coreflood simulation.
Table 2.3: Input data for 2-D cross-sectional simulations.
Table 2.4: Oil recovery data versus temperature.
Table 2.5: Simulation input data for thermal properties.
Table 2.6: Simulation input data for Reservoir B.
Table 2.7: Surfactant property data used in the Base-Case simulation for Reservoir B.
Table 2.8 : List of reservoir description input data for Reservoir C.
Table 2.9: Surfactant property data used in the Base-Case simulation for Reservoir C.
Table 2.10: List of modifications for the new Base Case.
Table 3.1: Results of water analysis of makeup water and formation water.
Table 3.2: List of elements and reactive species for ASP simulations.
Table 3.3: List of reactions for ASP simulations.
Table 3.4: Properties measured during coreflood experiments.
Table 3.5: Summary of Berea coreflood experiments.
Table 3.6: Comparison of simulated and measured retention data.
Table 3.7: Summary of reservoir coreflood results.
Table 3.8: Summary of reservoir coreflood data.
Table 3.9: UTCHEM parameters used in history match of KMAY7 coreflood.
Table 3.10: Key input data used in history match of reservoir coreflood.
Table 3.11: Statistical data for permeability field for each case.
Table 3.12: Optimum Bottomhole pressure for each producer.

TASK 2. OPTIMIZATION OF SURFACTANT FLOODING
Part II: Economic Analysis

Table 2.1: Average cost of drilling and equipping onshore oil wells.
Table 2.2: Direct monthly operating costs for secondary oil recovery in West Texas (per producing well).
Table 2.3: Depreciation schedule for 7 year property under MACRS.
Table 2.4: Federal income tax rates for corporations.
Table 3.1: Technical performance of the Case 1 surfactant flood.
Table 3.2: Profitability of the Case 1 surfactant flood.
Table 3.3: Profitability per barrel of oil produced, non-discounted and discounted at 10%, for the Case 1 surfactant flood.
Table 3.4: Technical performance of the Case 2 surfactant flood.
Table 3.5: Profitability of the Case 2 surfactant flood.

Table 3.6: Profitability per barrel of oil produced, non-discounted and discounted at 10%, for the Case 2 surfactant flood.
Table 4.1: Simulation runs at a polymer concentration of 1000 ppm.
Table 4.2: Simulation runs at a polymer concentration of 1500 ppm.
Table 4.3: Simulation runs at a polymer concentration of 2000 ppm.
Table 4.4: Simulation runs at a polymer concentration of 2500 ppm.
Table 4.5: Simulation runs at a polymer concentration of 3000 ppm.
Table 4.6: Technical performance at the economic limit with a polymer concentration of 1000 ppm.
Table 4.7: Technical performance at the economic limit with a polymer concentration of 1500 ppm.
Table 4.8: Technical performance at the economic limit with a polymer concentration of 2000 ppm.
Table 4.9: Technical performance at the economic limit with a polymer concentration of 2500 ppm.
Table 4.10: Technical performance at the economic limit with a polymer concentration of 3000 ppm.
Table 4.11: Technical performance of the optimum surfactant flooding design at the economic limit.
Table 4.12: Profitability of the optimum surfactant flooding design.
Table 4.13: Profitability per barrel of oil produced for the optimum surfactant flooding design.
Table 4.14: Profitability of surfactant floods with a polymer concentration of 1000 ppm.
Table 4.15: Profitability of surfactant floods with a polymer concentration of 1500 ppm.
Table 4.16: Profitability of surfactant floods with a polymer concentration of 2000 ppm.
Table 4.17: Profitability of surfactant floods with a polymer concentration of 2500 ppm.
Table 4.18: Profitability of surfactant floods with a polymer concentration of 3000 ppm.
Table 5.1: Determining the strategic variables using various profitability measures.
Table 5.2: Comparing the profitability of the optimum surfactant flooding design for an independent producer to an integrated producer.
Table 5.3: Comparing the discounted profitability per barrel of the optimum design for an independent producer to an integrated producer.
Table 5.4: Results of the Monte Carlo simulation.
Table 5.5: Comparing deterministic and probabilistic approaches to economic analysis.

List of Figures

TASK 1. HIGH-RESOLUTION, FULLY IMPLICIT, COMPOSITIONAL SIMULATION

Figure 3.1: Schematic representation of binodal curve, invariant point, and different phase regions in a ternary diagram.
Figure 3.2: Gridpoints used in the high-order finite-difference scheme.
Figure 3.3: Matrix structure for a three-dimensional, two-component problem using the fully implicit high-order method with 5x5x3 gridblocks.
Figure 4.1: Comparison of simulation results of one-dimensional convection-diffusion problems with analytical solutions.
Figure 4.2: Comparison of simulation results of one-dimensional convection-diffusion problems with those using low-order temporal scheme.
Figure 4.3: Error comparison of simulating one-dimensional convection-diffusion problem using low- or high-order spatial discretization scheme.
Figure 4.4: Error comparison of simulating one-dimensional convection-diffusion problem using IMPES simulator or fully implicit simulator.
Figure 4.5: Comparison of simulation results of one-dimensional waterflood with Buckley-Leverett solution.
Figure 4.6: Comparison of simulating one-dimensional waterflood using IMPES simulator or fully implicit simulator at a small timestep size.
Figure 4.7: Comparison of simulating one-dimensional waterflood using IMPES simulator or fully implicit simulator at a large timestep size.
Figure 4.8: Comparison of results of simulating capillary end effect with analytical solution.
Figure 4.9: Comparison of simulation results of one-dimensional gravity-inversion problem with analytical solution.
Figure 4.10: Comparison of simulation results of one-dimensional polymerflood with analytical solutions.
Figure 4.11: Comparison of simulation results of one-dimensional polymerflood using one-point upstream scheme with those of analytical solutions.
Figure 4.12: Comparison of simulation results of one-dimensional polymerflood using IMPES simulator with those of analytical solutions.
Figure 4.13: Comparison of simulation results of one-dimensional polymerflood using high-order scheme without flux limiting with those of analytical solutions.
Figure 4.14: Results of one-dimensional polymerflood simulation for verifying polymer property model.
Figure 4.15: Comparison of simulation results of two-dimensional tracer flood with analytical solution.
Figure 4.16: Comparison of tracer responses for hydraulic fracture diagnostic tests using IMPES simulator and implicit simulator.
Figure 4.17: Comparison of timestep sizes of simulations for hydraulic-fracture diagnostic tests using IMPES simulator and implicit simulator.
Figure 4.18: Tracer responses results for hydraulic-fracture diagnostic tests using implicit simulator.
Figure 4.19: Simulation results of two-dimensional waterflood using IMPES method.
Figure 4.20: Simulation results of two-dimensional waterflood using implicit method.
Figure 4.21: Comparison of simulation results of two-dimensional waterflood with those using low-order spatial scheme.
Figure 4.22: Well patterns for the two-dimensional, cross-sectional polymerflood simulation.
Figure 4.23: Simulation of a two-dimensional, cross-sectional polymerflood using the IMPES simulator and the fully implicit simulator with small timestep sizes.

Figure 4.24: Oil recovery and normalized effluent polymer concentration of simulating a two-dimensional, cross-sectional polymerflood using the IMPES simulator.
Figure 4.25: Water cut of simulating a two-dimensional, cross-sectional polymerflood using the IMPES simulator.
Figure 4.26: Oil recovery and normalized effluent polymer concentration of simulating a two-dimensional, cross-sectional polymerflood using the fully implicit simulator.
Figure 4.27: Water cut of simulating a two-dimensional, cross-sectional polymerflood using the fully implicit simulator.
Figure 4.28: Simulation of a two-dimensional, cross-sectional polymerflood with a high vertical permeability.
Figure 4.29: Water saturation and polymer concentration distributions with a high vertical permeability using the mobility rate-allocation method.
Figure 4.30: Water saturation and polymer concentration distributions with a high vertical permeability using the potential rate-allocation method.
Figure 4.31: Simulation of a two-dimensional, cross-sectional polymerflood with a low vertical permeability.
Figure 4.32: Water saturation and polymer concentration distributions with a low vertical permeability using the mobility rate-allocation method.
Figure 4.33: Water saturation and polymer concentration distributions with a low vertical permeability using the potential rate-allocation method.
Figure 4.34: Comparison with IMPES results of two-dimensional polymerflood simulation for verifying polymer-property model.
Figure 4.35: IMPES results of two-dimensional polymerflood simulation for verifying polymer-property model.
Figure 4.36: Implicit simulator results of two-dimensional polymerflood simulation for verifying polymer-property model.
Figure 4.37: Comparison of results of two-dimensional surfactant flood simulation with those of IMPES simulator at Courant number of 0.01.
Figure 4.38: Comparison of results of two-dimensional surfactant flood simulation with those of IMPES simulator at Courant number of 0.001.
Figure 4.39: Comparison of results of two-dimensional surfactant flood simulation with those of IMPES simulator at Courant number of 0.0001.
Figure 4.40: Well pattern for the three-dimensional tracer convection-diffusion simulation.
Figure 4.41: Simulation of a three-dimensional tracer flood using the IMPES simulator and the fully implicit simulator.
Figure 4.42: Simulation of a three-dimensional tracer flood using the IMPES simulator.
Figure 4.43: Simulation of a three-dimensional tracer flood using the fully implicit simulator.
Figure 4.44: Simulation of a three-dimensional tracer flood using the high-order scheme without TVD flux limiting or the low-order scheme.
Figure 4.45: Schematic of a nonuniform grid and its expansion ratio.
Figure 4.46: Simulation of a three-dimensional tracer flood using the IMPES simulator with a nonuniform grid.
Figure 4.47: Simulation of a three-dimensional tracer flood using the IMPES simulator with a nonuniform grid.
Figure 4.48: Well pattern for the three-dimensional polymerflood simulation.
Figure 4.49: Simulation of a three-dimensional polymerflood with horizontal well using the fully implicit simulator and the IMPES simulator.
Figure 4.50: Simulation of a three-dimensional polymerflood with horizontal well using the IMPES simulator.
Figure 4.51: Simulation of three-dimensional polymerflood with horizontal well using the fully implicit simulator.

TASK 2. OPTIMIZATION OF SURFACTANT FLOODING
Part I: Reservoir Modeling Studies

Figure 2.1: Capillary desaturation curves.
Figure 2.2: Low capillary number relative permeability curves.
Figure 2.3: Interfacial tension as a function of solubilization ratio.
Figure 2.4: Viscosity of xanthan gum polymer as a function of shear rate.
Figure 2.5: Schematic of phase behavior used in UTCHEM.
Figure 2.6: High capillary number relative permeability curves.
Figure 2.7: Microemulsion viscosity as a function of oil concentration.
Figure 2.8: Surfactant adsorption isotherm.
Figure 2.9: Polymer adsorption isotherm.
Figure 2.10: Comparison of simulated and laboratory oil recovery for water flood.
Figure 2.11: Comparison of simulated and laboratory pressure drop for water flood.
Figure 2.12: Comparison of simulated and laboratory chemical oil recovery for S/P process.
Figure 2.13: Comparison of simulated and laboratory oil cut for S/P process.
Figure 2.14: Comparison of simulated and laboratory pressure drop for S/P process.
Figure 2.15: Distribution of phase saturations at 0.2 PV (Time=0.032 Days).
Figure 2.16: Distribution of phase saturations at 0.4 PV (Time=0.064 Days).
Figure 2.17: Distribution of phase saturations at 0.73 PV (Time=0.117 Days).
Figure 2.18: Distribution of phase saturations at 2.43 PV (Time=0.39 Days).
Figure 2.19: Distributions of oil phase capillary number.
Figure 2.20: Distributions of residual oil saturation.
Figure 2.21: Phase diagram and history path of composition.
Figure 2.22: Distribution of surfactant and polymer concentrations at 0.2 PV (Time=0.032 DAYS).
Figure 2.23: Distribution of surfactant and polymer concentrations at 0.4 PV (Time=0.064 days).
Figure 2.24: Distribution of surfactant and polymer concentrations 0.73 PV (Time=0.116 days).
Figure 2.25: Distribution of surfactant and polymer concentrations 1.43 PV (Time=0.229 days).
Figure 2.26: Permeability distribution for the Reservoir A.
Figure 2.27: Oil recovery and oil cut for surfactant/polymer flooding for 2-D cross sectional simulations.
Figure 2.28: Simulated total oil production rate for surfactant/polymer flood.
Figure 2.29: Surfactant concentration for S/P flooding for 2-D cross sectional simulations.
Figure 2.30: Polymer concentration for S/P flooding for 2-D cross sectional simulations.
Figure 2.31: Surfactant adsorption for surfactant/polymer flood for 2D cross sectional simulations.
Figure 2.32: Oil saturation profiles for 13x1x3 2-D cross sectional simulation .
Figure 2.33: Effect of simulation gridblocks on oil recovery.
Figure 2.34: Effect of simulation gridblocks on oil cut.
Figure 2.35: Effect of simulation gridblocks on the produced total surfactant concentration.
Figure 2.36: Effect of injected surfactant concentrations on oil recovery for 2-D cross sectional simulations.
Figure 2.37: Effect of injected surfactant concentrations on oil recovery for 1-D simulations with constant amount of polymer injected.
Figure 2.38: Effect of chemical slug sizes on oil recovery for 2-D cross sectional simulations.
Figure 2.39: Effect of surfactant slug sizes on using same amount of chemical for 1-D simulations.
Figure 2.40: Effect of polymer concentrations on oil recovery for 2-D cross sectional simulations.
Figure 2.41: Effect of polymer concentrations on oil recovery and project life for 2-D cross sectional simulations.
Figure 2.42: Effect of injected polymer concentrations on oil recovery for 1-D simulations.

Figure 2.43: Effect of gravity on oil recovery for 2-D cross sectional simulations.
Figure 2.44: Oil saturation profiles with gravity effect at different pore volumes injected for the case of 0.5 vol.% injected surfactant concentration..
Figure 2.45: Oil saturation profiles when gravity effect is neglected.
Figure 2.46: Buoyancy effect on oil recovery for 2-D cross sectional simulations.
Figure 2.47: Effect of maximum heights of binodal curve on oil recovery for 2-D cross sectional simulations.
Figure 2.48: Schematic representation of phase diagram for three different heights of binodal curves.
Figure 2.49: Microemulsion viscosity for sensitivity analyses.
Figure 2.50: Effect of microemulsion viscosity parameters on oil recovery of coreflood.
Figure 2.51: Effect of microemulsion viscosity parameters on oil recovery for 2-D cross sectional simulations.
Figure 2.52: Interfacial tension vs. solubilization ratio at 122°F.
Figure 2.53: Effect of interfacial tension parameters on oil recovery of coreflood.
Figure 2.54: Effect of interfacial tension parameters on oil recovery for 2-D cross sectional simulations.
Figure 2.55: Effect of temperature on effective salinity of coreflood.
Figure 2.56: Effect of temperature on oil recovery for coreflood.
Figure 2.57: Temperature effect on produced surfactant concentration for coreflood.
Figure 2.58: Temperature effect on surfactant retained for 1-D simulations.
Figure 2.59: Effect of injection temperatures on oil recovery for 2-D cross sectional simulations.
Figure 2.60: Effect of temperatures on injection rate for 2-D cross sectional simulations.
Figure 2.61: Temperature profiles for injection T = 86°F for 2-D cross sectional simulation.
Figure 2.62: Temperature profiles for injection T = 122°F for 2D cross sectional simulations.
Figure 2.63: Surfactant concentration and temperature distribution in 8th layer for 2-D cross sectional simulations.
Figure 2.64: Surfactant concentration and effective salinity distribution in 8th layer for 2-D cross sectional simulations.
Figure 2.65: Residual oil saturation (Sorw) as a function of permeability.
Figure 2.66: Capillary desaturation curve for permeability-dependent Sorw (Case 3 Sorw=exp(-0.0161865k0.5)).
Figure 2.67: Capillary desaturation curve for permeability-dependent Sorw (Case 4 Sorw=exp(-0.001752905k0.75)).
Figure 2.68: Capillary desaturation curve for permeability-dependent Sorw (Case 5 Sorw=exp(-0.2336038k0.2)).
Figure 2.69: Effect of distributed Sorw on oil recovery.
Figure 2.70: Effect of distributed Sorw on oil rate.
Figure 2.71: Effect of distributed Sorw on water cut.
Figure 2.72: Oil concentration distributions at 0.5 PV injected (84 days) for different residual oil saturation distributions.
Figure 2.73: Oil concentration distributions at 1.8 PV injected (303 days) for different residual oil saturation distributions.
Figure 2.74: Effect of competitive adsorption on oil recovery for Reservoir A.
Figure 2.75: Oil concentration profiles for the Base Case.
Figure 2.76: Profiles of surfactant concentration overlaid by temperature contours in °F.
Figure 2.77: Profiles of surfactant concentration overlaid by polymer concentration contours in wt%.
Figure 2.78: Effect of polymer preflooding on oil recovery for Reservoir A.
Figure 2.79: Effect of polymer preflooding on surfactant concentration for Reservoir A.
Figure 2.80: Effect of polymer preflooding on surfactant adsorption .
Figure 2.81: Profiles of surfactant concentration overlaid by polymer concentration contours in wt% for 2-D cross sectional simulations.
Figure 2.82: Schematic of 3-D simulation grids.

Figure 2.83: Comparison of 3D and 2D surfactant/polymer simulations.
Figure 2.84: The location of the Reservoir B.
Figure 2.85: Permeability distribution for reservoir B.
Figure 2.86: Capillary desaturation curves.
Figure 2.87: Low capillary number oil and water relative permeability curves.
Figure 2.88: Phase relative permeability at high capillary number as a function of water saturation.
Figure 2.89: Type III ternary diagram.
Figure 2.90: Interfacial tension as a function of oil solubilization ratio.
Figure 2.91: Surfactant adsorption isotherm.
Figure 2.92: Microemulsion viscosity as a function of oil concentration.
Figure 2.93: Viscosity of xanthan polymer as a function of shear rate.
Figure 2.94: Polymer adsorption isotherm.
Figure 2.95: Oil and water viscosity as a function of temperature.
Figure 2.96: Effect of well type and location on oil recovery.
Figure 2.97: Effect of well type and location on oil recovery.
Figure 2.98: Effect of well type and location on oil cut.
Figure 2.99: Effect of well type and location on oil production rate.
Figure 2.100: Effect of well type and location on oil cut.
Figure 2.101: Effect of well type and location on project life.
Figure 2.102: Effect of location of producer on oil recovery.
Figure 2.103: Effect of location of producer on oil recovery.
Figure 2.104: Effect of location of producer on oil cut.
Figure 2.105: Effect of location of producer on oil production rate.
Figure 2.106: Effect of location of producer on injection rate.
Figure 2.107: Effect of location of producer on project life.
Figure 2.108: Effect of coordinate on oil recovery.
Figure 2.109: Effect of coordinate on oil recovery.
Figure 2.110: Effect of coordinate on oil production rate.
Figure 2.111: Effect of grid size on oil recovery.
Figure 2.112: Effect of grid size on oil recovery.
Figure 2.113: Effect of grid size on oil cut.
Figure 2.114: Effect of grid size on oil production rate.
Figure 2.115: Effect of grid size on injection rate.
Figure 2.116: Effect of grid size on project life.
Figure 2.117: Effect of temperature on oil recovery.
Figure 2.118: Effect of temperature on oil recovery.
Figure 2.119: Effect of temperature on oil cut.
Figure 2.120: Effect of temperature on oil production rate.
Figure 2.121: Effect of temperature on injection rate .
Figure 2.122: Temperature distribution of non-isothermal run.
Figure 2.123: Simulation gridblocks for Reservoir B.
Figure 2.124: Initial pressure distribution for Reservoir B.
Figure 2.125: Initial water saturation distribution for Reservoir B.
Figure 2.126: Oil recovery of the Base Case.
Figure 2.127: Oil cut of the Base Case.
Figure 2.128: Oil production rate of the Base Case.
Figure 2.129: Injection rate of the Base Case .
Figure 2.130: Project life of the Base Case.
Figure 2.131: Oil concentration distribution at 0.47 pore volumes injected.
Figure 2.132: Oil concentration distribution at 1.125 pore volumes injected.
Figure 2.133: Surfactant concentration distribution at 0.47 pore volumes injected.
Figure 2.134: Surfactant concentration distribution at 1.125 pore volumes injected.
Figure 2.135: Polymer concentration distribution at 0.47 pore volumes injected.

Figure 2.136: Polymer concentration distribution at 1.125 pore volumes injected.
Figure 2.137: Distribution of oil saturation at 0.47 pore volumes injected.
Figure 2.138: Distribution of oil saturation at 1.125 pore volumes injected.
Figure 2.139: Microemulsion saturation distribution at 0.47 pore volumes injected.
Figure 2.140: Microemulsion saturation distribution at 1.125 pore volumes injected .
Figure 2.141: Distribution of log of microemulsion/oil interfacial tension at 0.62 pore volumes injected.
Figure 2.142: Distribution of log of microemulsion/oil interfacial tension at 1.15 pore volumes injected.
Figure 2.143: Distribution of log of microemulsion/water interfacial tension at 0.62 pore volumes injected.
Figure 2.144: Distribution of log of microemulsion/water interfacial tension at 1.15 pore volumes injected.
Figure 2.145: Effect of duration of water injection prior to chemical on S/P oil recovery.
Figure 2.146: Effect of duration of water injection prior to chemical on S/P oil recovery.
Figure 2.147: Injection rate during water flood prior to S/P.
Figure 2.148: Effect of vertical permeability on oil recovery.
Figure 2.149: Effect of vertical permeability on oil recovery.
Figure 2.150: Effect of vertical permeability on oil cut.
Figure 2.151: Effect of vertical permeability on oil production rate.
Figure 2.152: Effect of vertical permeability on injection rate.
Figure 2.153: Effect of vertical permeability on project life.
Figure 2.154: Effect of amount of injected surfactant on oil recovery at 5% oil cut.
Figure 2.155: Effect of amount of injected surfactant on oil recovery.
Figure 2.156: Effect of amount of injected surfactant on oil recovery.
Figure 2.157: Effect of amount of injected surfactant on oil cut.
Figure 2.158: Effect of amount of injected surfactant on oil production rate.
Figure 2.159: Effect of amount of injected surfactant on injection rate.
Figure 2.160: Effect of amount of injected surfactant on project life.
Figure 2.161: Effect of amount of injected polymer on oil recovery at 5% oil cut.
Figure 2.162: Effect of amount of injected polymer on oil recovery.
Figure 2.163: Effect of polymer concentrations on oil recovery.
Figure 2.164: Effect of polymer concentrations on oil cut.
Figure 2.165: Effect of polymer concentrations on oil production rate.
Figure 2.166: Effect of amount of injected polymer on injection rate.
Figure 2.167: Effect of amount of injected polymer on project life.
Figure 2.168: Surfactant adsorption isotherm used in sensitivity study.
Figure 2.169: Effect of surfactant adsorption on oil recovery.
Figure 2.170: Effect of surfactant adsorption on oil recovery.
Figure 2.171: Effect of height of binodal curve at optimum salinity on oil recovery.
Figure 2.172: Effect of height of binodal curve at optimum salinity on oil recovery.
Figure 2.173: Oil desaturation curves used in the sensitivity study.
Figure 2.174: Effect of oil desaturation curves on oil recovery.
Figure 2.175: Effect of oil desaturation curves on oil recovery.
Figure 2.176: Residual oil saturations as a function of permeability.
Figure 2.177: Capillary desaturation curves for permeability-dependent Sorw (Sorw=exp(-0.88222k0.125)).
Figure 2.178: Capillary desaturation curves for permeability-dependent Sorw (Sorw=exp(-1.1048k0.0625)).
Figure 2.179: Capillary desaturation curves for permeability-dependent Sorw (Sorw=exp(-0.5665k0.25)).
Figure 2.180: Effect of residual oil saturations on chemical flood oil recovery.
Figure 2.181: Effect of residual oil saturations on chemical flood oil recovery.
Figure 2.182: Effect of residual saturations on tertiary cumulative oil production.

Figure 2.183: Effect of residual saturation on tertiary cumulative oil production.
Figure 2.184: Oil recovery as a function of pore volumes injected for the new Base Case simulation.
Figure 2.185: Oil production rate as a function of pore volumes injected for the new Base Case simulation.
Figure 2.186: Produced surfactant concentration as a function of pore volumes injected for the new Base Case simulation.
Figure 2.187: Produced polymer concentration as a function of pore volumes injected for the new Base Case simulation.
Figure 2.188: Project life as a function of pore volumes injected for the new Base Case simulation.
Figure 2.189: Effect of injected surfactant concentration on oil recovery.
Figure 2.190: Effect of injected surfactant concentration on produced surfactant concentration.
Figure 2.191: Effect of injected surfactant concentration on produced polymer concentration.
Figure 2.192: Effect of injected surfactant concentration on surfactant adsorption.
Figure 2.193: Effect of injected surfactant concentration on polymer adsorption.
Figure 2.194: Effect of slug size on oil recovery.
Figure 2.195: Effect of injected polymer concentration on oil recovery.
Figure 2.196: Effect of competitive adsorption on oil recovery.
Figure 2.197: Effect of competitive adsorption on produced surfactant concentration.
Figure 2.198: Effect of competitive adsorption on surfactant adsorption.
Figure 2.199: Effect of competitive adsorption on produced polymer concentration.
Figure 2.200: Effect of competitive adsorption on polymer adsorption.
Figure 2.201: Effect of competitive adsorption on oil recovery.
Figure 2.202: Effect of competitive adsorption on produced surfactant concentration.
Figure 2.203: Effect of competitive adsorption on surfactant adsorption.
Figure 2.204: Effect of competitive adsorption on produced polymer concentration.
Figure 2.205: Effect of competitive adsorption on polymer adsorption.
Figure 2.206: Surfactant adsorption isotherm.
Figure 2.207: Permeability distribution with the 200 md iso-surface.
Figure 2.208: Oil and water relative permeability curves at low capillary number.
Figure 2.209: Oil and water relative permeability curves at high capillary number.
Figure 2.210: Oil and microemulsion relative permeability curves at high capillary number.
Figure 2.211: Polymer adsorption isotherm.
Figure 2.212: Polymer viscosity as a function of polymer concentration and shear rate.
Figure 2.213: Polymer permeability reduction factor.
Figure 2.214: Capillary desaturation curves for oil, water, microemulsion phases.
Figure 2.215: Interfacial tension as a function of solubilization ratios.
Figure 2.216: Surfactant adsorption isotherm.
Figure 2.217: Phase behavior for the Type III region.
Figure 2.218: Cumulative oil recovery and oil cut as a function of pore volumes injected (Base Case).
Figure 2.219: Cumulative oil recovery as a function of project life.
Figure 2.220: Oil production as a function of pore volumes injected.
Figure 2.221: Total injection rate and bottomhole pressure as a function of pore volumes injected.
Figure 2.222: History of effluent surfactant concentration (Base Case).
Figure 2.223: History of effluent polymer concentration (Base Case).
Figure 2.224: History of effective salinity for the Base Case.
Figure 2.225: Oil concentration distribution with iso-surface of 0.1 for Base Case.
Figure 2.226: Surfactant concentration distribution with iso-surface of 0.001 for Base Case.
Figure 2.227: History of the effective salinity.
Figure 2.228: Effect of salinity gradient on oil recovery.
Figure 2.229: Effect of salinity gradient on oil recovery and project life.
Figure 2.230: Effect of salinity gradient on oil production rate.

Figure 2.231: Effect of salinity gradient on total injection rate.
Figure 2.232: Effect of salinity gradient on the produced surfactant concentration.
Figure 2.233: Effect of salinity gradient on surfactant adsorption.
Figure 2.234: Effect of salinity gradient on retained surfactant.
Figure 2.235: Distribution of oil concentration with iso-surface of 0.001 for salinity gradient case.
Figure 2.236: Distribution of surfactant concentration with iso-surface of 0.1 vol.% for salinity gradient case.
Figure 2.237: Comparison of oil recovery between constant salinity and salinity gradient case at different surfactant concentration.
Figure 2.238: Distribution of surfactant concentration with iso-surface of 0.1 vol.% for injected surf. = 0.8 vol.% for constant salinity case.
Figure 2.239: Distribution of oil concentration with iso-surface of 0.1 meq/ml for constant salinity case.
Figure 2.240: Distribution of surfactant concentration with iso-surface of 0.1 vol.% for injected surfactant = 0.8 vol.% fraction for salinity gradient case.
Figure 2.241: Distribution of oil concentration with iso-surface of 0.1 meq/ml for salinity gradient case.
Figure 2.242: Residual oil saturation (Sorw) as a function of permeability.
Figure 2.243: Capillary desaturation curves for permeability-dependent Sorw (Case 3 Sorw=exp(-1.1859127k0.04)) .
Figure 2.244: Capillary desaturation curves for permeability-dependent Sorw (Case 4 Sorw=exp(-0.941164k0.1)).
Figure 2.245: Effect of distributed Sorw on oil recovery.
Figure 2.246: Effect of distributed Sorw on oil recovery.
Figure 2.247: Effect of chemical interactions on oil recovery (Constant salinity).
Figure 2.248: Effect of chemical interactions on produced surfactant concentration (Constant salinity).
Figure 2.249: Effect of chemical interactions on surfactant adsorption (Constant salinity).
Figure 2.250: Effect of competitive adsorption with salinity gradient on oil recovery.
Figure 2.251: Effect of competitive adsorption with salinity gradient on produced surfactant concentration.
Figure 2.252: Effect of competitive adsorption with salinity gradient on surfactant adsorption .
Figure 2.253: Surfactant concentration distribution for constant salinity case.
Figure 2.254: Surfactant concentration distribution for salinity gradient design case.
Figure 3.1: Capillary desaturation curve used for coreflood history match.
Figure 3.2: Low capillary number relative permeability curves used for coreflood history match.
Figure 3.3: High capillary number (>10-2) relative permeability curves used for coreflood history match.
Figure 3.4: Type II(-) phase behavior used for KMAY7 coreflood history match.
Figure 3.5: Interfacial tension for oil/microemulsion used for coreflood history match.
Figure 3.6: Surfactant adsorption isotherm used in KMAY7 history match.
Figure 3.7: Surfactant adsorption as a function of pH used for KMAY7 history match.
Figure 3.8: Polymer adsorption isotherm used in KMAY7 history match.
Figure 3.9: Microemulsion phase viscosity.
Figure 3.10: Polymer viscosity as a function of shear rate used for KMAY7 history match.
Figure 3.11: Effect of salinity on polymer viscosity.
Figure 3.12: History match of cumulative oil recovery for KMAY7 Berea coreflood during waterflood.
Figure 3.13: History match of pressure drop for KMAY7 Berea coreflood during waterflood.
Figure 3.14: Oil recovery and oil cut as a function of pore volumes injected (Type II(-)).
Figure 3.15: Total surfactant concentration as a function of pore volumes injected (Type II(-)).
Figure 3.16: Polymer concentration as a function of pore volumes injected (Type II(-)).
Figure 3.17: pH as a function of pore volumes injected (Type II(-)).

Figure 3.18: Surfactant and effective salinity as a function of pore volumes injected (Type II(-)).
Figure 3.19: Pressure drop as a function of pore volumes injected (Type II(-)).
Figure 3.20: Sodium ion concentration as a function of pore volumes injected (Type II(-)).
Figure 3.21: Magnesium ion concentration as a function of pore volumes injected (Type II(-)).
Figure 3.22: Calcium ion concentration as a function of pore volumes injected (Type II(-)).
Figure 3.23: Chloride ion concentration as a function of pore volumes injected (Type II(-)).
Figure 3.24: Profile of calcium carbonate at 0.31 pore volumes injected (Type II(-)).
Figure 3.25: Comparison of pH for different cation exchange capacity.
Figure 3.26: Phase behavior of surfactant for Type III.
Figure 3.27: Oil recovery and oil cut as a function of pore volumes injected (Type III).
Figure 3.28: Surfactant concentration as a function of pore volumes injected (Type III).
Figure 3.29: Polymer concentration as a function of pore volumes injected (Type III).
Figure 3.30: pH as a function of pore volumes injected (Type III).
Figure 3.31: Pressure drop as a function of pore volumes injected (Type III).
Figure 3.32: Surfactant and polymer concentration profiles at 0.3 pore volumes injected (Type III).
Figure 3.33: Surfactant and polymer concentration profiles at 1.05 pore volumes injected (Type III).
Figure 3.34: Phase behavior of surfactant used in salinity gradient design.
Figure 3.35: Effective salinity and surfactant concentration as a function of pore volumes injected.
Figure 3.36: Comparison of oil recovery between the result of UTCHEM simulation and laboratory data (Salinity gradient).
Figure 3.37: Comparison of oil cut between the result of UTCHEM simulation and laboratory data (Salinity gradient).
Figure 3.38: Surfactant concentration as a function of pore volumes injected (Salinity gradient).
Figure 3.39: Polymer concentration as a function of pore volumes injected (Salinity gradient).
Figure 3.40: Pressure drop as a function of pore volumes injected (Salinity gradient).
Figure 3.41: pH as a function of pore volumes injected (Salinity gradient).
Figure 3.42: Comparison of the simulation results of oil recovery and oil cut with experimental data for KMAY5.
Figure 3.43: Surfactant concentration and salinity as a function of pore volumes injected (KMAY5).
Figure 3.44: Type II(-) phase behavior used for KMAY5 coreflood history match.
Figure 3.45: Microemulsion phase viscosity.
Figure 3.46: Capillary desaturation curves used for KMAY5 coreflood history match.
Figure 3.47: Interfacial tension for oil/microemulsion used for KMAY5 coreflood history match.
Figure 3.48: Oil recovery and oil cut as for the reservoir core (based on KMAY7 input parameters).
Figure 3.49: Pressure drop for reservoir core (based on KMAY7 input parameters).
Figure 3.50: Oil recovery and oil cut for reservoir core using Type II(-) phase behavior.
Figure 3.51: Pressure drop for reservoir core using Type II(-) phase behavior.
Figure 3.52: Permeability field for Layers 1 and 2.
Figure 3.53: Permeability field for Layers 3 and 4.
Figure 3.54: Permeability field for Layer 5.
Figure 3.55: Oil saturation field overlaid by porosity contour for Layer 1.
Figure 3.56: Oil saturation field overlaid by porosity contour for Layers 2 and 3.
Figure 3.57: Oil saturation field overlaid by porosity contour for Layers 4 and 5.
Figure 3.58: Initial pressure distribution for Layers 1 and 2.
Figure 3.59: Initial pressure distribution for Layers 3 and 4.
Figure 3.60: Initial pressure distribution for Layer 5.
Figure 3.61: Schematic of simulation grid and ell locations used in ASP pilot simulations.
Figure 3.62: Tracer response curve for Well No. 1 (uniform Pwf).
Figure 3.63: Tracer response curves for Well No. 2 (uniform Pwf).

Figure 3.64: Tracer response curve for Well No. 3 (uniform Pwf).
Figure 3.65: Tracer response curves for Well No. 6 (uniform Pwf).
Figure 3.66: Tracer response curves for Well No. 7 (uniform Pwf).
Figure 3.67: Tracer response curves for Well No. 8 (uniform Pwf).
Figure 3.68: Tracer response curve for Well No. 11 (uniform Pwf).
Figure 3.69: Tracer response curves for Well No. 12 (uniform Pwf).
Figure 3.70: Tracer response curve for Well No. 13 (uniform Pwf).
Figure 3.71: History of production rate as a function of pore volumes injected (uniform Pwf).
Figure 3.72: Tracer response curve for Well No. 1 (optimized Pwf).
Figure 3.73: Tracer response curves for Well No. 2 (optimized Pwf).
Figure 3.74: Tracer response curve for Well No. 3 (optimized Pwf).
Figure 3.75: Tracer response curves for Well No. 6 (optimized Pwf).
Figure 3.76: Tracer response curves for Well No. 7 (optimized Pwf).
Figure 3.77: Tracer response curves for Well No. 8 (optimized Pwf).
Figure 3.78: Tracer response curve for Well No. 11 (optimized Pwf).
Figure 3.79: Tracer response curves for Well No. 12 (optimized Pwf).
Figure 3.80: Tracer response curve for Well No. 13 (optimized Pwf).
Figure 3.81: History of production rates for all producers as a function of pore volumes injected (optimum bottomhole pressure).
Figure 3.82: Sweep pore volumes for each producer (optimized Pwf).
Figure 3.83: Oil recovery for water flooding, polymer flooding, AP flooding, and ASP flooding.
Figure 3.84: Oil recovery for water flooding, polymer flooding, and AP flooding for high polymer adsorption.
Figure 3.85: Oil recovery for water flooding, polymer flooding, AP flooding, and ASP flooding (Series II).
Figure 3.86: Oil recovery and oil cut as a function of time (Base Case).
Figure 3.87: Oil production rate as a function of time (Base Case).
Figure 3.88: Distribution of oil concentration of 0.1 iso-surface for base case.
Figure 3.89: Distribution of water concentration of 0.9 iso-surface for Base case.
Figure 3.90: Distribution of surfactant concentration of 0.002 iso-surface for base case.
Figure 3.91: Distribution of polymer concentration of 0.025 iso-surface for base case.
Figure 3.92: Distribution of pH of 10 iso-surface for base case.
Figure 3.96: Injection scheme for each enhanced oil recovery process.
Figure 3.97: Comparison of oil recovery for different enhanced oil recovery processes for Reservoir D.
Figure 3.98: Cumulative oil recovery as a function of amount of injected surfactant.
Figure 3.99: Comparison of oil recovery between dilute ASP slug and Base Case simulations.
Figure 3.100: Distribution of surfactant concentration of 0.2 vol.% iso-surface for dilute surfactant slug size case.
Figure 3.101: Distribution of surfactant concentrations of 0.9 iso-surface for Base Case and dilute surfactant slug size case.
Figure 3.102: Effect of phase behavior on the oil recovery.
Figure 3.103: Distributions of water concentration of 0.9 iso-surface for Type III Case.
Figure 3.104: Comparison of oil recovery between low chemical adsorption and Base Case.
Figure 3.105: Distributions of surfactant concentration of 0.2 vol% iso-surface for low chemical adsorption case.
Figure 3.106: Comparison of oil recovery between large polymer drive and Base Case.
Figure 3.107: Distributions of oil concentration of 0.1 iso-surface for enlarged polymer drive case.
Figure 3.108: Distributions of water concentration of 0.9 iso-surface for enlarged polymer drive case.
Figure 3.109: Oil and water relative permeabilities at low capillary number.

Figure 3.110: Relative permeability curves at high capillary number used for reservoir coreflood history match.
Figure 3.111: Phase behavior diagram used for reservoir coreflood history match.
Figure 3.112: Interfacial tension vs. solubilization ratio used for reservoir coreflood history match.
Figure 3.113: Surfactant adsorption isotherm used for reservoir coreflood history match.
Figure 3.114: Polymer adsorption isotherm used for reservoir coreflood history match.
Figure 3.115: Cumulative oil recovery and oil cut as a function of time for ASP field study based on reservoir core flooding data.
Figure 3.116: Comparison of oil recovery for different injection surfactant concentration.

TASK 2. OPTIMIZATION OF SURFACTANT FLOODING
Part II: Economic Analysis

Figure 2.1: Methodology used to determine constant dollar after-tax cash flows.
Figure 2.2: Posted prices for WTI (1925-1993).
Figure 2.3: Index of equipping costs for oil fields in the U.S.
Figure 2.4: Index of operating costs for oil fields in the U.S.
Figure 2.5: Definition of economic limit and investment efficiency.
Figure 3.1: Oil production and recovery efficiency versus time for the Case 1 surfactant flood.
Figure 3.2: Oil production and recovery efficiency versus pore volumes injected for the Case 1 surfactant flood.
Figure 3.3: The full forty-acre five-spot pattern used in the economic analysis of the Case 1 surfactant flood.
Figure 3.4: Cumulative DCF versus time for the Case 1 surfactant flood.
Figure 3.5: Cumulative DCF versus pore volumes injected for the Case 1 surfactant flood.
Figure 3.6: Oil production and recovery efficiency versus time for the Case 2 surfactant flood.
Figure 3.7: Oil production and recovery efficiency versus pore volumes injected for the Case 2 surfactant flood.
Figure 3.8: Cumulative DCF versus time for the Case 2 surfactant flood.
Figure 3.9: Cumulative DCF versus pore volumes injected for the Case 2 surfactant flood.
Figure 4.1: Recovery efficiency versus amount of surfactant injected with a polymer concentration of 1000 ppm.
Figure 4.2: Recovery efficiency versus amount of surfactant injected with a polymer concentration of 1500 ppm.
Figure 4.3: Recovery efficiency versus amount of surfactant injected with a polymer concentration of 2000 ppm.
Figure 4.4: Recovery efficiency versus amount of surfactant injected with a polymer concentration of 2500 ppm.
Figure 4.5: Recovery efficiency versus amount of surfactant injected with a polymer concentration of 3000 ppm.
Figure 4.6: Recovery efficiency versus amount of polymer injected with a surfactant concentration of 0.05 vol. %.
Figure 4.7: Recovery efficiency versus amount of polymer injected with a surfactant concentration of 0.10 vol. %.
Figure 4.8: Recovery efficiency versus amount of polymer injected with a surfactant concentration of 0.25 vol. %.
Figure 4.9: Recovery efficiency versus amount of polymer injected with a surfactant concentration of 0.50 vol. %.
Figure 4.10: Optimization of chemical slug size and surfactant concentration with a polymer concentration of 1000 ppm and an oil price of $18/bbl.
Figure 4.11: Optimization of chemical slug size and surfactant concentration with a polymer concentration of 1500 ppm and an oil price of $18/bbl.

Figure 4.12: Optimization of chemical slug size and surfactant concentration with a polymer concentration of 2000 ppm and an oil price of $18/bbl.
Figure 4.13: Optimization of chemical slug size and surfactant concentration with a polymer concentration of 2500 ppm and an oil price of $18/bbl.
Figure 4.14: Optimization of chemical slug size and surfactant concentration with a polymer concentration of 3000 ppm and an oil price of $18/bbl.
Figure 4.15: Optimization of chemical slug size and polymer concentration with a surfactant concentration of 0.05 vol. % and an oil price of $18/bbl.
Figure 4.16: Optimization of chemical slug size and polymer concentration with a surfactant concentration of 0.10 vol. % and an oil price of $18/bbl.
Figure 4.17: Optimization of chemical slug size and polymer concentration with a surfactant concentration of 0.25 vol. % and an oil price of $18/bbl.
Figure 4.18: Optimization of chemical slug size and polymer concentration with a surfactant concentration of 0.50 vol. % and an oil price of $18/bbl.
Figure 4.19: Optimization of polymer concentration at the optimum chemical slug size and surfactant concentration.
Figure 4.20: Optimization of surfactant concentration at the optimum chemical slug size and polymer concentration.
Figure 4.21: Oil production rate and recovery efficiency versus time for the optimum surfactant flooding design.
Figure 4.22: Oil production rate and recovery efficiency versus pore volumes injected for the optimum surfactant flooding design.
Figure 4.23: Cumulative DCF versus time for the optimum surfactant flooding design.
Figure 4.24: Optimization of surfactant injected at the economic limit with a polymer concentration of 2000 ppm.
Figure 4.25: Recovery efficiency versus pore volumes injected for two designs with similar amounts of surfactant injected.
Figure 4.26: Oil production rate versus pore volumes injected for two designs with similar amounts of surfactant injected.
Figure 4.27: Produced surfactant concentrations versus pore volumes injected for two designs with similar amounts of surfactant injected.
Figure 4.28: Cumulative DCF versus pore volumes injected for two designs with similar amounts of surfactant injected.
Figure 4.29: Optimization of chemical slug size and surfactant concentration with a polymer concentration of 1000 ppm and an oil price of $35/bbl.
Figure 4.30: Optimization of chemical slug size and surfactant concentration with a polymer concentration of 1500 ppm and an oil price of $35/bbl.
Figure 4.31: Optimization of chemical slug size and surfactant concentration with a polymer concentration of 2000 ppm and an oil price of $35/bbl.
Figure 4.32: Optimization of chemical slug size and surfactant concentration with a polymer concentration of 2500 ppm and an oil price of $35/bbl.
Figure 4.33: Optimization of chemical slug size and surfactant concentration with a polymer concentration of 3000 ppm and an oil price of $35/bbl.
Figure 4.34: Optimization of chemical slug size and polymer concentration with a surfactant concentration of 0.05 vol. % and an oil price of $35/bbl.
Figure 4.35: Optimization of chemical slug size and polymer concentration with a surfactant concentration of 0.10 vol. % and an oil price of $35/bbl.
Figure 4.36: Optimization of chemical slug size and polymer concentration with a surfactant concentration of 0.25 vol. % and an oil price of $35/bbl.
Figure 4.37: Optimization of chemical slug size and polymer concentration with a surfactant concentration of 0.50 vol. % and an oil price of $35/bbl.
Figure 4.38: Optimization of polymer concentration using investment efficiency and NPV at an oil price of $18/bbl.

Figure 4.39: Optimization of surfactant concentration using investment efficiency and NPV at an oil price of $18/bbl.
Figure 4.40: Optimization of polymer concentration using GROR and IRR at an oil price of $18/bbl.
Figure 4.41: Optimization of surfactant concentration using GROR and IRR at an oil price of $18/bbl.
Figure 4.42: Optimization of polymer concentration using investment efficiency and NPV at an oil price of $35/bbl.
Figure 4.43: Optimization of surfactant concentration using investment efficiency and NPV at an oil price of $35/bbl.
Figure 4.44: Optimization of polymer concentration using GROR and IRR at an oil price of $35/bbl.
Figure 4.45: Optimization of surfactant concentration using GROR and IRR at an oil price of $35/bbl.
Figure 5.1: Spider diagram for the optimum design using investment efficiency as the profitability measure.
Figure 5.2: Spider diagram for the optimum design using NPV as the profitability measure.
Figure 5.3: Spider diagram for the optimum design IRR as the profitability measure.
Figure 5.4: Spider diagram for the operating cost components.
Figure 5.5: Sensitivity of investment efficiency to oil price.
Figure 5.6: Various oil price forecasts (1995-2010).
Figure 5.7: Sensitivity of investment efficiency to real discount rate using various oil price forecasts.
Figure 5.8: Sensitivity of investment efficiency to surfactant and polymer price.
Figure 5.9: Sensitivity of investment efficiency to facilities and equipment cost.
Figure 5.10: Comparing the cumulative DCF versus time for an independent producer to an integrated producer.
Figure 5.11: Economic risk analysis using Monte Carlo simulation.
Figure 5.12: Oil price probability distribution used in the Monte Carlo simulation.
Figure 5.13: Polymer price probability distribution used in the Monte Carlo simulation.
Figure 5.14: Waterflood operating cost probability distribution used in the Monte Carlo simulation.
Figure 5.15: Chemical slug injection operating cost probability distribution used in the Monte Carlo simulation.
Figure 5.16: Facilities and equipment cost probability distribution used in the Monte Carlo simulation.
Figure 5.17: Examples of oil price forecasts from the Monte Carlo simulation.
Figure 5.18: Oil price forecast generated using Monte Carlo simulation showing the mean and confidence bands.
Figure 5.19: Cumulative DCF generated using Monte Carlo simulation showing the mean and confidence bands.
Figure 5.20: NPV distribution generated using Monte Carlo simulation.
Figure 5.21: Investment efficiency distribution generated using Monte Carlo simulation.
Figure 5.22: IRR distribution generated using Monte Carlo simulation.
Figure 5.23: GROR distribution generated using Monte Carlo simulation.

DEVELOPMENT OF COST-EFFECTIVE SURFACTANT FLOODING TECHNOLOGY

ABSTRACT

Task 1 of this research was the development of a high-resolution, fully implicit, finite-difference, multiphase, multicomponent, compositional simulator for chemical flooding. The major physical phenomena modeled in this simulator are dispersion, heterogeneous permeability and porosity, adsorption, interfacial tension, relative permeability and capillary desaturation, compositional phase viscosity, compositional phase density and gravity effects, capillary pressure, and aqueous-oleic-microemulsion phase behavior. Polymer and its non-Newtonian rheology properties include shear-thinning viscosity, permeability reduction, inaccessible pore volume, and adsorption. Options of constant or variable space grids and time steps, constant-pressure or constant-rate well conditions, horizontal and vertical wells, and multiple slug injections are also available in the simulator.

The solution scheme used in this simulator is fully implicit. The pressure equation and the mass-conservation equations are solved simultaneously for the aqueous-phase pressure and the total concentrations of each component. A third-order-in-space, second-order-in-time finite-difference method and a new total-variation-diminishing (TVD) third-order flux limiter are used that greatly reduce numerical dispersion effects. This latest numerical advance is a significant advantage over other reservoir simulation codes of all types that use one- and two-point upstream weighting, which is the industry standard despite its well-known and significant numerical inaccuracy. The pressures in nonaqueous phases are obtained from the capillary pressures, and the phase concentrations and saturations are obtained by flash calculations from the total concentrations.

The simulator has been verified by the good agreement between numerical results and analytical solutions. The simulation results for different chemical processes were also compared with the results using standard numerical approaches or using our existing high-resolution IMPES simulator. These comparisons check the correctness of the mathematical formulation, the finite-difference scheme, the physical property models, well models, spatial gridding and timestepping schemes, and the program coding. These comparisons also demonstrate the merit of our high-resolution fully implicit numerical method over standard numerical approaches and the computational efficiency over the IMPES simulator for problems with severe stability restrictions.

Task 2 of this research was the Optimization of Surfactant Flooding. We report on field scale simulations of various chemical processes and mechanisms in the first part of Task 2. UTCHEM was used to simulate surfactant/polymer flooding of three reservoirs representative of low, moderate, and high heterogeneous permeability distributions. Several factors such as the amount of chemicals, chemical adsorption, cation exchange, salinity gradient design, temperature effects on surfactant phase behavior, and low tension polymer injection scheme were studied in detail. The use of horizontal wells played an important role in the optimization of these chemical floods since the project time must be reduced to less than ten years to have any chance of economic success even when using high-efficiency surfactants as done here.

In a fourth reservoir study, we investigated alkaline/surfactant/polymer (ASP) flooding for a pilot with an inverted five-spot pattern and a total of 13 wells. This is the first time field-scale alkaline/surfactant/polymer flooding simulations with detailed reaction chemistry have been done. A tracer test simulation was used to optimize the injection and production rates of each well. A comparison of different improved oil recovery processes such as water, polymer, alkaline/polymer, surfactant/polymer, and alkaline/surfactant/polymer flooding was made. A series of sensitivity simulations was performed to evaluate the optimum design for the pilot.

We report on a detailed economic analysis of a surfactant/polymer flood of a typical U.S. onshore light-oil reservoir in the second part of Task 2. The main challenge of chemical flooding

at prevailing low oil prices is to reduce the cost. The UTCHEM simulation results were used with an economic model to optimize the design of a chemical flood. The optimum design consisted of a large chemical slug with a low surfactant concentration and a high polymer concentration and the use of a horizontal producer. The optimization process was found to be dependent on the profitability measure used. Investment efficiency was the preferred profitability measure and is recommended for evaluating and optimizing chemical flooding projects. The original chemical flood design was unprofitable at $18 per barrel of oil even when very favorable surfactant properties characteristic of the best available high-efficiency surfactants were used. However, after optimization the chemical flood of this particular light-oil reservoir was profitable even at this low oil price. Sensitivity analysis was used to determine the strategic economic variables for the optimum design and they were, in order of importance, oil price, polymer price, discount rate, and operating cost. Monte Carlo simulation was demonstrated as a technique to quantify the economic risk in the optimum surfactant flood design.

EXECUTIVE SUMMARY

The objective of this research was to develop cost-effective surfactant flooding technology by using surfactant simulation studies to evaluate and optimize alternative design strategies taking into account reservoir characteristics, process chemistry, and process design options such as horizontal wells.

Task 1 of this research was the development of a high-resolution, fully implicit, finite-difference, multiphase, multicomponent, compositional simulator for chemical flooding. The major physical phenomena modeled in this simulator are dispersion, heterogeneous permeability and porosity, adsorption, interfacial tension, relative permeability and capillary desaturation, compositional phase viscosity, compositional phase density and gravity effects, capillary pressure, and aqueous-oleic-microemulsion phase behavior. Polymer and its non-Newtonian rheology properties include shear-thinning viscosity, permeability reduction, inaccessible pore volume, and adsorption. Options of constant or variable space grids and time steps, constant-pressure or constant-rate well conditions, horizontal and vertical wells, and multiple slug injections are also available in the simulator.

The solution scheme used in this simulator is fully implicit. The pressure equation and the mass-conservation equations are solved simultaneously for the aqueous-phase pressure and the total concentrations of each component. A third-order-in-space, second-order-in-time finite-difference method and a new total-variation-diminishing (TVD) third-order flux limiter are used that greatly reduce numerical dispersion effects. This latest numerical advance is a significant advantage over other reservoir simulation codes of all types that use one- and two-point upstream weighting, which is the industry standard despite its well-known and significant numerical inaccuracy. The pressures in nonaqueous phases are obtained from the capillary pressures, and the phase concentrations and saturations are obtained by flash calculations from the total concentrations.

The simulator has been verified by the good agreement between numerical results and analytical solutions. The simulation results for different chemical processes were also compared with the results using standard numerical approaches or using our existing high-resolution IMPES simulator. These comparisons check the correctness of the mathematical formulation, the finite-difference scheme, the physical property models, well models, spatial gridding and timestepping schemes, and the program coding. These comparisons also demonstrate the merit of our high-resolution fully implicit numerical method over standard numerical approaches and the computational efficiency over the IMPES simulator for problems with severe stability restrictions.

Task 2 of this research was the Optimization of Surfactant Flooding. UTCHEM was used to simulate surfactant/polymr flooding simulations performed under Task 2. UTCHEM development has continued and several significant improvements have been made in the code during the past year. These improvements have the combined effect of making the code more versatile and efficient, which serves not only our needs better but those of a large number of external users. These users consist of not only the industrial sponsors of our enhanced oil recovery research at The University of Texas at Austin, but also a large and increasing number of academic users who use our code in a variety of oil recovery research. These users now include the following organizations:

ADREF
Amoco Production Co.
ARAMCO
Arco Oil & Gas Co.
BP Exploration, Inc.
California State University, Long Beach
Chevron Oil Field Research Co.
Clemson University
Conoco, Inc.
Cray Research
Pacific Northwest Laboratories
PETROBRAS
Petronas
Prairie View A&M
Rice University
Rogaland Research Institute
Sandia National Laboratories
Santa Fe Energy Resources
Schlumberger Well Services
Scientific Computing Associates, Inc.

DOE
Duke University
Elf Aquitaine
EPA
Exxon Production Research Company
Idaho National Engineering Laboratories (EG&G)
Institute for Energy Technology
INTERA, Inc.
INTEVEP, S.A.
Japan National Oil Corp.
Japan Petroleum Exploration Co., Ltd.
Kerr Laboratories
Kuwait University
Louisiana State University
Marathon Oil Company
Michigan Tech
Mobil Exploration and Producing Services
New Mexico Petroleum Recovery Research Center
Norsk Hydro
Oryx Energy Co.
Oxy USA, Inc.
Shell Development Co.
Shengli Geological Research Institute
Stanford University
Statoil
Technical University of Clausthal, Germany
Technical University of Denmark
Texaco, Inc.
Texas A&M University
Union Pacific Resources
Université Laval (Quebec, Canada)
University of Buenos Aires
University of Florida
University of Kansas
University of Michigan
University of Mining and Metallurgy - Poland
University of Oklahoma
University of São Paulo
University of Wyoming
UNOCAL
Xinjiang Research Institute of Exploration and Development

A significant effort is required to provide the code and its documentation to these users as well as some support on its use. However, we do benefit from feedback from these users and occasionally even add new features to the code. In addition to these application users, we also have a major collaborative research effort with Professors Mary Wheeler, Clint Dawson and Todd Arbogast to port UTCHEM to massively parallel computers as well as to develop new algorithms for future use. This research is sponsored by the High Performance Computing and Communications program of the federal government. This research is targeted at the use of massively parallel computers to solve Grand Challenge problems, which in our case means flow in permeable media problems with applications to both oil recovery and groundwater remediation. Some of our most recent UTCHEM development targeted to contaminant cleanup is sponsored by the Environmental Protection Agency. This effort includes such things as the addition of local mesh refinement, which will be very valuable to all of our applications. Thus, there is a large leverage on the research funds provided by this grant, among other benefits to this related activity.

The potential of improving surfactant flooding using horizontal wells has been systematically investigated. The potential for horizontal wells to accelerate the oil production and thus improve the discounted cash flow may seem obvious, but the precise improvement depends on many complex factors such as vertical permeability ratio and can only be assessed using realistic simulations. We performed the simulations for several reservoir descriptions including layered and stochastic. The location of the horizontal well is very important with respect to both the sweep efficiency and injectivity and must be in a good location to produce the desired results. The vertical permeability must be moderate to high for horizontal wells to give good results, although vertical drainholes off the horizontal injector can potentially give good results even for low vertical permeability. The combination of vertical producer and horizontal injector, under some conditions, does appear to have economic merit. However, these conditions are clear only after a careful study with realistic reservoir and process descriptions. These results were discussed in the previous reports.

We report on field scale simulations of various chemical processes and mechanisms in the first part of Task 2. UTCHEM was used to simulate surfactant/polymer flooding of three reservoirs representative of low, moderate, and high heterogeneous permeability distributions. Several factors such as the amount of chemicals, chemical adsorption, cation exchange, salinity gradient design, temperature effects on surfactant phase behavior, and low tension polymer injection scheme were studied in detail. The use of horizontal wells played an important role in the

optimization of these chemical floods since the project time must be reduced to less than ten years to have any chance of economic success even when using high-efficiency surfactants as done here.

In an attempt to include more realistic rock and fluid properties in the evaluation of surfactant flooding in different reservoir descriptions with properties suitable for surfactant flooding, we used permeability-dependent waterflood residual oil saturation rather than uniform residual saturations. Several permeability-residual oil saturation correlations were used. The simulation results for the three reservoirs studied here indicate that the tertiary oil recovered is more sensitive to the amount of target oil at the time of chemical flood than to the distribution of the oil saturation.

To evaluate the potential of improving the cost effectiveness of surfactant flooding, we performed, for the first time, low-tension polymerflood (LTPF) simulations taking into account competitive surfactant and polymer adsorption. These results indicate that the oil recovery is still good for the small amount of chemical used. The results might be too optimistic and are shown here only to illustrate the trend. The actual results will depend on the specific adsorption isotherms for the reservoir formation, surfactant and polymer solutions, and many other factors.

In a fourth reservoir study, we investigated alkaline/surfactant/polymer (ASP) flooding for a pilot with an inverted five-spot pattern and a total of 13 wells. This is the first time field-scale alkaline/surfactant/polymer flooding simulations with detailed reaction chemistry have been done. A tracer test simulation was used to optimize the injection and production rates of each well. A comparison of different improved oil recovery processes such as water, polymer, alkaline/polymer, surfactant/polymer, and alkaline/surfactant/polymer flooding was made. A series of sensitivity simulations was performed to evaluate the optimum design for the pilot.

We report on a detailed economic analysis of a surfactant/polymer flood of a typical U.S. onshore light-oil reservoir in the second part of Task 2. The main challenge of chemical flooding at prevailing low oil prices is to reduce the cost. The UTCHEM surfactant/polymer flood simulation results were used with an economic model to optimize the design of a chemical flood. The optimum design consisted of a large chemical slug with a low surfactant concentration and a high polymer concentration and the use of a horizontal producer. The optimization process was found to be dependent on the profitability measure used. Investment efficiency was the preferred profitability measure and is recommended for evaluating and optimizing chemical flooding projects. The original chemical flood design was unprofitable at $18 per barrel of oil even when very favorable surfactant properties characteristic of the best available high-efficiency surfactants were used. However, after optimization the chemical flood of this particular light-oil reservoir was profitable even at this low oil price. Sensitivity analysis was used to determine the strategic economic variables for the optimum design and they were, in order of importance, oil price, polymer price, discount rate, and operating cost. Monte Carlo simulation was demonstrated as a technique to quantify the economic risk in the optimum surfactant flood design.

UTCHEM Modeling Enhancements

UTCHEM development has continued and several significant improvements have been made in the code during the course of this research project. These improvements have the combined effect of making the code more versatile and efficient, which better serves not only our needs but those of a large number of external users in both petroleum, subsurface, and environmental engineering. The enhancements in UTCHEM include the following:

- A single-level adaptive grid refinement. The implementation strategy for grid refinement is based on domain decomposition where each zone is treated independently.
- 2-D cross-sectional curvilinear grid option.
- A dual porosity formulation to model tracer transport in fractured media.

- An option to calculate the interfacial tension between microemulsion/oil and microemulsion/brine using Chun Huh relationship. The only option previously available was based on Healy and Reed.
- Temperature-dependent surfactant phase behavior. Both the height of the binodal curve and the effective salinity are shifted to model the shift in surfactant/oil/water phase behavior with temperature.
- The component numbering scheme presently in UTCHEM has been changed to allow additional aqueous species.
- Options of chromium malonate gel and silicate gel systems for the application of in-depth gel treatment in addition to the previous option of polymer/chromium chloride gel.
- Allow for competitive surfactant adsorption in the presence of polymer. This option was added to adequately simulate the low tension polymer flooding. The surfactant adsorption model was modified such that the adsorbed surfactant concentration is reduced as a function of polymer concentration.
- Microbiological population model.
- Multiple reactive tracers.
- Reversible oil adsorption.
- Permeability-dependent surfactant and polymer adsorption model.
- Addition of gas tracers and an option for nonequilibrium mass transfer of gas tracers.
- An option to calculate up to three-phase hysteretic capillary-pressure and relative permeability functions using van Genuchten and Parker *et al.* models. The three phases are either oil/water/gas or three liquid phases of water/microemulsion/oil in the presence of surfactant. Both capillary-pressure and relative-permeability models are functions of capillary number.
- Allow for a compositional oleic phase and property models for the oil mixture: for example, surfactant phase behavior, viscosity, and density for organic mixtures.

TASK 1. HIGH-RESOLUTION, FULLY IMPLICIT, COMPOSITIONAL SIMULATION

1. Introduction

Enhanced oil recovery (EOR) is defined as any process that yields additional oil beyond that which a reservoir is able to produce because of its own natural energy (Willhite, 1986). This additional oil is recovered by injecting materials not normally present in the reservoir (Lake, 1989). The processes are combinations of various physical and chemical phenomena. The fluids consist of numerous components and phases with a wide variety of properties, and the porous media are composed of different types of architectural heterogeneities. Conventional simulation techniques are under great challenges to predict the performance of such complex processes.

Based on phase equilibrium, volume balance, Darcy's law, conservation of mass, and certain other assumptions, a mathematical model is derived incorporating all of the desired physical and pertinent flow phenomena. It is a system of highly coupled, time-dependent, nonlinear partial differential equations with associated initial and boundary conditions. Finding an analytical solution to this system of equations is in general impossible and a numerical solution must be pursued.

In order to obtain a realistic solution, many compositional models have been developed (Kazemi *et al.*, 1978; Pope and Nelson, 1978; Young and Stephenson, 1983; Datta Gupta *et al.*, 1986; Scott *et al.*, 1987). Compositional simulators model the flow of multiphase fluids consisting of mixtures of chemical components. The material-balance equations are best formulated with the component concentrations as the primary unknowns. The description of phase behavior leads to a highly nonlinear model. As computers become less expensive and more powerful and as the economic production of hydrocarbons becomes more complicated, compositional simulators are used more often. One of such simulators is UTCHEM, which has been developed at The University of Texas at Austin for simulating chemical flooding and has been widely used for various other applications for years (Saad, 1989; Delshad *et al.*, 1996).

The basic flow equations in the model include a parabolic pressure equation with a hyperbolic system of species equations. The accuracy of the numerical approximation and the computational efficiency are highly dependent on the techniques for solving these two kinds of partial differential equations. Finite-difference methods for parabolic equations have been analyzed and understood for a number of years (Richtmyer and Morton, 1977). With the use of parabolic equations in connection with conservation laws in reservoir simulation, additional features have emerged in both mathematical structure and numerical treatment that need to be studied (Trangenstein, 1986). Various finite-difference methods have been applied for the hyperbolic conservation laws (Peaceman, 1977; Le Veque, 1990; Celia and Gray, 1992). There are special difficulties associated with solving these systems that are not seen elsewhere and must be dealt with carefully in developing numerical methods. Standard finite-difference methods may work well for smooth solutions but can give disastrous results when discontinuities, which are common in the concentration fronts of many EOR processes, are present. Lower-order numerical methods have a large amount of "numerical viscosity" that smoothes the solution in much the same way physical viscosity would, but to an extent that is unrealistic by several orders of magnitude (Lantz, 1971; Fanchi, 1983). Higher-order methods such as Leonard's method (1979) are good in their higher-order accuracies and numerical smearing reduction effects but are plagued by numerical oscillations near fronts or overshoots caused by an additional monotonicity constraint (Patel *et al.*, 1985). In order to assure convergence to the correct physical solution of the conservation law, numerical methods should possess the following features: (1) high-order accuracy for smooth solutions and in smooth regions of a solution even when discontinuities are present elsewhere, (2) sharp resolution of discontinuities without excessive smearing, (3) the absence of spurious oscillations in the computed solution, (4) an appropriate form of consistency with the weak form of

the conservation law, and (5) nonlinear stability bounds that, together with consistency, guarantee convergence as the grid is refined. Methods with the accuracy and resolution properties indicated are often referred to as high-resolution methods (Le Veque, 1990). Typically, these methods require computation of an approximation to the solution with an infinitesimal amount of additional numerical diffusion and without the excessive smearing of sharp fronts. The two requirements need to be carefully balanced. For many methods, it is possible to show that the total variation of the solution is nonincreasing with time. This is enough to obtain some convergence results and also guarantees that spurious oscillations are not generated. Methods with this property are called total variation diminishing (TVD) methods. Using this requirement as a design tool has led to the development of many good numerical methods (Harten, 1983; Sweby, 1984; Roe, 1984; Yee, 1987; Le Veque, 1990). Our goal is to develop a numerical method having the desired high-resolution properties. The method should be computationally efficient such that increased accuracy in the resolution of sharp fronts is obtained less expensively with this method than by increased grid refinement with a more diffusive scheme. In recent years, we have studied the possibility of imposing high-order TVD flux limiting on the high-order flux functions to achieve a high-resolution scheme and apply the scheme to the system of partial differential equations. The scheme now has been used in our multidimensional, multicomponent, multiphase, finite-difference, IMPES-type compositional simulator UTCHEM for years, and a variety of simulation results of enhanced oil recovery (EOR) processes have shown that this scheme gives convergent, high-order, accurate results (Liu *et al.*, 1994).

The use of fully implicit versus IMPES methods is another issue in reservoir simulation (Aziz and Settari, 1979). With an IMPES method, an implicit method is selected for the pressure equation and an explicit method for the conservation law. With a fully implicit method, the entire system of flow equations is solved simultaneously, often through nonlinear iterations. For parabolic problems, the solution of the equations depends on the initial data throughout the entire computational domain. This leads to stability restrictions that require much smaller timestep sizes than those typically required for accuracy. As a result, implicit methods need to be used to avoid severe stability restrictions on timestep sizes. For a hyperbolic problem, there is a fundamental difference in the amount of numerical dispersion added by explicit and implicit methods. For explicit methods, smaller timestep sizes lead to increased numerical diffusion. Source of instability besides a Courant stability criterion for the explicitly updating step is in the pressure equation when the mobility terms contain a pressure dependence that is time-lagged. This instability can arise from simulating some EOR processes, such as shear-dependent viscosities in polymer flooding or the capillary-number dependence of relative permeabilities in surfactant flooding (Foulser and Goodyear, 1989). These factors lead to small timestep sizes for IMPES methods. On the other hand, standard implicit methods are more diffusive as their timestep sizes are increased. The degree of implicitness required to obtain stable solutions is problem-dependent, and both computational efficiency and accuracy are factors that need to be considered in practical reservoir simulations. The method produces a set of nonlinear algebraic equations and the system is solved using iteration (Au *et al.*, 1980). The solution of the associated Jacobian system becomes the most computationally intensive portion of the simulation. In order to take large timestep sizes, it is necessary to solve the nonlinear equations accurately. This increases the computational cost of nonlinear iterations. The standard fully implicit approaches usually adopt lower-order finite-difference schemes for both the temporal and spatial discretizations because of computational requirements, numerical oscillations associated with higher-order methods, and difficulties in the program coding and the implementation of the physical property models. The advantages of methods thus are overshadowed by the increased amount of numerical dispersion associated with large truncation errors of lower-order finite-difference schemes, which is especially detrimental to accurate field simulation and process design. This research attempts to improve the methods by employing a Crank-Nicolson scheme, which is second-order in time, along with our TVD high-order flux-limited scheme, which has already been proved to be successful in our IMPES simulator. The overall increase in accuracy through the use of the combination of these high-order schemes makes it possible to use large time and space grids without sacrificing accuracy and stability and to reduce computational cost.

In this report, we give a full description of the mathematical models in the simulator, including their basic assumptions, conservation equations, pressure equation, initial and boundary conditions, and physical property models. We also present our high-resolution finite-difference scheme, the construction of the Jacobian matrix corresponding to each physical property, flash calculation, and the fully implicit solution algorithms. Simulation results of various processes are then given to show the capabilities and numerical and computational features of the simulator.

2. Physical and Mathematical Model

2.1 General Description

A petroleum reservoir is a complicated mixture of porous rock, brine, and hydrocarbon fluids. Various physical effects, such as fluid viscosity, capillarity, adverse mobility ratio, rock heterogeneities, etc. conspire to inhibit the flow of fluids. Enhanced oil recovery processes generally involve the injection of fluids that alter the flow properties of the natural rock-fluid system in the reservoir. One major class of enhanced recovery techniques is chemical methods. The objectives of these methods vary depending on the chemical injected and the nature of the reservoir. One common chemical recovery technique is polymer flooding, which essentially amounts to waterflooding with water whose viscosity has been increased by the addition of a polymer. This tactic overcomes the adverse mobility ratio associated with many waterfloods. It can also help reduce the channeling effects caused by reservoir heterogeneities, thus increasing the volume of the reservoir swept by the injected water. Other types of chemical floods attempt to lower the interfacial tension between the resident oil and injected water, thus reducing the capillary effects that inhibit oil recovery. Among this latter class of chemical methods are surfactant flooding, in which the chemical injected directly lowers the interfacial tension between the oil and water.

The increase in the sophistication of enhanced oil recovery technologies has brought with it increased operating and material costs and therefore a greater demand for optimum process designs. Mathematical models of fluid flows in petroleum reservoirs have become key tools for engineers to develop and implement these designs. Using mathematical models together with accurate characterizations of the reservoir being modeled, the engineer can test various operating strategies, compare different recovery technologies, and formulate hypotheses in diagnosing the performance of ongoing projects. Improved computing technologies, including large-scale vector and parallel architectures, have also spurred the application of mathematical models by making simulations at realistic levels of resolution more feasible than ever before.

In an oil reservoir, molecular species can undergo transport within phases and exchange across phase boundaries. For example, many enhanced oil recovery processes rely on the effects of interphase mass transfer to alter fluid properties in ways that benefit oil production. The simulation of any of these phenomena requires a fully compositional formulation. For a mathematical model of chemical flooding processes, we simulate multiphase, multicomponent, three-dimensional flow in porous media. The basic governing equations consist of a mass-conservation equation for each component, an energy balance, Darcy's law generalized for multiphase flow, and an overall mass-conservation or continuity equation that determines the pressure. Various phenomena such as velocity-dependent dispersion, adsorption, chemical reactions, complex phase behavior, variable phase viscosities, and relative permeabilities are required to model chemical transport in oil reservoirs.

2.2 Basic Assumptions

The major assumptions used in the development of our mathematical model for chemical flooding processes are (Saad, 1989; Delshad *et al., 1996*)

- Solid phase is immobile.
- Fluids and rock are slightly compressible.
- Local thermodynamic equilibrium exists except for specified chemical reactions, *e.g.*, gelation of polymer, reacting tracers, and specified mass transfer of tracer components.
- Darcy's law applies (for non-Newtonian flow, apparent viscosity is used in Darcy's equation).
- Dispersion follows a generalization of Fick's law to multiphase flow in porous media.
- Ideal mixing holds (*i.e.*, volume changes on mixing are zero).

- Surfactant and polymer are treated as monospecies with no molecular weight distribution.
- Polymer, electrolytes, and tracers do not occupy any pore space.
- Fluid phase behavior is independent of the reservoir pressure.

Various other assumptions and detailed discussions of formulating specific physical models can be found in references (Pope and Nelson, 1978; Datta Gupta *et al.*, 1986; Camilleri *et al.*, 1987; Bhuyan *et al.*, 1988; Saad, 1989; Delshad *et al.*, 1996).

2.3 Mass Conservation Equations

With the slightly compressible flow assumptions, the mass-balance equation for component κ is (Saad, 1989; Delshad *et al.*, 1996)

$$\phi_R \frac{\partial}{\partial t}\left\{\tilde{C}_\kappa\left[1+\left(C_f + C_\kappa^0\right)\Delta P_R\right]\right\}$$

$$+\vec{\nabla}\bullet\left(1+C_\kappa^0\Delta P_R\right)\sum_{\ell=1}^{n_p}\left(C_{\kappa\ell}\vec{u}_\ell - \phi S_\ell \bar{\bar{K}}_{\kappa\ell}\bullet\vec{\nabla}C_{\kappa\ell}\right) = q_\kappa \qquad \kappa = 1, \ldots, n_c$$

The compressibility effects are functions of the pressure change ΔP, defined as

$$\Delta P = P_R - P_{R0}$$

where P_R is the pressure of a reference phase and P_{R0} is the pressure at which all compressibility reference values are defined. C_f is the pore volume compressibility and C_κ^0 is the compressibility of component κ. The overall concentration of each component κ is given by

$$\tilde{C}_\kappa = \left(1-\sum_{\kappa=1}^{n_{cv}}\hat{C}_\kappa\right)\sum_{\ell=1}^{n_p}S_\ell C_{\kappa\ell} + \hat{C}_\kappa$$

where n_{cv} is the number of volumetric components, $\hat{C}_\kappa$ is the volume of component κ adsorbed on the rock surface per unit pore volume, and $1-\sum_{\kappa=1}^{n_{cv}}\hat{C}_\kappa$ represents the reduction in pore volume because of adsorption.

Physical dispersion is modeled in a precise manner, using the full dispersion tensor. In a Cartesian coordinate system, it is given by

$$\bar{\bar{K}}_{\kappa\ell} = \begin{bmatrix} K_{xx\kappa\ell} & K_{xy\kappa\ell} & K_{xz\kappa\ell} \\ K_{yx\kappa\ell} & K_{yy\kappa\ell} & K_{yz\kappa\ell} \\ K_{zx\kappa\ell} & K_{zy\kappa\ell} & K_{zz\ell} \end{bmatrix}$$

The elements of the dispersion tensor for multiphase, multicomponent flow in permeable media including molecular diffusion are

$$K_{xx\kappa\ell} = \frac{D_{\kappa\ell}}{\tau} + \frac{\alpha_{L\ell}u_{x\ell}^2 + \alpha_{T\ell}\left(u_{y\ell}^2 + u_{z\ell}^2\right)}{\phi S_\ell |\vec{u}_\ell|}$$

$$K_{yy\kappa\ell} = \frac{D_{\kappa\ell}}{\tau} + \frac{\alpha_{L\ell} u_{y\ell}^2 + \alpha_{T\ell}\left(u_{z\ell}^2 + u_{x\ell}^2\right)}{\phi S_\ell |\vec{u}_\ell|}$$

$$K_{zz\kappa\ell} = \frac{D_{\kappa\ell}}{\tau} + \frac{\alpha_{L\ell} u_{z\ell}^2 + \alpha_{T\ell}\left(u_{x\ell}^2 + u_{y\ell}^2\right)}{\phi S_\ell |\vec{u}_\ell|}$$

$$K_{xy\kappa\ell} = K_{yx\kappa\ell} = \frac{u_{x\ell} u_{y\ell}\left(\alpha_{L\ell} - \alpha_{T\ell}\right)}{\phi S_\ell |\vec{u}_\ell|}$$

$$K_{yz\kappa\ell} = K_{zy\kappa\ell} = \frac{u_{y\ell} u_{z\ell}\left(\alpha_{L\ell} - \alpha_{T\ell}\right)}{\phi S_\ell |\vec{u}_\ell|}$$

$$K_{zx\kappa\ell} = K_{xz\kappa\ell} = \frac{u_{z\ell} u_{x\ell}\left(\alpha_{L\ell} - \alpha_{T\ell}\right)}{\phi S_\ell |\vec{u}_\ell|}$$

where

$$|\vec{u}_\ell| = \sqrt{u_{x\ell}^2 + u_{y\ell}^2 + u_{z\ell}^2}$$

The fluxes $u_{x\ell}$, $u_{y\ell}$, and $u_{z\ell}$, are modeled through the use of Darcy's law for multiphase flow through permeable media:

$$\vec{u}_\ell = -\bar{\bar{k}}\lambda_{r\ell}\left(\vec{\nabla}P_\ell - \gamma_\ell \vec{\nabla}D\right)$$

where $\bar{\bar{k}}$ is a diagonal permeability tensor.

We can also write the general conservation equations in the form

$$\phi_R \frac{\partial}{\partial t}\left\{\tilde{C}_\kappa\left[1 + \left(C_f + C_\kappa^0\right)\Delta P_R\right]\right\}$$

$$-\vec{\nabla}\bullet\left(1 + C_\kappa^0 \Delta P_R\right)\sum_{\ell=1}^{n_p}\left(C_{\kappa\ell}\bar{\bar{k}}\lambda_{r\ell}\bullet\left(\vec{\nabla}P_\ell - \gamma_\ell\vec{\nabla}D\right) + \phi S_\ell \bar{\bar{K}}_{\kappa\ell}\bullet\vec{\nabla}C_{\kappa\ell}\right) = q_\kappa$$

$$\kappa = 1, \ldots, n_c$$

2.4 Pressure Equation

The overall material balance equation is the summation of all volumetric component-conservation equations:

$$\phi_R C_t \frac{\partial P_R}{\partial t} + \vec{\nabla}\bullet\sum_{\ell=1}^{n_p}\vec{u}_\ell\bullet\left(1 + \Delta P_R\sum_{\kappa=1}^{n_{cv}} C_\kappa^0 C_{\kappa\ell}\right) = \sum_{\kappa=1}^{n_{cv}} q_\kappa$$

where C_t is the total compressibility defined as

$$C_t = C_f + \sum_{\kappa=1}^{n_{cv}} C_\kappa^0 \tilde{C}_\kappa$$

By substituting Darcy's law for the volumetric flux $\vec{u}_\ell$ and using the capillary pressure relations,

$$P_\ell = P_R + P_{c\ell R} \qquad \ell = 1, ..., n_p$$

the pressure equation is obtained in terms of the reference phase pressure P_R:

$$\phi_R C_t \frac{\partial P_R}{\partial t} - \vec{\nabla}\cdot\vec{\vec{k}}\cdot\lambda_{rTc}\vec{\nabla}P_R - \vec{\nabla}\cdot\vec{\vec{k}}\cdot\sum_{\ell=1}^{n_p}\left[\lambda_{r\ell c}\left(\vec{\nabla}P_{c\ell R} - \gamma_\ell\vec{\nabla}D\right)\right] = \sum_{\kappa=1}^{n_{cv}} q_\kappa$$

where

$$\lambda_{r\ell c} = \lambda_{r\ell}\left(1 + \Delta P_R \sum_{\kappa=1}^{n_{cv}} C_\kappa^0 C_{\kappa\ell}\right)$$

and

$$\lambda_{rTc} = \sum_{\ell=1}^{n_p}\lambda_{r\ell}\left(1 + \Delta P_R \sum_{\kappa=1}^{n_{cv}} C_\kappa^0 C_{\kappa\ell}\right)$$

The description and the derivation of the conservation equations and the pressure equation are given in detail in references (Saad, 1989; Delshad *et al.*, 1996).

2.5 Initial and Boundary Conditions

Problems involving the time dimension are always initial-value problems in time. The initial values of the concentration of each component must be specified at each point in the reservoir. For compressible flow cases, the initial pressure distributions are also required. The pressure equation is parabolic in nature and requires either the pressure or its normal derivative to be specified at each point on the boundary. The conservation equations have a hyperbolic element associated with the convective terms that requires that the composition of any fluid entering through the boundary be specified but requires no boundary condition on outflow boundaries, nor on any boundary through which no flow is allowed. Physical dispersion introduces a parabolic element to these equations and when present requires composition or its normal derivative to be specified on all boundaries through which dispersive flux is possible.

The basic boundary condition assumed in the model is no flow and no dispersive flux through all impermeable boundaries:

$$\vec{n} \bullet \vec{u}_\ell = 0$$

and

$$\vec{n} \bullet \vec{\vec{K}}_{\kappa\ell} \bullet \vec{\nabla} C_{\kappa\ell} = 0$$

where $\vec{n}$ is the unit vector normal to the boundary. The inflow and outflow conditions are specified as well conditions. For the inflow boundary, the normal component of the phase species flux must be known as a function of time. For flow in thermodynamic equilibrium, this condition can be imposed by specifying the total injection rate for each component or alternatively the overall composition and one pressure. For the outflow boundary, we require continuity of fluxes across

the reservoir wellbore interfaces and no physical dispersion within the wellbore (Lake *et al.*, 1984). The total flow rate or one pressure is specified and the capillary pressure is assumed to be zero in the wellbore.

2.6 Constitutive Relations

The basic governing equations are complemented by a number of constitutive relations that relate the number of phases present and their compositions, saturations, densities, viscosities, interfacial tensions, and capillary pressures to the overall component concentrations and pressure (Lake *et al.*, 1984). Further constitutive relations determine adsorption, residual saturation, and relative permeability.

A brief list of these relations is given here and the quantities appearing in brackets are the number of independent equations corresponding to each relation.

(1) Saturation constraint [1]

$$\sum_{\ell=1}^{n_p} S_\ell = 1$$

(2) Phase-concentration constraint [n_p]

$$\sum_{\kappa=1}^{n_{cv}} C_{\kappa\ell} = 1$$

(3) Total concentration definition [n_c]

$$C_\kappa = \sum_{\ell=1}^{n_p} C_{\kappa\ell} S_\ell$$

(4) The adsorption isotherms [n_c]

$$\hat{C}_\kappa = \hat{C}_\kappa\left(\bar{C}\right)$$

$\bar{C}$ is a vector with C_κ as its elements.

(5) Phase-equilibrium relations [$n_c(n_c-1)$]

$$f\left(\bar{\bar{C}}, \bar{C}\right) = 0$$

$\bar{\bar{C}}$ is a matrix with $C_{\kappa\ell}$ as its elements.

(6) Phase viscosities [n_p]

$$\mu_\ell = \mu_\ell\left(\bar{\bar{C}}, \bar{u}_\ell\right)$$

(7) Phase densities [n_p]

$$\rho_\ell = \rho_\ell\left(\bar{\bar{C}}, P_\ell\right)$$

(8) Relative permeabilities [n_p]

$$k_{r\ell} = k_{r\ell}\left(\bar{S}\right)$$

$\bar{S}$ is a vector with S_ℓ as its elements.

(9) Capillary pressure relations [n_p-1]

$$P_{c\ell i} = P_i - P_\ell$$

The conservation equations, the pressure equation, and the constitutive relations are the basic equations describing the isothermal, multicomponent, multiphase flow in permeable media. They result in $2n_c+ (5+n_c)n_p$ independent scalar equations equal to the number of dependent variables listed below.

(1) Total concentration of component κ, C_κ [n_c]
(2) Concentration of component κ adsorbed on the stationary phase, $\hat{C}_\kappa$ [n_c]
(3) Concentration of component κ in phase ℓ, $C_{\kappa\ell}$ [n_p-n_c]
(4) Phase saturation, S_ℓ [n_p]
(5) Relative permeabilities, $k_{r\ell}$ [n_p]
(6) Phase viscosities, μ_ℓ [n_p]
(7) Phase densities, ρ_ℓ [n_p]
(9) Phase pressures, P_ℓ [n_p]

3. Numerical Model

3.1 Physical-Property Calculations

In this section, we will describe the calculations of several physical properties modeled in the simulator, including phase behavior, adsorption, relative permeability and capillary desaturation, polymer viscosity, compositional phase viscosity, capillary pressure, phase density, and gravity.

3.1.1 Phase Behavior and Flash Calculations

We will describe the phase-equilibrium conditions and the algorithm with at most six components (water, oil, surfactant, polymer, anions, and divalent cations) and three phases (aqueous, oleic, and microemulsion), where water and oil are always volumetric components and surfactant is a volumetric component except for a special case discussed later. In the phase-equilibrium problem, we are given the total concentration of each component and want to determine which phase exists and calculate the saturations and the phase concentrations.

Ternary Diagram, Binodal Curve, Invariant Point, and Effective Salinity

Phase-equilibrium conditions can be described in terms of a ternary diagram and a binodal curve (Fig. 3.1). The apexes of the ternary diagram correspond to 100% water, oil, and surfactant concentrations. To simplify the discussion, we also assume a corner plait point. The boundaries of the various phase regions are determined in part by the binodal curve, and the shape of the binodal curve is affected by salinity.

There exists an aqueous-oleic two-phase region at very low surfactant concentrations (below the critical micelle concentration, abbreviated as CMC) and a single microemulsion-phase region at high surfactant concentration, above the binodal curve. Below the binodal curve, there may be two phases (the oleic and microemulsion phases or the aqueous and microemulsion phases) or all three phases depending on the position of the invariant point or the effective salinity.

The binodal curve is defined by the empirical relation known as Hand's rule (Hand, 1939). In this case, it is

$$\frac{C_{33}}{C_{13}} = A\left(\frac{C_{33}}{C_{23}}\right)^B.$$

Commonly B is taken to be -1, so that the binodal curve is symmetric in oil and water. A is linearly interpolated by

$$A = \begin{cases} A_1-(A_1-A_0)(1-C_{SE}/C_{SEO}) & C_{SE} \le C_{SEO} \\ A_1+(A_2-A_1)(C_{SE}/C_{SEO}-1) & C_{SE} > C_{SEO} \end{cases}$$

where A_0, A_1, and A_2 are related to the heights of binodal curve C_{3max0}, C_{3max1}, and C_{3max2} corresponding to the low, optimal, and high salinities, C_{SEL}, C_{SEO}, and C_{SEU}, respectively,

$$A_i = \left(\frac{2C_{3max,\,i}}{1-C_{3max,\,i}}\right)^2 \qquad (i= 0, 1, \text{and } 2)$$

and the effective salinity C_{SE} is given by

$$C_{SE} = C_5/C_1.$$

The optimal salinity C_{SEO} is taken to be the average of C_{SEL} and C_{SEU}. C_{3maxi}, C_{SEL}, and C_{SEU} are input values.

The concentrations at the invariant point M are a function of the ratio R_{SE}, defined as (Saad *et al.*, 1989)

$$R_{SE} = \frac{C_{SE}-C_{SEL}}{C_{SEU}-C_{SEL}}$$

and

$$(R_{SE}-C_{2M})/C_{3M} = \cos 60^{\circ}.$$

Since the invariant point is on the binodal curve and $C_{1M} = 1-C_{2M}-C_{3M}$, from Hand's equation, we can obtain

$$C_{2M} = \frac{1}{2(4-A)}\left\{2R_{SE}(4-A) + A - \sqrt{[2R_{SE}(4-A) + A]^2 - 16R_{SE}^2(4-A)}\right\}.$$

When C_{SE} approaches C_{SEL} and R_{SE} approaches 0, the invariant point moves to the water component apex, and there exist the oleic and microemulsion phases. When C_{SE} approaches C_{SEU} and R_{SE} approaches 1, the invariant point moves to the oleic component apex, and there exist the aqueous and microemulsion phases. When C_{SE} is in between C_{SEL} and C_{SEU}, a three-phase region opens up between the two-phase regions.

Concentrations C_1, C_3, and C_5 are chosen as part of the primary variables. The nonzero derivatives of R_{SE}, A, C_{2M}, C_{3M}, and C_{1M} with respect to these primary variables are as follows:

$$\frac{\partial R_{SE}}{\partial C_5} = 1/C_1/(C_{SEU}-C_{SEL})$$

$$\frac{\partial R_{SE}}{\partial C_1} = -C_{SE}\frac{\partial R_{SE}}{\partial C_5}$$

$$\frac{\partial A}{\partial C_5} = \begin{cases} (A_1-A_0)/C_{SEO}/C_1 & C_{SE} \le C_{SEO} \\ (A_2-A_1)/C_{SEO}/C_1 & C_{SE} > C_{SEO} \end{cases}$$

$$\frac{\partial A}{\partial C_1} = -C_{SE}\frac{\partial A}{\partial C_5}$$

$$\frac{\partial C_{2M}}{\partial C_i} = \frac{C_{2M}(1-2R_{SE}+C_{2M})\frac{\partial A}{\partial C_i} + 2[C_{2M}(4-A)-4R_{SE}]\frac{\partial R_{SE}}{\partial C_i}}{2(C_{2M}-R_{SE})(4-A)-A}$$

$$\frac{\partial C_{3M}}{\partial C_i} = 2\left(\frac{\partial R_{SE}}{\partial C_i} - \frac{\partial C_{2M}}{\partial C_i}\right)$$

$$\frac{\partial C_{1M}}{\partial C_i} = -\frac{\partial C_{2M}}{\partial C_i} - \frac{\partial C_{3M}}{\partial C_i} \qquad (i=1 \text{ and } 5)$$

Two-Phase Aqueous-Oleic

The fluid forms an aqueous-oleic mixture whenever

$C_3 \leq CMC.$

In this case, the solution of phase equilibrium is very simple: the number of phase is 2 and the surfactant is in the aqueous phase. The nonzero dependent variables oil concentration, phase concentrations, saturations, and derivatives with respect to the primary variables are

$$S_2 = 1 - C_1 - C_3$$

$$\frac{\partial S_2}{\partial C_i} = -1 \qquad \text{(i=1 and 3)}$$

$$S_1 = 1 - S_2$$

$$\frac{\partial S_1}{\partial C_i} = -\frac{\partial S_2}{\partial C_i} \qquad \text{(i=1 and 3)}$$

$$C_{11} = C_1/S_1$$

$$\frac{\partial C_{11}}{\partial C_1} = (1 - C_{11})/S_1$$

$$\frac{\partial C_{11}}{\partial C_3} = -C_{11}/S_1$$

$$C_{31} = 1 - C_{11}$$

$$\frac{\partial C_{31}}{\partial C_i} = -\frac{\partial C_{11}}{\partial C_i} \qquad \text{(i=1 and 3)}$$

Single Microemulsion Phase

The fluid forms a single microemulsion phase at high surfactant concentration of

$$C_3 > (AC_1C_2)^{1/2}.$$

In this case, the nonzero elements are

$$S_3 = 1$$

$$C_{33} = C_3$$

$$\frac{\partial C_{33}}{\partial C_3} = 1$$

$$C_{13} = C_1$$

$$\frac{\partial C_{13}}{\partial C_1} = 1$$

$$C_{23} = C_2$$

$$\frac{\partial C_{23}}{\partial C_i} = -1 \qquad \text{(i=1 and 3)}$$

Two-Phase Oleic-Microemulsion

The fluid forms oleic and microemulsion mixtures when the surfactant concentration satisfies

$$C_3 \le (AC_1C_2)^{1/2}$$

with a low effective salinity of

$$C_{SE} < C_{SEL}$$

or an intermediate effective salinity of

$$C_{SEL} \le C_{SE} \le C_{SEU}$$

with the concentration in the region of

$$C_2 > C_{2M} \text{ and } C_3 > C_1C_{3M}/C_{1M}.$$

The nonzero elements in this case are

$$C_{11} = 1$$

$$S_3 = C_1(1+R_{31}+R_{31}^2/A), \qquad (R_{31} = C_3/C_1)$$

$$\frac{\partial S_3}{\partial C_1} = 1 - \frac{R_{31}}{A}\left(R_{31} + \frac{C_3}{A}\frac{\partial A}{\partial C_1}\right)$$

$$\frac{\partial S_3}{\partial C_3} = 1+2R_{31}/A$$

$$\frac{\partial S_3}{\partial C_5} = -\frac{R_{31}C_3}{A^2}\frac{\partial A}{\partial C_5}$$

$$S_2 = 1-S_3$$

$$\frac{\partial S_2}{\partial C_i} = -\frac{\partial S_3}{\partial C_i} \qquad \text{(i=1, 3, and 5)}$$

$$C_{33} = C_3/S_3$$

$$\frac{\partial C_{33}}{\partial C_i} = -\frac{C_{33}}{S_3}\frac{\partial S_3}{\partial C_i} \qquad \text{(i=1 and 5)}$$

$$\frac{\partial C_{33}}{\partial C_3} = \left(1 - C_{33}\frac{\partial S_3}{\partial C_3}\right)/S_3$$

$$C_{13} = C_1/S_3$$

$$\frac{\partial C_{13}}{\partial C_1} = \left(1 - C_{13}\frac{\partial S_3}{\partial C_1}\right)/S_3$$

$$\frac{\partial C_{13}}{\partial C_i} = -\frac{C_{13}}{S_3}\frac{\partial S_3}{\partial C_i} \qquad (i=3 \text{ and } 5)$$

$$C_{23} = 1 - C_{13} - C_{33}$$

$$\frac{\partial C_{23}}{\partial C_i} = -\frac{\partial C_{13}}{\partial C_i} - \frac{\partial C_{33}}{\partial C_i} \qquad (i=1, 3, \text{ and } 5)$$

Two-Phase Aqueous-Microemulsion

The fluid forms aqueous and microemulsion mixtures when the surfactant concentration satisfies

$$C_3 \le (AC_1C_2)^{1/2}$$

with a high effective salinity of

$$C_{SE} > C_{SEU}$$

or an intermediate effective salinity of

$$C_{SEL} \le C_{SE} \le C_{SEU}$$

with the concentration in the region of

$$C_2 < C_{2M} \text{ and } C_3 > C_2C_{3M}/C_{2M}.$$

The nonzero elements in this case are

$$C_{11} = 1$$

$$S_3 = C_2(1+R_{32}+R_{32}^2/A) \qquad (R_{32} = C_3/C_2)$$

$$\frac{\partial S_3}{\partial C_1} = -\left(1+\frac{R_{32}}{A}\right)\left(R_{32} - \frac{C_3}{A}\frac{\partial A}{\partial C_1}\right)$$

$$\frac{\partial S_3}{\partial C_3} = (2+R_{32})R_{32}/A$$

$$\frac{\partial S_3}{\partial C_5} = -\frac{R_{32}C_3}{A^2}\frac{\partial A}{\partial C_5}$$

$$S_1 = 1 - S_3$$

$$\frac{\partial S_1}{\partial C_i} = -\frac{\partial S_3}{\partial C_i} \qquad \text{(i=1, 3, and 5)}$$

$$C_{33} = C_3/S_3$$

$$\frac{\partial C_{33}}{\partial C_i} = -\frac{C_{33}}{S_3}\frac{\partial S_3}{\partial C_i} \qquad \text{(i=1 and 5)}$$

$$\frac{\partial C_{33}}{\partial C_3} = \left(1 - C_{33}\frac{\partial S_3}{\partial C_3}\right)/S_3$$

$$C_{23} = C_2/S_3$$

$$\frac{\partial C_{23}}{\partial C_i} = -\left(1 + C_{23}\frac{\partial S_3}{\partial C_i}\right)/S_3 \qquad \text{(i=1 and 3)}$$

$$\frac{\partial C_{23}}{\partial C_5} = -\frac{C_{23}}{S_3}\frac{\partial S_3}{\partial C_5}$$

$$C_{13} = 1 - C_{23} - C_{33}$$

$$\frac{\partial C_{13}}{\partial C_i} = -\frac{\partial C_{23}}{\partial C_i} - \frac{\partial C_{33}}{\partial C_i} \qquad \text{(i=1, 3, and 5).}$$

Three-Phase Aqueous-Oleic-Microemulsion

The fluid forms aqueous, oleic, and microemulsion three-phase mixtures when the surfactant concentration satisfies

$$C_3 \le (AC_1C_2)^{1/2}$$

with an intermediate effective salinity of

$$C_{SEL} \le C_{SE} \le C_{SEU}$$

and the concentrations in the regions of

$$C_2 < C_{2M} \text{ and } C_3 < C_2C_{3M}/C_{2M}$$

or

$$C_2 > C_{2M} \text{ and } C_3 < C_1C_{3M}/C_{1M}.$$

The nonzero elements in this case are

$$C_{11} = 1$$

$$S_3 = C_3/C_{3M}$$

$$\frac{\partial S_3}{\partial C_i} = -\frac{S_3}{C_{3M}}\frac{\partial C_{3M}}{\partial C_i} \qquad \text{(i=1 and 5)}$$

$$\frac{\partial S_3}{\partial C_3} = \frac{1}{C_{3M}}$$

$$S_1 = C_1 - C_{1M} S_3$$

$$\frac{\partial S_1}{\partial C_1} = 1 - C_{1M}\frac{\partial S_3}{\partial C_1} - S_3\frac{\partial C_{1M}}{\partial C_1}$$

$$\frac{\partial S_1}{\partial C_3} = -\frac{C_{1M}}{C_{3M}}$$

$$\frac{\partial S_1}{\partial C_5} = -C_{1M}\frac{\partial S_3}{\partial C_5} - S_3\frac{\partial C_{1M}}{\partial C_5}$$

$$S_2 = 1 - S_1 - S_3$$

$$\frac{\partial S_2}{\partial C_i} = -\frac{\partial S_1}{\partial C_i} - \frac{\partial S_3}{\partial C_i} \qquad \text{(i=1, 3, and 5)}$$

$$C_{33} = C_{3M}$$

$$\frac{\partial C_{33}}{\partial C_i} = -\frac{\partial C_{3M}}{\partial C_i} \qquad \text{(i=1 and 5)}$$

$$C_{23} = C_{2M}$$

$$\frac{\partial C_{23}}{\partial C_i} = \frac{\partial C_{2M}}{\partial C_i} \qquad \text{(i=1 and 5)}$$

$$C_{13} = C_{1M}$$

$$\frac{\partial C_{13}}{\partial C_i} = \frac{\partial C_{1M}}{\partial C_i} \qquad \text{(i=1 and 5)}$$

3.1.2 Adsorption

Adsorption is modeled by a Langmuir-type isotherm and is irreversible. Polymer-adsorption isotherm is given by

$$\hat{C}_4 = \frac{a_4 C_4 S_\ell}{S_\ell + b_4 C_4}$$

where $\ell = 1$ if $S_1 > 0$ and $\ell = 3$ otherwise. Its derivatives are calculated by

$$\frac{\partial \hat{C}_4}{\partial C_i} = \frac{b_4 C_{4\ell} \hat{C}_4}{S_\ell + b_4 C_4} \frac{\partial S_\ell}{\partial C_i} \qquad (i=1,3,5)$$

$$\frac{\partial \hat{C}_4}{\partial C_4} = \frac{\hat{C}_4}{S_\ell + b_4 C_4} \frac{1}{C_{4\ell}}$$

Surfactant-adsorption isotherm is given by

$$\hat{C}_3 = \min\left(C_3, \frac{a_3 C_{3\ell}}{1 + b_3 C_{3\ell}}\right)$$

where $\ell = 3$ if $S_3 > 0$ and $\ell = 1$ otherwise. Its derivatives are calculated by

$$\frac{\partial \hat{C}_3}{\partial C_i} = \frac{\hat{C}_3}{C_{3\ell}(1 + b_3 C_3)} \frac{\partial C_{3\ell}}{\partial C_i} \qquad (i=1,3,5)$$

for $\dfrac{a_3 C_{3\ell}}{1 + b_3 C_{3\ell}} < C_3$

3.1.3 Interfacial-Tension Model

The interfacial tension of σ_{i3} (i=1,2) is computed by

$$\sigma_{i3} = F_{\sigma_{i3}} \sigma_{12} 10^{\left(G_{i2} + \frac{G_{i1}}{1+G_{i3}} - \lg \sigma_{12}\right) r_{i3}} \qquad \text{for} \quad r_{i3}<1$$

and

$$\sigma_{i3} = F_{\sigma_{i3}} 10^{G_{i2} + \frac{G_{i1}}{1+G_{i3} r_{i3}}} \qquad \text{for} \quad r_{i3}>1$$

where

$$r_{i3} = \frac{C_{i3}}{C_{i3}}$$

and

$$F_{\sigma i3} = \frac{1 - \exp(-C_{RMSi3})}{1 - \exp(-\sqrt{2})}$$

$$C_{RMS13} = \sqrt{(1 - C_{13})^2 + C_{23}^2 + C_{33}^2}$$

$$C_{RMS23} = \sqrt{(1 - C_{23})^2 + C_{13}^2 + C_{33}^2}$$

The derivatives of interfacial tension are computed by

$$\frac{1}{\sigma_{i3}}\frac{\partial\sigma_{i3}}{\partial C_k}=\frac{1}{F_{\sigma_{i3}}}\frac{\partial F_{\sigma_{i3}}}{\partial C_k}+r_{i3}\left(\frac{1}{C_{i3}}\frac{\partial\sigma_{i3}}{\partial C_k}-\frac{1}{\sigma_{33}}\frac{\partial\sigma_{33}}{\partial C_k}\right)\ln\frac{10^{G_{i2}+\frac{G_{i1}}{1+G_{i3}}}}{\sigma_{12}} \quad \text{for } r_{i3}<1$$

and

$$\frac{1}{\sigma_{i3}}\frac{\partial\sigma_{i3}}{\partial C_k}=\frac{1}{F_{\sigma_{i3}}}\frac{\partial F_{\sigma_{i3}}}{\partial C_k}-r_{i3}\left(\frac{1}{C_{i3}}\frac{\partial\sigma_{i3}}{\partial C_k}-\frac{1}{\sigma_{33}}\frac{\partial\sigma_{33}}{\partial C_k}\right)\frac{G_{i3}G_{i1}\ln 10}{\left(1+G_{i3}r_{i3}\right)^2} \quad \text{for } r_{i3}>1$$

where

$$\frac{1}{F_{\sigma i3}}\frac{\partial F_{\sigma i3}}{\partial C_k}=\frac{\exp(-C_{RMSi3})}{1-\exp(-C_{RMSi3})}\frac{\partial C_{RMSi3}}{\partial C_k}$$

$$\frac{\partial C_{RMS13}}{\partial C_k}=\frac{1}{C_{RMS13}}\left[-(1-C_{13})\frac{\partial C_{13}}{\partial C_k}+\frac{\partial C_{23}}{\partial C_k}+\frac{\partial C_{33}}{\partial C_k}\right]$$

$$\frac{\partial C_{RMS23}}{\partial C_k}=\frac{1}{C_{RMS23}}\left[-(1-C_{23})\frac{\partial C_{23}}{\partial C_k}+\frac{\partial C_{13}}{\partial C_k}+\frac{\partial C_{33}}{\partial C_k}\right]$$

(k=1,3,5)

3.1.4 Relative Permeability and Capillary Desaturation

Relative permeability and capillary desaturation in the simulator are modeled by

$$k_{r\ell}=k^0_{r\ell}S^{e_\ell}_{n\ell}$$

where

$$S_{n\ell}=\frac{S_\ell-S_{\ell r}}{1-\sum_{\ell=1}^{n_p}S_{\ell r}}$$

$$S_{\ell r}=S_{\ell rc}+\frac{S_{\ell rw}-S_{\ell rc}}{1+T_\ell N_{c\ell}}$$

$$k^0_{r\ell}=k^0_{r\ell c}+\frac{k^0_{r\ell w}-k^0_{r\ell c}}{1+T_\ell N_{c\ell}}$$

$$e_\ell=e_{\ell c}+\frac{e_{\ell w}-e_{\ell c}}{1+T_\ell N_{c\ell}}$$

and the capillary number is given by

$$N_{c\ell} = \frac{2.23 \times 10^{-5}}{\sigma_\ell} \sqrt{\left(k_x \frac{\partial \Phi}{\partial x}\right)^2 + \left(k_y \frac{\partial \Phi}{\partial y}\right)^2 \left(k_z \frac{\partial \Phi}{\partial z}\right)^2}$$

Depending on the phase environment, σ_ℓ assumes different values:

aqueous and oleic two-phase flow
ℓ=1 or 2 $\quad \sigma_\ell = \sigma_{12}$
aqueous and microemulsion two-phase flow
ℓ=1 or 3 $\quad \sigma_\ell = \sigma_{13}$
oleic and microemulsion two-phase flow
ℓ=2 or 3 $\quad \sigma_\ell = \sigma_{23}$
aqueous, oleic, and microemulsion three-phase flow
ℓ=1 $\quad \sigma_\ell = \sigma_{13}$
ℓ=2 $\quad \sigma_\ell = \sigma_{23}$
ℓ=3 $\quad \sigma_\ell = \sigma_{23}$ if $S_1 < S_{1r}$ and $S_2 > S_{2r}$
$\sigma_\ell = \sigma_{13}$ otherwise

Derivatives of relative permeability are computed by

$$\frac{1}{k_{r\ell}} \frac{\partial k_{r\ell}}{\partial C_i} = \left[1 - \frac{k^0_{r\ell c}}{k^0_{r\ell}} + \left(1 - \frac{e_{\ell c}}{e_\ell}\right) \ln S_{n\ell}\right] \frac{T_\ell N_{c\ell}}{1 + T_\ell N_{c\ell}} \frac{1}{\sigma_\ell} \frac{\partial \sigma_\ell}{\partial C_i} + \frac{e_\ell}{S_{n\ell}} \frac{\partial S_{n\ell}}{\partial S_{n\ell}}$$

where

$$\frac{1}{S_{n\ell}} \frac{\partial S_{n\ell}}{\partial S_{n\ell}} = \frac{1}{S_\ell - S_{\ell r}} \frac{\partial (S_\ell - S_{\ell r})}{\partial C_i} + \frac{1}{1 - \sum_{\ell=1}^{n_p} S_{\ell r}} \sum_{\ell=1}^{n_p} \frac{\partial S_{\ell r}}{\partial C_i}$$

and

$$\frac{\partial S_{\ell r}}{\partial C_i} = (S_{\ell r} - S_{\ell rc}) \frac{T_\ell N_{c\ell}}{1 + T_\ell N_{c\ell}} \frac{1}{\sigma_\ell} \frac{\partial \sigma_\ell}{\partial C_i}$$

3.1.5 Polymer Viscosity

Polymer solution viscosity can be expressed in general as

$$\mu_p = \mu_w \left(1 + \frac{f_\mu}{f_\gamma}\right)$$

where

$$f_\mu = A_{p1}(C_{4\ell}) C_{sep}^{S_p}$$

and

$$A_{p1}(C_{4\ell}) = A_{p1} C_{4\ell} + A_{p2} C_{4\ell}^2 + A_{p3} C_{4\ell}^3$$

measures polymer solution viscosity at zero shear rate and is a function of polymer and electrolyte concentrations. A_{p1}, A_{p2}, and A_{p3} are empirical constants for a given polymer, and C_{sep} is an effective salinity, defined for use in polymer-property calculations

$$C_{sep} = \max\left[\frac{C_5 + (\beta_p - 1)C_6}{C_1}, C_{sel}\right]$$

The effect of shear rate on polymer solution viscosity is measured by

$$f_\gamma = 1 + \left(\frac{\dot{\gamma}}{\dot{\gamma}^{1/2}}\right)^{P_\alpha - 1}$$

where

$$\dot{\gamma} = \dot{\gamma}_c \sqrt{\frac{u_{x\ell}^2/k_x + u_{y\ell}^2/k_y + u_{z\ell}^2/k_z}{\phi k_{r\ell} S_\ell}}$$

and $\dot{\gamma}_c$ and $\dot{\gamma}^{1/2}$ are input parameters.

The derivatives of the viscosity are calculated as follows:

$$\frac{1}{\mu_p}\frac{\partial \mu_p}{\partial C_i} = \left(\frac{1}{f_\mu}\frac{\partial f_\mu}{\partial C_i} - \frac{1}{f_\gamma}\frac{\partial f_\gamma}{\partial C_i}\right) \Big/ \left(1 + f_\gamma / f_\mu\right)$$

where

$$\frac{1}{f_\mu}\frac{\partial f_\mu}{\partial C_1} = \frac{1}{A_p}\frac{\partial A_p}{\partial C_1} - \frac{S_p}{C_1}$$

$$\frac{1}{f_\mu}\frac{\partial f_\mu}{\partial C_i} = \frac{1}{A_p}\frac{\partial A_p}{\partial C_i} \qquad (i=3,4)$$

$$\frac{1}{f_\mu}\frac{\partial f_\mu}{\partial C_5} = \frac{1}{A_p}\frac{\partial A_p}{\partial C_5} + \frac{S_p}{C_1 C_{sep}}$$

$$\frac{1}{f_\mu}\frac{\partial f_\mu}{\partial C_6} = \frac{S_p(\beta_p - 1)}{C_1 C_{sep}}$$

with

$$\frac{\partial A_p}{\partial C_i} = \left(A_{p1} + 2A_{p2}C_{4\ell} + 3A_{p3}C_{4\ell}^2\right)\frac{\partial C_{4\ell}}{\partial C_i} \qquad (i=1,3,4,5)$$

and

$$\frac{1}{f_\gamma}\frac{\partial f_\gamma}{\partial C_i} = -\frac{1}{2}\left(1 - 1/f_\gamma\right)\left(P_\alpha - 1\right)\left(\frac{1}{k_{r\ell}}\frac{\partial k_{r\ell}}{\partial C_i} + \frac{1}{S_\ell}\frac{\partial S_\ell}{\partial C_i}\right)$$

3.1.6 Compositional Phase Viscosity

The phase viscosity is calculated using

$$\mu_1 = C_{11}\mu_p \exp[\alpha_1(1-C_{11})] + C_{31}\alpha_3 \exp(\alpha_4 C_{11})$$
$$\mu_2 = \mu_o$$
$$\mu_3 = C_{13}\mu_p \exp[\alpha_1(1-C_{13})] + C_{23}\mu_o \exp[\alpha_2(1-C_{23})]$$
$$+C_{33}\alpha_3 \exp(\alpha_4 C_{13} + \alpha_5 C_{23})$$

The derivatives of the phase viscosity are calculated as follows:

$$\frac{\partial \mu_1}{\partial C_i} = \left[(1-\alpha_1 C_{11})\mu_p \frac{\partial C_{11}}{\partial C_i} + C_{11}\frac{\partial \mu_p}{\partial C_i}\right]\exp[\alpha_1(1-C_{31})] \qquad \text{(i=1,3)}$$
$$+\left(\frac{\partial C_{31}}{\partial C_i} + C_{31}\alpha_4 \frac{\partial C_{11}}{\partial C_i}\right)\alpha_3 \exp(\alpha_4 C_{11})$$

$$\frac{\partial \mu_1}{\partial C_i} = C_{11}\frac{\partial \mu_p}{\partial C_i}\exp[\alpha_1(1-C_{11})] \qquad \text{(i=4,5,6)}$$

$$\frac{\partial \mu_3}{\partial C_i} = \left[(1-\alpha_1 C_{13})\mu_p \frac{\partial C_{13}}{\partial C_i} + C_{13}\frac{\partial \mu_p}{\partial C_i}\right]\exp[\alpha_1(1-C_{13})]$$
$$+(1-\alpha_2 C_{23})\mu_o \frac{\partial C_{23}}{\partial C_i}\exp[\alpha_2(1-C_{23})] \qquad \text{(i=1,3,5)}$$
$$+\left[\frac{\partial C_{33}}{\partial C_i} + C_{33}\left(\alpha_4 \frac{\partial C_{13}}{\partial C_i} + \alpha_5 \frac{\partial C_{23}}{\partial C_i}\right)\right]\alpha_3 \exp(\alpha_4 C_{13} + \alpha_5 C_{23})$$

$$\frac{\partial \mu_3}{\partial C_i} = C_{13}\frac{\partial \mu_p}{\partial C_i}\exp[\alpha_1(1-C_{13})] \qquad \text{(i=4,6)}$$

3.1.7 Permeability Reduction

Permeability-reduction factor in the simulator is modeled by

$$R_k = 1 + \frac{(R_{kmax}-1)b_{rk}C_{4\ell}}{1+b_{rk}C_{4\ell}}$$

where

$$R_{kmax} = \left[1 - \frac{C_{rk}[\mu]^{1/3}\phi^{1/2}}{(k_x k_y)^{1/4}}\right]^{-4}$$

and $[\mu]$ is the intrinsic viscosity of the polymer solution

$$[\mu] = A_{p1} C_{sep}^{S_p}$$

The derivatives of the permeability-reduction factor are calculated as follows:

$$\frac{1}{R_k}\frac{\partial R_k}{\partial C_l} = (1-1/R_k)\left[\frac{1-1/R_k}{C_{4\ell}(1+b_{rk}C_{4\ell})}\frac{\partial C_{4\ell}}{\partial C_l} - \frac{4}{3}\frac{R_{kmax}(R_{kmax}^{1/4}-1)}{R_{kmax}-1}\frac{S_p}{C_l}\right]$$

$$\frac{1}{R_k}\frac{\partial R_k}{\partial C_i} = (1-1/R_k)\frac{1-1/R_k}{C_{4\ell}(1+b_{rk}C_{4\ell})}\frac{\partial C_{4\ell}}{\partial C_i} \qquad (i=3,4)$$

$$\frac{1}{R_k}\frac{\partial R_k}{\partial C_5} = (1-1/R_k)\left[\frac{1-1/R_k}{C_{4\ell}(1+b_{rk}C_{4\ell})}\frac{\partial C_{4\ell}}{\partial C_5} + \frac{4}{3}\frac{R_{kmax}\left(R_{kmax}^{1/4}-1\right)}{R_{kmax}-1}\frac{S_p}{C_1 C_{sep}}\right]$$

$$\frac{1}{R_k}\frac{\partial R_k}{\partial C_6} = \frac{4(1-1/R_k)}{3}\frac{R_{kmax}\left(R_{kmax}^{1/4}-1\right)}{R_{kmax}-1}\frac{S_p(\beta_p-1)}{C_1 C_{sep}}$$

3.1.8 Capillary Pressure

Capillary pressure for two phases is modeled as a function of interfacial tension, permeability, porosity, and saturation:

$$P_{c\ell i} = C_{pc}\frac{\phi^{1/2}}{(k_x k_y)^{1/4}}\frac{\sigma_{\ell i}}{\sigma_{12}}(1-S_{n\ell})^{n_{pc}}$$

and its derivatives are

$$\frac{\partial P_{c\ell i}}{\partial C_i} = P_{c\ell i}\left(\frac{1}{\sigma_{\ell i}}\frac{\partial \sigma_{\ell i}}{\partial C_i} - \frac{n_{pc}}{1-S_{n\ell}}\frac{\partial S_{n\ell}}{\partial C_i}\right) \qquad (i=1,3,5)$$

For three-phase water, oil, microemulsion flow,

$$P_{c13} = C_{pc}\frac{\phi^{1/2}}{(k_x k_y)^{1/4}}\frac{\sigma_{13}}{\sigma_{12}}(1-S_{n1})^{n_{pc}}$$

$$P_{c32} = C_{pc}\frac{\phi^{1/2}}{(k_x k_y)^{1/4}}\frac{\sigma_{32}}{\sigma_{12}}\left(\frac{S_{n2}}{S_{n3}+S_{n2}}\right)^{n_{pc}}$$

and the derivatives are

$$\frac{\partial P_{c13}}{\partial C_i} = P_{c13}\left(\frac{1}{\sigma_{13}}\frac{\partial \sigma_{13}}{\partial C_i} - \frac{n_{pc}}{1-S_{n1}}\frac{\partial S_{n1}}{\partial C_i}\right)$$

$$\frac{\partial P_{c32}}{\partial C_i} = P_{c32}\left[\frac{1}{\sigma_{32}}\frac{\partial \sigma_{32}}{\partial C_i} + \frac{n_{pc}}{S_{n2}}\frac{\partial S_{n2}}{\partial C_i} - \frac{n_{pc}}{S_{n3}+S_{n2}}\frac{\partial (S_{n3}+S_{n2})}{\partial C_i}\right] \qquad (i=1,3,5)$$

3.1.9 Phase Density, Gravity and Reservoir Dip

Phase specific weights are calculated in the simulator by

$$\gamma_1 = C_{11}w_1 + C_{31}w_3 + C_{41}w_4 + C_{51}w_5 + C_{61}w_6$$
$$\gamma_2 = w_2$$
$$\gamma_3 = C_{13}w_1 + C_{23}w_2 + C_{33}w_3 + C_{43}w_4 + C_{53}w_5 + C_{63}w_6$$

where specific weights of water (w_1), oil (w_2), and surfactant (w_3) are input values and w_4, w_5, and w_6 are given constant values in the simulator.

The derivatives of phase specific weights are

$$\frac{\partial \gamma_1}{\partial C_i} = \frac{\partial C_{11}}{\partial C_i} w_1 + \frac{\partial C_{31}}{\partial C_i} w_3 + \frac{\partial C_{41}}{\partial C_i} w_4 + \frac{\partial C_{51}}{\partial C_i} w_5 + \frac{\partial C_{61}}{\partial C_i} w_6 \qquad (i=1,3)$$

$$\frac{\partial \gamma_1}{\partial C_i} = \frac{\partial C_{i1}}{\partial C_i} w_i \qquad (i=4,6)$$

$$\frac{\partial \gamma_1}{\partial C_5} = \frac{\partial C_{41}}{\partial C_i} w_4 + \frac{\partial C_{51}}{\partial C_i} w_5 + \frac{\partial C_{61}}{\partial C_i} w_6$$

$$\frac{\partial \gamma_3}{\partial C_i} = \frac{\partial C_{13}}{\partial C_i} w_1 + \frac{\partial C_{23}}{\partial C_i} w_2 + \frac{\partial C_{33}}{\partial C_i} w_3 + \frac{\partial C_{43}}{\partial C_i} w_4 + \frac{\partial C_{53}}{\partial C_i} w_5 + \frac{\partial C_{63}}{\partial C_i} w_6$$

(i=1,3,5)

$$\frac{\partial \gamma_3}{\partial C_i} = \frac{\partial C_{i3}}{\partial C_i} w_i \qquad (i=4,6)$$

For a reservoir with an x-direction dip angle of θ_x and a y-direction dip angle of θ_y, the depth is calculated by

$$D(x,y,z) = x\sin\theta_x + \left(y\sin\theta_y + z\cos\theta_y\right)\cos\theta_x + D_0$$

where D_0=D(0,0,0) and x=y=z=0, at i=1,j=1, and k=1.

The angle between each reservoir coordinate direction and gravity direction is given by

$$\alpha_x = \cos^{-1}(\sin\theta_x)$$

$$\alpha_y = \cos^{-1}(\cos\theta_x \sin\theta_y)$$

$$\alpha_z = \cos^{-1}(\cos\theta_x \cos\theta_y)$$

These angles are needed when computing gravity head for wells completed parallel to different coordinate directions.

3.2 High-Order Temporal Discretization

Applying Taylor's expansion to function f(t) at time level t^n and t^{n+1}, we can obtain the following:

$$f^{n+1} - \Delta t\left(\frac{\partial f}{\partial t}\right)^{n+1} = f^n + \Delta t\left(\frac{\partial f}{\partial t}\right)^n + O\left(\Delta t^2\right)$$

where $\Delta t = t^{n+1} - t^n$. This expression is called the Crank-Nicolson scheme and has second-order accuracy. We will use the scheme as the basis for our temporal discretizations in the governing equations.

3.3 High-Order Spatial Discretization

The discrete approximation of first spatial derivative can be written in general as

$$\left(\frac{\partial f}{\partial x}\right)_i = \frac{f_{i+1/2} - f_{i-1/2}}{\Delta x_i} + O\left(\Delta x^p\right)$$

where p is the order of the scheme. For flow from $x_{i-1/2}$ to $x_{i+1/2}$ and uniform grid, we have following schemes:

First-order scheme (one-point upstream weighting)

$$f_{i+1/2} = f_i$$

Second-order scheme (two-point upstream weighting)

$$f_{i+1/2} = (-f_{i-1} + 3f_i)/2$$

Third-order scheme (two-point upstream, one-point downstream weighting)

$$f_{i+1/2} = (-f_{i-1} + 5f_i + f_{i+1})/6$$

We will use the third-order scheme as the basis to build our spatial discretization scheme while leaving first- and second-order schemes as options in the simulator.

3.4 TVD Method and Flux Limiter

For flow from $x_{i-1/2}$ to $x_{i+1/2}$, we can write the flux in the form

$$f_{i+1/2} = f_i + \varphi_i(f_{i+1} - f_i)$$

where φ represents the flux-limiter function. The magnitude of the limiting depends on the smoothness of the data, measured by the ratio of consecutive gradients r:

$$r_i = (f_i - f_{i-1})/(f_{i+1} - f_i)$$

The derivatives of the flux function are given by

$$\frac{\partial f_{i+1/2}}{\partial f_{i-1}} = -\left(\frac{\partial \varphi}{\partial r}\right)_i$$

$$\frac{\partial f_{i+1/2}}{\partial f_i} = 1 - \varphi_i + (1 + \varphi_i)\left(\frac{\partial \varphi}{\partial r}\right)_i$$

$$\frac{\partial f_{i+1/2}}{\partial f_{i+1}} = \varphi_i - r_i\left(\frac{\partial \varphi}{\partial r}\right)_i$$

We can express φ to be a function of r in general as

$$\varphi(r) = ar + b$$

Corresponding to different schemes, we have

First-order scheme

$$a_i = b_i = 0$$

Second-order scheme

$$a_i = \Delta x_i/(\Delta x_{i-1} + \Delta x_i),\ b_i = 0$$

High-order scheme for uniform grid (p=3)

$$a_i = 1/6,\ b_i = 1/3$$

High-order scheme for nonuniform grid (p=2)

$$a_i = \Delta x_i \Delta x_{i+1}/[(\Delta x_{i-1} + \Delta x_i)(\Delta x_{i-1} + 2\Delta x_i + \Delta x_{i+1})],$$

$$b_i = \Delta x_i(\Delta x_{i-1} + 2\Delta x_i)/[(\Delta x_i + \Delta x_{i+1})(\Delta x_{i-1} + 2\Delta x_i + \Delta x_{i+1})]$$

The total variation (TV) of a solution C(x,t) is defined as (Harten, 1983)

$$TV(C) = \sup \sum_{i=1}^{N} |C(x_i,t)-C(x_{i-1},t)|$$

where the solution is defined in the domain $x \in [x_1,. x_N]$ and the supremum is taken over all subdivisions of the domain. If the solution is total variation diminishing (TVD), then we have

$$TV(C(x,t_2)) \leq TV(C(x,t_1)) \qquad \text{for } t_2 \geq t_1$$

When a numerical solution C_i^n is sought to approximate the solution $C(x_i, t^n)$, it is reasonable to require that the variation of the discretized solution be diminishing for all grid functions C^n:

$$TV(C^{n+1}) \leq TV(C^n)$$

If we use a TVD method, then

$$TV(C^n) \leq TV(C^0) \leq TV(C(x,t_0))$$

for all $n \geq 0$.

One difficulty associated with numerical approximations of discontinuous solutions is that oscillations may appear near the discontinuity. With the TVD requirements, these oscillations are eliminated since any of these oscillations in the solution would give a larger total variation. This means in particular that oscillations cannot arise near an isolated propagating discontinuity if the initial data are monotonic.

In a flux-limiter method, we attempt to hybridize the high-order flux, which works well in smooth regions, and the low-order upwind flux, which behaves well near discontinuities, into a single flux that becomes the high-order flux in smooth regions and the low-order upwind flux near discontinuities. The hybridizing is controlled by the limiter function, which allows the scheme to have the greatest extent of higher-order accuracy under the TVD constraint. Applying TVD conditions to flux function, we can have the following expression for flux limiter (Liu, 1993; Liu *et al.*, 1995):

$$\varphi_i = \begin{cases} 0 & r_i \in (-\infty, 0) \\ r_i & r_i \in (0, b_i/(1-a_i)) \\ a_i r_i + b_i & r_i \in (b_i/(1-a_i), (1-b_i)/a_i) \\ 1 & r_i \in ((1-b_i)/a_i, +\infty) \end{cases}$$

3.5 Governing Equations

The spatial domain of the simulator is a rectangular prism and the Cartesian coordinate system used is referred to as (x, y, z). The finite-difference grid is block-centered and numbered from 1 to $N_x N_y N_z$, where N_x, N_y, and N_z correspond to the number of gridblocks in each direction. The volume of the m^{th} block (i, j, k) is $\Delta V_m = \Delta x_m \Delta y_m \Delta z_m$.

Most variables, including pressure, concentrations, adsorbed concentrations, saturations, capillary pressures, and phase properties such as density, viscosity, interfacial tension, and relative permeabilities are calculated and stored at gridblock centers. Some auxiliary variables, such as transmissibilities and phase velocities, are evaluated at the faces between gridblocks.

Applying the finite-difference approximations to the mass-conservation equations and the pressure equation, we obtain a system of finite-difference equations.

The component conservation equation for component κ at gridpoint m is

$$(F_{a\kappa})_m^{n+1} + \Delta t^{n+1}(F_{t\kappa} + F_{s\kappa})_m^{n+1}/2 = (F_{a\kappa})_m^n - \Delta t^{n+1}(F_{t\kappa} + F_{s\kappa})_m^n/2.$$

$F_{a\kappa}$ is the total accumulation term

$$(F_{a\kappa})_m = \left\{\left[\left(1 - \sum_{\kappa=1}^{n_{cv}} \hat{C}_\kappa\right)C_\kappa + \hat{C}_\kappa\right]\phi_R \Delta V\left[1 + (C_\kappa + C_\kappa^0)\Delta P\right]\right\}_m,$$

and $F_{t\kappa}$ is the total transport term.

$$(F_{t\kappa})_m = \Delta y_j \Delta z_k\left[(f_{t\kappa})_{i+1/2} - (f_{t\kappa})_{i-1/2}\right] + \Delta z_k \Delta x_i\left[(f_{t\kappa})_{j+1/2} - (f_{t\kappa})_{j-1/2}\right]$$
$$+ \Delta x_i \Delta y_j\left[(f_{t\kappa})_{k+1/2} - (f_{t\kappa})_{k-1/2}\right]$$

where $f_{t\kappa}$ includes both dispersive and convective fluxes. In the x direction

$$(f_{t\kappa})_{i+1/2} = \sum_{\ell=1}^{n_p}\left[(1 + C_\kappa^0 \Delta P)(C_{\kappa\ell} u_{x\ell} + N_{x\kappa\ell})\right]_{i+1/2}$$

and for $(u_{x\ell})_{i+1/2} > 0$, we compute $(C_{\kappa\ell})_{i+1/2}$ and $(u_{x\ell})_{i+1/2}$ by

$$(C_{\kappa\ell})_{i+1/2} = (C_{\kappa\ell})_i + \varphi\left[r(C_{\kappa\ell})\right]_{i+1/2}\left[(C_{\kappa\ell})_{i+1} - (C_{\kappa\ell})_i\right]$$
$$(u_{x\ell})_{i+1/2} = (T_x)_{i+1/2}(\lambda_\ell)_{i+1/2}\left[(P_\ell)_i - (P_\ell)_{i+1} + (\gamma_\ell)_{i+1/2}(D_i - D_{i+1})\right]$$

where T and λ are transmissibility and mobility

$$(T_x)_{i+1/2} = 2/\left[(\Delta x)_{i+1}/(k_x)_{i+1} + (\Delta x)_i/(k_x)_i\right]$$
$$(\lambda_\ell)_{i+1/2} = (\lambda_\ell)_i + \varphi\left[r(\lambda_\ell)\right]_{i+1/2}\left[(\lambda_\ell)_{i+1} - (\lambda_\ell)_i\right]$$

and the specific weight at the interblock boundary is approximated by pore-volume weighting:

$$(\gamma_\ell)_{i+1/2} = \frac{(V_p)_i(\gamma_\ell)_i + (V_p)_{i+1}(\gamma_\ell)_{i+1}}{(V_p)_i + (V_p)_{i+1}}$$

The mobility term here includes relative permeability, viscosity, and permeability reduction

$$\lambda_\ell = \frac{k_{r\ell}}{\mu_\ell R_k}$$

and its derivative is computed by

$$\frac{1}{\lambda_\ell}\frac{\partial \lambda_\ell}{\partial C_i} = \frac{1}{k_{r\ell}}\frac{\partial k_{r\ell}}{\partial C_i} - \frac{1}{\mu_\ell}\frac{\partial \mu_\ell}{\partial C_i} - \frac{1}{R_k}\frac{\partial R_k}{\partial C_i}$$

Dispersive flux in the x direction for $(u_{x\ell})_{i+1/2} > 0$ is given by

$$(N_{x\kappa\ell})_{i+1/2} = (K_{xx\kappa\ell})_m \left[(C_{\kappa\ell})_i - (C_{\kappa\ell})_{i+1}\right] / \left[(\Delta x_i + \Delta x_{i+1})/2\right]$$
$$+ (K_{xy\kappa\ell})_m \left[(C_{\kappa\ell})_{j-1} - (C_{\kappa\ell})_{j+1}\right] / \left[(\Delta y_{j-1} + \Delta y_{j+1})/2 + \Delta y_j\right]$$
$$+ (K_{xz\kappa\ell})_m \left[(C_{\kappa\ell})_{k-1} - (C_{k\ell})_{j+1}\right] / \left[(\Delta z_{k-1} + \Delta z_{k+1})/2 + \Delta z_k\right]$$

$F_{s\kappa}$ is the source and sink term, which includes wells constrained by either rate or pressure. The pressure equation at gridpoint m is

$$(F_a)_m^{n+1} + \Delta t^{n+1}(F_t + F_s)_m^{n+1}/2 = (F_a)_m^n - \Delta t^{n+1}(F_t + F_s)_m^n/2$$

where the accumulation term F_a is

$$(F_a)_m = \left\{ C_f + \sum_{\kappa=1}^{n_{cv}} C_\kappa^0 \left[\left(1 - \sum_{\kappa=1}^{n_{cv}} \hat{C}_\kappa\right) C_\kappa + \hat{C}_\kappa \right] \right\}_m (\phi_R \Delta V \Delta P)_m$$

and the transport term F_t is

$$(F_t)_m = \Delta y_j \Delta z_k \left[(f_t)_{i+1/2} - (f_t)_{i-1/2}\right] + \Delta z_k \Delta x_i \left[(f_t)_{j+1/2} - (f_t)_{j-1/2}\right]$$
$$+ \Delta x_i \Delta y_j \left[(f_t)_{k+1/2} - (f_t)_{k-1/2}\right]$$

where f_t is the convective flux and in the x direction for $(u_{x\ell})_{i+1/2} > 0$ is given by

$$(f_t)_{i+1/2} = \sum_{\ell=1}^{n_p} \left[\left(1 + \Delta P \sum_{\kappa=1}^{n_{cv}} C_\kappa^0 C_{\kappa\ell}\right) u_{x\ell} \right]_{i+1/2}$$

3.6 Well Models

The inflow and outflow conditions in the simulator are specified as well conditions. The ways in which wells are handled in the simulator have a significant impact on the simulation results. The following well options have been included in the simulator:

1. An arbitrary number of injectors and producers in any gridblock can be specified.
2. Wells can be completed parallel to any coordinate direction with full or partial completion.
3. Both the injectors and producers can be shut in or opened and well type can be switched anytime during the simulation run.
4. Multiple slugs with different component concentrations can be specified for each injector.
5. Well constraint can be specified either by constant rate or constant flowing bottomhole pressure.

In an areal flow, the well model is interpreted as a point-source or -sink term, but in cross-sectional flow, the well model is interpreted as a line-source or -sink term, and distributing the total flow into each layer is necessary. There are two different rate allocation methods: the mobility allocation method and the potential allocation method (Nolen and Berry, 1972; Aziz and Settari,

1979). The mobility allocation method assures that the difference of potential between the wellbore and the gridblock is the same for all blocks communicating with the given well. The rate is therefore allocated to each layer according to the ratios of mobility in each layer. The potential method accounts for the fact that the potential difference between the wellbore and the gridblock containing the well may differ in each layer so that the potential difference is taken into account and the flow rate entering into each layer is according to the ratios of both mobility and potential. In a layered reservoir, the fluid flowing in the vertical direction depends on the degree of communication with adjacent layers. If the adjacent layers are well-communicating, the fluid flows vertically easily; the resistance to fluid flow is low and as a result, the potential difference between will be small. Conversely, if the adjacent layers have poor communication, the fluid will hardly flow vertically; the resistance to flow is high and so is the potential difference. Accordingly, the potential difference is not always the same for all layers and the mobility allocation method is not suitable then. We have adopted the potential allocation method in the simulator.

3.6.1 Phase-Productivity Index

For one-dimensional (x direction) and cross-sectional (x-z cross-section) simulations, the phase-productivity index is given by

$$PI_\ell = \frac{\sqrt{k_x k_y}\,\Delta y \Delta z}{\Delta x}\lambda_\ell$$

For two-dimensional areal and three-dimensional simulations, the phase-productivity index is computed as

$$PI_\ell = \frac{\sqrt{k_x k_y}\,\Delta z}{\ln\left(\frac{r_o}{r_w}\right)}\lambda_\ell$$

The equivalent radius, r_0, is calculated using Peaceman's model:

$$r_o = 0.28\sqrt{\frac{\sqrt{k_x/k_y}\,\Delta y^2 + \sqrt{k_y/k_x}\,\Delta x^2}{\sqrt[4]{k_x/k_y} + \sqrt[4]{k_y/k_x}}}$$

The well is assumed to be at the center of the gridblock that contains the well.

3.6.2 Gravity Head

The gravity effect is considered in computing the well bottomhole flowing pressure by

$$(P_w)_m = (P_w)_1 + H_m$$

where H is the gravity head

$$H_m = \gamma_1 \frac{\Delta D_1}{2} + \gamma_m \frac{\Delta D_m}{2} + \sum_{i=2}^{m-1} \gamma_i \Delta D_i$$

and

$$\gamma_m = \frac{\sum_{\ell=1}^{n_p} (\lambda_\ell \gamma_\ell)_m}{\sum_{\ell=1}^{n_p} (\lambda_\ell)_m}$$

3.6.3 Bottomhole Pressure for Rate-Constrained Wells

The bottomhole pressure for rate-constrained wells is computed by

$$(P_w)_1 = \frac{Q_w + \sum_{m=1}^{N_{wb}} \left[\sum_{\ell=1}^{n_p} PI_\ell (P_\ell - H) \right]_m}{\sum_{m=1}^{N_{wb}} \left(\sum_{\ell=1}^{n_p} PI_\ell \right)_m}$$

where Q_w is the total flow rate and N_{wb} is the number of gridblocks that contain the well.

3.6.4 Injection Rate

The flow rate of component κ at the m-th gridblock in a injector is computed by

$$(q_\kappa)_m = C_{\kappa w} \left(\sum_{\ell=1}^{n_p} PI_\ell (P_w - P_\ell) \right)_m$$

For a rate-constrained injector, $C_{\kappa w}$ is given by

$$C_{\kappa w} = \frac{\sum_{\ell=1}^{n_p} C_{\kappa \ell w} q_{\ell w}}{\sum_{\ell=1}^{n_p} q_{\ell w}}$$

and $q_{\ell w}$ is the injection rate of each phase.

$$C_{\kappa w} = \sum_{\ell=1}^{n_p} C_{\kappa \ell w} f_{\ell w}$$

For a pressure-constrained injector, $C_{\kappa w}$ is given by

$$C_{\kappa w} = \sum_{\ell=1}^{n_p} C_{\kappa \ell w} f_{\ell w}$$

and $f_{\ell w}$ is the fractional flow rate of each phase.

3.6.5 Production Rate

The flow rate of component κ at the m-th gridblock in a producer is computed by

$$(q_\kappa)_m = \left(\sum_{\ell=1}^{n_p} C_{\kappa\ell} PI_\ell (P_w - P_\ell) \right)_m$$

3.7 Solution of the Nonlinear System of Equations

We have derived a system of finite-difference equations in their residual form. At each gridpoint, there are total of n_c residual equations consisting of n_c-1 component conservation equations and one pressure equation. We first need to define a set of independent variables or primary variables. Besides the reference-phase pressure, we choose n_c-1 relevant total concentrations as other primary variables. The remaining total concentration, phase saturations, phase concentrations, pressures, and physical properties are secondary variables and obtained using constitutive relations.

The nonlinear system of residual equations is linearized and solved using a Newton iteration, defined by

$$J \delta P = -f,$$

where J is the Jacobian matrix formed by differentiating the nonlinear system of residual equations $f(P)$ with respect to the primary variables P. The Jacobian matrix and the residual equations are updated at the end of each iteration, and the iteration continues until the relative changes in the primary variables between two successive approximations are small enough to satisfy given tolerance criteria.

For a three-dimensional simulation problem of n_c components using $N_x N_y N_z$ gridblocks, the total number of equations is $n_c N_x N_y N_z$. The Jacobian matrix is constructed such that the primary variable indices are the faster-changing indices in the solution vector. With the high-order scheme, a total of 25 gridpoints may be involved in the finite-difference equations (Fig. 3.2) and a maximum number of $25n_c - 6$ partial differentiation computations may be required for each equation to build the Jacobian matrix. The matrix structure of simulating a three-dimensional, two-component problem using the high-order scheme and a 5x5x3 grid is shown in Figure 3.3.

For simulation problems with rate-constrained multicell wells, the constraint conditions provide additional equations, and the bottomhole pressure of each well needs to be solved at the same time along with all primary variables. A special solution method is adopted in the simulator and described here.

We set the system of equations of primary variables and bottomhole pressures as

$$\begin{bmatrix} A_{11} & A_{12} \\ A_{21} & A_{22} \end{bmatrix} \begin{bmatrix} u_1 \\ u_2 \end{bmatrix} = \begin{bmatrix} b_1 \\ b_2 \end{bmatrix}$$

with the components defined as

- A_{11} main Jacobian matrix with a size of n_t by n_t
- b_1 main right-side vector with a size of n_t
- A_{12} matrix formed by derivatives of allocated injection rate with respect to bottomhole pressures with a size of n_t by n_w
- A_{21} matrix formed by derivatives of constraint conditions with respect to primary variables with a size of n_w by n_t
- A_{22} matrix formed by derivatives of constraint conditions with respect to bottomhole pressures with a size of n_w by n_w
- b_2 Vector formed by $-f_{p_w}$ with a size of n_w
- u_1 Solution vector of primary variables with a size of n_t

u_2 Solution vector of bottomhole pressures with a size of n_w

We can rewrite the system as

$$\begin{cases}(A_{22}-A_{21}A_{11}^{-1}A_{12})u_2=b_2-A_{21}A_{11}^{-1}b_1\\ A_{11}u_1=b_1-A_{12}u_2\end{cases}$$

and solve for u_1 and u_2 by the procedure 1 through 7.

1 Solve for interim solution ξ from a set of system of equations $A_{11}\xi=A_{12}$

2 Solve for interim solution η from the system of equations $A_{11}\eta=b_1$

3 Compute $\tilde{A}_{22}=A_{22}-A_{21}\xi$

4 Compute $\tilde{b}_2=b_2-A_{21}\eta$

5 Solve for solution u_2 from the system of equations $\tilde{A}_{22}u_2=\tilde{b}_2$

6 Compute $\tilde{b}_1=b_1-A_{12}u_2$

7 Solve for solution u_1 from the system of equations $A_{11}u_1=\tilde{b}_1$

The solution of the linear system of equations represents the most costly aspect of a fully implicit simulator. Using an efficient solution solver will greatly improve the efficiency of the simulator.

3.8 Timestepping Algorithms

The choice of timestep size is dictated by accuracy considerations and stability constraints. Since a fully implicit solution technique is employed, the numerical solution is stable for all timestep sizes. There are, however, other limitations that must be considered. For example, Newton's method is guaranteed to converge only from good starting guesses. For a simulation problem, there may be some times when solution gradients are very large, such as near breakthrough. Simply using the solution of the last timestep as the starting guess for the current timestep may not converge. In addition, some important physical phenomena may be missed by using an arbitrarily large timestep size.

Using the past information of the relative changes in the primary variables to decide the current timestep size is a strategy employed by most timestepping algorithms. The timestep size selection is based on the information from the most recent iterations and user-specified maximum and minimum timestep sizes denoted Δt_{max} and Δt_{min}, such that the current timestep size is limited.

Besides constant timestepping, which often requires a smaller timestep size to guarantee convergence and takes more simulation time, we employ the following timestepping algorithm for the simulator:

$$\Delta t^{n+1} = \min\left\{\Delta t_{max}, \max\left[\frac{\Delta u_{lim}\Delta t^n}{\max\limits_{\kappa=1}^{n_c}\left(\frac{u_\kappa^n - u_\kappa^{n-1}}{u_\kappa^{n-1}}\right)}, \Delta t_{min}\right]\right\}$$

where u denotes the primary variables and Δu_{lim} is a user-specified tolerance of relative changes of primary variables during two consecutive timesteps.

The timestep size chosen by any of the timestepping selection algorithms is not guaranteed to produce convergence. A recovery feature is included in the simulator to continue the simulation in case an iteration fails, indicated when iteration steps exceed the maximum iteration numbers allowed by the user. It stores the necessary information of the last timestep, automatically reduces the current timestep size, and restarts the iteration until a successful iteration is completed with a suitable timestep size.

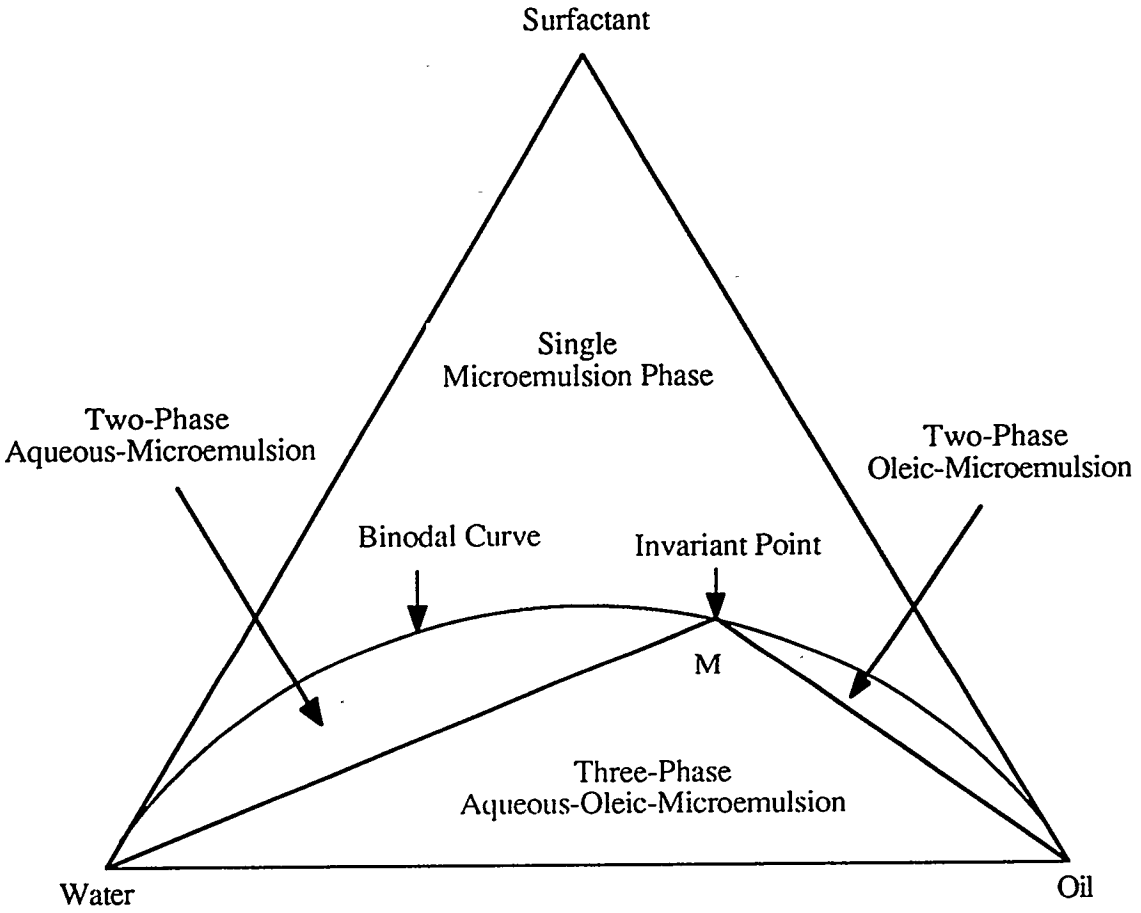


Fig. 3.1. Schematic representation of binodal curve, invariant point, and different phase regions in a ternary diagram.

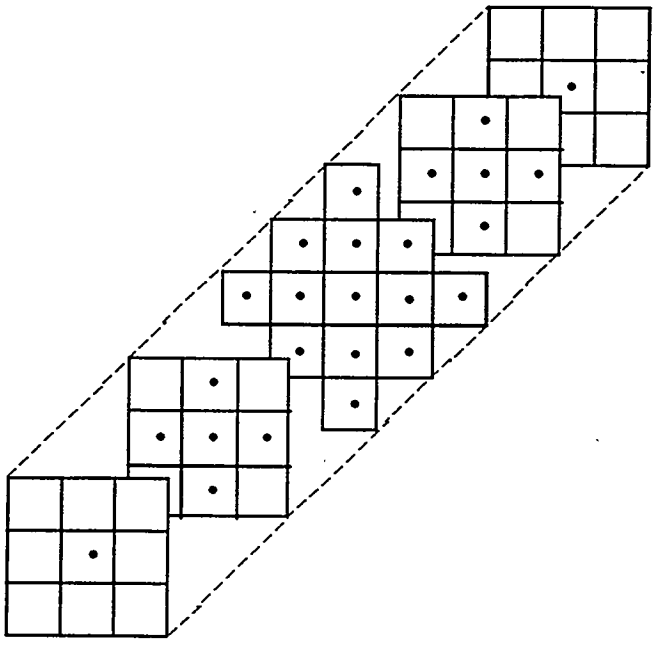


Fig. 3.2. Gridpoints used in the high-order finite-difference scheme.

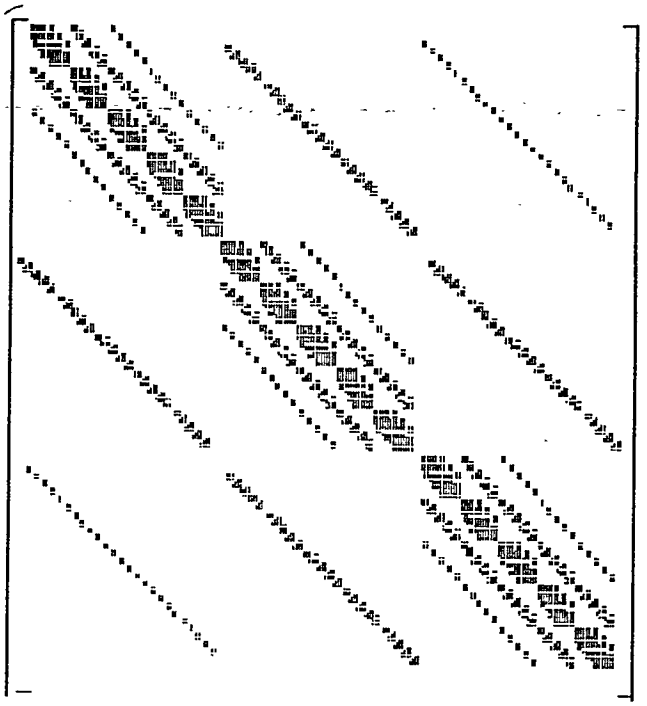


Fig. 3.3. Matrix structure for a three-dimensional, two-component problem using the fully implicit high-order method with 5x5x3 gridblocks.

4. Simulation Results

4.1 One-Dimensional Convection-Diffusion Problem

Simulation of one-dimensional tracer flood was conducted using 100 gridblocks and the tracer profiles at 0.5 pore volumes injected were obtained.

4.1.1 Comparison with Analytical Solutions

To establish the validity of the formulation of the conservation equations, the results were compared with the analytical solution of the convection-diffusion equation. Two runs were made, one with a Peclet number (the ratio of convective to dispersive transport) of 100 and the other one of 1000. The comparisons are shown in Fig. 4.1 and the agreement is good for both Peclet numbers. The Courant numbers (measure of dimensionless timestep size) for both runs are 0.5.

4.1.2 Comparison with Low-Order Temporal Scheme

Since large timestep size can be used for a implicit simulator, time-truncation error becomes more important, and higher accuracy is required for the time-discretization scheme. A second-order temporal discretization scheme has been used in our simulator and described earlier. We ran the problem of Peclet number of 1000 with a large timestep size of Courant number 1.5 and compared the results with those using the first-order time scheme. The comparison is shown in Fig. 4.2; we find severe numerical front-smearing effects with the lower-order time scheme.

4.1.3 Comparison with Low-Order Spatial Scheme

Lower-order space discretization one- and two-point upstream schemes are available in the simulator for comparison purposes. These are the conventional finite-difference schemes employed by most fully implicit simulators. We ran the problem of Peclet number of 100 with one-point upstream weighting scheme and used timestep sizes of Courant numbers ranging from 0.05 to 3. An error analysis was conducted to compare the difference and is shown in Fig. 4.3. Note that we used the same high-order temporal discretization scheme here, and the errors were mainly caused by different spatial discretization schemes unless very large timestep sizes were used, when time-truncation errors became dominant.

4.1.4 Comparison with IMPES method

The problem of Peclet number 100 was simulated using the IMPES method with different timestep sizes, and the numerical errors were compared with those using the implicit method. Figure 4.4 shows that the errors of the IMPES method increase dramatically as timestep size increases, and the method becomes unstable as the Courant number approaches 1. The errors of implicit method are almost the same at small Courant numbers, which can be explained by the second-order temporal accuracy of the simulator.

4.2 One-Dimensional Waterflood

Simulations of one-dimensional waterflood were conducted using 100 gridblocks.

4.2.1 Comparison with Buckley-Leverett Solution

The Buckley-Leverett equation (Buckley and Leverett, 1958) describes the problem of one-dimensional two-phase flow in a porous medium:

$$S_t+f_x(S) = 0$$

where the flux f(S) is a known function of S, the saturation of one phase. The initial condition S(x,0) = 0 and a boundary condition S(0,t) = 1 are applied. Without some form of dissipation, the equation is hyperbolic in nature.

The fractional-flow function for the Buckley-Leverett problem tested is

$$f(S) = S^2/[S^2+(1-S)^2/3]$$

This gives a mobility ratio of 3 with the front at position x = 0.3 at time t = 0.2. Simulation was conducted using a Courant number of 0.5 and the water saturation profile at 0.2 pore volumes injected is shown in Fig. 4.5. The simulated solution matches the analytical solution very well except for small numerical smearing at the displacement fronts.

4.2.2 Comparison with IMPES method

The IMPES method is less stable when simulating both convection-dominated and dissipation-dominated problems. The dissipation is mainly provided by dispersive forces for miscible displacements and by capillary forces for immiscible displacements. The problem with a Rapoport and Leas number (the ratio of viscous to capillary forces) (Rapoport and Leas, 1953, 1958) of 5 is simulated using both methods with Courant numbers of 0.1 and 0.5. Figures 4.6 and 4.7 show the results of two methods match well at a small timestep size of Courant number 0.1 and the instability of the IMPES method at a large timestep size of Courant number 0.5.

4.2.3 Capillary End Effect

The boundary conditions on the outflow boundary coupled with the requirement that the phase pressure be continuous across the boundary results in a phenomenon called the "capillary end effect" (Richardson *et al.*, 1952; Amyx *et al.*, 1960). An analytical solution of the saturation profile along a one-dimensional, homogeneous porous medium is given by Richardson *et al.* (1952). A one-dimensional simulation example by Chang (1990) is used to check the implementation of the outflow boundary condition in the simulator. The problem has a Rapoport and Leas number of 2.78 and a residual oil saturation of 0.35. Figure 4.8 shows the good agreement between the analytical solution and the simulation results. A Courant number of 1 was used.

4.2.4 Gravity-Inversion Problem

A gravity-induced countercurrent flow or gravity-inversion problem was simulated to test the gravity model in the simulator. We assume a vertical reservoir with both the injector and producer placed at the bottom. The reservoir was initially filled with heavy water and then injected with light oil. The gravity number, a ratio of gravity to viscous pressure gradients based on the endpoint oil relative permeability (Lake, 1989), is 22. The water saturation profile is shown in Fig. 4.9 and compared with the analytical solution. The Courant number used is 0.2.

4.3 One-Dimensional Polymerflood

One-dimensional polymerflood simulations were conducted. The problem was the same as that simulated by Holing *et al.* (1990). The porous medium was initially filled with 70% oleic-phase fluid and 30% aqueous-phase fluid with 0.9 wt% polymer, then injected with 100% aqueous-phase fluid with 0.1 wt% polymer. There was no adsorption, permeability reduction, or physical dispersion. Inaccessible pore volume, and capillary and gravity effects were also

neglected. The input data for this run are listed in Table 4.1. One hundred gridblocks and a Courant number of 0.5 were used for the simulation.

4.3.1 Comparison with Analytical Solution

The analytical solutions for this problem were calculated using fractional-flow theory (Pope, 1980). Figure 4.10 shows the simulation results. Good resolution in both the water saturation and polymer concentration fronts is obtained and the numerical solution matches the analytical solution well.

4.3.2 Comparison with Low-Order Spatial Scheme

Figure 4.11 shows the results simulated using the one-point upstream scheme. In contrast to the high-order scheme, both the water saturation and polymer concentration shocks are spread out, which results in inaccurate prediction of both recoveries and breakthrough times and leads to erroneous conclusions.

4.3.3 Comparison with IMPES Method

Under the same conditions used by the implicit simulator, the problem was simulated using the IMPES simulator and unstable results are obtained and shown in Fig. 4.12.

4.3.4 Effect of TVD Flux Limiting

Figure 4.13 demonstrates the importance of flux limiting. Both overshoots and undershoots appear in the water saturation and polymer concentration profiles obtained using the high-order scheme without flux-limiting.

4.3.5 Polymer-Property Model Verification

To verify the polymer-property model in the simulator, simulation including complete polymer properties was conducted and production histories of oil recovery, water cut, and effluent polymer concentration up to 1.5 pore volumes injected were compared with those of UTCHEM IMPES simulator and are shown in Fig. 4.14. The two results agree quite well except for some apparent numerical effects in the water-cut curve of the IMPES result. Two simulations used the same 80 gridblocks and a Courant number of 0.1 for the IMPES simulation and 0.5 for the implicit simulation. A complete description of the input is given in Table 4.2.

4.4 Two-Dimensional Tracer Flood

4.4.1 Comparison with Analytical Solution

An analytical solution is available for an ideal tracer flow at unit mobility ratio for a homogeneous five-spot well pattern (Abbaszadeh-Dehghani and Brigham, 1984). The simulation domain is one-quarter of the well pattern with a length of 330 ft. A 30x30 grid and a Courant number of 1 were used to simulate the flow of a 2% PV tracer slug with a longitudinal dispersivity of 0.66 ft and a Peclet number of 500. The effluent tracer concentration is normalized by the product of slug size and the square root of the Peclet number. Figure 4.15 shows a comparison of the analytical solution with the simulation results. The overall match is very good, and the small discrepancy between the two solutions can be reduced using finer grids and smaller timestep sizes.

4.4.2 Hydraulic-Fracture Diagnostic Test

This set of simulations was prepared for future simulations of hydraulic-fracture diagnostic tests, in which very high contrasts in permeability and porosity exist and a very nonuniform grid needs to be used. In the simulation shown, the ratio of high permeability to low permeability is 1200, high porosity to low porosity is 67, large gridblock size to small gridblock size in the x direction is 1000 and in the y direction is 100. Tracer responses were observed from two horizontal wells. The simulations were first conducted using both IMPES and implicit methods with variable timesteps and a 10x16 grid . The timestep size limits are same for both methods. The results of tracer responses from one of the producers are shown in Fig. 4.16 and the agreement is good. Records of timestep size actually used during the simulations are shown in Fig. 4.17. We notice that the curve for the implicit method is smoother than the other one, which verifies its numerical stability advantage over the IMPES method. For the implicit method, the results are good at a Courant number of 10 (Fig. 4.18), while the IMPES method fails at a Courant number of 1.3.

4.5 Two-Dimensional Waterflood

Two-dimensional waterflood simulation was conducted with reservoir dimensions, properties, and well pattern the same as those for the case of tracer flood in a five-spot pattern. The reservoir has an initial oil saturation of 0.8. The mobilities of water and oil are characterized by S^2 and $(1-S)^2/2$, where S is the water saturation. A 10x10 grid was used. Figure 4.12 shows the results of the IMPES formulation, which failed at a Courant number of 1, while the results of the fully implicit formulation are almost the same at Courant numbers of 0.1 and 3.

4.5.1 Comparison with IMPES Method

Figures 4.19 and 4.20 show the simulation results of oil recovery, water-oil ratio, and water cut using the IMPES and the fully implicit methods. The IMPES method failed at a Courant number of 1, while the fully implicit method is good even at a Courant number of 3 and its results are almost the same as those of Courant number 0.1.

4.5.2 Comparison with Low-Order Spatial Scheme

The simulation was also conducted using the one-point upstream scheme (Fig. 4.21). Water cut and water-oil-ratio curves show early breakthroughs compared with the results of the high-resolution method.

4.6 Two-Dimensional Polymerflood

4.6.1 Cross-Sectional Simulation

The simulation domain is 10 ft in the x direction, 1 ft in the y direction, and 5 ft in the z direction with a porosity of 0.2. The permeabilities in each direction are the same, 200 md. A 10x1x5 uniform grid was used. An injector was placed from (1,1,1) to (1,1,5) and a producer goes from (5,1,1) to (5,1,5) (Fig. 4.22a). The reservoir has an initial oil saturation of 0.8. The mobilities of aqueous and oleic phases are characterized by S^2/μ_a and $(1-S)^2/\mu_o$, where S is the aqueous phase saturation and μ_a and μ_o are the aqueous and oleic phase viscosities, respectively. μ_o equals 2 cp and μ_1 is calculated by $(1+10C_{41})$ cp, where C_{41} is the polymer concentration in the aqueous phase. The longitudinal dispersivity is 0.1 ft. Capillary pressure endpoint is 3.16 psi(darcy)$^{1/2}$, corresponding to a Rapoport and Leas number of 5. 0.1 wt% polymer was injected continuously for 1 day with an injection rate of 10 ft^3/day, which gave a total injection of 1 pore volume.

The results of oil recovery, water cut, and effluent normalized polymer concentration were obtained. At a timestep size of 0.001 days (Courant number of 0.01), the agreement between the results of the IMPES simulator and the implicit simulator is good (Fig. 4.23). At a timestep size of 0.01 days (Courant number of 0.1), the results of the IMPES simulator show some differences in the polymer concentration curves (Fig. 4.24) and water-cut curves (Fig. 4.25) compared with the results at a Courant number of 0.01, and become unstable at a timestep size of 0.05 days (Courant number of 0.5), as characterized by oscillations in all recovery curves. For the fully implicit simulator, the results show nearly no changes in all recovery curves (Figs. 4.26 and 4.27) at larger timestep sizes.

4.6.2 Potential Rate Allocation Method

To test our well model and to compare the mobility rate-allocation method with the potential rate-allocation method, we used the same two-dimensional, cross-sectional polymerflood test case except that the production well was only completed at the top layer (Fig. 4.22b) to induce the vertical pressure difference and vertical flow. We simulated the case using UTCHEM5.3 for the mobility rate-allocation method and the fully implicit simulator for the potential rate-allocation method. A small timestep size of 0.001 days (Courant number of 0.01) was used for UTCHEM simulation to avoid numerical effects.

We first used a vertical permeability of 200 md, which is equal to the horizontal permeability, assuming the degree of communication with adjacent layers is relatively good in this case. Figure 4.28 shows the polymer concentration and oil production histories, and Figs. 4.29 and 4.30 show the water saturation and polymer concentration distributions at 0.5 pore volumes injected. There is little difference using the two rate-allocation methods for this case. We next used a vertical permeability of 2 md, which is 0.01 times the horizontal permeability, and consider this to be a poor communicating case. Figure 4.31 indicates apparent differences in the polymer concentration and oil production histories using the two rate-allocation methods. These differences can also be found in the water saturation and polymer concentration distributions (Figs. 4.32 and 4.33), where the mobility method gives a more uniform displacement than the potential method.

4.6.3 Polymer-Property Model Verification

To verify the simulator's polymer-property model for the two-dimensional problem, simulations including complete polymer properties were conducted. A polymer slug of 1/2 pore volume with polymer concentration of 0.1 wt% was injected and followed by chase water of another 1/2 pore volume. A description of the input is given in Table 4.3. The production histories of oil recovery, water cut, and effluent polymer concentration were compared with those of UTCHEM IMPES simulator and are shown in Fig. 4.34, and the two results agree quite well at a Courant number of 0.1. A larger timestep size of Courant number of 0.5 was then used for both methods and the results are shown in Figs. 4.35 and 4.36. The IMPES method produced quite different water cut and polymer slug curves from those at the small timestep size, while results from the implicit method have almost no change.

4.7 Two-Dimensional Surfactant Flood

A two-dimensional surfactant flood simulation was conducted. Surfactant related physical properties included in the test were aqueous-oleic-microemulsion phase behavior, surfactant adsorption, interfacial tension, compositional phase viscosity, relative permeability, and capillary desaturation. A description of the input data is given in Table 4.4.

A timestep size of 80 days, corresponding to a Courant number of 1, was used for the implicit simulator and the production histories of oil recovery, oil cut, and surfactant concentration were compared with those of the IMPES simulator using a timestep size of 0.8 days (Courant number of 0.01) (Fig. 4.37). The oil recovery and oil-cut curves agree well in general. The IMPES

result of surfactant concentration has severe numerical effects, characterized by oscillations, which causes a low oil recovery as the simulation closed to 3 pore volumes injected. There were some improvements as we reduced the timestep sizes to 0.08 days (Courant number of 0.001) (Fig. 4.38) and 0.008 days (Courant number of 0.0001), respectively (Fig. 4.39). The numerical effects, however, can still be observed.

4.8 Three-Dimensional Tracer Flood

4.8.1 Comparison with IMPES Method

The simulation domain is a cube with an edge of 5 ft and a porosity of 0.2. The permeabilities in each direction are the same, 200 md. The injected fluid with tracer has properties identical to those of the resident fluid in the domain. A 5x5x5 uniform grid was used with an injection well at (1,1,1) and a production well at (5,5,5) (Fig. 4.40). Injection rate was 0.2 ft^3/day and the total injection time was 375 days, which gave a total injection of 3 pore volumes. One test had a longitudinal dispersivity of 0.1 ft and the other, 1 ft, which gives Peclet numbers of 5 and 50, respectively. The transverse dispersivity was 0 for all tests.

To establish the validity of the three-dimensional formulation of the conservation equations, simulations were conducted using the UTCHEM5.3 and the fully implicit simulator with the same timestep size of 0.5 days, corresponding to a Courant number of 0.5. Tracer production histories are shown in Fig. 4.41. Good agreement between the two simulator results was obtained for both Peclet numbers. We then increased the timestep size to compare the stabilities of the IMPES method and fully implicit method. Figure 4.42 gives the results of the IMPES simulator and shows that the simulator produced unstable results at a timestep size of 0.6 days (Courant number 0.6) for a Peclet number of 5 and at 1.1 days (Courant number 1.1) for a Peclet number of 50. Figure 4.43 shows the results of the fully implicit simulator. Contrary to the IMPES simulator results, the stability is preserved even at a timestep size of 10 days (Courant number of 10), and there are no significant differences between the results using the timestep sizes of 0.5, 5, and 10 days (Courant numbers of 0.5, 5, and 10) because of the high-order time accuracy.

4.8.2 Comparison with Conventional Schemes

Results are given here to show the numerical effects of the low-order scheme or the high-order scheme without flux-limiting for three-dimensional problems. We tested the same three-dimensional convection-diffusion problem with a Peclet number of 500 using the high-order scheme without flux limiting and one-point upstream scheme with a Courant number of 5. Figure 4.44 gives the normalized tracer concentration at the cubic center and clearly shows the numerical overshoots created by the high-order scheme without flux limiting and numerical smearing created by the one-point upstream scheme.

4.8.3 Nonuniform Grid Test

The grid shown in Fig. 4.45 was used to verify our nonuniform grid formulation for the three-dimensional problem. We define an expansion ratio R, the ratio of the adjacent gridblock size, to measure the grid nonuniformity. Figure 4.46 shows the tracer production-history results. The results of using the uniform grid are almost identical to those of using the nonuniform grid with an expansion ratio of 10. A timestep size with an average Courant number of 0.5 was used for both grids. For the IMPES method, because of its Courant stability restriction, the smaller gridblocks cause stability problems when using grids of larger expansion ratio. Figure 4.47 demonstrates that for the same problem, the IMPES method becomes unstable at an expansion ratio of 1.85 with the same timestep size used by the fully implicit simulator.

4.9 Three-Dimensional Polymerflood with Horizontal Wells

4.9.1 Horizontal-Well Model Verification

A simulation of three-dimensional polymerflood using a horizontal well was conducted to verify the horizontal well model in the simulator. The simulation domain is 165 ft in the x direction, 165 ft in the y direction, and 25 ft in the z direction with a porosity of 0.25. The permeabilities in each direction are 200 md. A 5x5x5 uniform grid was used. A horizontal injector was placed from (1,1,3) to (5, 1, 3) and a vertical producer from (3,5,1) to (3,5,5) (Fig. 4.48). The reservoir fluid initial conditions and properties are the same as those of the two-dimensional simulation case. 0.1 wt% polymer was injected continuously for 90.75 days with an injection rate of 1,875 ft^3/day, which gave a total injection of 1 pore volume.

The results of oil recovery, water cut, and effluent normalized polymer concentration were obtained using the UTCHEM5.3 and the fully implicit simulator with the TVD high-order scheme. At a timestep size of 0.363 days (Courant number 0.1), the two simulators gave almost the same results (Fig. 4.49)

4.9.2 Comparison with IMPES method

At a larger timestep size of 4 days (Courant number 1.1), the results of the IMPES simulator became unstable, characterized by oscillations and lower oil recovery (Fig. 4.50), while the results of the fully implicit simulator show nearly no change (Fig. 4.51) in all recovery curves at larger timestep sizes of 3.63 and 7.26 days (Courant number 1.0 and 2.0).

4.10 Computational Efficiency

4.10.1 Two-Dimensional Surfactant Flood

In the case of two-dimensional surfactant flood simulations, we have show that the IMPES simulator produces unstable results, characterized by oscillations in the surfactant concentration curve. These numerical effects will inaccurately predict oil recovery. Although reducing the timestep sizes can improve the solution, the improvements are limited. In the case we have run, the results at a timestep size 0.008 days (Courant number of 0.0001) are still not as good as those of the implicit simulator (Fig. 4.39) , which used a timestep size of 80 days (Courant number of 1). The computation cost because of this numerical stability difference is huge. For the results shown in Fig. 4.39, the CPU time on a DEC-α workstation for the IMPES simulator was 8250 seconds, while for the implicit simulator it was 239 seconds, a ratio of 34.5.

4.10.2 Three-Dimensional Tracer Flood

Since solving the linear system of equations is the most costly part of the total computation of an implicit simulator, using efficient solvers can greatly improve the computational efficiency. Study has been done using both a direct solver (band-LU decomposition) and an iterative solver (ORTHOMIN with Jacobi preconditioner (Oppe *et al.*, 1988) for a three-dimensional tracer flood problem, and the results were also compared with those obtained using our IMPES simulator (UTCHEM). The comparison demonstrates the implicit simulator is more computationally efficient than the IMPES simulator when the iterative solver is used.

The reservoir simulation domain is rectangular with a size of 1000 ft x 1000 ft x 100 ft in x, y, and z directions, respectively, and a porosity of 0.2. The permeabilities in each direction are 200 md. The injected fluid with tracer has properties identical to those of the resident fluid. A 10x10x10 uniform grid was used with an injector at (1,1,1) and a producer at (10,10,10). The injection rate was 1781 bbl/day and the total injection time was 6000 days (3 pore volumes). To

establish the validity of the iterative solver used, tracer production histories obtained using the iterative solver were compared with those using the direct solver and identical results were achieved. The CPU time ratio of using the direct solver to the iterative solver is about 124 on a DEC-α workstation. We then compared the results and CPU time of the implicit simulator with those of the UTCHEM simulator. Good agreement was achieved when a small timestep size was used, 0.16 days for the UTCHEM simulator and 2 days for the implicit simulator, corresponding to Courant numbers of 0.08 and 1.0. The IMPES simulator, however, failed at a timestep size of 0.17 days, corresponding to a Courant number of 0.085, while the implicit simulator, because of its stability and the high-order time accuracy, gave good results even when using a timestep size of 200 days, corresponding to a Courant number of 100. There are no significant differences in the results using the timestep sizes of 2, 20, and 200 days, corresponding to Courant numbers of 1, 10, and 100. The CPU time for the implicit simulator using the iterative solver with a timestep size of 200 days is 614 seconds compared with 9127 seconds for the IMPES simulator with a timestep size of 0.16 days, a speedup of 14.8.

Table 4.1 Input data for Holing's one-dimensional polymerflood

Length (ft)	100
Width (ft)	1
Depth (ft)	1
Grid	100x1x1
Absolute permeability (md)	100
Porosity	1.0
Residual water saturation	0.0
Residual oil saturation	0.0
Initial water saturation	0.3
Initial polymer concentration (wt%)	0.9
Injection rate (ft^3/day)	1.0
Injected water saturation	1.0
Injected polymer concentration (wt%)	0.1
Water endpoint relative permeability	1.0
Oil endpoint relative permeability	1.0
Water relative-permeability exponent	2.0
Oil relative-permeability exponent	2.0
Water viscosity (cp)	0.5
Oil viscosity (cp)	0.35
Polymer-viscosity parameters ($wt\%^{-1}$)	
A_{p1}	2.0
A_{p2}	0.0
A_{p3}	0.0

Effects of adsorption, permeability reduction, physical dispersion, inaccessible pore volume, capillary pressure, and gravity were neglected.

Table 4.2 Input data for one-dimensional polymerflood for validating polymer properties

Parameters	Values
Dimensions of reservoir simulated	1 ft x 0.1 ft x 0.1 ft
Number of gridblocks in the x, y, and z directions	80x1x1
Permeability	3000 md
Porosity	0.25
Initial reservoir pressure	145 psi
Initial water saturation	0.6
Initial salinity expressed in total equivalent anions	0.6 meq/ml
Initial calcium ions concentration	0.1 meq/ml
Relative permeability	
Aqueous Phase:	
Residual saturation	0.15
Endpoint relative permeability	0.14
Exponent of the relative permeability curve	2.2
Oleic Phase:	
Residual saturation	0.15
Endpoint relative permeability	0.9
Exponent of the relative permeability curve	1.4
Water viscosity	0.42 cp
Oil viscosity	2.5 cp
Polymer-viscosity parameters	
AP1	70 $(wt\%)^{-1}$
AP2	100 $(wt\%)^{-2}$
AP3	10000 $(wt\%)^{-3}$
$\dot{\gamma}_c$	10
$\dot{\gamma}_{1/2}$	190 sec^{-1}
P_α	1.8
S_p	0.175
β_p	2
C_{SE1}	0.01 meq/ml
Effective porosity to polymer	0.9
Permeability-reduction factor	
b_{rk}	1000
c_{rk}	0.02
Parameters for polymer adsorption	
A_{41}	1
A_{42}	0.
B_4	100 1/wt%
Longitudinal dispersivity	0.01 (ft)
Transverse dispersivity	0.0
Bottomhole pressure for pressure-constrained producer	145 psi
Water injection rate for rate-constrained injector	0.02 (ft^3/day)
Injected polymer concentration	0.05 wt%

Table 4.3 Input data for two-dimensional polymerflood for validating polymer properties

Parameters	Values
Dimensions of reservoir simulated	1000 ft x 1000 ft x 100 ft
Number of gridblocks in the x, y, and z directions	5x5x1
Permeability	200 md
Porosity	0.2
Initial reservoir pressure	14.7 psi
Initial water saturation	0.45
Initial salinity expressed in total equivalent anions	0.65 meq/ml
Initial calcium ions concentration	0.133 meq/ml
Relative permeability	
Aqueous Phase:	
Residual saturation	0.15
Endpoint relative permeability	0.14
Exponent of the relative permeability curve	2
Oleic Phase:	
Residual saturation	0.4
Endpoint relative permeability	0.9
Exponent of the relative permeability curve	2
Water viscosity	0.42 cp
Oil viscosity	1.2 cp
Polymer-viscosity parameters	
AP1	70 $(wt\%)^{-1}$
AP2	100 $(wt\%)^{-2}$
AP3	10000 $(wt\%)^{-3}$
$\dot{\gamma}_c$	10
$\dot{\gamma}_{1/2}$	190 sec^{-1}
P_α	1.8
S_p	0.175
β_p	2
C_{SE1}	0.01 meq/ml
Effective porosity to polymer	0.9
Permeability-reduction factor	
b_{rk}	1000
c_{rk}	0.02
Parameters for polymer adsorption	
A_{41}	1
A_{42}	0.
B_4	100 1/wt%
Longitudinal dispersivity	12 (ft)
Transverse dispersivity	0.0
Bottomhole pressure for pressure-constrained producer	14.7 psi
Water injection rate for rate-constrained injector	10000 (ft^3/day)
Injected polymer slug size	0.5 PV
Polymer concentration	0.1 wt%

Table 4.4 Input data for two-dimensional surfactant flood

Parameters	Values
Dimensions of reservoir simulated	1000 ft x 1000 ft x 100 ft
Permeability	200 md
Porosity	0.2
Initial reservoir pressure	14.7 psi
Initial water saturation	0.45
Initial salinity expressed in total equivalent anions	0.65 meq/ml
Initial calcium ions concentration	0.133 meq/ml
Relative permeability at low capillary number	
Aqueous phase:	
Residual saturation	0.15
Endpoint relative permeability	0.14
Exponent of the relative permeability curve	2
Oleic phase:	
Residual saturation	0.4
Endpoint relative permeability	0.9
Exponent of the relative permeability curve	2
Microemulsion phase:	
Residual saturation	0.15
Endpoint relative permeability	0.14
Exponent of the relative permeability curve	2.0
Relative permeability at high capillary number	
Aqueous phase:	
Residual saturation	0
Endpoint relative permeability	1
Exponent of the relative permeability curve	2
Oleic phase:	
Residual saturation	0
Endpoint relative permeability	1
Exponent of the relative permeability curve	2
Microemulsion phase:	
Residual saturation	0
Endpoint relative permeability	1
Exponent of the relative permeability curve	2
Interfacial tension parameter	
Aqueous-microemulsion interface	
G11	13
G12	-14.8
G13	0.007
Oleic-microemulsion interface	
G21	13
G22	-14.5
G23	0.01
Water-oil interface	
$\log_{10}\sigma_{wo}$	1.3

Table 4.4 Input data for two-dimensional surfactant flood (cont'd.)

Capillary desaturation	
Capillary desaturation curve parameter T_{11}	1865
Capillary desaturation curve parameter T_{22}	59074
Capillary desaturation curve parameter T_{33}	364
Water viscosity	0.42 cp
Oil viscosity	1.2 cp
Phase behavior	
Critical micelle concentration (CMC)	0.0001
Height of binodal curve:	
HBNC70	0.12
HBNC71	0.03
HBNC72	0.08
Surfactant salinity range	
CSEL	0.5 meq/ml
CSEU	0.8 meq/ml
Microemulsion viscosity parameters	
ALPHA1	0
ALPHA2	0
ALPHA3	0
ALPHA4	0.000865
ALPHA5	4.153
Parameters for surfactant adsorption	
A_{31}	1
A_{32}	0
B_3	1000
Longitudinal dispersivity	12 ft
Transverse dispersivity	0.4 ft
Bottom hole pressure for pressure-constrained producer	14.7 psi
Water injection rate for rate-constrained injector	10000 ft^3/day
Surfactant concentration	0.005 vol. fr.
Salinity expressed in total equivalent anions	0.65 meq/ml
Calcium ions concentration	0.133 meq/ml

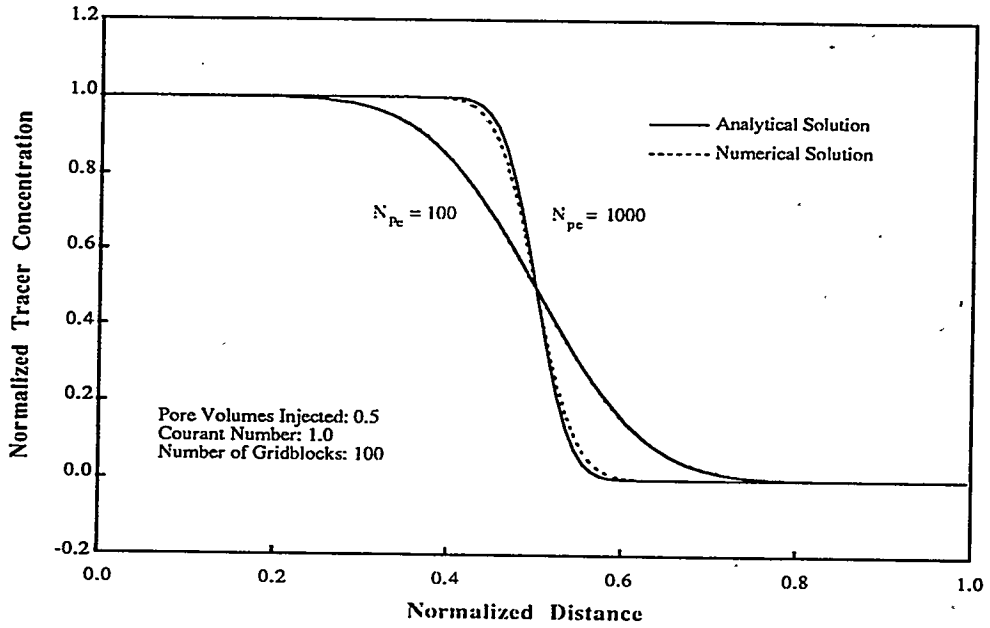


Fig. 4.1. Comparison of simulation results of one-dimensional convection-diffusion problems with analytical solutions.

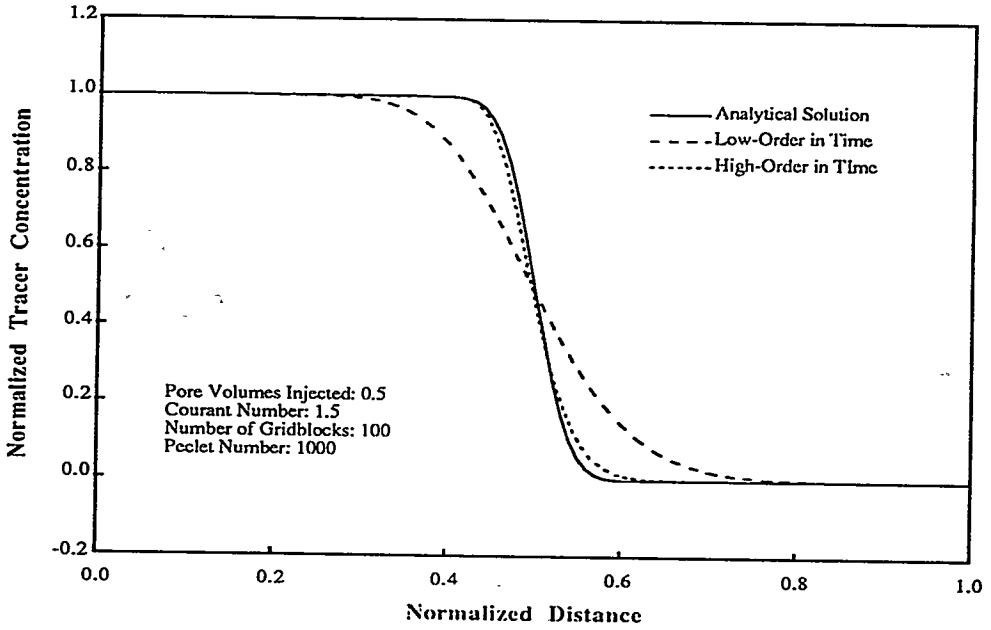


Fig. 4.2. Comparison of simulation results of one-dimensional convection-diffusion problems with those using low-order temporal scheme.

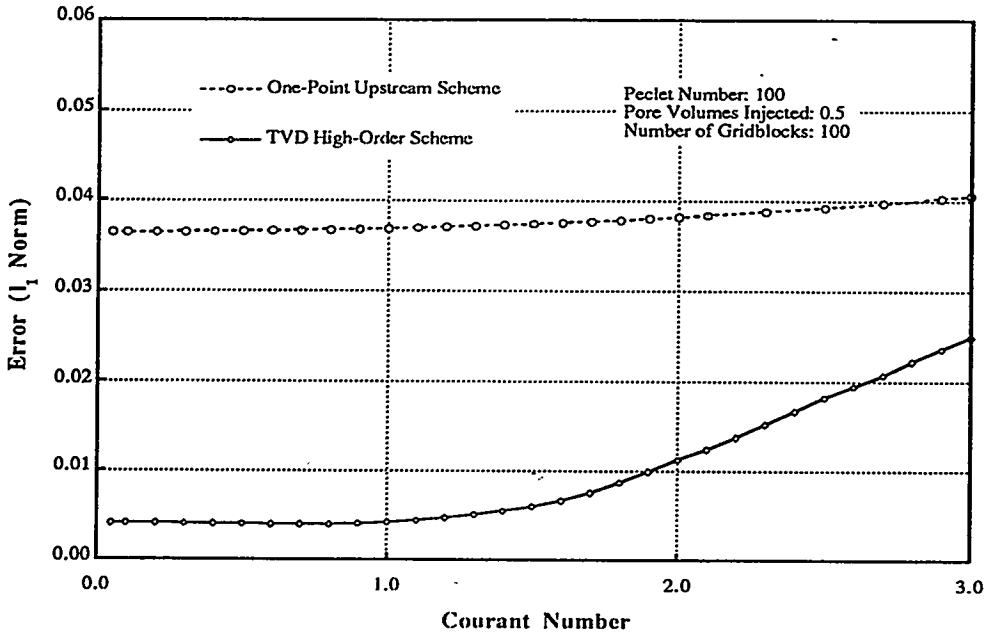


Fig. 4.3. Error comparison of simulating one-dimensional convection-diffusion problem using low- or high-order spatial discretization scheme.

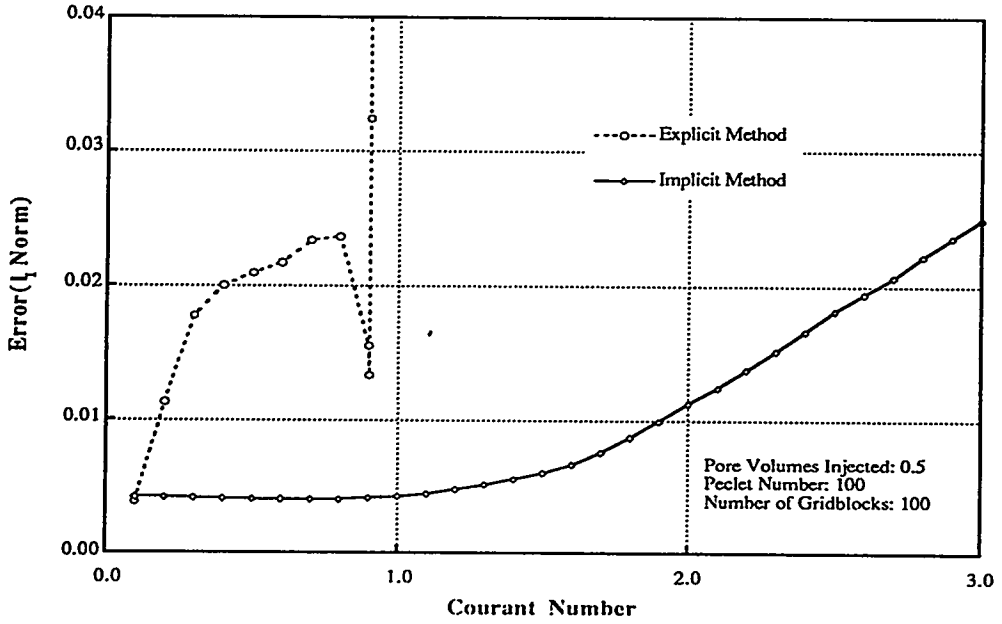


Fig. 4.4. Error comparison of simulating one-dimensional convection-diffusion problem using IMPES simulator or fully implicit simulator.

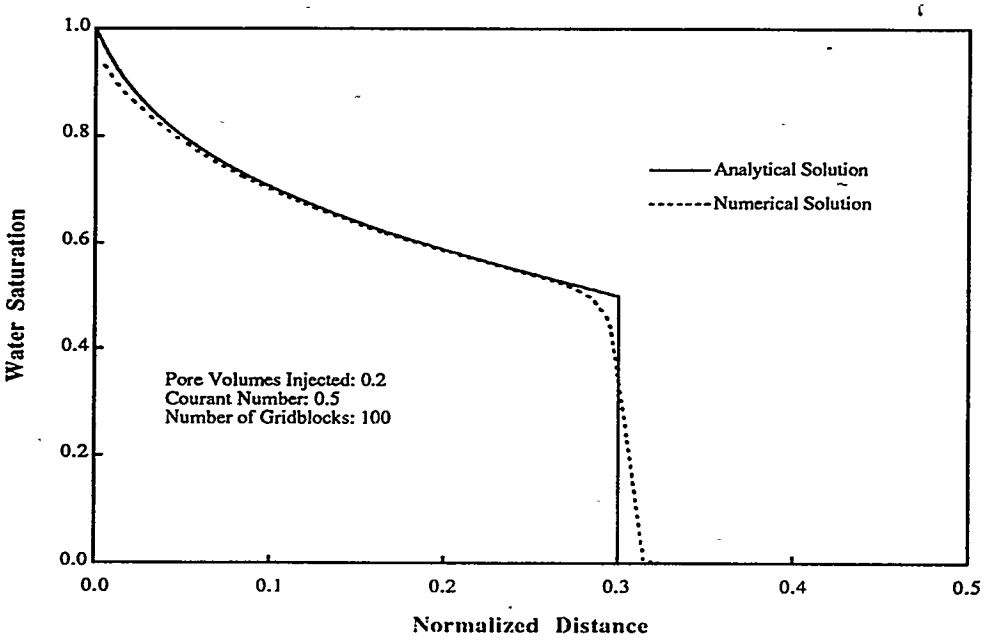


Fig. 4.5. Comparison of simulation results of one-dimensional waterflood with Buckley-Leverett solution.

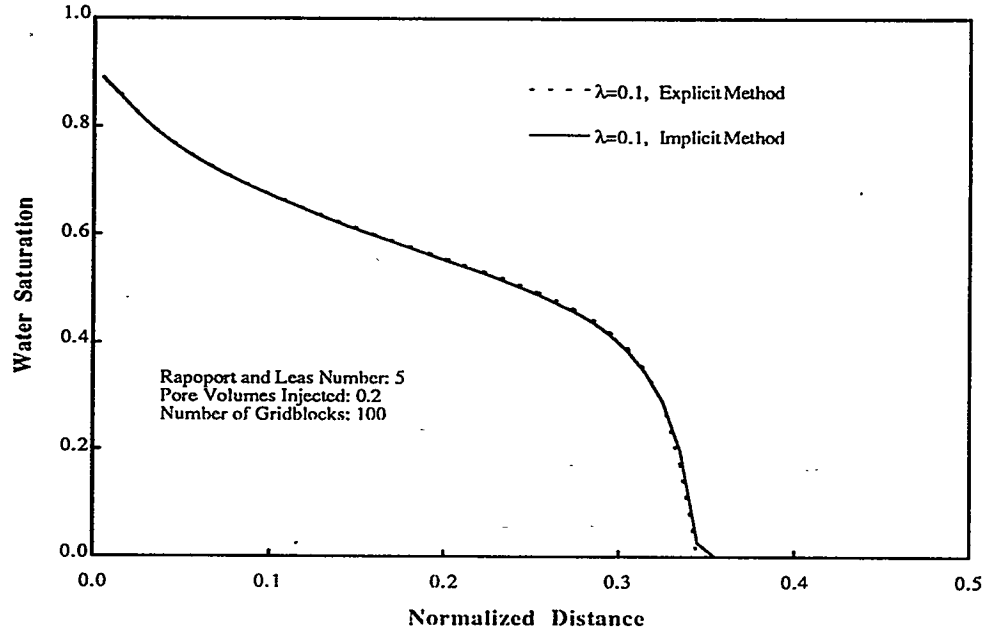


Fig. 4.6. Comparison of simulating one-dimensional waterflood using IMPES simulator or fully implicit simulator at a small timestep size.

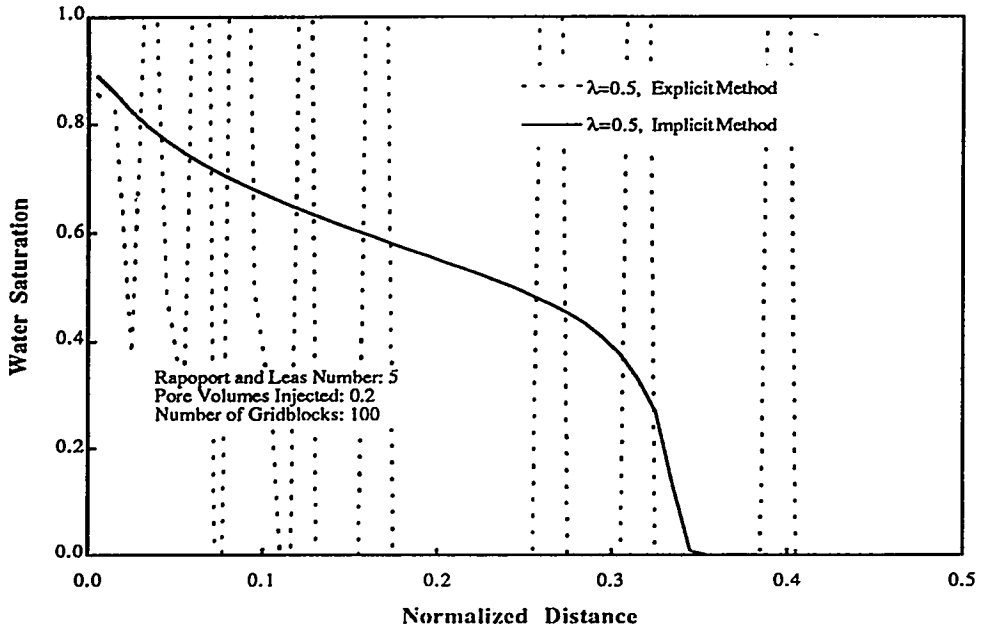


Fig. 4.7. Comparison of simulating one-dimensional waterflood using IMPES simulator or fully implicit simulator at a large timestep size.

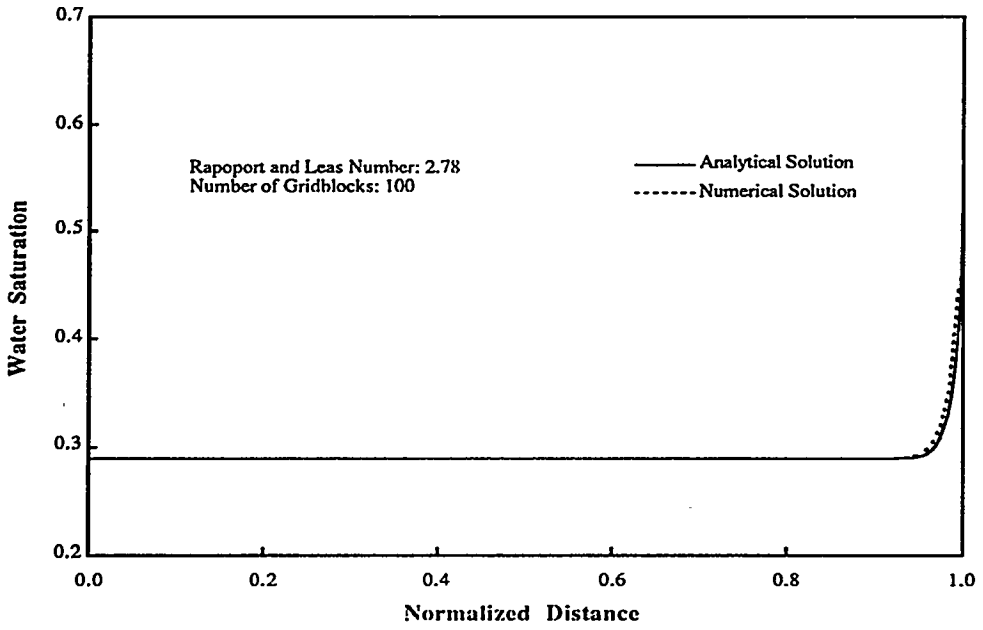


Fig. 4.8. Comparison of results of simulating capillary end effect with analytical solution.

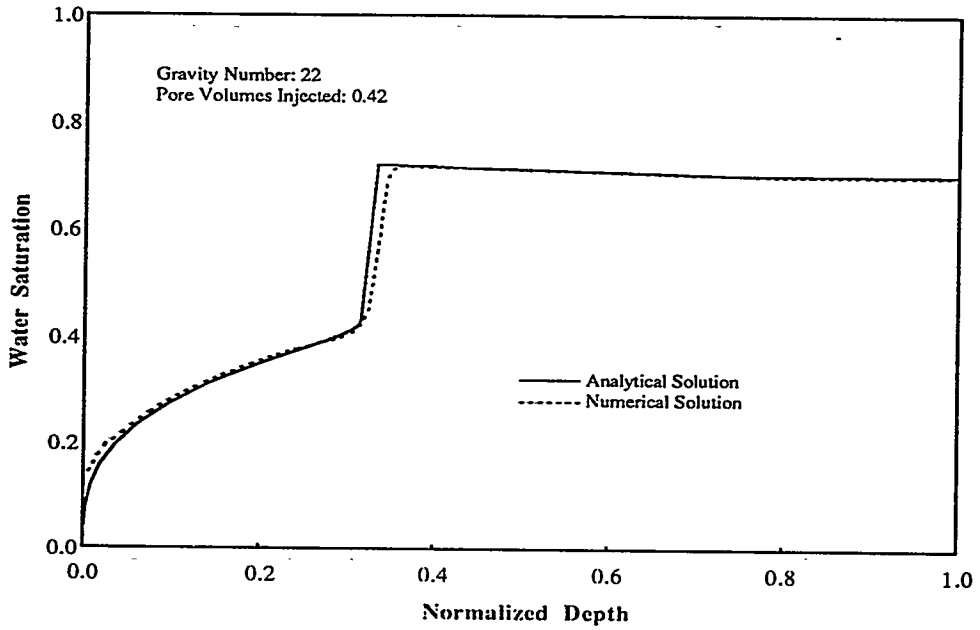


Fig. 4.9. Comparison of simulation results of one-dimensional gravity-inversion problem with analytical solution.

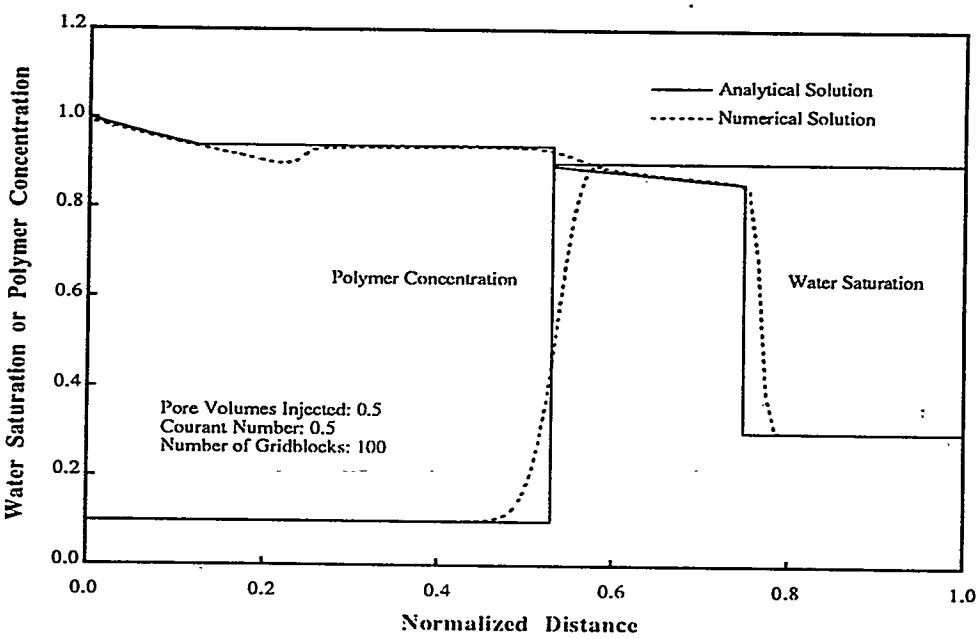


Fig. 4.10. Comparison of simulation results of one-dimensional polymerflood with analytical solutions.

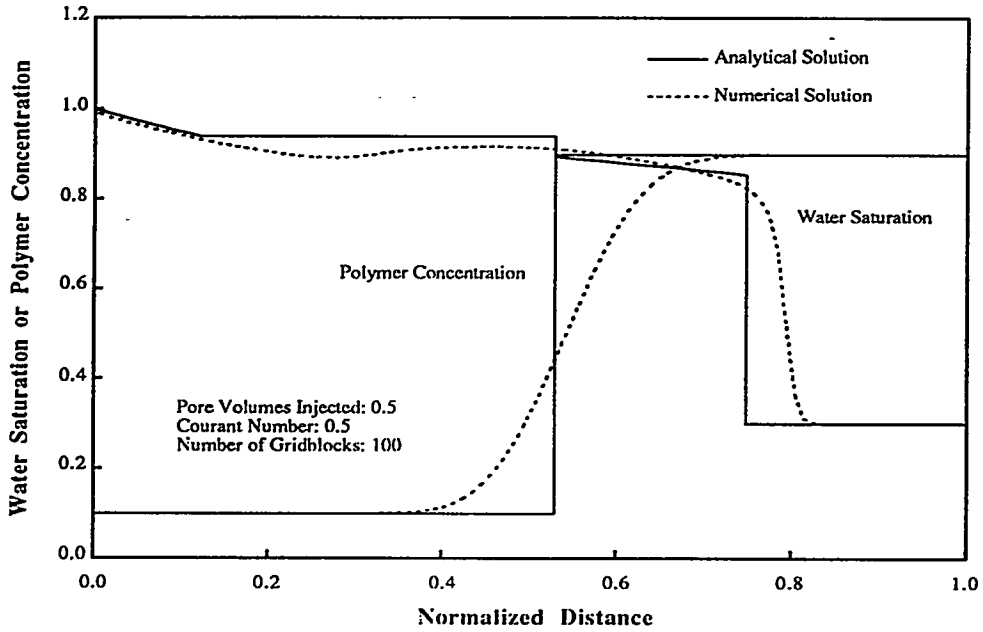


Fig. 4.11. Comparison of simulation results of one-dimensional polymerflood using one-point upstream scheme with those of analytical solutions.

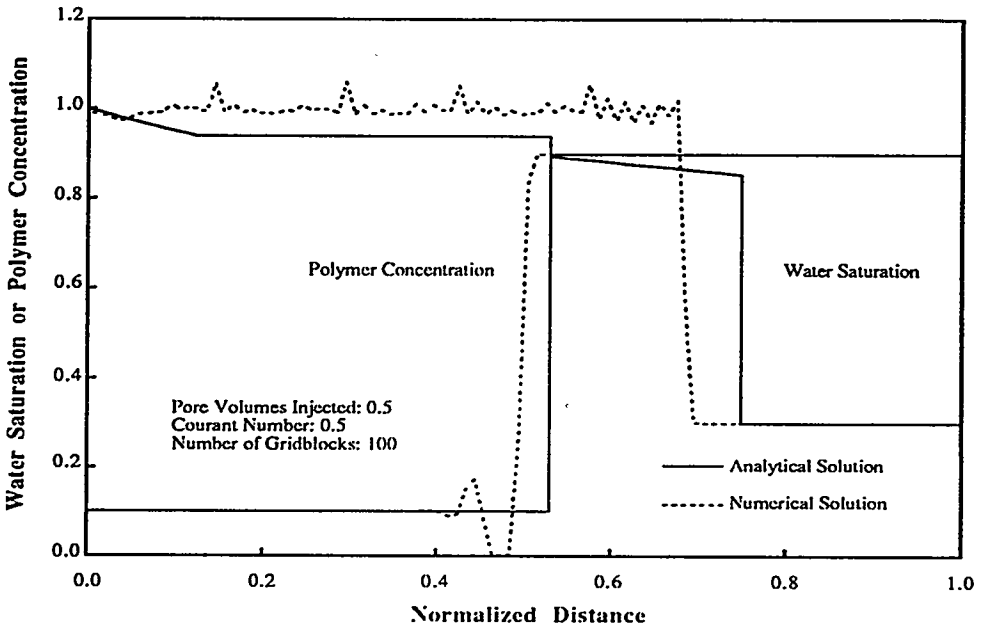


Fig. 4.12. Comparison of simulation results of one-dimensional polymerflood using IMPES simulator with those of analytical solutions.

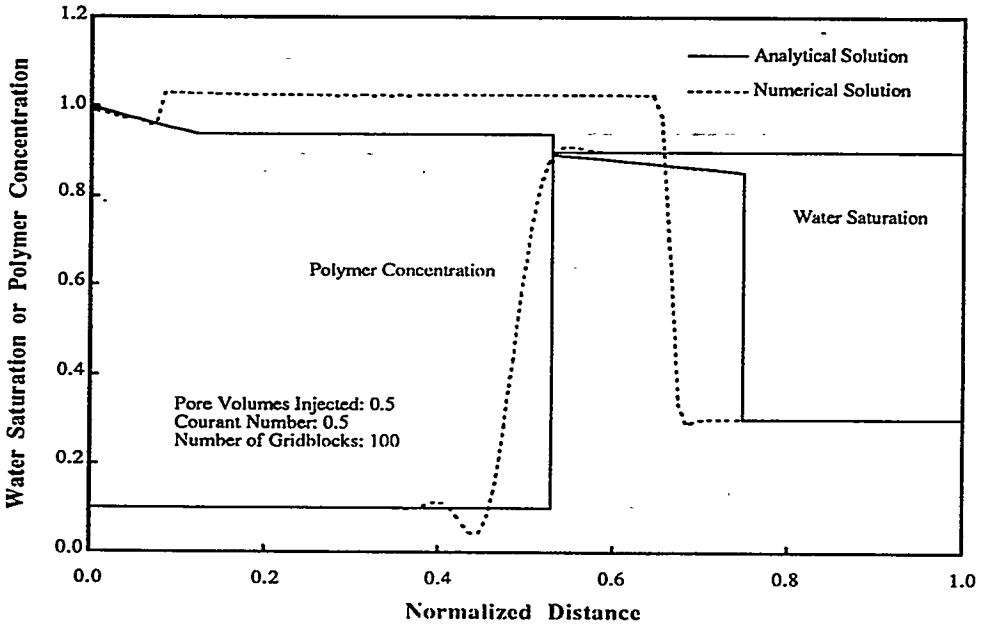


Fig. 4.13. Comparison of simulation results of one-dimensional polymerflood using high-order scheme without flux limiting with those of analytical solutions.

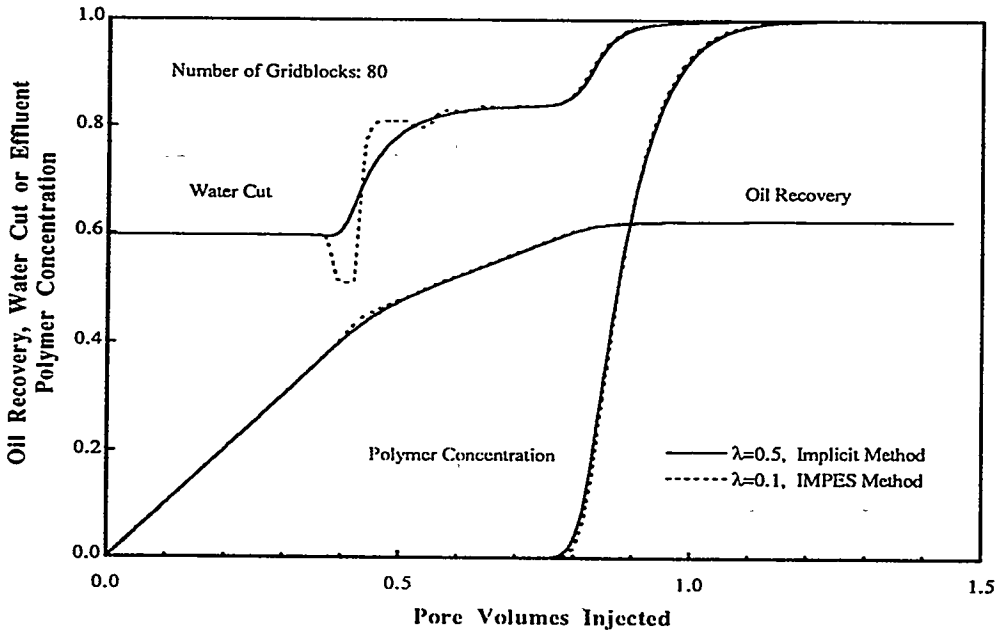


Fig. 4.14. Results of one-dimensional polymerflood simulation for verifying polymer property model.

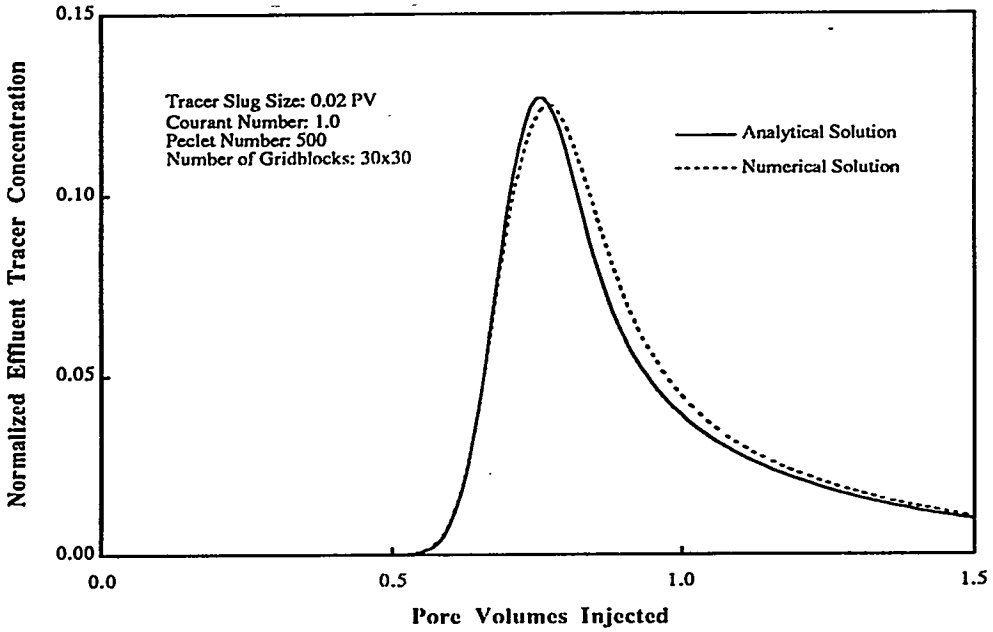


Fig. 4.15. Comparison of simulation results of two-dimensional tracer flood with analytical solution.

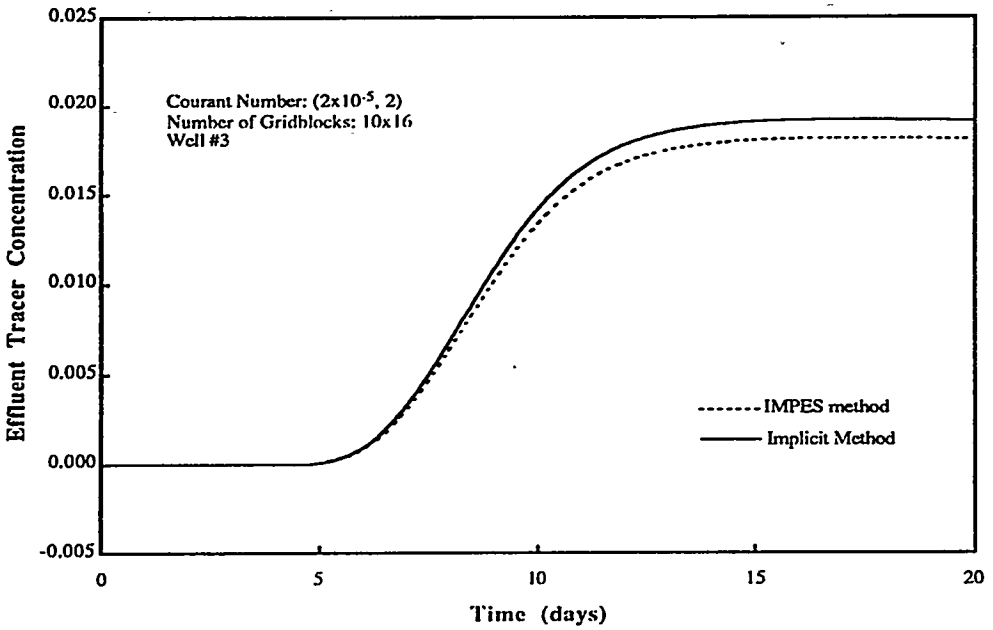


Fig. 4.16. Comparison of tracer responses for hydraulic fracture diagnostic tests using IMPES simulator and implicit simulator.

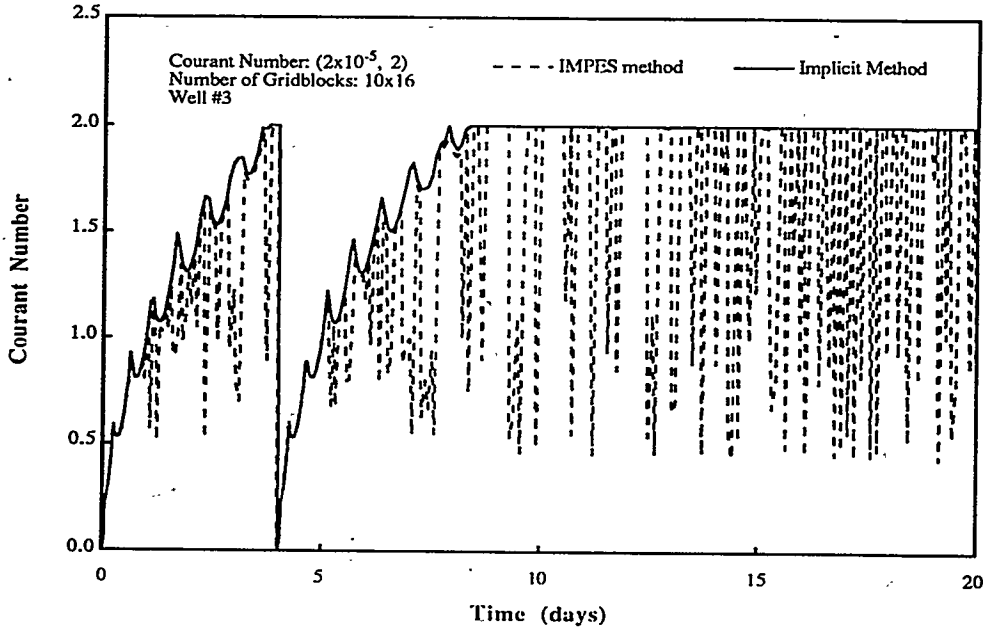


Fig. 4.17. Comparison of timestep sizes of simulations for hydraulic-fracture diagnostic tests using IMPES simulator and implicit simulator.

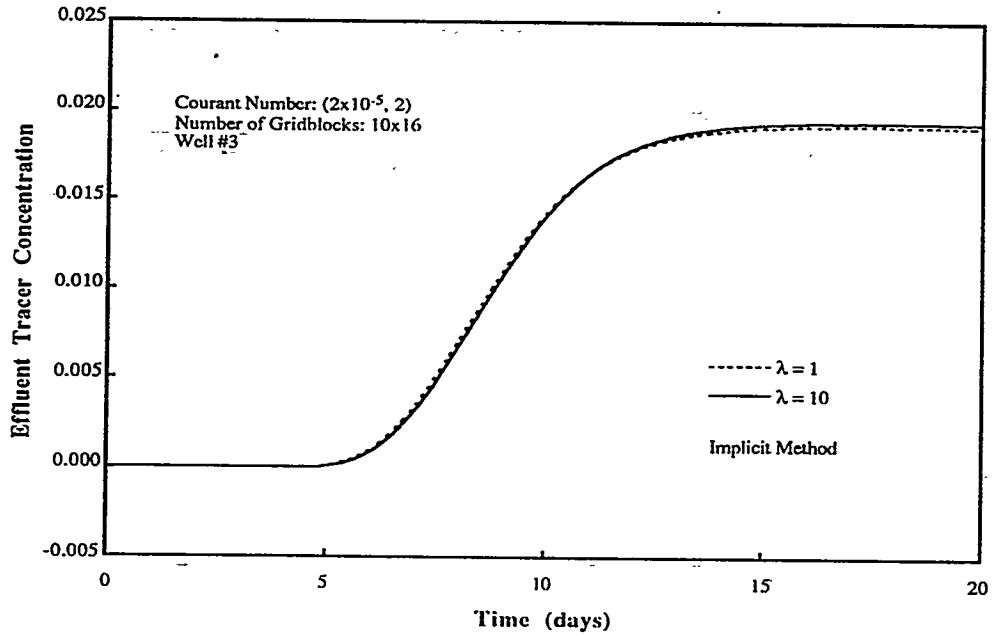


Fig. 4.18. Tracer responses results for hydraulic-fracture diagnostic tests using implicit simulator.

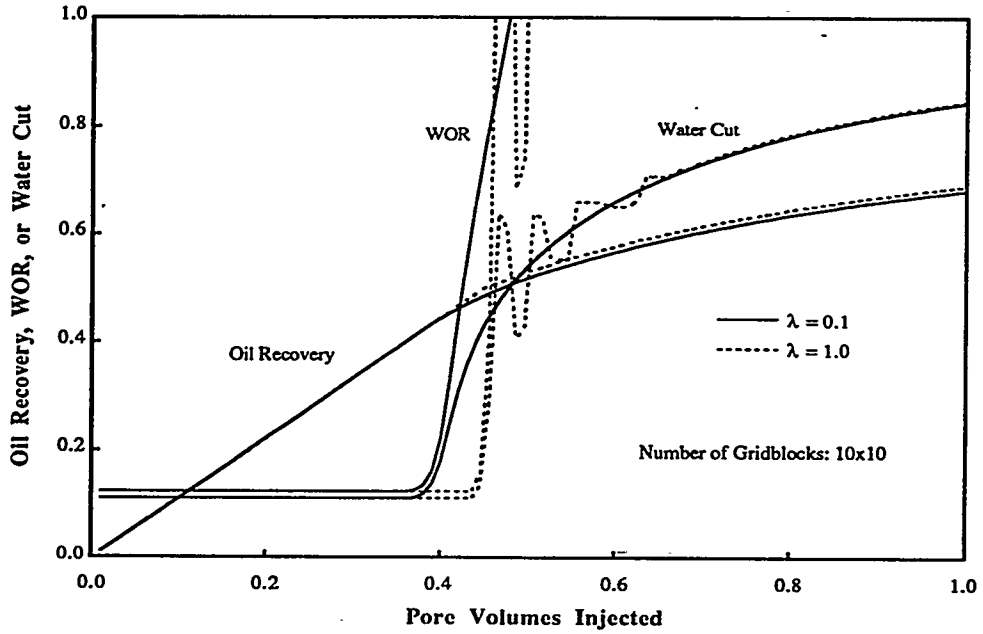


Fig. 4.19. Simulation results of two-dimensional waterflood using IMPES method.

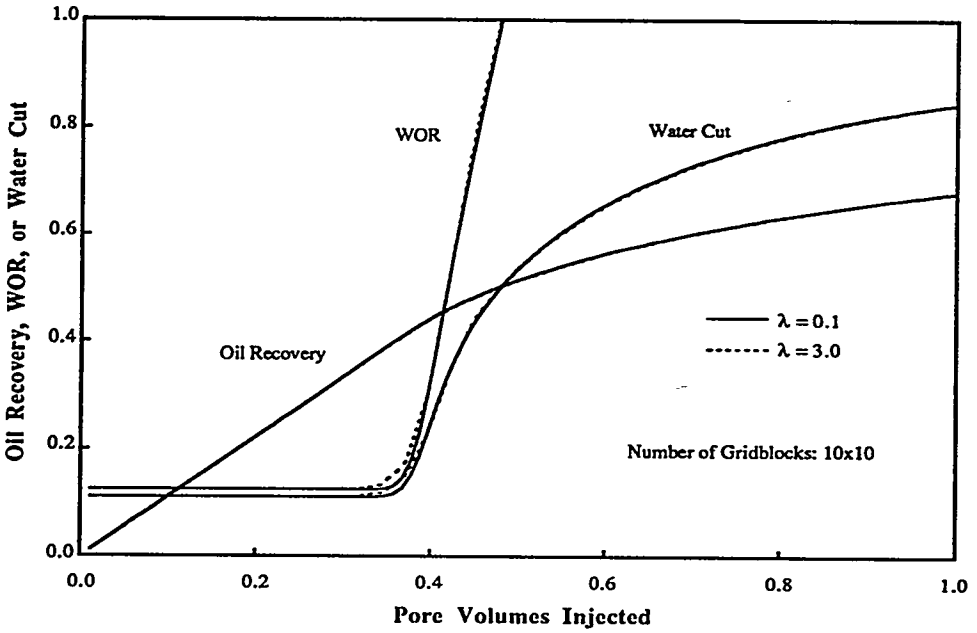


Fig. 4.20. Simulation results of two-dimensional waterflood using implicit method.

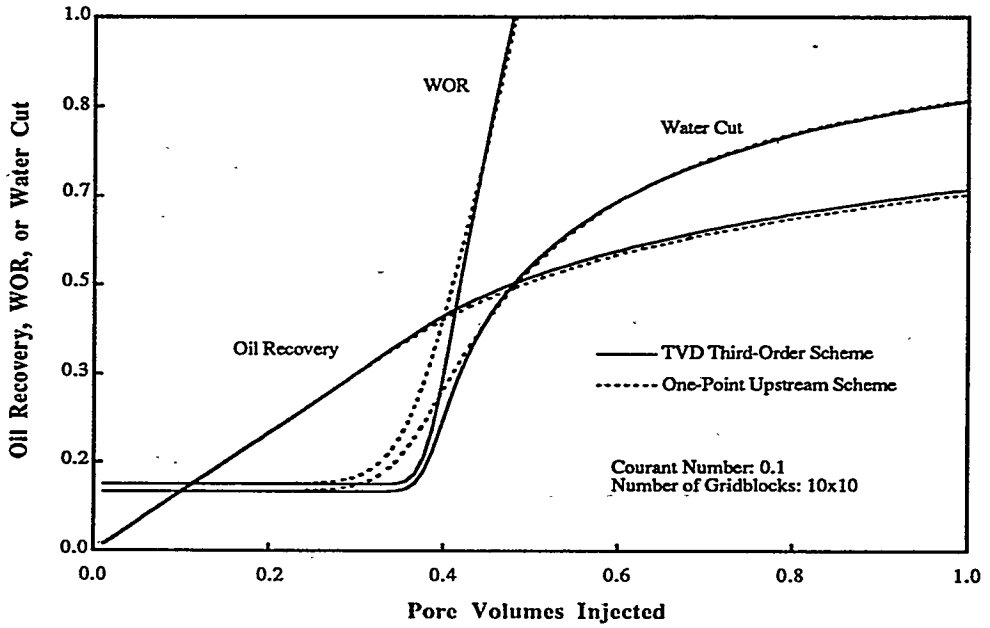


Fig. 4.21. Comparison of simulation results of two-dimensional waterflood with those using low-order spatial scheme

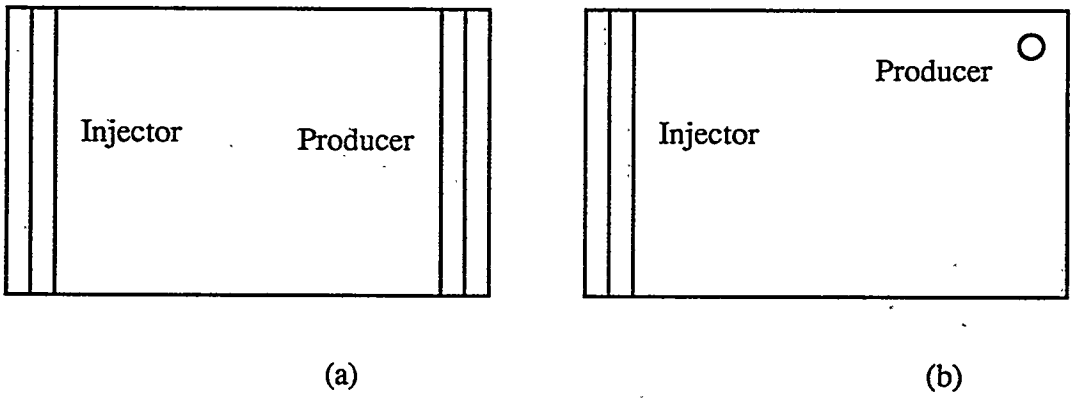


Fig. 4.22. Well patterns for the two-dimensional, cross-sectional polymerflood simulation

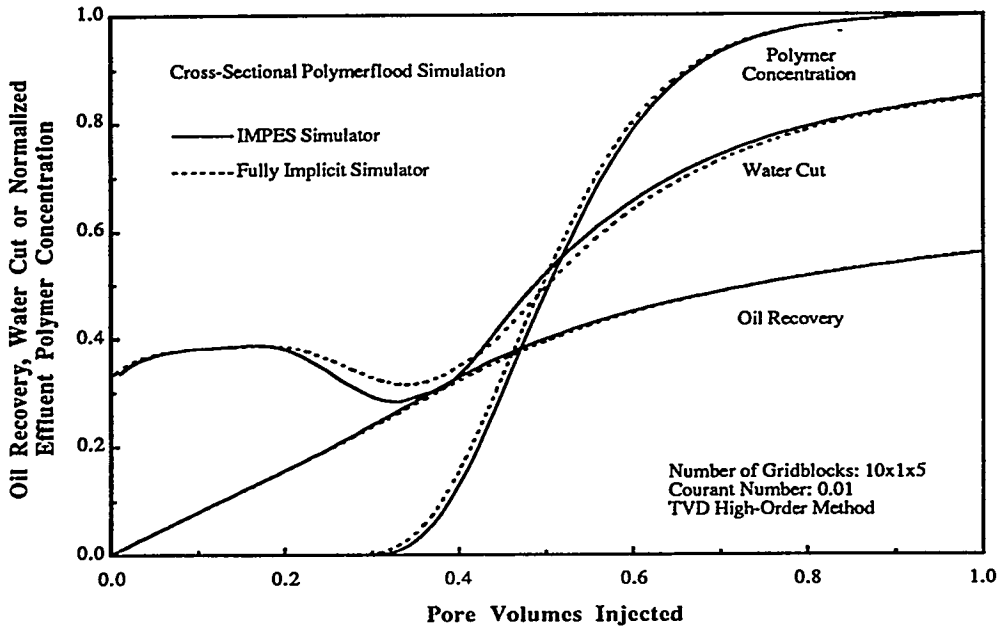


Fig. 4.23. Simulation of a two-dimensional, cross-sectional polymerflood using the IMPES simulator and the fully implicit simulator with small timestep sizes.

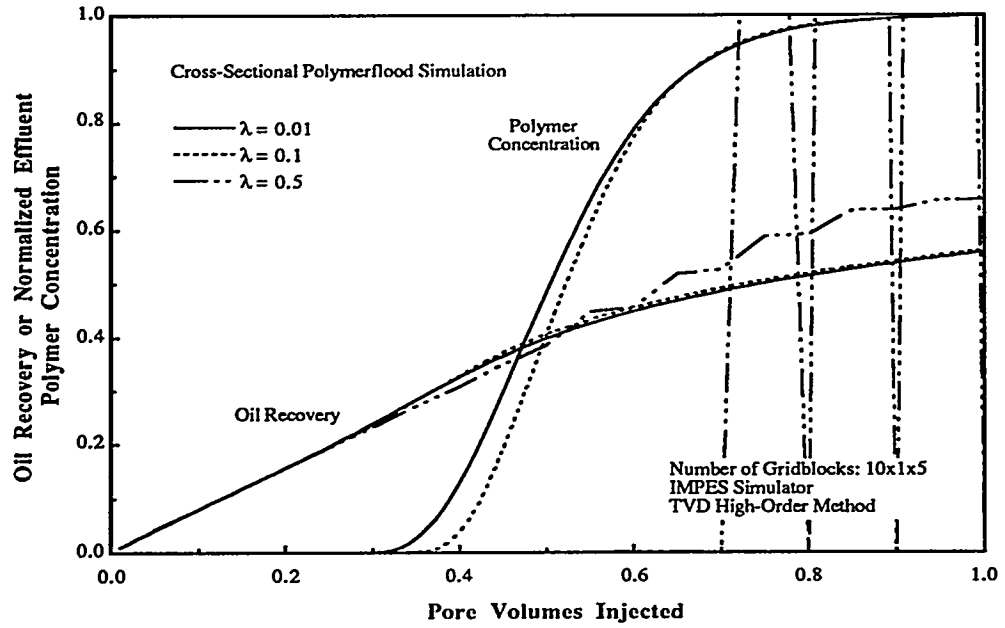


Fig. 4.24. Oil recovery and normalized effluent polymer concentration of simulating a two-dimensional, cross-sectional polymerflood using the IMPES simulator.

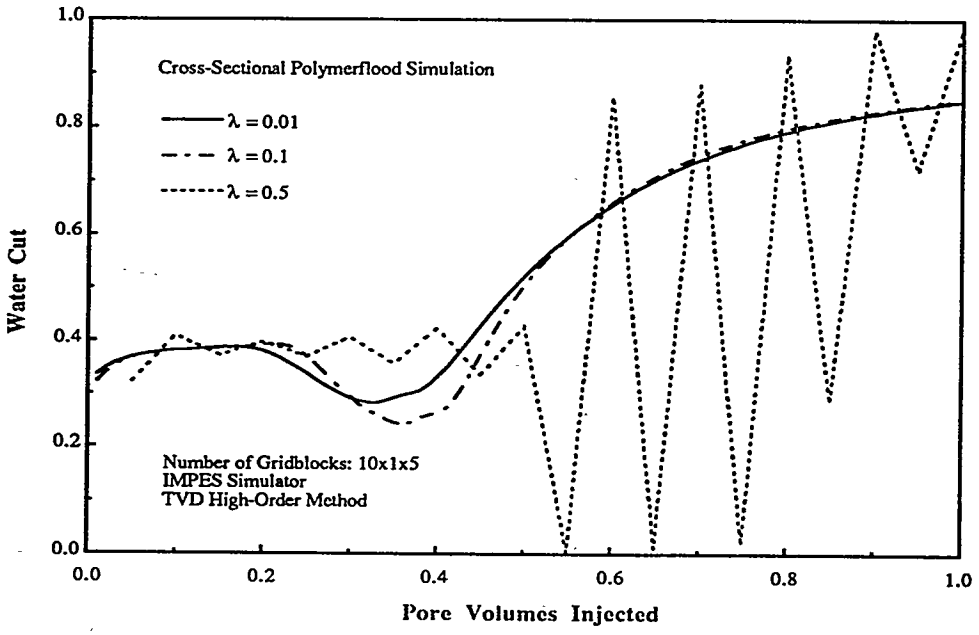


Fig. 4.25. Water cut of simulating a two-dimensional, cross-sectional polymerflood using the IMPES simulator.

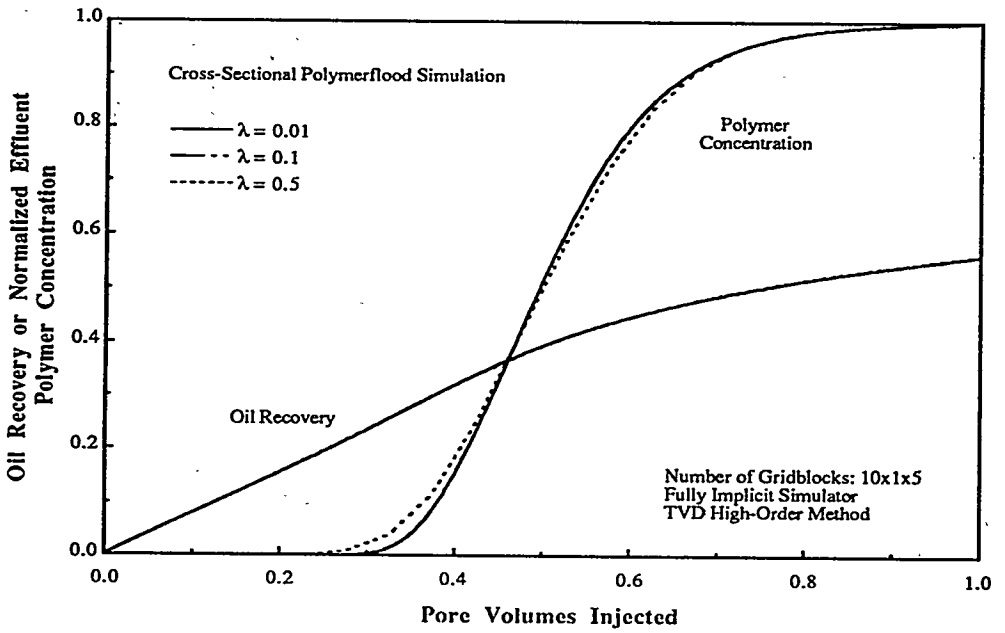


Fig. 4.26. Oil recovery and normalized effluent polymer concentration of simulating a two-dimensional, cross-sectional polymerflood using the fully implicit simulator.

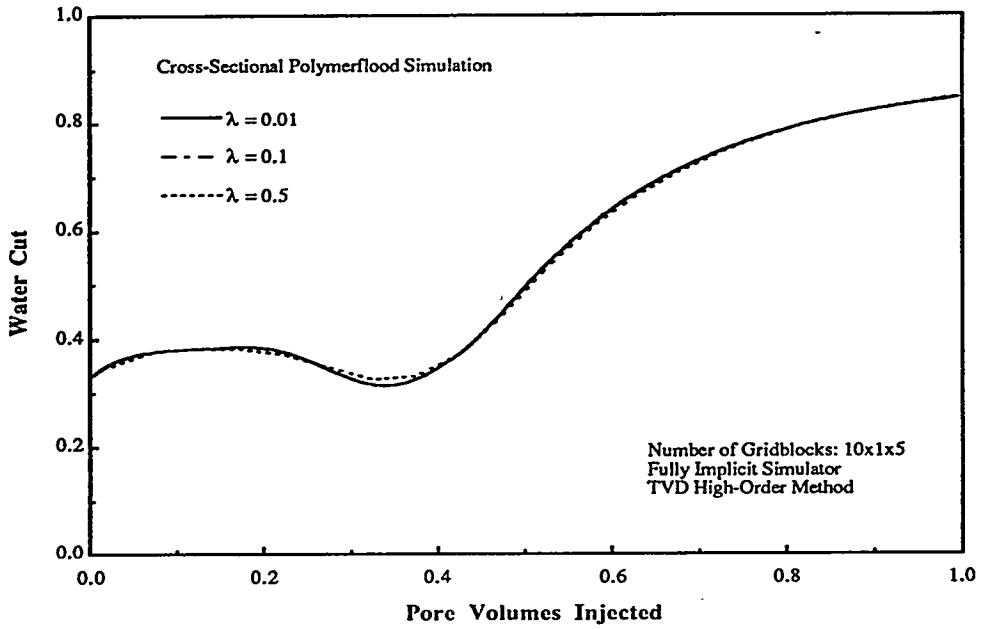


Fig. 4.27. Water cut of simulating a two-dimensional, cross-sectional polymerflood using the fully implicit simulator.

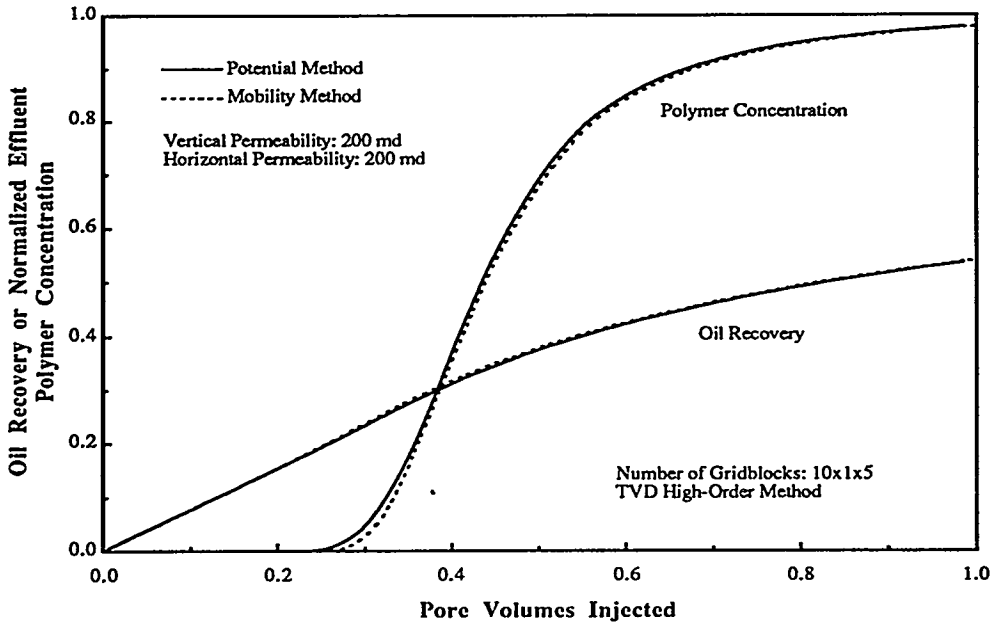
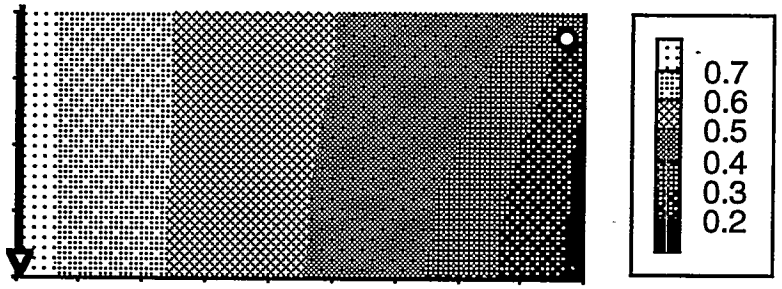
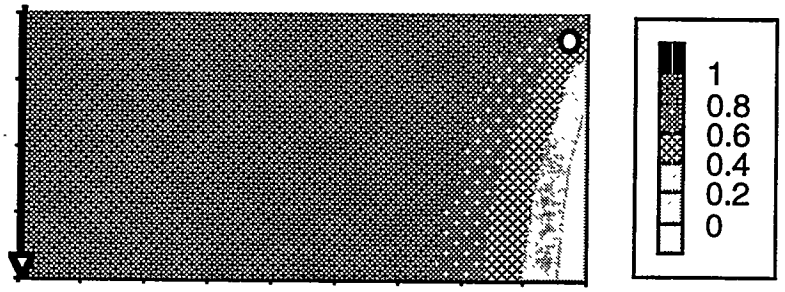


Fig. 4.28. Simulation of a two-dimensional, cross-sectional polymerflood with a high vertical permeability.

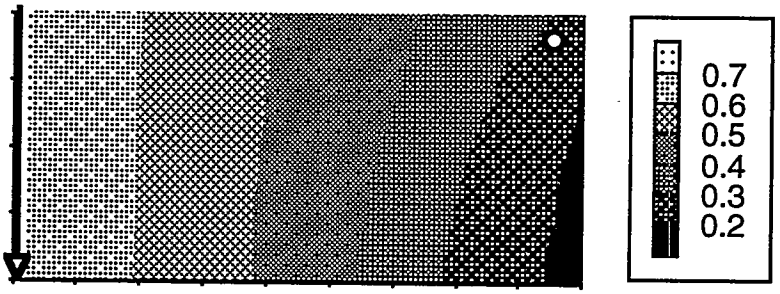


Water Saturation, Mobility Method, kz=kx, PVI: 0.5

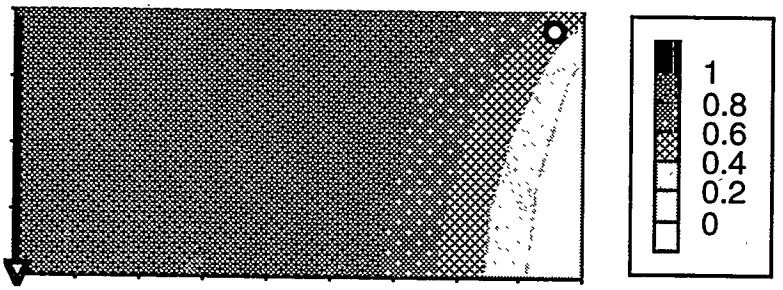


Polymer Concentration, Mobility Method, kz=kx, PVI: 0.5

Fig. 4.29. Water saturation and polymer concentration distributions with a high vertical permeability using the mobility rate-allocation method.



Water Saturation, Potential Method, kz=kx, PVI: 0.5



Polymer Concentration, Potential Method, kz=kx, PVI: 0.5

Fig. 4.30. Water saturation and polymer concentration distributions with a high vertical permeability using the potential rate-allocation method.

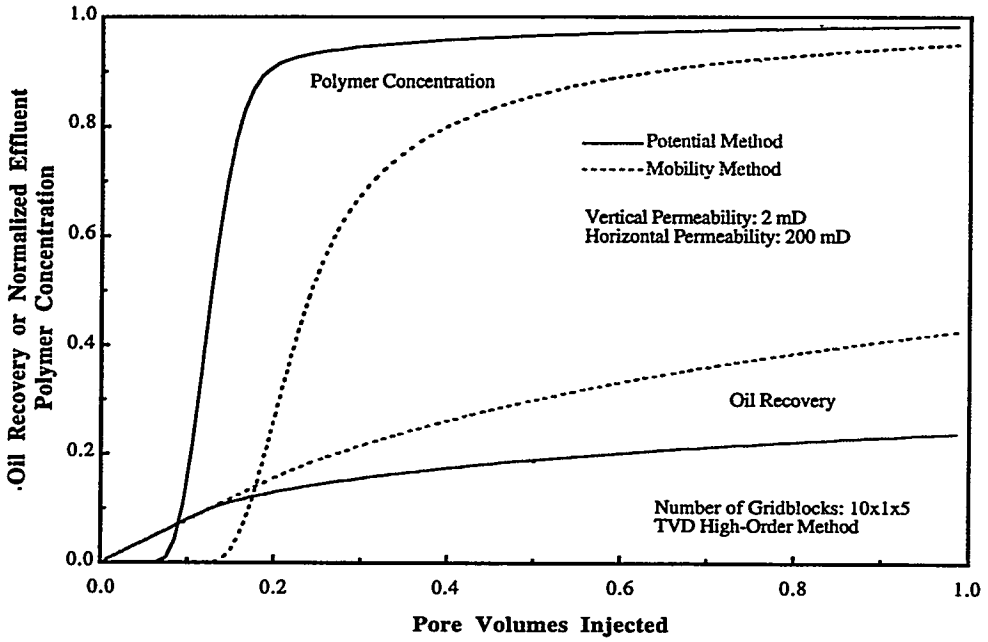
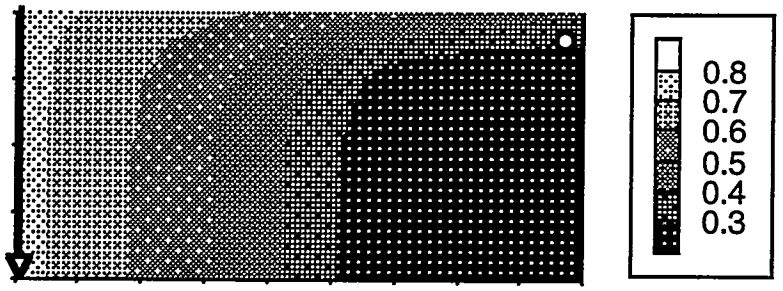
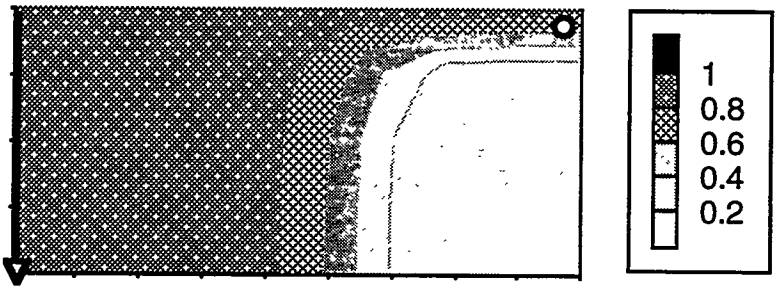


Fig. 4.31. Simulation of a two-dimensional, cross-sectional polymerflood with a low vertical permeability.

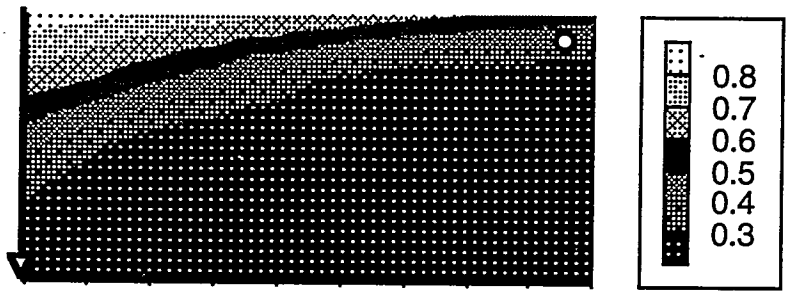


Water Saturation, Mobility Method, kz=0.01kx, PVI: 0.5

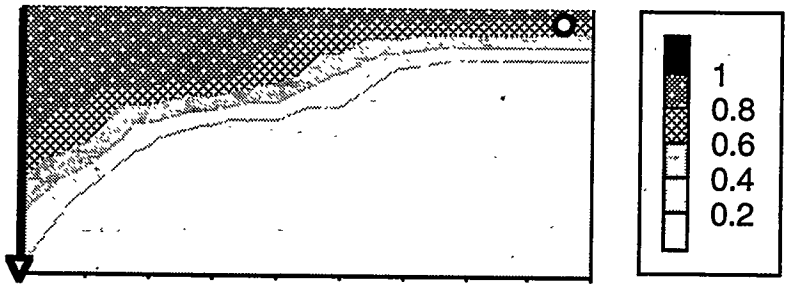


Polymer Concentration, Mobility Method, kz=0.01kx, PVI: 0.5

Fig. 4.32. Water saturation and polymer concentration distributions with a low vertical permeability using the mobility rate-allocation method.



Water Saturation, Potential Method, kz=0.01kx, PVI: 0.5



Polymer Concentration, Potential Method, kz=0.01kx, PVI: 0.5

Fig. 4.33. Water saturation and polymer concentration distributions with a low vertical permeability using the potential rate-allocation method.

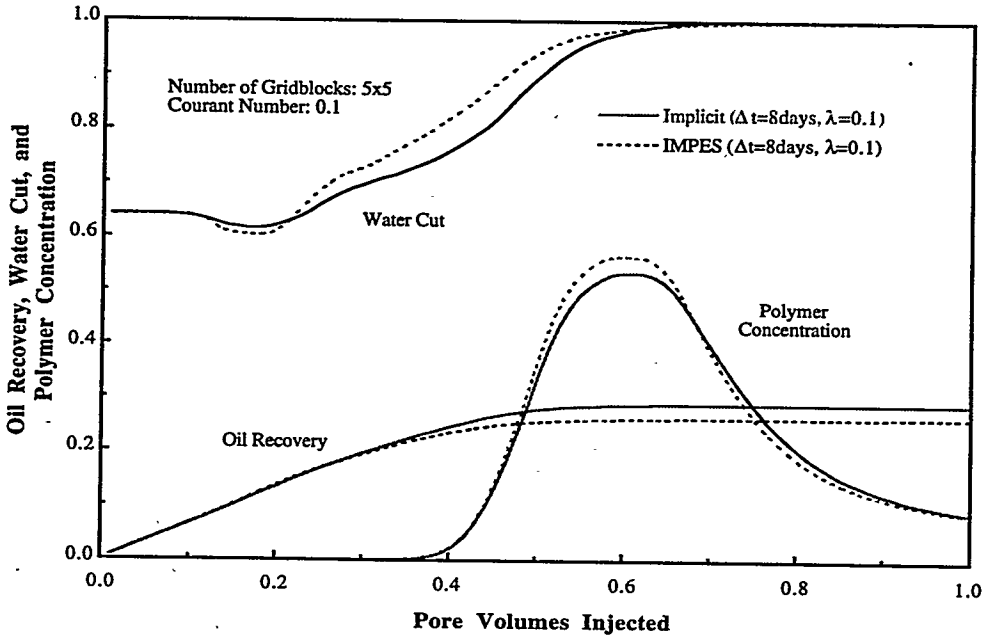


Fig. 4.34. Comparison with IMPES results of two-dimensional polymerflood simulation for verifying polymer-property model.

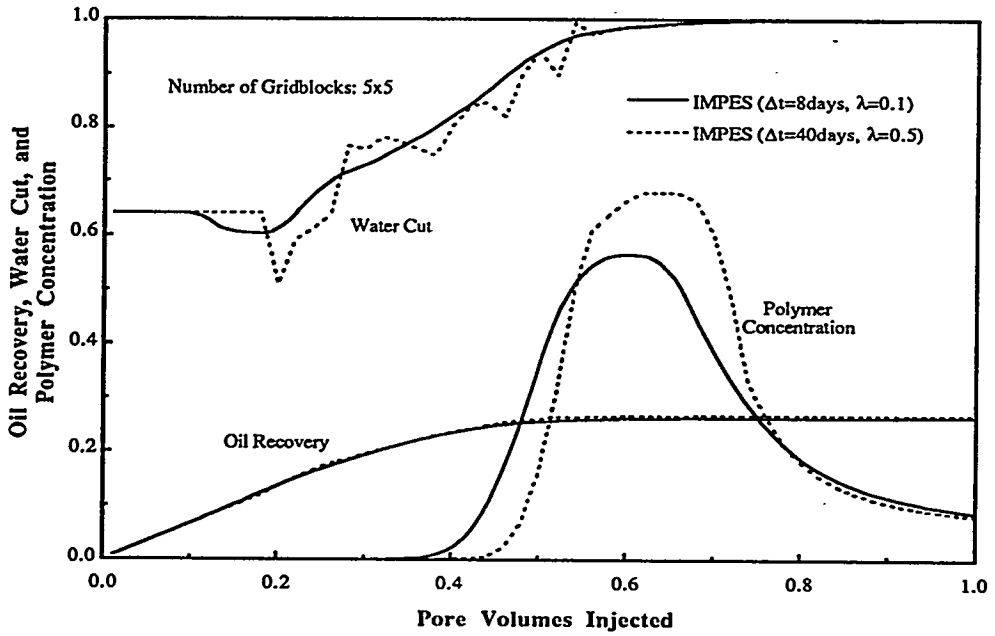


Fig. 4.35. IMPES results of two-dimensional polymerflood simulation for verifying polymer-property model.

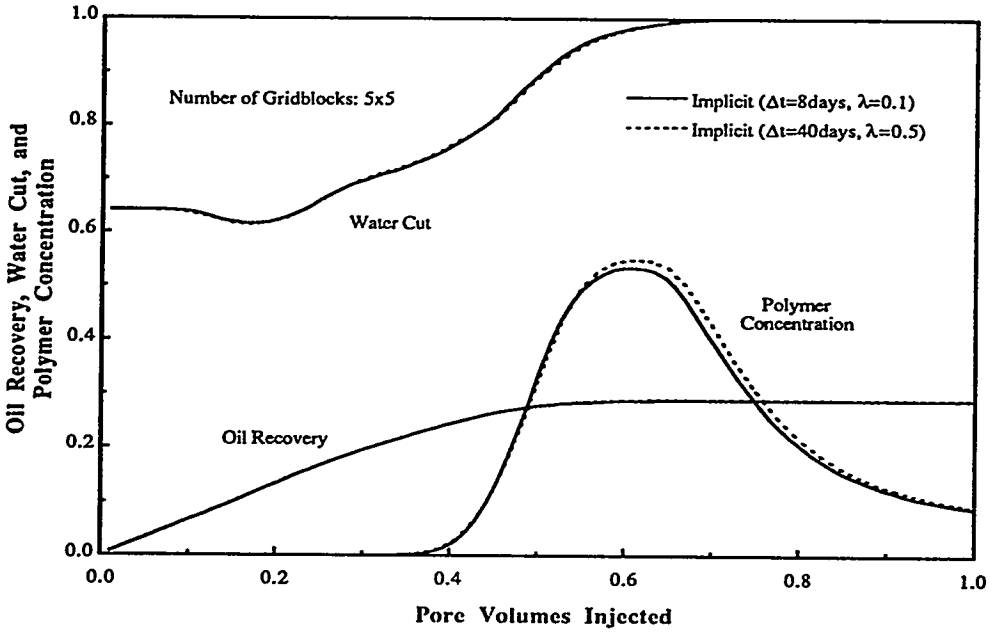


Fig. 4.36. Implicit simulator results of two-dimensional polymerflood simulation for verifying polymer-property model.

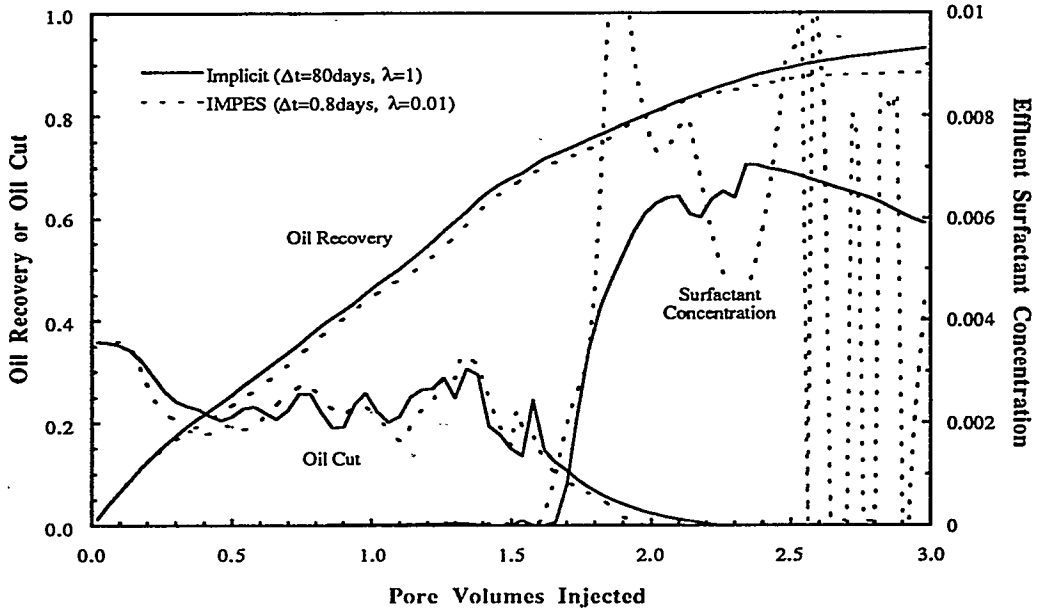


Fig. 4.37. Comparison of results of two-dimensional surfactant flood simulation with those of IMPES simulator at Courant number of 0.01.

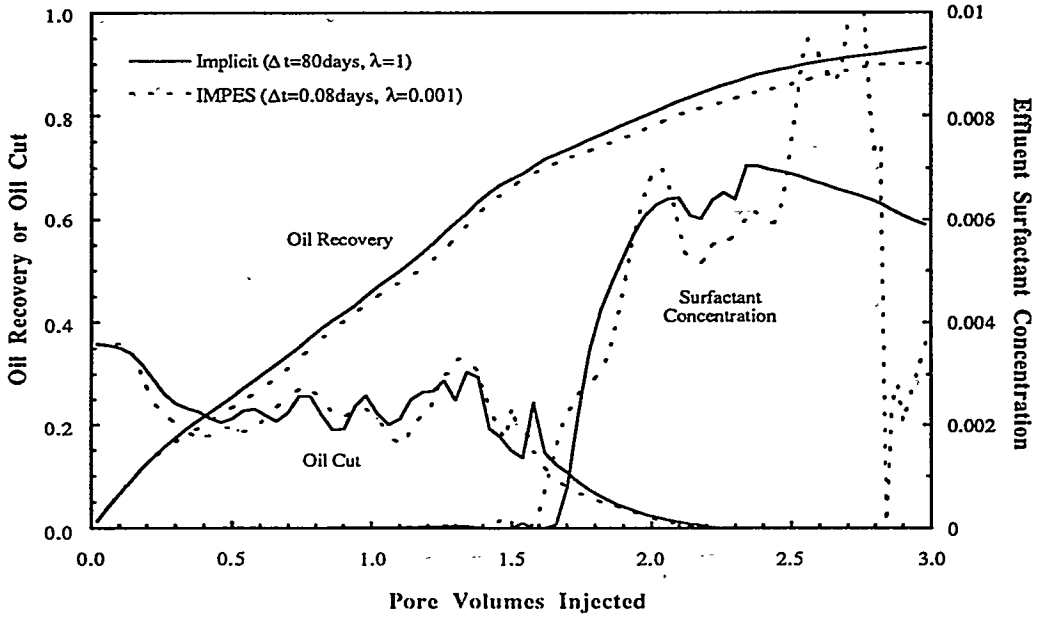


Fig. 4.38. Comparison of results of two-dimensional surfactant flood simulation with those of IMPES simulator at Courant number of 0.001.

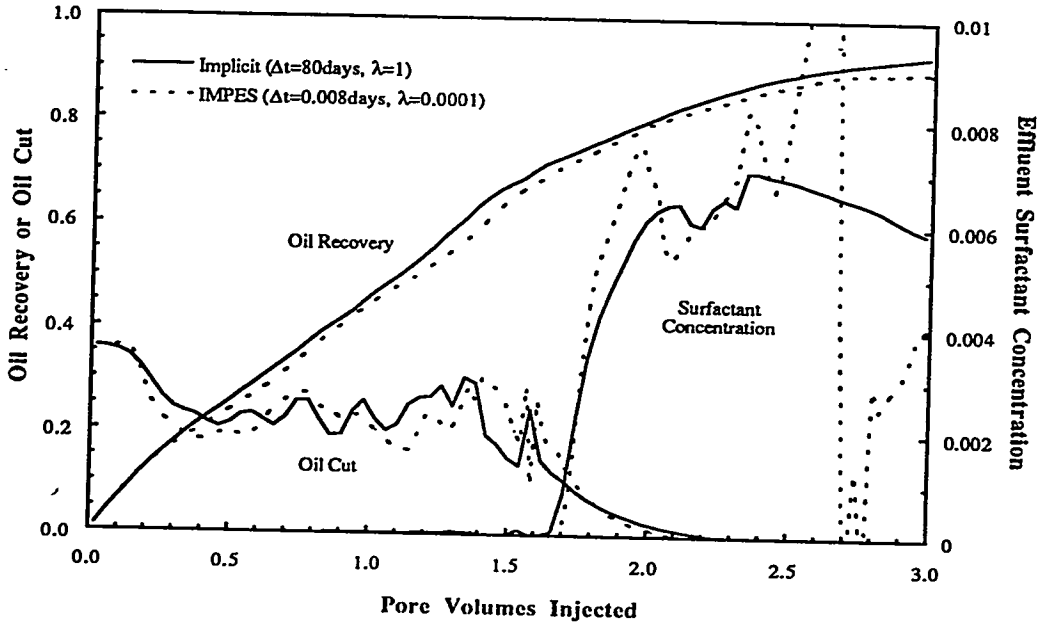


Fig. 4.39. Comparison of results of two-dimensional surfactant flood simulation with those of IMPES simulator at Courant number of 0.0001.

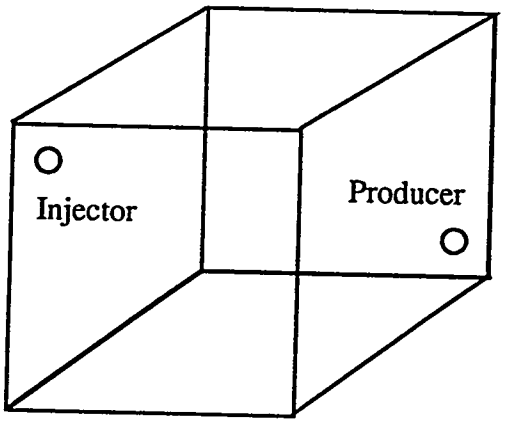


Fig. 4.40. Well pattern for the three-dimensional tracer convection-diffusion simulation.

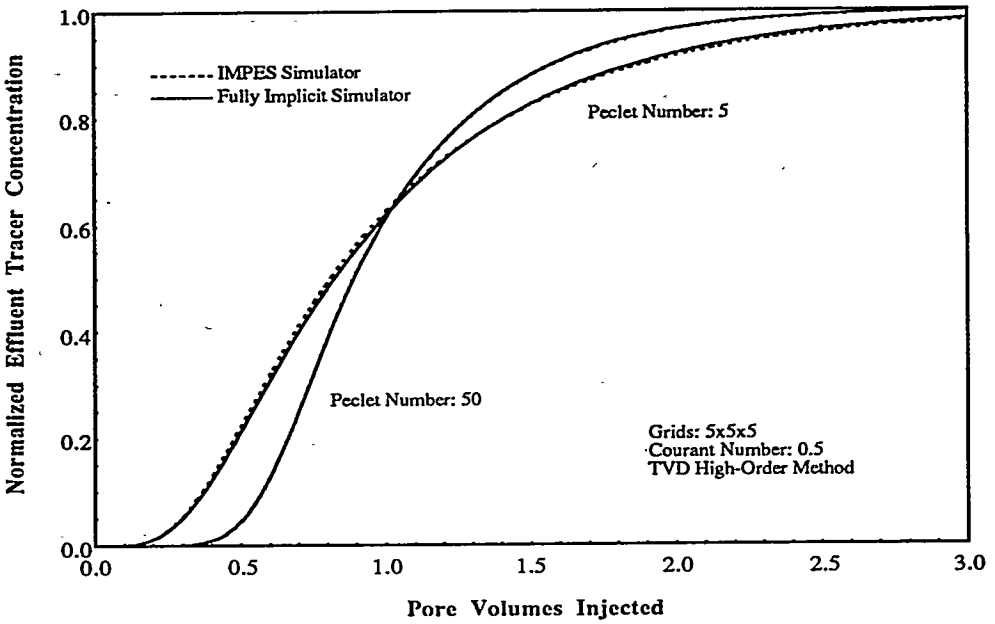


Fig. 4.41. Simulation of a three-dimensional tracer flood using the IMPES simulator and the fully implicit simulator.

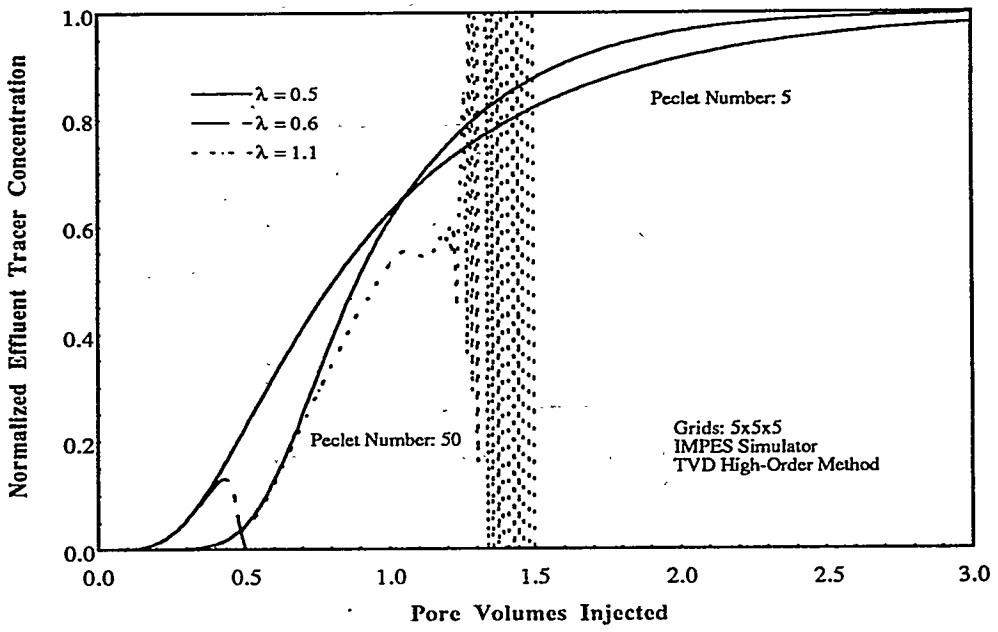


Fig. 4.42. Simulation of a three-dimensional tracer flood using the IMPES simulator.

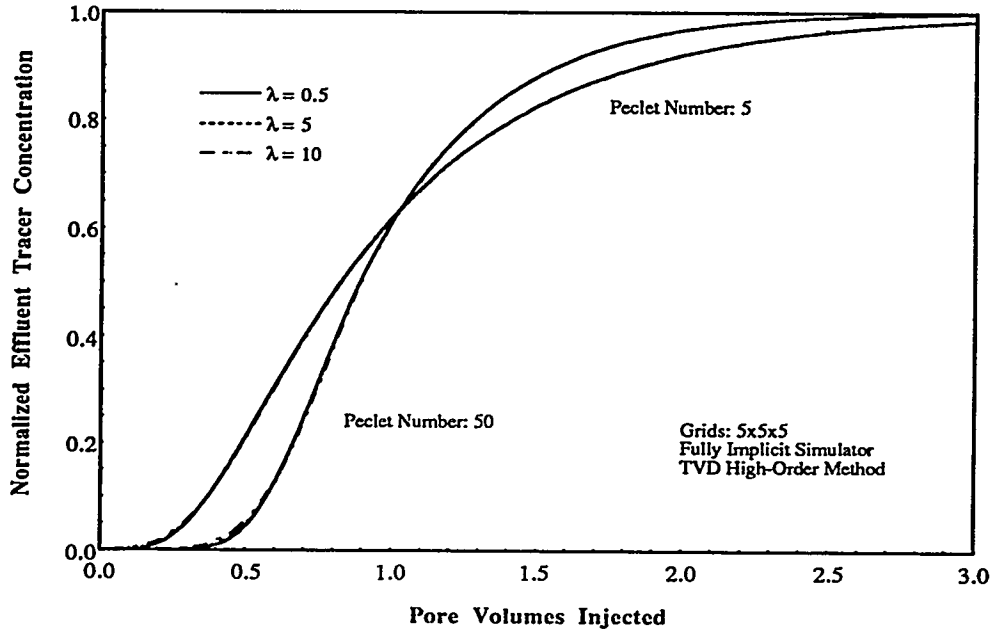


Fig. 4.43. Simulation of a three-dimensional tracer flood using the fully implicit simulator.

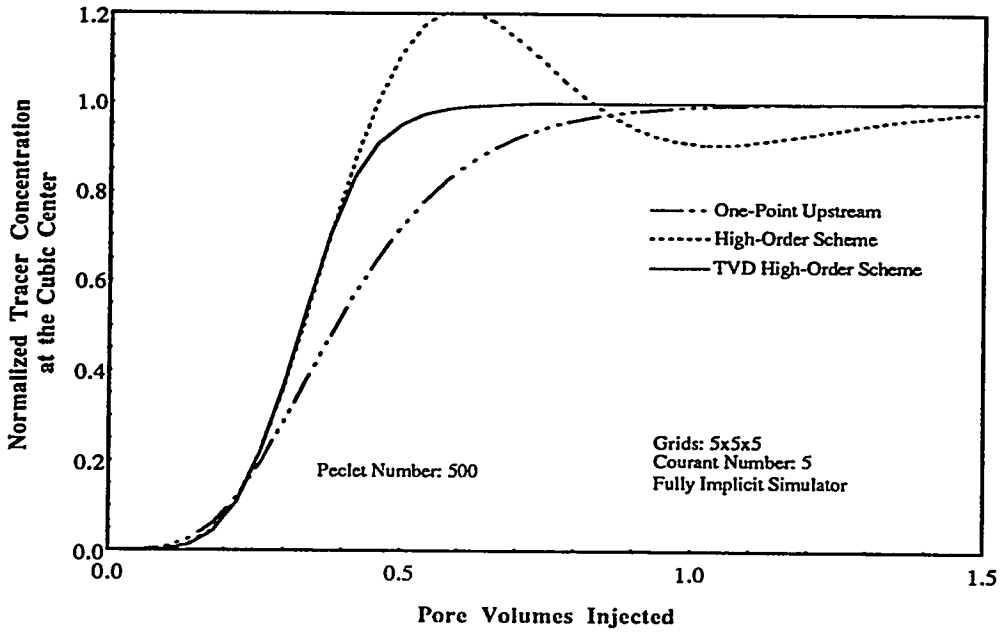


Fig. 4.44. Simulation of a three-dimensional tracer flood using the high-order scheme without TVD flux limiting or the low-order scheme.

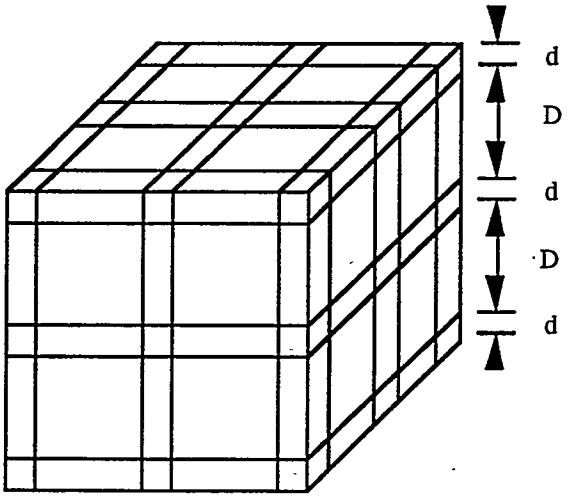


Fig. 4.45. Schematic of a nonuniform grid and its expansion ratio.

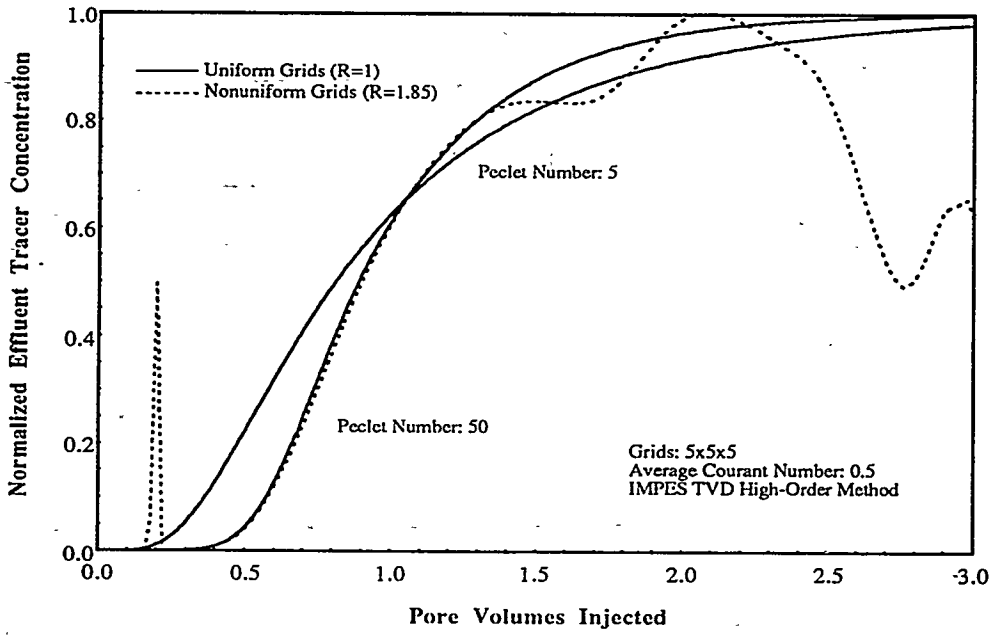


Fig. 4.46. Simulation of a three-dimensional tracer flood using the IMPES simulator with a nonuniform grid.

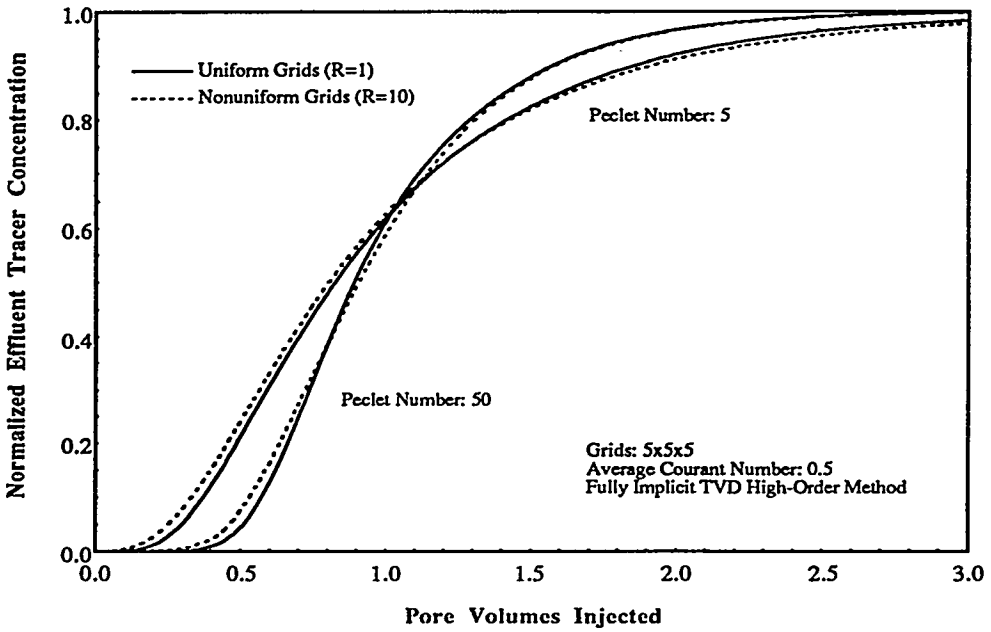


Fig. 4.47. Simulation of a three-dimensional tracer flood using the IMPES simulator with a nonuniform grid.

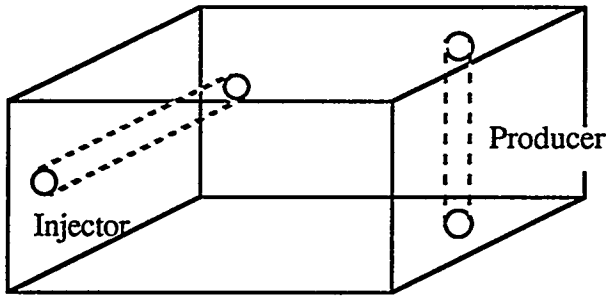


Fig. 4.48. Well pattern for the three-dimensional polymerflood simulation.

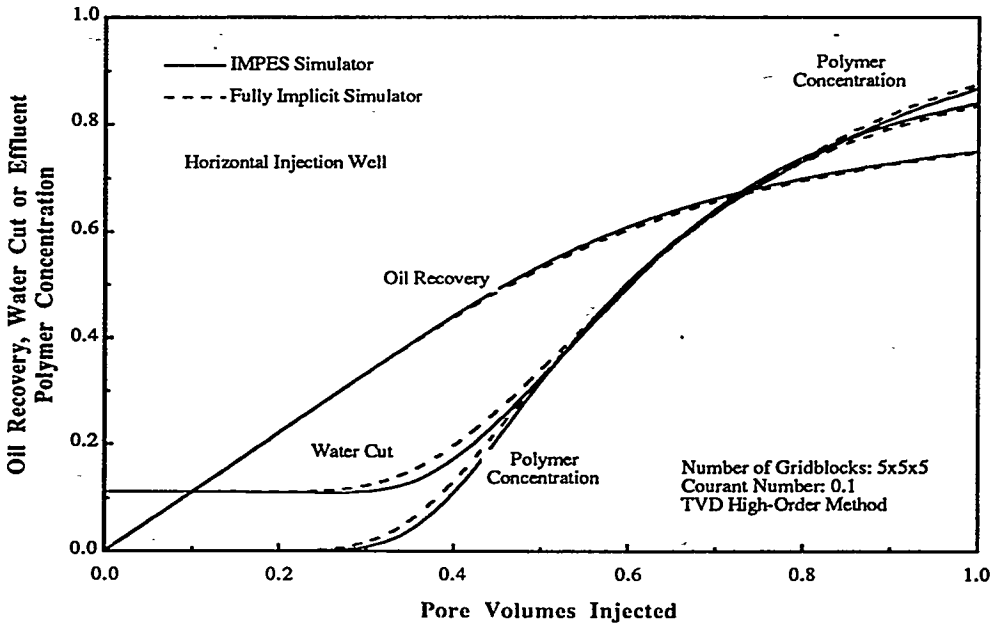


Fig. 4.49. Simulation of a three-dimensional polymerflood with horizontal well using the fully implicit simulator and the IMPES simulator.

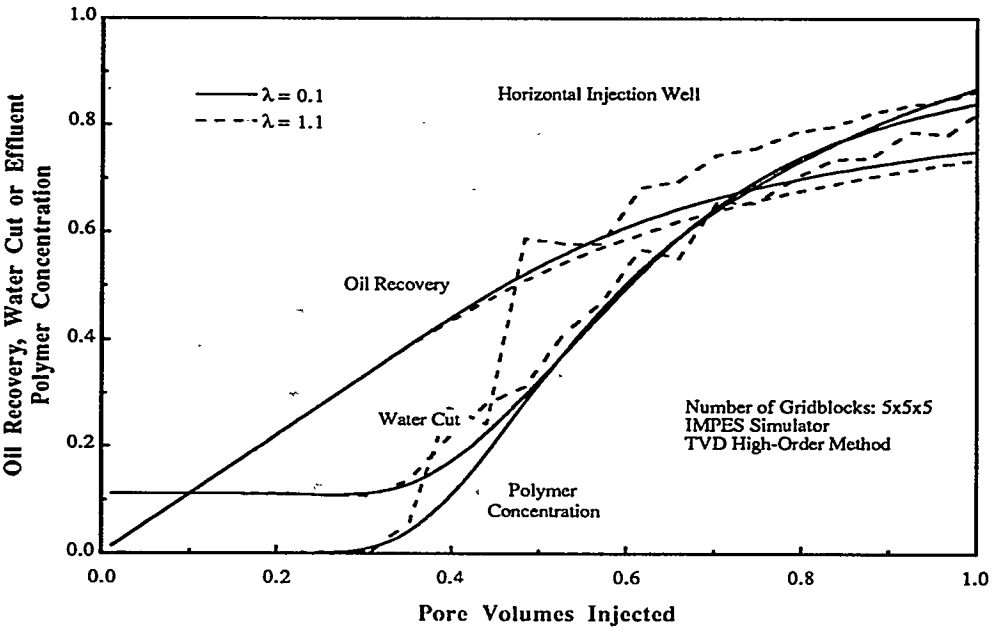


Fig. 4.50. Simulation of a three-dimensional polymerflood with horizontal well using the IMPES simulator.

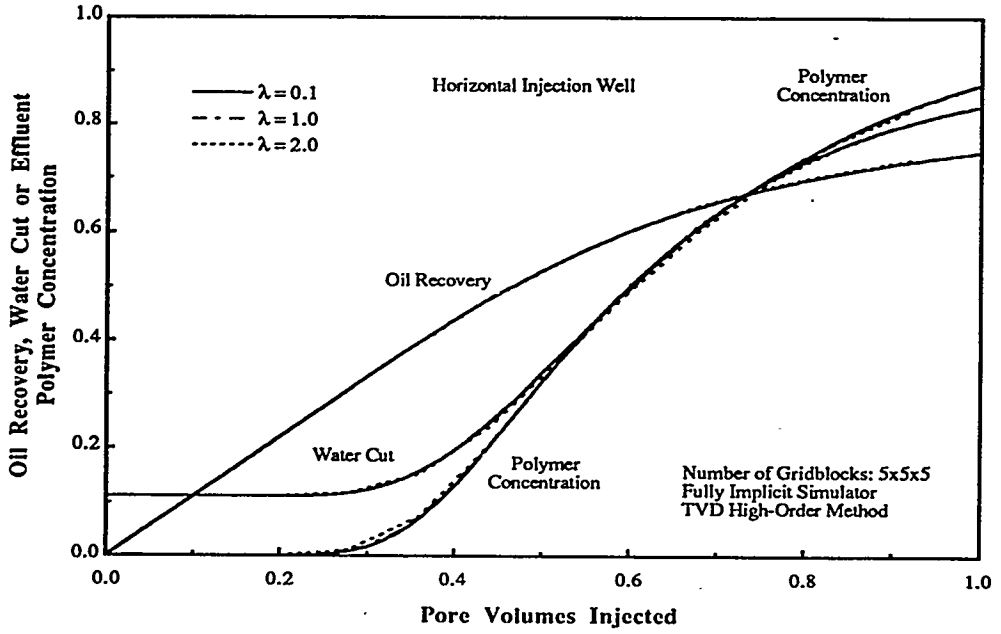


Fig. 4.51. Simulation of a three-dimensional polymerflood with horizontal well using the fully implicit simulator.

5. Summary, Conclusions, and Recommendations

5.1 Summary and Conclusions

A high-resolution, fully implicit, finite-difference, multiphase, multicomponent, compositional simulator for chemical flooding has been developed and is described in this report.

The major physical phenomena modeled in the simulator are dispersion, heterogeneous permeability and porosity, adsorption, interfacial tension, relative permeability and capillary desaturation, compositional phase viscosity, compositional phase density and gravity effects, capillary pressure, and aqueous-oleic-microemulsion phase behavior. Polymer and its non-Newtonian rheology properties include shear-thinning viscosity, permeability reduction, inaccessible pore volume, and adsorption. Options of constant or variable space and time grids, constant-pressure or constant-rate well conditions, horizontal and vertical wells, and multiple slug injections are also available in the simulator.

The solution scheme used in this simulator is fully implicit. The pressure equation and the mass-conservation equations are solved simultaneously for the aqueous-phase pressure and the total concentrations of each component. The pressures in nonaqueous phases are obtained from the capillary pressures, and the phase concentrations and saturations are obtained by flash calculations from the total concentrations. The finite-difference discretization scheme is third-order-in-space, second-order-in-time and a new total-variation-diminishing (TVD) third-order flux limiter is used for reducing numerical dispersion effects. Under the TVD constraints, the third-order TVD flux limiter is constructed using the third-order flux function to the greatest extent possible for the purpose of achieving high-order accuracy. Numerical oscillations associated with the high-order schemes without flux limiting are eliminated. The high-resolution scheme maintains high-order accuracy with nonuniform grids. TVD constraints are applied to the species fluxes and the phase fluxes by imposing the TVD third-order flux-limiter functions to the approximations of interface convections and interface relative permeabilities.

Conventional simulation techniques are based on classical finite-difference methods. The feature of these methods is that they are built on constant-coefficient stencils. Lower-order spatial discretization schemes have excessive front-smearing effects, resulting in erroneous solutions unless very fine grids are used, which is impractical because of the computational cost. Higher-order schemes are good at reducing excessive numerical dispersion effects and are suitable for problems having a certain amount of physical dispersion. They are, however, plagued by spurious oscillations in the neighborhood of discontinuities. Such oscillations are not only undesirable but often lead to a breakdown in the stability of the scheme and to nonphysical results. The effects are particularly severe when modeling many enhanced oil recovery processes. The conventional implicit methods with either the first-order or the high-order spatial discretizations have no Courant number restrictions and are unconditionally stable, but suffer from excessive numerical diffusion caused by lower-order time accuracy as larger Courant numbers are used.

This latest numerical advance in the new simulator is a significant advantage over other reservoir simulation codes of all types that use one- and two-point upstream weighting, which is the industry standard despite its well-known and significant numerical inaccuracy.

The simulator has been verified by the good agreements between numerical results and analytical solutions. The simulation results of different processes have also been compared with the results using standard numerical approaches or using our existing high-resolution IMPES simulator. The comparisons ensure the correctness of the mathematical formulations, the finite-difference schemes, the physical-property models, well models, spatial gridding and timestepping schemes, and the program coding. The comparison also demonstrates the merit of our high-resolution fully implicit numerical method over standard numerical approaches and the computational efficiency over the IMPES simulator for problems with severe stability restrictions.

5.2 Recommendations

5.2.1 Improvements of Physical-Property Models

There are certain first or second kind of discontinuities, and infinite points exist in the functions or their derivatives describing physical properties modeled in the simulator. Examples of these are CMC criteria in the phase-behavior model, permeability-reduction-factor limits in the permeability-reduction model, C_{SEI} definition in the polymer viscosity model, derivatives of interfacial tension and adsorptions, etc.. Further studies are recommended to find the degree of these discontinuities and how seriously these discontinuities may affect the simulations for different processes. Some of these discontinuities in derivatives may be removable and can be treated using standard methods. Some may need special treatments.

The quality of Jacobian matrix evaluation is a kep factor to the convergence of the Newton iteration of the implicit simulator. There are variables in the physical-property models containing terms that are flux-dependent, such as the elements of the physical dispersion tensor, shear rate, capillary number, etc. In the current simulator, fluxes contained in these terms are treated as constants and updated each iteration. Further studies need to be made to find if the Jacobian matrix should include these derivatives. To answer the question, we need to compare the cost of more Newton iterations without these kinds of Jacobian evaluations with the cost of fewer iterations with Jacobian evaluations. For the evaluation itself, we also need to decide if we should do it numerically or analytically. In most cases, all the questions and answers are processes-dependent.

The development of high-resolution numerical simulation techniques has made it meaningful to use more realistic models to describe chemical, physical, and geological properties with respect to transport processes in permeable media. Based on these models, the new-generation general-purpose simulator will have broad features with the capability of simulating problems of different types. The integrated mathematical model of the simulator based on conservation of mass and energy will incorporate all of the desired physical and pertinent flow phenomena. The formulation of mass-conservation equations involves a wide variety of species of different types: organic, electrolyte, inorganic, surfactant, microbial, and tracers. These species can form whatever phases thermodynamics dictate (e.g., aqueous, oleic, gas, microemulsion, gel, or foams) as a function of composition and temperature. General boundary conditions should be available to facilitate simulating various problems. In addition to general-purpose well models, other boundary conditions should be included to allow for open and closed surfaces. Arbitrary specification of all primary dependent variables and fluxes should be possible on these surfaces.

5.2.2 Improvements of Numerical Models

Further studies of high-resolution simulation techniques can be made in several areas. One option is to develop fully multidimensional methods, which are still deficient in mathematical theory (Le Veque, 1988). Most current multidimensional numerical methods are based on the theory of one-dimensional results, which can only be carried over to a certain extent. Multidimensional effects do play a strong role in the solution locally, and any approach that only solves a one-dimensional problem in the coordinate directions is clearly not using all the available information. Shock waves at a large angle to the coordinate directions will be less well-resolved than shocks aligned with the grid. In practical calculations this is sometimes avoided by choosing grids that fit the problem well, so the shock wave is nearly aligned with the grid. Methods are evolving in the direction of using more information about multidimensional behavior. One possibility is to determine the direction of primary wave propagation, based on the data, rather than simply using the coordinate directions, and to employ wave propagation in other directions as well (Le Veque, 1988; Powell and Van Leer, 1989).

The numerical model should be a discrete analog to the mathematical model with the highest degree of accuracy within the constraints of the cost and availability of computing power. Some important new features of the model should be (1) adaptive spatial gridding in three dimensions

with effective properties, which means the spatial grid automatically refines or coarsens as needed locally, with the properties of the medium such as permeability recomputed on the new grid using renormalization theory or other theoretically correct scaling, and the grid should easily accommodate faults and other common geological features, (2) an adaptive implicit method for the solution scheme, which operates with different levels of implicitness as a function of both space and time rather than a fixed degree of implicitness in the entire simulation domain, with level shifting being accomplished automatically without user intervention, achieving substantial reduction in computing time and storage requirements compared to fully implicit formulations while still yielding unconditionally stable solutions, (3) an optimal timestepping algorithm which provides an efficient way for estimating the timestep size sequence as a function of spatial gridding and relative changes in the solution, with the produced timestep sizes guaranteeing the convergence of a Newton iteration for the implicit formulation and minimizing the truncation error of the finite-difference scheme, (4) adaptive parallelization, which means the solution to the numerical model should be obtained by automatically taking advantage of a wide range of processors and having different solvers depending on the number of processors and the type of problem to maximize efficiency, and (5) a user-friendly interface for different types of applications, with the input menu driven with optional expert advice and a database of physical properties available and the output in a form that can be readily used with visualization software. All these new features need to be studied in the near future, using the latest numerical simulation methods and computing technologies.

6. Nomenclature

a_4	=	Polymer adsorption parameter
a_{41}	=	Polymer adsorption parameter
a_{42}	=	Polymer adsorption parameter
A_{p1}, A_{p2}, A_{p3}	=	Polymer viscosity parameters
b_4	=	Polymer adsorption parameter
b_{rk}	=	Parameter in permeability reduction-factor equation
C_{4a}	=	Concentration of polymer in aqueous phase
c_{rk}	=	Permeability-reduction parameter, L
C_f	=	Pore compressibility, $M^{-1}LT^2$
C_t	=	Total compressibility, $M^{-1}LT^2$
$\tilde{C}_\kappa$	=	Overall concentration of component κ
$\hat{C}_\kappa$	=	Adsorbed concentration of component κ
C_κ^0	=	Compressibility of component κ, $M^{-1}LT^2$
$C_{\kappa\ell}$	=	Concentration of component κ in phase ℓ
C_{p_c}	=	Capillary pressure endpoint parameter, MT^{-2}
C_{SEP}	=	Effective salinity for polymer
$D_{\kappa\ell}$	=	Molecular diffusion, L^2T^{-1}
e_ℓ	=	Relative-permeability exponent of phase ℓ
$F_{a\kappa}$	=	Overall accumulation of component κ, L^3
$F_{t\kappa}$	=	Overall transport of component κ, L^3T^{-1}
$F_{q\kappa}$	=	Overall source or sink of component κ, L^3T^{-1}
$\vec{F}_\kappa$	=	Overall mass flux of component κ, $ML^{-2}T^{-1}$
J	=	Jacobian matrix
k	=	Permeability, L^2
$\vec{\vec{k}}$	=	Permeability tensor
k_a	=	Horizontal permeability, L^2
$k_{r\ell}$	=	Relative permeability of phase ℓ
k_s	=	Permeability-deviation coefficient
$k_{r\ell}^0$	=	Endpoint relative permeability for phase ℓ
$\overline{K}$	=	Dispersion coefficient, L^3T^{-1}
$\vec{\vec{K}}$	=	Dispersion tensor
$K_{xx\kappa\ell}, K_{yy\kappa\ell}$ $K_{zz\kappa\ell}$	=	Diagonal elements of the dispersion tensor for component κ in phase ℓ, L^2T^{-1}
$K_{xyk\ell}, K_{xzk\ell}$ $K_{yxk\ell}, K_{yzk\ell}$ $K_{zxk\ell}, K_{zyk\ell}$	=	Off-diagonal elements of the dispersion tensor for component κ in phase ℓ, L^2T^{-1}

n_c	=	Total number of components
n_{cv}	=	Total number of volume-occupying components
n_p	=	Total number of phases
n_{p_c}	=	Capillary-pressure exponent
N_b	=	Total number of gridblocks
N_i	=	Number of iterations
N_g	=	Gravity number
N_{Pe}	=	Peclet number (L/α)
N_{RL}	=	Rapoport and Leas number
N_x, N_y, N_z	=	Number of gridblocks in the x, y, and z directions
$P_{c\ell\ell'}$	=	Capillary pressure between phases ℓ and ℓ', $ML^{-1}T^{-2}$
P_ℓ	=	Phase pressure, $ML^{-1}T^{-2}$
P_R	=	Reference pressure, $ML^{-1}T^{-2}$
P_{wf}	=	Well flowing pressure, $ML^{-1}T^{-2}$
P_α	=	Exponent for calculating shear-rate dependence of polymer viscosity
P_Δ	=	Cell Peclet number ($\Delta x/\alpha$)
PI	=	Productivity index, $M^{-1}L^4T$
q_κ	=	Unit volumetric source or sink of component κ, T^{-1}
$q_{\kappa f}$	=	Unit volumetric injection/production rate of component κ, T^{-1}
$q_{\kappa r}$	=	Unit volumetric reaction rate of component κ, T^{-1}
Q	=	Rate, L^3T^{-1}
r	=	Ratio of consecutive gradients
R_k	=	Permeability reduction factor
R_m	=	A random number with a normal distribution
S_ℓ	=	Phase saturation
$S_{n\ell}$	=	Normalized phase saturation
S_p	=	Exponent for calculating salinity dependence of polymer viscosity
$S_{\ell r}$	=	Residual saturation of phase ℓ
S_{wi}	=	Initial water saturation
Δt	=	Timestep size, T
T	=	Transmissibility, L^3; Temperature, K
$\vec{u}_\ell$	=	Flux, LT^{-1}
Δx, Δy, Δz	=	Gridblock sizes in the x, y, and z directions, L

Greek Symbols

$\alpha_{L\ell}$	=	Longitudinal dispersivity of phase ℓ, L
$\alpha_{T\ell}$	=	Transverse dispersivity of phase ℓ, L
β_P	=	Effective salinity parameter for polymer viscosity

$\dot{\gamma}_{1/2}$	=	Shear rate at which polymer viscosity is one-half the polymer viscosity at zero shear rate, T^{-1}
$\dot{\gamma}_c$	=	Coefficient in equivalent shear-rate equation
γ_ℓ	=	Specific weight of phase ℓ, $ML^{-2}T^{-2}$
λ	=	Courant number; mobility , $M^{-1}LT$
μ_ℓ	=	Phase viscosity, $ML^{-1}T^{-1}$
$[\mu]$	=	Intrinsic polymer viscosity
μ_p	=	Polymer solution viscosity, $ML^{-1}T^{-1}$
μ_w	=	Water viscosity, $ML^{-1}T^{-1}$
ϕ	=	Porosity
ϕ_R	=	Porosity at reference pressure
φ	=	Flux-limiter function
Φ	=	Potential, $ML^{-1}T^{-2}$

Subscripts and Superscripts

a	=	Accumulation term index
a, w	=	Aqueous phase index
i, j, k	=	Spatial indexes in the x, y, and z directions
κ	=	Component index
ℓ	=	Phase index
L	=	Longitudinal
n	=	Timestep index
o	=	Oleic phase
q	=	Source or sink term index
r	=	Residual; relative property
t	=	Transport term index
T	=	Transverse

7. References

Abbaszadeh-Dehghani, M. and W.E. Brigham: "Analysis of Well-to-Well Tracer Flow To Determine Reservoir Layering," *J. Pet. Tech.* (Oct. 1984) **36**, 1753-1762.

Amyx, J.W., D.M. Bass, and R. L. Whiting: *Petroleum Reservoir Engineering: Physical Properties*, McGraw-Hill Book Company, New York (1960).

Au, A.D.K., A. Behie, B. Rubin, and P.K.W. Vinsome: "Techniques For Fully Implicit Reservoir Simulation," paper SPE 9302 presented at the 1980 SPE Annual Tech. Conf., Dallas, TX, Sep. 21-24.

Aziz, K. and A. Settari: *Petroleum Reservoir Simulation*, Applied Science Publishers, London (1979).

Bhuyan, D., L.W. Lake, and G.A. Pope: "Mathematical Modeling of High-pH Chemical Flooding," paper SPE/DOE 17398 presented at the 1988 SPE/DOE Symposium on Enhanced Oil Recovery, Tulsa, OK, April 17-20.

Buckley, S.E. and M.C. Leverett: "Mechanism of Fluid Displacements in Sands," *Trans.*, AIME (1958) **146**, 107-116.

Camilleri, D., A. Fil, G.A. Pope, B. Rouse, and K. Sepehrnoori: "Improvements in Physical Property Models Used in Micellar/Polymer Flooding," *SPE Reser. Eng.* (1987) **2**, No. 4, 433-440.

Celia, M. A. and W.G. Gray: *Numerical Methods for Differential Equations*, Prentice Hall, Englewood Cliffs, NJ (1992).

Chang, Y.: "Development of a Three-Dimensional, Equation-of-State Compositional Reservoir Simulator for Miscible Gas Flooding," Ph.D. dissertation, U. of Texas, Austin (Aug. 1990).

Datta Gupta, A., G.A. Pope, K. Sepehrnoori, and R.L. Thrasher: "A Symmetric, Positive Definite Formulation of a Three-Dimensional Micellar/Polymer Simulator," *SPE Reser. Eng.* (Nov. 1986) **1**, 622-632.

Delshad, M., G.A. Pope, and K. Sepehrnoori: "A Compositional Simulator for Modeling Surfactant Enhanced Aquifer Remediation. 1: Formulation," *J. of Contam. Hydro.*, in press, 1996.

Fanchi, J.R.: "Multidimensional Numerical Dispersion," *Soc. Pet. Eng. J.* (Jan. 1983) **23**, 143-151.

Foulser, R.W.S. and S.G. Goodyear: "Improved Stability of the IMPES Formulation for Chemical Flooding," paper SPE 18417 presented at the 1989 SPE Symposium on Reservoir Simulation, Houston, TX, Feb. 6-8.

Hand, D.B.: "Dineric Distribution: I. The distribution of a Consolute Liquid between Two Immiscible Liquids," *J. of Physics and Chem.* (1939) **34**, 1961-2000.

Harten, A.: "High Resolution Schemes for Hyperbolic Conservation Laws," *SIAM Rev.* (1983) **25**, No. 1, 35-67.

Holing, K., J. Alvestad, and J. Trangenstein: "The Use of Second-Order Godunov-type Methods for Simulating EOR Processes in Realistic Reservoir Models," *Proc.*, 2nd European Conference on the Mathematics of Oil Recovery, Paris (Nov. 1990) 101-111.

Kazemi, H., C.R. Vestal, and G. Deane Shank: "An Efficient Multicomponent Numerical Simulator," *Soc. Pet. Eng. J.* (Oct. 1978) **18**, 355-368.

Lake, L.W.: *Enhanced Oil Recovery*, Prentice Hall, Englewood Cliffs, NJ (1989).

Lake, L.W., G.A. Pope, G.F., Carey, and K. Sepehrnoori: "Isothermal, Multiphase, Multicomponent Fluid Flow in Porous Media. Part I: Description and Mathematical Formulation," *In Situ* (1984) **8**, No. 1, 1-40.

Lantz, R.B.: "Quantitative Evaluation of Numerical Diffusion (Truncation Error)," *Soc. Pet. Eng. J.* (Sep. 1971) **11**, 315-320.

Le Veque, R.J.: "High Resolution Finite Volume Methods on Arbitrary Grids via Wave Propagation," *J. Comp. Phys.* (1988) **78**, No. 1, 36-63.

Le Veque, R.J.: *Numerical Methods for Conservation Laws*, Lectures in Mathematics, Birkhauser Verlag, Basel (1990).

Liu, J., M. Delshad, G.A Pope, and K. Sepehrnoori: "Application of Higher-Order Flux-Limited Methods in Compositional Simulation," *Trans. in Porous Media* (1994) **16**, No. 1, 1-30.

Liu, J., G.A. Pope, and K. Sepehrnoori: "A High-Resolution, Fully Implicit Method for Enhanced Oil Recovery Simulation," paper SPE 29098, proceedings of the 1995 SPE Symposium on Reservoir Simulation, San Antonio, TX, Feb. 12-15.

Oppe, T.C., W. D. Joubert, and D.R. Kincaid: *"NSPCG User's Guide Version 1.0,* A Package for Solving Large Sparse Linear Systems by Various Iterative Methods," Center for Numerical Analysis, U. of Texas, Austin (April 1988).

Patel, M.K., N.C. Markatos, and M. Cross: "A Critical Evaluation of Seven Discretization Schemes for Convection-Diffusion Equations," *Int. J. for Numer. Methods in Fluids* (1985) **5**, No. 5, 225-244.

Peaceman, D.W.: *Fundamentals of Numerical Reservoir Simulation*, Elsevier Science Publishers, Amsterdam (1977).

Pope, G.A.: "The Application of Fractional Flow Theory to Enhanced Oil Recovery," *Soc. Pet. Eng. J.* (1980) **20**, No. 3, 191-205.

Pope, G.A. and R.C. Nelson: "A Chemical Flooding Compositional Simulator," *Soc. Pet. Eng. J.* (Oct. 1978) **18**, 339-354.

Powell, K.G. and B. Van Leer: "A Genuinely Multidimensional Upwind Cell-Vertex Scheme for the Euler Equations," AIAA Paper 89-0095, Reno, NV (1989).

Rapoport, L.A. and W.J. Leas: "Properties of Linear Waterfloods," *Trans.*, AIME (1953) **198**, 139-148.

Rapoport, L.A. and W.J. Leas: "Laboratory Studies of Five-Spot Waterflood Performance," *Trans.*, AIME (1958) **213**, 113-120.

Richardson, J.G., J.K. Kerver, J.A. Hafford, and J.S. Osoba: "Laboratory Determination of Relative Permeability," *Trans.*, AIME (1952) **195**, 187-196.

Richtmyer, R.D. and K.W. Morton: *Difference Methods for Initial Value Problems*, Interscience, New York (1977).

Roe, P.L.: "Generalized Formulation of TVD Lax-Wendroff Schemes," *ICASE Report* No. 84-53 (Oct. 1984).

Saad, N.: "Field Scale Simulation of Chemical Flooding," Ph.D. dissertation, U. of Texas, Austin (Aug. 1989).

Saad, N., G.A. Pope, and K. Sepehrnoori: "Simulation of Big Muddy Surfactant Pilot," *Soc. Pet. Eng. J.*. (Feb. 1989) **29**, 23-34.

Scott, T., L.J. Roberts, S.R. Sharpe, P.J. Clifford, and K.S. Sorbie: "In-Situ Gel Calculations in Complex Reservoir Systems using a New Chemical Flood Simulator," *SPE Reser. Eng.* (Nov. 1987) **2**, 634-646.

Sweby, P.K.: "High Resolution Schemes Using Flux Limiters for Hyperbolic Conservation Laws" *SIAM J. Numer. Analysis* (1984) **21**, No. 5, 995-1011.

Trangenstein, J.A.: *Multi-Phase Flow in Porous Media: Mechanics, Mathematics and Numerics*, Lecture Notes, IBM Scientific Center, Bergen, Norway (1986).

Willhite, G.P.: *Waterflooding*, Textbook Series **3**, Soc. Pet. Eng., Dallas, TX (1986).

Yee, H.C.: "Construction of Explicit and Implicit Symmetric TVD Schemes and Their Applications," *J. Comp. Phys.* (1987) **68**, No. 1, 151-179.

Young, L.C. and R.E. Stephenson: "A Generalized Compositional Approach for Reservoir Simulation," *Soc. Pet. Eng. J.* (Oct. 1983) **23**, 727-742.

TASK 2. OPTIMIZATION OF SURFACTANT FLOODING

Part I: Reservoir Modeling Studies

1. UTCHEM Modeling Enhancements

UTCHEM development has continued and several significant improvements have been made in the code during the course of this research project. These improvements have the combined effect of making the code more versatile and efficient, which better serves not only our needs but those of a large number of external users in both petroleum, subsurface, and environmental engineering. The enhancements in UTCHEM include the following:

- A single-level adaptive grid refinement. The implementation strategy for grid refinement is based on domain decomposition where each zone is treated independently (Edwards, 1996).
- 2-D cross-sectional curvilinear grid option.
- A dual porosity formulation to model tracer transport in fractured media (Liang *et al.*, 1995).
- An option to calculate the interfacial tension between microemulsion/oil and microemulsion/brine using Chun Huh relationship (Huh, 1979). The only option previously available was based on Healy and Reed (1974).
- Temperature-dependent surfactant phase behavior. Both the height of the binodal curve and the effective salinity are shifted to model the shift in surfactant/oil/water phase behavior with temperature (Delshad *et al.*, 1996).
- The component numbering scheme presently in UTCHEM has been changed to allow additional aqueous species.
- Options of chromium malonate gel and silicate gel systems for the application of in-depth gel treatment in addition to the previous option of polymer/chromium chloride gel (Kim, 1995).
- Allow for competitive surfactant adsorption in the presence of polymer. This option was added to adequately simulate the low tension polymer flooding. The surfactant adsorption model was modified such that the adsorbed surfactant concentration is reduced as a function of polymer concentration (Wu, 1996).
- Microbiological population model.
- Multiple reactive tracers.
- Reversible oil adsorption.
- Permeability-dependent surfactant and polymer adsorption model (Delshad *et al.*, 1996).
- Addition of gas tracers and an option for nonequilibrium mass transfer of gas tracers.
- An option to calculate up to three-phase hysteretic capillary-pressure and relative permeability functions using van Genuchten (1980) and Parker *et al.* (1987) models. The three phases are either oil/water/gas or three liquid phases of water/microemulsion/oil in the presence of surfactant. Both capillary-pressure and relative-permeability models are functions of capillary number.

- Allow for a compositional oleic phase and property models for the oil mixture: for example, surfactant phase behavior, viscosity, and density for organic mixtures.

2. Optimization of Surfactant/Polymer Flooding for Three Reservoirs

In this study, we attempt to optimize the design of surfactant/polymer (S/P) flooding by analyzing in detail the reservoir processes taking place in three different reservoirs. New modeling features of UTCHEM were applied to obtain a realistic reservoir description and precise description of physical properties. These features include temperature effects on the phase behavior of surfactant and phase viscosity, competitive adsorption between surfactant and polymer, curvilinear grids, and Huh's interfacial tension model.

The best surfactants for enhanced oil recovery appear to be sulfates or sulfonates of alcohols that have branched hydrophobes and have had ethylene oxide and/or propylene oxide moieties added in the number appropriate for the particular reservoir conditions of crude oil, salinity, and temperature. In this study, we have referred to predecessors such as Shupe (1989) and Wellington and Richardson (1995) for a surfactant that is likely to perform best.

The optimization for each reservoir is presented. The mechanisms of the surfactant/polymer process in low, moderate and high heterogeneity reservoirs are discussed in detail. The introduction is followed by the presentation of an optimized S/P process for Reservoir A. Then the optimizations for Reservoirs B and C are shown.

2.1 Introduction

For the optimization of chemical flooding, sensitivity analysis simulations were performed. Three reservoirs with significantly different properties, initial conditions, and different degrees of heterogeneity (low, medium, and high) were studied. Application of horizontal wells, location of the horizontal wellbore, nonisothermal condition, permeability-distributed residual oil saturation, and the sensitivity of each of these to reservoir description are examples of sensitivity factors simulated. The new injection scheme with high-efficiency surfactant such as low-tension polymer flood (LTPF) was studied. The LTPF design has the potential of reducing the front end and total chemical costs, since a small amount of surfactant and a low concentration of surfactant are used in chemical flooding. There are a number of laboratory studies on the interactions between polymers and surfactants during a LTPF (Austad *et al.*, 1994; Austad and Taugbøl, 1993; Kalpakci *et al.*, 1993).

Kalpakci *et al.* (1993), Austad *et al.* (1993), and other recent researchers indicate that the very best of the synthetic ethoxy and propoxy sulfate and sulfonate surfactants can still be effective under these dilute conditions. This is thought to be in part due to the very low surfactant adsorption in the presence of polymer. It is believed that polymer of a certain type, when propagated with and ahead of the surfactant bank in the appropriate amount, can potentially reduce surfactant adsorption. The polymer-induced shift of the surfactant phase behavior is not considered in this study, because the discrepancy among experiments on this matter is too large and the effect is thought to be small.

These simulations show that some S/P floods can be very efficient when the optimum design for some reservoirs is obtained by systematic simulations and careful analysis of the results. The detailed results and discussions in the following sections are introduced by the classification of reservoirs.

2.2 Optimization Design for Reservoir A

Reservoir A is an offshore North Sea sandstone reservoir. The permeability distribution has a relatively low heterogeneity and is in the range of 5 to 16 darcies. High permeability and porosity are important characteristics of this reservoir. For simplification, a 2-D vertical cross-section of the reservoir was chosen for the simulations presented here. The main concerns in this reservoir are the effects of the injection scheme and the chemical and physical properties. Both 2-D

and 1-D sensitivity simulations were performed to thoroughly understand the process mechanisms. A 3-D simulation was also performed at the end to evaluate the difference between 2-D and 3-D behavior.

Experimental coreflood results were first history matched to obtain the physical property data. An approach to fit experimental data to the physical models in UTCHEM is demonstrated. Applying these data to Reservoir A, we have investigated the sensitivity of a polymer-assisted surfactant flood to the following parameters: injected surfactant concentration, S/P slug size, polymer concentration, phase behavior, surfactant/polymer interactions, surfactant viscosity, interfacial tension, permeability-dependent residual oil saturation, and polymer preflooding. Gravity, buoyancy, and temperature effects were also evaluated. The discussion and analysis of surfactant/polymer mechanisms from the simulation results are presented in the following sections.

2.2.1 Coreflood Simulations

A Bentheimer rock coreflood result was history matched to estimate some of the physical-property parameters. Eleven coreflood results were provided. Since the first coreflood (named NL1) had most clearly defined core properties, its results were used for the coreflood history match. This coreflood result was representative of the whole series of experiments because the other ten corefloods differed only in the slug size or concentration of injected surfactant.

2.2.1.1 Descriptions of Coreflood

The S/P corefloods were done with Bentheimer rock. The permeability of these cores ranged from 1,400 to 2,912 md. The average porosity was 0.22. The length of these cores was 1 ft and cores were oriented horizontally in all experiments. These experiments exhibited abnormal pressure-drop increases. The pressure drop increased and reached a maximum at the end of surfactant injection, then decreased in both the polymer drive and water postflush. High-viscosity emulsions may have occurred during the core displacement.

For coreflood NL1, the diameter and the length were 0.125 and 1 feet, respectively. The porosity was 0.229 and the brine permeability was 2,912 md. The coreflood data are listed in Table 2.1. The Bentheimer core was flooded with oil at 122°F until the water saturation reached 0.147. Then the core was flooded with synthetic sea water for 0.61 PV. The oil saturation was close to the residual oil saturation at the end of this waterflooding. The injection scheme for the chemical flood was

S/P slug	: 0.43 PV of 0.5 vol.% of surfactant with 500 ppm of xanthan gum in synthetic sea water,
Polymer drive	: 0.5 PV of 500 ppm xanthan gum in synthetic sea water, and
Postflush	: 4.9 PV of synthetic sea water.

The surfactant used in this study was characterized by a short ethylene oxide chain between a branched hydrophobic tail and the sulfonate group. The critical micelle concentration (CMC) was 0.01 vol.%. The surfactant phase behavior was Type II(-). The sea-water anion and divalent concentrations were 22,258 mg/ℓ (0.627 meq/mℓ) and 5,320 mg/ℓ (0.133 meq/mℓ), respectively. The upper limit and lower limit effective salinities of the three-phase region were 31,950 (0.9 meq/mℓ) and 27,950 mg/ℓ (0.65 meq/mℓ), respectively.

2.2.1.2 Processing Experimental Data to UTCHEM Model

In this section, we show an approach to apply the experimental data to the mathematical model used in UTCHEM. The curve-fitting package used in this study is a built-in function of a commercial program, Microsoft Excel. The fitting of the oil-phase desaturation curve is demonstrated. The model used to describe the desaturation curve in UTCHEM is

$$S_{\ell r} = S_{\ell rc} + \frac{S_{\ell rw} - S_{\ell rc}}{1 + T_\ell N_{c\ell}}, \ \ell = 1,2,3.$$

The residual-phase saturations can be measured from corefloods. The capillary number is given by

$$N_{c\ell} = \frac{\sqrt{\left(k_x \frac{\partial \Phi_\ell}{\partial x}\right)^2 + \left(k_y \frac{\partial \Phi_\ell}{\partial y}\right)^2 + \left(k_z \frac{\partial \Phi_\ell}{\partial z}\right)^2}}{\sigma_{\ell\ell}}, \ \ell = 1,2,3.$$

The objective function used to estimate the value of the parameter T_ℓ was

$$F = \sum_{k=1}^{n} \left(S_{\ell,\text{calculated}} - S_{\ell,\text{experiment}} \right)_k^2$$

where n is the number of experimental measurements. Applying a function called "solver" in Microsoft Excel, the minimum value of this objective function was determined. The results are shown in Figure 2.1. Similarly, the experimental data for relative permeability at low capillary number, interfacial tension, polymer viscosity, and surfactant phase behavior were regressed to estimate the best values of various parameters. Figures 2.2 through 2.5 show the results for each model. The height of the binodal curve at zero salinity is very low (0.03), which indicates an efficient surfactant.

When no data were available to estimate a parameter, typical values or values from history matching coreflood results were used. For this reason, relative permeability at high capillary number (Figure 2.6) and the water and microemulsion capillary-desaturation parameters (Figure 2.1) were taken from Delshad (1990). The microemulsion viscosity was assumed to be a linear function of the oil and water concentrations, since insufficient data were available to estimate the dependence on surfactant concentration (Figure 2.7). The adsorption isotherm for surfactant (Figure 2.8) and polymer (Figure 2.9) were estimated from the history match of the experimental corefloods. The measured retentions for surfactant and polymer were 0.2 mg/g of rock and 8.44 μ g/g of rock at the end of the coreflood. These are both low values.

2.2.1.3 Simulation of Coreflood

Applying the above-mentioned injection scheme and given physical properties, a Base Case of 1-D S/P simulation was performed. The key input parameters for the history match are listed in Table 2.2. 80 gridblocks were used for all simulations. The porosity and permeability were assumed to be uniform. The height of the binodal curve was a constant equal to 0.03, since the salinity was kept constant in Type II(-) environment. The initial oil saturation for the chemical flood was assumed to be equal to the reported residual oil saturation of 0.395. This is because the residual oil saturation and the oil recovery reported for the waterflood were inconsistent. Nonetheless, the waterflood was simulated. Figures 2.10 and 2.11 compare the simulated oil recovery and pressure drop with the experimental data. The experimental measurement of pressure drop at 0.61 PV is much higher than the simulated value. The reason for this high value is unknown, but can indicate either a plugging problem or a measurement problem.

Figures 2.12 through 2.14 show the calculated and experimental values of the chemical flood oil recovery, oil cut, and pressure drop. The simulated oil recovery and oil cut match the laboratory data very well. The simulated pressure drop is much lower than the experimental data. Figures 2.15 through 2.18 show the saturation profiles at 0.2, 0.4, 0.73, and 2.43 PV. The residual oil was mobilized by injected surfactant and formed an oil bank (Figures 2.15 and 2.16). The simulated oil bank breakthrough occurred at 0.4 PV. Oil production stopped at 1.3 PV during the water flush. The simulated oil saturation decreased from 0.26 at the core outlet to zero at the

inlet (injector). The mechanisms that caused this distribution include reduction of interfacial tension and solubilization of oil in the microemulsion.

Figures 2.19 and 2.20 show the capillary number and the residual oil saturation profiles at different times. The surfactant reduced the residual oil to about 0.03 by decreasing the interfacial tension between the microemulsion and oil phases. In Figure 2.20, the residual oil saturation is reduced to zero in the gridblocks near the injector at 0.43 PV (end of S/P slug). Since the lowest residual oil saturation reduced by IFT is near 0.03 but not zero, the balance of the reduction must be due to solubilization of the remaining oil in the micelles. A solubilization front develops and corresponds to the well-known jump from a tie line to the injected composition (Pope, 1980; Helfferich, 1981; Hirasaki; 1981). During the polymer drive and postflush period, the surfactant concentration decreased because of dilution and the solubilization decreased correspondingly. Thus, the oil saturation increased with the distance away from the injector. Figure 2.21 shows a schematic ternary diagram for surfactant, water, and oil components with the history path of phase equilibrium compositions.

Figures 2.22 through 2.25 show the distribution of polymer and surfactant at different times. The mobility ratio between the microemulsion and oil bank was 0.08 at 0.43 PV. It is well-known that the lower mobility ratio, the more piston-like the displacement will be. The simulated results indicate that the mobility control was good.

The model predicted the polymer front was ahead of the surfactant front because the relative amount of the adsorbed polymer was lower than that of adsorbed surfactant. The simulated polymer adsorption was 16% of the amount of injected polymer (8.5μ g/g rock), and the simulated surfactant adsorption was 78% of the volume of injected surfactant (0.19 mg/g rock). The retention of both surfactant and polymer agreed well with laboratory data. Since no microemulsion can be trapped in a Type II(-) phase environment, the amount of adsorbed surfactant is the total retained surfactant in the core.

2.2.2 2-D Vertical Cross-Sectional Simulation

Reservoir A is a high-permeability sandstone reservoir. The net-pay zone of the reservoir is 26 ft with a dip angle of 16 degrees. This field consists of three main sandstone layers. The deepest and the most shallow part of the top layer are 6,200 ft and 5,757 ft under the North Sea. Since the x and y axe are scaled differently, the dip angle in Figure 2.26 is not drawn to scale. The permeability varies from 5.8 darcies in the top layer to 16 darcies in the bottom layer (Figure 2.26). The average porosity is 0.335. High permeability and porosity with low heterogeneity is a notable characteristic of this reservoir. The dimensions of the vertical cross section chosen for the simulations are 1,351 ft x 82 ft x 26 ft in x, y, and z directions. Two vertical wells are included. The injector is placed in the deepest part of the reservoir, since this design can benefit from the gravity force. A grid of 13 by 1 by 3 was first used. The average gridblock size is 101 ft by 80 ft by 9 ft.

The physical-property parameters were based upon the coreflood studies except as noted because of different rock or fluids. The input data are presented in Table 2.3. The injection scheme was as follows:

Waterflooding	: 0.65 PV of sea water with the total equivalent anions of 22,258.5 mg/ℓ and calcium ions of 2,660 mg/ℓ,
S/P slug	: 0.2 PV of 0.5 vol.% of surfactant with 500 ppm of xanthan gum in sea water,
Polymer drive	: 0.1 PV of 500 ppm polymer (xanthan gum) in synthetic sea water, with a tapered concentration of 250 ppm for 0.1 PV, and
Postflush	: 1.45 PV of sea water.

The waterflood was stopped when the water cut reached 94%.

Applying this injection scheme under assumed isothermal conditions, a simulation was performed. Figures 2.27 through 2.32 show the oil recovery, oil cut, oil production rate, produced surfactant and polymer concentrations, surfactant adsorption, and oil saturation profiles.

The chemical oil recovery was 34 % of ROIP, which is not considered high enough to be a successful chemical flood in this environment. The surfactant adsorption shown in this case is 0.18 mg/g rock. Adsorption is low since this reservoir formation contains very little clay and has a very low surface area per unit rock mass. The low produced surfactant concentration (Figure 2.29) is an indication that there was not sufficient amount of surfactant injected. The oil bank floated above the injection front because of the density difference between the oleic and microemulsion phases (Figure 2.32). Because of the permeability distribution, the injected fluids flew through the bottom layer much faster than the ones in top layer and caused a smear-like injection front.

To evaluate the effect of reservoir discretization, mesh-refinement simulations were done to determine the number of gridblocks required for an accurate simulation. Two cases with grids of 26x1x3 and 26x1x8 were investigated. Figures 2.33 through 2.35 show the oil recovery, oil cut, and the produced surfactant concentration as a function of pore volumes injected. The oil recovery did not change very much as the grid was refined. However, since the CPU times for the fine 26x1x8 grid were still affordable (90 seconds in DEC Alpha workstation), all subsequent simulations were done using the finest grid.

2.2.3 Sensitivity Analyses

To optimize and investigate mechanisms of the S/P process, a series of sensitivity analyses established on the 1-D and 2-D Base Cases was performed. The sensitivity factors included the chemical amount and slug size and microemulsion properties. Also, gravity and buoyancy effects on the oil recovery were evaluated.

2.2.3.1 Surfactant Concentration

To study the effect of surfactant concentration on 2-D cross-sectional S/P flooding, we considered 0.5, 1.0, and 1.5 vol.% injected surfactant concentration with 0.2 PV as the slug size. Figure 2.36 shows that the cumulative oil recovery increased by more than a factor of two with the increase of the surfactant concentration from the Base Case value of 0.5 to 1 vol.%. It is clear that the amount of injected surfactant in the Base Case was insufficient, which is consistent with our discussion in the previous section.

For 1-D simulation, surfactant concentrations of 0.5 (Base Case), 0.625, 0.75, 1.0, 1.5, 2.0, and 2.5 vol.% were considered. The slug size for S/P was kept constant at 0.43 PV. Figure 2.37 shows the cumulative oil recovery as a function of the amount of injected surfactant expressed as pore volume multiplied by concentration. There is a sharp increase in the amount of oil recovery when the surfactant concentration was raised from 0.5% to 0.625%. However, only a gradual increase in the cumulative oil recovery was caused by any higher surfactant concentration.

Both coreflood and 2-D vertical cross-sectional simulations show that cumulative oil recovery is very sensitive to surfactant concentration, especially when the injected surfactant concentration is low. Also, the core and reservoir respond very well when a surfactant with a higher concentration is injected. Thus, a careful determination of an optimum concentration of surfactant in the chemical slug is essential in a successful S/P flood, especially with low injected surfactant concentration.

2.2.3.2 Surfactant/Polymer Slug Size

To estimate the sensitivity to the S/P slug size for 2-D cross-sectional simulations, we considered four values of 0.2 (Base Case), 0.4, 0.6, and 0.8 PV for S/P slug sizes. In all these runs, surfactant and polymer concentrations were kept constant at the Base Case values of 0.5 vol.% and 500 ppm, respectively. The whole injection process was kept constant at 1.8 PV by reducing the postflush size accordingly.

Figure 2.38 shows oil recovery as a function of S/P slug size. The increase in the slug size improves the oil recovery almost linearly. There is a 54% difference in oil recovery between the Base Case (0.2 PV) and the case with 0.6 PV surfactant slug. Based on the results presented in Section 2.2.3.1 and the above-mentioned S/P slug size sensitivity, the duration of S/P slug for the 2-D Base Case is modified to either 0.4 or 0.6 PV. This change can result in a better Base Case and make the other sensitivity analysis results more meaningful and realistic.

The sensitivity analysis of 1-D simulations to S/P slug size was run with the amount of injected surfactant as a constant. The S/P slug sizes studied were 0.215 PV of 3 vol.% surfactant, 0.43 PV of 1.5 vol.% surfactant, and 0.93 PV of 0.7 vol.% surfactant. Figure 2.39 shows the effect of surfactant slug size with constant injected amount of chemical on the cumulative oil recovery. The largest difference in the cumulative oil recovered for the three above-mentioned cases is only 2%.

These simulation results show that the oil recovery is not very sensitive to the S/P slug size when a sufficient and fixed amount of chemical is injected. Since the permeability distributions for both core and reservoir are in the low-heterogeneity case, the surfactant reaches the target oil in a similar way for both concentrated and dilute S/P slug-size cases. Also, the low adsorption helps the dilute slug case maintain its efficiency. This insensitivity to the chemical slug size holds only when the formation rock has a low heterogeneity and low adsorption.

2.2.3.3 Polymer Concentration

To evaluate the sensitivity of the S/P flood to polymer concentration in the vertical cross-sectional simulations, concentrations of 250, 500 (Base Case), 750, and 1,000 ppm were evaluated. The S/P slug size was increased from the Base Case value of 0.2 PV to 0.6 PV and the injected surfactant concentration kept constant at 0.5 vol.%. Figure 2.40 shows the sensitivity of the cumulative oil recovered to the amount of polymer injected expressed as polymer concentration multiplied by pore volume.

The improvement of sweep efficiency caused by a high polymer concentration leads to an increase of oil recovery. A 5% increase in cumulative oil recovery was observed when polymer concentration was raised from 250 to 1,000 ppm. The increase was 2% when polymer concentrations of 500 and 1,000 ppm were compared. Figure 2.41 shows the increased project life caused by lower injectivity with higher polymer concentrations. Since the shear rate near the injection well is underestimated in our model, the actual injectivity may not decrease as much as predicted.

To study the effect of polymer concentration on 1-D coreflood simulations, polymer concentrations of 500 (Base Case), 750 and 1,000 ppm were evaluated. The injected surfactant concentration was kept constant (0.5 vol.%). Figure 2.42 shows the effect of the amount of polymer used (expressed as polymer concentration multiplied by pore volume) on cumulative oil recovered. The amount of oil recovery increased by an additional 10% when the polymer concentration increased from 500 ppm to 1,000 ppm. This is similar to the experimental coreflood results in which the oil recovery increased by 17.4% when the polymer concentration increased from 500 ppm to 1,000 ppm. Since detailed coreflood data were not available, an attempt was not made to match the experimental oil recovery.

The 1-D simulations showed a greater sensitivity to polymer concentration than the 2-D cross-sectional simulations. The 1-D simulations were run with a rate constraint on the injection well, whereas the 2-D runs were made with both the pressure and maximum rate imposed; hence injectivity affected the recovery for the 2-D simulations but not the 1-D simulations.

2.2.3.4 Gravity and Buoyancy

To evaluate the gravitational effects on 2-D simulations, two simulations were run with the corresponding UTCHEM gravity option turned on and off. The injection and production wells were under a pressure constraint in these simulations. The S/P slug size was 0.6 PV and the injected surfactant was 0.5%. The oil recovery for the nongravity case turned out only slightly

lower (Figure 2.43). The project life increased by 15% when gravity was turned on because of a lower injectivity during the polymer-drive period.

Figures 2.44 and 2.45 show the oil saturation profiles. The formation and propagation of the oil bank differ greatly in the two cases except that the profiles at the 1.8 PV injected (end of project life) are similar. The final net effect on the cumulative oil recovery between the two cases is small because the permeability distribution dominates the sweep efficiency.

The oil bank floats to the top of the reservoir because of the density difference between water and oil and the buoyancy effect caused by gravity. Vertical crossflow was enhanced by gravity and resulted in a less uniform vertical distribution of the oil bank. It is remarkable how little effect this had on the oil recovery (Figure 2.43). Recall that this reservoir has a 16 degree dip and the water is injected downdip, which is the favorable location to take advantage of gravity.

Two simulations were performed to assess the importance of the buoyancy term in the capillary number on the oil recovery (Jin, 1995). The UTCHEM simulator was modified to eliminate the buoyancy term in the capillary number so that the importance of this term could be evaluated by making comparison runs. Both simulations injected 0.4 PV surfactant (surfactant concentration is 0.5 vol.%) and polymer (polymer concentration is 500 ppm for 0.3 PV and 250 ppm for 0.1 PV). Figure 2.46 shows that the oil recovery slightly improved with an increase in the capillary number caused by buoyancy.

Oil recovery in this case was not found to be very sensitive to the gravity or buoyancy effect, but fluid and pressure distributions are. The gravitational effect on fluid flow is a function of the injection rate, since the ratio of the viscosity and gravity terms depends on the injection rate. Both effects would also be greater in three-dimensional cases because of the lower velocities along slow streamlines.

2.2.3.5 Microemulsion Properties

To investigate the sensitivity of physical properties on the oil recovery and to assess the uncertainty of experimental measurements, the microemulsion phase behavior, viscosity, and the interfacial tension models were studied. Although some parameters had little effect on the oil recovery in these cases, this cannot be assumed to hold for other reservoirs.

(i) Phase Behavior

The surfactant phase behavior was changed by changing the height of the binodal curve (HBNC). For the test cases, the values of the maximum height of the binodal curve were 0.05, 0.03 (Base Case), and 0.01. The maximum height of the binodal curve is a very important input parameter in almost all surfactant simulations. Here the S/P slug is 0.6 PV and injected surfactant concentration is 0.5 vol.%.

Figure 2.47 demonstrates the sensitivity of the oil recovery to HBNC. It can be seen that the oil recovery increases as HBNC decreases. For the Base Case (HBNC 0.03), for example, the oil recovery is almost 50% more compared to Case 1 in which HBNC is 0.05. Lower values of HBNC correspond to higher values of oil solubilized in the micelles (higher solubilization ratio) and thus lower IFT.

Figure 2.48 is a schematic representation of a phase diagram with three different heights of the binodal curve. Point A is assumed to represent the composition at a certain time in a simulation. This point is located in the single-phase region for Case 3 (HBNC = 0.01) but in the two-phase region for Cases 1 and 2. Since there is no capillary force in single-phase flow, surfactant used in Case 3 can locally displace all of the residual oil. For Case 2, the two phases are the oleic phase and the microemulsion phase represented by Point B, and for Case 1 the oleic phase and the microemulsion phase represented by Point C are the two phases. It is clear that the oil concentration is higher at Point B than in Point C, which indicates a higher capacity of the surfactant to solubilize oil in Case B. Since the oil recovery is very sensitive to this parameter, the precise measurement of surfactant phase behavior is strongly recommended.

(ii) Microemulsion Viscosity Model

To investigate the effect of microemulsion viscosity on oil recovery, two simulations were performed. There are five parameters (α_1 to α_5) that describe the microemulsion viscosity modeled in UTCHEM. The model can be described as

$$\mu_\ell = c_{1\ell}\mu_p \exp[\alpha_1(c_{2\ell}+c_{3\ell})] + c_{2\ell}\mu_2 \exp[\alpha 2(c_{1\ell}+c_{3\ell})] + c_{3\ell}\alpha_3 \exp[\alpha_4 c_{1\ell} + \alpha_5 c_{2\ell}] \qquad \ell=1,3$$

The effect of surfactant concentration on the microemulsion viscosity was neglected in this study, since insufficient data were available to estimate the dependence on surfactant concentration. The microemulsion viscosity was studied by changing the input parameters ALPHA1 (α_1) and ALPHA2 (α_2).

Figure 2.49 shows the microemulsion viscosity as a function of oil concentration. Both 1-D and 2-D simulations were performed to study the sensitivity of oil recovery to the microemulsion viscosity. In the 2-D simulation, the S/P slug was 0.4 PV with 0.5 vol.% surfactant concentration. Figures 2.50 and 2.51 show the oil recovery as a function of pore volumes injected for the two viscosity cases and indicate that oil recovery is not very sensitive to microemulsion viscosity. The sweep efficiency did not improve significantly by using the nonlinear model for microemulsion viscosity.

(iii) Interfacial Tension

In addition to the modified Reed-Healy model (Healy and Reed, 1974; Hirasaki, 1981; Delshad *et al.*, 1996), UTCHEM has an option to compute the interfacial tension using a modified Chun-Huh interfacial tension model (Huh, 1979; Delshad *et al.*, 1996). To study the sensitivity of oil recovery to interfacial tension, the values of 0.1, 0.2, 0.3, and 0.35 were used for the constant C in the Chun-Huh model. Figure 2.52 shows the interfacial tension computed as a function of oil solubilization ratio for both models. Most published IFT data can be fit with a value for C of 0.3 ± 0.2 (Huh, 1979; Graciaa *et al.*, 1982; Barakat *et al.*, 1983). Figures 2.53 and 2.54 show the sensitivity of the oil recovery to interfacial tension. There was a 10% decrease in the final oil recovery when parameter C was increased from 0.1 to 0.35 for both 1-D and 2-D simulations. A value of C=0.2 seems to give the best agreement with this coreflood data, but it would be better to base its value on IFT data.

2.2.4 Temperature Effect

To evaluate the effect of temperature on oil recovery, both 1-D and 2-D S/P floods were simulated. Since experimental measurements of surfactant phase behavior as a function of temperature were not available, these simulation results are only qualitative and demonstrate the general trend predicted by the UTCHEM temperature-dependent phase-behavior model. The general tendency is for the optimum salinity of sulfonates to increase as temperature increases.

2.2.4.1 Temperature Effect on Corefloods

Several 1-D simulations were run at different temperatures to obtain the trend in the oil recovery versus temperature and compare it to that observed in the laboratory (Table 2.4). A history match of the coreflood results was not attempted because of the lack of critical data such as phase behavior at different temperatures and thermal properties. In addition, the only available data on the temperature dependency of the oil recovery were obtained from a coreflood with different properties than that on which the history match was performed (Table 2.4). The final oil recovered for the history-matched coreflood at 122°F was 0.806. The oil recovery for the coreflood experiment listed in Table 2.4 is only 0.64 (of the residual oil saturation).

Simulations at 158, 122 (Base Case), and 86°F were performed. The effective salinity at 86°F is in the Type III region, and at 122 and 158°F it is in the Type II(-) region because of the usual shift in phase behavior with temperature. Figure 2.55 shows the salinity distribution versus pore volumes injected for three cases. The phase behavior and phase property input data were based on the measured values given at 122°F. Other input data were taken from the 1-D simulations. Thermal properties are given in Table 2.5.

Figure 2.56 shows the oil recovery as a function of temperature and indicates that, as with the laboratory data, the highest oil recovery is obtained at temperature of 122°F. The difference in oil recovery between the experimental corefloods and the simulations is at least in part because a different core was used, but the trend with temperature is similar. Figures 2.57 and 2.58 show the produced surfactant concentration and the surfactant retained as functions of pore volumes injected, respectively. The surfactant adsorption and retention at 86^{0}F are much higher than for the other two cases. This is due to the trapping of microemulsion under the Type III condition but not under the Type II(-) cases. Type II microemulsion contains high concentration of surfactant, so even a small amount of phase trapping results in a large surfactant retention. This problem can be avoided by using either a salinity gradient or a constant salinity in the Type II(-) region. Microemulsion trapping cannot occur under Type II(-) condition, since the microemulsion and aqueous drive are miscible (Pope and Bavière, 1991). The change in oil recovery with temperature is thus an indirect consequence rather than from the temperature per se.

2.2.4.2 Temperature Effect on 2-D Cross-Sectional Simulations

Temperature gradients must be considered for North Sea chemical floods, since cold sea water is typically the only available injection water. To investigate the effect of temperature in a 2-D vertical cross-sectional reservoir, three cases were simulated:

(A) Constant temperature of 158°F,
(B) Injection temperature of 122°F in a 158°F reservoir, and
(C) Injection temperature of 86°F in a 158°F reservoir.

The heat gain from the overburden and underburden rocks was modeled with UTCHEM. The input data for the 2-D simulations were taken from the Base Case with the exception of injected surfactant slug (0.4 PV) and temperature-related parameters. The bottomhole pressures were 4,121 and 3,771 psi for injector and producer wells, respectively.

Figure 2.59 shows that the oil recovery is the highest for the lowest injected temperature of 86^{0}F. Figure 2.60 shows that higher injectivity occurs in Cases B and C. High injectivity helps to shorten the project life but does not greatly increase oil recovery. The temperature gradient in the formation is the main cause for this divergence. The reservoir temperatures at different injection times are shown in Figures 2.61 and 2.62. Figures 2.63 and 2.64 show the surfactant concentration and effective salinity in the bottom gridblocks. The temperature of the surfactant is lower because of the injection of water colder than the initial formation temperature of 158 °F. This is favorable since the effective salinity is now just below the lower critical salinity (Type III), which gives a favorable combination of high oil solubilization (and then very low IFT) and low retention, since trapping still does not occur just below the Type III region. However, if the temperature decreased too much, the results would be worse, just as they were for the coreflood at 86°F. Both accurate phase behavior data as a function of temperature and accurate simulations would be required to optimize a chemical flood under these condition and to avoid undue risk.

In summary, temperature had a significant effect on the oil recovery in both coreflood and 2-D vertical cross-sectional simulations. The simulated coreflood results showed the same trend as the experimental measurements. A temperature gradient is an important design factor for this high-permeability reservoir with moderate initial reservoir temperature (158°F). The precise phase behavior as a function of temperature must be modeled for such a case, and each surfactant for use will be different in its temperature dependence. A change of even one ethylene oxide or propylene oxide unit in the surfactant (sulfate or sulfonate) will in general make a difference in the

temperature dependence. Nonionics containing ethylene oxide units will have a completely different behavior (opposite trend).

2.2.5 Permeability-Dependent Waterflood Residual Oil Saturation

To investigate the effect of the waterflood residual-oil saturation (S_{orw}) distributions on oil recovery, S_{orw} was first uniformly increased from 0.25 (Base Case) to 0.30 (Case 2). Since it is very plausible that higher-permeability regions have lower S_{orw}, simple empirical correlations relating S_{orw} to reservoir permeability (Kocberber and Collins, 1990)were used to assign the waterflood residual-oil saturation to each gridblock. The distributions studied were

Case 3 : $S_{orw} = \exp(-0.016187\ k^{0.5})$

Case 4 : $S_{orw} = \exp(-0.001753\ k^{0.75})$

Case 5 : $S_{orw} = \exp(-0.233604\ k^{0.2})$

Since a constant S_{orw} of 0.25 was used in the Base Case, a volume-weighted S_{orw} of 0.25 was also preserved in these distributions. Figure 2.65 shows S_{orw} as a function of permeability. Figures 2.66 through 2.68 show the oil-phase capillary-desaturation curve (CDC) of the lowest, average, and highest permeability gridblocks for each distribution (Cases 3 through 5). CDCs corresponding to a waterflood residual-oil saturation of 0.25 are also shown in these figures. The residual-oil saturation ranges from about 18 to 30% in Case 3 (Figure 2.66), from 14 to 32% in Case 4 (Figure 2.67), and from 22 to 27% in Case 5 (Figure 2.68).

Figures 2.69 through 2.71 show the results of these simulations. Figures 2.72 and 2.73 show the oil concentration profiles at 0.5 and 1.8 PV injected, respectively. Figure 2.69 shows that except for Case 2, where S_{orw} was held constant at 0.30, the permeability-dependent S_{orw} cases (Cases 3 through 5) yielded about the same chemical-flood cumulative oil recoveries as Case 1. In Case 2, when S_{orw} was held constant at 0.30 during the waterflood prior to the S/P flood, the least amount of oil was recovered during the waterflood (about 66% of ROIP) compared to the other cases with either constant S_{orw} of 0.25 (Base Case, 71% of ROIP) or variable S_{orw} but preserving a volume-weighted S_{orw} of 0.25 (Cases 3 to 5). Consequently, the chemical-flood target oil volume for Case 2 is the largest, thus resulting in the highest chemical-flood cumulative oil recovery.

Waterflood oil recovery for Cases 3 through 5 are 69.84%, 69.09%, and 70.59% of OOIP, respectively. Figure 2.69 shows that Case 4 yielded the second-highest chemical-flood final oil recovery, followed by Case 3. For all practical purposes, the cumulative oil recoveries for Cases 3 through 5 are the same as Case 1. Figure 2.72 shows that the chemical-flood oil bank response is the strongest and sharpest when the range of residual oil saturation in the reservoir is the largest (Case 4). This effect is also demonstrated by Figures 2.70 and 2.71.

Figure 2.73 shows the oil concentration at the end of the water drive (1.8 PV injected). The oil concentration in the lower permeability regions that have less mobilized by the surfactant is higher in Cases 3 through 5 than in Case 1. On the other hand, the oil concentration in the high-permeability regions is lower in Case 3 through Case 5 than in Case 1. Hence, this apparent insensitivity of the final oil recovery to the S_{orw} distributions used in our study can be attributed to offsetting factors. Regardless, the final oil recovery is remarkably insensitive to even large variation in residual-oil saturation to water. This is contrary to what has often been claimed to be a major problem with chemical flooding oil reservoir that have been waterflooded to high water cuts. The very high vertical permeability (and hence crossflow) in this reservoirs may be the reason for this unexpected performance.

2.2.6 Surfactant/Polymer Interactions

To study the effect of competitive adsorption between the surfactant and polymer components, a new Base Case was designed and simulated. The waterflood up to 94% water cut was used as in the original Base Case. After the waterflooding, 0.4 PV of 0.5 vol.% surfactant

was injected at a constant rate of 2,000 B/D. The surfactant slug contained 500 ppm for 0.3 PV and 250 ppm for 0.1 PV. The chemical slug was then followed by chase water for 1.45 PV. The simulation included a temperature gradient, since the initial reservoir temperature was 158°F and the injected water temperature was 122°F. This new Base Case is referred to as a low-tension polymer flood (LTPF) since only very small amounts of low-concentration surfactant and polymer are coinjected, and since competitive adsorption will be included in some cases studied.

The oil recovery is about 57% for the Base Case LTPF with this very small amount of injected surfactant (Figure 2.74). The polymer/surfactant interactions are not included in this simulation. Profiles of oil concentration at several times are shown in Figure 2.75. Figure 2.76 shows the profiles of surfactant concentration overlaid by the temperature contours at several pore volumes injected. The temperature front is ahead of the chemical slug for most of the flood (0.7 PV).

Figure 2.77 shows the profiles of the surfactant concentration overlaid by the polymer concentration contours. The results show the presence of polymer ahead of the surfactant slug. Maximum adsorption concentrations corresponding to the injected concentration were 0.36 mg/g rock for surfactant and 33 μg/g rock for polymer.

To investigate the impact of competitive adsorption between surfactant and polymer, we repeated the Base Case simulation with the competition from polymer included in the surfactant adsorption calculations. The sensitivity of LTPF oil recovery to surfactant adsorption with competition from polymer is shown in Figure 2.74. The oil recovery increased from 56 to 77% because of the reduced surfactant adsorption. The surfactant adsorption decreased from 0.26 to 0.09 mg/g rock because of competitive adsorption. This is a 65% reduction. These results might be too optimistic and are shown here to only illustrate the trend. The adsorption-reduction factor needs a well-designed core displacement to get suitable values. Also, the 2-D cross-section case usually shows high sweep efficiency from the S/P slug that does not hold for a 3-D reservoir. Although these results are not very realistic, the trends represented in these simulations help us understand the important effect of chemical adsorption on oil recovery.

To ensure that enough polymer is propagated ahead of the surfactant slug to fully benefit from the competitive adsorption, the Base Case was repeated but with an injection of 0.2 PV polymer solution with 250 ppm concentration prior to the injection of the S/P slug (referred to as polymer preflooding in the figures). Figure 2.78 shows that the oil production response is faster, as expected because of a better mobility control in the latter case. The final oil recovery, however, is about the same with or without the polymer preflood.

To see whether this preinjection leads to a high oil recovery because of polymer/surfactant interactions, a simulation was run with the competitive adsorption included. The oil recovery increased from 54% to 74%, an incremental recovery of 20% (Figure 2.78), while the corresponding figure was 22% for the case without the polymer preflood (Figure 2.74). Therefore, the only advantage of polymer injection prior to the chemical slug in this reservoir under the conditions studied is the faster oil recovery response (Figure 2.78). The ultimate recovery is fairly insensitive to the inclusion of polymer preflood.

Figures 2.79 and 2.80 show the produced surfactant concentration and the adsorbed surfactant concentration. The profiles of surfactant concentration overlaid by the polymer concentration contours at several pore volumes injected in the polymer preflooding case are shown in Figure 2.81. The results indicate that high concentrations of polymer propagated ahead of the surfactant during the entire flood.

2.2.7 A 3-D Simulation

One 3-D simulation was done just to get some idea of the importance of three-dimensional effects for this two-well surfactant pilot. The 3-D field was treated as a block of nine slices used in our 2-D cross-sectional simulations. The injector and producer wells were positioned in the fifth slice as shown in Figure 2.82. All physical properties and well constraints remained the same as for the constant-temperature 2-D runs (original Base Case) with a 0.4 PV S/P slug size. Figure

2.83 shows the cumulative oil recovery as a function of pore volumes injected for both 2-D and 3-D runs. The oil recovery and the breakthrough are very different because of an entirely different streamline pattern in the two cases. However, use of 2-D runs to understand the effect of physical properties and for design parameters appears to be acceptable in reservoir study, except for the final simulations, and has the advantage of simplicity and low cost.

2.2.8 Summary and Conclusions for Reservoir A

The effects of the injection scheme and surfactant physical properties on oil recovery in a high-permeability formation were studied. These effects and mechanisms were revealed after performing both 1-D and 2-D simulations. For corefloods, experimental data were successfully matched by UTCHEM. The simulator predicted the same trend in oil recovery with temperature as observed in the corefloods.

The input parameters obtained from the coreflood history match were used along with available reservoir description data to set up a 2-D vertical cross-sectional study. This is the first time that temperature effect and competitive adsorption have been used in field-scale S/P simulations. Our conclusions based on these results are as follows :

1. The temperature gradient in this chemical flood caused by injecting cold water improved the performance of the chemical flood.
2. Modeling suggests that reduction in surfactant adsorption because of competitive adsorption of polymer significantly improves the performance of the chemical flood. This occurs when the polymer front is ahead of the surfactant front, as in this case, and thus adsorbs first. However, not enough data are available to be sure that this competitive adsorption effect is real.
3. Oil recovery changed very little when the grid was refined from 13x1x4 to 26x1x8.
4. In this reservoir, the permeability-dependent residual-oil saturation shows the chemical oil recovery is more sensitive to the amount of target oil after waterflood than to the oil distribution.

Although the optimized injection scheme based on the 2-D simulations is not suitable for 3-D cases, we take advantage of lower CPU time and simplicity of a 2-D cross section to understand the process mechanisms.

2.3 Optimization Design for Reservoir B

To further study the potential of the S/P process for a sandstone reservoir, Reservoir B was investigated. Reservoir B is an offshore North Sea sandstone reservoir. The location and area of the reservoir are shown in Figure 2.84. The permeability distribution is moderately heterogeneous and the shape of reservoir is highly irregular. There have been two vertical wells in this pilot so far. The average oil saturation was 0.8, which is far away from the residual oil situation.

In this study, the S/P process is treated as a supplement to waterflooding. In order to avoid the numerical uncertainties, mesh refinement and the grid geometry studies were first performed. The production strategies for the application of horizontal wells and the temperature gradient caused by injecting cold water were then studied to construct a Base Case.

The Base Case was applied for a series of sensitivity analyses. The sensitivity factors for reservoir properties included vertical-to-horizontal permeability ratio and permeability-dependent residual-oil saturation. For the physical-property and interaction factors, duration of water injection before chemical injection, amount of injected surfactant, amount of injected polymer, surfactant adsorption, surfactant phase behavior, capillary-desaturation curve for the oil phase, and competitive adsorption between surfactant and polymer were studied.

2.3.1 Reservoir Description and Injection Scheme

Reservoir B formation consists of channel and sheet sandstones (fine to medium grained), deposited in a braided and low sinuosity river environment. Associated with sandstones are shales deposited in floodplains and in lacustrine basins. The shales can represent flow barriers. The flow communication is moderate to good and is variable in the upper layers (Skjaveland and Kleppe, 1992). For this pilot, there are eight layers in the z direction. Permeability in the horizontal direction ranged from 14 md for the lowest permeability layer at the bottom (Layer 8) to 700 md for the highest (Layer 4). Permeability for the other layers ranged from 30 to 80 md. The vertical-to-horizontal permeability ratio was 0.2. Figure 2.85 shows the permeability distribution for this reservoir. It is indicated clearly that the formation pinches out and layer channeling exists in this reservoir. Porosity is in the range of 0.06 to 0.24. The reservoir temperature is 194°F at the average depth of 8,050 ft (top of Layer 1) under the North Sea. The water and oil viscosity are 0.27 and 0.29 cp, respectively. The initial salinity of the formation water is 23,785 mg/ℓ (0.627 meq/mℓ).

Xanthan gum was chosen as the injection polymer because of its stability in high-salinity brine and at high temperature. High injection concentration of the polymer was absolutely necessary for the control of layer channeling, although the endpoint mobility ratio was 0.8 for waterflooding. The polymer adsorption (10 μg/g of rock) was low in this reservoir. Surfactant used in this study was the same type as used in Reservoir A. Experiments showed that the phase behavior of the surfactant remained stable at high temperature. Also, surfactants covering a large range of salinity (from 0.5 to 2.0 times sea-water salinity) in optimum salinity were available. The surfactant adsorption level was typical (0.23 mg/g rock) and the CMC was 0.01 vol.%.

Since the surfactant and polymer applied in this reservoir were similar to those used in Reservoir A, some physical parameters for surfactant and polymer properties were taken from Reservoir A. Other physical parameters of injected fluids were either extracted from the laboratory data or are typical values for specified surfactant and polymer. Figures 2.86 through 2.95 show the capillary-desaturation curves, relative-permeability curves at low and high capillary numbers, ternary diagram, oil/microemulsion interfacial tension as a function of oil solubilization ratio, surfactant adsorption isotherm, microemulsion viscosity as a function of oil concentration, polymer viscosity as a function of concentration and shear rate, polymer adsorption isotherm, and oil and water viscosities as a functions of temperature.

In each simulation discussed, we first waterflooded the reservoir for a year followed by a dilute slug of surfactant/polymer. The wells were operated either at the constant injection pressure of 6,206 psi or constant injection rate of 25,409 bbls/day (for horizontal wells only) and constant production pressure of 2,175 psi. The salinity was kept constant at 23,785 mg/ℓ (0.627 meq/mℓ), which is slightly above the optimum salinity of 20,412 mg/ℓ (0.575 meq/mℓ) and is in the Type III phase environment. The injection scheme for the S/P process is

S/P slug : 0.4 PV of 0.5 vol.% of surfactant with 500 ppm of xanthan gum in sea water,
Polymer drive : 0.2 PV of 500 ppm polymer (xanthan gum) in sea water, and
Postflush : 0.43 PV of sea water.

The high effectiveness of those injected chemicals account for these remarkably small quantities. Tables 2.6 and 2.7 list the key parameters of input data for reservoir properties and surfactant properties.

2.3.2 Base Case Simulation

The production strategy was first studied to examine the benefits of applying horizontal wells. The grid geometry and discretization were then evaluated to avoid numerical uncertainties. Since the shape of reservoir was highly irregular, grid geometry became a concern. Also, the effects of temperature on the surfactant phase behavior for Reservoir B was evaluated for the Base Case.

2.3.2.1 Production Strategies

To investigate the significance of the well orientation and well location, we performed the following simulations using a 3-D Cartesian grid of 13 x 7 x 8, in the x, y, and z directions with constant bottomhole pressure injector and producer under isothermal conditions:

(A) Horizontal injector is located in the 10th gridblock in the 7th layer and is extended from gridblocks 2 to 7 in the y direction. Horizontal producer is located in the first gridblock in the 4th layer and is perforated from gridblocks 1 to 7 in the y direction.

(B) Line-drive vertical injector is perforated in Layers 6 to 8 and located in the x and y coordinates of (10,4). Vertical producer perforated in layers 1 to 8 is located at (1,4).

(C) Line-drive vertical injector is perforated in Layers 1 to 8 and is located in the x and y coordinates of (1,4). Vertical producer is perforated in the 7 to 8 Layers and is located at (11,4).

(D) Horizontal injector is located in the 10th gridblock in the 7th layer and extends from gridblock 2 - 7 in the y-direction. Vertical producer is perforated in Layers 1 - 8 and is located at (1,4).

The results are shown in Figures 2.96 through 2.101. Figures 2.96 and 2.98 show that the project life is 9 years for the horizontal producer (Case A) compared to 13 years for the vertical producer (Case D) for an oil cut of 5%. The oil recovery is about the same in these two cases and is equal to 64% of remaining oil in place (ROIP). Figure 2.97 indicates that the sweep efficiency is almost the same at the end of pore volume injected for the case with a vertical injector and a vertical producer (Case B). Two horizontal wells, as well as a horizontal injector and a vertical producer, lead to the highest injectivity among the four cases (Figures 2.100 and 2.101). Since no constraints were imposed on the maximum injection rates in these simulations, the injection rate was extremely high during the postflush. A provided maximum rate constraint (36,327 B/D) was applied to eliminate the unrealistically high injection rate. Figure 2.100 indicates that the water postflush injection rate exceeded the maximum injection rate in Case A. The injection rate for the chemical flood remained well below this limit in all simulation cases. However, the constraint on the maximum injection rates was imposed on the other sensitivity analyses. The production strategy in Case A, two horizontal wells, was applied for sensitivity simulations because this design can cause the highest oil recovery within the shortest project life.

In an attempt to further improve the sweep efficiency, we moved the horizontal producer located in Layer 4 in the Base Case to either Layer 2 or 8. A skin factor of -3 was used to compensate for the low permeability values in the order of 100 md in those layers. Figures 2.102 through 2.107 show oil recovery as a function of project life and pore volumes injected, oil cut, oil production rate, injection rate, and time vs. pore volumes injected. Figure 2.102 indicates that the project life increased but the oil recovery was not tremendously improved. The project life in the two cases was prolonged because of the low permeability of the producers (Figures 2.102 and 2.107). Figure 2.103 shows that the sweep efficiency was not greatly improved when producers were placed in a low-permeability zone. The sweep efficiency was controlled by the permeability channeling in Layer 4. The injection fluid front stayed sharp before reaching Layer 4. After the fluids moved into Layer 4, the high permeability in the x direction hastened the fluids into the producer, bypassing most the target oil in Layers 6 through 8. Oil recovery and injectivity were not sensitive to these changes. The horizontal well was still kept in Layer 4 for the Base Case.

2.3.2.2 Grid Geometry

To reduce the uncertainty caused by the grid geometry, the effects of using the Cartesian coordinate and curvilinear grids with pressure-constraint injector were investigated. Figures 2.108 through 2.110 show the small sensitivity of the 3-D S/P process simulation to the grid geometry. The difference in the oil production rate is due to the difference in the initial pore volumes and the oil in place with the two grid geometries. Since the initial temperature of this pilot was 194 °F and that of the injection fluid was 68°F, the effect of the temperature on the surfactant was not

negligible. In the following sections, a curvilinear grid scheme was used in most simulations except when non-isothermal effects were studied. The temperature equation is currently not available for curvilinear grid.

2.3.2.3 Grid Refinement

The gridblocks used for both curvilinear and Cartesian grids were 13x7x8 in x, y, and z directions. 728 gridblocks were used to describe the reservoir and the average size of a gridblock was 332 ft x 482 ft x 7.4 ft. To investigate the numerical accuracy of the results with use of large gridblocks with curvilinear geometry, mesh refinement simulations were performed. The number of gridblocks was increased only in the horizontal direction in a run and both in the horizontal and vertical directions in another. The resulting refinements were (1) 27x7x8 and (2) 27x7x15.

Figures 2.111 through 2.116 show the insensitivity of simulation results to the grid refinement. The histories of oil recovery, oil cut, and oil production rate resemble one another. The injection rates in the latter two are higher than in the former. Since the shear rate near the wellbore is simulated more precisely in the latter two cases, lower polymer viscosity and higher injectivity are predicted. The CPU time (on a DEC Alpha workstation) for the three cases were 41 minutes, 1 hour 40 minutes, and 2 hours 40 minutes for the Base Case and Case (1) and Case (2), consecutively. Based on the numerical accuracy and CPU consumption, the gridblock of 13x7x8 from the Base Case was used in all other sensitivity analyses.

2.3.2.4 Temperature Effect

In this section, a 3-D Cartesian grid S/P simulation was performed with an injected water temperature of 68°F and an initial reservoir temperature of 194°F. The Base Case with the two horizontal wells was used. The input parameters for temperature sensitivity were reasonably estimated for the type of surfactant (branched hydrophobe sulfonate with a small number of EOs and POs). The temperature effect on the polymer is implicitly included in the polymer viscosity model because the calculation of polymer viscosity included water and oleic phase viscosity. The stability of polymer under the thermal effect was not considered in the study. The energy balance on the reservoir including the heat gains/losses from the overburden and underburden rocks is considered in this study. Both the shift of the effective salinity and the height of the binodal curve with temperature are also used (Table 2.7). Figures 2.117 through 2.121 compare the results of the constant- and variable-temperature simulations for the oil recovery as a function of time and pore volumes injected, oil cut, cumulative oil production, and injection rate. The lower cumulative oil recovery in the variable-temperature simulation is caused by the lower injectivity of the more viscous water at the colder injection temperature of 68°F (Figures 2.118 and 2.121). On the other hand, the higher viscosity of cold water improves the sweep efficiency (Figure 2.118).

Temperature profiles as expected indicate only a few degrees of cooling in the high-permeability layer (Layer 4) after 0.4 PV cold-water injection (Figure 2.122) and a large temperature decrease for Layer 7 where the cold water is being injected. Meanwhile, the surfactant front has already moved into Layer 4. The temperature front moves far behind the surfactant front. Therefore, temperature effects on the height of the binodal curve and effective salinity were insignificant in this pilot. Since the temperature change hardly affected oil recovery or caused a notable effect on the surfactant properties, subsequent simulations were performed isothermally.

Temperature effects seen in Reservoir B are very different from those in Reservoir A. Lower permeability causes the heat transfer by the fluid flowing through reservoir to be reduced. These results emphasize the importance of performing sensitivity simulations for each reservoir of interest before the final optimum design is recommended. However, other factors such as a longer waterflood before surfactant injection and thermal sensitivity of a surfactant would allow for a larger temperature effect.

2.3.2.5 Description of Base Case

From the results of the above-mentioned simulations, a Base Case was constructed. The Base Case was simulated with a 3-D isothermal at 194°F using the curvilinear grid with a horizontal constant bottomhole pressure injector and a horizontal constant pressure production well. The injector and producer were operated at constant bottomhole pressures of 6,206 psi and 2,175 psi. 13x7x8 gridblocks with curvilinear grid geometry were used. The grid geometry is shown in Figure 2.123. Initial water-phase pressure and initial water-saturation distributions are shown in Figures 2.124 and 2.125, respectively. The horizontal wells were located in Layer 4 (producer) and Layer 7 (injector) and were perforated along the width of the corresponding layer. The total injection including the initial waterflood was 1.15 PV.

Figures 2.126 through 2.130 show cumulative oil recovery as a fraction of ROIP (3,764,155 bbls), oil cut, oil production rate, injection rate, and time vs. pore volume. These results show that it took about 8.5 years to finish injecting 1.15 PV for the chemical flood including the 1-year waterflood preceding the chemical flood. The oil recovery was 56.2% of the remaining oil in place, which would be considered good for a tertiary oil recovery chemical flood with such a small amount of chemical.

To obtain a more quantitative view of surfactant efficiency, an improved oil-recovery index and surfactant-efficiency indicator were used to help understand how well a surfactant works. The definition of improved oil recovery index (IOR) as

$$IOR = \frac{Rec_{chemical} - Rec_{water}}{Rec_{water}}$$

where $Rec_{chemical}$ = cumulative oil produced from chemical flooding and Rec_{water} = cumulative oil produced from waterflood, and the surfactant efficiency as

$$S_{eff} = \frac{Rec_{chemical} - Rec_{water}}{\text{Amount of injected surfactant}},$$

Units : m^3 of oil/ton of surfactant.

For this Base Case, the surfactant efficiency is 51 (m^3 oil/ton surfactant), which is relatively high for an S/P flood. IOR is 0.41, since the S/P process was treated as a secondary oil recovery process.

Figures 2.131 through 2.140 show the distributions of oil, surfactant, and polymer concentrations and oil and microemulsion saturations at 0.47 PV (in the S/P slug) and 1.125 PV (in post-water injection) injected for the Base Case. Profiles of interfacial tension are plotted in Figures 2.141 through 2.144. Figures 2.131 and 2.132 indicate that oil distributed under Layer 4 was not heavily in contact with chemical agents. It is clear that the injected chemicals follow the path of high-permeability zones and bypass the area under the producer (Figures 2.133 through 2.136).

The oil saturation is reduced to nearly zero for gridblocks with active surfactant (after satisfying the adsorption) concentration above the critical micelle concentration (Figures 2.137 and 2.138). This is due to the ultralow IFT caused by the Type III phase behavior of the surfactant. The IFT distributions (Figures 2.141 to 2.144) show the consistency with the oil-saturation distribution.

2.3.3 Sensitivity of Starting Time for Chemical Slug

In order to study the effect of the chemical injection timing, we examined a case with no water injection and another with a long water injection of about 7 years prior to the surfactant slug injection. Results are shown in Figures 2.145 through 2.147. Figure 2.145 shows the cumulative oil recovered as a fraction of oil in place at the beginning of the project. For the purpose of

comparison, the oil recoveries are at a fixed oil cut of 5% for the three cases studied. The amount of oil recovered is fairly insensitive to the starting time of the chemical injection (Figure 2.145).

The additional oil recovered in the latter case is partly due to the high injection rate during the waterflood prior to the chemical slug (Figure 2.147). However, the long waterflood increased the project life by 6 years from the Base Case, as shown in Figure 2.146. Although the injection timing may affect the economic analysis, the case with a year-long waterflooding was kept as the Base Case.

2.3.4 Effect of Vertical Permeability

In this section, the sensitivity analysis of vertical permeability was performed with a constant-bottomhole-pressure injector. The previous works on the applications of horizontal wells (Lim, 1993; Dakhlia *et al.*, 1995) have shown the strong effect of the vertical-to-horizontal permeability ratio on the oil recovery for the reservoirs being studied. To investigate the effect of vertical permeability on this reservoir, the vertical-to-horizontal permeability ratio was first reduced from 0.2 of the Base Case to 0.02. A simulation was also conducted where the vertical permeability is equal to the horizontal permeability (k_v/k_h ratio of 1). The results are shown in Figures 2.148 through 2.153.

Figure 2.148 indicates that the lowest k_v/k_h ratio leads to the highest sweep efficiency. Because of the high permeability in Layer 4, the higher the k_v/k_h ratio, the more easily layer channeling occurred. On the other hand, the lowest k_v/k_h ratio caused a low injectivity and a prolonged project life (Figures 2.149, 2.150, and 2.152). The project life increased from 10 years to 15 years when the k_v/k_h ratio decreased by an order of magnitude (Figure 2.153). Based on a project life of 10 years, the cumulative oil recovery was lowest for the k_v/k_h ratio of 0.02, i.e., about 58% of ROIP compared to the Base Case cumulative oil recovery of about 63.5% of ROIP.

The reduction in the project life was insignificant when the k_v/k_h ratio was increased from 0.2 to 1, thus implying that the crossflow was almost maximum even at a k_v/k_h ratio of 0.2. Because of the formation pinchout, the layer channeling, and the large aspect ratio in x and z directions, the capability for crossflow at a k_v/k_h ratio of 0.2 is as high as for a k_v/k_h ratio of 1.0. Thus, application of horizontal wells in this pilot is very suitable.

2.3.5 Effect of Injection Scheme and Chemical Property

To optimize injection schemes such as amount of surfactant and polymer injected, we first varied the concentrations of the injected surfactant concentration with constant slug size (0.4 PV injected) and constant polymer concentration. Then the amount of surfactant injected was kept constant and the polymer concentration was changed. The initial simulations were performed without considering the surfactant and polymer interactions, e.g., reduced surfactant adsorption in the presence of the polymer. Also, the injector was constrained to constant bottomhole pressure. For the purpose of estimating the uncertainty of experimental measurement, the sensitivity analyses including surfactant adsorption, surfactant phase behavior, and oil-phase desaturation curve are studied in this section. The detailed results are discussed in the following sections.

2.3.5.1 Amount of Injected Surfactant

The injected surfactant concentrations were changed from 0.5 vol.% of the Base Case to 0.2 and 1 vol.%. The results are shown in Figures 2.154 through 2.160. The project life was shortened from 10 years for the Base Case to 9 years for the higher surfactant concentration of 0.01 (Figure 2.156). The incremental oil recovered was only 3.4% even when the amount of surfactant injected was doubled (Figure 2.154). Because of the layer channeling, most bypassed oil still was not in contact with the high-surfactant-concentration front.

The surfactant front in the high-injection-concentration case moved into Layer 4 faster than in the low-concentration case and caused a higher injectivity during the S/P slug. Effective reduction of the effect of heterogeneity becomes the most difficult task in this reservoir. Regardless of this additional restraint, based on the incremental oil recovery, the most attractive case is that with the injected surfactant concentration of 0. 5 vol.%.

2.3.5.2 Amount of Injected Polymer

The injected polymer concentration was increased from 250 ppm in the Base Case to 400 ppm in both the surfactant slug and polymer drive (Figures 2.161 to 2.167). We also studied a case without polymer injection. The injection time for 1.15 PV injected was increased from 10 years to nearly 14 years (Figures 2.163 and 2.167) because of the lower injectivity of the higher polymer concentration of 400 ppm. The cumulative oil recovered, however, was increased from 63.5% to 65.5% by increasing the polymer concentration (Figures 2.161 and 2.162).

If an oil cut of 0.05 is used as the economic limit, then, as seen from Figure 2.164, the cumulative oil recovered at the project life of 8 years with 250 ppm polymer as in the Base Case is actually higher than for the 400 ppm in the later case. The simulation results from the case without polymer seem attractive in terms of both oil recovery (57%) and short project life of 8.5 years, but are not realistic. It is well-known that polymers are needed for mobility control and integrity of the surfactant slug. The phenomenon of fingering was not observed in the simulation results because large gridblocks were used in simulations. We must emphasize that this physical phenomenon, although invisible in the simulation results, will take place in a real-world situation. It is extremely risky to accept the simulation results of this case without polymer.

2.3.5.3 Surfactant Adsorption

The surfactant adsorption corresponding to the surfactant concentration of 0.5 vol.% was increased from 0.2 mg/g rock of the Base Case to 0.6 and 1.0 mg/g rock to study the sensitivity of the S/P flood to surfactant adsorption (Figure 2.168). The results are shown in Figures 2.169 and 2.170. The S/P oil recovery is sensitive to the adsorption level of surfactant. The oil recovery decreases from the 63% of the Base Case to 58% for the highest adsorption value studied here. Because of the layer channeling, rock surfaces contacted by the surfactant are mostly distributed in high-permeability paths. The effect of surfactant adsorption is not as significant as expected.

2.3.5.4 Surfactant Phase Behavior

The height of the binodal curve at the optimum salinity (HBNC71 on the plots) was the parameter studied for its sensitivity to the surfactant phase behavior. The cumulative oil recovery and the interfacial tension are in general very sensitive to this parameter. Figures 2.171 and 2.172 show the results of the effect of the height of the binodal curve on oil recovery. There is a 5% oil recovery difference with a 13% increase or decrease in the height of the binodal curve (0.03) in the Base Case at the project life of 9 years.

An accurate measurement of this parameter from a laboratory phase-behavior study is essential to make reasonable oil-recovery predictions for the S/P process. The above values of the height of the binodal curve at optimum salinity conditions assume the use of one of the best available surfactants.

2.3.5.5 Oil Capillary-Desaturation Curve

Two desaturation curves for the oil phase were considered for the sensitivity study to oil capillary-desaturation curve (CDC). The CDC curve used in the Base Case has a critical capillary number of 10^{-7} and the capillary number at which the residual oil goes to zero is about 10^{-2} (Figure 2.173). The Base Case CDC curve was shifted to the right, where the critical capillary number is

$3x10^{-6}$ and oil is completely mobilized at $7x10^{-2}$. The provided experimental data are also shown in Figure 2.173.

The simulation results showed no sensitivity to the oil CDC (Figures 2.174 and 2.175). The reason is that, for the gridblocks where the surfactant is active, the capillary number is far greater than 10^{-2}. Because of ultralow interfacial tensions, the residual oil is totally mobilized. This would not be true for a less-efficient surfactant. Careful examination of surfactant properties is very important in constructing an optimum design for the S/P process.

These simulation results indicate that measurements of the surfactant properties such as phase-behavior parameters, adsorption isotherms, and desaturation curves for the oil phase are very important to make the simulation results highly representative of the responses from the reservoir. Although the oil recovery does not seem very sensitive to the parameters in some cases, we only can draw conclusions after very careful sensitivity analyses with the understanding of reservoir characterization. Also, all of the above results will be applied to economic analyses for a qualitative understanding of the uncertainty of experimental measurement on oil recovery. These results are discussed by Vaskas (1996).

To further improve the reservoir description for the simulations closer to the real situations, a permeability-dependent residual-oil saturation to water-phase sensitivity analysis is introduced in the following sections. Also, a new Base Case is presented and the cases for sensitivity of surfactant slug size and amount of polymer are repeated to understand the effect of the residual-oil distributions on the oil recovery.

2.3.6 Permeability-Dependent Waterflood Residual-Oil Saturation

Up to now, all simulations were conducted using a constant waterflood residual-oil saturation (S_{orw}) at a low capillary number of 0.25 in all the gridblocks. In this section, the impact of S_{orw} is investigated. First, S_{orw} was uniformly increased from 0.25 to 0.3. Since S_{orw} is correlated with permeability, subsequent simulations were conducted using an empirical correlation to assign the waterflood S_{orw} to each gridblock. The distributions studied were

(A) $S_{orw} = \exp(-0.88222\, k^{0.125})$,
(B) $S_{orw} = \exp(-1.1048\, k^{0.0625})$, and
(C) $S_{orw} = \exp(-0.5665\, k^{0.25})$.

In these distributions, a volume-weighted average S_{orw} of 0.25 was preserved. Figure 2.176 shows S_{orw} as a function of permeability using the above correlations. Various S_{orw} values were investigated for each correlation. Figures 2.177 through 2.179 show the oil-phase capillary-desaturation curve of the lowest- and highest-permeability gridblocks for each distribution, consecutively. The residual oil saturation ranges from 13% to 33% in the first distribution, from about 19% to about 29% in the second distribution, and from 5% to 40% in the third distribution.

Figures 2.180 and 2.181 show the results of these simulations under the condition of constant-rate injector. The chemical-flood performance of Reservoir B is quite insensitive to the waterflood residual-oil saturation. This insensitivity can be attributed to the early initiation of the chemical flood (only a year after waterflood). At the initiation of chemical flooding, the initial oil saturations in the waterflooded gridblocks are still very much above the residual saturation.

We repeated three of the above cases, namely the case with $S_{orw} = 0.25$, the case with $S_{orw} = 0.3$, and the case where S_{orw} is a function of permeability ($S_{orw} = \exp[-0.88222\, k^{0.125}]$), under tertiary conditions. The reservoir was first waterflooded for 1 PV (about 7 years) prior to the commencement of chemical flood. Figures 2.182 and 2.183 show the cumulative oil production for the three cases during the chemical-flood project life. As the chemical-flood target oil volume was greatest when an S_{orw} of 0.3 was used, it also yielded the highest cumulative oil

production. The case with the distributed S_{orw} gave the lowest tertiary oil production, even though the volume-weighted S_{orw} was also equal to 0.25.

This is partly caused by the correlation used to produce the S_{orw} distribution, a higher-permeability reservoir will yield a lower residual-oil saturation. Also, because of the presence of a very high-permeability layer in this reservoir, the displacement was dominated by channeling effects. Hence, the sweep is poor and the contacted gridblocks are mostly those with higher permeability, contributing to the channeling phenomenon. Consequently, the chemical-flood target oil volume in these gridblocks is less than in the other two cases.

To make the simulations more realistic, Case A of variable residual-oil saturation (as a function of permeability) was chosen as the Base Case and was called the new Base Case. Although there are no experimental data to validate the correlation used for this pilot, it is believed that the distribution of Case A is reasonably assumed for this reservoir. Also, the decrease in injectivity of the chemical flood because of the higher viscosity of the polymer may be somewhat overestimated, since the shear rate in the very large gridblocks near wells is underestimated. To simplify this problem, the injection rate was considered to be constant for the following sensitivity analyses. Since the bottomhole pressure of the injector was ignored, whether the wellbore pressure exceeded the formation fracture pressure or not was not analyzed.

2.3.7 Sensitivity Analyses for the New Base Case

In the new Base Case, the injector was under a rate constraint of 25,409 B/D (2,571 m^3/d) and oil residual saturation was based on the permeability distribution. Figures 2.184 through 2.188 show cumulative oil recovery as a fraction of oil in place at the start of waterflood, oil production rate, produced surfactant concentration, produced polymer concentration, and the time vs. pore volume injected. These results show that it takes about 8.5 years to inject 1.15 PV for the chemical flood including the 1-year waterflood preceding the chemical flood. The project life is shortened by a year from the original Base Case.

To examine carefully the effect of amount of injected chemicals and slug size, the simulations of amount of injected surfactant and polymer were repeated based on the new Base Case. In addition, the sizes of S/P slugs were investigated by keeping the amount of injected chemical constant but reducing the injection duration to half of the new Base Case (0.2 PV).

2.3.7.1 Amount of Surfactant and Slug Size

The sensitivity analyses of surfactant were performed first, and the injected polymer concentration was kept constant at 250 ppm for 0.6 PV. To investigate the uncertainty from the amount of injected surfactant concentration, the injected surfactant concentrations were varied from 0.5 vol.% of the Base Case to 0.25 and 0.75 vol.%. The results are shown in Figures 2.189 through 2.193. The incremental oil recovered by increasing the amount of injected surfactant from 0.5 to 0.75 vol.% was only 2%. The incremental oil recovered was nearly 6% by increasing the injected concentration from 0.25 to 0.5 vol.%, since most of the surfactant was adsorbed for the case with lower injected concentration (Figures 2.190 and 2.192). Compared to the sensitivity analyses for the results discussed in Section 2.3.5.1, the incremental recovery for the rate-constrained injector is not as much as that for a pressure-constraint injector. Because the target oil of this new Base Case is less than the previous Base Case, the high-concentration front of surfactant does not have much extra oil to mobilize.

To further study the injection slug size of S/P, the chemical amounts were kept the same but the injection duration was reduced to half of the new Base Case (0.2 PV). Figure 2.194 shows the oil recovery as a function of pore volumes injected. It is indicated that oil recovery is not sensitive to the S/P slug size because of the low chemical adsorptions for the pilot. Since the injection scheme has a large impact on the cash flow, the results were applied for the economic analyses to obtain the optimum case. The detailed economic analysis can be found in Vaskas (1996).

2.3.7.2 Amount of Polymer

The sensitivity analyses for the amount of injected polymer were performed for the new Base Case. The injected polymer concentration was increased from 250 ppm in the new Base Case to 500 ppm and 750 ppm in both the surfactant slug and polymer drive. A case without polymer was also studied. The cumulative oil recovered increased from 63.5 to 74% with the increase in the polymer concentration from the Base Case value of 250 ppm to 750 ppm (Fig. 2.195). The sweep efficiency improved significantly by increasing the polymer concentration. Since the capacity of the injection facility and formation fracture pressure are not considered in the simulations, the results may be somehow optimistic. However, application of high concentration of polymer to overcome the high-permeability channeling and to improve the sweep efficiency has been shown in this study.

2.3.8 Polymer/Surfactant Interactions

To investigate the effect of polymer/surfactant interactions, e.g., reduced surfactant adsorption, the model that treated the calculation of adsorbed surfactant as a function of adsorbed polymer concentration was used. Figures 2.196 through 2.200 show these results. The competitive adsorption has very little effect on the oil recovery for this case. Figure 2.198 shows the effect of polymer in reducing the adsorbed surfactant concentration from 0.043 to 0.02 mg/g rock. The insensitivity of oil recovery to the level of adsorbed surfactant in this case is due to the small chemical contact area (layer channeling) and a low surfactant adsorption in the new Base Case.

To further investigate this, the maximum surfactant adsorption corresponding to the injected concentration of 0.5 vol.% was increased from 0.1 to 0.42 mg/g rock and the above simulations were repeated. The results are presented in Figures 2.201 through 2.205, where higher sensitivity to the surfactant adsorption is shown. The surfactant adsorption isotherm is shown in Figure 2.206. From the breakthrough times of surfactant and polymer, it is clear that the polymer flows ahead of the surfactant as predicted by the model. Because of the layer channeling, the effect of competitive adsorption between surfactant and polymer on oil recovery is reduced.

2.3.9 Summary and Conclusions for Reservoir B

The potential of LTPF using horizontal wells with moderate permeability and porosity was investigated. The new features such as curvilinear grid geometry option, temperature effect on the surfactant phase behavior, and competitive adsorption model were applied for this study. This is the first time that the curvilinear grid geometry has been used in field-scale S/P simulations with UTCHEM.

We can draw the following conclusions from the field-scale simulation results:

1. For this field, the use of horizontal wells and the optimization of the well locations were essential to reduce the project life to 10 years.
2. The high vertical permeability in this reservoir makes it favorable for horizontal wells.
3. A high polymer concentration is required to prevent channeling through a very high-permeability layer in this reservoir.
4. Refinement of the grid from 13x7x8 to 27x7x15 made only a small change in the oil recovery.
5. In Reservoir B, the temperature effect is not significant. The lagging of heat transport behind the surfactant front causes this insensitivity. This contradicts the results obtained from Reservoir A, which is a reservoir with high permeability .
6. The effect of competitive adsorption is not significant for Reservoir B. Layer channeling, formation pinchout, and low surfactant adsorption caused the injection fluid to contact a small area of reservoir and low chemical adsorption. This phenomenon reduces the effect of the surfactant/polymer interactions.

To reduce the effect of layer channeling on the S/P process, gel treatments may be one of the best ways to improve the sweep efficiency. Kim (1996) presented the application of cross-linking gel treatment for this reservoir. The gel treatment was investigated for the injector, producer, and both injector and producer to obtain the best sweep efficiency. The results showed that the gel treatment did improve the performance of the S/P process after the profile control by the cross-linking gel treatment, which is consistent with our conclusions.

2.4 Optimized Design for Reservoir C

Sensitivity analysis and optimum injection scheme for the S/P process were studied for a high-heterogeneity U.S. onshore light-oil sandstone reservoir, Reservoir C. A stochastic method was used to generate the permeability distribution with the average permeability of 50 md and Dykstra-Parsons coefficient of 0.8. A high-efficiency surfactant with the physical properties based on the one reported by Shupe (1989) was used.

A series of simulations was performed. The sensitivity parameters included the salinity gradient and constant salinity design, amount of injected surfactant and polymer, permeability-dependent residual-oil saturation to water phase, competitive adsorption, vertical-to-horizontal permeability ratio (k_v/k_h), and permeability realization.

The optimum injection scheme was obtained by economic analysis. The chemical slug, surfactant concentration, and polymer concentration were the variables for optimization process. The results show that the profitability was greatly improved after the optimization.

2.4.1 Reservoir Description

To simplify the reservoir description, a quarter-symmetry element of a 40-acre five-spot pattern was modeled. The quarter-five-spot was 660 ft in both x and y directions with a thickness of 140 ft. The reservoir is an idealization of an actual midcontinent U.S. sandstone oil reservoir. High heterogeneity and low porosity are the main characteristics of this reservoir. This reservoir is a potential candidate for surfactant flooding since it has already been waterflooded to near its economic limit and is otherwise subject to abandonment.

The permeability description was generated by matrix decomposition method (Yang, 1990). A Dykstra-Parsons coefficient of 0.8 (the standard deviation of the logarithm of the permeability is 1.609) and a geometric mean of 50 md were used. A spherical variogram and a log-normal permeability distribution were used. The correlation lengths were 660 feet in the x and y directions and 28 feet in the z direction. Several different permeability realizations were made. The effect of different permeability realizations can be found in Dakhlia (1995).

Figure 2.207 shows the x-direction permeability isosurface for 200 md. Local channeling and pinchout were observed from the permeability distribution. The permeability ranges from 1 to 2,000 md. The vertical-to-horizontal permeability ratio was 0.1. The porosity was uniform and equal to 0.136. The initial oil saturation was 0.8 and the depth of the top layer was 3,500 ft with uniform initial pressure of 900 psi. The UTCHEM input data for the are listed in Table 2.8.

2.4.2 Base Case for S/P Flooding

The simulation grid was 11x11x5 and Δx, Δy, and Δz were 60 ft x 50 ft x28 ft was used for discretization. Two vertical wells were first chosen for the Base Case. The reservoir was first waterflooded for a long duration (40 years) until 98% water cut was reached. The temperature changes were not considered in this case, since the temperature difference between formation and injection water was reduced by the long waterflood.

Polymer properties are based on the typical data available for xanthan gum. Surfactant property data correspond to a high efficiency EO-PO type surfactant (Shupe, 1989). The critical micelle concentration (CMC) was 6×10^{-3} vol.%. This value is on the order of 4.1×10^{-3} vol.%

measured by Kalpakci *et al.* (1990). The surfactant adsorption of 0.08 mg/g rock is similar to the levels observed in the Loudon field pilot (Maerker and Gale, 1992; Reppert *et al.*, 1990).

The physical properties used in simulations are shown in Figures 2.208 through 2.217. Figures 2.208 and 2.209 show the oil and water relative-permeability curves used at low and high capillary numbers, respectively. Figure 2.210 presents the relative-permeability curve for microemulsion and oil phases at high capillary numbers. Polymer properties such as adsorption isotherm, viscosity versus shear rate, and the permeability-reduction factor are shown in Figures 2.211 through 2.213. Surfactant properties and phase behavior are shown in Figures 2.214 through 2.217. The ternary diagram was based on the Type III phase environment of the oil, surfactant, and water mixture at anions of 0.611 meq/mℓ (21,690 mg/ℓ).

To approximate conditions prior the onset of tertiary oil recovery, the reservoir was first waterflooded with a low initial-water saturation of 0.2 until a water cut of 98% was reached. The resulting pressure and saturation distributions were then used as the initial condition for the S/P process simulations. The average oil saturation was 0.31 at the end of the waterflood. The injection scheme applied for the Base Case was as follows :

S/P slug : 0.2 PV of 2.5 vol.% of surfactant with 1,000 ppm of xanthan gum in the brine,
Polymer drive : 0.5 PV of 1,000 ppm polymer (xanthan gum) in the brine, and
Postflush : 3.25 PV of brine.

The total anion concentration of makeup water (brine) for the constant-salinity case was 21,690 mg/ℓ which was identical to that of the formation water. The wells were vertical and pressure-constrained with 1,000 psi pressure drop between the injector and the producer. The key input parameters for the Base Case are given in Table 2.9.

Figures 2.218 through 2.224 show oil recovery as a function of both pore volumes and project life, oil production rate, injection rate, produced surfactant and polymer concentrations, and effective salinity. The oil production rate and injection rate are shown for a full five-spot pattern. The oil recovery is 0.68 based on the remaining oil in place (ROIP) for a project life of 30 years (Figures 2.218 and 2.219). Figure 2.222 shows a large amount of surfactant was produced. A high polymer concentration is required for a suitable mobility control (endpoint mobility ratio was 0.05) because of the unfavorable endpoint mobility ratio of 1.4 for waterflood. The low injectivity due in part to the underestimation of the well gridblock shear rate has a negative effect on this Base Case (Figure 2.221). A maximum injection rate of 2,000 B/D was used to avoid an unrealistically high injection rate during the postflush period.

Figures 2.225 and 2.226 show the distributions of oil and surfactant concentrations at different times. The oil in the high- and moderate-permeability zones is recovered very well. At the end of the project, some oil was trapped in the corner opposite to the producer. Surfactant had contacted a large volume of reservoir at the end of the polymer drive. During the postflush, water channeled into the high-permeability path and forced the surfactant front to flow to the opposite side of the producer and to be trapped in the top and bottom layers. These results indicate that the oil recovery is good, but the high consumption of surfactant and the long project life hurt the economics. Shortening the project life and reducing the amount of surfactant are the way to make a better design for Reservoir C. Prior to the sensitivity analyses, a salinity-gradient design is introduced.

2.4.3 Salinity-Gradient Design

One of the advantages of the salinity-gradient design is the reduction of surfactant retention. Many other advantages are discussed by Pope and Bavière (1991). This scheme is especially suitable for onshore reservoirs, since alternate sources of water are usually available to inject and this can be used to great advantage in some cases. To study the effect of a salinity gradient for Reservoir C, a salinity-gradient design (Figure 2.227) was used. Input data remained the same as for the Base Case with the exception of the initial formation and injected salinities. The initial anion concentration was 0.97 meq/mℓ (34,435 mg/ℓ), which was above the upper salinity for the

three-phase window. During the S/P slug injection, the anion concentration was kept at 0.611 meq/mℓ (21,300 mg/ℓ) within the three-phase window. Then, the polymer drive and postflush anion concentrations were 0.4 meq/mℓ (14,200 mg/ℓ) below the lower effective salinity limit of the three-phase window.

Applying this scheme, a salinity gradient was simulated. Figures 2.228 and 2.229 compare the oil recoveries for constant salinity and salinity-gradient design. Though the latter exhibited an increased sweep efficiency during the S/P slug and polymer drive, its overall oil recovery was less than that of the former. Figure 2.230 shows the effect of the sweep efficiency on the oil production rate. Because of the higher viscosity of the microemulsion in the Type II(+) region and the smooth viscosity gradient, the chemical front performed like a piston-like displacement, but there was a reduction in the injectivity (Figure 2.231).

Comparison of the breakthrough time and peak concentration of produced surfactant (Figure 2.232) shows that the salinity-gradient design sharpens the front and delays chemical breakthrough time. Figures 2.233 and 2.234 show that the use of the salinity-gradient design reduces the surfactant adsorption but not the surfactant retention. This is surprising, since the advantages of a salinity gradient have been demonstrated many times in both corefloods and field pilots. One possible explanation is that this gradient was too steep.

Most effects of salinity gradient in coreflood were observed in the field-scale simulation with the exception of lower surfactant retention. Figures 2.235 and 2.236 show the oil and surfactant concentrations at different injection times for the salinity-gradient case. The high heterogeneity of the permeability field and the channeling near the injector are the main factors causing high trapping of surfactant in the salinity-gradient case .

Comparison of Figures 2.225 and 2.235 show that the oil in the high-permeability zone was displaced quickly in the salinity-gradient case during the polymer drive. Since the oil in the high-permeability path is almost perfectly displaced by the sharp front, the postflush water for the salinity-gradient case meets less resistance in the high-permeability path than in the constant-salinity case. Thus, the postflush water following the high-permeability path travels to the producer and pushes low IFT fluids to the opposite side of the producer. Also, the Type II(-) phase behavior causes higher relative permeability for the water phase (two- phase flow) than that in the Type III constant-salinity case (three-phase flow). These factors prevent the oil recovery for the salinity-gradient case from increasing very much during the water drive (Figure 2.228). All of this indicates that optimization of the salinity gradient is needed.

To further study the effect of salinity-gradient design, the injected surfactant concentration was varied to 3, 2.5 (Base Case), 1.25, 0.8, and 0.2 vol.% for 0.25 PV injected. The amount of polymer was kept constant at 0.25 PV of 0.1 wt% for the S/P slug and 0.5 PV of 0.1 wt% for the polymer drive. Both constant-salinity and salinity-gradient designs were tested in each case. Figure 2.237 shows the oil recovery as a function of the amount of surfactant after injection of 3 PV. For the constant-salinity case, the oil recovery has a sharp decrease when the surfactant concentration falls below 1.25 vol.%. (Figure 2.237) The oil recovery for the Base Case is located on the plateau and is clearly too high to be cost-effective. When smaller amounts of surfactant are injected, the salinity-gradient design gives higher oil recovery, and these are the conditions of most interest economically. For small amounts of injected surfactant, the residual oil, even distributed in the high-permeability zone near the producer, does not get a chance to be produced (Figures 2.238 and 2.239).

The oil recovery for the salinity-gradient case has a similar shape to that in the constant-salinity case, except that its sharp decline starts at 0.8 vol.% (Figure 2.237). The salinity-gradient effects are more significant in the cases with low surfactant-concentration injection. Since the salinity-gradient design has reduced surfactant adsorption, it has more active surfactants than in a constant salinity case (Figures 2.238 and 2.240). Also, this effect causes a slower decrease in oil recovery when the surfactant concentration is reduced. Figure 2.241 shows the distribution of oil concentration. The oil distributed near the well area is displaced better than in the constant-salinity run (Figure 2.239). The effect of local channeling on the high-permeability path is reduced because having enough surfactant to mobilize residual oil is the main factor for high oil recovery.

In summary, the salinity-gradient design can be applied to reduce the amount of surfactant required. The favorable condition for this design is at low surfactant concentration. The surfactant concentration can be 0.8 vol.% (0.25 PV) with a salinity design to give an oil recovery of 0.53, but with a 30-year project life, which is much too long. Application of horizontal wells is one way to shorten the project life. Dakhlia (1995) indicated that the combination of a horizontal injector with a vertical producer was favorable for Reservoir C. Thus, a horizontal injector was used in the following sections.

2.4.4 Permeability-Dependent Residual-Oil Saturation

The waterflood residual-oil saturation (S_{orw}) was uniform and was equal to 0.25 in the simulations in the previous sections. To investigate the effect of both the magnitude and the distribution of a nonuniformity of residual-oil saturation on the S/P process using stochastic permeability distributions, (1) S_{orw} was increased from 0.25 (Case 1) to 0.3 (Case 2) and (2) two sets of permeability-dependent S_{orw} distributions were investigated as follows:

Case 3: $S_{orw} = \exp(-1.1859127\ k^{0.04})$

Case 4: $S_{orw} = \exp(-0.941164\ k^{0.1})$

A volume-weighted S_{orw} of 0.25 was used in these oil distributions.

A horizontal injector was placed along the y direction and in the second layer. The producer was vertical. A constant pressure drop of 1,000 psi was applied. The constant-salinity design and injection scheme for the Base Case were kept. Figure 2.242 shows S_{orw} as a function of permeability. Figures 2.243 and 2.244 show the oil-phase capillary-desaturation curve (CDC) of the lowest- and highest-permeability gridblocks for Cases 3 and 4. CDC corresponding to a waterflood residual oil saturation of 0.25 is also shown in these figures. S_{orw} ranges from 19% to 32% in Case 3 (Figure 2.243) and from 12% to 44% in Case 4 (Figure 2.244).

Figures 2.245 and 2.246 show the cumulative oil produced as a function of both pore volumes injected and time for the cases studied. These results indicate that the oil recovery is more sensitive to the amount of targeted oil than how it is distributed, which was also observed for Reservoirs A and B. Prior to surfactant injection, the reservoir was waterflooded with 2.81 PV of water. The water cut at the initiation of S/P flood is about 98%. The cumulative oil recovery is the highest for Case 2 ($S_{orw} = 0.3$). This can be attributed to the fact that, because of the higher S_{orw} in Case 2 than in Case 1 (25%) or Cases 3 and 4 where a volume-weighted average S_{orw} of 25% was also preserved, less oil was recovered during waterflooding in Case 2. Hence, the chemical-flood target oil volume is the largest in Case 2. Even though Cases 3 and 4 have the same volume-weighted average S_{orw} (on a reservoir-wide basis) as Case 1 (constant S_{orw} of 25%), it is observed that the cumulative oil recovery for Case 3 is higher than that of Case 1, while the recovery for Case 4 is higher than that of Case 3. This is also an indication that as the range in the S_{orw} distribution increases (as in Case 4 compared to Case 3), less oil can be recovered through waterflooding, and hence a higher chemical-flood target oil volume exists. The residual oil distribution of Case 3 was used in the following sections to make the reservoir description as realistic as possible.

2.4.5 Effect of Competitive Adsorption

To explore the potential of low-tension polymer flooding (LTPF) as an alternative to the traditional S/P process in an effort to increase the cost-effectiveness of surfactant flooding, we altered the amount of chemical injected to model the conditions of LTPF. The salinity-gradient and polymer-preflooding designs were also investigated.

2.4.5.1 New Base Case

Based on the results in the previous sections, the surfactant concentration was reduced from 0.5 to 0.25 vol.% and the slug size was increased from 0.25 to 0.40 PV. The total amount of surfactant used for this design was equal to the 0.8 vol.% surfactant of 0.25 PV case (discussed in Section 2.4.3). The polymer concentration was 1,000 ppm in both the 0.4 PV surfactant slug and 0.5 PV polymer drive. The polymer drive was then followed by 2.1 PV chase water. To eliminate the effect of injectivity in these runs in order to better understand the impacts of the small amount of chemicals and the chemical interactions, the simulations discussed here were performed at a constant rate of 2,244 B/D. The residual oil was distributed in accordance with the permeability field as in Case 3 in the previous section. A constant salinity was used.

2.4.5.2 Competitive Adsorption

To investigate the effects of S/P interactions in this high-heterogeneity reservoir, a simulation that took competitive adsorption into account was performed. For the purpose of comparison, a case without polymer injection was also simulated. Figure 2.247 shows the oil recovery as a function of pore volumes injected for three cases. The oil recovery for the case without polymer injection is 22%, almost half of that in the new Base Case. Mobility control for viscous oil and reduction of channeling for high-heterogeneity permeability distribution are the main reasons for using high polymer concentration. Since the gridblock size used in this study was large, the fingering phenomenon was not observed for the case without polymer. The surfactant/polymer interactions resulted in a 6% increase in the oil recovery in the competitive adsorption case over the new Base Case.

Figures 2.248 and 2.249 show the produced surfactant concentration and the adsorption versus pore volumes injected. The surfactant adsorption decreased by 75% from 0.08 (Base Case) to 0.02 mg/g rock by competitive adsorption. Because of less surfactant contact with formation, the case without polymer injection has lower surfactant adsorption than with polymer. Although the reduction of surfactant adsorption may be too optimistic, these simulation results show the importance of competitive adsorption in a design where only a small amount surfactant is injected.

2.4.5.3 Competitive Adsorption with Salinity Gradient

To further study the salinity-gradient effect on the design of LTPF, two simulations were performed. The salinity-gradient design as mentioned in Section 2.4.3 was applied for both cases, with one of them taking the surfactant/polymer interactions into consideration. Figure 2.250 compares the oil recovery of these two cases with that of the new Base Case. There is a 4% increase in oil recovery because of the salinity-gradient design and 3% because of competitive adsorption. The sweep efficiency was improved by the salinity-gradient design.

Figure 2.251 shows the produced surfactant concentration versus pore volumes injected. The salinity-gradient case has a later breakthrough time because of the favorable mobility control. The produced surfactant concentration increases significantly in the competitive adsorption case, though again it may be too optimistic to make this prediction. Figure 2.252 compares surfactant adsorption for three cases. The surfactant adsorption for the salinity-gradient design is higher than that for the constant salinity case, which is opposite to what was expected. The reason was that the surfactant contacted more of the reservoir during the salinity-gradient flood. This result nicely illustrates the need to carefully simulate and understand each case studied.

Figures 2.253 and 2.254 compare the surfactant concentration of the 1×10^{-4} isosurface during the polymer drive and postflush and clearly indicate that the surfactant contacted a larger volume of the reservoir in the salinity-gradient flood. Since later the sweep efficiency increased and a local reduction of the surfactant adsorption by the use of the salinity gradient design occurred, the surfactant contacted much more low-permeability rock than for the constant-salinity

flood, and this led to higher overall loss of surfactant from surfactant adsorption for the constant-salinity case and the salinity-gradient design case.

2.4.6 Optimum Injection Scheme

The purpose of this study was to apply the discounted-cash-flow method and risk analysis to the optimization of chemical flooding to find out under what conditions at current U.S. oil prices chemical flooding might be profitable if optimized using current process and oil field technologies.

The new Base Case presented in Section 2.4.5.1 was modified and was applied for the optimization process. The modifications included geometric average of permeability field, residual oil and water saturation at low capillary number, oil viscosity, and porosity. Constant-salinity design was applied to the sensitivity simulations in this section. Table 2.10 lists the modified values of each parameter. A formation fracture pressure limit of 2,250 psia was applied to the constant-rate injector in order to prevent fracturing the formation.

A economic model based on discounted-cash-flow method was used. The detailed description of the economic model can be found in Vaskas (1996), Wu *et al.* (1996), and in Part II (Economic Analysis) of Task 2 of this report.

Table 2.1: Coreflood data for Reservoir A

Rock	Bentheimer
Length, cm	30.4
Diameter, cm	3.8
Porosity, fraction	0.229
Pore volume, mℓ	76.8
Temperature, °F	122
Pressure, psi	435
Permeability, md	2912
Permeability at S_{oi}, md	2664
Permeability at S_{or}, md	401
Permeability at S_{orc}, md	1970
S_{wi}	0.147
S_{or}	0.395
S_{orc}	0.096
μ_w, cp	0.42
μ_o, cp	2.5
Injection rate, mℓ/s	0.00556
Waterflood, PV	0.60
Surfactant/polymer slug, PV	0.43
Polymer drive, PV	0.5
Chase water, PV	4.9
Surfactant conc., vol.%	0.5
Polymer conc., ppm	500

Table 2.2: Input data for coreflood simulation (Variables as defined in Saad (1989).)

Dimensions of core simulated, ft	0.9974 x 0.1105 x 0.1105
Number of gridblocks in the x direction	80
Uniform gridblock sizes, ft	0.0125 x 0.1089 x 0.1089
Porosity	0.229
Permeability, md	2192
Initial core pressure, psia	145.04
Initial water saturation	0.605
Salinity expressed in total equivalent anions, meq/mℓ	0.627
Calcium ions , meq/mℓ	0.133
Height of the binodal curve	
HBNC70	0.03
HBNC71	0.03
HBNC72	0.03
Lower effective salinity, meq/mℓ	0.65
Higher effective salinity, meq/mℓ	0.9
Critical micelle concentration, vol. fraction	0.0001
Interfacial tension	
G11	13.0
G12	-14.8
G12	0.007

Table 2.2: Input data for coreflood simulation (cont'd.)

G21	13.2
G22	-14.5
G23	0.01
Capillary desaturation parameters	
T11	1865
T22	28665
T33	364.2
Residual water saturation	0.147
Residual oil saturation	0.395
Water endpoint relative permeability	0.137
Oil endpoint relative permeability	0.915
Exponent of the water relative permeability curve	2.182
Exponent of the oil relative permeability curve	1.4048
Water viscosity, cp	0.42
Oil viscosity, cp	2.5
Polymer viscosity parameters:	
ap1	73.0
ap2	1006.0
ap3	10890.
$\dot{\gamma}_c$	10.0
$\dot{\gamma}_{1/2}$	187.985
P_α	1.843
S_p	0.0
β_p	2.0
Case1	0.01
Inaccessible pore volume for polymer	0.9
Permeability reduction factors:	
b_{rk}	1000
c_{rk}	0.0186
Polymer adsorption parameters:	
a41	1.1
a42	0.0
b4	100
Surfactant adsorption parameters:	
a31	2.2
a32	0.0
b3	1000
Longitudinal dispersivity, ft	0.02
Transverse dispersivity, ft	0.0

Table 2.3: Input data for 2-D cross-sectional simulations*

Dimensions of core simulated, ft	1315 x 82.02 x 26
Number of gridblocks in the x, y, z directions	26 x 1 x 8
Average gridblock sizes, ft	50.5 x 82.02 x 3.25
Average (arithmetic) of porosity, md	0.229
Geometric average of permeability in x direction, md	7349
Initial pressure, psia	3771.04
Initial water saturation	0.147
Salinity expressed in total equivalent anions meq/mℓ	0.627
Calcium ions , meq/mℓ	0.133
Residual water saturation	0.147
Residual oil saturation	0.25
Water viscosity, cp	0.42
Oil viscosity, cp	2.5
Longitudinal dispersivity, ft	16
Transverse dispersivity, ft	0.4

*The physical properties that are not listed here are the same as 1-D coreflood data.

Table 2.4: Oil recovery data versus temperature

Temperature (°F)	Measured Oil Recovery	Simulated Oil Recovery
86	0.54	0.789
122	0.64	0.884
158	0.42	0.746

Table 2.5: Simulation input data for thermal properties

	Laboratory data	UTCHEM Input*
Phase behavior parameters:		
HBNT0	-----	0.00017
HBNT1	-----	0.0017
HBNT2	-----	0.00017
β_T	-----	0.00415
Formation rock and fluid heat properties		
Rock density	2.65 g/cc	165.43 lb/ft^3
Reservoir thermal conductivity	2.8846 W/m°K	40 (day-ft-°F)$^{-1}$
Rock heat capacity	2.347x106 J/m^3°K	0.2117 BTU/lb°F
Water heat capacity	4186 J/kg°K	1.0 BTU/lb°F
Oil heat capacity	2093 J/kg°K	0.5 BTU/lb°F
Surfactant heat capacity	-----	1.0 BTU/lb°F
Overburden and underburden thermal conductivity	2.524 W/m°K	35 (day-ft-°F)$^{-1}$

* This column shows the provided laboratory data in English units

Table 2.6: Simulation input data for Reservoir B

Reservoir dimension, ft	4656.8 x 3376.1x 288.0
Number of gridblocks in the x, y, z directions	13 x 7 x 8
Average gridblock sizes, ft	358.2 x 482.3 x 36
Volume-weighted avg. porosity, fraction	0.1265
Arithmetic average permeability in x direction, md	112
Vertical-to-horizontal permeability ratio	0.2
Average (volume) initial water saturation	0.2313
Salinity expressed in total equivalent anions meq/mℓ	0.627
Calcium ions , meq/mℓ	0.133
Residual water saturation	0.125
Residual oil saturation	0.25
Water viscosity, cp (90°C)	0.27
Oil viscosity, cp (90°C)	0.29
Oil formation volume factor (constant), B/STB	1.444
Water formation volume factor, B/STB	1.01
Oil compressibility, psi^{-1}	1.8279×10^{-5}
Water compressibility, psi^{-1}	1.52317×10^{-5}
Formation compressibility, psi^{-1} (P_{ref} = 4,350 psia)	4.8276×10^{-6}
Constant injection rate, B/D	25,409
Production pressure, psia	2,175

Table 2.7: Surfactant property data used in the Base-Case simulation for Reservoir B (Variables are defined in Saad (1989).)

	Base case (constant temp.)	Variable temp.
Phase behavior parameters :		
HBNC70	0.03	0.12
HBNC71	0.03	0.03
HBNC72	0.03	0.04
HBNT1	------	0.00017
HBNT2	------	0.00017
HBNT3	------	0.00017
C2PLC	0.0	0.0
C2PRC	1.0	1.0
CMC	0.0001	0.0001
CSEL	0.50	0.50
CSEU	0.65	0.66
CSET	0.0	0.00415
Parameters for interfacial model :		
G11	13.	13.
G12	-14.8	-14.8
G13	0.007	0.007
G21	13.2	13.2
G23	-14.5	-14.5
G33	0.010	0.010

Table 2.7: Surfactant property data used in the Base-Case simulation for Reservoir B (cont'd.)

Parameters for surfactant adsorption:		
AD31	0.2	0.2
AD32	3.19	3.19
B3D	1000	1000

Polymer properties

Polymer viscosity parameters:	
ap1	73
ap2	1006
ap3	10809
$\dot{\gamma}_c$	10
$\dot{\gamma}_{1/2}$	188
P_α	1.84
S_p	0.0
β_p	2.0
Case1	0.01
Inaccessible pore volume	0.9
Permeability reduction factors:	
b_{rk}	1000
c_{rk}	0.0186
Polymer adsorption parameters:	
a41	1.1
a42	0.0
b4	100

Table 2.8: List of reservoir description input data for Reservoir C

Dimensions of the quarter a five-spot	660 ft x 660 ft x 140 ft
Porosity	0.136
Type of permeability distribution	log-normal
Geometric average permeability	50.55 md
Standard deviation of the log permeability	1.609
Arithmetic average permeability	181.8 md
Range of permeability	0.293 md — 4343 md
Correlation length in x, y, and z directions	660 ft x 660 ft x 28 ft
Vertical to horizontal permeability ratio	0.1
Residual water saturation	0.14
Residual oil saturation	0.25
Water viscosity	0.74 cp
Oil viscosity	7.78 cp
Endpoint water-oil mobility ratio	1.393
Brine salinity assumed all anions	0.611 meq/mℓ
Divalent cation concentration of brine	0.1275 meq/mℓ

Table 2.8: List of reservoir description input data for Reservoir C (cont'd.)

Injection pressure	1250 psi
Production pressure	250 psi
Number of gridblocks in the x, y and z directions	11 x 11 x 5
Gridblock sizes in the x, y, and z directions	60 ft x 60 ft x 28 ft
Effective length to thickness ratio	1.49
Maximum injection rate per quarter a five-spot	500 B/D

Table 2.9: Surfactant property data used in the Base-Case simulation for Reservoir C

Surfactant properties

	Input values
Phase behavior parameters:	
HBNC70	0.01
HBNC71	0.016
HBNC72	0.1
C2PLC	0
C2PRC	1
CMC	6×10^{-5}
CSEL	0.611
CSEU	0.55
CSET	0.916
Parameters for desaturation curves:	
T11	1865
T22	59074
T33	364.2
Parameters for interfacial model:	
G11	13.
G12	-14.8
G13	0.007
G21	13.
G23	-14.5
G33	0.01
Parameters for surfactant adsorption:	
AD31	1.0
AD32	0.5
B3D	1000

Table 2.9: Surfactant property data used in the Base-Case simulation for Reservoir C (cont'd.)

Polymer properties

Polymer viscosity parameters:	
ap1	81
ap2	2700
ap3	2500
$\dot{\gamma}_c$	20
$\dot{\gamma}_{1/2}$	10
P_α	1.8
S_p	0.1695
β_p	10
Case1	0.01
Inaccessible pore volume	0.8
Permeability reduction factors:	
b_{rk}	1000
c_{rk}	0.0186
Polymer adsorption parameters:	
a41	3.016
a42	0.0
b4	1000

Table 2.10: List of modifications for the new Base Case

Input parameters	New Base Case	Original Base Case
Porosity	0.2	0.136
Geometric average Permeability, md	200	50
Residual water saturation	0.3	0.14
Residual oil saturation	0.3	0.25
Residual microemulsion saturation	0.3	0.14
Oil viscosity	4.0	7.78

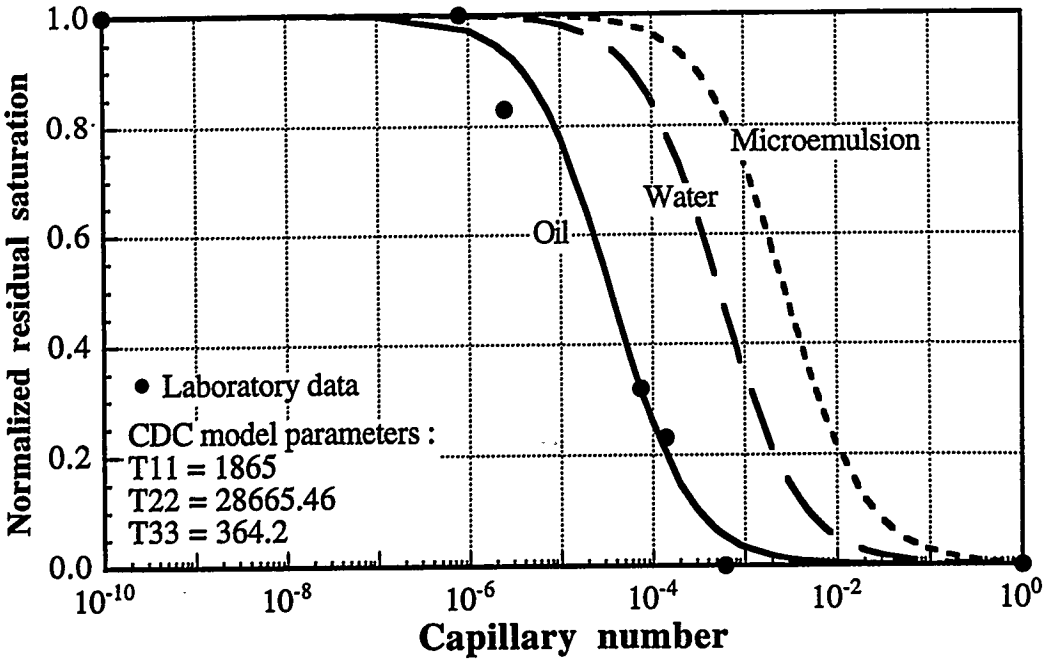


Figure 2.1 Capillary desaturation curves

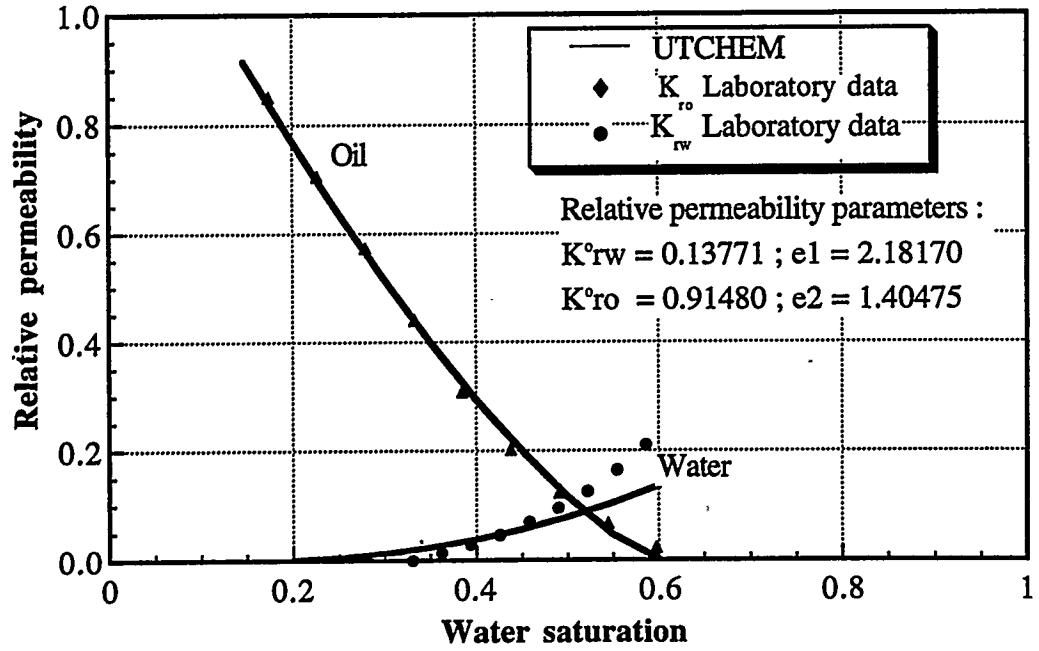


Figure 2.2 Low capillary number relative permeability curves

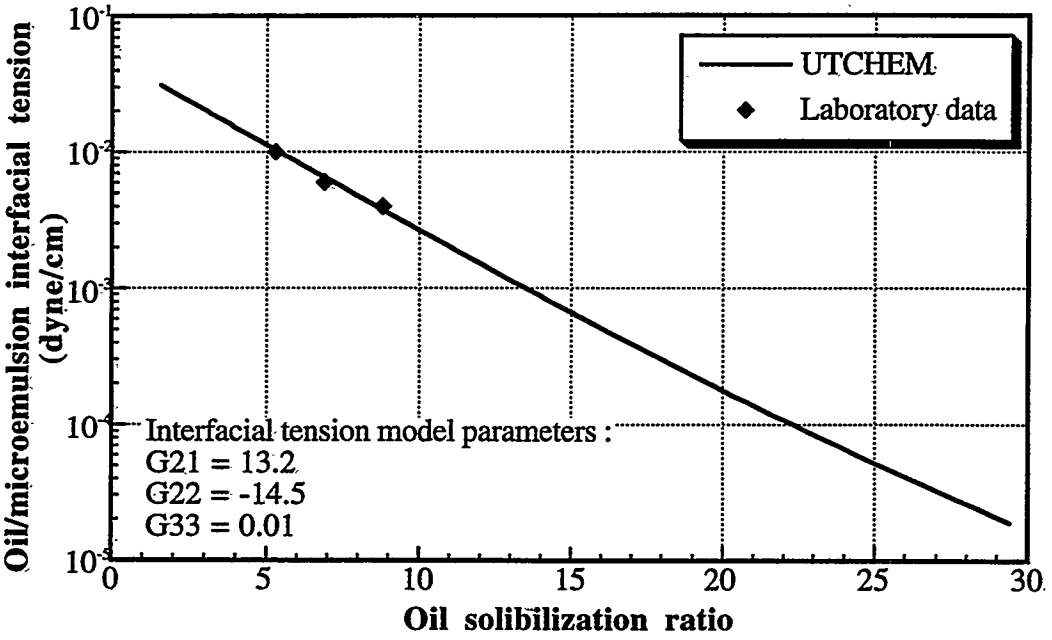


Figure 2.3 Interfacial tension as a function of solubilization ratio

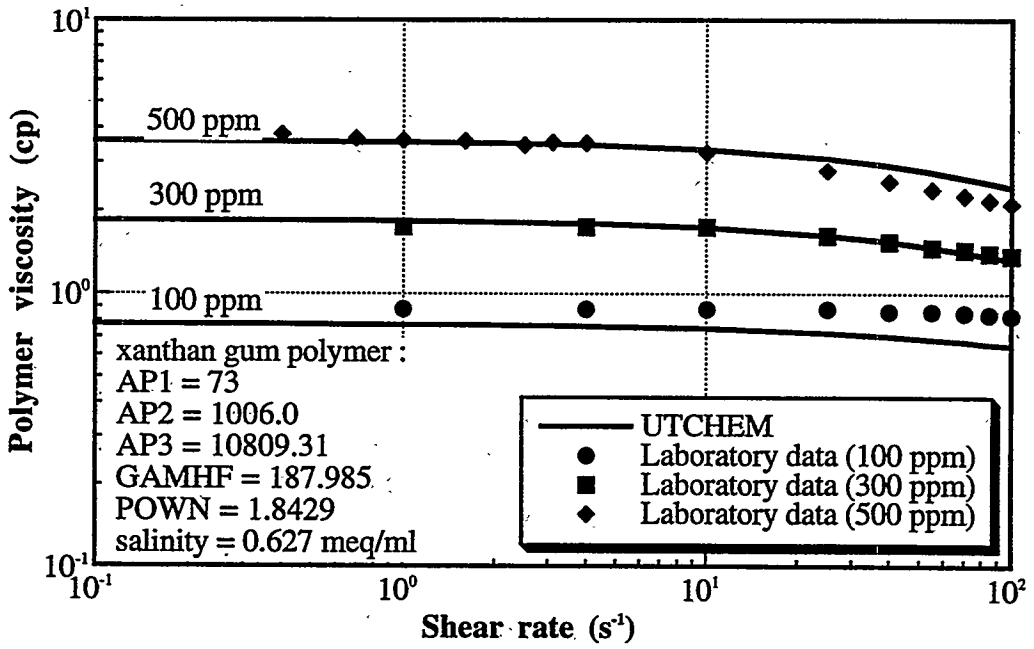


Figure 2.4 Viscosity of xanthan gum polymer as a function of shear rate

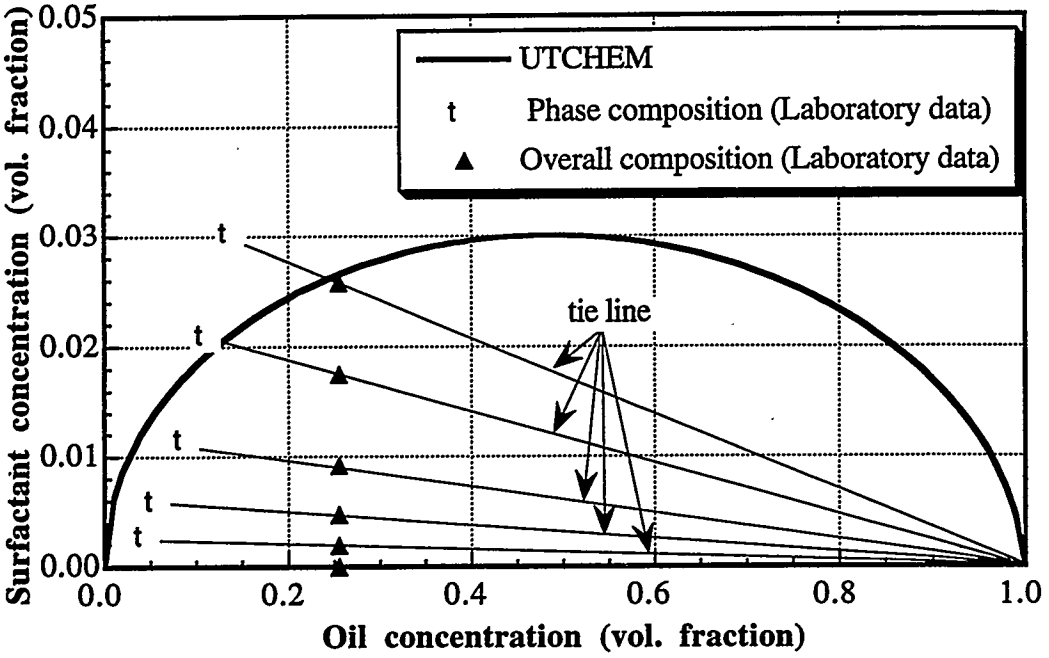


Figure 2.5 Schematic of phase behavior used in UTCHEM

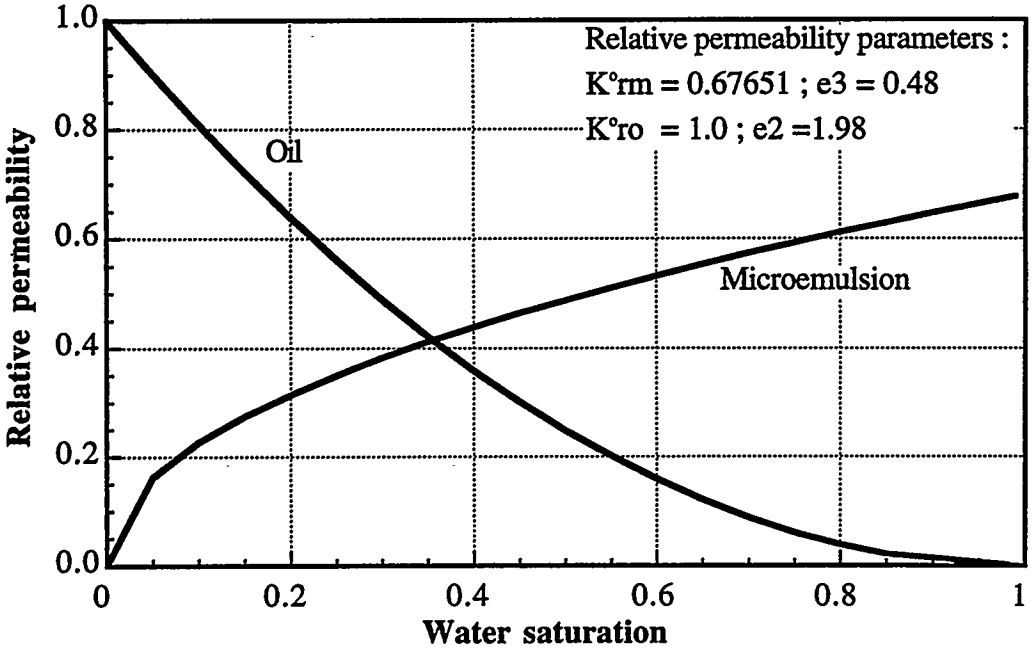


Figure 2.6 High capillary number relative permeability curves

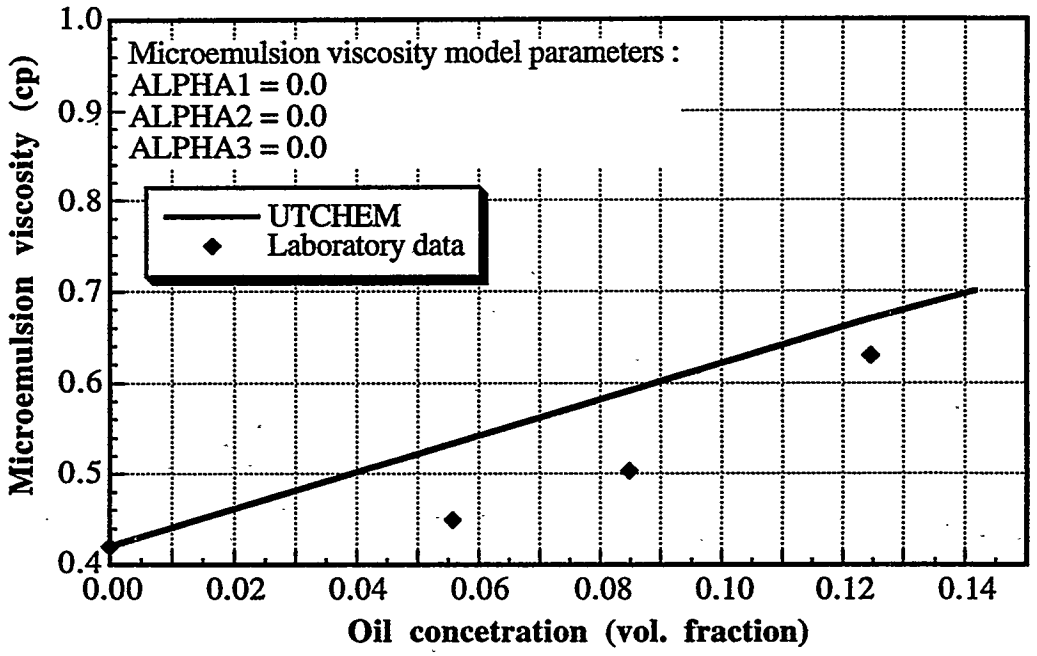


Figure 2.7 Microemulsion viscosity as a function of oil concentration

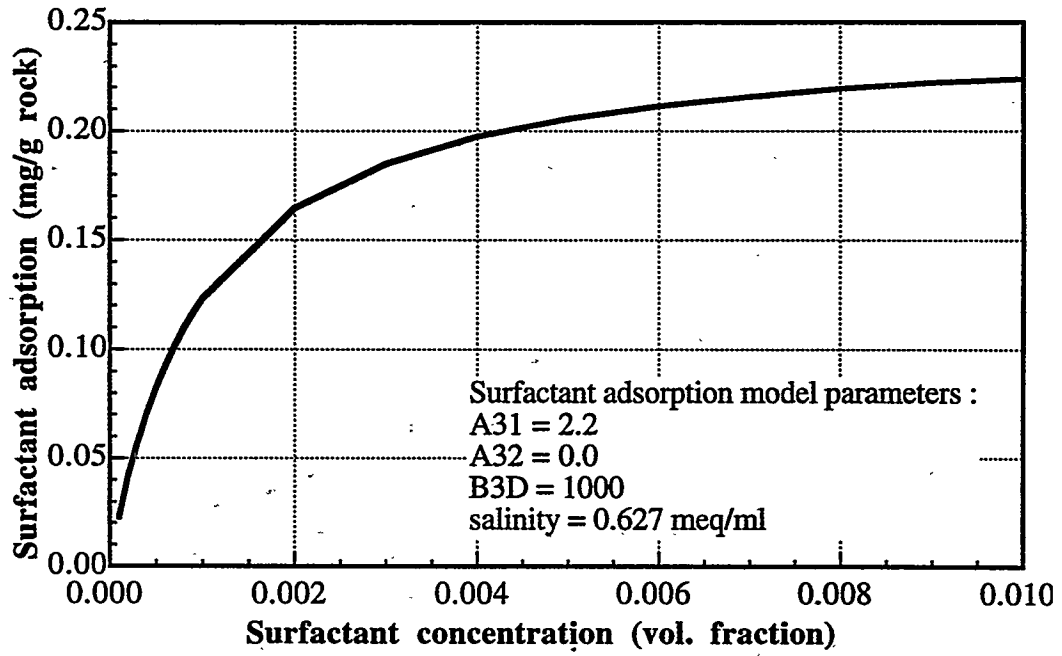


Figure 2.8 Surfactant adsorption isotherm

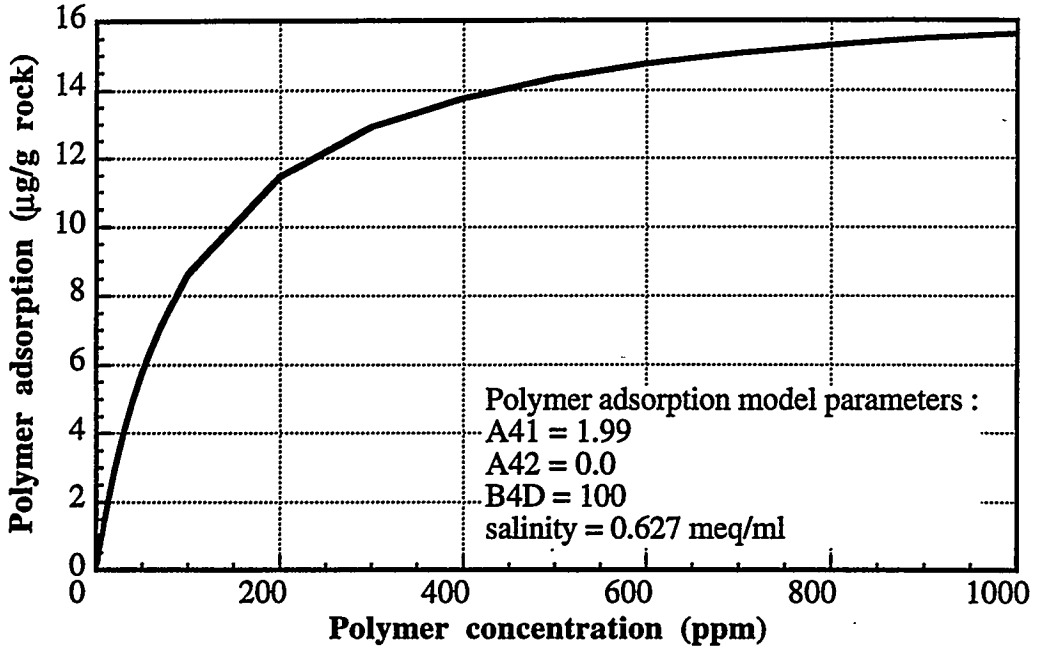


Figure 2.9 Polymer adsorption isotherm

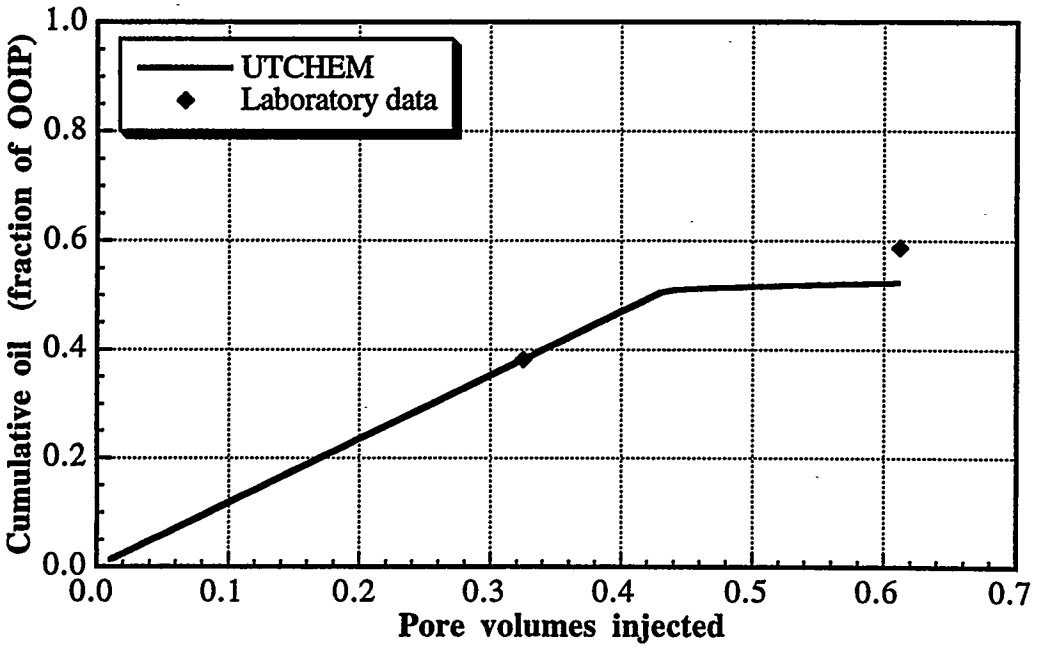


Figure 2.10 Comparison of simulated and laboratory oil recovery for water flood

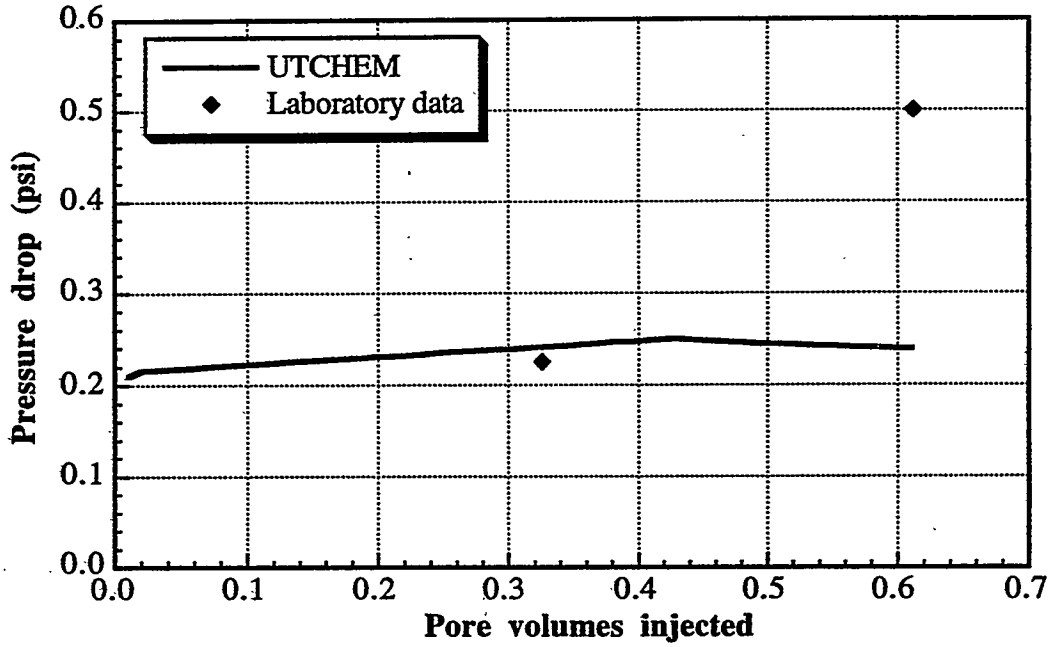


Figure 2.11 Comparison of simulated and laboratory pressure drop for water flood

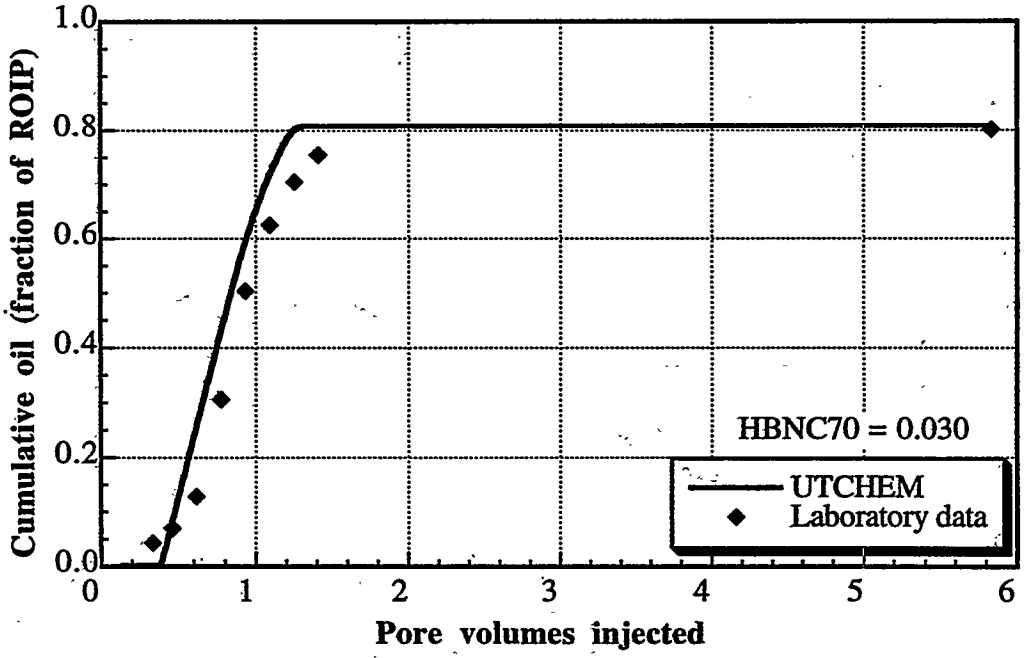


Figure 2.12 Comparison of simulated and laboratory chemical oil recovery for S/P process

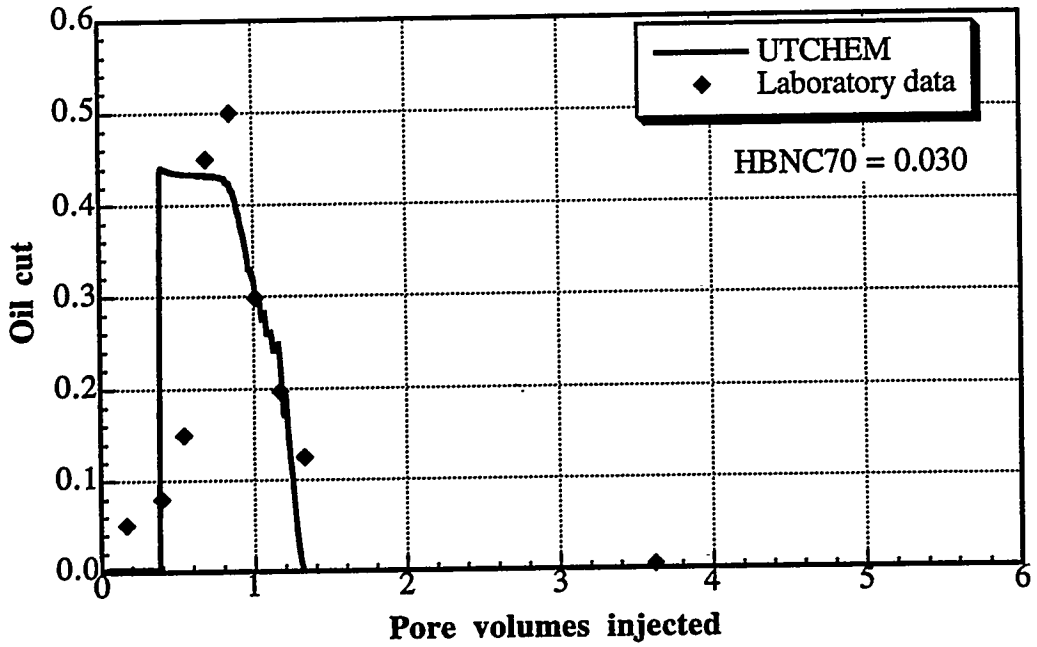


Figure 2.13 Comparison of simulated and laboratory oil cut for S/P process

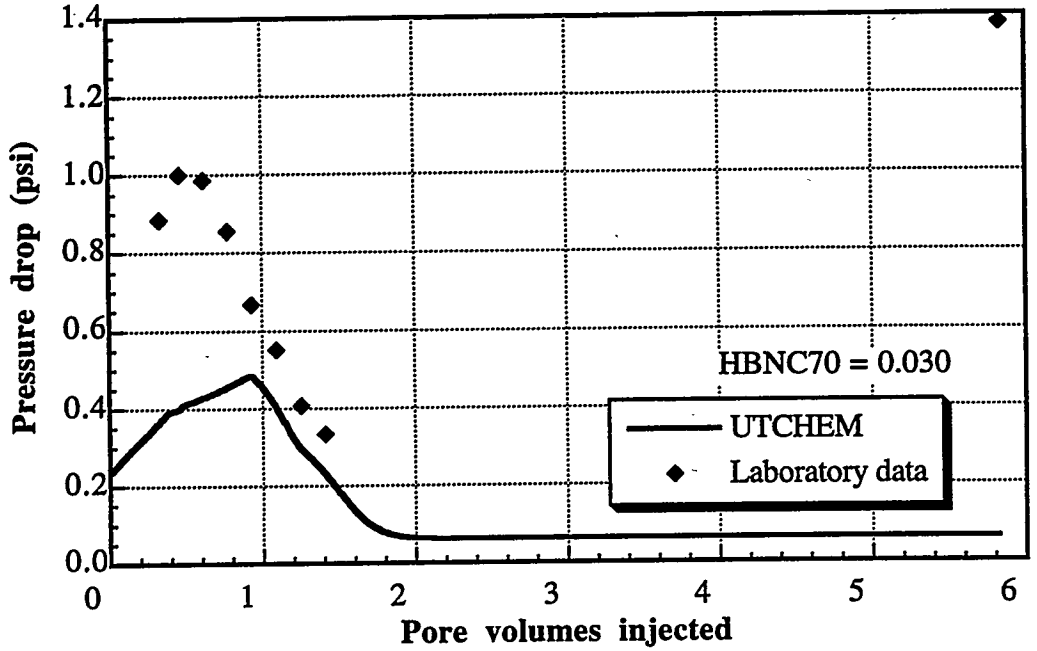


Figure 2.14 Comparison of simulated and laboratory pressure drop for S/P process

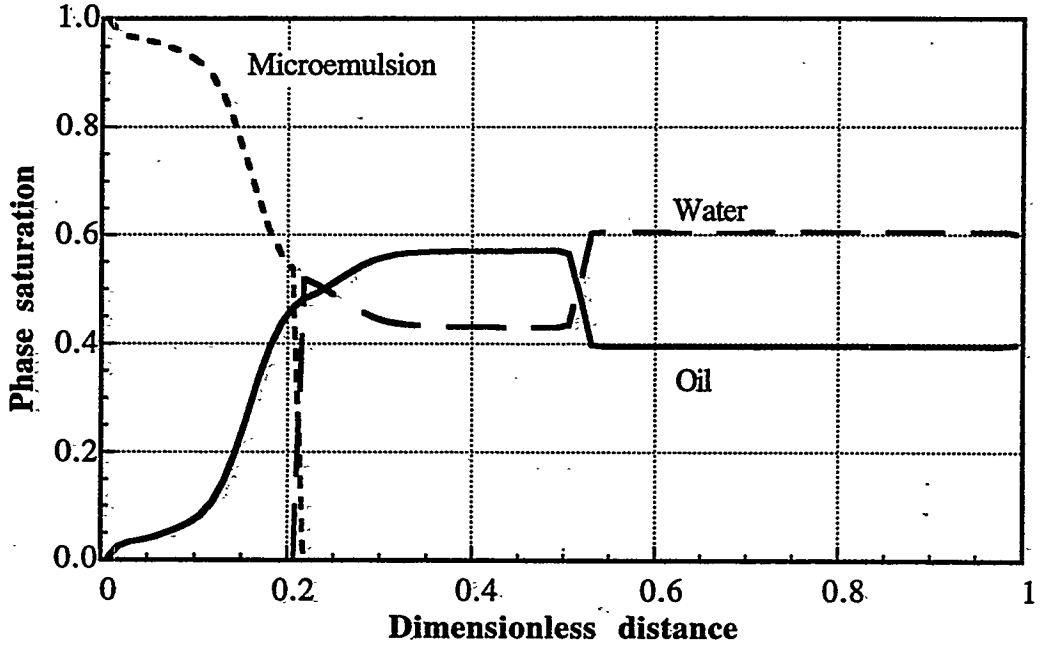


Figure 2.15 Distribution of phase saturations at 0.2 PV (Time=0.032 Days)

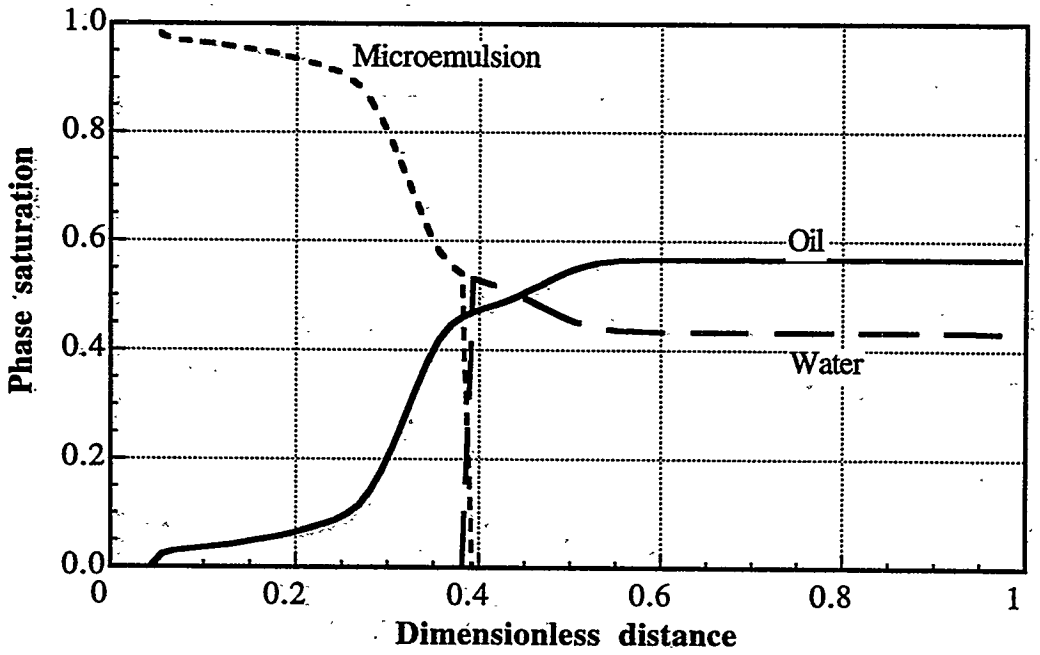


Figure 2.16 Distribution of phase saturations at 0.4 PV (Time=0.064 Days)

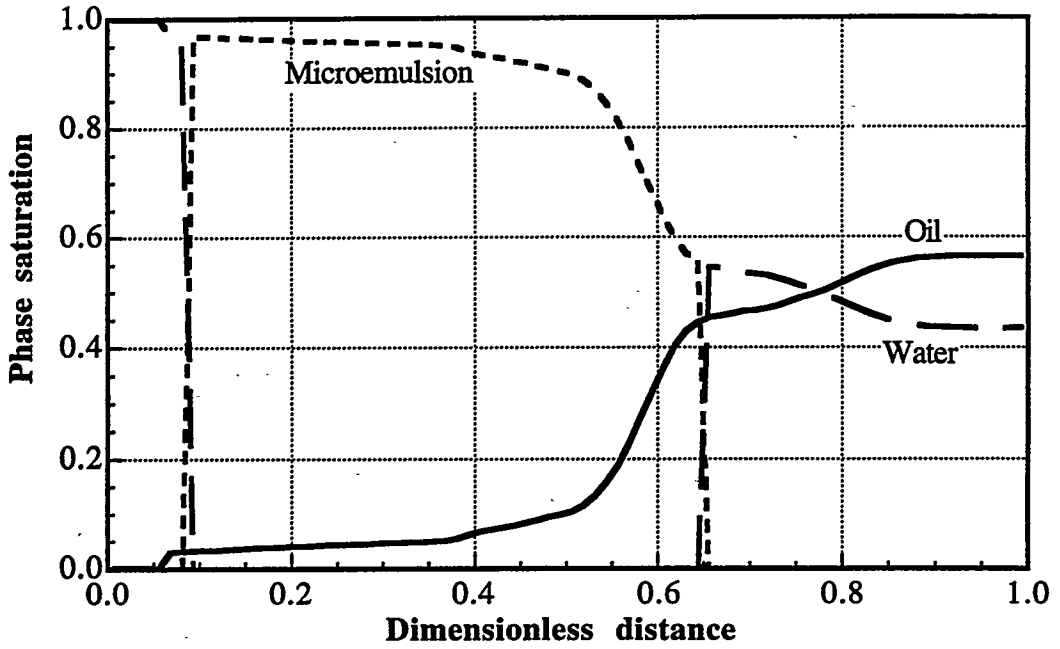


Figure 2.17 Distribution of phase saturations at 0.73 PV (Time=0.117 Days)

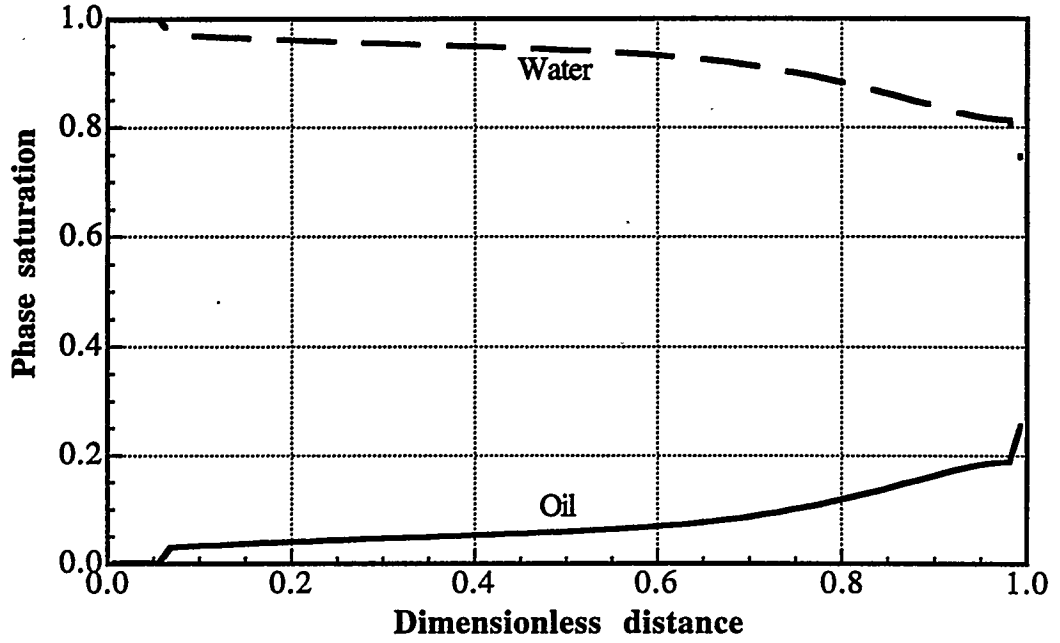


Figure 2.18 Distribution of phase saturations at 2.43 PV (Time=0.39 Days)

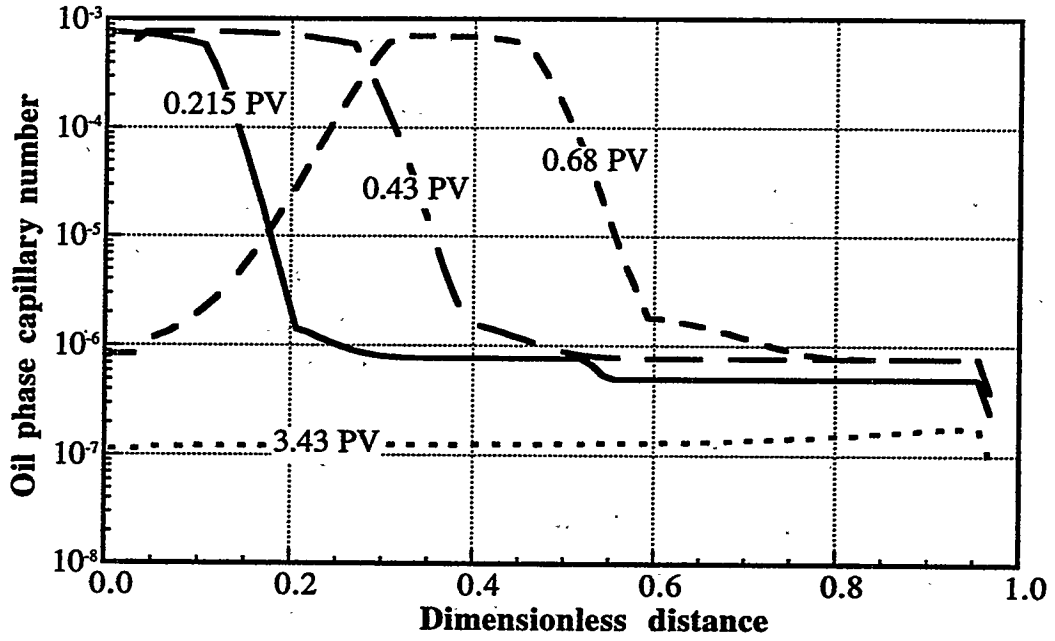


Figure 2.19 Distributions of oil phase capillary number

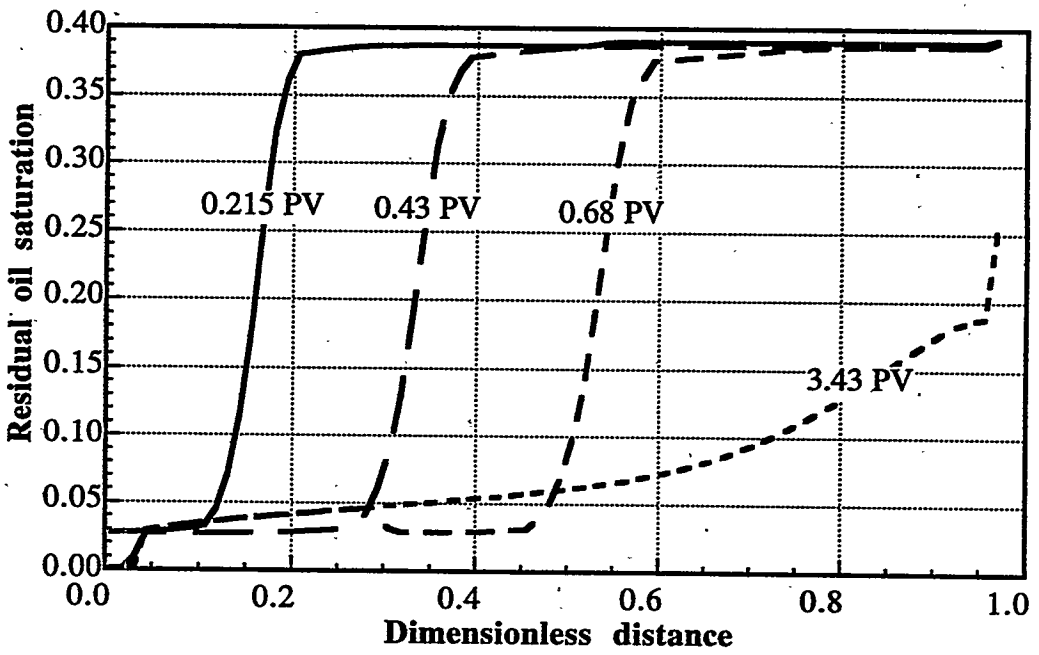


Figure 2.20 Distributions of residual oil saturation

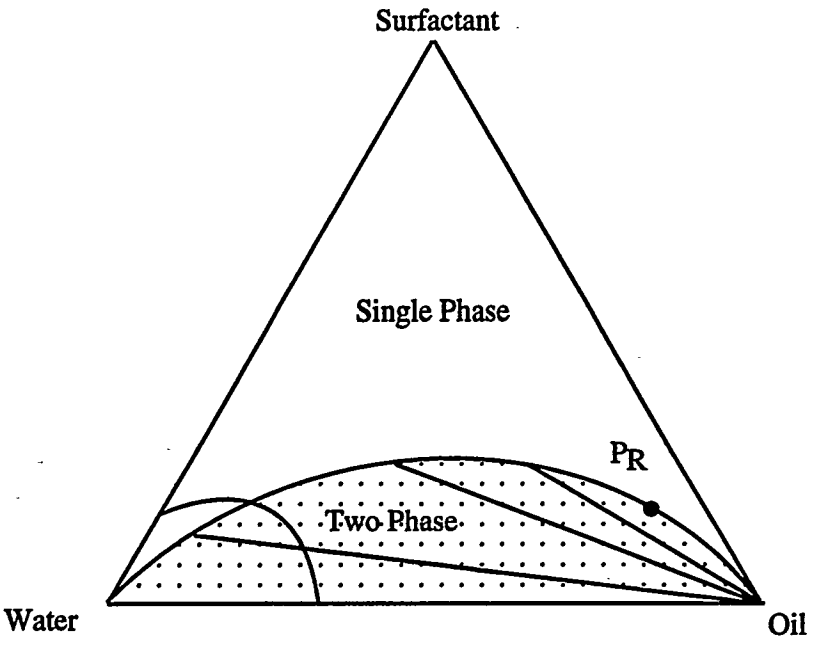


Figure 2.21 Phase diagram and history path of composition

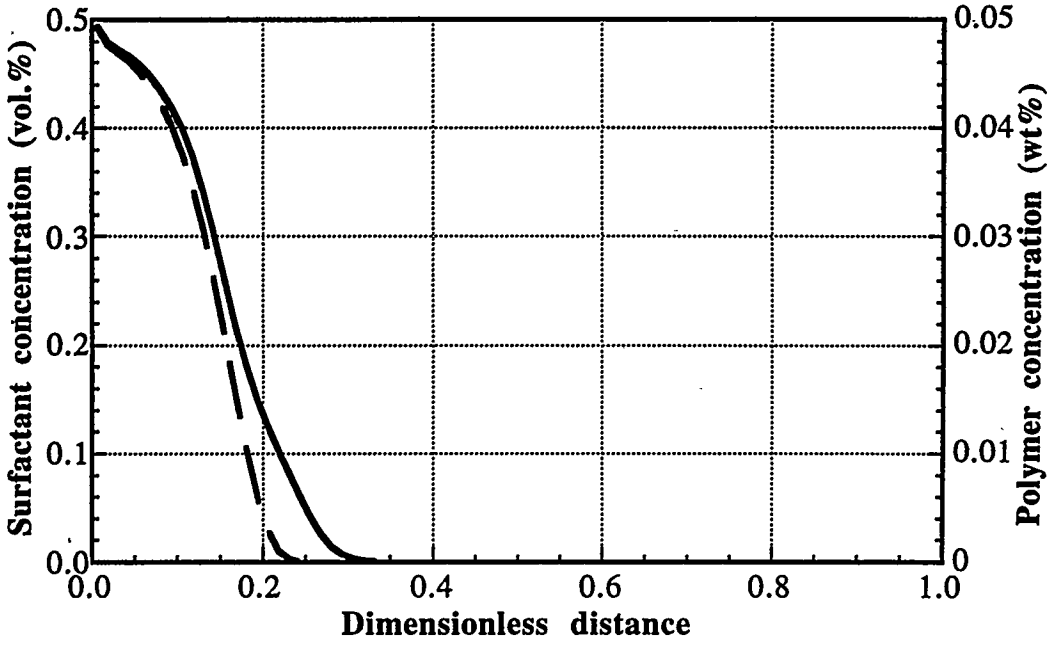


Figure 2.22 Distribution of surfactant and polymer concentrations at 0.2 PV (Time=0.032 DAYS)

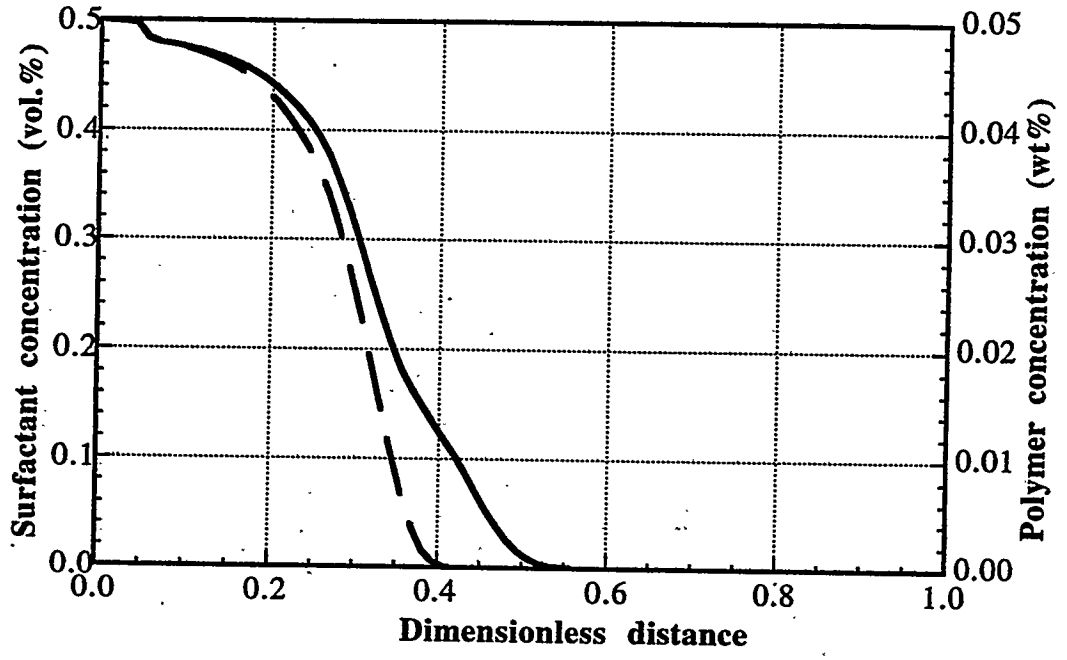


Figure 2.23 Distribution of surfactant and polymer concentrations at 0.4 PV (Time=0.064 days)

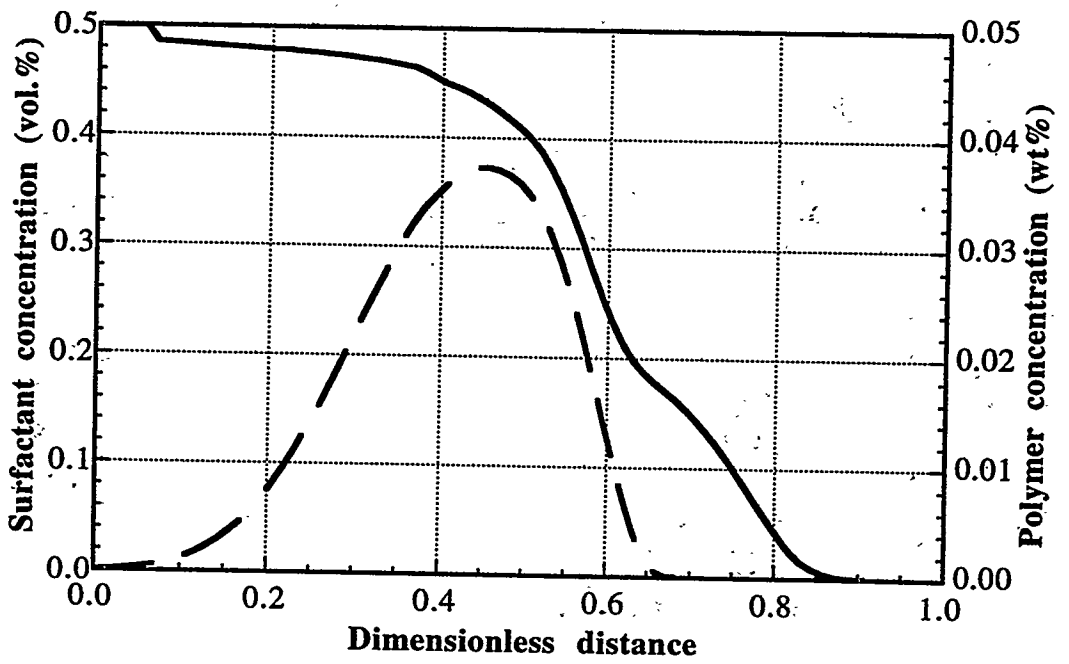


Figure 2.24 Distribution of surfactant and polymer concentrations 0.73 PV (Time=0.116 days)

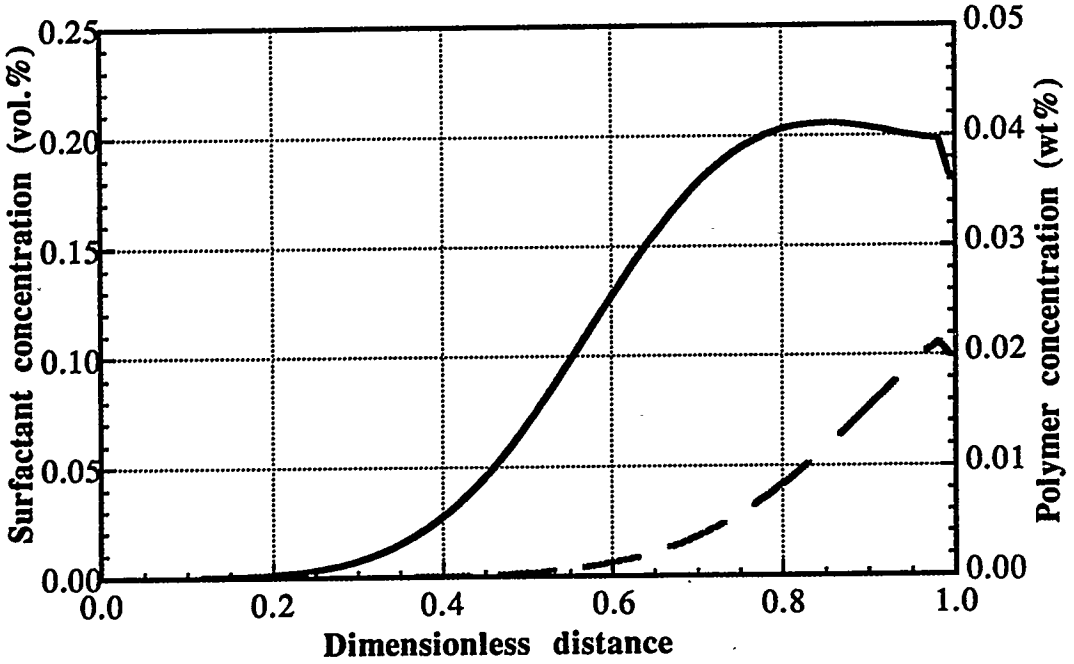


Figure 2.25 Distribution of surfactant and polymer concentrations 1.43 PV (Time=0.229 days)

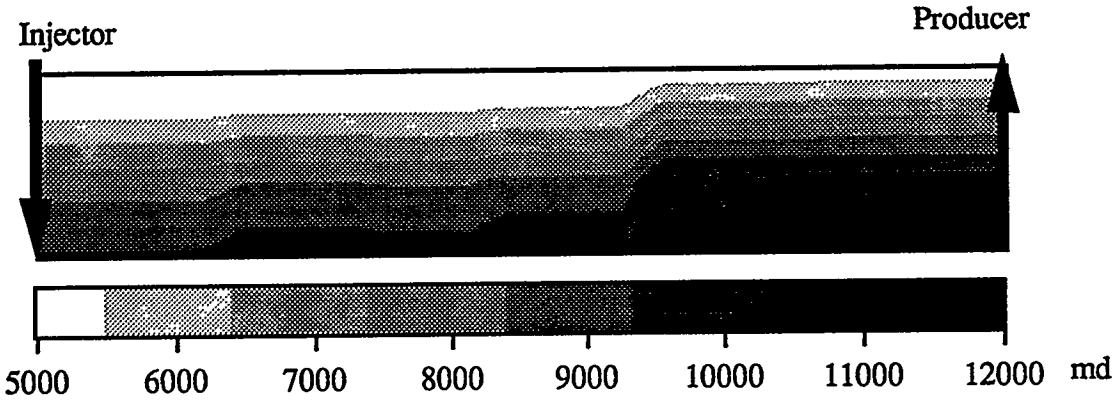


Figure 2.26 Permeability distribution for the Reservoir A

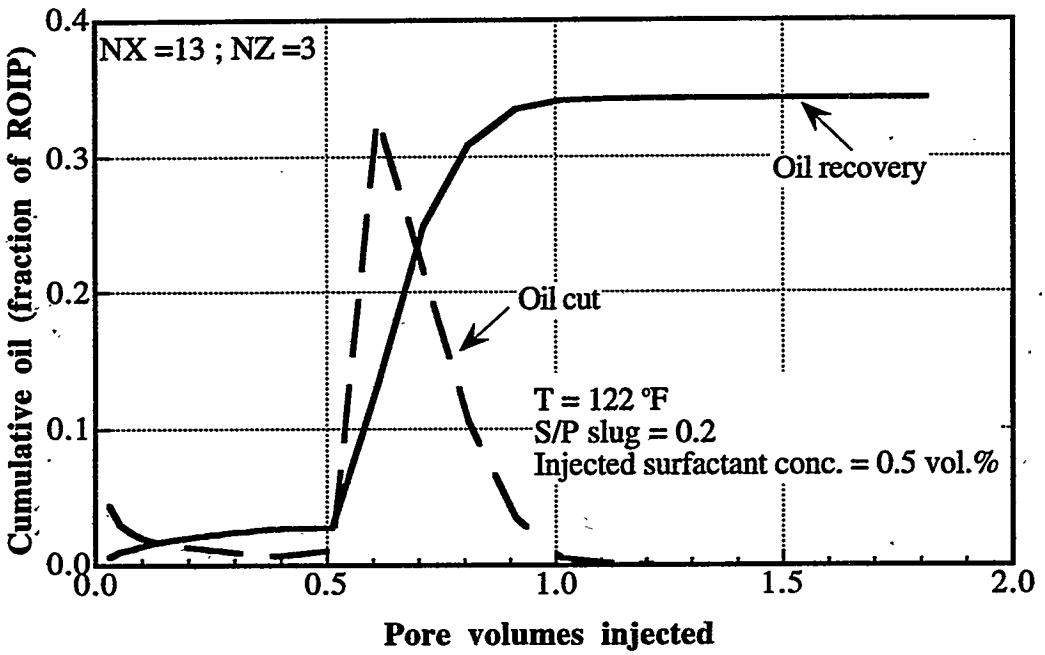


Figure 2.27 Oil recovery and oil cut for surfactant/polymer flooding for 2-D cross sectional simulations

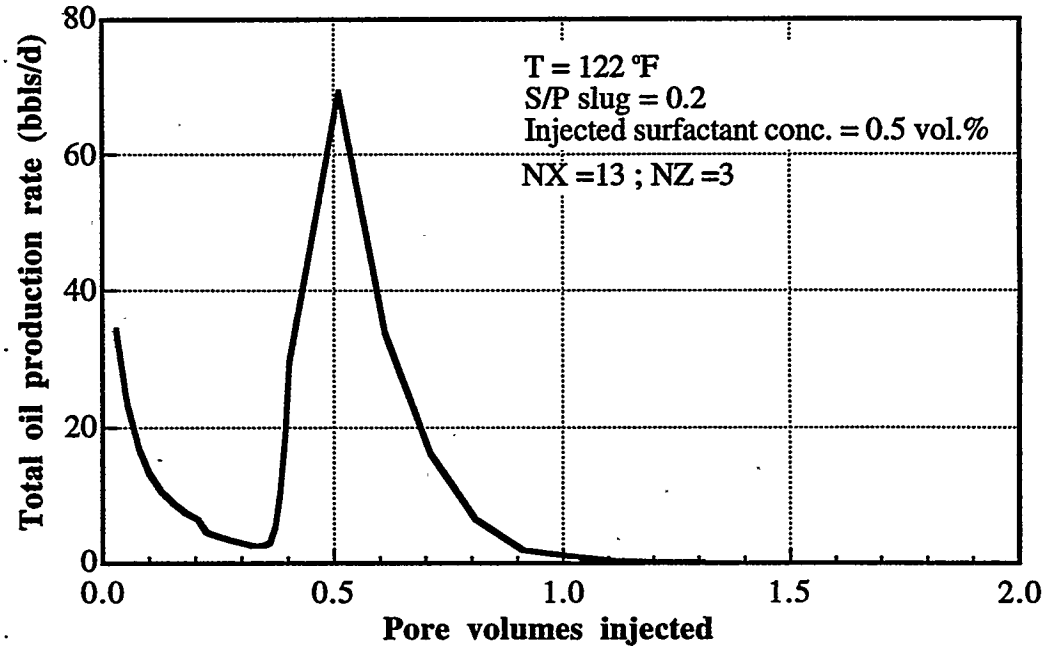


Figure 2.28 Simulated total oil production rate for surfactant/polymer flood

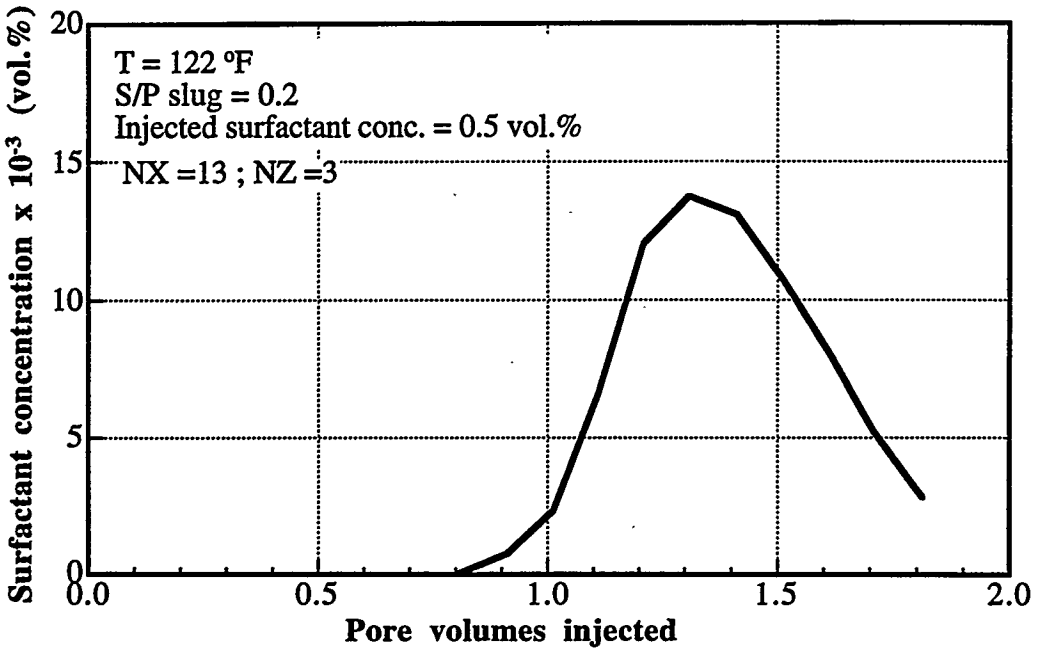


Figure 2.29 Surfactant concentration for S/P flooding for 2-D cross sectional simulations

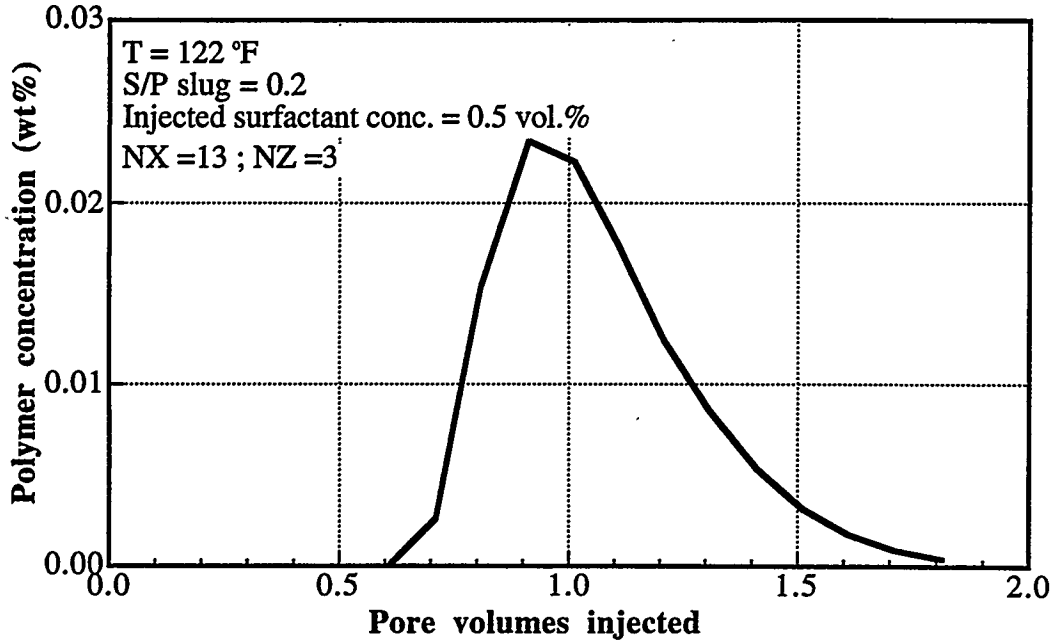


Figure 2.30 Polymer concentration for S/P flooding for 2-D cross sectional simulations

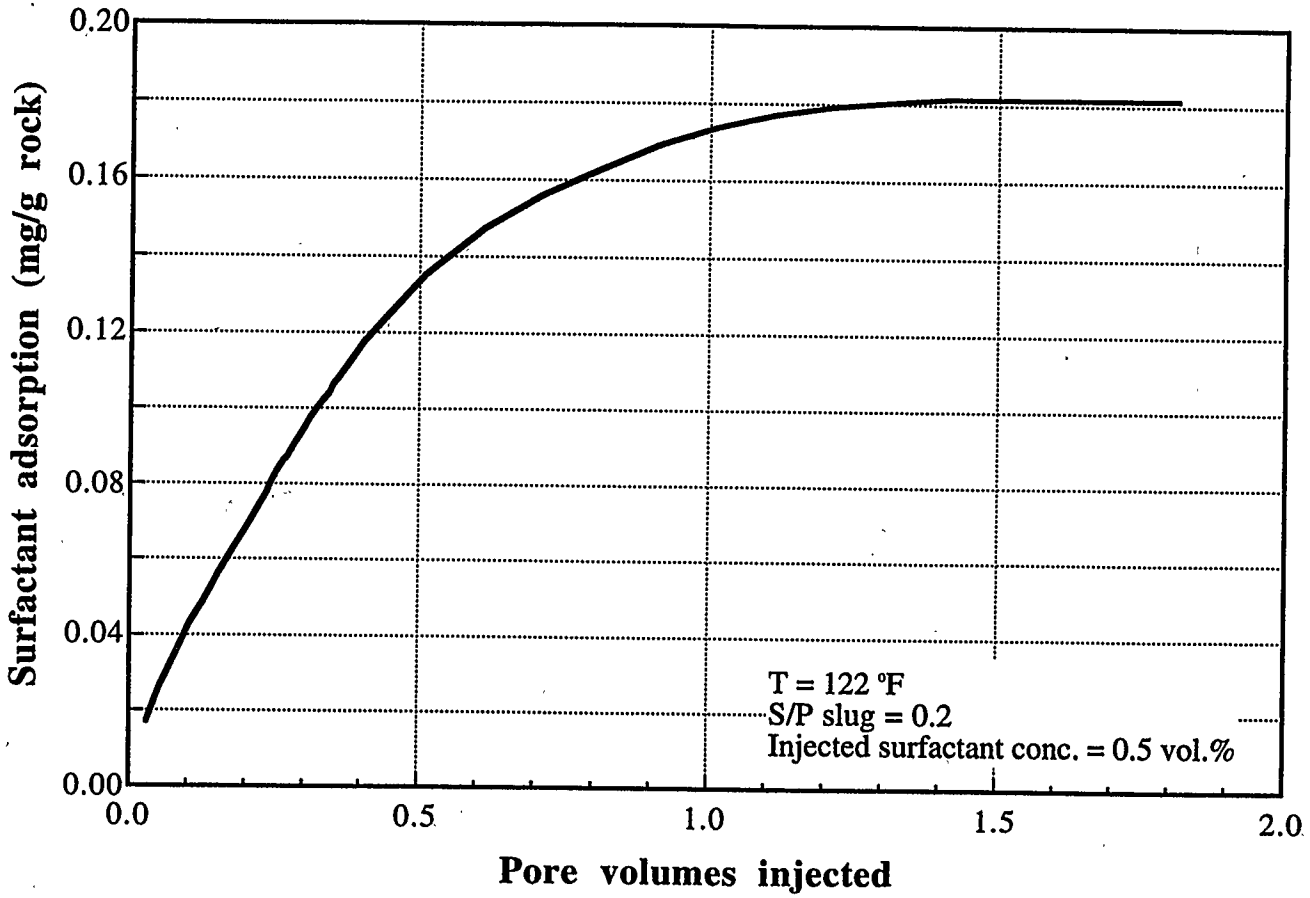


Figure 2.31 Surfactant adsorption for surfactant/polymer flood for 2D cross sectional simulations

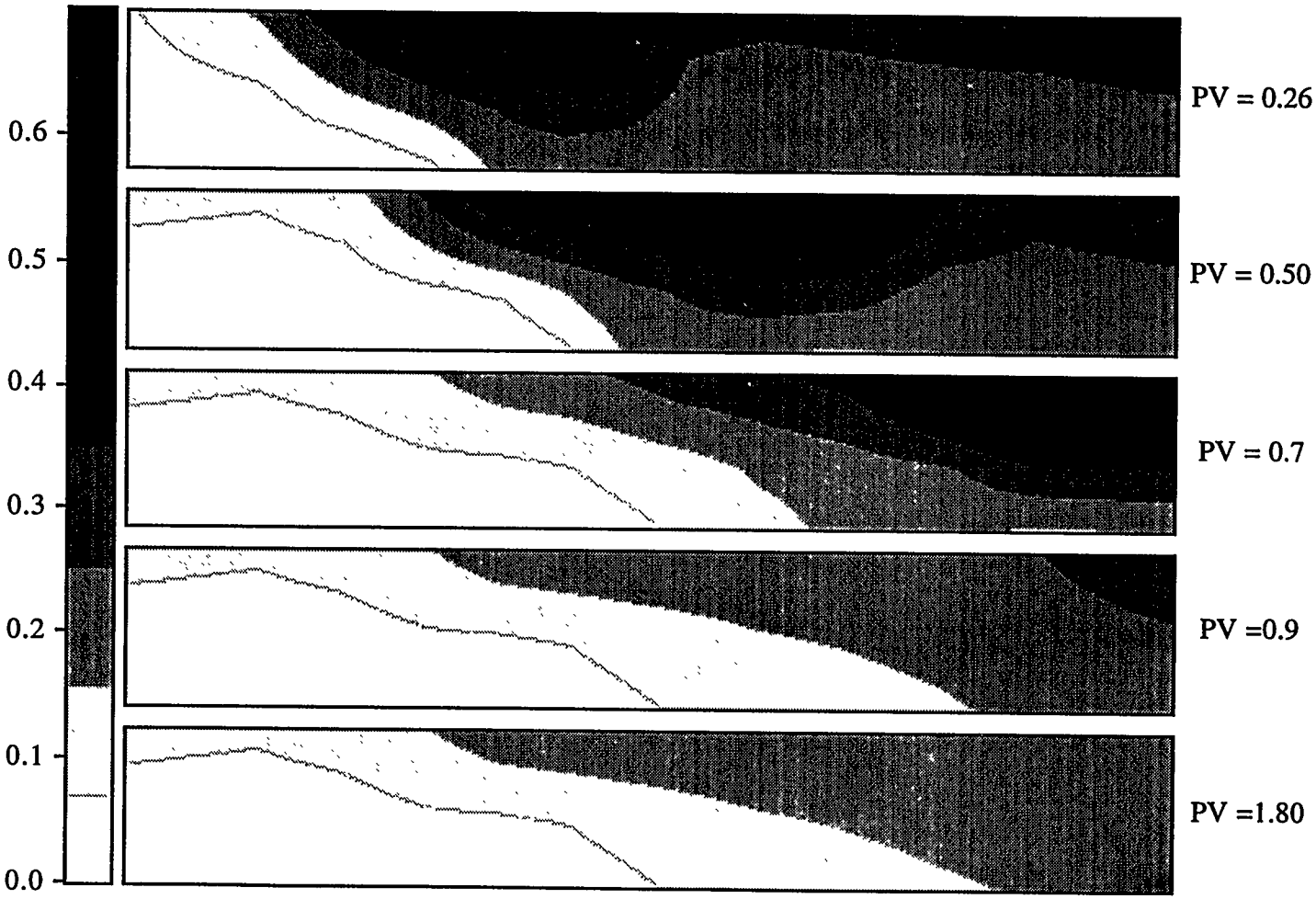


Figure 2.32 Oil saturation profiles for 13x1x3 2-D cross sectional simulation

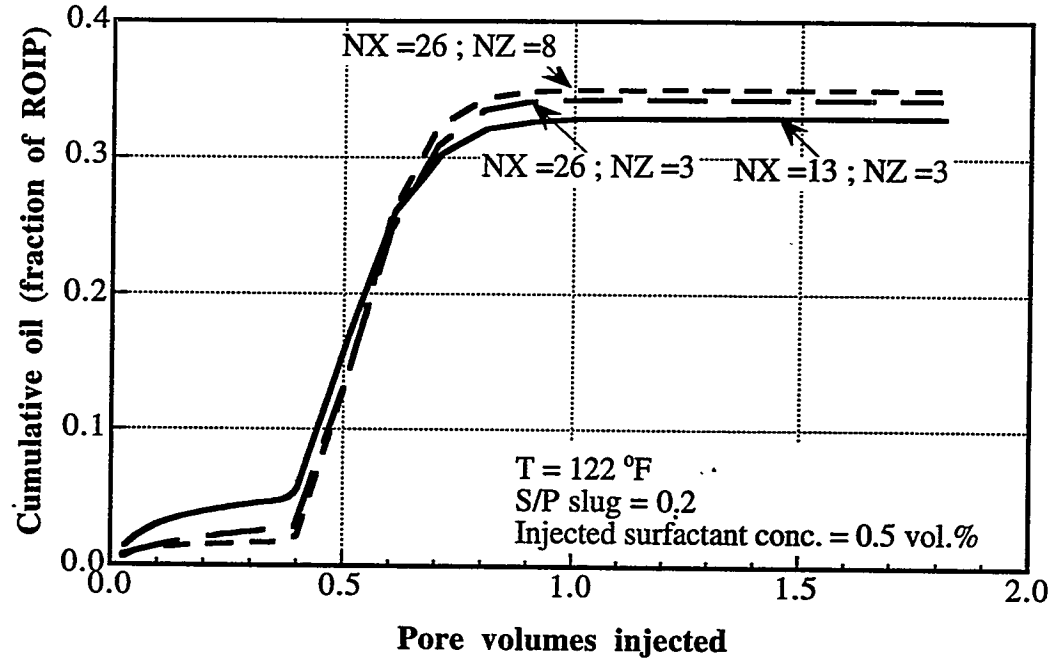


Figure 2.33 Effect of simulation gridblocks on oil recovery

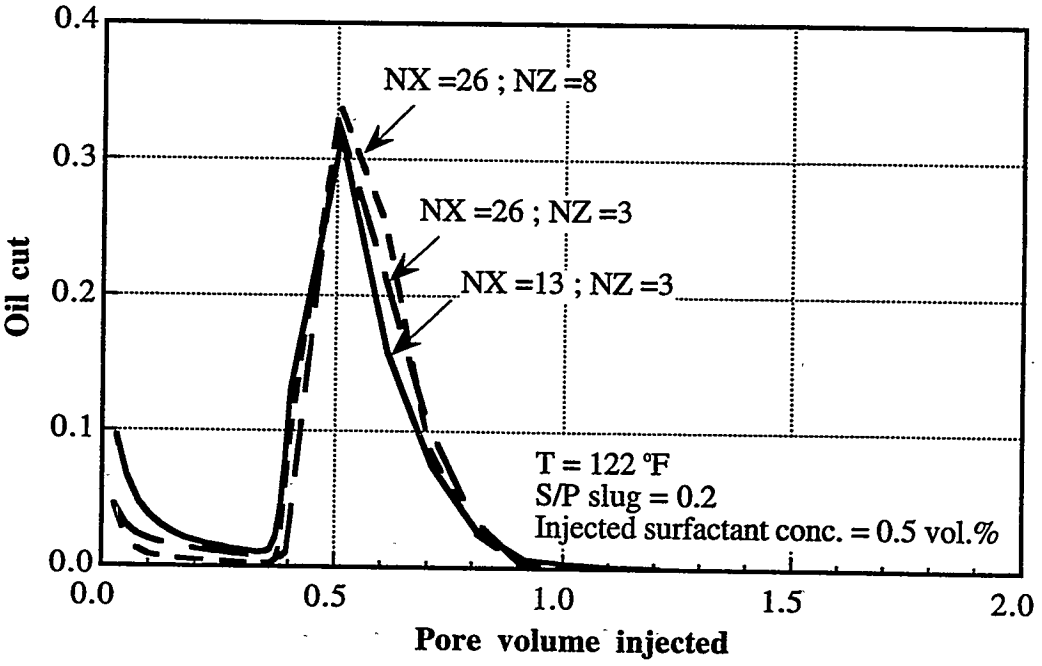


Figure 2.34 Effect of simulation gridblocks on oil cut

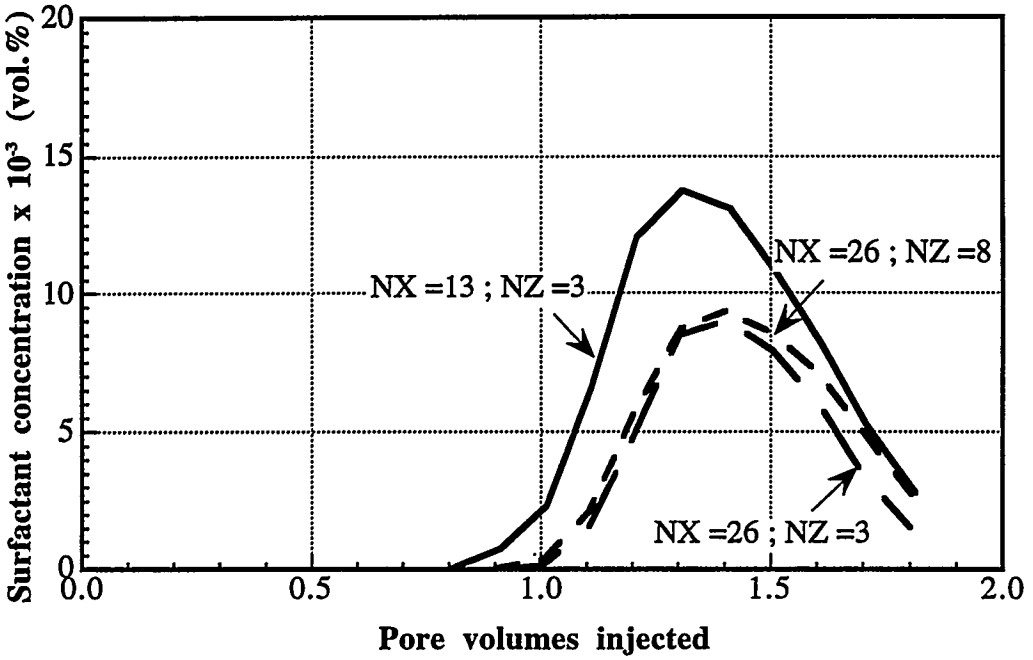


Figure 2.35 Effect of simulation gridblocks on the produced total surfactant concentration

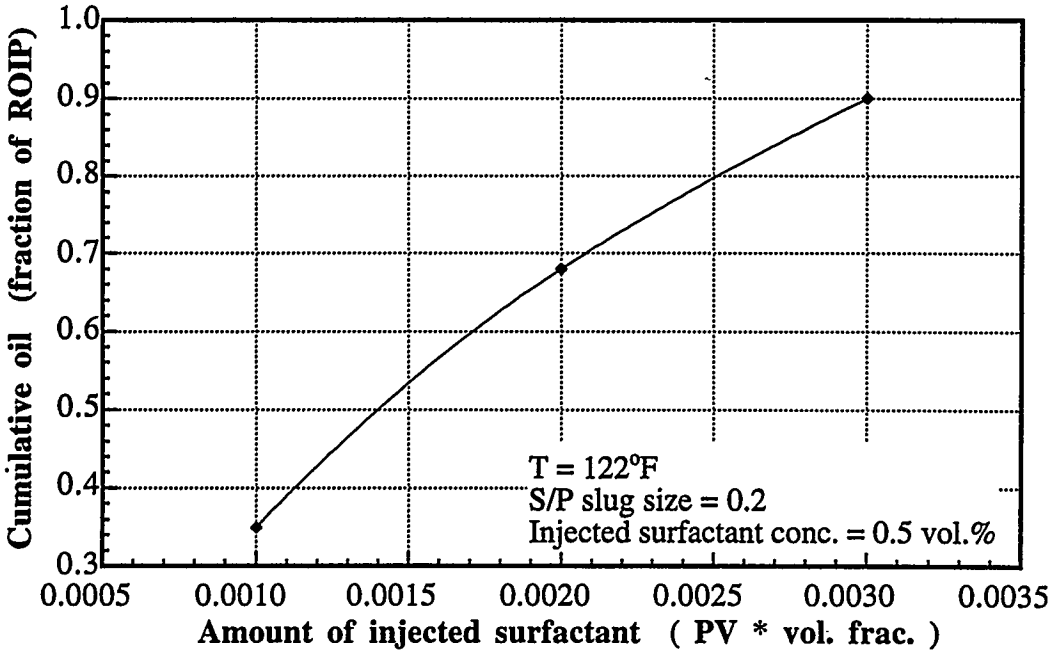


Figure 2.36 Effect of injected surfactant concentrations on oil recovery for 2-D cross sectional simulations

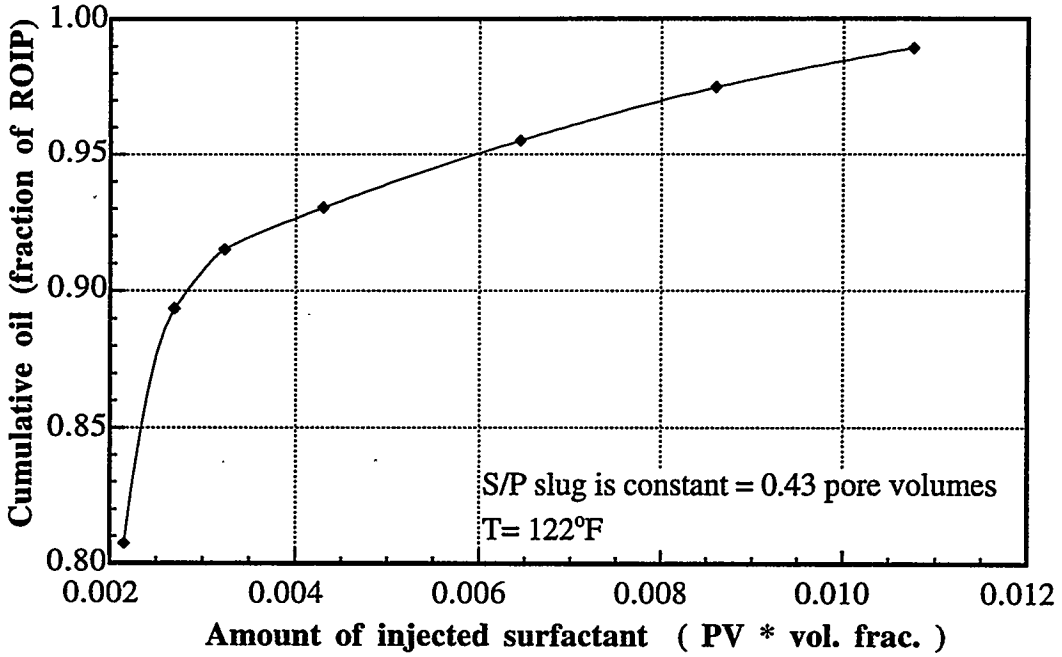


Figure 2.37 Effect of injected surfactant concentrations on oil recovery for 1-D simulations with constant amount of polymer injected

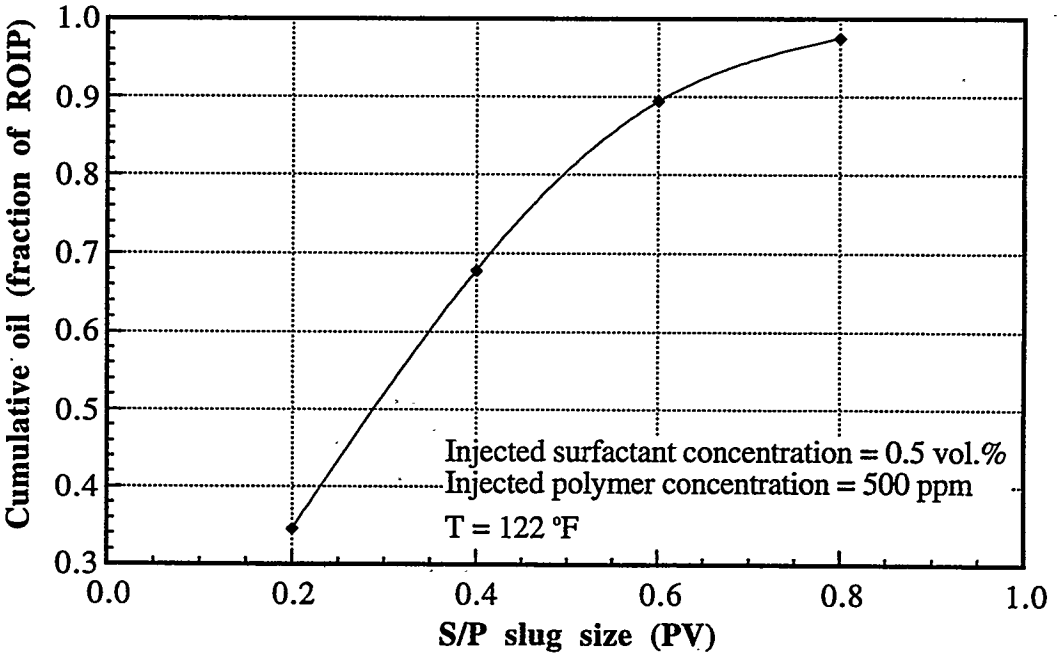


Figure 2.38 Effect of chemical slug sizes on oil recovery for 2-D cross sectional simulations

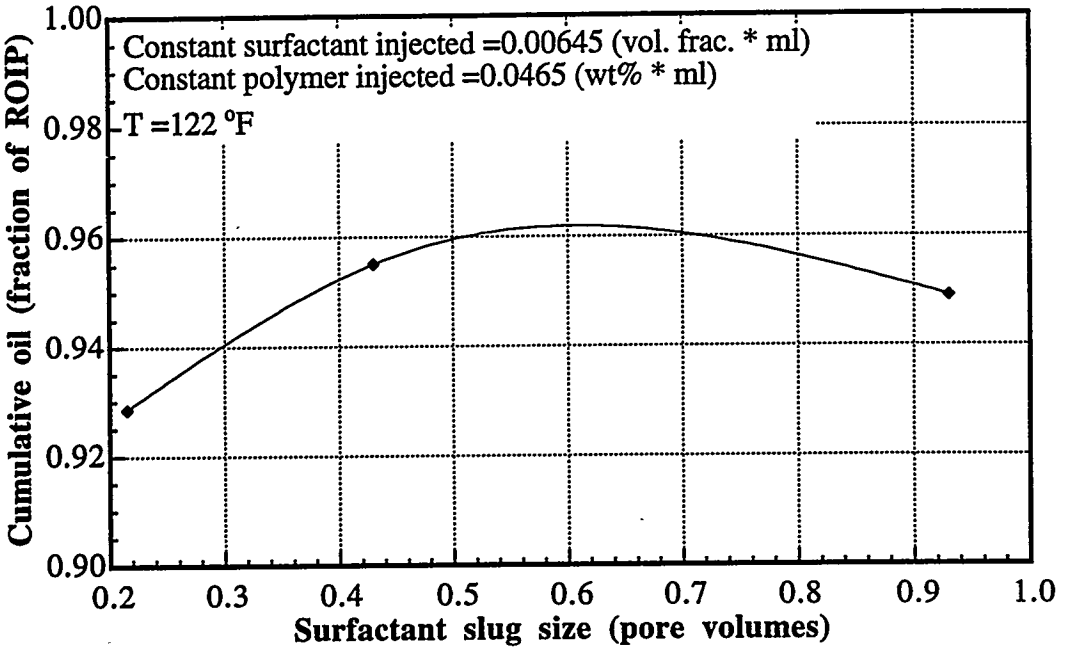


Figure 2.39 Effect of surfactant slug sizes on using same amount of chemical for 1-D simulations

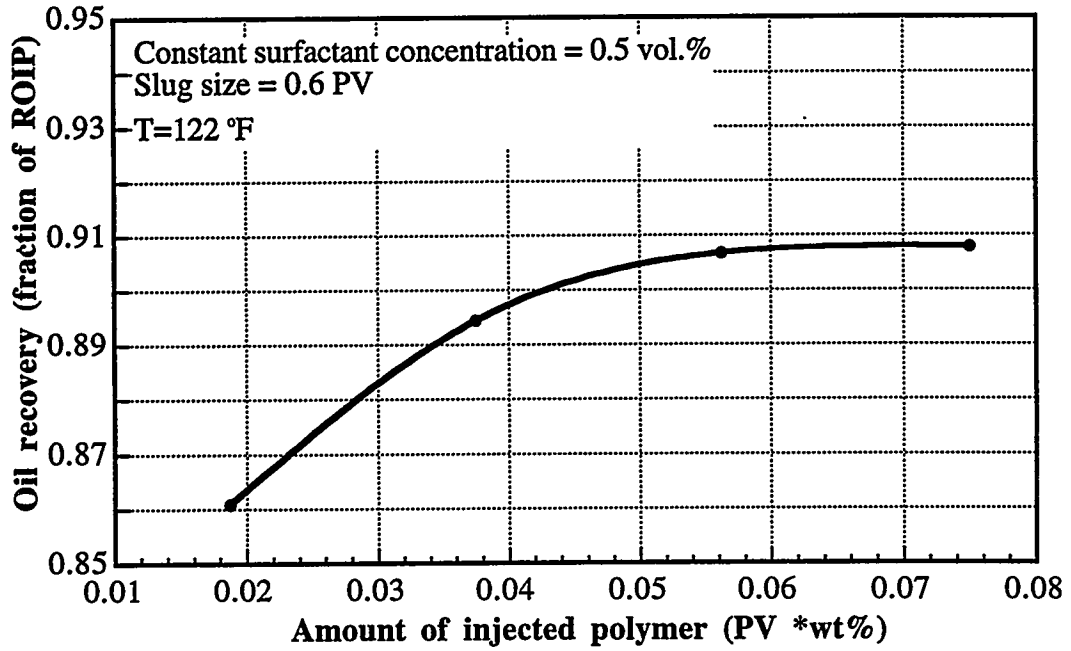


Figure 2.40 Effect of polymer concentrations on oil recovery for 2-D cross sectional simulations

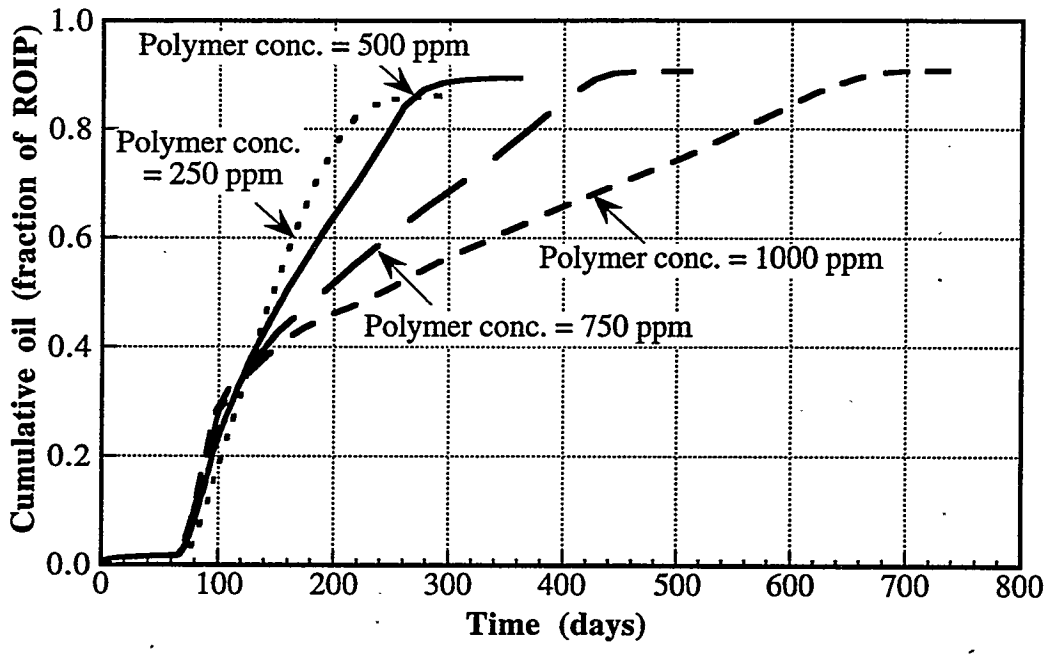


Figure 2.41 Effect of polymer concentrations on oil recovery and project life for 2-D cross sectional simulations

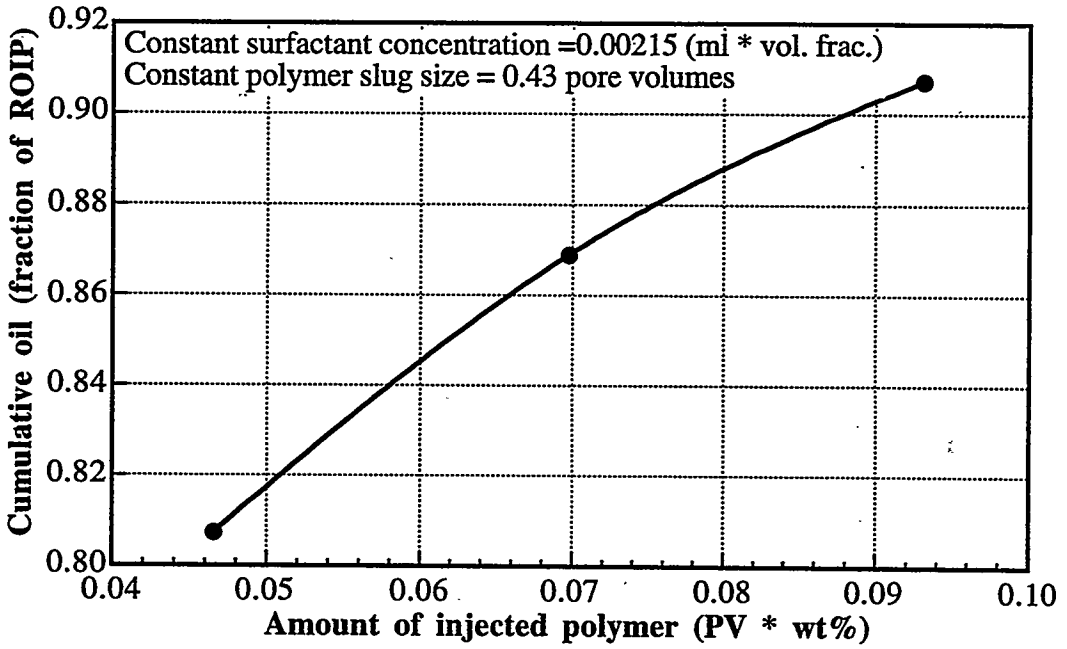


Figure 2.42 Effect of injected polymer concentrations on oil recovery for 1-D simulations

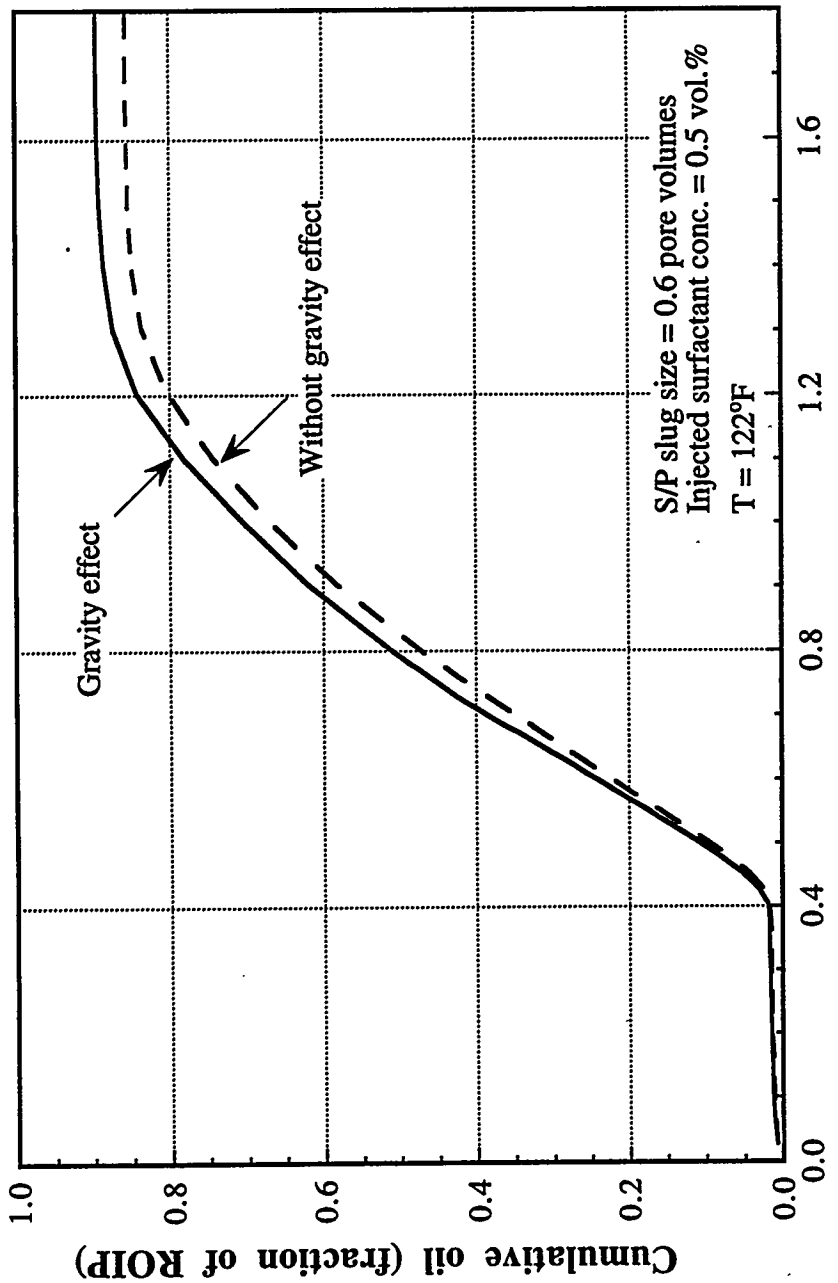


Figure 2.43 Effect of gravity on oil recovery for 2-D cross sectional simulations

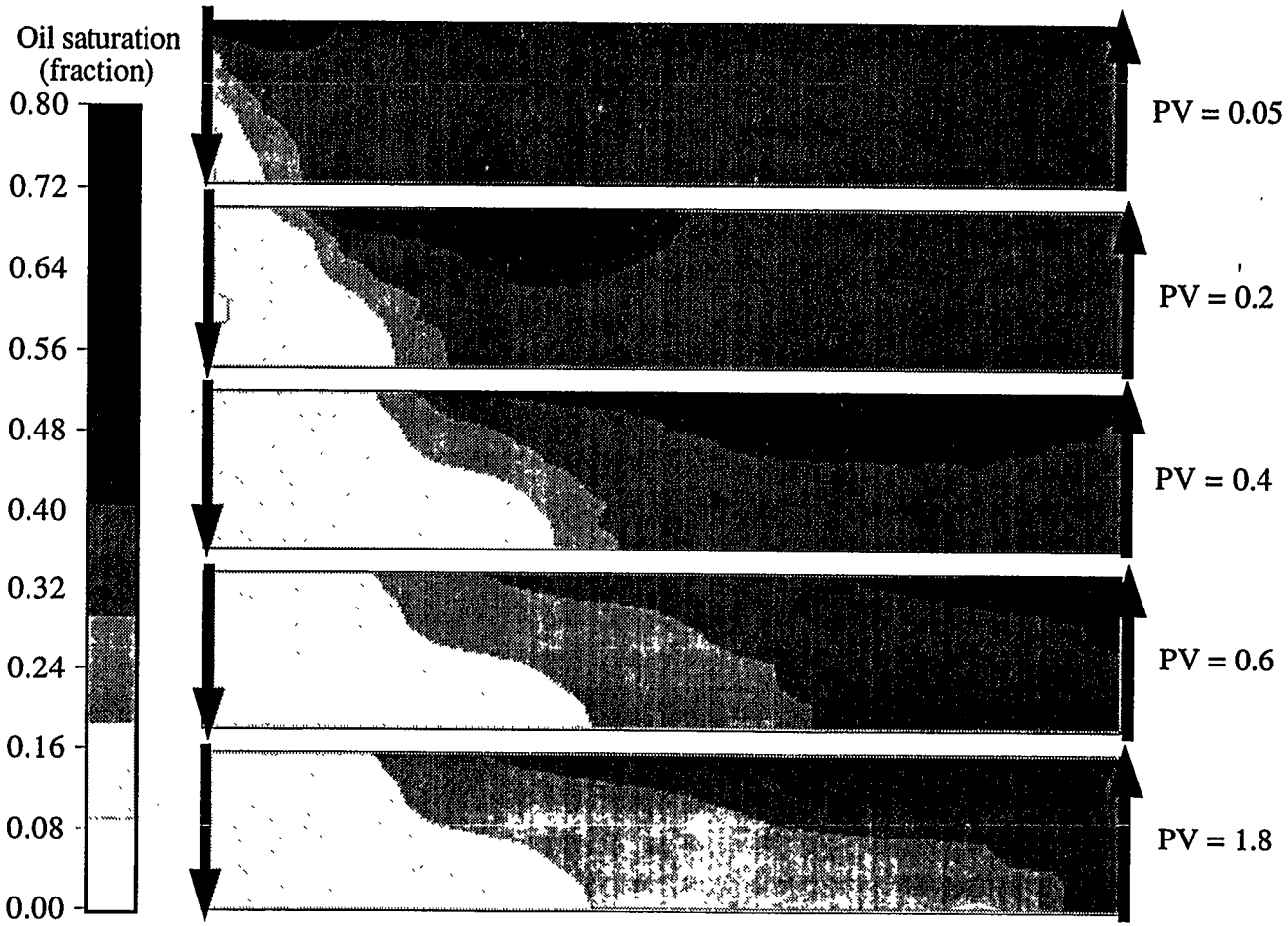


Figure 2.44 Oil saturation profiles with gravity effect at different pore volumes injected for the case of 0.5 vol.% injected surfactant concentration.

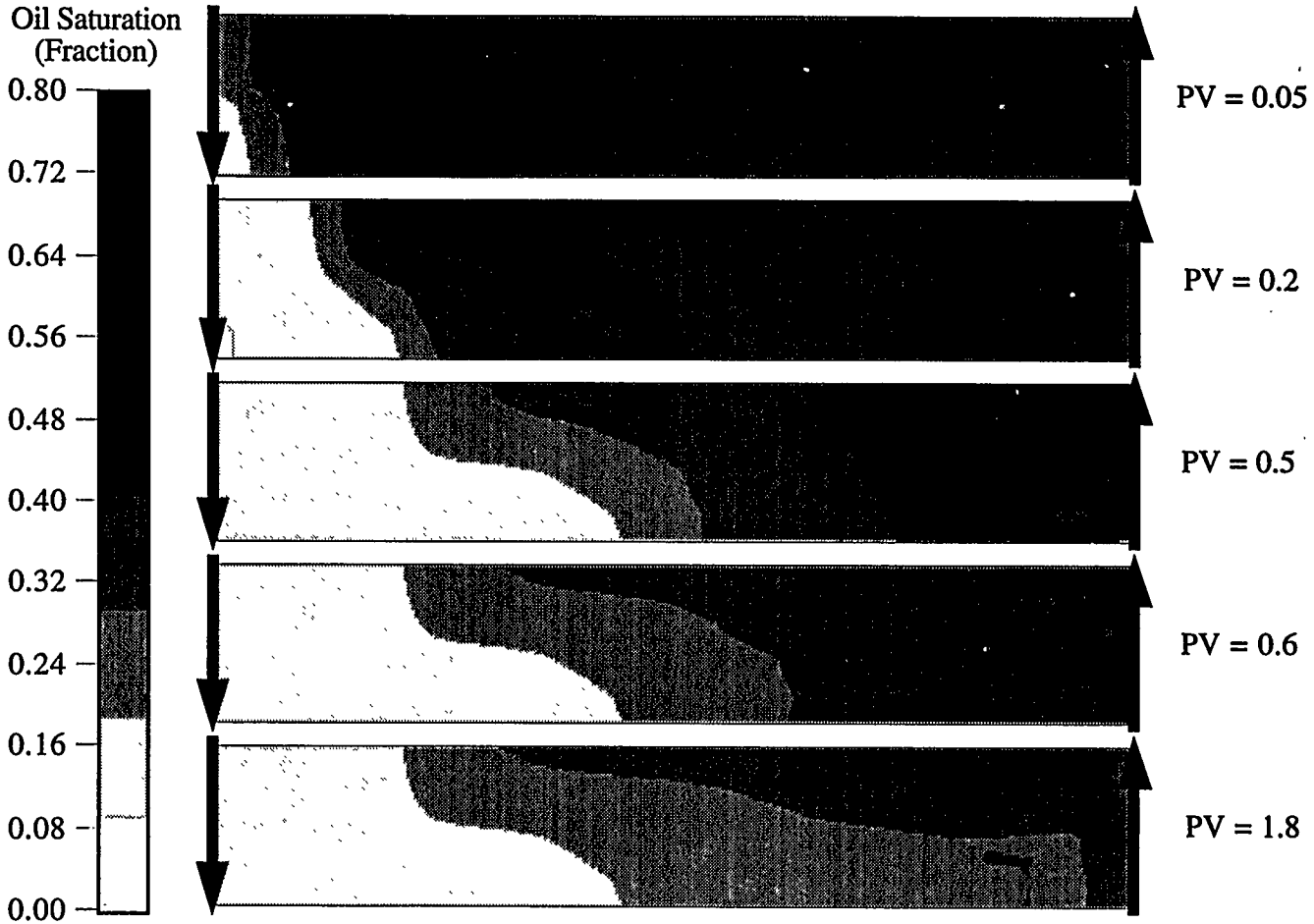


Figure 2.45 Oil saturation profiles when gravity effect is neglected

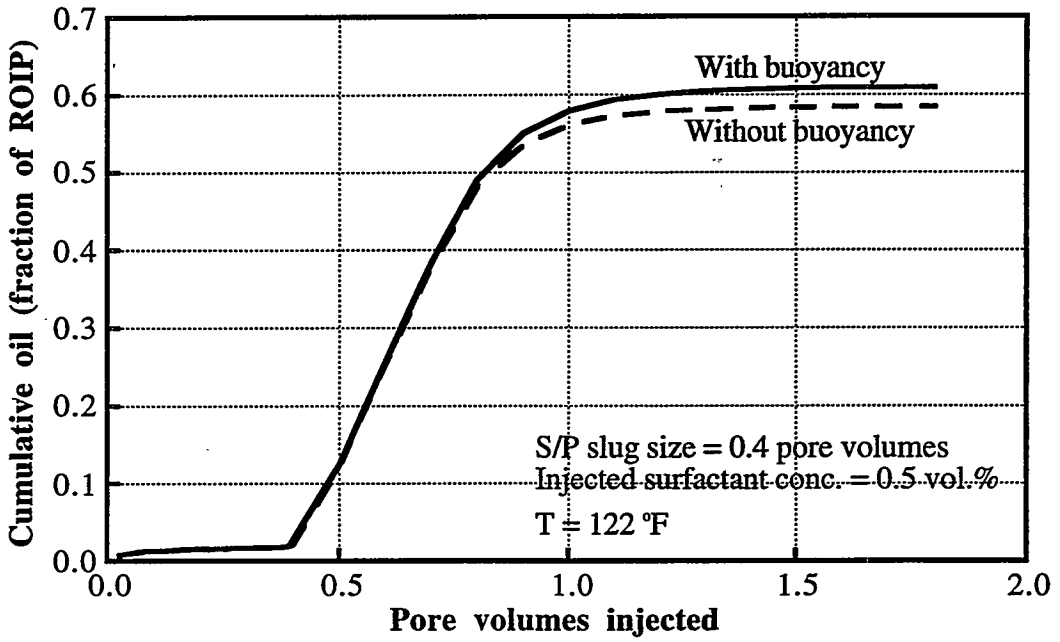


Figure 2.46 Buoyancy effect on oil recovery for 2-D cross sectional simulations

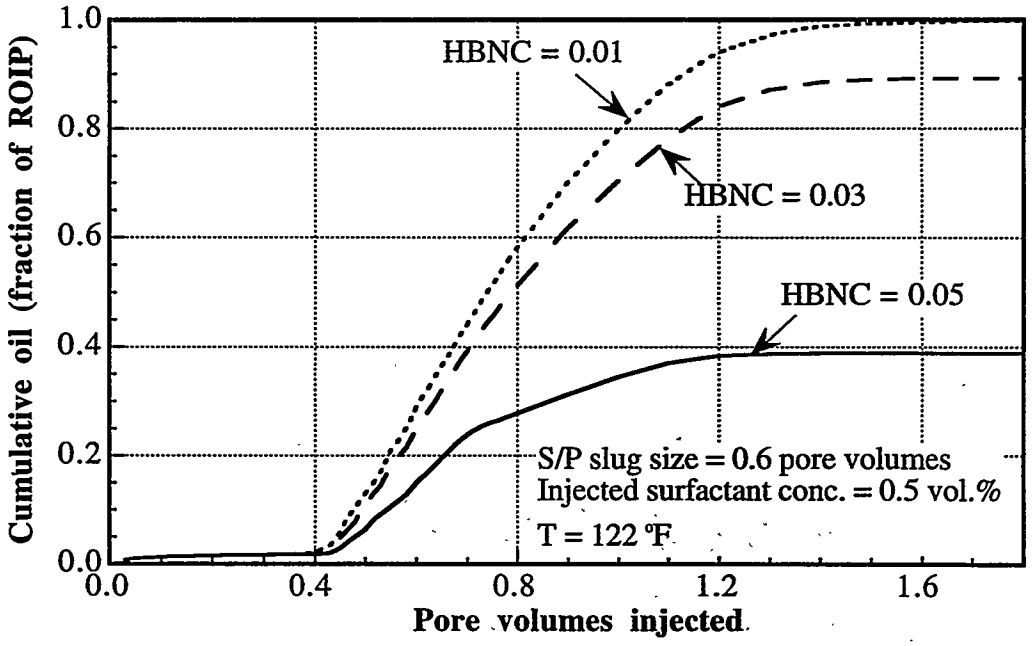


Figure 2.47 Effect of maximum heights of binodal curve on oil recovery for 2-D cross sectional simulations

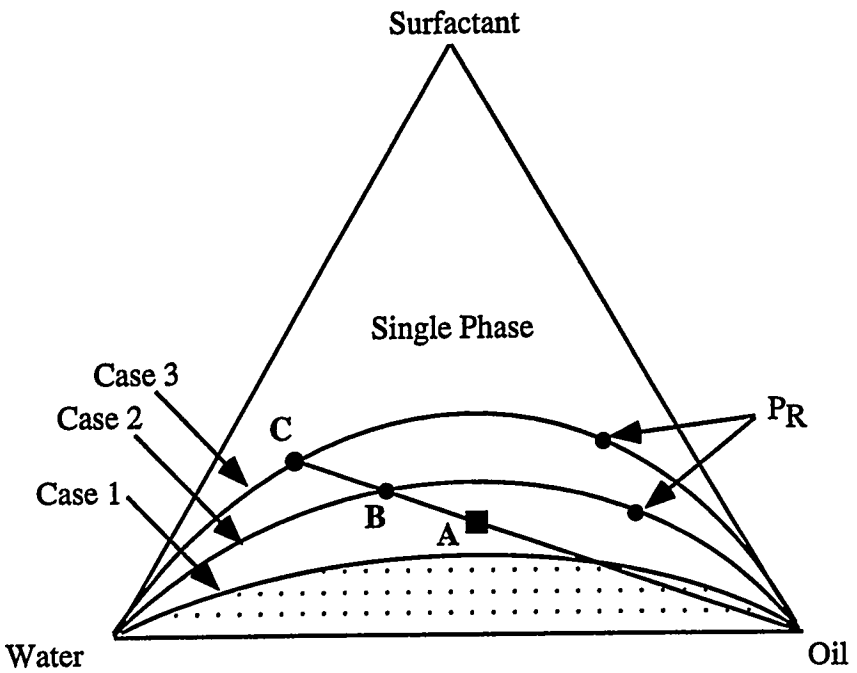


Figure 2.48 Schematic representation of phase diagram for three different heights of binodal curves

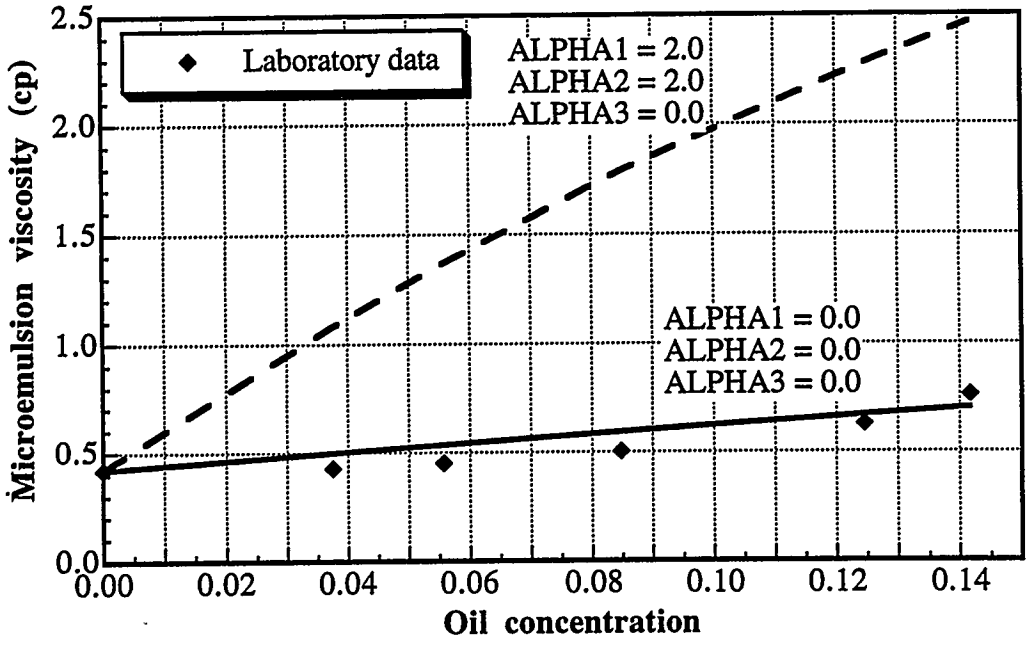


Figure 2.49 Microemulsion viscosity for sensitivity analyses

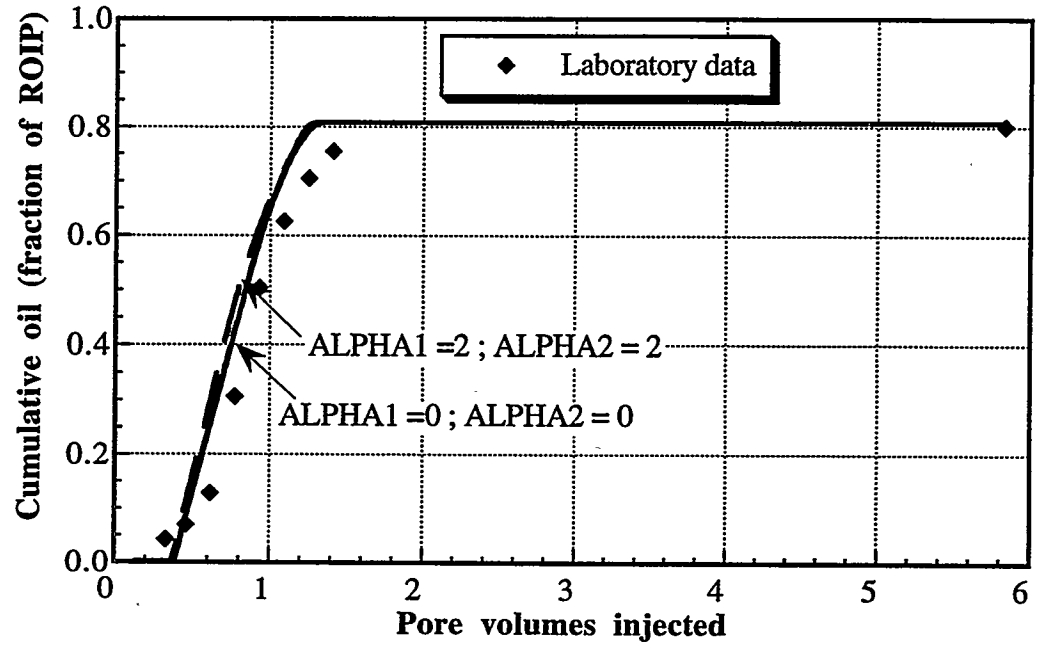


Figure 2.50 Effect of microemulsion viscosity parameters on oil recovery of coreflood

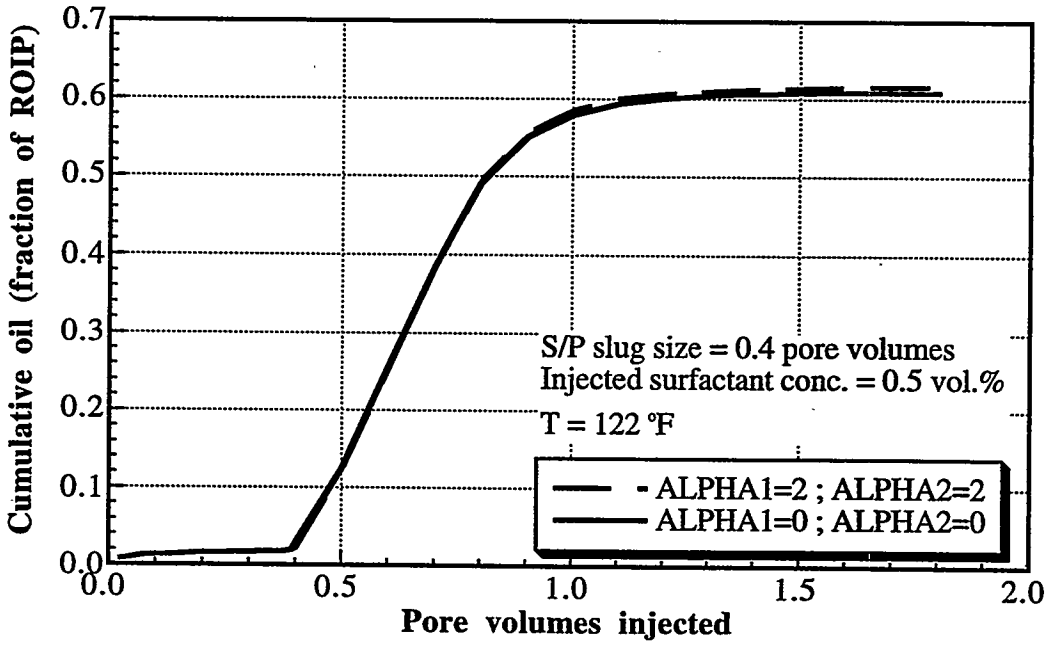


Figure 2.51 Effect of microemulsion viscosity parameters on oil recovery for 2-D cross sectional simulations

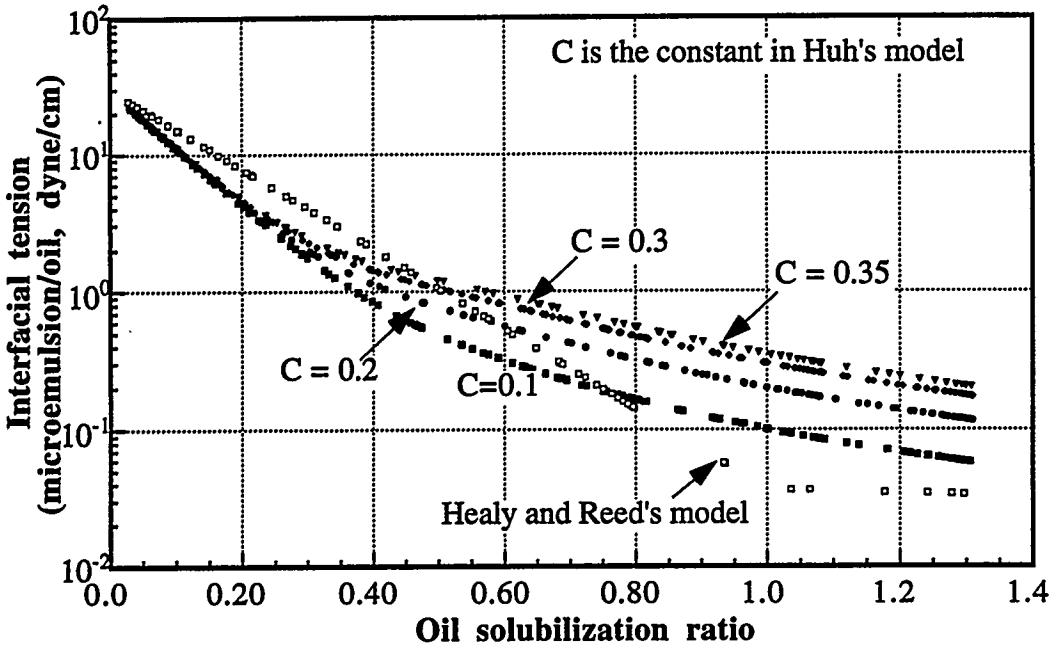


Figure 2.52 Interfacial tension vs. solubilization ratio at 122 °F

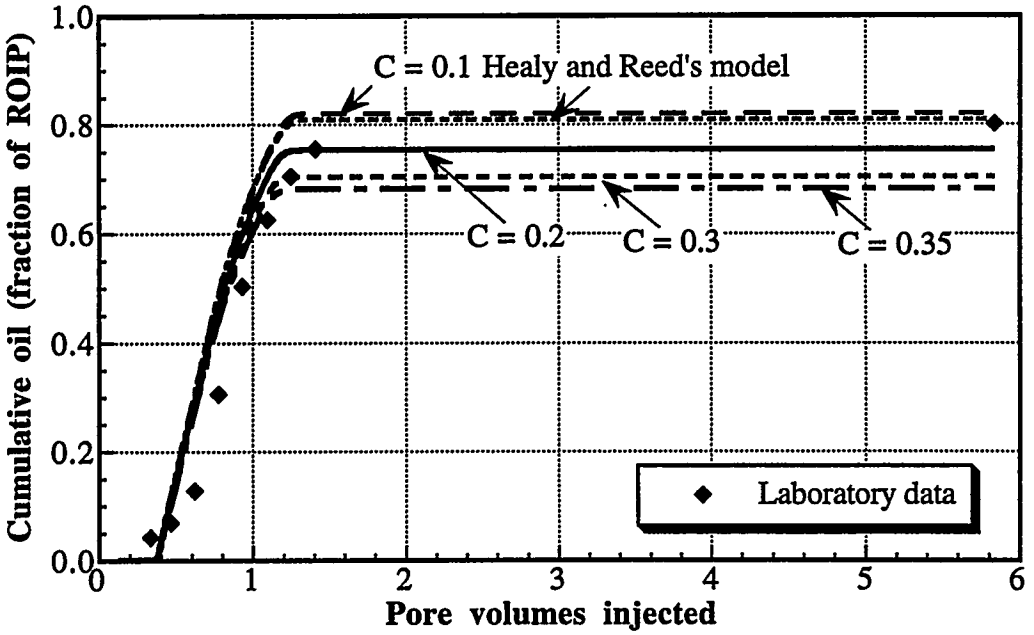


Figure 2.53 Effect of interfacial tension parameters on oil recovery of coreflood

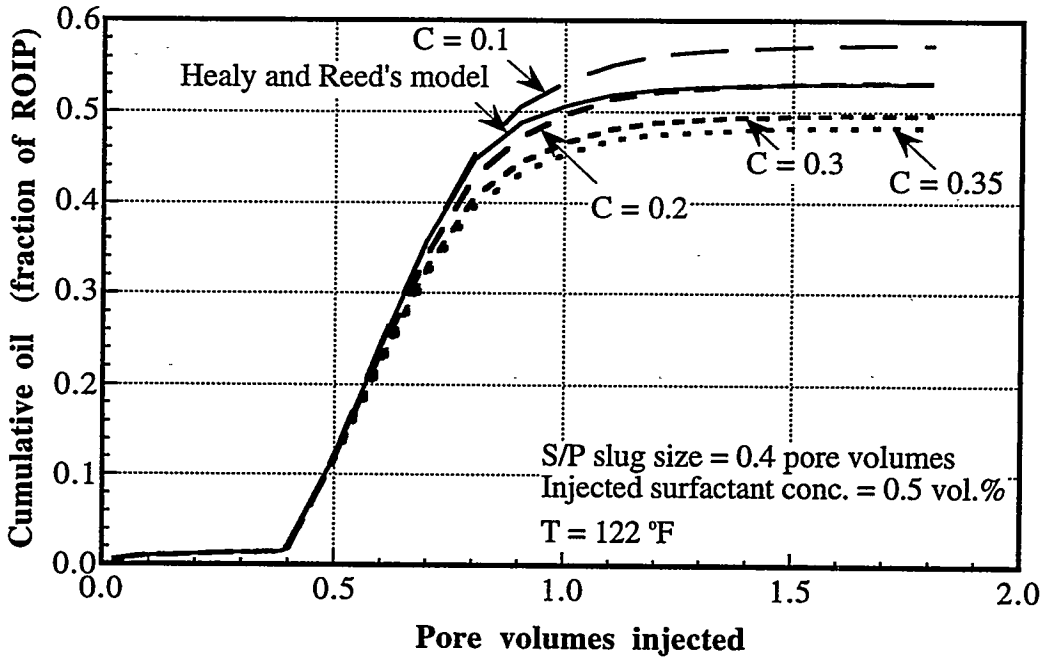


Figure 2.54 Effect of interfacial tension parameters on oil recovery for 2-D cross sectional simulations

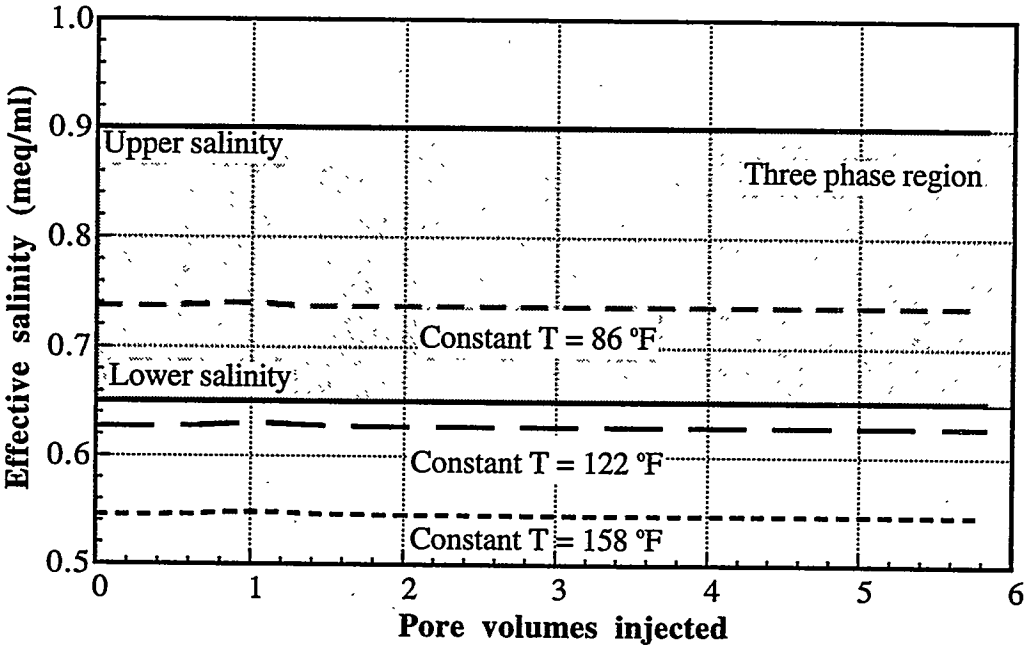


Figure 2.55 Effect of temperature on effective salinity of coreflood

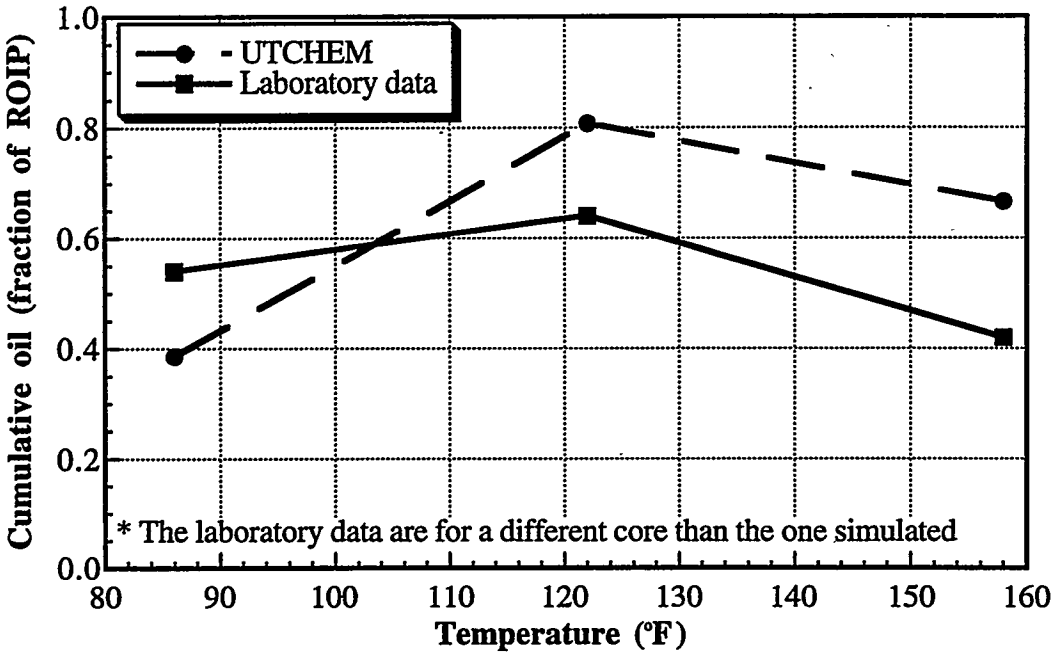


Figure 2.56 Effect of temperature on oil recovery for coreflood

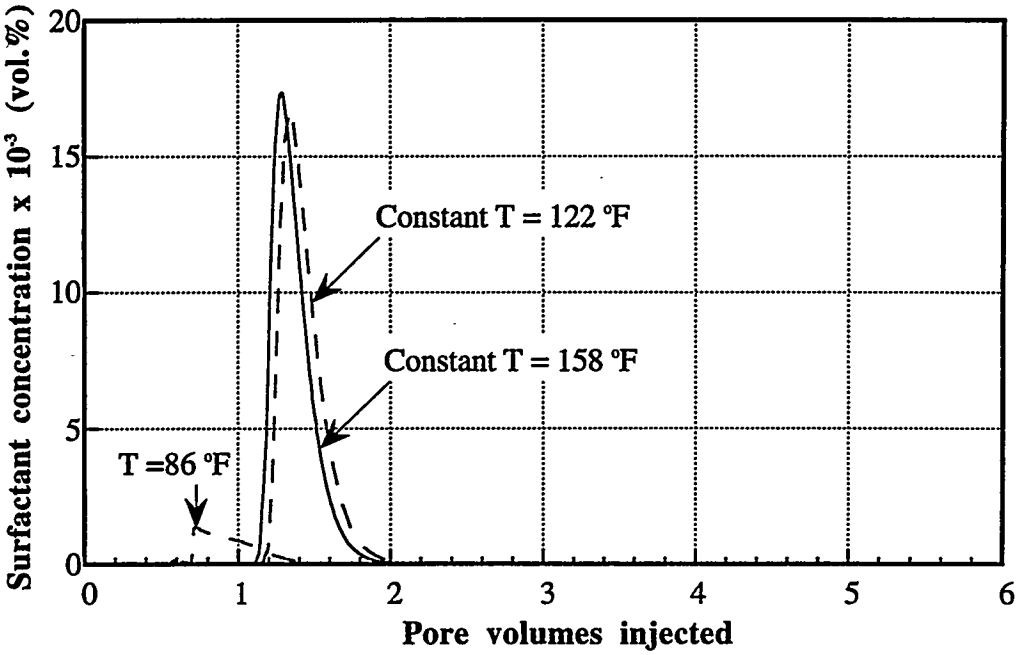


Figure 2.57 Temperature effect on produced surfactant concentration for coreflood

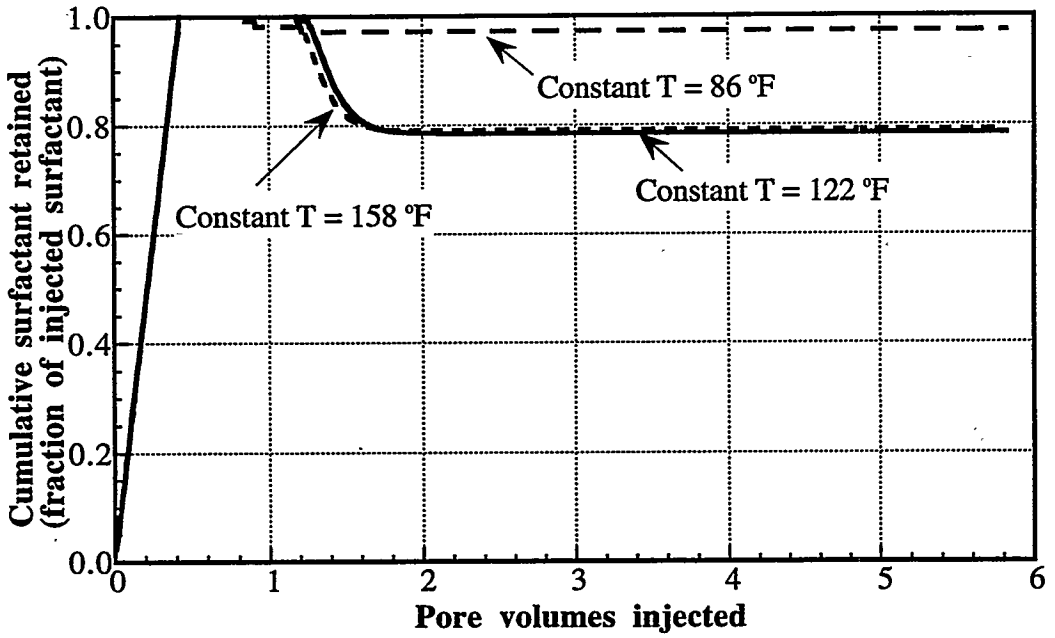


Figure 2.58 Temperature effect on surfactant retained for 1-D simulations

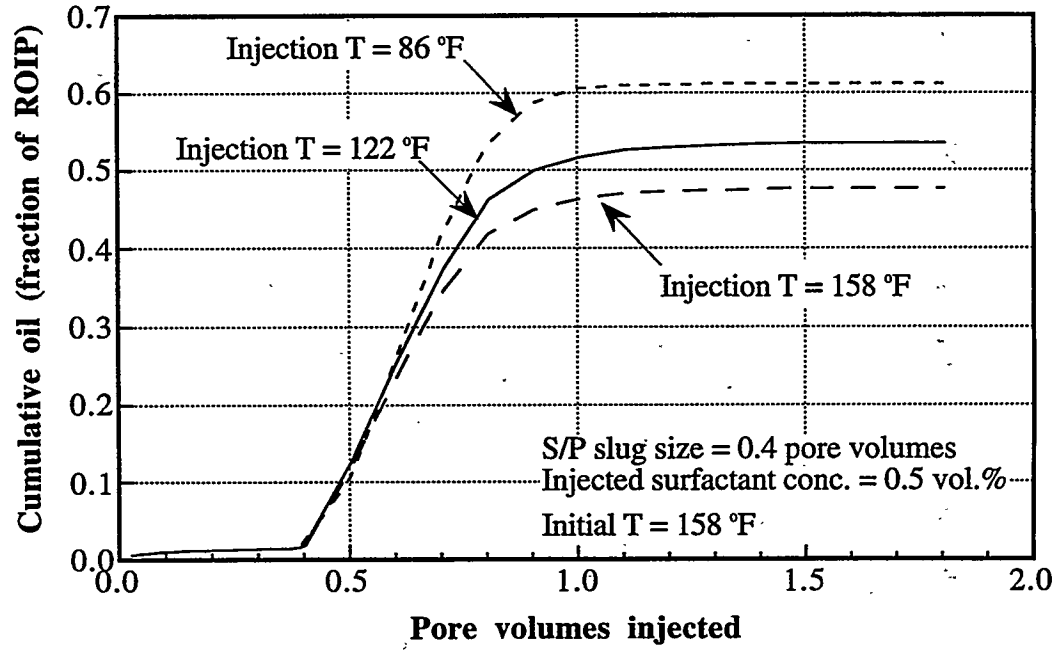


Figure 2.59 Effect of injection temperatures on oil recovery for 2-D cross sectional simulations

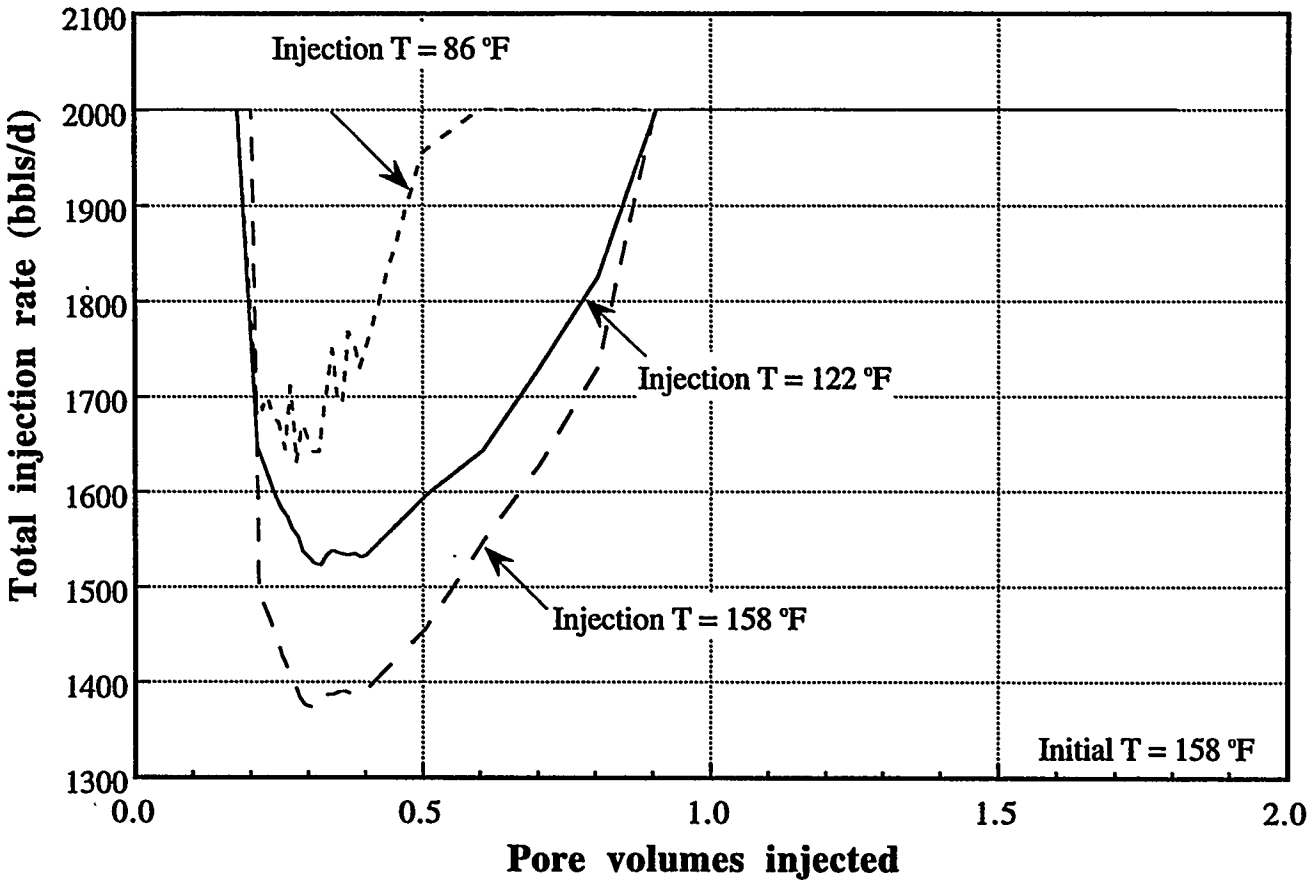


Figure 2.60 Effect of temperatures on injection rate for 2-D cross sectional simulations

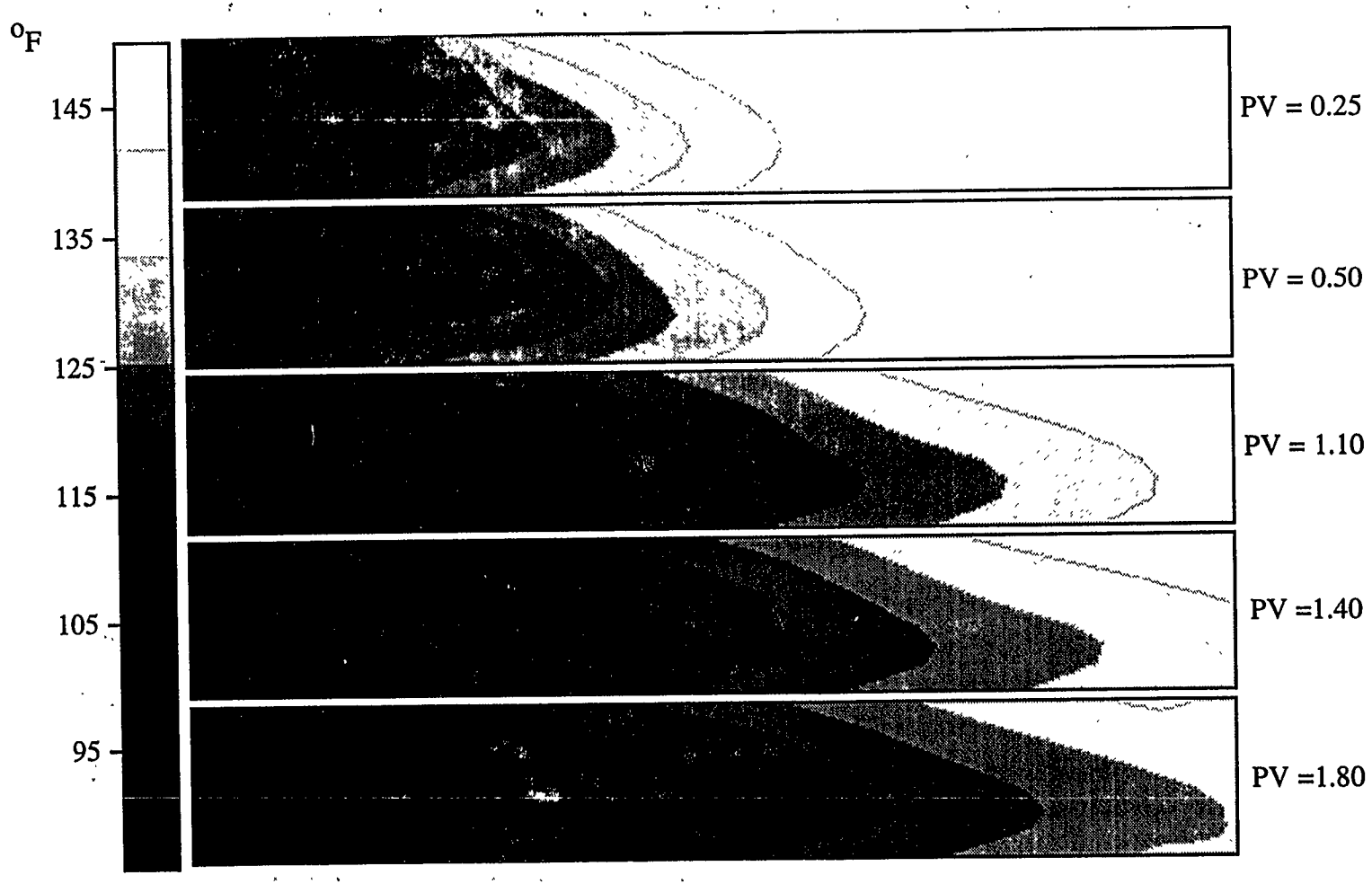


Figure 2.61 Temperature profiles for injection T = 86 °F for 2-D cross sectional simulation

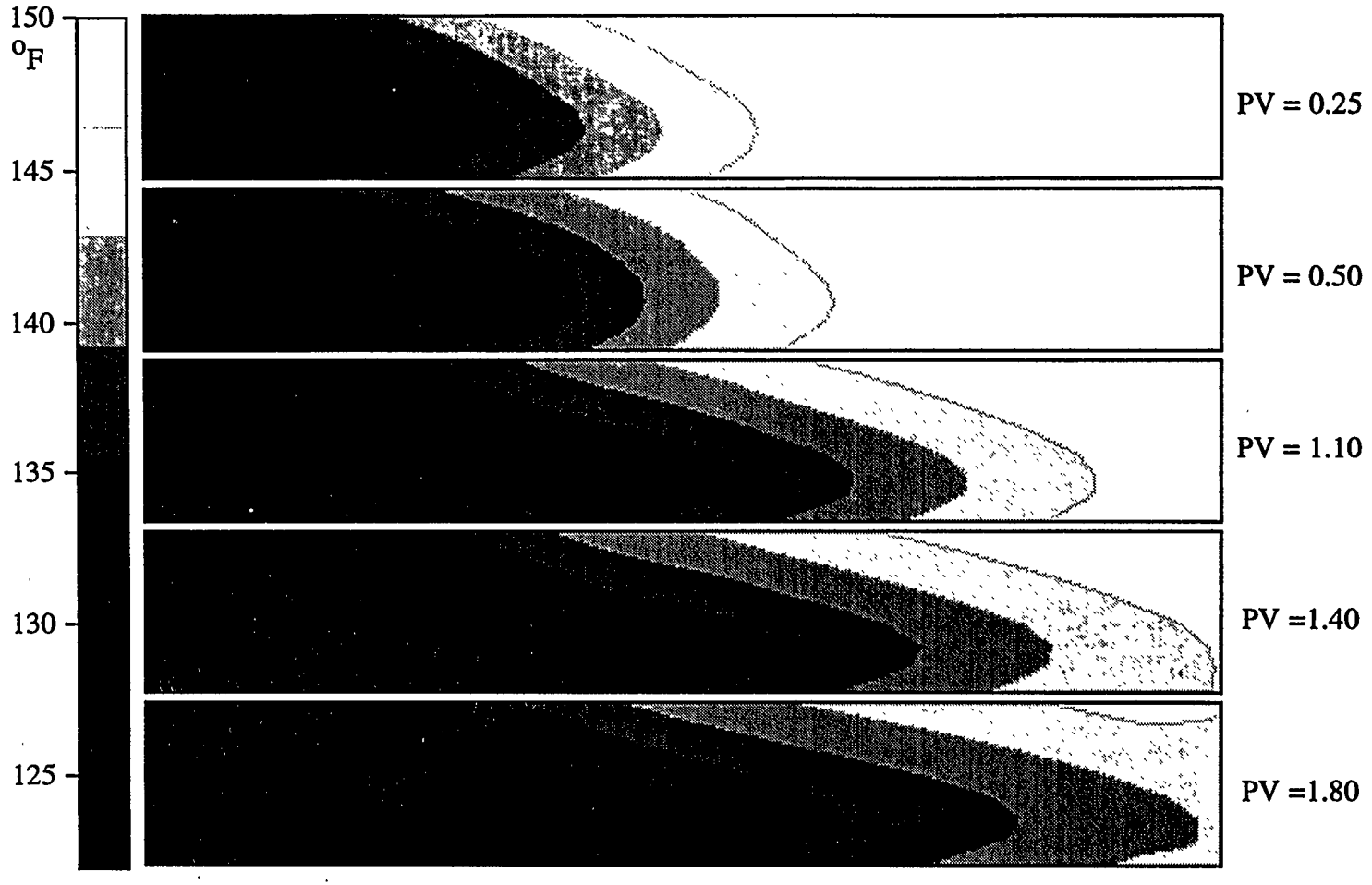


Figure 2.62 Temperature profiles for injection T = 122 °F for 2D cross sectional simulations

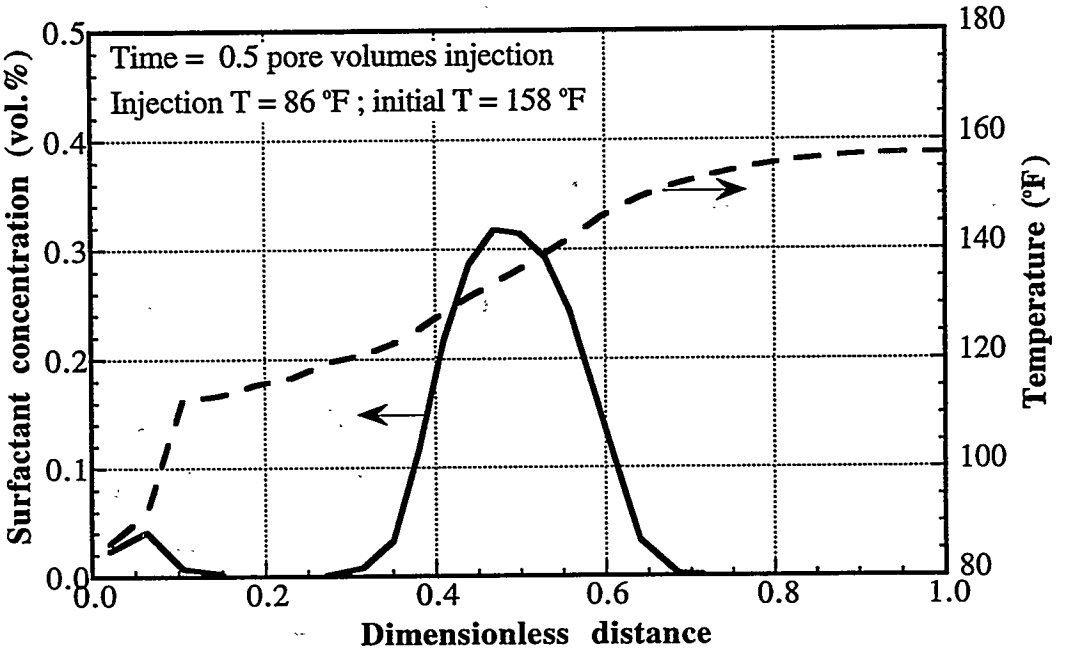


Figure 2.63 Surfactant concentration and temperature distribution in 8th layer for 2-D cross sectional simulations

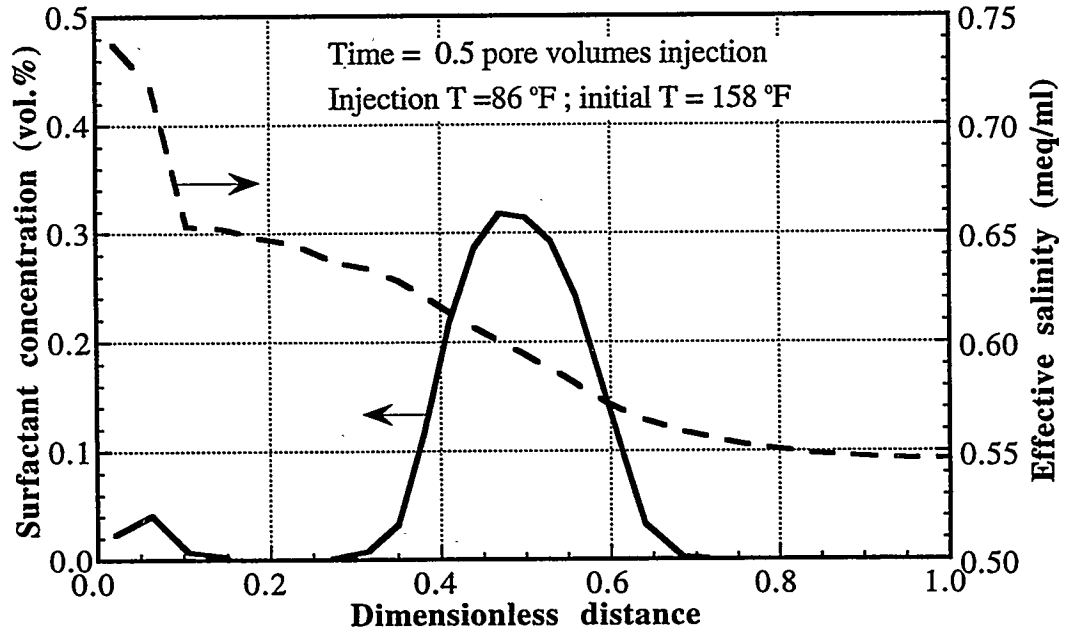


Figure 2.64 Surfactant concentration and effective salinity distribution in 8th layer for 2-D cross sectional simulations

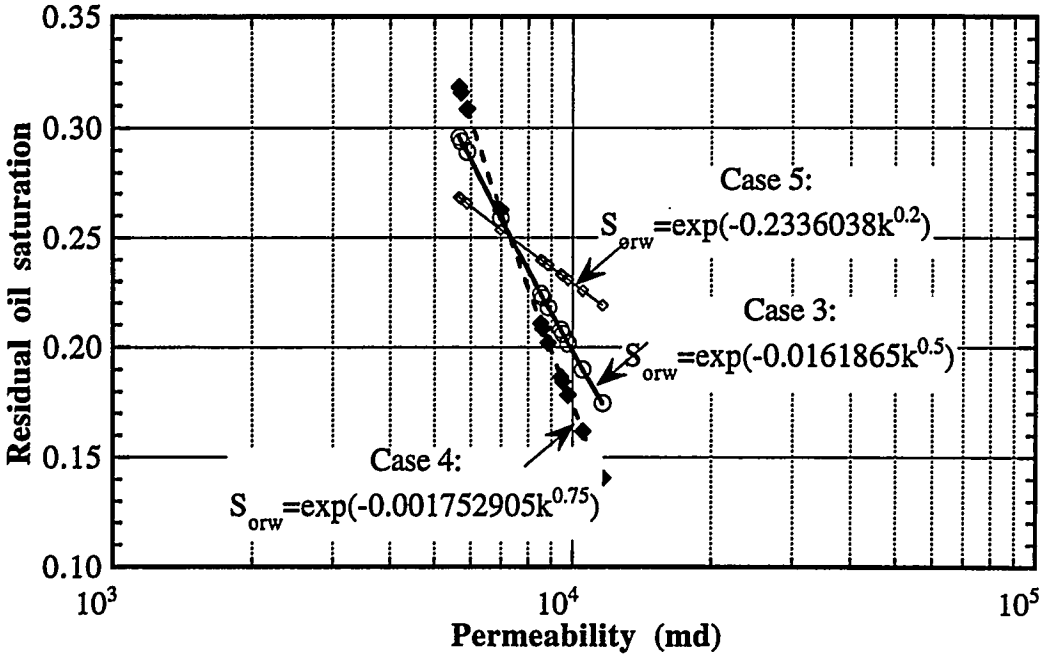


Figure 2.65 Residual oil saturation (S_{orw}) as a function of permeability

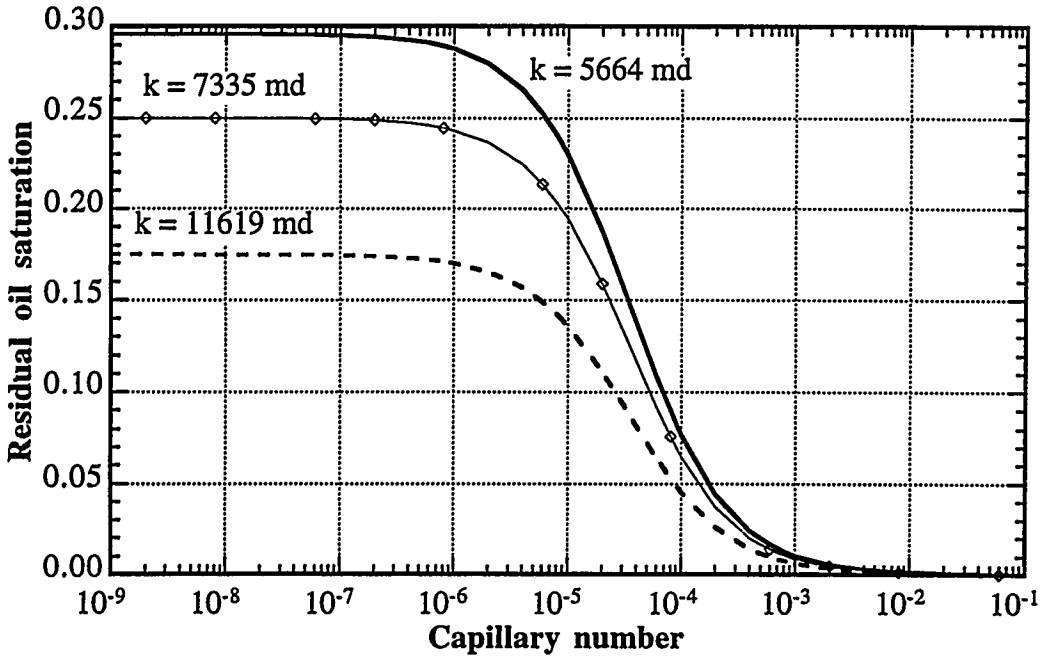


Figure 2.66 Capillary desaturation curve for permeability-dependent S_{orw} (Case 3: $S_{orw}=\exp(-0.0161865k^{0.5})$)

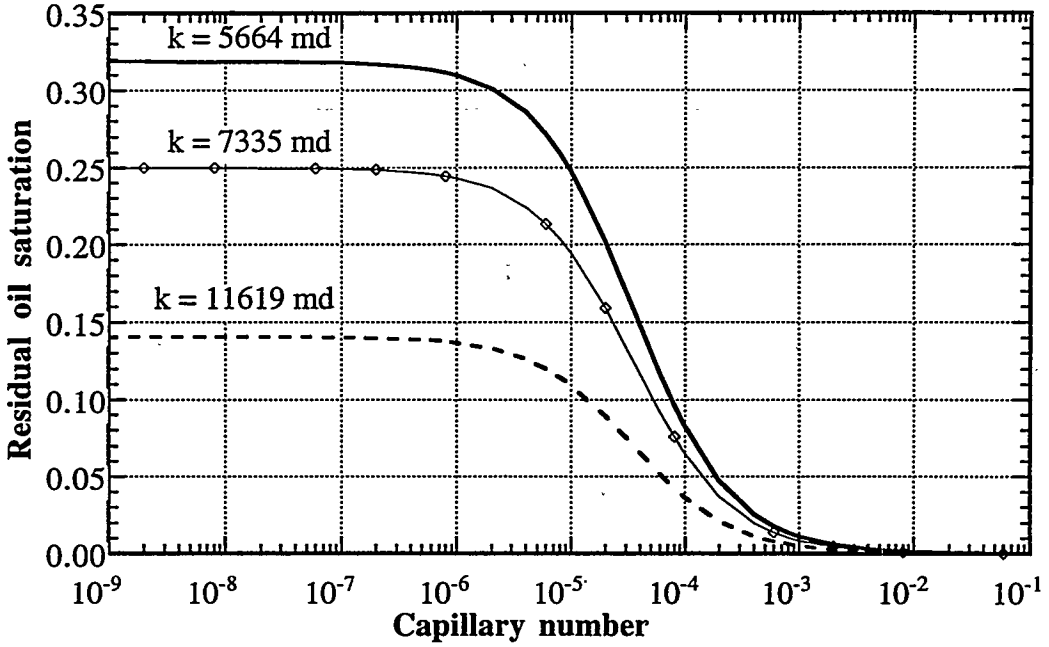


Figure 2.67 Capillary desaturation curve for permeability-dependent S_{orw} (Case 4: $S_{orw}=\exp(-0.001752905k^{0.75})$)

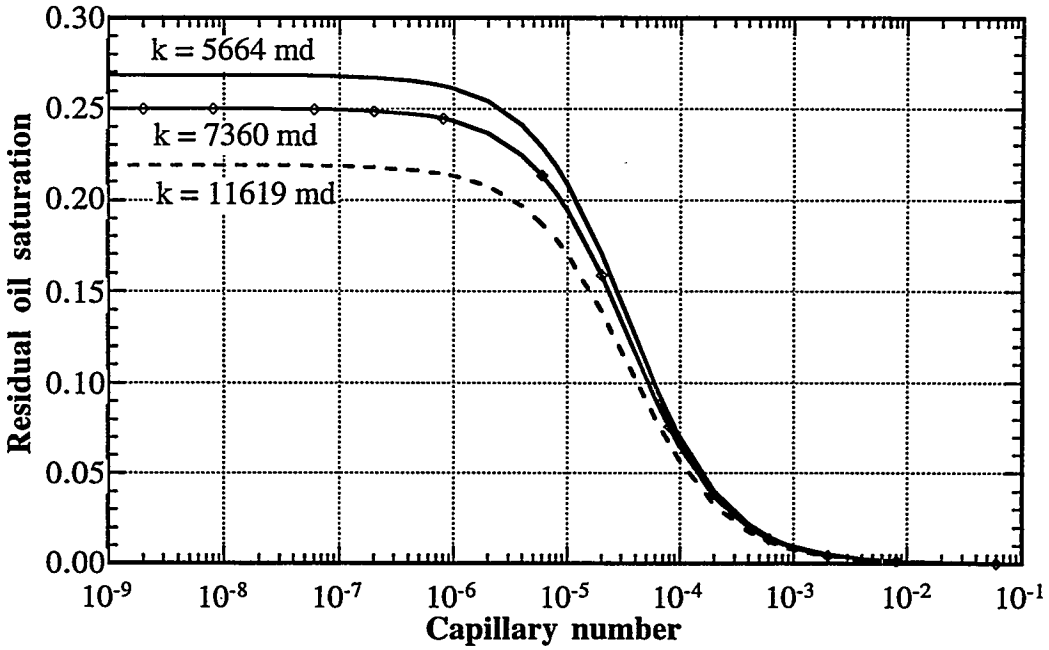


Figure 2.68 Capillary desaturation curve for permeability-dependent S_{orw} (Case 5: $S_{orw}=\exp(-0.2336038k^{0.2})$)

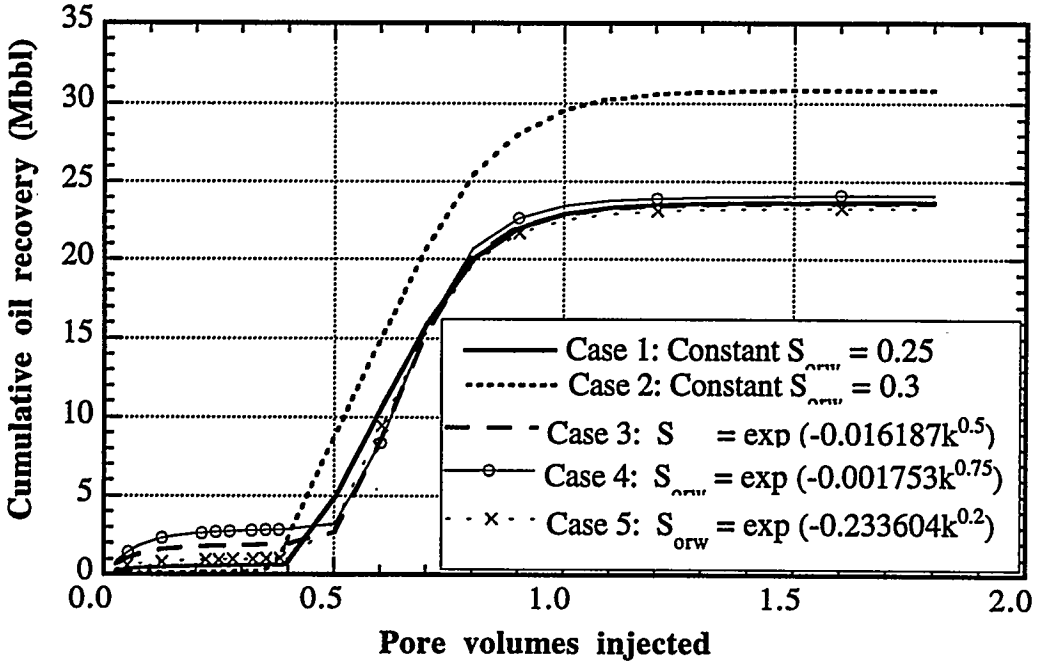


Figure 2.69 Effect of distributed S_{orw} on oil recovery

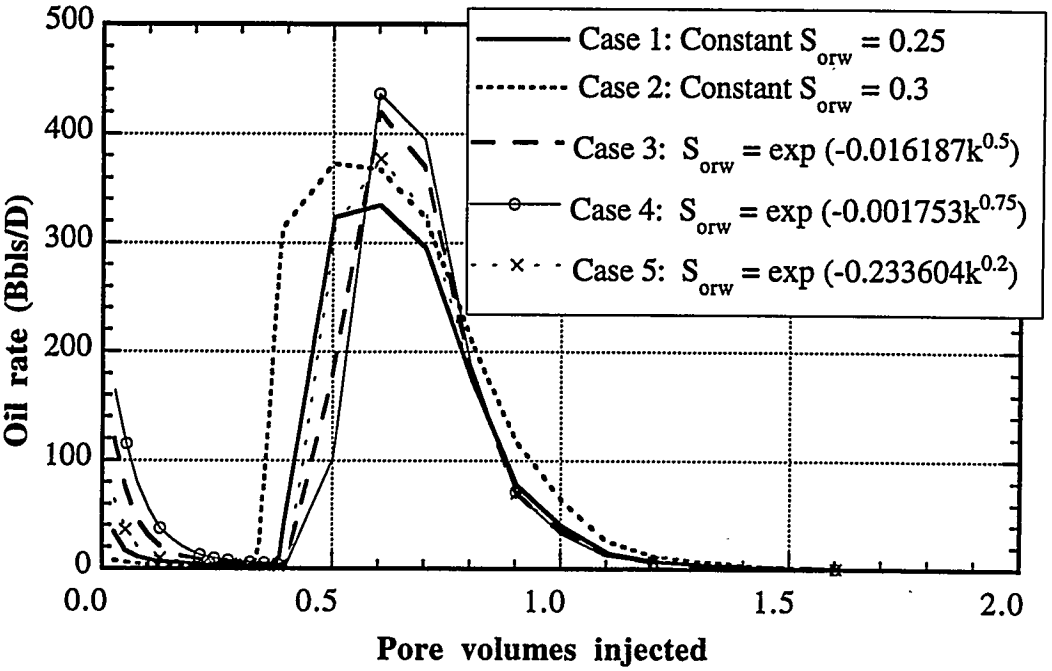


Figure 2.70 Effect of distributed S_{orw} on oil rate

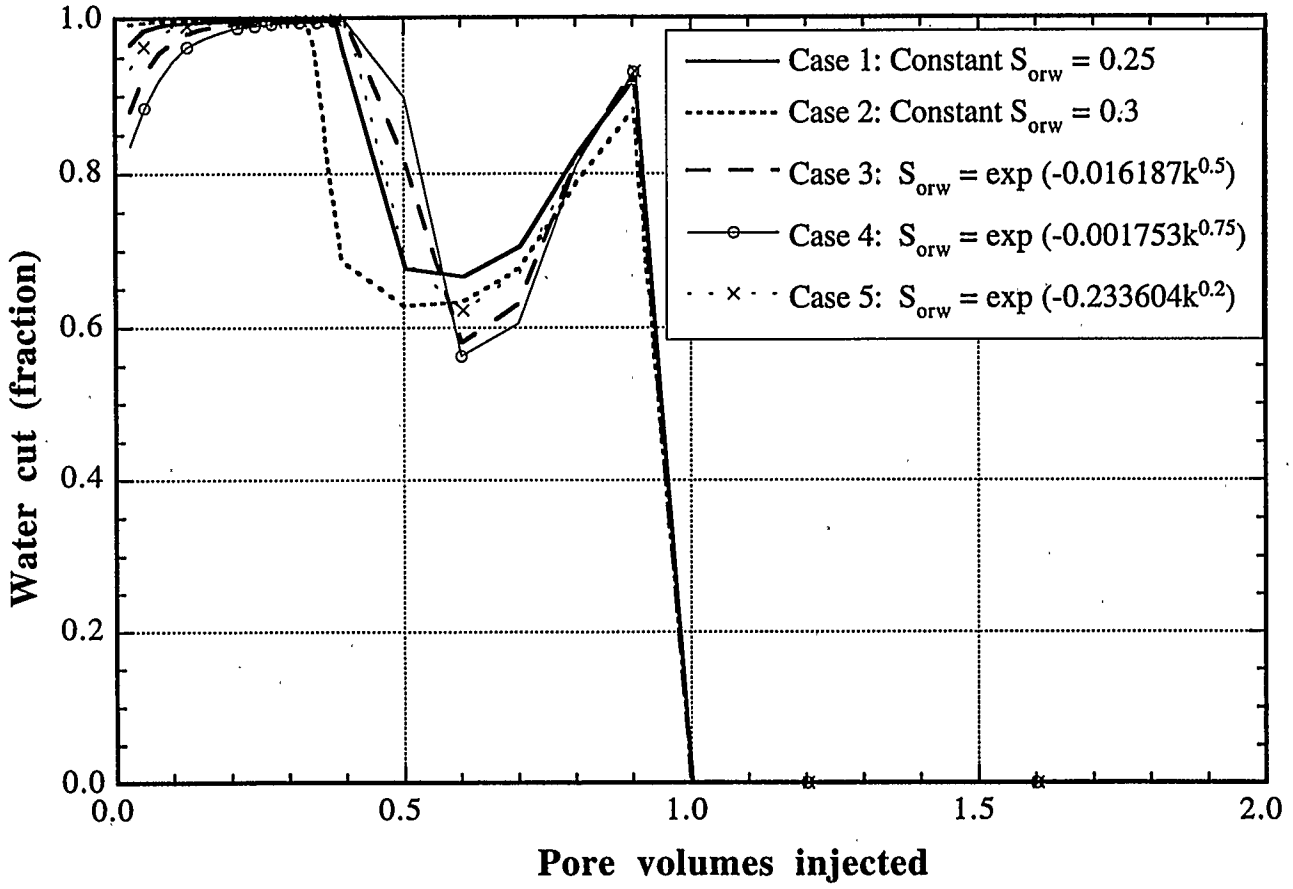


Figure 2.71 Effect of distributed S_{orw} on water cut

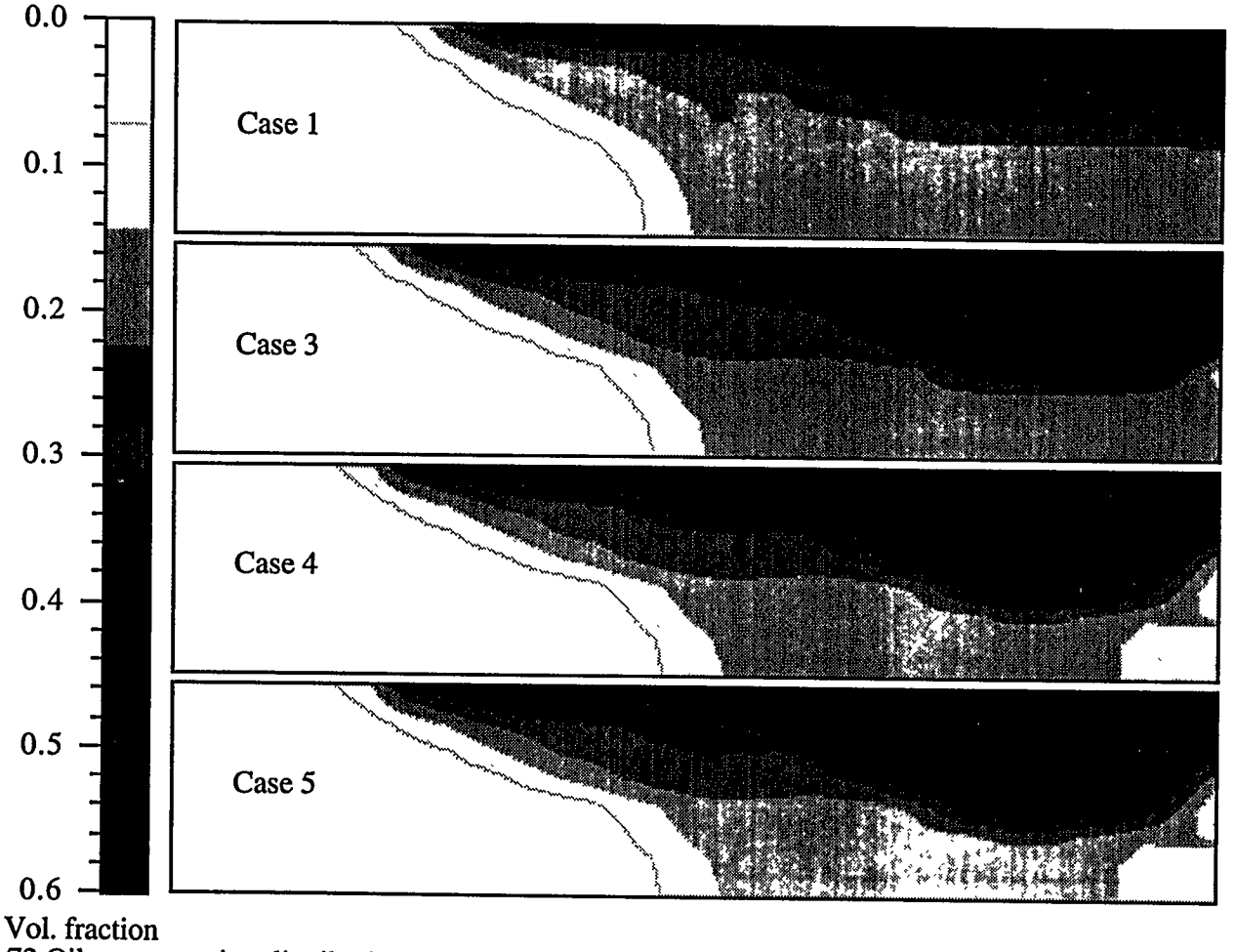


Figure 2.72 Oil concentration distributions at 0.5 PV injected (84 days) for different residual oil saturation distributions

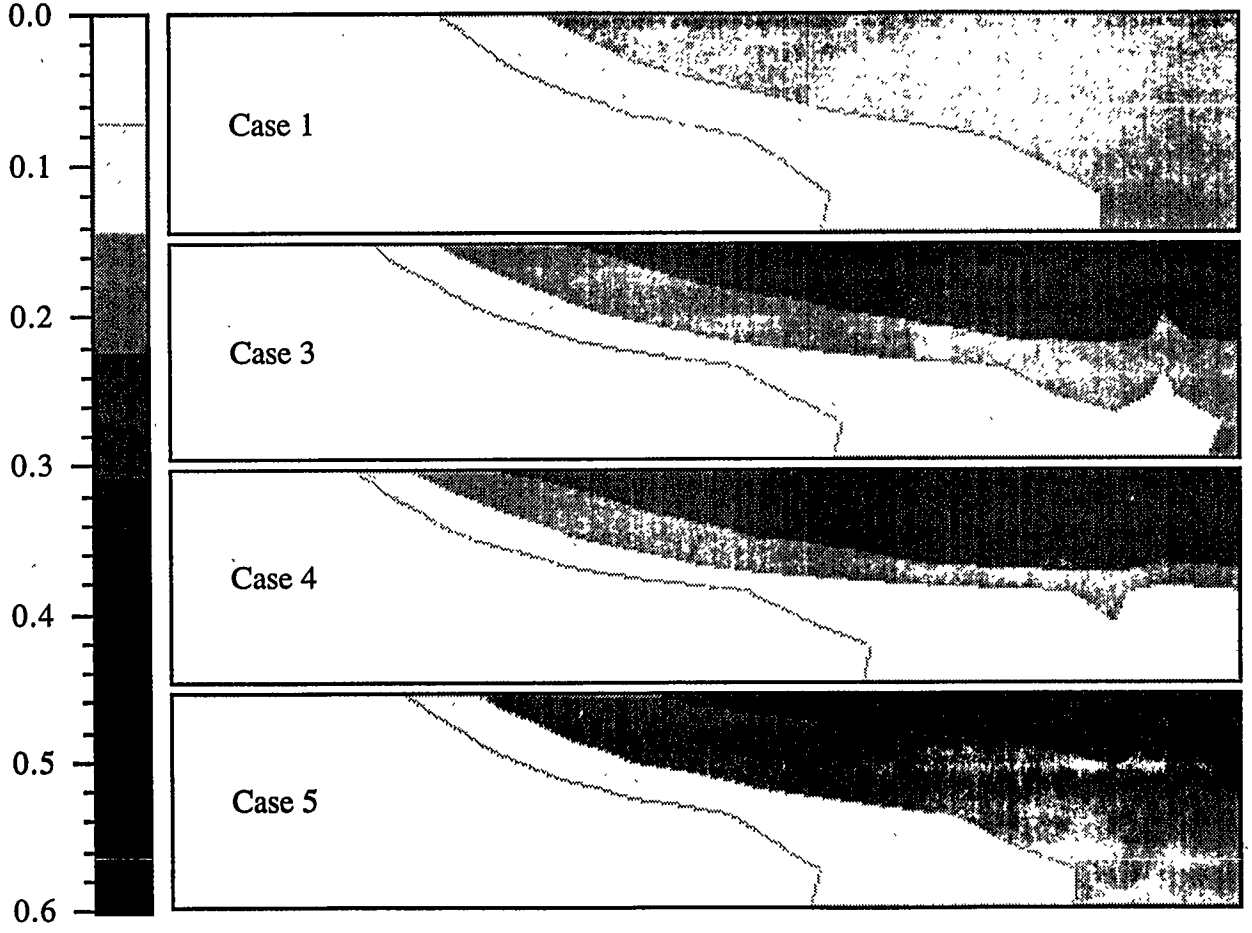


Figure 2.73 Oil concentration distributions at 1.8 PV injected (303 days) for different residual oil saturation distributions

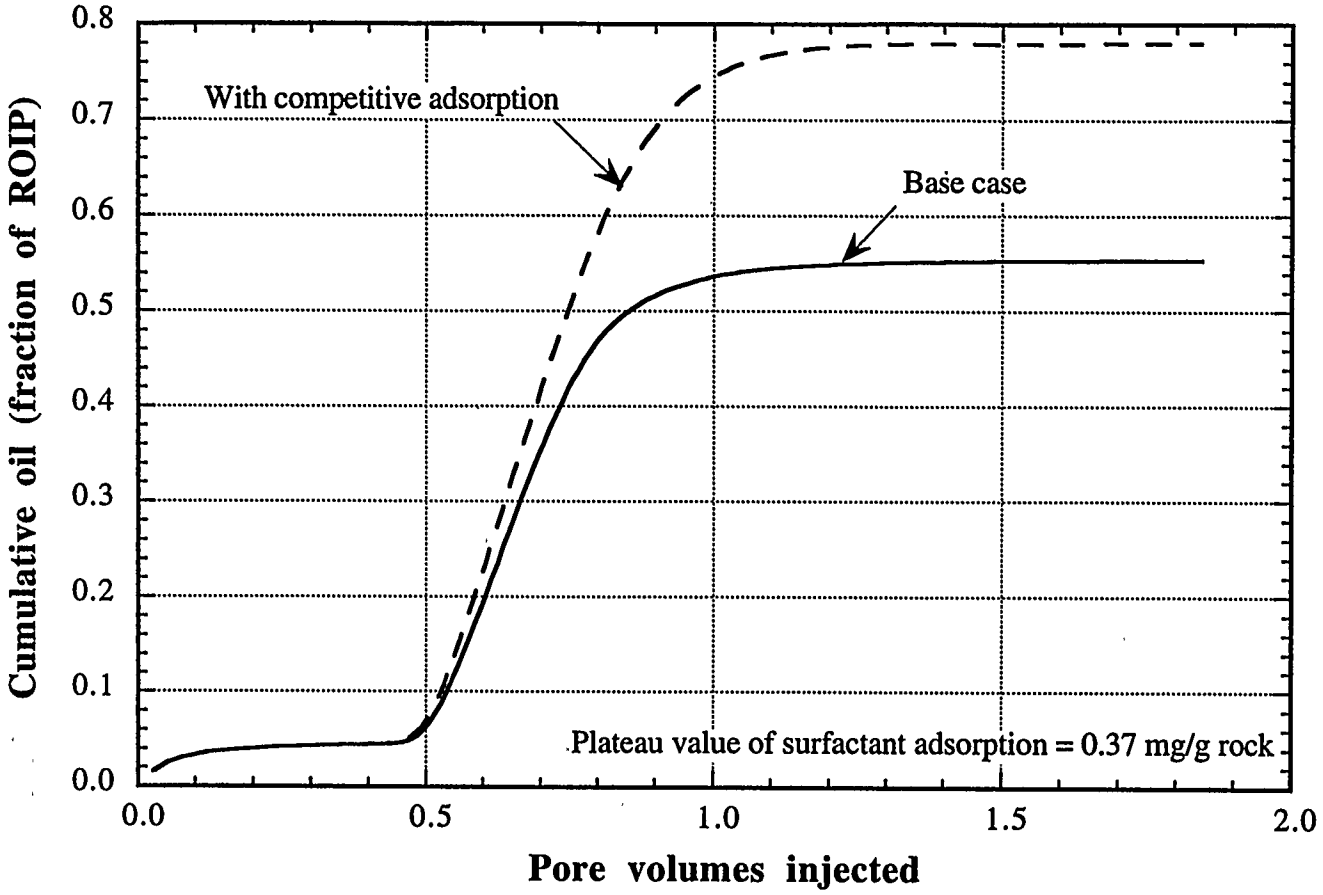


Figure 2.74 Effect of competitive adsorption on oil recovery for Reservoir A

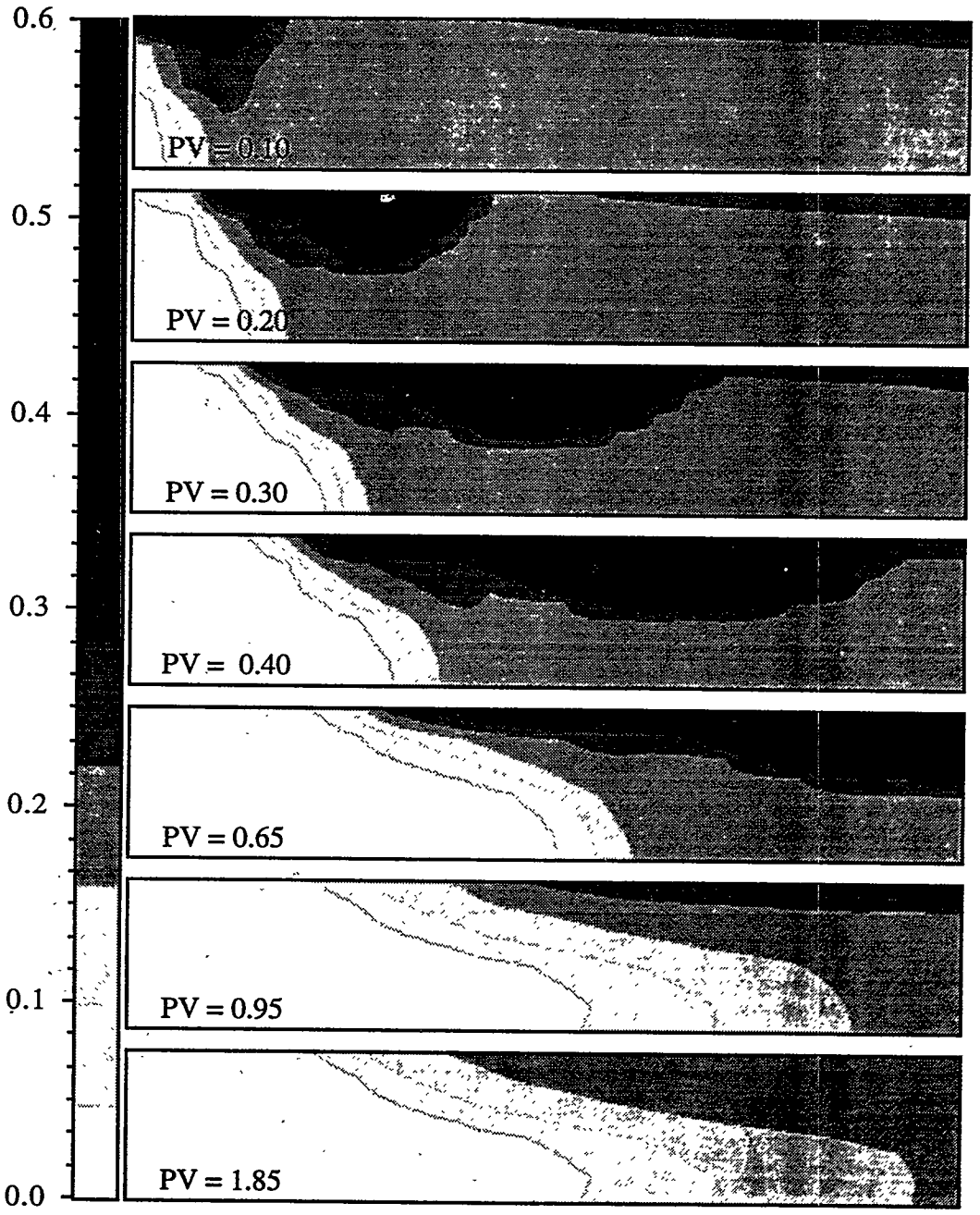


Figure 2.75 Oil concentration profiles for the Base Case

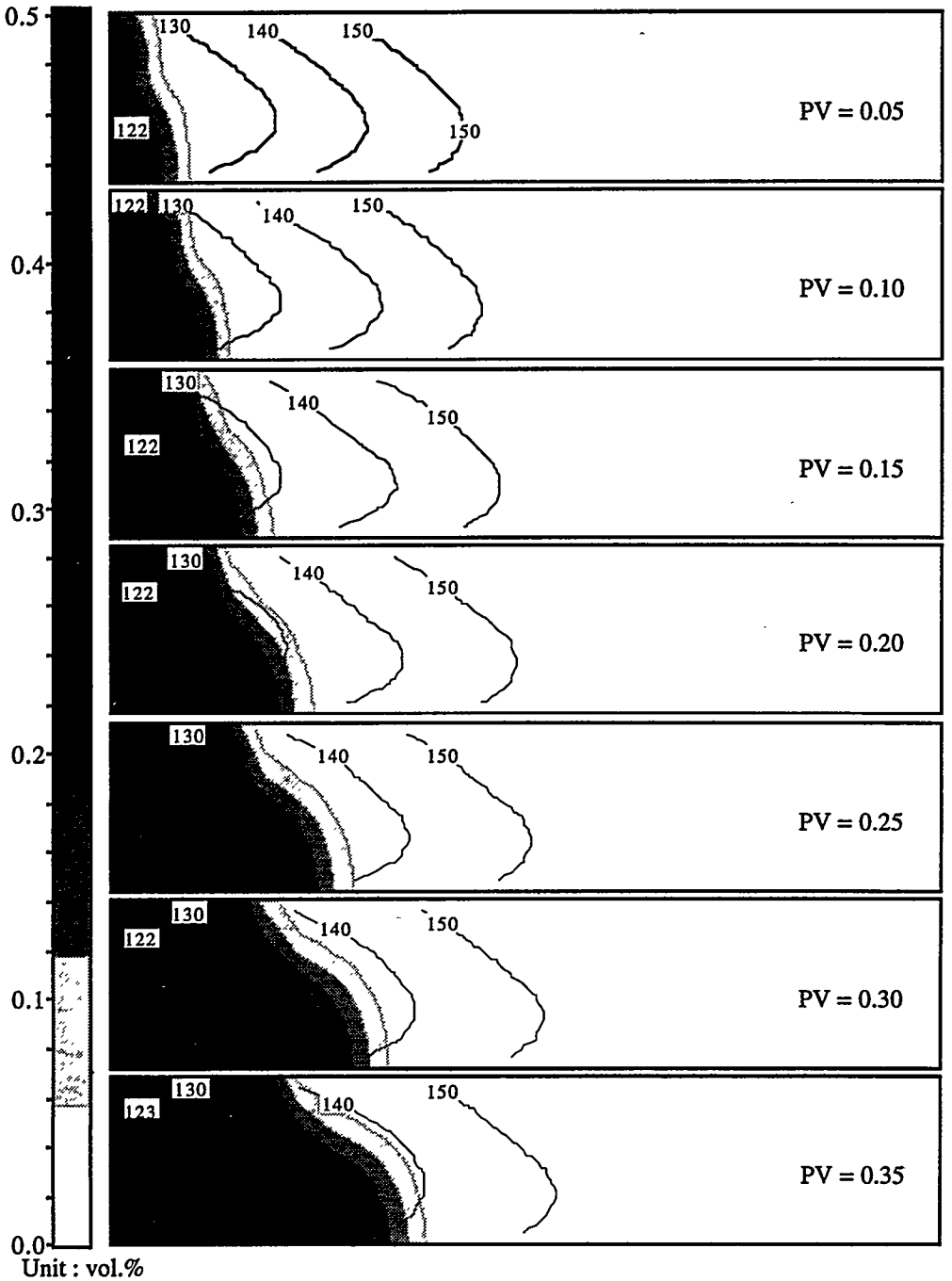


Figure 2.76 Profiles of surfactant concentration overlaid by temperature contours in °F

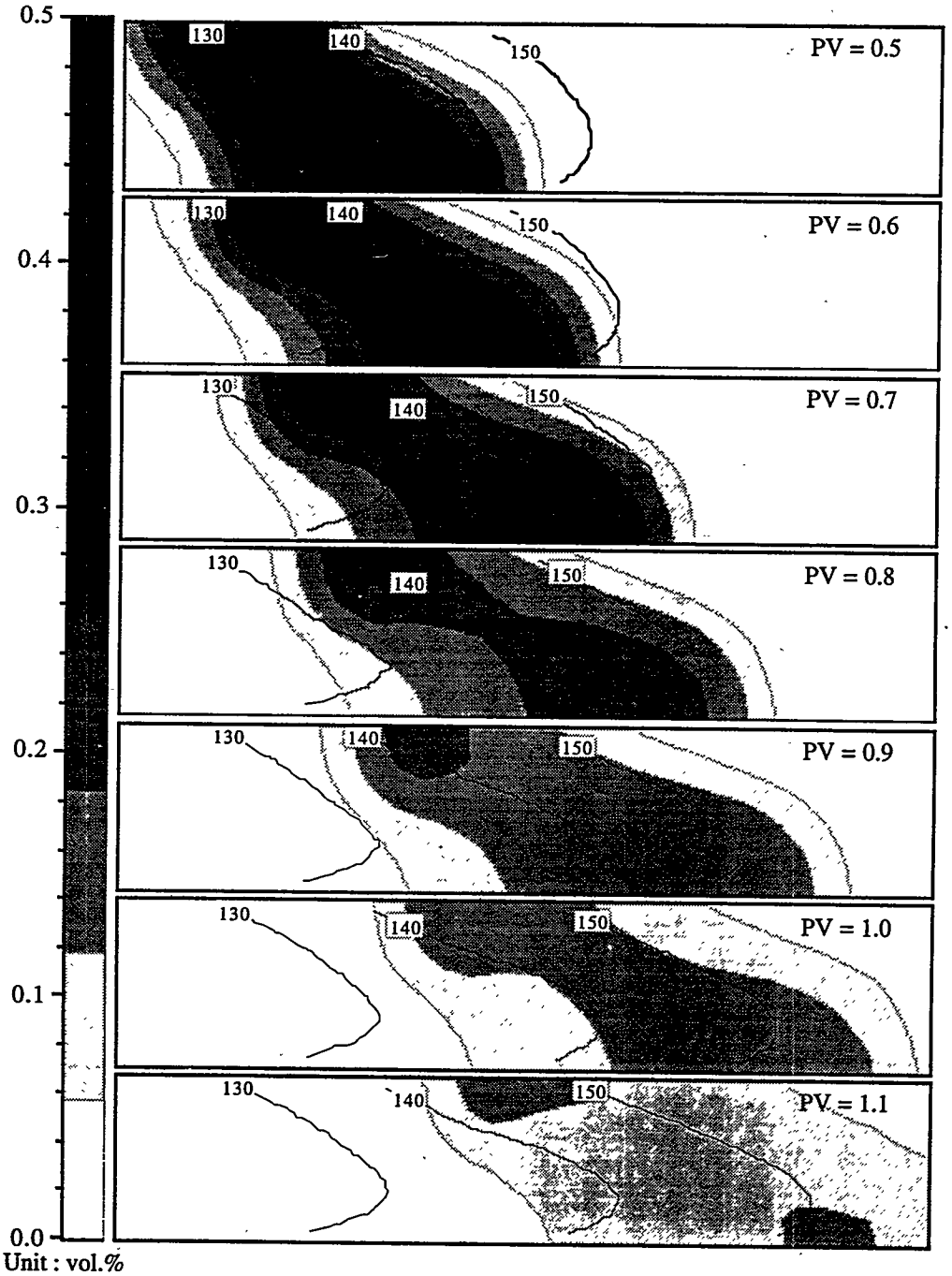
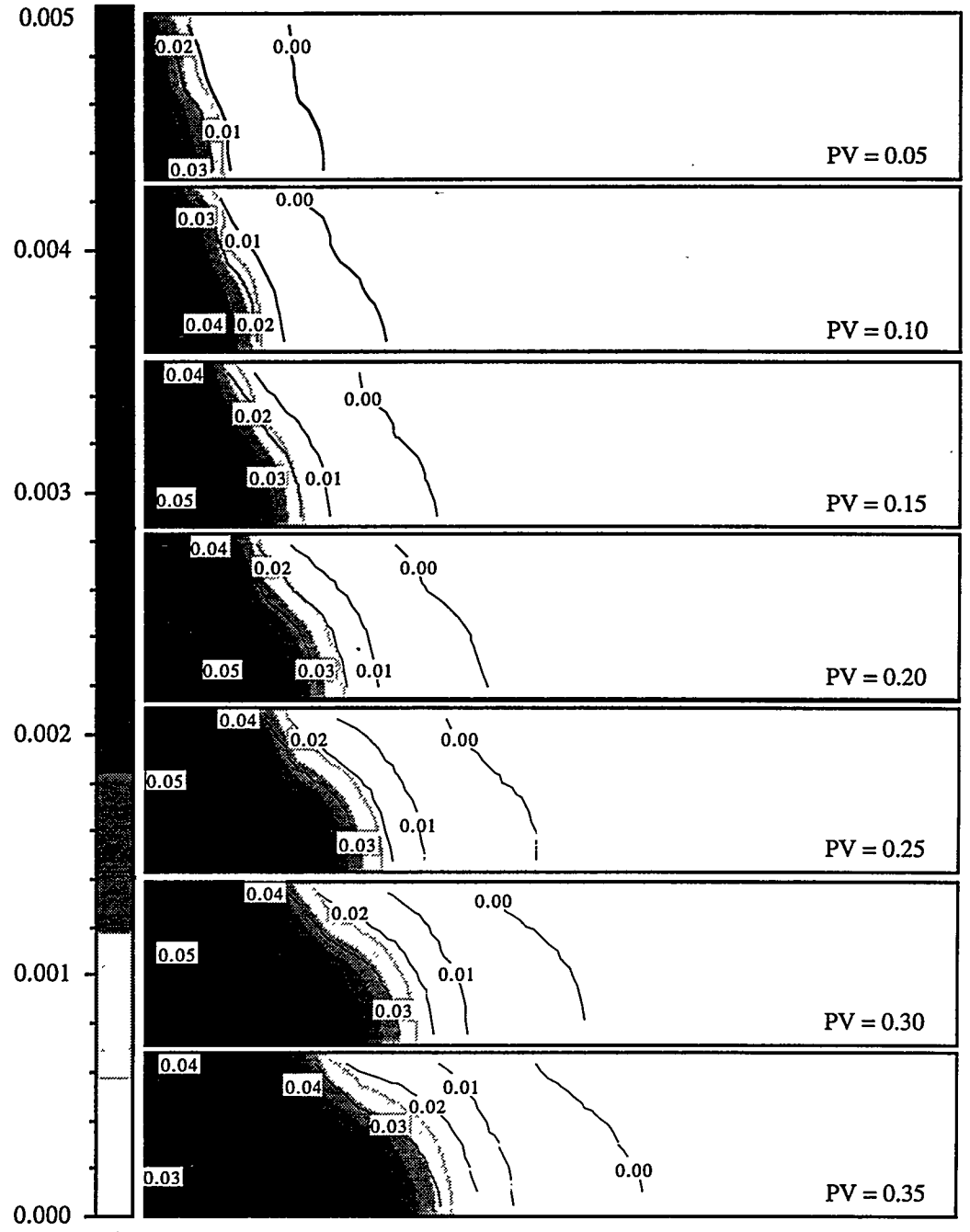


Figure 2.76 (Continued) Profiles of surfactant concentration overlaid by temperature contours in °F



Unit : vol. fraction

Figure 2.77 Profiles of surfactant concentration overlaid by polymer concentration contours in wt%

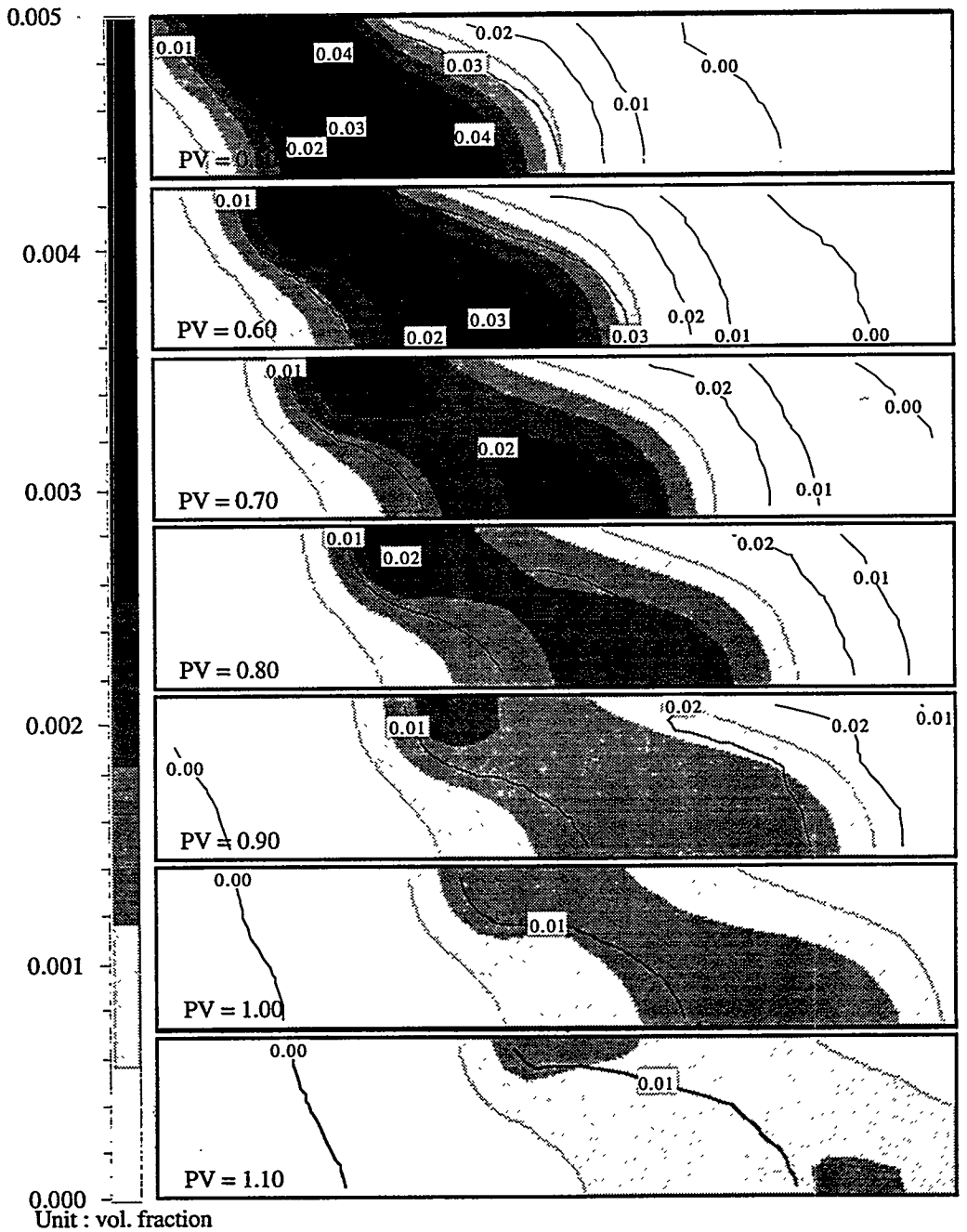


Figure 2.77 (Continued) Profiles of surfactant concentration overlaid by polymer concentration contours in wt%

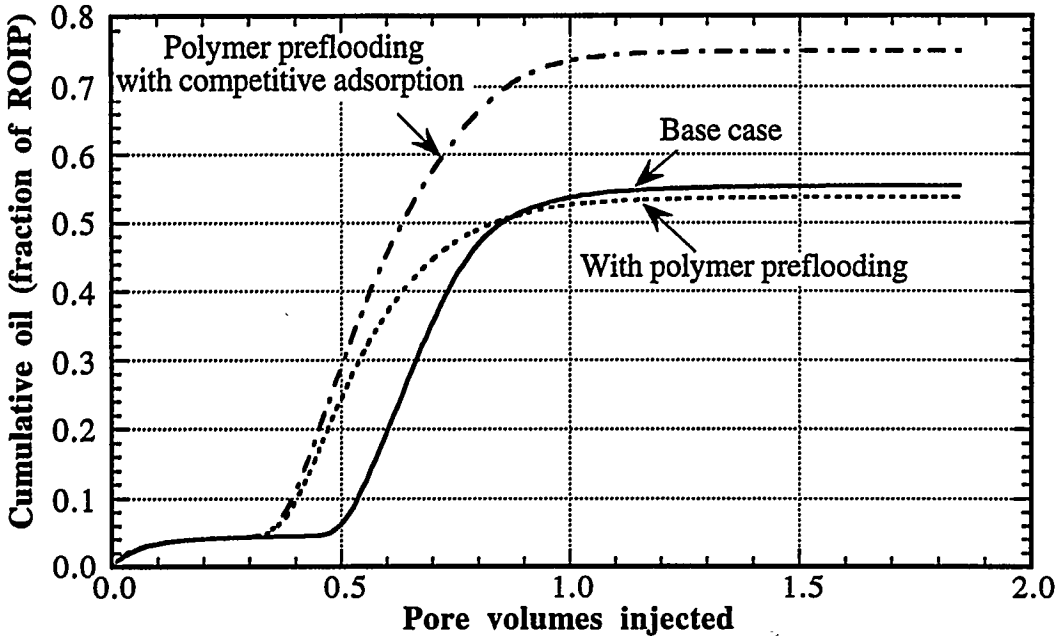


Figure 2.78 Effect of polymer preflooding on oil recovery for Reservoir A

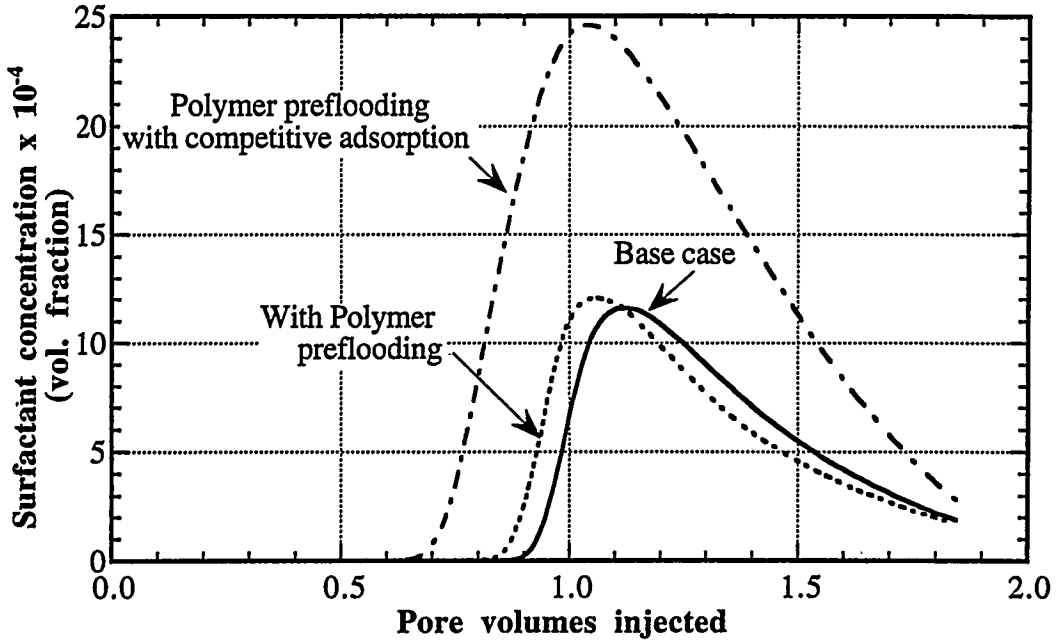


Figure 2.79 Effect of polymer preflooding on surfactant concentration for Reservoir A

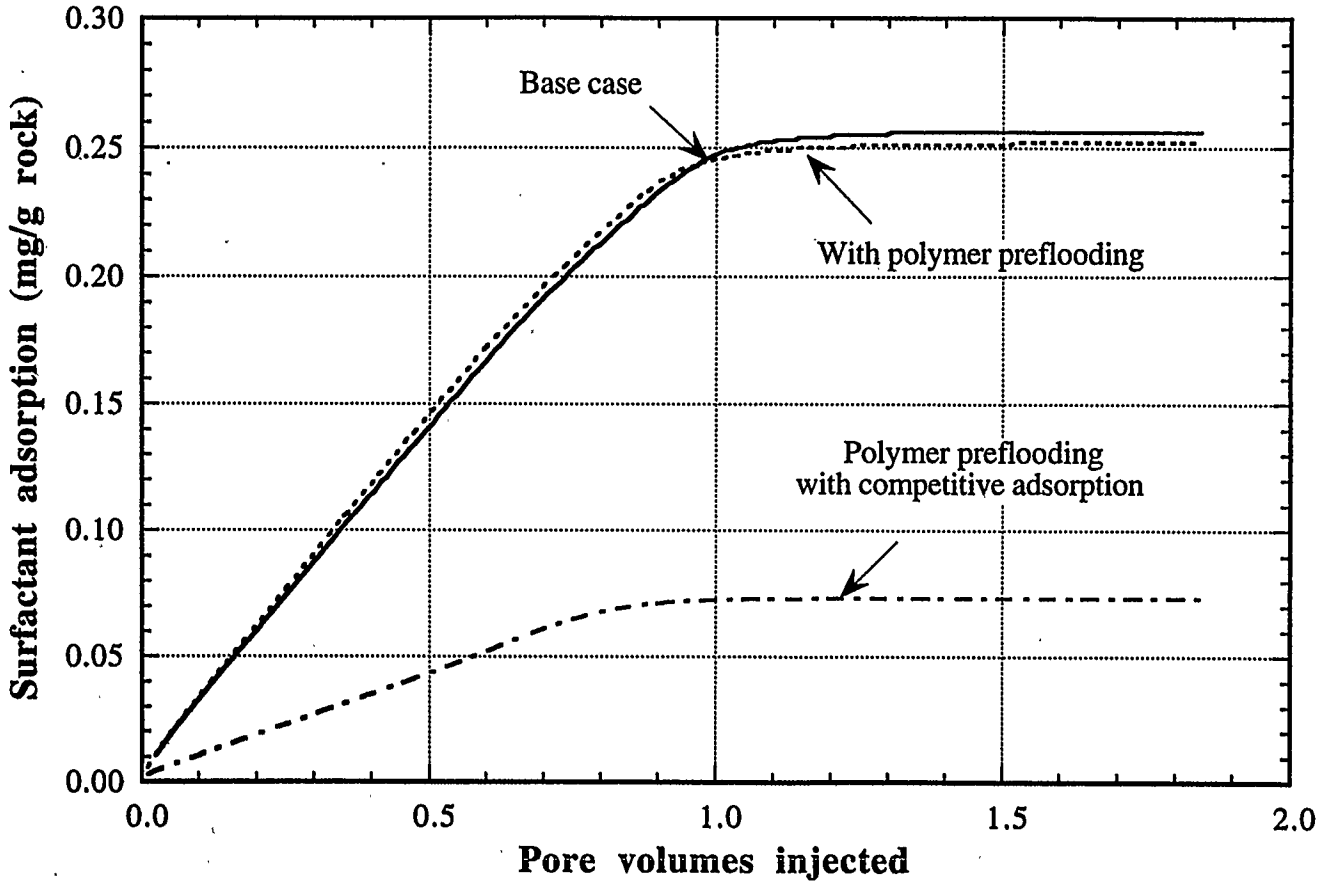


Figure 2.80 Effect of polymer preflooding on surfactant adsorption

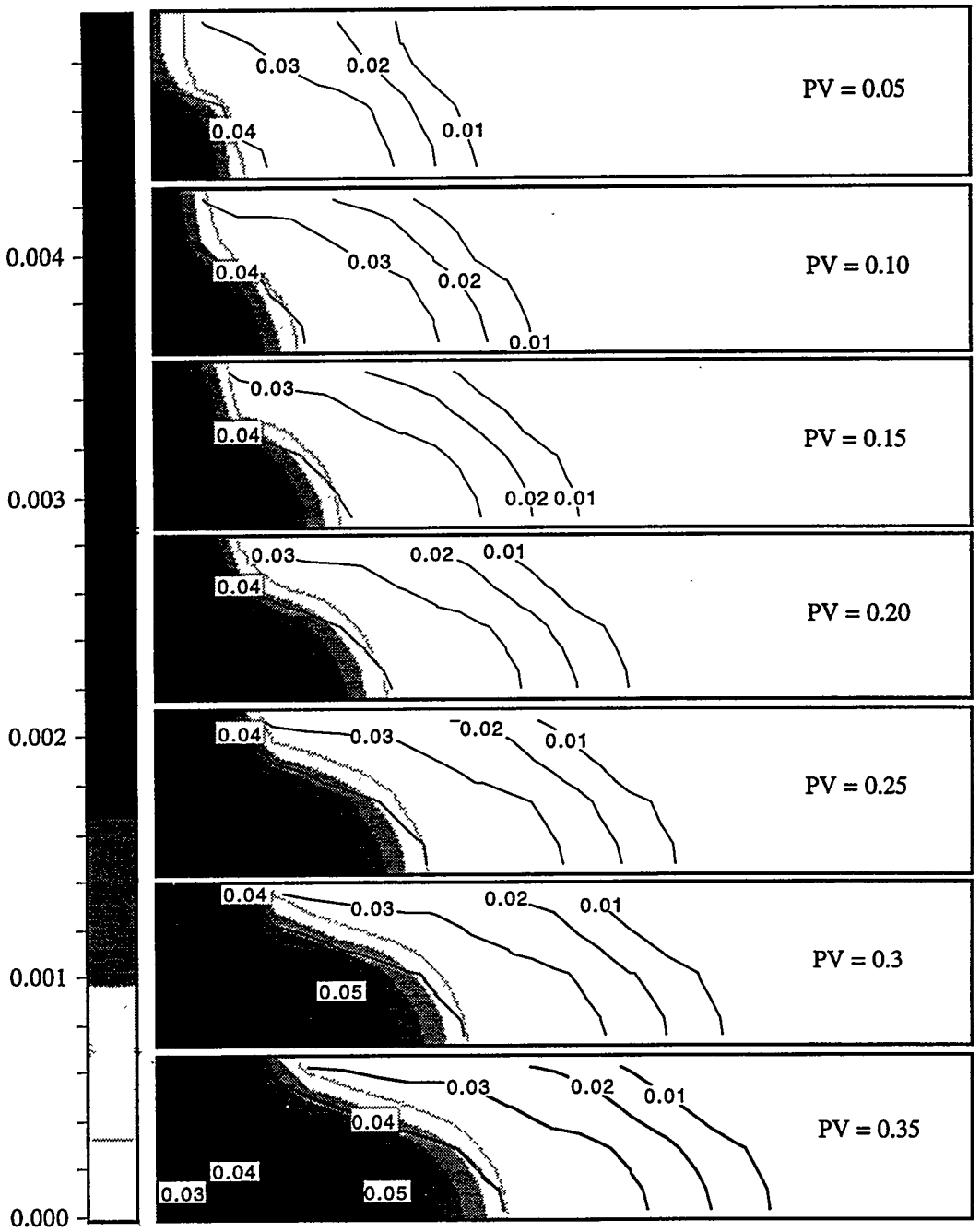


Figure 2.81 Profiles of surfactant concentration overlaid by polymer concentration contours in wt% for 2-D cross sectional simulations

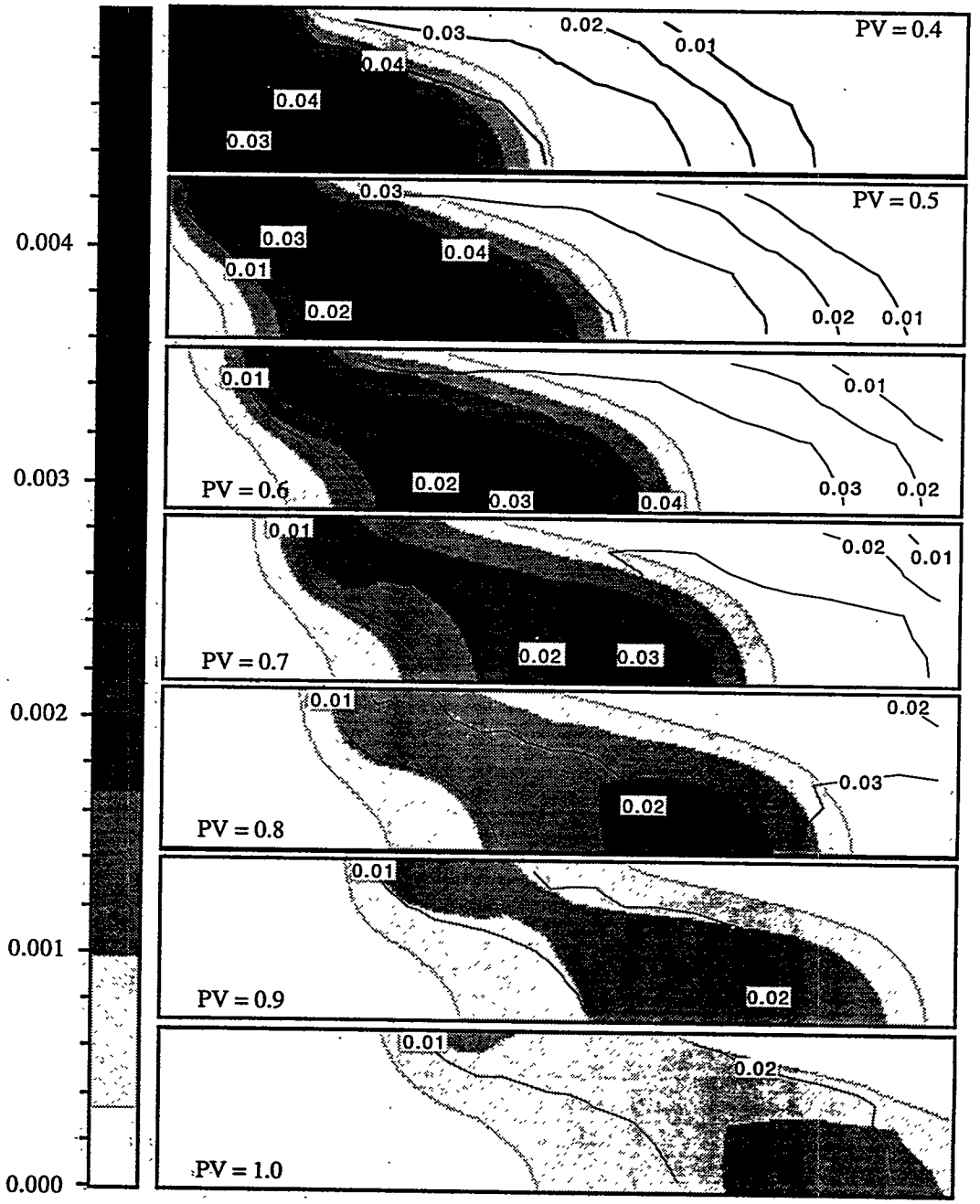


Figure 2.81 (Continued) Profiles of surfactant concentration overlaid by polymer concentration contours in wt% for 2-D cross sectional simulations

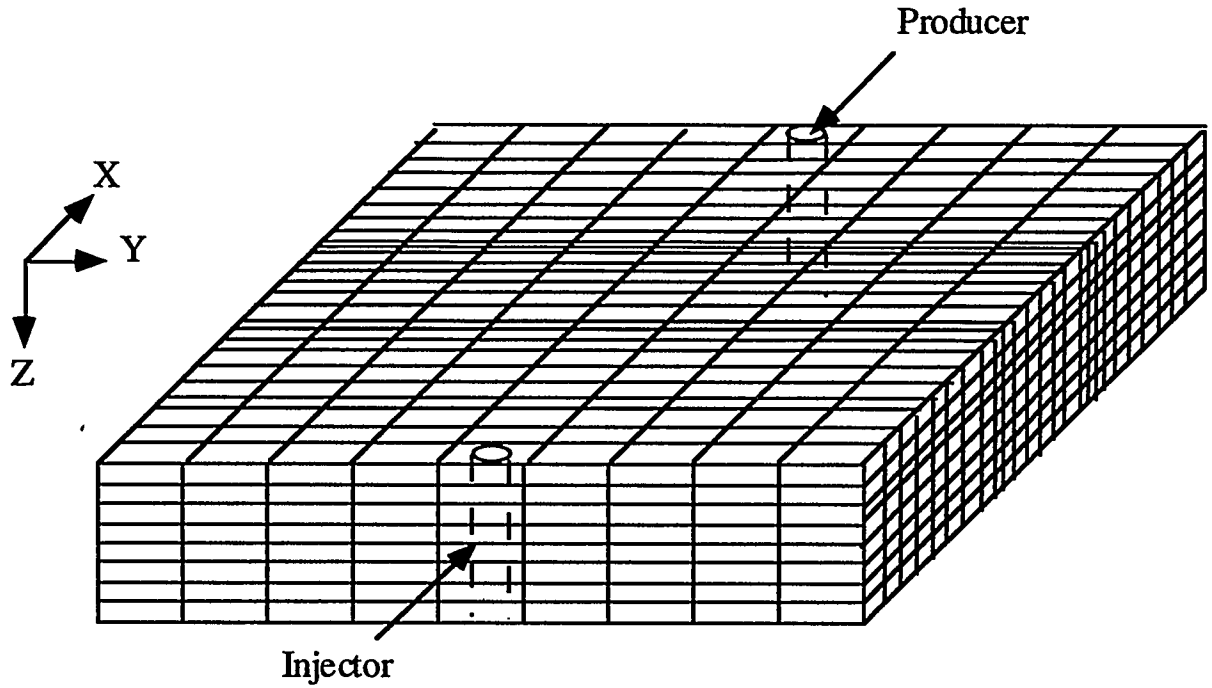


Figure 2.82 Schematic of 3-D simulation grids

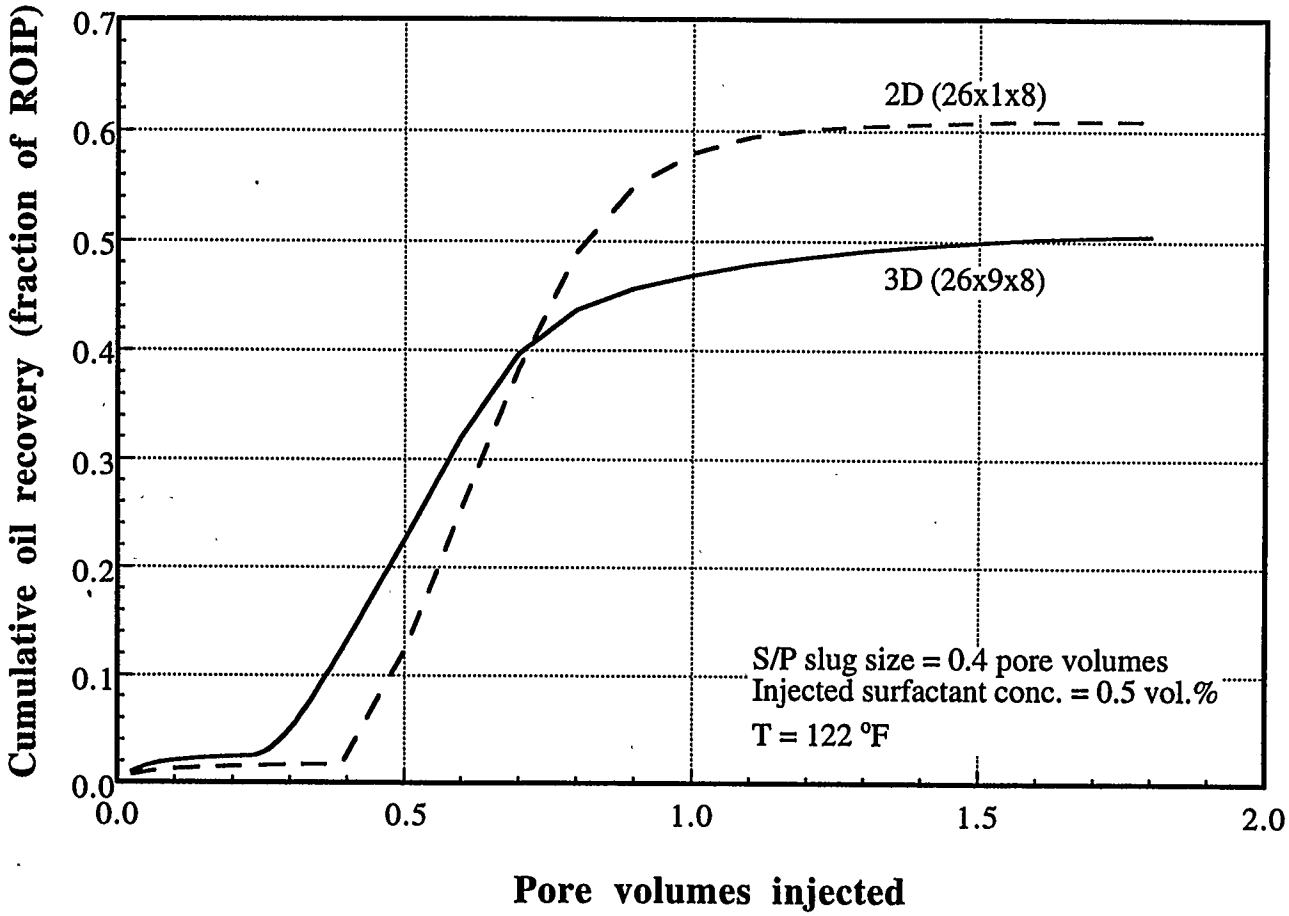


Figure 2.83 Comparison of 3D and 2D surfactant/polymer simulations

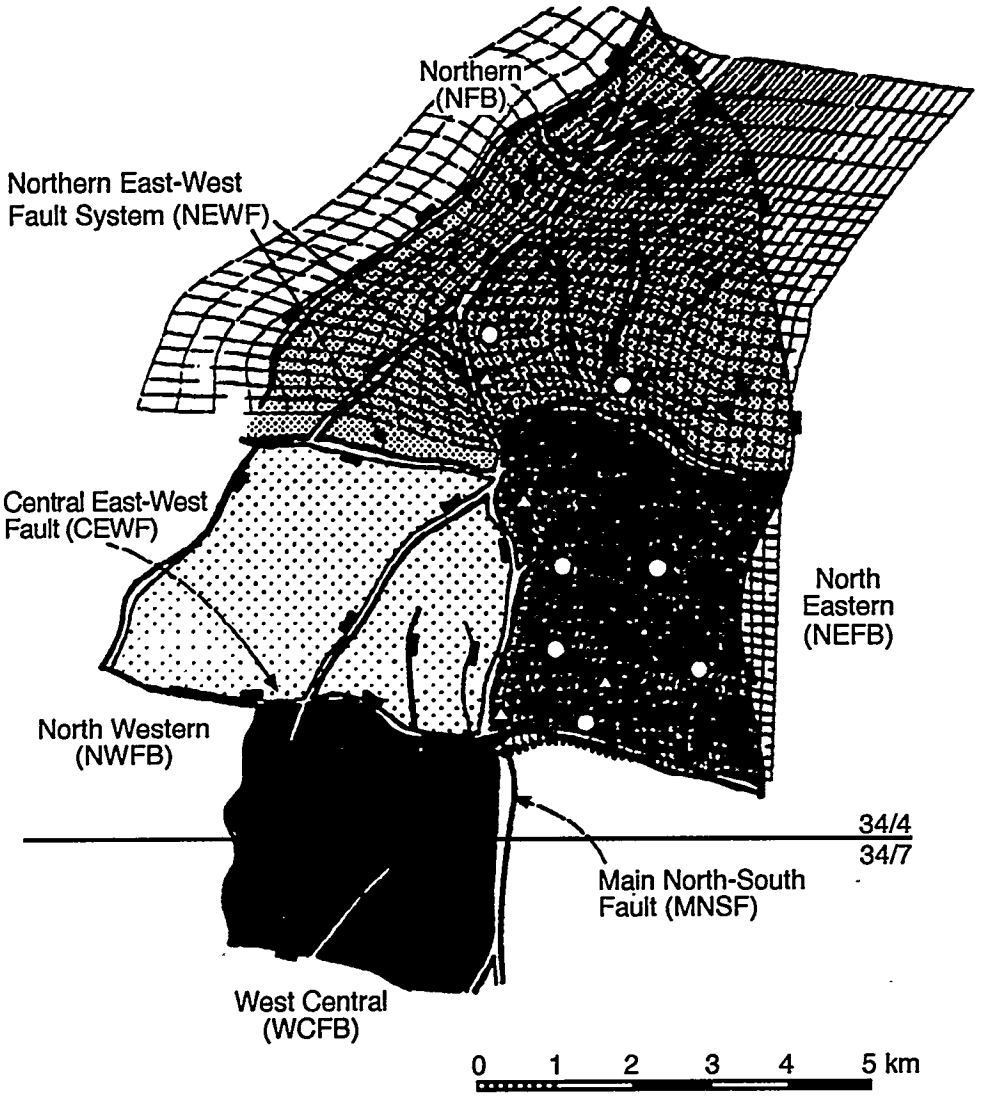


Figure 2.84 The location of the Reservoir B

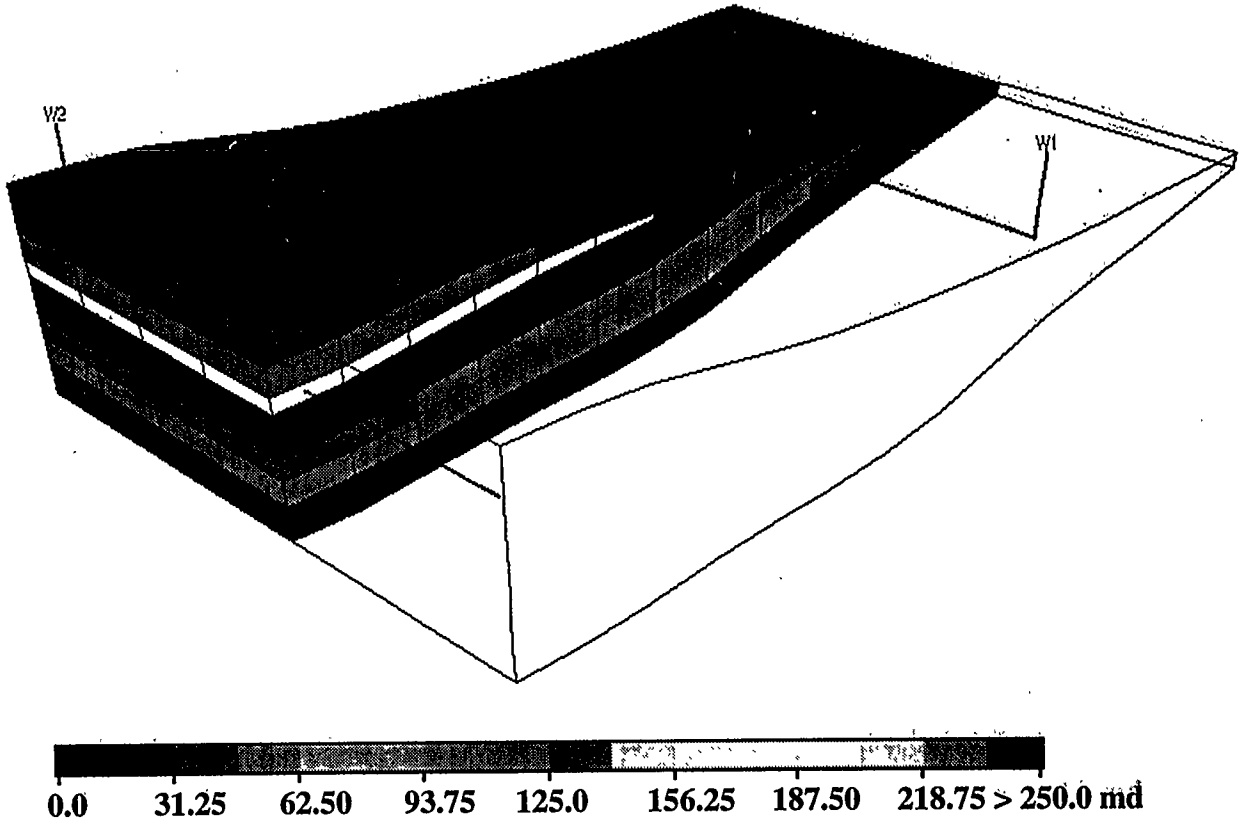


Figure 2.85 Permeability distribution for reservoir B

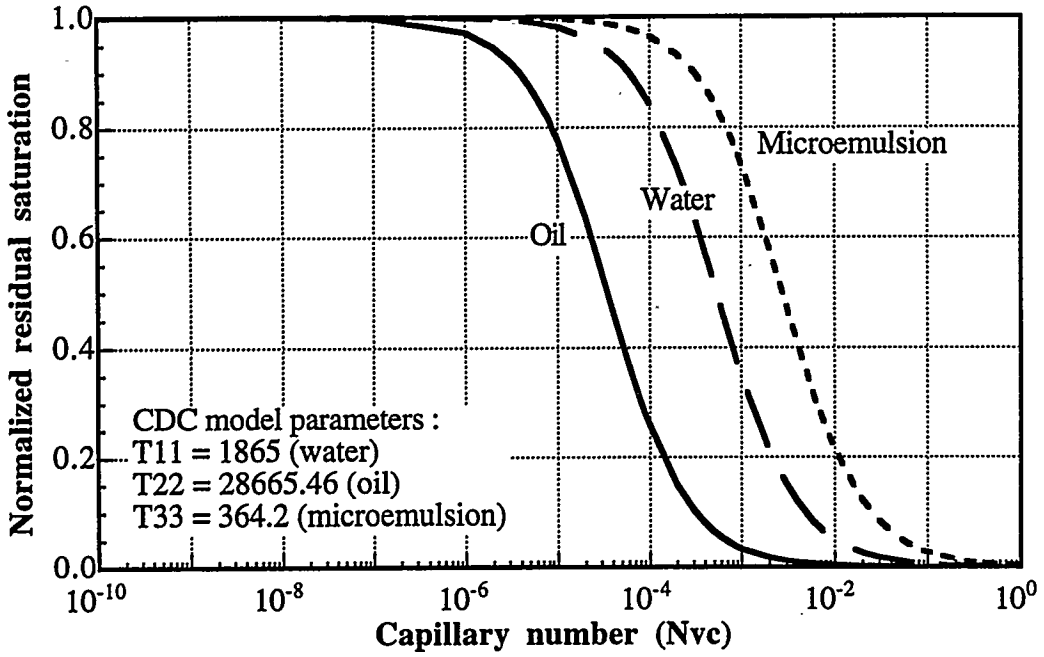


Figure 2.86 Capillary desaturation curves

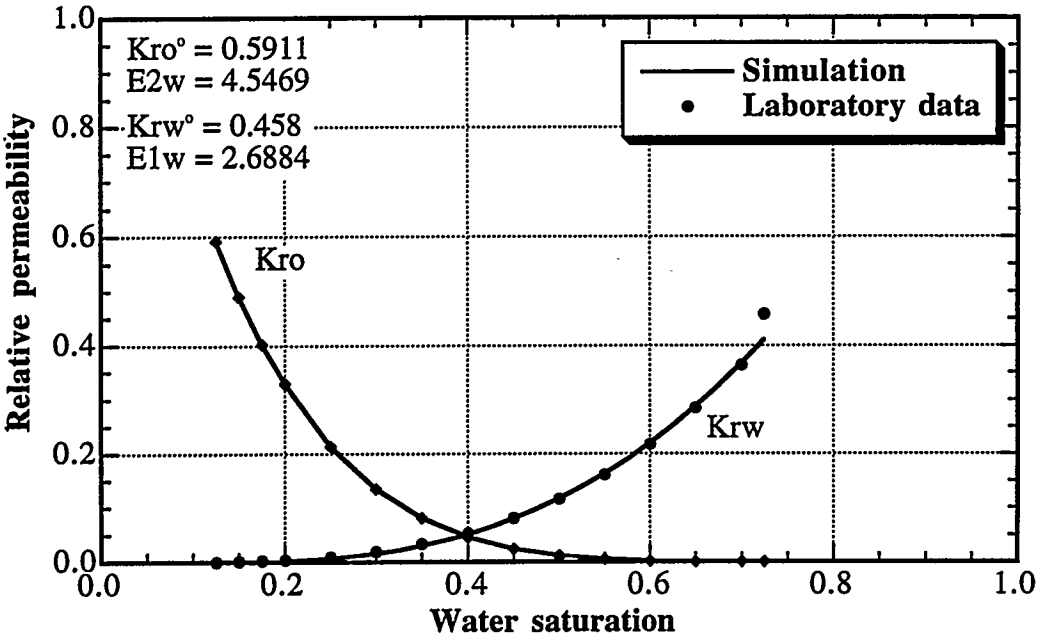


Figure 2.87 Low capillary number oil and water relative permeability curves

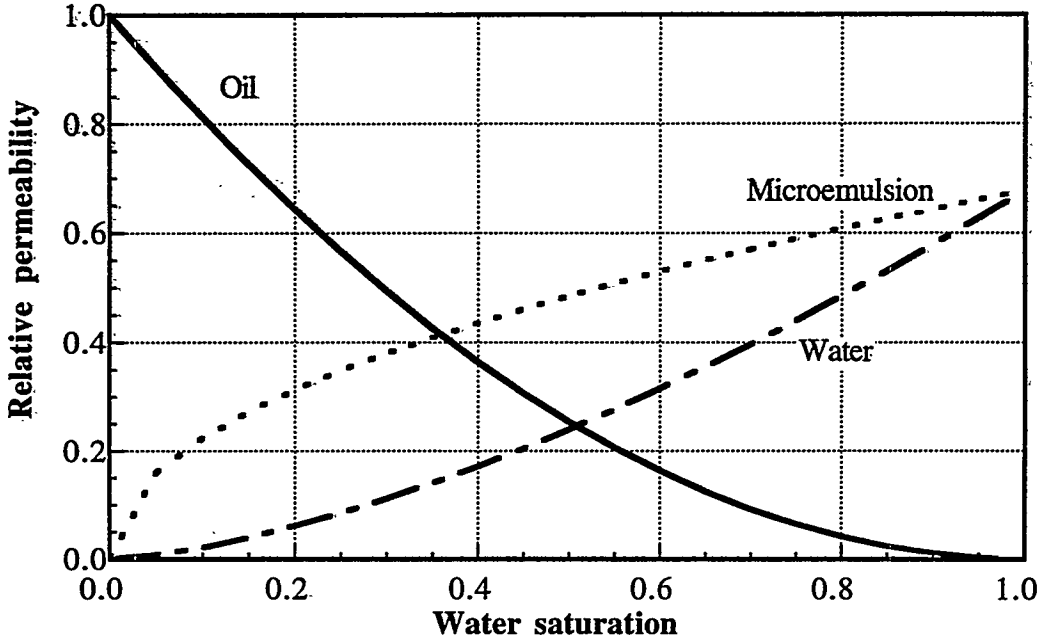


Figure 2.88 Phase relative permeability at high capillary number as a function of water saturation

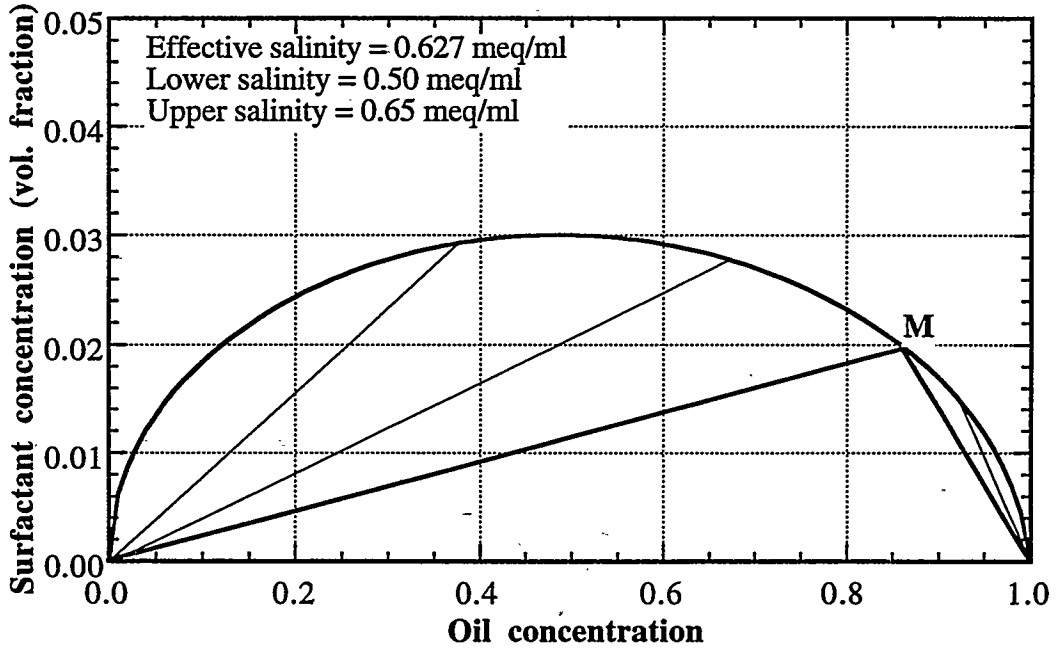


Figure 2.89 Type III ternary diagram

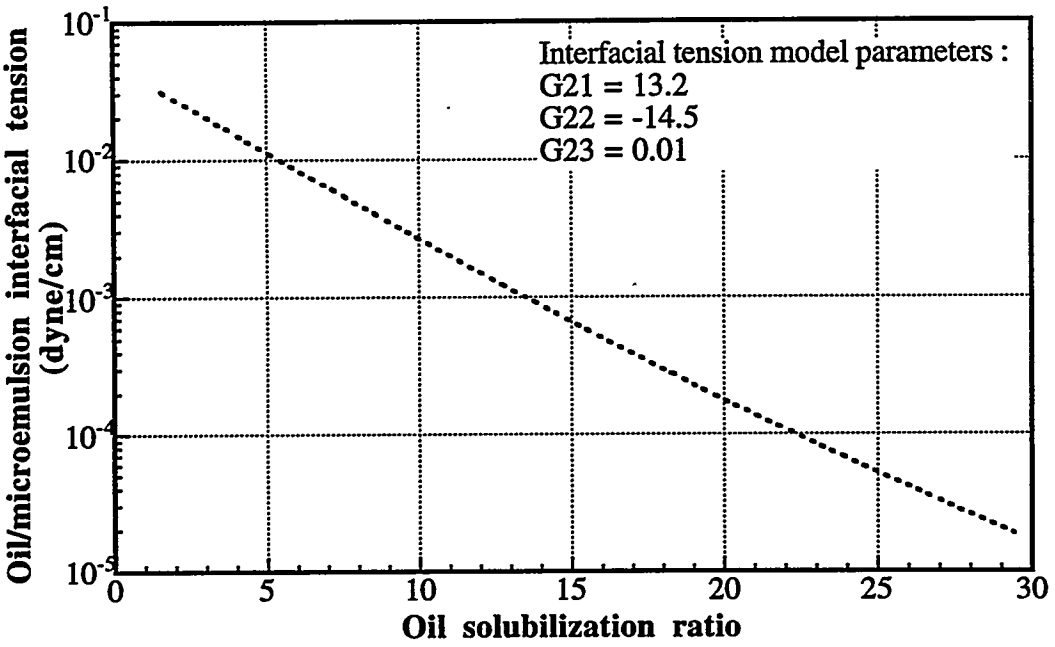


Figure 2.90 Interfacial tension as a function of oil solubilization ratio

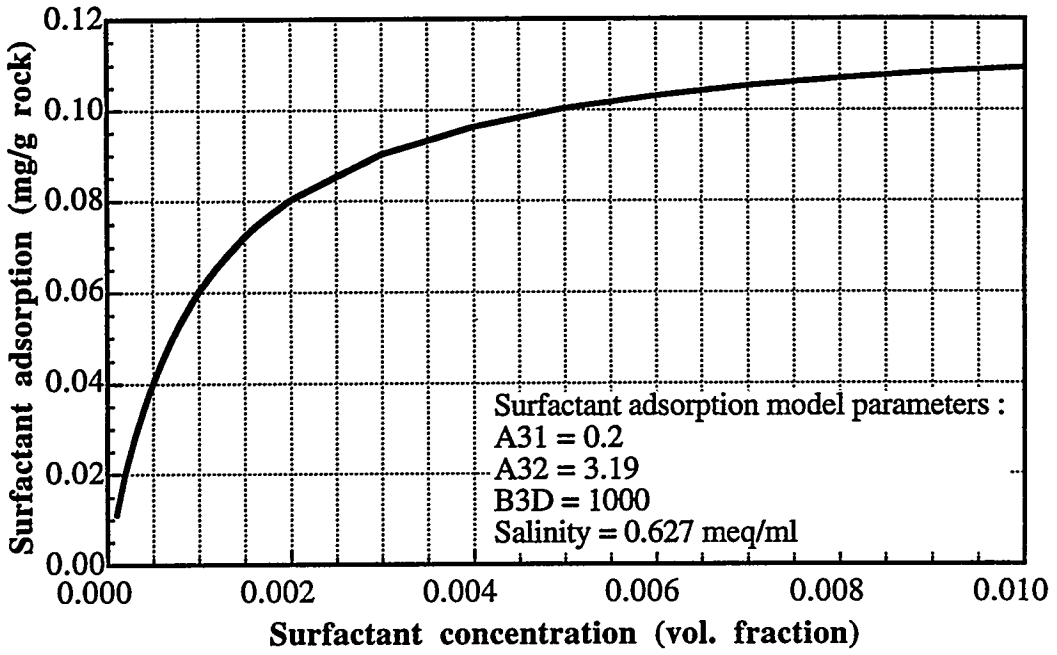


Figure 2.91 Surfactant adsorption isotherm

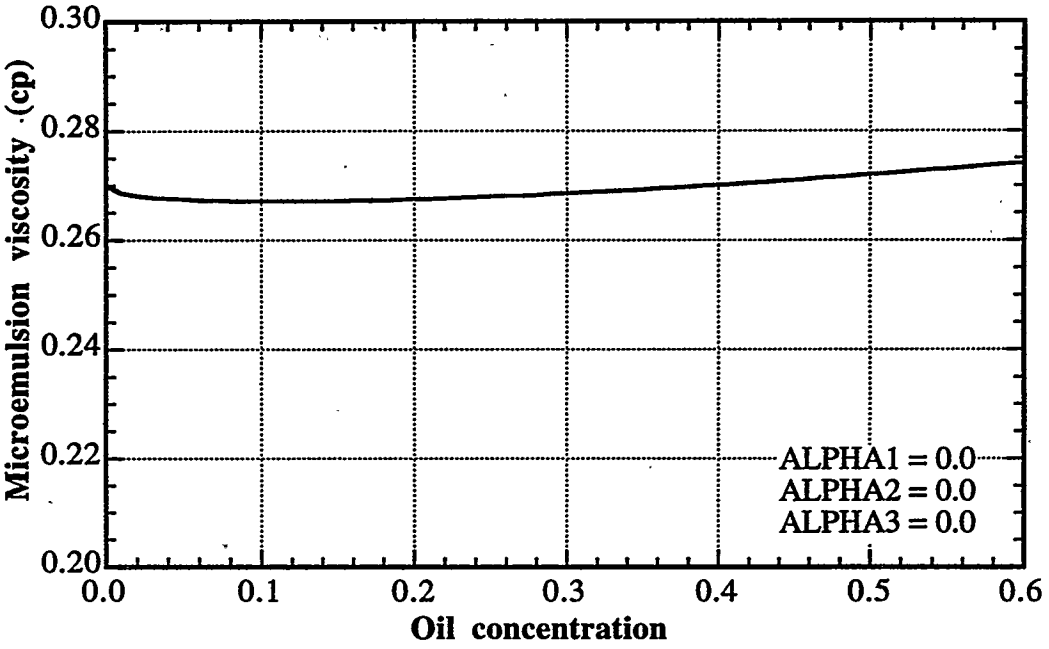


Figure 2.92 Microemulsion viscosity as a function of oil concentration

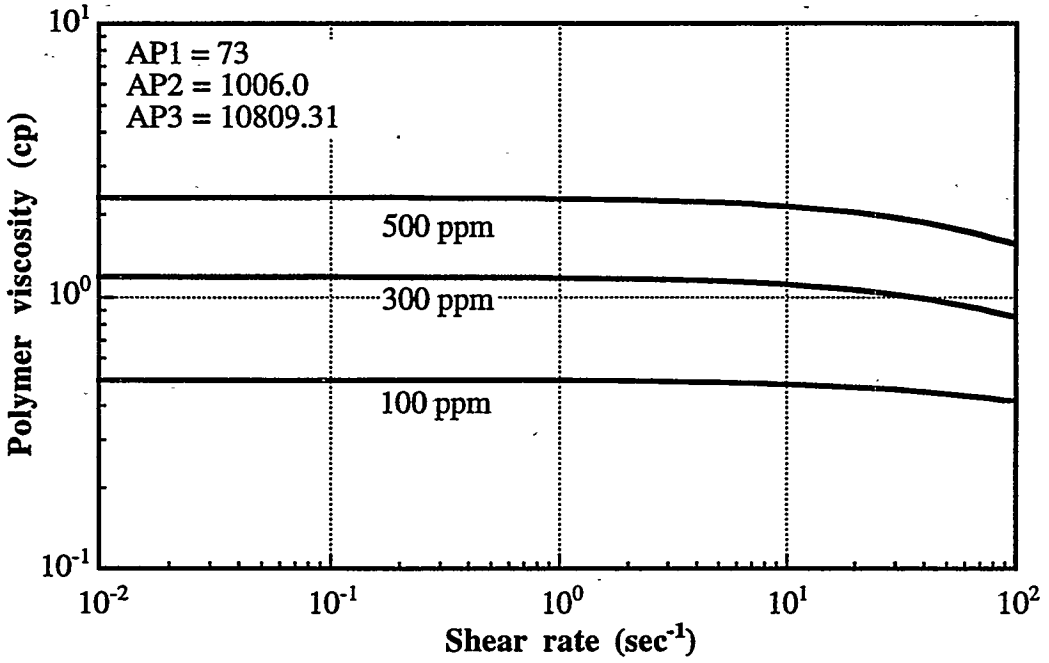


Figure 2.93 Viscosity of xanthan polymer as a function of shear rate

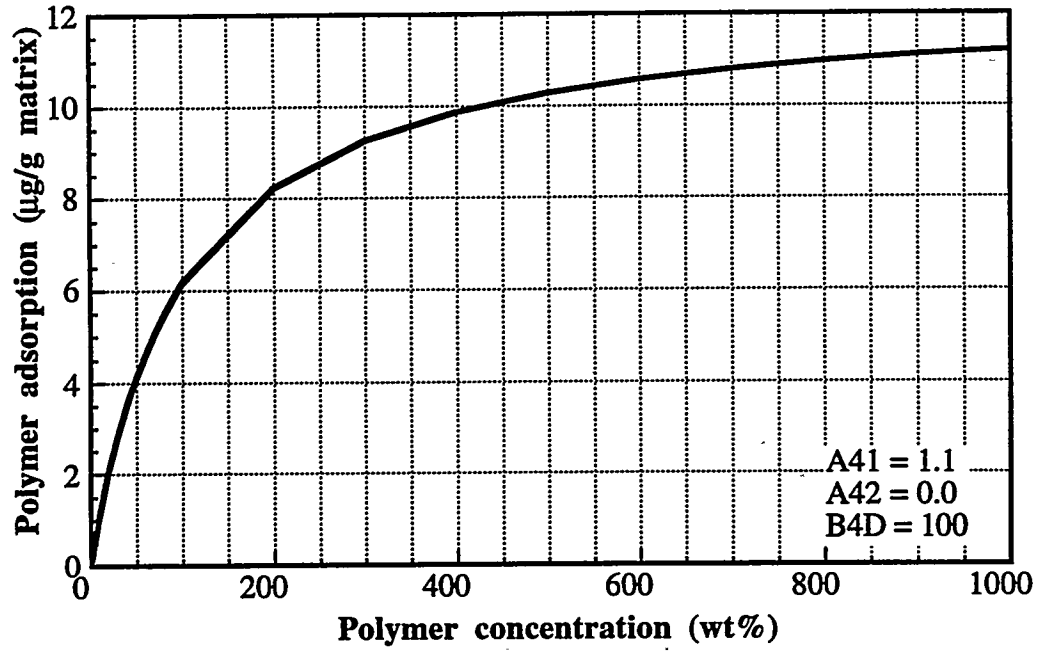


Figure 2.94 Polymer adsorption isotherm

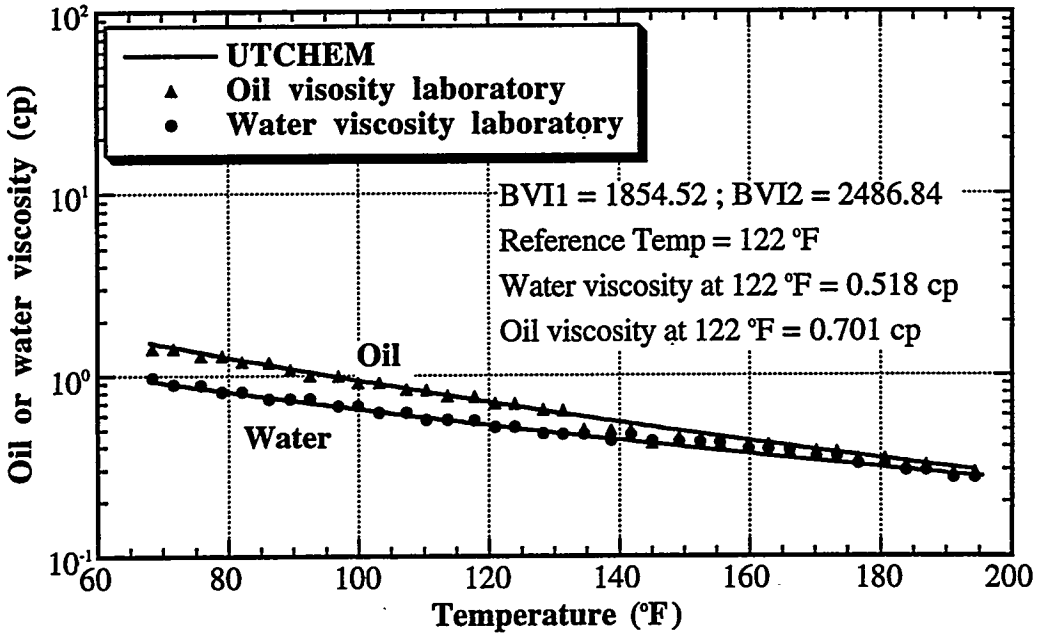


Figure 2.95 Oil and water viscosity as a function of temperature

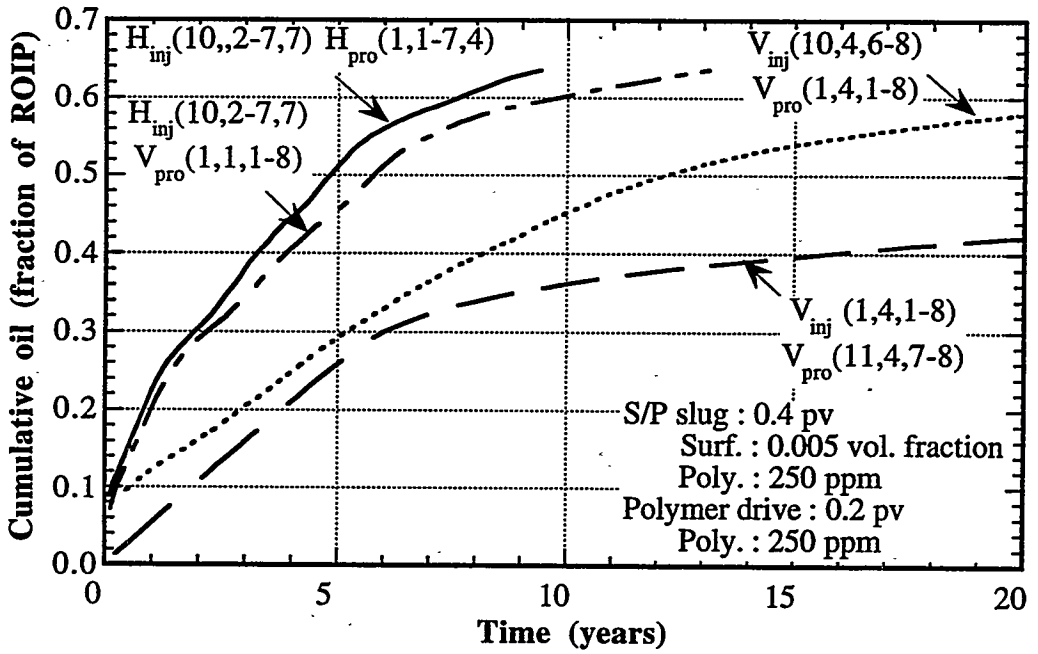


Figure 2.96 Effect of well type and location on oil recovery

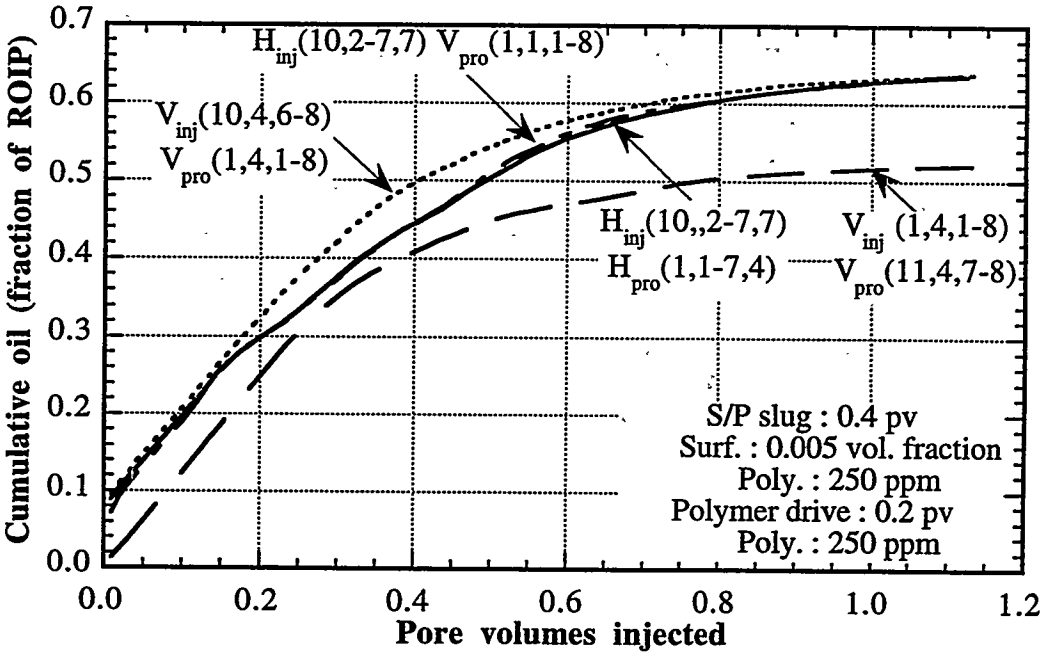


Figure 2.97 Effect of well type and location on oil recovery

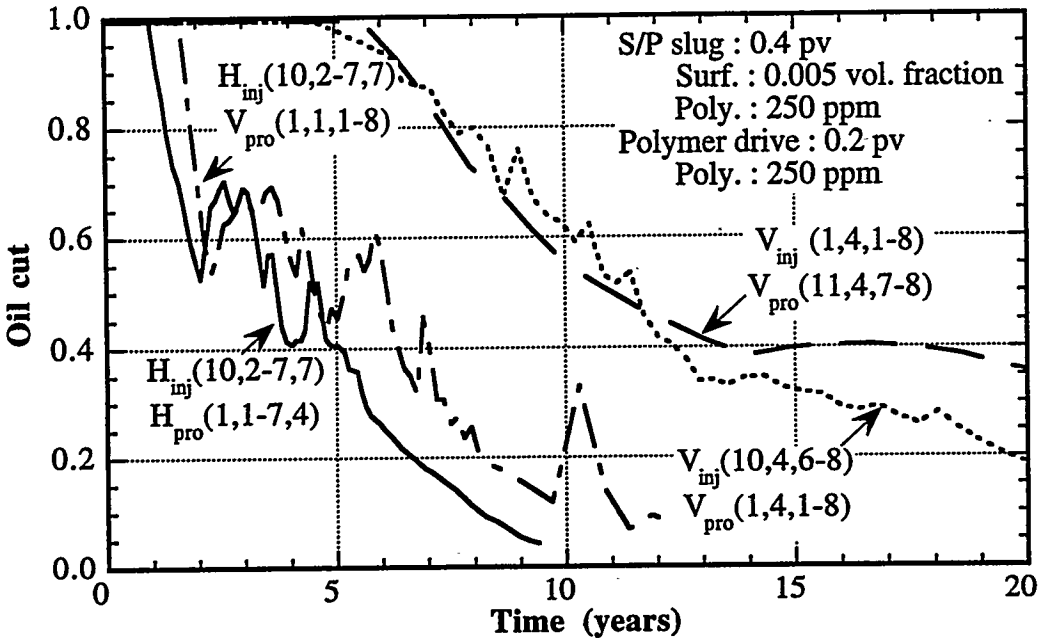


Figure 2.98 Effect of well type and location on oil cut

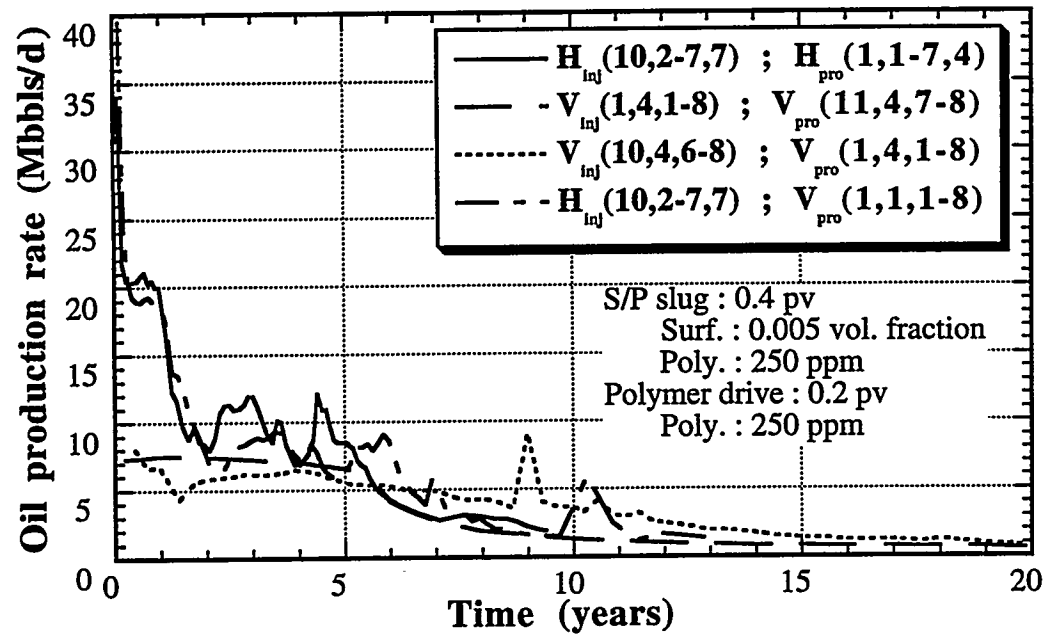


Figure 2.99 Effect of well type and location on oil production rate

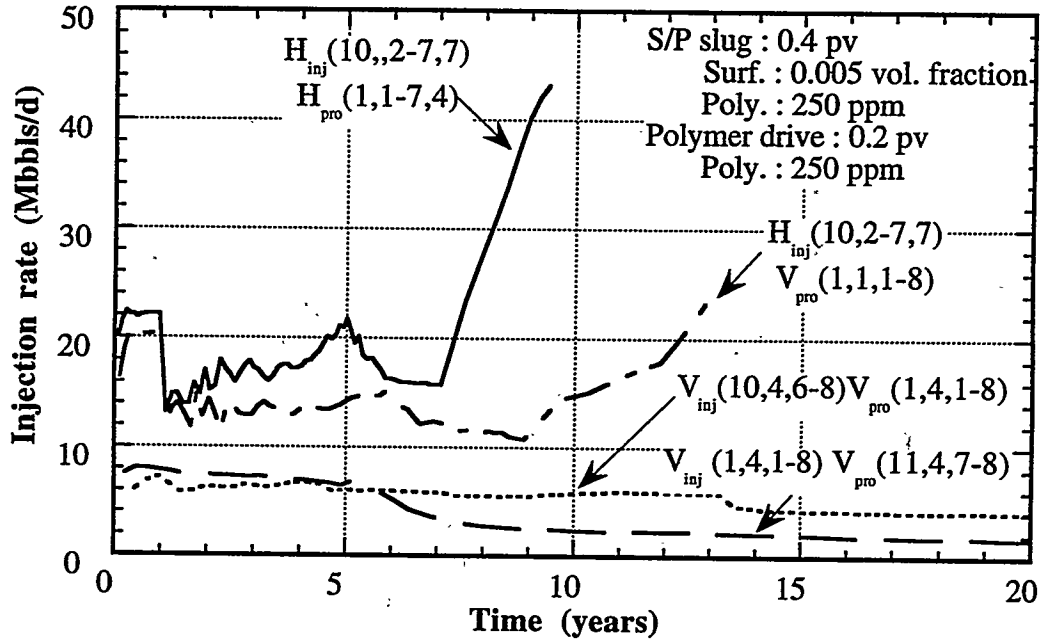


Figure 2.100 Effect of well type and location on oil cut

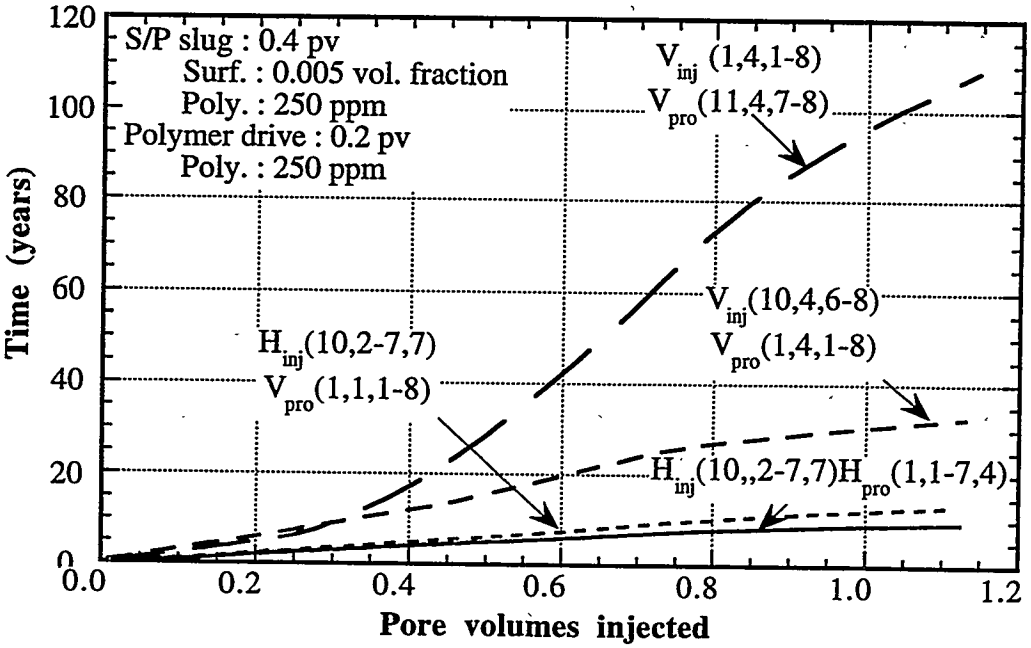


Figure 2.101 Effect of well type and location on project life

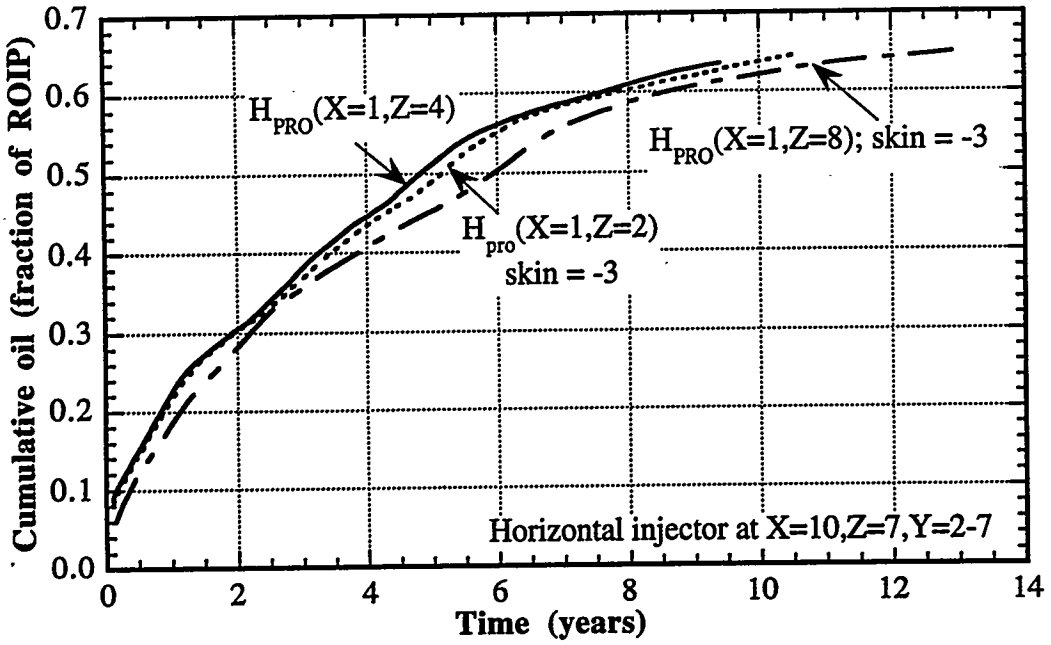


Figure 2.102 Effect of location of producer on oil recovery

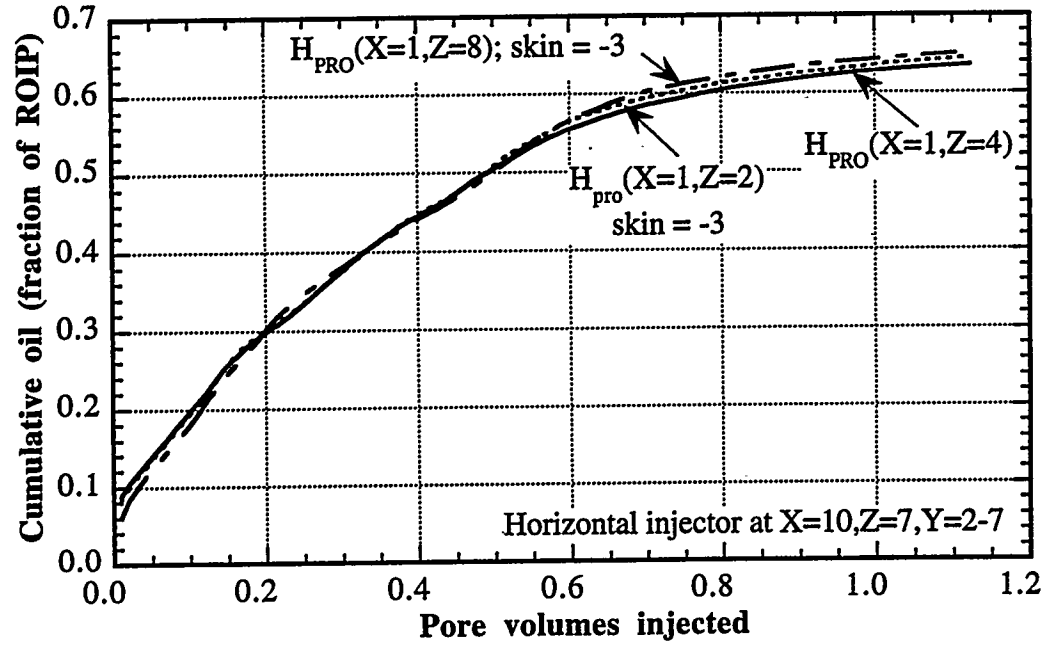


Figure 2.103 Effect of location of producer on oil recovery

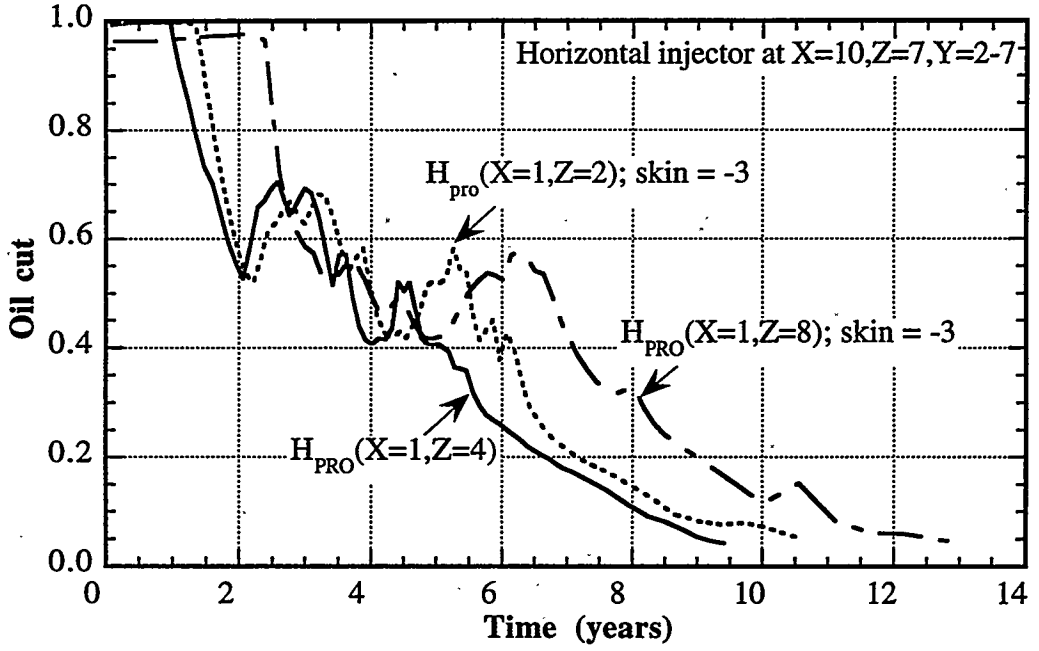


Figure 2.104 Effect of location of producer on oil cut

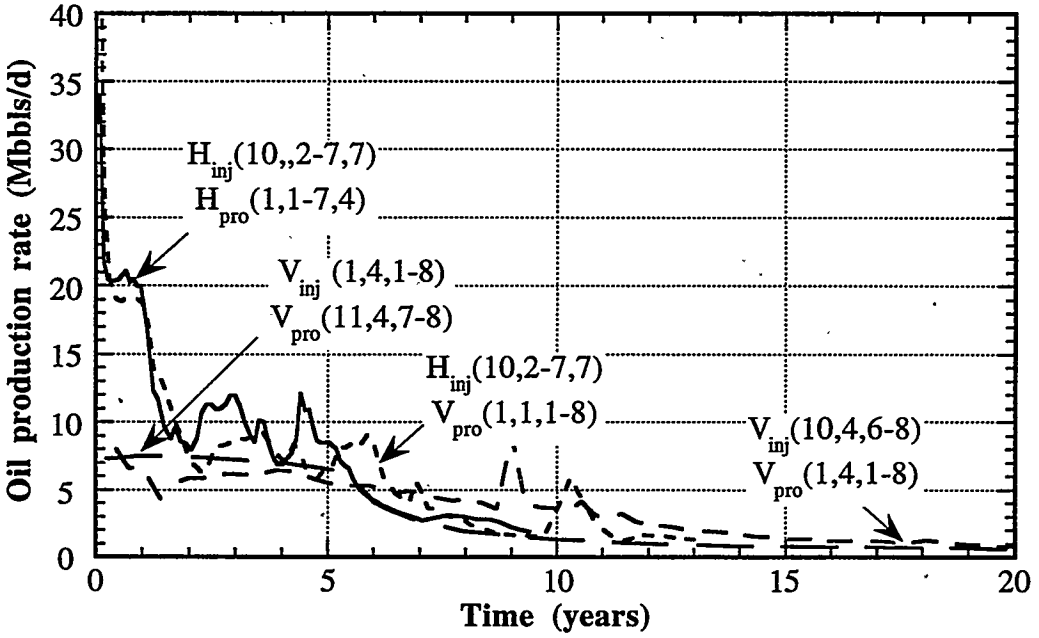


Figure 2.105 Effect of location of producer on oil production rate

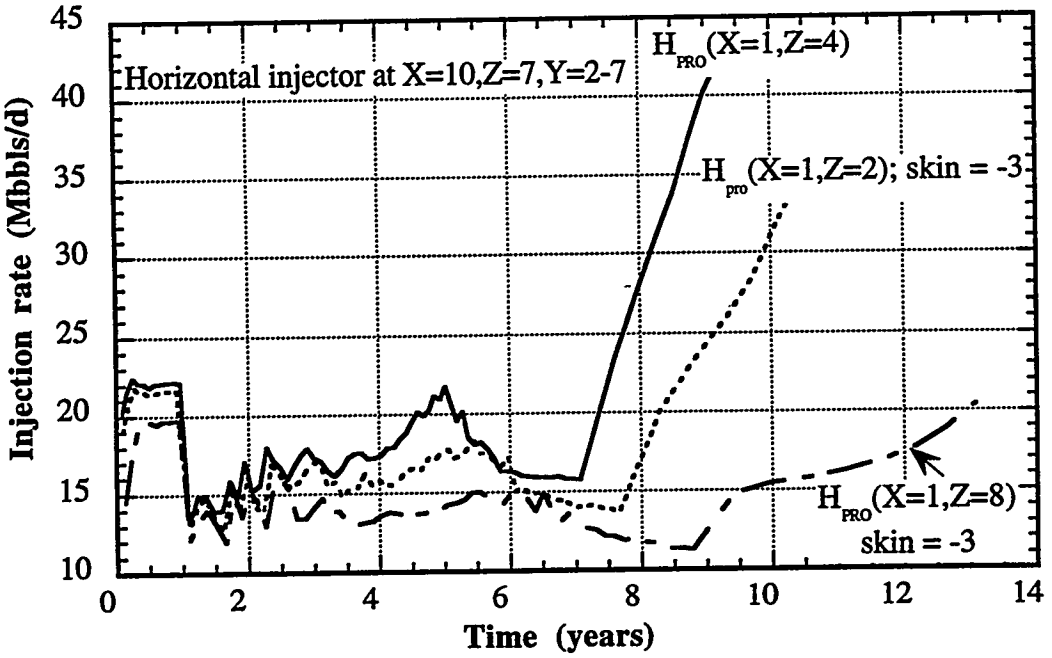


Figure 2.106 Effect of location of producer on injection rate

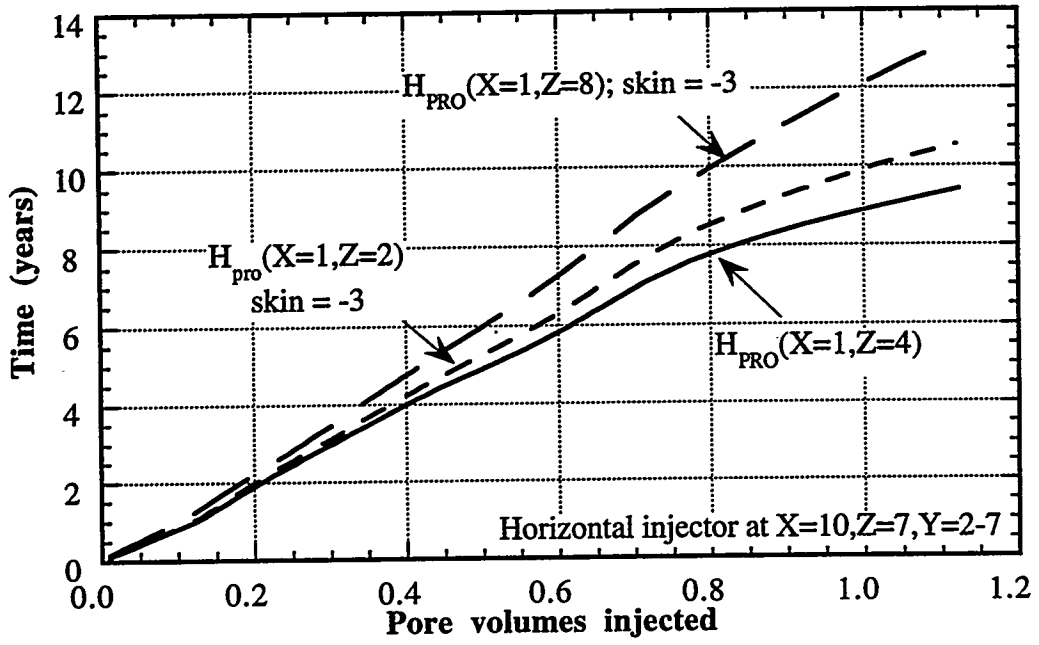


Figure 2.107 Effect of location of producer on project life

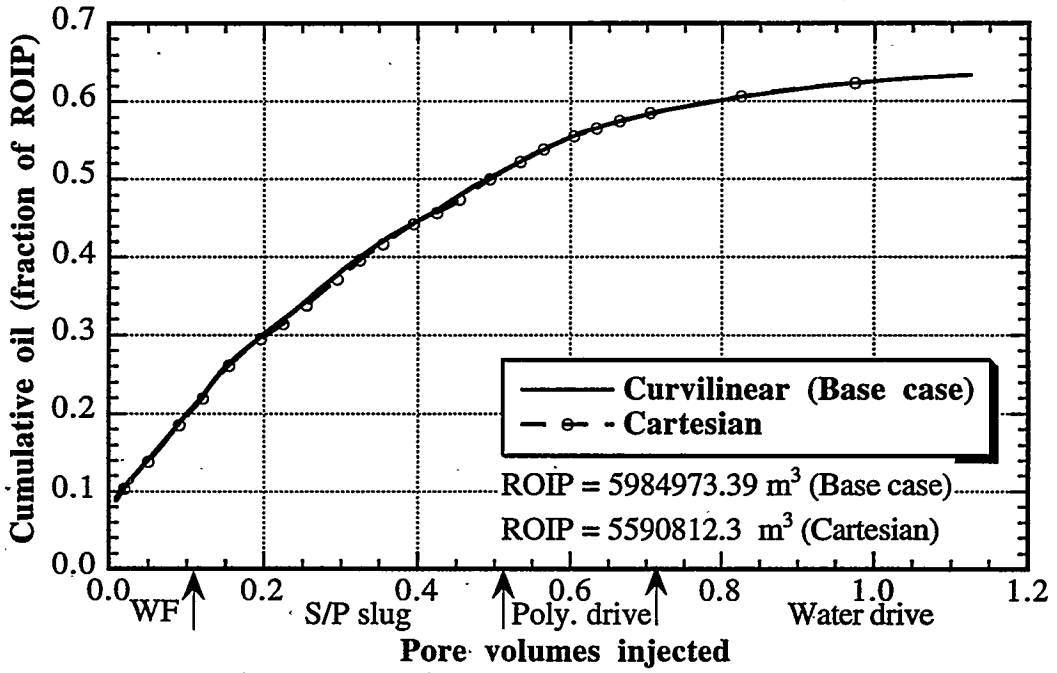


Figure 2.108 Effect of coordinate on oil recovery

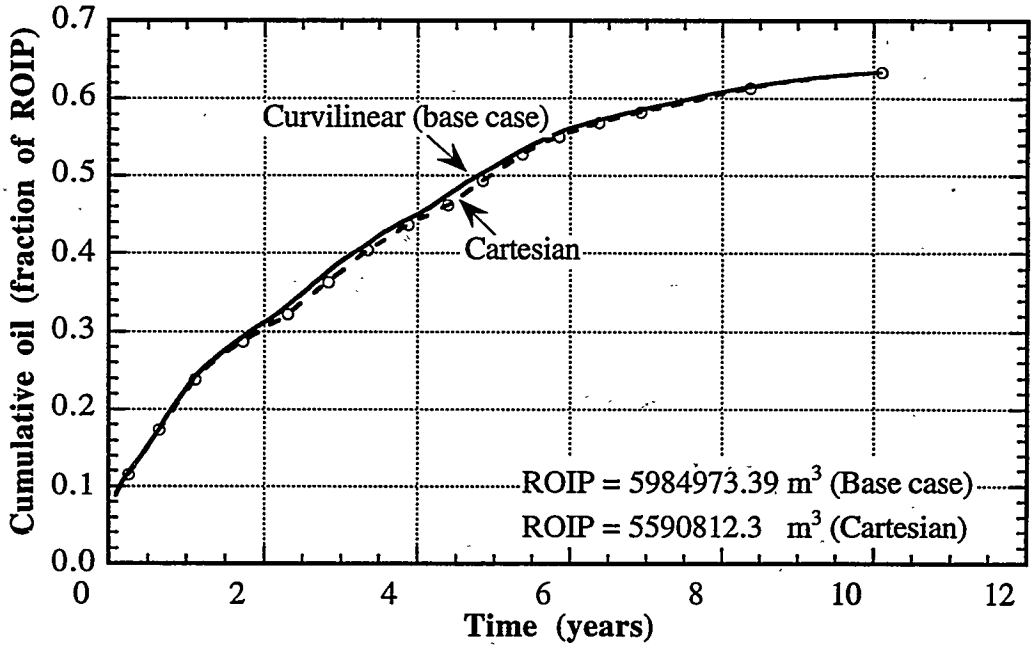


Figure 2.109 Effect of coordinate on oil recovery

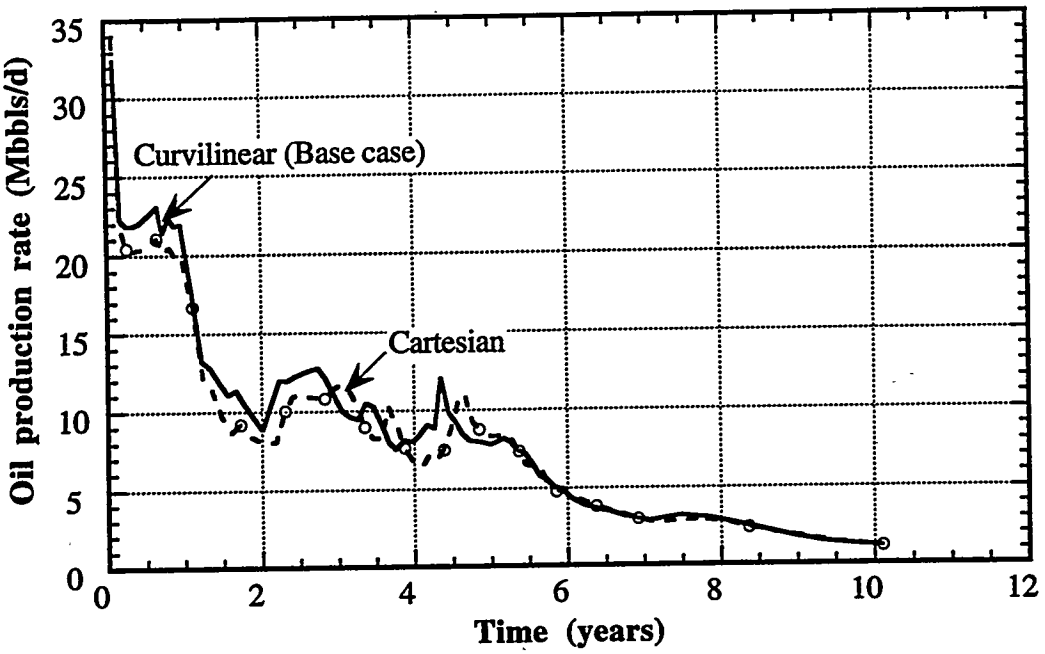


Figure 2.110 Effect of coordinate on oil production rate

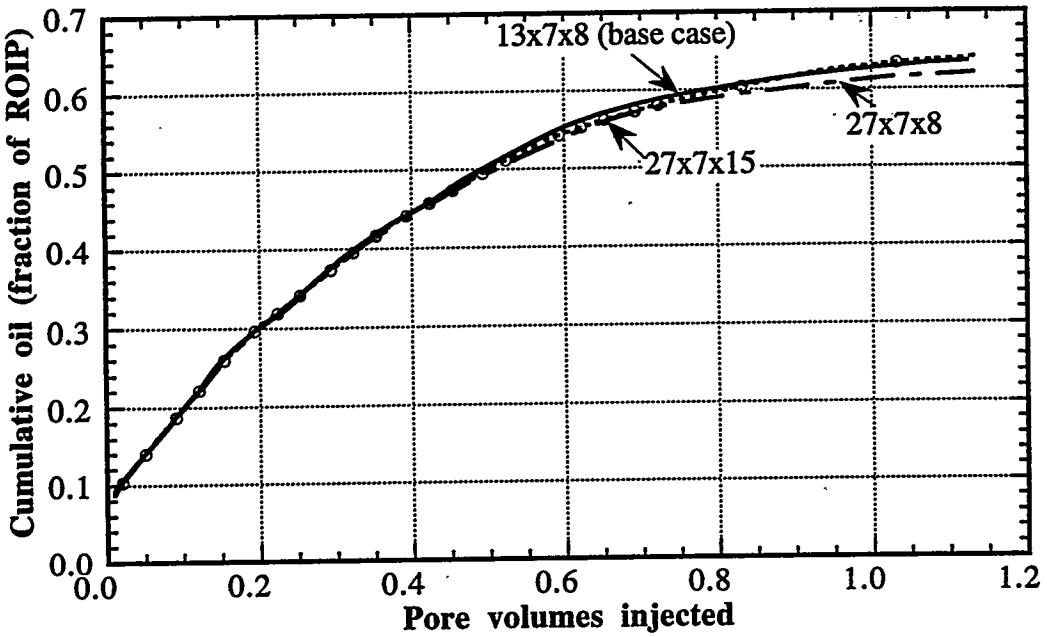


Figure 2.111 Effect of grid size on oil recovery

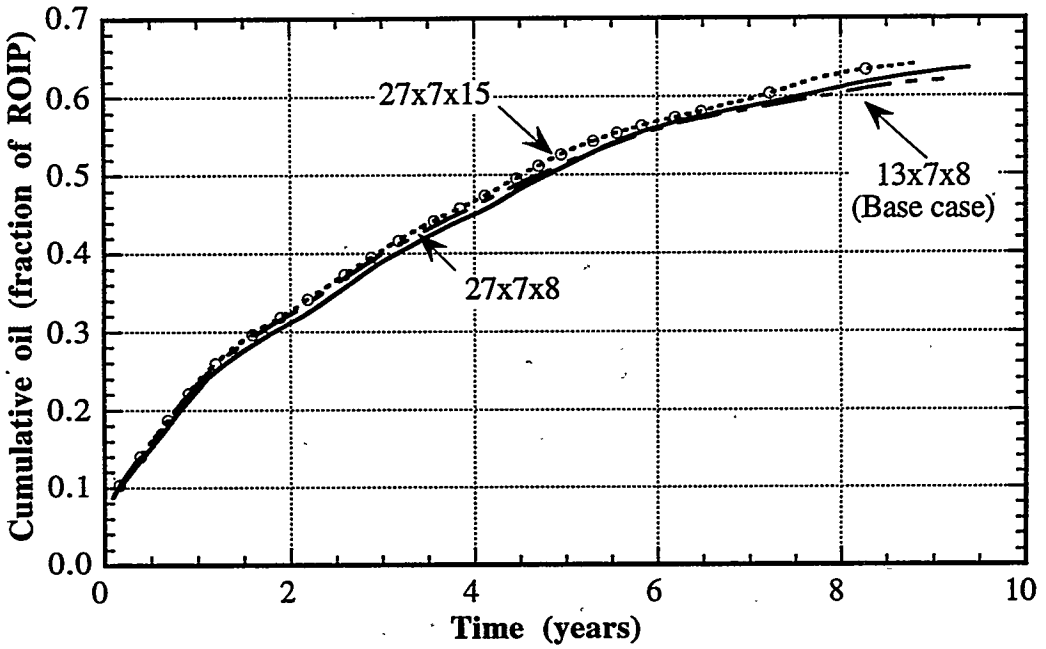


Figure 2.112 Effect of grid size on oil recovery

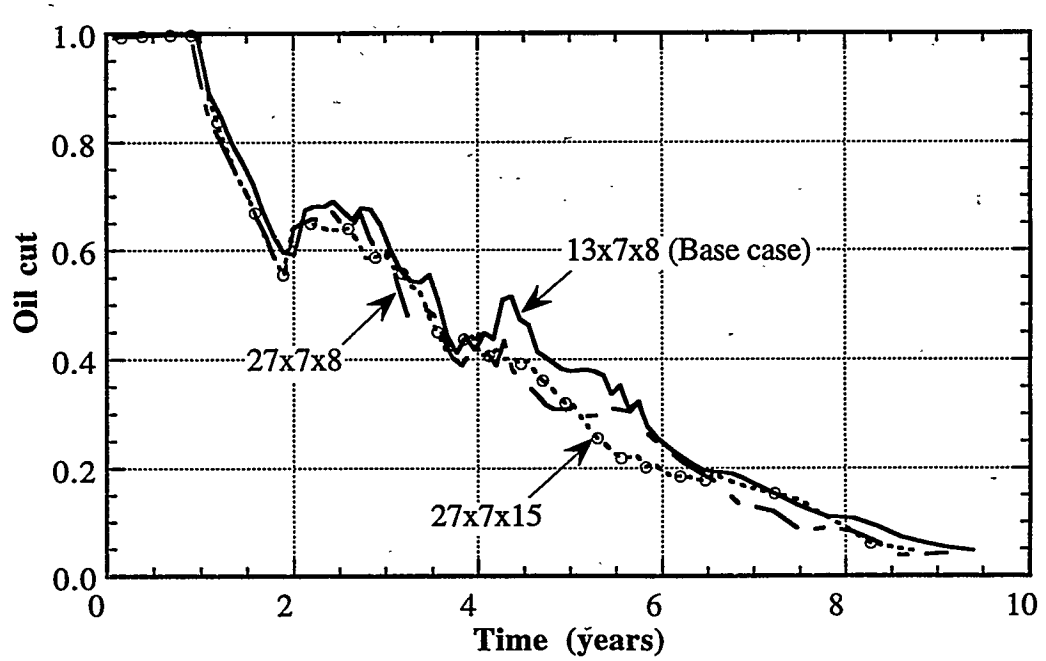


Figure 2.113 Effect of grid size on oil cut

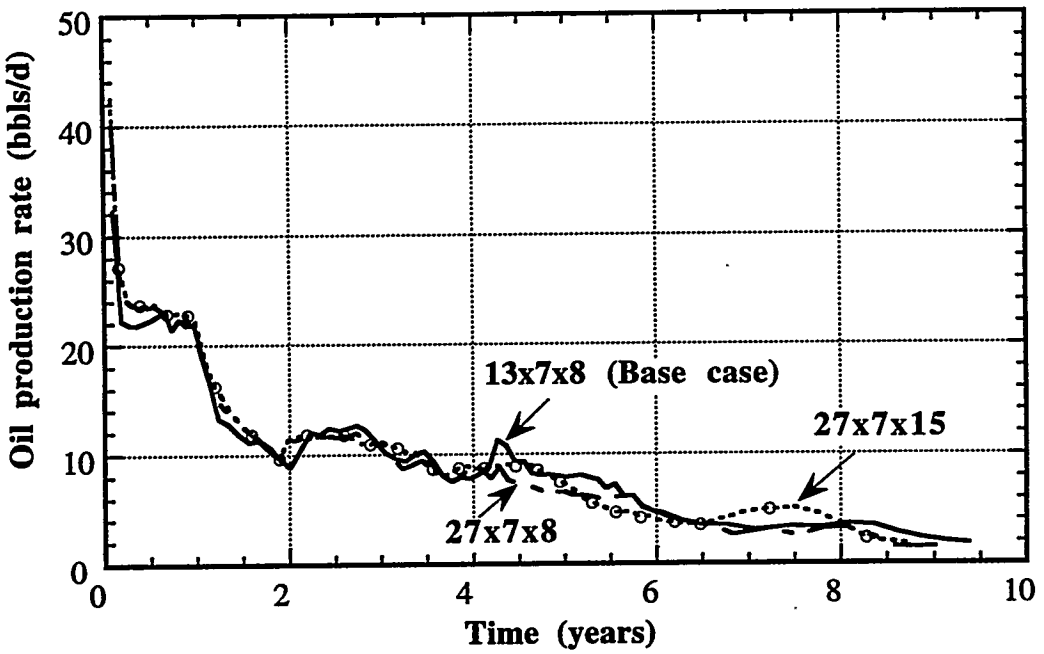


Figure 2.114 Effect of grid size on oil production rate

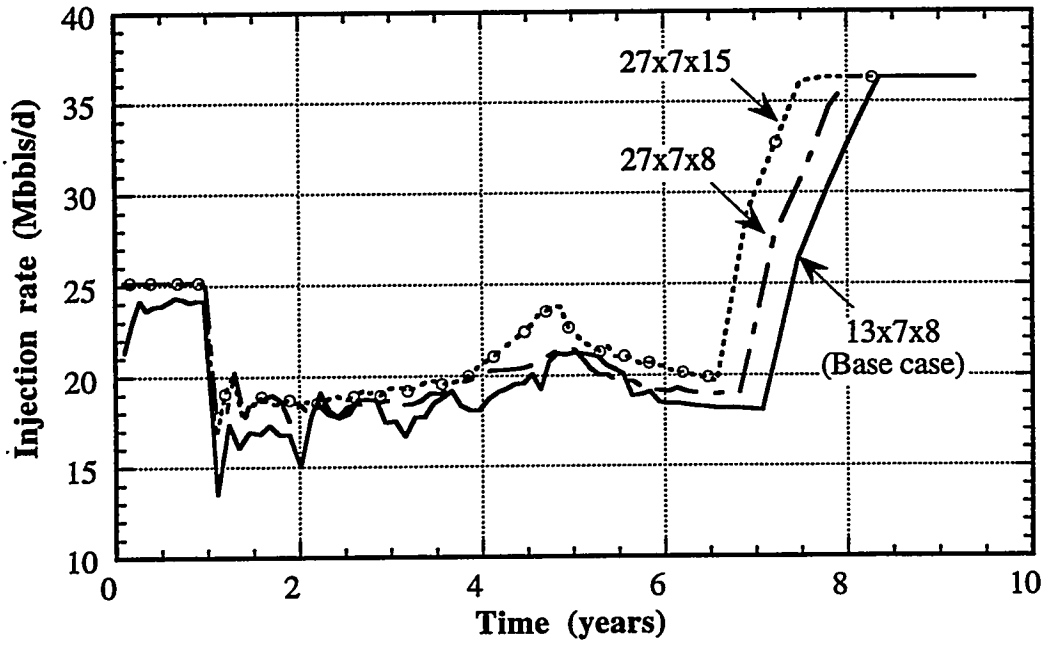


Figure 2.115 Effect of grid size on injection rate

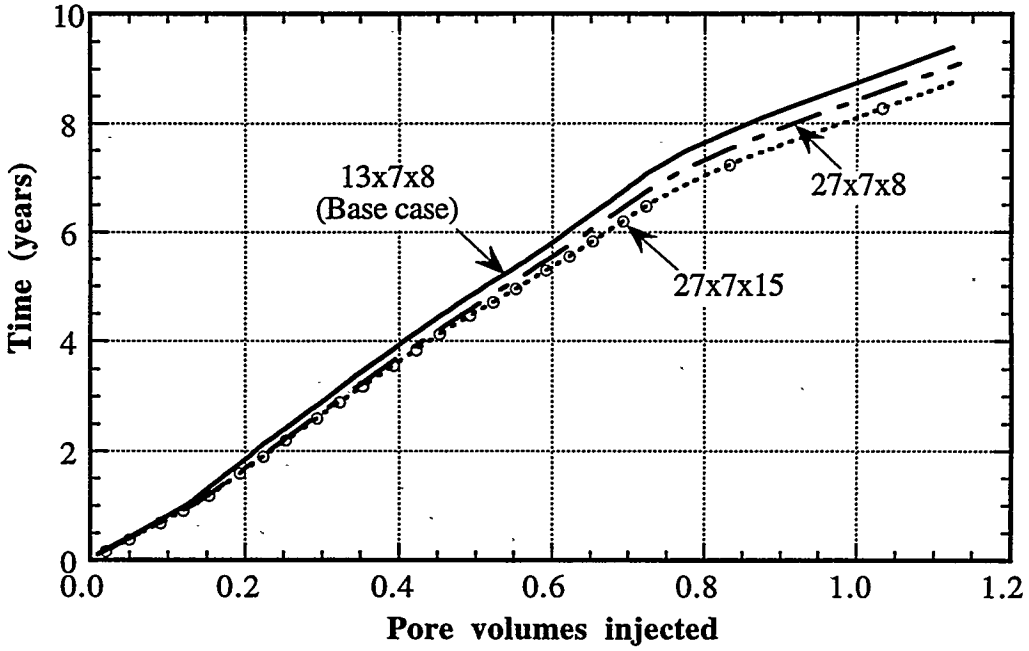


Figure 2.116 Effect of grid size on project life

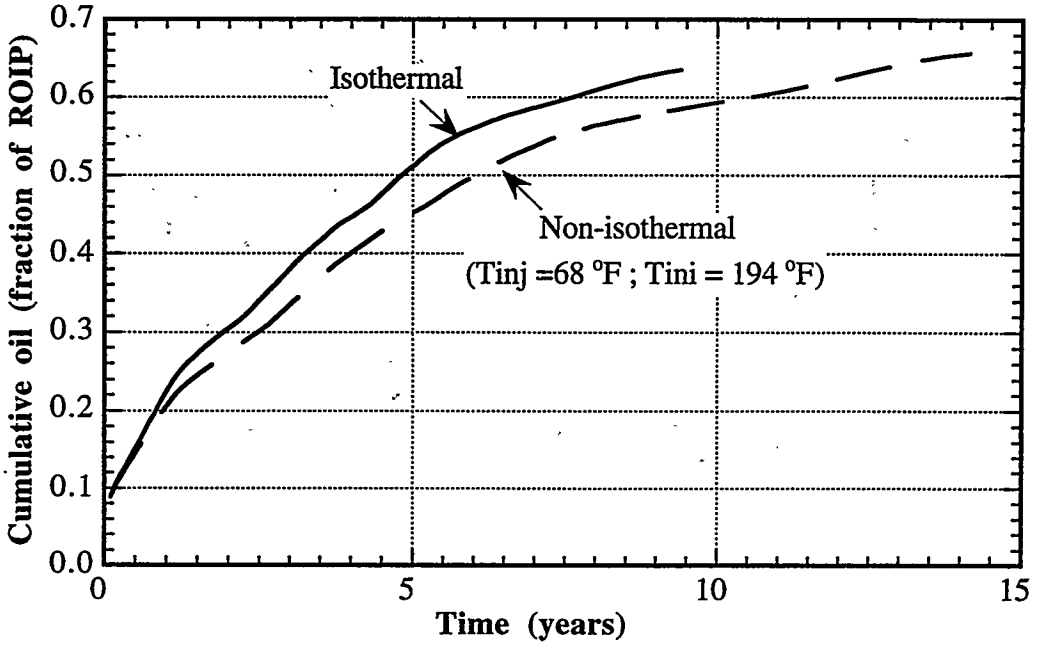


Figure 2.117 Effect of temperature on oil recovery

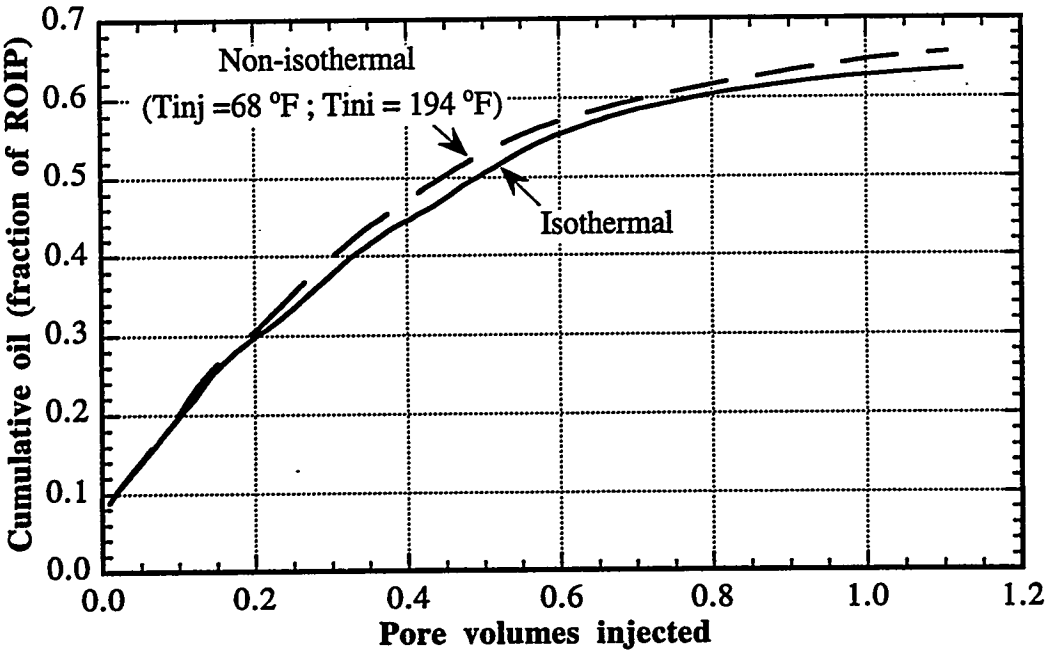


Figure 2.118 Effect of temperature on oil recovery

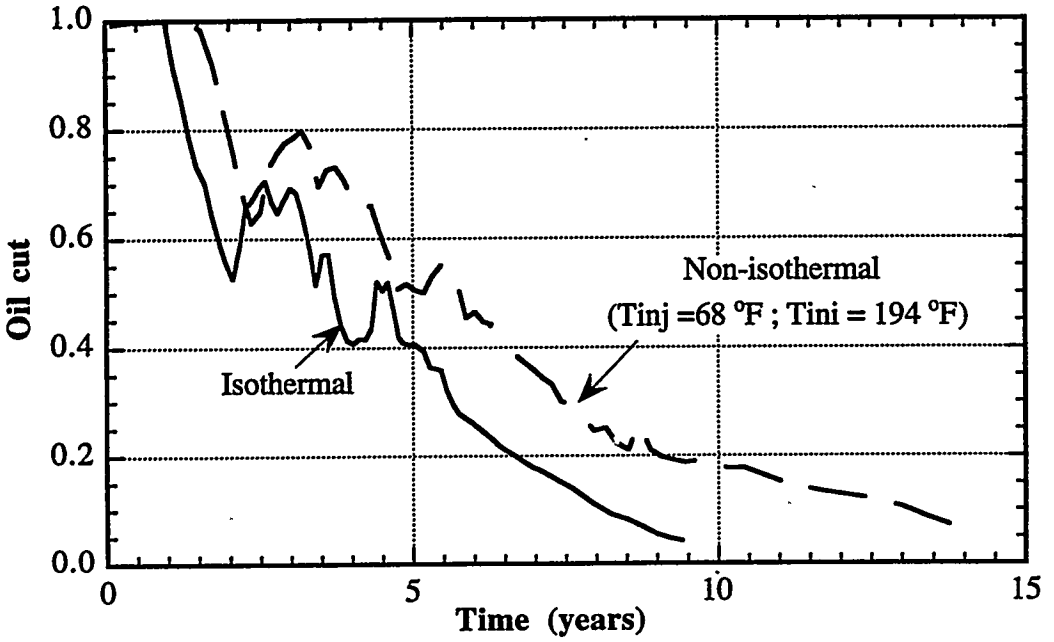


Figure 2.119 Effect of temperature on oil cut

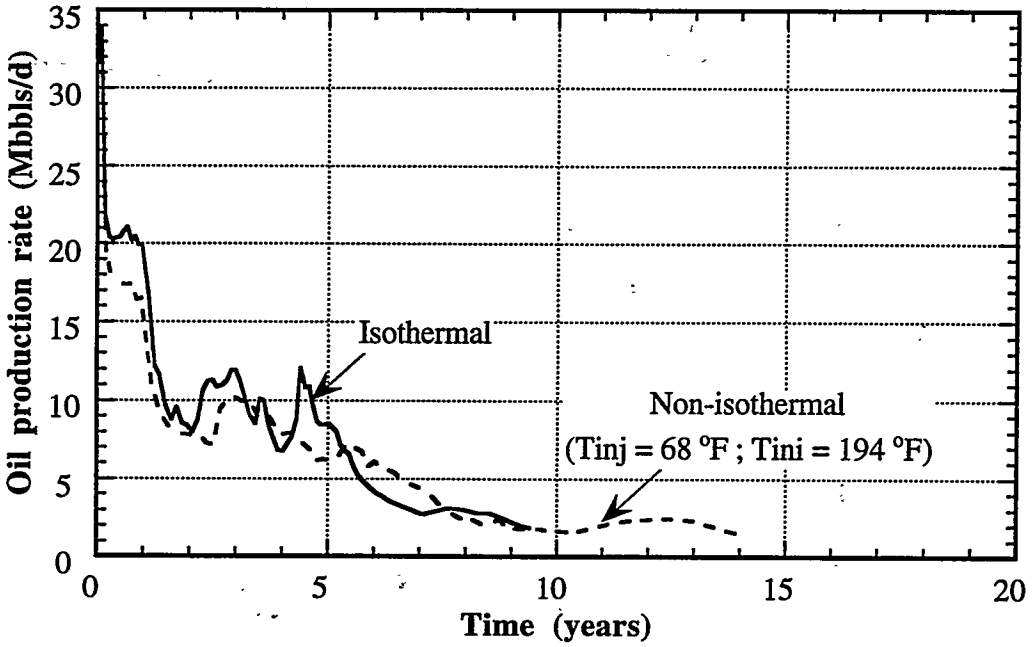


Figure 2.120 Effect of temperature on oil production rate

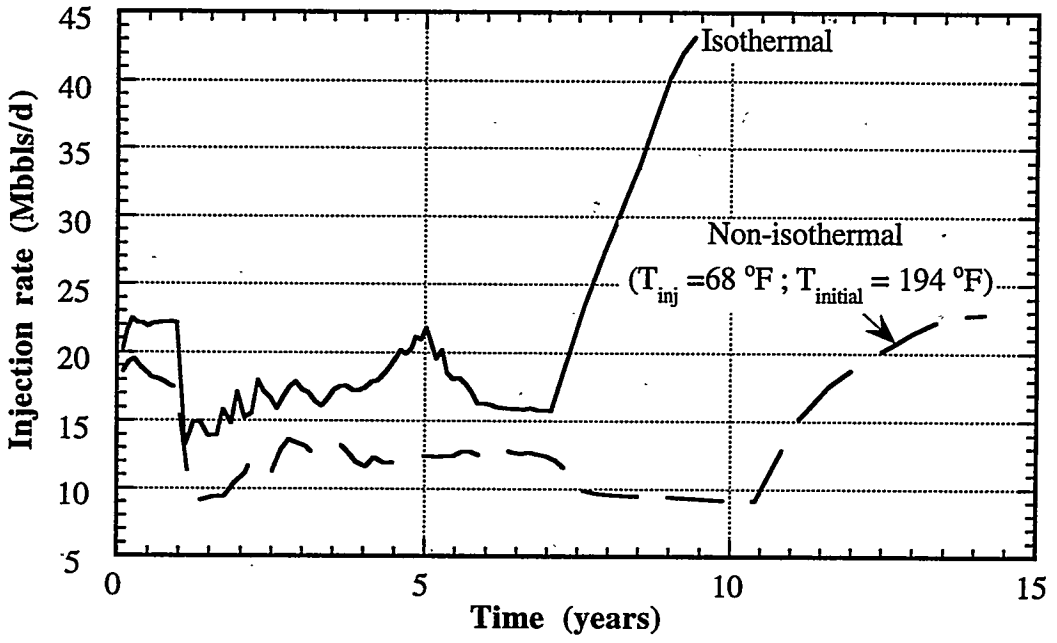


Figure 2.121 Effect of temperature on injection rate

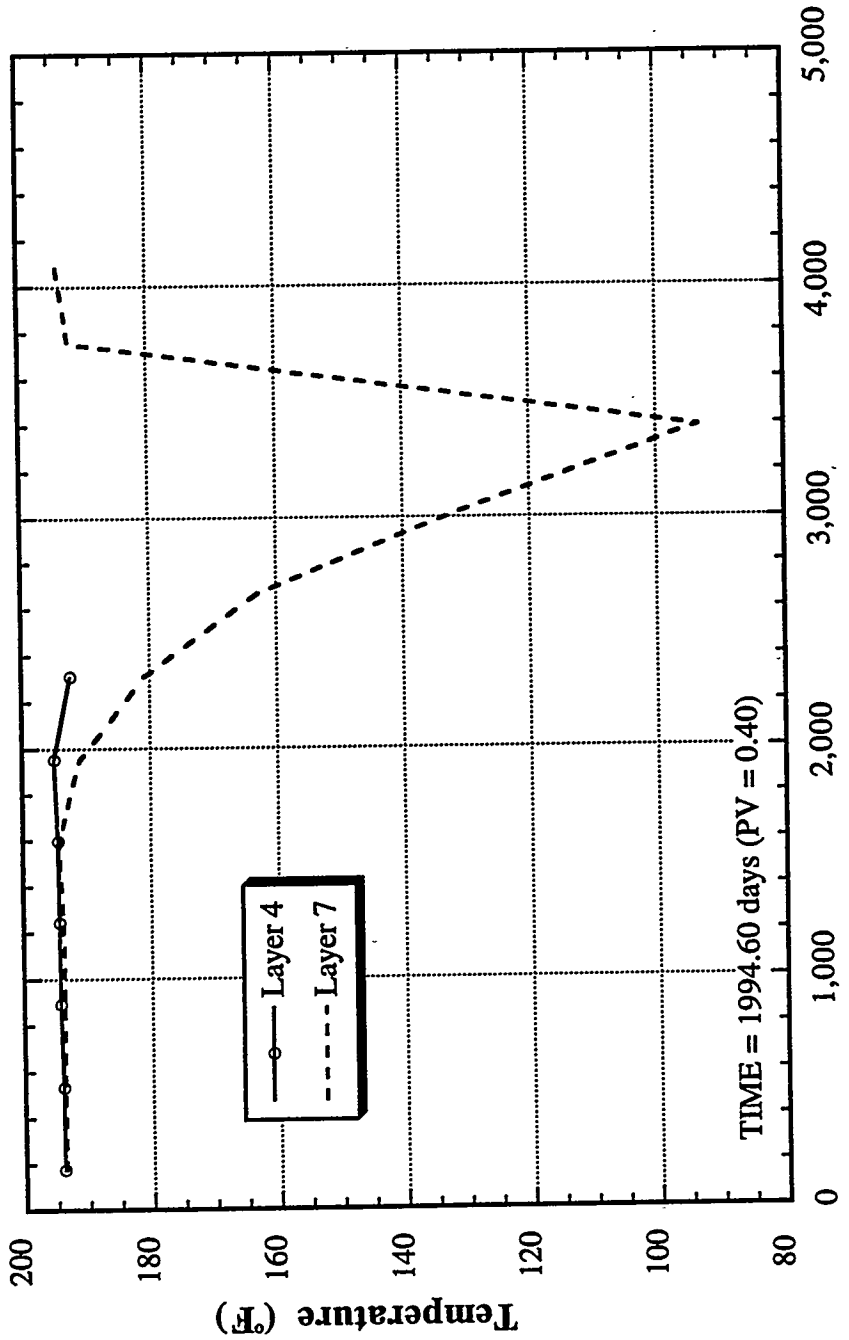


Figure 2.122 Temperature distribution of non-isothermal run

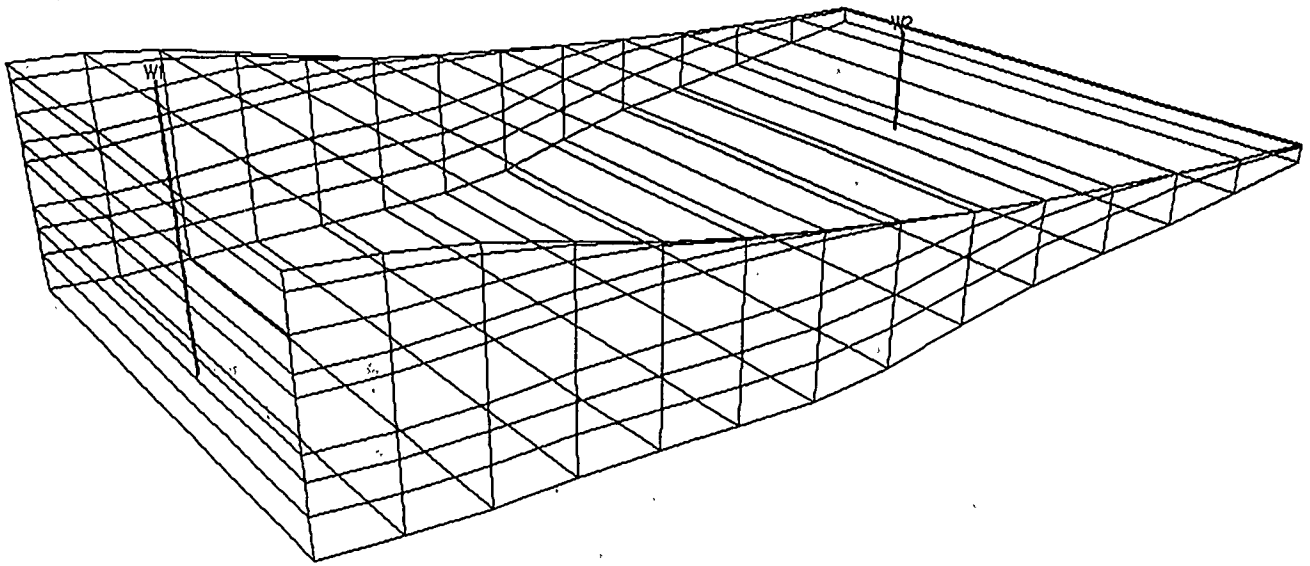


Figure 2.123 Simulation gridblocks for Reservoir B

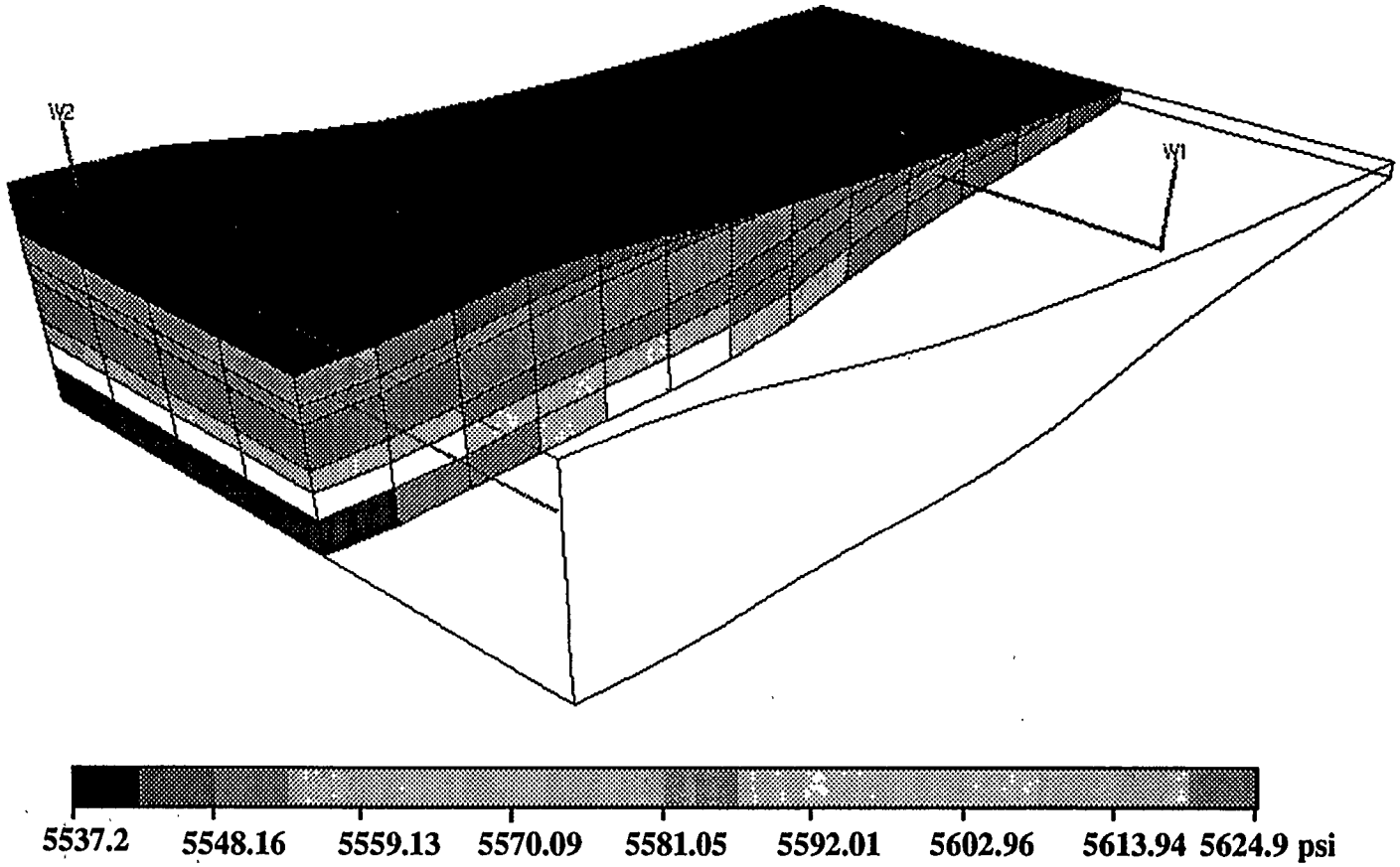


Figure 2.124 Initial pressure distribution for Reservoir B

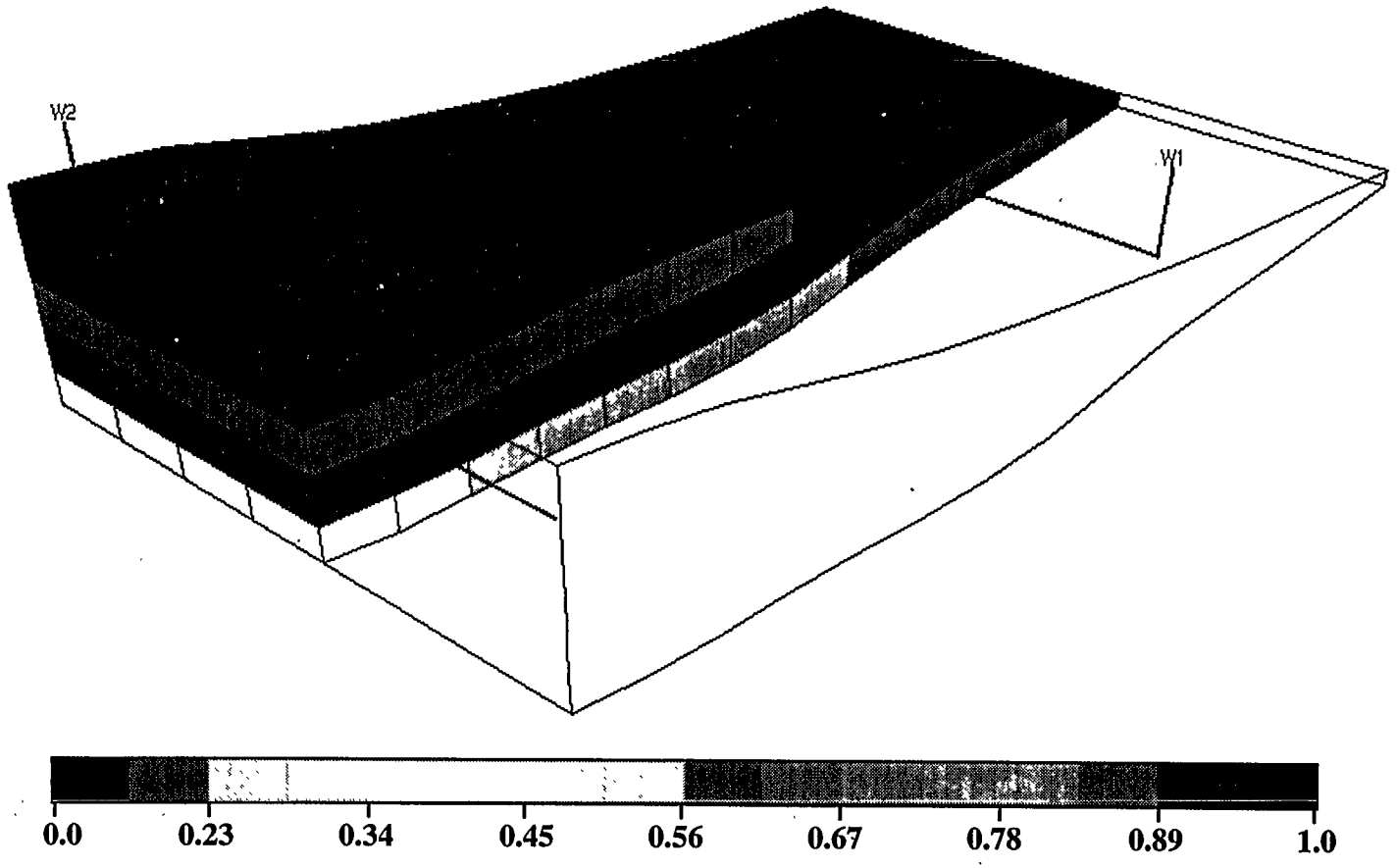


Figure 2.125 Initial water saturation distribution for Reservoir B

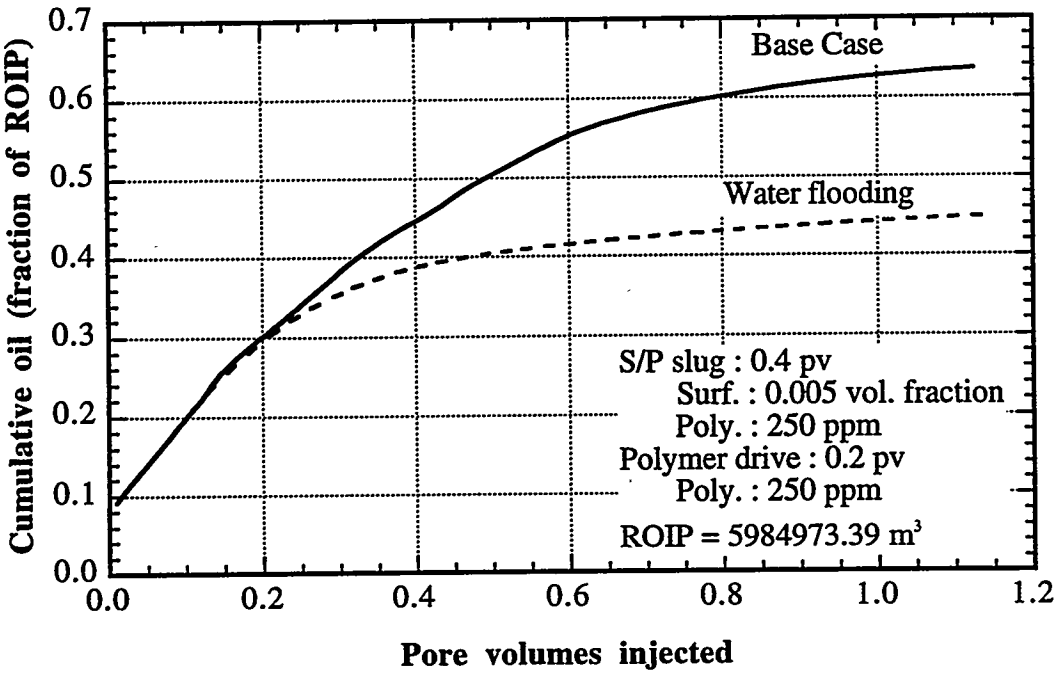


Figure 2.126 Oil recovery of the Base Case

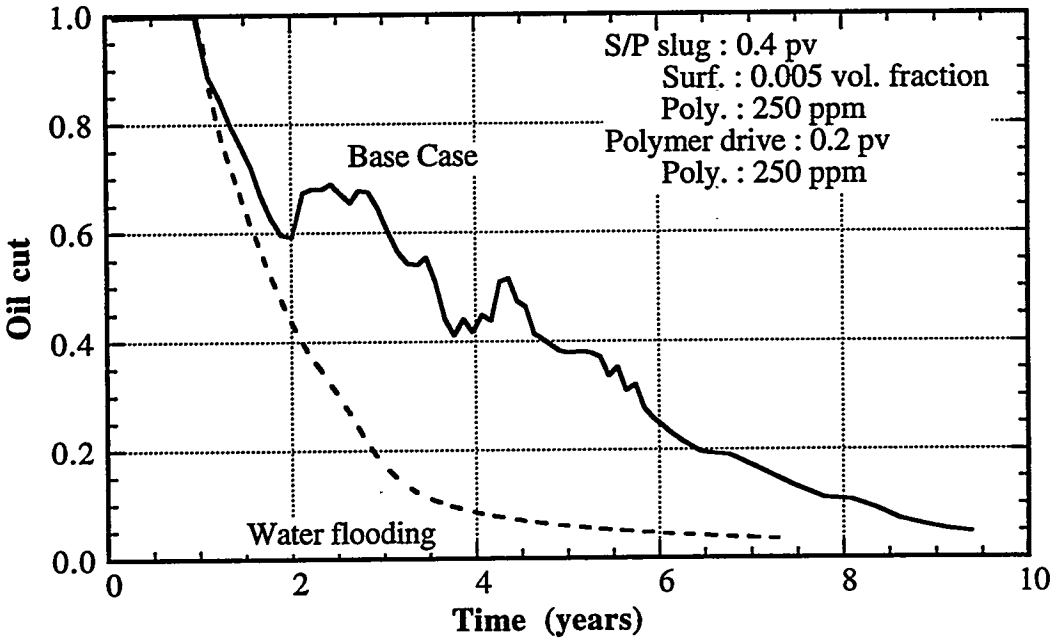


Figure 2.127 Oil cut of the Base Case

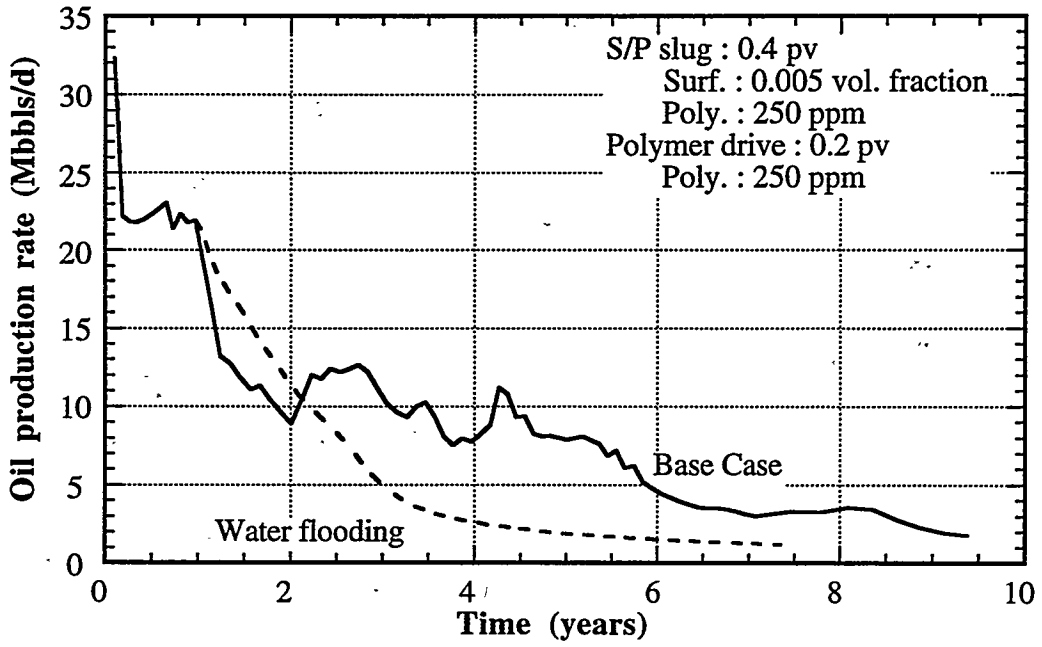


Figure 2.128 Oil production rate of the Base Case

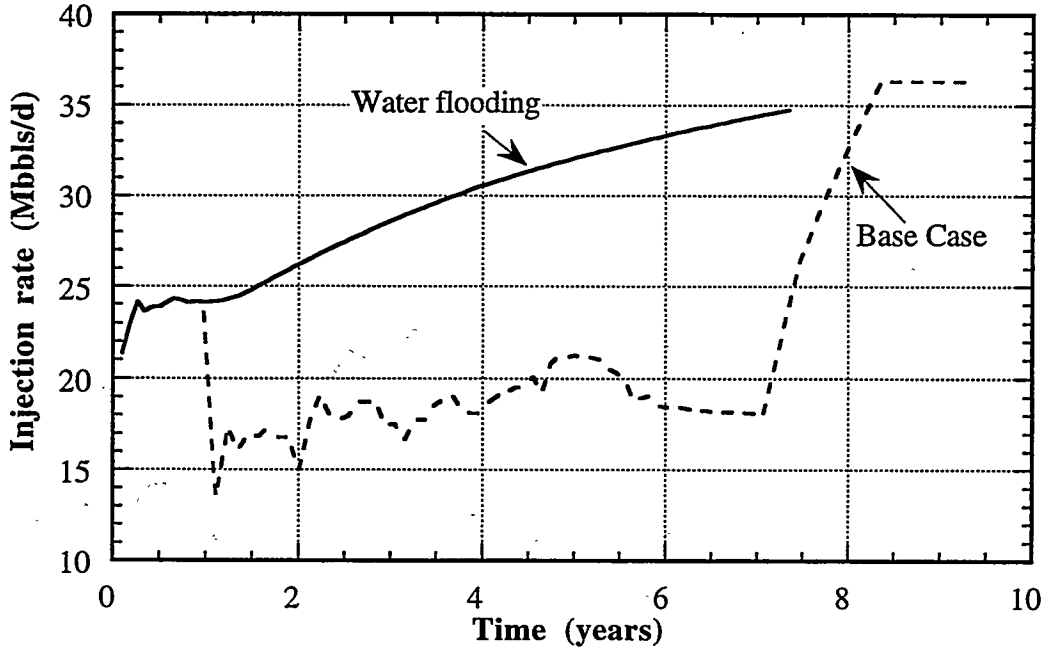


Figure 2.129 Injection rate of the Base Case

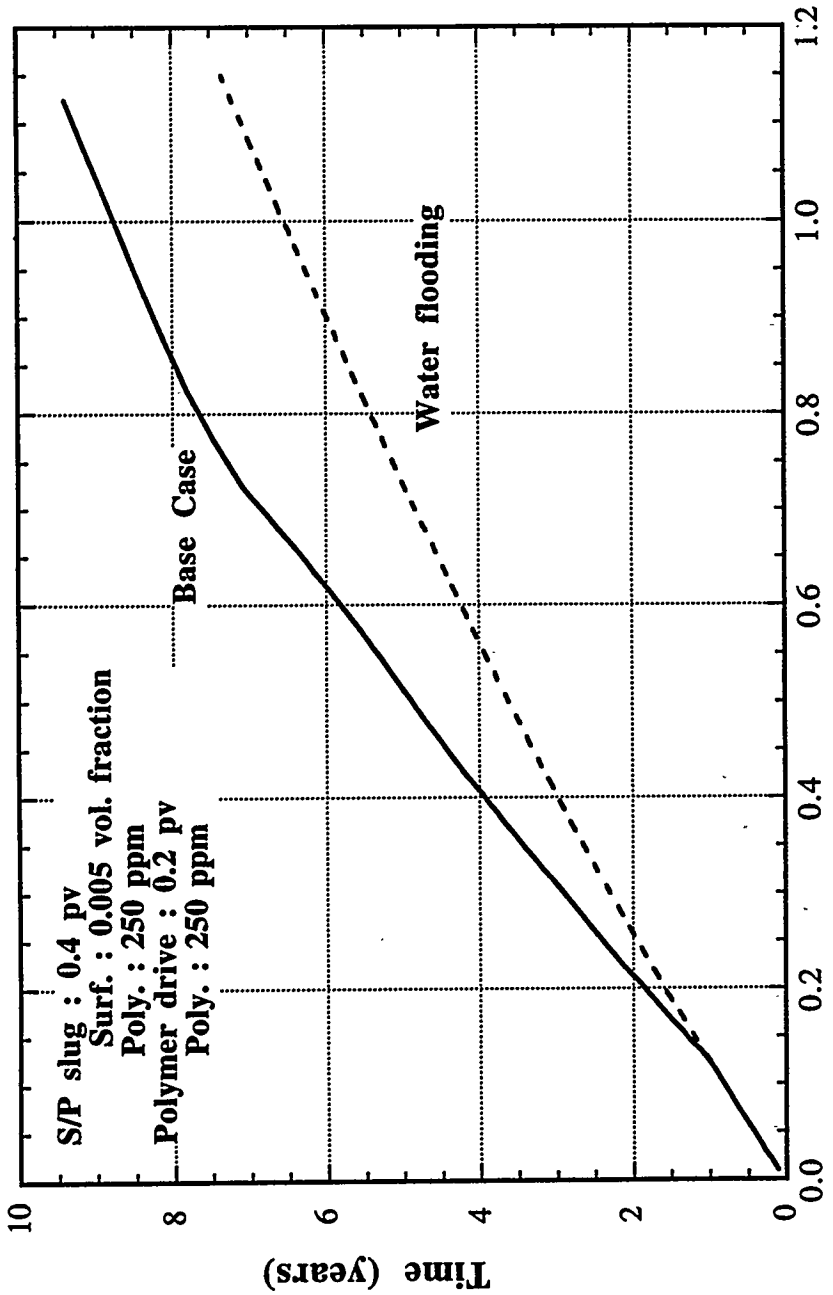


Figure 2.130 Project life of the Base Case

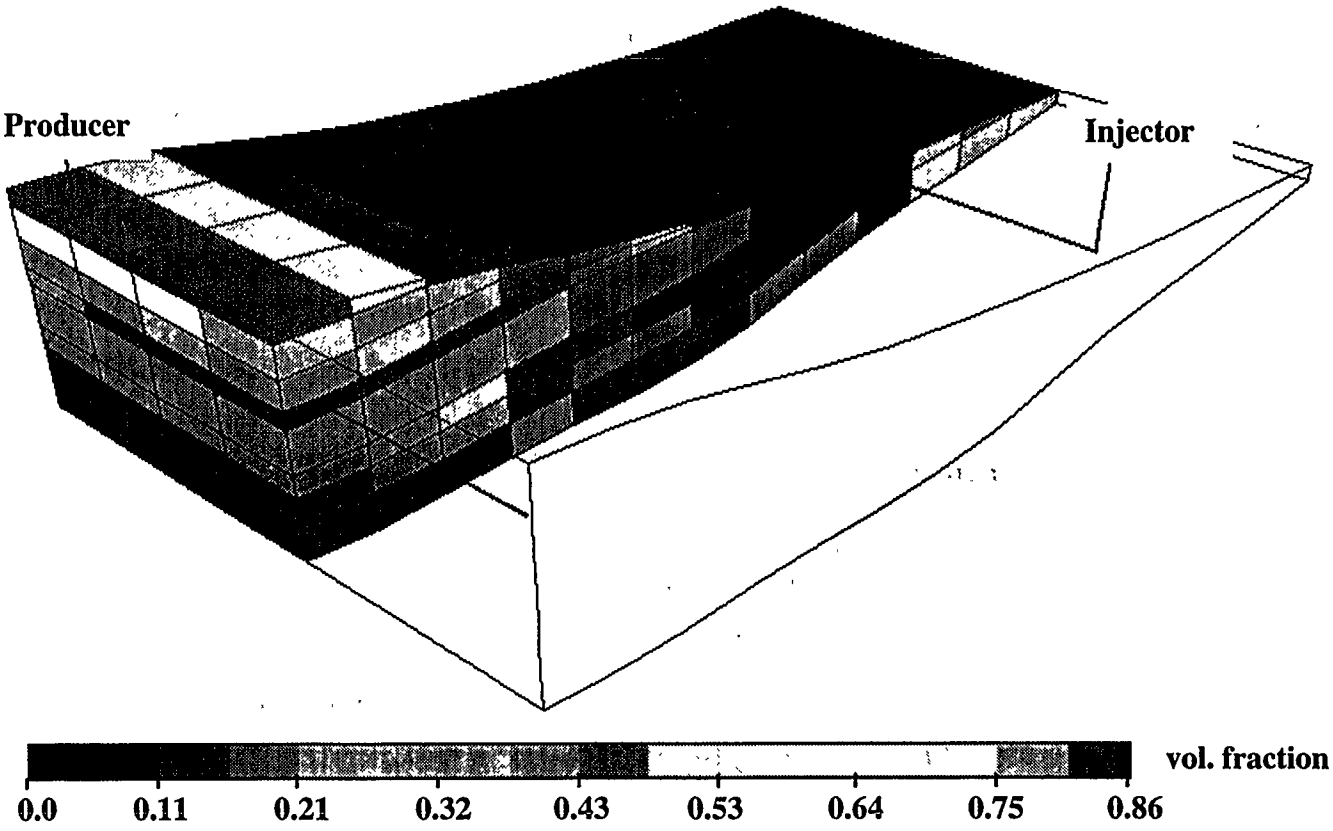


Figure 2.131 Oil concentration distribution at 0.47 pore volumes injected

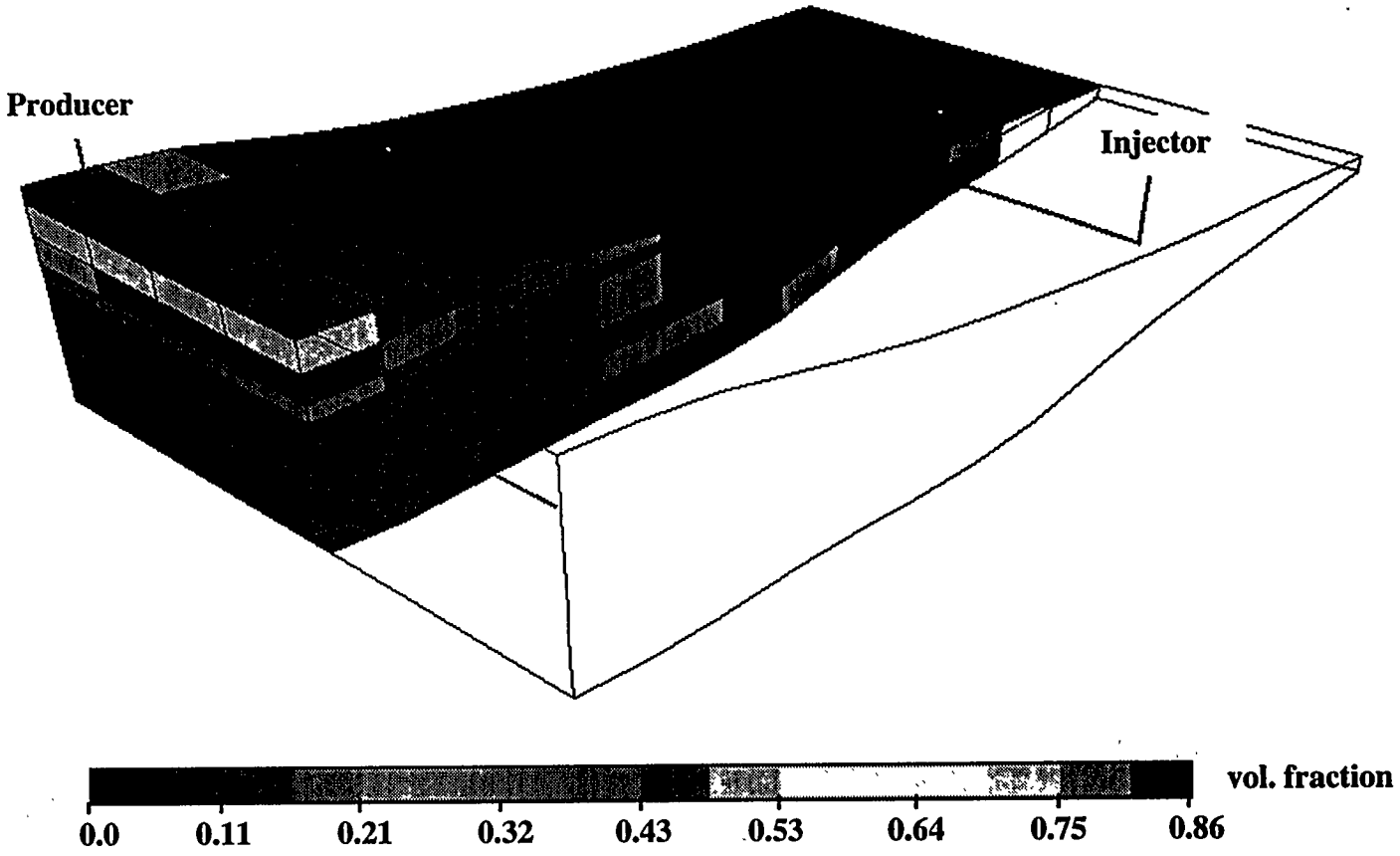


Figure 2.132 Oil concentration distribution at 1.125 pore volumes injected

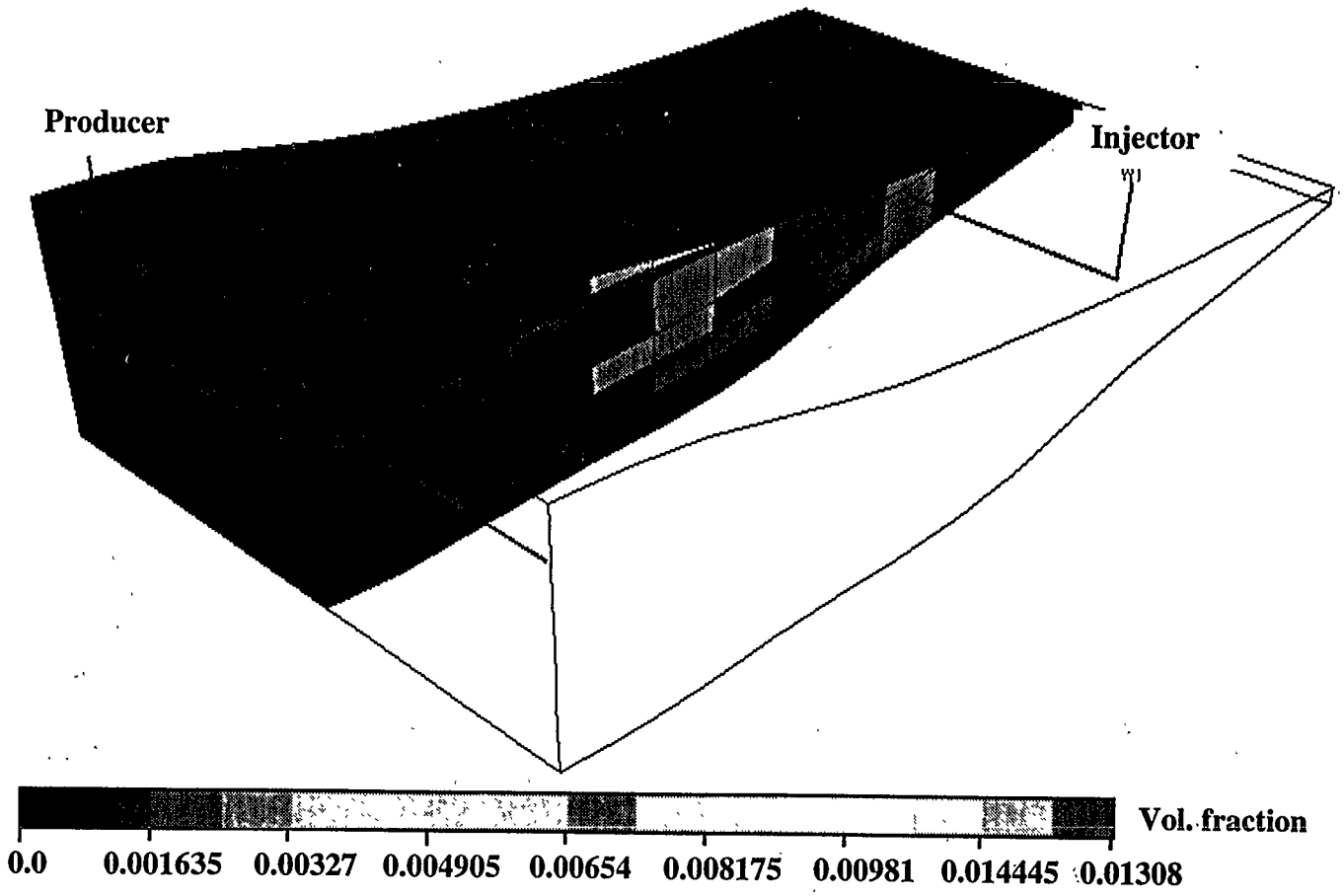


Figure 2.133 Surfactant concentration distribution at 0.47 pore volumes injected

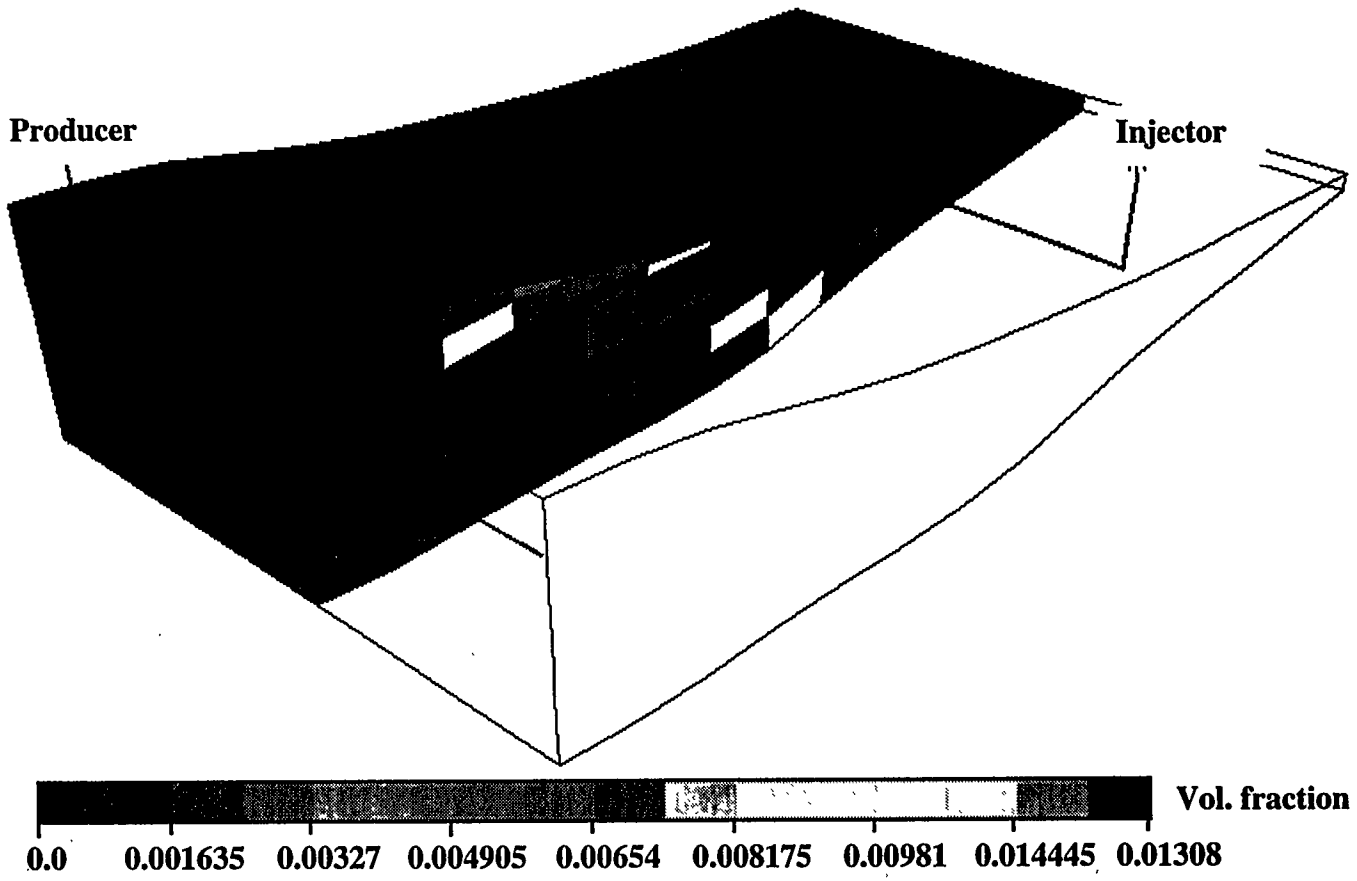


Figure 2.134 Surfactant concentration distribution at 1.125 pore volumes injected

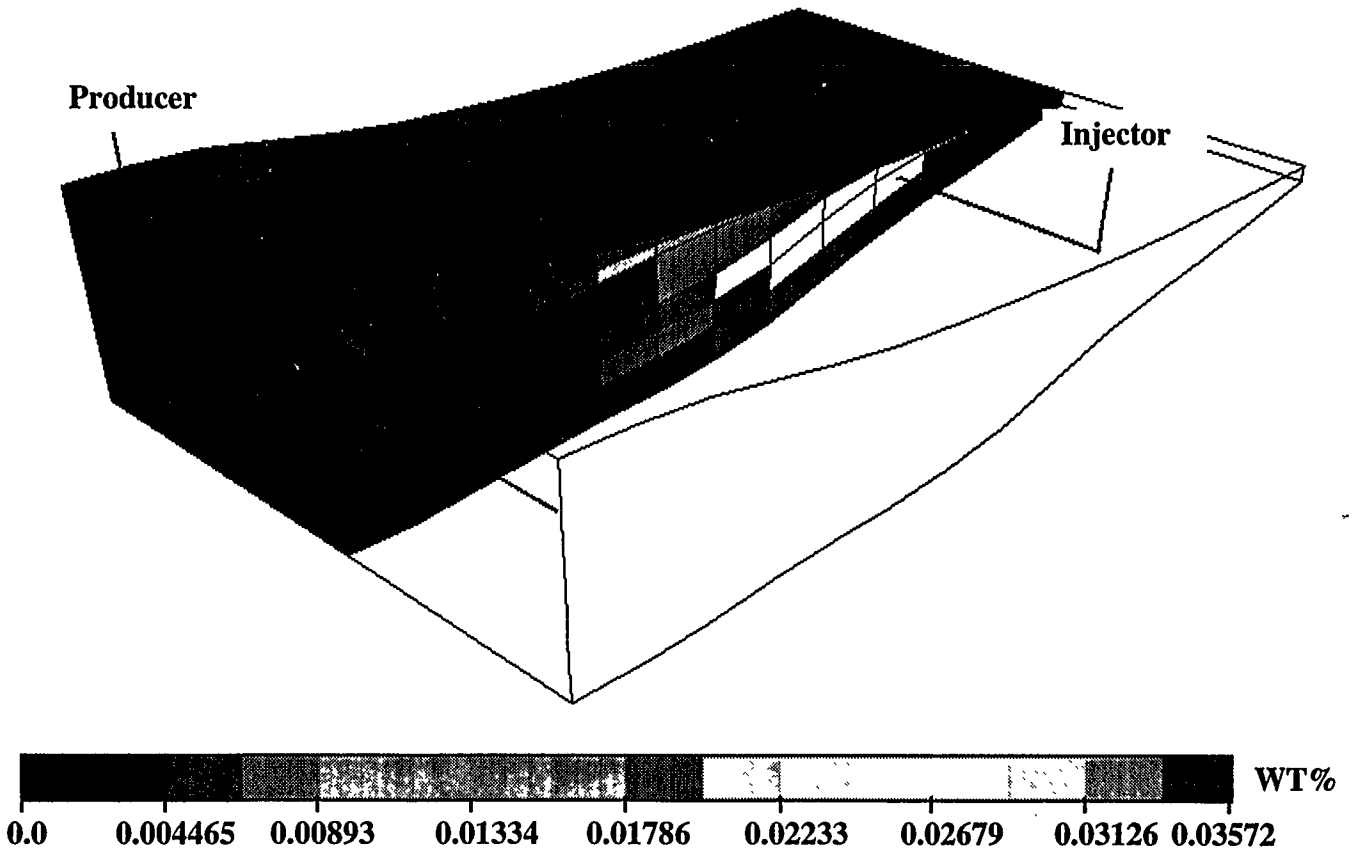


Figure 2.135 Polymer concentration distribution at 0.47 pore volumes injected

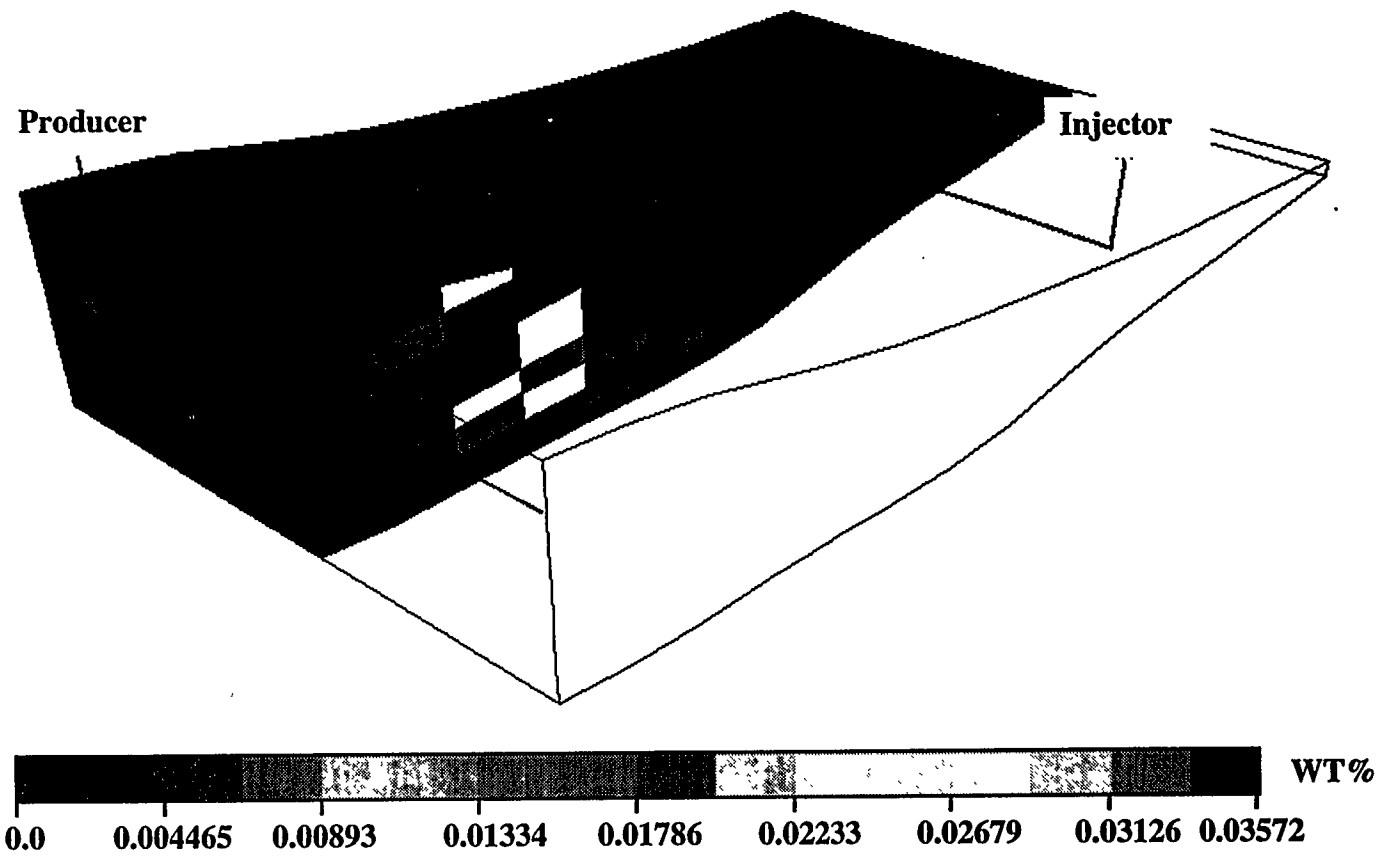


Figure 2.136 Polymer concentration distribution at 1.125 pore volumes injected

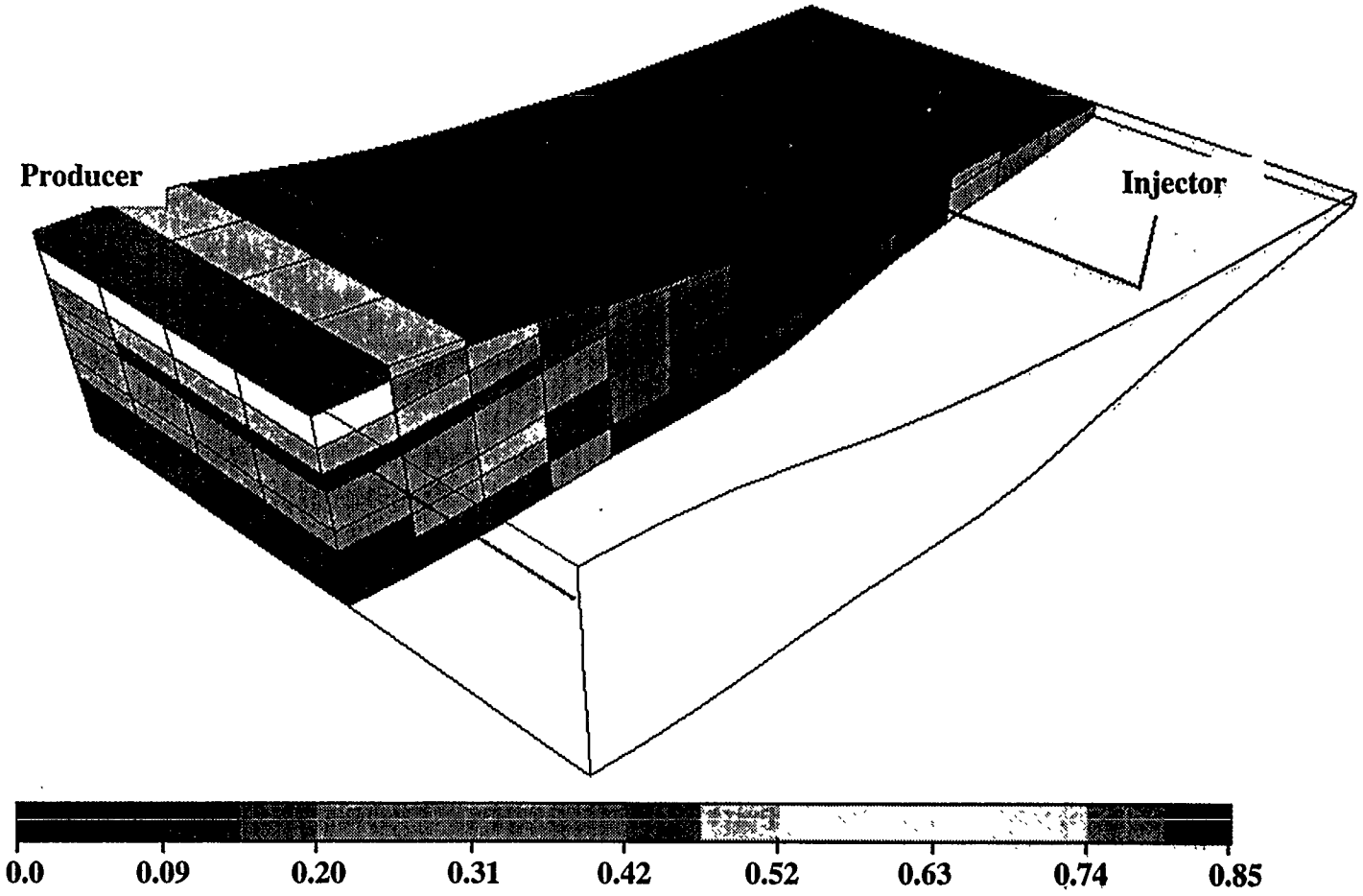


Figure 2.137 Distribution of oil saturation at 0.47 pore volumes injected

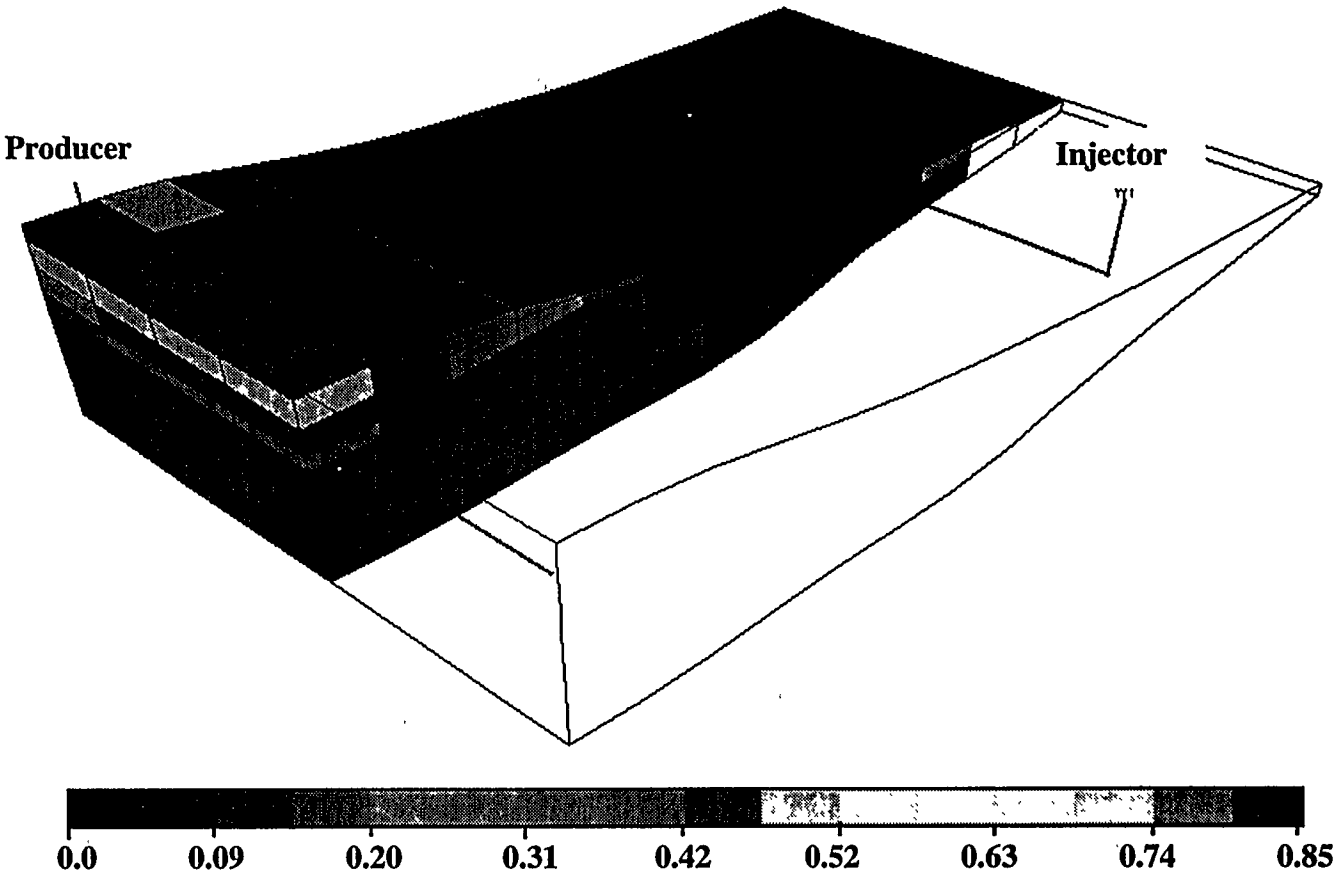


Figure 2.138 Distribution of oil saturation at 1.125 pore volumes injected

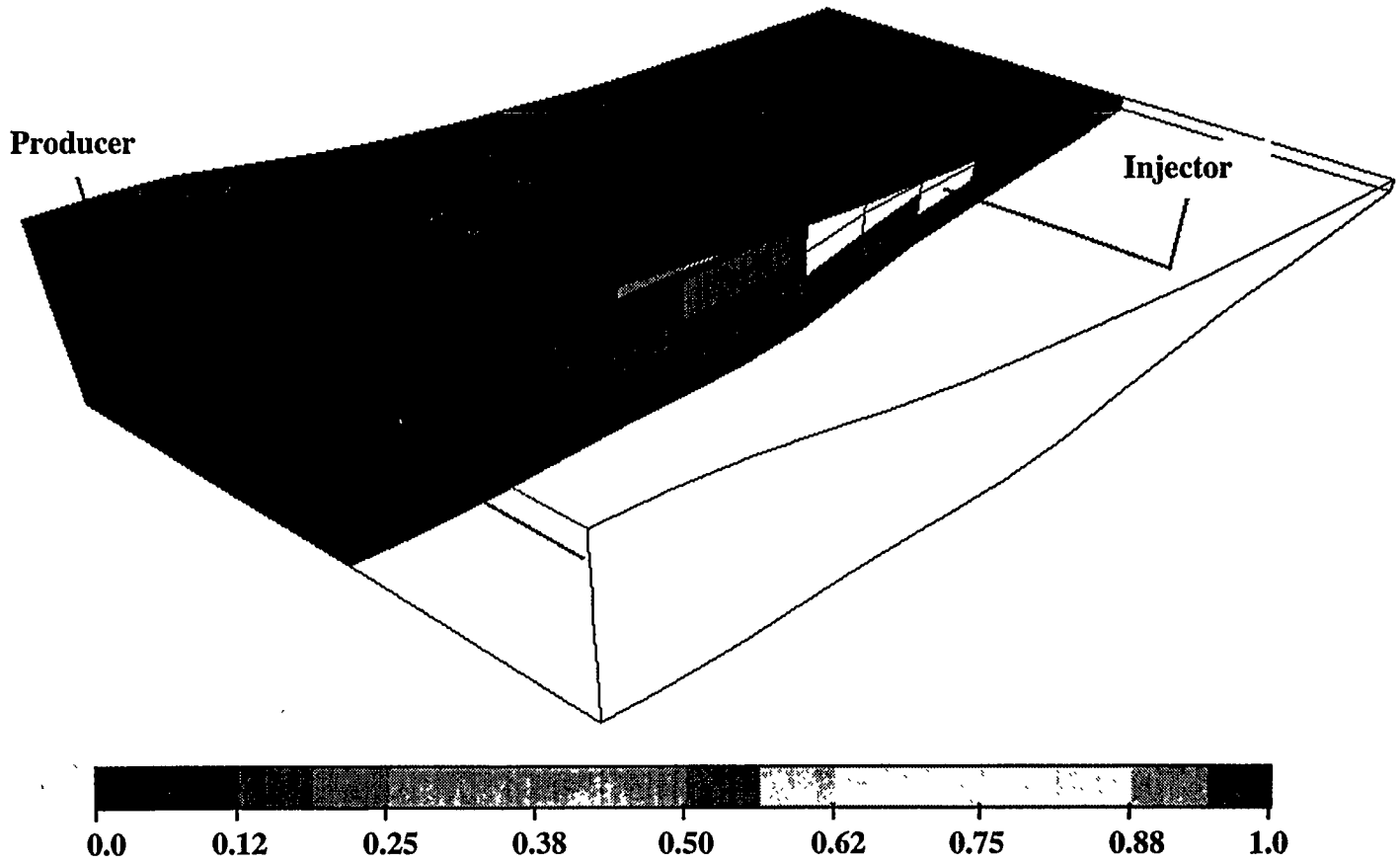


Figure 2.139 Microemulsion saturation distribution at 0.47 pore volumes injected

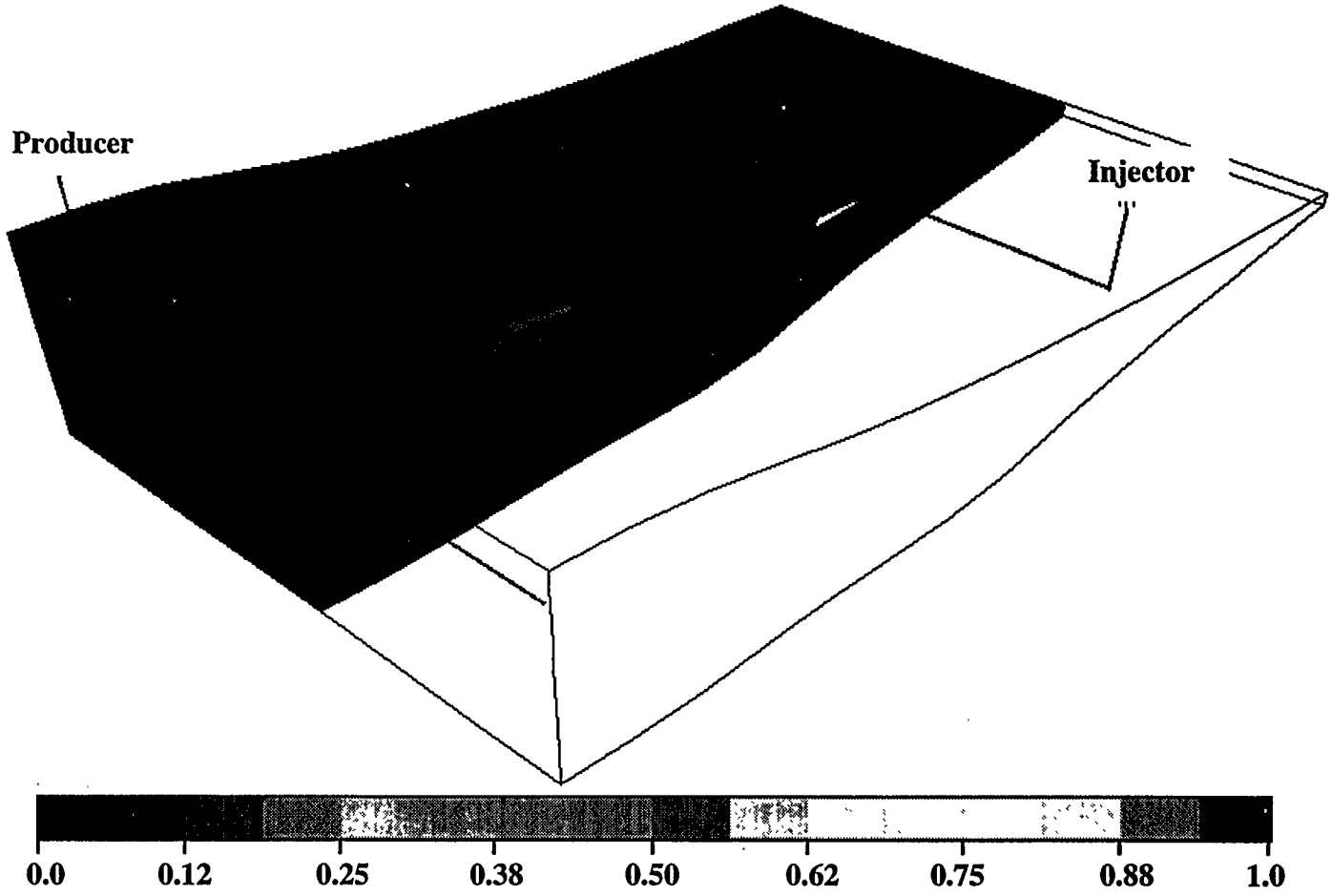


Figure 2.140 Microemulsion saturation distribution at 1.125 pore volumes injected s.

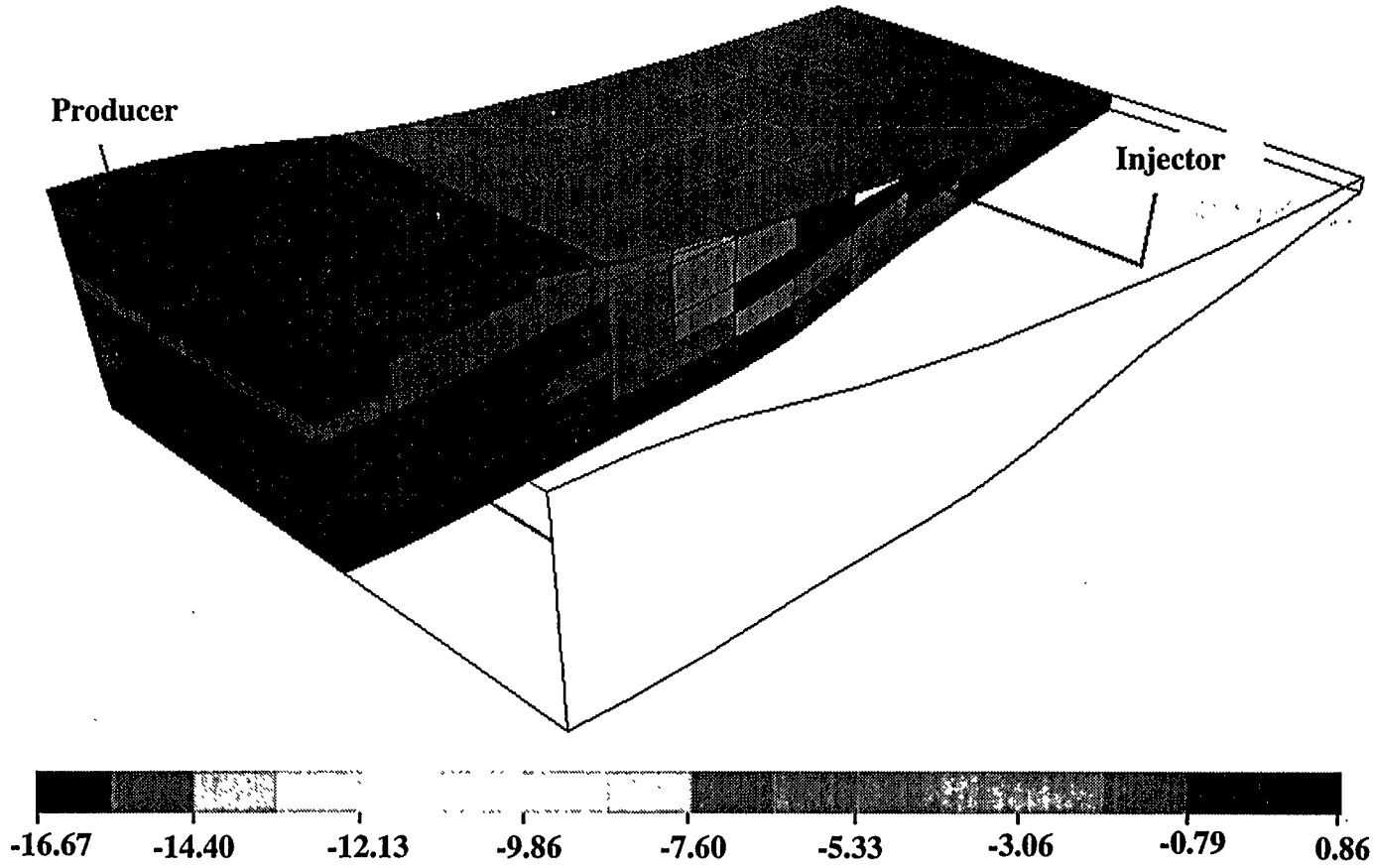


Figure 2.141 Distribution of log of microemulsion/oil interfacial tention at 0.62 pore volumes injected

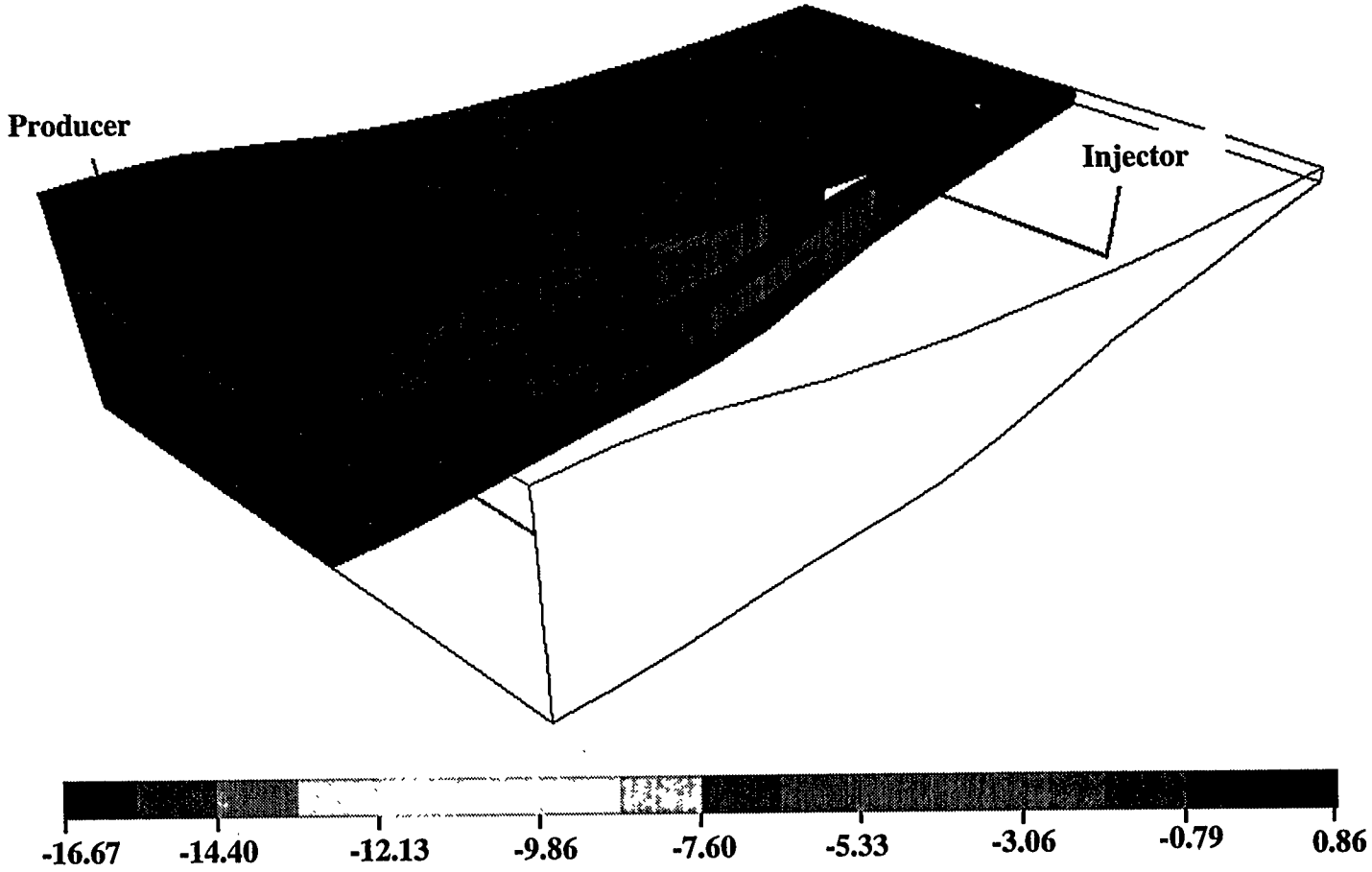


Figure 2.142 Distribution of log of microemulsion/oil interfacial tention at 1.15 pore volumes injected

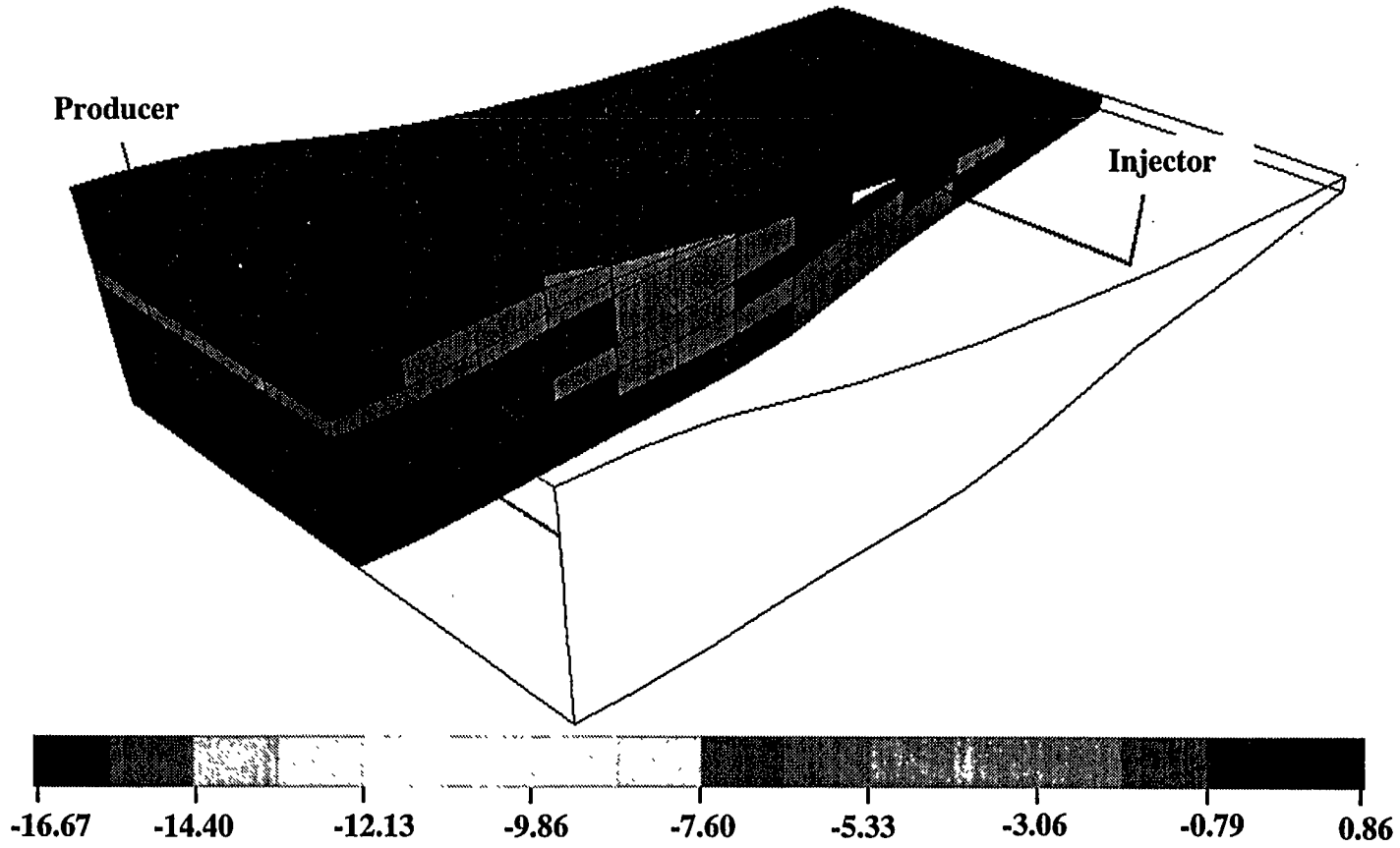


Figure 2.143 Distribution of log of microemulsion/water interfacial tention at 0.62 pore volumes injected

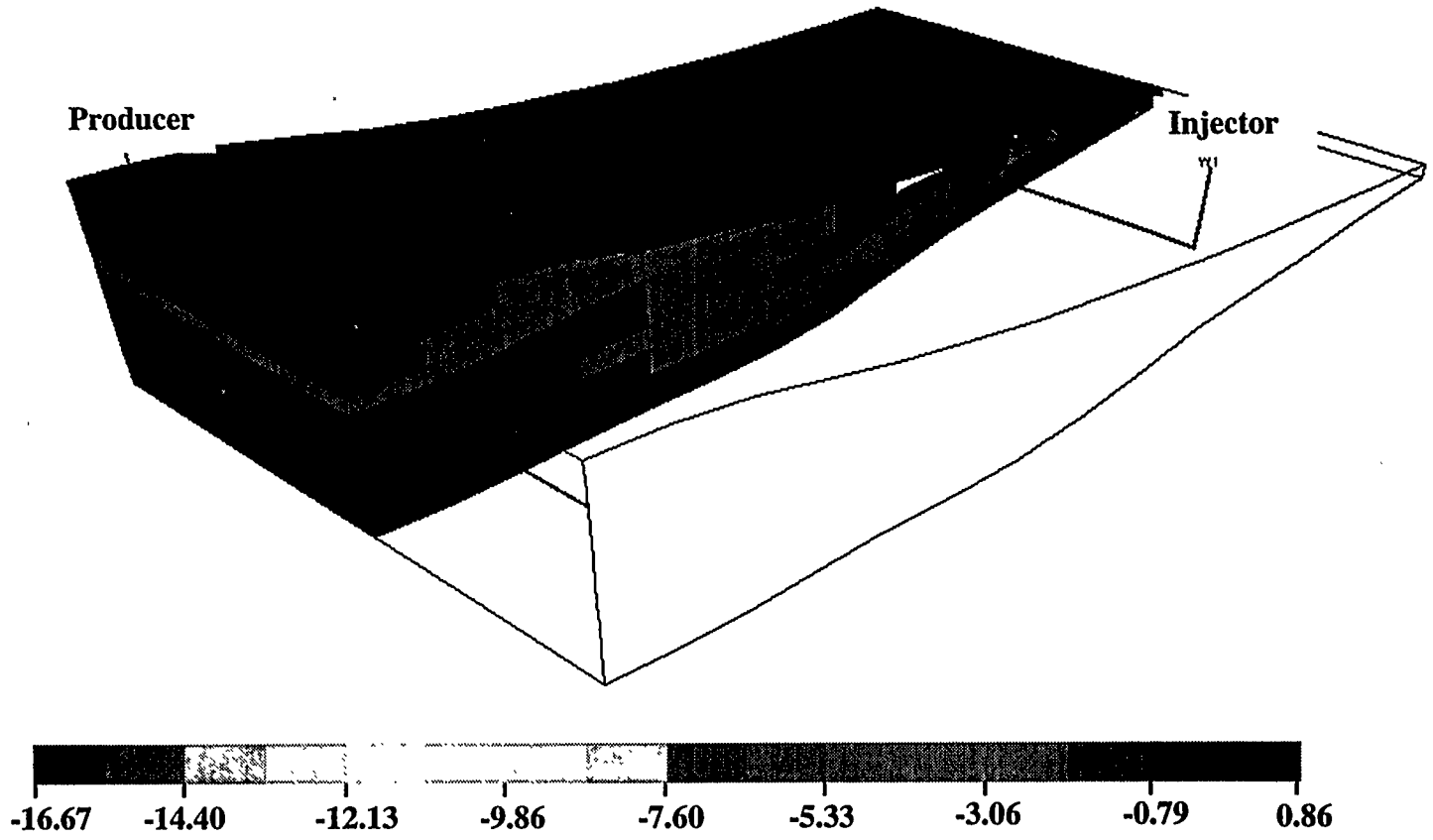


Figure 2.144 Distribution of log of microemulsion/water interfacial tention at 1.15 pore volumes injected

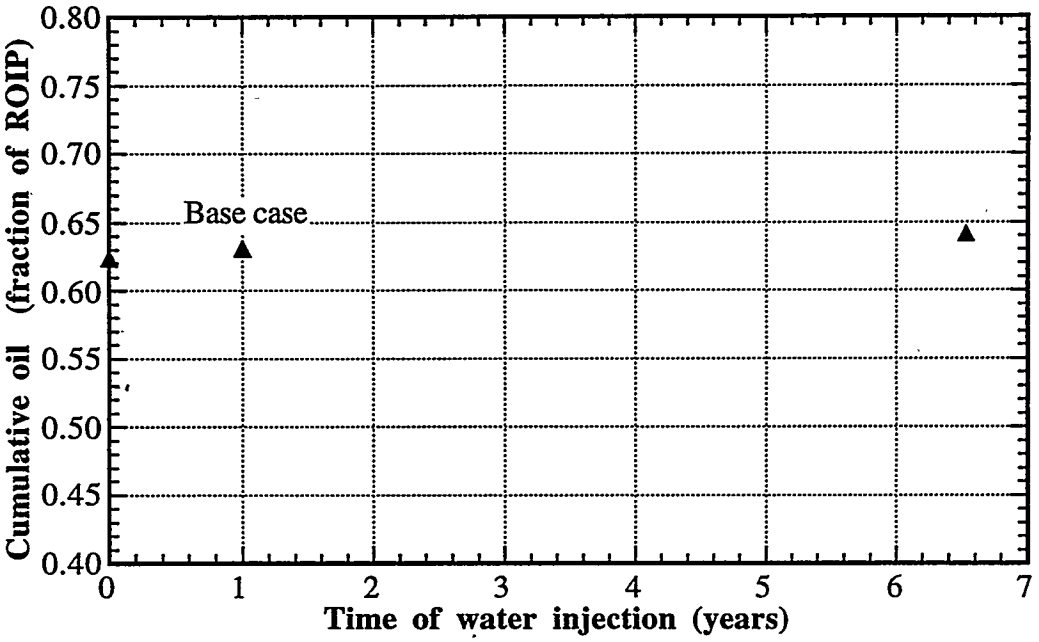


Figure 2.145 Effect of duration of water injection prior to chemical on S/P oil recovery

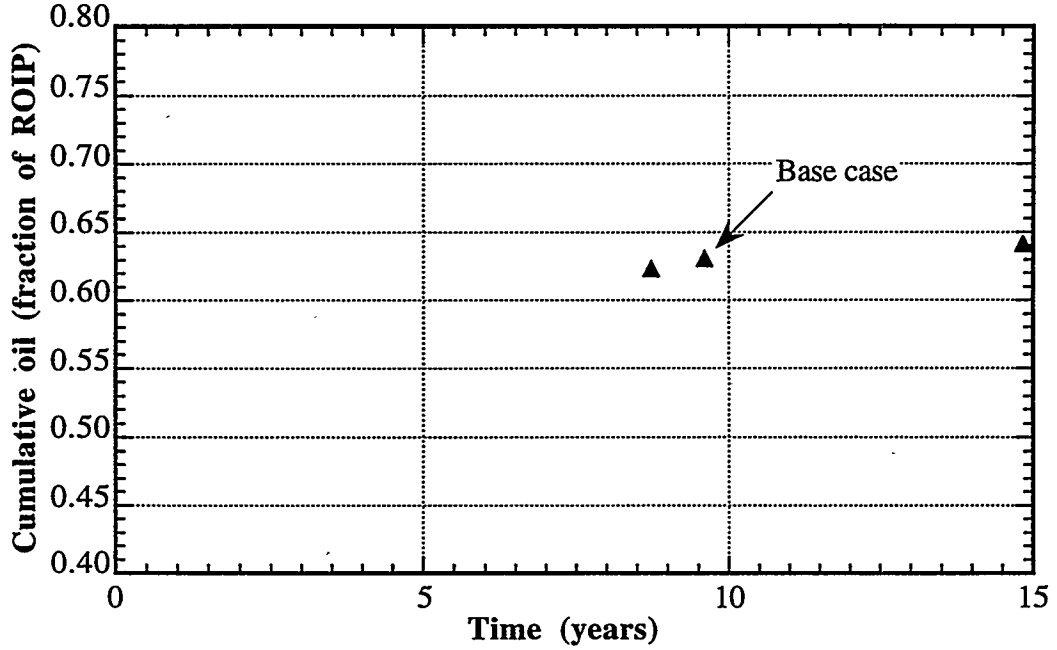


Figure 2.146 Effect of duration of water injection prior to chemical on S/P oil recovery

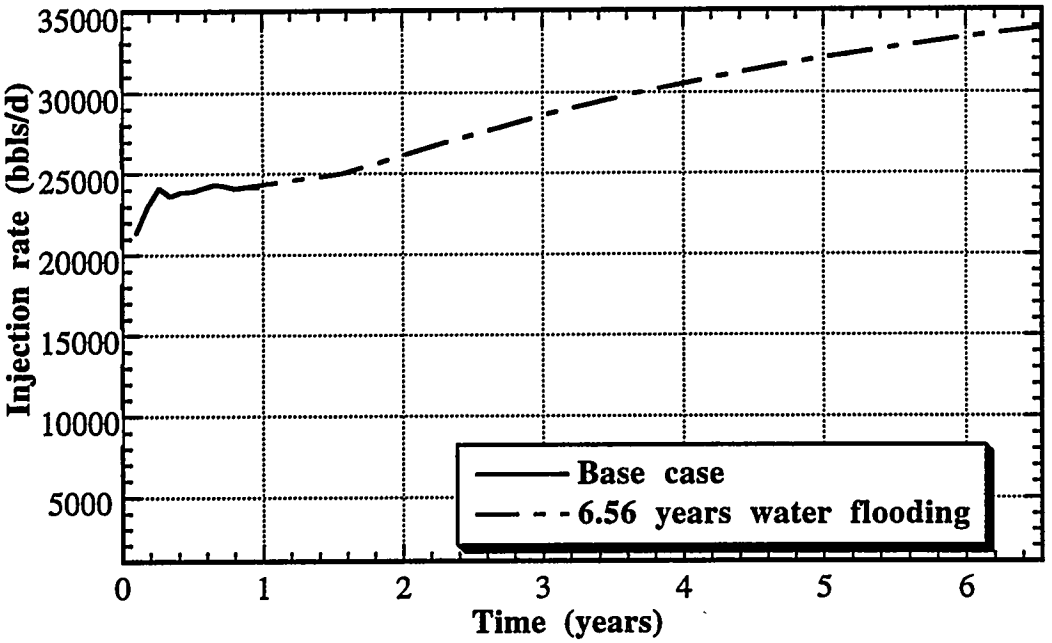


Figure 2.147 Injection rate during water flood prior to S/P

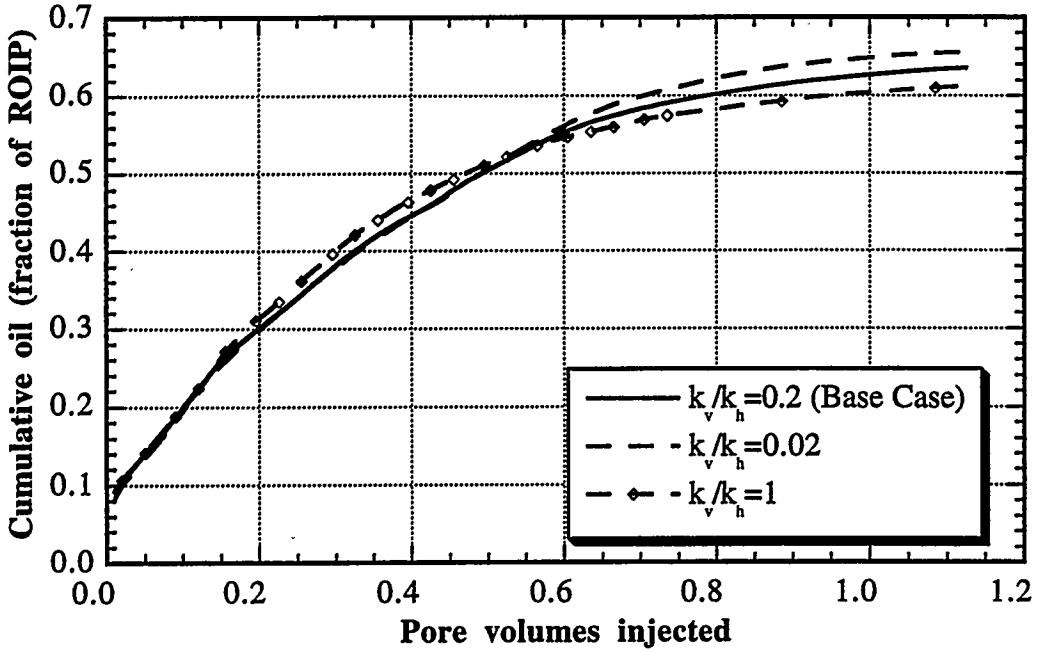


Figure 2.148 Effect of vertical permeability on oil recovery

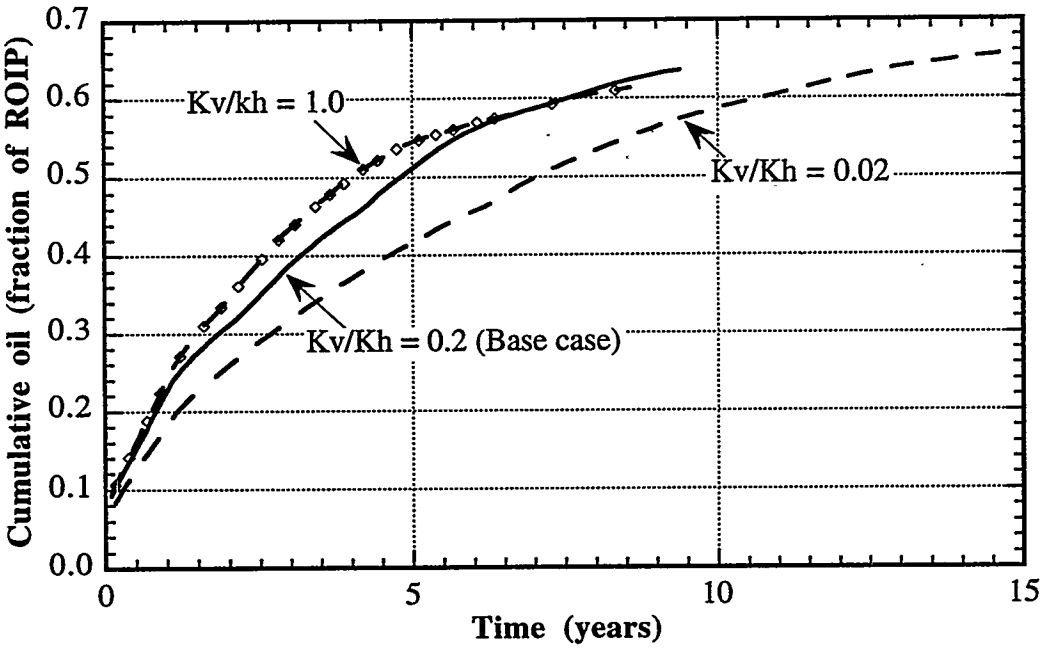


Figure 2.149 Effect of vertical permeability on oil recovery

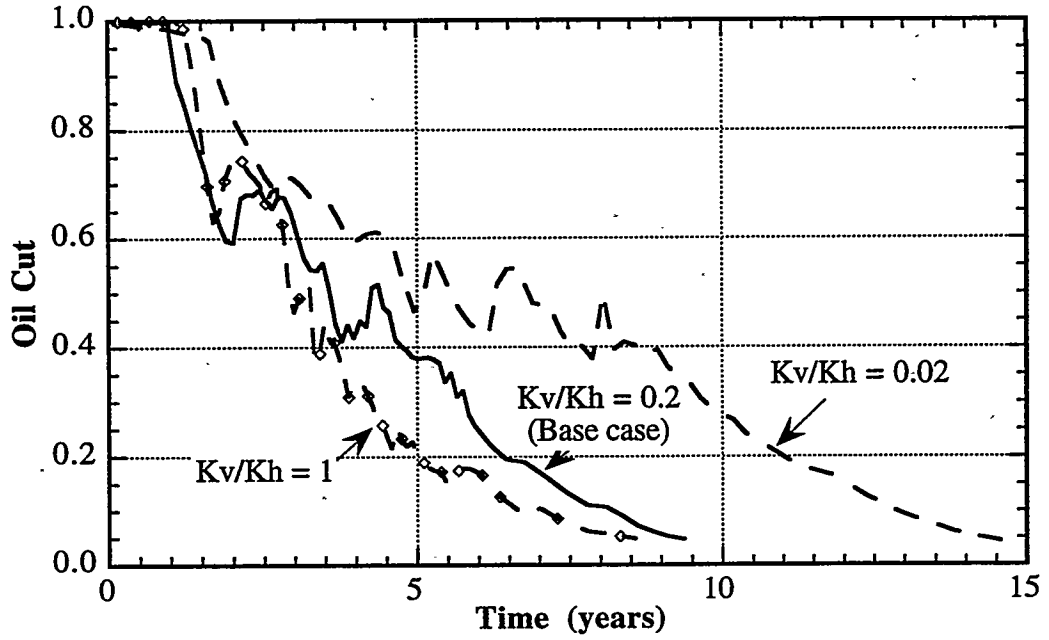


Figure 2.150 Effect of vertical permeability on oil cut

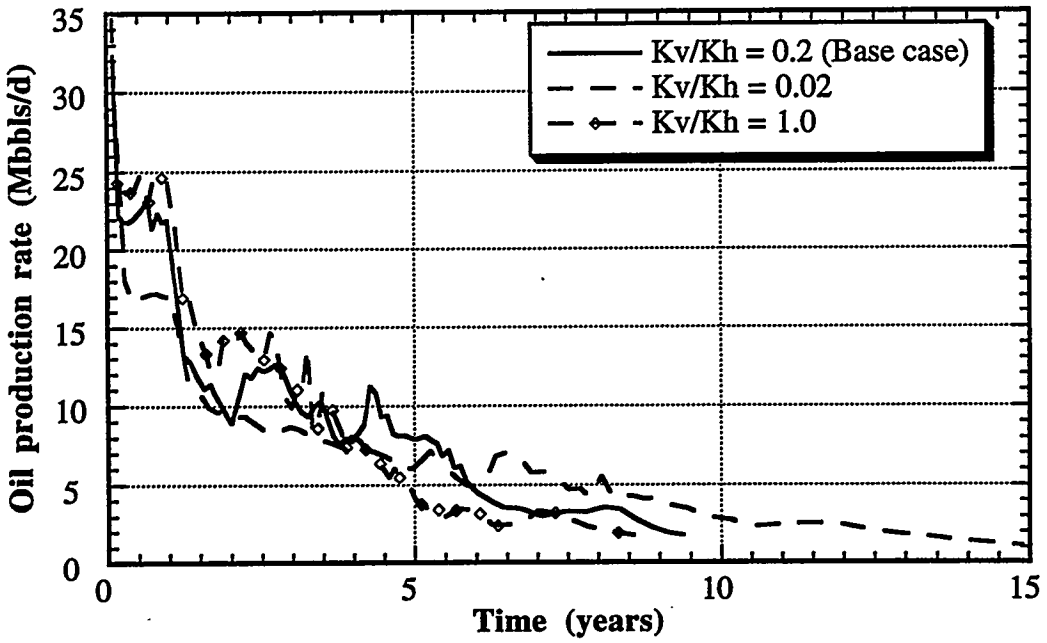


Figure 2.151 Effect of vertical permeability on oil production rate

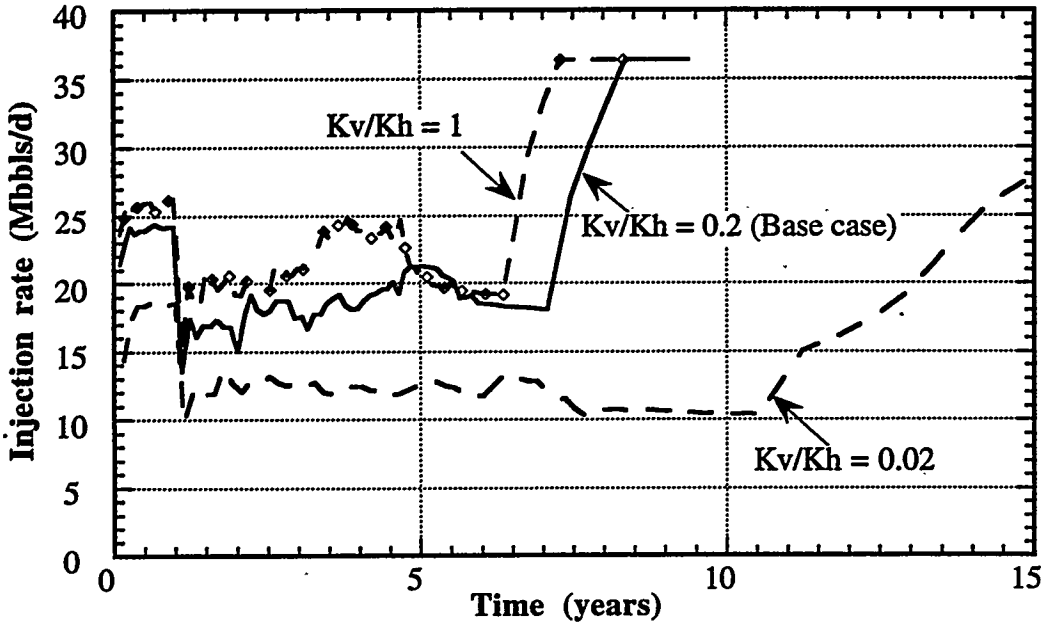


Figure 2.152 Effect of vertical permeability on injection rate

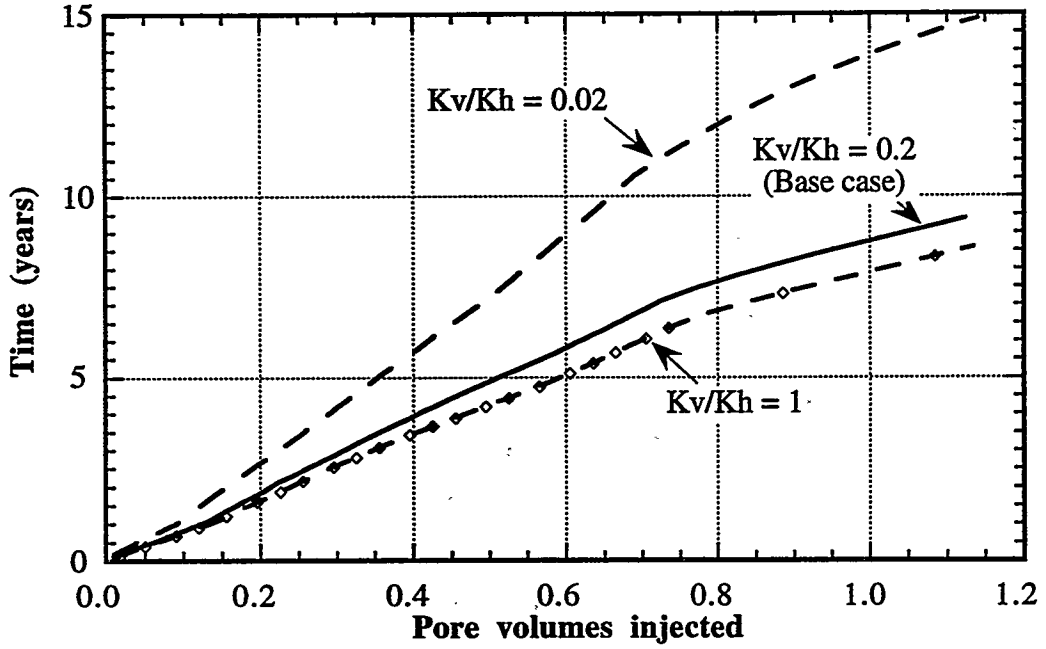


Figure 2.153 Effect of vertical permeability on project life

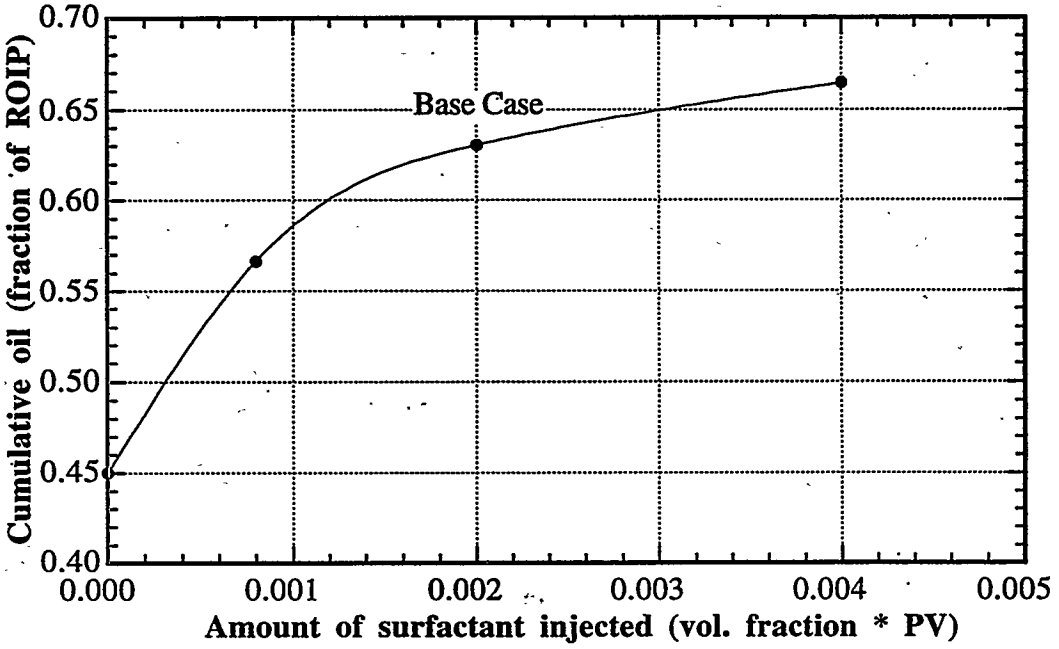


Figure 2.154 Effect of amount of injected surfactant on oil recovery at 5% oil cut

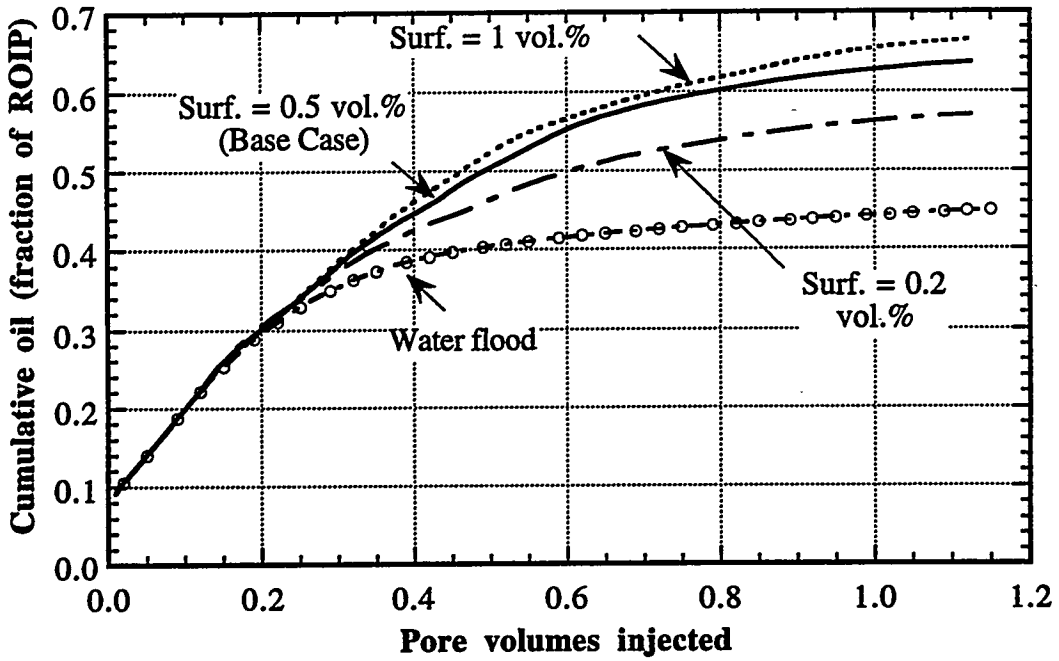


Figure 2.155 Effect of amount of injected surfactant on oil recovery

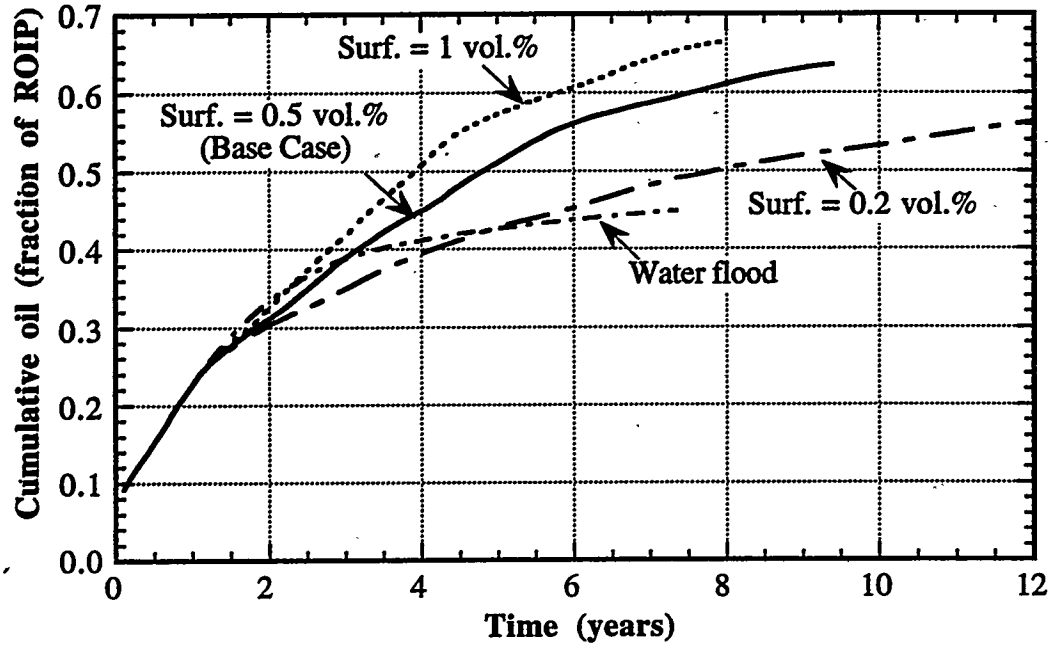


Figure 2.156 Effect of amount of injected surfactant on oil recovery

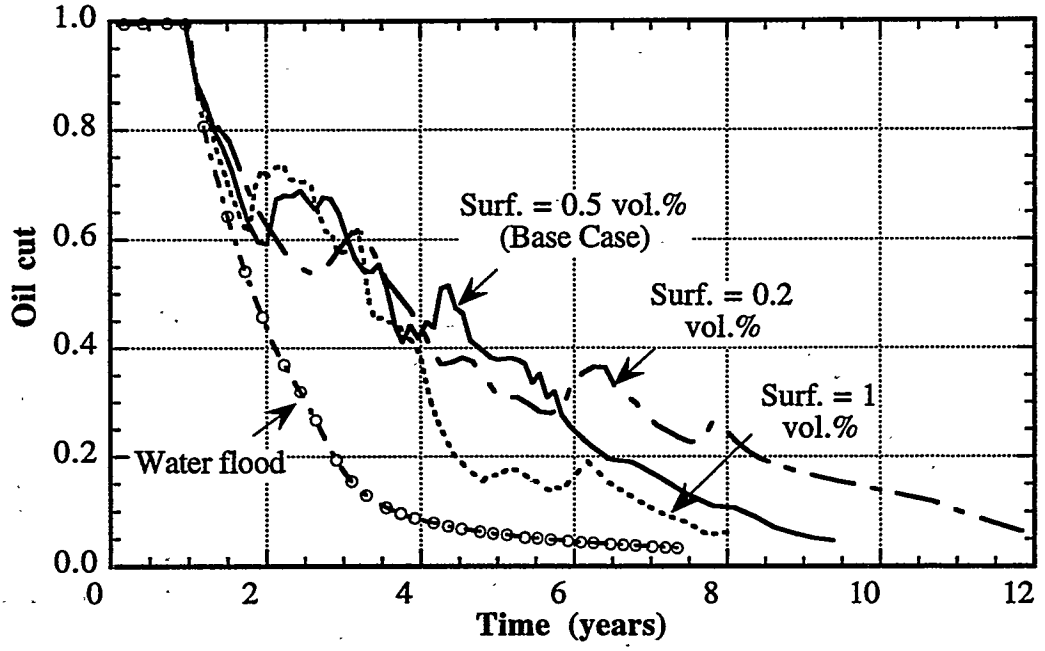


Figure 2.157 Effect of amount of injected surfactant on oil cut

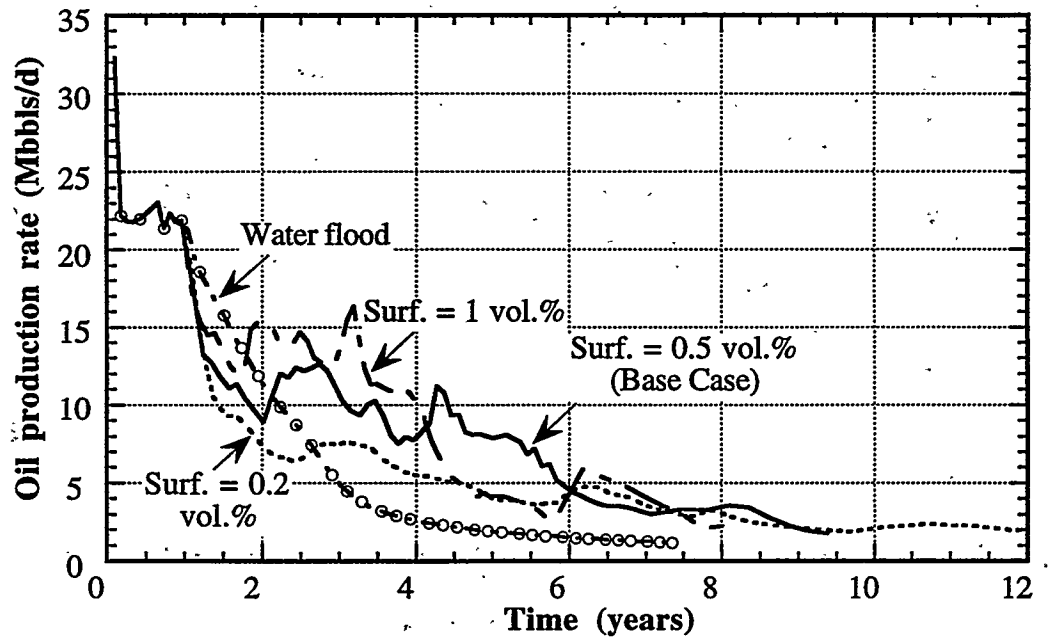


Figure 2.158 Effect of amount of injected surfactant on oil production rate

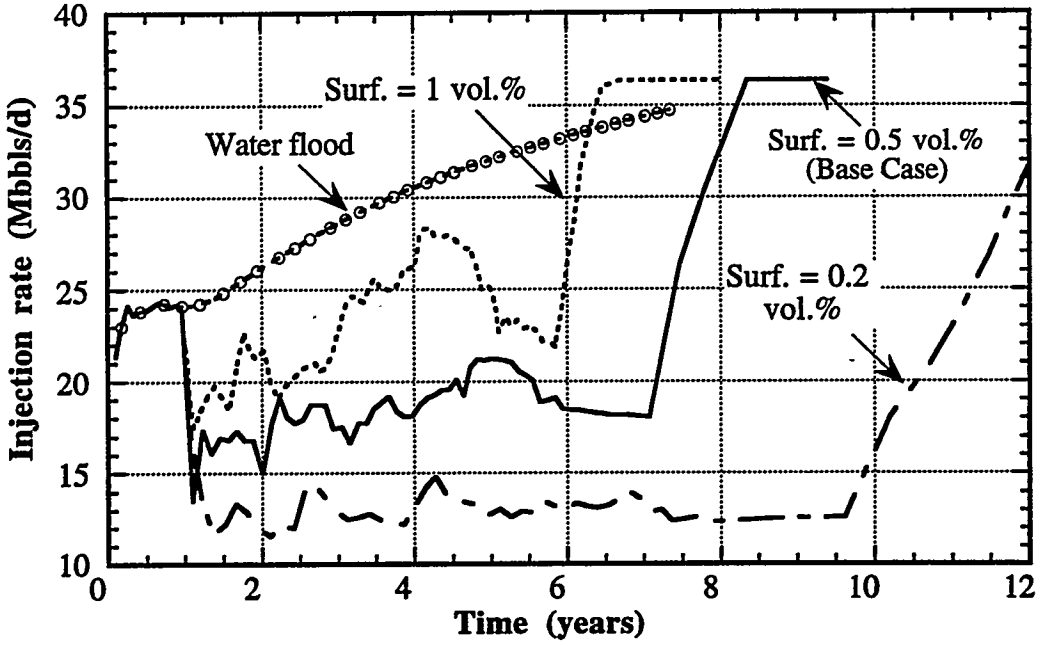


Figure 2.159 Effect of amount of injected surfactant on injection rate

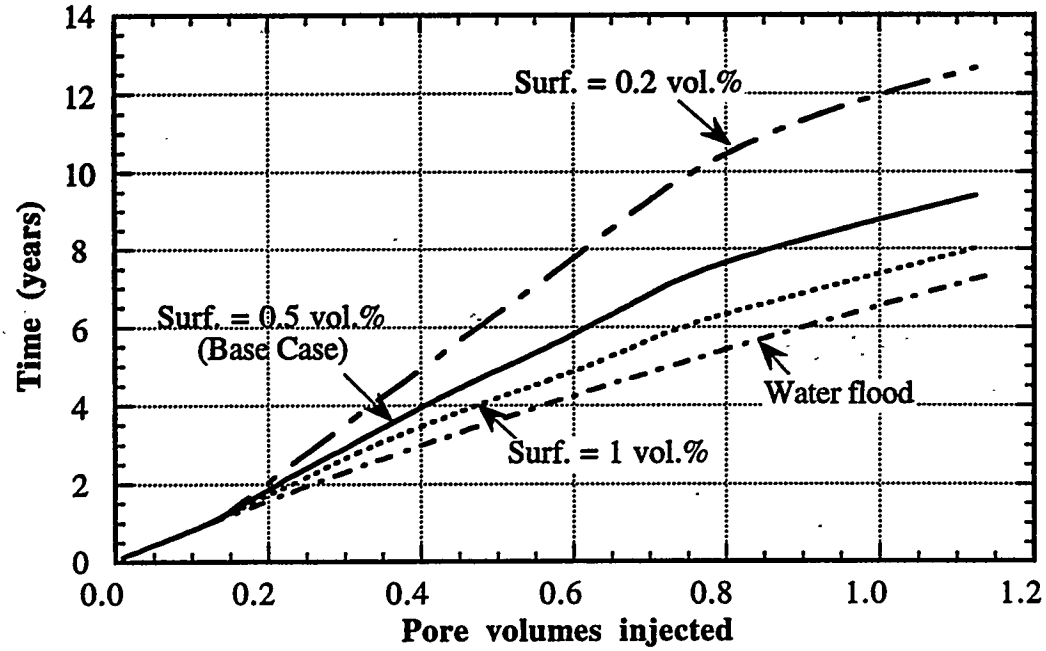


Figure 2.160 Effect of amount of injected surfactant on project life

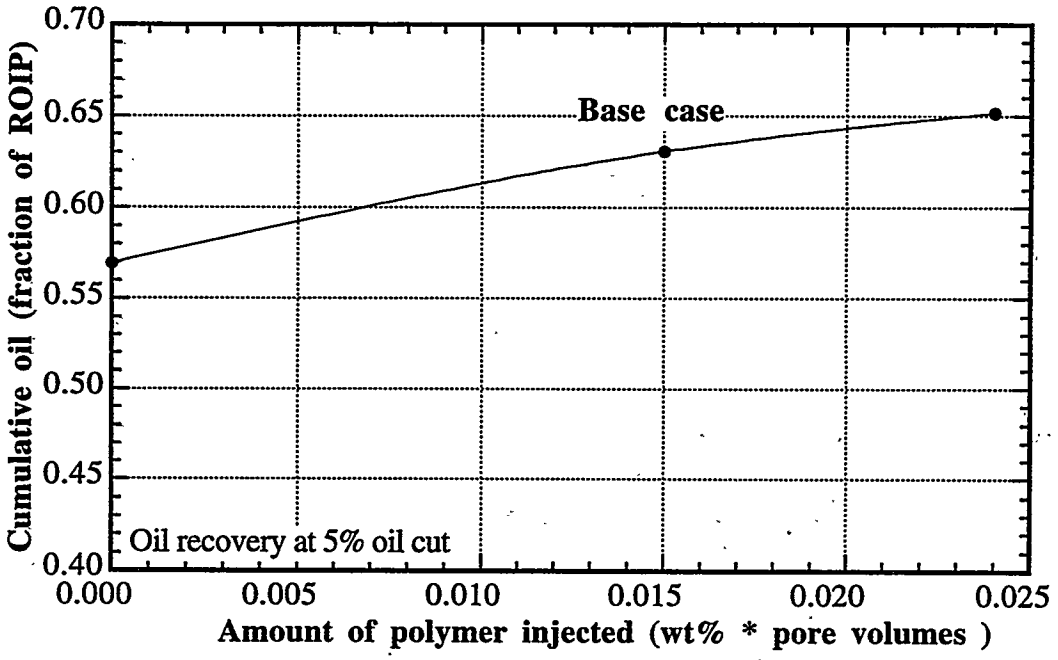


Figure 2.161 Effect of amount of injected polymer on oil recovery at 5% oil cut

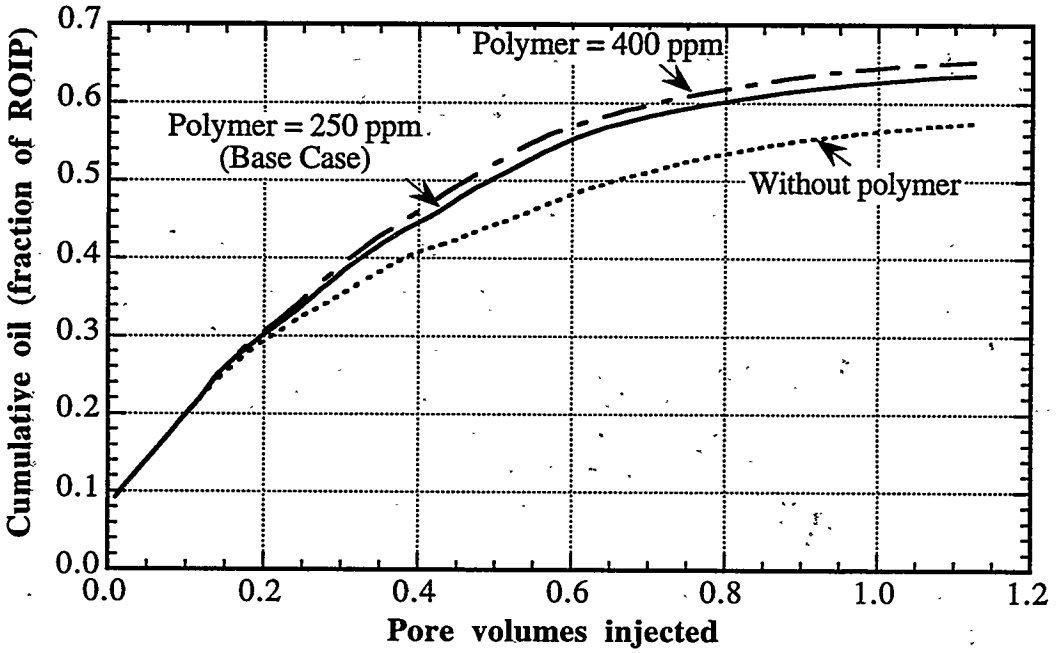


Figure 2.162 Effect of amount of injected polymer on oil recovery

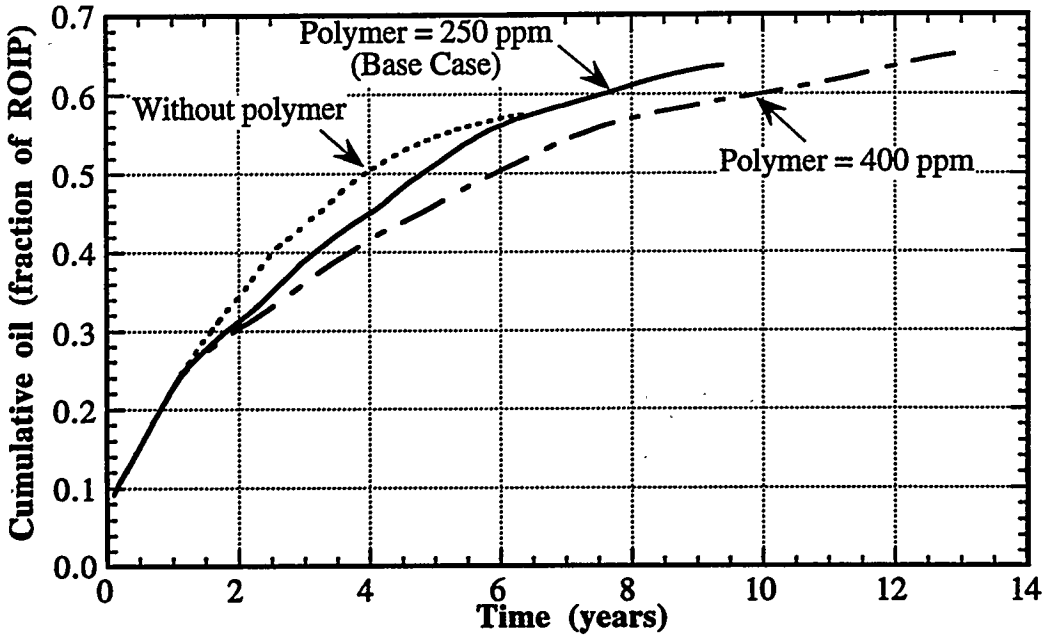


Figure 2.163 Effect of polymer concentrations on oil recovery

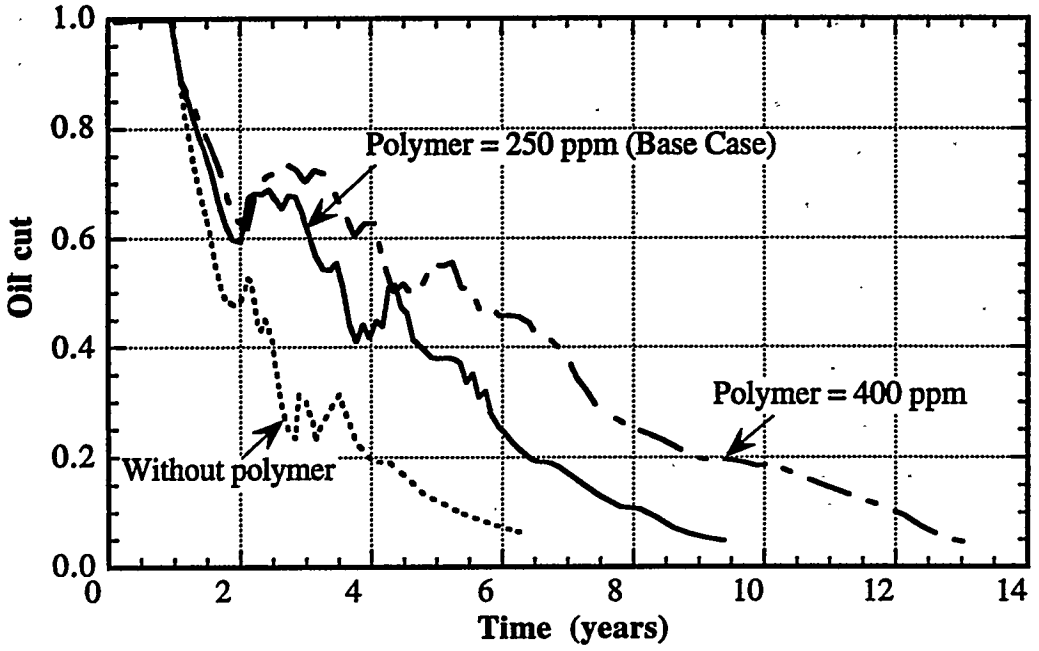


Figure 2.164 Effect of polymer concentrations on oil cut

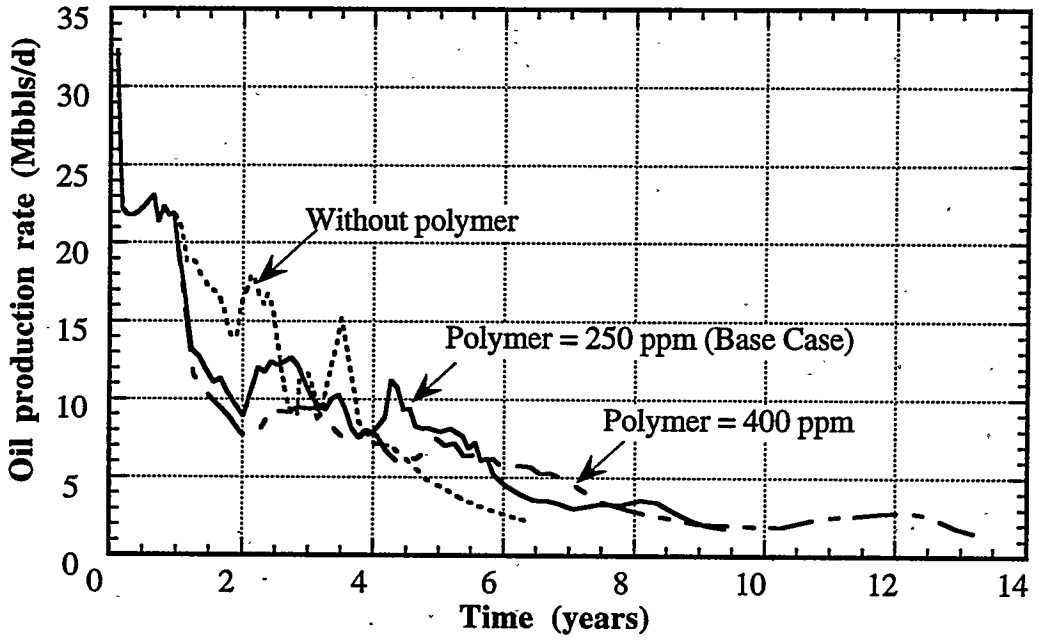


Figure 2.165 Effect of polymer concetrations on oil production rate

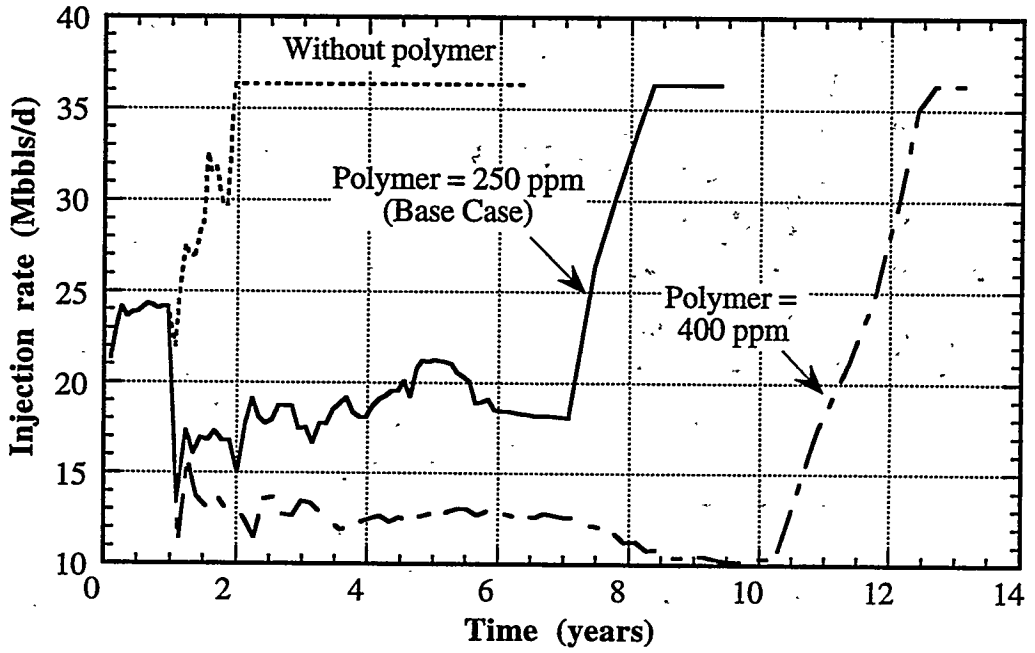


Figure 2.166 Effect of amount of injected polymer on injection rate

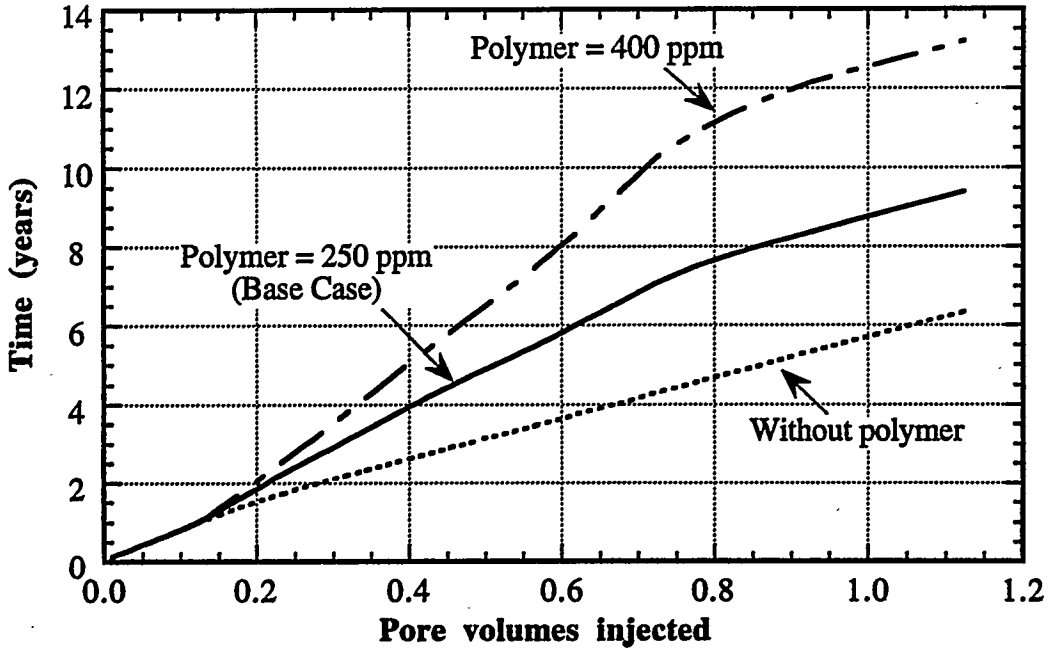


Figure 2.167 Effect of amount of injected polymer on project life

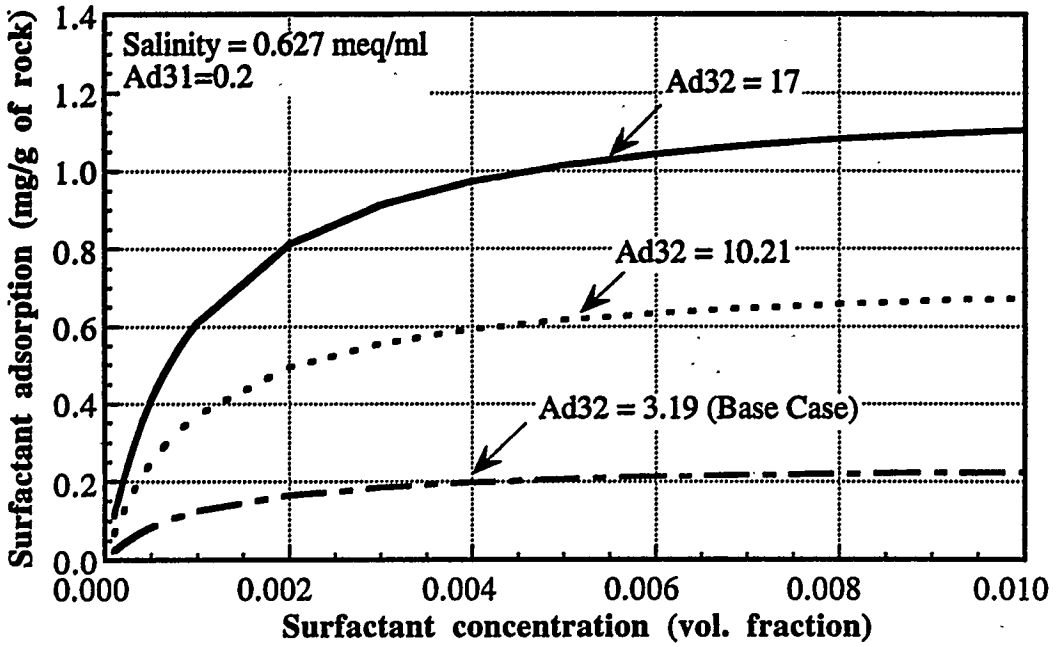


Figure 2.168 Surfactant adsorption isotherm used in sensitivity study

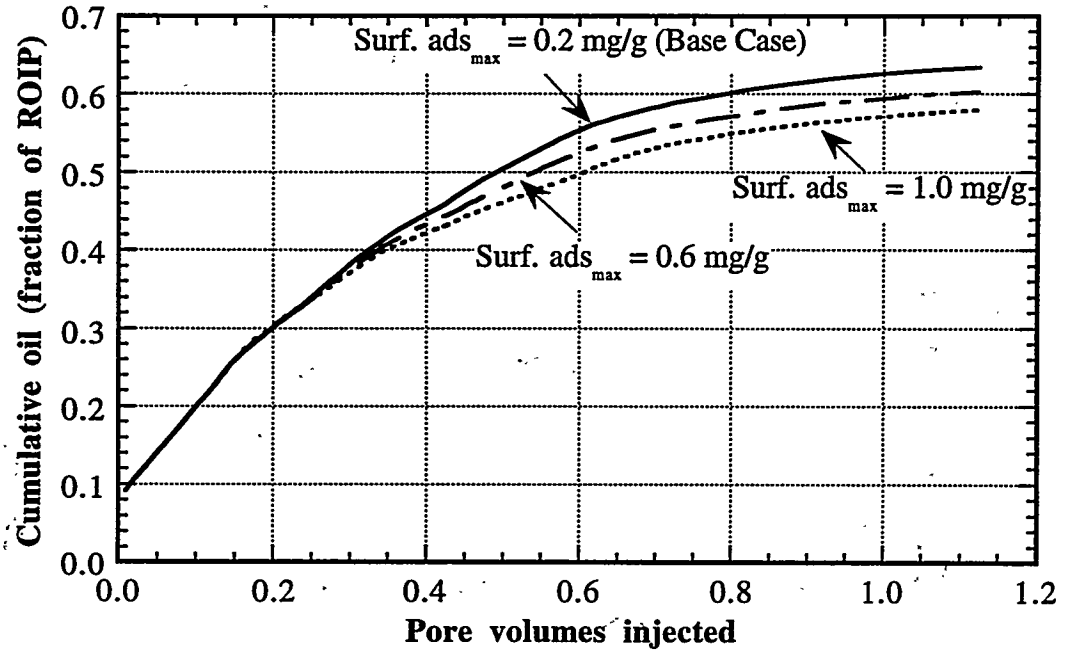


Figure 2.169 Effect of surfactant adsorption on oil recovery

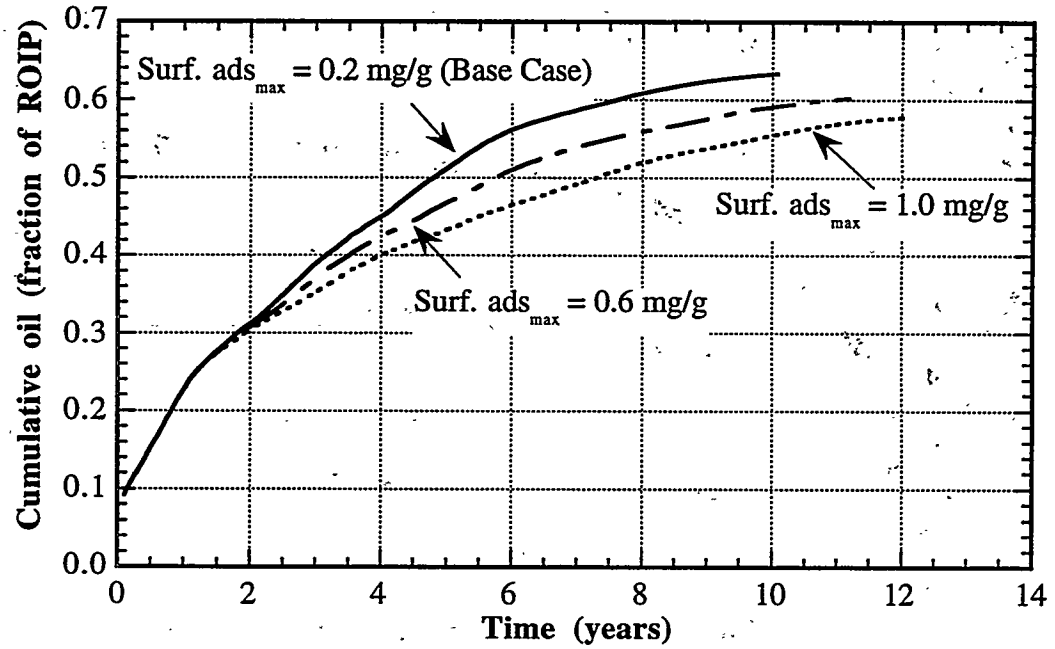


Figure 2.170 Effect of surfactant adsorption on oil recovery

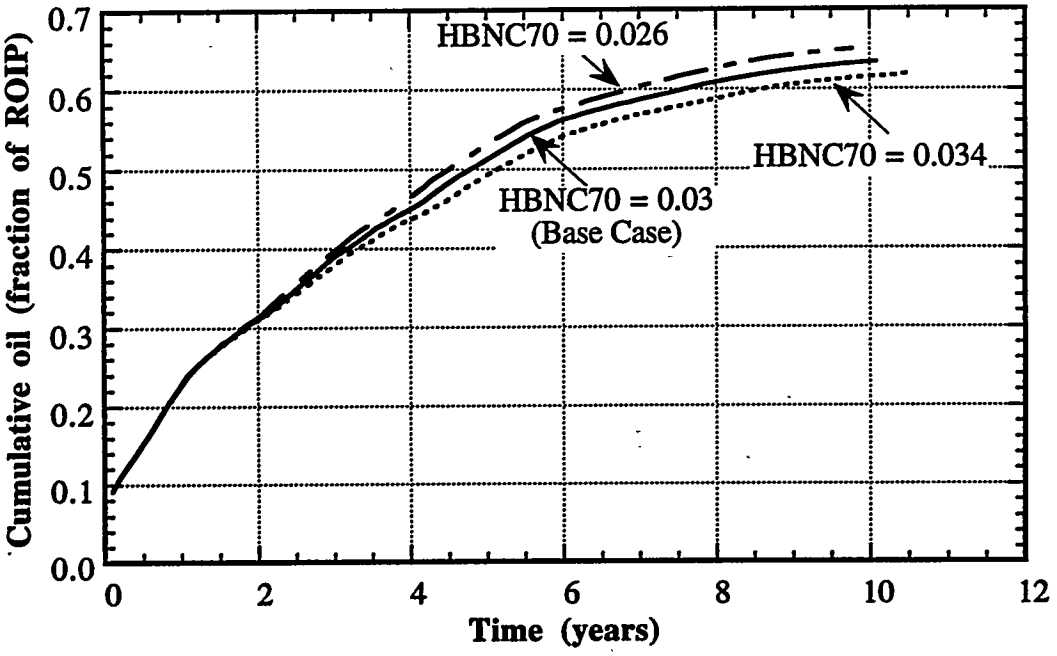


Figure 2.171 Effect of height of binodal curve at optimum salinity on oil recovery

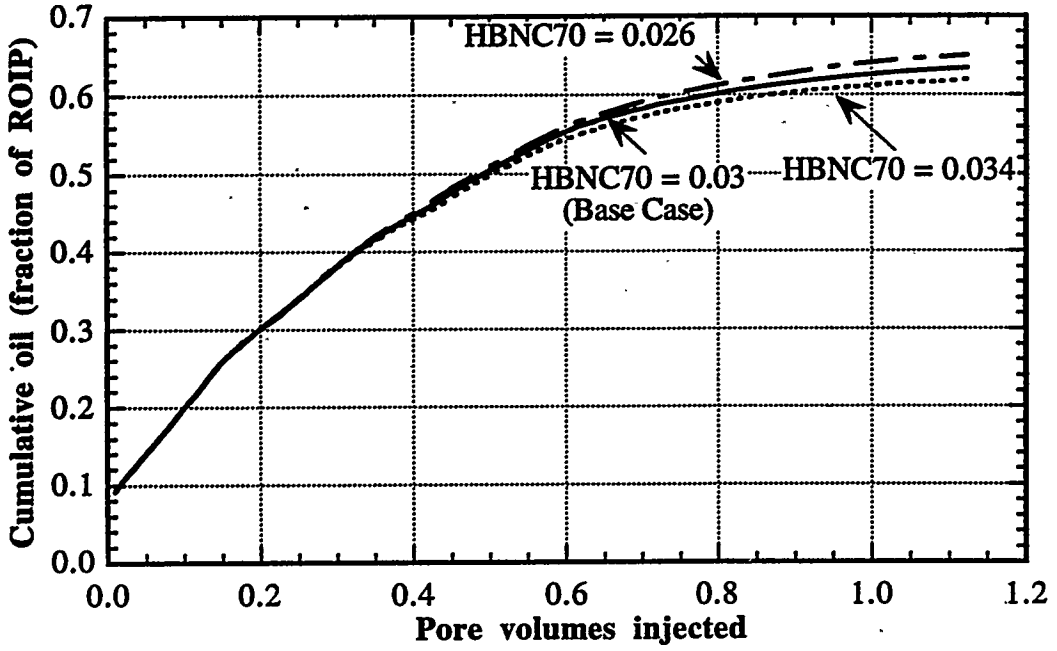


Figure 2.172 Effect of height of binodal curve at optimum salinity on oil recovery

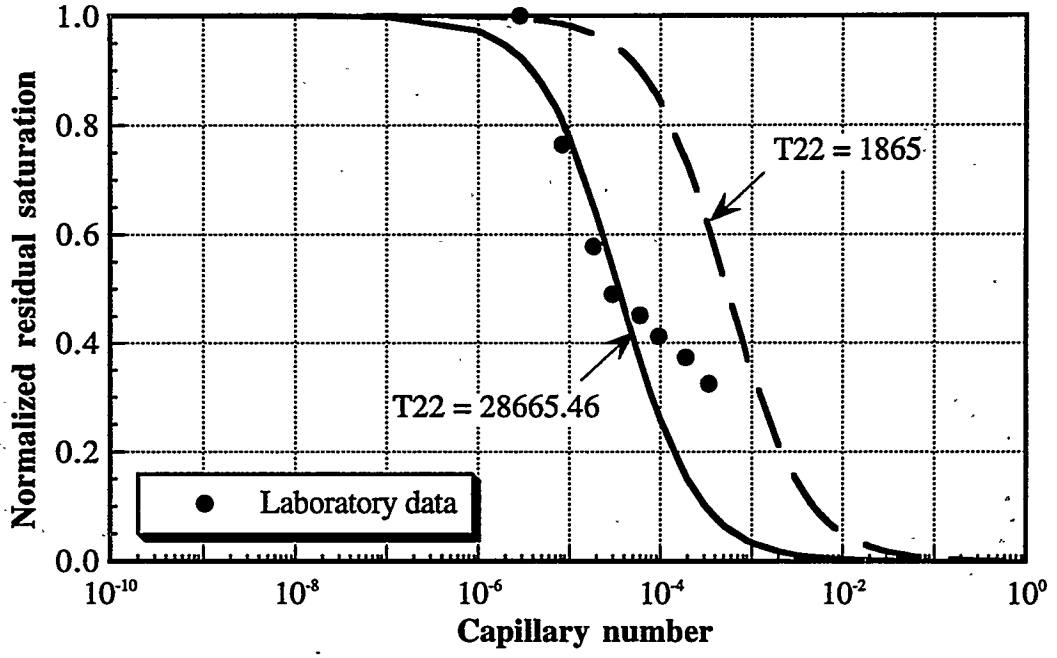


Figure 2.173 Oil desaturation curves used in the sensitivity study

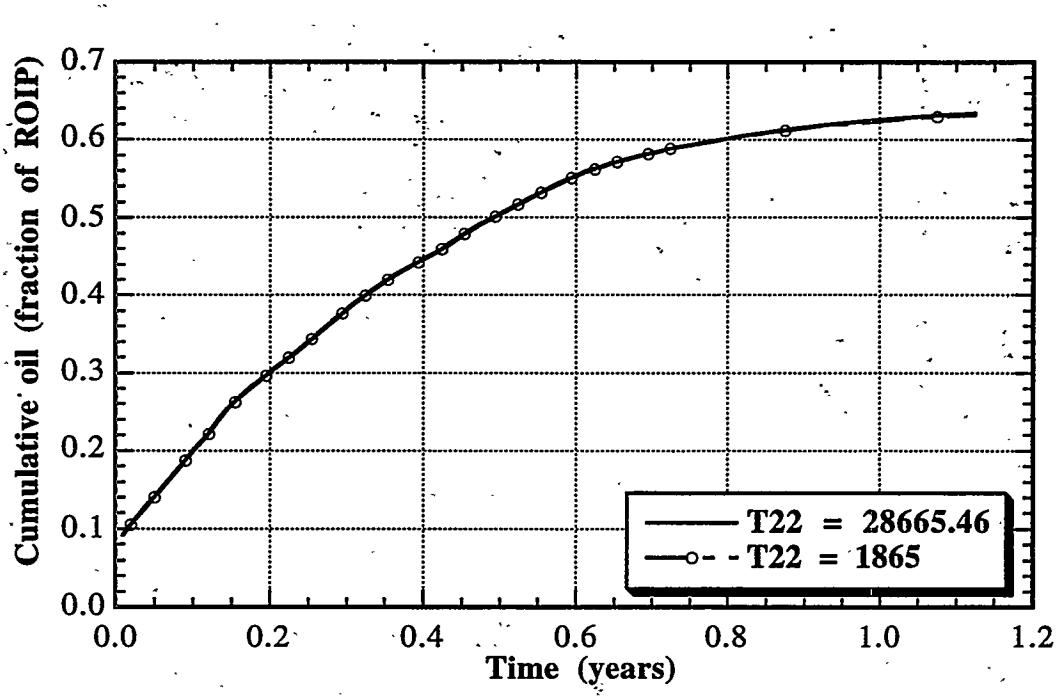


Figure 2.174 Effect of oil desaturation curves on oil recovery

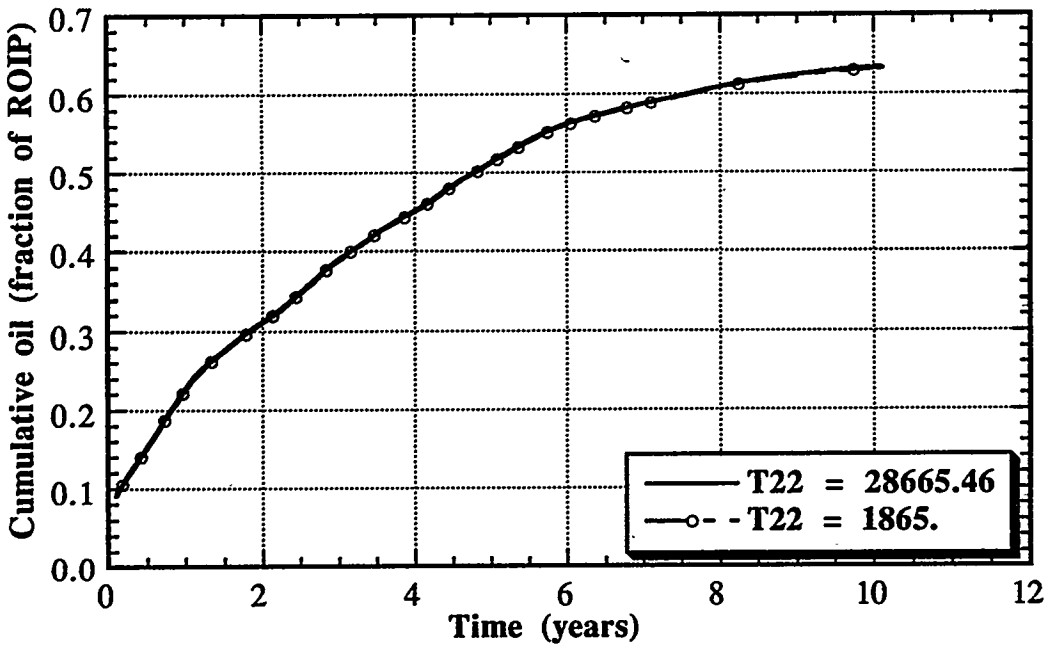


Figure 2.175 Effect of oil desaturation curves on oil recovery

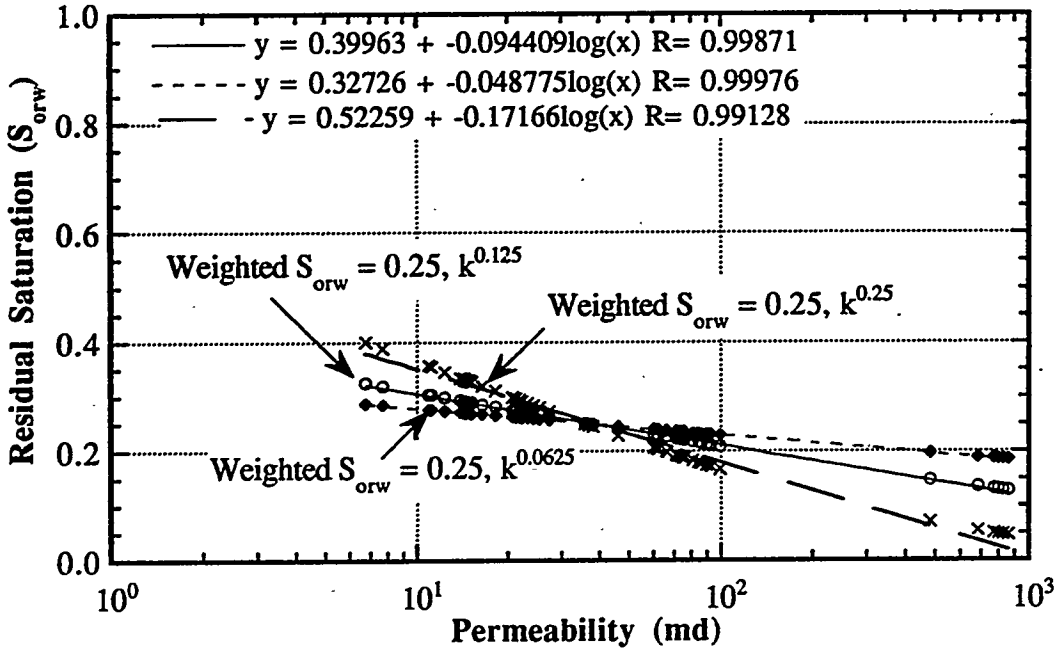


Figure 2.176 Residual oil saturations as a function of permeability

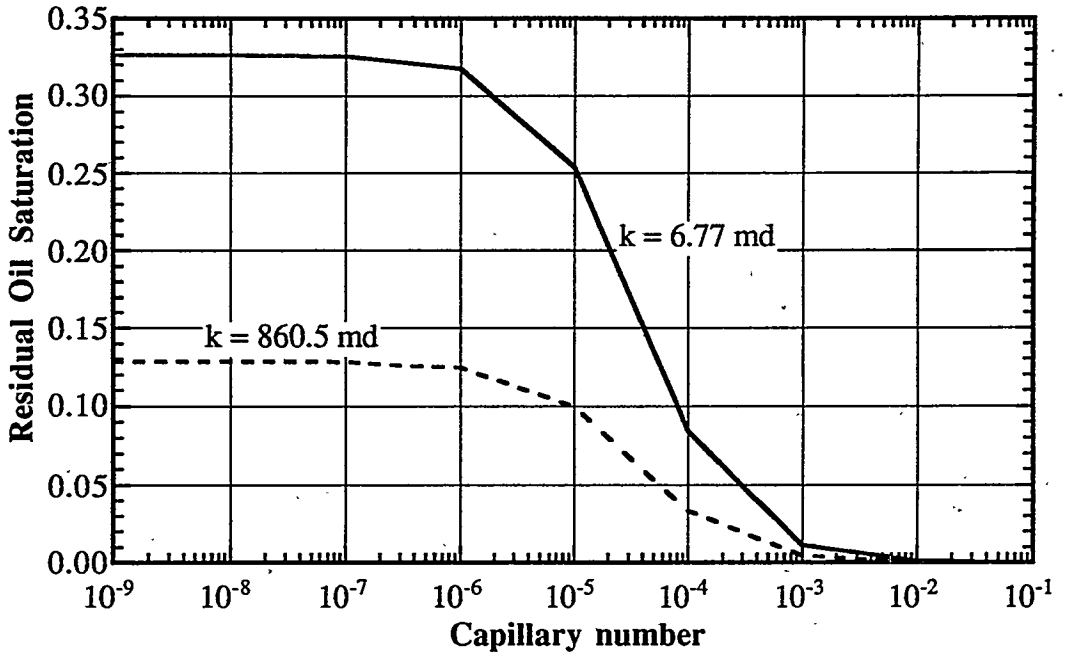


Figure 2.177 Capillary desaturation curves for permeability-dependent S_{orw} ($S_{orw}=\exp(-0.88222k^{0.125})$)

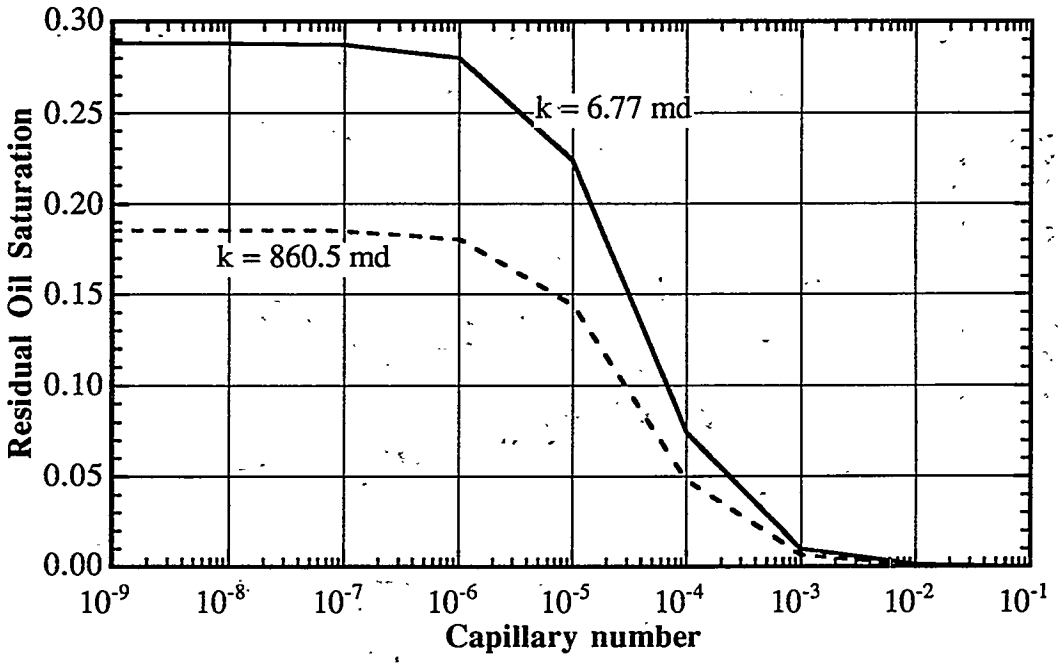


Figure 2.178 Capillary desaturation curves for permeability-dependent S_{orw} ($S_{orw}=\exp(-1.1048k^{0.0625})$)

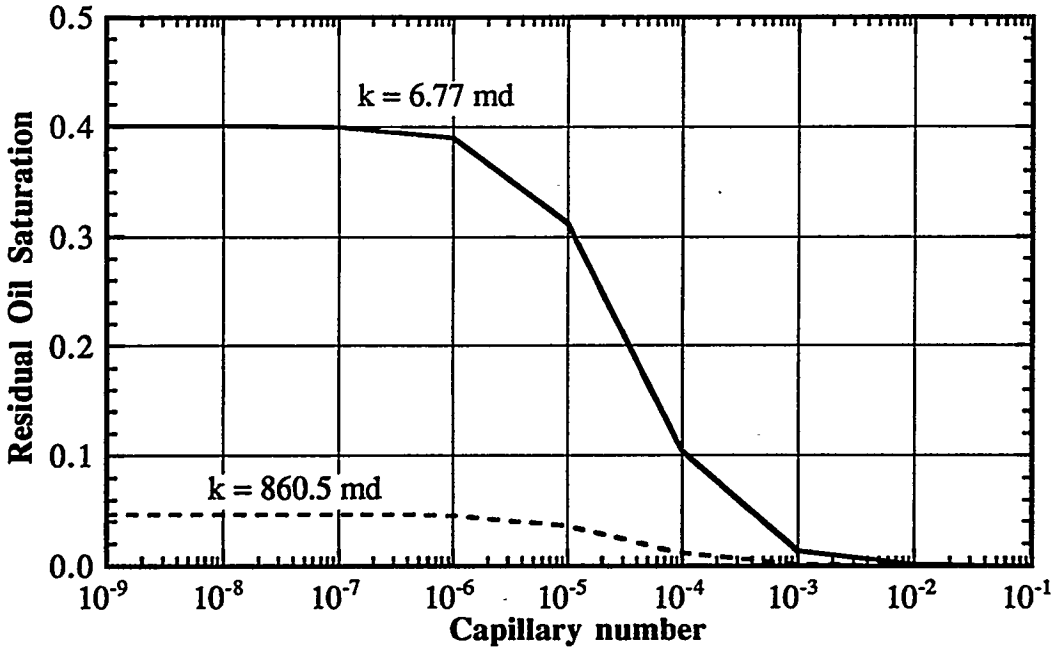


Figure 2.179 Capillary desaturation curves for permeability-dependent S_{orw} ($S_{orw}=\exp(-0.5665k^{0.25})$)

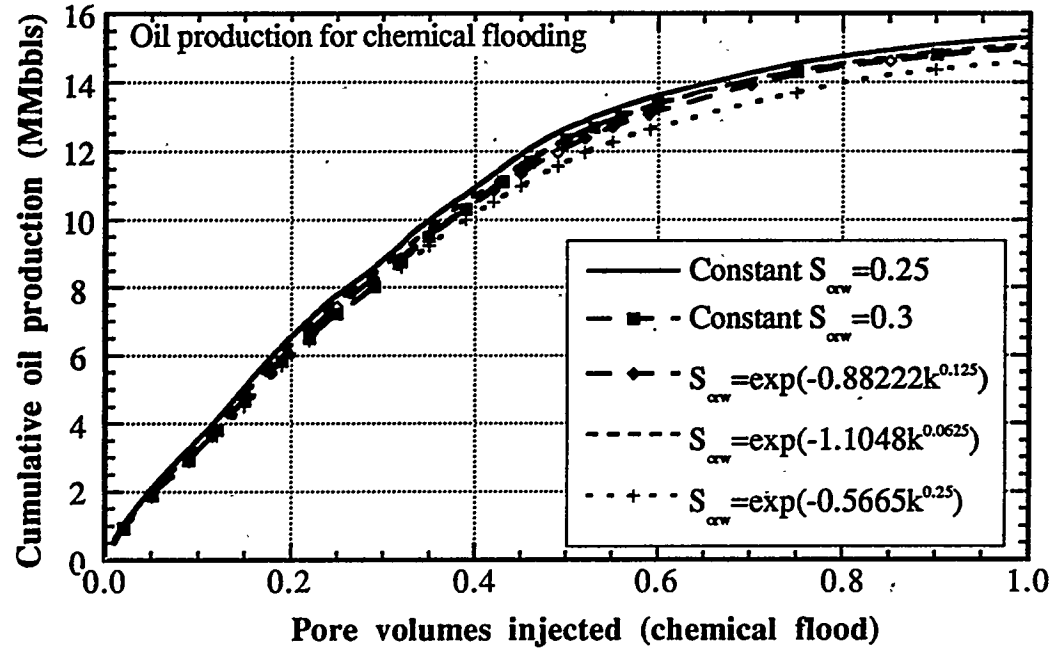


Figure 2.180 Effect of residual oil saturations on chemical flood oil recovery

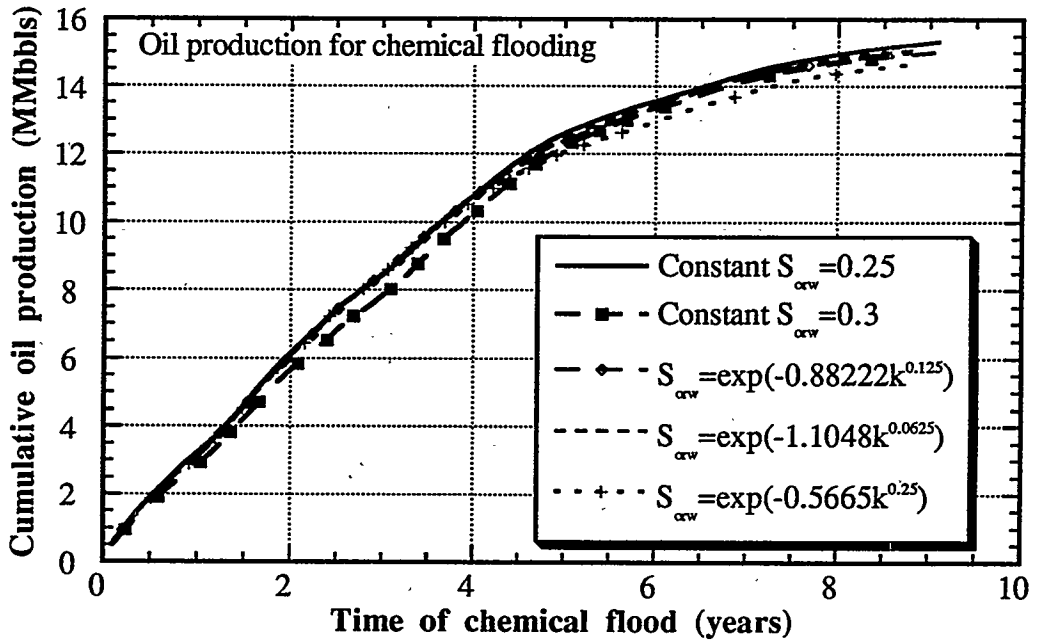


Figure 2.181 Effect of residual oil saturations on chemical flood oil recovery

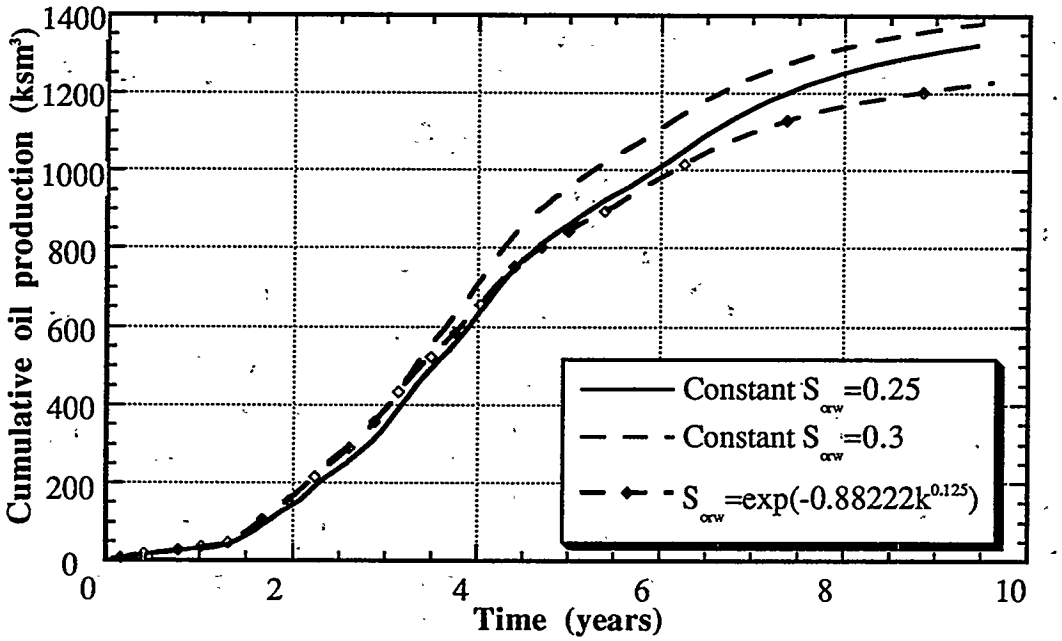


Figure 2.182 Effect of residual saturations on tertiary cumulative oil production

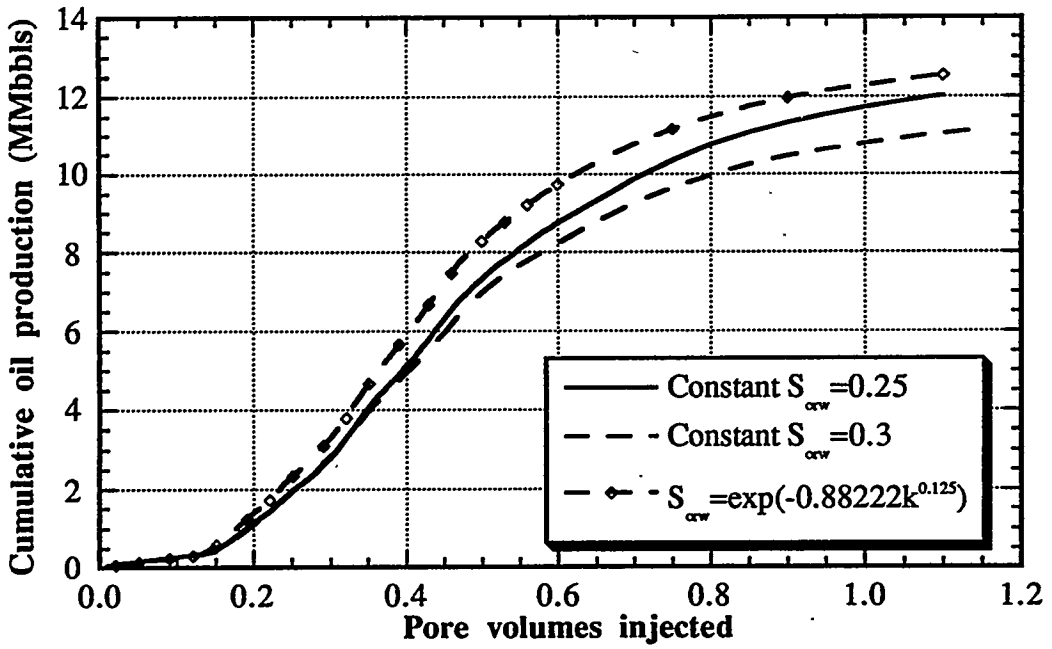


Figure 2.183 Effect of residual saturation on tertiary cumulative oil production

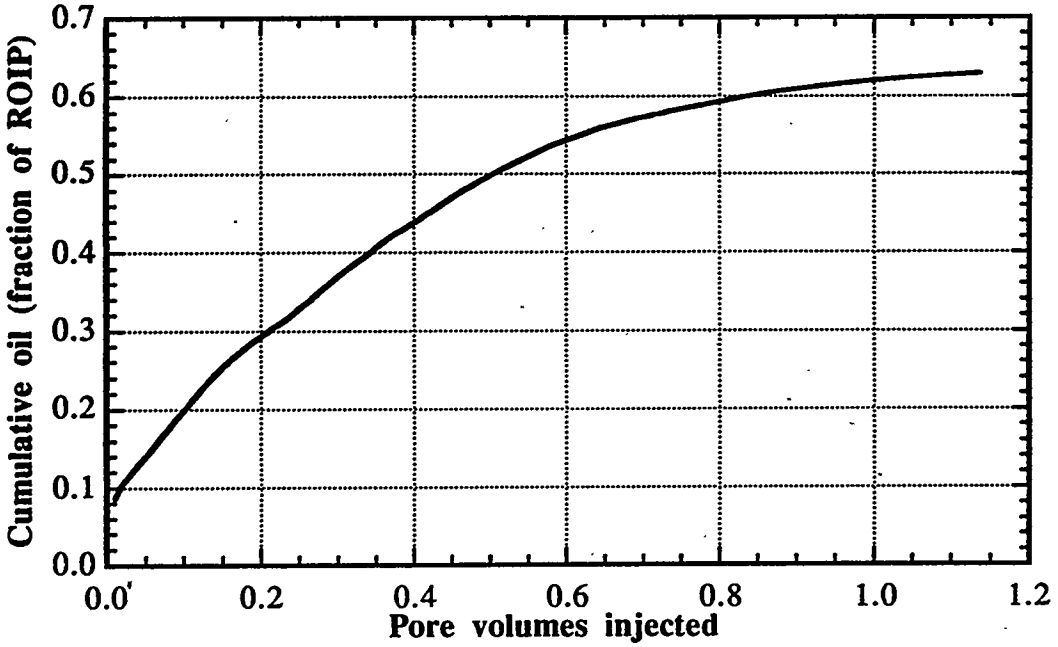


Figure 2.184 Oil recovery as a function of pore volumes injected for the new Base Case simulation

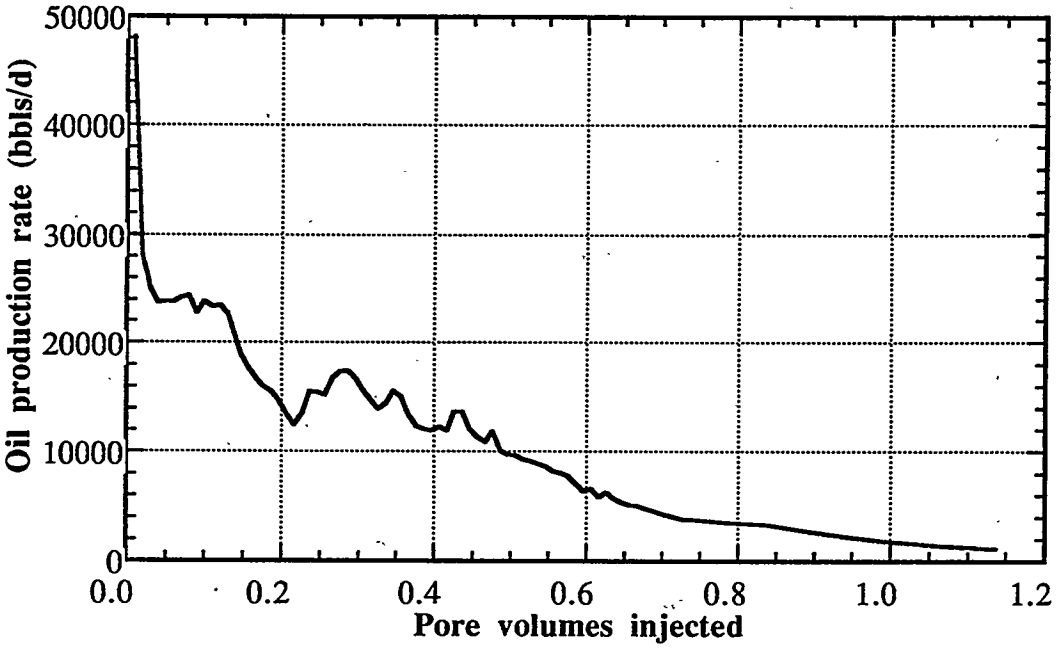


Figure 2.185 Oil production rate as a function of pore volumes injected for the new Base Case simulation

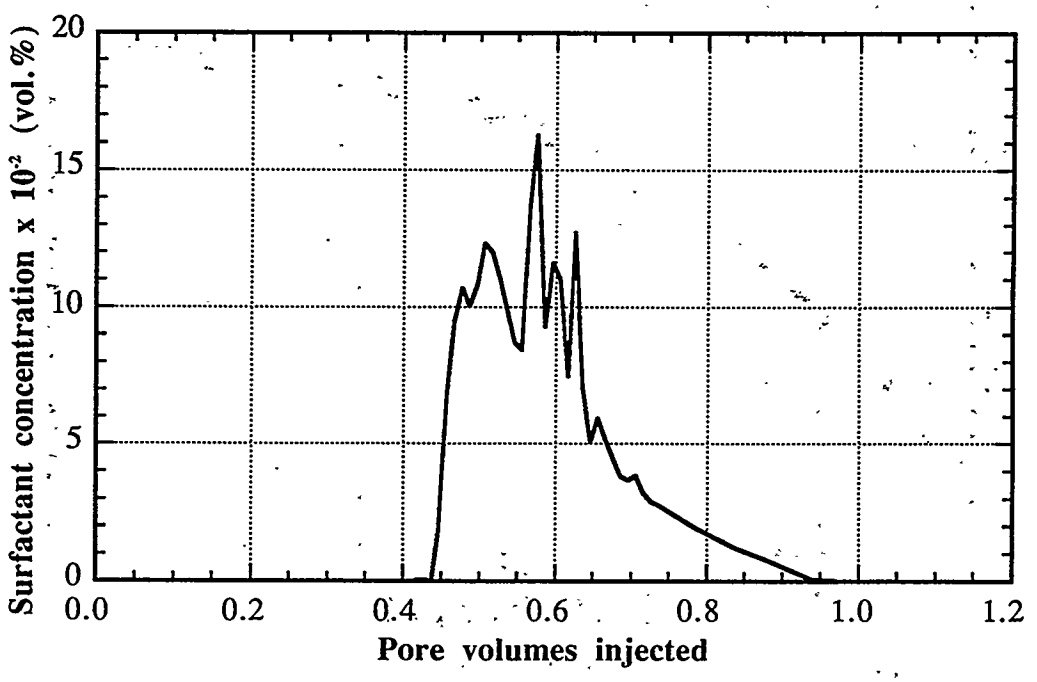


Figure 2.186 Produced surfactant concentration as a function of pore volumes injected for the new Base Case simulation

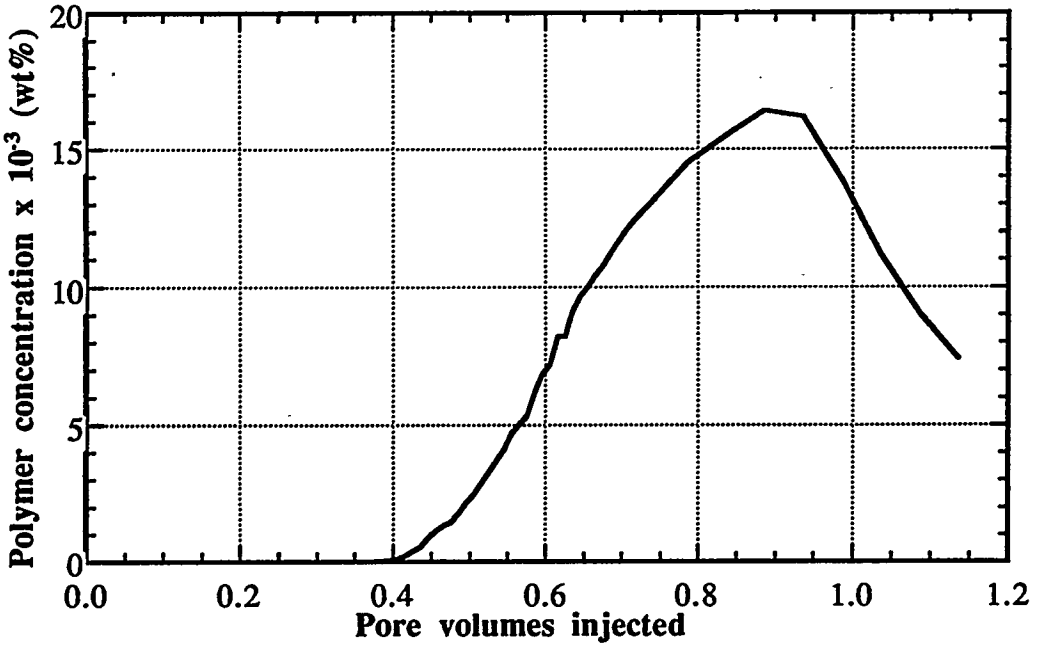


Figure 2.187 Produced polymer concentration as a function of pore volumes injected for the new Base Case simulation

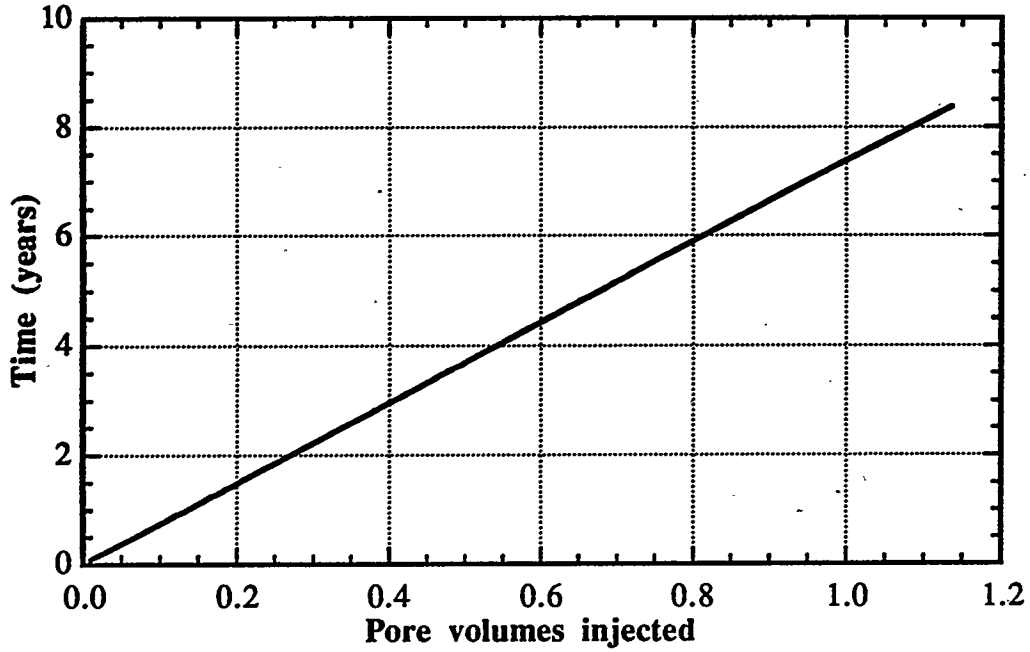


Figure 2.188 Project life as a function of pore volumes injected for the new Base Case simulation

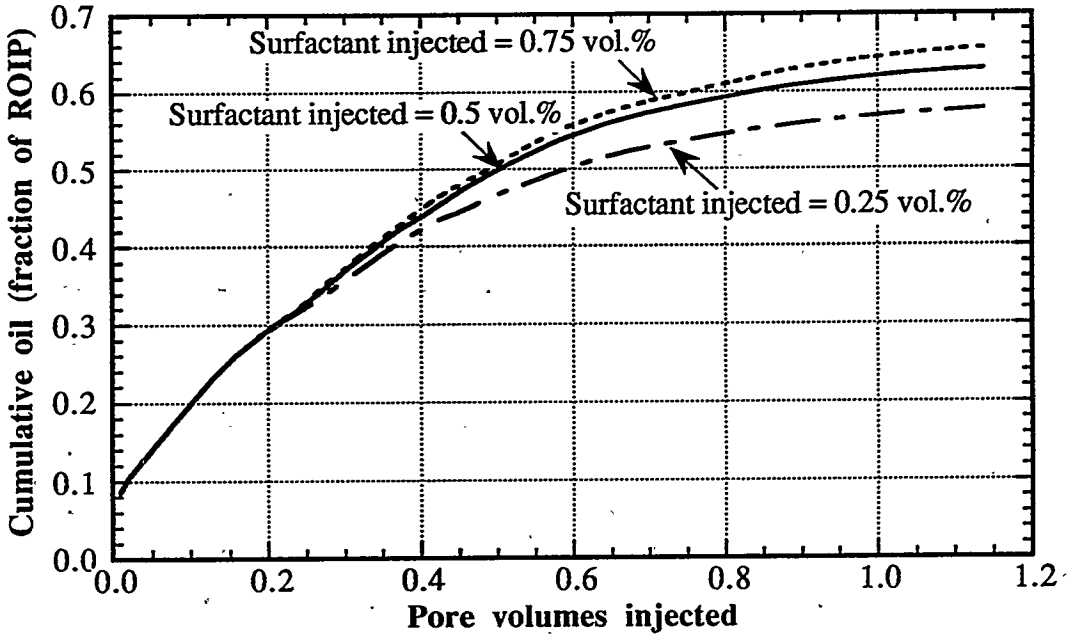


Figure 2.189 Effect of injected surfactant concentration on oil recovery

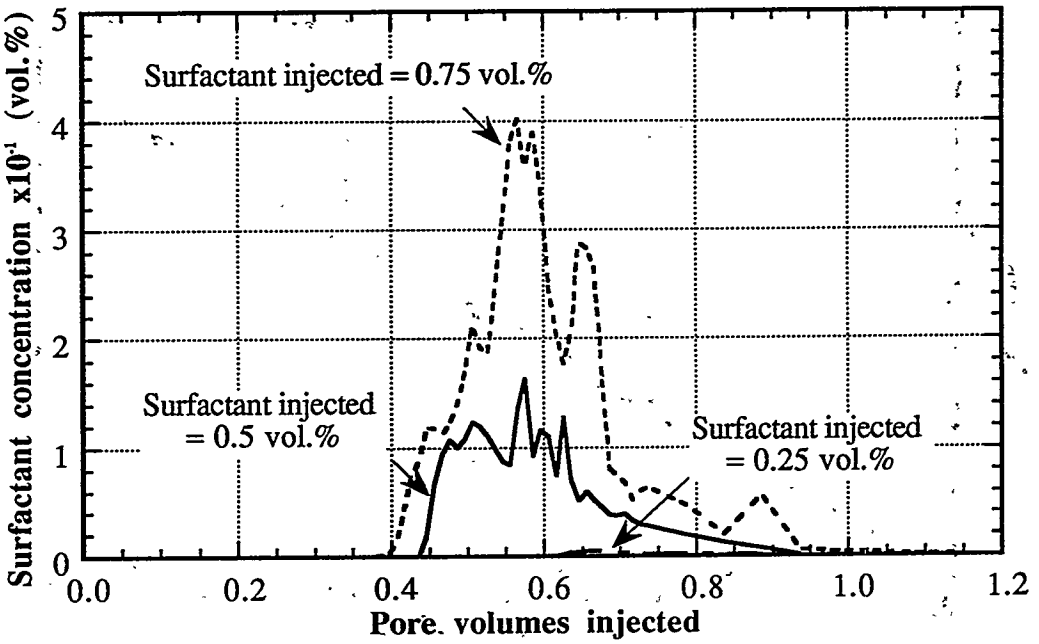


Figure 2.190 Effect of injected surfactant concentration on produced surfactant concentration

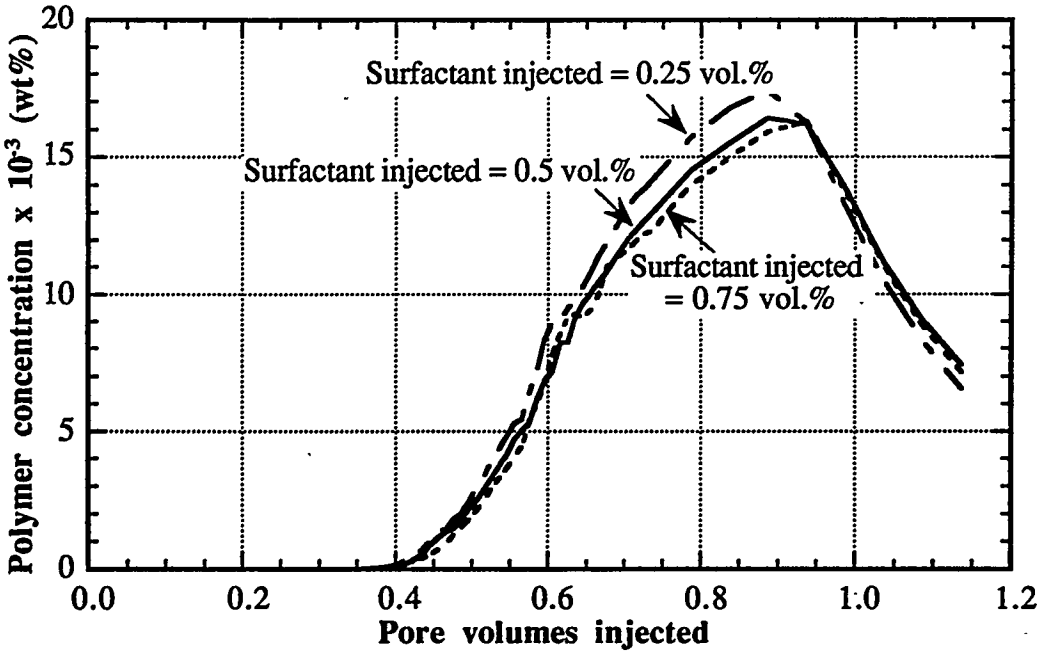


Figure 2.191 Effect of injected surfactant concentration on produced polymer concentration

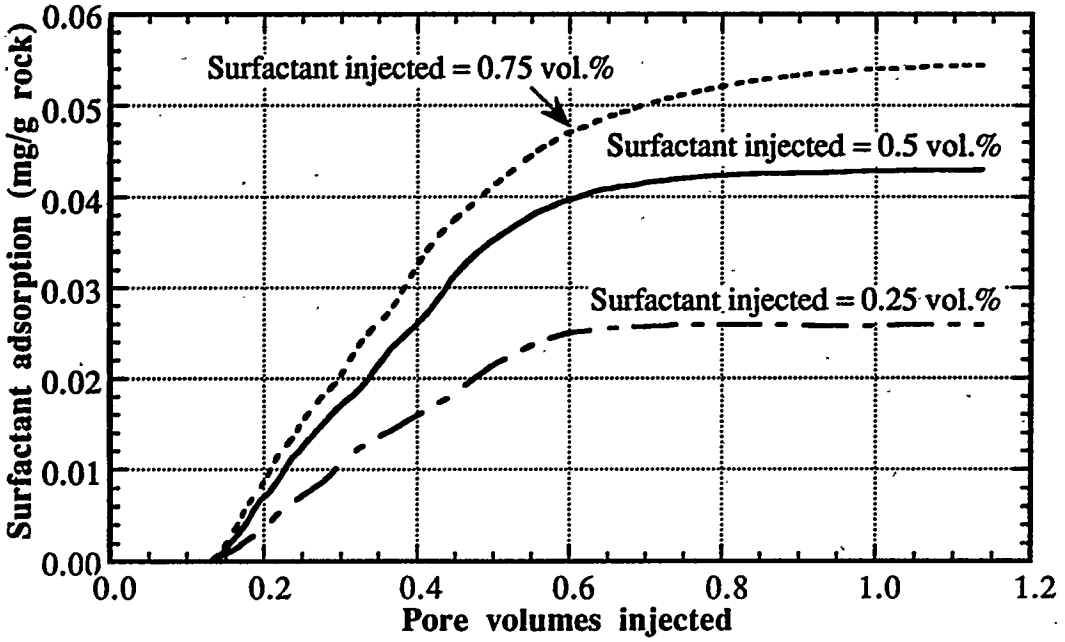


Figure 2.192 Effect of injected surfactant concentration on surfactant adsorption

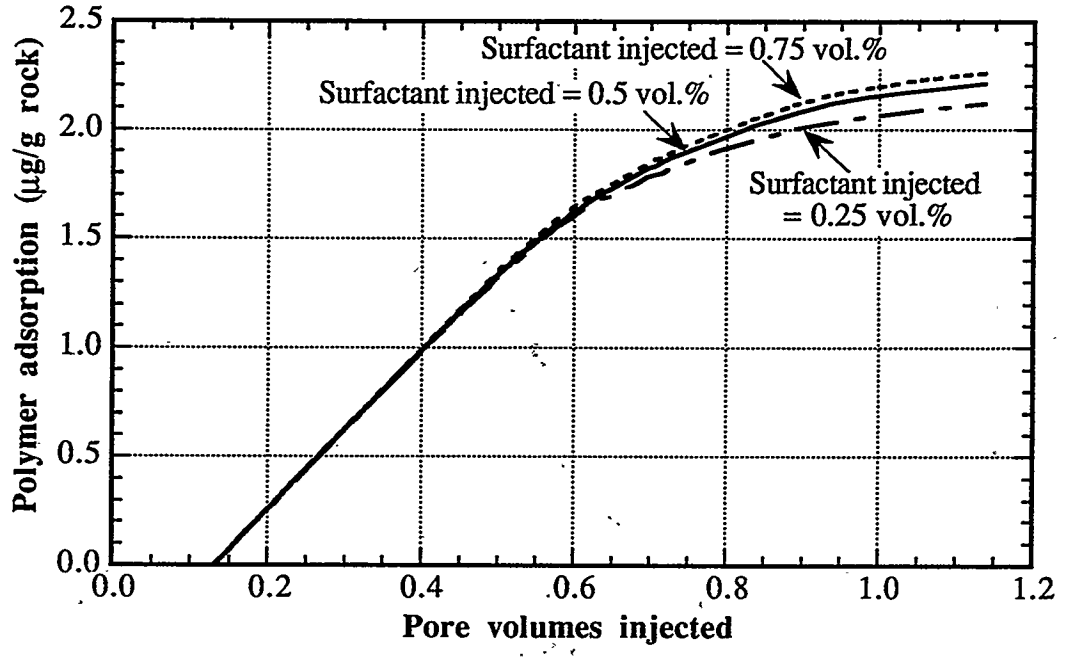


Figure 2.193 Effect of injected surfactant concentration on polymer adsorption

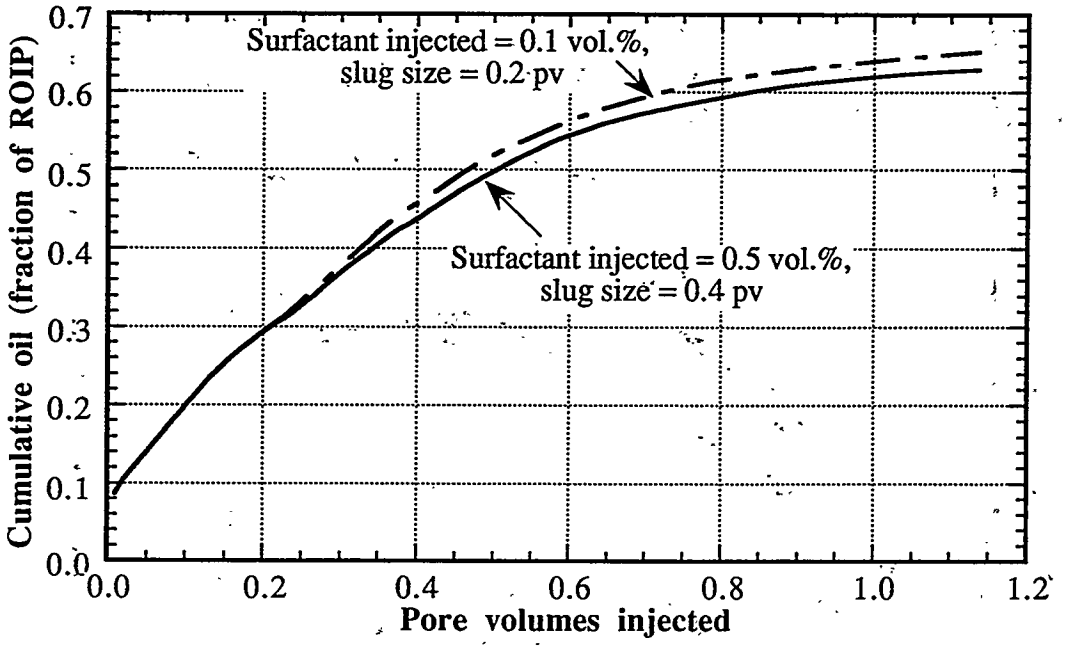


Figure 2.194 Effect of slug size on oil recovery

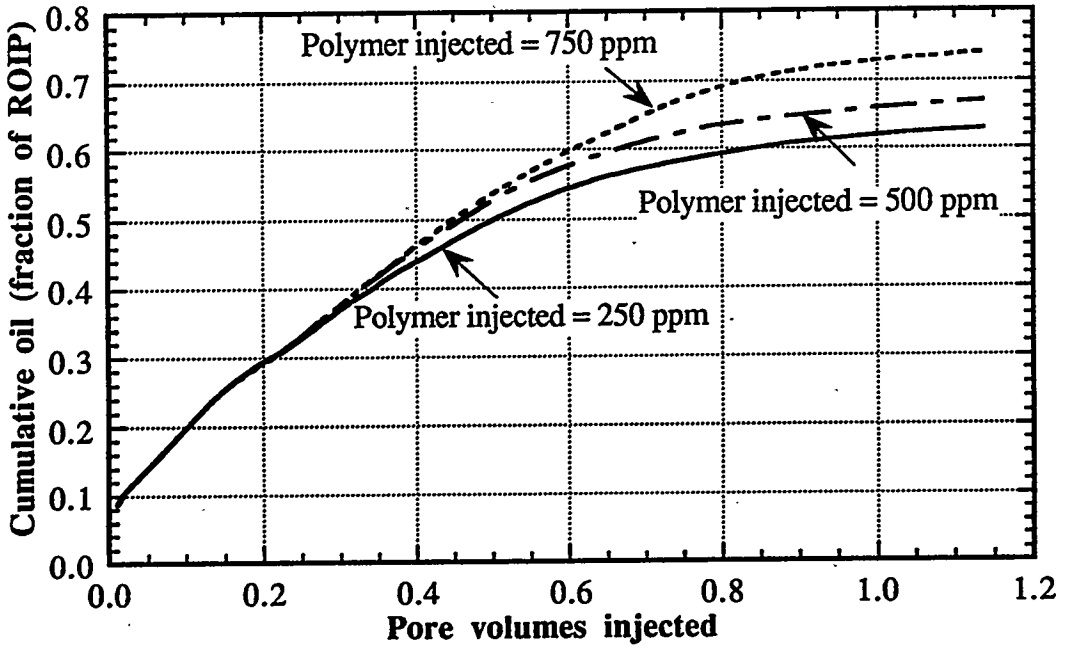


Figure 2.195 Effect of injected polymer concentration on oil recovery

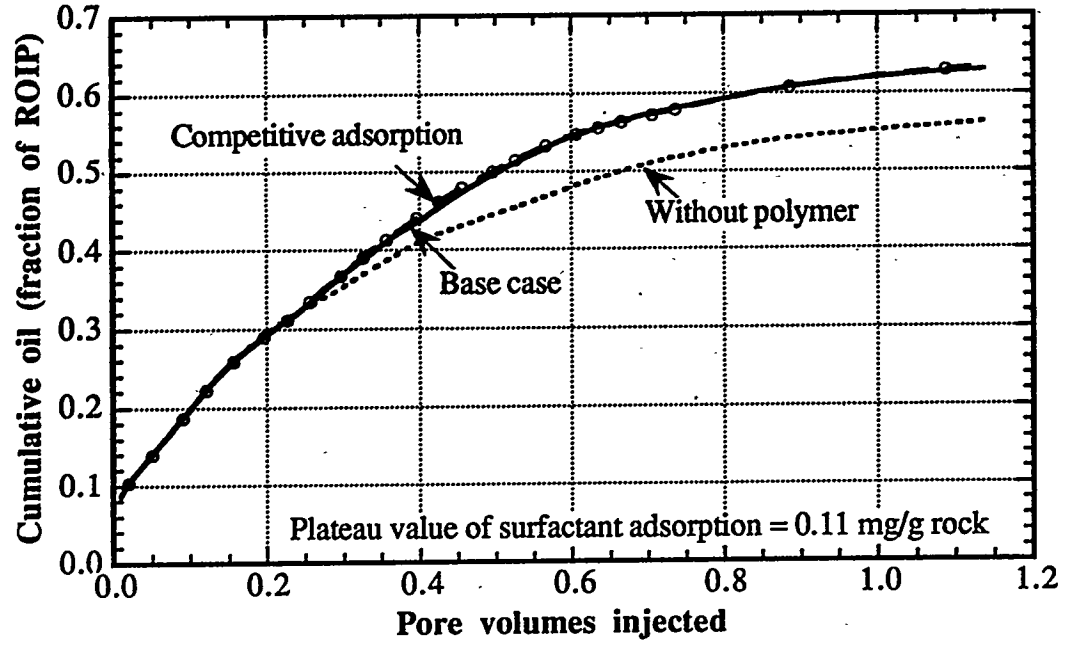


Figure 2.196 Effect of competitive adsorption on oil recovery

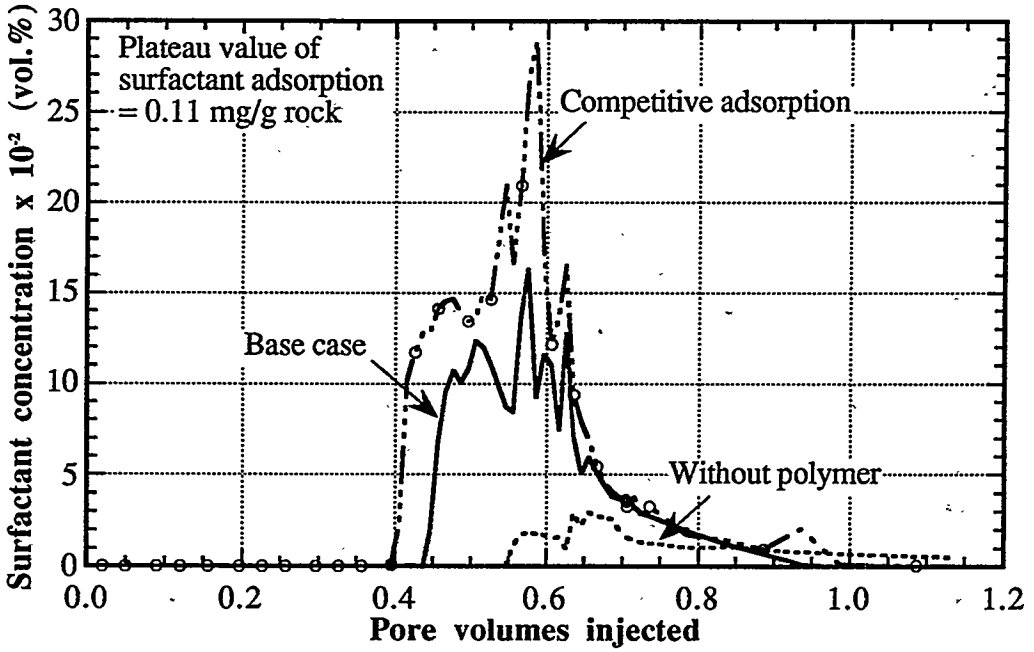


Figure 2.197 Effect of competitive adsorption on produced surfactant concentration

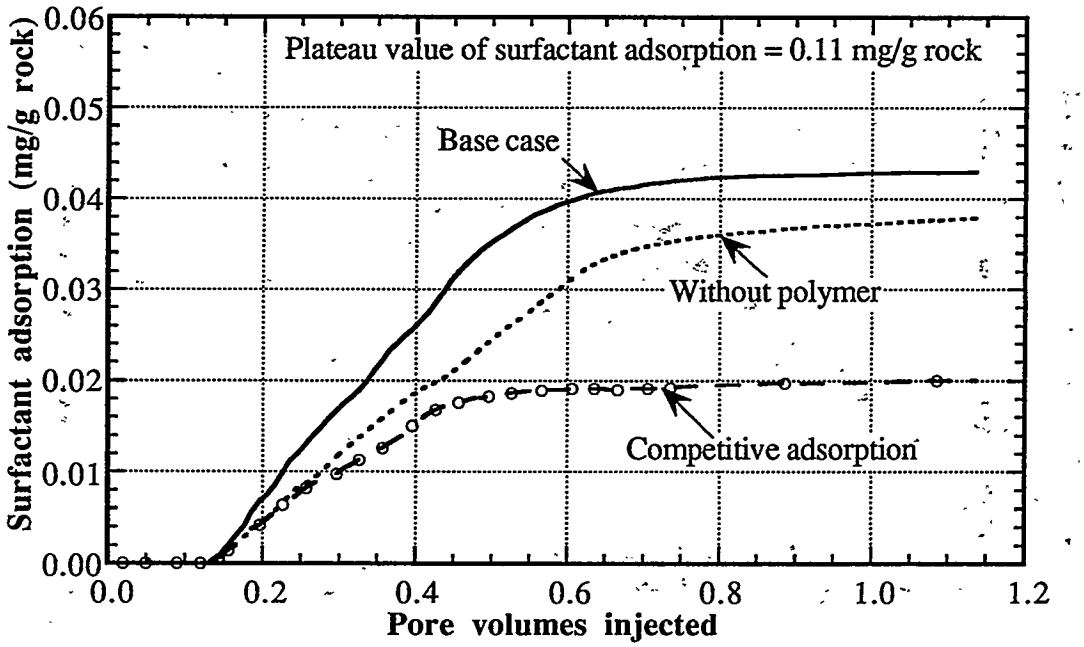


Figure 2.198 Effect of competitive adsorption on surfactant adsorption

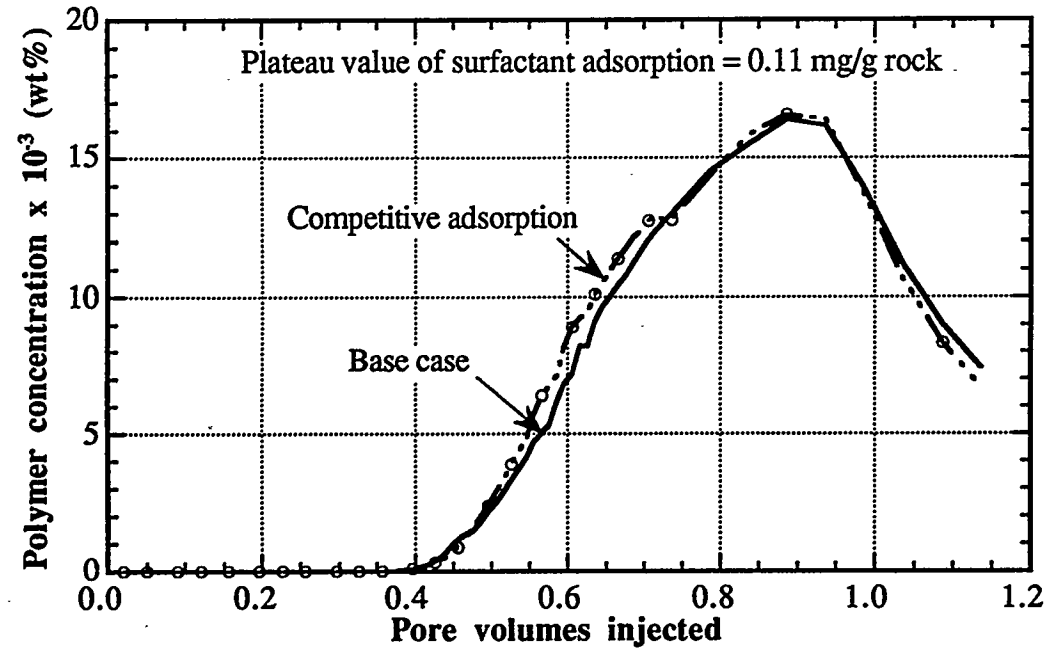


Figure 2.199 Effect of competitive adsorption on produced polymer concentration

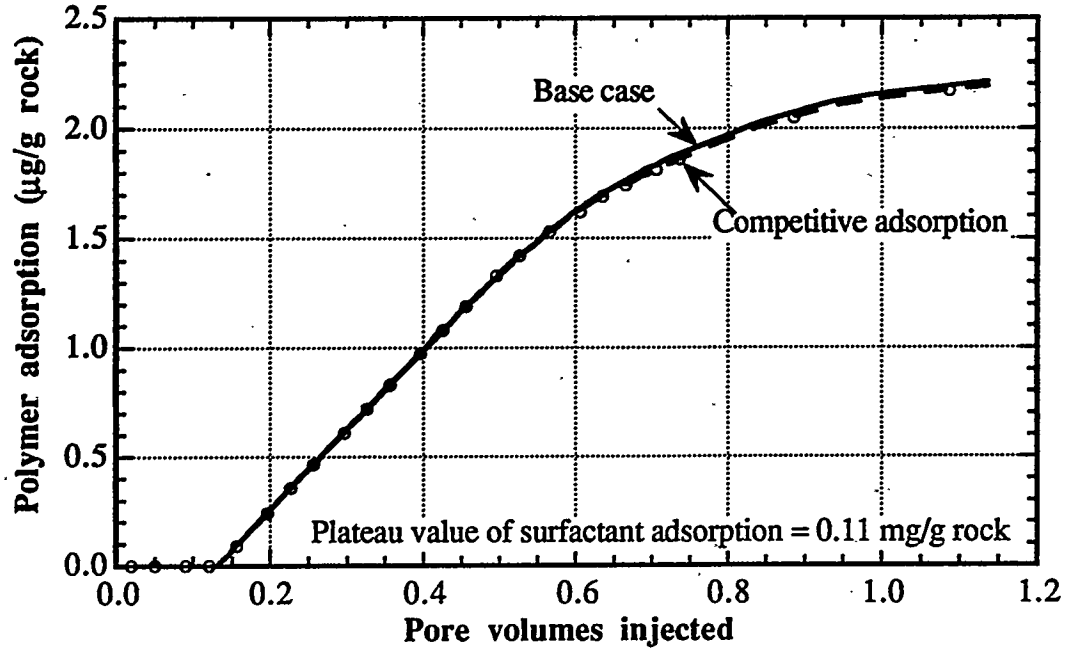


Figure 2.200 Effect of competitive adsorption on polymer adsorption

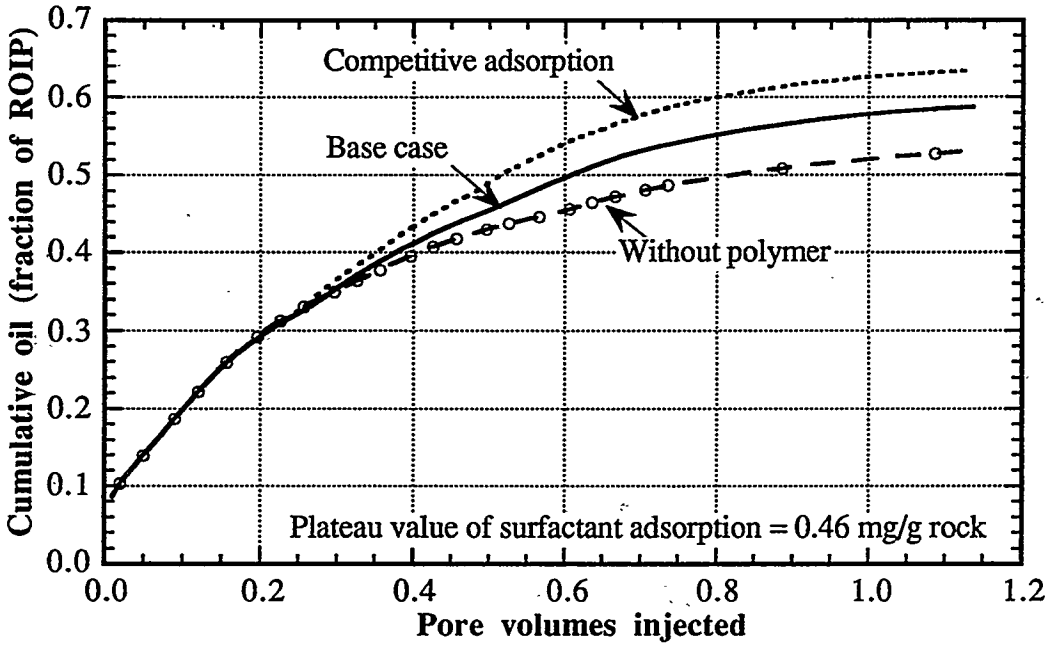


Figure 2.201 Effect of competitive adsorption on oil recovery

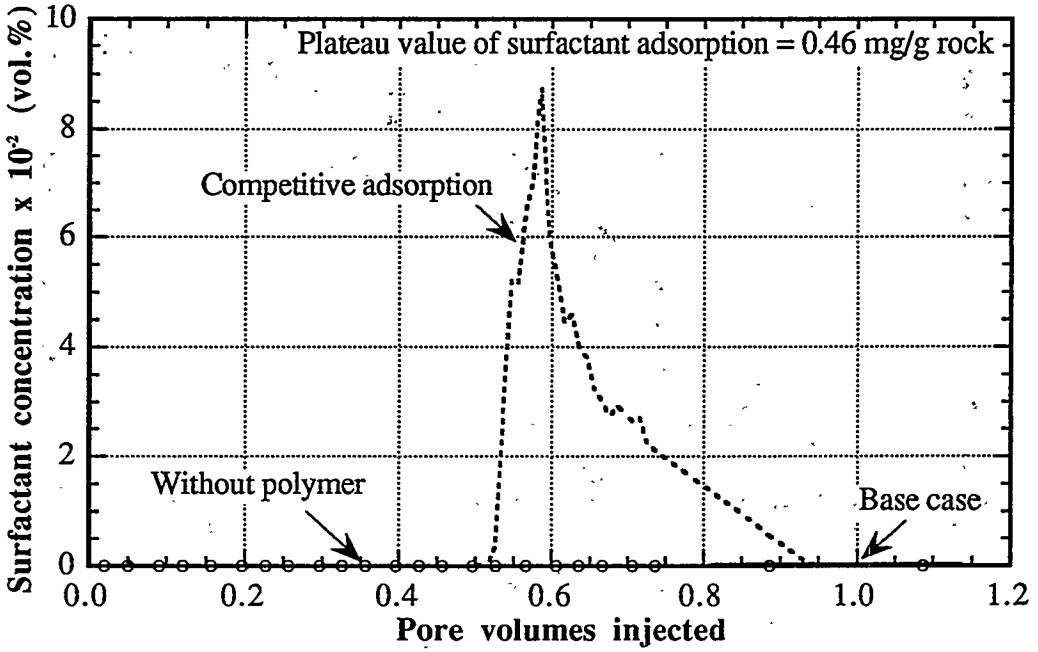


Figure 2.202 Effect of competitive adsorption on produced surfactant concentration

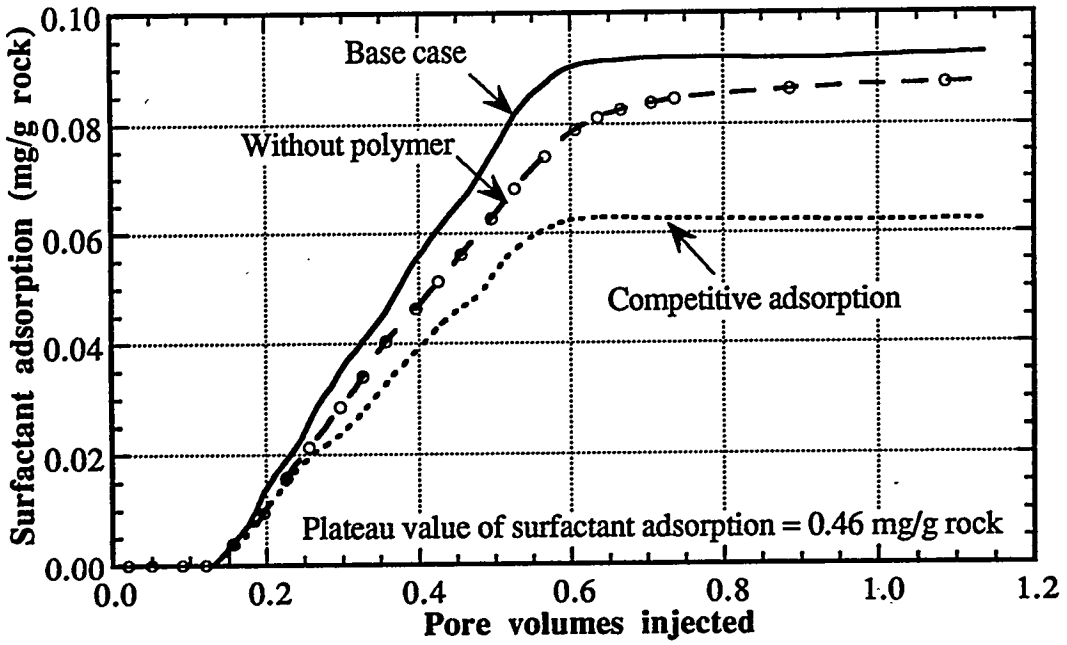


Figure 2.203 Effect of competitive adsorption on surfactant adsorption

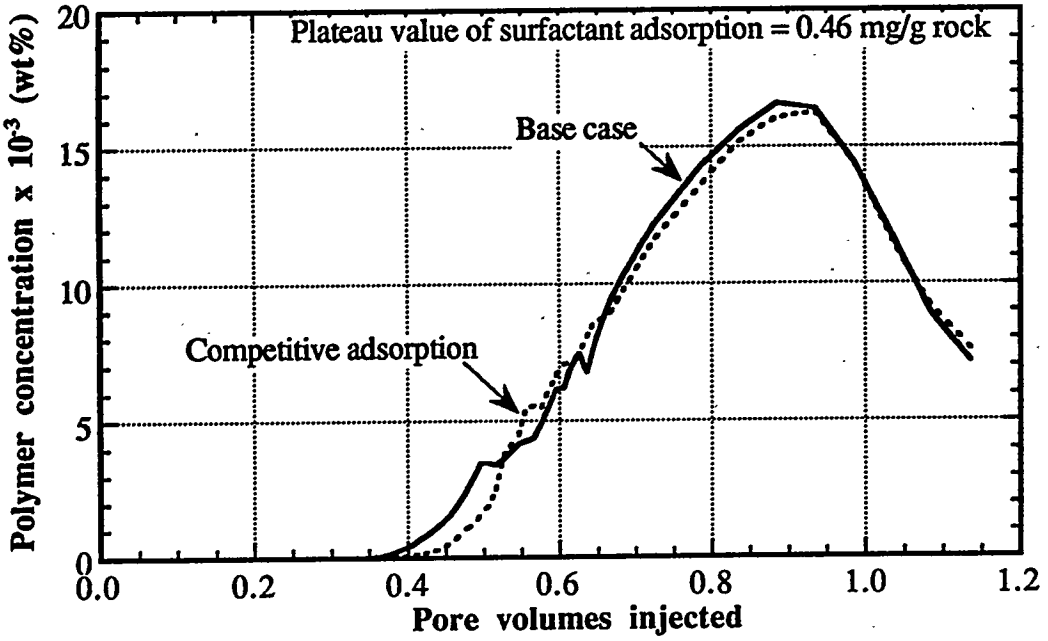


Figure 2.204 Effect of competitive adsorption on produced polymer concentration

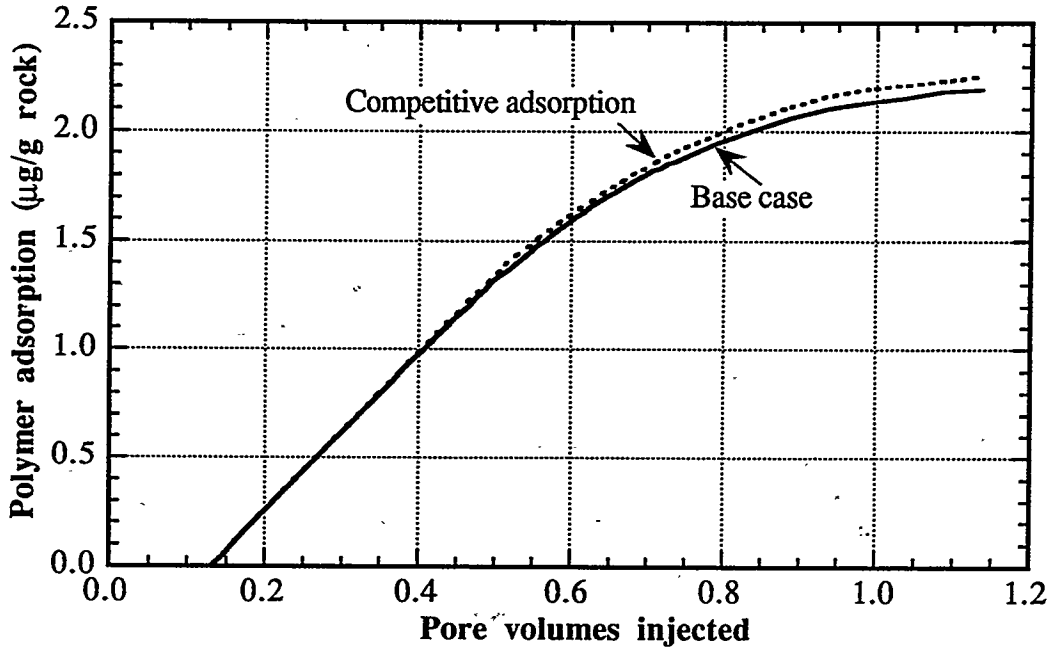


Figure 2.205 Effect of competitive adsorption on polymer adsorption

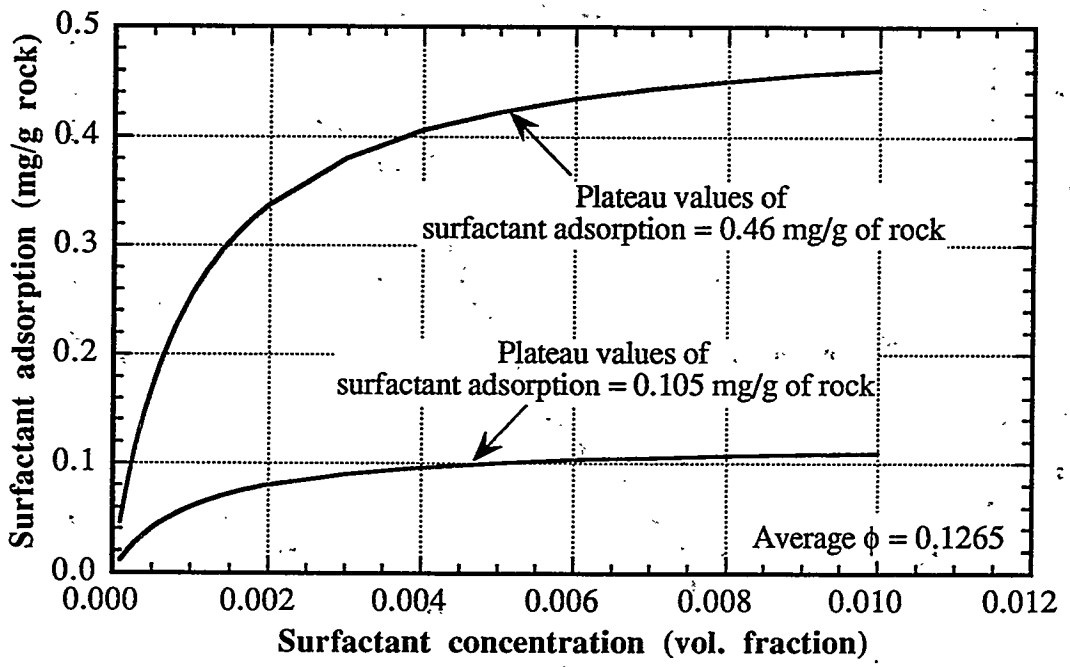


Figure 2.206 Surfactant adsorption isotherm

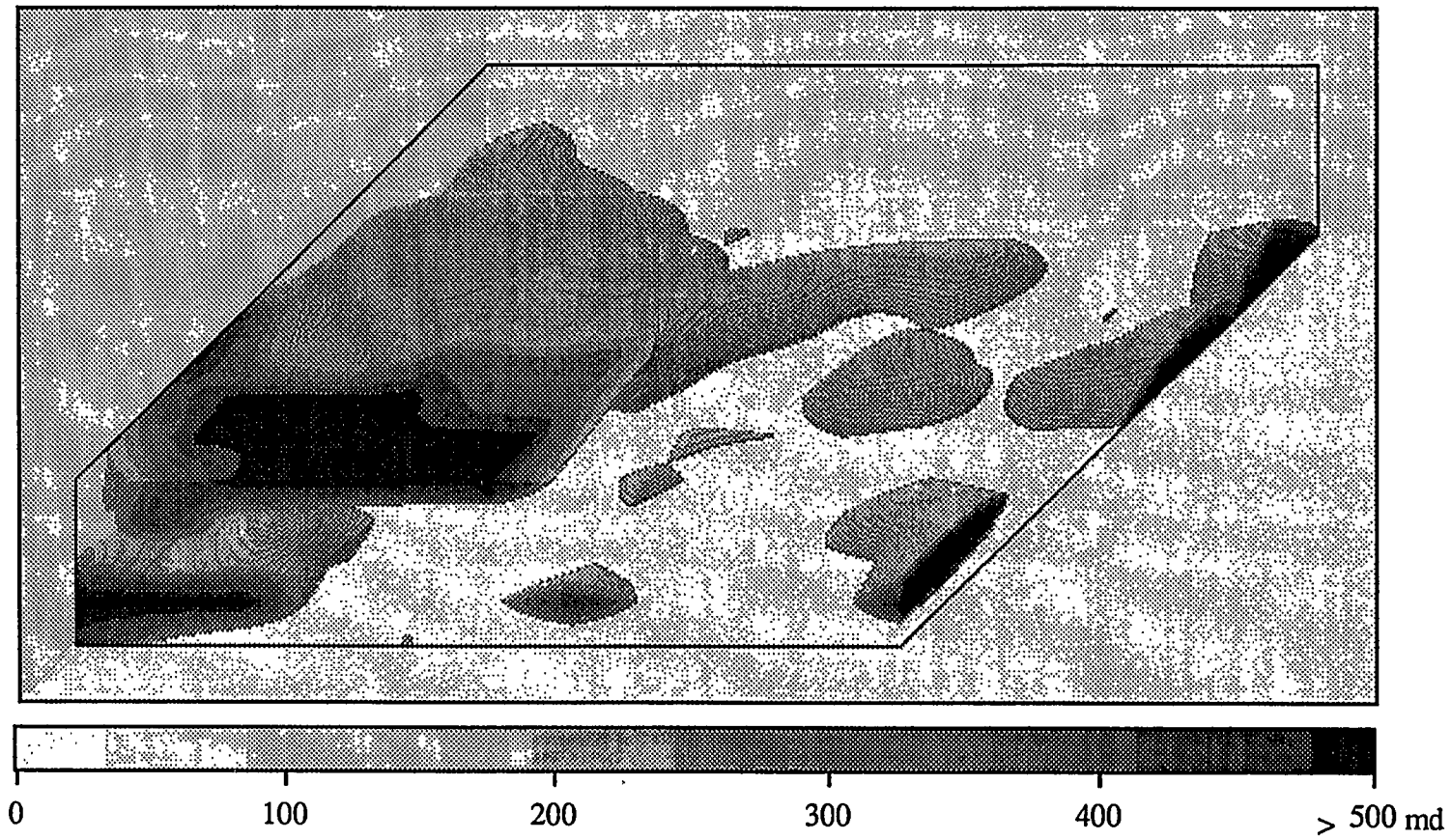


Figure 2.207 Permeability distribution with the 200 md iso-surface

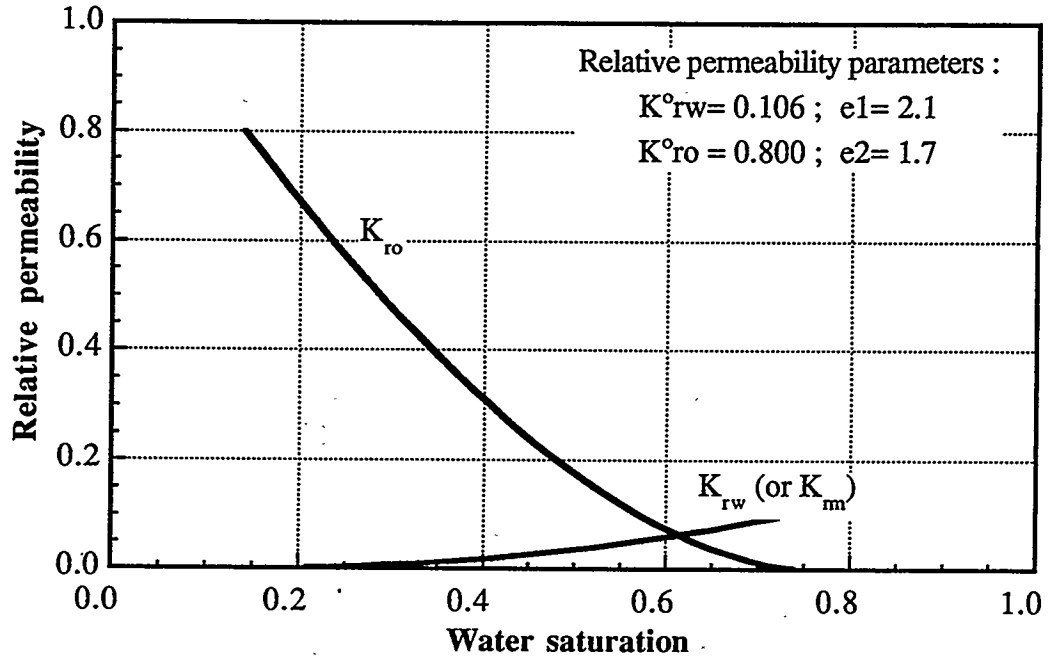


Figure 2.208 Oil and water relative permeability curves at low capillary number

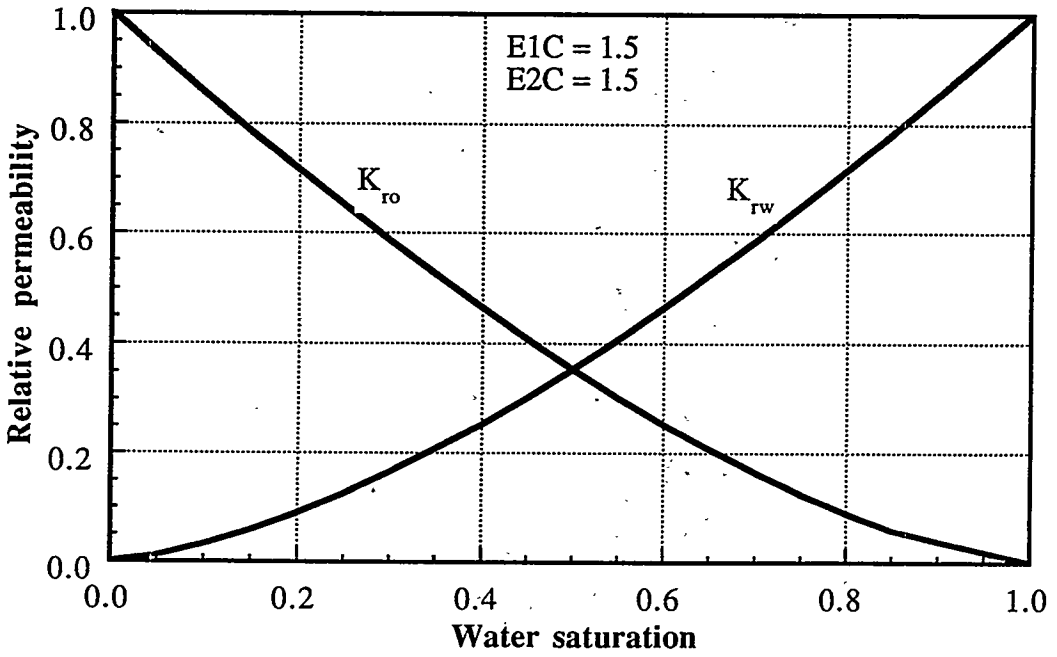


Figure 2.209 Oil and water relative permeability curves at high capillary number

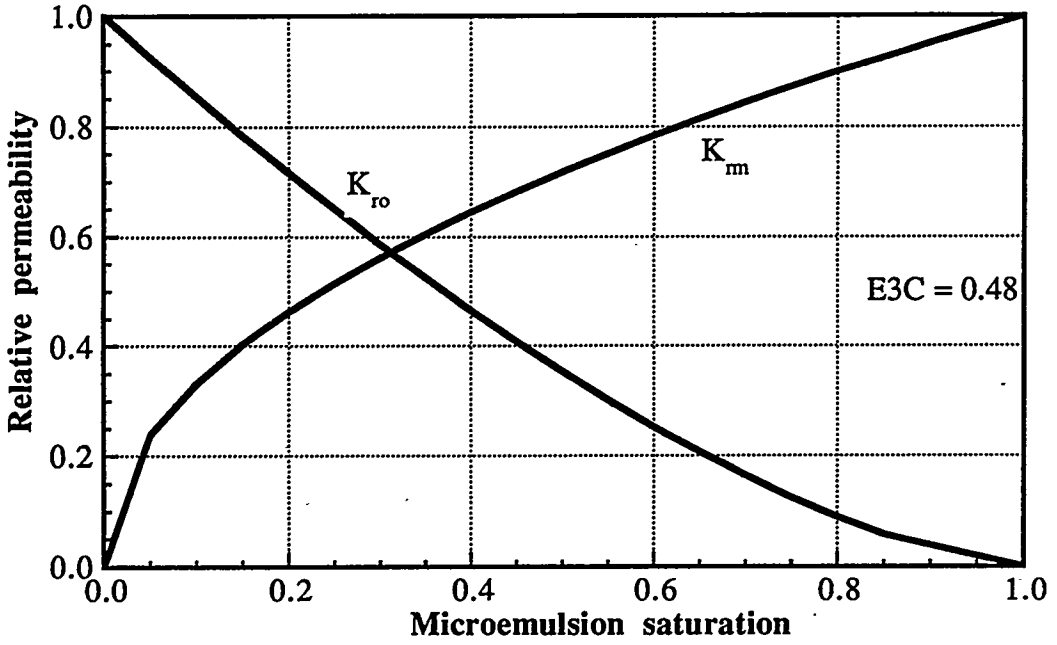


Figure 2.210 Oil and microemulsion relative permeability curves at high capillary number

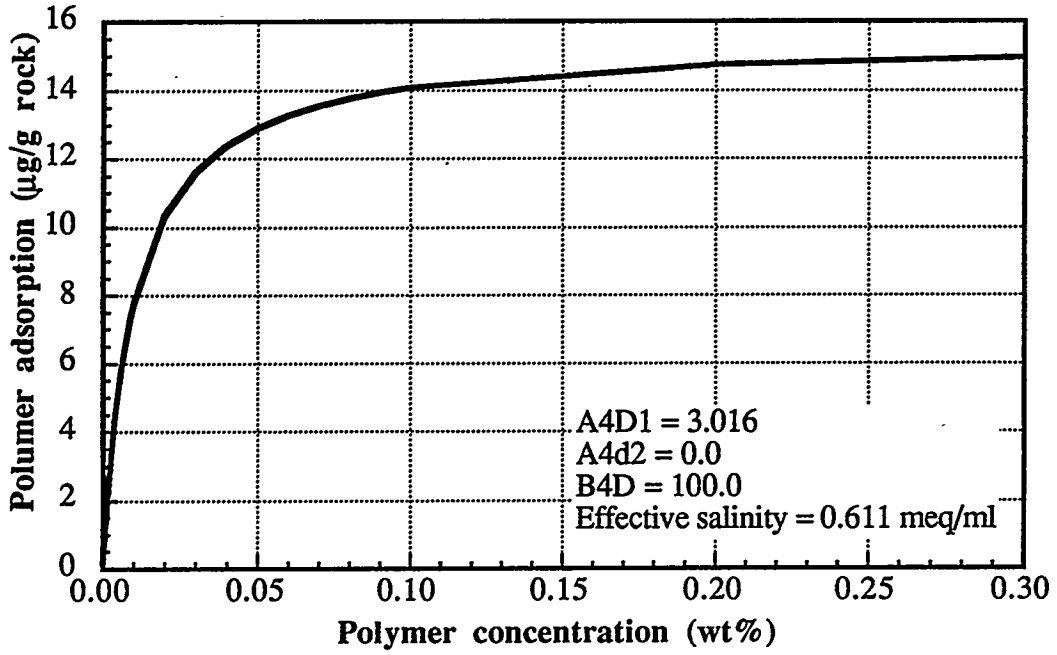


Figure 2.211 Polymer adsorption isotherm

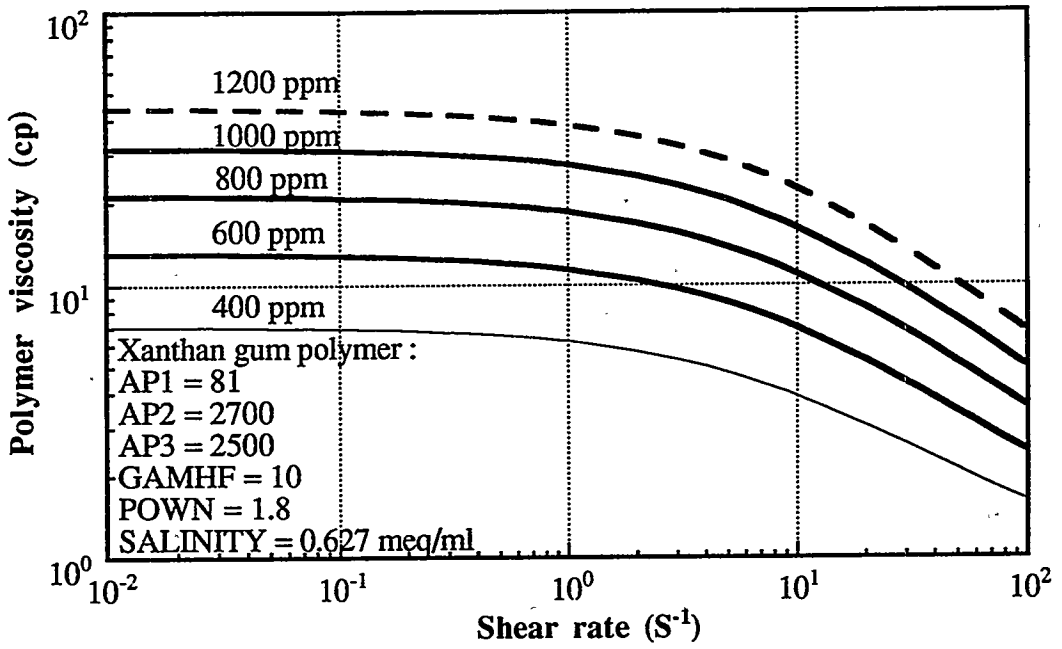


Figure 2.212 Polymer viscosity as a function of polymer concentration and shear rate

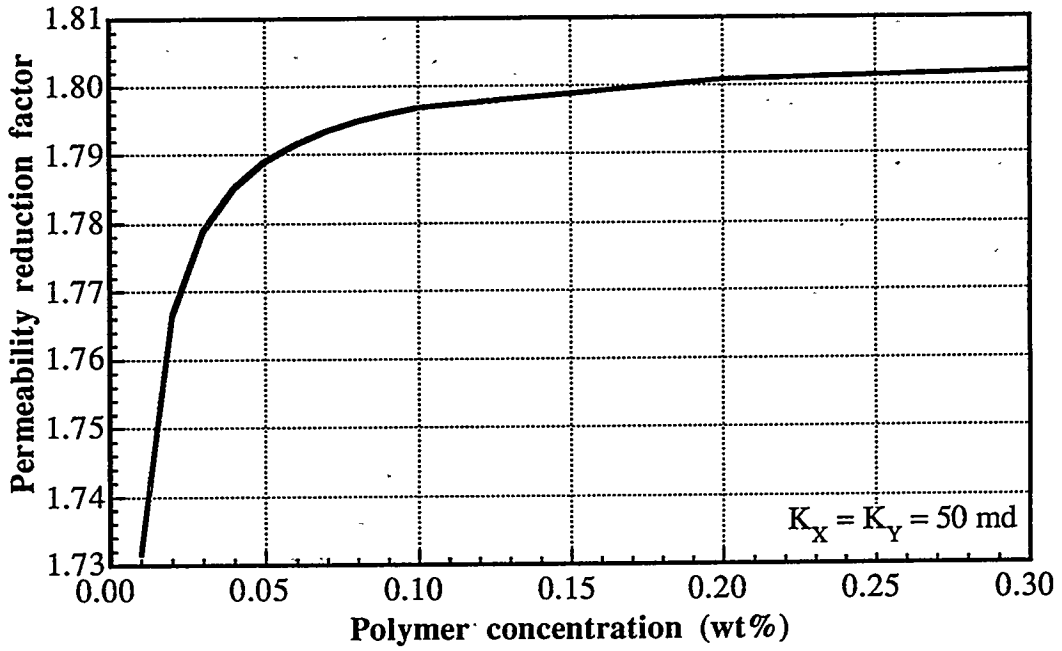


Figure 2.213 Polymer permeability reduction factor

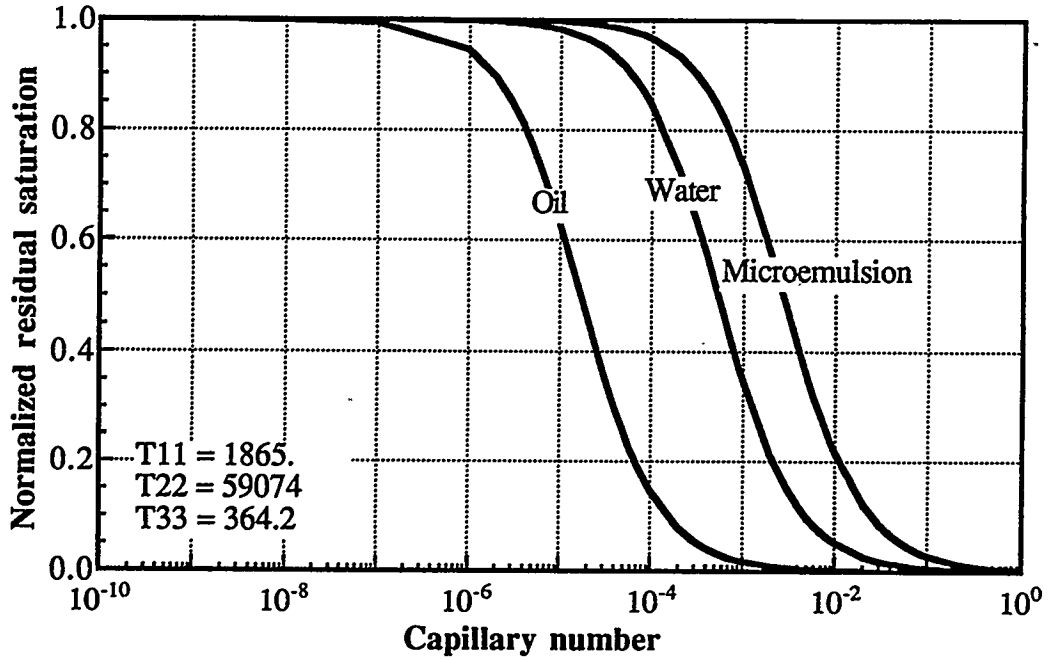


Figure 2.214 Capillary desaturation curves for oil, water, microemulsion phases

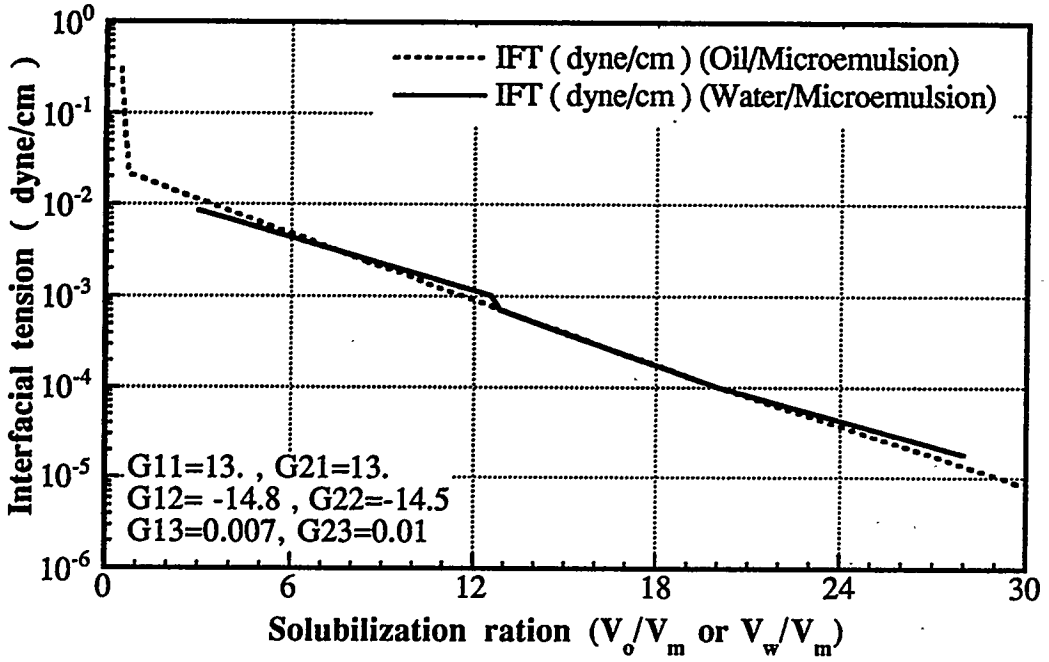


Figure 2.215 Interfacial tension as a function of solubilization ratios

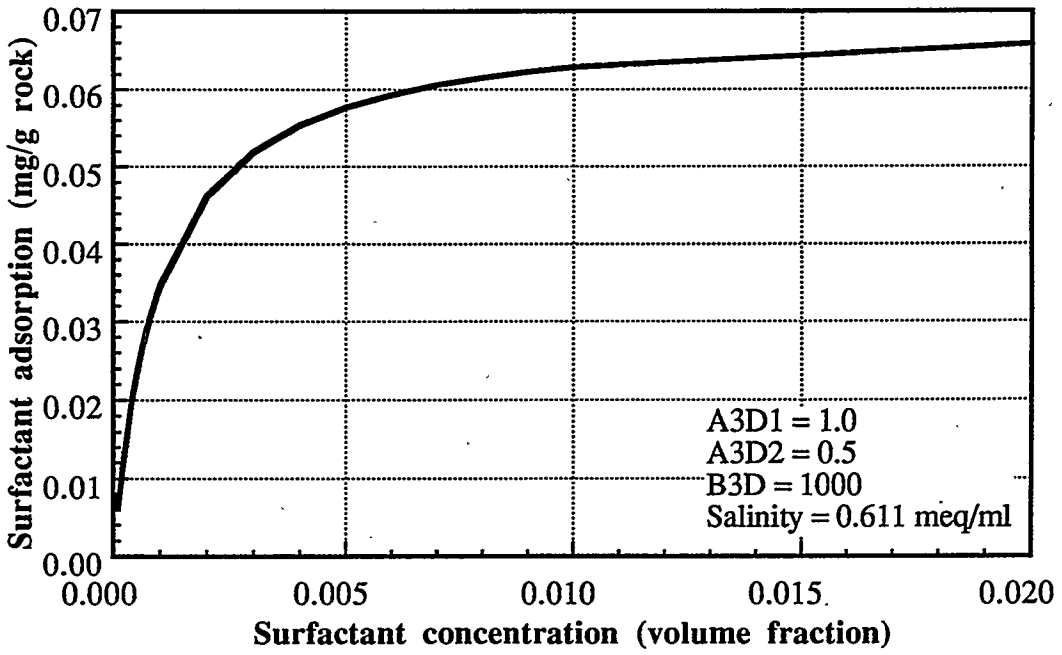


Figure 2.216 Surfactant adsorption isotherm

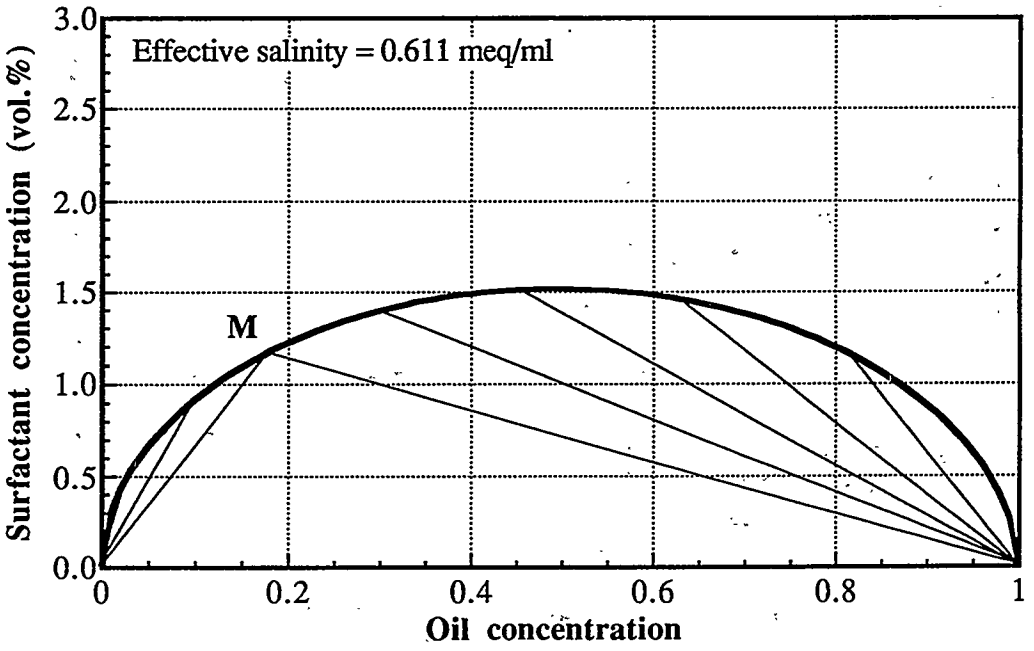


Figure 2.217 Phase behavior for the Type III region

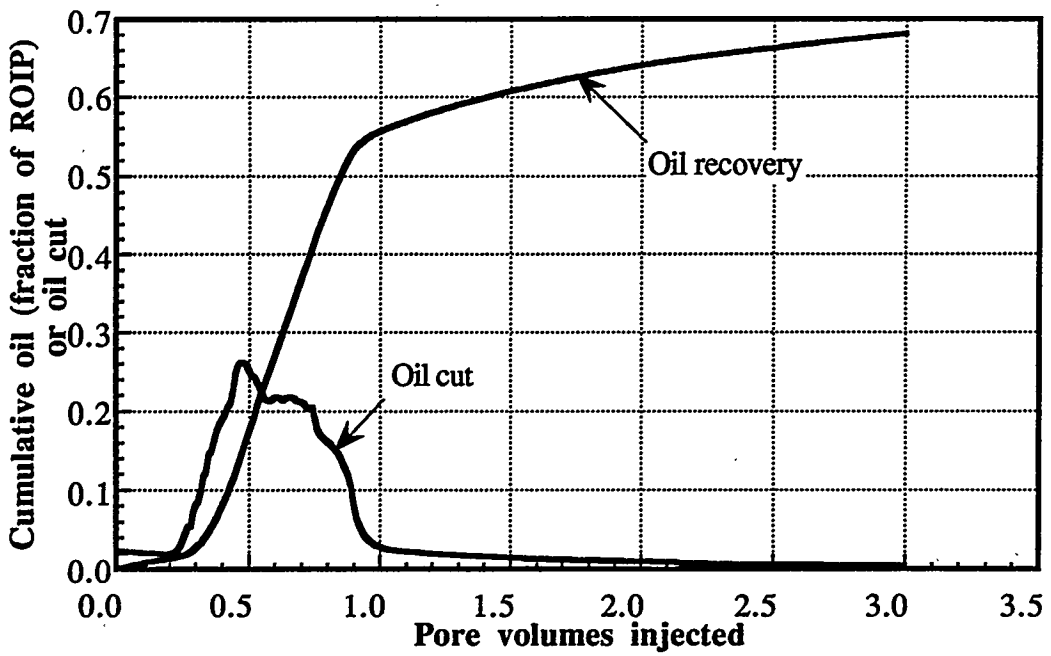


Figure 2.218 Cumulative oil recovery and oil cut as a function of pore volumes injected (Base Case)

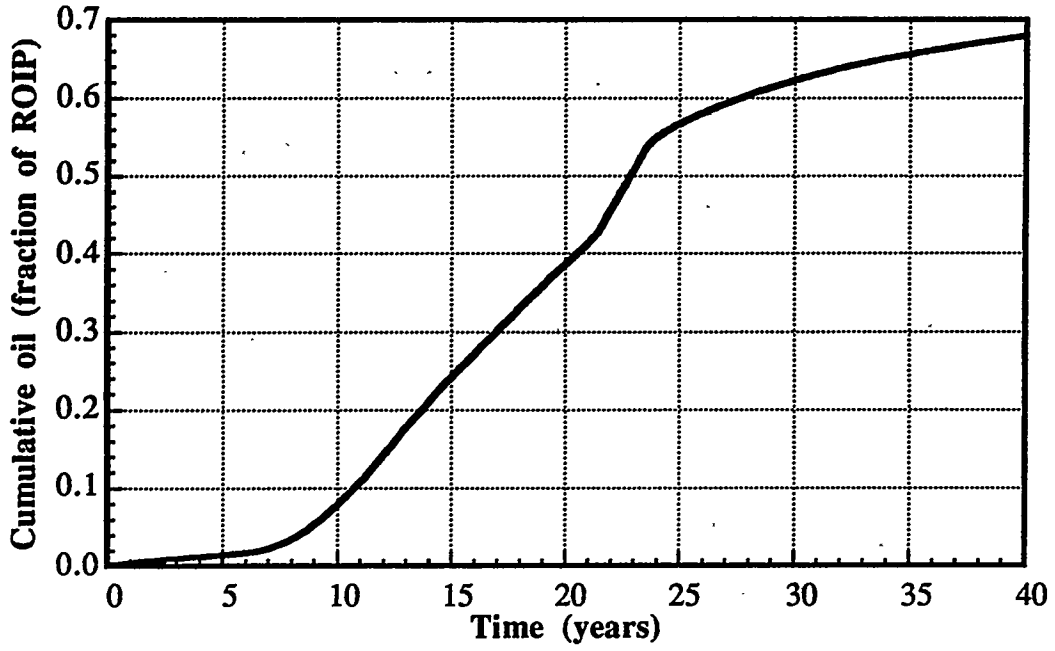


Figure 2.219 Cumulative oil recovery as a function of project life

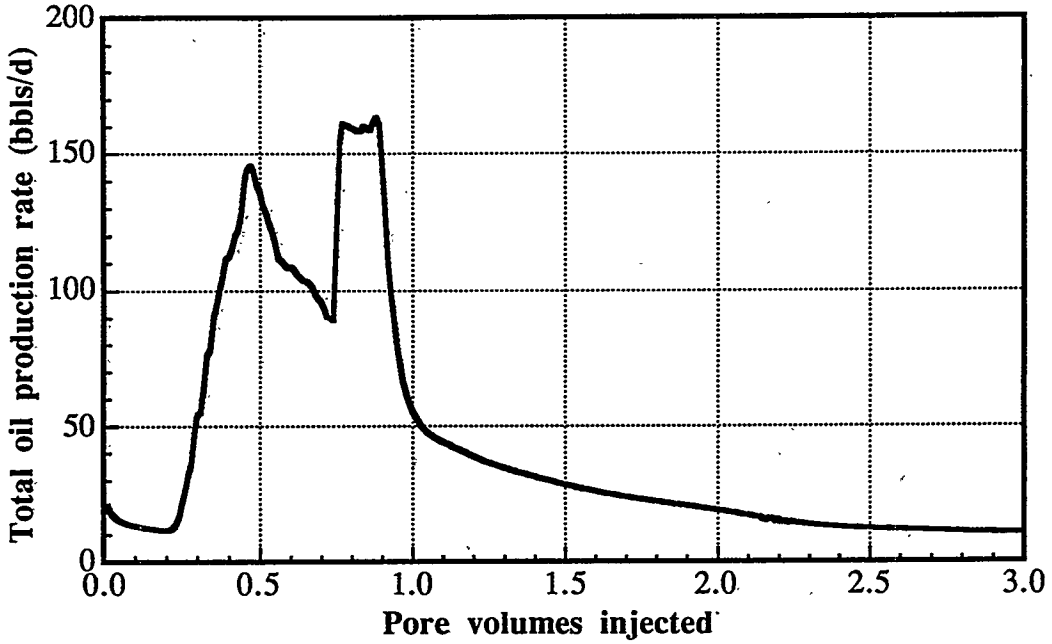


Figure 2.220 Oil production as a function of pore volumes injected

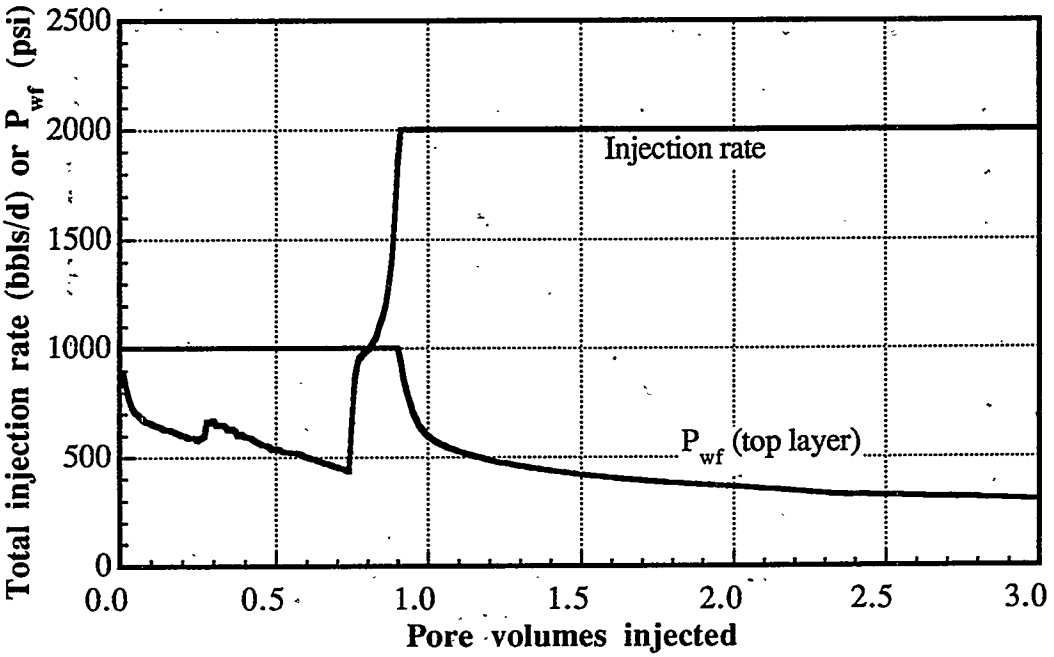


Figure 2.221 Total injection rate and bottomhole pressure as a function of pore volumes injected

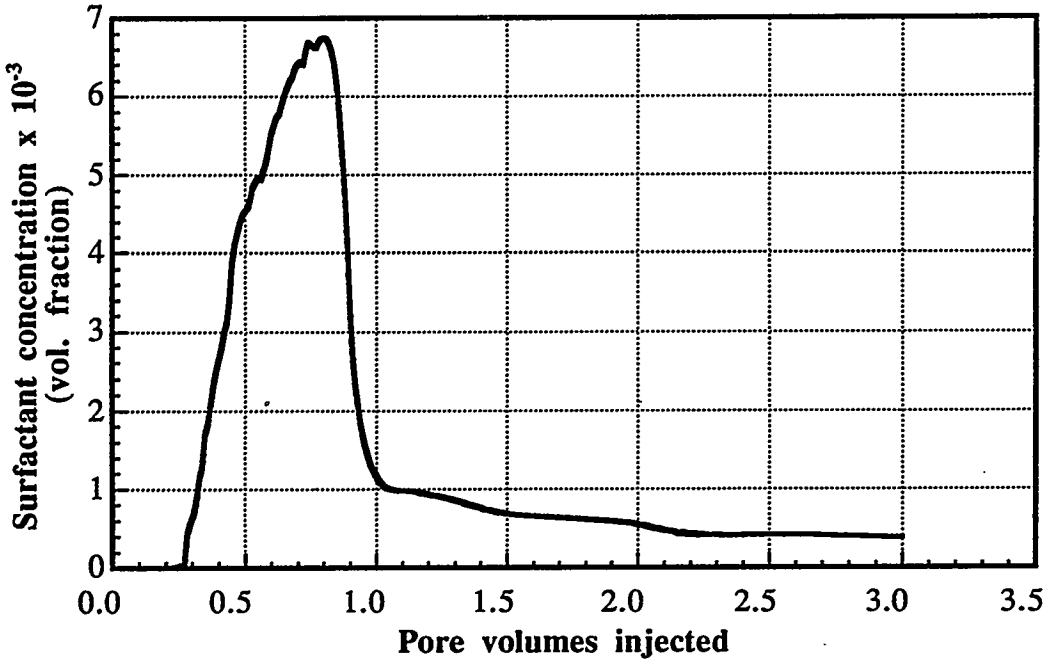


Figure 2.222 History of effluent surfactant concentration (Base Case)

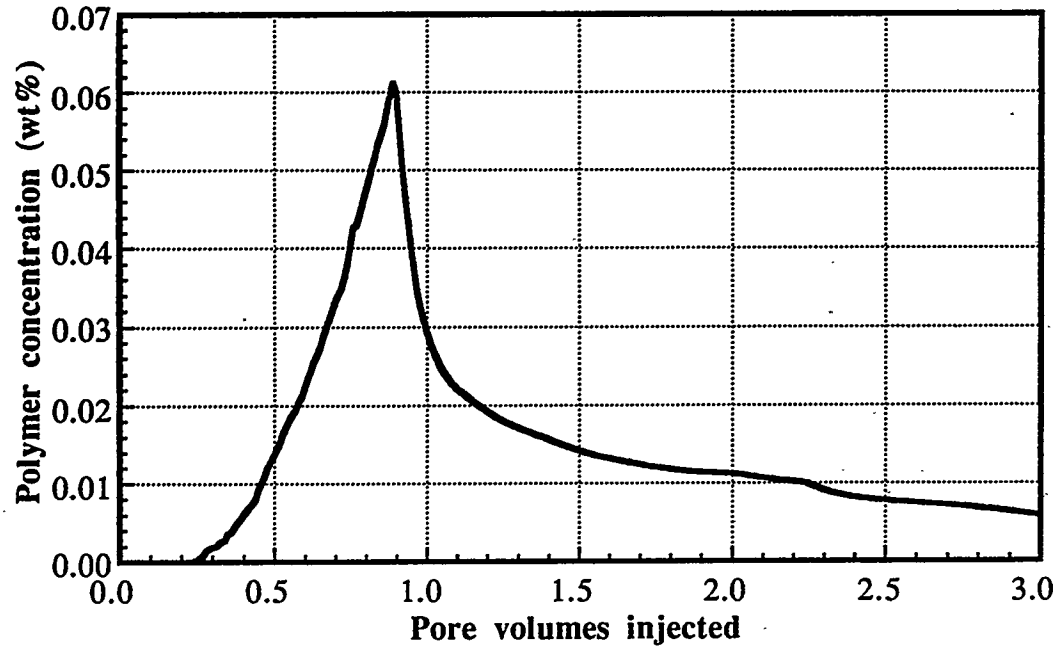


Figure 2.223 History of effluent polymer concentration (Base Case)

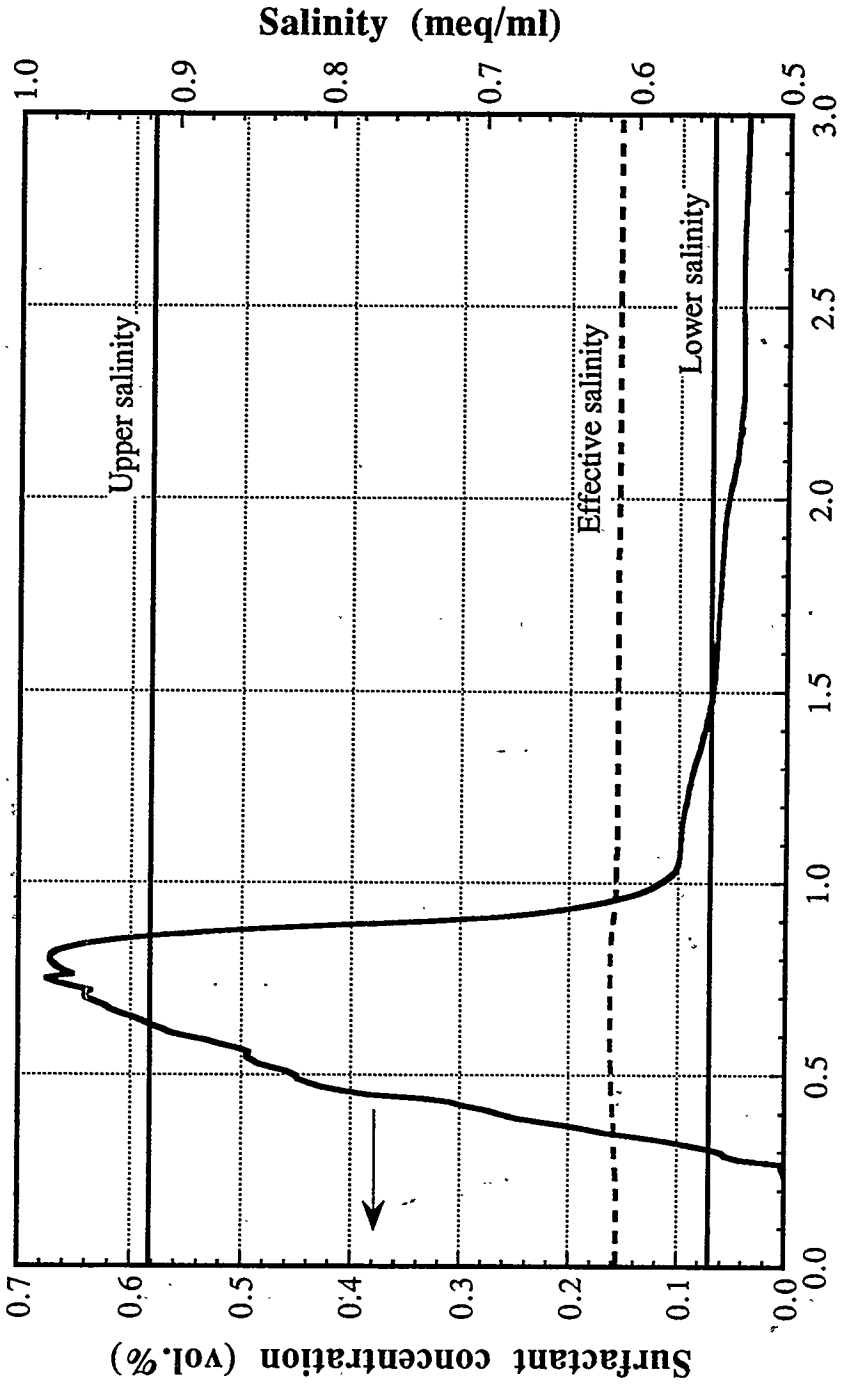
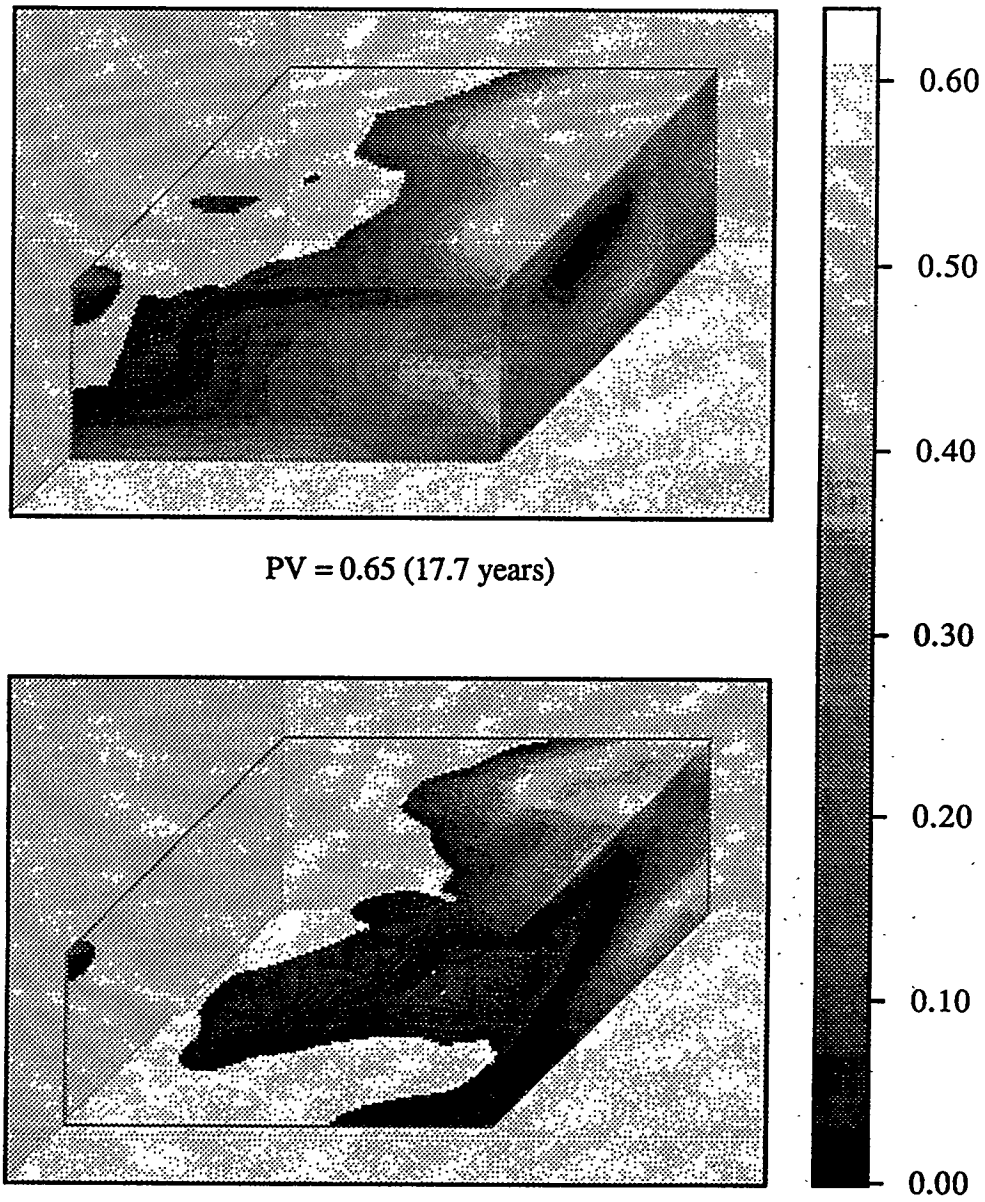


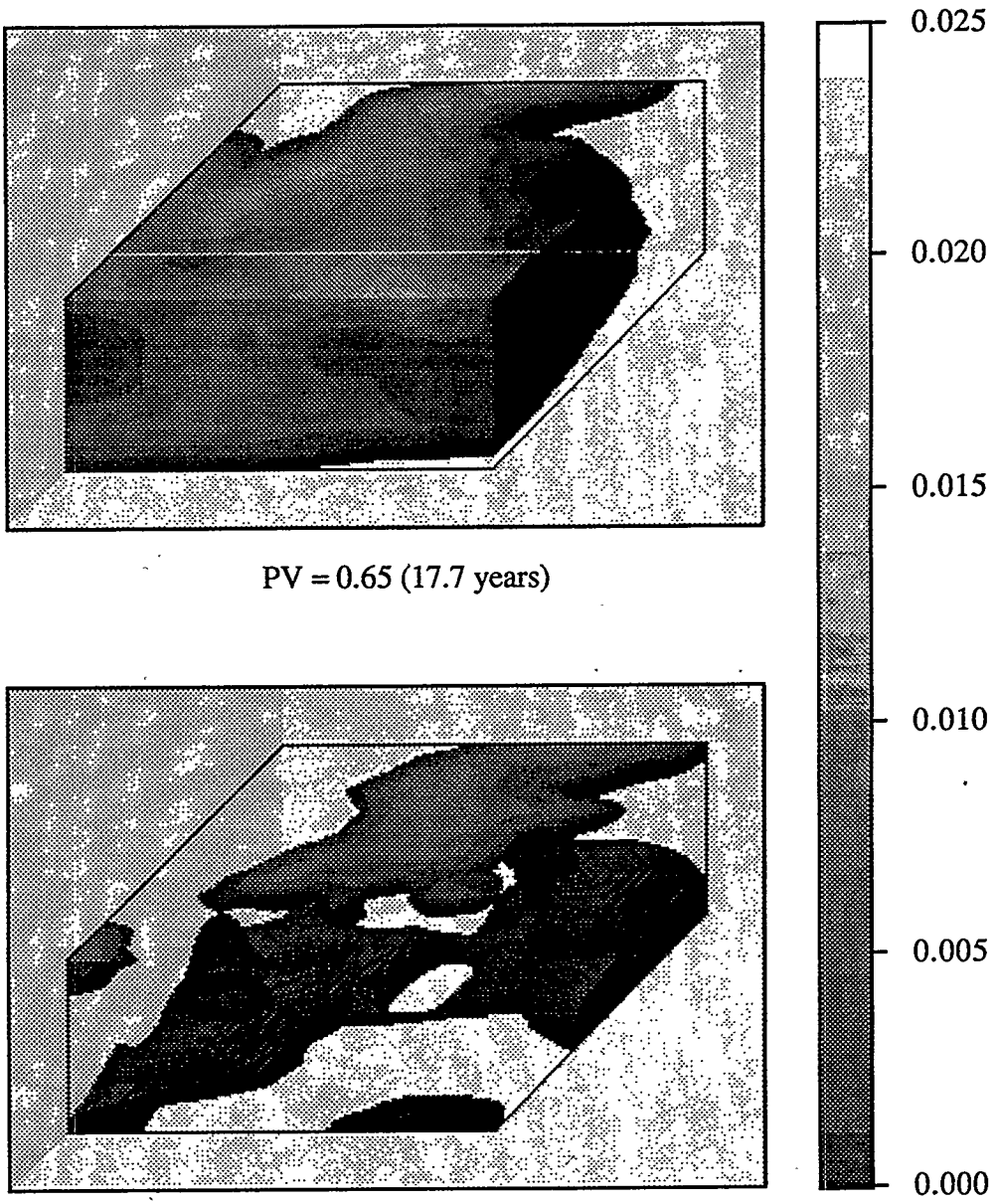
Figure 2.224 History of effective salinity for the Base Case



PV = 0.65 (17.7 years)

PV = 2.75 (38.6 years)

Figure 2.225 Oil concentration distribution with iso-surface of 0.1 for Base Case



PV = 0.65 (17.7 years)

PV = 2.75 (38.6 years)

Figure 2.226 Surfactant concentration distribution with iso-surface of 0.001 for Base Case

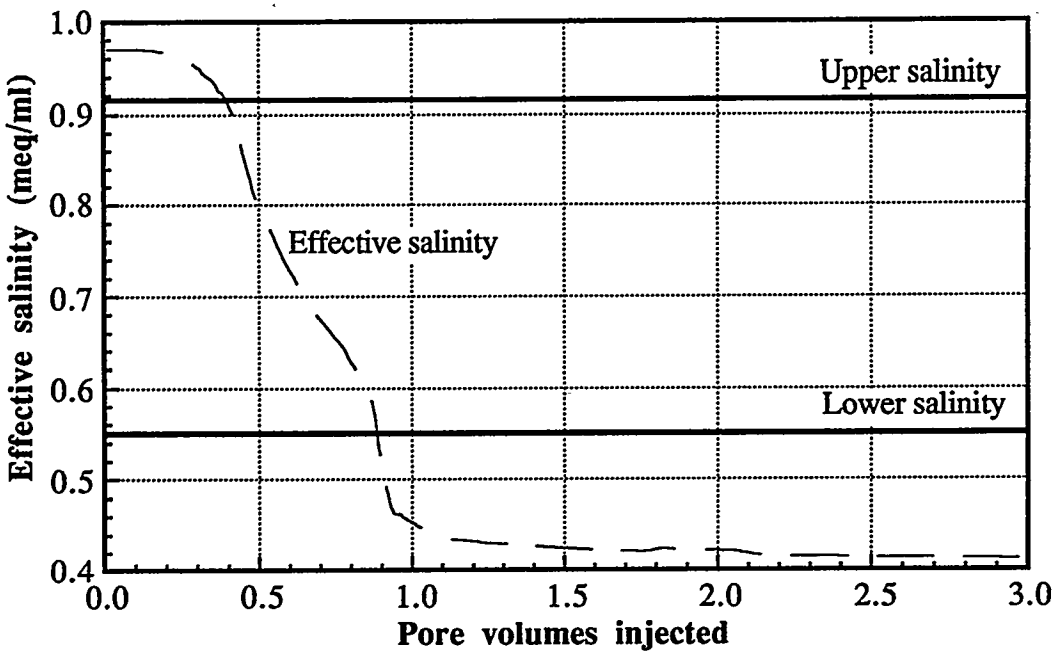


Figure 2.227 History of the effective salinity

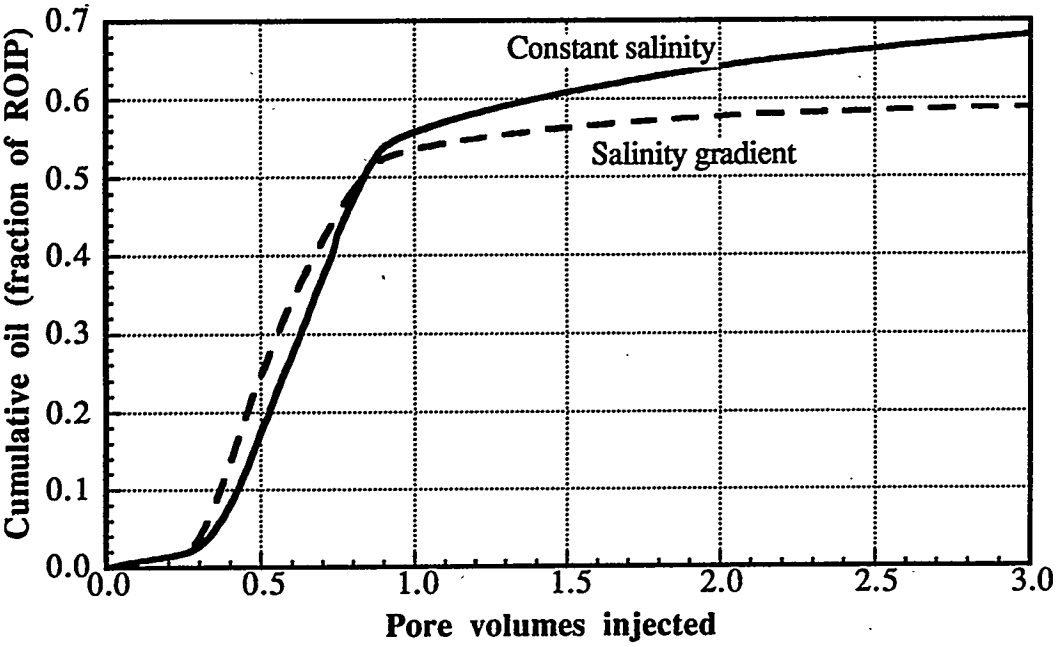


Figure 2.228 Effect of salinity gradient on oil recovery

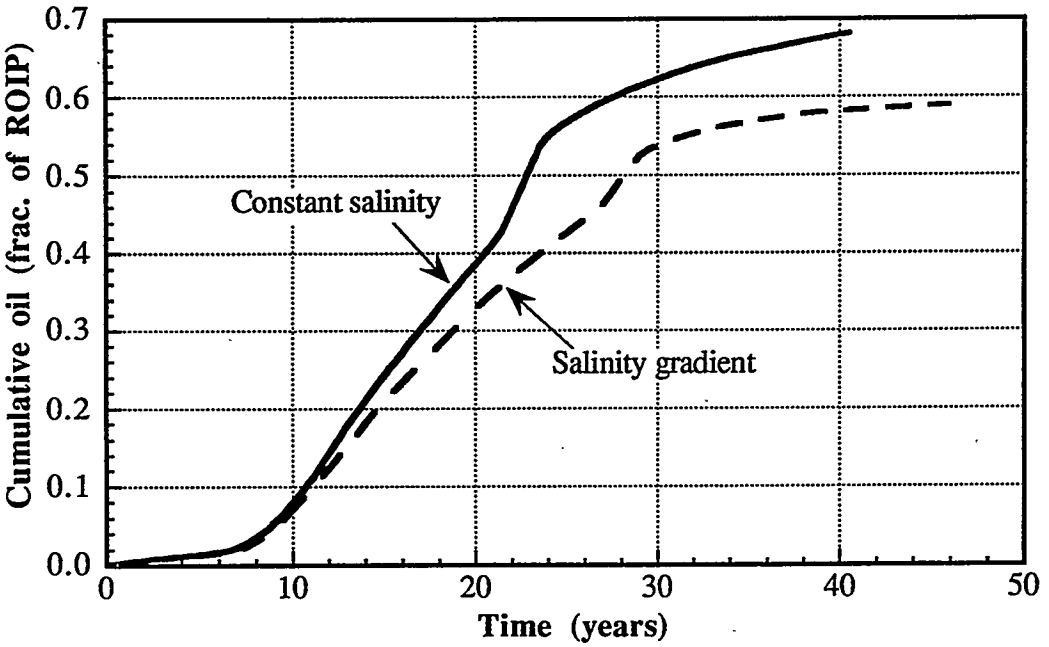


Figure 2.229 Effect of salinity gradient on oil recovery and project life

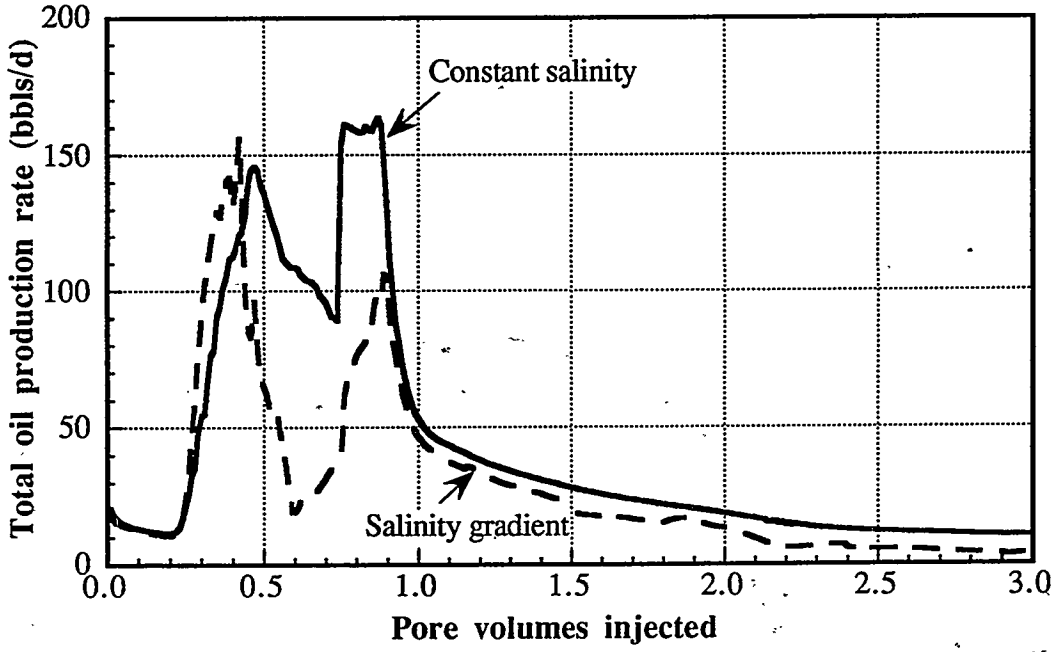


Figure 2.230 Effect of salinity gradient on oil production rate

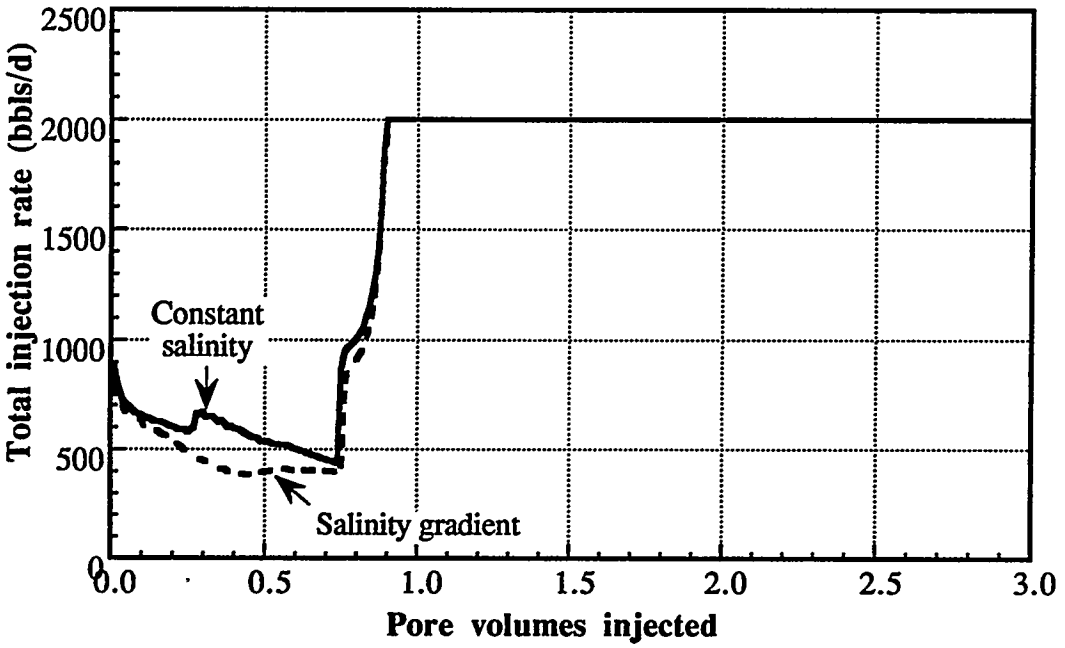


Figure 2.231 Effect of salinity gradient on total injection rate

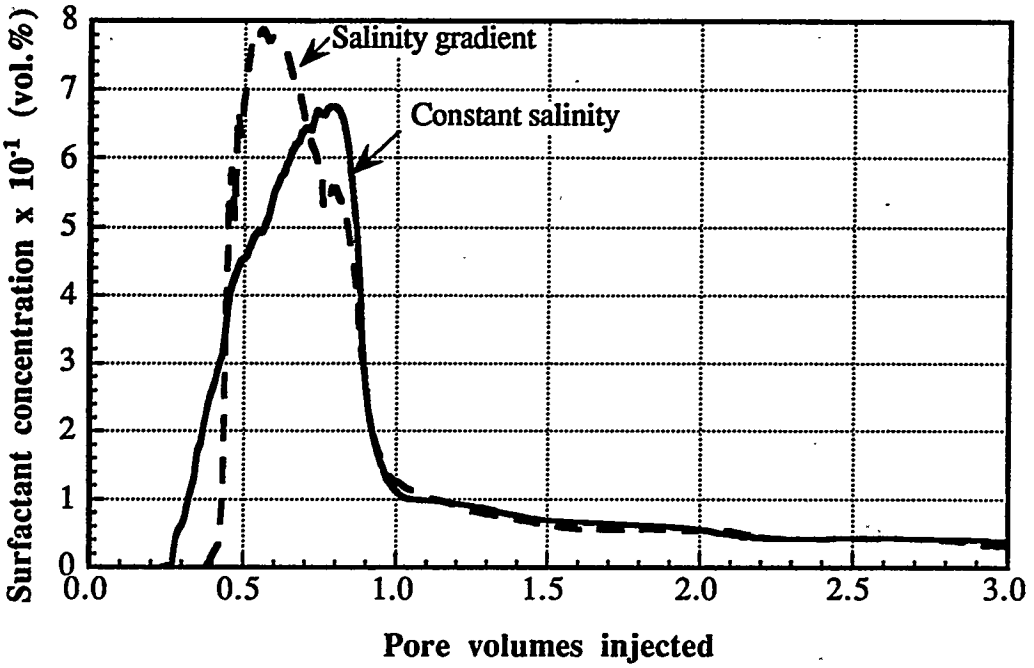


Figure 2.232 Effect of salinity gradient on the produced surfactant concentration

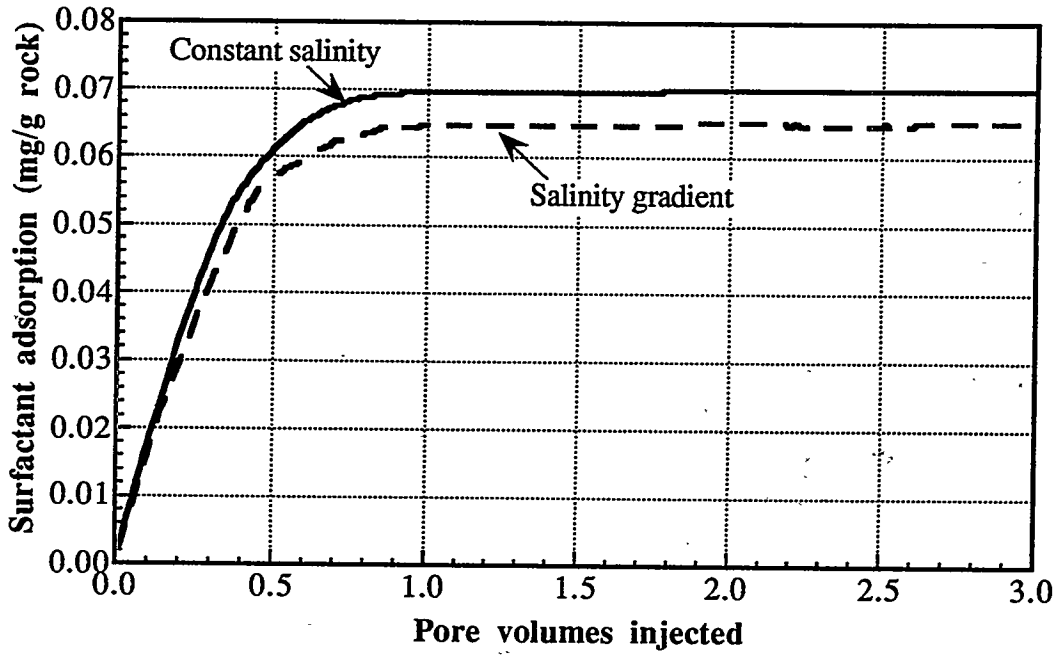


Figure 2.233 Effect of salinity gradient on surfactant adsorption

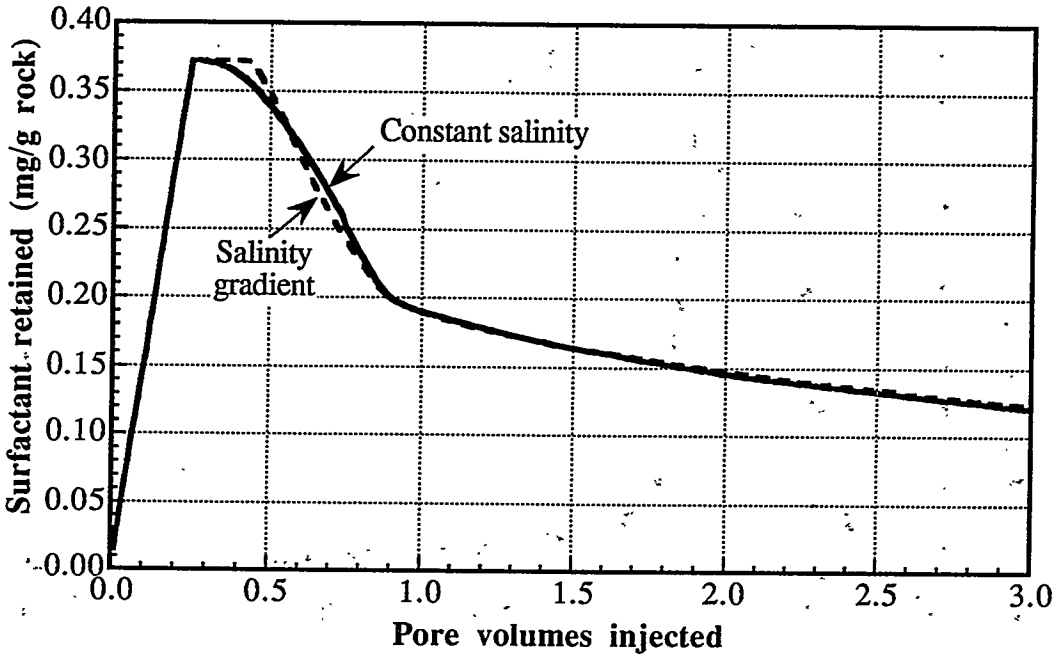
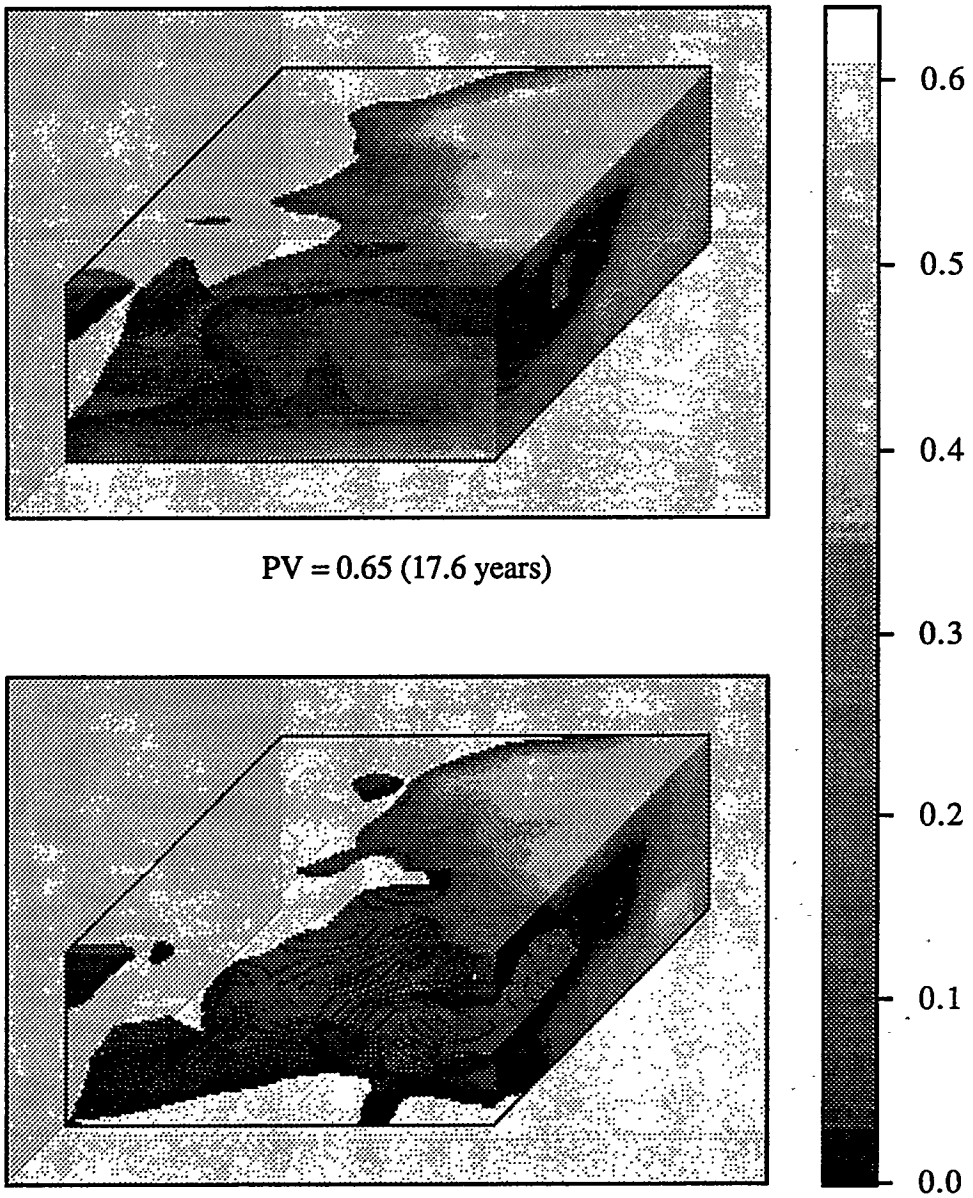


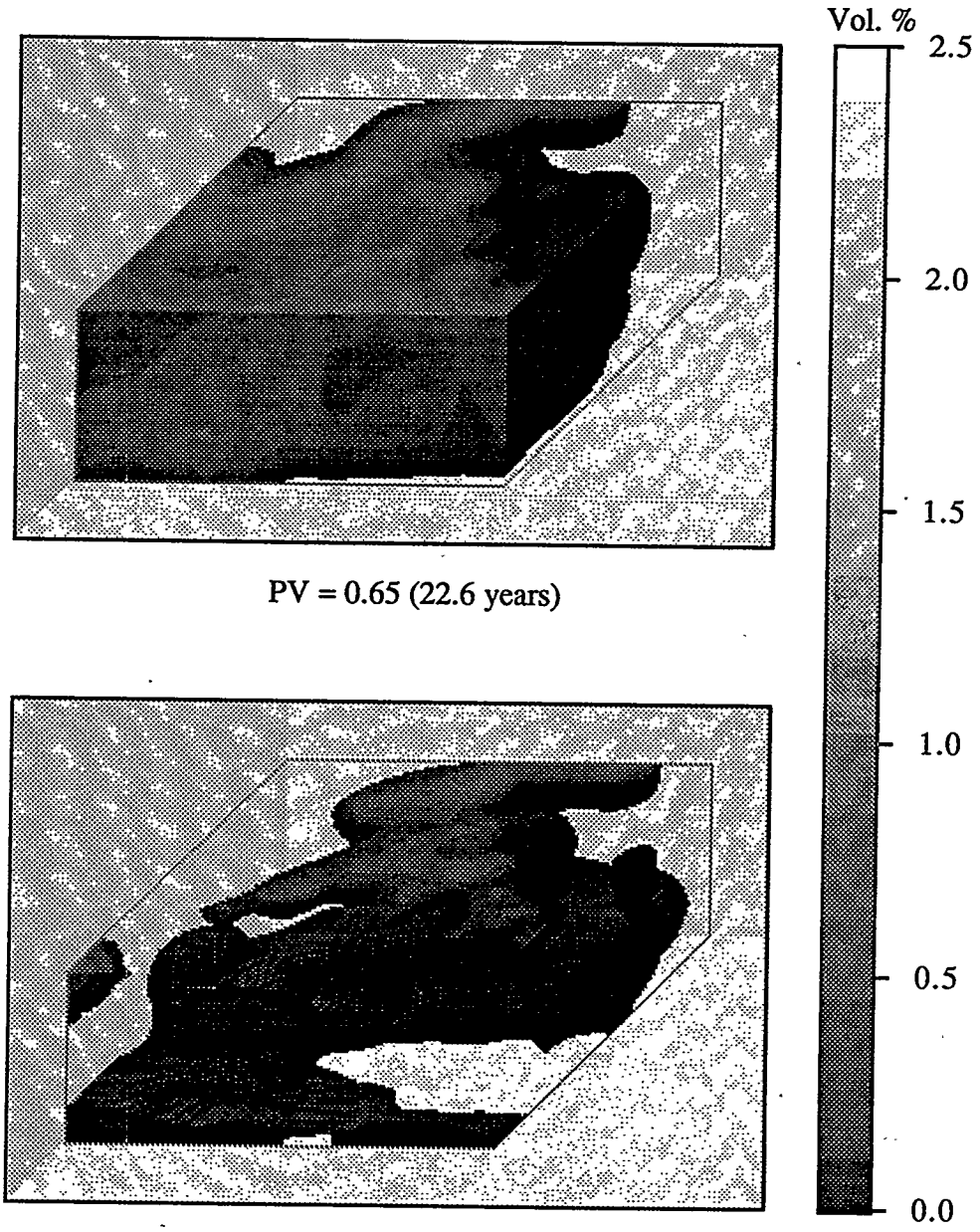
Figure 2.234 Effect of salinity gradient on retained surfactant



PV = 0.65 (17.6 years)

PV = 2.75 (38.6 years)

Figure 2.235 Distribution of oil concentration with iso-surface of 0.001 for salinity gradient case



PV = 0.65 (22.6 years)

PV = 2.75 (44 years)

Figure 2.236 Distribution of surfcatnt concentration with iso-surface of 0.1 vol.% for salinity gradient case

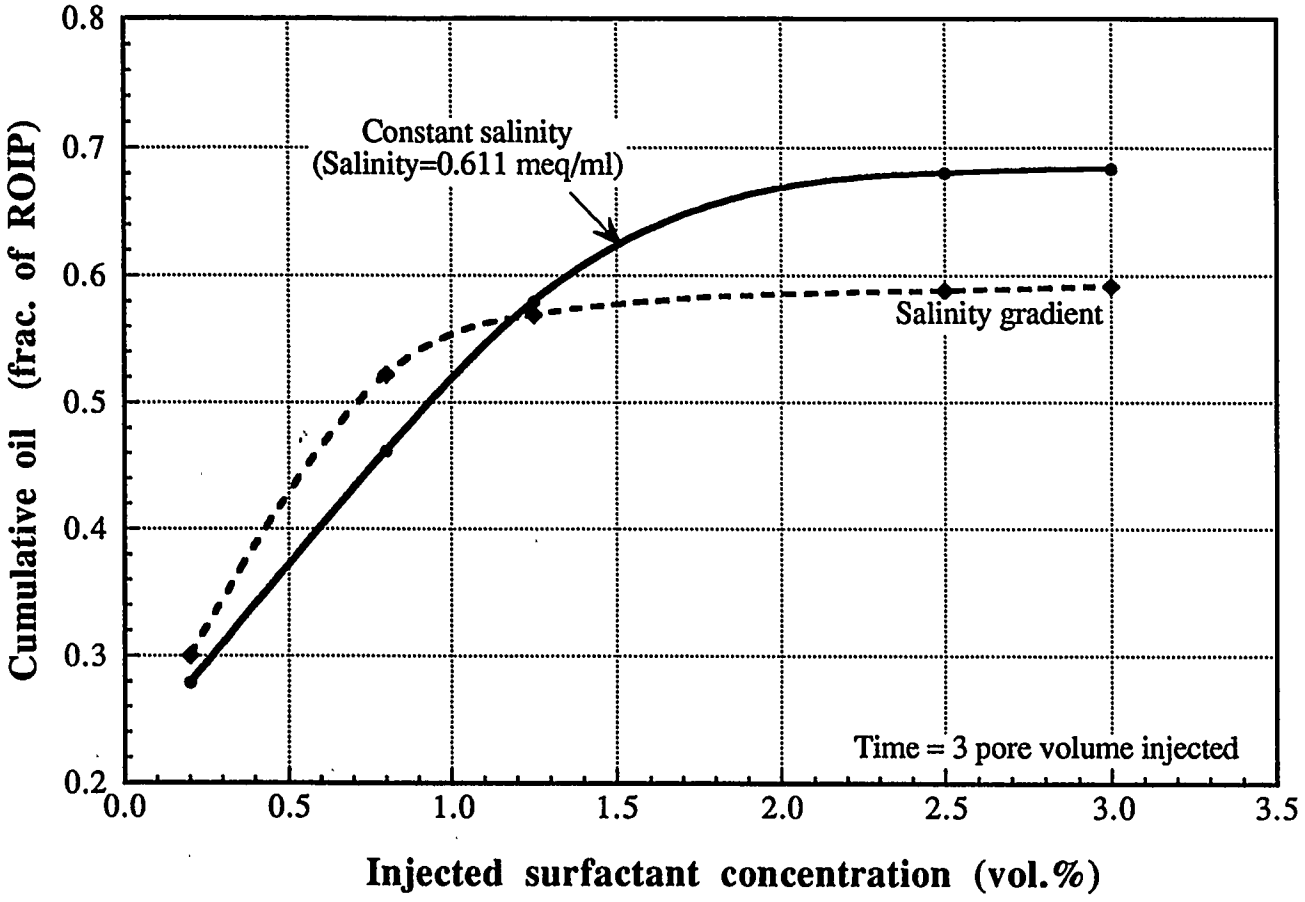


Figure 2.237 Comparison of oil recovery between constant salinity and salinity gradient case at different surfacatnt concentration

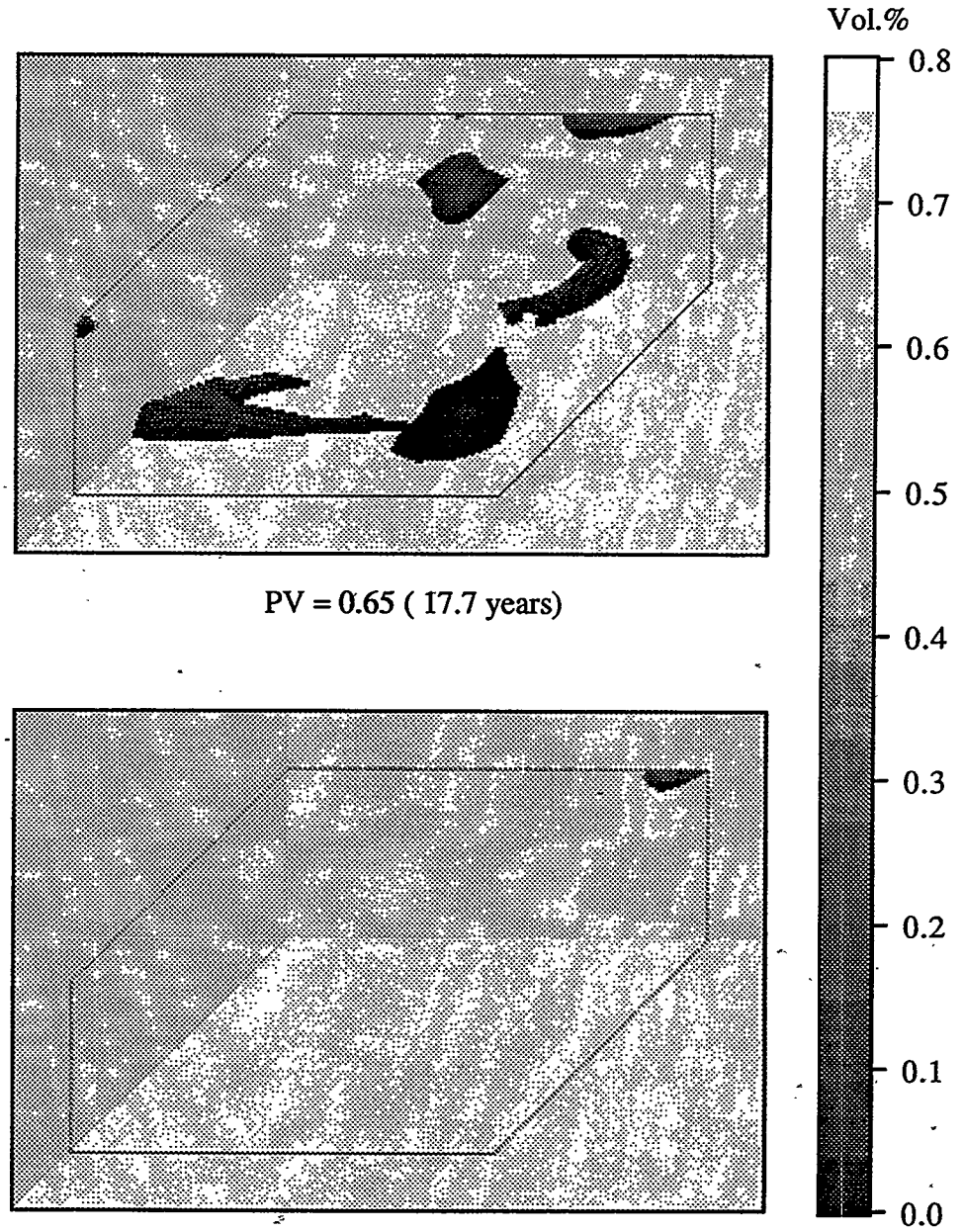
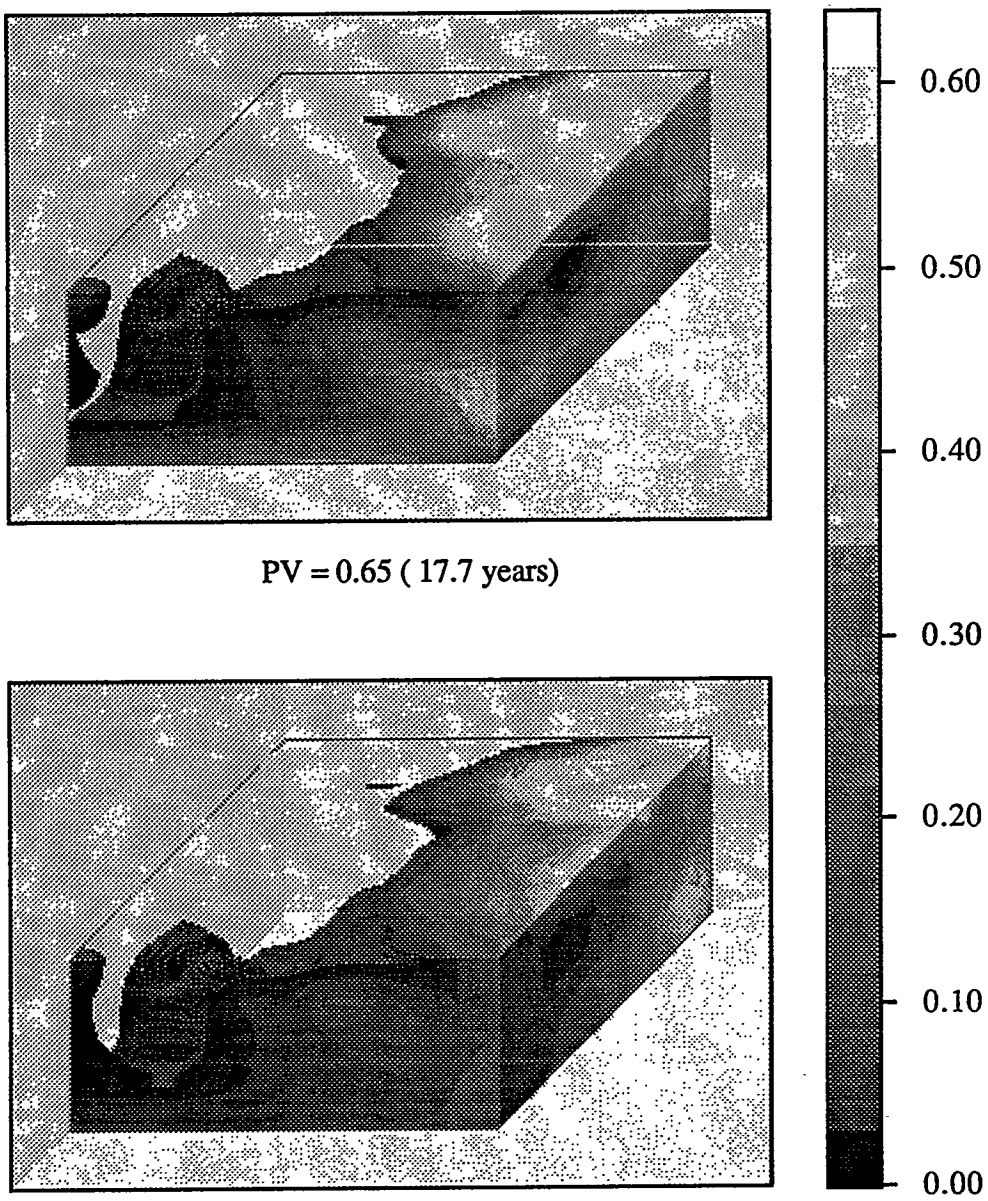


Figure 2.238 Distribution of surfactant concentration with iso-surface of 0.1 vol.% for injected surf. = 0.8 vol.% for constant salinity case



PV = 0.65 (17.7 years)

PV = 2.75 (50.0 years)

Figure 2.239 Distribution of oil concentration with iso-surface of 0.1 meq/ml for constant salinity case

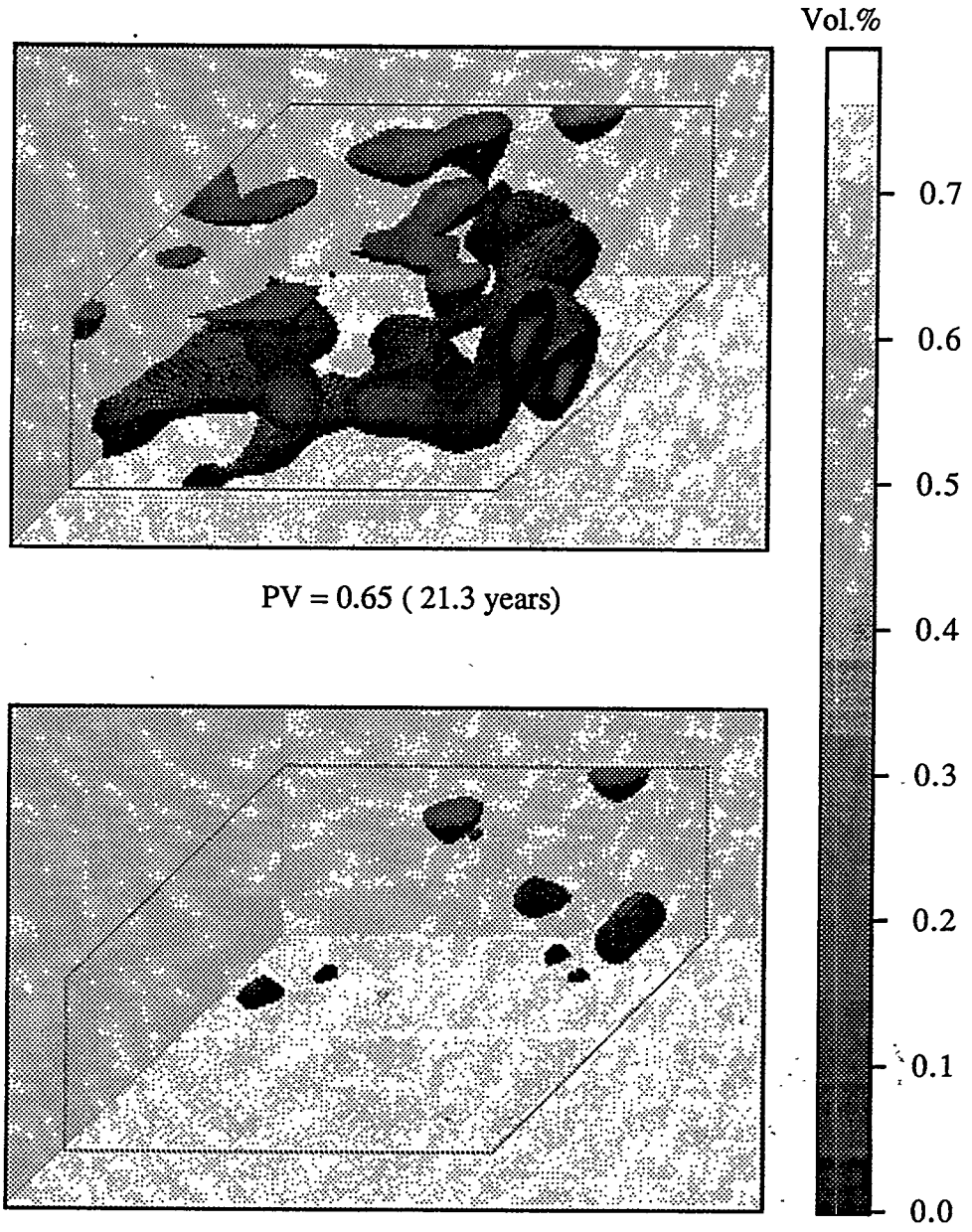
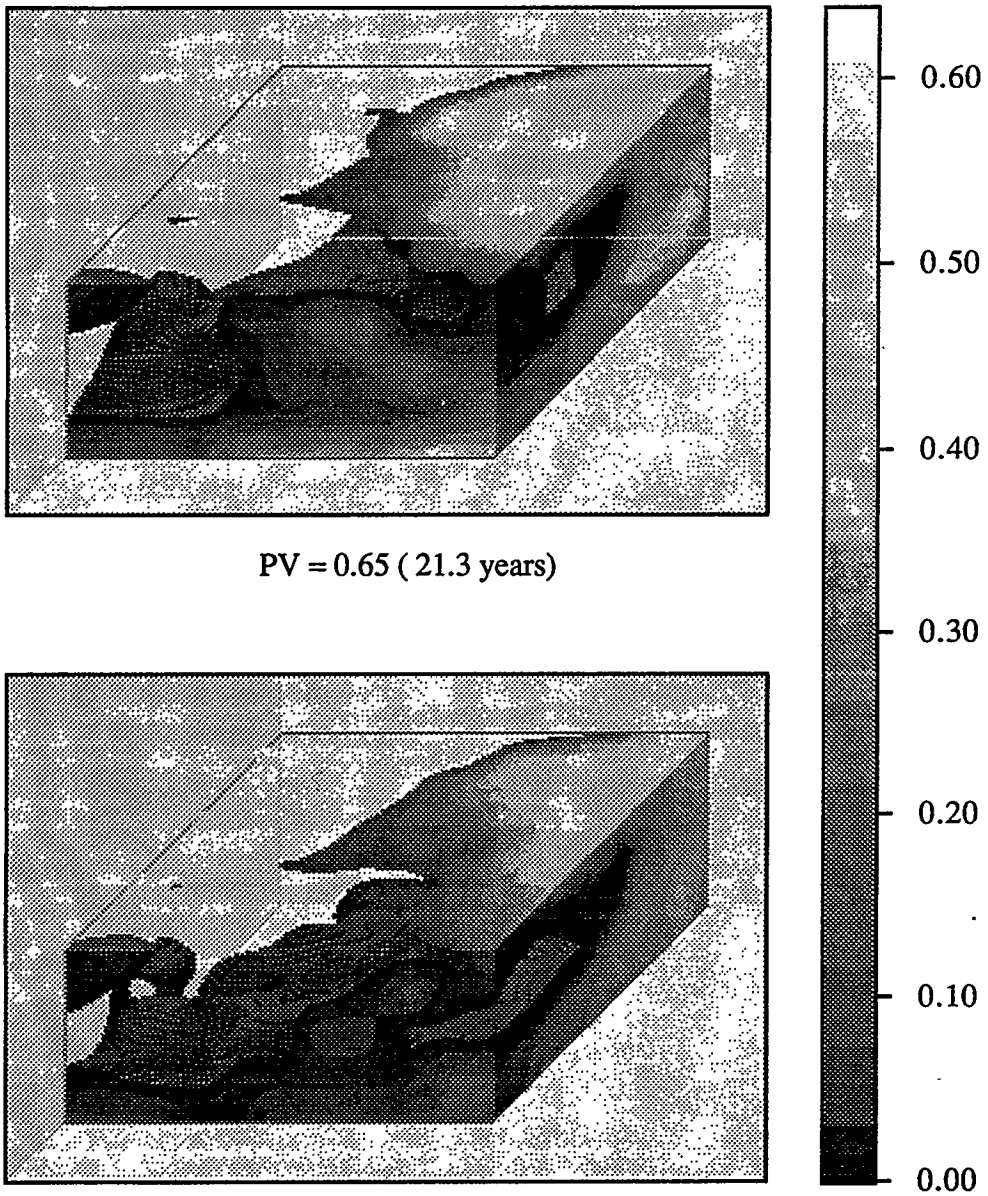


Figure 2.240 Distribution of surfactant concentration with iso-surface of 0.1 vol.% for injected surfactant = 0.8 vol.% fraction for salinity gradient case



PV = 0.65 (21.3 years)

PV = 2.75 (45.0 years)

Figure 2.241 Distribution of oil concentration with iso-surface of 0.1 meq/ml for salinity gradient case

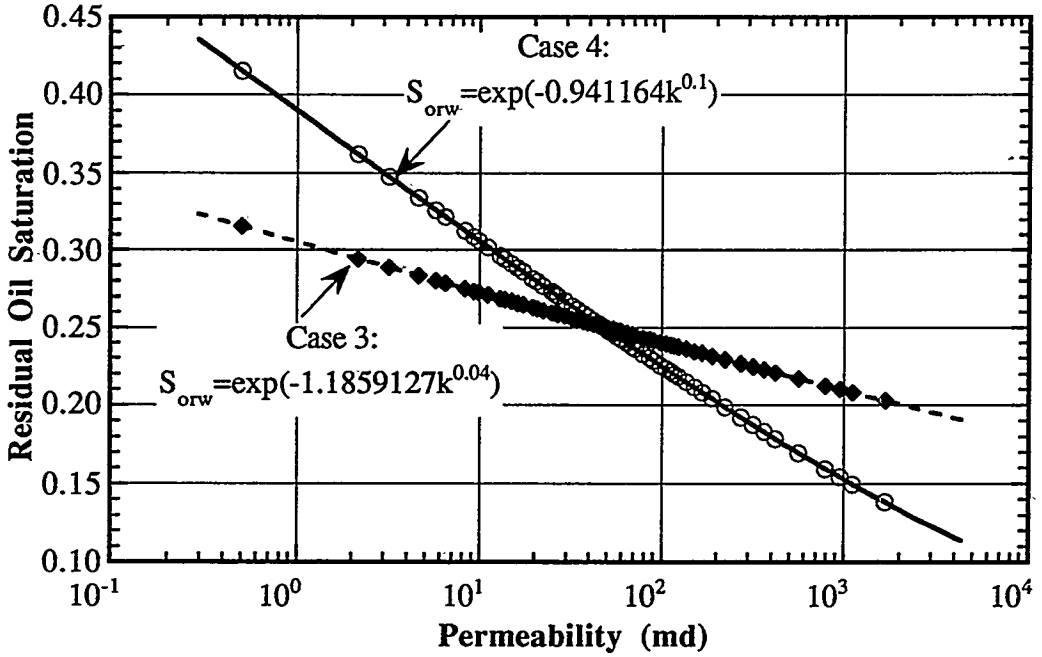


Figure 2.242 Residual oil saturation (S_{orw}) as a function of permeability

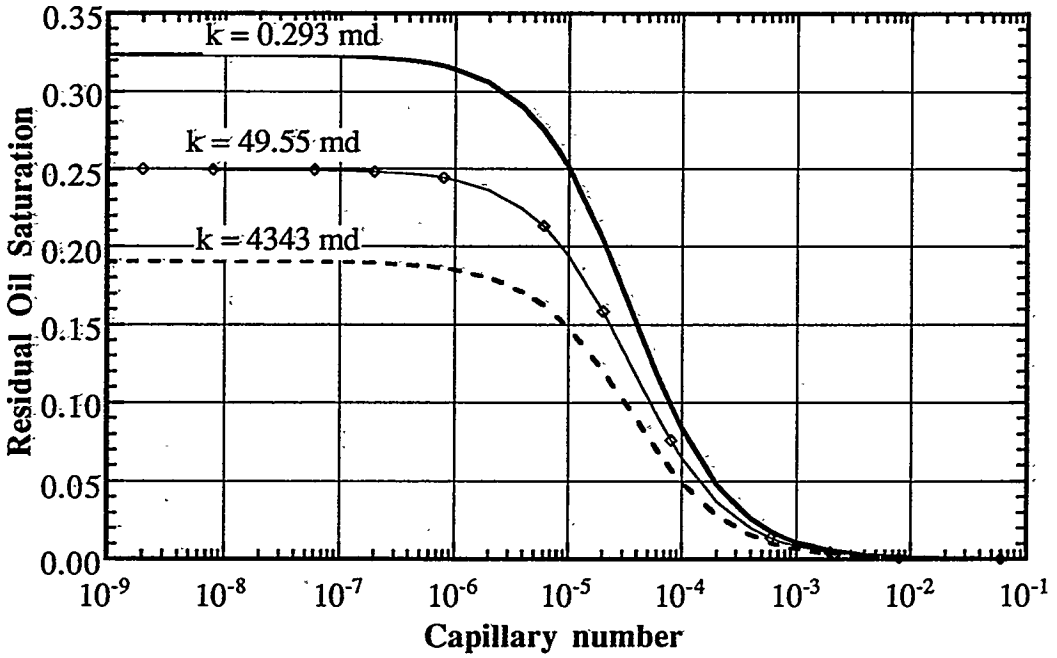


Figure 2.243 Capillary desaturation curves for permeability-dependent S_{orw} (Case 3: S_{orw}=exp(-1.1859127k$^{0.04}$))

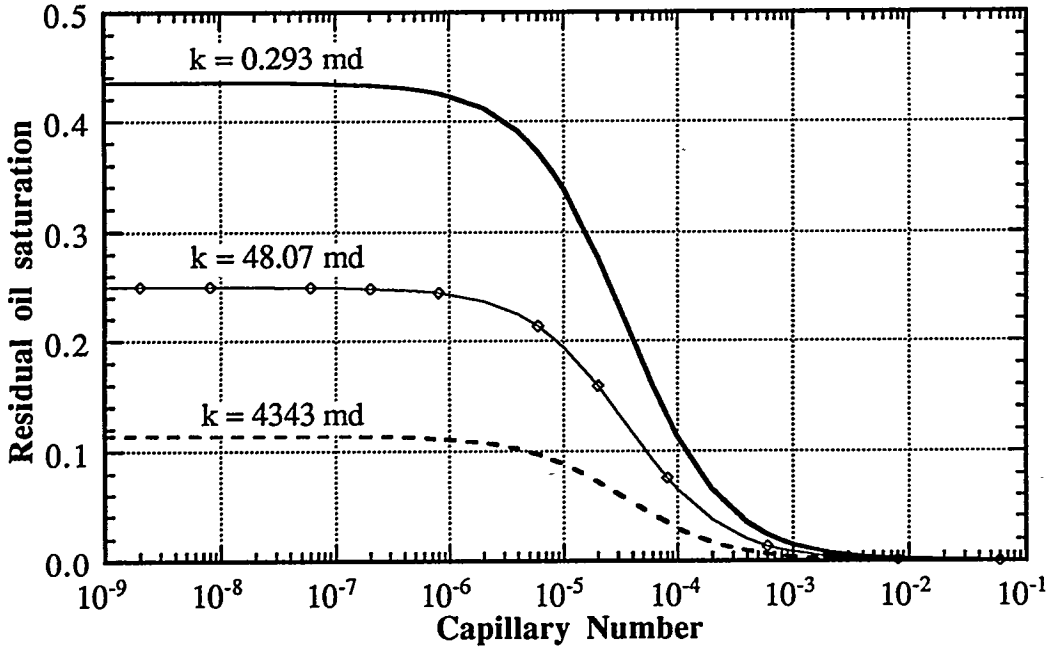


Figure 2.244 Capillary desaturation curves for permeability-dependent S_{orw} (Case 4: $S_{orw}=\exp(-0.941164k^{0.1})$)

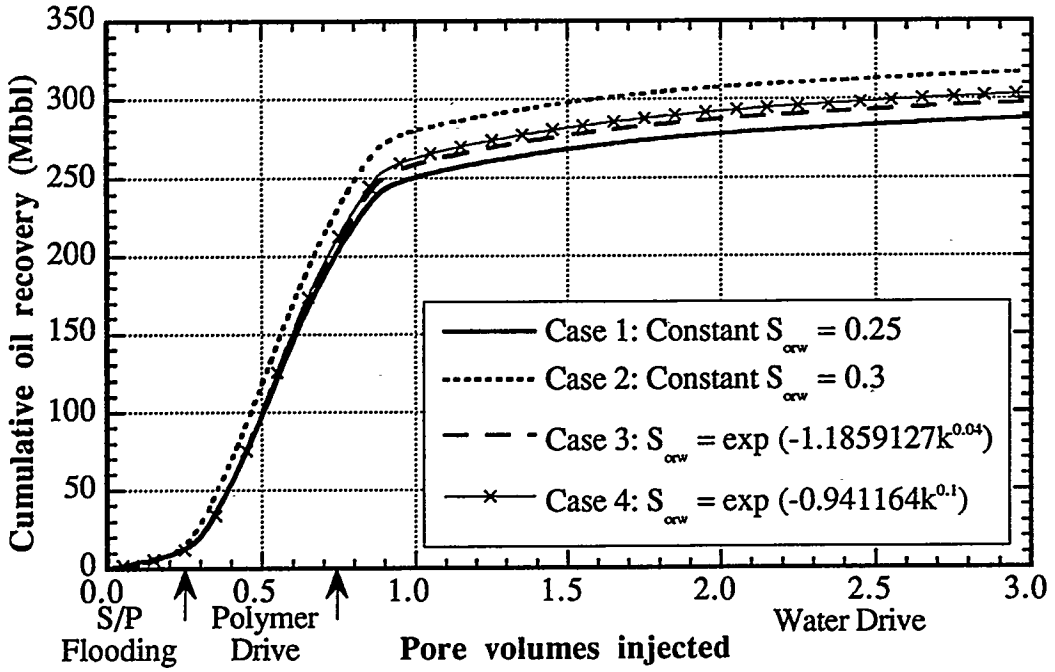


Figure 2.245 Effect of distributed S_{orw} on oil recovery

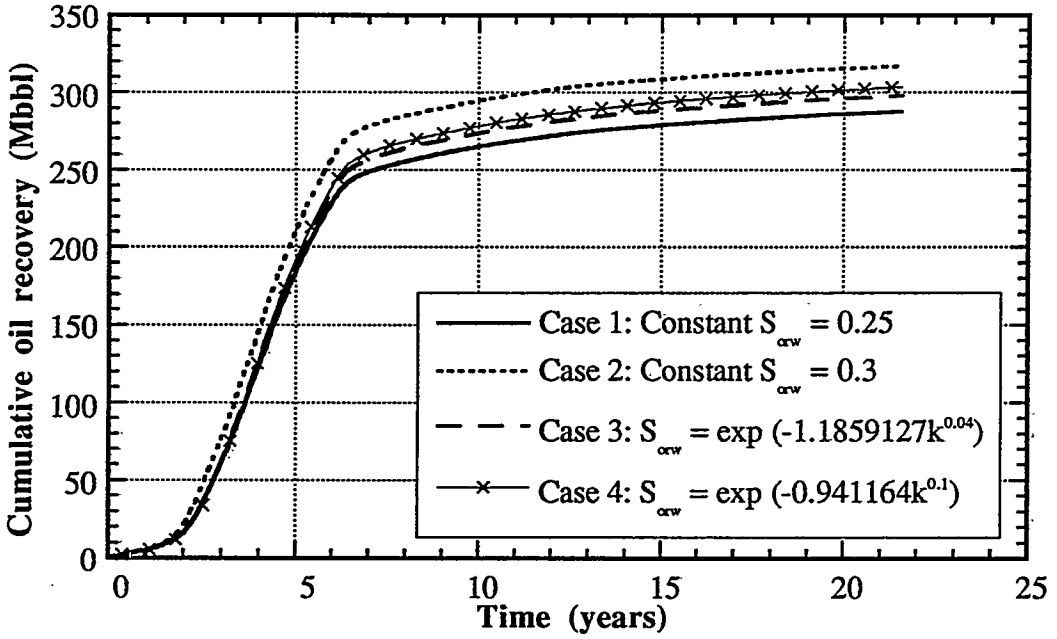


Figure 2.246 Effect of distributed S_{orw} on oil recovery

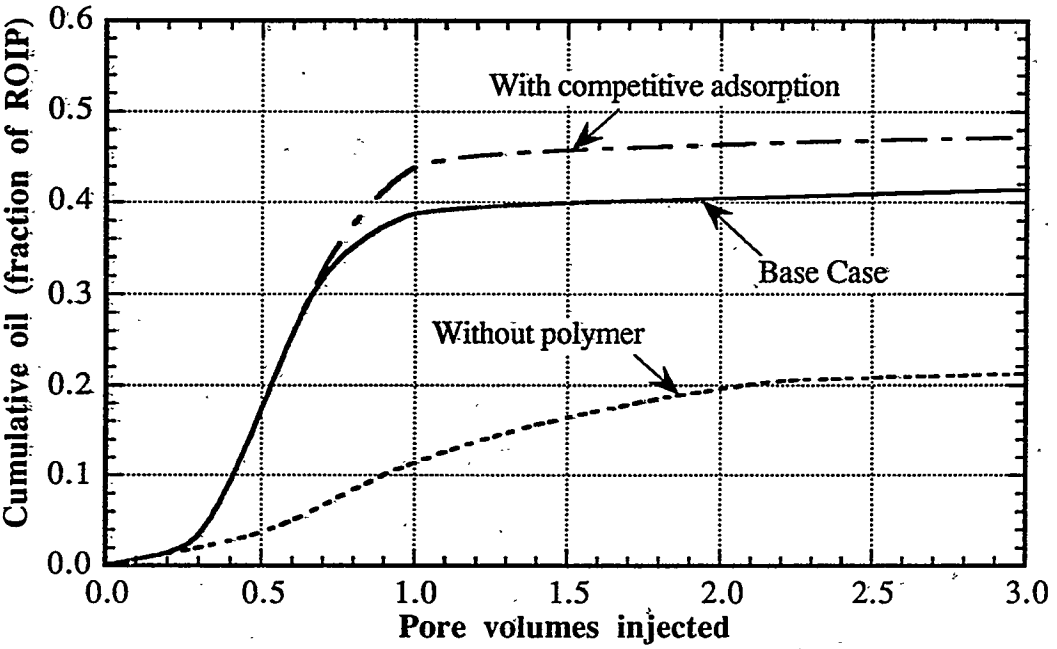


Figure 2.247 Effect of chemical interactions on oil recovery (Constant salinity)

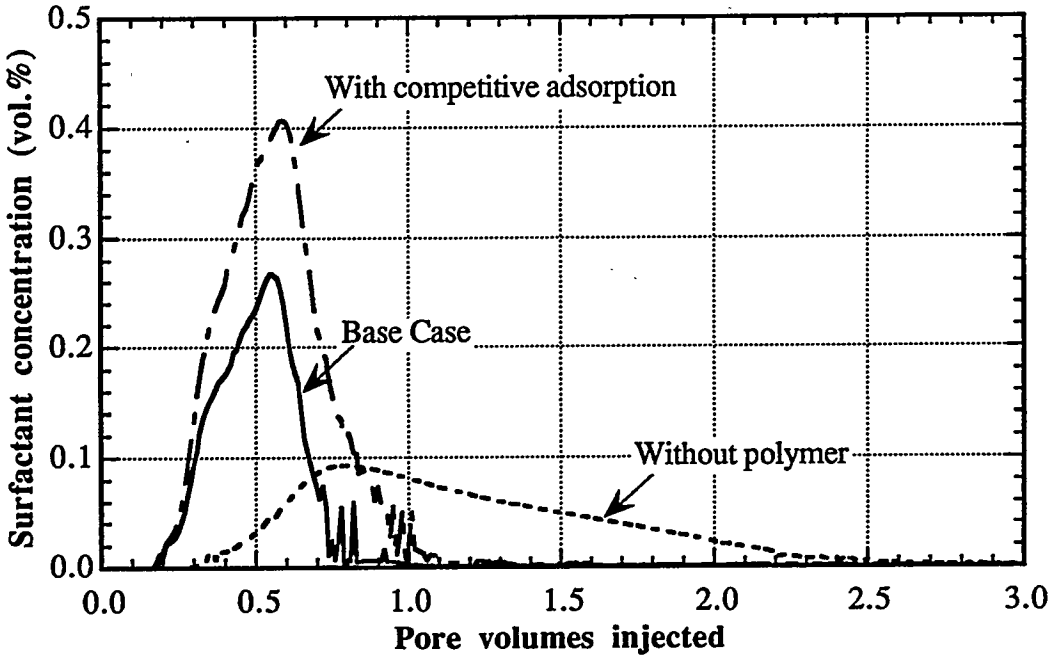


Figure 2.248 Effect of chemical interactions on produced surfactant concentration (Constant salinity)

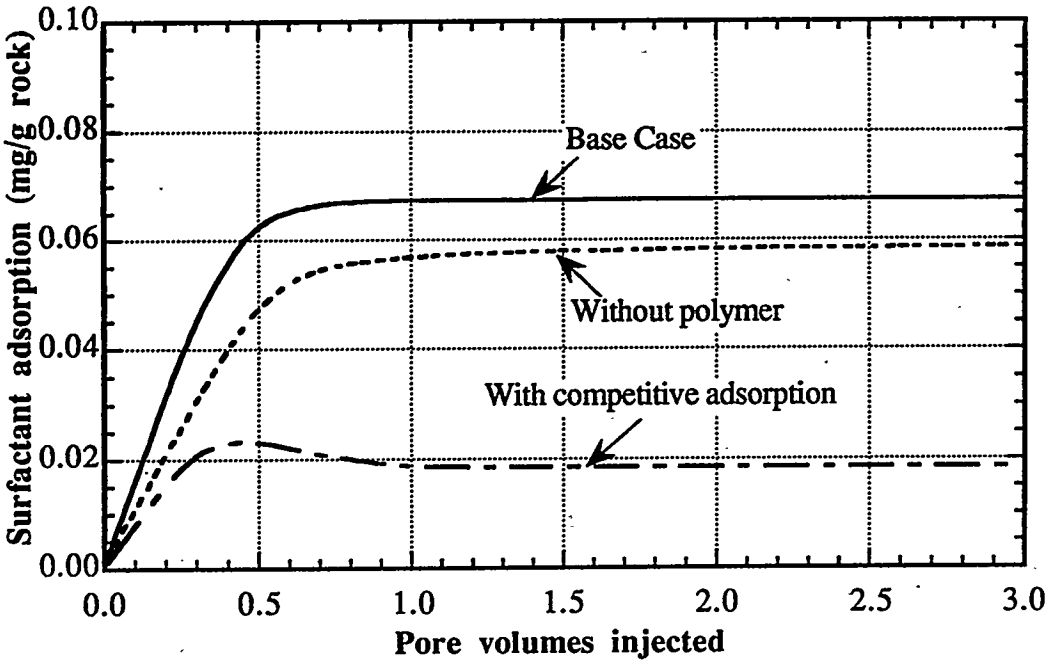


Figure 2.249 Effect of chemical interactions on surfactant adsorption (Constant salinity)

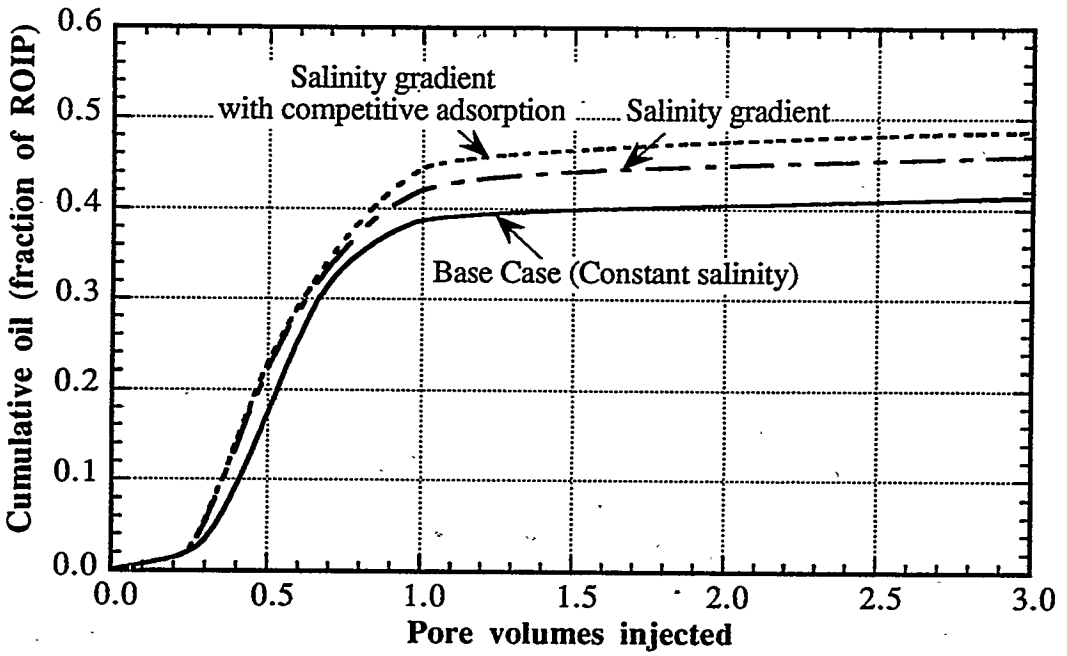


Figure 2.250 Effect of competitive adsorption with salinity gradient on oil recovery.

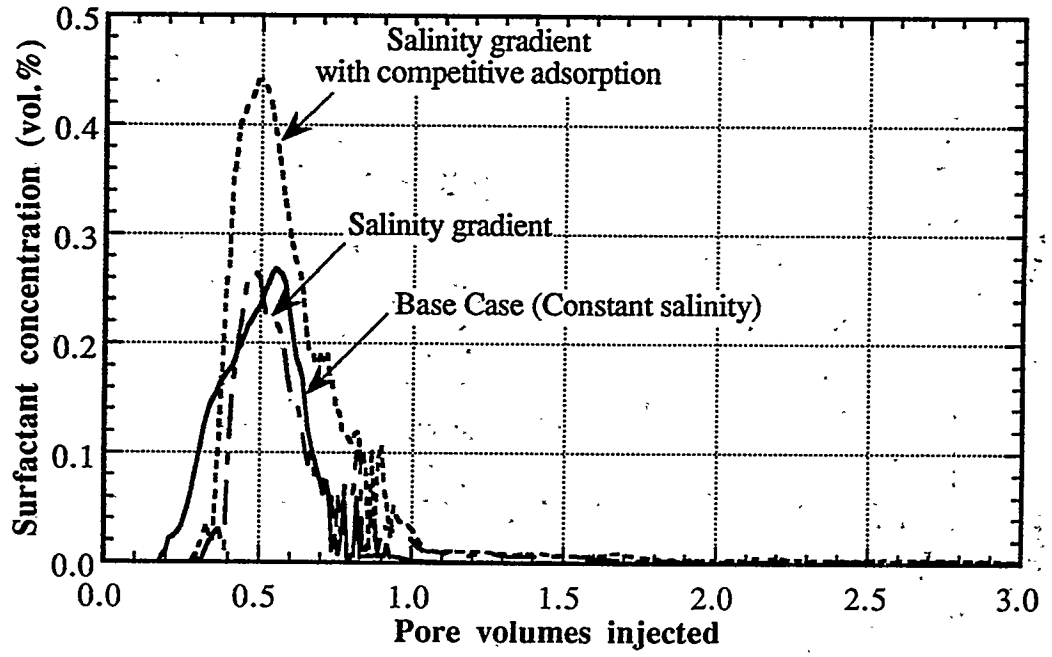


Figure 2.251 Effect of competitive adsorption with salinity gradient on produced surfactant concentration

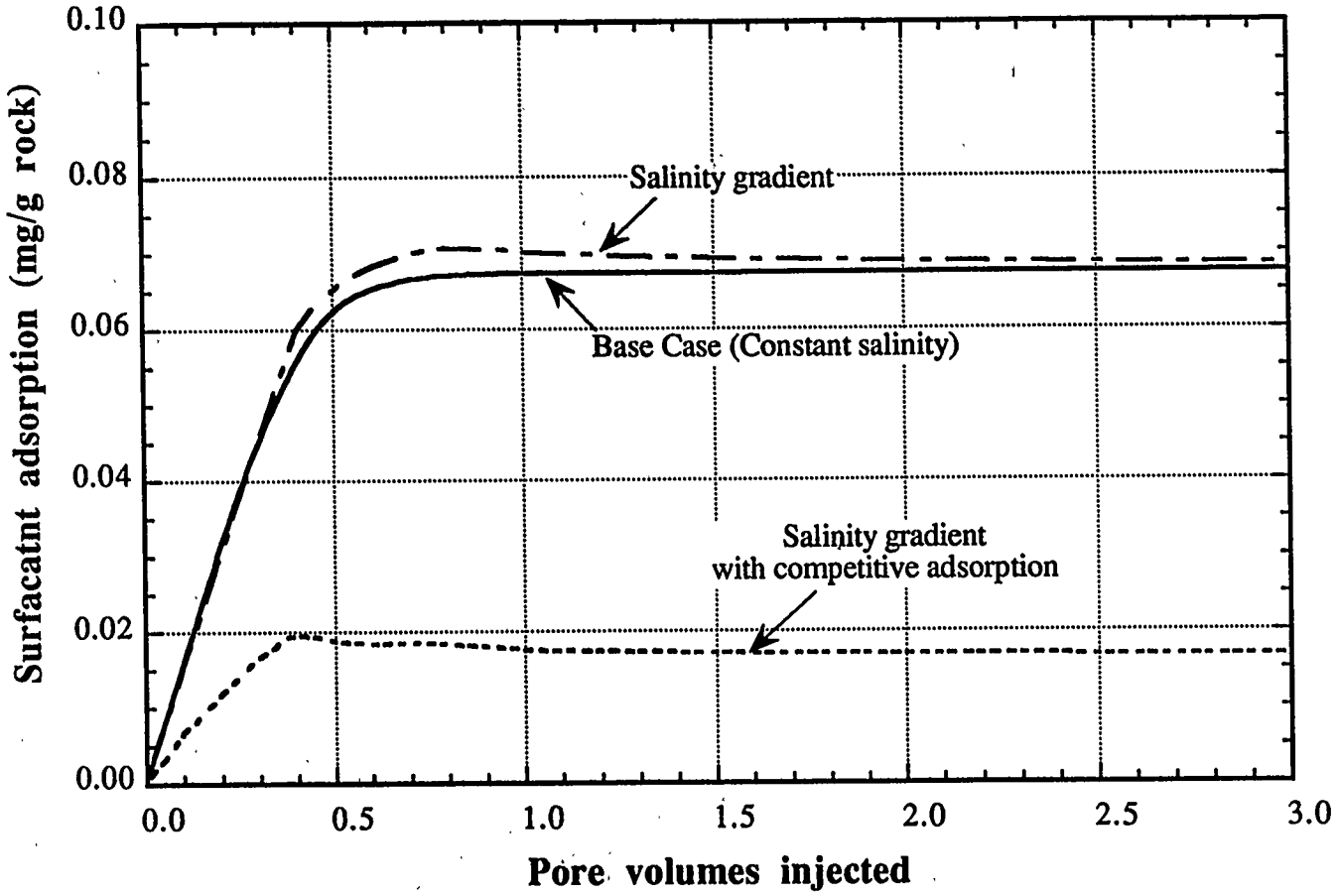


Figure 2.252 Effect of competitive adsorption with salinity gradient on surfactant adsorption

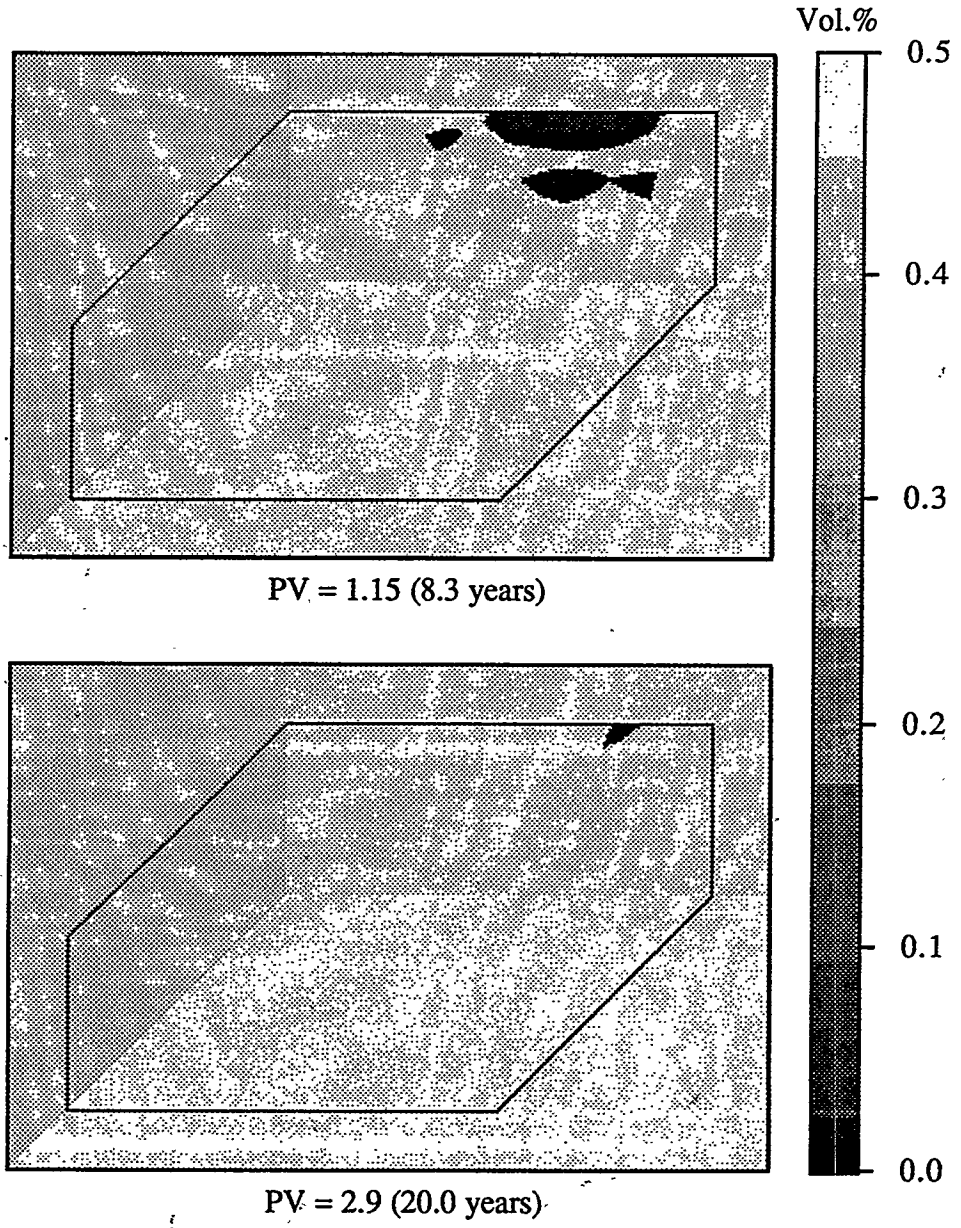


Figure 2.253 Surfactant concentration distribution for constant salinity case

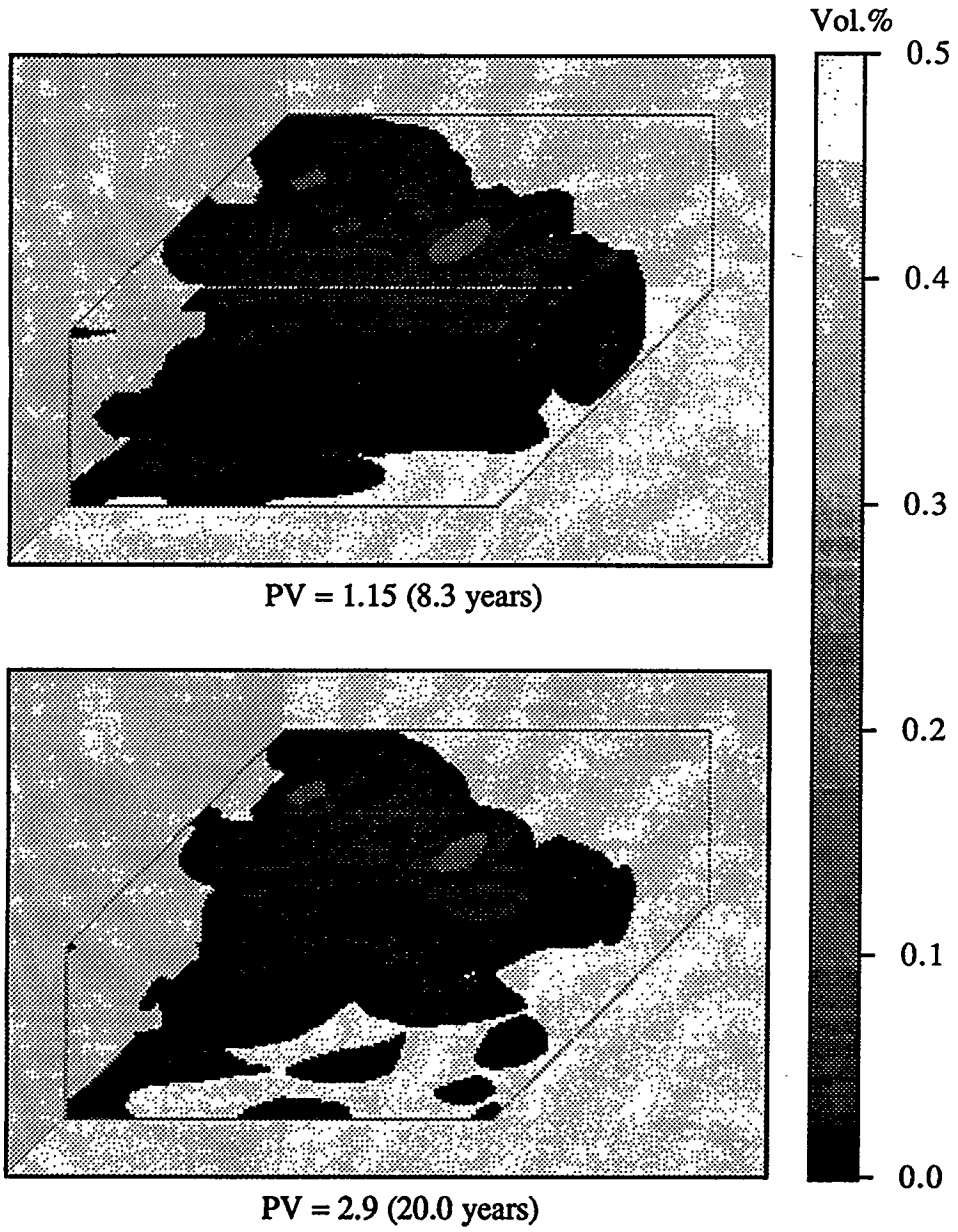


Figure 2.254 Surfactant concentration distribution for salinity gradient design case

3. Optimization of Alkaline/Surfactant/ Polymer Flooding for Reservoir D

A three-dimensional, alkaline/surfactant/polymer (ASP) pilot design was studied using UTCHEM. Several series of field-scale simulations were performed to investigate the ASP process and to compare it with alternative processes. Actual field data and coreflood results were used as much as possible to estimate simulator input parameter values.

The chemicals and the chemical reactions are first described. Then, history matches of coreflood results are shown for both Berea cores and reservoir core. A field-scale tracer test simulation is introduced. In the last two sections, results of field-scale sensitivity simulations are presented.

3.1 Introduction

The objective of this study was to investigate the potential of the ASP process for a pilot. An analysis of the complex ASP mechanisms in this reservoir is very important. Reservoir simulation is a good tool for performing sensitivity analyses. In this study, a series of three-dimensional ASP simulations was performed for the sensitivity analysis. The sensitivity of the oil recovery to the amount of surfactant and polymer, slug-size design, and chemical adsorption were determined. A comparison of the ASP process with other processes such as alkaline/polymer (AP), surfactant/polymer (SP), polymer (P), and waterfloods was made. In addition, tracer simulations were performed to determine how to balance the pattern and evaluate the swept volume between the injector and producer well pair.

Several categories of reactions were used to describe the ASP mechanisms. They are *in situ* generated surfactant, precipitation/dissolution of minerals, cation exchange with clay and micelle, and reduction of surfactant adsorption. Data from two Berea cores and one reservoir core were history matched to obtain estimates of property parameters. Permeability, porosity, initial water saturation, and initial pressure distributions were stochastically described using a matrix decomposition method (Yang, 1990) that was conditioned with the available core data.

These simulation results revealed a high potential of the ASP process to improve the cost-effectiveness of chemical flooding in this reservoir. This study has included elements of the chemistry of the ASP process not previously feasible on a field scale as well as combined these mechanistic process elements with three-dimensional stochastic reservoir descriptions for the first time.

3.2 ASP Chemicals and Reactions

The main factors considered in selecting alkaline agents were their ability to maintain a favorable pH under reservoir conditions, the mineralogy of the reservoir, and the composition of formation and makeup waters. Reservoir D is an onshore sandstone reservoir with a temperature of 71.6°F. The river water (used as makeup water, KRW) and formation water (KFW) contain low concentrations of sodium, calcium, magnesium, and carbonate ions (Table 3.1).

Sodium carbonate (Na_2CO_3) was selected as the alkaline agent in this pilot over other alkaline chemicals such as sodium hydroxide (NaOH) and sodium orthosilicate (Na_4SiO_4). Several factors contributed to this selection. These chemicals have similar efficiency in improving oil recovery (Burk, 1987; Al-Hashim *et al.*, 1996). However, sodium carbonate is less expensive than the other two. Sodium hydroxide and sodium orthosilicate will sometimes react with the rocks, which will cause a high consumption of these alkaline agents. If the divalent cation concentration is low, then precipitation of calcium carbonate ($CaCO_3$) and magnesium carbonate ($MgCO_3$) will not be excessive even if sodium carbonate is used. These coreflood results demonstrate that it is possible to propagate a pH of 11 using Na_2CO_3.

The surfactant was a petroleum sulfonate and was made in-house to reduce the cost. A hydrolyzed polyacrylamide polymer was chosen because it is suitable at low temperature (71.6°F) and low salinity and is less expensive than xanthan gum polymer and most other water-soluble polymers.

To describe the ASP geochemistry, seven elements, eighteen fluid species, four solid species, four clay-exchange cations, and three surfactant-exchange cations were included based upon the formation water and the minerals in the reservoir formation rocks (Table 3.2). The elements and pseudo-elements chosen in this study were hydrogen, sodium, calcium, magnesium, carbonate, acid (from HA_O), and water (H_2O). The acid was included because the mechanism of *in situ* generated surfactant is essential to model the ASP process properly. The chemical reactions among all species are shown in Table 3.3. Twenty chemical reactions are needed to describe these mechanisms. The equilibrium constants (K) for each reaction were obtained from the National Bureau of Standards (1974) or Lake (1989). A preprocessor program named EQBATCH was run to obtain equilibrium data to be used as initial data for UTCHEM.

3.3 Core-Flooding History Match

To obtain the physical-property data and to validate the simulation model, three coreflood results were used for history matching. Two experiments were performed in Berea sandstone and one was performed in a reservoir core. The properties measured in each core are listed in Table 3.4. Since many key data such as surfactant phase behavior and oil capillary desaturation were not available, a precise core flooding history match was difficult to make. An enormous number of simulations were needed to compensate for this unavailability of key data.

3.3.1 History Match of Berea Corefloods

Two corefloods, KMAY5 and KMAY7, were considered for history matching out of several ASP core displacement results provided. The cores used were 188 and 200 md Berea sandstone. The core length was 1 ft and the diameter was 1.5 inch. Detailed core descriptions are given in Table 3.5. The crude oil was a diluted stock tank oil with a viscosity of 24.3 cp. The acid number of the crude oil was 1.96 mg KOH/g oil. The cores were initially saturated with formation water, then flooded with the crude to residual water saturation, and were waterflooded with formation water to residual oil saturation before the chemical flood was conducted. The injection rate was 0.5 cc/min (0.0254 ft^3/day) during the ASP slug injection. The pH of the injected ASP slug was 11. The formation water pH was 7.8.

A review of the coreflood results revealed abnormal pressure drops in the KMAY7 coreflood, along with early breakthrough times for oil, surfactant, and polymer. The pressure drop can be calculated based on Darcy's law during the postflush period. The calculated pressure drop is 0.72 psi (assuming a relative permeability of 0.2 at a water saturation of 0.9) compared to 2.3 psi measured. This indicated a possible plugging of the core during the displacement. High-viscosity emulsion was observed in the produced samples, and this might explain the plugging behavior. Though KMAY5 was the best experiment to history match, it lacked the produced-water analysis data and pressure-drop data. Therefore, KMAY7, which was identical to KMAY5 with the exception of 0.5 wt% of NaCl added to the polymer drive, was used.

Using the available physical-property data, a series of one-dimensional simulations was performed. In these 1-D simulations, 80 uniform gridblocks were used. KMAY7 was matched first. The phase-behavior type was the most important parameter. Three phase-behavior cases are discussed below starting with a Type II(-) case. This approach had to be taken since the true phase behavior was not known (no actual phase diagrams were available).

3.3.1.1 KMAY7: Type II(-) Phase Behavior

Type II(-) phase behavior was first used to model the ASP coreflood data of KMAY7. Figures 3.1 through 3.11 show the physical properties and corresponding UTCHEM input parameters used in the best history match of the coreflood results. The computed phase diagram (Figure 3.4) showed a low binodal curve (0.025) at optimum salinity. The CMC for this surfactant was 0.01 vol.%. The plateau of the surfactant adsorption isotherm had a relatively high value of 1 mg/g rock (Figure 3.6). Figure 3.7 shows the effect of pH on the plateau value of the surfactant adsorption isotherm. The plateau value of the polymer adsorption isotherm is 76 μg/g rock (Figure 3.8). Figure 3.9 shows the microemulsion-phase viscosity as a function of oil concentration. The oil viscosity used here was 24.3 cp, which is different from the 17.2 cp used in the reservoir simulations. The polymer viscosity as a function of shear rate is shown in Figure 3.10. Figure 3.11 shows the effect of salinity on the polymer viscosity. Since hydrolyzed polyacrylamide polymer was used, the effect of salinity on the polymer viscosity was significant.

The waterflooding performance was first modeled. Figures 3.12 and 3.13 compare simulated and experimental waterflood oil recovery, oil cut, and pressure drop. Both plots indicate that the simulation results matched the measured data quite well. The endpoint relative permeability for the water phase was the most important parameter that either needed to be measured or adjusted.

Figures 3.14 through 3.23 compare the ASP experimental data and simulation results. The oil recovery, oil cut, and pH matched well (Figures 3.14 and 3.17). To match the oil recovery and oil cut, the height of the binodal curve was adjusted to a low value of 0.0265. The model predicted later breakthrough times for both surfactant (Figure 3.15) and polymer (Figure 3.16) and failed to match the experimental pressure drop (Figure 3.19). The retained surfactant and polymer concentrations were close to those measured in the laboratory (Table 3.6). The salinity was kept under the lower limit of a three-phase window (Figure 3.18).

The simulated pH was very close to the experimental values (Figure 3.17). This indicated that the chemical reactions were described correctly. The results also showed a reasonable comparison of simulated and measured produced sodium and chloride ion concentrations (Figures 3.20 and 3.23). The simulated calcium and magnesium ion concentrations did not match the laboratory data very well (Figures 3.21 and 3.22). Calcium carbonate ($CaCO_3$) was the only solid to precipitate in our simulation results (Figure 3.24). Because of this precipitation, the model predicted a much lower concentration of calcium than the experimental measurement. Precipitation reactions are assumed to occur instantaneously in the model. This may not be a valid assumption for these experiments. The underestimation of the chloride ion concentration caused deviation of the predicted magnesium ion concentration from the laboratory data at early time. The alkaline consumption was calculated to be 3.6 mole% from precipitation, 3.16 mole% from cation exchange, and 0.6 mole% from reaction with oil acid based on the simulation results.

To investigate the effect of the cation exchange capacity, we ran three cases with cation exchange capacities higher than in the previous case (0.2 meq/100 g of rock). The new cation exchange capacities were 2.5, 3.75, and 5 meq/100 g of rock. Figure 3.25 compares the predicted pH for these three cases. The simulated and experimental pH values matched poorly for these three high cation-exchange-capacity values. This shows a high sensitivity of pH to the cation exchange capacity.

In KMAY7, high-viscosity emulsion was observed in the produced samples. This viscous emulsion may have caused surfactant and polymer channeling to the end of the core, which would explain their early breakthrough. Also, a core plug at the time of the ASP slug injection may have caused the calcium and magnesium ions to rush to the end of the core without reacting with carbonate ions. Matching of these early breakthrough times and abnormally high pressure drop would require a nontrivial model modification and further information on the experiments. This, however, is beyond the scope of this study.

In summary, the simulation results with Type II(-) phase behavior are in reasonable agreement with the experimental measurements except for surfactant and polymer breakthrough times and the calcium and magnesium ion concentrations.

3.3.1.2 KMAY7 : Type III Phase Behavior

For this case, input data were identical to those used in the Type II(-) model with an exception that Type III phase behavior was used (Figure 3.26). Comparisons of the simulated and experimental oil recovery, oil cut, surfactant and polymer concentrations, pH, and pressure drop are shown in Figures 3.27 through 3.31. The Type III phase environment model incorrectly predicted a nearly perfect oil recovery at the end of the coreflood (Figure 3.27). The simulated produced surfactant concentration showed a sharp and narrow peak while the laboratory data leveled off (Figure 3.28). This is because the small phase volume of microemulsion causes a local high-surfactant concentration.

Figures 3.32 and 3.33 show surfactant and polymer concentration profiles. Because of low interfacial tension, the microemulsion-phase capillary number was very high (≥ 0.1) and the residual microemulsion saturation was reduced to almost zero. Therefore, the surfactant moved faster than the polymer front. The simulated pH still matched the data quite well (Figure 3.30).

The results showed that the use of Type III phase behavior was not ideal in fitting the coreflood results. To further study the possibility of matching coreflood data by using Type III phase behavior, a salinity-gradient design that varied the effective salinity from Type III to Type II(-) environment was introduced.

3.3.1.3 KMAY7: Salinity-Gradient Case

In the third case, we attempted using the salinity gradient to restrain the effective salinity in the three-phase window during the ASP slug and then dropping it back into the Type II(-) environment. The phase-behavior diagram is shown in Figure 3.34. Figure 3.35 shows the effective salinity and surfactant concentration as a function of pore volumes injected. Figures 3.36 through 3.41 compare simulated results with laboratory data for oil recovery, oil cut, produced surfactant and polymer concentrations, pressure drop, and pH.

In Figures 3.36 and 3.37, both KMAY7 and KMAY5 data are compared with simulation results. The simulated oil recovery was between those of the two experiments. As mentioned before, these two experiments were identical except for the salinity in the polymer drive. The effective salinities were 0.1 and 0.185 meq/mℓ for KMAY7 and KMAY5, respectively. The oil recovery, however, was 93% for KMAY5 and 71% for KMAY7. Although the polymer viscosity was reduced by adding 0.5 wt% of NaCl (0.085 meq/mℓ) to the polymer drive, this would not be the main cause of the lower oil recovery. The difference of 22% in oil recovery translated to only 5 mℓ of oil. It was suspected that this difference was at least partially caused by experimental error and variation due to several factors.

The simulated oil cut, produced surfactant and polymer concentrations, and pressure drop did not compare well with the laboratory data (Figures 3.37 through 3.40). But the pH matched the measured data well in this case (Figure 3.41). This indicates the insensitivity of pH to the surfactant phase behavior.

In summary, the waterflood results for KMAY7 were successfully predicted by the model. The comparison for the ASP flood was not as good because of both coreflood problems and lack of critical data on surfactant phase behavior. The simulation results, however, agreed fairly well for the KMAY7 oil recovery, pH, concentration of sodium ion, and amount of both polymer and surfactant retention when the flood was modeled as a Type II(-) environment.

Before applying the physical properties for the field studies, the uncertainty of oil recovery for the KMAY7 and KMAY5 cases needs to be addressed. As mentioned before, there was a 22% difference in oil recovery between these two cases. The oil recovery for the KMAY5 case was

believed to be the more realistic. Although the KMAY5 results are not described here in detail, we attempted to match the KMAY5 data based on the modification of KMAY7 input data.

Modifying the data from the KMAY7 with Type II(-) environment, we matched the coreflood results for the KMAY5 case. Figure 3.42 shows the good history match of oil recovery and oil cut. The produced salinity history (Figure 3.43) indicated that the Type II(-) phase behavior was present in all coreflooding processes. The adjusted parameters included the height of the binodal curve at zero salinity, microemulsion-phase viscosity, oil capillary-desaturation curve, and interfacial tension. Figures 3.44 through 3.47 show the modified physical properties described by those new parameters.

3.3.2 Reservoir Coreflooding Simulations

The oil recovery, oil cut, pressure drop, and chemical retention were the only data available on the coreflood with reservoir core (Table 3.7). Table 3.8 summarizes the reservoir core data. The core length was 0.2 ft and the permeability 95 md. The oil viscosity was 24.3 cp. The injection rate during the ASP slug was 0.2 ft/day. It appears that the core was plugged as the ASP slug was injected. Both the high pressure gradient of 215 psi/ft and early breakthrough (0.13 PV after ASP slug injected) of oil are indicative of plugging.

The first simulation was based upon the parameters from the history match of the Berea coreflood (KMAY7) with the input of Table 3.9 except that the core length, permeability, porosity, residual saturations, injected concentrations, slug sizes, flow rate, and polymer and surfactant retentions were based on the reservoir coreflood data (Table 3.7). The oil recovery and pressure drop are shown in Figures 3.48 and 3.49. The simulated pressure drop and oil cut were significantly different from those measured in the laboratory. Therefore, those input parameters that are dependent on the rock type such as the parameters for the capillary-trapping curve and relative-permeability curves were adjusted first. Other parameters adjusted were the height of binodal curve at zero salinity and the microemulsion-viscosity parameters. Input parameters that were changed from KMAY7 are listed in Table 3.10.

Figures 3.50 and 3.51 compare the simulated and laboratory oil recovery, oil cut, and pressure drop results for the reservoir coreflood. The simulated oil recovery and oil cut showed a similar trend as the experimental data, but the experimental oil breakthrough and peak were much earlier than those simulated (Figure 3.50). The simulated surfactant and polymer retentions were 0.13 mg/g rock and 138 μg/g rock, respectively. These retention values were very close to the laboratory data (0.12 mg/g rock for surfactant and 150 μg/g rock for polymer). The pressure drop during the water preflush and water postflush were successfully matched, but the measured pressure drop during chemical injection was about four times as high as the simulated values.

Next field-scale simulations were performed using the physical parameters from the reservoir coreflood history match. The main difference between the physical properties of the reservoir core and the Berea core is the adsorption level of surfactant and polymer.

3.4 Field-Scale Simulations

A number of field cases were simulated to understand the mechanisms of the ASP process in this pilot. Permeability, porosity, and initial water-saturation distributions were generated using a matrix decomposition method (MDM). A field-scale tracer test was then run to find an optimum bottomhole pressure for each producer to keep the flow balanced in the main five-spot pattern. Two sets of sensitivity analyses for the optimum pilot design were performed based on the optimum bottomhole pressure condition .

3.4.1 Reservoir Characterization

The pilot was stochastically described in terms of permeability, porosity, reservoir thickness, initial oil saturation, and initial pressure using a matrix decomposition method. A

spherical variogram and a log-normal permeability distribution were used. The geometric average permeability was 99 md and the average porosity was 0.2. Crude oil viscosity was 17.2 cp at the reservoir temperature of 71.6°F. Average initial oil saturation was 0.4 and the residual oil saturation was 0.32. Figures 3.52 through 3.60 show the conditioned stochastic permeability field, the initial oil saturation fields overlaid by porosity contours, and the initial pressure distribution for each layer. These descriptions were generated for a pilot area 184.8 m long x 184.8 m wide using a grid of 14 x 14 in the x and y directions for each of the five layers. These distributions were conditioned using permeability, porosity, thickness, initial pressure, and initial oil saturation data taken from 13 wells in the pilot area (Table 3.11).

To assess uncertainty, three different realizations and two variable correlation lengths were investigated (Table 3.11). The results indicate that, based on the data from 13 wells, the permeability distribution was insensitive to either the realization or the correlation length. The Case No. 1, Table 3.11, permeability field was used for all simulations.

In Case No. 1, Layers 4 and 5 were low-permeability zones with an average of 74 and 54 md. The average permeabilities of Layers 1, 2, and 3 were 164, 134, and 150 md. Examination of the permeability distribution for each layer revealed a large variation in permeability between layers at the location of injectors between layers. For example, Injector Well No. 9 was located in a 50-md area in Layer 1 but in a 400-md area in Layer 2. This kind of distribution causes a layer channeling or a poor sweep efficiency for injected chemicals. The permeability in the vertical direction was calculated as a function of horizontal permeability (k_x) using

$$k_z = 0.5379k_x - 34.0602.$$

When this correlation produced negative values, a vertical permeability of 1 md was assigned.

3.4.2 Tracer Simulations

Tracer simulations were used to estimate the amount of each tracer required to estimate the swept volume between injectors and producers and to adjust the bottomhole pressure of the producers to improve the sweep efficiency. Figure 3.61 shows the grid and well locations for the pilot. Four tracers were injected: Tracer 1 for Well No. 4, Tracer 2 for Well No. 5, Tracer 3 for Well No. 9, and Tracer 4 for Well No. 10. For simplicity, we assumed that the tracers were nonpartitioning, nonadsorbing chemical tracers with a detection limit on the order of 1 ppm. Examples of these tracers are sodium bromide and sodium iodide (Zemel, 1995).

The tracers were injected at 107 B/D (17 m^3/d) for 18 days followed by 1,582 days of waterflooding. The tracer simulations were initially performed with a uniform bottomhole pressure of 4,500 kPa (653 psia) for the producers. The tracer response curves shown in Figures 3.62 through 3.70 indicated an unbalanced pattern. Figure 3.71 shows the total fluid production for each producer. Well No. 7, which was located in the center of the five-spot pattern, did not show a high productivity. The bottomhole pressures of the producers were then adjusted in an attempt to optimize the production rates and to balance the five-spot pattern. The adjusted bottomhole pressures are given in Table 3.12. Figures 3.72 through 3.80 show the tracer responses at each production well. The tracer curves are now closer to each other for Well No. 7 (Figure 3.76). The total production for each well is shown in Figure 3.81. Well No. 7 showed the highest total production rate among all producers.

The swept volumes between wells were calculated based on the moment analysis in the tracer response curve (Maroongroge, 1994; Jin *et al.*, 1994). The swept volume for a given well pair is defined as the volume of the reservoir contacted by the tracer as it flowed between an injector and a producer. The total swept volume for all four injectors was 193,624 bbls (30,786 m^3). Figure 3.82 shows the swept volume for each producer, with the highest value of 37,736 (6,000 m^3) for Well No. 7. The produced tracer concentrations were very small after 1,000 days of injection. Therefore, the injected tracer concentration was calculated by assuming that the detection limit of 1 ppm (C_{limit}) was equal to the lowest normalized tracer concentration at 1,000 days (C_{nor}) for each tracer at each production well. The injected concentration (C_o) for tracers was then calculated by

$$C_o = \frac{C_{nor}}{C_{limit}}$$

The amount of tracer injected was then computed by multiplying the injected concentration by the volume of tracer injected (306 m^3). It was estimated that 600 kg of each chemical tracer would be the minimum amount needed based on the 1 ppm detection limit. Design details such as tracer type and the method of tracer detection were not part of this study and not needed for these simulations but would be needed for an actual tracer project in the field. The purpose here was to use a hypothetical tracer test to aid in the optimization of the chemical flood. This is an unusual but highly useful approach that should be made more often.

3.4.3 ASP Simulations

Four series of field-scale sensitivity simulations were performed to examine the potential of the ASP process in this reservoir. Two series of simulations were performed before the KMAY5 and reservoir core flood results became available. Unknown physical properties such as phase behavior of surfactant were assigned some typical values and chemical adsorption was treated as a sensitivity parameter in these simulations. The other two series were run based on the history match results for both Berea core and reservoir core displacements after the coreflood results were provided.

3.4.3.1 ASP Field-Scale Simulation - Series I and II

The objective of this series was to investigate the potential of using *in situ* surfactant to mobilize oil. Table 3.13 lists the injection schemes for Series I. Figure 3.83 shows the oil recoveries for ASP, alkaline/polymer (AP) flood, polymer flooding, and waterflood for low plateau values of surfactant and polymer adsorptions (0.15 mg/g of rock and 8 μg/g of rock). The oil recovery for the ASP process was 16.5 % of the remaining oil in place (ROIP) of 189,674 bbls (30,158 m^3), which was 3.5% higher than for the AP process.

We repeated the polymer and AP simulations using a plateau polymer adsorption of 80 μg/g of rock (based on Berea coreflood data) instead of 8 μg/g of rock. Figure 3.84 shows the oil recovery of AP and polymer flooding in comparison with waterflooding. The total oil recovery decreased significantly with the increase in the polymer adsorption. The mobility control from polymer was undoubtedly very important for this high-viscosity crude oil (17.2 cp). Also, the sweep efficiency was strongly affected by the amount of polymer in the heterogeneous reservoir. It was concluded that injecting a sufficient amount of polymer was very important.

Based on the results from Series I, a high concentration of injected surfactant in the ASP slug and a large polymer drive were applied in Series II. The injection scheme used in Series II is listed in Table 3.14. The alkaline agent (Na_2CO_3) was reduced from 1.8 to 1.6 wt% to be consistent with the core flood. The plateau adsorption for surfactant and polymer were 0.25 mg/g of rock and 8 μg/g of rock. Figure 3.85 shows the total oil recovery for ASP, AP, polymer, and waterflooding. The processes were stopped at 1% oil cut. The oil recovery improved significantly in the ASP and AP processes. Comparison of the AP floods of Series I and II indicated polymer improved the sweep efficiency and created the 6% increase in oil recovery.

A higher surfactant concentration in the ASP slug and a longer polymer drive in Series II led to a 15% increase in oil recovery for the ASP process. Improvement in the sweep efficiency and oil mobilization was the main cause for this higher oil recovery. However, the amount of surfactant and polymer needed to be optimized.

3.4.3.2 ASP Field-Scale Simulation - Series III

Series III simulations were performed based on the physical parameters from the KMAY5 Berea coreflood matched with Type II(-) phase behavior. The plateau values of chemical adsorption in this series were based on the Berea coreflood results of 1.0 mg/g of rock and 80 μg/g of rock for surfactant and polymer, respectively. Also, the input parameters of surfactant phase behavior, phase capillary-desaturation curves, and polymer properties were kept the same as in the Berea coreflood simulation. Several coreflood input parameters needed to be changed for the field-scale application. The cation exchange capacity was 8.5 meq/100 g of rock for the reservoir (0.2 meq/100 g of rock for the Berea core). Oil viscosity, dispersivity parameters, and relative permeability were also changed to the reservoir condition.

The Series III simulations included sensitivity to the amount of surfactant, surfactant-slug size, amount of polymer, phase behavior, and surfactant and polymer adsorption. A Base Case was first simulated. The injection scheme for the ASP Base Case is given below :

Water Preflush : 0.2 pore volumes (225 days) of makeup water with 1.5 wt% of NaCl were injected.

ASP Slug : 0.3 pore volumes (337.5 days) of 1.6 wt% Na_2CO_3, 2 vol. % of surfactant, and 0.15 wt% polymer in makeup water were injected.

Polymer drive : 0.13 pore volumes (152.5 days) of 1,500 ppm polymer in makeup water were injected.

Postflush : 0.79 pore volumes (885 days) makeup water were injected.

In this design, 50 tons of polymer and 459 tons of surfactant were injected.

Figure 3.86 shows the total oil recovery and oil cut as a function of pore volumes injected. The oil recovery was 23.6% of ROIP at the end of the project life. The IOR was 9.7 and S_{eff} was 13.8 for the Base Case. The surfactant efficiency was low. Oil-bank breakthrough was at 325 days (0.31 PV) after water injection or 100 days (0.11 PV) after ASP injection. The total produced oil was 44,730 bbls (7,112 m^3) at the end of the project life (Figure 3.87). The surfactant and polymer retention were 53% of total surfactant injected (0.31 mg/g of rock) and 60% of total polymer injected (38 μ g/g of rock). The adsorption for surfactant was 0.20 mg/g of rock and that for polymer was 29 μ g/g of rock. 90% of surfactant retention and 76% of polymer retention were caused by the formation adsorption. Figure 3.88 shows the isosurface of 0.1 for oil concentration distribution at different times. Injection Wells No. 4 and No. 5 showed high oil mobilization in the top three layers, but injection Wells No. 9 and No. 10 were less efficient in the first layer.

To demonstrate the effect of permeability heterogeneity more clearly, the isosurface of 0.9 for water concentration is shown in Figure 3.89. Figures 3.90 and 3.91 show the distribution of surfactant and polymer concentrations. The isosurface for surfactant is 0.2 vol.% and for polymer 0.025 wt%. For Wells No. 9 and No. 10, the main contact area was distributed in Layers 2 and 3 (Figure 3.89). The injection fluid was unevenly distributed in each layer for every injector. Clearly, the heterogeneous permeability distribution caused the injection fluid to move into high-permeability layers (Layers 1, 2, and 3) (Figures 3.90 and 3.91). On the other hand, the low-permeability layers (Layers 4 and 5) took less chemicals than the other layers. Figure 3.92 shows the distribution of the pH isosurface (pH=10). The high cation exchange capacity of this formation caused a large consumption of injected alkalinity and prevented the high-pH (>10) front from moving as fast as the surfactant front, thus reducing the chemical adsorption as much as desired (Figures 3.90 and 3.92). The consumption of alkalinity was calculated to be 2.4 mole% from precipitation, 36.3 mole% from cation exchange, and 0.19 mole% from reaction with oil acid based on the simulation results.

Figures 3.93 through 3.95 show the distribution of sodium and calcium ion concentrations and the calcium carbonate solid phase concentration. The sodium ion concentration distribution was similar to the surfactant concentration distribution. Low calcium ion concentration is distributed through the reservoir, especially near the wellbore (Figure 3.94), which would reduce the divalent effect on the surfactant efficiency. The cause of lower calcium ion concentration near

the wellbore was the precipitation of calcium carbonate (Figure 3.95). However, very little precipitation of calcium carbonate occurred.

It can be concluded that the main reasons for the low efficiency of surfactant were high surfactant adsorption, high cation exchange capacity of clay, and heterogeneity of permeability, which causes an uneven distribution of the injected fluids and local channeling.

Before we performed the sensitivity simulations for the ASP process, several oil-recovery processes were run. These processes included water, polymer, alkaline/polymer, surfactant/polymer, and alkaline/surfactant/polymer flooding. The injection scheme for each process is shown in Figure 3.96. The chemical concentrations were the same for each process. The concentrations of surfactant and polymer were 2 vol.% and 1,500 ppm, respectively. The alkaline concentration was 1.6 wt% of sodium carbonate (Na_2CO_3). Figure 3.97 compares the oil recovery for these processes. Both water and polymer flooding are not favorable in this reservoir, since the average initial oil saturation (0.4) was close to the average residual oil saturation (0.32), which means a small target oil for both processes. The alkaline/polymer process was not favorable because of a high chemical consumption caused by the high cation exchange capacity. The *in situ* generated surfactant would not efficiently mobilize oil because of its high adsorption.

The S/P process showed a 12% increase in oil recovery over polymer flooding. Injecting enough surfactant to decrease the IFT and to mobilize oil was important for recovering the residual oil. The ASP process showed another 6% increase over surfactant/polymer flooding. Table 3.15 compares surfactant adsorption and retention of the ASP and S/P processes. There was a 51.2% reduction in surfactant adsorption because of the increase in pH when Na_2CO_3 was injected. The Na_2CO_3 also causes the generation of surfactant when it reacts with the organic acid that partitions into the water from the crude oil. Both of these mechanisms result in more active surfactant available to mobilize and recover the residual oil and account for the higher recovery of the ASP process compared to S/P.

3.4.3.2.1 Amount of Surfactant and ASP Slug Size

Based on the results of the Base Case ASP simulation, a lower surfactant concentration of 1 vol.% (Case 1) and 0.5 vol.% (Case 2) were used. Table 3.16 summarizes the simulation results for these three cases. The final oil recovery decreased from 23.6% to 18.7% to 14.3% as the amount of injected surfactant was reduced. There was a 9% difference in oil recovery between the Base Case and Case 2. Figure 3.98 shows the oil recovery as a function of the amount of surfactant injected. The case with zero surfactant is just a polymer flood and recovers only about 2% of ROIP. The values of S_{eff} and IOR for each case are given in Table 3.16.

In an attempt to gain a higher efficiency and a lower retention of surfactant, the ASP slug size was investigated. The amount of surfactant and polymer injected was kept unchanged from the Base Case. The injected concentration of surfactant in the ASP slug was one-half of that in the Base Case but the slug size was doubled to 0.6 PV (Case 3). The injection scheme is listed in Table 3.17. The final oil recovery decreased from 23.6% to 19.5% (Figure 3.99). The cumulative oil production equaled 36,912 bbls (5,869 m^3) at the end of the project life. The efficiency of the surfactant was 11.1 and the surfactant retention was 0.25 mg/g of rock. Comparing the isosurface plots of surfactant concentration (Figures 3.90 and 3.100), the surfactant distribution was very similar. Although the chemical slug was larger in Case 3, surfactant bypassed the target oil and channeled to the producers because of the heterogeneous permeability. The lower surfactant retention in Case 3 showed more surfactant was produced than for the Base Case.

It was suspected the lower oil recovery for Case 3 was due to the reduction of the polymer concentration in the ASP slug. To eliminate the effect caused by a low polymer concentration in the ASP slug, a test case (Case 4) was run after increasing the polymer concentration from 1,000 ppm to 1,500 ppm in the ASP (0.6 PV) slug and from 500 ppm to 700 ppm for polymer drive (0.14 PV). The oil recovery in Case 4 was 21.8%. The amount of polymer injected exceeded that in the Base Case by 24.5 tons, but the oil recovery did not increase very much (Table 3.17).

Single-phase microemulsion flow was observed near the wellbore for these three cases. Figure 3.101 compares the area for single-phase microemulsion flow between the Base Case and Case 4. The isosurface shown in these plots was representative of the area with 90 vol.% of single-phase microemulsion saturation. The Base Case exhibited a larger area than Case 4. This can be attributed to the surfactant phase behavior, heterogeneous permeability distribution, and relatively high adsorption of surfactant for the dilute-slug design. The surfactant adsorption near the wellbore gridblocks was 35% and 60% of the surfactant for the Base Case and dilute-slug designs, respectively. The enlarged slug of surfactant again bypassed the target oil and was produced.

Using an enlarged slug size with a low concentration of surfactant agent was not suitable for this pilot. Comparison of these results with those in the previous section of this report shows that sensitivity factors vary a lot from one reservoir to another. These factors were revealed only after a systematic simulation and detailed analysis.

3.4.3.2.2 Phase Behavior and Chemical Adsorption

Surfactant adsorption and phase behavior are the key parameters for the ASP and SP processes. To understand the uncertainty of these two parameters for this pilot, two simulations were run. First, a Type III phase behavior during the ASP slug injection was applied (Case 5 in Table 17) by adjusting the salinity window of 0.22 meq/mℓ for lower limit and 0.33 meq/mℓ for upper limit. Also the height of the binodal curve for the low-salinity condition was increased from 0.0265 (Base Case) to 0.1. Figure 3.102 shows a 4.3% uncertainty in oil recovery (10,154 bbls difference) for surfactant phase behavior. The isosurfaces of 0.9 for water concentration at different times for Case 5 are seen in Figure 3.103. Compared to the Base Case (Figure 3.89), Case 5 showed more surfactant flowing into the low-permeability zones because of the ultralow interfacial tension occurring in the Type III region. In Case 5, additional contact between the surfactant and formation rock surface caused larger surfactant adsorption (0.22 mg/g rock) and retention (0.34 mg/g rock) than in the Base Case (0.20 and 0.31 mg/g rock for surfactant adsorption and retention). Oil recovery and distribution of injected fluids were shown to be sensitive to the surfactant phase behavior. A precise surfactant phase-behavior experiment is strongly recommended, since the performance of ASP flooding is highly dependent on the surfactant phase behavior.

Second, the surfactant adsorption plateau was reduced to 0.5 mg/g of rock and polymer adsorption to 15 μ g/g of rock. The other physical properties were kept the same as those in the Base Case. Figure 3.104 shows little improvement in the oil recovery from that in the Base Case. The cumulative oil production for this case equaled 48,176 bbls (7,660 m^3), and this was an increase of only 3,447 bbls (548 m^3). The surfactant efficiency was 15, still low. Surfactant and polymer adsorptions were 0.12 mg/g of rock and 6.7 μ g/g of rock. The retentions were 0.23 mg/g of rock and 23.5 μ g/g of rock for surfactant and polymer. The adsorption of chemicals decreased, but the retention did not decrease significantly. Figure 3.105 shows the distribution of the surfactant isosurface of 0.2 vol.%. The surfactant concentration was clearly higher than that in the Base Case (Figure 3.90) near injection Wells No. 4, No. 5, and No. 10 because of the reduction of surfactant adsorption, but its distribution was similar to that of the Base Case. The oil in low-permeability layers was still bypassed by the injection fluids, although the injection front contained higher concentrations of surfactant and polymer. The improvement in sweep efficiency and the mobilization of oil were constrained because of the heterogeneity.

3.4.3.2.3 Amount of Polymer

In Case 7, the polymer-drive size was increased from 0.14 to 0.3 PV. The total amount of polymer was 72.5 tons (22.5 tons more than in the Base Case). Oil recovery increased 5.4% (Figure 3.106) to 29.0%, which is 10,270 bbls (1633 m^3) more than that for the Base Case. Figure 3.107 shows the oil distribution with the 0.1 isosurface at different times. Figure 3.108

shows the water distribution with the 0.9 isosurface. Comparison of these plots to those of the Base Case (Figures 3.88 and 3.89) shows the sweep efficiency was improved by enlarging the polymer drive. Injecting enough polymer to reduce the effect of heterogeneity (local channeling) is very important for this pilot.

In summary, results from the simulation Series I, II, and III revealed a significant sensitivity of oil recovery to the amount of polymer injected. Polymer played a very important role in the ASP process because improvement of sweep efficiency and reduction of the local channeling had a significant effect on oil recovery. The enlarged slug size with low surfactant concentration was not efficient in mobilizing oil because of the high adsorption and high cation exchange capacity with the surfactant and alkaline agents. Injecting a high-concentration surfactant and a large polymer drive are the key to achieving high oil recovery. Applying the design experiences from Series I, II, and III simulations, a final set of sensitivity simulations were performed with the physical properties based on the reservoir coreflood.

3.4.4 ASP Simulations Based on Reservoir Coreflood

The physical properties for the simulations performed in this section were based on the reservoir coreflood (Table 3.18). Figures 3.109 through 3.115 show the physical properties based on these modified parameters. Figure 3.109 shows the relative permeability and UTCHEM model curve at low capillary number. Figure 3.110 shows the phase relative permeability at the high capillary number used in this case. Surfactant phase behavior and interfacial tension are shown in Figures 3.111 and 3.112. Surfactant and polymer adsorption with plateau values of 0.68 mg/g of rock and 80 μg/g of rock are shown in Figures 3.113 and 3.114. Most input parameters for physical properties were taken from the Series III simulations, with the exception of rock properties such as relative permeability and chemical adsorption.

Simulation Series I, II, and III showed the importance of injecting a large amount of polymer. Thus, the amount of polymer was not considered as a sensitivity analysis factor in this section and was set to 0.18 wt% for 0.8 PV (both the ASP slug, 0.5 PV, and the polymer drive, 0.3 PV). On the other hand the amount of surfactant and ASP slug size were the main factors considered in this case. The injection scheme for Series IV was as follows :

Water Preflush : 0.2 pore volumes (225 days) of makeup water with 1.0 wt% of KCl.
ASP Slug : 0.5 pore volumes (562.5 days) of 1.4 wt% Na_2CO_3, 0.3 vol. % of surfactant, and 0.18 wt% polymer in makeup water.
Polymer Drive : 0.3 pore volumes (337.5 days) of 1,800 ppm polymer and 0.7 wt% NaCl in makeup water were injected.
Postflush : 0.42 pore volumes (475 days) makeup water.

The amounts of chemical injected were 107 tons of polymer and 111 tons of surfactant. Figure 3.115 shows the oil recovery for this ASP flood. The amount of injected surfactant was not enough to mobilize oil.

To approach the optimum amount of injected surfactant, two simulations were performed with surfactant concentrations of 0.6 and 1 vol.% with 0.5 PV slug size, which corresponds to 224 and 372 tons of injected surfactant. The amount of injected surfactant (for the 1 vol.% case) was still less than that for the Series III design based on the Berea core data (459 tons). Figure 3.116 compares the oil recoveries for each of these cases. The oil recovery increased 8% as the surfactant concentration increased from 0.6 to 1 vol.%. The uncertainty of the oil recovery among the sensitivity cases was similar to that in the previous series (Figure 3.98). High concentration of surfactant was necessary to obtain higher oil recovery for both cases because of the high surfactant adsorption and the high cation exchange capacity of the formation rock.

3.5 Summary and Conclusions

A compositional simulator (UTCHEM) has been modified to better handle alkaline/surfactant/polymer flooding simulations. It has been successfully applied to optimize the

ASP process for a three-dimensional pilot and history match of three coreflood results. The laboratory data were used to the maximum possible extent to estimate simulation input parameters. Results predicted by the modified geochemical option showed a reasonable match with the coreflood results. The ability of UTCHEM to rigorously account for the very complicated chemical reactions between the injection fluids and the formation fluids and rocks is the key to this study because of the complex mechanisms of ASP flooding.

A comparison of oil recovery among different processes was made. Several sensitivity studies were also performed. In addition, a tracer-test simulation was used to optimize the well rates by adjusting the pressures. This is the first field-scale ASP simulation study that includes detailed reaction chemistry. Furthermore, these simulations were done using conditioned stochastic permeability fields. The results of our field-scale simulation study suggest the following conclusions:

1. The ASP process has a high potential to improve the cost-effectiveness of chemical flooding because of the low price of alkaline chemicals and the reduction of the amount of surfactant required to efficiently mobilize oil.
2. High adsorption of surfactant and cation exchange capacity made the alkaline/polymer process unsuitable for this pilot.
3. Polymer plays an important role in ASP flooding. To improve the sweep efficiency, to maintain a favorable mobility ratio, and to avoid channeling, a large amount of polymer is required.
4. High-pH fluids to reduce the adsorption of surfactant and generate *in situ* the surfactant decrease the consumption of surfactant. In this pilot, the reduction of surfactant adsorption is especially important.
5. A tracer test is important for understanding the swept volumes for each injector and producer pair and the balancing of the well pattern. Tracers also provide information on the connections and heterogeneity distribution between wells.

Although the modified geochemical model has worked well so far, the ASP simulations are computationally time-consuming (10 hours per run on a DEC Alpha 3000/500 workstation). Vectorization and parallelization of the code should be considered to reduce such consumption.

4. References

Aldejain, A.: "Simulation of Surfactant and Tracer Flooding in Naturally Fractured Reservoirs," Category A Research, 13th Annual Report, Enhanced Oil and Gas Recovery Research Program, Center for Petroleum and Geosystems Engineering, The University of Texas, Austin (April 1996).

Al-Hashim, H.S., V. Obiora, H.Y. Al-Yousef, F. Fernandez, and W.A. Nofal: "Alkaline Surfactant Polymer Formulation for Saudi Arabian Carbonate Reservoirs," paper SPE/DOE 35353 presented at the 10th SPE/DOE Symposium on Improved Oil Recovery, Tulsa, OK, Apr. 21-24, 1996.

Austad, T., I. Fjelde, K. Veggeland, and K. Taugbøl: "Physicochemical Principles of Low Tension Polymer Flood," *J. Pet. Sci. Eng.* (1994) **10**, 255-269.

Austad, T., and K. Taugbøl : "Polymer Gradient as an Alternative to the Salinity Gradient for Controlling the Effects of Dispersion and Retention in LTPF," paper presented at the 14th IEA Collaborative Project on Enhanced Oil Recovery Workshop and Symposium, Salzburg, Germany, Oct. 17-21, 1993.

Barakat Y., L.N. Fortney, R.S. Schechter, W.H. Wade, S.H. Yiv, and A. Graciaa: "Criteria for Structuring Surfactants to Maximize Solubilization of Oil and Water Part II-Alkyl Benzene Sodium Sulfonates," *J. Colloid Interface Sci.* (1983) **92**, No. 2, 561-574.

Baumann, R.H. and A.G. Pulsipher: "States Pass Measures to Help Producers during Tough Times," *Oil and Gas J.* (Nov. 1994) 56-59.

Burk, J.H.: "Comparison of Sodium Carbonate, Sodium Hydroxide, and Sodium Orthosilicate for EOR," *SPE Reser. Eng.* (Feb. 1987) 9-16.

Dakhlia, H.: "A Simulation Study of Polymer Flooding and Surfactant Flooding Using Horizontal Wells," Ph.D. dissertation, U. of Texas, Austin (Aug. 1995).

de Blanc, P.C.: "A Three-dimensional, Multicomponent, Multiphase Subsurface Biodegradation Simulation Model," Ph.D. dissertation, U. of Texas, Austin (1996).

Delshad, M., G.A. Pope, and K. Sepehrnoori: "A Compositional Simulator for Modeling Surfactant Enhanced Aquifer Remediation," in press, *J. Cont. Hydrol.*, 1996.

Edwards, M.: "Local Grid Refinement with a High Resolution Scheme in Three Dimensional Simulator," Category A Research, 13th Annual Report, Enhanced Oil and Gas Recovery Research Program, Center for Petroleum and Geosystems Engineering, The University of Texas, Austin (April 1996).

Graciaa, A., L.N. Fortney, R.S. Schechter, W.H. Wade, S.H. Yiv: "Criteria for Structuring Surfactants to Maximize Solubilization of Oil and Water: Part 1-Commercial Nonionics," *SPEJ* (Oct. 1982) 743-749.

Healy, R.N. and R.L. Reed: "Physicochemical Aspects of Microemulsion Flooding," *SPEJ* (Oct. 1974) 491-501.

Helfferich, F.G.: "Theory of Multicomponent, Multiphase Displacement in Porous Media," *SPEJ* (Feb. 1981) 51-62.

Hirasaki, G.J.: "Application of the Theory of Multicomponent, Multiphase Displacement to Three-Component, Two-Phase Surfactant Flooding," *SPEJ* (Apr. 1981) 191-204.

Huh, C.: "Interfacial Tensions and Solubilizing Ability of a Microemulsion Phase that Coexists with Oil and Brine," *J. Colloid Interface Sci.* (1979) **71**, No. 2, 408-426.

Jin, M.: "A Study of Nonaqueous Phase Liquid Characterization and Surfactant Remediation," Ph.D. dissertation, U. of Texas, Austin (Aug. 1995).

Jin, M., M. Delshad, D.C. McKinney, G.A. Pope, K. Sepehrnoori, C. Tilburg, and R.E. Jackson: "Subsurface NAPL Contamination: Partitioning Tracer Test for Detection, Estimation and Remediation Performance Assessment," in *Toxic Substances and the Hydrologic Science,* A.R. Dutton (ed.), American Institute of Hydrology, Minneapolis, MN (1994).

Kalpakci, B., T.G. Arf, J.W. Barker, A.S. Krupa, J.C. Morgan, and R.D. Neira: "The Low-Tension Polymer Flood Approach to Cost-Effective Chemical EOR," SPE/DOE paper 20220 presented at the 7th SPE/DOE Symposium on Enhanced Oil Recovery, Tulsa, OK, Apr. 22-25, 1990.

Kalpakci, B., T.G. Arf, D.M. Grist, S.B. Hyde, O. Vikane, and S. Espedal: "A Preliminary Evaluation of an LTPF Process for STATFIORD Field, Norway," paper presented at the 7th European IOR Symposium, Moscow, Russia, Oct. 27-29, 1993.

Kim, H.S.: "Simulation Study of Gel Conformance Treatments," Ph.D. dissertation, U. of Texas, Austin (May 1995).

Kocberber, S. and R.E. Collins: "Impact of Reservoir Heterogeneity on Initial Distributions of Hydrocarbons," paper SPE 20547 presented at the 65th Annual Technical Conference and Exhibition of the SPE, New Orleans, LA, Sep. 23-26, 1990.

Lake, L.W.: *Enhanced Oil Recovery*, Prentice Hall, Englewood Cliffs, NJ (1989).

Liang, Z., M.A. Miller, and K. Sepehrnoori: "Implementation of a Dual Porosity Model in UTCHEM," Category A Research, 12th Annual Report, Enhanced Oil and Gas Recovery Research Program, Center for Petroleum and Geosystems Engineering, The University of Texas, Austin (March 1995).

Maerker, J.M. and W.W. Gale: "Surfactant Flood Process Design for Loudon," *SPE Reser. Eng.* (Feb. 1992) 36-44.

Maroongroge, V.: "Modeling and Application of Tracers for Reservoir Characterization," Ph.D. dissertation, U. of Texas, Austin (Dec. 1994).

National Bureau of Standards, U.S. Department of Commerce, Washington D.C. (1974).

Parker, J.C., R.J. Lenhard, and T. Kuppusamy: "A Parametric Model for Constitutive Properties Governing Multiphase Flow in Porous Media," *Water Resour. Res.* (1987) **23** (4) 618.

Pope, G.A. and R.C. Nelson: "A Chemical Flooding Compositional Simulator," *SPEJ* (Oct. 1978) **18**, 339-354.

Pope, G.A. and M. Bavière: "Reduction of Capillary forces by Surfactant," *Basic Concepts in Enhanced Oil Recovery Processes*, M. Bavière (ed.), Elsevier Science Publishing Loudon, 1991.

Reppert, T.R., J.R. Bragg, J.R. Wilkinson, T.M. Snow, N.K. Maer Jr., and W.W. Gale: "Second Ripley Surfactant Flood Pilot Test," paper SPE 20219 presented at the 7th SPE/DOE Enhanced Oil Recovery Symposium, Tulsa, OK, Apr. 22-25, 1990.

Shupe, R.D.: "Process for Secondary Oil Recovery Utilizing Propoxylated Ethoxylated Surfactants in Seawater," U.S. Patent No. 4,886,120 (Dec. 1989).

van Genuchten, M.T.: "A Closed-Form Equation for Predicting the Hydraulic Conductivity of Unsaturated Soils," *Soil Sci. Soc. Am. J.*, (1980) **44**, 892.

Vaskas, A.J.: "Optimization of Surfactant Flooding: An Economic Approach," M.S. thesis, U. of Texas, Austin (May 1996).

Wellington, S.L. and E.A. Richardson: "Low Surfactant Concentration Enhanced Waterflooding," paper SPE 30748 presented at the 70th Annual Technical Conference and Exhibition of the SPE, Dallas, TX, Oct. 22-25, 1995.

Wu, W.: "Optimization of Field-Scale Chemical Floodings Using Numerical Modeling," PhD dissertation, U. of Texas, Austin (May, 1996).

Wu, W., A. Vaskas, M. Delshad, G.A. Pope, and K. Sepehrnoori: "Design and Optimization of Low-Cost Chemical Flooding," paper SPE 35355 presented at the 10th SPE/DOE Symposium on Improved Oil Recovery, Tulsa, OK, Apr. 21-24, 1996.

Yang, A.-P.: "Stochastic Heterogeneity and Dispersion," Ph.D. dissertation, U. of Texas, Austin (Dec. 1990).

Zemel, B.: *Tracers in the Oil Field*, Developments in Petroleum Science 43, Elsevier Science (1995).

Table 3.1: Results of water analysis of makeup water and formation water

	Formation water (KFW)		Makeup water (KRW)	
Name of Ions	meq/ml	mg/l	meq/ml	mg/l
Na^+	0.1043	2398.90	0.0023	52.9
Mg^{2+}	0.003	36.46	0.00095	11.54
Ca^{2+}	0.00271	54.1	0.00336	67.13
Cl^-	0.05892	2041.73	0.00109	39.00
HCO_3^-	0.04301	2623.36	0.0025	152.55
CO_3^{2-}	0.008	240.00	0.002	6.00
SO_4^{2-}	-------	-------	0.0028	134.56

Table 3.2: List of elements and reactive species for ASP simulations

Elements or pseudo-element:	Hydrogen (reactive), Sodium, Calcium, Magnesium, Carbonate, A (from acid HA), Chlorine,
Independent aqueous or oleic species:	H^+, Na^+,Ca^{2+}, Mg^{2+},CO_3^{2-}, HA_o, H_2O
Dependent aqueous or oleic species:	$Ca(OH)^+$, $Mg(OH)^+$, $Ca(HCO_3)^+$, HA_w, $Mg(HCO_3)^+$, OH^-, HCO_3^-, A^-, H_2CO_3, $CaCO_3^o$, $MgCO_3^o$
Solid species:	$CaCO_3$ (Calcite), $Ca(OH)_2$ (Calcium hydroxide), $MgCO_3$ (Magnesite), $Mg(OH)_2$ (Magnesium hydroxide)
Adsorbed cations:	$\overline{H}^+$, $\overline{Na}^+$, $\overline{Ca}^{2+}$, $\overline{Mg}^{2+}$
Adsorbed cations on micelles:	$\overline{\overline{Na}}^+$, $\overline{\overline{Ca}}^{2+}$, $\overline{\overline{Mg}}^{2+}$

Table 3.3: List of reactions for ASP simulations

Aqueous reactions	Equilibrium constant
$H_2O \overset{K_1^{eq}}{\rightleftarrows} H^+ + OH^-$	$K_1^{eq} = [H^+]\,[OH^-]$
$HA_w + OH^- \overset{K_2^{eq}}{\rightleftarrows} A^- + H_2O$	$K_2^{eq} = \dfrac{[A^-]\,[H^+]}{[HA_w]}$
$H^+ + CO_3^{2-} \overset{K_3^{eq}}{\rightleftarrows} HCO_3^-$	$K_3^{eq} = \dfrac{[HCO_3^-]}{[H^+]\,[CO_3^{2-}]}$
$Ca^{2+} + H_2O \overset{K_4^{eq}}{\rightleftarrows} Ca(OH)^+ + H^+$	$K_4^{eq} = \dfrac{[Ca(OH)^+]\,[H^+]}{[Ca^{2+}]}$
$Mg^{2+} + H_2O \overset{K_5^{eq}}{\rightleftarrows} Mg(OH)^+ + H^+$	$K_5^{eq} = \dfrac{[Mg(OH)^+]\,[H^+]}{[Mg^{2+}]}$
$Ca^{2+} + H^+ + CO_3^{2-} \overset{K_6^{eq}}{\rightleftarrows} Ca(HCO_3)^+$	$K_6^{eq} = \dfrac{[Ca(HCO_3)^+]}{[Ca^{2+}]\,[CO_3^{2-}][H^+]}$
$Mg^{2+} + H^+ + CO_3^{2-} \overset{K_7^{eq}}{\rightleftarrows} Mg(HCO_3)^+$	$K_7^{eq} = \dfrac{[Mg(HCO_3)^+]}{[Mg^{2+}]\,[CO_3^{2-}][H^+]}$
$2H^+ + CO_3^{2-} \overset{K_8^{eq}}{\rightleftarrows} H_2CO_3$	$K_8^{eq} = \dfrac{[H_2CO_3]}{[CO_3^{2-}][H^+]^2}$
$Ca^{2+} + CO_3^{2-} \overset{K_9^{eq}}{\rightleftarrows} CaCO_3^o$	$K_9^{eq} = \dfrac{[CaCO_3^o]}{[Ca^{2+}]\,[CO_3^{2-}]}$
$Mg^{2+} + CO_3^{2-} \overset{K_{10}^{eq}}{\rightleftarrows} MgCO_3^o$	$K_{10}^{eq} = \dfrac{[MgCO_3^o]}{[Mg^{2+}]\,[CO_3^{2-}]}$
Partitioning of HA	**Partition coefficient**
$HA_o \overset{K_D}{\rightleftarrows} HA_w$	$K_D = \dfrac{[HA_w]_{water}}{[HA_o]_{oil}}$

Table 3.3: List of reactions for ASP simulations (cont'd.)

Dissolution reactions	Solubility product
$CaCO_3 \overset{K_1^{sp}}{\rightleftarrows} Ca^{2+} + CO_3^{2-}$	$K_1^{sp} = [Ca^{2+}]\,[CO_3^{2-}]$
$MgCO_3 \overset{K_2^{sp}}{\rightleftarrows} Mg^{2+} + CO_3^{2-}$	$K_2^{sp} = [Mg^{2+}]\,[CO_3^{2-}]$
$Ca(OH)_2 \overset{K_3^{sp}}{\rightleftarrows} Ca^{2+} + 2OH^-$	$K_3^{sp} = [Ca^{2+}][H^+]^{-2}$
$Mg(OH)_2 \overset{K_4^{sp}}{\rightleftarrows} Mg^{2+} + 2OH^-$	$K_4^{sp} = [Mg^{2+}][H^+]^{-2}$
Exchange reactions (on matrix)	**Exchange equilibrium constant**
$2\overline{Na}^+ + Ca^{2+} \overset{K_1^{ex}}{\rightleftarrows} 2Na^+ + \overline{Ca}^{2+}$	$K_1^{ex} = \dfrac{[\overline{Ca}^{2+}]\,[Na^+]^2}{[Ca^{2+}]\,[\overline{Na}^+]^2}$
$2\overline{Na}^+ + Mg^{2+} \overset{K_2^{ex}}{\rightleftarrows} 2Na^+ + \overline{Mg}^{2+}$	$K_2^{ex} = \dfrac{[\overline{Mg}^{2+}]\,[Na^+]^2}{[Mg^{2+}]\,[\overline{Na}^+]^2}$
$\overline{H}^+ + Na^+ + OH^- \overset{K_3^{ex}}{\rightleftarrows} \overline{Na}^+ + H_2O$	$K_3^{ex} = \dfrac{[Na^+]\,[\overline{H}^+]}{[\overline{Na}^+]\,[H^+]}$
Exchange reactions (on micelle)	**Exchange equilibrium constant**
$2\overline{\overline{Na}}^+ + Ca^{2+} \overset{K^{exm}}{\rightleftarrows}{}^{1} 2Na^+ + \overline{\overline{Ca}}^{2+}$	$K_1^{exm} = \dfrac{[\overline{\overline{Ca}}^{2+}]\,[Na^+]^2}{[\overline{\overline{Na}}^+]^2\,[Ca^{2+}]}$
	where $K_1^{exm} = \beta_1^{exm}\{[A^-] + [S^-]\}$
$2\overline{\overline{Na}}^+ + Mg^{2+} \overset{K^{exm}}{\rightleftarrows}{}^{2} 2Na^+ + \overline{\overline{Mg}}^{2+}$	$K_2^{exm} = \dfrac{[\overline{\overline{Mg}}^{2+}]\,[Na^+]^2}{[\overline{\overline{Na}}^+]^2\,[Mg^{2+}]}$
	where $K_2^{exm} = \beta_2^{exm}\{[A^-] + [S^-]\}$

Table 3.4: Properties measured during coreflood experiments

Porosity
Permeability
Initial water saturation
Relative permeability (Low capillary number)
Water viscosity
Oil viscosity
Polymer viscosity
Surfactant retention
Polymer retention

Table 3.5: Summary of Berea coreflood experiments

1. Summary of KMAY7 coreflood data

Core length, cm	26.75
Core diameter, cm	3.8
Pore volume, cc	60.28 (0.00212 ft^3)
Temperature	Ambient
Permeability, md	206.6
Oil perm. at residual water, md	236
Water perm. at residual oil, md	6.5
Porosity, fraction	0.1988
Oil viscosity, cp	24.3
Oil density, g/cc	0.84
Waterflooding:	
Formation water (KFW), PV	0.4786
Residual water saturation	0.3829
Residual oil saturation to water	0.3807
Injection rate, cc/min	0.5 (0.02543 ft^3/day)
ASP flooding:	
1.5 % NaCl in KRW, PV	0.2
2% surfactant, 1500 ppm polymer, 1.6% Na_2CO_3 in KRW, PV	0.31
1500 ppm polymer, 0.5% NaCl in KRW, PV	1.05
KFW postflush, PV	1.7
Injection rate, cc/min	0.05
Residual oil saturation (S_{orc})	0.1090
Surfactant retention, mg/g rock	0.3
Polymer retention, mg/g rock	0.06

Table 3.5: Summary of Berea coreflood experiments (cont'd.)

2. Summary of KMAY5 coreflood data

Core length, cm	27.95
Core diameter, cm	3.81
Pore volume, cc	59.68
Temperature	Ambient
Permeability, md	188.2
Oil perm. at residual water, md	248
Water perm. at residual oil, md	---
Porosity, fraction	0.1873
Oil viscosity, cp	24.3
Oil density, g/cc	0.84
Waterflooding:	
Formation water (KFW), PV	0.4786
Residual water saturation	0.3258
Residual oil saturation to water	0.371
Injection rate, cc/min	---
ASP flooding:	
1.5 % NaCl in KRW, PV	0.2
2% surfactant, 1500 ppm polymer, 1.6% Na_2CO_3 in KRW, PV	0.31
1500 ppm polymer KRW, PV	1.05
KFW postflush, PV	1.7
Injection rate, cc/min	0.05
Residual oil saturation (S_{orc})	0.0243

Table 3.6: Comparison of simulated and measured retention data

Case Name	Retained surfactant (mg/g rock)	Retained polymer (mg/g rock)
KMAY7 coreflood	0.3	0.065
Model Type II (-)	0.3	0.057
Model Type III	0.08	0.063
Model Salinity Gradient	0.07	0.054

Table 3.7a: Summary of reservoir coreflood results

Initial oil saturation ,%	57.38
Residual oil saturation (after water flood)	0.3402
Slug A (Preflush)	1.0% KCl for 0.5 pv
Slug B (ASP Slug)	ASP fluid for 0.5 pv
Slug C (Polymer drive)	0.15% Polymer 0.7% NaCl for 0.3 pv
Water flooding oil recovery, % (OOIP)	40.71
Chemical flooding oil recovery, % (OOIP)	23.93
Total oil recovery, % (OOIP)	64.64
Remaining oil in place (after water flooding), %	40.36

Table 3.7b: Retention data for reservoir core

Surfactant retention, mg/g rock	0.12
Polymer retention, mg/g rock	0.15
Alkaline (Na_2CO_3) loss, mg/g rock	0.28

Table 3.7c: Reservoir coreflood data used for history matching

PV injected	Ave. PV injected	Oil rec	Oil cut	Pressure drop, psi
0.13	0.065	0.2321	1	20.58
0.54	0.335	0.3393	0.15	7.35
0.95	0.745	0.3786	0.06	5.88
1.36	1.155	0.3929	0.02	5.88
1.77	1.565	0.4071	0.02	4.41
2.29	2.03	0.425	0.02	4.41
2.8	2.545	0.5393	0.129	44.1
3.1	2.95	0.6107	0.1351	44.1
4.12	3.61	0.6464	0.02	4.851
5.15	4.635	0.6464	0	3.675
6.17	5.66	0.6464	0	3.234
7.2	6.685	0.6464	0	2.94

Table 3.8: Summary of reservoir coreflood data

Core length, cm	6.25
Core diameter, cm	3.8
Pore volume, cc	22.29 (0.0007871 ft^3)
Temperature	Ambient
Permeability, md	95
Porosity, fraction	0.3144
Oil viscosity, cp	17.2
Oil density, g/cc	0.84
Waterflooding:	
Formation water (KFW), PV	1.77
Residual water saturation	0.4262
Residual oil saturation to water	0.3402
Injection rate, cc/min	0.5 (0.02543 ft^3/day)
ASP flooding:	
1.0 % KCl in KRW, PV	0.5
0.3% surfactant, 1800 ppm polymer, 1.4% Na_2CO_3 in KRW, PV	0.5
1500 ppm polymer, 0.7% NaCl in KRW, PV	0.3
KFW postflush, PV	4.1
Injection rate, cc/min	0.05
Surfactant retention, mg/g rock	0.12
Polymer retention, mg/g rock	0.15

Table 3.9: UTCHEM parameters used in history match of KMAY7 coreflood

Parameters	
Phase behavior:	
HBNC70	0.026
HBNC71	0.025
HBNC72	0.12
CSEL7	0.33
CSEU7	0.53
Capillary-desaturation curve:	
T11	1865
T22	8000
T33	364.2
Relative permeability at low capillary number:	
P1RW	0.028
P2RW	1.0
P3RW	0.028
E1W	1.12
E2W	1.3
E3W	1.12
Relative permeability at high capillary number:	
P1RC	0.5
P2RC	1.0
P3RC	1.0
E13C	1.1
E23C	1.1
E31C	0.35
IFT using Huh's model:	
CHUH	0.35
Microemulsion viscosity:	
ALPHA1	2.5
ALPHA2	2.5
ALPHA3	60.
ALPHA4	1.
ALPHA5	1.7

Table 3.10: Key input data used in history match of reservoir coreflood

Phase behavior:	
Type II(-)	
HBNC70	0.06
HBNC71	0.025
HBNC72	0.12
Lower salinity (CSEL7) , meq/ml	0.33
Upper salinity (CSEU7), meq/ml	0.53
Oil desaturation curve parameter:	
T22	59074
Microemulsion phase viscosity:	
ALPHA1	0.5
ALPHA2	0.5
ALPHA3	0.0
ALPHA4	1.0
ALPHA5	1.7
Adsorption model parameters:	
Surfactant	
AD31	12.0
AD32	10.0
B3D	1000.0
Polymer	
AD41	14.0
AD42	6.0
B4D	100.0
Relative permeability (low capillary number):	
P1RW	0.205
P2RW	1.0
E1w	1.87
E2w	1.7

Table 3.11: Statistical data for permeability field for each case

Case Number	Layers	Mean (md)	V_{DP}	Seed number	λ_x^* (ft)
1	1	164.3	0.39	87654	184.8
	2	133.8	0.37		
	3	150.3	0.35		
	4	74.07	0.29		
	5	53.92	0.27		
2	1	176.7	0.40	12345	184.8
	2	132.5	0.37		
	3	155.4	0.35		
	4	78.70	0.29		
	5	52.22	0.31		
3	1	168.9	0.39	98765	184.8
	2	132.1	0.37		
	3	151.3	0.36		
	4	77.46	0.30		
	5	52.87	0.30		
4	1	169.0	0.39	772891	184.8
	2	133.2	0.37		
	3	150.1	0.34		
	4	74.22	0.29		
	5	53.63	0.28		
5	1	164.7	0.38	87654	369.6
	2	130.8	0.36		
	3	148.3	0.35		
	4	73.34	0.29		
	5	51.20	0.26		
6	1	121.9	0.43	87654	92.40
	2	136.0	0.38		
	3	162.7	0.35		
	4	79.59	0.31		
	5	66.12	0.32		

Ratio of correlation lengths.: $\lambda_x / \lambda_y = 1$; $\lambda_x / \lambda_z = 92.4$

*λ_x : Correlation length in x direction

Table. 3.12: Optimum Bottomhole pressure for each producer

Well No.	Bottom hole pressure (kPa)
1	4500
2	5300
3	4850
6	4700
7	4500
8	4700
11	4750
12	4750
13	4750

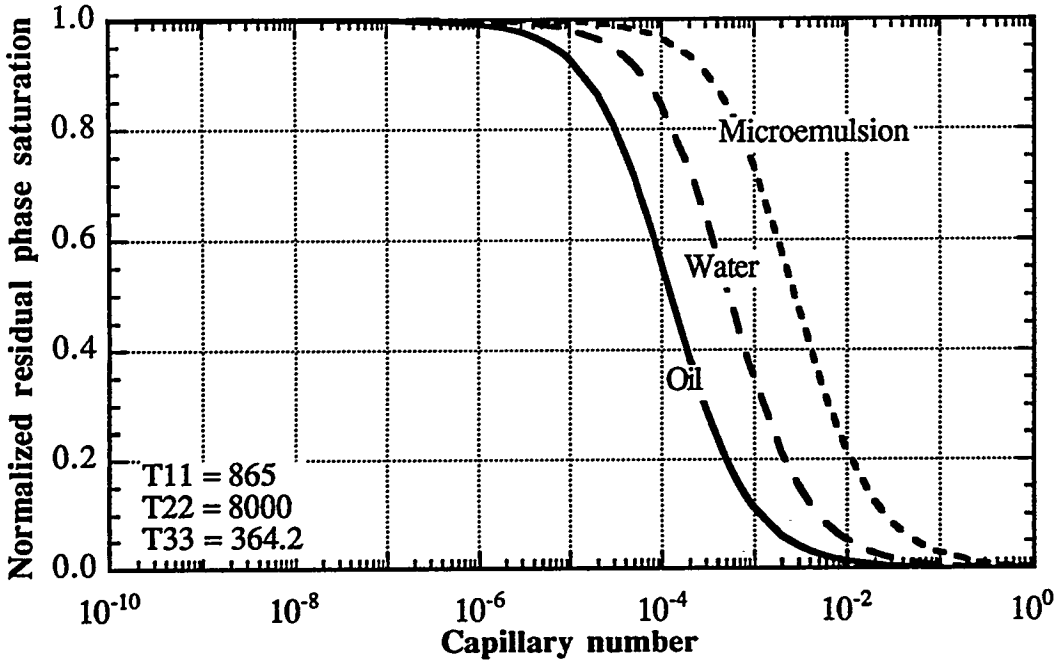


Figure 3.1 Capillary desaturation curve used for coreflood history match

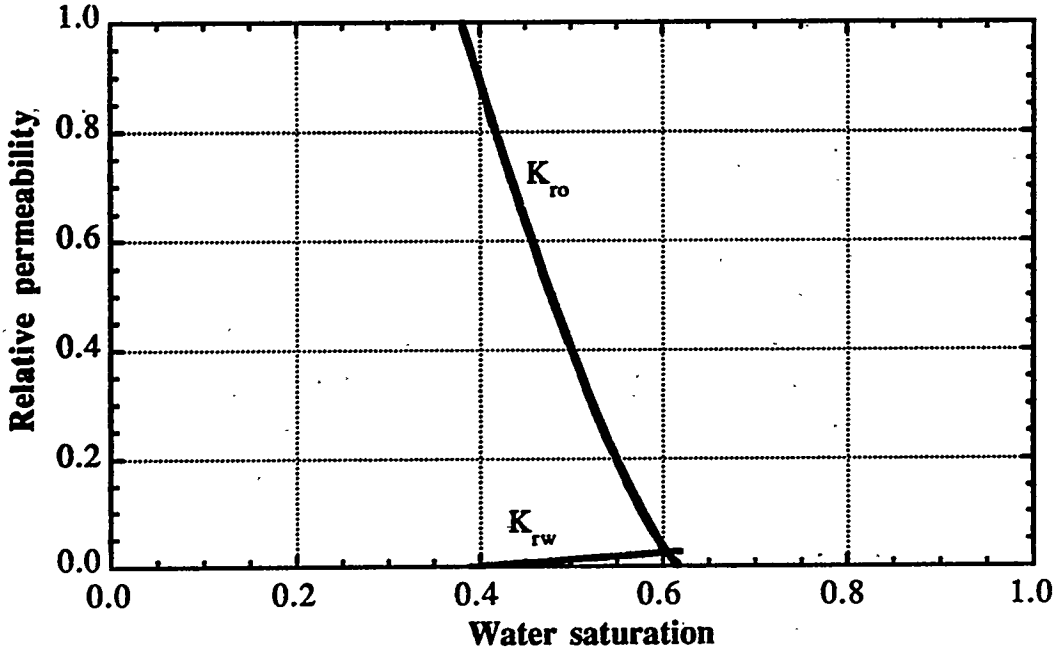


Figure 3.2 Low capillary number relative permeability curves used for coreflood history match

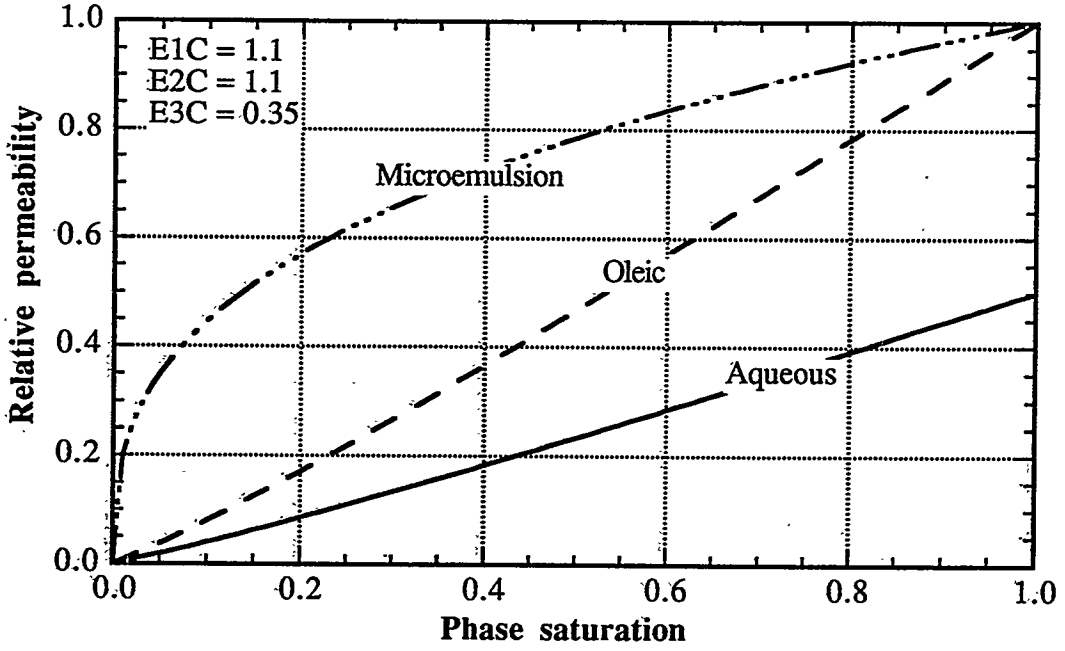


Figure 3.3 High capillary number (>10^{-2}) relative permeability curves used for coreflood history match

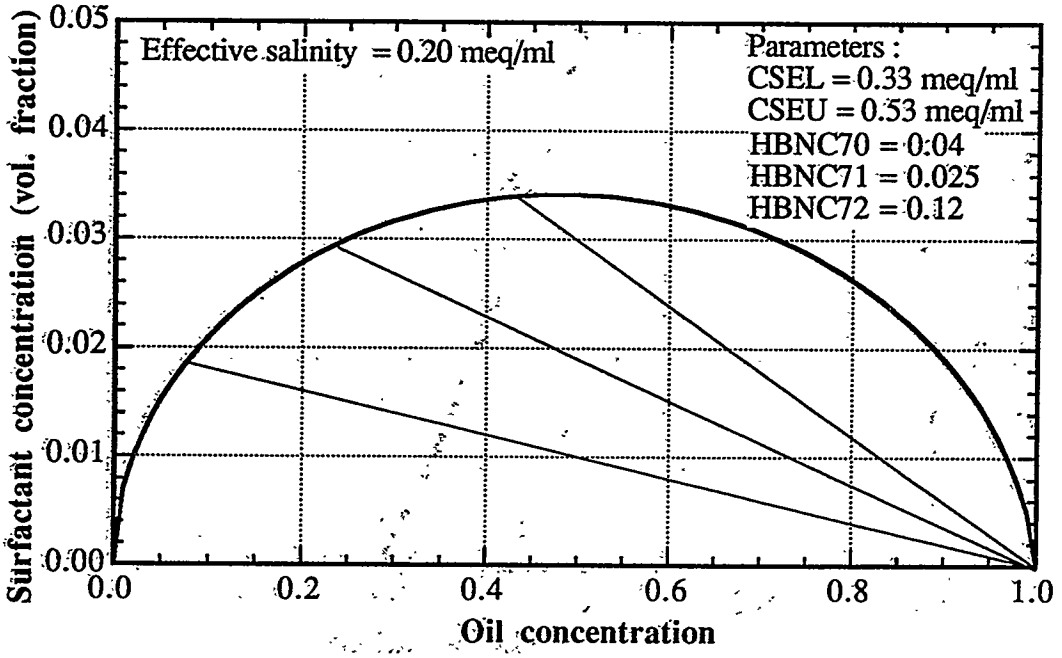


Figure 3.4 Type II(-) phase behavior used for KMAY7 coreflood history match

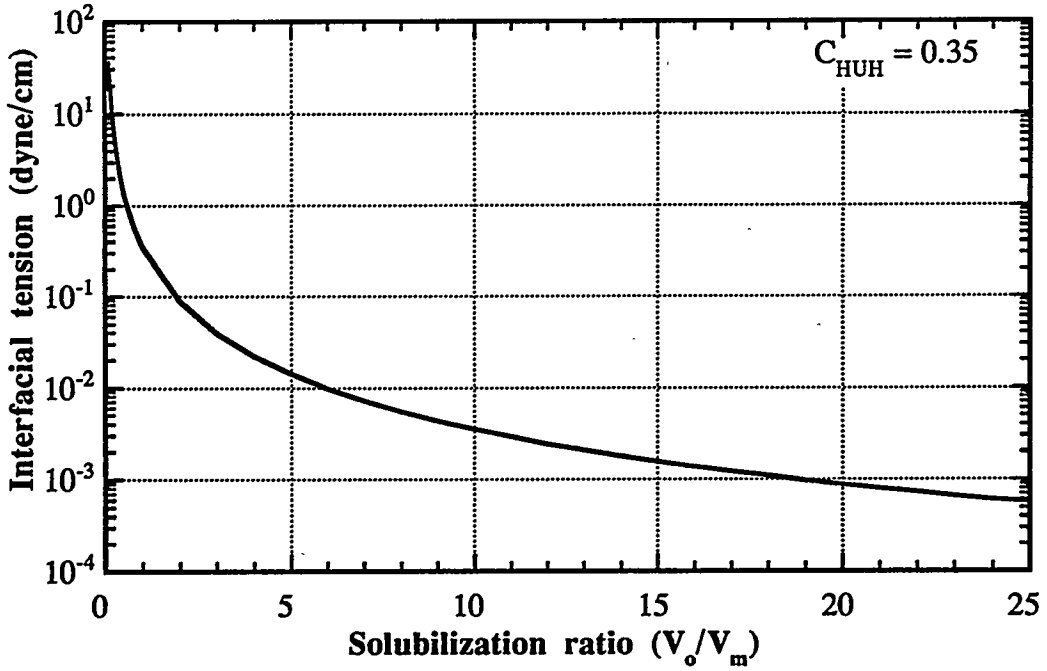


Figure 3.5 Interfacial tension for oil/microemulsion used for coreflood history match

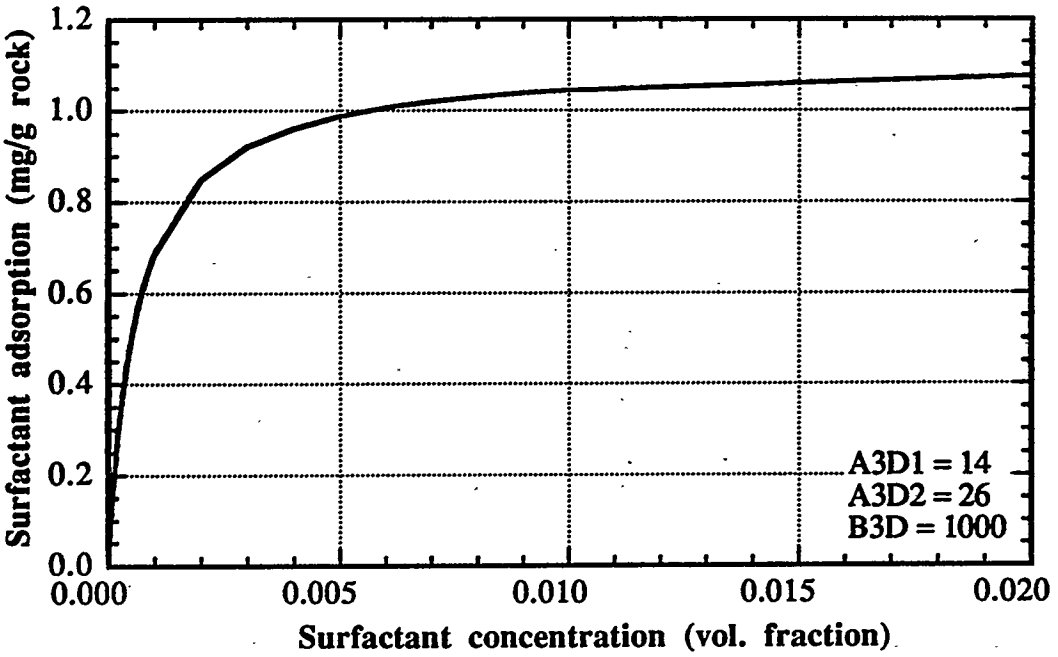


Figure 3.6 Surfactant adsorption isotherm used in KMAY7 history match

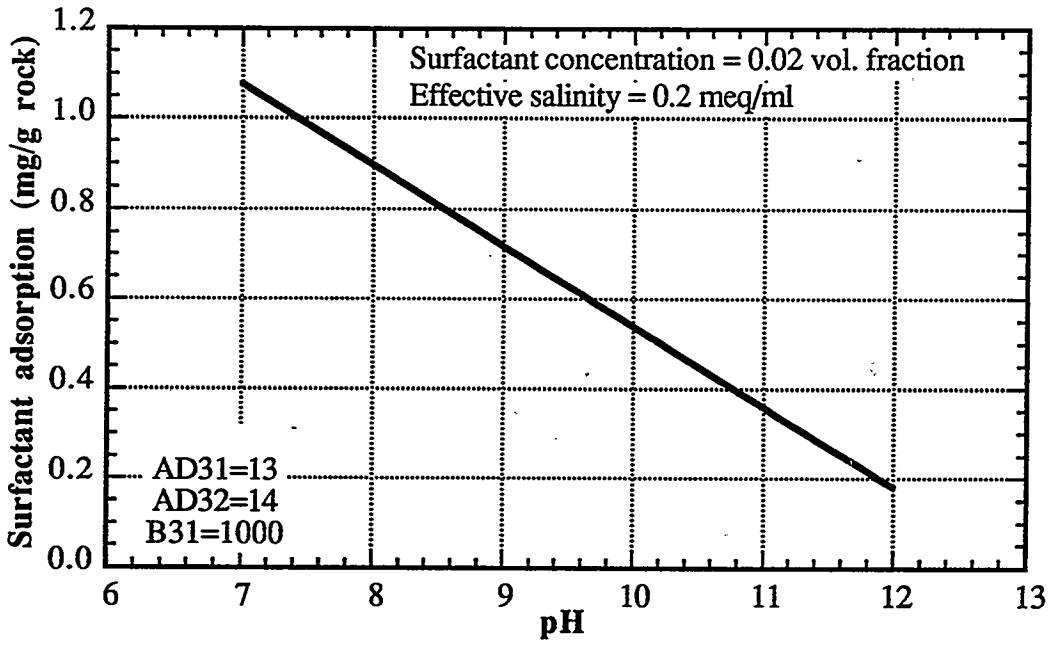


Figure 3.7 Surfactant adsorption as a function of pH used for KMAY7 history match

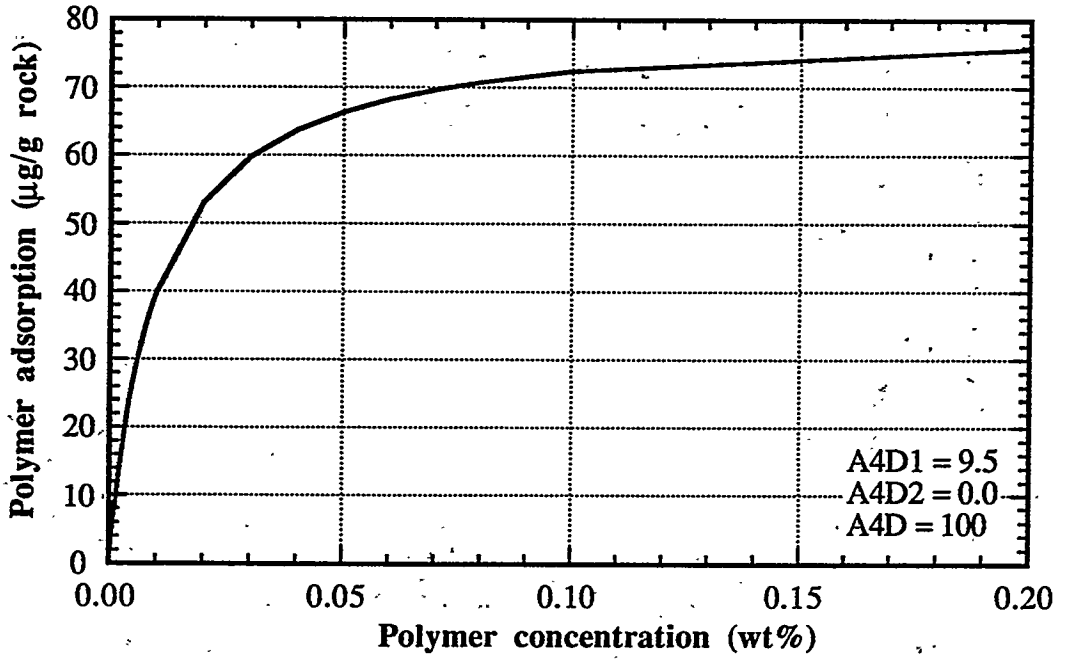


Figure 3.8 Polymer adsorption isotherm used in KMAY7 history match

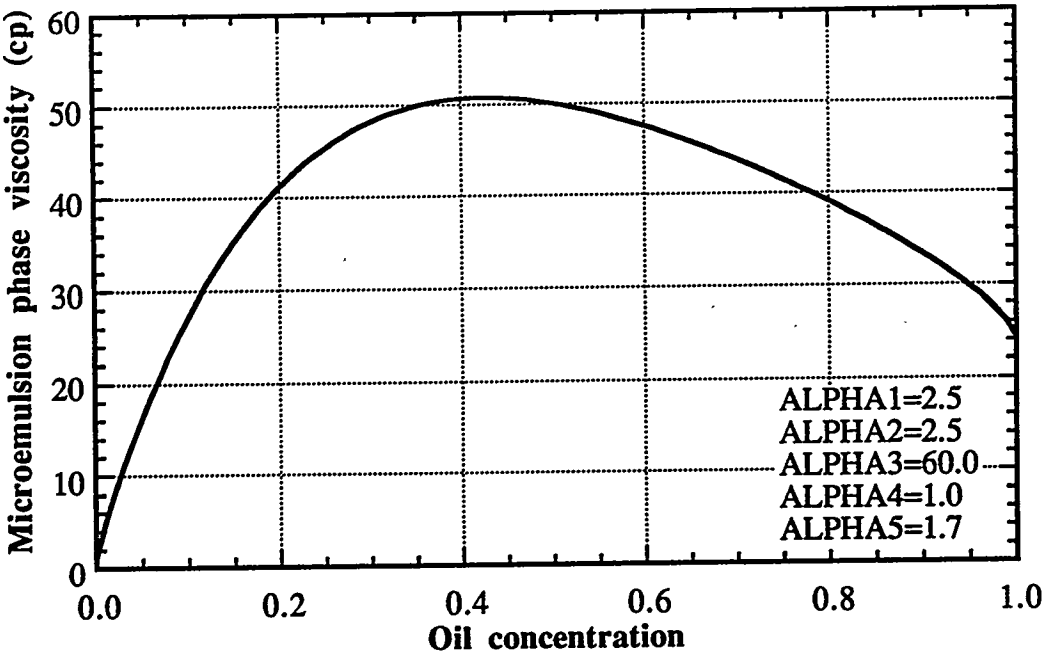


Figure 3.9 Microemulsion phase viscosity

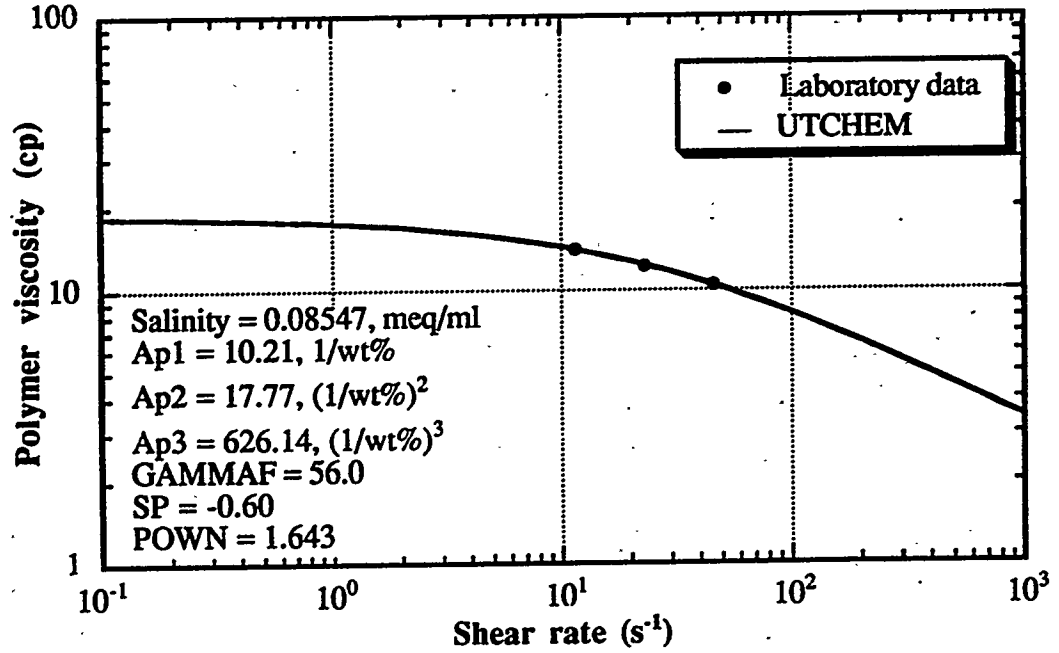


Figure 3.10 Polymer viscosity as a function of shear rate used for KMAY7 history match

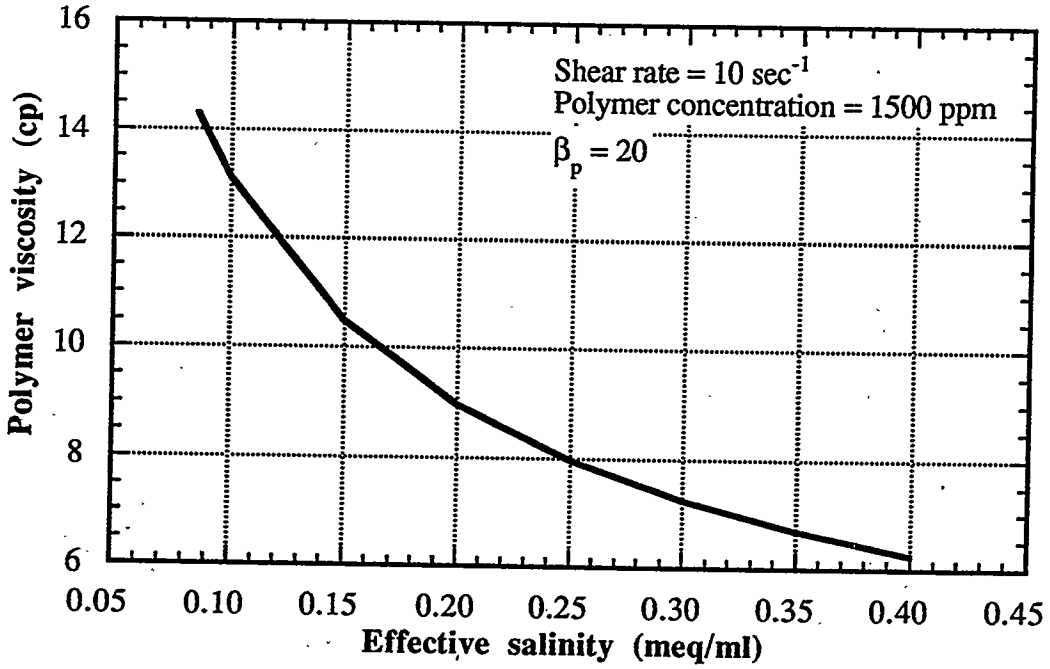


Figure 3.11 Effect of salinity on polymer viscosity

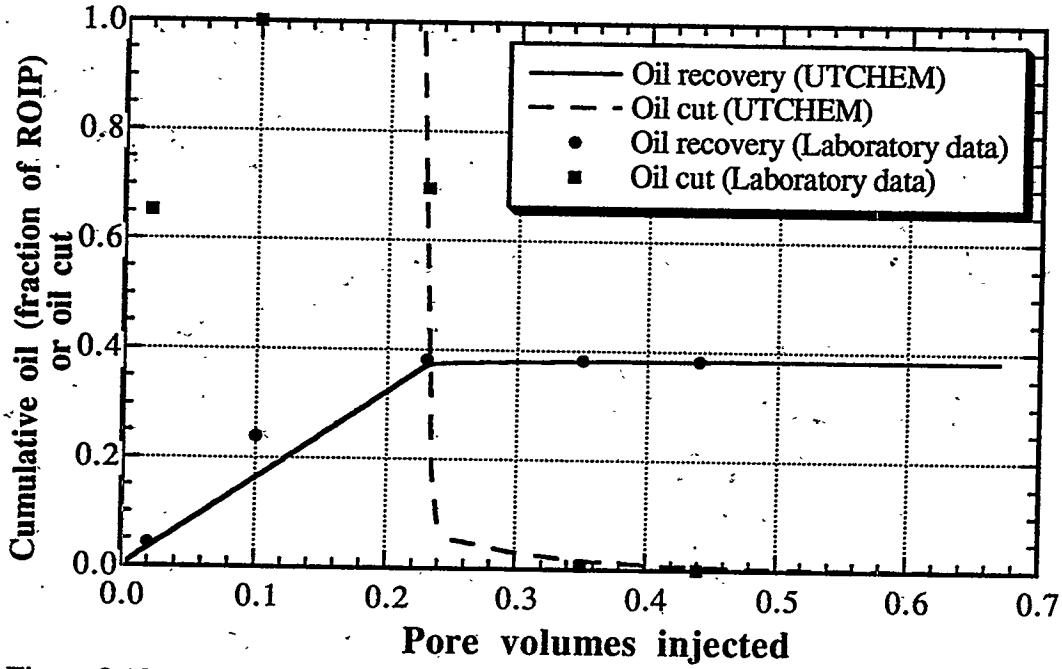


Figure 3.12 History match of cumulative oil recovery for KMAY7 Berea coreflood during waterflood

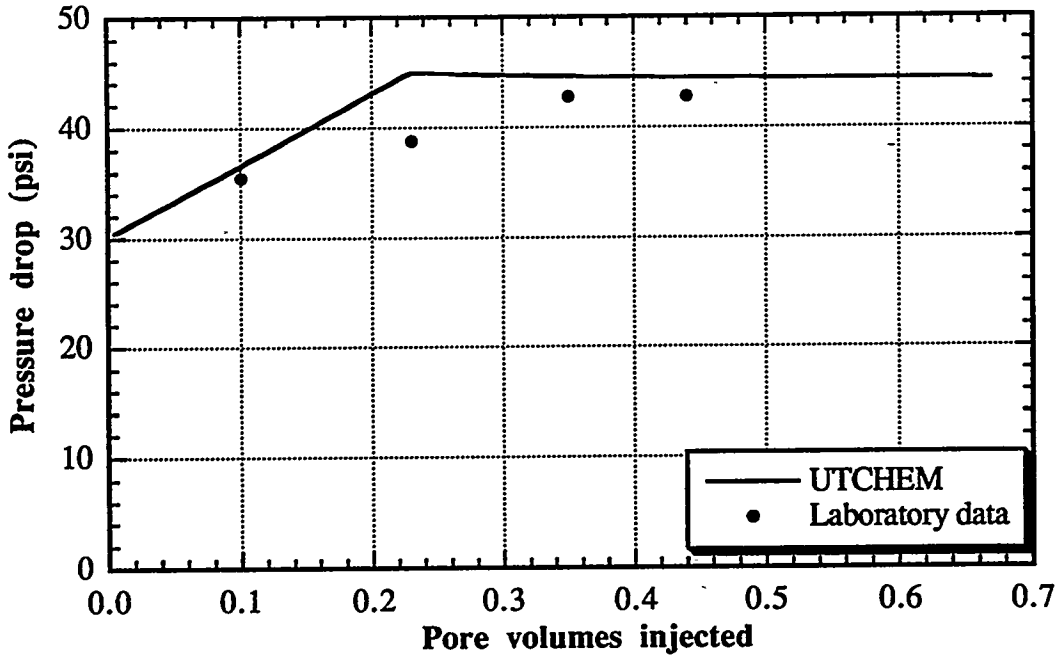


Figure 3.13 History match of pressure drop for KMAY7 Berea coreflood during waterflood

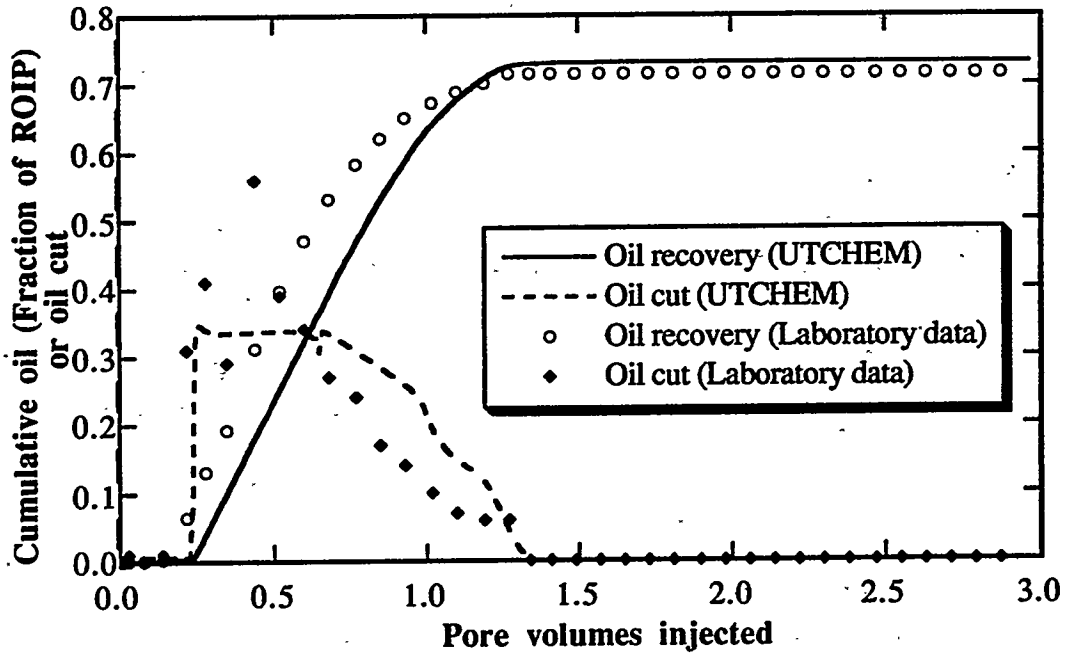


Figure 3.14 Oil recovery and oil cut as a function of pore volumes injected (Type II(-))

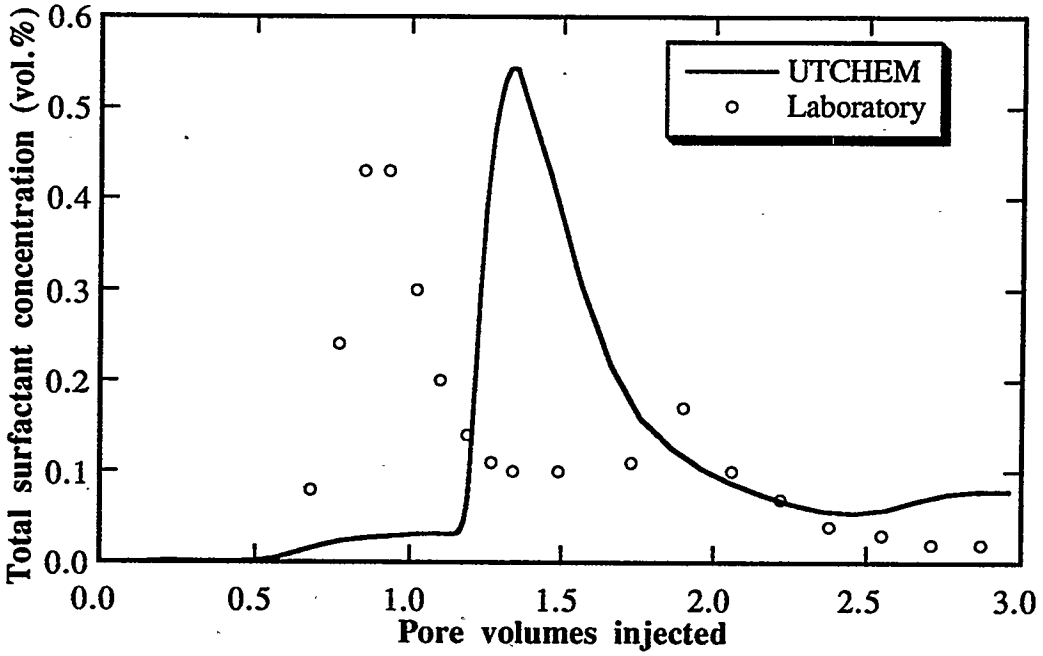


Figure 3.15 Total surfactant concentration as a function of pore volumes injected (Type II(-))

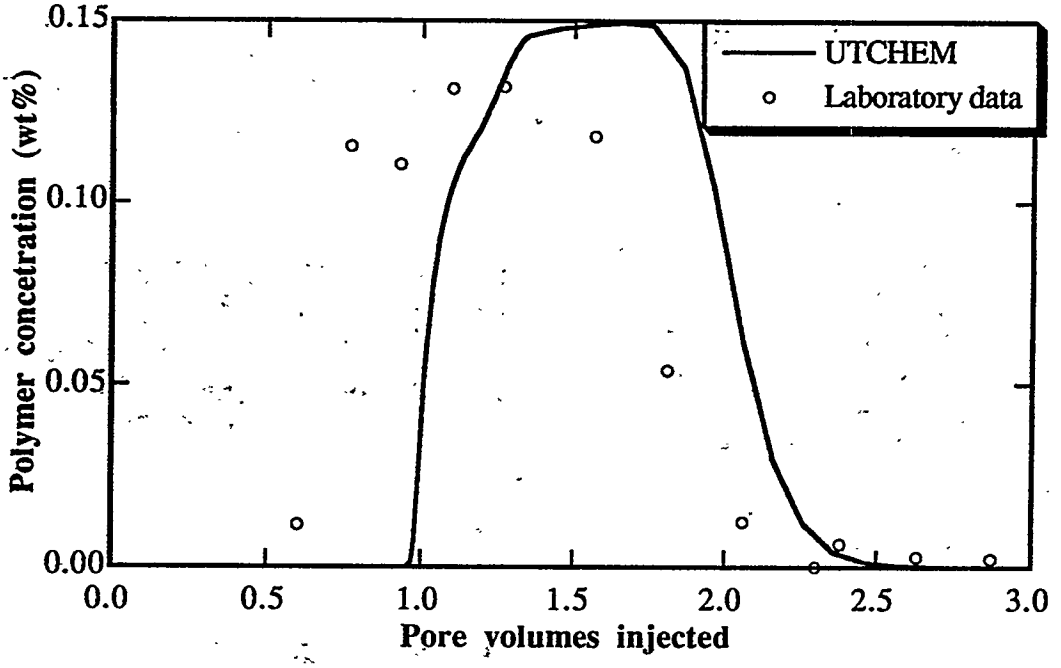


Figure 3.16 Polymer concentration as a function of pore volumes injected (Type II(-))

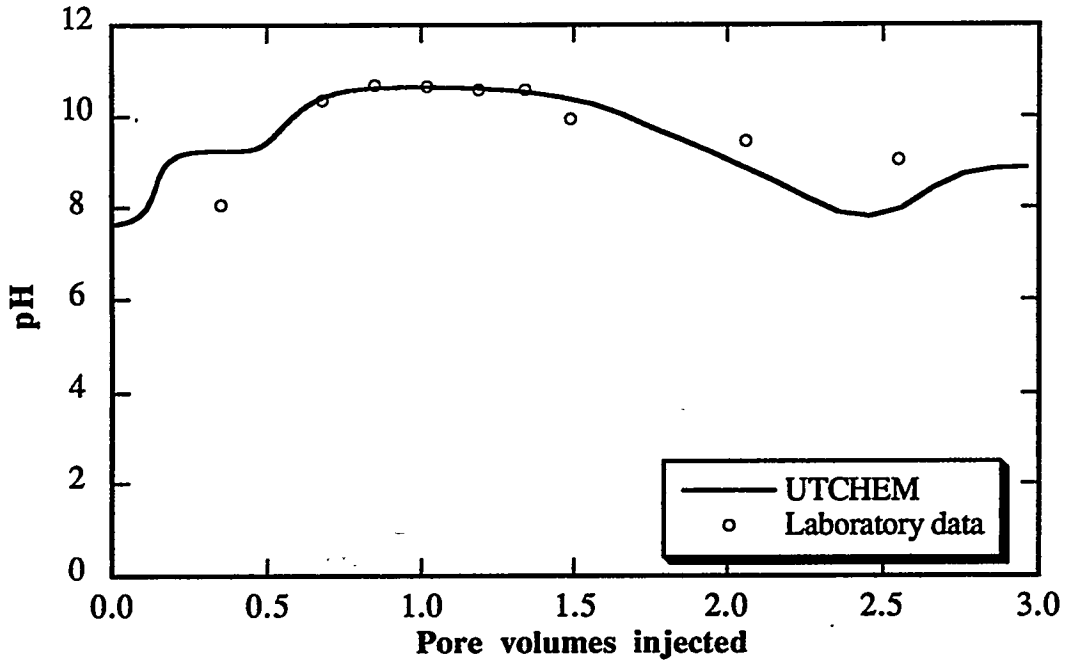


Figure 3.17 pH as a function of pore volumes injected (Type II(-))

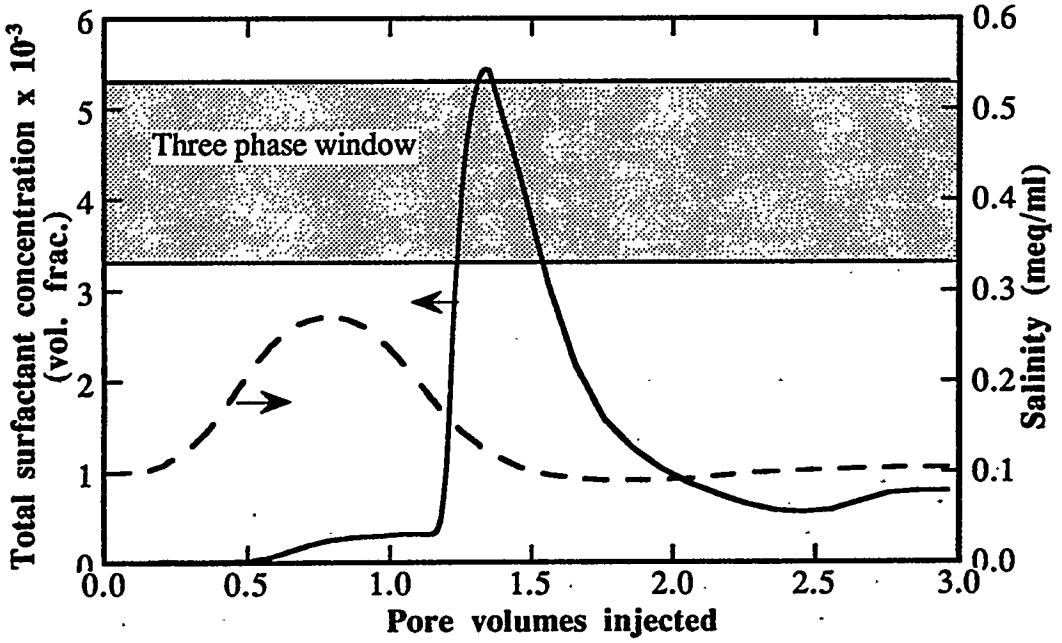


Figure 3.18 Surfactant and effective salinity as a function of pore volumes injected (Type II(-))

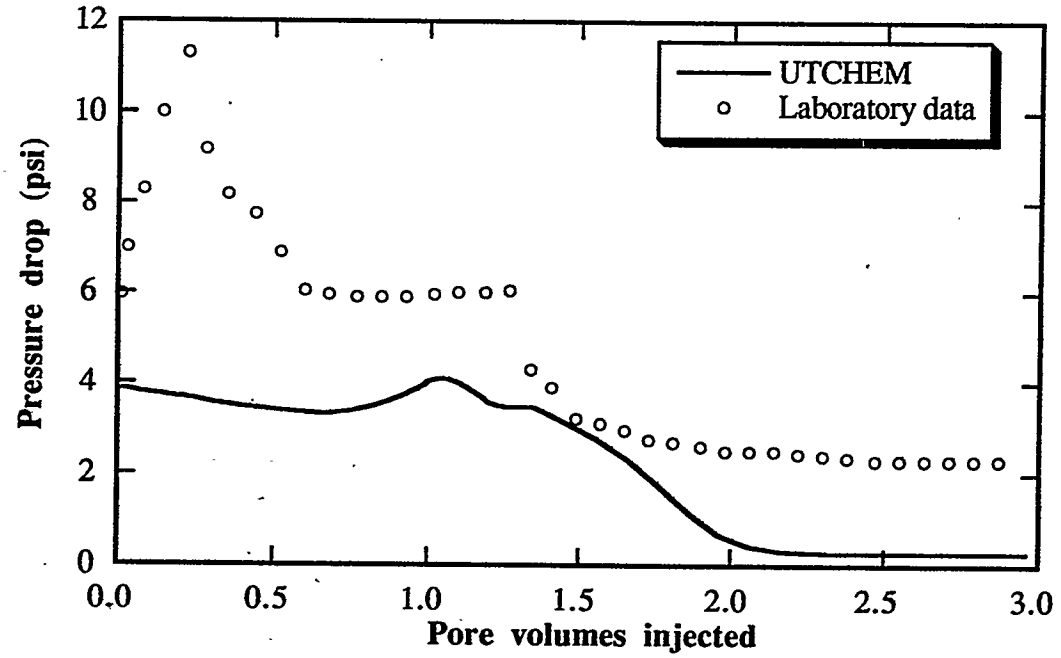


Figure 3.19 Pressure drop as a function of pore volumes injected (Type II(-))

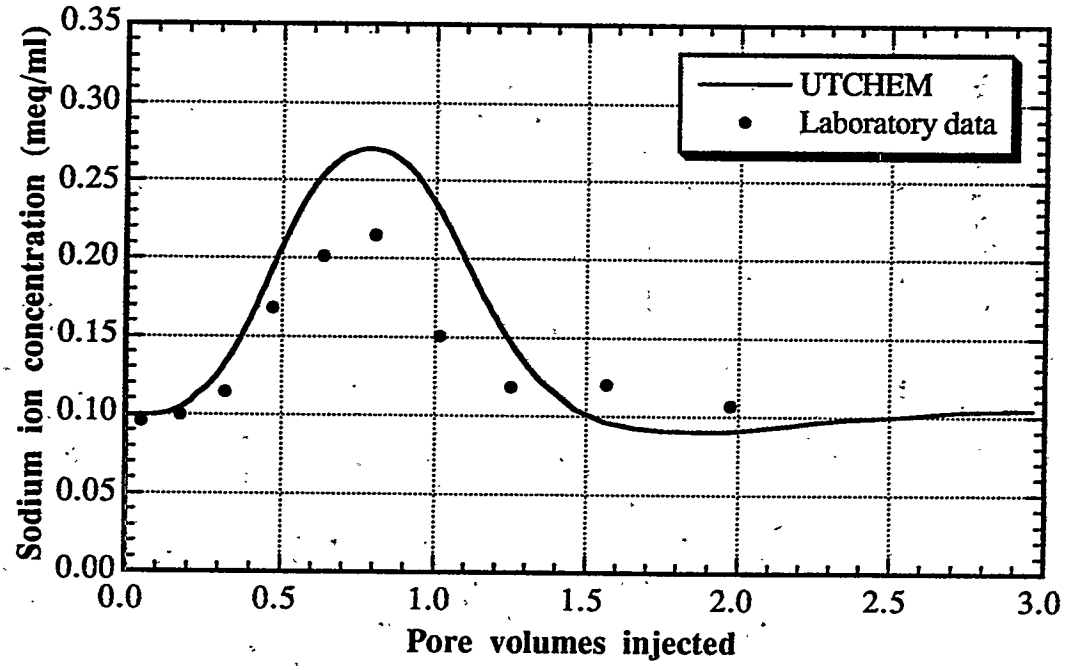


Figure 3.20 Sodium ion concentration as a function of pore volumes injected (Type II(-))

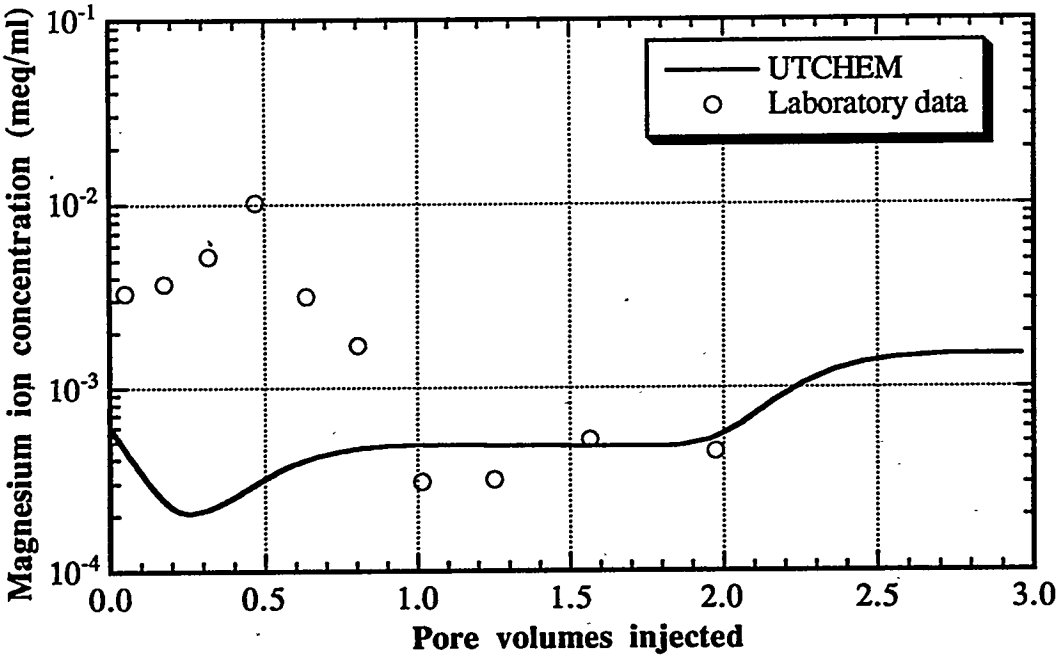


Figure 3.21 Magnesium ion concentration as a function of pore volumes injected (Type II(-))

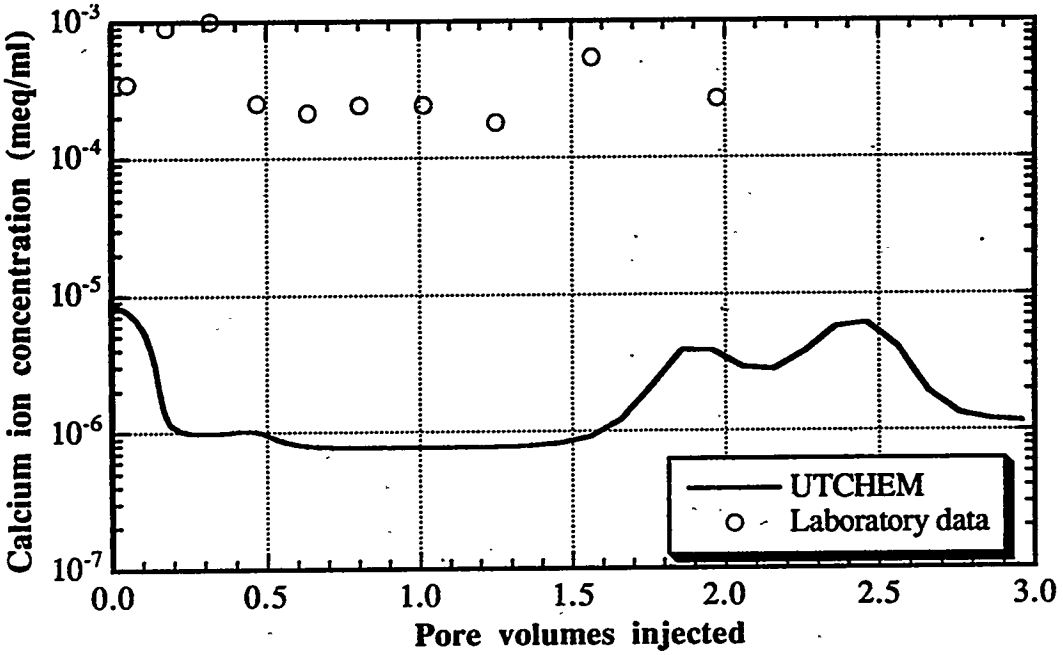


Figure 3.22 Calcium ion concentration as a function of pore volumes injected (Type II(-))

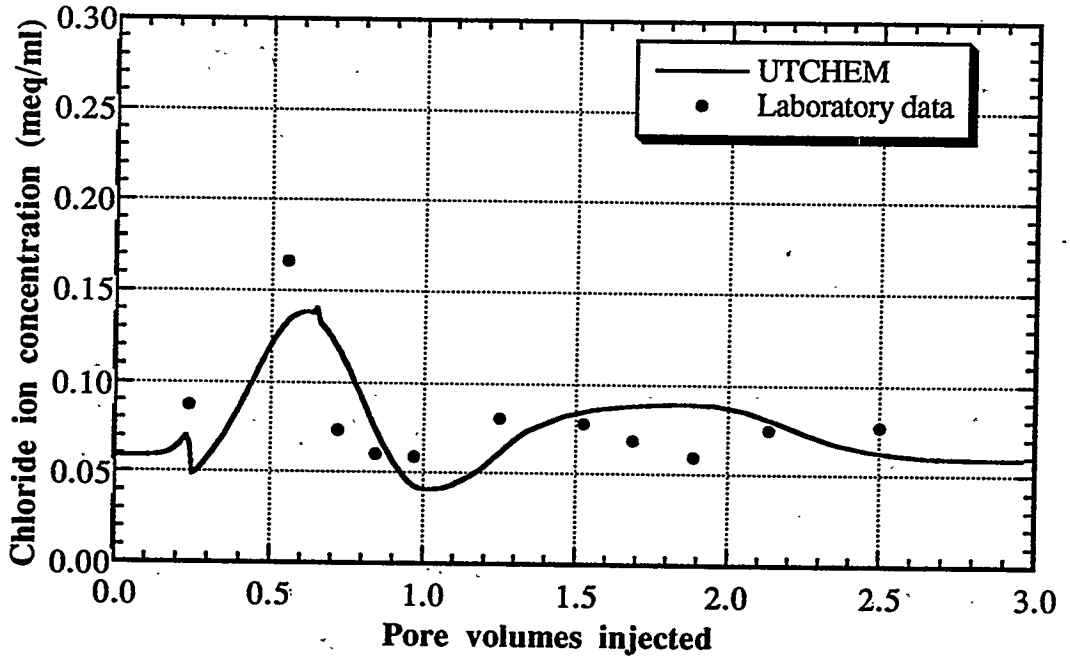


Figure 3.23 Chloride ion concentration as a function of pore volumes injected (Type II(-))

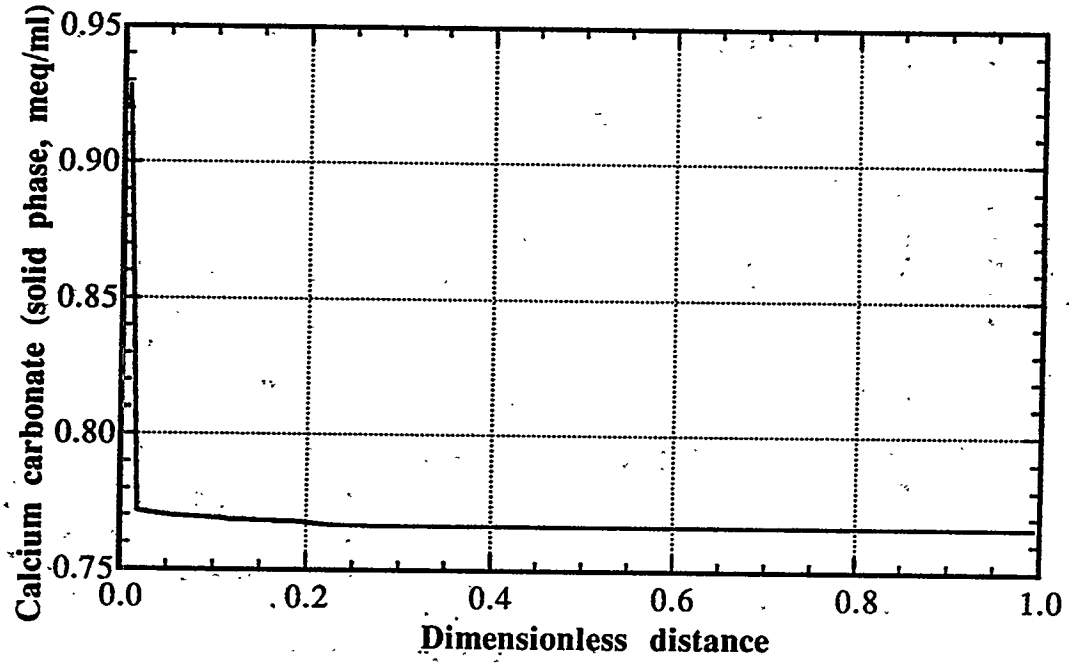


Figure 3.24 Profile of calcium carbonate at 0.31 pore volumes injected (Type II(-))

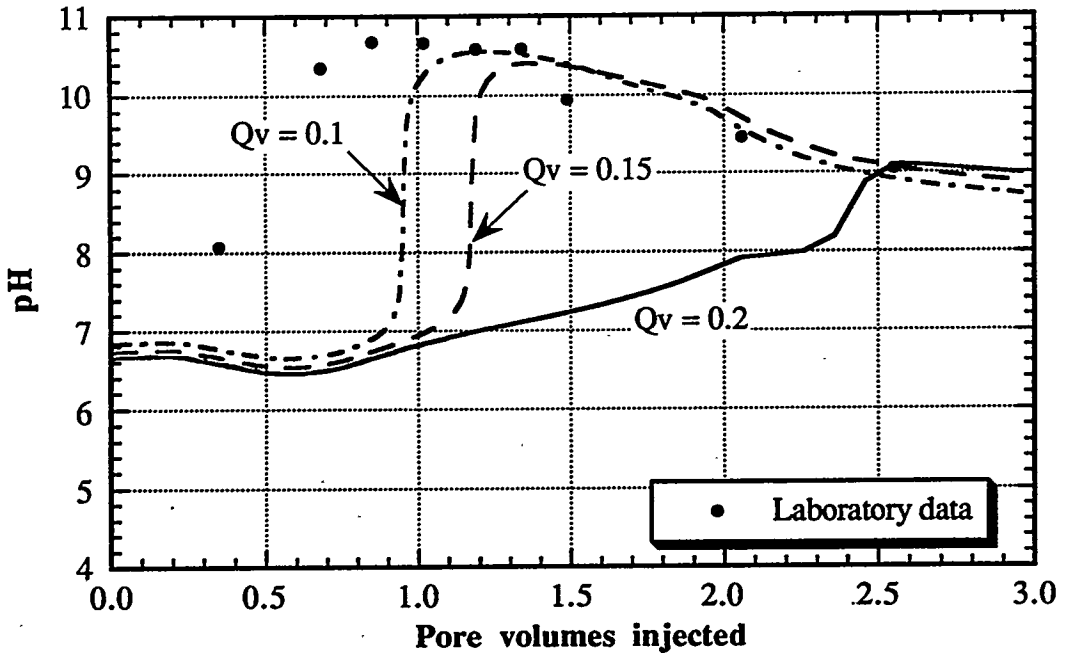


Figure 3.25 Comparison of pH for different cation exchange capacity

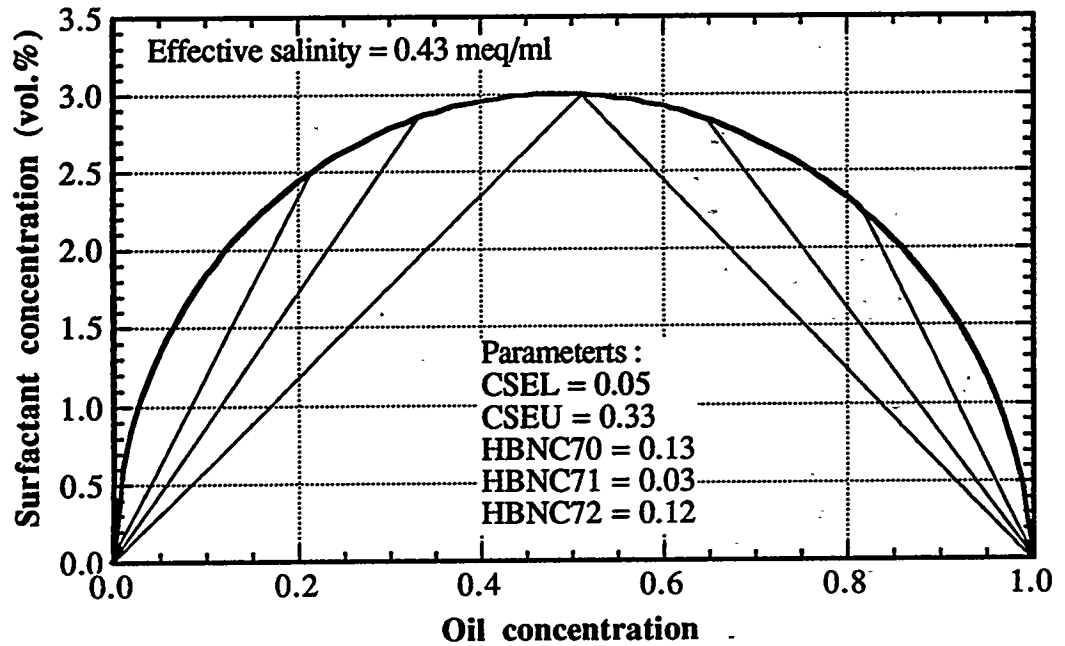


Figure 3.26 Phase behavior of surfactant for Type III

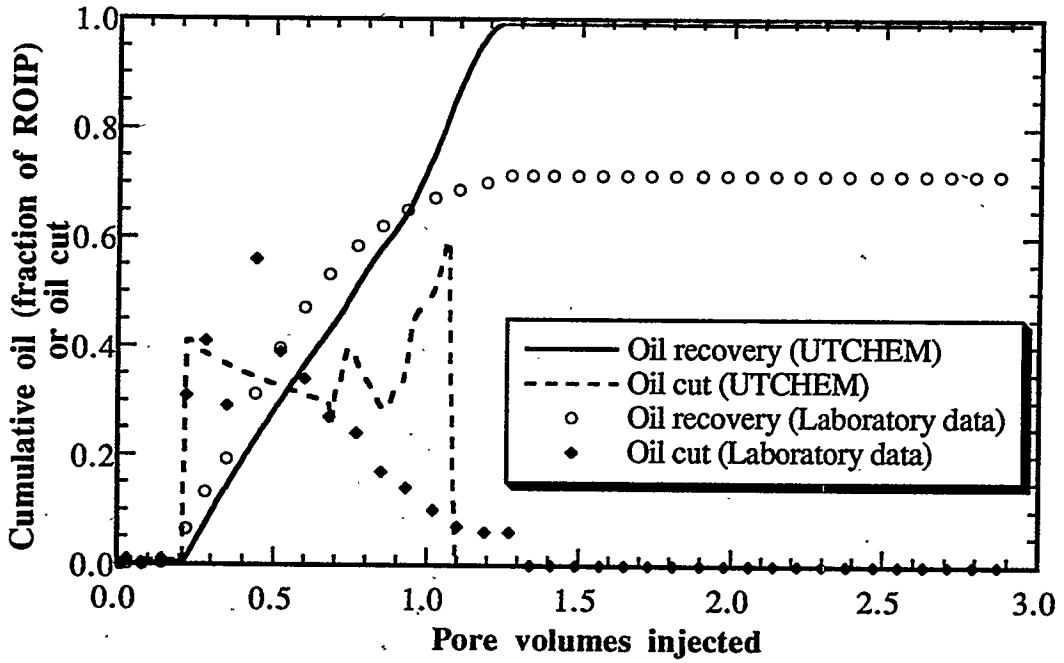


Figure 3.27 Oil recovery and oil cut as a function of pore volumes injected (Type III)

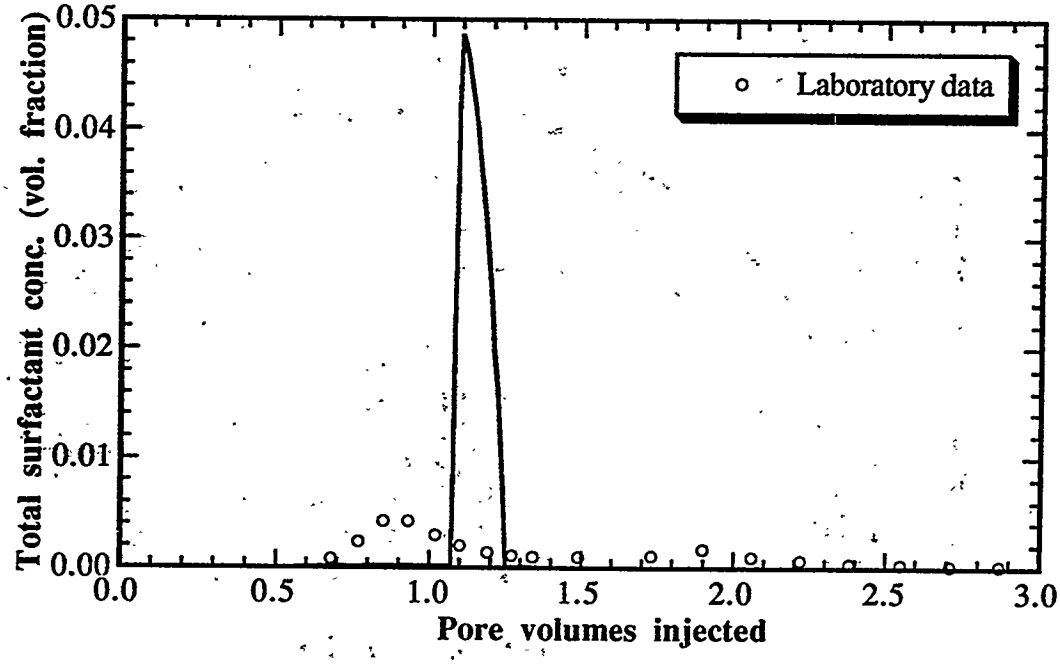


Figure 3.28 Surfactant concentration as a function of pore volumes injected (Type III)

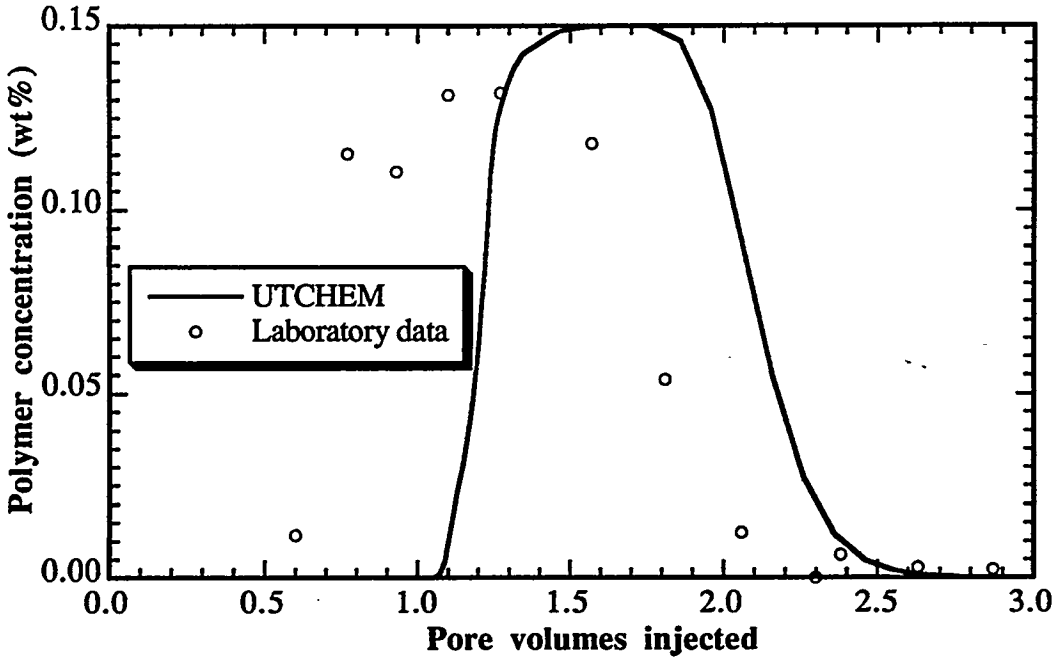


Figure 3.29 Polymer concentration as a function of pore volumes injected (Type III)

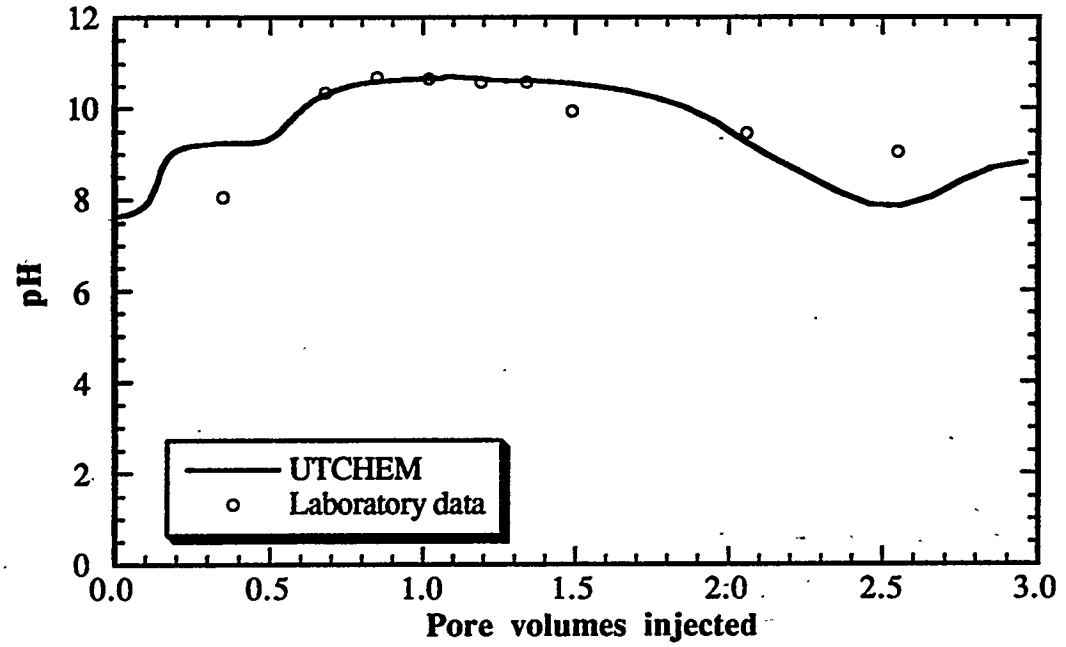


Figure 3.30 pH as a function of pore volumes injected (Type III)

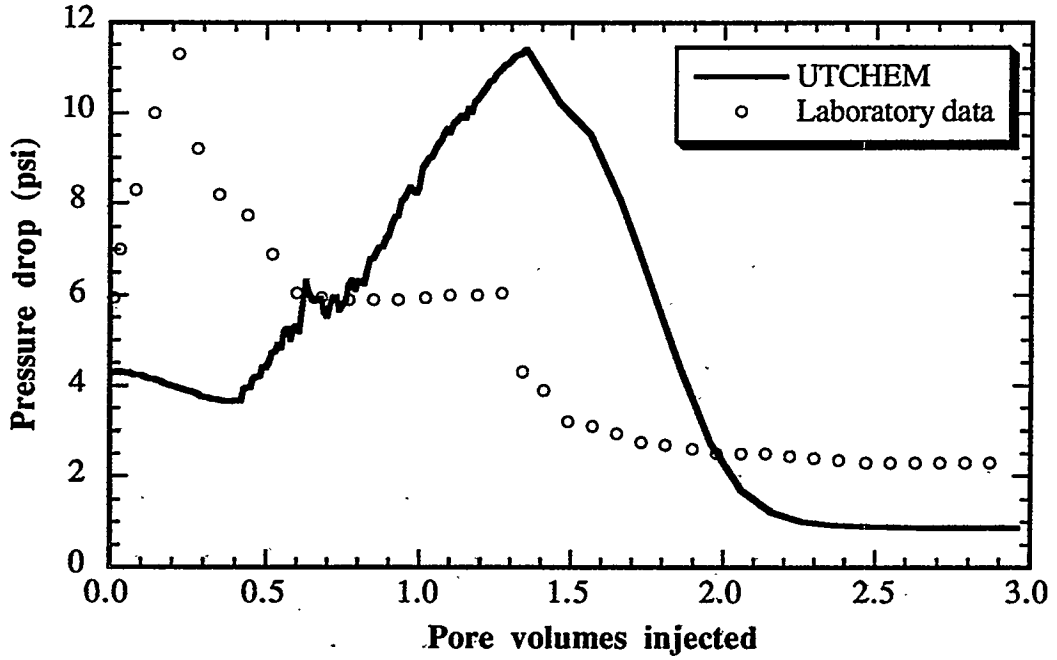


Figure 3.31 Pressure drop as a function of pore volumes injected (Type III)

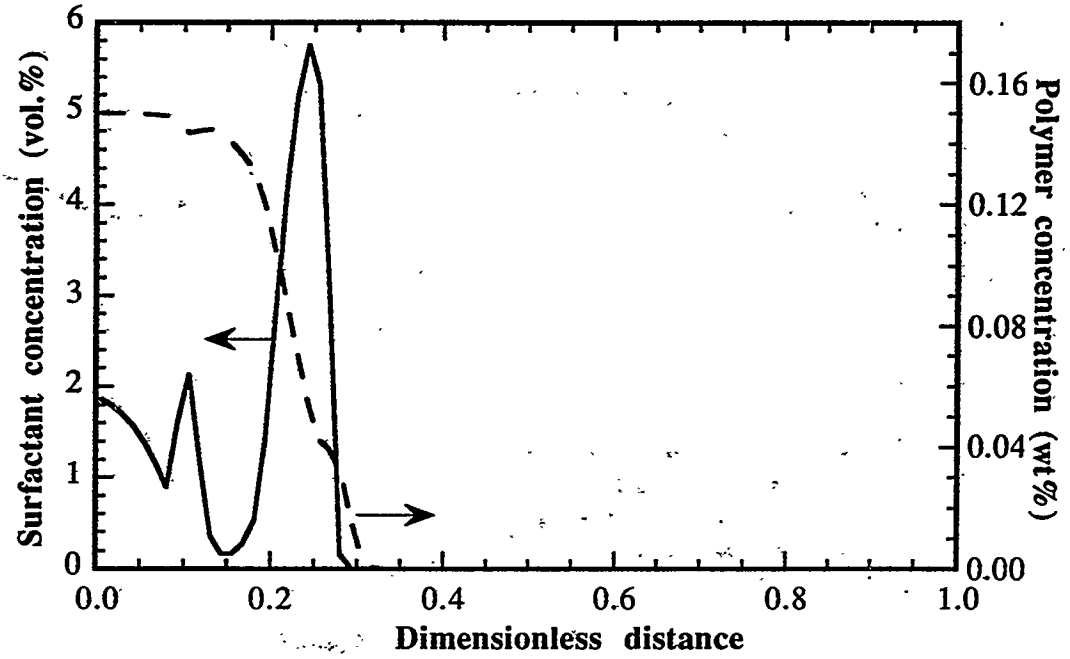


Figure 3.32 Surfactant and polymer concentration profiles at 0.3 pore volumes injected (Type III)

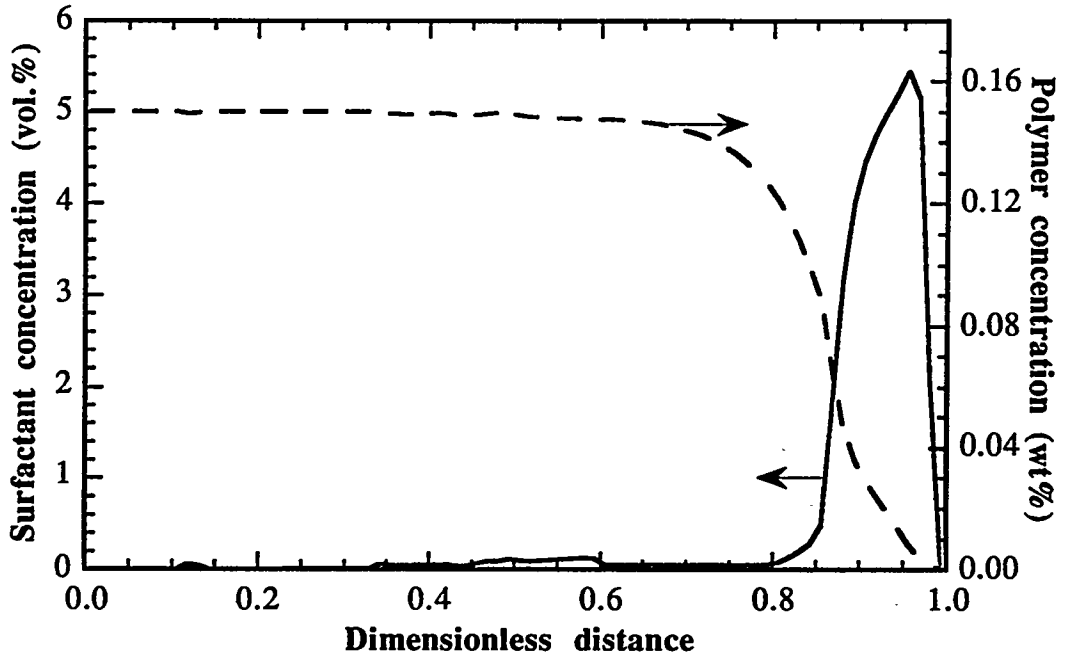


Figure 3.33 Surfactant and polymer concentration profiles at 1.05 pore volumes injected (Type III)

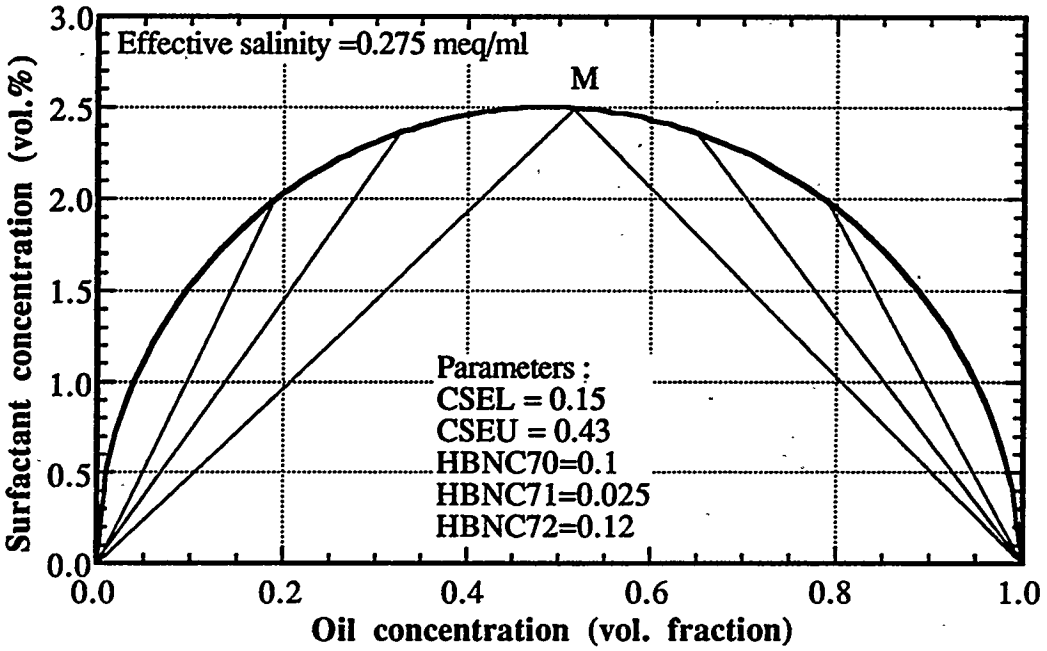


Figure 3.34 Phase behavior of surfactant used in salinity gradient design

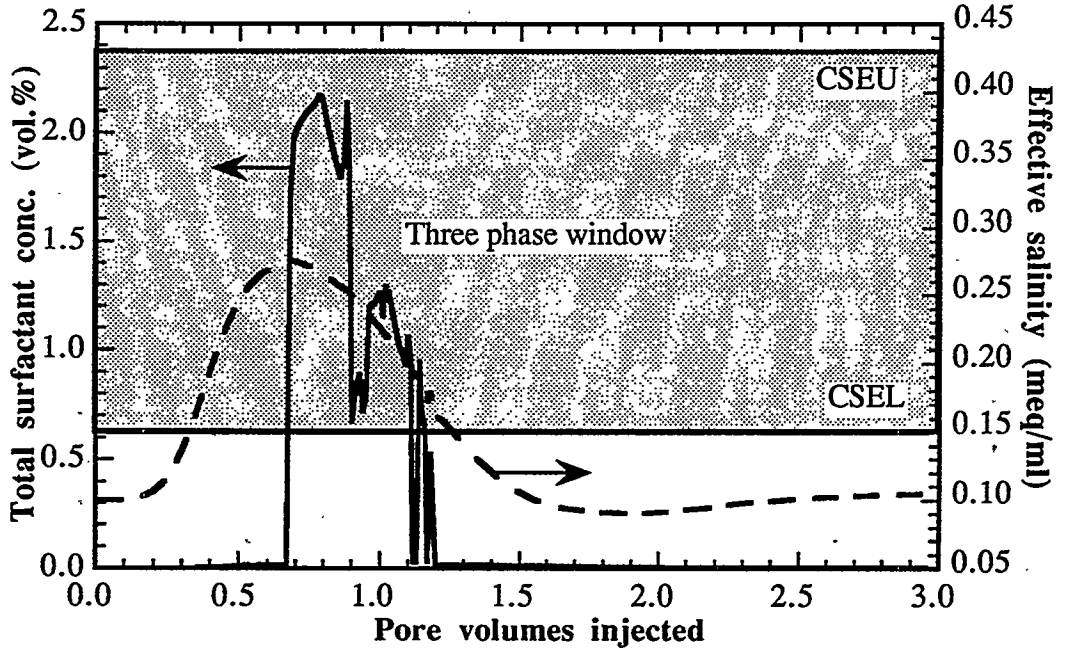


Figure 3.35 Effective salinity and surfactant concentration as a function of pore volumes injected

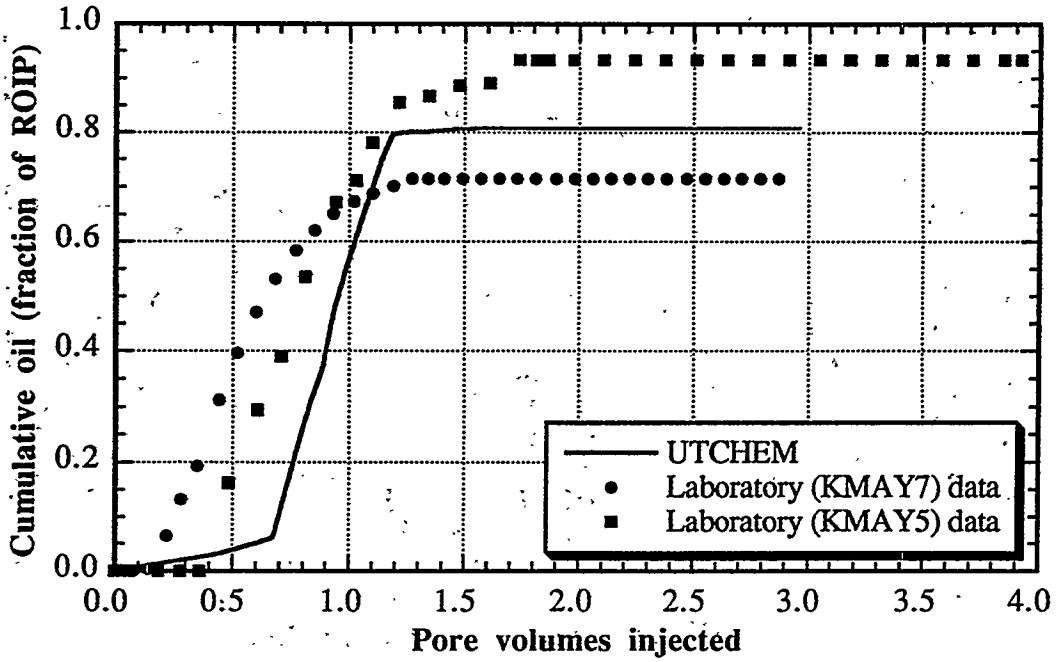


Figure 3.36 Comparison of oil recovery between the result of UTCHEM simulation and laboratory data (Salinity gradient)

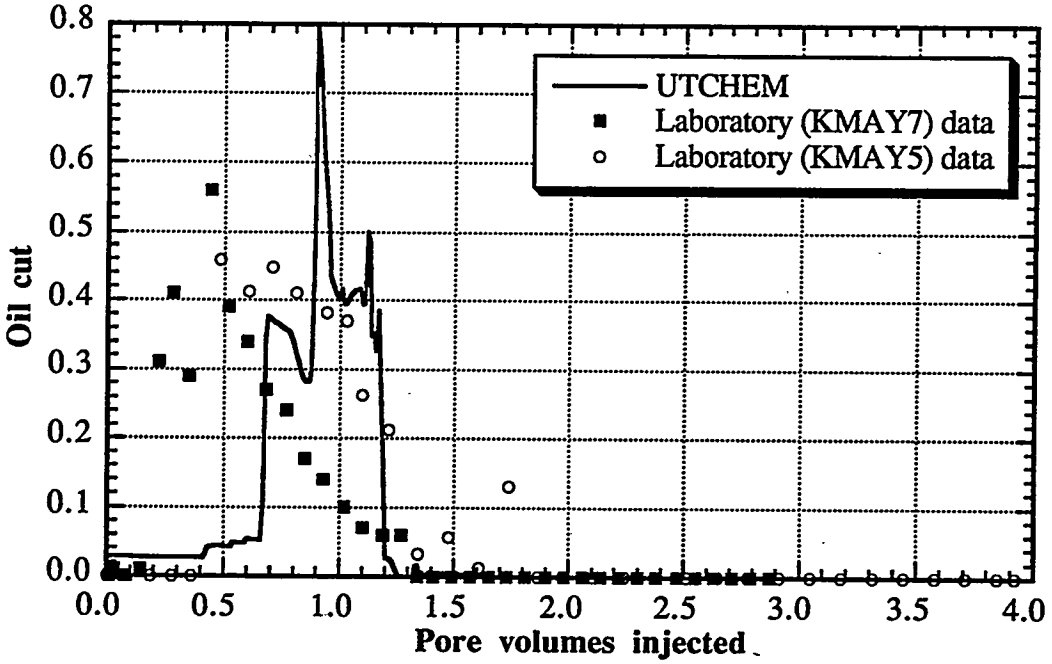


Figure 3.37 Comparison of oil cut between the result of UTCHEM simulation and laboratory data (Salinity gradient)

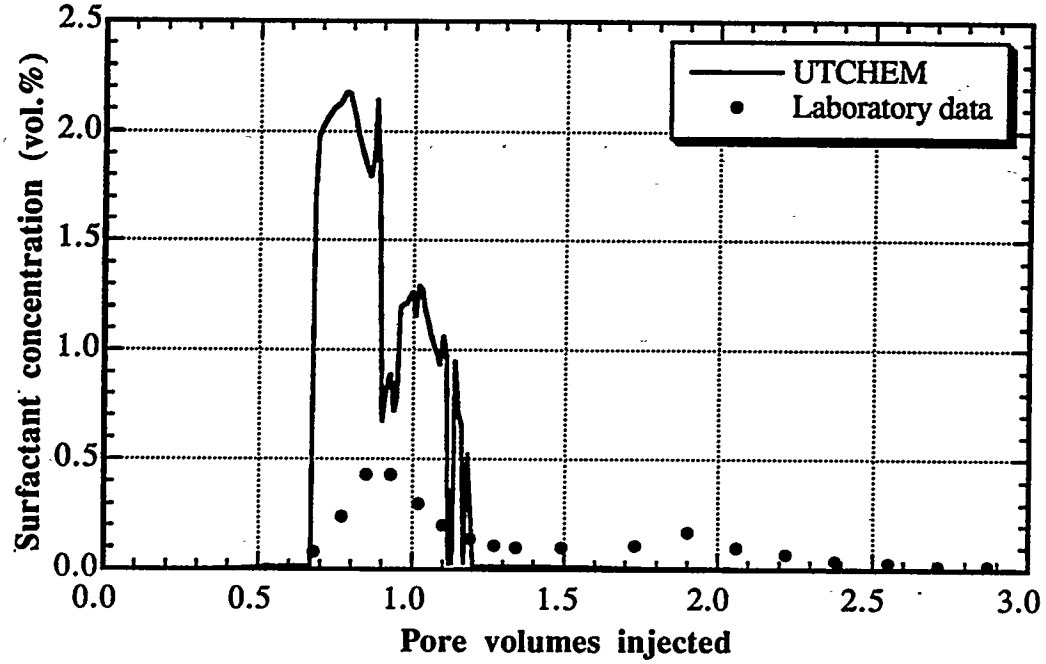


Figure 3.38 Surfactant concentration as a function of pore volumes injected (Salinity gradient)

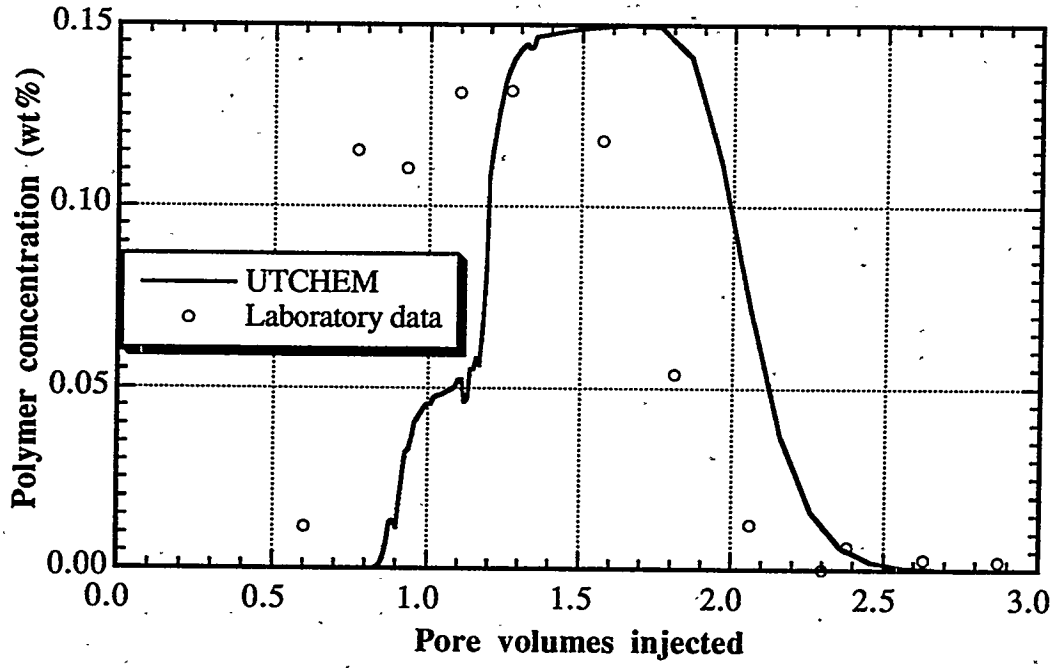


Figure 3.39 Polymer concentration as a function of pore volumes injected (Salinity gradient)

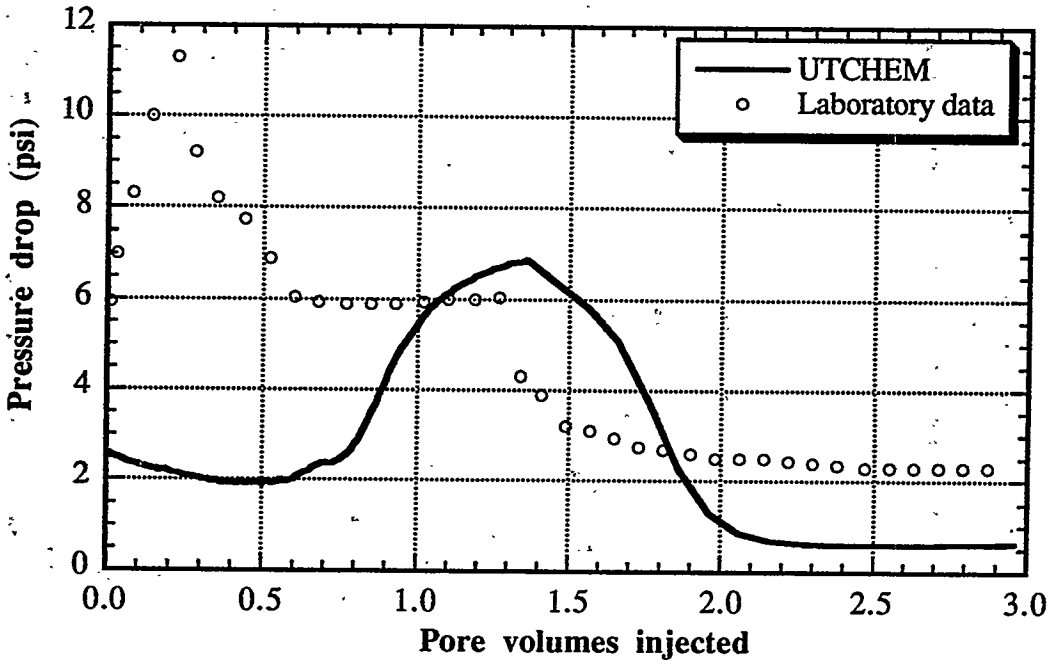


Figure 3.40 Pressure drop as a function of pore volumes injected (Salinity gradient)

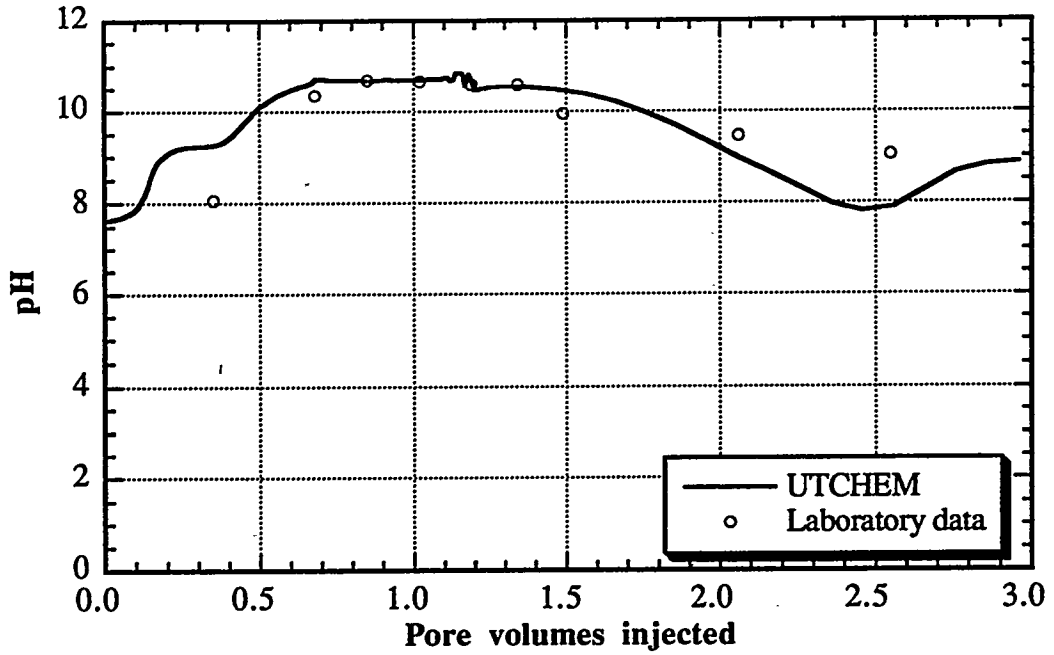


Figure 3.41 pH as a function of pore volumes injected (Salinity gradient)

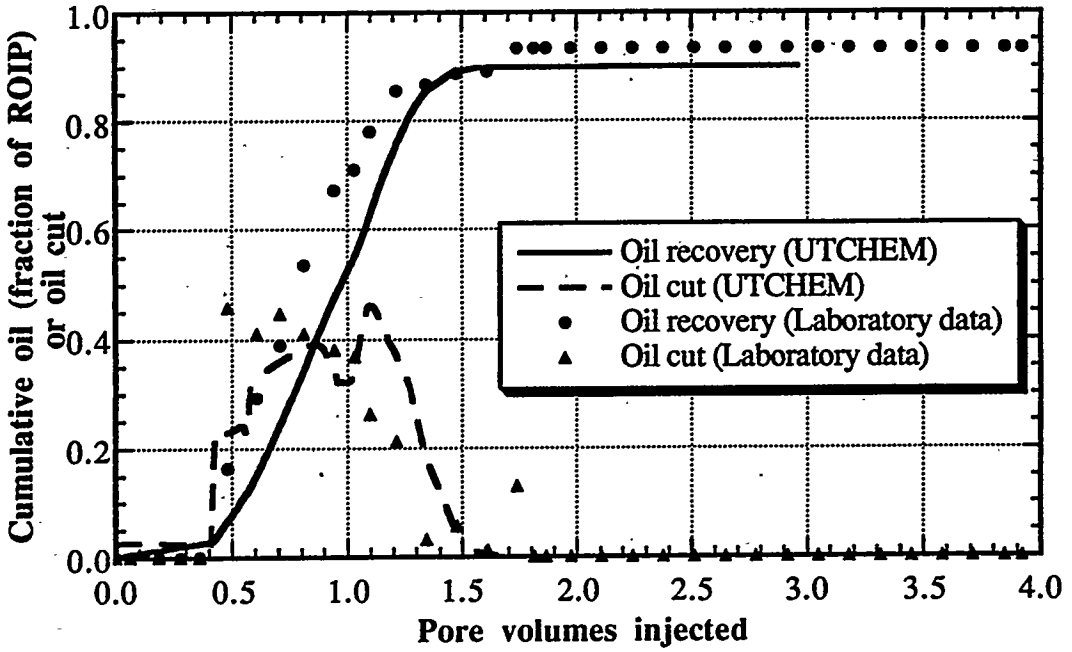


Figure 3.42 Comparison of the simulation results of oil recovery and oil cut with experimental data for KMAY5

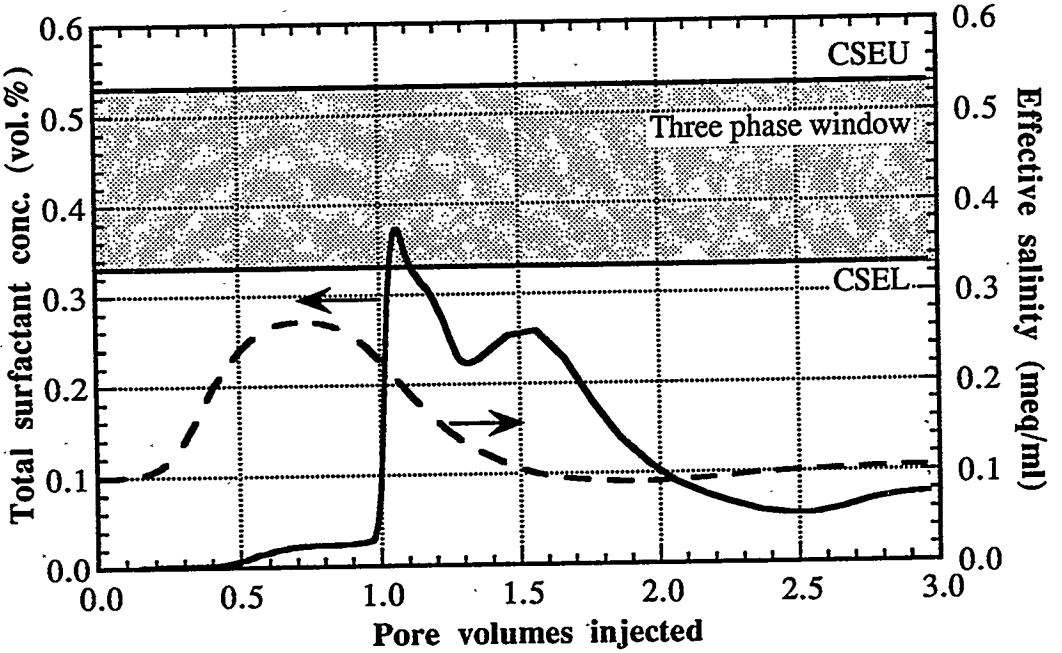


Figure 3.43 Surfactant concentration and salinity as a function of pore volumes injected (KMAY5)

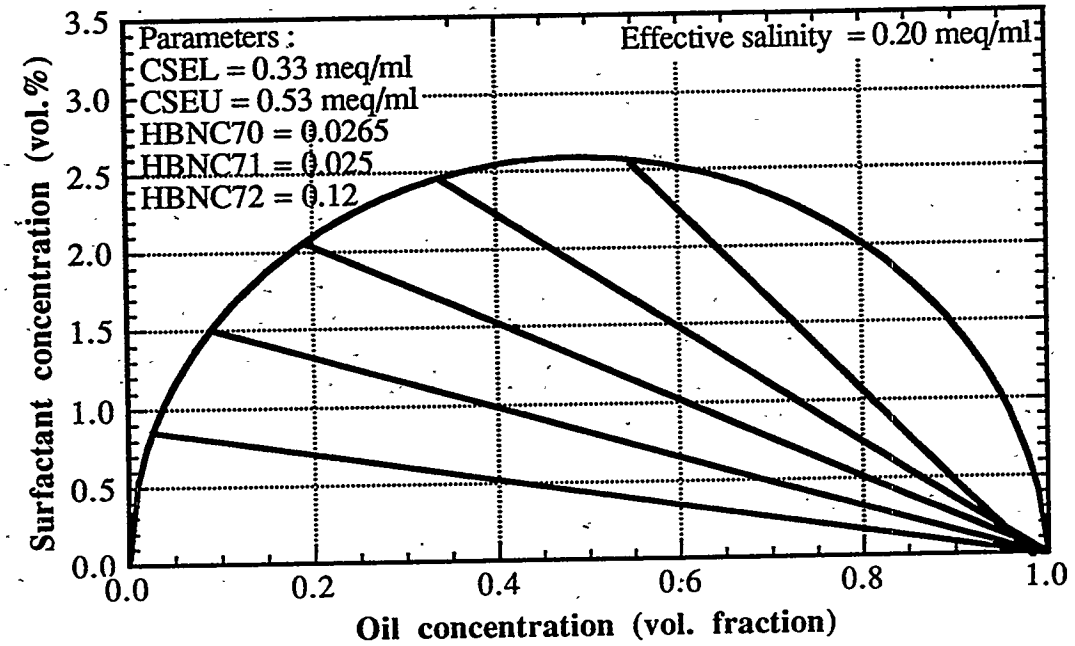


Figure 3.44 Type II(-) phase behavior used for KMAY5 coreflood history match

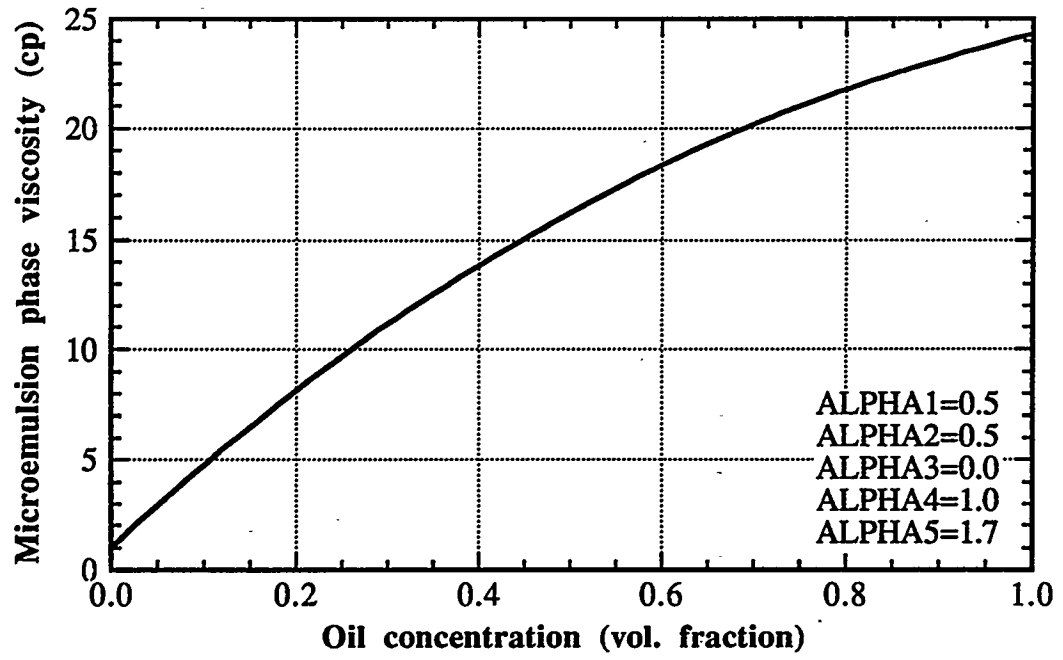


Figure 3.45 Microemulsion phase viscosity

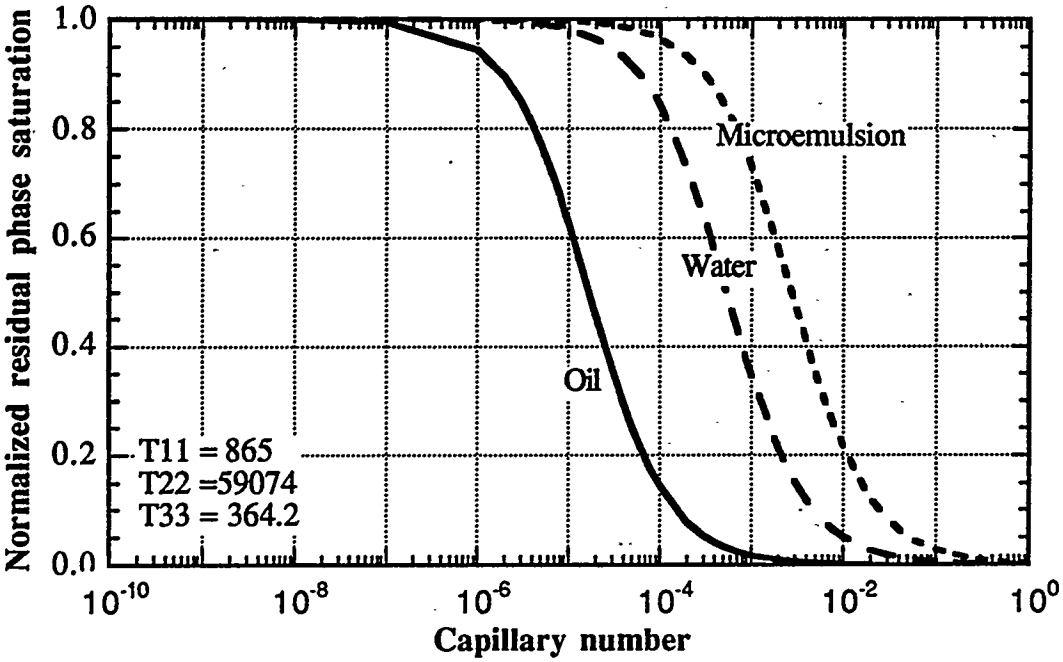


Figure 3.46 Capillary desaturation curves used for KMAY5 coreflood history match

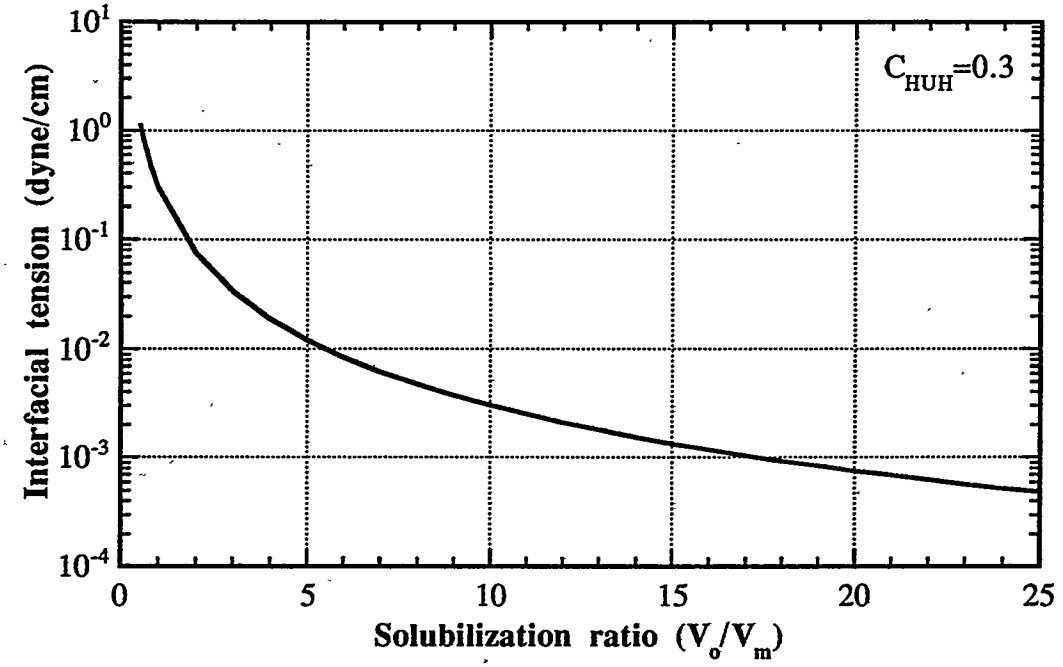


Figure 3.47 Interfacial tension for oil/microemulsion used for KMAY5 coreflood history match

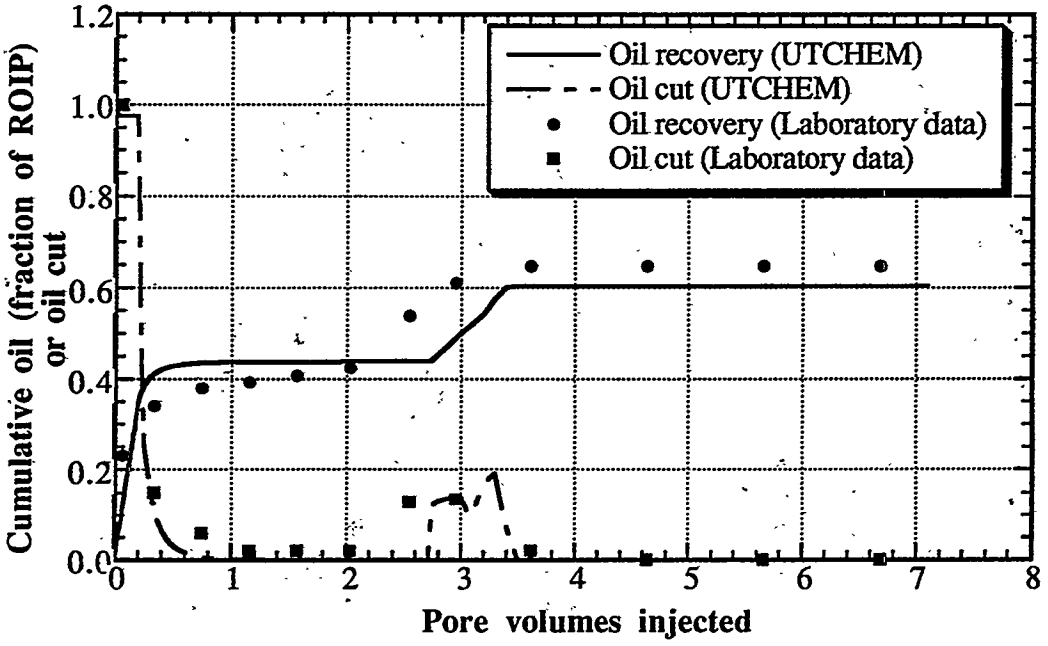


Figure 3.48 Oil recovery and oil cut as for the reservoir core (based on KMAY7 input parameters)

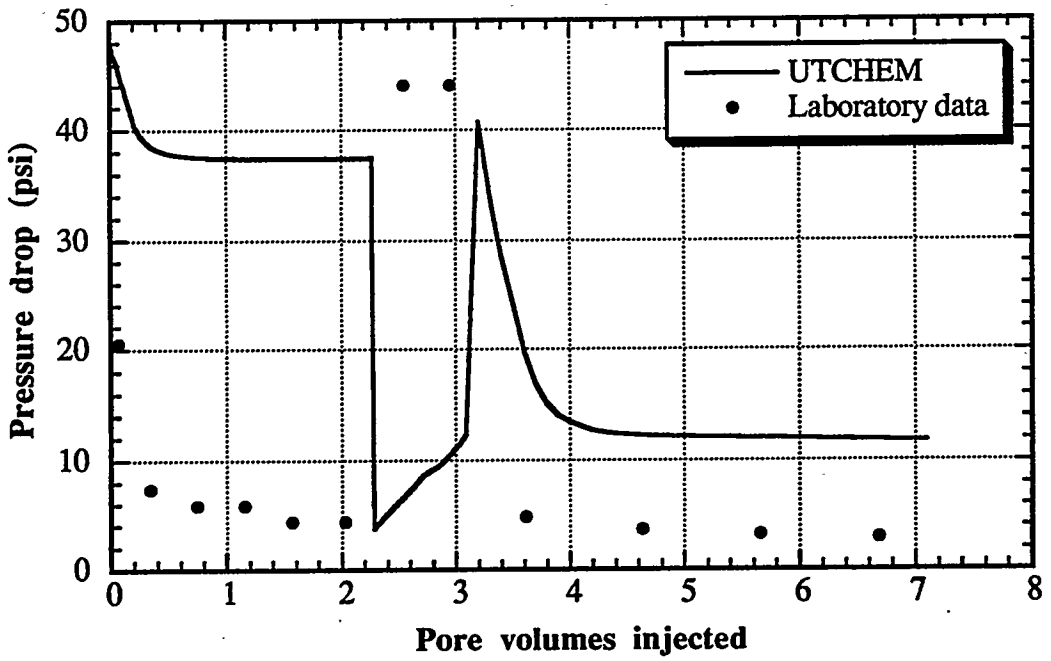


Figure 3.49 Pressure drop for reservoir core (based on KMAY7 input parameters)

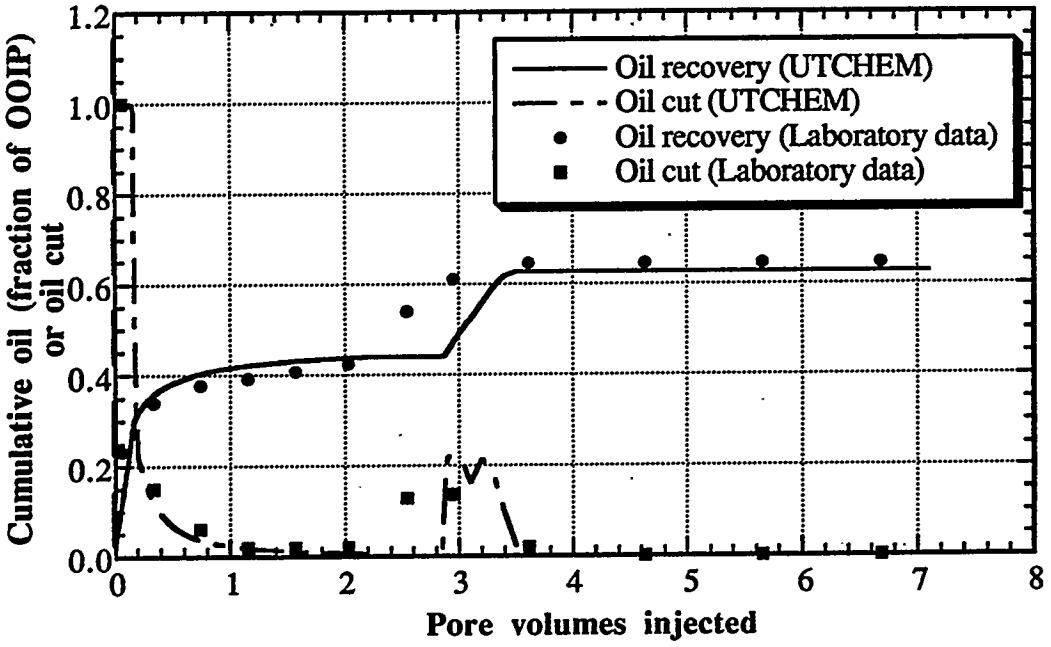


Figure 3.50 Oil recovery and oil cut for reservoir core using Type II(-) phase behavior

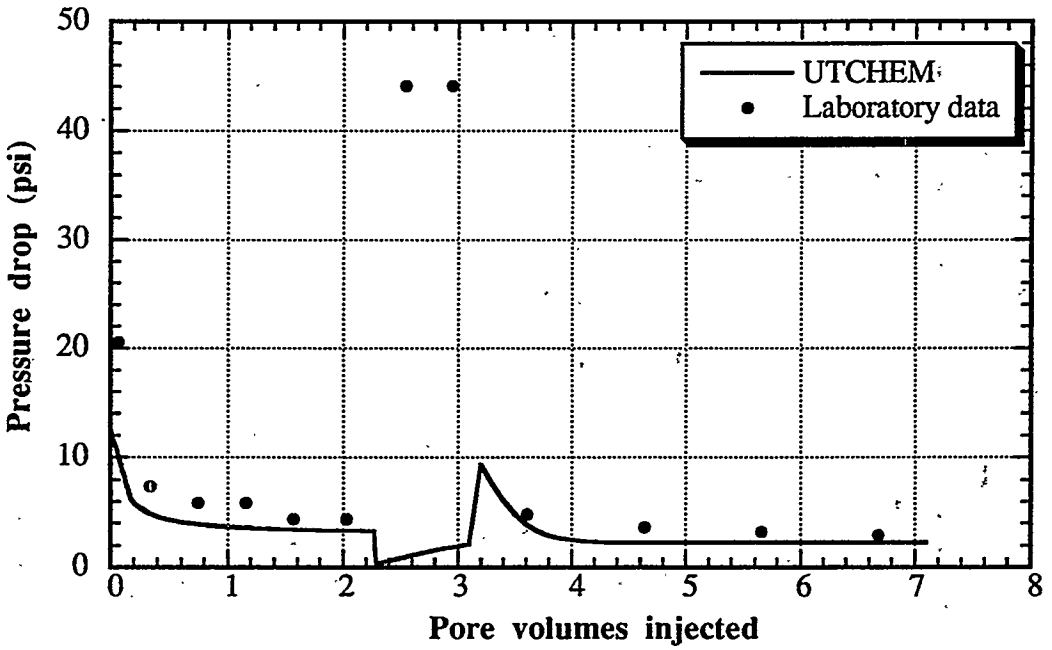
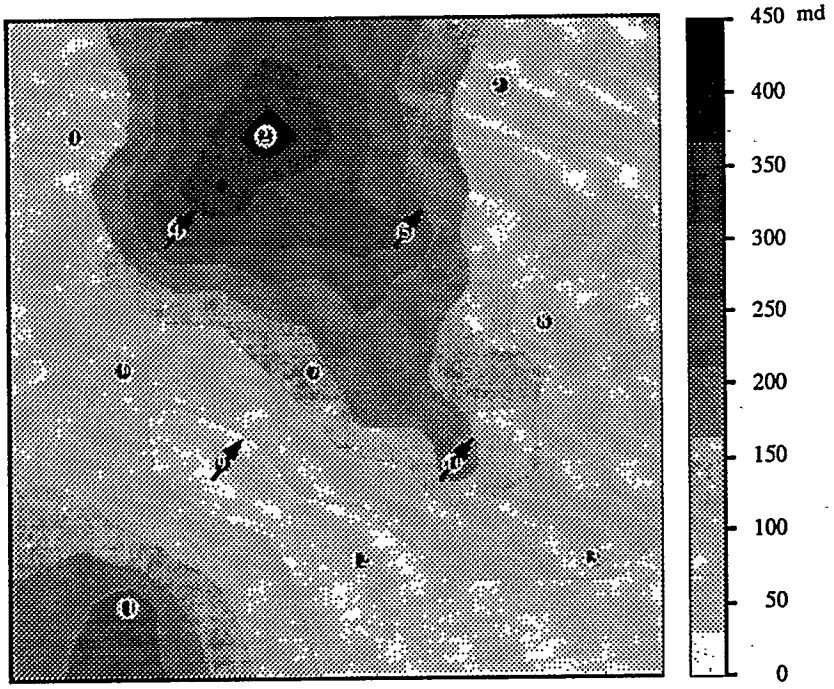
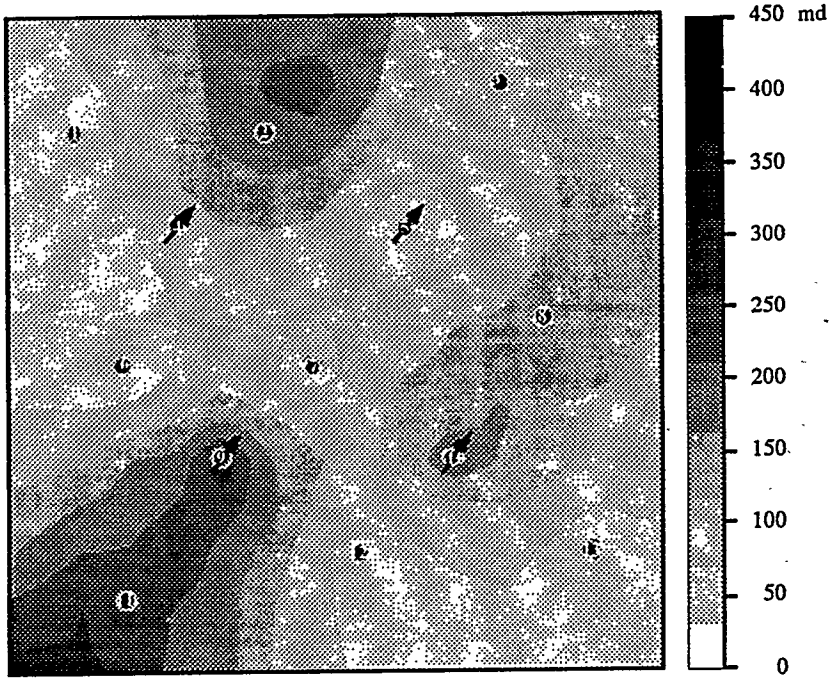


Figure 3.51 Pressure drop for reservoir core using Type II(-) phase behavior

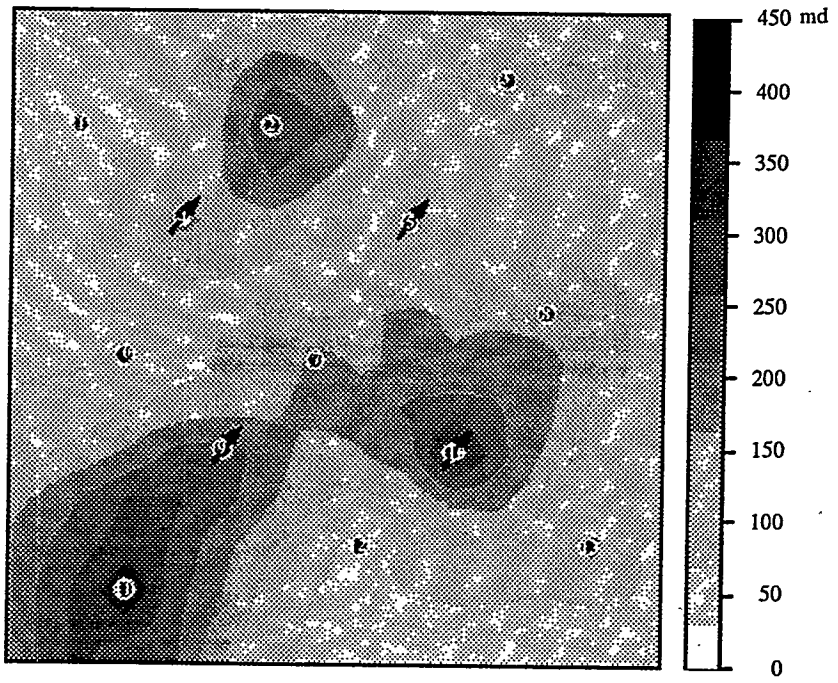


Layer 1

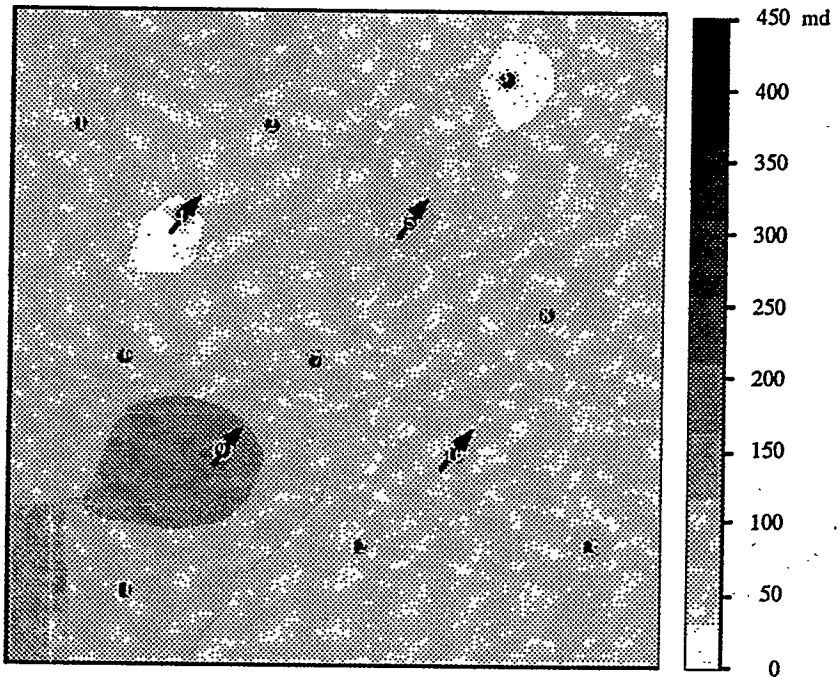


Layer 2

Figure 3.52 Permeability field for Layers 1 and 2



Layer 3



Layer 4

Figure 3.53 Permeability field for Layers 3 and 4

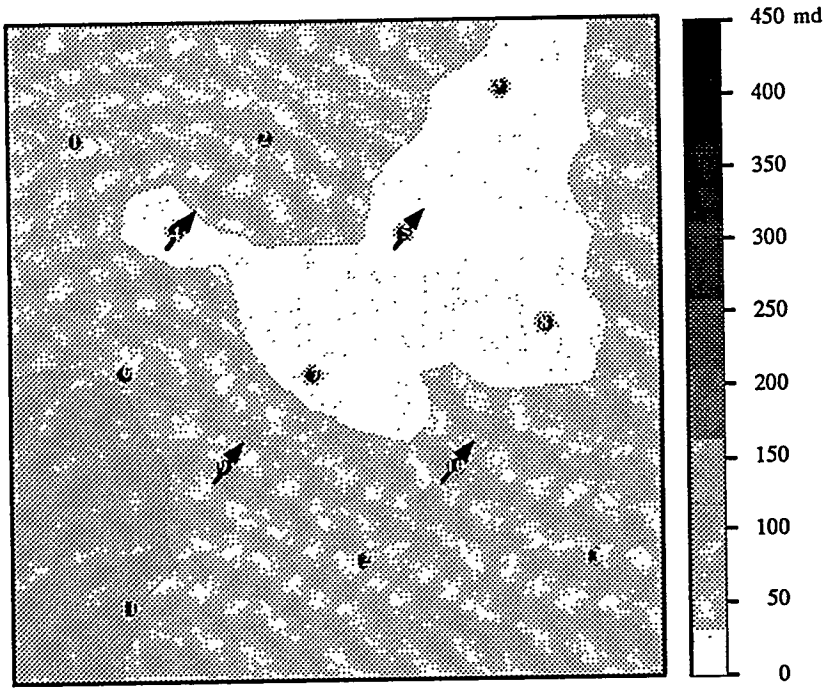


Figure 3.54 Permeability field for Layer 5

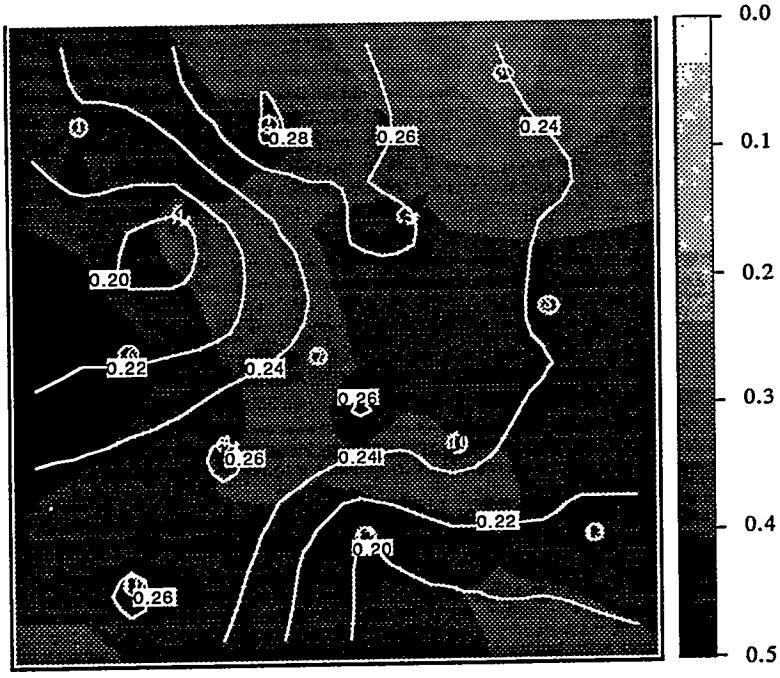
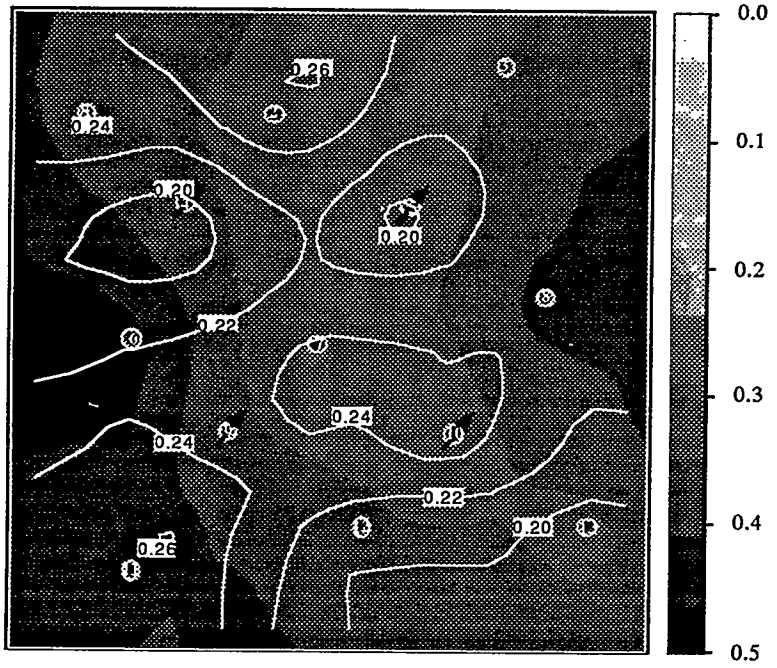
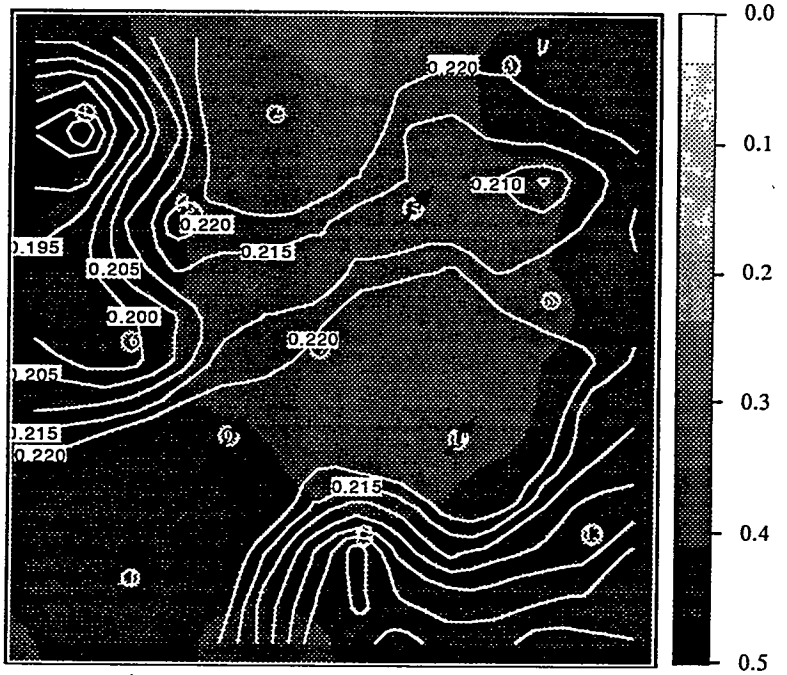


Figure 3.55 Oil saturation field overlaid by porosity contour for Layer 1

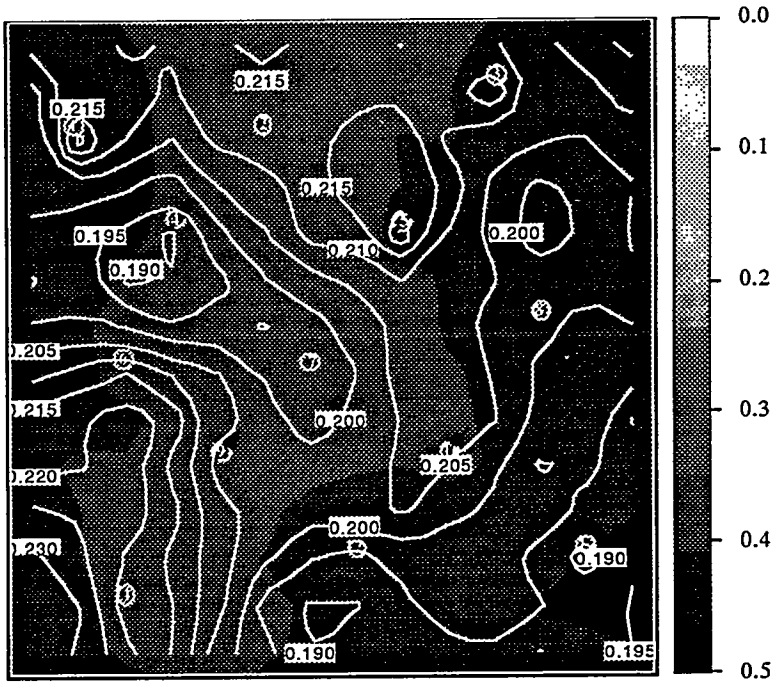


Layer 2

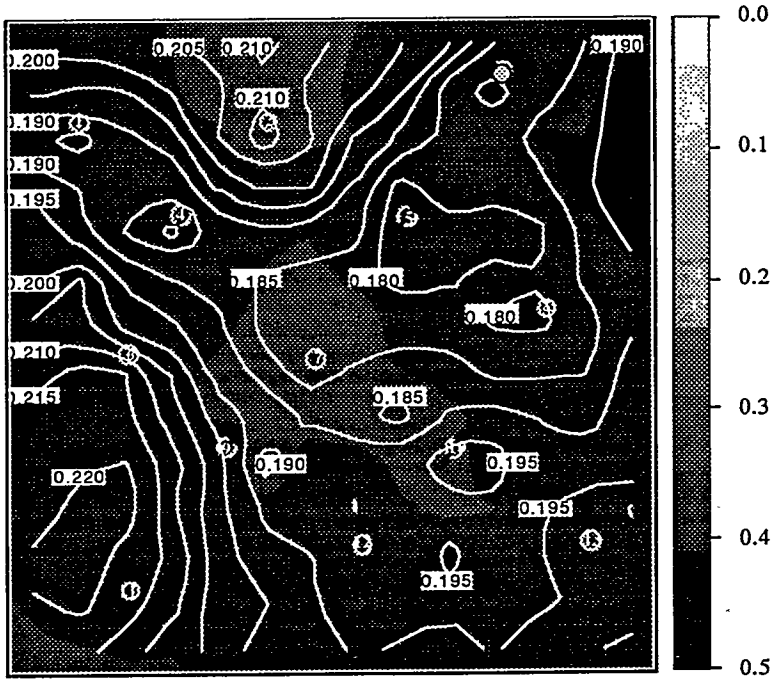


Layer 3

Figure 3.56 Oil saturation field overlaid by porosity contour for Layers 2 and 3

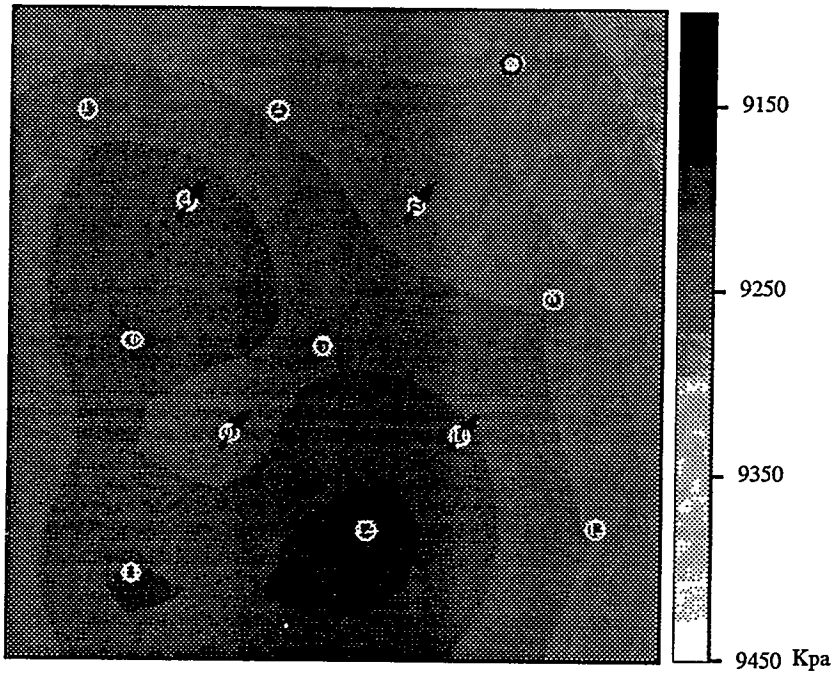


Layer 4

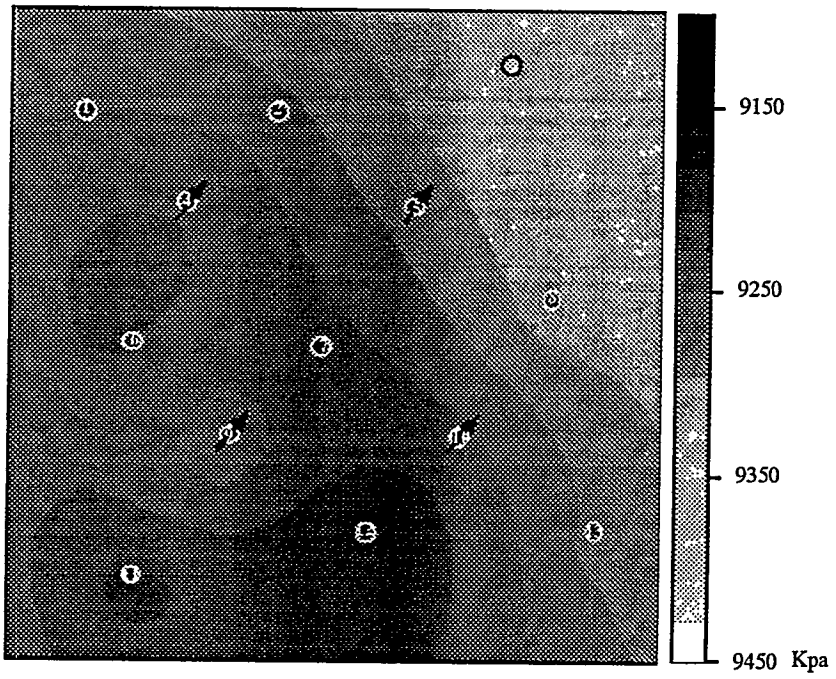


Layer 5

Figure 3.57 Oil saturation field overlaid by porosity contour for Layers 4 and 5

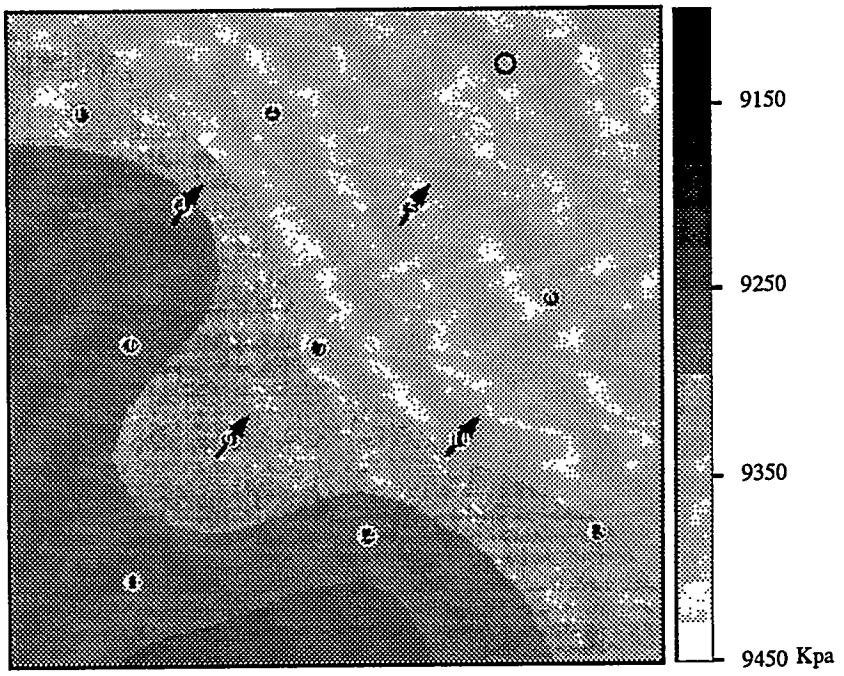


Layer 1

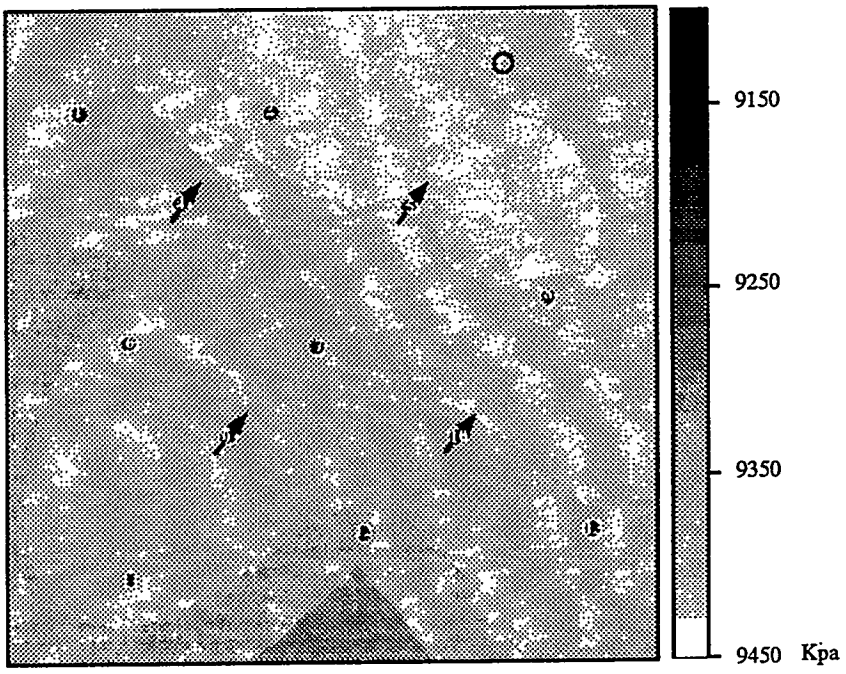


Layer 2

Figure 3.58 Initial pressure distribution for Layers 1 and 2



Layer 3



Layer 4

Figure 3.59 Initial pressure distribution for Layers 3 and 4

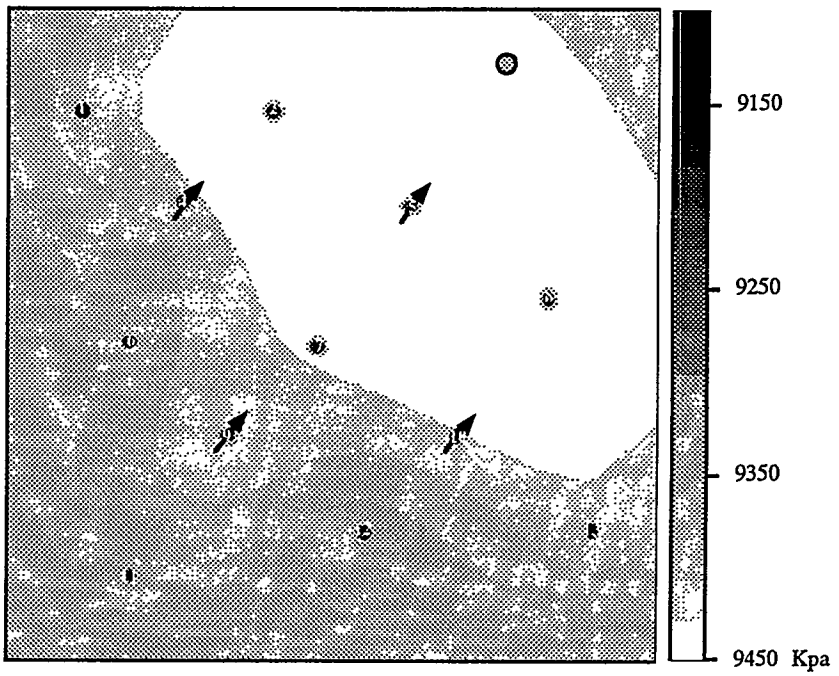


Figure 3.60 Initial pressure distribution for Layer 5

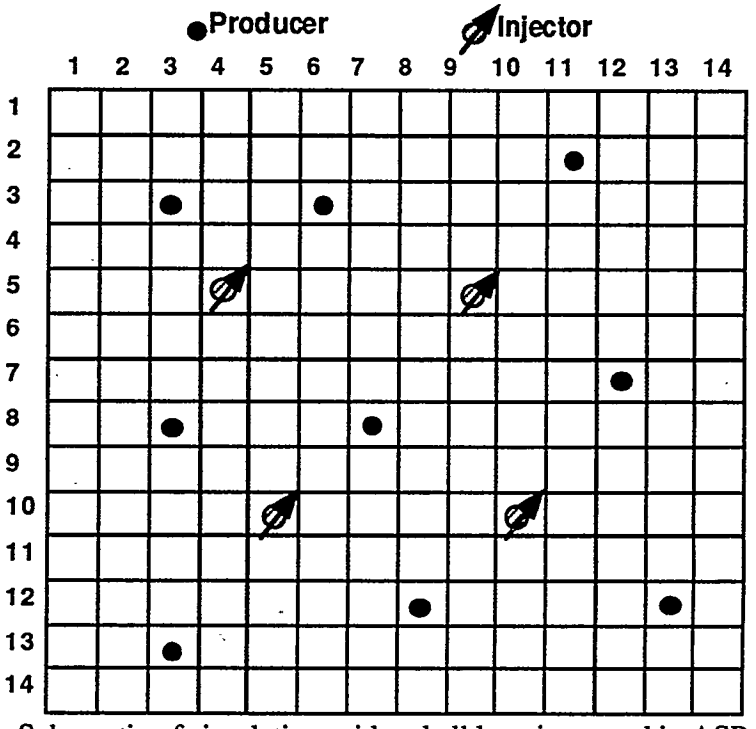


Figure 3.61 Schematic of simulation grid and ell locations used in ASP pilot simulations

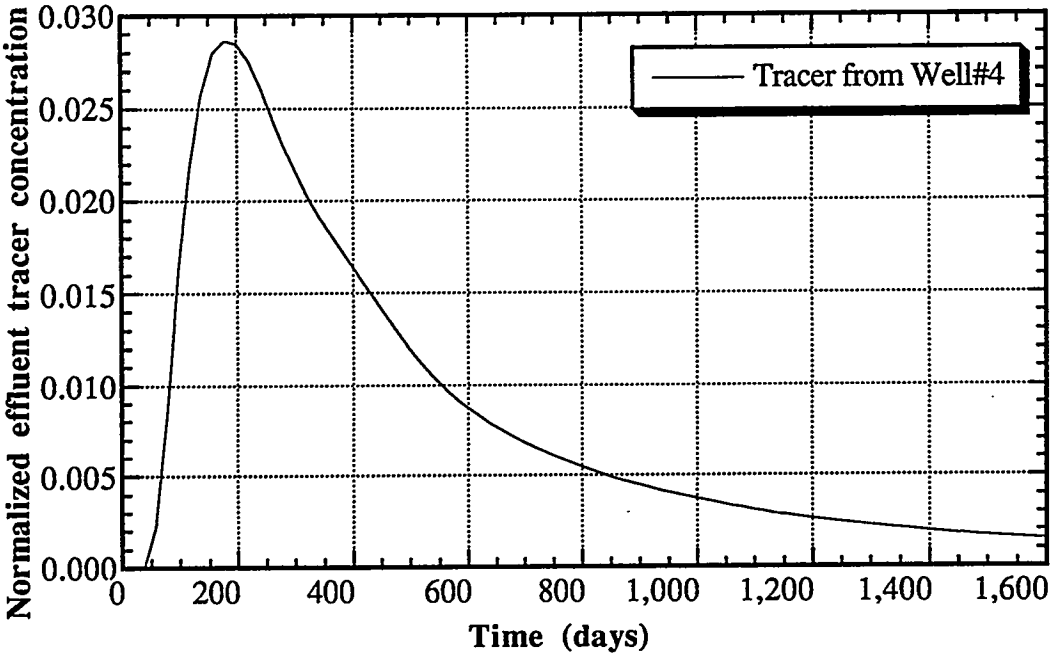


Figure 3.62 Tracer response curve for Well#1 (uniform P_{wf})

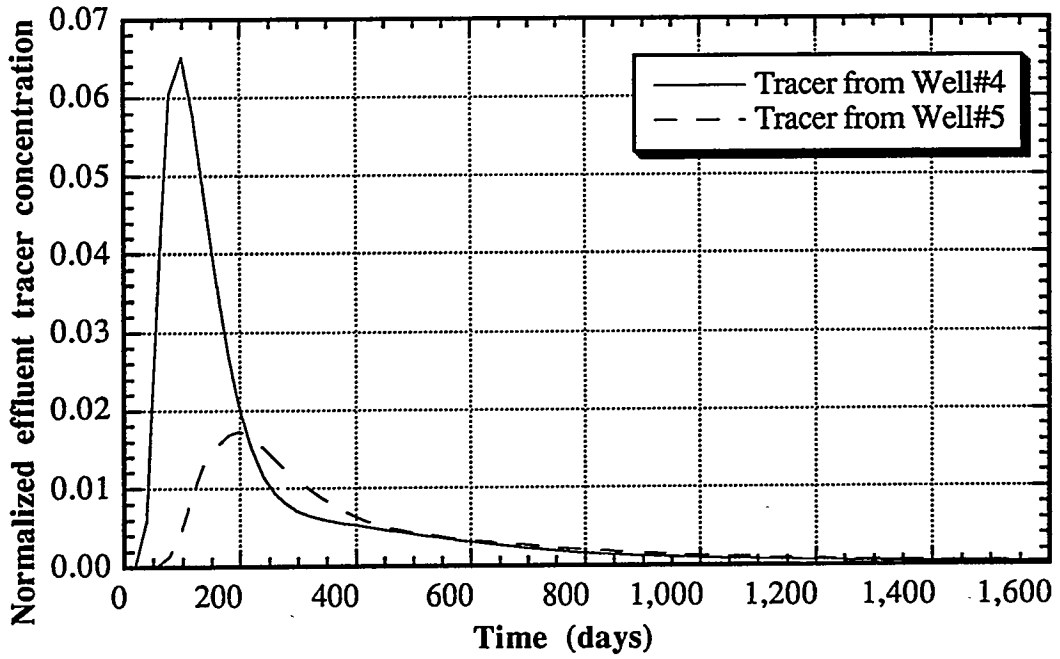


Figure 3.63 Tracer response curves for Well#2 (uniform P_{wf})

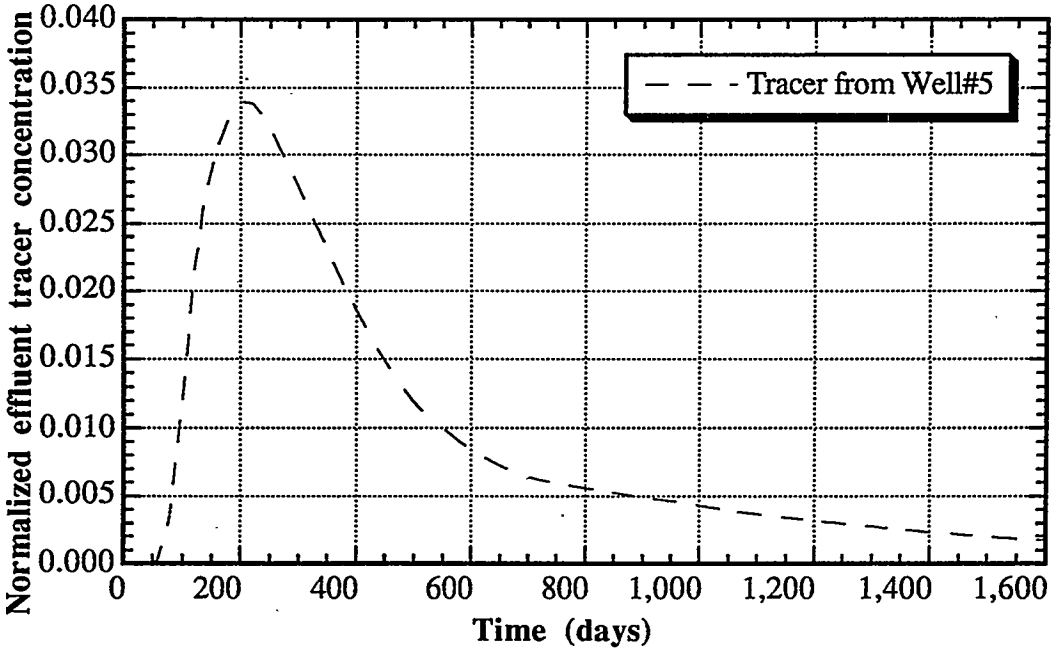


Figure 3.64 Tracer response curve for Well#3 (uniform P_{wf})

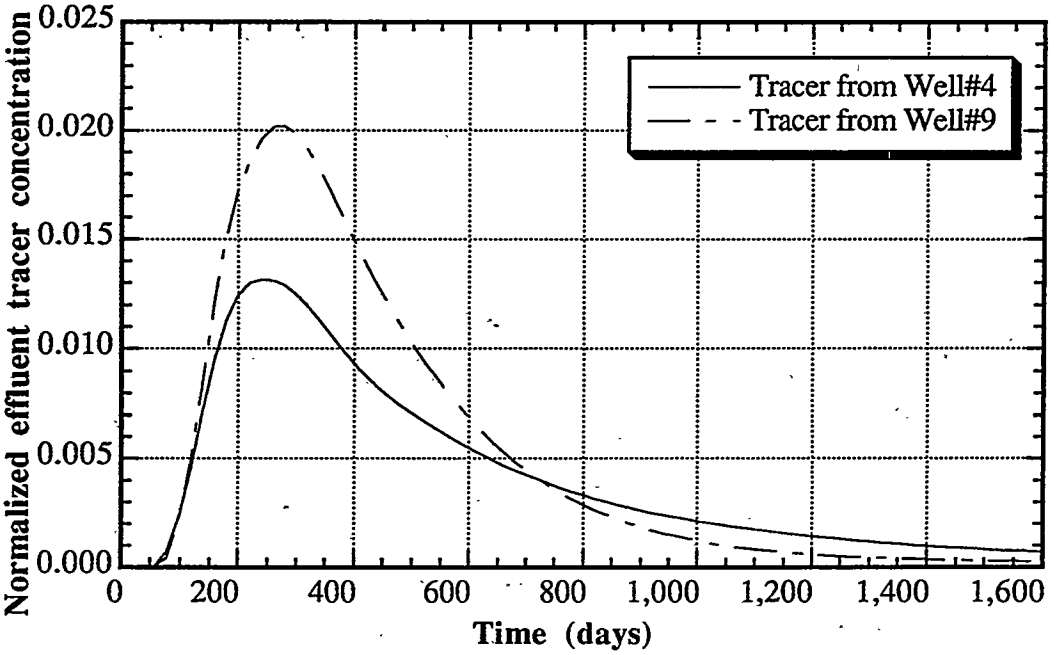


Figure 3.65 Tracer response curves for Well#6 (uniform P_{wf})

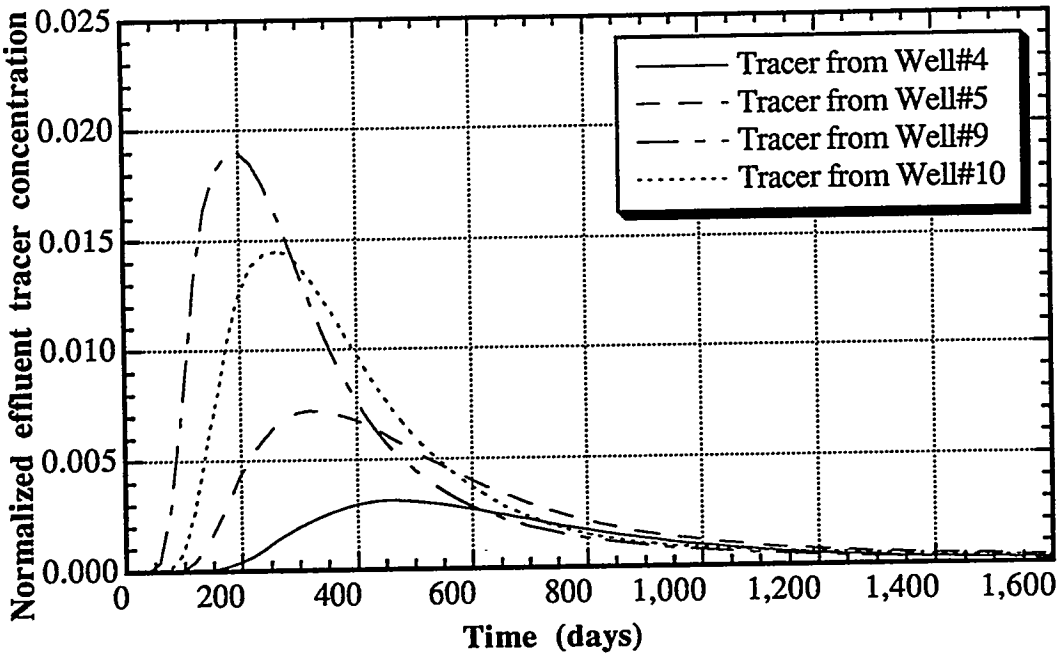


Figure 3.66 Tracer response curves for Well#7 (uniform P_{wf})

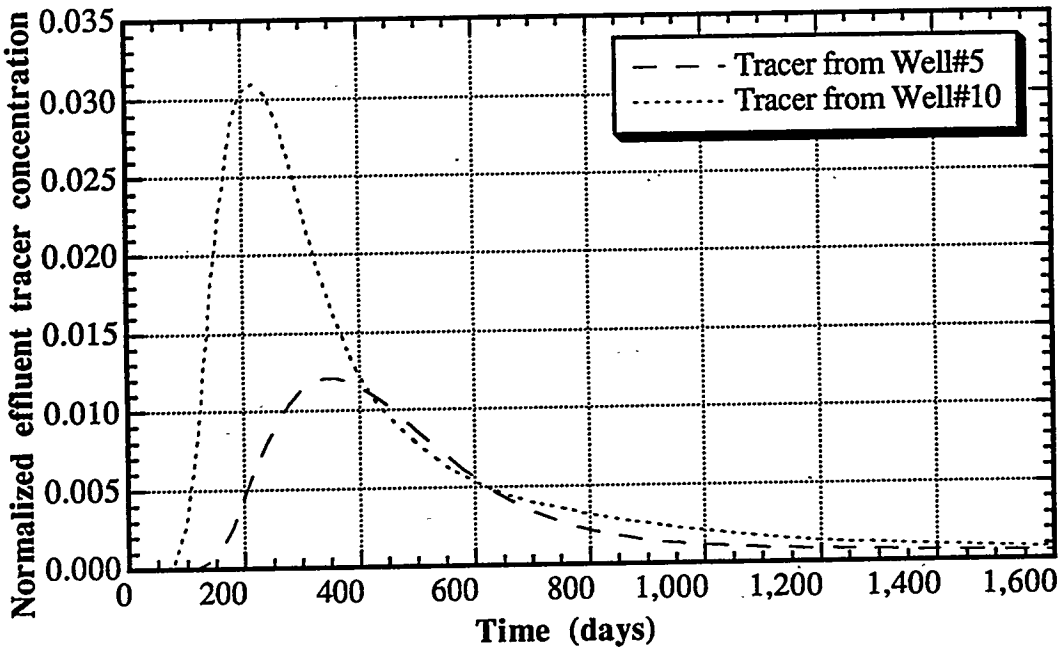


Figure 3.67 Tracer response curves for Well#8 (uniform P_{wf})

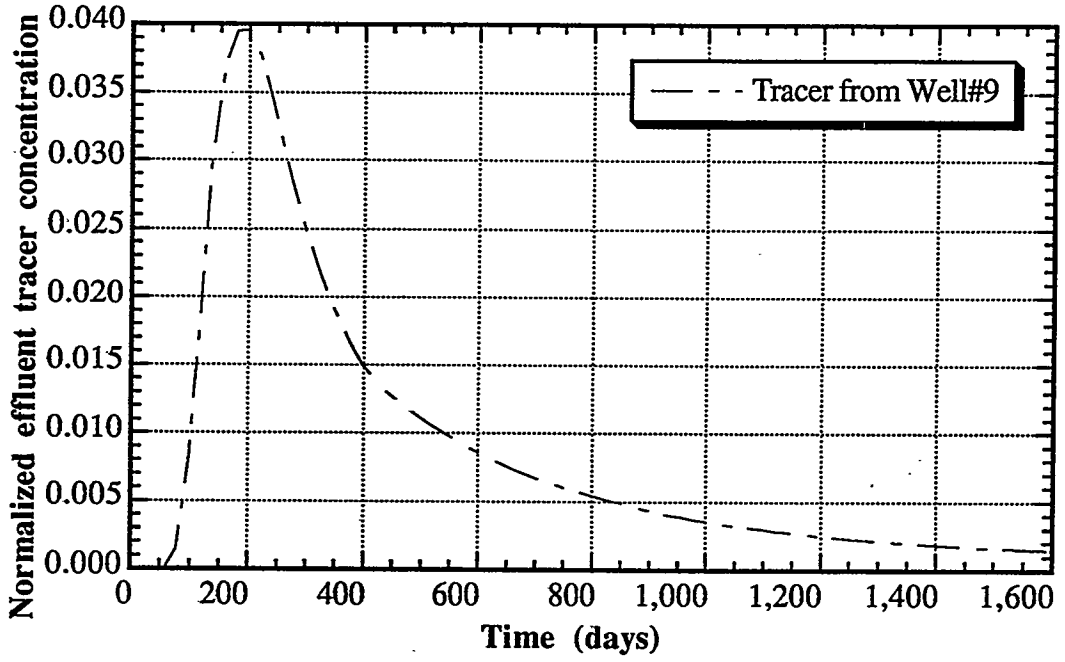


Figure 3.68 Tracer response curve for Well#11 (uniform P_{wf})

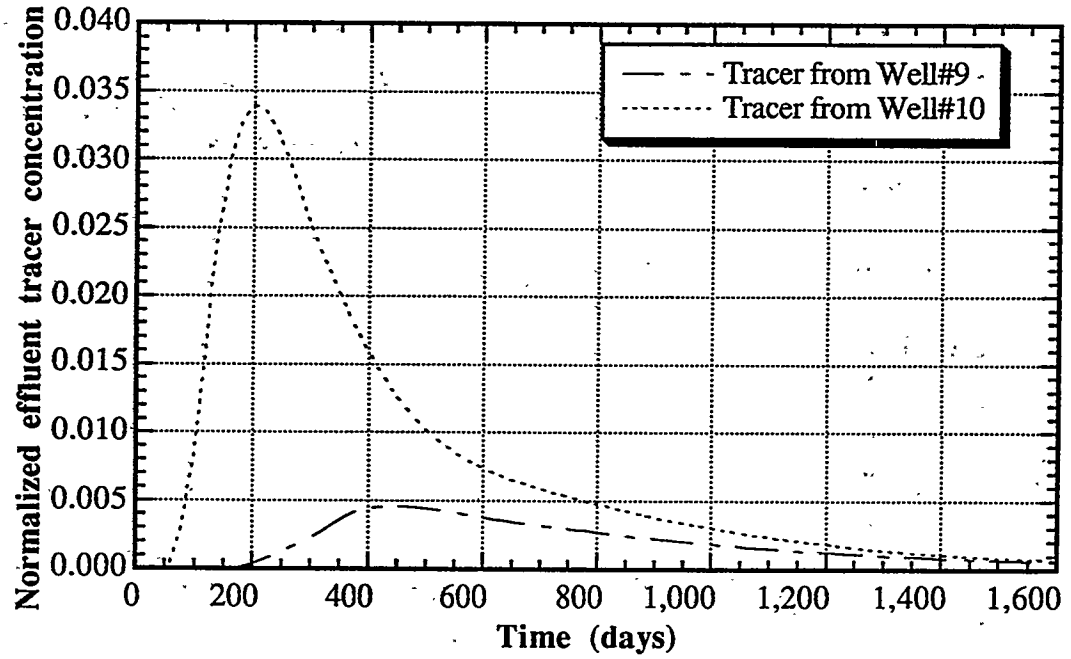


Figure 3.69 Tracer response curves for Well#12 (uniform P_{wf})

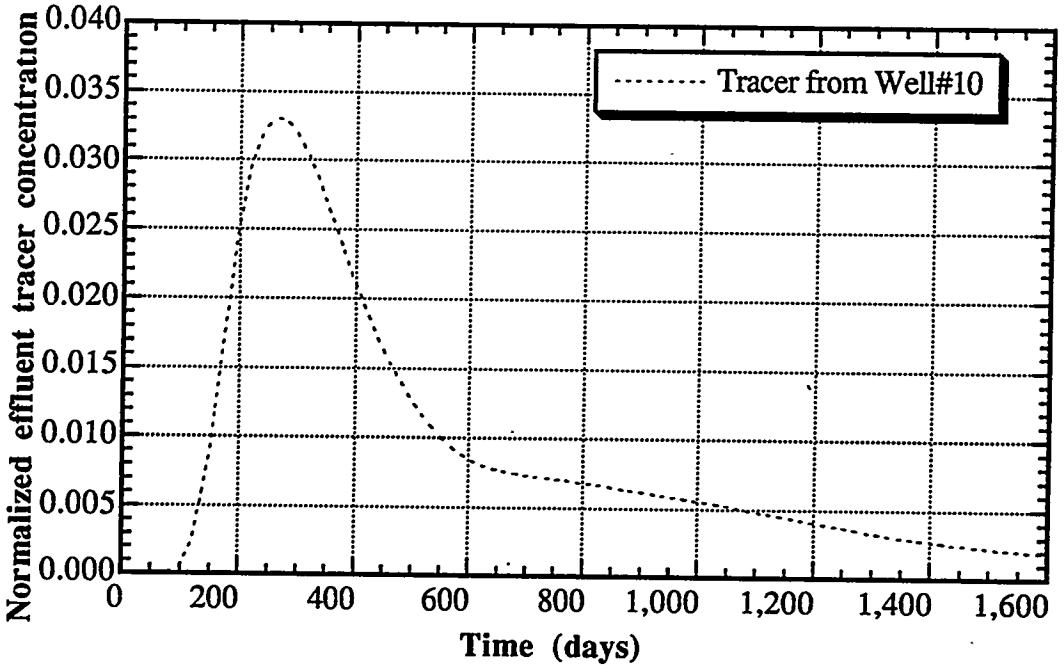


Figure 3.70 Tracer response curve for Well#13 (uniform P_{wf})

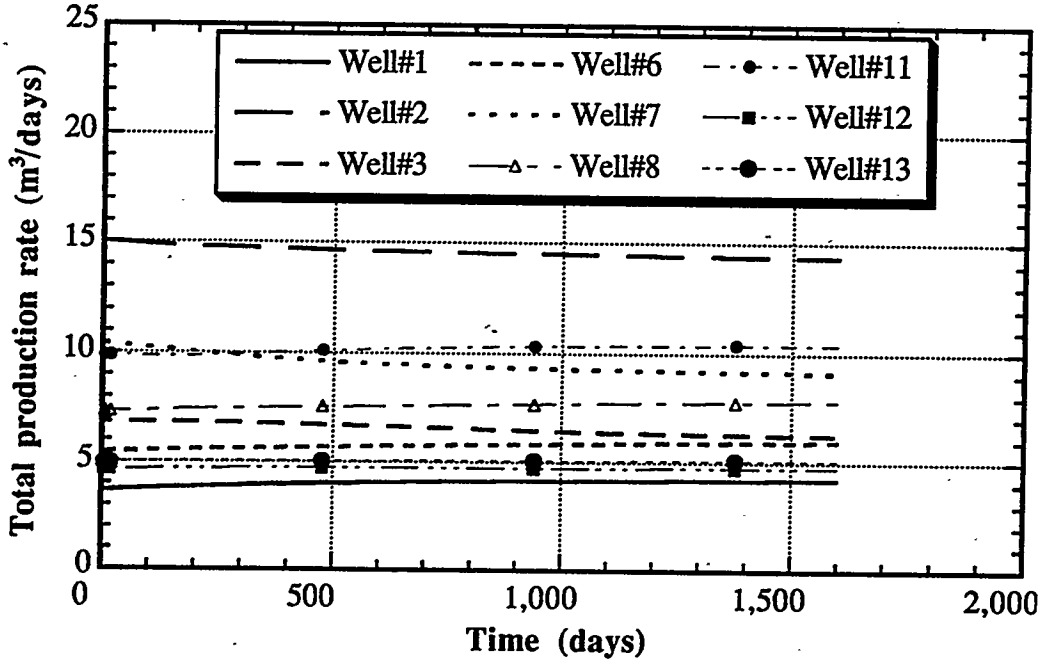


Figure 3.71 History of production rate as a function of pore volumes injected (uniform P_{wf})

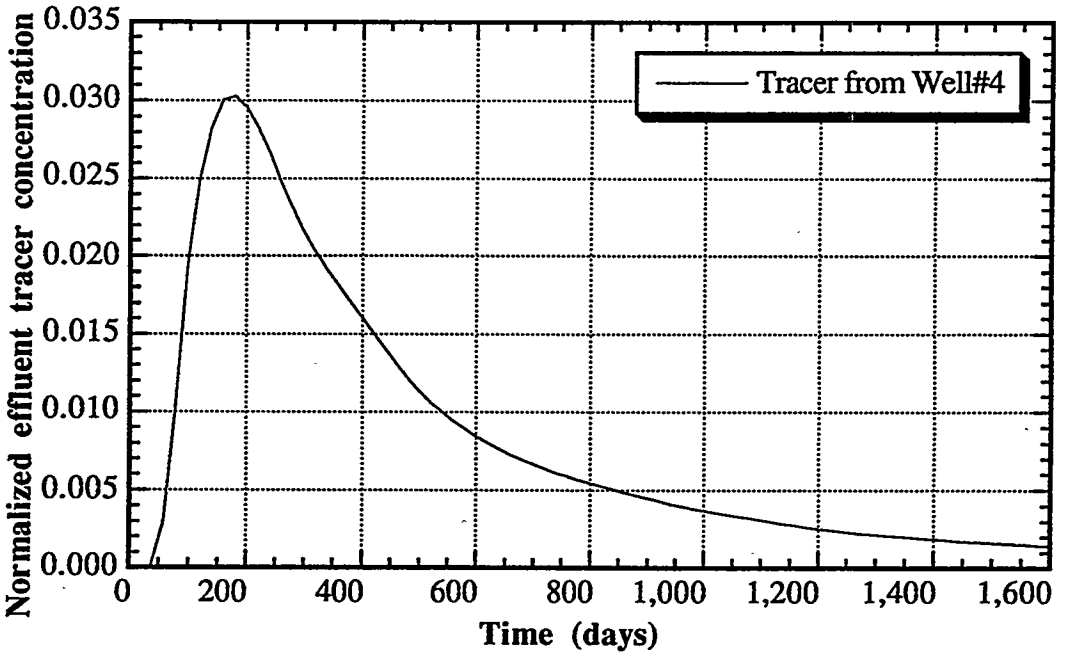


Figure 3.72 Tracer response curve for Well#1 (optimized P_{wf})

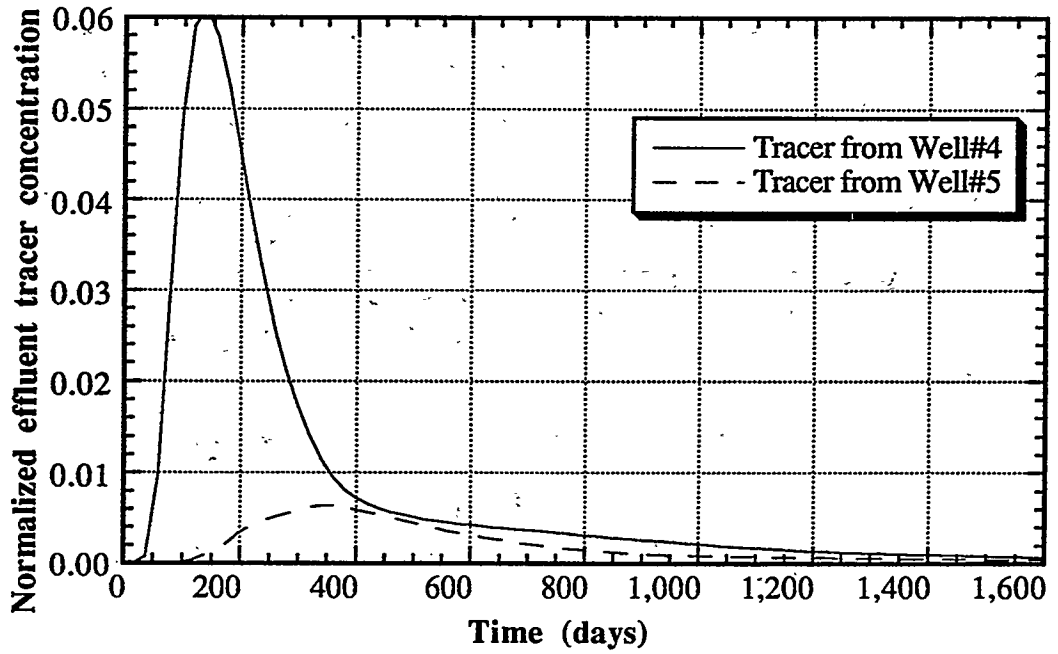


Figure 3.73 Tracer response curves for Well#2 (optimized P_{wf})

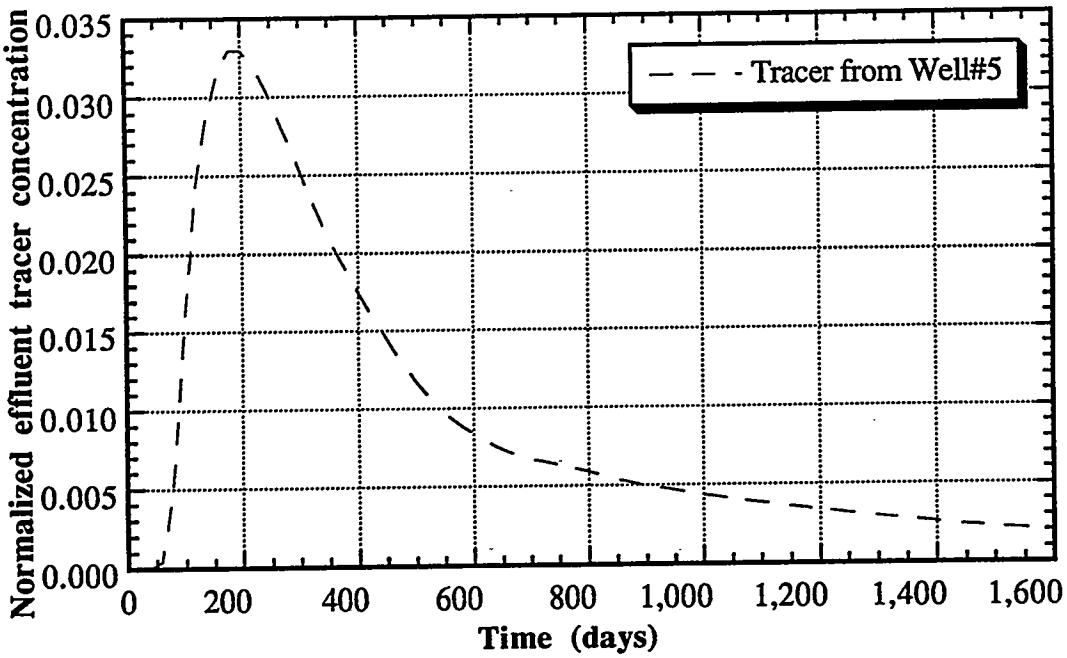


Figure 3.74 Tracer response curve for Well#3 (optimized P_{wf})

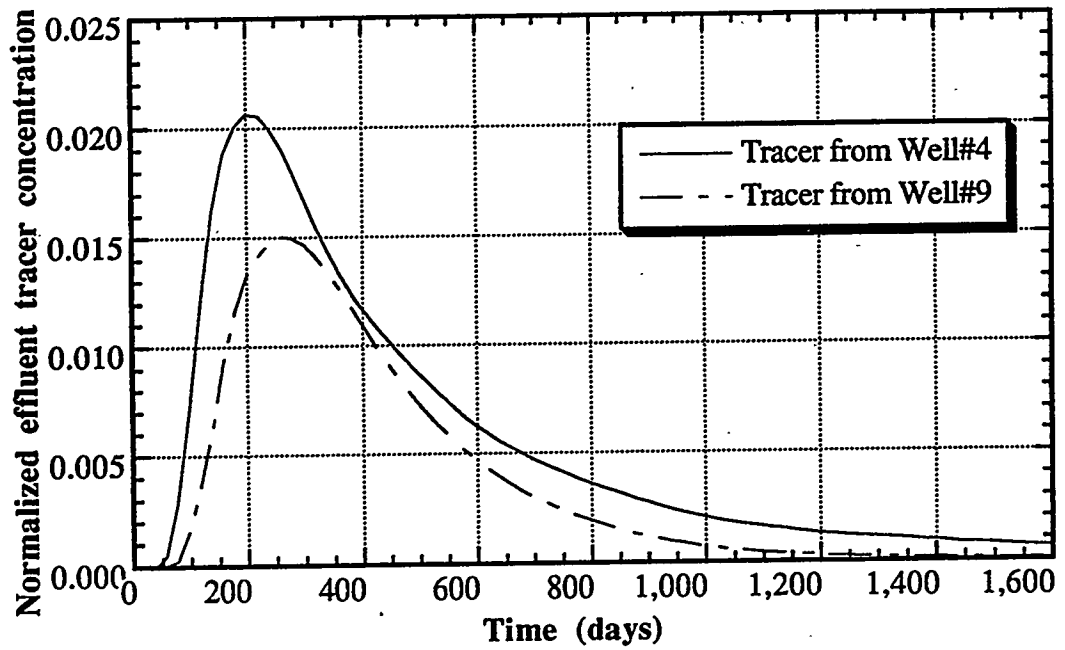


Figure 3.75 Tracer response curves for Well#6 (optimized P_{wf})

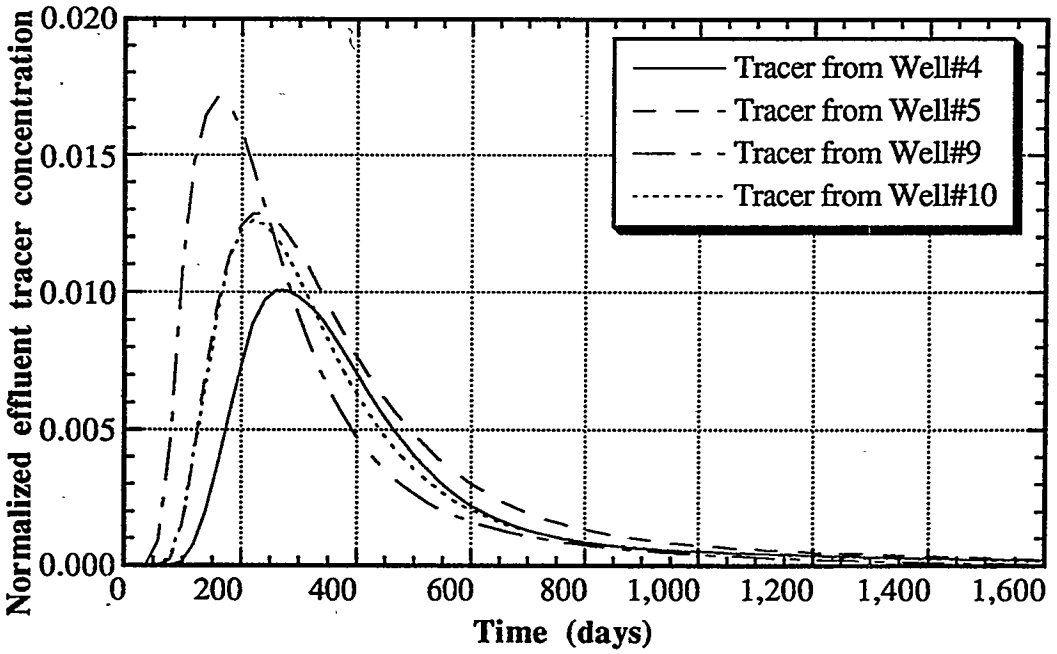


Figure 3.76 Tracer response curves for Well#7 (optimized P_{wf})

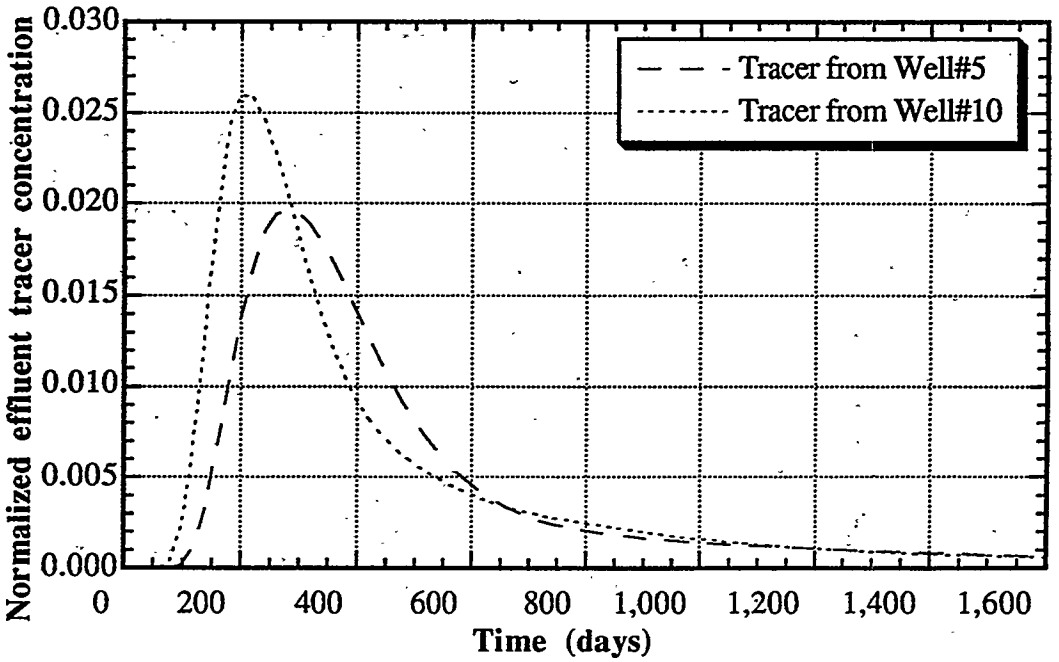


Figure 3.77 Tracer response curves for Well#8 (optimized P_{wf})

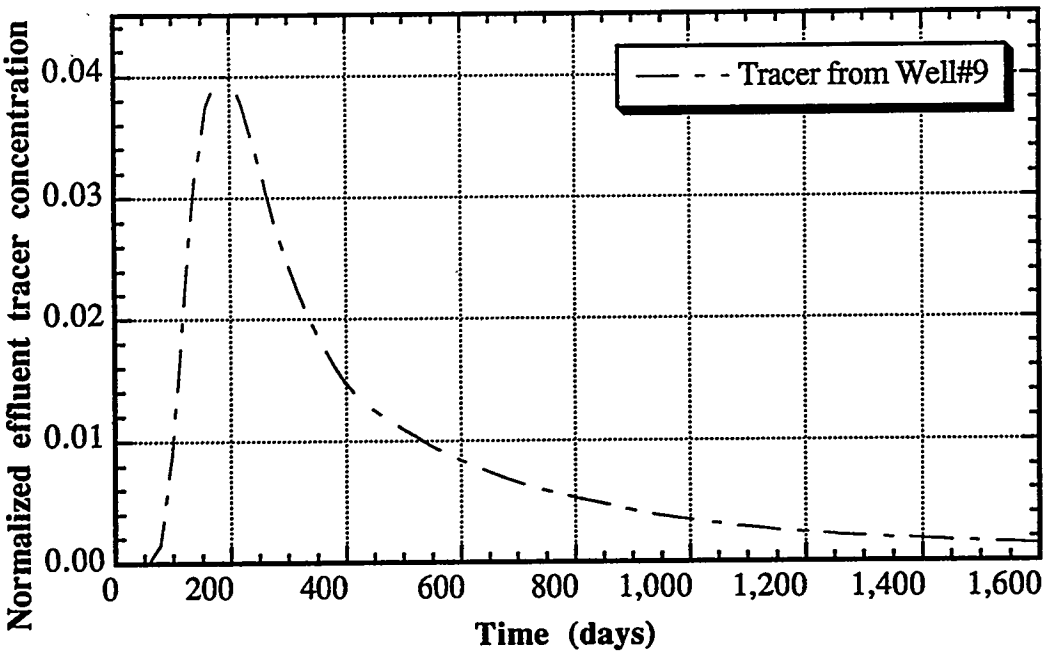


Figure 3.78 Tracer response curve for Well#11 (optimized P_{wf})

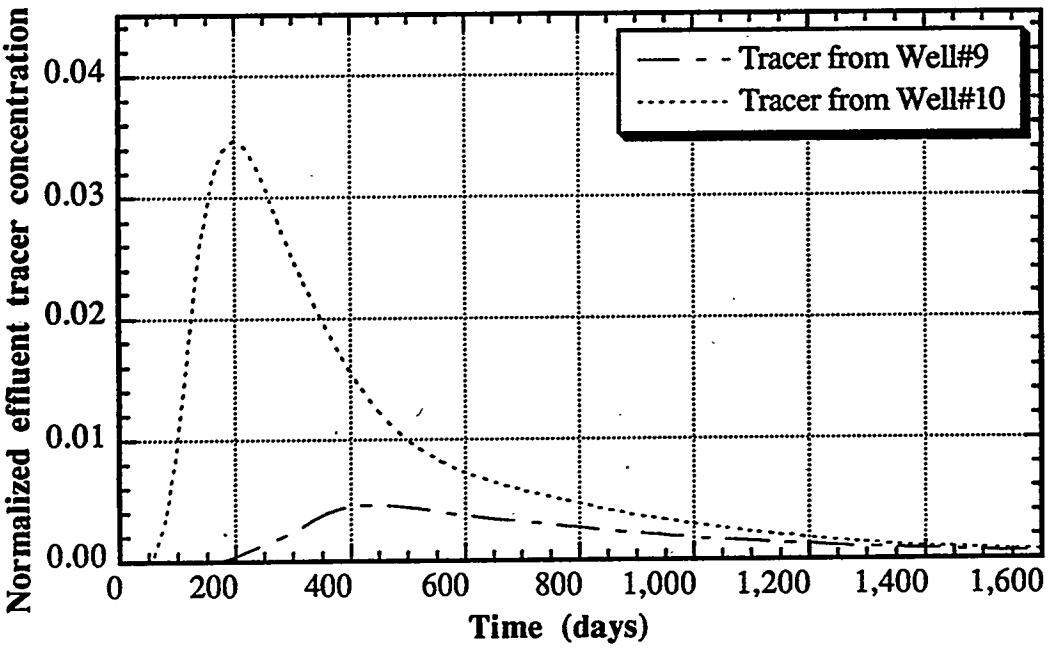


Figure 3.79 Tracer response curves for Well#12 (optimized P_{wf})

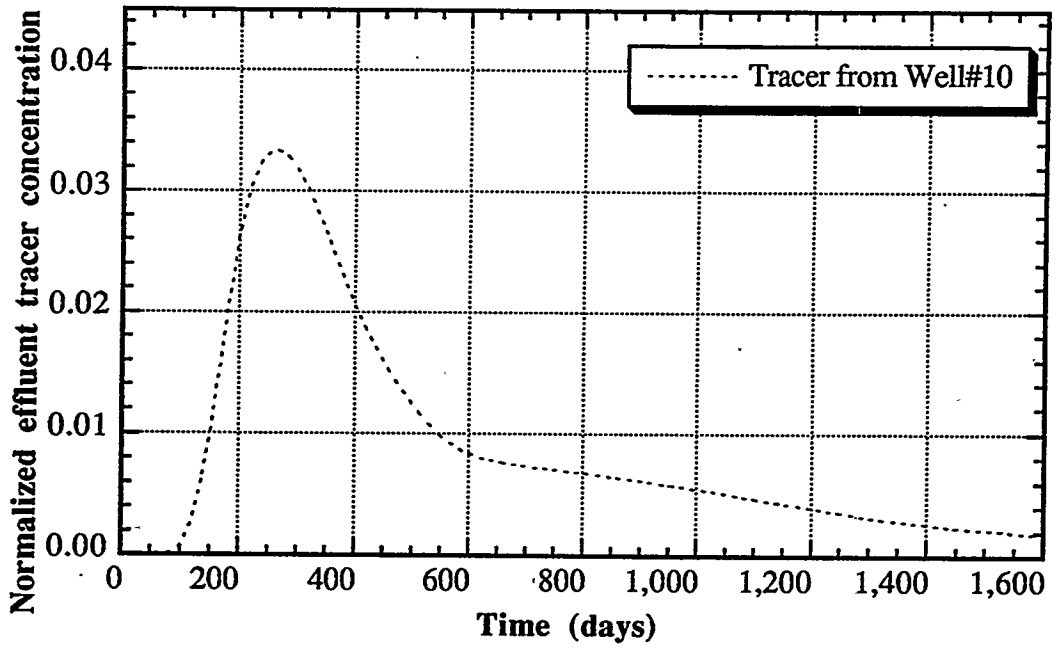


Figure 3.80 Tracer response curve for Well#13 (optimized P_{wf})

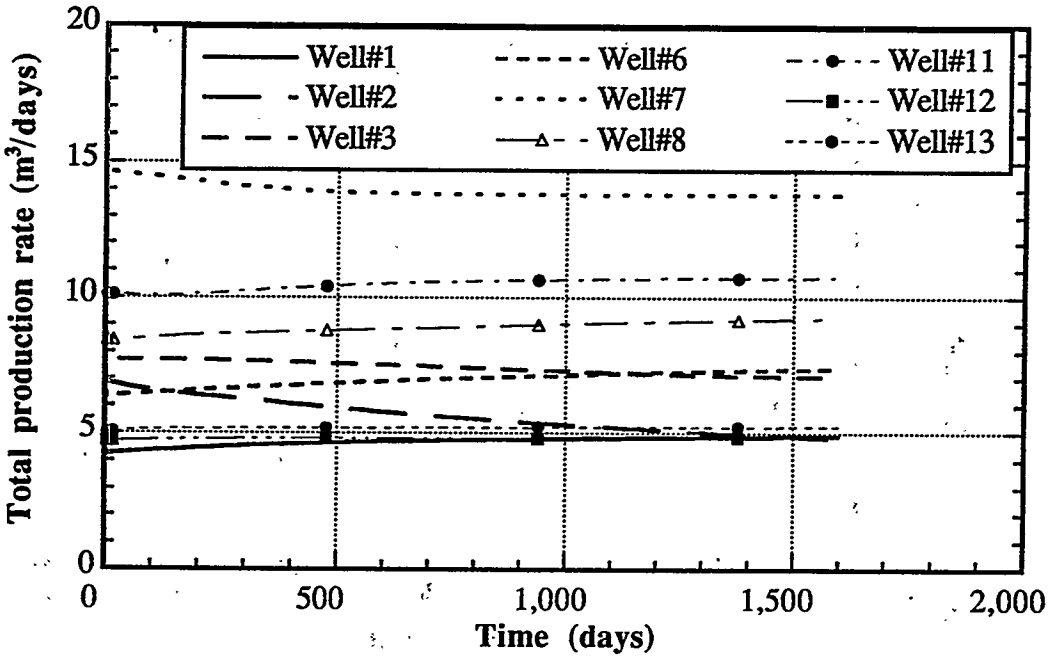


Figure 3.81 History of production rates for all producers as a function of pore volumes injected (optimum bottomhole pressure)

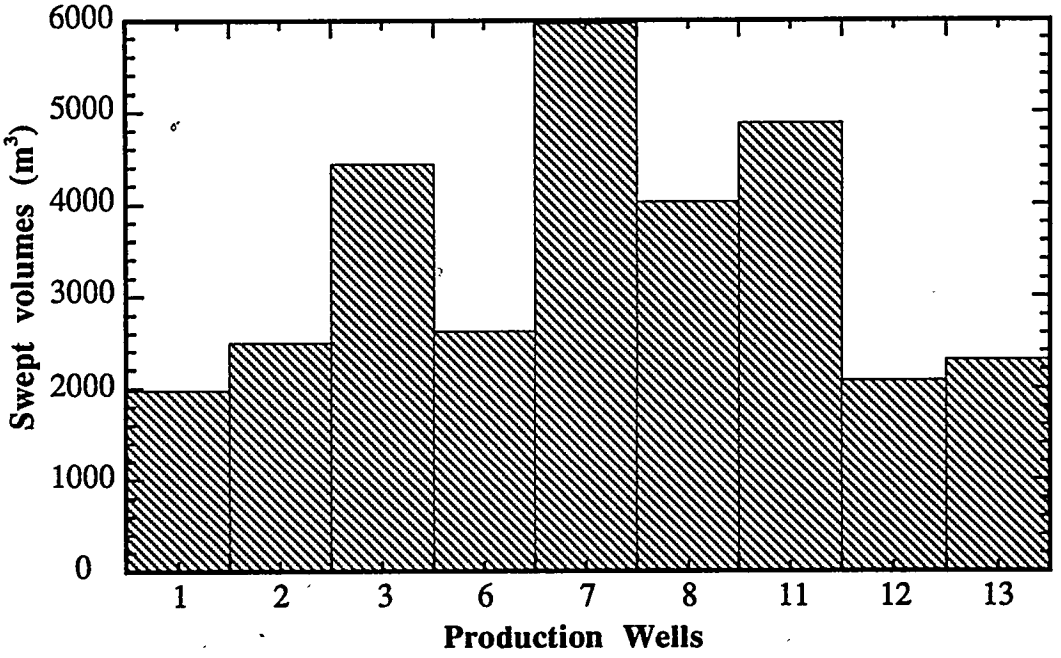


Figure 3.82 Sweep pore volumes for each producer (optimized P_{wf})

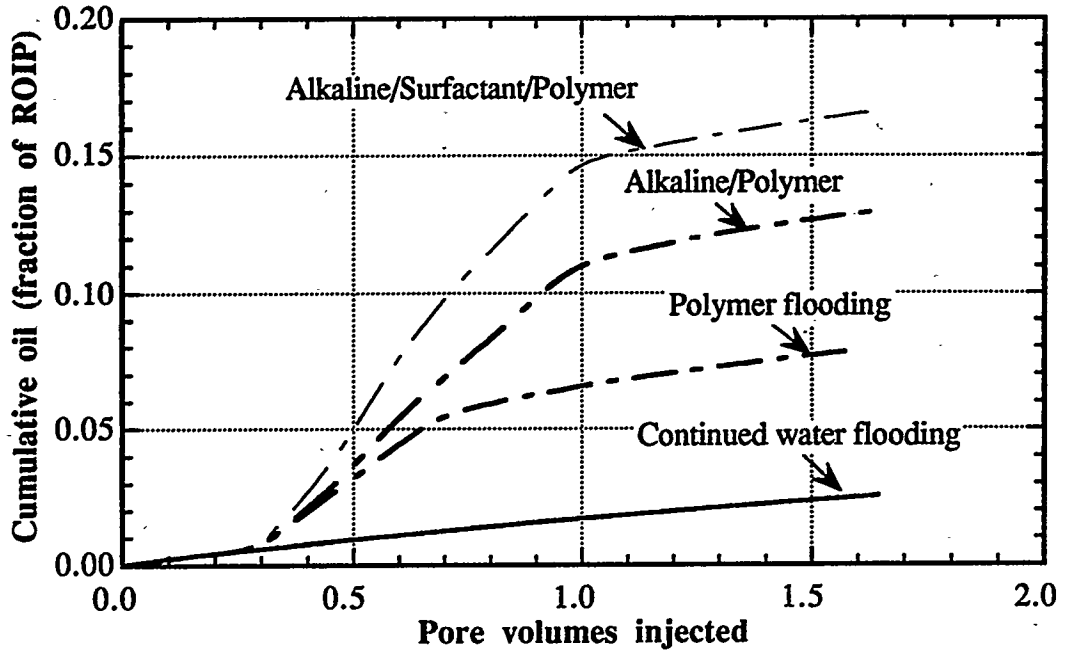


Figure 3.83 Oil recovery for water flooding, polymer flooding, AP flooding, and ASP flooding

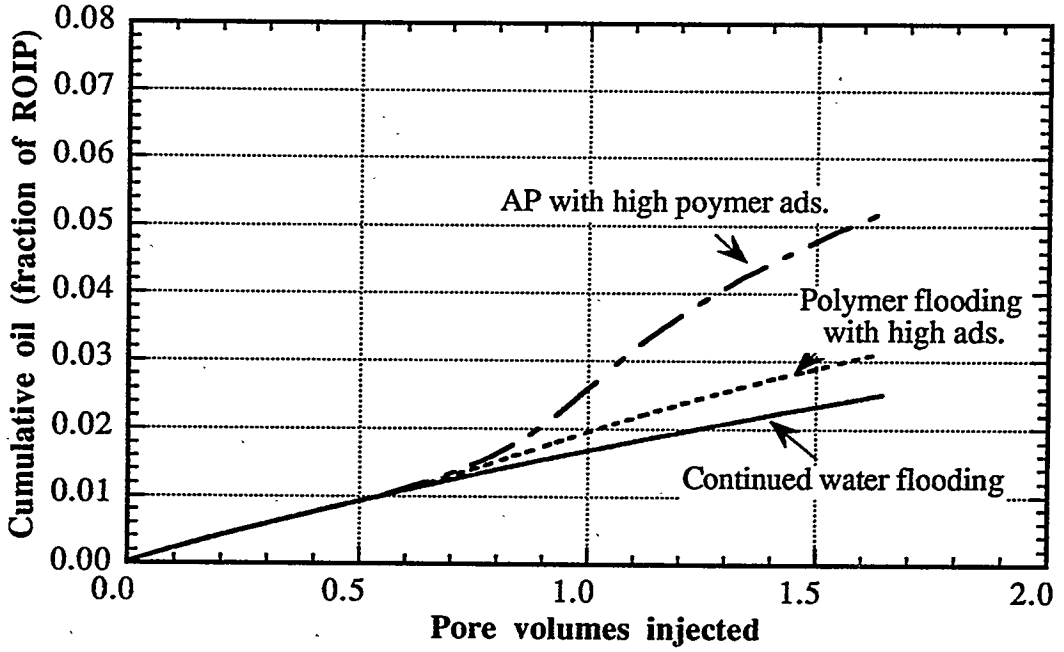


Figure 3.84 Oil recovery for water flooding, polymer flooding, and AP flooding for high polymer adsorption

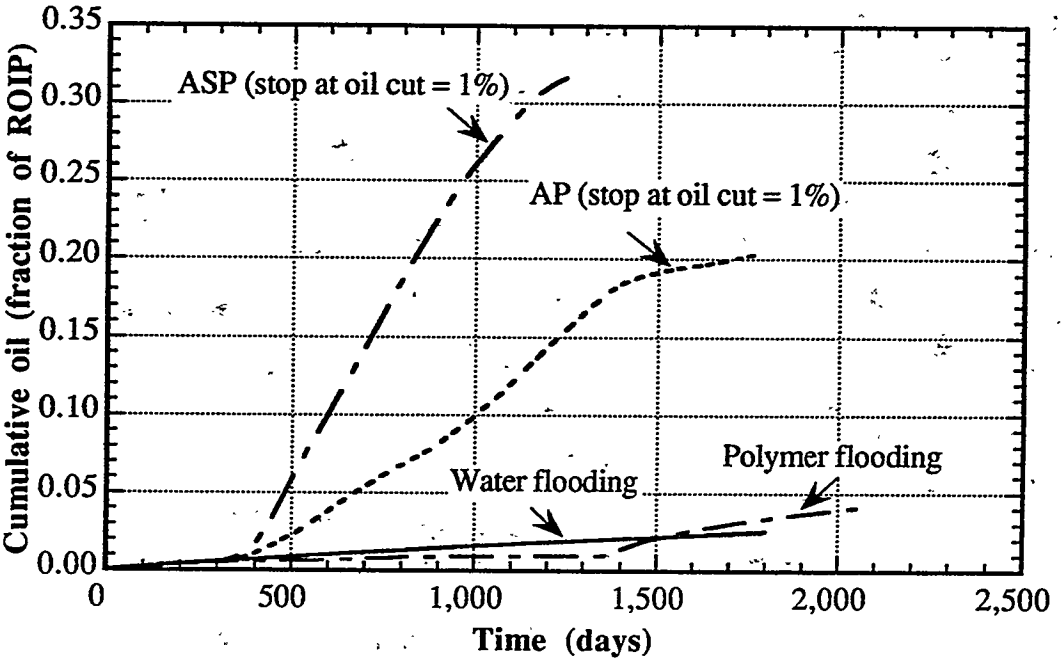


Figure 3.85 Oil recovery for water flooding, polymer flooding, AP flooding, and ASP flooding (Series II)

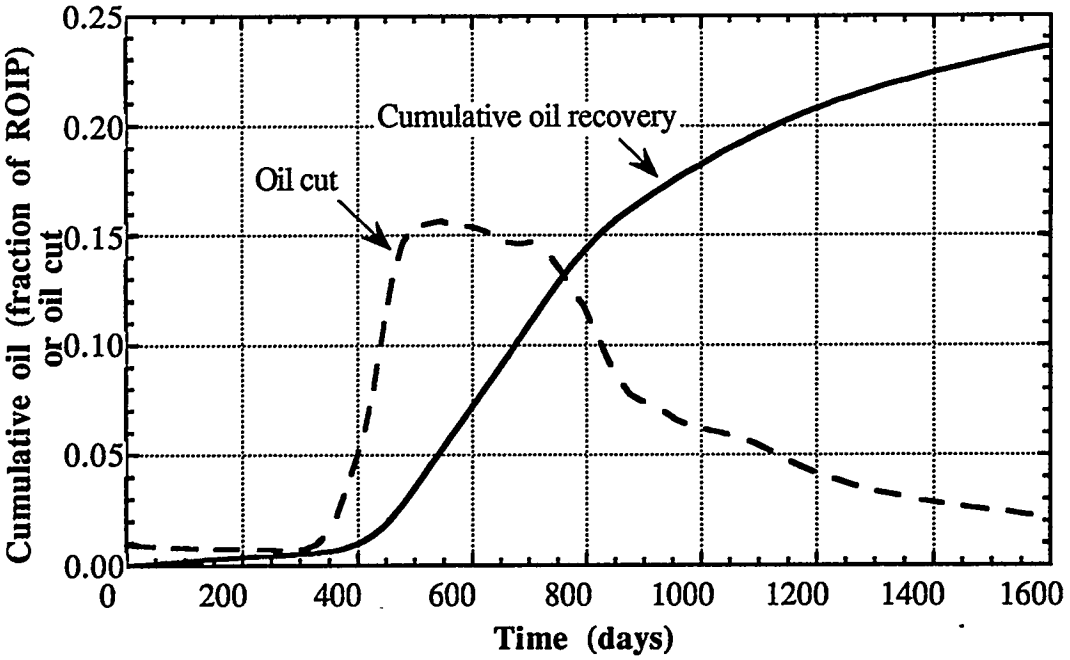


Figure 3.86 Oil recovery and oil cut as a function of time (Base Case)

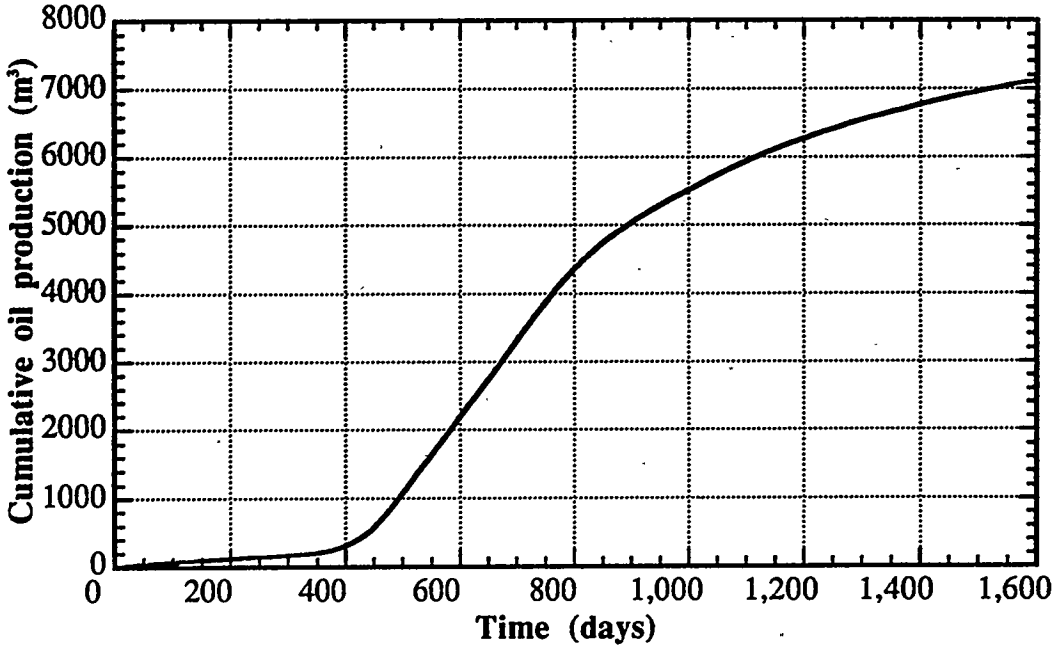


Figure 3.87 Oil production rate as a function of time (Base Case)

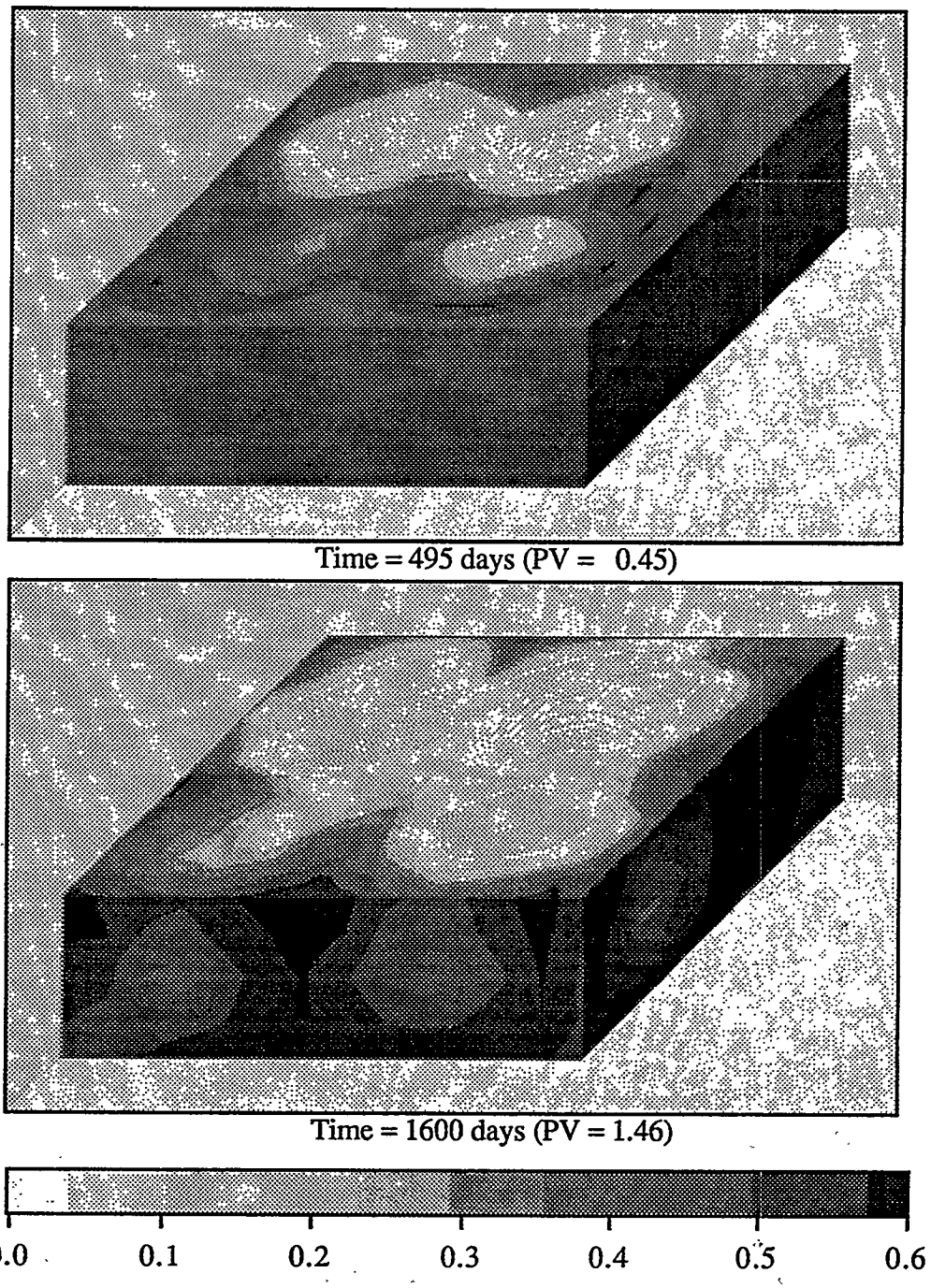
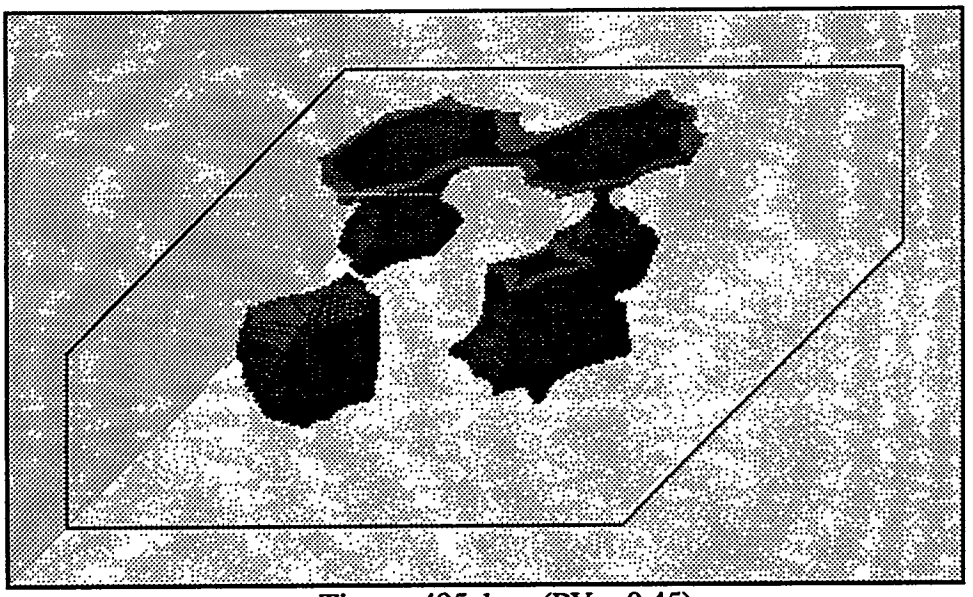
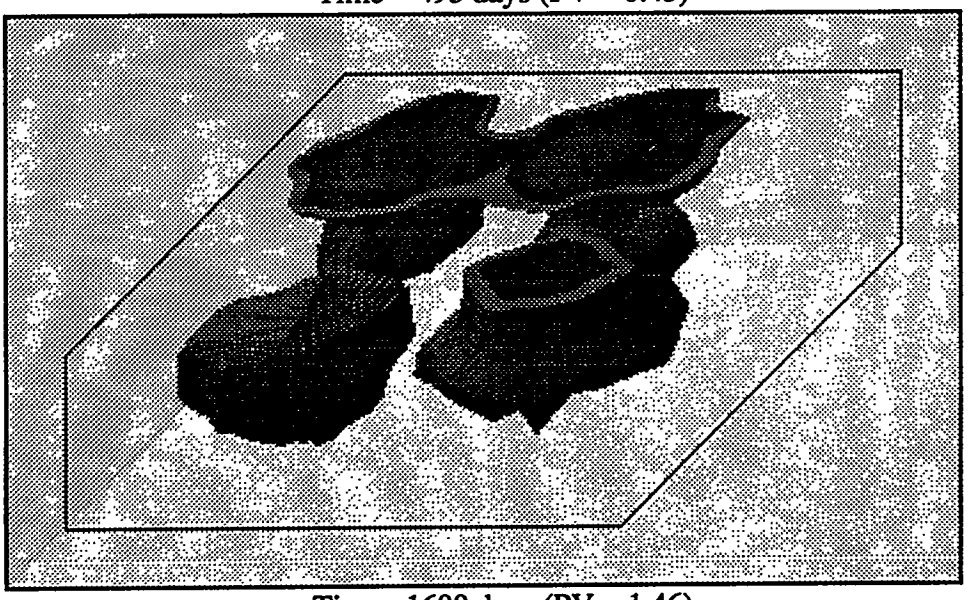


Figure 3.88 Distribution of oil concentration of 0.1 iso-surface for base case



Time = 495 days (PV = 0.45)



Time =1600 days (PV = 1.46)

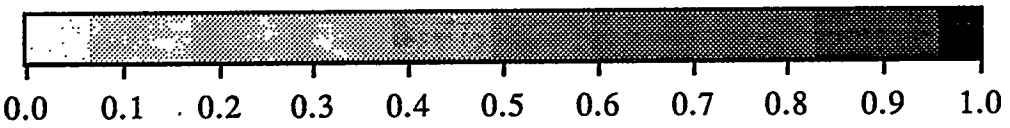


Figure 3.89 Distribution of water concentration of 0.9 iso-surface for Base case

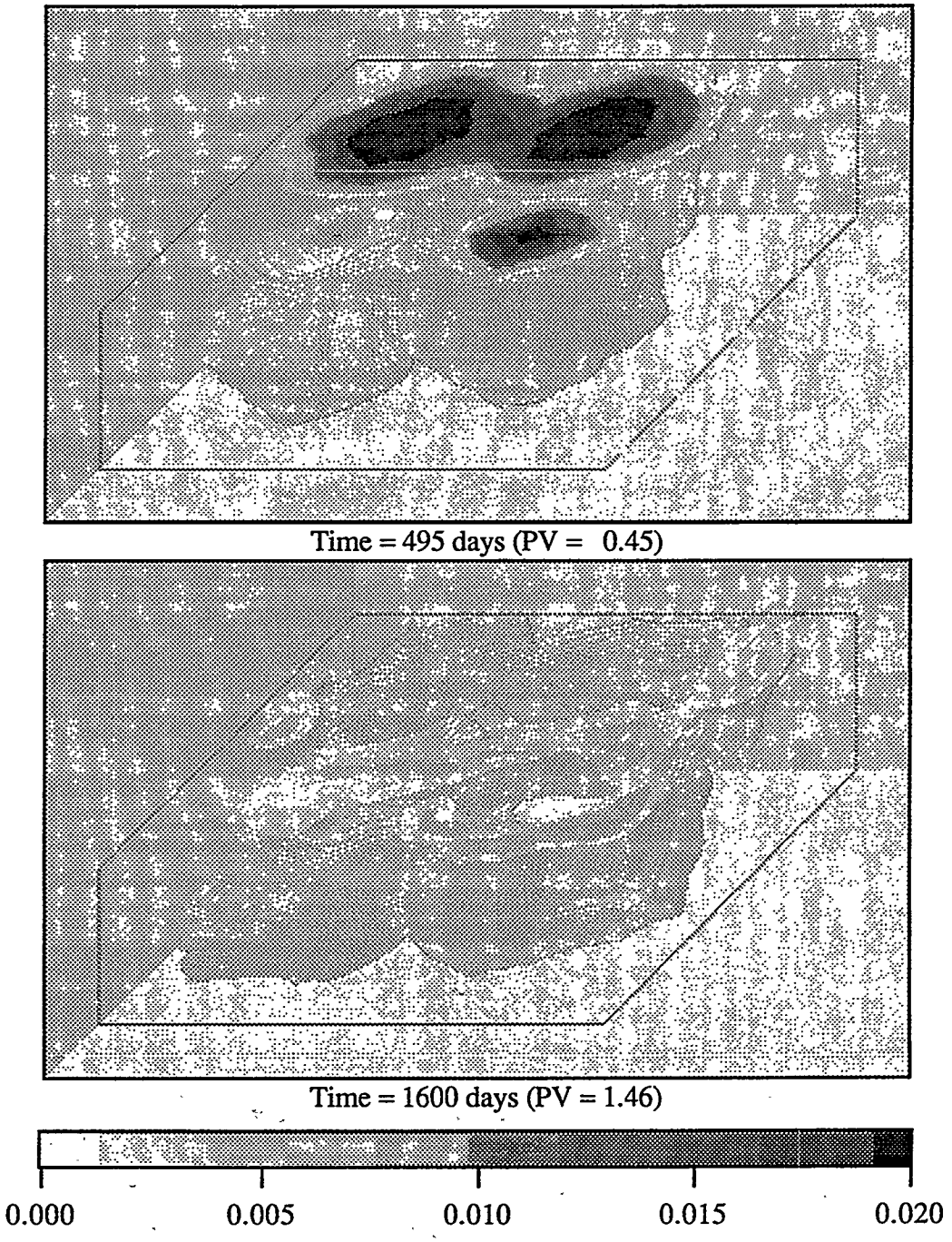


Figure 3.90 Distribution of surfactant concentration of 0.002 iso-surface for base case

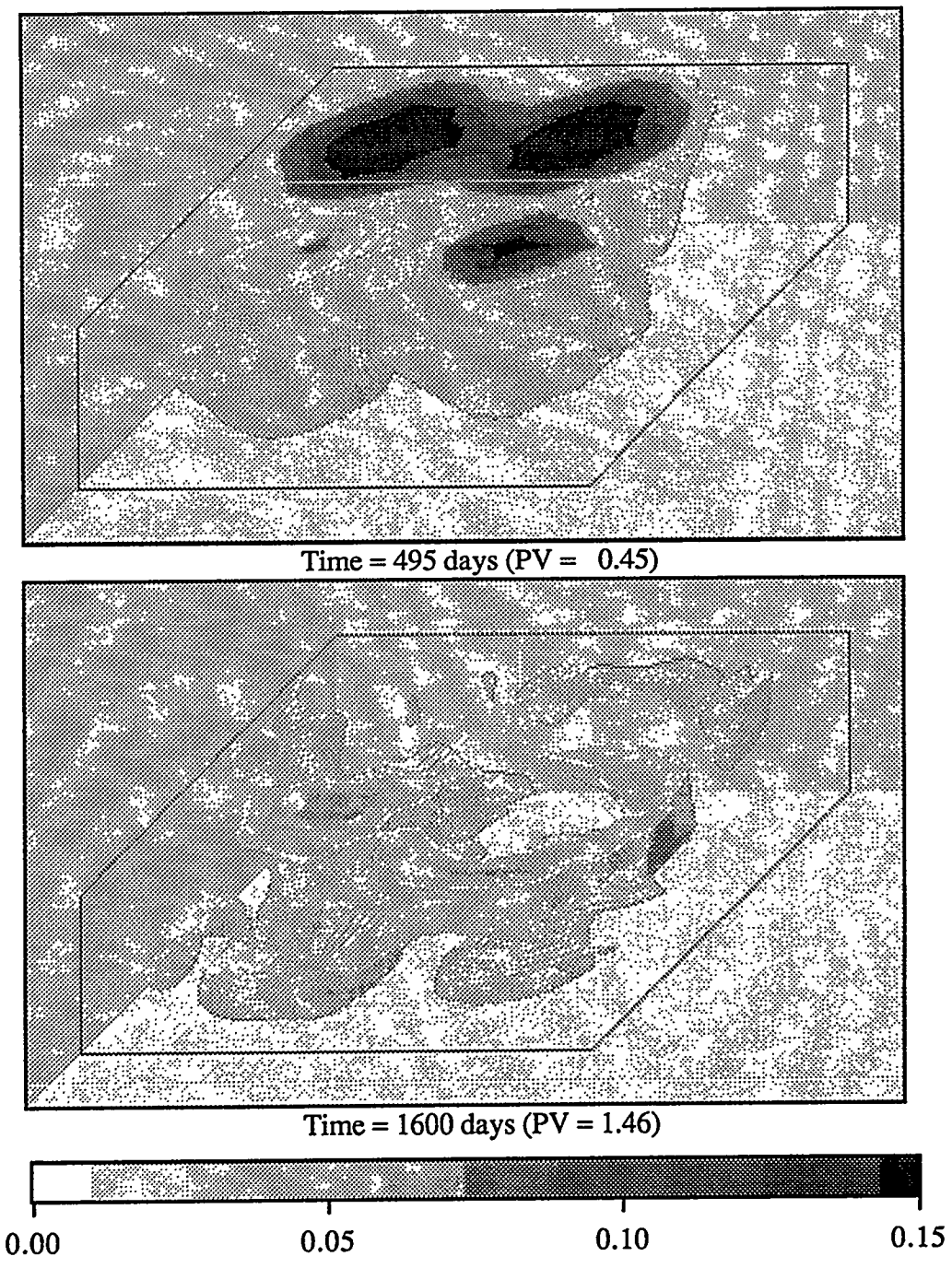
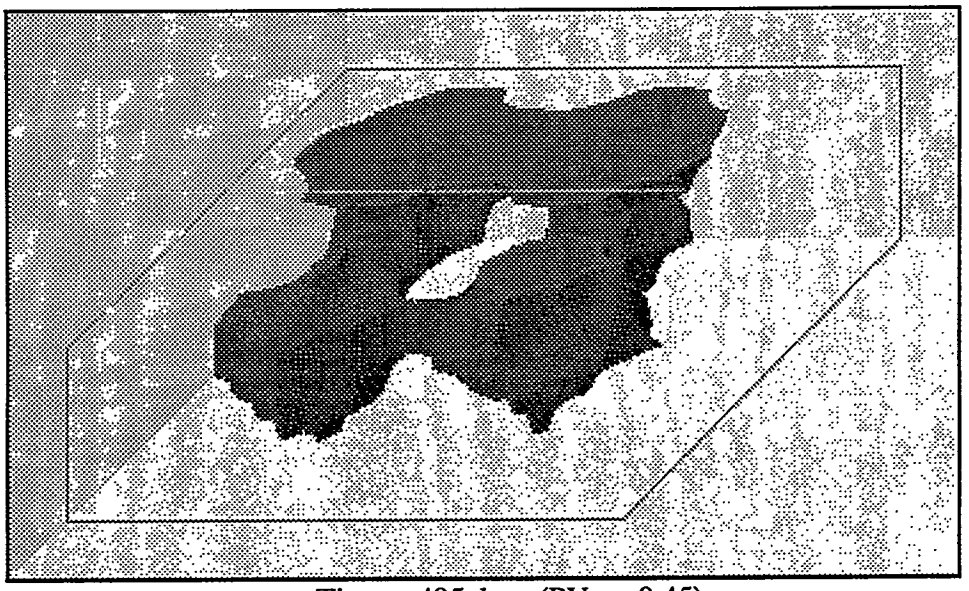
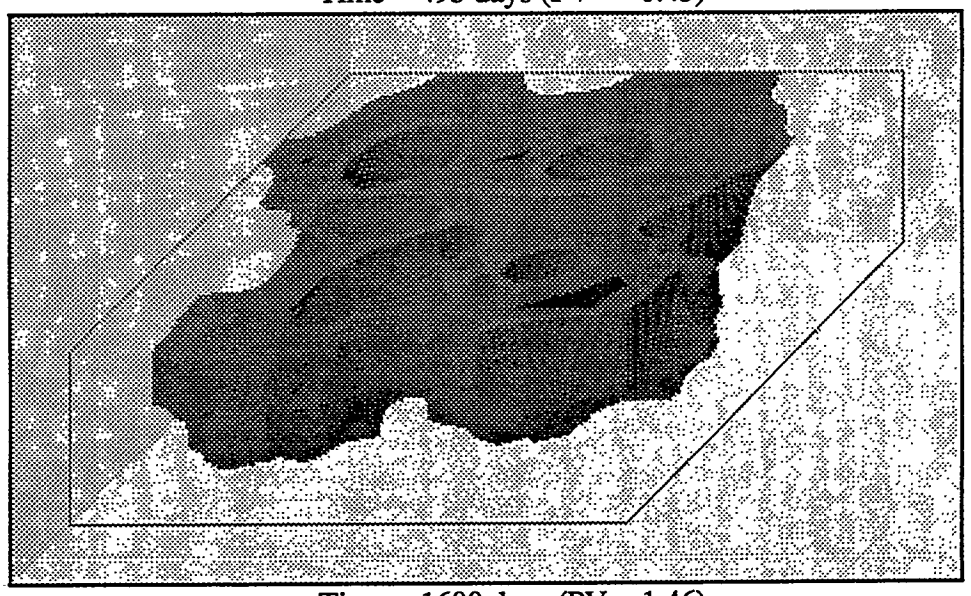


Figure 3.91 Distribution of polymer concentration of 0.025 iso-surface for base case



Time = 495 days (PV = 0.45)



Time = 1600 days (PV = 1.46)

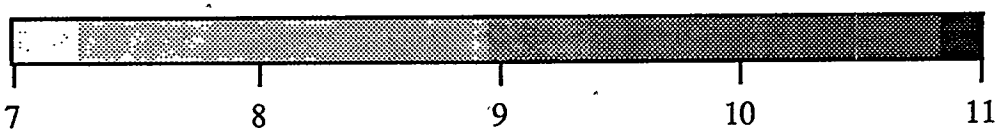


Figure 3.92 Distribution of pH of 10 iso-surface for base case

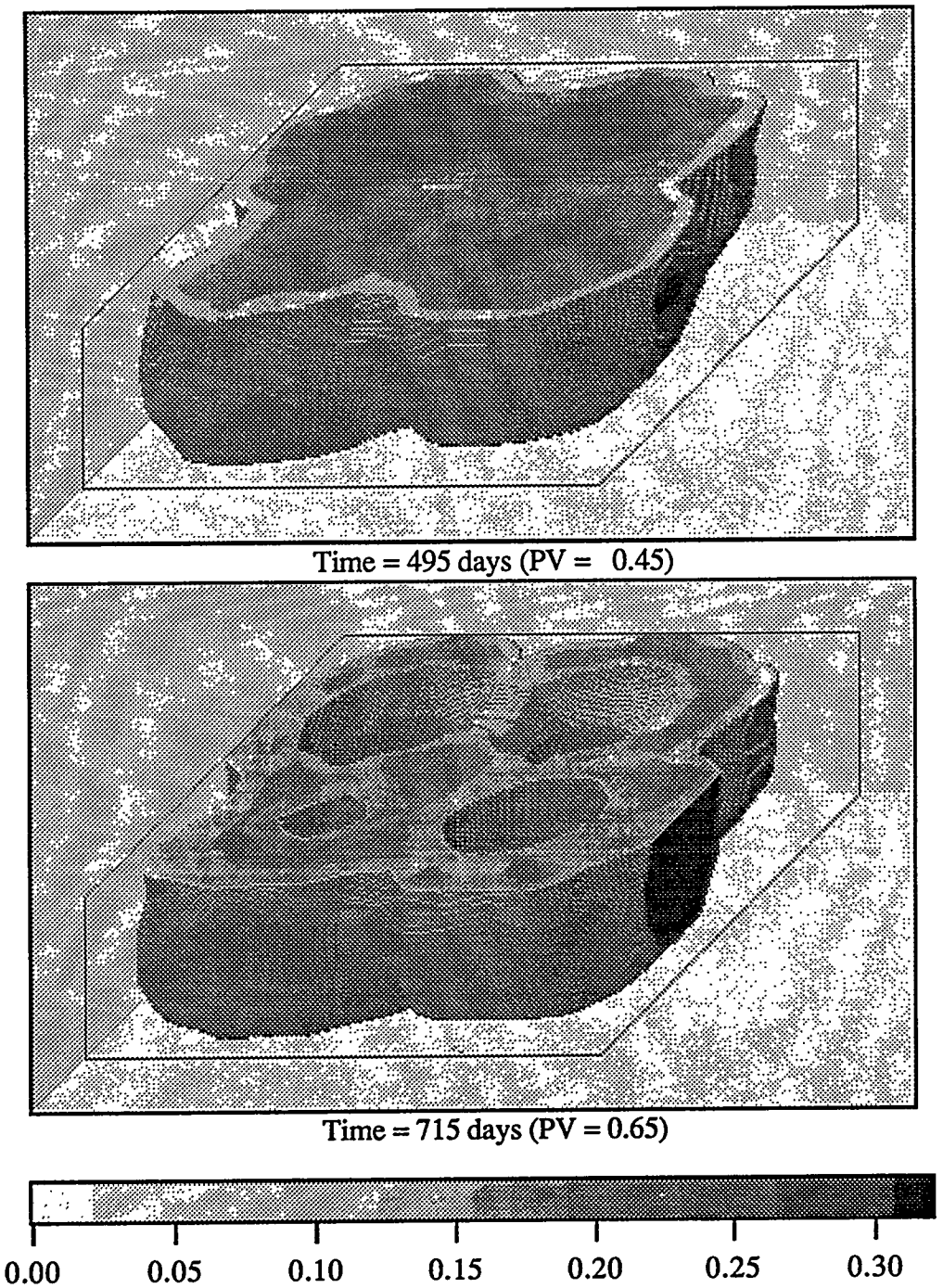


Figure 3.93 Distribution of sodium ion concetration of 0.15 meq/ml iso-surface

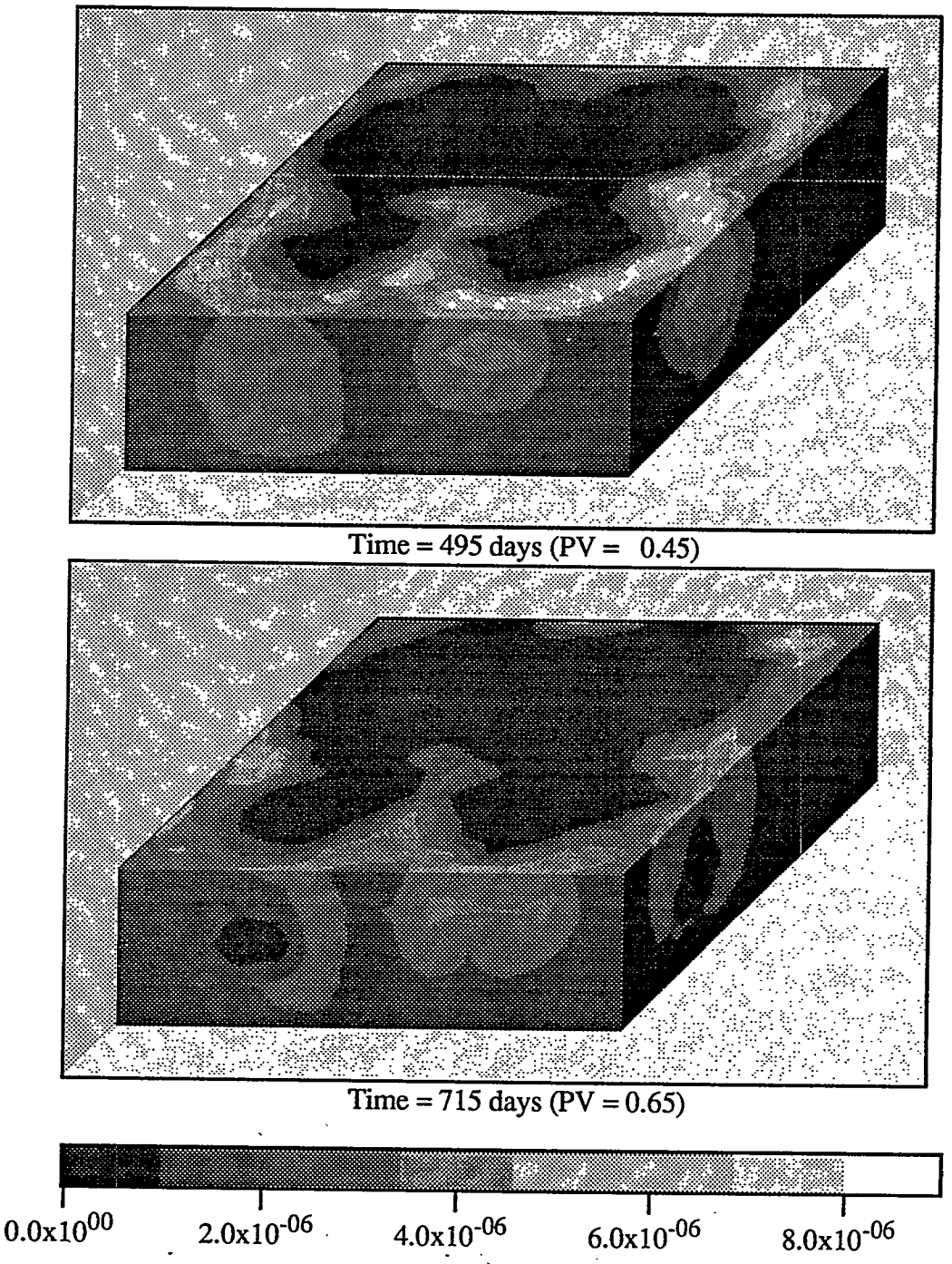


Figure 3.94 Distribution of calcium ion concetration (meq/ml)

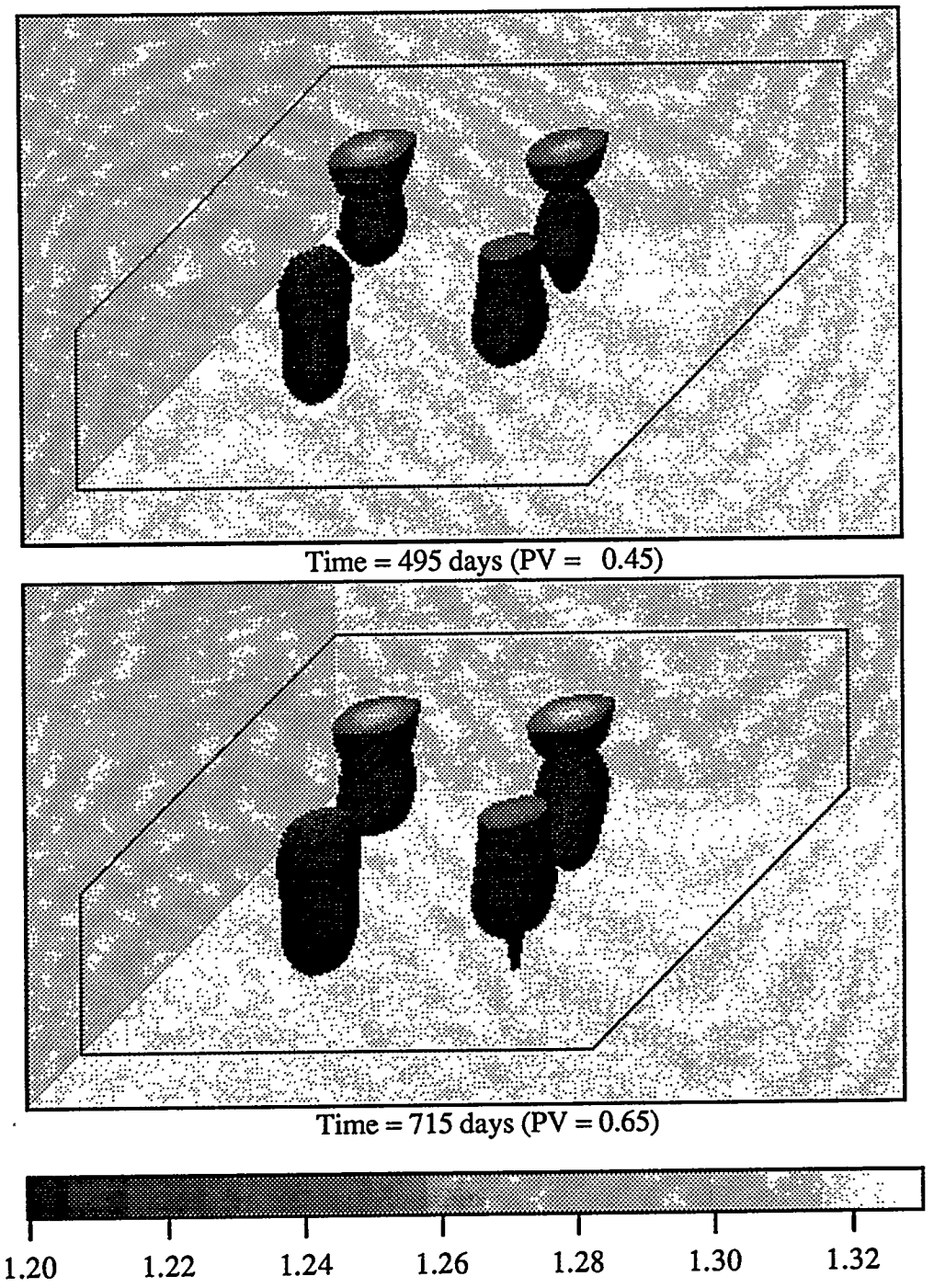


Figure 3.95 Distribution of calcium ion concetration of 1.22 meq/ml iso-surface

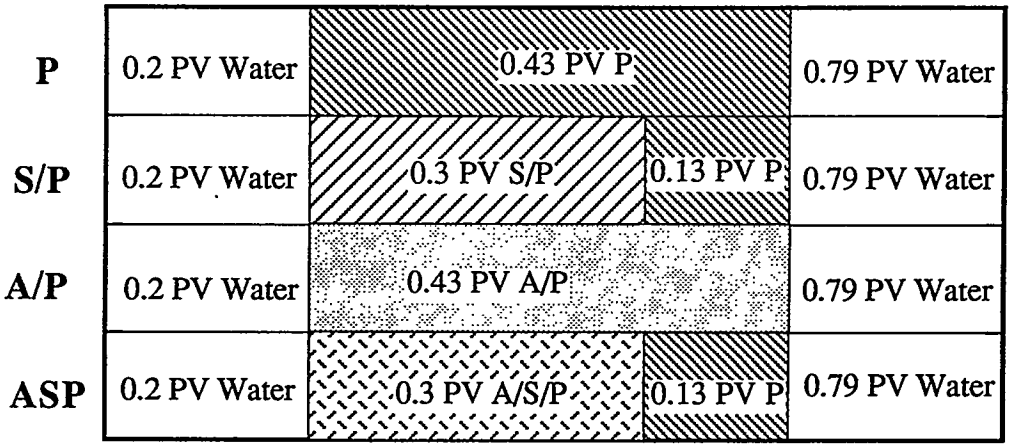


Figure 3.96 Injection scheme for each enhanced oil recovery process

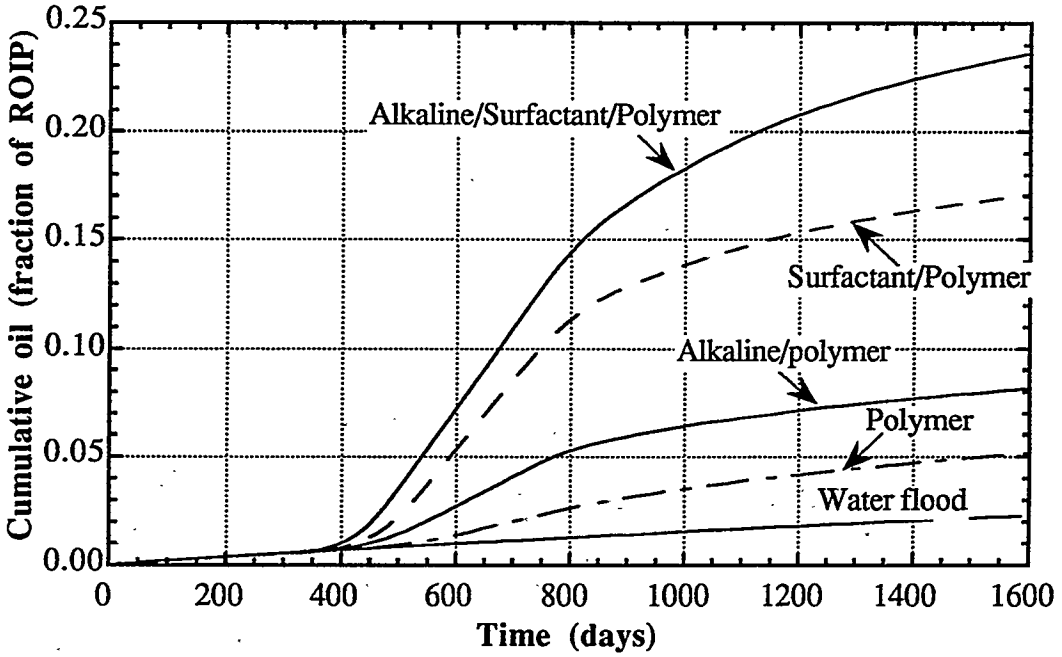


Figure 3.97 Comparison of oil recovery for different enhanced oil recovery processes for Reservoir D

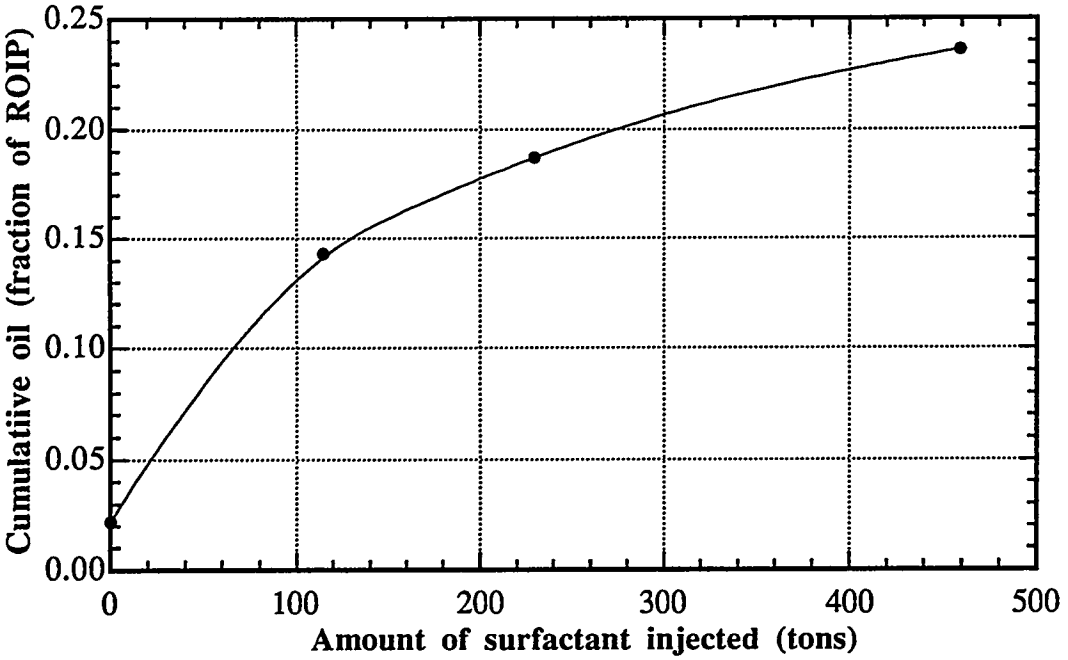


Figure 3.98 Cumulative oil recovery as a function of amount of injected surfactant

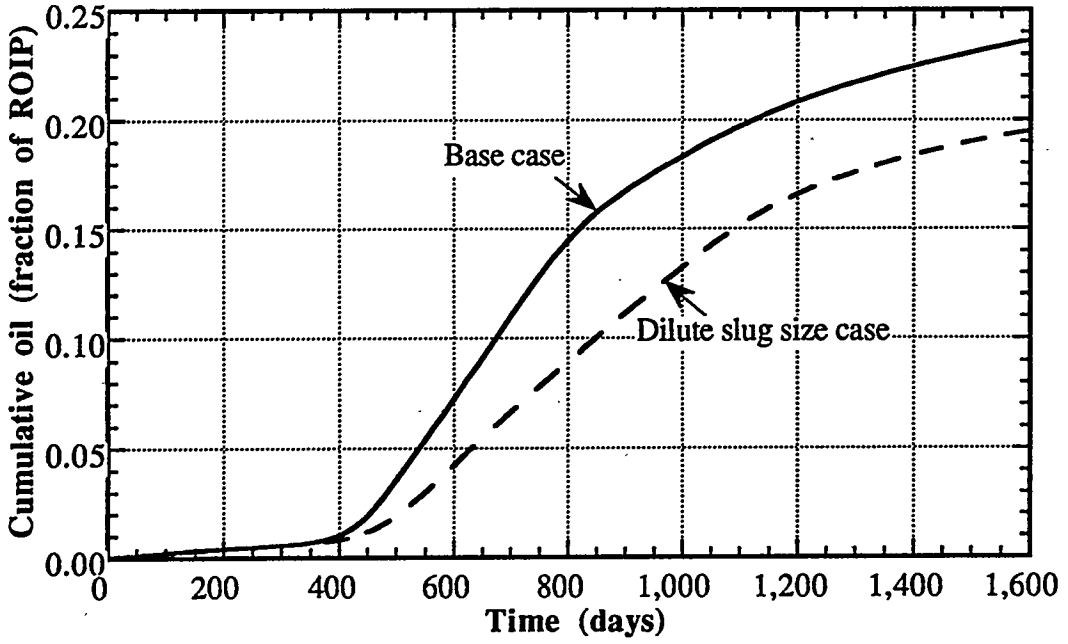


Figure 3.99 Comparison of oil recovery between dilute ASP slug and Base Case simulations

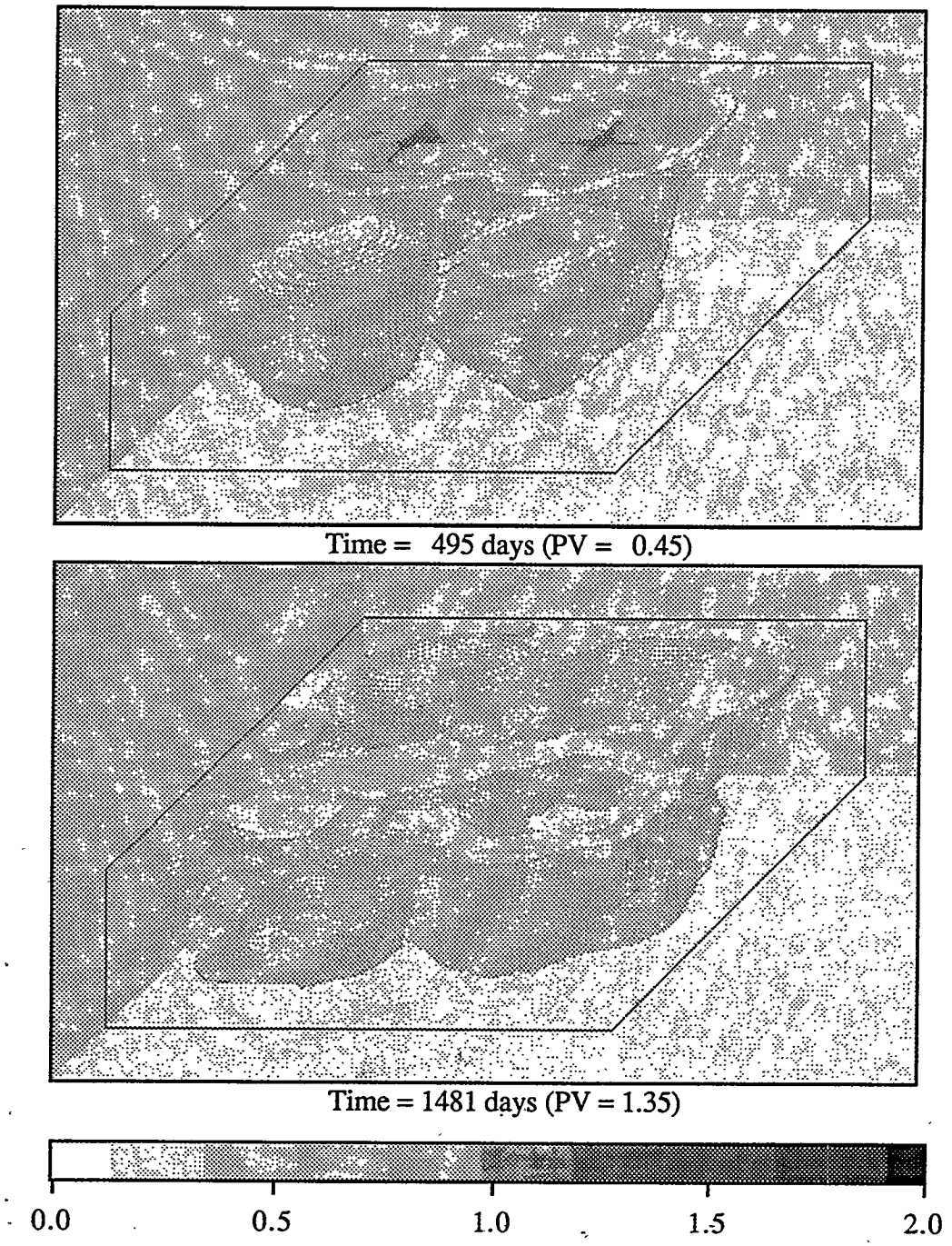
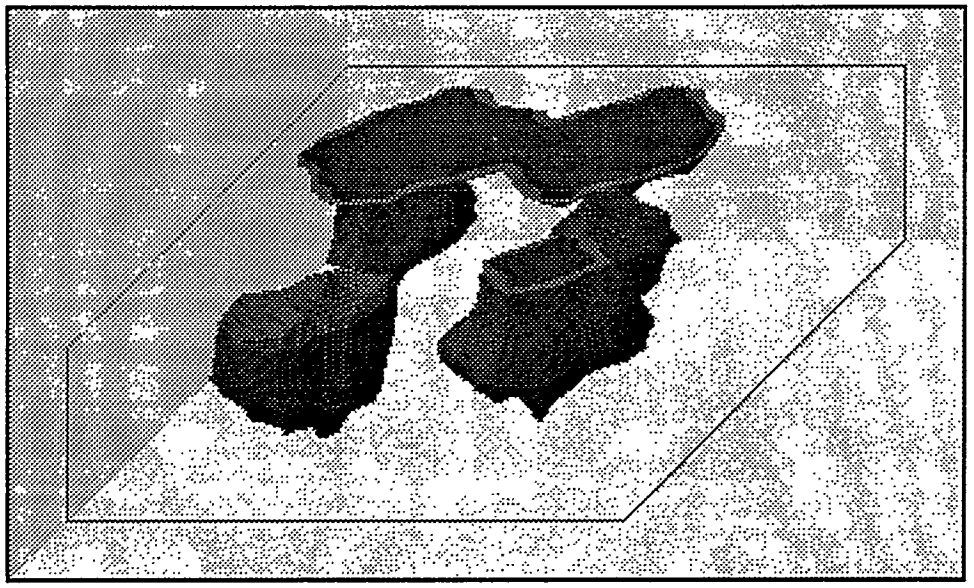
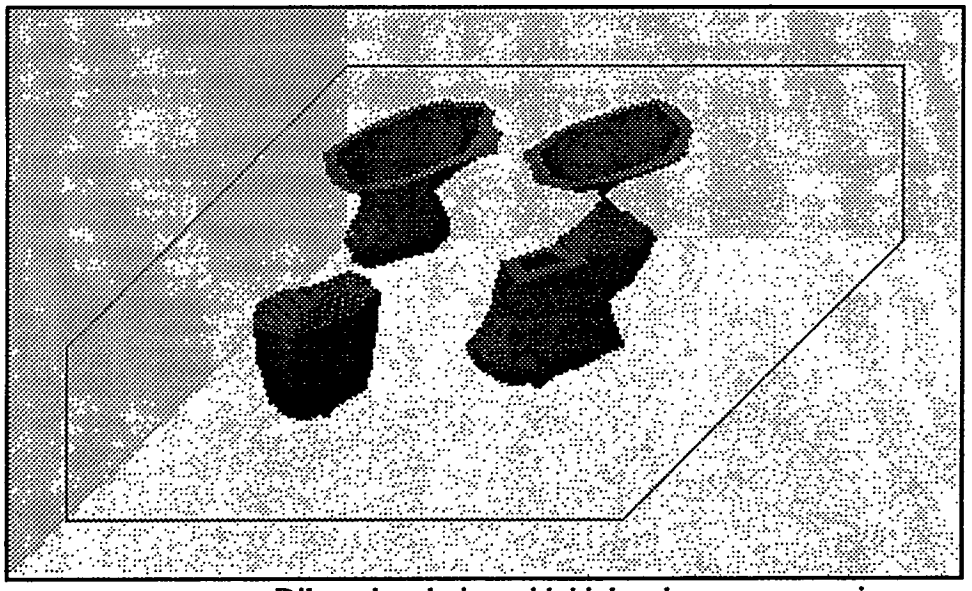


Figure 3.100 Distribution of surfactant concentration of 0.2 vol.% iso-surface for dilute surfactant slug size case



Base case



Dilute slug design with high polymer concetration

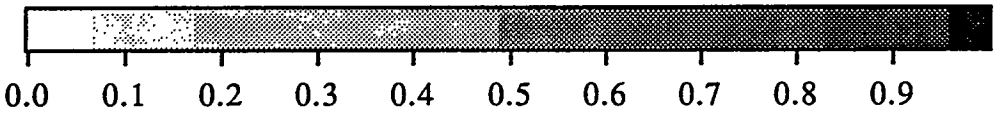


Figure 3.101 Distribution of surfactant concentrations of 0.9 iso-surface for Base Case and dilute surfactant slug size case

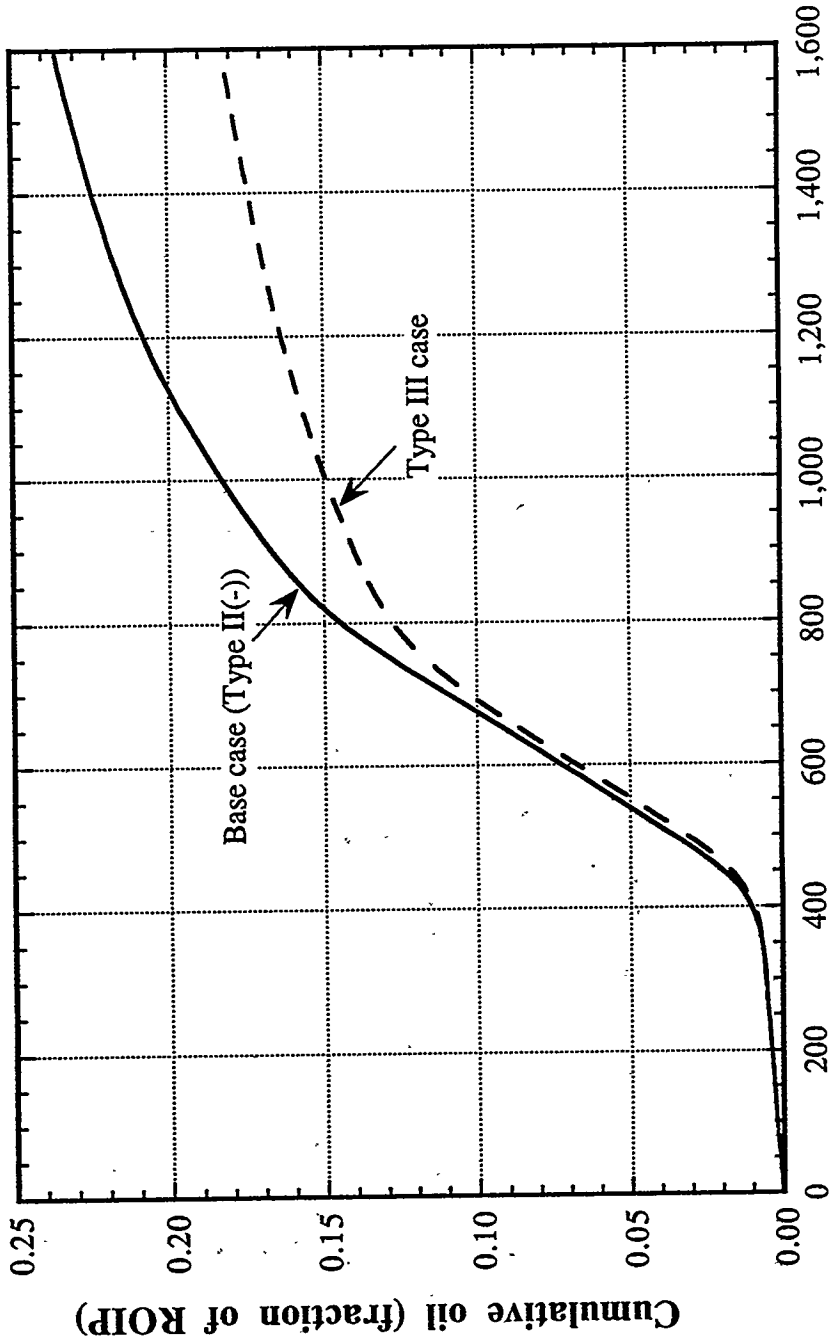


Figure 3.102 Effect of phase behavior on the oil recovery

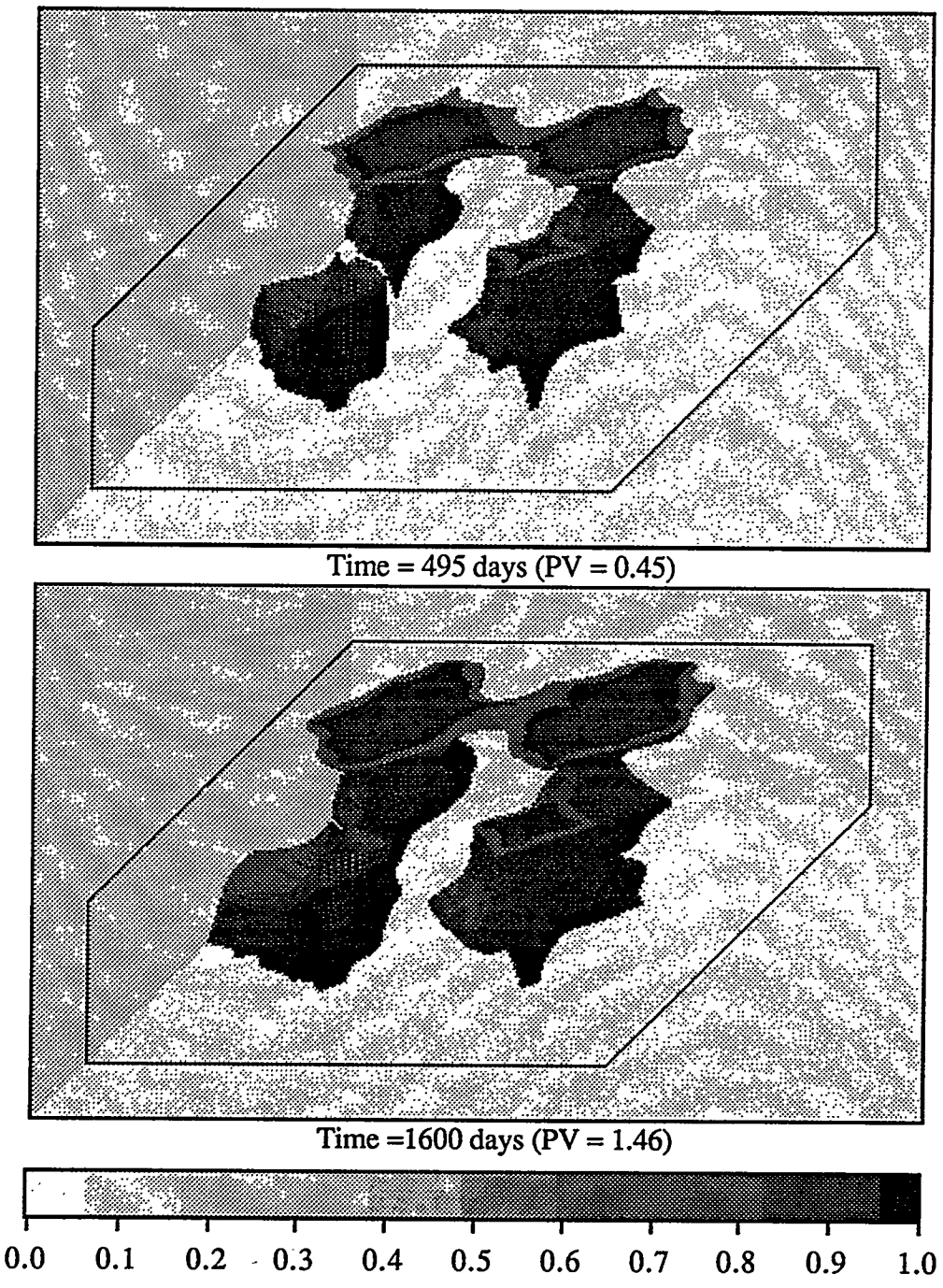


Figure 3.103 Distributions of water concentration of 0.9 iso-surface for Type III Case

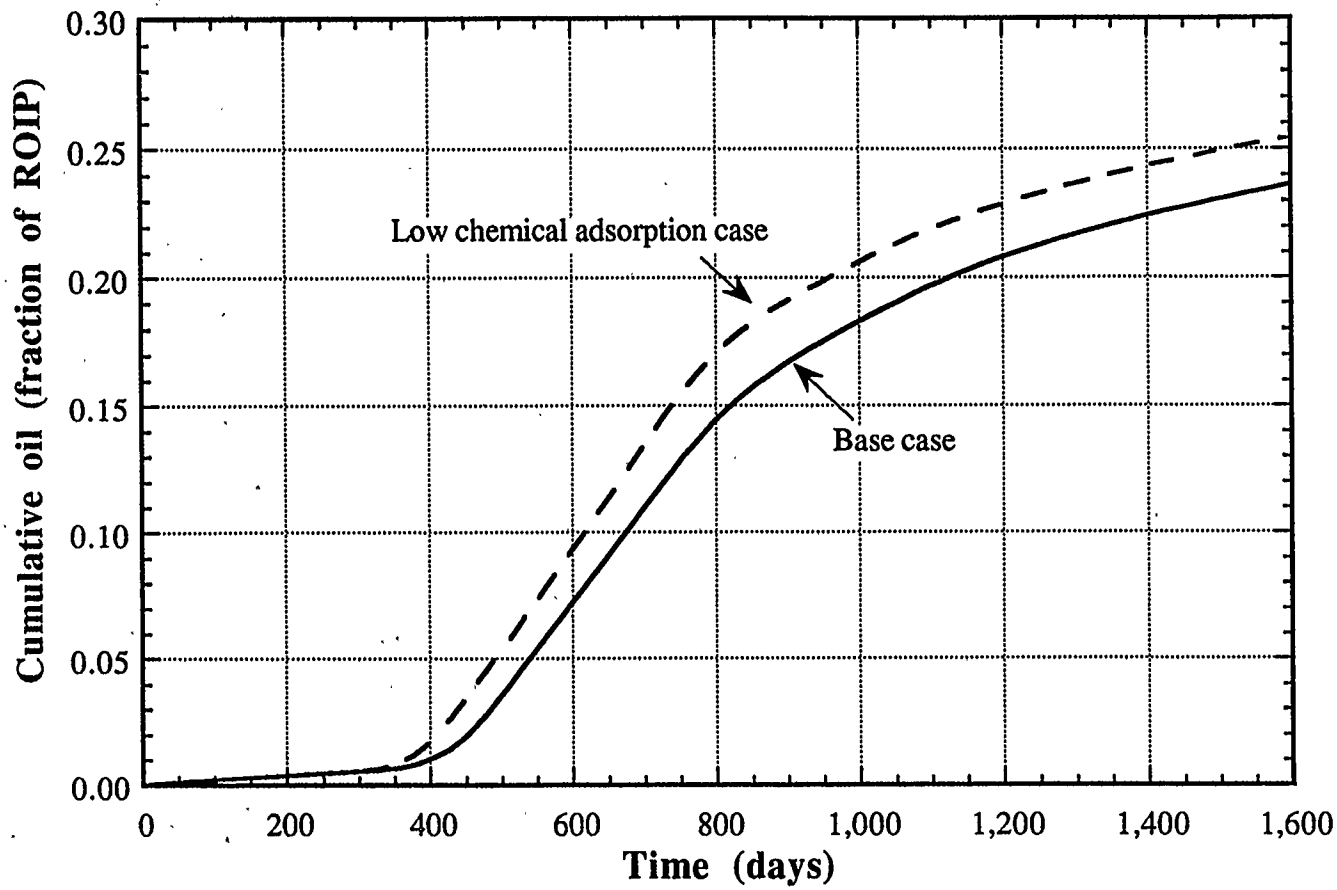


Figure 3.104 Comparison of oil recovery between low chemical adsorption and Base Case

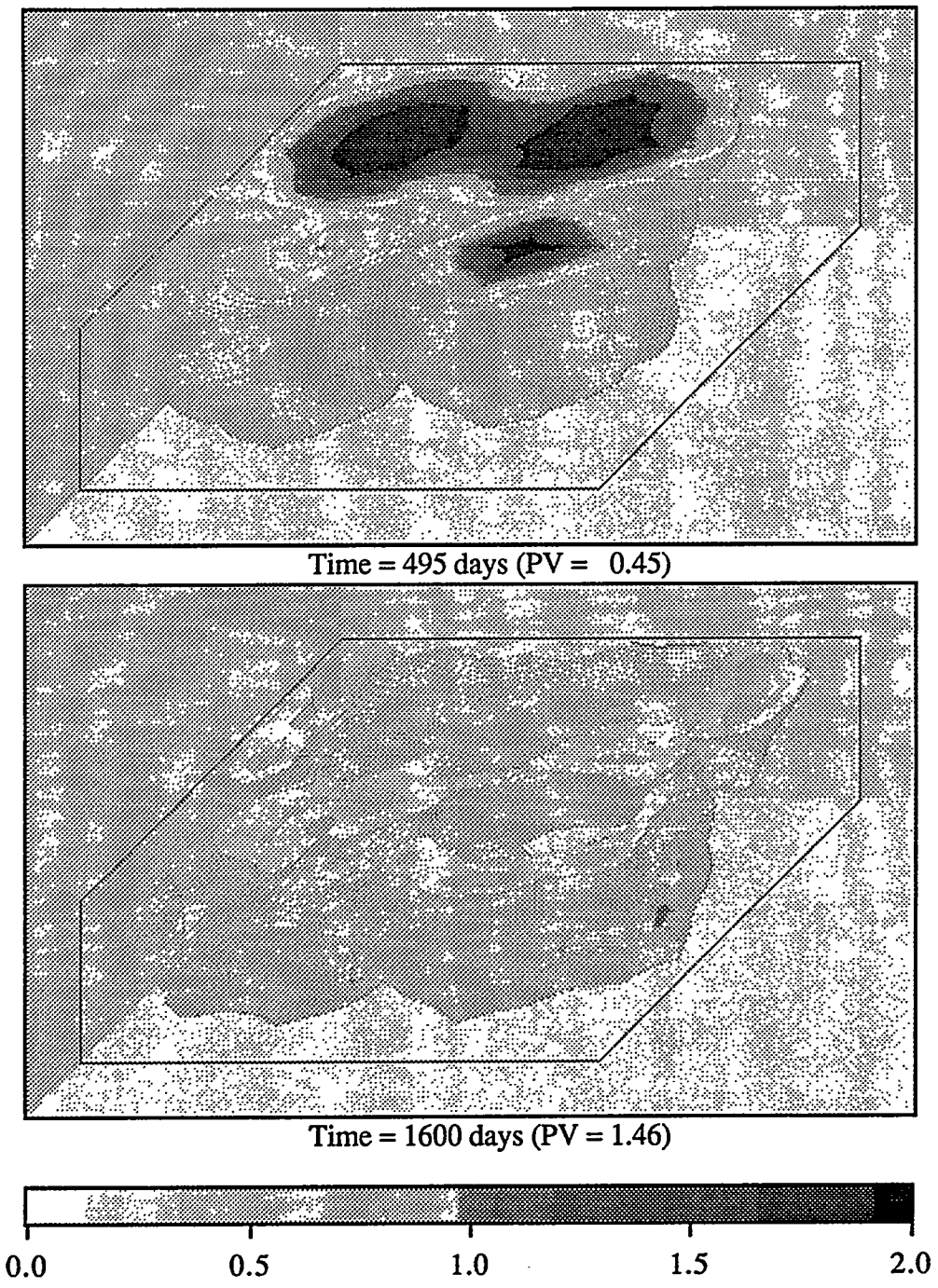


Figure 3.105. Distributions of surfactant concentration of 0.2 vol% iso-surface for low chemical adsorption case

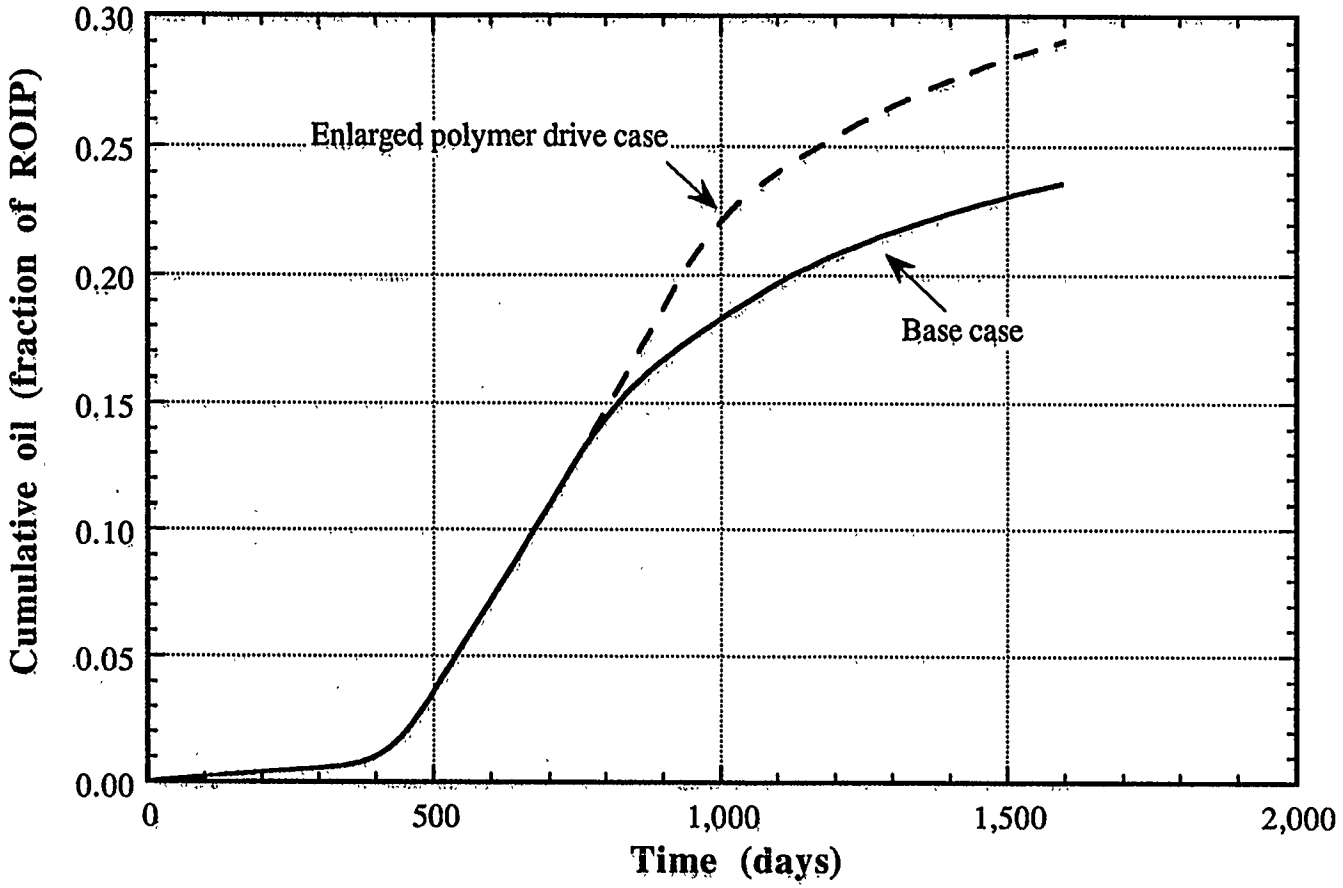


Figure 3.106 Comparison of oil recovery between large polymer drive and Base Case

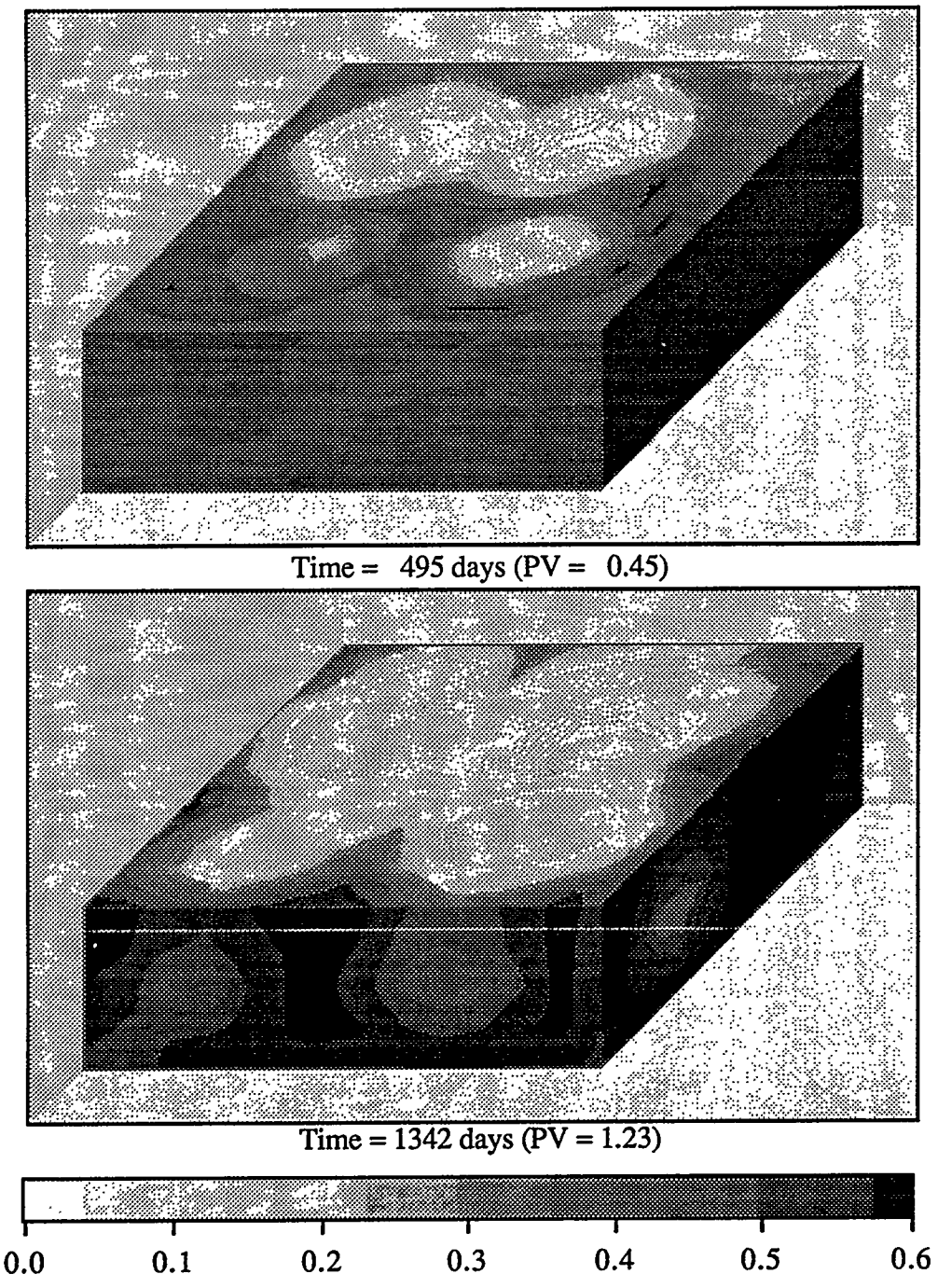


Figure 3.107 Distributions of oil concentration of 0.1 iso-surface for enlarged polymer drive case

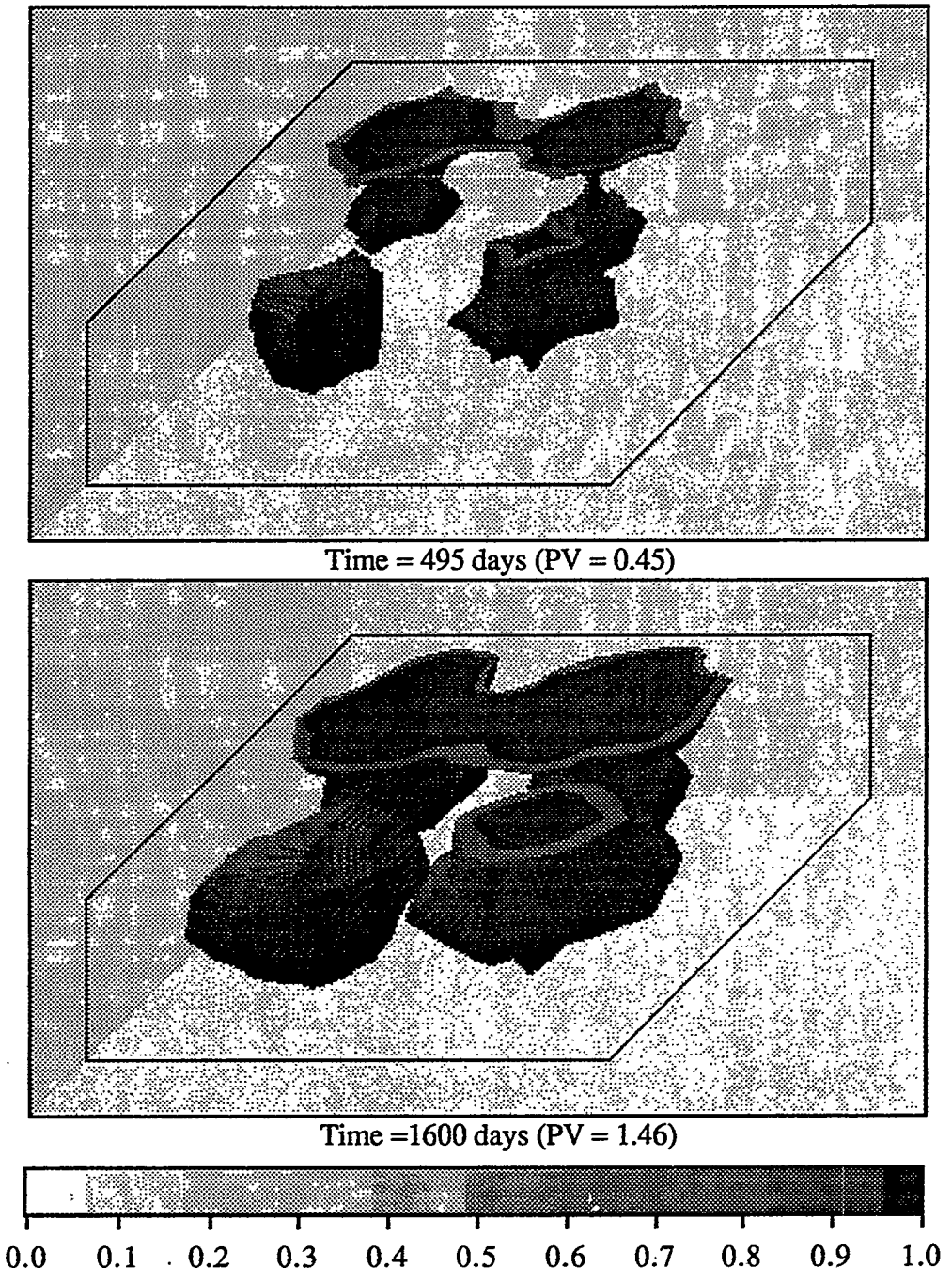


Figure 3.108 Distributions of water concentration of 0.9 iso-surface for enlarged polymer drive case

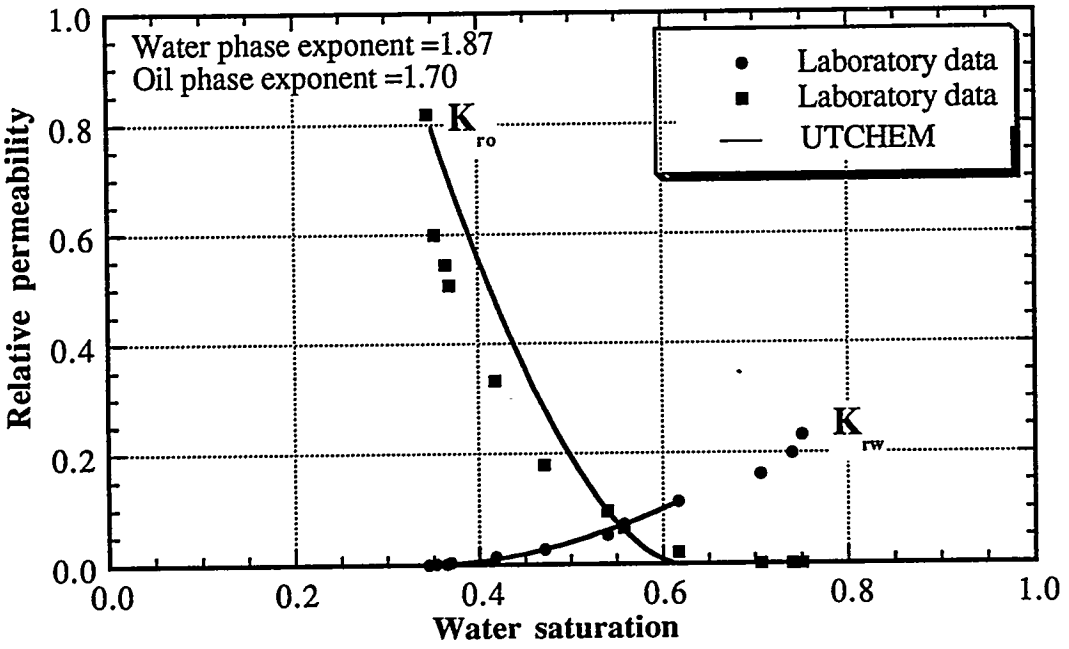


Figure 3.109 Oil and water relative permeabilities at low capillary number

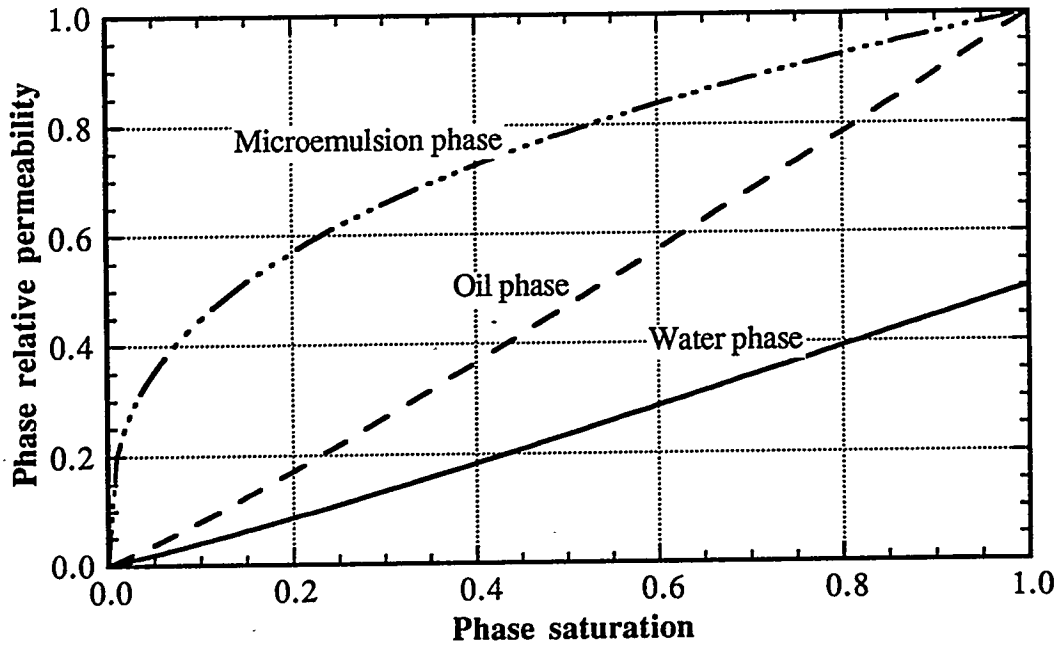


Figure 3.110 Relative permeability curves at high capillary number used for reservior coreflood histor match

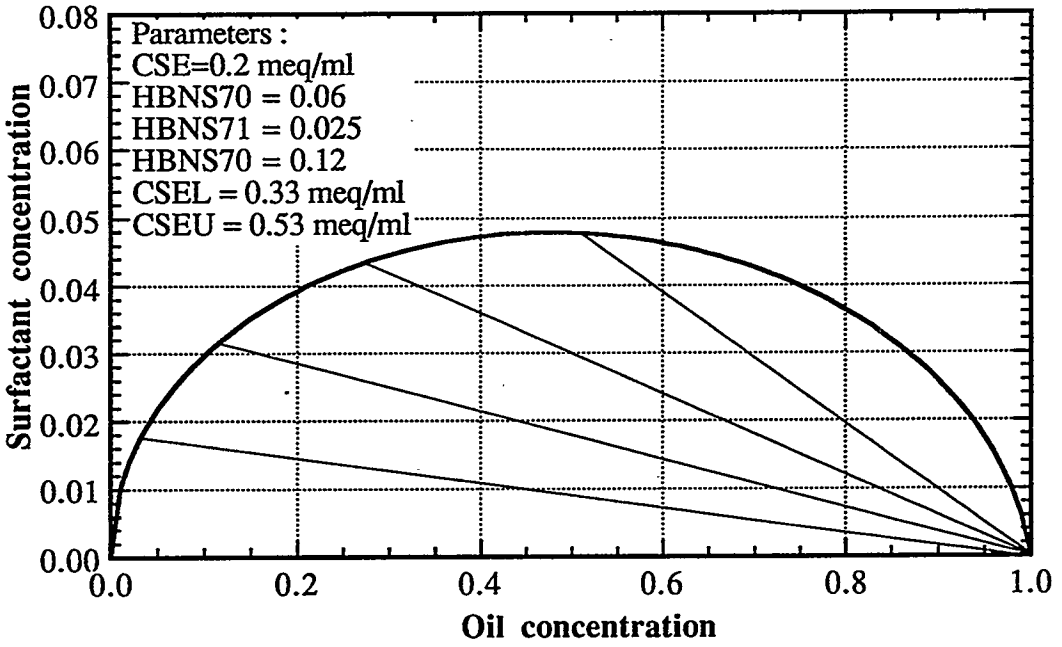


Figure 3.111 Phase behavior diagram used for reservior coreflood history match

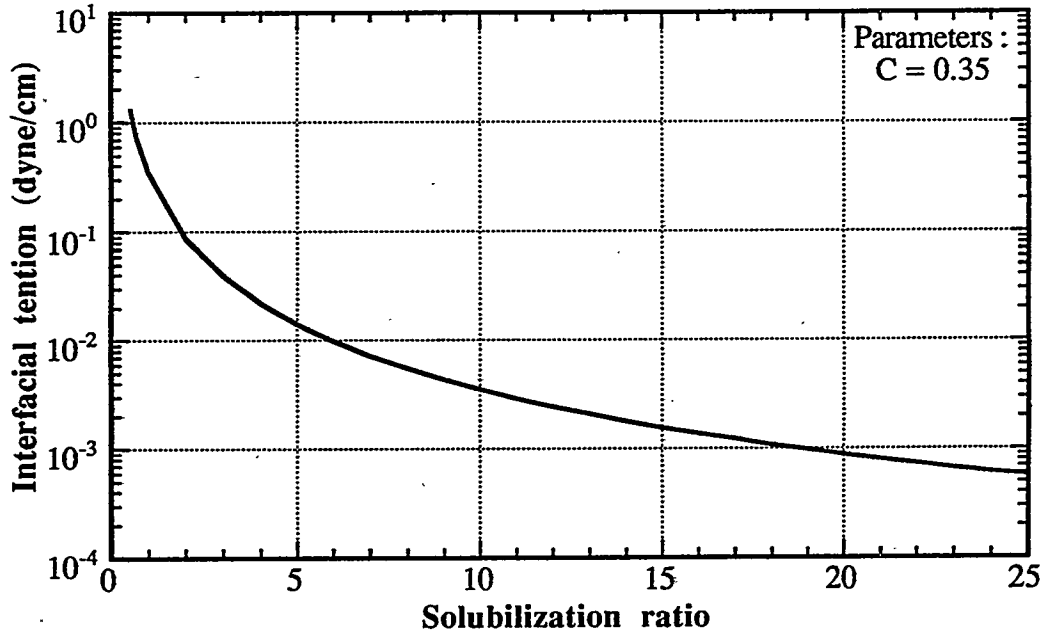


Figure 3.112 Interfacial tension vs. solubilization ratio used for reservior coreflood history match

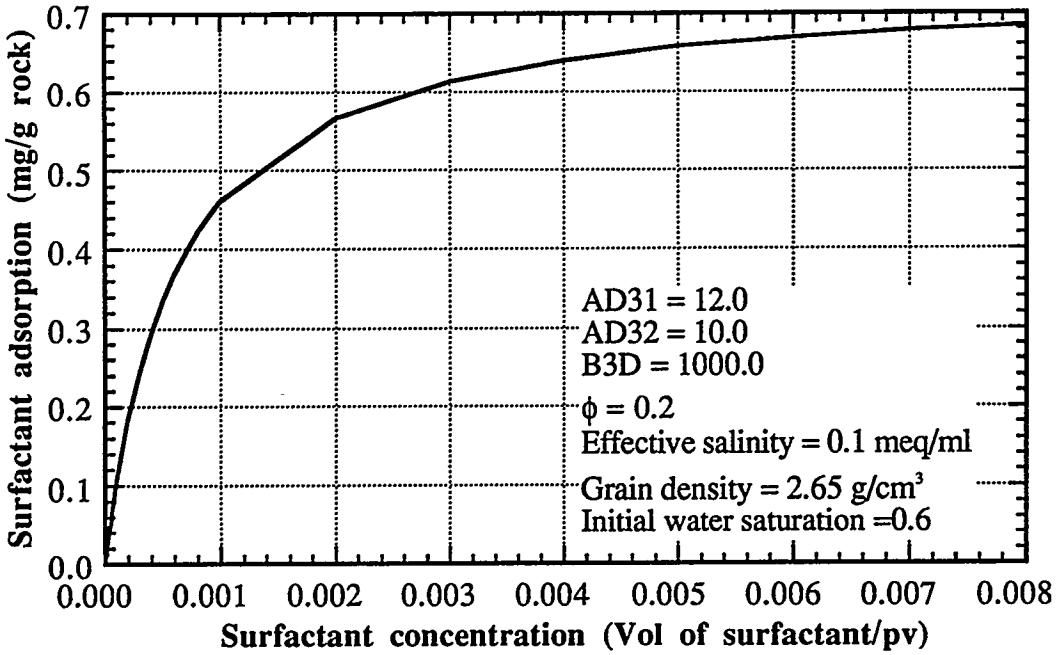


Figure 3.113 Surfactant adsorption isotherm used for reservoir coreflood history match

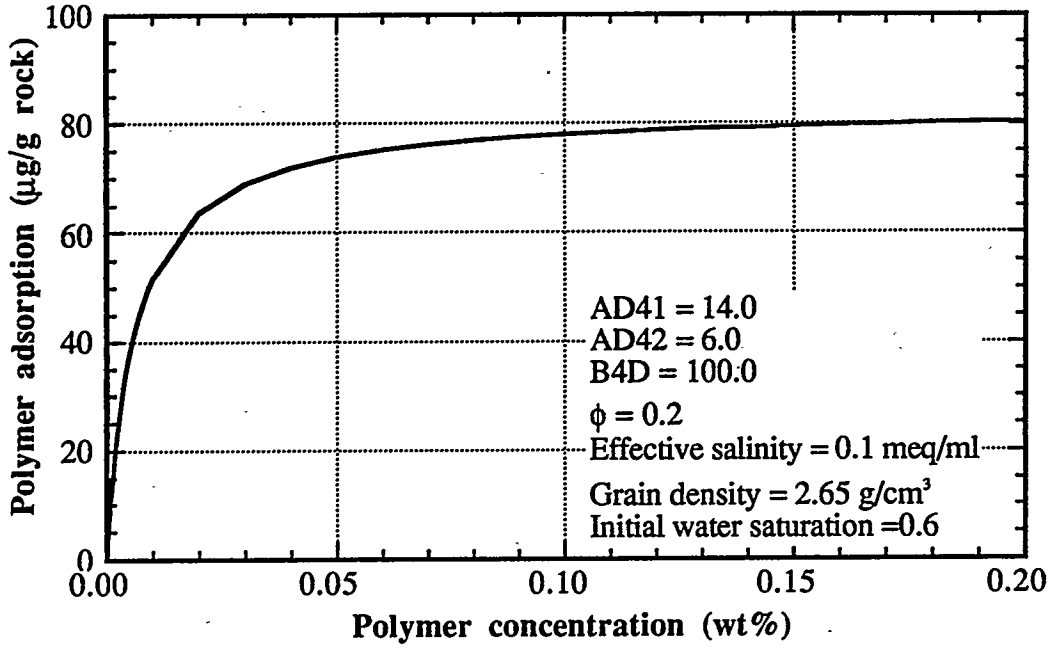


Figure 3.114 Polymer adsorption isotherm used for reservoir coreflood history match

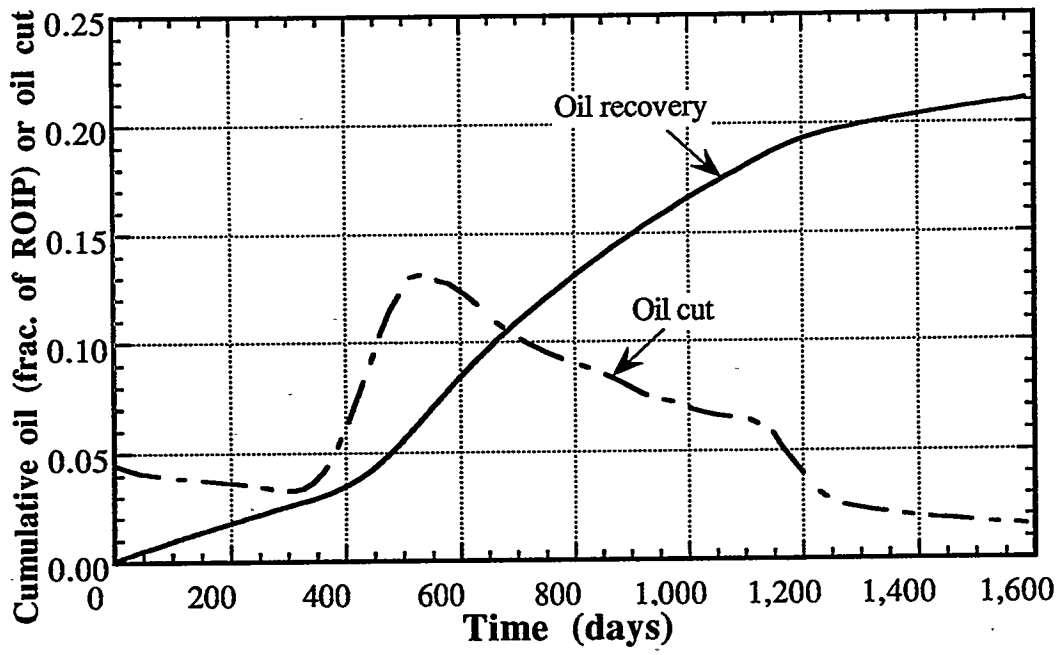


Figure 3.115 Cumulative oil recovery and oil cut as a function of time for ASP field study based on reservoir core flooding data

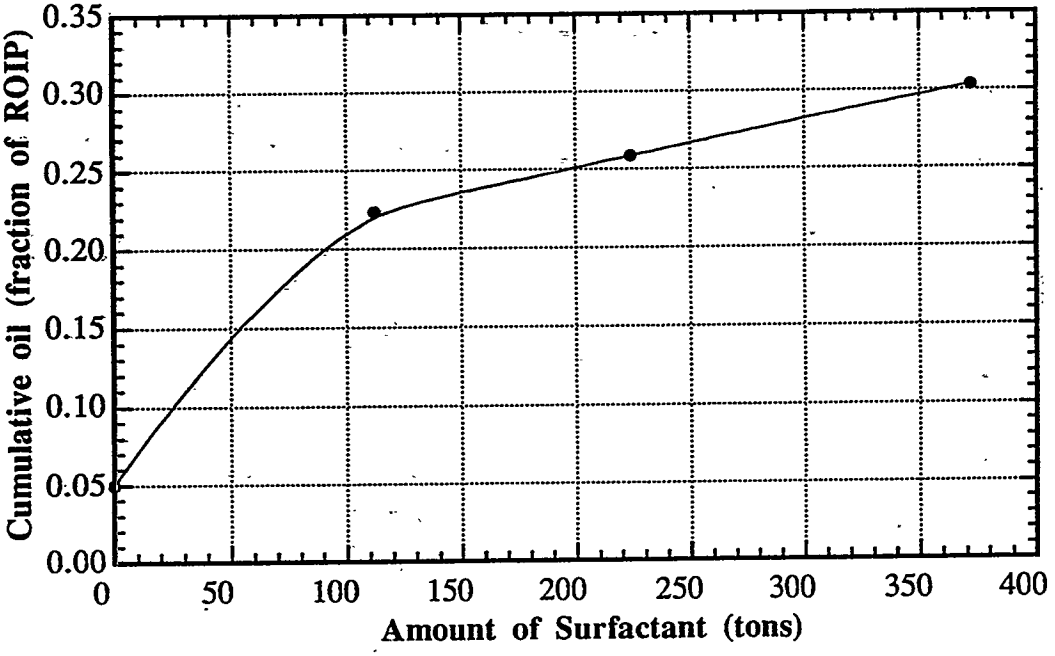


Figure 3.116 Comparison of oil recovery for different injection surfactant concentration

TASK 2. OPTIMIZATION OF SURFACTANT FLOODING

Part II: Economic Analysis

1. Introduction

1.1 Background

Surfactant flooding, which is also referred to as micellar-polymer flooding, is an enhanced oil recovery (EOR) process that involves the injection of a chemical slug, containing surfactant, to lower the interfacial tension between oil and water. This mobilizes oil that was initially trapped by viscous and capillary forces and improves the oil recovery. The chemical slug often contains polymer to improve the sweep efficiency and preserve the often more costly surfactant. Alcohol is usually contained in the chemical slug to obtain gel-free microemulsions and improve the compatibility of the surfactant and polymer (Austad *et al.*, 1993). The chemical slug is followed by a slug of water containing polymer in solution, then an injection of drive water until the project reaches completion.

The first surfactant flooding system was introduced in the late 1920's as a large pore volume (up to 50%) of a low concentration (less than 2.5%) active surfactant solution. In the late 1950's, a second type of surfactant system was introduced that used a much smaller surfactant slug with a high concentration (5% to 12%) active surfactant. Maraflood™ and Uniflood™ are patented processes that were developed using high surfactant concentration systems. These processes were used in field-scale projects with some technical success, but at current oil prices are not considered economical.

Surfactant flooding is considered a high risk process and has not made a significant contribution to U.S. EOR production, because of high chemical costs, low and uncertain oil prices, the relatively long project life, and the lack of confidence in the performance of the process. For the high oil recovery potential of surfactant flooding to be realized, the process needs to be more cost-effective.

The availability of synthetic surfactants that are active at very low concentrations and under reservoir conditions of high salinities and temperatures has lead to the development of some low-cost surfactant systems. These types of surfactants contain both ethoxy and propoxy groups in the same molecule (Maerker and Gale, 1992). A surfactant system that contained this type of surfactant with xanthan gum as the polymer was used in a technically successful surfactant flood pilot test (Reppert *et al.*, 1990). Synthetic surfactants were also used in the development of low surfactant concentration (0.4%) enhanced waterflooding (Wellington and Richardson, 1995).

A new approach to low-cost chemical flooding, termed Low Tension Polymer Flooding (LTPF), was proposed by Kalpakci *et al.* (1990). The LTPF process combines the effectiveness of surfactants with the control of polymers by using polymer compatible surfactants. Typical LTPF component concentrations are about 0.3% surfactant and 500 to 800 ppm polymer in brine. The chemical slug is followed by a 0.5 pore volume graded viscosity polymer buffer. Preliminary studies of the LTPF process show it is sensitive to slug size, surfactant phase behavior, and adsorption loss levels (Kalpakci *et al.*, 1993).

The application of horizontal wells in chemical enhanced oil recovery has several benefits, including increased injectivity and better sweep efficiency (Dakhlia *et al.*, 1995; Taber and Seright, 1992). Dakhlia *et al.* showed that the project life for a surfactant flood in a five-spot pattern could

be reduced by a factor of 2 using a horizontal injector and a vertical producer. The reduction in project life has a favorable effect on project economics and was a key factor in this optimization study. The application and benefits of horizontal wells in carbon dioxide flooding have been studied by Lim *et al.* (1994, 1992).

1.2 Research Objective

The objective of this research is to determine the optimum surfactant flood design, based on economic performance, for a typical domestic onshore sandstone oil reservoir.

1.3 Overview

In order to economically evaluate the surfactant flooding process, an economic model was developed, based on the discounted cash flow method of economic analysis. This model was designed to be flexible, so that it could be used to evaluate other chemical flooding processes, such as polymer flooding and caustic flooding. The assumptions made in the economic model and all of its components are described in detail in the next section.

The application of the economic model is demonstrated in Section 3, where several surfactant flooding case studies are presented. Reservoir simulations were used to predict the performance of surfactant flooding two different reservoirs. The surfactant flood design for each reservoir makes use of a horizontal injection well to reduce the project life. A synthetic surfactant that is active at very low concentrations and compatible with the polymer (xanthan gum) was used in the chemical slug, without the need for alcohol cosolvent. Reservoir descriptions are provided and each surfactant flood is evaluated using the economic model.

In Section 4, one of the case studies is selected for optimization. The optimization process is based on economic performance and uses reservoir simulation to predict the performance of each surfactant flooding design. An iterative approach that evaluates variations in the chemical slug size, surfactant concentration, and polymer concentration was used to determine the optimum design. The sensitivity of the optimization process to oil price and different profitability measures is also presented.

The profitability of the optimum design is based on the economic environment described in Section 2. It is very unlikely that the economic model will accurately predict future prices, costs, and tax rates, so there is some uncertainty in the outcome. Methods for evaluating risk and uncertainty in surfactant flooding are presented in Section 5, using the optimum surfactant flood design as a case study. Sensitivity analysis was used to identify which economic variables have the greatest impact on the uncertainty in the profitability of the optimum design. Monte Carlo simulation was used to demonstrate how economic risk in surfactant flooding can be quantified.

Section 6 summarizes the results and conclusions of this work and provides recommendations related to the evaluation and optimization of surfactant flooding.

2. Chemical Flooding Economic Model

2.1 Introduction

An economic model, called the Chemical Flooding Economic Model (CFEM), was developed to economically evaluate chemical flooding processes in the United States. The CFEM can be used to evaluate surfactant flooding, polymer flooding, caustic flooding, or any combination of these.

Oil recovery from chemical flooding was predicted using a compositional reservoir simulator, called UTCHEM, developed at The University of Texas at Austin. The UTCHEM simulator has been validated through comparisons with field data for a surfactant/polymer flood (Saad *et al.*, 1989) and also used to simulate polymer flooding (Takagi *et al.*, 1992) and high pH alkaline/surfactant/polymer (ASP) flooding (Bhuyan *et al.*, 1991; Wu, 1996).

The CFEM was developed using a commercially available spreadsheet application, which provided many of the financial and statistical functions required. Inputs for the CFEM include chemical oil recovery, capital costs, operating costs, taxation rates, oil and chemical prices, inflation, and other variables that define the economic environment. These inputs were used to generate constant dollar after-tax cash flows. Discounted cash flow analysis was applied to these cash flows, taking into account the time value of money, to determine project profitability.

Discounted cash flow analysis was used by Chapman (1994) to evaluate ASP flooding. Chapman used decline curve analysis to predict future oil recovery and a simplified estimation of operating cost. Economic analysis using the CFEM is more comprehensive because it uses reservoir simulations for a more realistic prediction of chemical flood performance and an operating cost estimate that is sensitive to the types of injected and produced fluids.

This chapter describes the CFEM in detail, stating all assumptions made and values used to define the base case.

2.2 Chemical Flood Description

The CFEM can evaluate chemical flood designs that contain some or all of the following, expressed in pore volumes (PV): water preflush, chemical slug, polymer drive, and water drive. A combination of alkali, surfactant, or polymer at different concentrations can be used in the chemical slug composition. The polymer concentration used in the chemical slug does not need to be constant and may be changed for the polymer drive.

A large number of variables are used in a reservoir description, but only two are required in the CFEM calculations. The reservoir pore volume, expressed in barrels (bbl), is used to calculate the chemical quantities required by the chemical flood. The remaining oil in place (ROIP), also expressed in barrels, is used to calculate the performance of the chemical flood.

For a given chemical injection schedule, the amount of each chemical required was calculated using their chemical concentration and assuming their density is approximately that of water. The equations used to calculate chemical quantities are

$$W_a = W_w V_{slug} C_a$$

$$W_s = V_w V_{slug} \rho_w C_s$$

$$W_p = W_w \left(V_{slug} C_{ps} + V_{drive} C_{pd} \right)$$

where

W_a = amount of alkali required (lb)
W_s = amount of surfactant required (lb)
W_p = amount of polymer required (lb)
W_w = amount of water in one pore volume (lb)
V_w = amount of water in one pore volume (ft^3)
V_s = chemical slug size (PV)
V_p = polymer drive size (PV)
ρ_w = density of water (lb/ft^3)
C_s = concentration of alkali in chemical slug (weight fraction)
C_s = concentration of surfactant in chemical slug (volume fraction)
C_{ps} = concentration of polymer in chemical slug (weight fraction)
C_{pd} = concentration of polymer in polymer drive (weight fraction)

These calculations are performed automatically in the CFEM spreadsheet. To define a chemical flood, the CFEM requires the injection schedule to be expressed in pore volumes and the chemical concentrations to be given in the units specified above.

2.3 Data Acquisition

UTCHEM was used to predict the injection and production profiles for various chemical floods. Relevant data were extracted from the simulation output files using a utility application, called EXHIS, developed by a former student. The data extracted were the pore volumes injected, time (days), total fluid injection (ft^3), total fluid injection rate (ft^3/day), cumulative oil recovery (fraction), total fluid production (ft^3), total fluid production rate (ft^3/day), and the produced concentrations of water, oil, surfactant, and polymer, expressed as fractions. These data were imported as text files into a spreadsheet template to put the data into the desired format. The spreadsheet template automatically produces plots of the following variables versus time and pore volumes injected: total fluid injection rate in barrels per day (B/D), total fluid production rate (B/D), oil production rate (B/D), cumulative oil recovery (%), oil cut (%), water cut (%), produced surfactant concentration (%), and produced polymer concentration (%).

The CFEM determines after-tax cash flows on an annual basis, so it was necessary to reduce the simulation data to an annualized data set. Linear interpolation and various spreadsheet functions were used to condense the simulation data set to annual values for pore volumes injected, fluid injected (bbl), oil production (bbl), and water production (bbl). The annualized data were then copied into the CFEM spreadsheet to evaluate the profitability of the chemical flood.

2.4 Predicting After-Tax Cash Flows

The methodology used to predict the future after-tax cash flows for a chemical flooding project is illustrated in Figure 2.1. The following sections explain the assumptions made by the CFEM to obtain each component of the cash flow.

2.4.1 Revenue

The revenue from a chemical flood is from the sale of oil produced and is calculated by multiplying the current oil price by the amount of oil production. The CFEM base case assumes the chemical flood operator has a 100% working interest and has to pay a 12.5% royalty to the owner of the property. The royalty payment is taken directly from gross revenue, and the remaining revenue is the operator's net revenue before deducting operating expenses and income tax.

There is no single benchmark for pricing crude oil from different sources, and the price is generally a function of the API gravity and the sulfur content. Lighter (higher API gravity) crude oils are desirable because they tend to yield more gasoline by volume than heavier crude oils. Sulfur is undesirable because it gives refined products an undesirable odor and increases their corrosiveness. The CFEM uses West Texas Intermediate (WTI), which is the major price reference in the U.S., as an oil price benchmark.

The posted price history of WTI, in current and constant 1980 dollars, is shown in Figure 2.2 (Pennwell, 1994). Since the first oil shock in 1974, oil prices have been extremely volatile. In the past 20 years, the current oil price has fluctuated between $10/bbl and $37/bbl, and only in recent years has it shown some stability at between $16 and $20/bbl. The constant 1980 dollar oil price is as volatile as the current dollar price, which suggests that oil prices are not driven by U.S. inflation.

There are numerous oil price forecasts available from petroleum consulting firms and government agencies. However, these forecasts often try to anticipate large fluctuations in price, which if used, can greatly affect the attractiveness of the project being evaluated. The oil price used in the CFEM base case was $18/bbl, which was the current price of WTI when the analysis was performed. The oil price forecast for the CFEM base case assumes that oil prices increase at the inflation rate. The sensitivity of the CFEM to various oil price forecasts is given in Section 5. The U.S. inflation rate was assumed to be constant at 3% per year, which is a reasonable assumption, since the average U.S. inflation rate from 1926 to 1992 was 3.1% (Rao, 1996).

2.4.2 Capital Costs

There are many additional capital costs associated with implementing a chemical flood at either the secondary or tertiary level. The additional capital costs for a chemical flood depend on the suitability, availability, and condition of the existing wells and equipment from the preceding waterflood. The different types of capital costs included in the CFEM are workover costs, development drilling costs (tangible and intangible), facilities and equipment costs, and leasehold costs. Abandonment costs and revenues from salvage of equipment were not included in the CFEM.

2.4.2.1 Workover Costs

The existing wells available for the chemical flood were assumed to require a well workover. The well workover costs were assumed to be 20% of the cost of drilling and equipping a new well. It was assumed that no additional workovers were required during the chemical flood.

2.4.2.2 Development Drilling Costs

Depending on the design of the proposed chemical flood, additional drilling may be required in the form of infill drilling to reduce the pattern size or the addition of horizontal wells. For income-tax purposes, the costs of drilling and developing an oil and gas property are classified into two categories: tangible and intangible. Tangible drilling and development costs include physical assets, such as casing, pumps, tubing, flow lines, and separators, which can be recovered through depreciation. Intangible drilling costs are expenditures made by an operator for wages, fuel, repairs, hauling, supplies, etc., which have no salvage value. In general, intangible drilling costs account for 60 to 70% of the total well cost (SPE, 1995). The intangible drilling costs used in the CFEM were assumed to be 60% of the total well costs.

Drilling costs in the United States for onshore reservoirs were obtained from a 1993 survey (American Petroleum Institute, 1994). The results of this survey were assumed to be representative of current drilling costs in the United States and used for estimating drilling costs in the CFEM. Costs reported in the survey included all tangible and intangible costs for drilling dry holes and

productive wells and the costs of equipping productive wells with a "Christmas tree" installation. In 1993, the average cost of drilling a horizontal oil well was $78.85 per foot at an average length of 11,174 feet. Drilling and equipping costs for onshore oil wells in the U.S. are summarized in Table 2.1 as a function of depth interval.

2.4.2.3 Facilities and Equipment Costs

The equipment and facilities from a preceding waterflood were assumed to be readily available at no additional cost. However, additional facilities and equipment are required for chemical storage, mixing of chemicals, oil treatment (heater treaters, skim tanks, centrifuges), and disposal of produced fluids. The cost of such facilities can vary widely, depending on the company, the size of the project, the type of chemical flood, the chemical properties, and the geographical location. Without this information, it is very difficult to estimate the cost of additional facilities and equipment for a chemical flood. The CFEM assumes there are no additional costs and the significance of this assumption is discussed later in Section 5.

2.4.2.4 Leasehold Cost

The leasehold cost is the expenditure associated with the acquisition of an economic interest in an oil and gas property. An economic interest exists if you have a legal interest in the natural resource in place and you have the right to income from the extraction and sale of the resource. The CFEM assumes that the leasehold cost has already been recovered during primary or secondary production. It is therefore treated as a sunk cost.

2.4.3 Operating Costs

There are two types of operating costs in oil and gas production: direct and indirect. Direct operating costs are those that are essential to production operations, such as labor, power, equipment repair and maintenance, fluid injection, and oil treatment. Indirect operating costs are also referred to as overhead and include expenditures such as legal and office expenses that are not directly attributable to the property but are considered as ordinary business expenses. The CFEM bases case assumes that overhead is allocated as a percentage of direct operating costs and equal to 20%.

There are three basic methods for predicting direct operating costs: constant cost per barrel, constant cost per well, and constant cost per platform (Bradley and Wood, 1994). All of these methods have limitations, but a fixed operating cost is often preferred because unit costs can be misleading. For example, a well producing 80 barrels per day will generally cost about the same as a well producing 10 barrels per day, but this will not be the case if a cost per barrel is used (Thompson and Wright, 1984). However, the cost of operating a chemical flood depends on the types of fluids and the fluid rates, so a cost per barrel is also desirable.

A realistic chemical flooding operating cost estimate was made by using a combination of fixed and variable operating costs. Fixed operating costs were assumed to be the costs of operating a waterflood and the variable costs were the additional operating costs associated with chemical injection and treatment of produced fluids. Waterflood operating costs were obtained from reports on domestic oil field production operations (DOE/EIA; 1994). The costs were reported on an annual basis for a waterflood with 10 production wells and 11 injection wells, producing 290 barrels of fluid per day. The direct monthly operating costs for secondary recovery in West Texas as a function of depth are shown in Table 2.2. To estimate operating costs for higher production rates, the operating cost versus production rate relationship was assumed to be constant.

The operating cost index for oil field production operations from 1976 to 1993 is shown in Figure 2.4. This index looks very similar to the equipping cost index shown in Figure 2.3.

Operating costs have been declining in real terms since about 1982 because of lower oil prices and increased competition among service companies. However, this trend is not expected to continue, and the CFEM base case assumes that operating costs and chemical prices will escalate at the inflation rate. Escalation refers to the rise or fall of a specific commodity because of inflation, environmental and engineering changes, and the forces of supply and demand (Stermole, 1984).

2.4.3.1 Chemical Injection Operating Costs

There are additional operating costs associated with chemical injection facilities that have to blend, shear, filter, and inject the chemical slug and polymer drive. Operating costs during the chemical slug injection were assumed to be more than those during the polymer drive because of the increased complexity of handling and mixing the chemicals. The National Petroleum Council (NPC) estimates chemical slug injection and polymer drive costs to be $0.20 and $0.10 per barrel of fluid, respectively (NPC, 1984). The operating cost index in Figure 2.3 shows that 1984 operating costs were only marginally lower than present operating costs, so the NPC estimates were used in the CFEM.

Chemical costs are considered an operating expense for taxation purposes and are significant in most chemical floods. Chemical injection volumes can be as high as one pore volume, so the chemical price is critical to the outcome of the project. The CFEM assumes that all chemicals are commercially available and do not need to be manufactured by the company. The types of chemicals used and the cost to obtain them vary significantly for each chemical flooding project. The chemical price depends on the type of chemical, the chemical quality, the chemical quantity, the supplier, and negotiations with the supplier. The chemical prices used in this study are given in the case studies presented in the next chapter.

2.4.3.2 Treatment of Produced Fluids

A common operational problem with chemical flooding is the treatment of produced oil. Problems with treating produced fluid emulsions have been reported in surfactant/polymer flooding (Johnson *et al.,* 1988; Dreher and Shoppman, 1985) and in polymer flooding (Jiachao *et al,* 1994). Mechanical treatment of produced fluids does not always result in pipeline quality oil, so chemical demulsifiers are often added to help break the emulsions.

Some oil companies have been successful at finding cost-effective ways to separate the produced emulsions. Exxon has developed and patented an inexpensive and efficient temperature-based separation technique for produced emulsions from its second Ripley surfactant flood pilot. The emulsion treating costs for this pilot were under $0.05 per barrel of emulsion treated and the surfactant was reusable (Reppert *et al.,* 1990). Marathon was able to reduce its chemical treating cost from $1.20 to $1.70 per barrel to about $0.55 per barrel of oil produced for their M-1 micellar-polymer project by using polyoxypropylene amines (POPAs) as demulsifiers. The POPAs were able to improve the oil quality and substantially reduce the amount of fluid-processing equipment required (Duke, 1994).

In general, a large capital investment in treatment facilities will result in low chemical treating costs, and a small capital investment will result in high chemical treating costs (Johnson *et al.,* 1988). The CFEM assumes that any stable produced emulsions can be economically separated using a combination of mechanical separation and chemical treatment techniques. An oil treatment cost of $0.50 per barrel of oil produced was assumed. An additional cost of $0.03 per barrel was also included in the CFEM for the disposal of produced water (NPC, 1984).

2.4.4 Oil and Gas Taxation

The tax law for oil and gas transactions is complex and constantly changing. Tax treatment of oil and gas transactions differs greatly from other industries and other natural resources. This

section is an overview of common oil and gas transactions: depreciation, depletion, treatment of intangible drilling costs, property taxes, production taxes, income taxes, and tax credits. The CFEM does not attempt to calculate the alternative minimum tax (AMT) because it is difficult to understand and calculate.

2.4.4.1 Depreciation

Depreciation is a book transaction that reduces the tax liability of the operator. It is a measure of the declining value of associated plant and equipment. The purpose of the tax allowance is to compensate the owner for the exhaustion, wear and tear, and obsolescence of plant and equipment.

The Modified Accelerated Cost Recovery System (MACRS) is the name given to the tax rules that govern the recovery through depreciation of the cost of property used in trade or business placed in service after 1986. The MACRS classifies assets for the exploration and production of petroleum as seven-year property (Internal Revenue Service, Pub. 534, 1995). The CFEM assumes that all projects being evaluated represent future investments, so all tangible capital costs are eligible for MACRS depreciation.

The depreciation deduction on oil and gas equipment is computed using the 200 percent declining balance method with an automatic switch to the straight line method in order to maximize the tax deduction. A half-year of depreciation is allowable for the year the property is placed in service. Table 2.3 gives the depreciation schedule for seven-year property in terms of depreciation factors. To calculate the depreciation for a given year, the purchase price of the depreciable property is multiplied by the depreciation factor.

2.4.4.2 Depletion

Depletion is a book transaction that allows the asset value of a natural resource to be gradually expensed over the life of the project. The objective of the depletion allowance is to permit the taxpayer a reasonable deduction for the estimated cost of the exhausted reserves. Depletable items can include leasehold costs, geological and geophysical costs, and lease bonuses. There are two types of depletion allowances: cost depletion and percentage depletion.

Cost depletion is calculated by multiplying the depletable basis in the property by the production in that year, divided by the reserves at the beginning of that year. The depletion allowance is calculated each year until the depletable basis is zero. The CFEM base case assumes that there is no leasehold cost or any other depletable basis, so no there is no cost depletion. However, the CFEM spreadsheet contains the equations necessary to calculate cost depletion if a depletable basis exists.

In general, percentage depletion is not allowed for oil or gas wells, except for certain oil and gas producers. Percentage depletion for oil and gas is limited to small producers and royalty owners who qualify for a 15% rate for an average daily production of up to 1,000 barrels of oil equivalent. This is known as the independent producers and royalty owners (IPRO) exemption.

Percentage depletion is calculated by multiplying gross depletable income from the property during a tax year by a certain percentage. Gross depletable income does not include any rents, royalties, and lease bonuses, which are depletable income to the payee. The depletion deduction must not exceed 100% of taxable income before the depletion deduction and the maximum deduction that may be claimed under IPRO is limited to 65% of the taxable income. When the 65% limit applies, the disallowed amount is carried over to the following year and can be carried over for an indefinite period. When determining the taxable income limit, net operating losses should not be deducted from gross income period (Burke and Starcher, 1993; Internal Revenue Service, Pub. 535, 1995).

The taxpayer must adjust the depletable basis for either cost or percentage depletion, whichever is highest. The CFEM base case assumes that the mineral lease is owned and operated

by an integrated oil company, which is not eligible for percentage depletion. The effects of the tax code on project profitability for independent and integrated producers is presented in Section 5.

2.4.4.3 Treatment of Intangible Drilling Costs

The tax law differs for independent and integrated oil companies with respect to the treatment of intangible drilling and development costs. Independent companies are allowed to expense 100% of the cost in the year that it was incurred. However, integrated oil companies can only deduct 70% of intangible drilling costs. They must capitalize the remaining 30% and amortize (straight-line) them over a 60-month period starting in the month the costs were incurred. (Internal Revenue Service, Pub. 535, 1995). The CFEM base case assumes that the operator is an integrated oil company and any additional drilling costs are for development purposes.

2.4.4.4 Severance and Ad Valorem Taxes

In most states there are taxes on the production of oil and gas. However, in recent years, many of the major oil producing states have offered tax incentives to expand oil and gas production in an attempt to increase energy-based revenues. In Texas, there is a tax incentive for enhanced oil recovery projects. The tax incentives vary from state to state, but in most cases involve a reduction in severance taxes. For example, the severance tax rate in Texas is reduced from 4.6% to 2.3% for qualified EOR projects (Baumann and Pulsipher, 1994).

Ad valorem taxes are property taxes that are imposed by the county governing the lease. The methods used to appraise oil and gas properties as the basis for ad valorem tax can be quite complex. The CFEM simplifies the calculation of severance and ad valorem taxes by combining them into a single production tax of 8% on gross revenue before any rents or royalties are paid.

2.4.4.5 Income Tax

Income tax laws are different for corporations and individuals. Income from oil and gas properties may be taxed by both state and federal governments. State corporate income taxes range from 0% in Texas to 10.5% in Pennsylvania (NPC, 1994). The federal income tax system for corporations is a progressive system with rates ranging from 15% to 39% depending on taxable income, as shown in Table 2.4 (Internal Revenue Service, Pub. 542, 1995). The CFEM uses an effective tax rate to combine federal and state income taxes into one calculation. Assuming state taxes can be deductible for calculating federal taxes, the effective rate is (Stermole, 1984)

$$\textit{Effective tax rate} = s + f(1-s)$$

where s is the state tax rate and f is the federal tax rate, expressed as fractions.

Before calculating income tax, any operating losses carried forward from the previous year are deducted from taxable income. The CFEM base case assumes a state tax rate of 5% and a federal tax rate of 35%, assuming the corporation has a taxable income greater than $18.3 million, which includes most oil companies. This equals an effective tax rate of 38.25%. The income tax rate was assumed to remain constant throughout the life of the project, even though past experience tells us that this is unlikely in the US, considering the frequency of changes in the tax code.

2.4.4.6 Tax Credits

To address the concern of declining domestic production, the National Energy Strategy introduced a tax credit for qualified EOR projects in 1990. The tax credit is equal to 15% of a taxpayer's qualified EOR costs and is deducted from taxes otherwise owed. The impact of the EOR tax credit on enhanced oil recovery production has been investigated (Brashear *et al.*, 1991).

The qualified EOR costs that form the base for the tax credit include tangible property costs, intangible drilling costs, and tertiary injectant costs. The EOR tax credit is not available to

taxpayers who are subject to the AMT in a given year. If the tax credit is not available because of the AMT, then the unused portion may be carried forward. Additional limitations on the application of the EOR tax credit are (Mandelker, 1992)

- The credit is only available to owners of operating mineral interests in a EOR property. Royalty owners and other economic but nonworking interests are not eligible for the credit.
- The costs of acquiring an existing qualified EOR project are not eligible for the credit.
- The EOR credit is gradually phased out in any year in which the crude oil wellhead price is greater than $28/bbl adjusted for inflation.

The CFEM does not calculate the AMT, so the tax credit may completely offset the payable income tax. Unused portions of the tax credit are carried forward indefinitely.

2.4.5 Adjustments

After paying income taxes and deducting any tax credit, the remaining cash flow is the net income of the project (Figure 2.1). However, this does not represent the actual cash flow, because depreciation, depletion, amortization, and losses forward have been deducted and do not represent real cash flows. In addition, the capital costs that cannot be expensed represent a real cash flow and need to be deducted from net income. The sum of net income, depreciation, depletion, amortization, and losses forward minus the capital costs represents the current dollar after-tax cash flow. These cash flows are then corrected for inflation to give constant dollar cash flows to be used in discounted cash flow analysis.

2.5 Discounted Cash Flow Analysis

The discounted cash flow (DCF) method of economic analysis allows individual projects to be evaluated and/or compared with other projects. DCF methods are widely used in the petroleum industry and are used by most companies as their primary method of investment analysis (Dougherty and Sarkar, 1993). DCF analysis gives less weight to future incomes by applying a discount rate to the predicted cash flows, thereby taking into account the time value of money. Before presenting the different profitability measures used by the CFEM, the chemical flooding economic limit is defined and methods for selecting an appropriate discount rate are discussed.

2.5.1 Definition of Economic Limit

An economic limit needs to be defined so profitability measures can be calculated for the anticipated life of the chemical flooding project. The project life depends on many factors, but the critical variables are likely to be oil price and production, which control the project revenue. The CFEM defines economic limit as the time when the cumulative discounted cash flow reaches a maximum, as shown in Figure 2.5.

2.5.2 Selecting a Discount Rate

Discount rate is also referred to as cost of capital, hurdle rate, opportunity cost, and minimum required rate of return. The appropriate discount rate is either the cost to acquire additional capital or the return that could be obtained by investing in an alternative opportunity (Seba, 1987). Subjective measures are the most commonly used in the petroleum industry, followed by weighted average cost of capital (Dougherty and Sarkar, 1993). The weighted average of the cost of debt and equity is the weighted average cost of capital for a firm. In general, the cost of debt is cheaper than the cost of equity.

The CFEM assumes that the chemical flood is financed on an all-equity basis, which was why no loan financing was included when predicting future cash flows. The real discount rate for the CFEM base case was chosen subjectively to be a minimum required rate of return of 10%, which is equivalent to a 13.3% nominal discount rate, assuming an inflation rate of 3%. A real discount rate has to be used instead of a nominal rate because the predicted cash flows have already been corrected for inflation (Figure 2.1)

2.5.3 Net Present Value

Net Present Value (NPV) is also known as present value profit and is an excellent screening criterion. It is calculated by discounting the predicted constant dollar cash flows at the real discount rate. An NPV greater than zero indicates that the project meets the investors minimum required rate of return. It provides the value in dollars that a successful investment will add to the net value of the investor. NPV can be used to evaluate individual projects and compare different projects with the same initial investment. However, if the initial investment differs between projects, NPV should not be used to rank projects, because it gives no indication of profitability per dollar invested.

2.5.4 Internal Rate of Return

Internal Rate of Return (IRR) is also referred to as the discounted cash flow rate of return (DCFROR) or profitability index (PI) and is the most commonly used discounting method of investment analysis by petroleum companies (Dougherty and Sarkar, 1993). IRR is the discount rate that, when applied to the predicted cash flows, gives a zero NPV, or the discount rate that equates the present value of inflows to the present value of outflows. A project is considered profitable if the IRR is greater than the discount rate or minimum required rate of return. A disadvantage with IRR is that it can have multiple rates of return when there are more than one cash flow sign change. High values of IRR can be misleading because the calculation of IRR assumes reinvestment at IRR, which heavily penalizes cash flows late in the project (Seba, 1987).

2.5.5 Discounted Return on Investment

Discounted Return on Investment (DROI) is also referred to as the present value ratio (PVR) and capital productivity index (CPI). It is simply the NPV divided by the discounted initial investment. It is a useful ranking criterion because it can be used to maximize profitability per dollar invested.

2.5.6 Investment Efficiency

Investment Efficiency is similar to DROI and is calculated by dividing NPV by the most negative cumulative discounted cash flow. Figure 2.5 illustrates the calculation of investment efficiency. The maximum cumulative discounted cash flow is the NPV calculated at the economic limit. Several authors have recognized the suitability of this profitability measure to petroleum projects (Clapp, 1994; Stermole, 1984; NPC, 1984). It is particularly suited to EOR projects because of their high front-end costs. Chemical costs and low production rates contribute to an increased period of negative cash flows, which reach a much greater negative cash flow than projects that have only an initial capital investment.

2.5.7 Growth Rate of Return

Growth Rate of Return (GROR) is also referred to as wealth growth rate, appreciation of equity, and percentage gain on investment. GROR is most useful when IRR and DROI give contradictory results and another ranking criterion is required. GROR is the compound interest rate at which the investment grows, which is analogous to interest rates paid by banks. The calculation of GROR requires a common time horizon to compare investments. GROR is calculated using the following equation (Capen *et al.*, 1976):

$$GROR = \left(\frac{PW}{I} + 1\right)^{1/t} (1+r) - 1$$

where I is the present value of initial negative cash flows discounted at the reinvestment rate, r, and PW is the present value of all cash flows discounted at the reinvestment rate. The reinvestment rate of return should be equal to or higher than the discount rate, depending on the method used to determine the discount rate. If the discount rate represents the company's cost of capital, then the reinvestment rate should be greater than the discount rate. If the discount rate represents the rate of return that could be obtained from other investment opportunities (opportunity cost), then the discount rate is equal to the reinvestment rate (Stermole, 1984). The CFEM uses a 10-year project life and assumes that the reinvestment rate is equal to the discount rate (10%) to calculate GROR.

2.5.8 Payback Period

The payback period is calculated by accumulating cash flows over successive years until the present value is zero. Discounted payback period measures the number of years it takes to achieve the required rate of return, which is useful as a measure of the risk and liquidity of the project. Nondiscounted payback period measures the number of years required to recover the initial investment. The main disadvantage with using payback is that it does not take into consideration the cash flows or profitability after payback is achieved.

2.5.9 Profitability Per Barrel

The chemical flooding economics are also presented on a per barrel of oil recovered basis, discounted and nondiscounted. The after-tax cash flow is broken down into the main cash flow streams: revenue, royalty, capital costs, operating costs, chemical costs, taxes, and profit. The operating cost and chemical cost per barrel of oil produced are of particular interest and are often used as benchmarks for evaluating projects. This type of analysis is also useful for checking the accuracy of the cash flow calculations.

2.6 Chemical Flood Performance

2.6.1 Recovery Efficiency

The recovery efficiency is defined as the cumulative oil recovery at the economic limit (bbl) divided by the ROIP (bbl) at the start of the chemical flood, expressed as a percentage. The cumulative oil recovery is the incremental oil produced by the chemical flood over that by a waterflood. If the chemical flood is preceded by a waterflood that has been waterflooded to its economic limit, then all the oil recovered can be considered as purely tertiary.

2.6.2 Chemical Efficiencies

Chemical efficiency is defined as the cumulative oil produced (bbl) divided by the amount of chemical used (lb), calculated at the economic limit. The CFEM calculates the chemical efficiencies for each chemical used in the chemical flood. High values are desirable, which indicates that the chemical flood is efficiently mobilizing the remaining oil in place for each pound of chemical injected.

Table 2.1: Average cost of drilling and equipping onshore oil wells

Depth interval (ft)	Average drilling cost ($/ft)
0 - 1,249	$46.33
1,250 - 2,499	$47.89
2,500 - 3,749	$43.94
3,750 - 4,999	$41.07
5,000 - 7,499	$45.49
7,500 - 9,999	$53.78
10,000 - 12,499	$78.60
12,500 - 14,999	$94.97

Table 2.2: Direct monthly operating costs for secondary oil recovery in West Texas (per producing well)

Depth (ft)	Operating Cost
2000	$16,538
4000	$22,822
6000	$24,339

Table 2.3: Depreciation schedule for seven-year property under MACRS

Year	Depreciation Factor
1	14.28%
2	24.49%
3	17.49%
4	12.49%
5	8.93%
6	8.93%
7	8.93%
8	4.46%

Table 2.4: Federal income tax rates for corporations

Taxable income	Tax rate
$0 - $50,000	15%
$50,001 - $75,000	25%
$75,001 - $100,000	34%
$100,001 - $335,000	39%
$335,001 - $10,000,000	34%
$10,000,001 - $15,000,000	35%
$15,000,001 - $18,333,333	38%
$18,333,334 +	35%

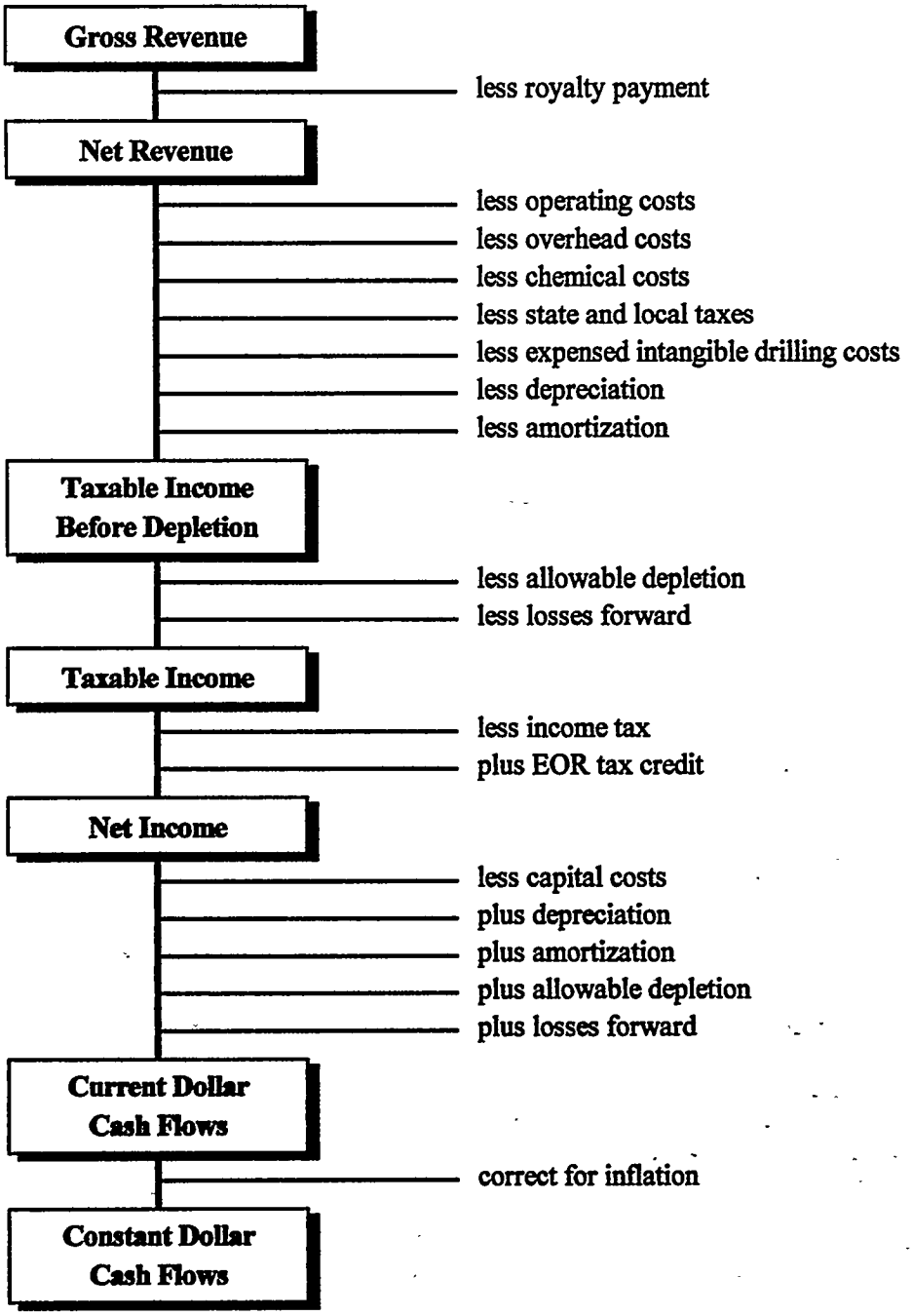


Figure 2.1: Methodology used to determine constant dollar after-tax cash flows

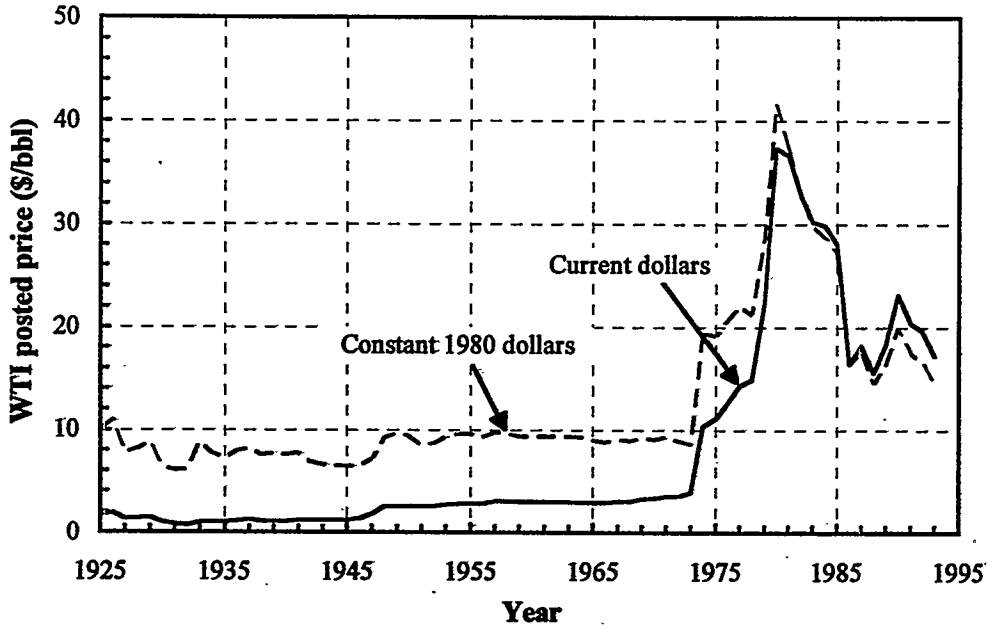


Figure 2.2: Posted oil prices for WTI (1925-1993)

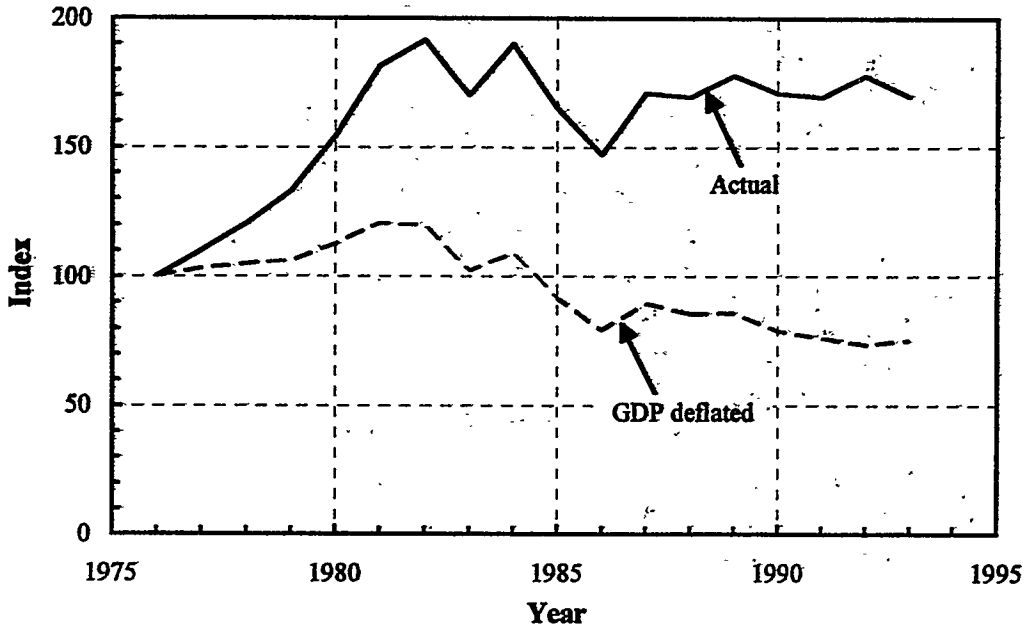


Figure 2.3: Index of equipping costs for oil fields in the U.S. (DOE/EIA, 1994)

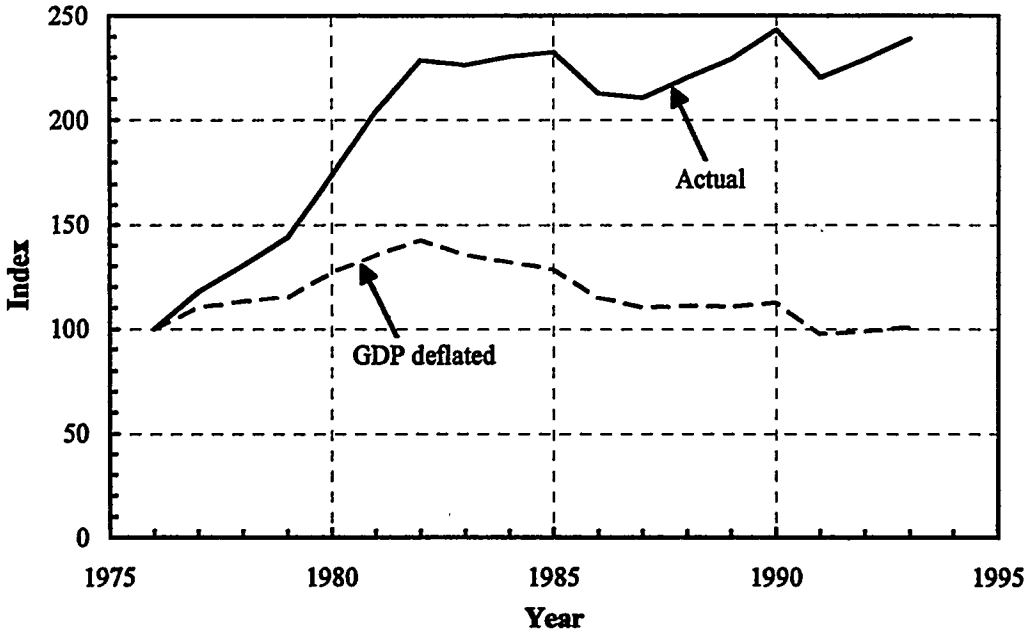


Figure 2.4: Index of operating costs for oil fields in the U.S. (DOE/EIA, 1994)

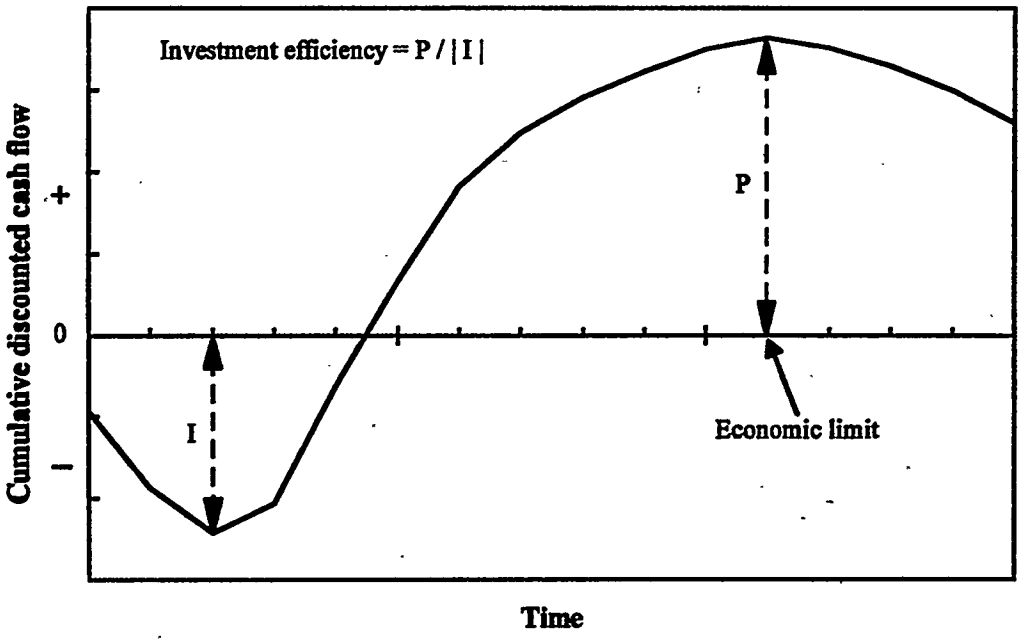


Figure 2.5: Definition of economic limit and investment efficiency

3. Surfactant Flooding Case Studies

3.1 Introduction

To demonstrate how the CFEM is used to evaluate chemical flooding processes, two domestic onshore surfactant flooding case studies are presented in this chapter. Each case has a different reservoir and a different surfactant flooding design. The surfactant flood performance for each reservoir was simulated using the UTCHEM simulator and evaluated using the CFEM.

3.2 Onshore Surfactant Flood: Case 1

The first case study is a surfactant flood of an onshore U.S. midcontinent sandstone oil reservoir with a low average permeability (50 md) and a depth of 3500 ft. A simulation study of this reservoir has been performed by Dakhlia (1995), who investigated the performance of surfactant flooding using horizontal wells and the sensitivity of surfactant flooding performance to various reservoir and operating parameters. Dakhlia did not determine the optimum surfactant flood design for this reservoir, technically or economically.

3.2.1 Reservoir Description and Simulation

A quarter-symmetry element of a forty-acre five-spot pattern with a horizontal injector and a vertical producer was used in the surfactant flood simulation. Its dimensions were 660 ft in the x direction, 660 ft in the y direction, and 140 ft in the z direction. The porosity was uniform and equal to 13.6%. A permeability field was statistically generated using a program based on the matrix decomposition method (Yang, 1990). The standard deviation of the logarithm of the permeability was 1.609, which corresponds to a Dykstra-Parsons coefficient of 0.8. The geometric mean permeability was 50.55 md. The correlation lengths were 660 ft in the x direction, 660 ft in the y direction, and 28 ft in the z direction. The vertical to horizontal permeability ratio was equal to 0.1. Oil viscosity was 7.78 cp and water viscosity was 0.74 cp at reservoir conditions. The endpoint water-oil mobility ratio was 1.393.

The quarter five-spot was first initialized with a high oil saturation of 80%, and a waterflood was simulated using vertical wells until a 98% water cut was reached. This was assumed to be the waterflooding economic limit, so the incremental oil produced from the surfactant flood was considered purely tertiary.

Injection pressure was held constant at 1250 psi, and the production pressure was held constant at 250 psi. The injection rate was monitored during the water drive and if it exceeded 2000 B/D for a full five-spot pattern, the injection well was switched to a constant rate of 2000 B/D. The chemical injection schedule for this surfactant flood simulation was as follows:

- Chemical slug: 0.25 PV of fluid with a surfactant concentration of 2.50 vol. % and a polymer concentration of 1000 ppm
- Polymer drive: 0.50 PV of fluid with a polymer concentration of 1000 ppm
- Water drive: until a 99% water cut was reached.

Xanthan gum was used as the polymer because it is less sensitive to salinity and hardness than hydrolyzed polyacrylamide polymers. The surfactant used was a synthetic surfactant that is active at low concentrations. Surfactant adsorption for this reservoir is 0.08 mg/g rock.

The remaining oil in place (ROIP), before starting the chemical flood, was 454,942 bbl for a full forty-acre five-spot pattern, which is equal to an initial oil saturation of 30.8%. The oil

production profile and the recovery efficiency from the surfactant flood simulation are shown in Figure 3.2, as a function of time, and in Figure 3.3, as a function of pore volumes injected, for a full forty-acre five-spot pattern. The recovery efficiency after 3.5 PV injected, and 31 years, was 61.31% ROIP. However, a majority of this oil has been recovered after about 10 years and 0.90 PV of fluid injection. This relatively short project life is due to the benefits of increased injectivity from the horizontal injection wells.

3.2.2 Economic Analysis

The economic analysis of this simulated surfactant flood was based on a full forty-acre five-spot pattern, which meant that the simulation results and reservoir size were increased by a factor of four. A full forty-acre five-spot pattern consists of four horizontal injection wells and one vertical production well, as shown in Figure 3.3. It was assumed that this pattern was repeated many times throughout the field, so the four wells at the corners of the pattern only inject a quarter of their capacity to this pattern. Hence, the total contribution of the injection wells is equivalent to one full injection well.

The cost of drilling a 1320 ft. horizontal injection well was calculated at a rate of $78.75 per foot, which is about $104,000 ($73,000 intangible and $31,000 tangible) for a new horizontal well. Workover costs for the vertical production wells, which were assumed to be already in place, were 20% of the cost of drilling a new well. The average cost of drilling an oil well to a depth of 3500 ft is $43.94 per foot (Table 2.1), which is about $154,000 for a new well. This corresponds to a workover cost of about $31,000 for each well. There are effectively two wells that need to be worked over, so the total workover cost for this pattern is $62,000. The fixed operating cost for this pattern was calculated using Table 2.2 and is equal to about $21,250 per month for a reservoir at 3500 ft.

It was assumed that the polymer (xanthan gum) was manufactured on-site for approximately $1.50/lb. The surfactant (tridecyl propoxylated sulfate) can be purchased for about $1.50/lb in large quantities with the desired properties at temperatures less than 170 °F.

Using the specific prices and costs determined for this surfactant flood, the CFEM was used to calculate the profitability. Table 3.1 summarizes the technical performance of the surfactant flood when the economic limit was reached. At the economic limit, this surfactant flood has injected 0.89 PV of fluid and has injected only 0.14 PV of the water drive. The recovery efficiency at the economic limit is 51.98% ROIP, which is about 84% of the oil that would be recovered after 3.5 PV of fluid injected, if the chemical flood were continued past the economic limit.

The profitability of this surfactant flood is given in Table 3.2. At the economic limit of 10 years, this surfactant flood is making a large loss, with a NPV of -$9.65 million. Payback is never achieved, and all the other profitability measures indicate that this surfactant flood should not be considered for investment.

Table 3.3 shows the profitability per barrel of oil produced, nondiscounted and discounted. The poor economic performance of this surfactant flood is from the cost of the injected chemicals, which was about $29/bbl of oil produced (discounted). A discounted basis is preferred because it takes into account the timing of the cash flows, which will give less weight to cash flows later in the project and more to those early in the project. The discounted chemical cost per barrel is significantly higher than on a nondiscounted basis, because most of the chemical cost is incurred early in the project.

The cumulative DCF versus time and pore volumes injected is shown in Figures 3.4 and 3.5, respectively. At about 10 years, or 0.9 PV injected, the cumulative DCF has reached a maximum, so this is the economic limit for this surfactant flood. This surfactant flood has a very large capital exposure of about $12 million during the chemical slug, which is never recovered. The surfactant efficiency was only 0.07 bbl/lb (Table 3.1), which indicates that a surfactant concentration of 2.5 vol. % is not efficient at recovering the remaining oil in place. A design with

a lower concentration should be considered to reduce the chemical cost and hopefully improve the surfactant efficiency and profitability.

3.3 Onshore Surfactant Flood: Case 2

A second reservoir was created hypothetically, with more favorable reservoir properties than the reservoir from case 1, which had a lower porosity and permeability than a typical domestic onshore sandstone reservoir. A lower concentration surfactant flood was applied to this reservoir and evaluated using the CFEM.

3.3.1 Reservoir Description and Simulation

The hypothetical reservoir inherited all the properties from the Case 1 reservoir, except the porosity was increased to 20%, and the geometric mean of the permeability field was increased to 200 md. This reservoir was also initialized with a high initial oil saturation of 80% and waterflooded until a 98% water cut was reached. The chemical injection schedule for surfactant flooding this reservoir was as follows:

- Chemical slug: 0.60 PV of fluid with a surfactant concentration of 0.50 vol. % and a polymer concentration of 2000 ppm
- Polymer drive: 0.50 PV of fluid with a polymer concentration of 2000 ppm
- Water drive: 1.9 PV

The injection rate was held constant at 2243 B/D, for a full five-spot pattern, but since this surfactant flood uses a relatively high polymer concentration, the injection pressure was monitored. If the maximum bottomhole pressure exceed 2250 psi, the injection rate was switched to a variable rate, at a constant injection pressure of 2250 psi. The same pattern size, pattern spacing, and well arrangement were used.

Increasing the porosity resulted in an increase in the remaining oil in place, because the same initial oil saturation was used. The remaining oil in place for this hypothetical reservoir was 782,013 bbl, which is equal to an initial oil saturation of 36.0%. The oil production profile and the recovery efficiency from the surfactant flood simulation are shown in Figures 3.6 and 3.7, as a function of time and pore volumes injected, respectively. The recovery efficiency after 3 PV injected, and 33 years, was 85.49% ROIP. However, a majority of this oil has been recovered after about 14 years and 1.4 PV of fluid injection. The recovery efficiency and the oil production rates are substantially higher for this surfactant flood than for the Case 1 surfactant flood. The higher permeability and higher initial oil saturation (at the start of the surfactant flood) of this hypothetical reservoir are the main contributing factors to this improved performance.

3.3.2 Economic Analysis

All of the prices and costs used in the Case 1 surfactant flood apply to this case. The CFEM determined the economic limit to be 13 years, and the technical performance at this point is summarized in Table 3.4. At the economic limit, the surfactant flood has injected 1.19 PV of fluid and has injected only 0.09 PV of the water drive. The recovery efficiency at the economic limit is 84.23% ROIP, which is 99% of the oil that would be recovered after 3 PV of fluid injected. A surfactant efficiency of 0.27 bbl/lb is much higher than for the Case 1 surfactant flood, because of the lower surfactant concentration used.

At the economic limit, this surfactant flood has an NPV of $0.7 million, which is greater than zero, so this design meets the minimum required rate of return of 10%. An IRR of 12.11% also indicates that this surfactant flood is profitable. DROI is equal to 4.35, which seems attractive, but this profitability measure can be misleading when evaluating chemical flooding projects, because it does not take into account the negative cash flows early in the project from the

cost of the injected chemicals. Investment efficiency includes these negative cash flows in its definition of investment and is only 0.10 in this case, which is not very favorable. An investment efficiency of 1.0 or higher is considered favorable for EOR projects (Goodyear and Gregory, 1994). The other profitability measures given by the CFEM are summarized in Table 5.5.

Table 5.6 gives the profitability per barrel for this surfactant flood. A discounted chemical cost of $10.83/bbl is almost a third that of Case 1, and the operating cost is also significantly less. These appear to be the main factors contributing to the better economic performance of this case. The lower chemical cost per barrel is due to the lower surfactant concentration used and the better surfactant efficiency for this surfactant flood.

The cumulative DCF versus time and pore volumes injected is shown in Figures 3.7 and 3.8, respectively. The cumulative DCF appears to have reached a maximum during the polymer drive, but when the water drive starts, a new maximum is reached, because of the savings in chemical costs. At about 3 years, or 0.3 PV injected, the maximum capital exposure is about $7 million. An NPV of $0.7 million is not a significant profit for this amount of capital risk. This illustrates why investment efficiency is a suitable profitability measure for chemical flooding projects.

3.4 Conclusions

In this section, two different surfactant floods were simulated using the UTCHEM simulator and then evaluated using the CFEM. The first surfactant flood case was found to be very unprofitable, with an NPV of -$9.65 million. A discounted chemical cost of $29/bbl of oil produced was the main reason for the poor economic performance of this surfactant flood.

The second case was based on a hypothetical reservoir, with the same properties as the Case 1 reservoir, but with a higher porosity and permeability, closer to those typical of domestic onshore sandstone oil reservoirs. Surfactant flooding this reservoir was marginally profitable based on NPV and IRR, but an investment efficiency of 0.10, indicates that this case is not that favorable. A significantly lower chemical cost and a lower operating cost per barrel of oil produced were the contributing factors to the better economics of this case compared to Case 1.

One surfactant flooding design was evaluated for each reservoir, but to determine the full economic potential of surfactant flooding these reservoirs, the optimum design needs to be determined. Within the technical constraints of the surfactant flooding process, the optimum design should be based on profitability.

Table 3.1: Technical performance of the Case 1 surfactant flood

Economic limit (PV)	0.89
Chemical slug injected (PV)	0.25
Polymer slug injected (PV)	0.50
Water drive injected (PV)	0.14
Cumulative oil recovery (bbl)	927,629
Recovery efficiency (% ROIP)	50.98
Surfactant used (lb)	12,938,365
Polymer used (lb)	1,552,604
Surfactant efficiency (bbl/lb)	0.07
Polymer efficiency (bbl/lb)	0.06

Table 3.2: Profitability of the Case 1 surfactant flood

Profitability Measure	
Economic limit (years)	10
Internal rate of return (%)	n/a
Net present value (millions $)	-9.65
Discounted return on investment	-58.14
Investment efficiency	-0.77
Growth rate of return (%)	-5.03
Payback period (years)	Never
Discounted payback period (years)	Never

Table 3.3: Profitability per barrel of oil produced, nondiscounted and discounted at 10%, for the Case 1 surfactant flood

	Nondiscounted $/bbl	**Discounted $/bbl**
Revenue	18.00	18.00
Royalty	2.25	2.25
Capital cost	0.21	0.35
Operating cost	5.60	5.95
Chemical cost	20.48	28.61
Taxes	1.44	1.44
Profit	-11.98	-20.60

Table 3.4: Technical performance of the Case 2 surfactant flood

Economic limit (PV)	1.19
Chemical slug injected (PV)	0.60
Polymer slug injected (PV)	0.50
Water drive injected (PV)	0.09
Cumulative oil recovery (bbl)	2,634,630
Recovery efficiency (% ROIP)	84.23
Surfactant used (lb)	9,133,113
Polymer used (lb)	6,697,617
Surfactant efficiency (bbl/lb)	0.29
Polymer efficiency (bbl/lb)	0.17

Table 3.5: Profitability of the Case 2 surfactant flood

Profitability Measure	
Economic limit (years)	13
Internal rate of return (%)	12.11
Net present value (millions $)	0.70
Discounted return on investment	4.35
Investment efficiency	0.10
Growth rate of return (%)	11.08
Payback period (years)	6.69
Discounted payback period (years)	8.31

Table 3.6: Profitability per barrel of oil produced, nondiscounted and discounted at 10%, for the Case 2 surfactant flood

	Nondiscounted $/bbl	**Discounted $/bbl**
Revenue	18.00	18.00
Royalty	2.25	2.25
Capital cost	0.06	0.11
Operating cost	2.76	2.88
Chemical cost	9.01	10.83
Taxes	1.44	1.44
Profit	2.47	0.48

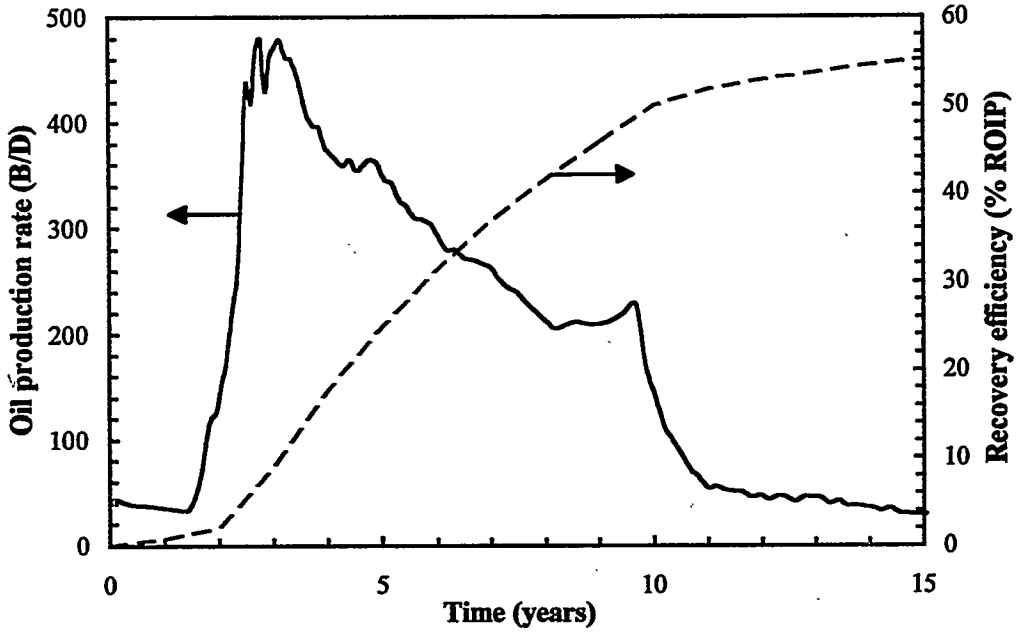


Figure 3.1: Oil production rate and recovery efficiency versus time for the Case 1 surfactant flood

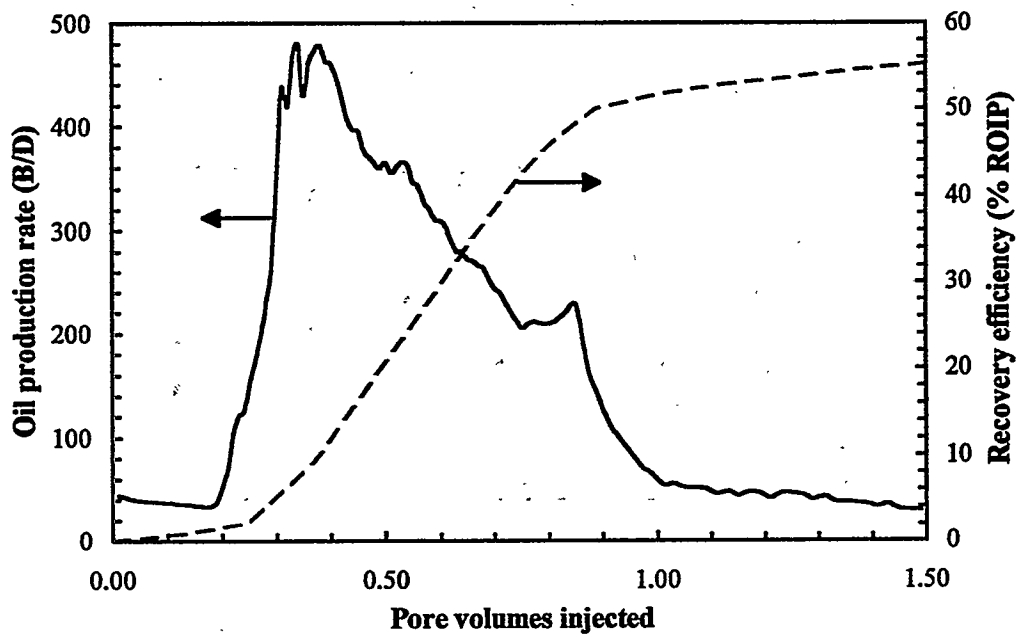


Figure 3.2: Oil production rate and recovery efficiency versus pore volumes injected for the Case 1 surfactant flood

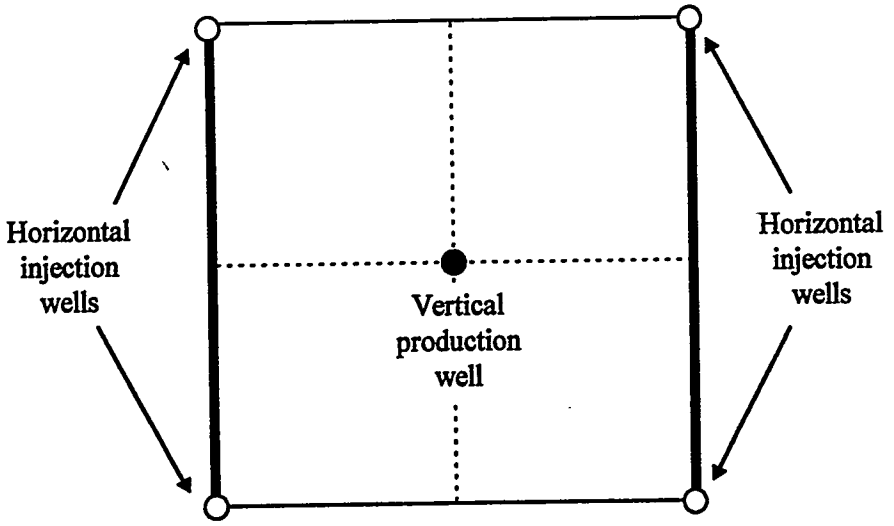


Figure 3.3: The full forty-acre five-spot pattern used in the economic analysis of the Case 1 surfactant flood

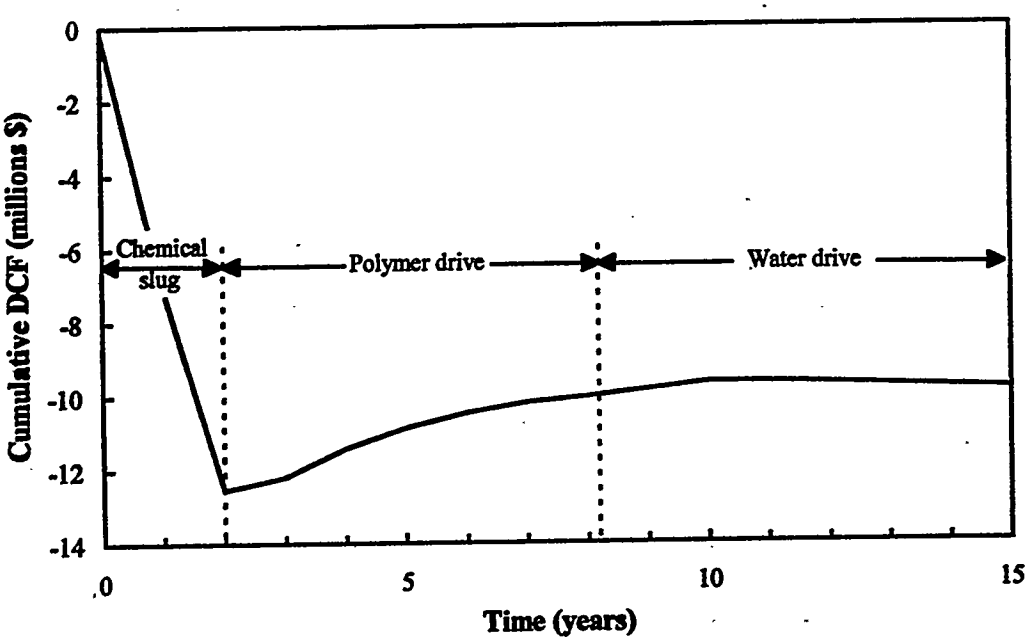


Figure 3.4: Cumulative DCF versus time for the Case 1 surfactant flood

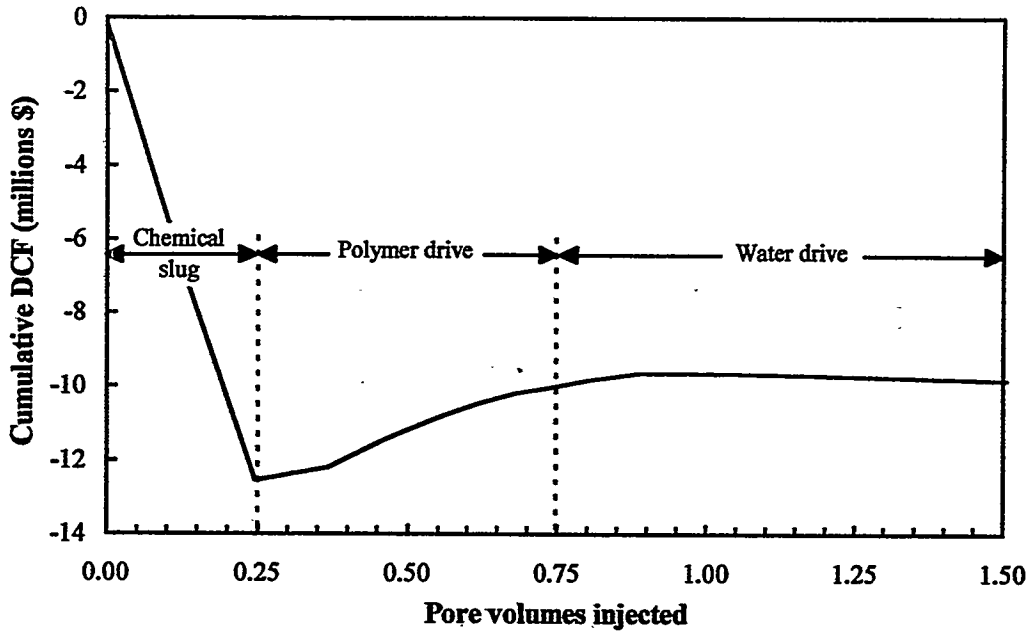


Figure 3.5: Cumulative DCF versus pore volumes injected for the Case 1 surfactant flood

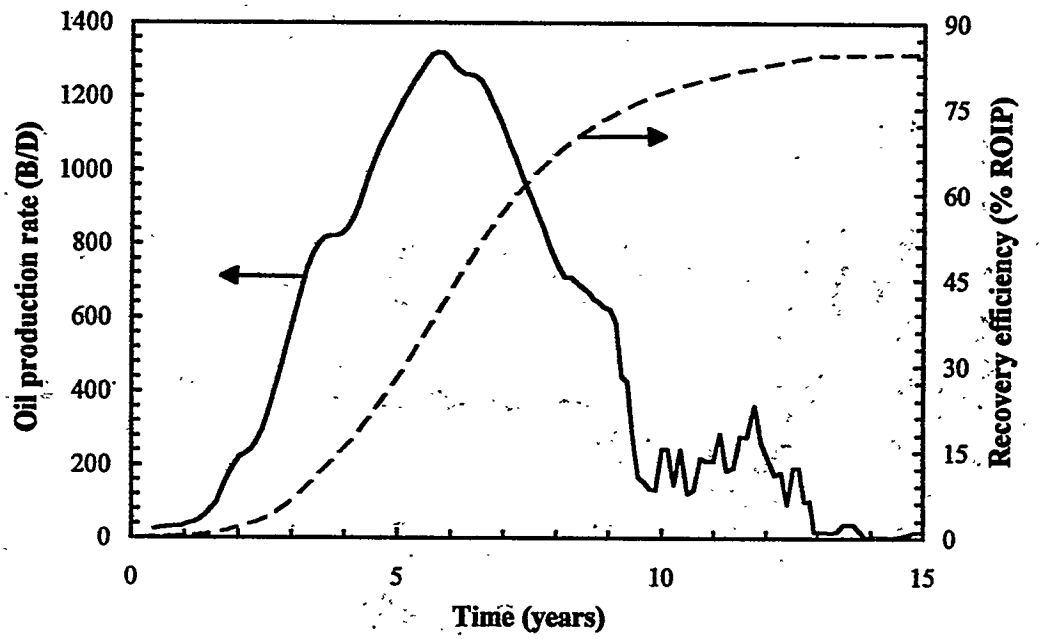


Figure 3.6: Oil production rate and recovery efficiency versus time for the Case 2 surfactant flood

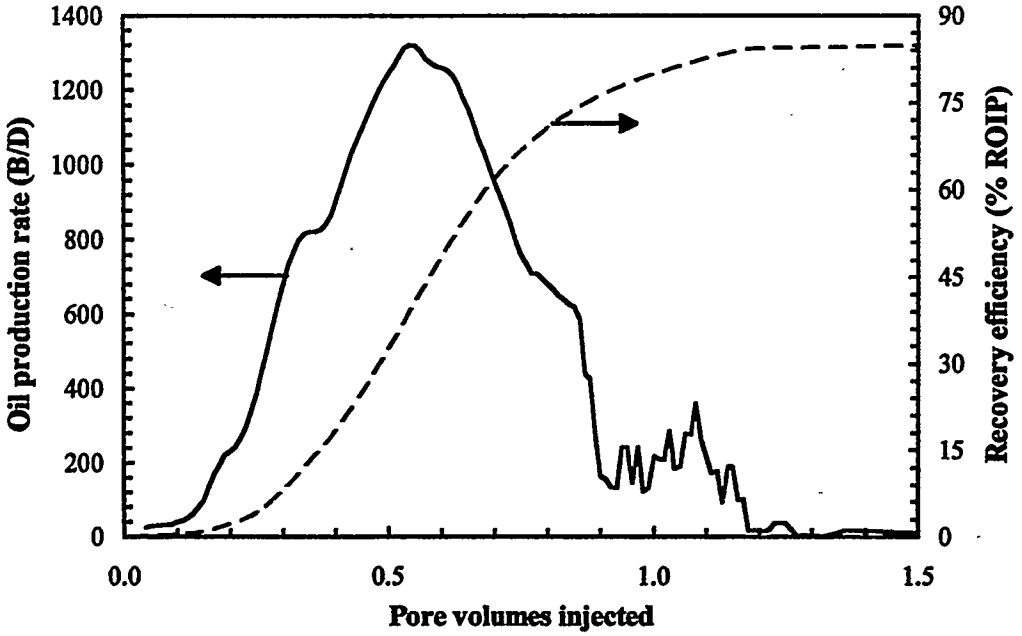


Figure 3.7: Oil production rate and recovery efficiency versus pore volumes injected for the Case 2 surfactant flood

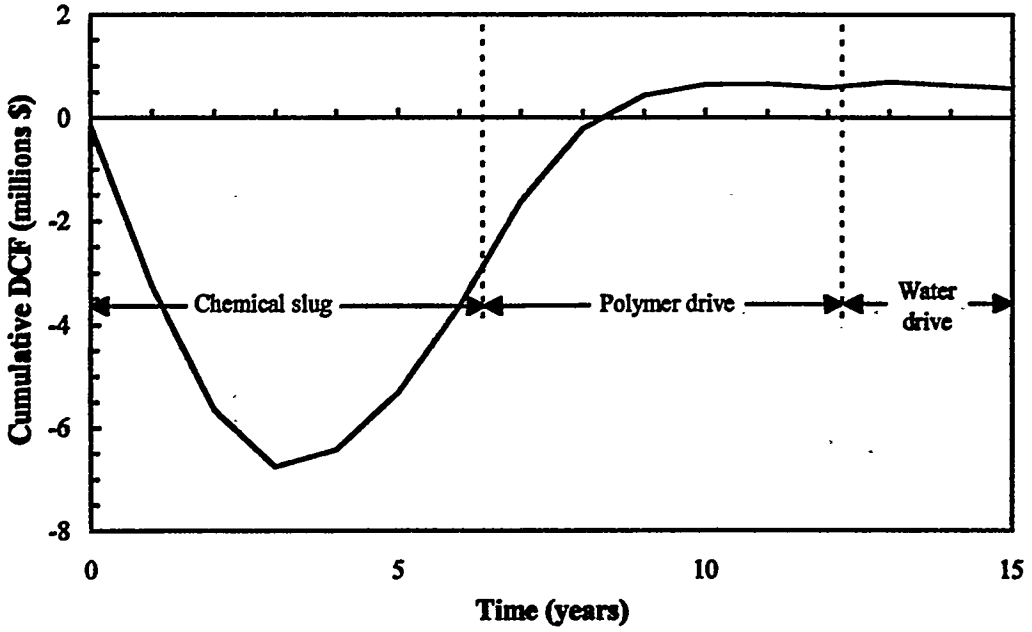


Figure 3.8: Cumulative DCF versus time for the Case 2 surfactant flood

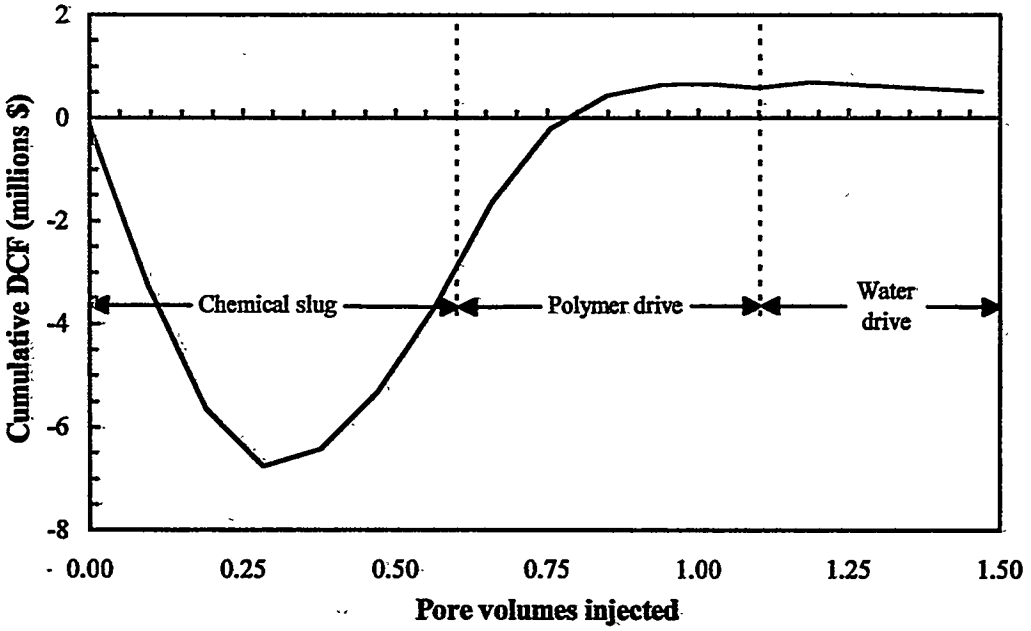


Figure 3.9: Cumulative DCF versus pore volumes injected for the Case 2 surfactant flood.

4. Optimization of Surfactant Flooding

4.1 Introduction

In the process of implementing a commercial surfactant flooding project, the operator needs to determine the optimal chemical slug sizes and concentrations to maximize profit. In practice, it is difficult to determine the optimum design because it is not possible to exactly predict the performance of the surfactant flood. Even if the production profile were known, the project profitability is uncertain because of the difficulty in predicting future prices, costs, and tax rates. However, reservoir simulation and economic modeling can be used to advantage by performing an optimization study. Most companies combine this approach with field pilots before attempting a commercial operation.

Reservoir simulation has been used by Jakobsen and Hovland (1994) to optimize well arrangements and surfactant slug sizes in North Sea reservoirs. The analysis by Jakobsen and Hovland uses surfactant flooding as a supplement to waterflooding and assumes the surfactant concentration is constant at 3%. Barua *et al.* (1986) presented a method to optimize surfactant flooding using a simplistic mathematical model to determine the surfactant flood performance. The analysis by Barua *et al.* assumed the surfactant concentration was constant at 5%, and only optimized the surfactant slug size.

The objective of this work is to comprehensively optimize surfactant flooding for a given reservoir, by considering variations in the chemical slug sizes and the chemical concentrations. The second surfactant flood case presented in the previous chapter was based on a hypothetical reservoir and was found to be marginally profitable. This chapter presents the optimization of surfactant flooding of this reservoir in detail, and the sensitivity of the optimization process to oil price and various profitability measures.

4.2 Evaluating Mutually Exclusive Projects

The optimization of surfactant flooding for a specific reservoir requires analysis of mutually exclusive projects. Mutually exclusive projects are projects where the acceptance of one project means the rejection of all the others (Thompson and Wright, 1984). Incremental analysis is often used to compare mutually exclusive projects that have different initial investments and rates of return. However, all the surfactant flood designs in the optimization process have the same initial investment, so the incremental investment is zero. Therefore, to determine the optimum surfactant flood design, each design was evaluated on a stand-alone basis. The design with the greatest profitability was chosen as the optimum design.

4.3 Selecting a Suitable Profitability Measure

If the operator of the surfactant flood has no capital constraints, then the project with the highest NPV should be selected, because it maximizes the wealth of the company. A more common situation is that the company has limited capital resources and must select a project that will yield the maximum return on the available investment capital. Therefore, the alternative with the greatest profitability per dollar invested should be selected (Seba, 1987). Profitability measures that take into account the investment include IRR, DROI, investment efficiency, and GROR.

Jakobsen and Hovland (1994) and Barua *et al.* (1986) used NPV as their primary profitability measure to optimize surfactant flooding. Barua *et al.* made the assumption that the

company would want to maximize wealth and did not use a profitability per dollar invested. Jakobsen and Hovland did not discuss why NPV was used as their profitability measure.

In this study, it was assumed that capital resources are limited, so investment efficiency was used as the primary measure to rank the different designs. The suitability of investment efficiency as a profitability measure for EOR projects was discussed in Section 2. The effect of different profitability measures on the optimization process is presented later in this chapter.

4.4 Optimization of Surfactant Flooding

The optimization of surfactant flooding for this reservoir required 84 simulations. During the optimization process, the chemical slug size, the surfactant concentration, and the polymer concentration were varied. It was not necessary to optimize the polymer drive size, because the most profitable design reached its economic limit during the chemical slug.

The optimization process required simulation runs with polymer concentrations of 1000 ppm, 1500 ppm, 2000 ppm, 2500 ppm, and 3000 ppm. At each polymer concentration, the surfactant concentration and chemical slug size were varied and optimized. The surfactant concentrations used were 0.05 vol. % , 0.10 vol. %, 0.25 vol. %, and 0.50 vol. %. The optimization process did not consider surfactant concentrations less than 0.05 vol. % because the surfactant will not be effective if its concentration is too close to or below the critical micelle concentration (CMC). The CMC used in this study was 0.006 %, which is typical of highly effective synthetic surfactants, and lower values have been reported by Kalpakci *et al.* (1993, 1990). Chemical slug sizes ranged from 0.1 PV to 2.0 PV, depending on the surfactant concentration used.

4.4.1 Technical Performance

All the simulation runs and their recovery efficiency at 3 PV injected are summarized in Tables 4.1 to 4.5. The highest recovery efficiency of all the designs considered was 96.5% ROIP, which corresponds to simulation run *utnew184*. This is not necessarily the optimum recovery efficiency, but the highest of all the designs considered.

The recovery efficiency at 3 PV injected for all the simulated designs is plotted against the amount of surfactant injected, while holding the polymer concentration constant, in Figures 4.1 to 4.5. For a given amount of surfactant injected, the recovery efficiency decreases with increasing surfactant concentration. The higher concentration designs (0.25 vol. % and 0.50 vol. %) produce only slightly more oil than designs at 0.10 vol. %, which suggests that the additional surfactant being injected is not effective at mobilizing more oil. These trends are observed at all polymer concentrations.

Recovery efficiency is also plotted against the amount of polymer injected, while holding the surfactant concentration constant, in Figures 4.6 to 4.9. At a surfactant concentration of 0.05 vol. %, there is clearly an increase in oil recovery as the polymer concentration is increased. As the surfactant concentration is increased, the difference in oil recovery between the low polymer concentration designs and the high concentration designs is less significant. At surfactant concentrations of 0.25 vol. % and 0.50 vol. %, and for a given amount of polymer injected, the highest recovery efficiencies are achieved by designs with a polymer concentration of 1000 ppm.

However, a high recovery efficiency does not imply that the design is profitable. Each of the designs mentioned above were economically evaluated using the CFEM. The profitability of the designs depends on when the economic limit is reached and how much oil has been recovered at that time. The technical performance of the surfactant flood designs at the economic limit are summarized in Tables 4.6 to 4.10. The economic life of the surfactant floods varies between 7 and 13 years. Of all the designs evaluated, about 60% reach the polymer drive and only about 25% reach the water drive.

There is a large variation in surfactant efficiency among the designs, ranging from 1.89 to 0.23 barrels of oil produced per pound of surfactant injected (bbl/lb). The most efficient design uses a surfactant concentration of 0.05 vol. % and a polymer concentration of 3000 ppm. The surfactant efficiency generally decreases as the surfactant concentration increases. An increase in polymer concentration also improves the surfactant efficiency for a given surfactant concentration.

The polymer efficiency is not as sensitive to the design as the surfactant efficiency, ranging from 0.15 bbl/lb to 0.34 bbl/lb. The design with the highest polymer efficiency uses a surfactant concentration of 0.05 vol. % and a polymer concentration of 1000 ppm. At higher surfactant concentrations, the polymer efficiency decreases because many of these designs have used some or all of the polymer drive when the economic limit is reached. As the polymer concentration is increased, there is only a slight decrease in polymer efficiency at a given surfactant concentration. This means that increasing the polymer concentration is an efficient way to improve the oil recovery without increasing the chemical cost per barrel of oil produced.

4.4.2 Determining the Optimum Design

Optimization focuses on the relative profitability, not the absolute profitability, of the designs, which is why it was not necessary to accurately estimate all initial capital costs. The optimum design was determined using investment efficiency as the profitability measure.

Investment efficiency was plotted against the design chemical slug size, instead of the actual slug size injected at the economic limit, to allow easier interpretation of the design with the optimum chemical slug size. At a polymer concentration of 1000 ppm. the optimum design has a chemical slug of 1.0 PV and a surfactant concentration of 0.10 vol. %, as shown in Figure 4.10. Project profitability decreases rapidly as the surfactant concentration is increased above 0.10 vol. %.

The optimization of designs with higher polymer concentrations are shown in Figures 4.11 to 4.14. As the polymer concentration is increased, the relative profitability of designs with a surfactant concentration of 0.05 vol. % improves. At all polymer concentrations, except for 1000 ppm, the optimum design has a surfactant concentration of 0.05 vol. % and a design chemical slug size of 1.0 PV. Larger chemical slug sizes give the same project profitability because the CFEM evaluates each design at its economic limit. If the economic limit is reached while still injecting the chemical slug, then increasing the slug size past the economic limit is redundant. The actual pore volumes injected at the economic limit are given in Tables 4.6 to 4.10, which summarize the technical performance of each design.

Figures 4.15 to 4.18 show the optimization results when the surfactant concentration is held constant and the polymer concentration varied. The optimum polymer concentration varies depending on the surfactant concentration. In general, the relative profitability of the various polymer concentration designs is not consistent across the range of surfactant concentrations. For example, at a surfactant concentration of 0.10 vol. % (Figure 4.16), the least profitable polymer concentration is 3000 ppm. However, at a surfactant concentration of 0.50 vol. % (Figure 4.18), a polymer concentration of 3000 ppm almost gives the optimum design. At the optimum chemical slug size of 1 PV and the optimum surfactant concentration of 0.05 vol. %, the optimum polymer concentration is 2000 ppm (Figure 4.15).

To get a clearer picture of the optimum design, investment efficiency is plotted against surfactant concentration in Figure 4.19. At the optimum chemical slug size and surfactant concentration, the optimum polymer concentration is clearly 2000 ppm. However, the profitability at polymer concentrations of 1500 and 2500 ppm is only marginally less than at 2000 ppm. When making the final decision, the 1500 ppm design may be favored by the operator, because of the technical risks associated with using a high polymer concentration.

At the optimum chemical slug size and polymer concentration, investment efficiency is plotted against the surfactant concentration, as shown in Figure 4.20. An optimum surfactant concentration was not determined, even with a surfactant concentration as low as 0.05 vol. %.

Lower surfactant concentrations were not considered because of the increased technical risk at concentrations close to the CMC.

The simulation run corresponding to the optimum design is *utnew82*. According to Table 4.1, this design has reached its economic limit at 0.79 PV injected, which is less than the design chemical slug size of 1.0 PV. Optimization of surfactant flooding for this reservoir has shown that the most economical design has a large chemical slug with the lowest surfactant concentration, and no polymer drive. To determine the full economic potential of the optimum design, it was necessary to run another simulation using the optimum chemical slug size (0.79 PV) and no polymer drive. This simulation run, corresponding to this optimum design, was called *utnewopt*. Ideally, the CFEM and UTCHEM simulator should be integrated, so the chemical injection schedule can be adjusted during runtime, when the economic limit is reached.

The technical performance of the optimum design is summarized in Table 4.11. At the economic limit of 10 years and 0.86 PV injected, the recovery efficiency is 57.5 % ROIP, which is about 99% of the oil that would be recovered after 3 PV injected. The oil production rate and recovery efficiency are plotted against time and pore volumes injected in Figures 4.21 and 4.22, respectively. These plots clearly show that most of the oil is recovered after 10 years or 0.9 PV injected.

The profitability of the optimum design is summarized in Table 4.11. All of the profitability measures indicate that this design is very attractive. However, not all of the initial capital costs were estimated, so the profitability of this design and the other designs could be misleading. The capital costs included were the workover costs for vertical wells already in place and the costs of drilling the horizontal injection wells. The calculation of these costs was explained in the first case study in Section 3. Additional facilities and equipment costs were not estimated, but this should not affect the optimization process because the capital costs were assumed to be the same for all the designs, which does not affect the relative profitability of the designs. An NPV of $4.3 million suggests that at least an additional $4.3 million could be spent on facilities and equipment, in addition to the workover and drilling costs, without exceeding the minimum required rate of return. This is not taking into account the benefits of capital recovery through depreciation, so the maximum capital expenditure could be significantly higher.

Cumulative DCF versus time for the optimum design is shown in Figure 4.23. This plot illustrates the high front end cost associated with the chemical injection and when the economic limit is reached. The economic limit is reached only one year after the chemical slug injection is completed.

The profitability of the optimum design, on a per barrel of oil produced basis, is given in Table 4.13. The chemical cost is a substantial cost component, consuming almost 30% of the revenue from production. However, a chemical cost of $5.39 per barrel of oil produced is relatively low compared to surfactant flooding projects implemented in the 1980's, which had chemical costs between $14 and 25/bbl of oil produced (Martin, 1992). Many of these surfactant floods used high surfactant concentrations between 2 and 5%, which is one of the several reasons why the chemical cost was high. This relatively low chemical cost of the optimum design is the main reason for its profitability.

The optimum surfactant flood design for this reservoir is similar to a Low Tension Polymer Flood (LTPF), proposed by Kalpakci *et al.* (1993, 1990). The chemicals used in this study are similar to those used in the LTPF process but less expensive to manufacture. Coreflood experiments by Kalpakci *et al.* used surfactant concentrations between 0.1 and 0.3 % and polymer concentrations between 500 and 750 ppm in the chemical slug, followed by a 0.5 PV graded polymer drive. Kalpakci *et al.* observed that substantial oil could still be recovered at a surfactant concentration of 0.10 vol. %. The optimum design differs from the designs used by Kalpakci *et al.*, with a slightly lower surfactant concentration (0.05 vol. %), a much higher polymer concentration (2000 ppm), and no polymer drive.

The results at 0.1 vol. % surfactant concentration are almost as favorable as the optimum design, and may be preferred because the technical risks are higher at very low surfactant concentrations. The surfactant efficiency is considerably higher than the polymer efficiency in the optimum and many other designs when the polymer concentration is greater than the surfactant

concentration. Most surfactant floods have traditionally used a lower polymer concentration than the surfactant concentration.

To gain a better understanding of why the lower concentration designs are more profitable for this reservoir, a higher concentration design was compared to the optimum design. A design with approximately the same amount of surfactant injected at the economic limit was chosen for comparison. The selection of this higher concentration design is shown in Figure 4.24. Simulation run *utnew111* corresponds to a design with a surfactant concentration of 0.50 vol. %, a polymer concentration of 2000 ppm, and a chemical slug size of 0.1 PV.

The recovery efficiencies of the two designs are plotted against pore volumes injected in Figure 4.25. At about 0.85 PV, the optimum design has reached its maximum recovery efficiency of about 58 % ROIP. The higher concentration design produced significantly less oil, reaching a maximum of 37 % ROIP at about 0.7 PV injected. This suggests that a small slug size combined with a relatively high surfactant concentration does not contact much of the target oil in this reservoir.

The oil production profiles for each design are shown in Figure 4.26 as a function of pore volumes injected. Up to about 0.4 PV injected, the production profiles correlate well, but thereafter the production rate for the higher concentration design falls rapidly. The maximum production rates for each design are about equal, which suggests that the higher concentration design is not mobilizing any more oil than the optimum design in a given time period.

The produced surfactant concentrations are plotted against pore volumes injected in Figure 4.27. Surfactant breakthrough for both designs is at about 0.1 PV injected. The surfactant front for the optimum case takes about 1.0 PV to channel through the reservoir, while it only takes about 0.4 PV for the higher concentration design. Surfactant concentrations produced by the optimum design are as low as 3 times the CMC. It is desirable to keep the produced surfactant concentration well above the CMC to ensure that the interfacial tension (IFT) between the oil and water is reduced to the lowest possible value, making it easier to mobilize the remaining oil in place. IFT increases rapidly below the CMC of a surfactant. Depending on the association between the surfactant and polymer, the lowest IFT is obtained for some systems at or above the CMC (Austad *et al.*, 1993). However, for a few surfactants the IFT is approximately constant above the CMC, assuming constant electrolyte composition and temperature, which was done in these simulations (Wu, 1996). The optimization process did not consider designs with surfactant concentrations lower than 0.05 vol. % because they are too close to the CMC.

The difference in cumulative DCF versus pore volumes injected for each design is shown in Figure 4.28. The poor economic performance of the higher concentration design is due to the large capital exposure at the start of the surfactant flood and the lack of revenue from oil production. The investment efficiency of the optimum design is 1.90, while it is only 0.29 for the higher concentration design, thereby taking into account the capital risk of each design. The maximum capital exposure of the optimum design is about $2.5 million, while it is about $4.0 million for the higher concentration design.

The petroleum industry has recognized for a long time that very dilute surfactant floods would be most favorable if they could be done successfully, i.e., if they could find a surfactant that is active and these low concentrations and under reservoir conditions, and inexpensive to manufacture. Surfactants of this type were not available until recently, and were taken advantage of in this study. Another factor in the optimum design, which differs from early attempts to make chemical flooding economical, is the use of a large amount of a suitable polymer to improve sweep efficiency. The horizontal injection well used in this study made it possible to use relatively high polymer concentrations without the reduced injectivity observed in chemical floods with vertical wells.

4.4.3 Effect of Oil Price

The effect of oil price on the optimization process was determined by re-evaluating the designs with a higher oil price of $35/bbl. The optimization results at $35/bbl, while holding the

polymer concentration constant, are shown in Figures 4.29 to 4.33. For all polymer concentrations, the optimum surfactant concentration is the same as at $18/bbl. However, the higher oil price has increased the optimum chemical slug size to 1.25 PV (Figure 4.31), but only 1.19 PV of the chemical slug has been injected at the economic limit. In general, the higher oil price increased the economic limit of all the designs.

The optimization results at $35/bbl, while holding the surfactant concentration constant, are shown in Figures 4.34 to 4.37. The higher oil price has affected the relative profitability of different polymer concentrations, but the optimum polymer concentration is still 2000 ppm, at a surfactant concentration of 0.05 vol. % (Figure 4.34).

4.4.4 Effect of Profitability Measures

The profitability of all the designs considered in the optimization process is shown in Tables 4.14 to 4.18. These tables summarize all of the relevant profitability measures produced by the CFEM, including the discounted chemical and operating costs per barrel of oil produced. DROI is not included in these tables because the initial capital cost does not include additional facilities and equipment costs, resulting in misleading values for DROI. In addition, the relative profitability of the designs using NPV gives the same results as DROI because the initial capital cost is the same for all the designs. The optimum value for each profitability measure has been highlighted.

Payback is not a suitable profitability measure for the optimization process, because it does not take into account the profit after payback is achieved. It is a good indicator of the capital risk associated with a particular surfactant flood design. The shortest payback period was 3.29 years (undiscounted) and 3.49 years (discounted) for the design corresponding to simulation run *utnewl21*. The payback period increases as the surfactant concentration increases, because of greater capital exposure at higher concentrations. Variations in the polymer concentration appear to have no effect on the payback period.

The discounted chemical cost per barrel of oil produced varies considerably among the designs, ranging from $4.86/bbl (27% of revenue) to $11.27/bbl (63% of revenue). As the surfactant concentration increases, the chemical cost per barrel increases, because of poorer surfactant efficiencies at higher concentrations. The chemical cost per barrel does not change significantly over the range of polymer concentrations. The design with the lowest chemical cost per barrel is not the optimum design, because it has a higher operating cost per barrel of oil produced, which offsets the lower chemical cost.

Lower operating costs per barrel of oil produced are observed at higher surfactant concentrations because of the higher recovery efficiencies of these designs. An interesting observation is that the sum of the discounted chemical and operating costs per barrel is at a minimum for the optimum surfactant flood design.

The effect of using NPV instead of investment efficiency as the profitability measure is shown in Figure 4.38. NPV clearly gives a different optimum polymer concentration than investment efficiency. At a polymer concentration of 3000 ppm, NPV still has not reached an optimum. Optimization of the surfactant concentration using investment efficiency and NPV is shown in Figure 4.39. NPV gives a higher optimum surfactant concentration than investment efficiency of 0.10 vol. %.

GROR gives the same optimization results as investment efficiency as shown by comparing Figures 4.38 to 4.41. This is expected because the reinvestment rate and discount rate are equal at 10%. In this case, GROR is simply the equivalent rate of return for investment efficiency.

The optimization of the polymer concentration using IRR and GROR is shown in Figure 4.40. This plot shows that IRR and GROR give different optimization results. IRR favors the higher polymer concentration designs compared to GROR. The optimization of surfactant concentration using IRR and GROR is shown in Figure 4.41. IRR and GROR give the same results, with IRR being more sensitive to the surfactant concentration than GROR, which is expected.

The effect of the profitability measures on the optimization process was also determined at a higher oil price of $35/bbl, as shown in Figures 4.42 to 4.45. At the higher oil price, the same conclusions can be made about the profitability measures. Investment efficiency and GROR give the same results. With a higher oil price, and greater profitability, NPV gives very different results than the other profitability measures. NPV gives an optimum polymer concentration of 3000 ppm (Figure 4.42) and an optimum surfactant concentration of 0.25 vol. % (Figure 4.43). In general, NPV favors the higher concentration designs, which have a higher front-end cost but maximize profit. IRR gives the same optimum surfactant concentration as GROR, but gives a higher optimum polymer concentration of 2500 ppm (Figure 4.44).

Investment efficiency is preferred over NPV because companies do not have unlimited capital resources and are not able to invest in all of the projects under consideration. To determine which projects should be undertaken, a suitable profitability measure must be used to rank potential investments, so that the return from the available investment capital is maximized.

4.5 Conclusions

Using the UTCHEM reservoir simulator and the CFEM, an optimum surfactant flood design, based on profitability, was determined for a domestic onshore reservoir. The optimum design has a large chemical slug (0.79 PV), with a low surfactant concentration (0.05 vol. %), a relatively high polymer concentration (2000 ppm), and no polymer drive. This design takes advantage of highly efficient synthetic surfactants that are active at low concentrations and compatible with xanthan gum polymer. The optimum design is very similar to the LTPF process, without the polymer drive, and with a much higher polymer concentration.

The optimum design was highly profitable, with a IRR of 51.8% and an NPV of $4.3 million. An investment efficiency of 1.9 indicates that this design is able to recover almost twice the amount of capital exposed at any time in the project. The CFEM assumed that there were no additional facilities and equipment costs, so the profitability of this design may be misleading. However, the NPV suggests that the additional facilities and equipment cost could be at least $4.3 million and still meet the minimum required rate of return. The additional capital costs to perform a surfactant flood on a forty-acre five-spot pattern are not likely to be this high.

The profitability of the surfactant flood designs was most sensitive to the surfactant concentration used. As the surfactant concentration was increased, the surfactant efficiency decreased, resulting in substantially higher chemical costs per barrel of oil produced and a lower project profitability. Variations in the polymer concentration, at a constant slug size and surfactant concentration, did not have much impact on profitability. The profitability of the optimum design does not change significantly between 1500 ppm and 2500 ppm.

In the past, the economics of surfactant flooding has suffered because of the injectivity reduction associated with the injection of polymer. The key to the success of the optimum design is the use of a horizontal injection well, which significantly reduces the project life. The horizontal injection well improves the injectivity, allowing the benefits of higher polymer concentrations to be utilized. Further work needs to be done on the relative profitability of well arrangements with various combinations of horizontal and vertical wells. The effect of well spacing on profitability also needs to be determined.

Investment efficiency and GROR are recommended as profitability measures for evaluating and optimizing surfactant flooding projects. These measures are favored because they include the initial negative cash flows, typical of EOR projects, as part of the investment. Using NPV as the profitability measure gives a very different optimum design than does investment efficiency, favoring higher surfactant and polymer concentrations. NPV should not be used as a ranking tool, because its use assumes that the company has unlimited capital resources and is able to invest in all projects that meet the minimum required rate of return. DROI is not a suitable measure for optimization because it does not take into account the different levels of capital risk in surfactant flooding projects.

Table 4.1: Simulation runs at a polymer concentration of 1000 ppm

Name of simulation run	Chemical slug size (PV)	Surfactant concentration (vol %)	Recovery efficiency at 3 PV injected (% ROIP)
utnew1	0.75	0.05	41.95
utnew2	1.00	0.05	47.42
utnew3	1.25	0.05	51.69
utnew4	1.50	0.05	55.60
utnew11	0.50	0.10	41.33
utnew12	1.00	0.10	60.38
utnew13	1.50	0.10	69.69
utnew14	2.00	0.10	74.99
utnew21	0.25	0.25	35.04
utnew22	0.50	0.25	52.93
utnew23	0.75	0.25	67.21
utnew24	1.00	0.25	74.57
utnew25	1.25	0.25	78.64
utnew31	0.10	0.50	26.63
utnew32	0.20	0.50	37.62
utnew33	0.40	0.50	57.03
utnew34	0.60	0.50	69.90

Table 4.2: Simulation runs at a polymer concentration of 1500 ppm

Name of simulation run	Chemical slug size (PV)	Surfactant concentration (vol. %)	Recovery efficiency at 3 PV injected (% ROIP)
utnew41	0.75	0.05	51.19
utnew42	1.00	0.05	57.93
utnew43	1.25	0.05	62.90
utnew44	1.50	0.05	66.42
utnew51	0.50	0.10	49.44
utnew52	1.00	0.10	70.29
utnew53	1.50	0.10	78.71
utnew54	2.00	0.10	82.19
utnew60	0.25	0.25	42.19
utnew61	0.50	0.25	65.46
utnew62	0.75	0.25	78.49
utnew63	1.00	0.25	82.41
utnew64	1.25	0.25	85.61
utnew71	0.10	0.50	31.96
utnew72	0.20	0.50	45.54
utnew73	0.40	0.50	70.08
utnew74	0.60	0.50	80.13

Table 4.3: Simulation runs at a polymer concentration of 2000 ppm

Name of simulation run	Chemical slug size (PV)	Surfactant concentration (vol. %)	Recovery efficiency at 3 PV injected (% ROIP)
utnew81	0.75	0.05	59.84
utnew82	1.00	0.05	68.73
utnew83	1.25	0.05	73.59
utnew84	1.50	0.05	77.37
utnew91	0.50	0.10	55.72
utnew92	1.00	0.10	78.97
utnew93	1.50	0.10	84.99
utnew94	2.00	0.10	87.66
utnew100	0.25	0.25	48.10
utnew101	0.50	0.25	75.04
utnew102	0.75	0.25	83.70
utnew103	1.00	0.25	88.03
utnew104	1.25	0.25	90.84
utnew111	0.10	0.50	36.83
utnew112	0.20	0.50	52.62
utnew113	0.40	0.50	78.59
utnew114	0.60	0.50	85.49

Table 4.4: Simulation runs at a polymer concentration of 2500 ppm

Name of simulation run	Chemical slug size (PV)	Surfactant concentration (vol. %)	Recovery efficiency at 3 PV injected (% ROIP)
utnew121	0.75	0.05	69.58
utnew122	1.00	0.05	76.87
utnew123	1.25	0.05	80.77
utnew124	1.50	0.05	83.06
utnew131	0.50	0.10	61.85
utnew132	1.00	0.10	85.27
utnew133	1.50	0.10	89.80
utnew134	2.00	0.10	92.65
utnew140	0.25	0.25	53.25
utnew141	0.50	0.25	82.77
utnew142	0.75	0.25	89.16
utnew143	1.00	0.25	92.91
utnew144	1.25	0.25	94.78
utnew151	0.10	0.50	40.73
utnew152	0.20	0.50	59.57
utnew153	0.40	0.50	83.99
utnew154	0.60	0.50	89.94

Table 4.5: Simulation runs at a polymer concentration of 3000 ppm

Name of simulation run	Chemical slug size (PV)	Surfactant concentration (vol. %)	Recovery efficiency at 3 PV injected (% ROIP)
utnew161	0.75	0.05	75.70
utnew162	1.00	0.05	81.58
utnew163	1.25	0.05	85.28
utnew171	0.50	0.10	69.56
utnew172	1.00	0.10	88.37
utnew173	1.50	0.10	93.50
utnew180	0.25	0.25	59.44
utnew181	0.50	0.25	86.35
utnew182	0.75	0.25	92.92
utnew183	1.00	0.25	95.30
utnew184	1.25	0.25	96.53
utnew191	0.10	0.50	44.18
utnew192	0.20	0.50	65.15
utnew193	0.40	0.50	87.33
utnew194	0.60	0.50	92.75

Table 4.6: Technical performance at the economic limit with a polymer concentration of 1000 ppm

Name of simulation run	Economic limit (years)	Economic limit (PV)	Chemical slug used (PV)	Polymer drive used (PV)	Water drive used (PV)	Recovery efficiency (% ROIP)	Surfactant efficiency (bbl/lb)	Polymer efficiency (bbl/lb)
utnew1	8	0.75	0.75	0.00	0.00	37.12	1.02	0.34
utnew2	9	0.85	0.85	0.00	0.00	40.53	0.98	0.33
utnew3	9	0.85	0.85	0.00	0.00	40.53	0.98	0.33
utnew4	9	0.85	0.85	0.00	0.00	40.53	0.98	0.33
utnew11	8	0.75	0.50	0.25	0.00	36.53	0.75	0.30
utnew12	11	1.04	1.00	0.04	0.00	55.57	0.57	0.28
utnew13	11	1.04	1.04	0.00	0.00	55.62	0.55	0.28
utnew14	11	1.04	1.04	0.00	0.00	55.62	0.55	0.28
utnew21	9	0.85	0.25	0.50	0.10	33.41	0.55	0.25
utnew22	9	0.85	0.50	0.35	0.00	48.87	0.40	0.24
utnew23	12	1.13	0.75	0.38	0.00	64.19	0.35	0.22
utnew24	13	1.23	1.00	0.23	0.00	68.59	0.28	0.19
utnew25	10	0.94	0.94	0.00	0.00	58.90	0.26	0.18
utnew31	8	0.75	0.10	0.50	0.15	24.50	0.50	0.23
utnew32	9	0.85	0.20	0.50	0.15	35.38	0.36	0.21
utnew33	11	1.04	0.40	0.50	0.14	55.58	0.29	0.20
utnew34	13	1.23	0.60	0.50	0.13	67.94	0.23	0.17

Table 4.7: Technical performance at the economic limit with a polymer concentration of 1500 ppm

Name of simulation run	Economic limit (years)	Economic limit (PV)	Chemical slug used (PV)	Polymer drive used (PV)	Water drive used (PV)	Recovery efficiency (% ROIP)	Surfactant efficiency (bbl/lb)	Polymer efficiency (bbl/lb)
utnew41	8	0.75	0.75	0.00	0.00	46.57	1.28	0.32
utnew42	9	0.85	0.85	0.00	0.00	50.16	1.21	0.30
utnew43	9	0.85	0.85	0.00	0.00	50.16	1.21	0.30
utnew44	9	0.85	0.85	0.00	0.00	50.16	1.21	0.30
utnew51	8	0.75	0.50	0.25	0.00	45.94	0.94	0.29
utnew52	10	0.94	0.94	0.00	0.00	62.36	0.68	0.27
utnew53	10	0.94	0.94	0.00	0.00	62.36	0.68	0.27
utnew54	10	0.94	0.94	0.00	0.00	62.36	0.68	0.27
utnew60	7	0.65	0.25	0.40	0.00	38.57	0.63	0.25
utnew61	9	0.85	0.50	0.35	0.00	60.92	0.50	0.25
utnew62	11	1.04	0.75	0.29	0.00	72.25	0.40	0.22
utnew63	9	0.85	0.85	0.00	0.00	65.07	0.32	0.20
utnew64	9	0.85	0.85	0.00	0.00	65.07	0.32	0.20
utnew71	8	0.70	0.10	0.50	0.10	30.77	0.63	0.23
utnew72	8	0.75	0.20	0.50	0.05	43.45	0.45	0.22
utnew73	11	1.04	0.40	0.50	0.14	68.28	0.35	0.21
utnew74	13	1.23	0.60	0.50	0.13	78.63	0.27	0.17

Table 4.8: Technical performance at the economic limit with a polymer concentration of 2000 ppm

Name of simulation run	Economic limit (years)	Economic limit (PV)	Chemical slug used (PV)	Polymer drive used (PV)	Water drive used (PV)	Recovery efficiency (% ROIP)	Surfactant efficiency (bbl/lb)	Polymer efficiency (bbl/lb)
utnew81	9	0.78	0.75	0.03	0.00	55.36	1.52	0.29
utnew82	9	0.79	0.79	0.00	0.00	56.06	1.47	0.29
utnew83	9	0.79	0.79	0.00	0.00	56.06	1.47	0.29
utnew84	9	0.79	0.79	0.00	0.00	56.06	1.47	0.29
utnew91	7	0.64	0.50	0.14	0.00	49.35	1.01	0.29
utnew92	9	0.83	0.83	0.00	0.00	64.74	0.81	0.27
utnew93	9	0.83	0.83	0.00	0.00	64.74	0.81	0.27
utnew94	9	0.83	0.83	0.00	0.00	64.74	0.81	0.27
utnew100	7	0.60	0.25	0.35	0.00	43.53	0.72	0.24
utnew101	10	0.91	0.50	0.41	0.00	70.87	0.58	0.24
utnew102	10	0.93	0.75	0.18	0.00	74.91	0.41	0.21
utnew103	8	0.75	0.75	0.00	0.00	65.67	0.36	0.20
utnew104	8	0.75	0.75	0.00	0.00	65.67	0.36	0.20
utnew111	7	0.56	0.10	0.46	0.00	33.18	0.68	0.21
utnew112	9	0.75	0.20	0.50	0.05	51.20	0.53	0.22
utnew113	11	1.03	0.40	0.50	0.13	76.87	0.39	0.21
utnew114	13	1.19	0.60	0.50	0.09	84.23	0.29	0.17

Table 4.9: Technical performance at the economic limit with a polymer concentration of 2500 ppm

Name of simulation run	Economic limit (years)	Economic limit (PV)	Chemical slug used (PV)	Polymer drive used (PV)	Water drive used (PV)	Recovery efficiency (% ROIP)	Surfactant efficiency (bbl/lb)	Polymer efficiency (bbl/lb)
utnew121	10	0.74	0.74	0.00	0.00	61.28	1.70	0.28
utnew122	10	0.74	0.74	0.00	0.00	61.28	1.70	0.28
utnew123	10	0.74	0.74	0.00	0.00	61.28	1.70	0.28
utnew124	10	0.74	0.74	0.00	0.00	61.28	1.70	0.28
utnew131	8	0.65	0.50	0.15	0.00	55.89	1.15	0.27
utnew132	10	0.78	0.78	0.00	0.00	68.96	0.91	0.26
utnew133	10	0.78	0.78	0.00	0.00	68.96	0.91	0.26
utnew134	10	0.78	0.78	0.00	0.00	68.96	0.91	0.26
utnew140	8	0.61	0.25	0.36	0.00	49.21	0.81	0.24
utnew141	10	0.82	0.50	0.32	0.00	73.89	0.61	0.23
utnew142	11	0.87	0.75	0.12	0.00	77.86	0.43	0.20
utnew143	9	0.78	0.78	0.00	0.00	72.81	0.38	0.19
utnew144	9	0.78	0.78	0.00	0.00	72.81	0.38	0.19
utnew151	7	0.52	0.10	0.42	0.00	35.92	0.74	0.21
utnew152	11	0.77	0.20	0.50	0.07	58.42	0.60	0.22
utnew153	13	0.98	0.40	0.50	0.08	82.30	0.42	0.20
utnew154	11	0.89	0.60	0.29	0.00	81.10	0.28	0.16

Table 4.10: Technical performance at the economic limit with a polymer concentration of 3000 ppm

Name of simulation run	Economic limit (years)	Economic limit (PV)	Chemical slug used (PV)	Polymer drive used (PV)	Water drive used (PV)	Recovery efficiency (% ROIP)	Surfactant efficiency (bbl/lb)	Polymer efficiency (bbl/lb)
utnew161	11	0.70	0.70	0.00	0.00	64.25	1.89	0.27
utnew162	11	0.70	0.70	0.00	0.00	64.25	1.89	0.27
utnew163	11	0.70	0.70	0.00	0.00	64.25	1.89	0.27
utnew171	9	0.65	0.50	0.15	0.00	61.88	1.27	0.25
utnew172	10	0.72	0.72	0.00	0.00	69.82	1.00	0.26
utnew173	10	0.72	0.72	0.00	0.00	69.82	1.00	0.26
utnew180	8	0.59	0.25	0.34	0.00	53.57	0.88	0.23
utnew181	10	0.75	0.50	0.25	0.00	74.77	0.61	0.22
utnew182	9	0.72	0.72	0.00	0.00	72.83	0.42	0.19
utnew183	9	0.72	0.72	0.00	0.00	72.83	0.42	0.19
utnew184	9	0.72	0.72	0.00	0.00	72.83	0.42	0.19
utnew191	7	0.49	0.10	0.39	0.00	38.07	0.78	0.20
utnew192	9	0.66	0.20	0.46	0.00	60.31	0.62	0.21
utnew193	11	0.80	0.40	0.40	0.00	79.10	0.41	0.18
utnew194	12	0.83	0.60	0.23	0.00	82.01	0.28	0.15

Table 4.11: Technical performance of the optimum surfactant flood design at the economic limit

Economic limit (years)	10
Economic limit (PV)	0.86
Chemical slug used (PV)	0.79
Polymer drive used (PV)	0.00
Water drive used (PV)	0.07
Recovery efficiency (% ROIP)	57.50
Surfactant used (millions lb)	1.20
Polymer used (millions lb)	4.80
Surfactant efficiency (bbl/lb)	1.50
Polymer efficiency (bbl/lb)	0.30

Table 4.12: Profitability of the optimum surfactant flood design

Internal rate of return (%)	51.80
Net present value (millions $)	4.27
Discounted return on investment	26.66
Investment efficiency	1.90
Growth rate of return (%)	22.36
Payback period (years)	3.33
Discounted payback period (years)	3.53

Table 4.13: Profitability per barrel of oil produced for the optimum surfactant flood design

	Discounted $/bbl	% of revenue
Revenue	18.00	
Royalty	2.25	12.5
Capital cost	0.15	8.3
Operating cost	3.35	18.6
Chemical cost	5.39	29.9
Taxes	2.96	16.4
Profit	3.90	21.6

Table 4.14: Profitability of surfactant floods with a polymer concentration of 1000 ppm

Name of simulation run	IRR (%)	NPV (millions $)	Investment efficiency	GROR (%)	Payback period (years)	Discounted payback (years)	Chemical cost ($/bbl)	Operating cost ($/bbl)
utnew1	39.21	2.35	1.37	19.92	3.77	4.05	4.86	4.47
utnew2	39.65	2.47	1.44	20.27	3.77	4.05	4.94	4.53
utnew3	39.65	2.47	1.44	20.27	3.77	4.05	4.94	4.53
utnew4	39.65	2.47	1.44	20.27	3.77	4.05	4.94	4.53
utnew11	33.32	2.10	1.04	18.11	4.08	4.45	5.64	4.28
utnew12	37.45	3.12	1.54	20.76	4.08	4.44	5.74	4.02
utnew13	37.22	3.05	1.50	20.57	4.08	4.45	5.79	4.04
utnew14	37.24	3.05	1.51	20.58	4.08	4.44	5.79	4.03
utnew21	19.64	1.08	0.34	13.27	4.38	4.83	7.18	4.62
utnew22	21.82	1.93	0.56	14.98	5.29	5.86	7.50	3.67
utnew23	22.06	2.24	0.65	15.62	5.41	6.22	7.97	3.65
utnew24	20.46	1.81	0.52	14.73	5.40	6.22	8.77	3.73
utnew25	19.49	1.51	0.44	14.06	5.41	6.22	8.99	3.64
utnew31	11.87	0.20	0.06	10.66	4.72	6.11	8.16	5.23
utnew32	12.35	0.39	0.08	10.83	5.01	6.00	8.91	4.29
utnew33	11.31	0.36	0.06	10.62	6.42	8.27	9.88	3.62
utnew34	7.71	-0.76	-0.12	8.57	8.19	Never	11.27	3.57

Table 4.15: Profitability of surfactant floods with a polymer concentration of 1500 ppm

Name of simulation run	IRR (%)	NPV (millions $)	Investment efficiency	GROR (%)	Payback period (years)	Discounted payback (years)	Chemical cost ($/bbl)	Operating cost ($/bbl)
utnew41	48.17	3.45	1.73	21.60	3.44	3.67	5.10	3.62
utnew42	48.32	3.52	1.76	21.75	3.44	3.67	5.23	3.70
utnew43	48.32	3.52	1.76	21.75	3.44	3.67	5.23	3.70
utnew44	48.32	3.52	1.76	21.75	3.44	3.67	5.23	3.70
utnew51	37.33	2.99	1.28	19.46	4.04	4.36	5.81	3.52
utnew52	40.16	3.90	1.67	21.36	4.04	4.36	5.94	3.39
utnew53	40.16	3.90	1.67	21.36	4.04	4.36	5.94	3.39
utnew54	40.16	3.90	1.67	21.36	4.04	4.36	5.94	3.39
utnew60	24.58	1.88	0.55	14.89	4.29	4.65	7.16	3.49
utnew61	26.57	3.13	0.84	16.93	5.07	5.51	7.18	3.06
utnew62	25.91	3.15	0.85	16.96	5.08	5.59	7.91	3.12
utnew63	24.32	2.57	0.69	15.83	5.08	5.59	8.48	3.08
utnew64	24.32	2.57	0.69	15.83	5.08	5.59	8.48	3.08
utnew71	17.32	0.86	0.24	12.40	4.16	4.76	8.01	4.23
utnew72	16.70	1.26	0.24	12.37	4.81	5.53	8.54	3.42
utnew73	15.54	1.66	0.26	12.55	5.91	6.85	9.14	3.04
utnew74	11.58	0.53	0.08	10.88	7.07	9.43	10.68	3.10

Table 4.16: Profitability of surfactant floods with a polymer concentration of 2000 ppm

Name of simulation run	IRR (%)	NPV (millions $)	Investment efficiency	GROR (%)	Payback period (years)	Discounted payback (years)	Chemical cost ($/bbl)	Operating cost ($/bbl)
utnew81	51.61	4.15	1.85	22.13	3.33	3.53	5.45	3.26
utnew82	51.72	4.21	1.87	22.25	3.33	3.53	5.45	3.25
utnew83	51.72	4.21	1.87	22.25	3.33	3.53	5.45	3.25
utnew84	51.72	4.21	1.87	22.25	3.33	3.53	5.45	3.25
utnew91	37.78	3.48	1.31	19.60	4.10	4.39	5.99	3.05
utnew92	40.24	4.33	1.63	21.16	4.10	4.39	6.13	3.02
utnew93	40.24	4.33	1.63	21.16	4.10	4.39	6.13	3.02
utnew94	40.24	4.33	1.63	21.16	4.10	4.39	6.13	3.02
utnew100	25.84	2.30	0.61	15.36	4.31	4.64	7.26	3.11
utnew101	27.55	3.68	0.91	17.34	5.01	5.44	7.39	2.84
utnew102	26.18	3.36	0.83	16.84	5.01	5.48	8.24	2.85
utnew103	24.86	2.86	0.70	16.03	5.01	5.48	8.52	2.81
utnew104	24.86	2.86	0.70	16.03	5.01	5.48	8.52	2.81
utnew111	19.00	1.11	0.29	12.80	3.96	4.50	8.37	3.59
utnew112	18.60	1.80	0.32	13.09	4.78	5.41	8.43	3.11
utnew113	17.06	2.26	0.33	13.22	5.76	6.61	9.08	2.76
utnew114	12.11	0.70	0.10	11.08	6.69	8.31	10.83	2.88

Table 4.17: Profitability of surfactant floods with a polymer concentration of 2500 ppm

Name of simulation run	IRR (%)	NPV (millions $)	Investment efficiency	GROR (%)	Payback period (years)	Discounted payback (years)	Chemical cost ($/bbl)	Operating cost ($/bbl)
utnew121	52.00	4.59	1.82	22.03	3.29	3.49	5.69	3.07
utnew122	52.00	4.59	1.82	22.03	3.29	3.49	5.69	3.07
utnew123	52.00	4.59	1.82	22.03	3.29	3.49	5.69	3.07
utnew124	52.00	4.59	1.82	22.03	3.29	3.49	5.69	3.07
utnew131	37.03	3.82	1.28	19.44	4.15	4.43	6.31	2.90
utnew132	38.73	4.47	1.49	20.53	4.15	4.43	6.41	2.91
utnew133	38.73	4.47	1.49	20.53	4.15	4.43	6.41	2.91
utnew134	38.73	4.47	1.49	20.53	4.15	4.43	6.41	2.91
utnew140	25.67	2.53	0.61	15.39	4.36	4.68	7.51	2.98
utnew141	26.91	3.81	0.86	17.04	5.01	5.44	7.65	2.69
utnew142	25.07	3.26	0.74	16.24	5.02	5.48	8.59	2.80
utnew143	24.43	2.99	0.68	15.83	5.02	5.48	8.77	2.71
utnew144	24.43	2.99	0.68	15.83	5.02	5.48	8.77	2.71
utnew151	19.36	1.27	0,30	12.91	3.95	4.48	8.61	3.31
utnew152	19.09	2.08	0.35	13.33	4.81	5.42	8.47	3.03
utnew153	16.66	2.22	0.31	13.01	5.73	6.55	9.39	2.73
utnew154	11.18	0.39	0.05	10.58	6.56	8.46	11.24	2.68

Table 4.18: Profitability of surfactant floods with a polymer concentration of 3000 ppm

Name of simulation run	IRR (%)	NPV (millions $)	Investment efficiency	GROR (%)	Payback period (years)	Discounted payback (years)	Chemical cost ($/bbl)	Operating cost ($/bbl)
utnew161	49.28	4.63	1.65	21.25	3.32	3.51	6.02	3.00
utnew162	49.28	4.63	1.65	21.25	3.32	3.51	6.02	3.00
utnew163	49.28	4.63	1.65	21.25	3.32	3.51	6.02	3.00
utnew171	35.74	4.06	1.22	19.12	4.21	4.48	6.62	2.80
utnew172	36.54	4.43	1.33	19.70	4.21	4.48	6.72	2.80
utnew173	36.54	4.43	1.33	19.70	4.21	4.48	6.72	2.80
utnew180	25.14	2.74	0.61	15.34	4.43	4.76	7.76	2.76
utnew181	25.05	3.58	0.74	16.27	5.06	5.51	8.08	2.62
utnew182	22.90	2.88	0.60	15.27	5.07	5.57	9.02	2.64
utnew183	22.90	2.88	0.60	15.27	5.07	5.57	9.02	2.64
utnew184	22.90	2.88	0.60	15.27	5.07	5.57	9.02	2.64
utnew191	18.63	1.27	0.28	12.71	3.99	4.58	8.98	3.13
utnew192	18.66	2.15	0.34	13.27	4.88	5.54	8.84	2.70
utnew193	15.22	1.76	0.23	12.32	5.76	6.68	10.00	2.59
utnew194	9.12	-0.29	-0.04	9.57	6.72	Never	11.70	2.70

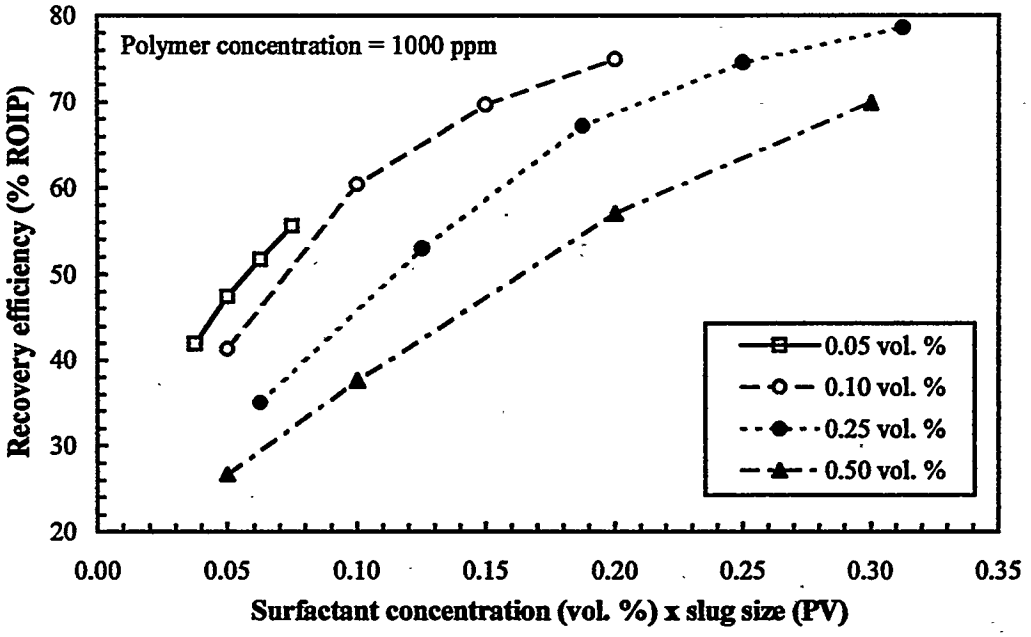


Figure 4.1: Recovery efficiency versus amount of surfactant injected with a polymer concentration of 1000 ppm

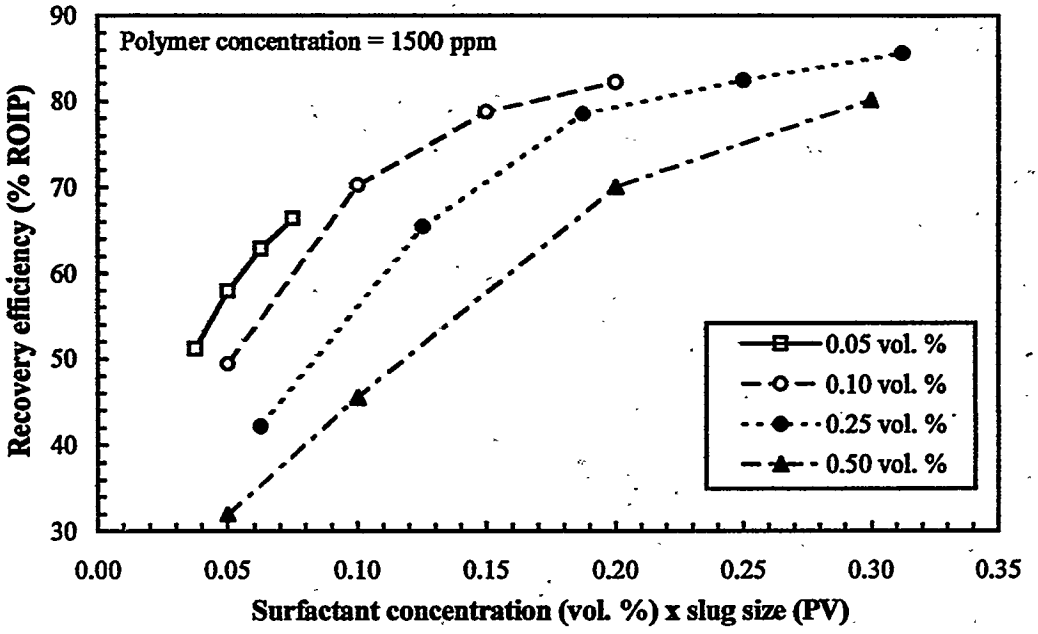


Figure 4.2: Recovery efficiency versus amount of surfactant injected with a polymer concentration of 1500 ppm

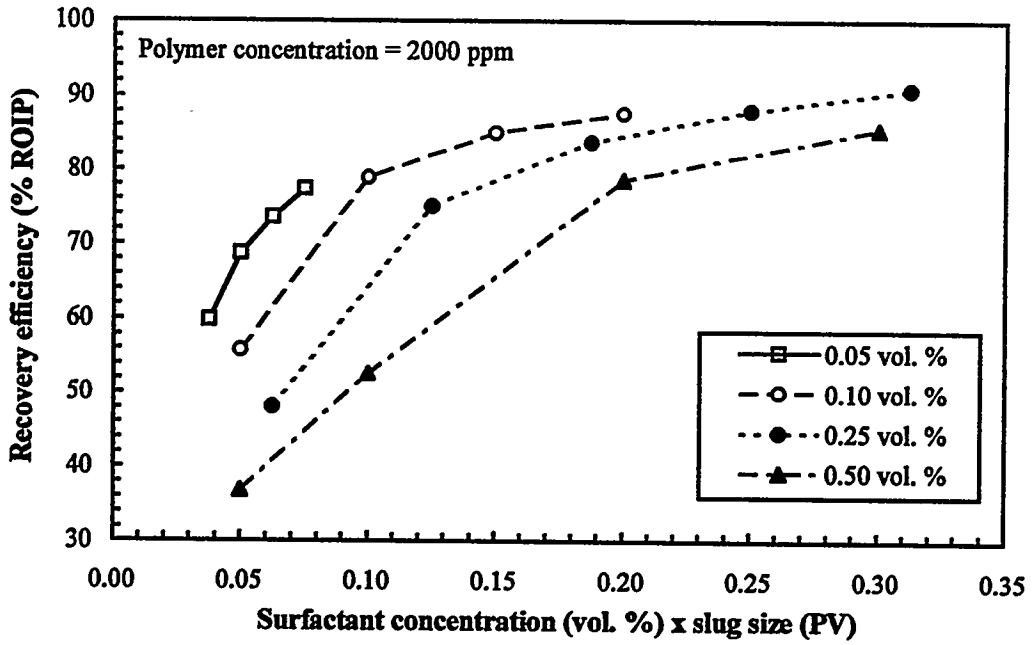


Figure 4.3: Recovery efficiency versus amount of surfactant injected with a polymer concentration of 2000 ppm

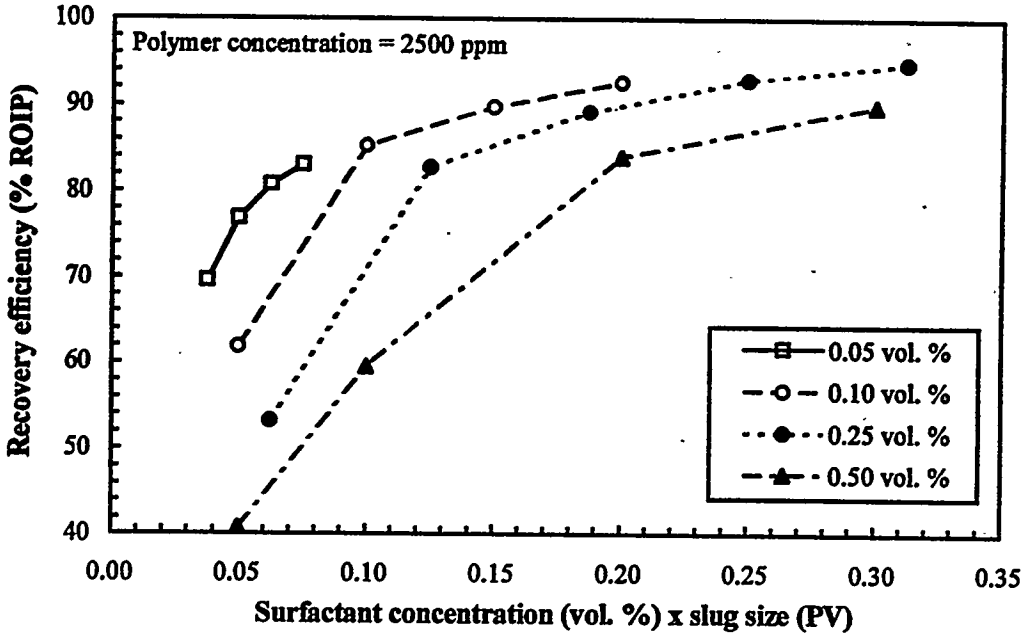


Figure 4.4: Recovery efficiency versus amount of surfactant injected with a polymer concentration of 2500 ppm

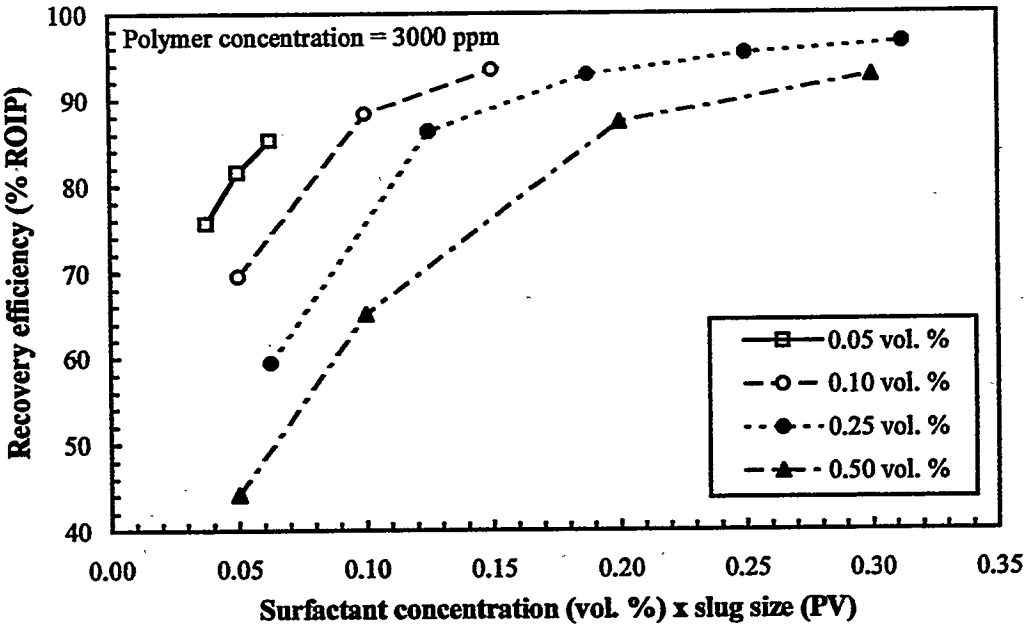


Figure 4.5: Recovery efficiency versus amount of surfactant injected with a polymer concentration of 3000 ppm

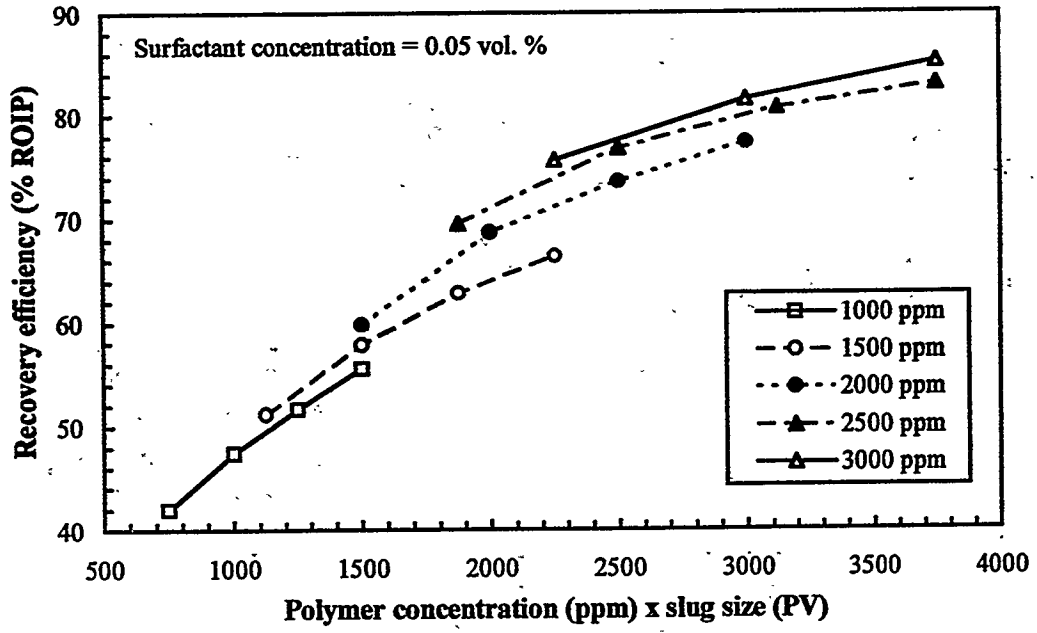


Figure 4.6: Recovery efficiency versus amount of polymer injected with a surfactant concentration of 0.05 vol. %

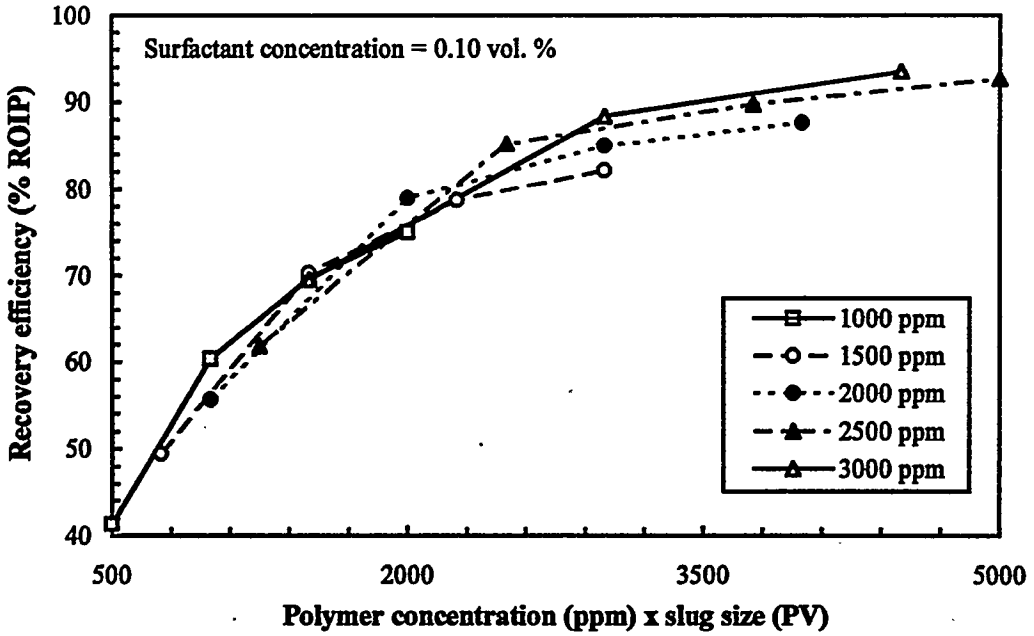


Figure 4.7: Recovery efficiency versus amount of polymer injected with a surfactant concentration of 0.10 vol. %

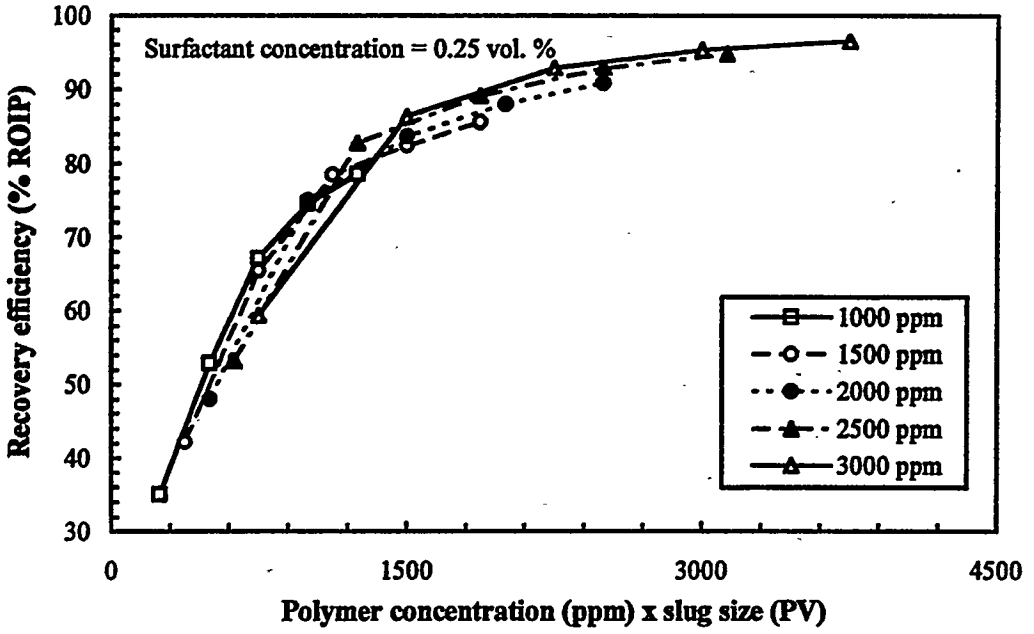


Figure 4.8: Recovery efficiency versus amount of polymer injected with a surfactant concentration of 0.25 vol. %

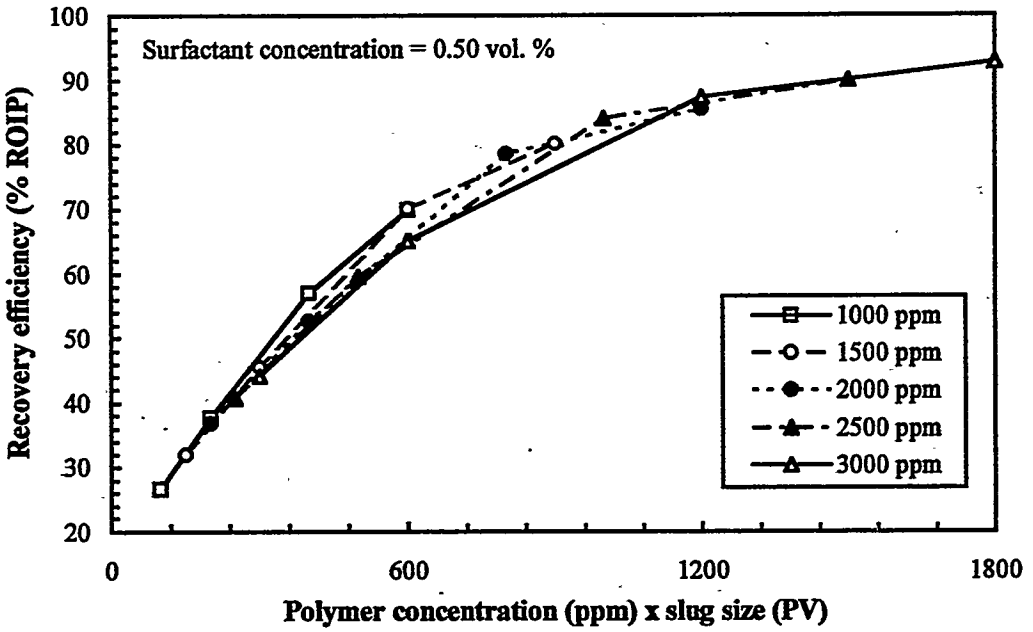


Figure 4.9: Recovery efficiency versus amount of polymer injected with a surfactant concentration of 0.50 vol. %

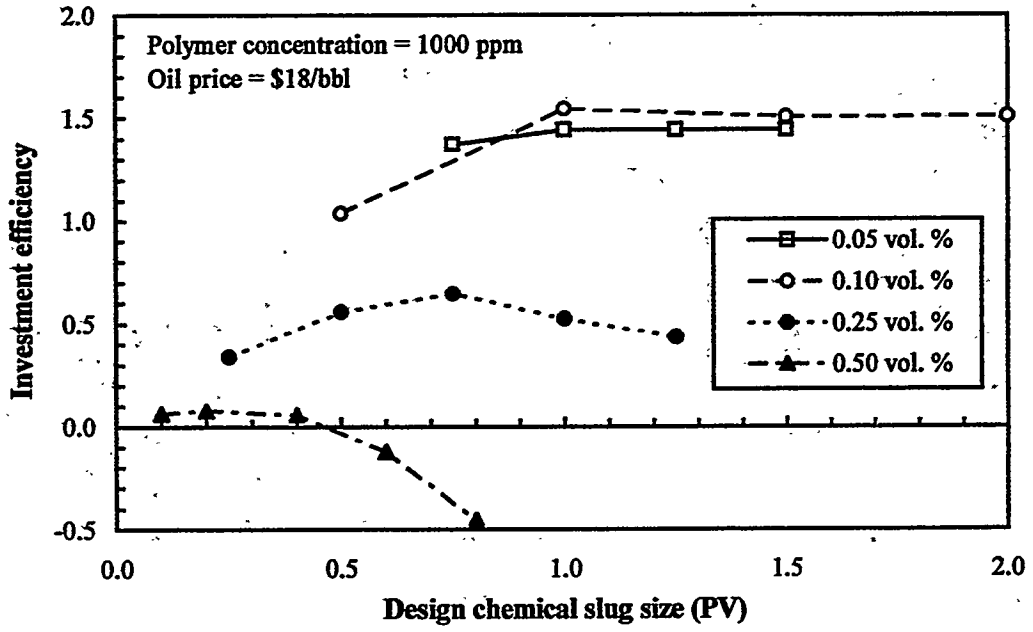


Figure 4.10: Optimization of chemical slug size and surfactant concentration with a polymer concentration of 1000 ppm and an oil price of $18/bbl

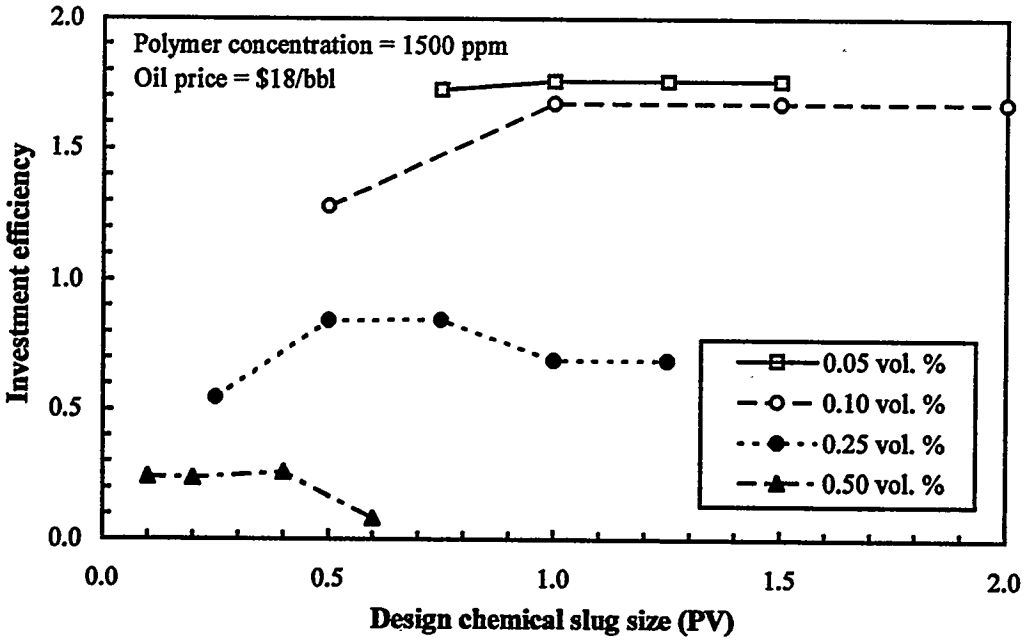


Figure 4.11: Optimization of chemical slug size and surfactant concentration with a polymer concentration of 1500 ppm and an oil price of $18/bbl

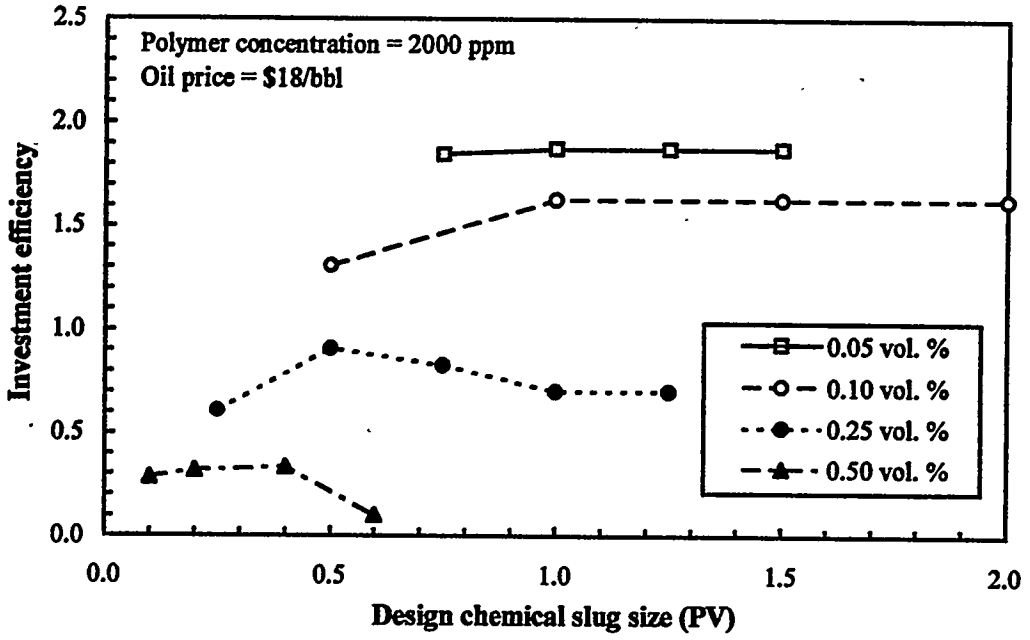


Figure 4.12: Optimization of chemical slug size and surfactant concentration with a polymer concentration of 2000 ppm and an oil price of $18/bbl

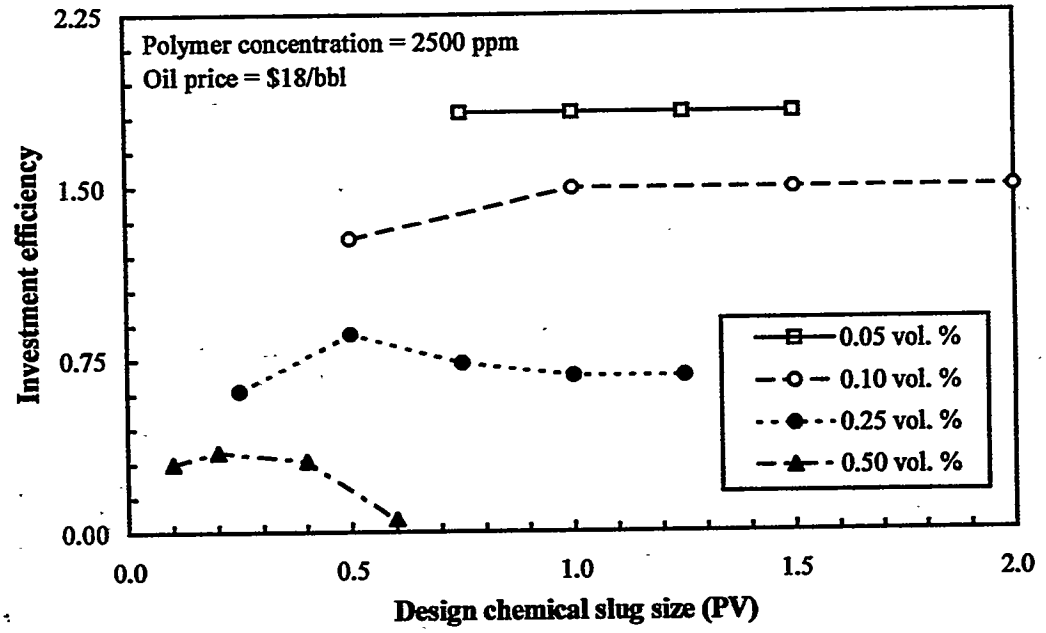


Figure 4.13: Optimization of chemical slug size and surfactant concentration with a polymer concentration of 2500 ppm and an oil price of $18/bbl

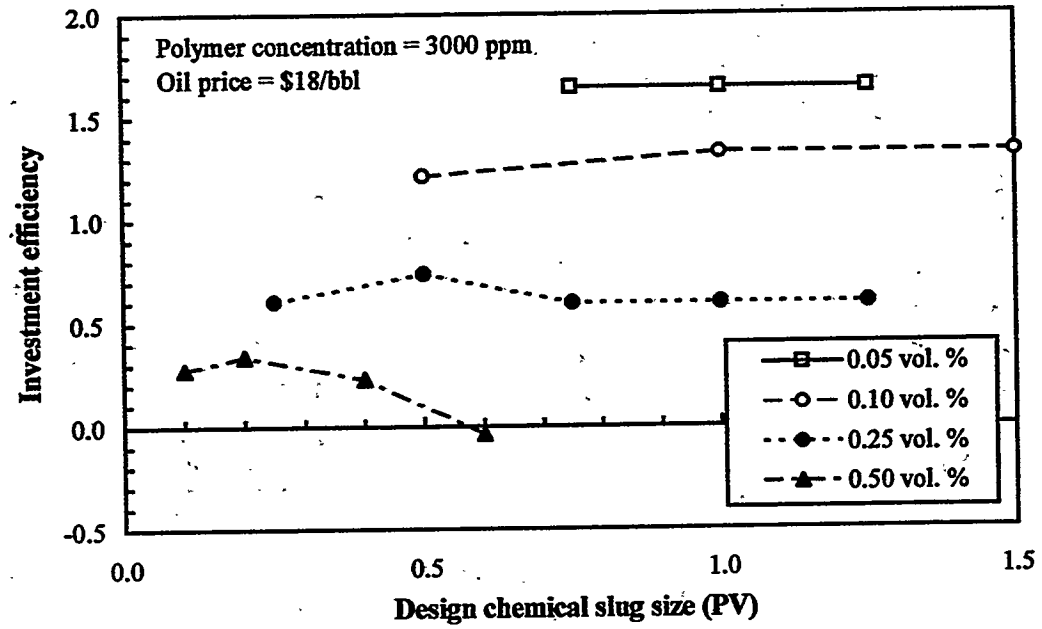


Figure 4.14: Optimization of chemical slug size and surfactant concentration with a polymer concentration of 3000 ppm and an oil price of $18/bbl

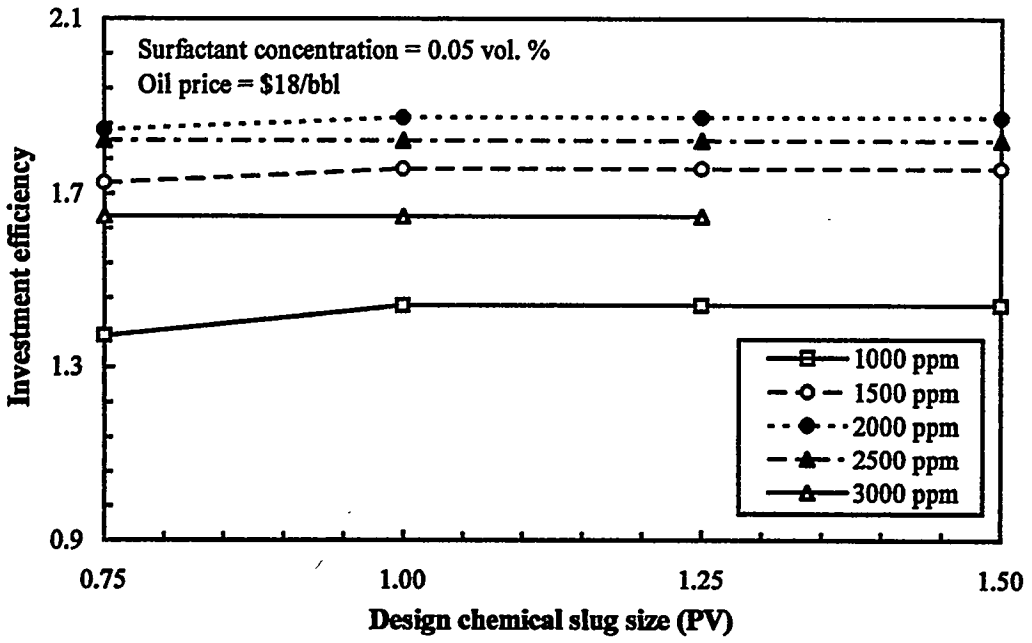


Figure 4.15: Optimization of chemical slug size and polymer concentration with a surfactant concentration of 0.05 vol. % and an oil price of $18/bbl

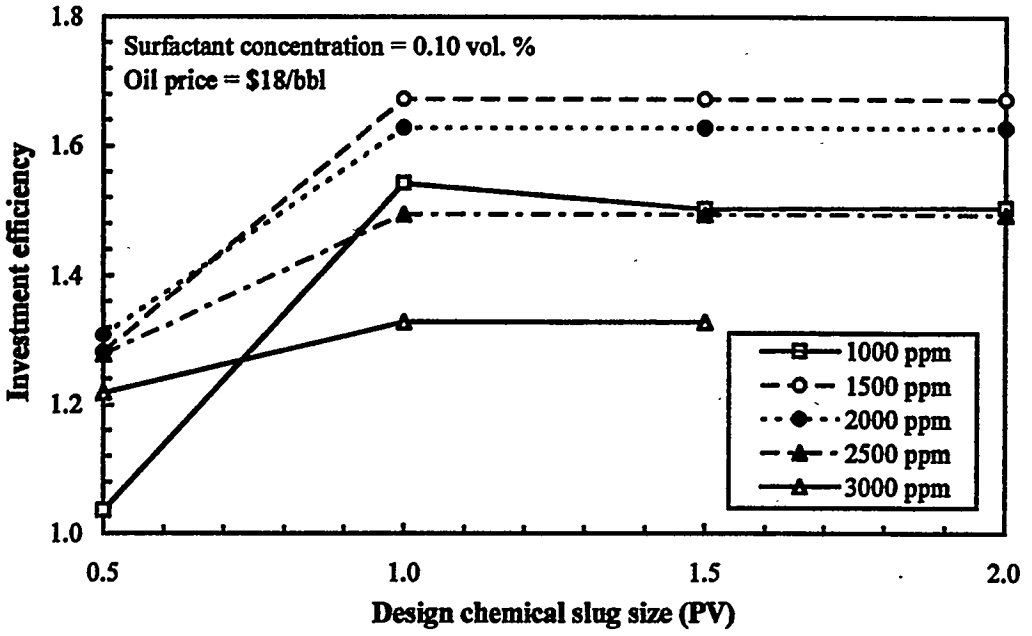


Figure 4.16: Optimization of chemical slug size and polymer concentration with a surfactant concentration of 0.10 vol. % and an oil price of $18/bbl

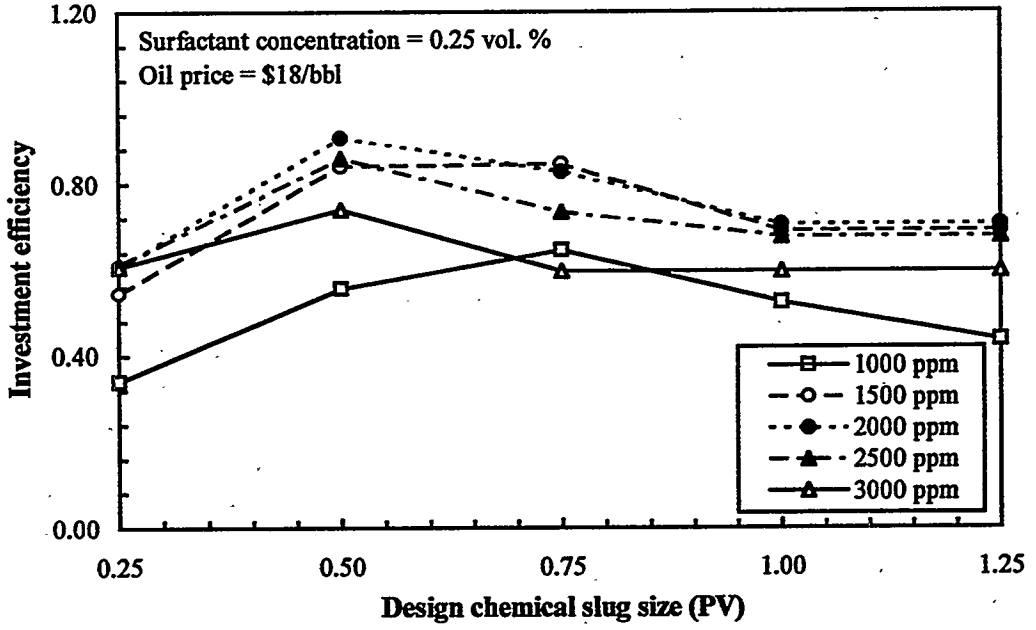


Figure 4.17: Optimization of chemical slug size and polymer concentration with a surfactant concentration of 0.25 vol. % and an oil price of $18/bbl

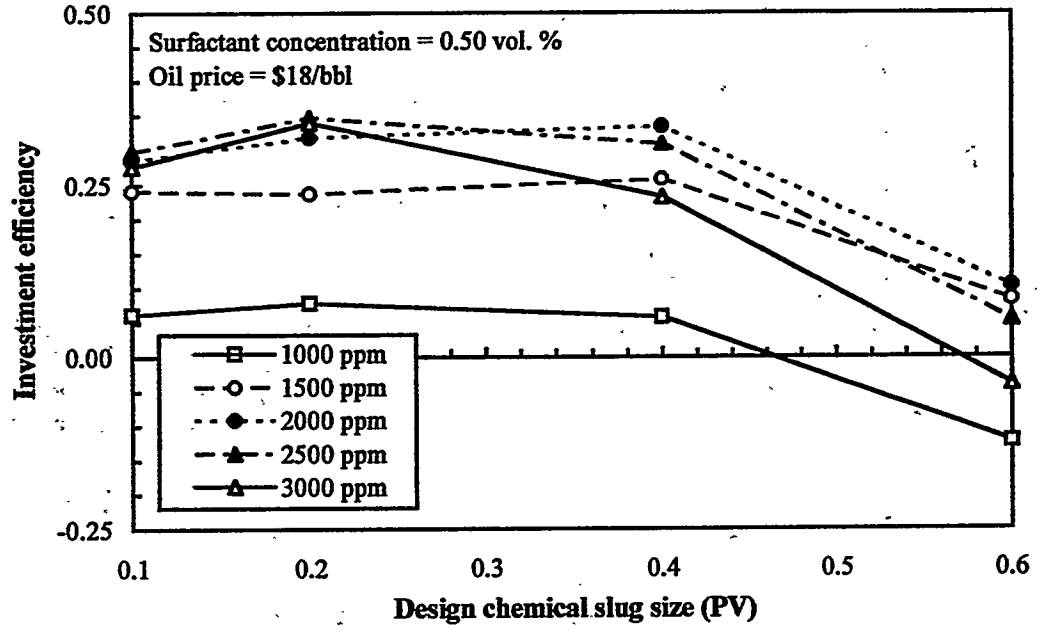


Figure 4.18: Optimization of chemical slug size and polymer concentration with a surfactant concentration of 0.50 vol. % and an oil price of $18/bbl

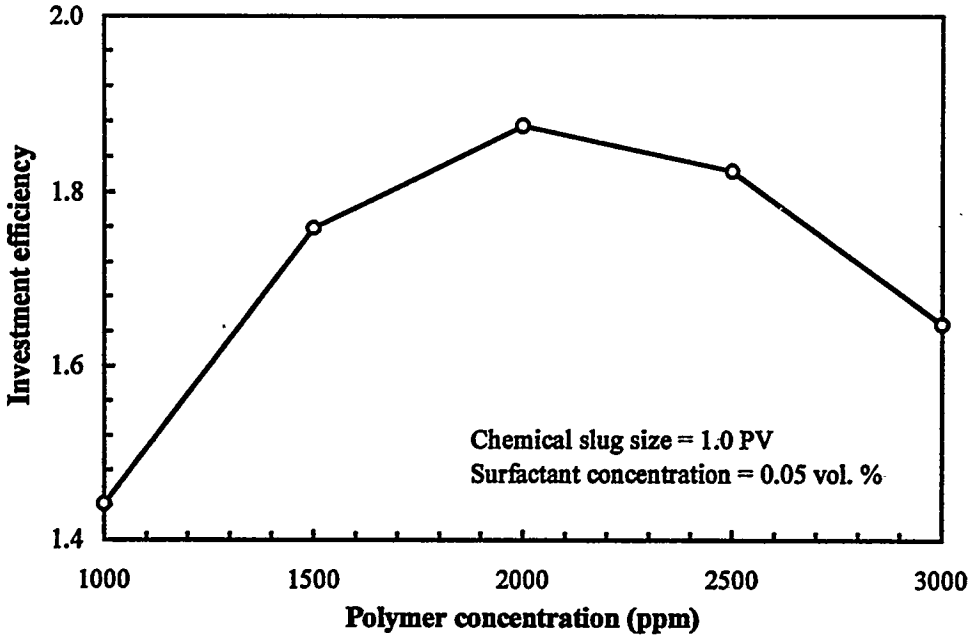


Figure 4.19: Optimization of polymer concentration at the optimum chemical slug size and surfactant concentration

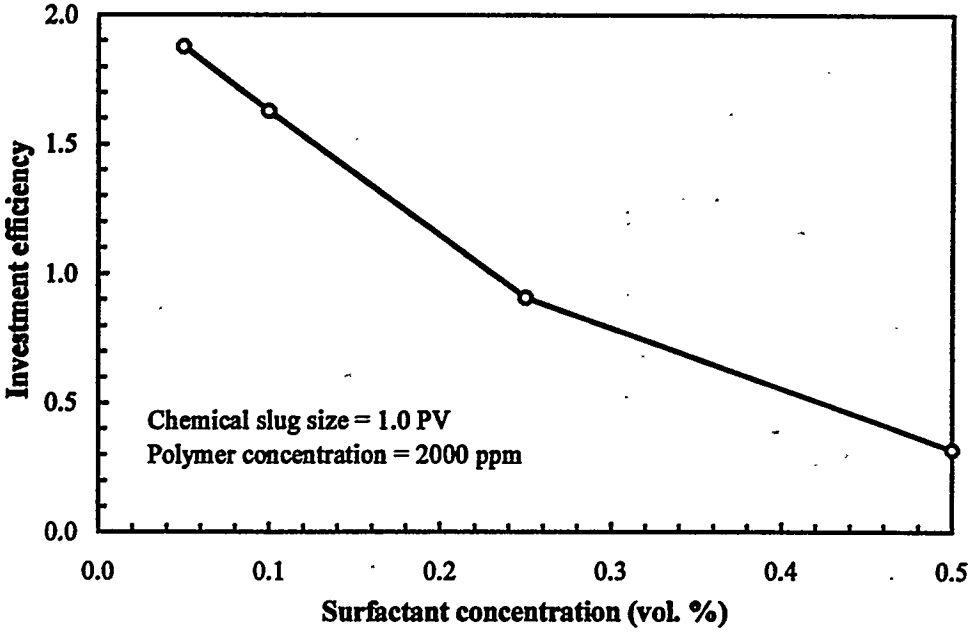


Figure 4.20: Optimization of surfactant concentration at the optimum chemical slug size and polymer concentration

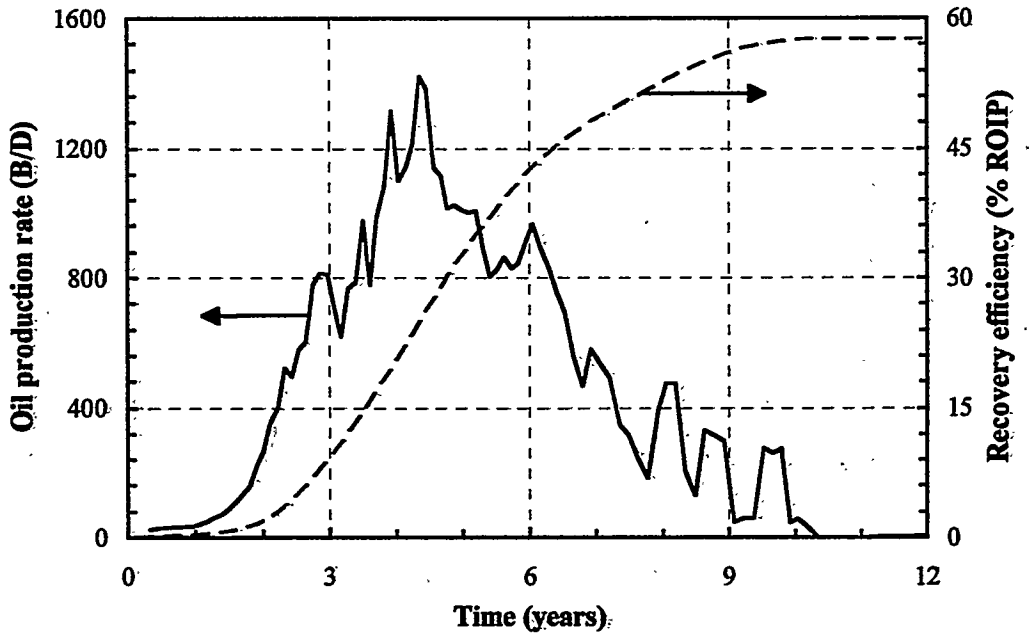


Figure 4.21: Oil production rate and recovery efficiency versus time for the optimum surfactant flooding design

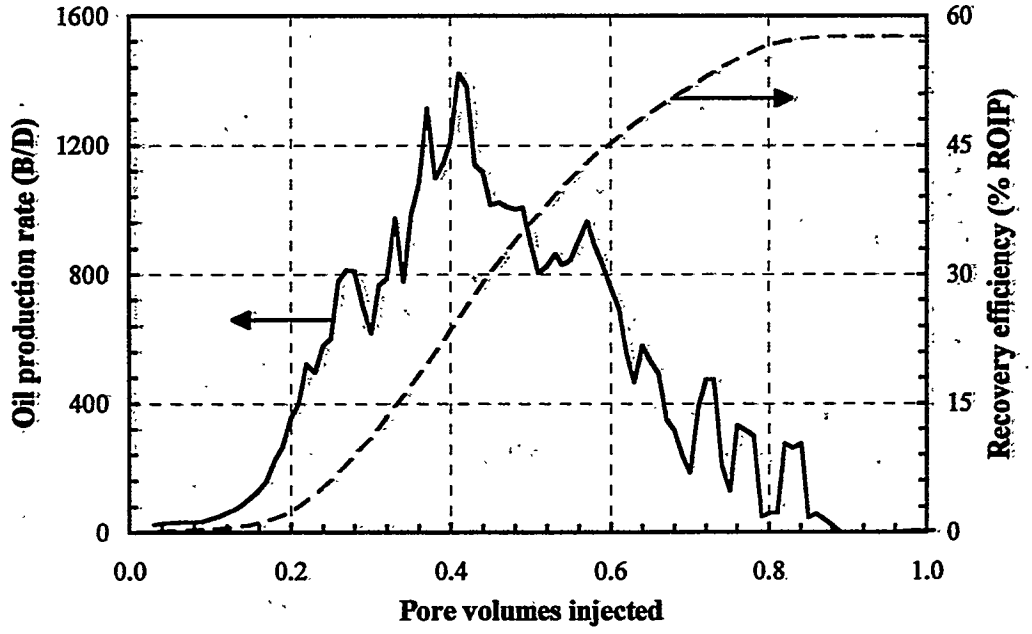


Figure 4.22: Oil production rate and recovery efficiency versus pore volumes injected for the optimum surfactant flooding design

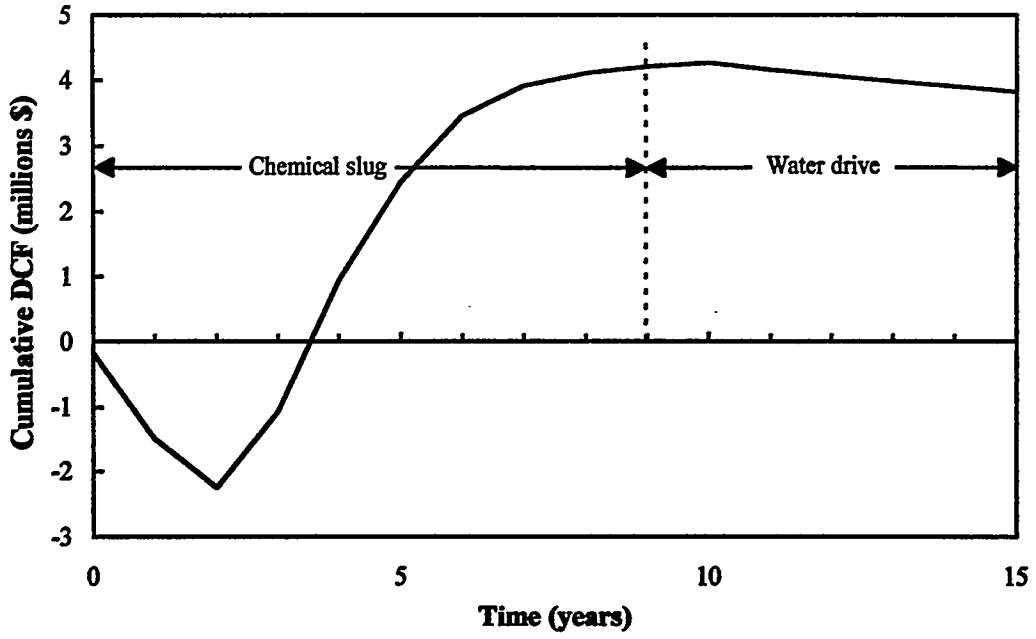


Figure 4.23: Cumulative DCF versus time for the optimum surfactant flooding design

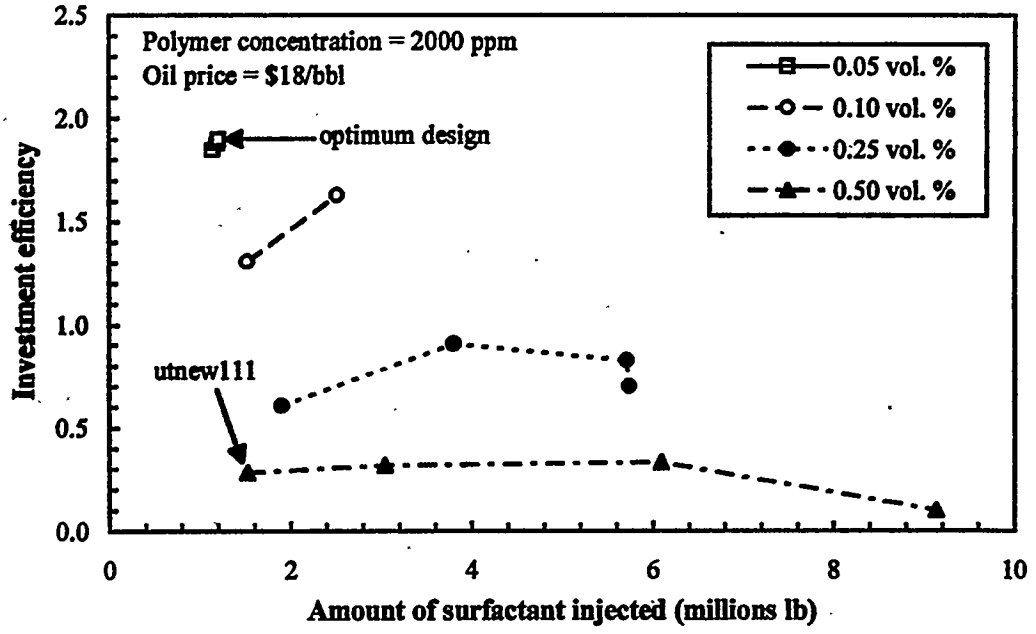


Figure 4.24: Optimization of surfactant injected at the economic limit with a polymer concentration of 2000 ppm

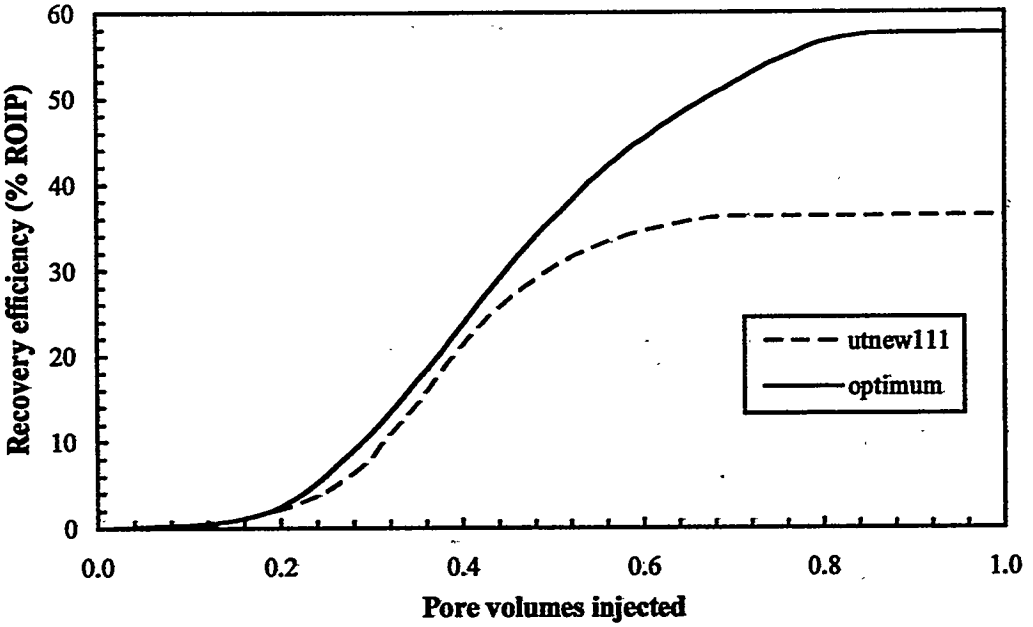


Figure 4.25: Recovery efficiency versus pore volumes injected for two designs with similar amounts of surfactant injected

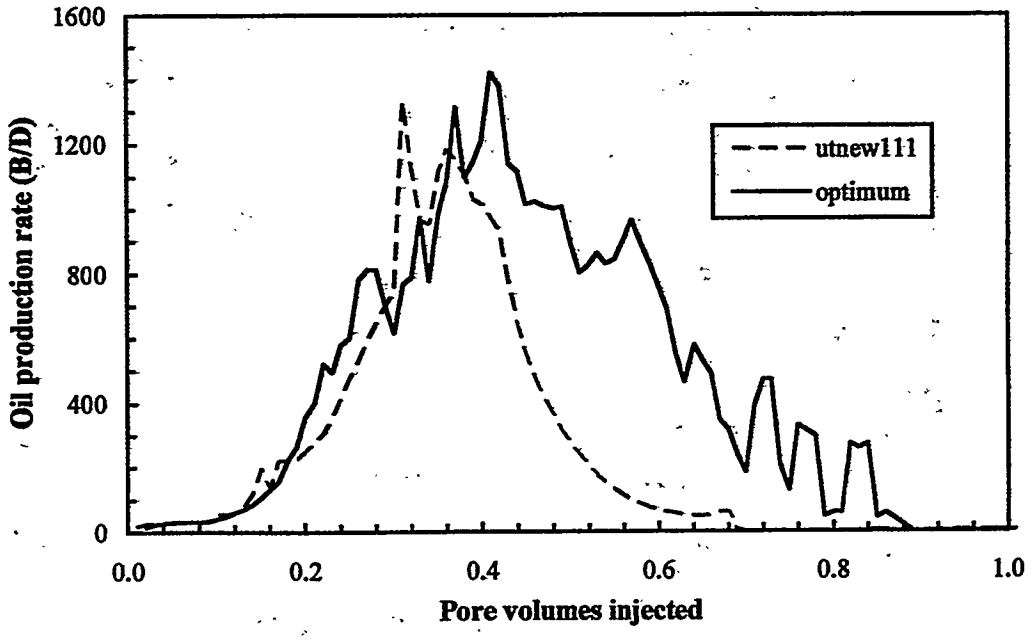


Figure 4.26: Oil production rate versus pore volumes injected for two designs with similar amounts of surfactant injected

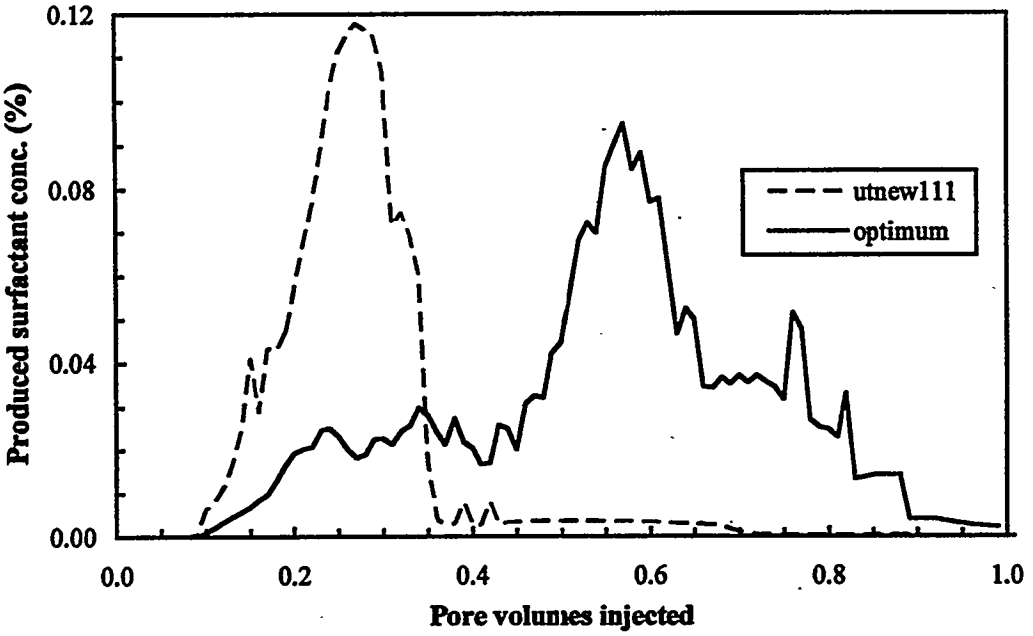


Figure 4.27: Produced surfactant concentration versus pore volumes injected for two designs with similar amounts of surfactant injected

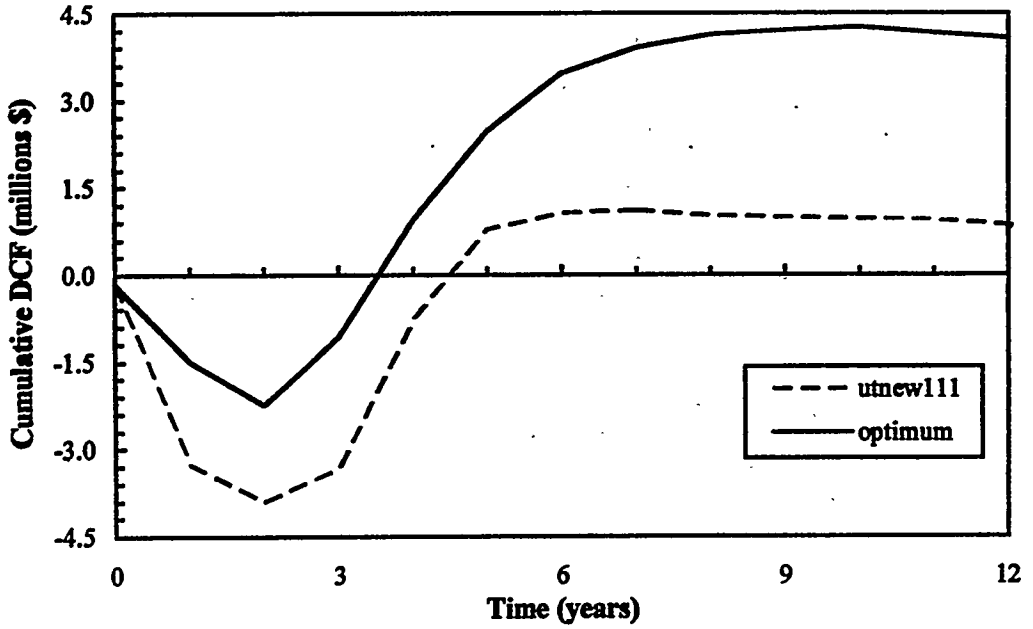


Figure 4.28: Cumulative DCF versus pore volumes injected for two designs with similar amounts of surfactant injected

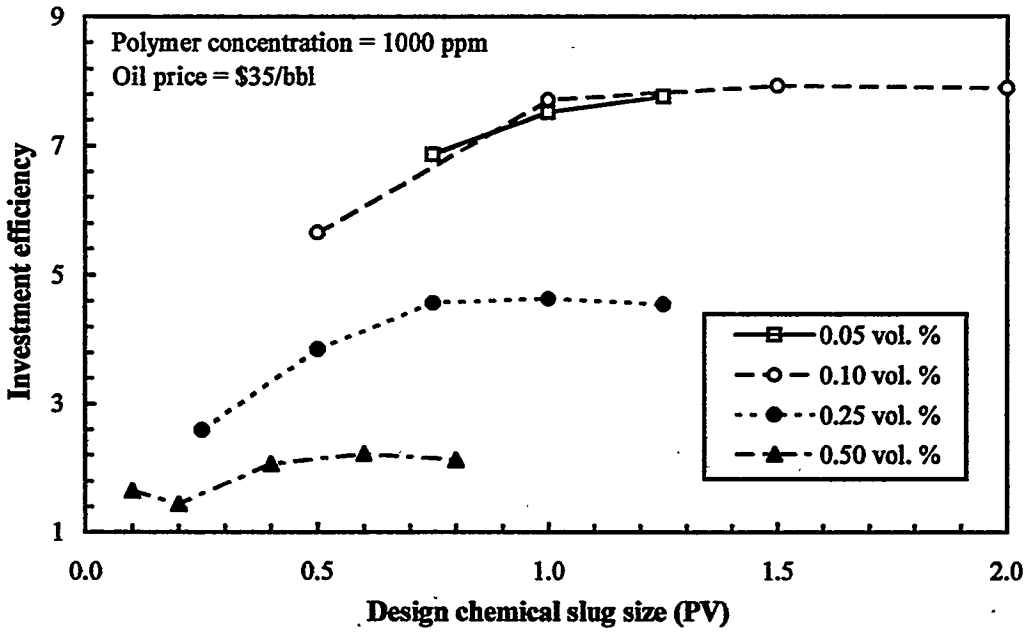


Figure 4.29: Optimization of chemical slug size and surfactant concentration with a polymer concentration of 1000 ppm and an oil price of $35/bbl

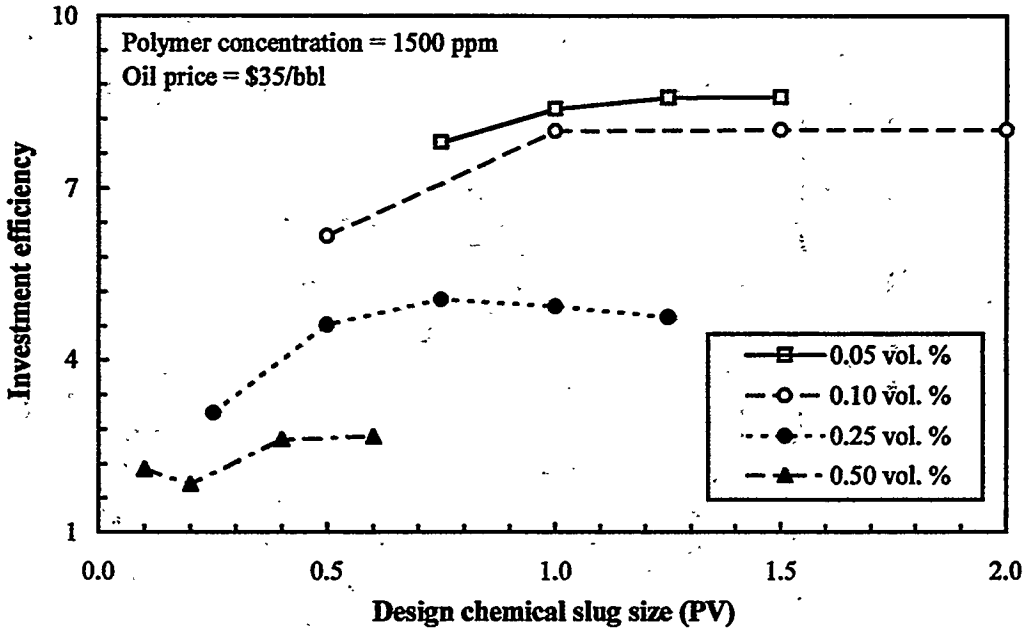


Figure 4.30: Optimization of chemical slug size and surfactant concentration with a polymer concentration of 1500 ppm and an oil price of $35/bbl

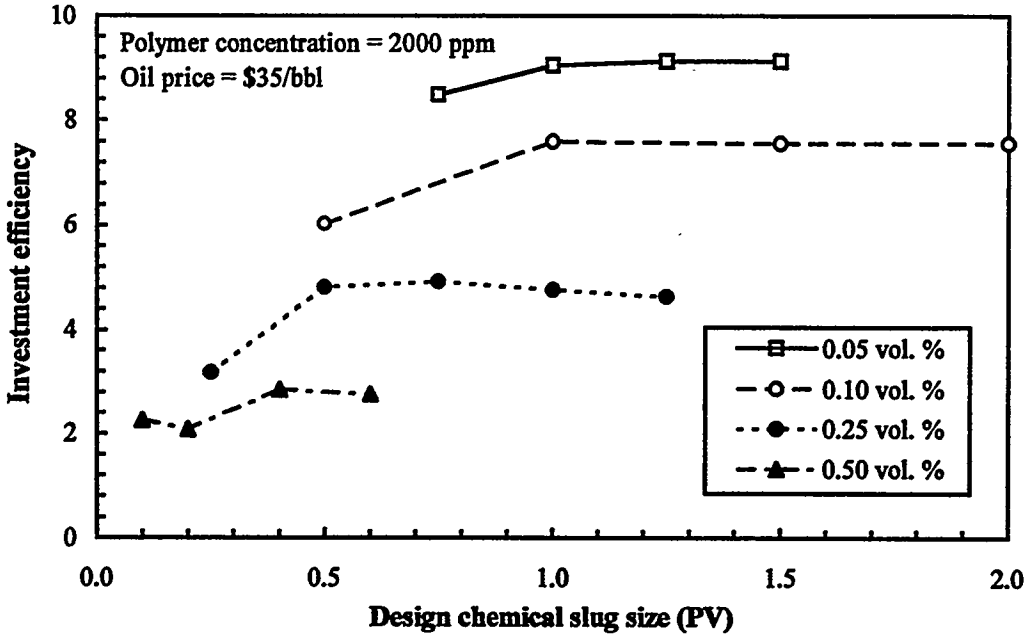


Figure 4.31: Optimization of chemical slug size and surfactant concentration with a polymer concentration of 2000 ppm and an oil price of $35/bbl

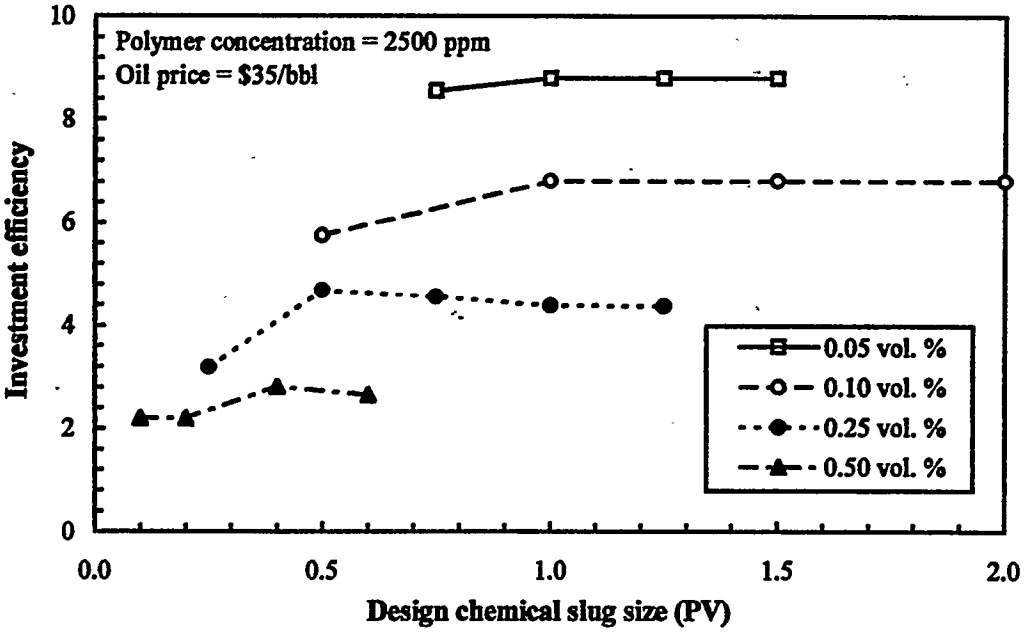


Figure 4.32: Optimization of chemical slug size and surfactant concentration with a polymer concentration of 2500 ppm and an oil price of $35/bbl

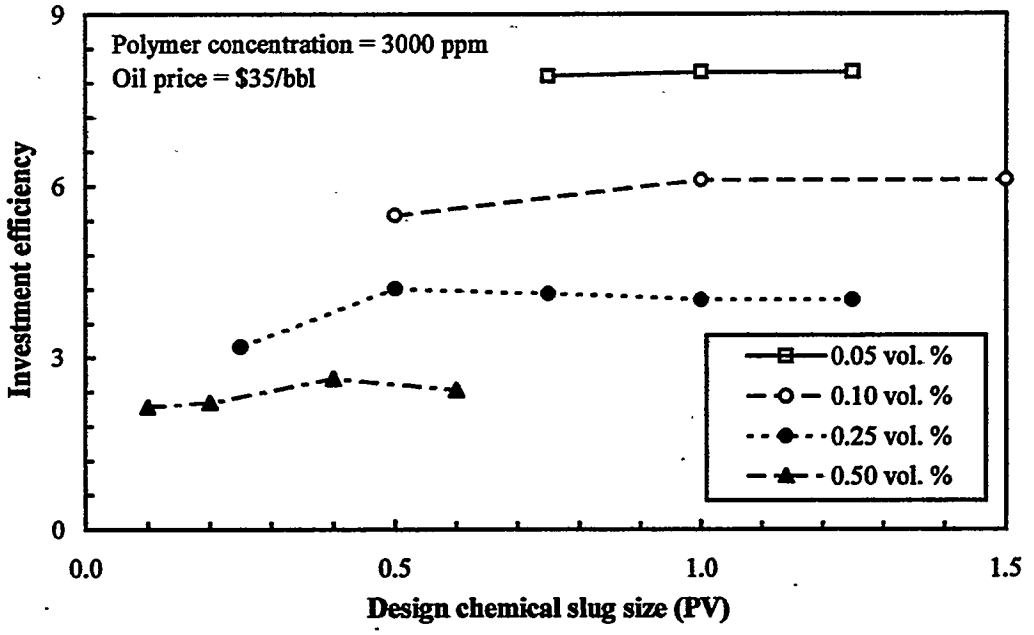


Figure 4.33: Optimization of chemical slug size and surfactant concentration with a polymer concentration of 3000 ppm and an oil price of $35/bbl

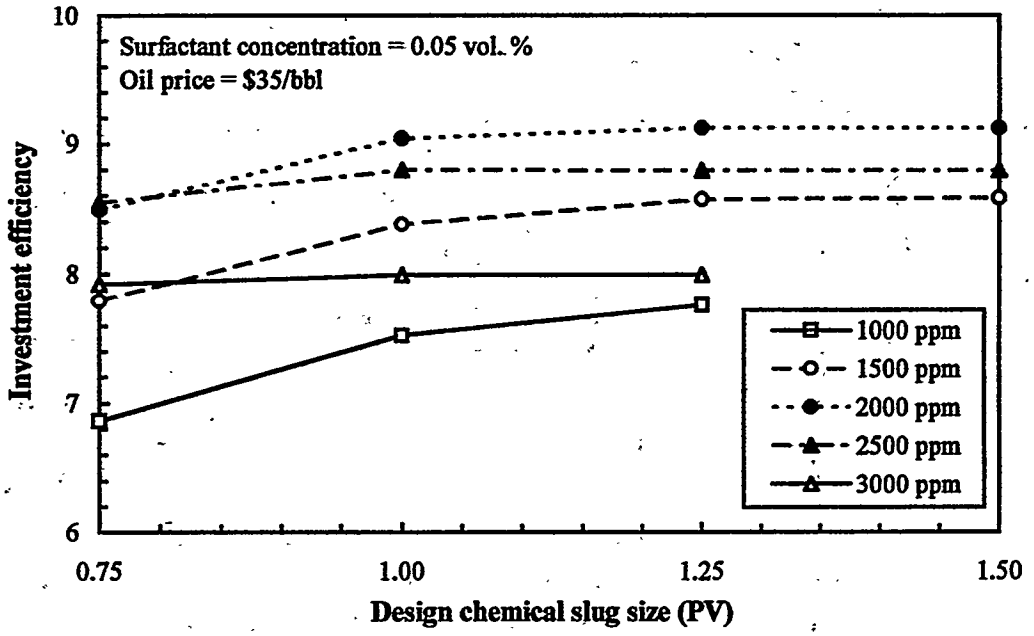


Figure 4.34: Optimization of chemical slug size and polymer concentration with a surfactant concentration of 0.05% and an oil price of $35/bbl

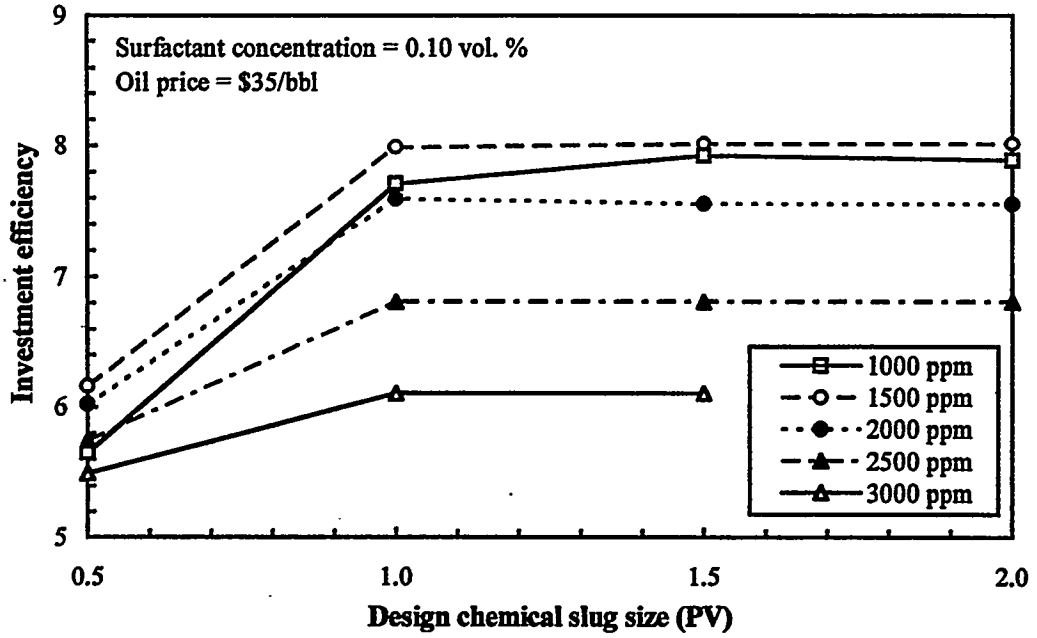


Figure 4.35: Optimization of chemical slug size and polymer concentration with a surfactant concentration of 0.10% and an oil price of $35/bbl

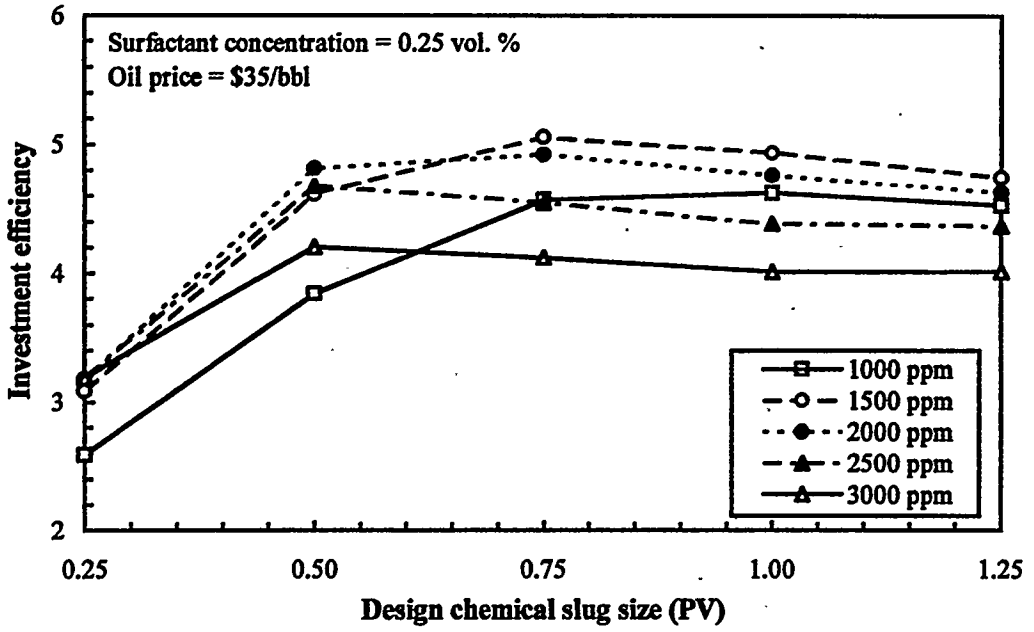


Figure 4.36: Optimization of chemical slug size and polymer concentration with a surfactant concentration of 0.25% and an oil price of $35/bbl

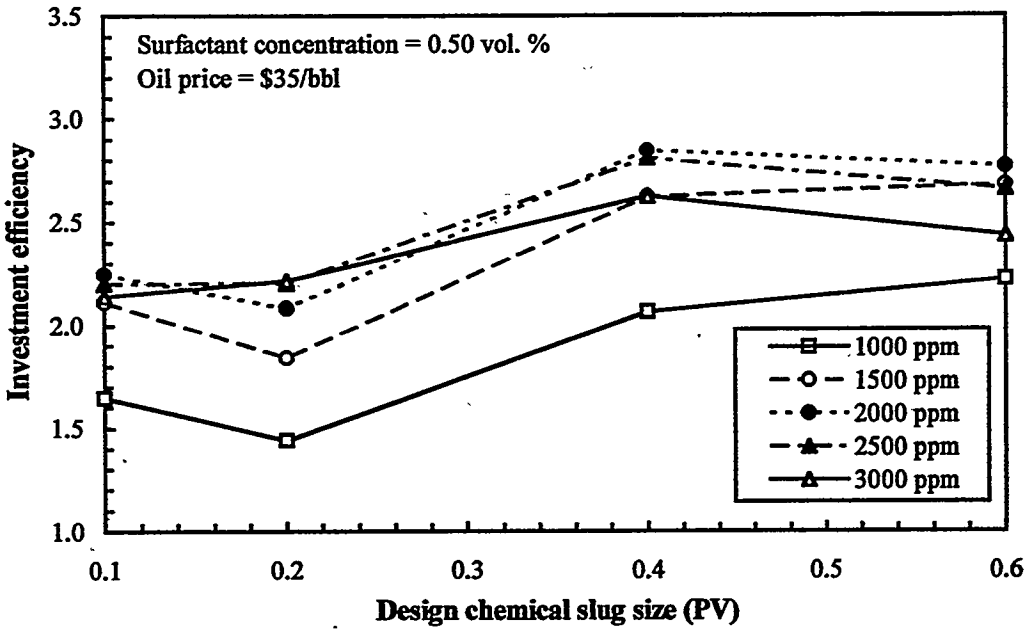


Figure 4.37: Optimization of chemical slug size and polymer concentration with a surfactant concentration of 0.50% and an oil price of $35/bbl

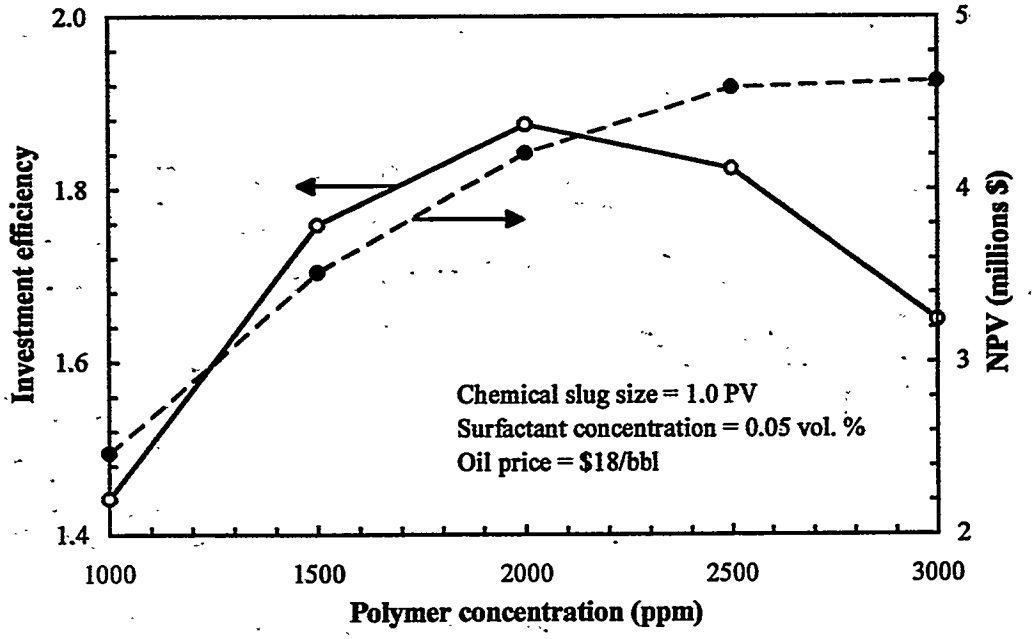


Figure 4.38: Optimization of polymer concentration using investment efficiency and NPV at an oil price of $18/bbl

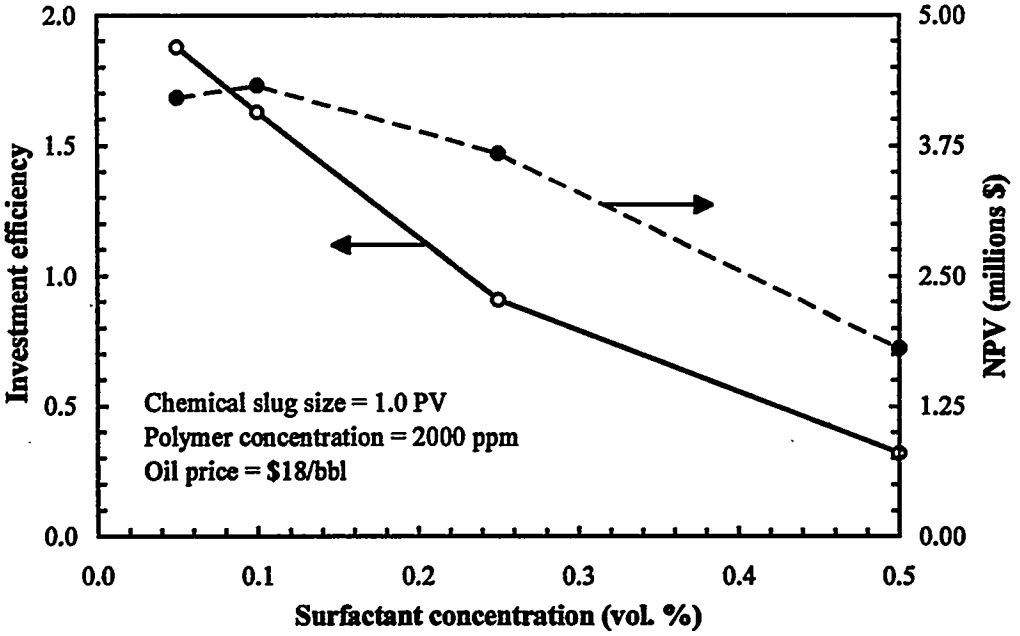


Figure 4.39: Optimization of surfactant concentration using investment efficiency and NPV at an oil price of $18/bbl

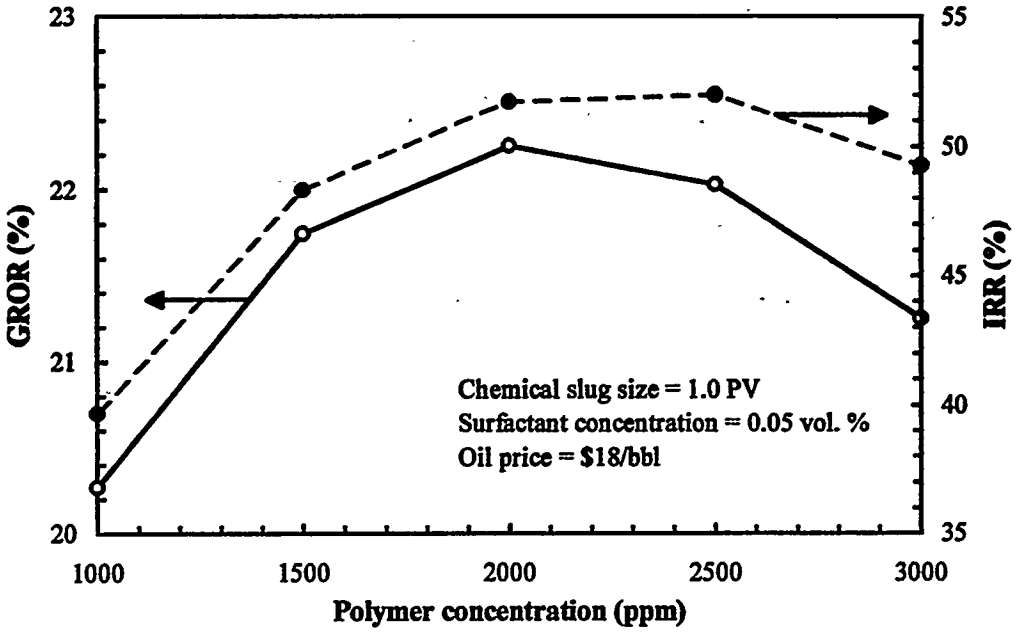


Figure 4.40: Optimization of polymer concentration using GROR and IRR at an oil price of $18/bbl

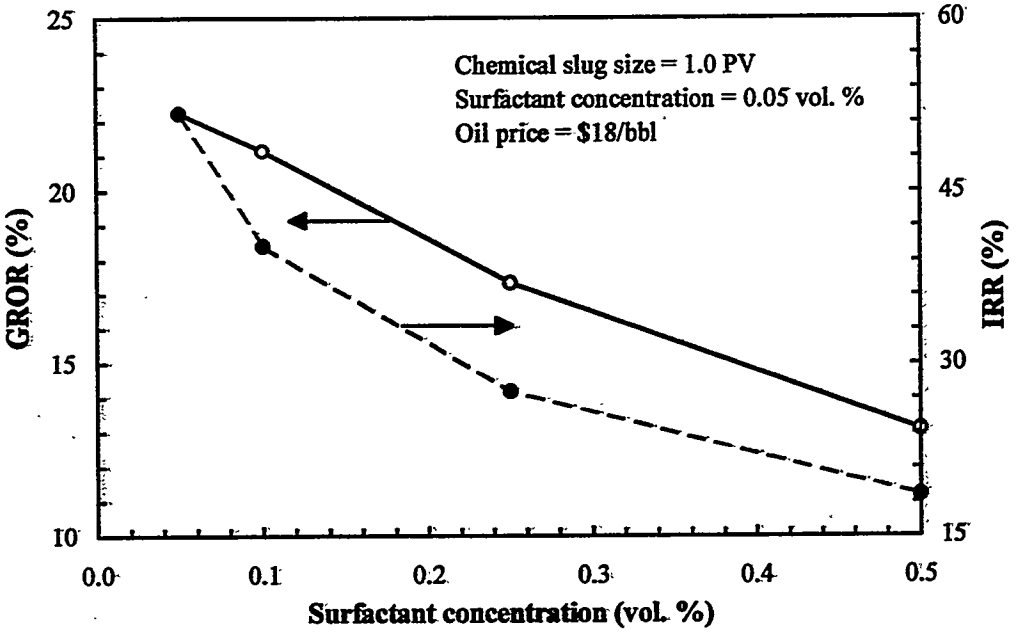


Figure 4.41: Optimization of surfactant concentration using GROR and IRR at an oil price of $18/bbl

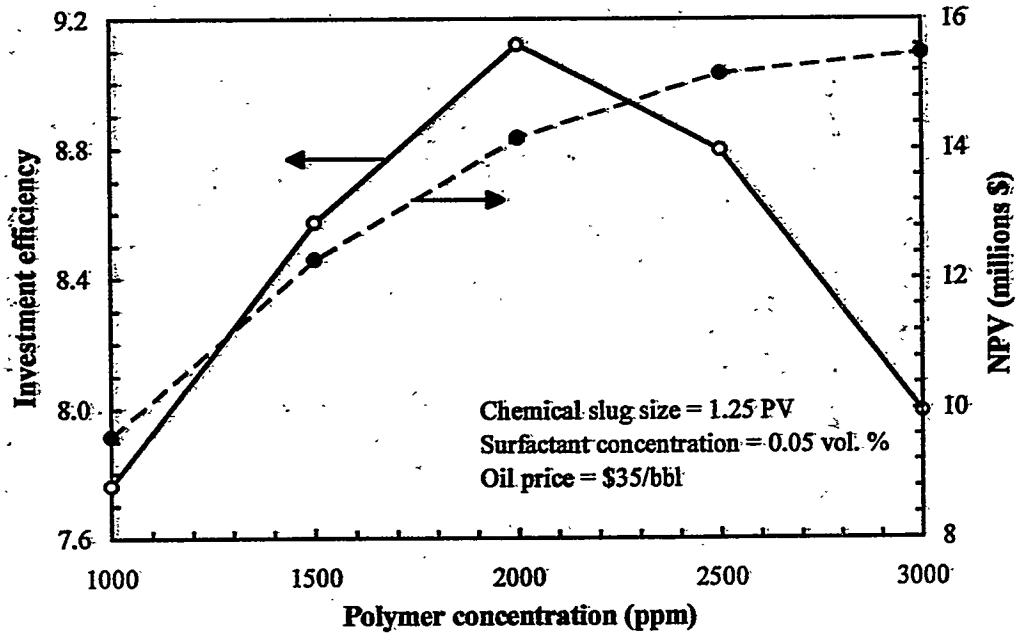


Figure 4.42: Optimization of polymer concentration using investment efficiency and NPV at an oil price of $35/bbl

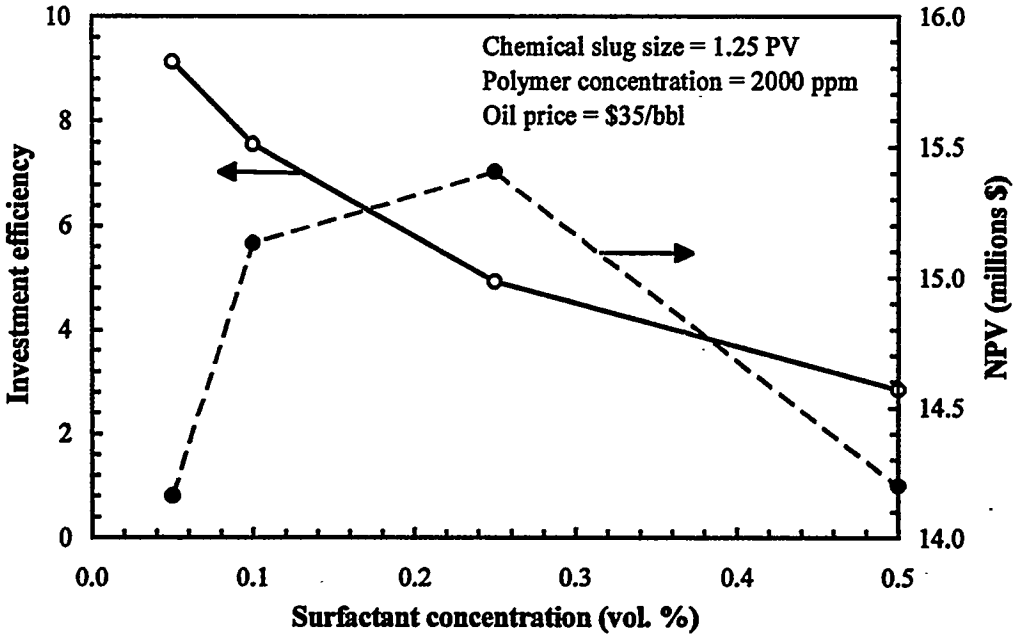


Figure 4.43: Optimization of surfactant concentration using investment efficiency and NPV at an oil price of $35/bbl

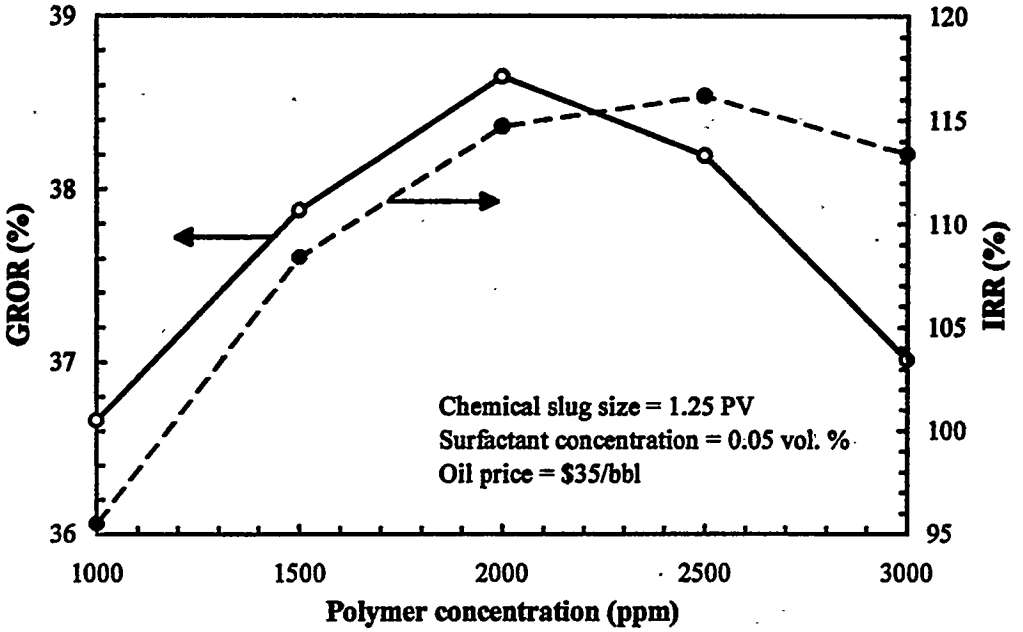


Figure 4.44: Optimization of polymer concentration using GROR and IRR at an oil price of $35/bbl

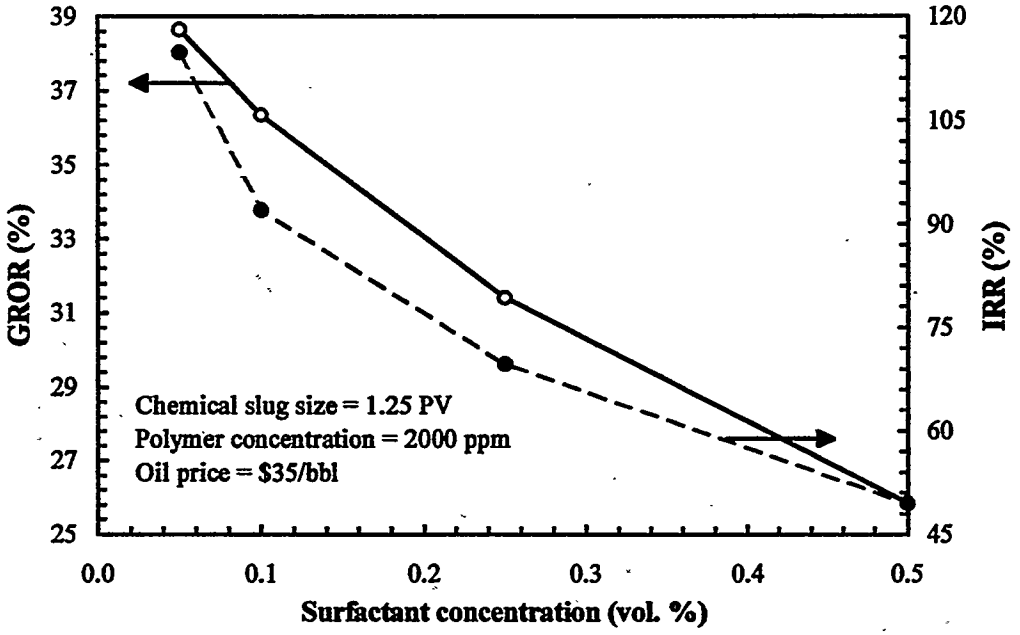


Figure 4.45: Optimization of surfactant concentration using GROR and IRR at an oil price of $35/bbl

5. Evaluating Risk and Uncertainty in Surfactant Flooding

5.1 Introduction

Economic analysis is not complete without some consideration of the risk and uncertainty associated with a project. The DCF analysis of the optimum design is a one-point analysis that represents a "best guess" or the "most likely" economic conditions. This type of one-point analysis is acceptable if there is no uncertainty in the variables or the project is relatively small and insignificant.

A project is considered to have risk if there is the possibility of economic loss. The probability and magnitude of economic loss determines whether the project is classified as high risk or low risk. Uncertainty is the recognition that there is more than one possible outcome, with each outcome having a certain probability of occurrence. If there is no chance of economic loss there is no risk, but there is still uncertainty about the degree of success of the project (Seba, 1987).

The risks of exploration and development of primary and secondary recovery projects are relatively well known and understood. However, the application of EOR projects is perceived to have higher risks, even though they may be as profitable as traditional exploration and production projects. A chemical flooding project has considerable technical risk associated with the process efficiency, and there is uncertainty in the recoverable reserves despite the availability of reservoir data.

The performance of a chemical flood is sensitive to many physical and chemical properties of the reservoir. Determining which variables are of most importance, their interdependencies, and their impact on the simulated production profile was not included in this study, because of the large number of variables that need to be considered and the long simulation runtimes.

Methods of evaluating economic risk and uncertainty are presented in this chapter, using the optimum surfactant flood design as a case study.

5.2 Sensitivity Analysis

The most common method for evaluating uncertainty is sensitivity analysis. Sensitivity analysis is a means of identifying those critical variables that if changed could considerably affect the profitability of the project. The sensitivity of a variable is indicated by the change in a profitability measure for a specified change in the variable. There are an infinite number of variables that affect the outcome of a project, and it is not possible to include all of them in an economic analysis. With limited resources, it is necessary to determine which economic variables have the greatest impact on project profitability. These variables are called strategic economic variables and are determined using a plot called a "spider diagram."

The CFEM made no estimate of the cost of additional facilities and equipment. Sensitivity analysis can be used to determine the importance of this capital cost, and therefore the significance of this assumption. To perform sensitivity analysis on the cost of additional facilities and equipment, a rough estimate of this capital cost is required. A spider diagram can then be used to compare the sensitivity of this cost to the sensitivity of the other economic variables. The cost of additional facilities and equipment depends on the suitability and availability of existing equipment from the preceding waterflood, and was assumed to be $1 million.

5.2.1 Determining the Strategic Variables

The strategic economic variables for the optimum surfactant flood design were determined using a spider diagram. To create the spider diagram, a number of the economic variables used by the CFEM were varied by a percentage factor, one at a time, to determine their effect on a specified profitability measure. The economic variables considered were oil price, discount rate, chemical prices, operating cost, facilities and equipment cost, production tax rate, and the EOR tax credit rate. These variables were varied by ±100% from their base case values. The variation in operating cost was made by changing each operating cost component by uniformly the same percentage factor. Investment efficiency, NPV, and IRR were used as the profitability measures.

The spider diagrams for each profitability measure are shown in Figures 5.1 to 5.3, and the ranking of the strategic variables is given in Table 5.1. There is clearly a difference in the strategic variables depending on which profitability measure is used. Oil price is the most important variable, which is expected. NPV and investment efficiency both rank polymer price, discount rate, and operating cost as the next most important variables. However, IRR gives much more weighting to the facilities and equipment (F & E) cost, because high values of IRR favor cash flows early in the project, as discussed in Section 2. Changes in the discount rate does not effect IRR because the calculation of IRR is independent of the discount rate.

NPV ranks the chemical prices, particularly the surfactant price, lower than the other measures. As mentioned in previous chapters, NPV is not a suitable profitability measure for ranking surfactant flooding projects, because it does not give a profitability per dollar invested. Investment efficiency recognizes the importance of chemical prices on the project profitability by using the maximum cumulative DCF as the investment. For example, higher chemical prices will increase the capital exposure at the start of the project, making it more difficult to achieve payback, resulting in a lower value for investment efficiency. NPV does decrease with higher chemical prices, but does not measure the increase in capital risk. IRR indirectly accounts for the increased capital risk because its calculation favors the early cash flows.

Investment efficiency is the preferred profitability measure, and the strategic economic variables were chosen to be those that resulted in a greater than 50% change in investment efficiency. From Figure 5.1 and Table 5.1, the strategic variables are, in order of importance, oil price, polymer price, discount rate, operating cost, and the additional cost of facilities and equipment.

A spider diagram is based on percentage variations from the base case values, so if the base case value is incorrect, the results can change significantly. For example, if the additional facilities and equipment costs were much less than $1 million, then it would probably rank below the surfactant price. This type of analysis is strongly dependent on the accuracy of the base case values, so the results should be treated with caution.

Operating cost was identified as one of the strategic economic variables for the optimum design, but the CFEM uses six operating cost components to determine the total operating cost. Sensitivity analysis was also applied to each operating cost component to rank them in order of importance, and the resulting spider diagram is shown in Figure 5.4. A 100% increase in operating cost results in a 54 % decrease in the investment efficiency. Figure 5.4 shows that the fixed waterflood operating cost is the most important component of the operating cost estimate, responsible for 46% of the profitability decrease, followed by the chemical slug injection cost (27%), overhead cost (15%), oil treatment cost (10%), then the produced water disposal cost (4%). The optimum design does not have a polymer drive, which is why the polymer drive injection cost does not appear in this analysis.

5.2.2 Sensitivity to Oil Price and Discount Rate

The sensitivity of investment efficiency to oil price is shown in Figure 5.4, for oil prices ranging from $10/bbl to $35/bbl. This figure indicates that the break-even oil price for the

optimum design is about $12.50/bbl. This analysis is helpful to determine the minimum oil price required to meet the minimum required rate of return, but the profitability can be misleading. The main problem with this type of analysis is that it assumes that the oil price in year 0 is a value other than the most certain price, the current spot market price, and then escalates that price at the inflation rate of 3% (the CFEM base case oil price forecast).

A more realistic and meaningful approach to evaluating oil price sensitivity is to use the current oil price as the year 0 price and make various forecasts from that point. The CFEM uses a constant real price of $18/bbl as the base case oil price forecast. There appears to be no correlation between oil prices and inflation (Figure 2.2), so a constant nominal price of $18/bbl was also used as a forecast. Three other oil price forecasts were obtained from a report by the U.S. Department of Energy (DOE) and the Energy Information Administration (EIA), which provided a reference case, a worst case, and a best case, in constant 1993 dollars (DOE/EIA, 1995). The forecasts were changed to current dollars per barrel, assuming an inflation rate of 3%. The different oil price forecasts considered are shown in Figure 5.6, in current dollars per barrel.

The profitability of each oil price forecast is shown in Figure 5.7, as a plot of investment efficiency versus real discount rate. At the base case discount rate of 10%, the profitability varies considerably among the oil price forecasts, with the investment efficiency ranging from 0.43 to 1.91. As the discount rate increases, the relative profitability among the forecasts is reduced, because a high discount rate makes future cash flows less significant. The discount rate at which the investment efficiency is zero is equal to the IRR for that oil price forecast. The least favorable forecast has an IRR of about 20%, which indicates that the optimum design is profitable over the range of oil price forecasts considered.

5.2.3 Sensitivity to Chemical Prices

The sensitivity of investment efficiency to surfactant and polymer prices is shown in Figure 5.8. Each chemical price was varied separately while keeping the other constant at the base case value, which is $1.50/lb for both chemicals. This figure shows that the polymer price is more important than the surfactant price. If the polymer price were more than $3/lb, the optimum design would no longer be profitable. The polymer price is more important because the optimum polymer concentration is four times the optimum surfactant concentration.

5.2.4 Sensitivity to Facilities and Equipment Costs

The maximum amount that could be spent on additional facilities and equipment was determined using a break-even analysis, shown in Figure 5.9. The investment efficiency is equal to zero when the facilities and equipment cost is about $5.8 million. It is highly unlikely that a surfactant flood using a forty-acre five-spot pattern would require this much investment.

5.2.5 Independent Versus Integrated Producers

In the past, many of the large EOR projects were operated by the integrated (major) oil companies. However, many integrated oil companies have sold or are selling off some of the large onshore oil and gas properties that are EOR candidates to pursue international prospects. Independent producers are purchasing these properties, often with a lack of expertise and personnel required to implement sophisticated EOR projects. Large independent producers with sufficient capital and staff may consider any of the EOR processes that can be justified economically. Small independent producers are suited to the less complicated, low-cost EOR methods, such as polymer flooding and steamflooding (Martin, 1994).

The independent producer has several tax advantages over an integrated producer. The tax advantages for the independent producer are in the treatment of intangible drilling costs and the depletion allowance (see Section 2 for more detail). The profitabilities of the optimum surfactant

flood design for an independent producer and an integrated producer are compared in Table 5.2. There is a significant economical benefit for an independent producer, with the profitability of the optimum design being increased by 38%, based on investment efficiency. Discounted profitability per barrel for the two cases is given in Table 5.3. This table shows that the improved profitability is due to a reduction in taxes from $2.68/bbl to $1.44/bbl. Figure 5.10 compares the cumulative DCF for each case. Over the initial years of negative cash flows, there is no difference between the two types of producers because no income tax is being paid. However, as soon as the cumulative DCF becomes positive, the tax savings for the independent producer significantly increase the profitability of the optimum design.

5.3 Risk Analysis

When deciding on an investment opportunity in the petroleum industry, the final decision is usually based on a balance between risk and reward. A profitable project may be ignored if the probability of economic loss is too high. There are many different types of risks that may affect the outcome of a project. This study focuses only on economic risk, but other types of risk that may be quantified in a risk assessment include technical risk, political risk, legal risk, financial risk, and environmental risk.

There are a number of different ways in which petroleum companies account for risk Some of the common methods used are raising the discount rate, shortening the payback period, applying probability factors to cash flows, and simulation techniques. Raising the discount rate is the most popular method used by petroleum companies, while probability factors and simulation techniques are the most popular for consulting companies (Dougherty and Sarkar, 1993). Raising the discount rate is not recommended because it assumes that risk increases with time and penalizes cash flows late in the project. If a project has reached payback, most of the economic risk is gone, but a risk-adjusted discount rate would continue to penalize subsequent cash flows, which could make a good project look unprofitable.

Sensitivity analysis identified which economic variables have the greatest impact on the uncertainty in the project profitability, but the uncertainty in each variable has not been quantified. The uncertainty in a variable can be quantified by assigning a probability of occurrence to the possibility of a certain outcome. The probability of getting a head can be found by tossing a coin a large number of times. This is an example of an objective probability, which can be demonstrated and tested, but there is no similar basis to determine the outcome of a chemical flooding project. Therefore, subjective probabilities are commonly used to quantify uncertainty, based on experience and judgment. Subjective probabilities are sometimes based on past frequencies of occurrence and the Baysian hypothesis that these frequencies will occur in the future (Ikoku, 1985).

The effect of uncertainty on the project profitability can be determined using the expected value concept - a method for combining profitability estimates with quantitative estimates of risk to yield a risk-adjusted decision criterion. The expected value of an outcome is obtained by multiplying the probability of occurrence by the conditional value that is received if the outcome occurs. The expected value of a decision alternative is the sum of the expected values of each possible outcome that could occur if the decision alternative is accepted (Newendorp, 1975).

An expected value can be expressed in many ways, but the most common is the expected monetary value (EMV), or expected NPV. When choosing among several mutually exclusive projects, the project with the highest positive expected NPV should be selected. The expected value concept can be also be applied to the other profitability measures used in the CFEM.

Monte Carlo simulation and decision-tree analysis are the principal evaluation techniques that use the expected value concept to incorporate judgments about risk and uncertainty into an economic analysis. Monte Carlo simulation is a more comprehensive technique because uncertainties are expressed in the form of probability distributions instead of single-point estimates. The resulting profitability distribution reflects the full range of possible outcomes.

Monte Carlo simulation has been used to assess risk in polymer flooding projects (Goodyear and Gregory, 1994; Schulyer and Hochanadel, 1991). The following sections explain

the Monte Carlo simulation technique and demonstrate how it was used to assess economic risk in the optimum surfactant flood design.

5.3.1 Monte Carlo Simulation

In an economic analysis, where the cash flow input data are stochastic in nature, there can be an infinite number of possible outcomes for the project. Monte Carlo simulation is a technique used to carry out a large number of individual project evaluations, each with different input values selected from their subjective probability distributions in random combinations. After a large number of iterations, the result is a list of expected values for each possible project outcome. A continuous probability distribution for an expected value can be approximated by presenting the results as a histogram. The accuracy of the distribution depends on the number of iterations performed by the simulation. To produce a reliable output distribution, 500 or more iterations may be required (Allen, 1991). The procedure for economic risk analysis using Monte Carlo simulation is shown in Figure 5.11.

To perform the Monte Carlo simulation, a spreadsheet add-on application, called @RISK, was used to define the subjective probability distributions and generate output probability distributions for the optimum surfactant flood design. The strategic variables, determined in the sensitivity analysis, were used as the inputs for the simulation.

5.3.1.1 Selecting Probability Distributions

The CFEM assumes that the oil price escalates uniformly at the inflation rate. Using simulation, it is possible to generate random oil price forecasts by defining an oil price probability distribution for each year of the project. A lognormal subjective probability distribution was used to define uncertainty in the oil price in a given year. This distribution was used because the probability of a higher oil price is perceived to be higher than that of a lower oil price. The most certain oil price is the current oil price, so this price was used as the mean for the lognormal distribution. For subsequent years, the predicted price for the previous year was used as the mean. The standard deviation was held constant at $4/bbl. A lower limit of $10/bbl was used, because some resistance is expected from companies as oil prices approach their finding costs. The oil price distribution for the first year of the project is shown in Figure 5.12.

The next most important strategic variable was the polymer price, which has a base case value of $1.50/lb. To obtain polymer at this price, it was assumed that the operator already manufactured the xanthan gum for other projects, and it could be supplied at this price with no additional capital costs. However, if the polymer were to be purchased commercially, the price could be significantly higher. A triangular distribution was used to define the uncertainty in the polymer price, with $1.50/lb being the lower limit and the most likely value. A polymer price of $3/lb was used as the upper limit. The probability distribution for polymer price is shown in Figure 5.13.

The discount rate is an important strategic variable, but is generally known with some certainty and is often set by the company's corporate management. It was assumed that the base case discount rate of 10% was certain, and therefore, no probability distribution was required.

To define uncertainty in the operating cost, it was not necessary to consider all the operating cost components. Sensitivity analysis showed that the waterflood operating cost and the chemical slug injection operating cost have the greatest impact on the operating cost sensitivity. Normal distributions were used, with the base case value as the mean, as shown in Figures 5.14 and 5.15.

The facilities and equipment cost was shown to be an important variable, based on the assumption that the cost is about $1 million. A normal distribution was used to define the uncertainty in the facilities and equipment cost, with a relatively large standard deviation, to reflect

the high uncertainty in this value. The probability distribution for the facilities and equipment cost is shown in Figure 5.16.

5.3.1.2 Simulation Results

Using the probability distributions defined for the strategic variables, the @RISK program was used to run a Monte Carlo simulation for 1000 trials using the Latin Hypercube sampling method. Normally, a Monte Carlo simulation generates random numbers for a probability distribution over the entire range of values for that distribution. This requires a large number of trials to obtain results that approximate the true shape of the distribution. Latin Hypercube sampling is more precise than conventional Monte Carlo sampling because the entire range of the distribution is sampled in a more even, consistent manner, by dividing the probability distribution into intervals of equal probability (Startzman and Wattenbarger, 1985).

Samples of various oil price forecasts generated by the Monte Carlo simulation are shown in Figure 5.17. The mean oil price forecast and confidence bands at 10% and 90% are shown in Figure 5.18. A 10% confidence band gives the oil price at which there is a 10% chance that the price is below this value. The mean oil price forecast is fairly conservative, predicting the oil price in 20 years to be about $25/bbl in current dollars. Simulated oil price forecasts by Schulyer and Hochanadel (1991) predicted the oil price to be about $80/bbl in 20 years, which seems very optimistic.

The results of the simulation are summarized in Table 5.4. NPV and investment efficiency appear to be the most suitable profitability measures for this type of analysis. The simulation received 154 errors out of the 1000 trials when calculating IRR, which was probably due to outcomes with multiple rates of return, or with no solution. Errors were also reported in the calculation of GROR.

The previous analysis of the optimum design uses a deterministic approach that considers only one possible outcome. Monte Carlo simulation is a probabilistic approach that considers a range of outcomes. The results from these two approaches are compared in Table 5.5. The expected NPV for the optimum design is $1.78 million, which is substantially less than the NPV using a deterministic approach of $3.57 million. There are two reasons for the lower profitability of the probabilistic approach. Firstly, the mean oil price forecast generated by the simulation was pessimistic compared to that of the CFEM base case forecast. Second, the triangular probability distribution used for polymer price had a mean of $2/lb, which is higher than the base case value of $1.50/lb. These factors decreased revenues while increasing the chemical cost, which reduced the profitability of the optimum design.

The mean cumulative DCF with 10% and 90% confidence bands is shown in Figure 5.19. This figure illustrates the large uncertainty in the outcome of the optimum design. The difference in cumulative DCF between the confidence bands is about $16 million.

The probability distributions for each probability measure are shown in Figures 5.20 to 5.23. The NPV distribution is reasonably continuous and resembles a lognormal distribution, which is expected, since a lognormal distribution was used to define uncertainty in the oil price. The distribution for investment efficiency is similar to the NPV distribution, except the negative values converge to -1, which is the lowest value investment efficiency can have. The distributions for IRR and GROR look very different from those for investment efficiency and NPV. NPV is the preferred profitability measure for economic risk analysis because it can be calculated for all possible outcomes and produces a relatively continuous distribution of outcomes.

The economic risk in the optimum design is quantified by the probability of an outcome having an expected NPV below zero. In this case, the probability of economic loss is 33%, which is not likely to be acceptable because of the large front-end investment associated with the project. The expected investment efficiency is only 0.53, which indicates that the rewards for taking this risk are not that great. Utility theory, or preference theory, is an extension of the expected value concept, and is often used as a quantitative measure to determine how much money a company is prepared to invest at different levels of risk.

The standard deviation is a measure of the dispersion of values around the mean, or expected value. The larger the standard deviation, the greater the uncertainty in the outcome. A standard deviation of $3.4 million for the NPV distribution is double the expected NPV, which suggests the outcome of this project is very uncertain. This uncertainty is a result of the large range of values used in defining the probability distributions for oil price and polymer price. If these prices could be estimated with greater confidence and a smaller range were used, then the uncertainty in the project outcome would decrease. Unfortunately, when evaluating projects, the variables that are most certain in value are often the most insignificant.

5.4 Conclusions

Sensitivity analysis was applied to the optimum surfactant flood design, and the strategic economic variables were determined using a spider diagram. The strategic variables differed depending on which profitability measure was used. Investment efficiency was used because of its suitability as a profitability measure for chemical flooding projects. The strategic economic variables are, in order of importance, oil price, polymer price, discount rate, and the cost of additional facilities and equipment. The surfactant price had little impact on profitability because a very low surfactant concentration is used in the optimum design.

The profitability of the optimum surfactant flood design was determined for both an independent producer and an integrated producer. An independent producer has several tax advantages, which were equivalent to a 38% increase in the investment efficiency for the optimum design. This economic benefit and the comparatively low cost of the optimum design should make it a suitable investment opportunity for independent producers.

Subjective probability distributions were used to define uncertainties in the strategic economic variables. These distributions were used as inputs for Monte Carlo simulation, to assess the economic risk in the optimum surfactant flood design. The expected NPV was $1.8 million, with a standard deviation of $3.4 million, which indicates that there is considerable uncertainty in the outcome of the project. The optimum design has a 33% probability of economic loss, which would probably be unacceptable because of the considerable capital exposure in the early years of the project. An expected investment efficiency of 0.53 indicates that the financial gains for taking this risk are not that great.

The results of the Monte Carlo simulation indicate that the profitability of the optimum surfactant flood design is marginal, especially when the probability of economic loss is taken into account. However, when using quantitative methods to evaluate risk, there can be a tendency to place too much emphasis on the results. The oil price forecast generated by the simulation was conservative, which was why the simulation results were less profitable than those of the base case analysis.

A comprehensive risk assessment of chemical flooding should also include uncertainties in the variables that have a strong influence on the technical performance of the chemical flood. Identifying the strategic technical variables for a surfactant flood was not part of this study, but should be included in future studies. In particular, different permeability field realizations, surfactant adsorptions, and CMC values are likely to affect the surfactant flood performance.

Table 5.1: Determining the strategic variables using various profitability measures

Importance ranking	Investment efficiency	NPV	IRR
1	Oil price	Oil price	Oil price
2	Polymer price	Discount rate	Polymer price
3	Discount rate	Polymer price	F & E cost
4	Operating cost	Operating cost	Operating cost
5	F & E cost	Production tax	Production tax
6	Surfactant price	Inflation rate	Surfactant price
7	Production tax	EOR tax credit	EOR tax credit
8	EOR tax credit	F & E cost	Inflation rate
9	Inflation rate	Surfactant price	Discount rate

Table 5.2: Comparing the profitability of the optimum surfactant flood design for an independent producer to that of an integrated producer

Profitability measure	Independent	Integrated
Economic limit (years)	10	10
Internal rate of return (%)	39.23	33.79
Net present value (millions $)	4.93	3.57
Discounted return on investment	4.25	3.08
Investment efficiency	1.52	1.10
Growth rate of return (%)	20.65	18.48
Payback period (years)	3.61	3.61
Discounted payback period (years)	3.93	3.93

Table 5.3: Comparing the discounted profitability per barrel of the optimum design for an independent producer to that of an integrated producer

	Independent ($/bbl)	Integrated ($/bbl)
Revenue	18.00	18.00
Royalty	2.25	2.25
Capital cost	1.06	1.06
Operating cost	3.35	3.35
Chemical cost	5.39	5.39
Taxes	1.44	2.68
Profit	4.51	3.27

Table 5.4: Results of the Monte Carlo simulation

	NPV (millions $)	Investment efficiency	IRR (%)	GROR (%)
Mean	1.78	0.53	24.51	12.42
Standard deviation	3.43	0.96	17.14	8.71
Minimum	-6.06	-0.91	-27.21	-36.95
Maximum	13.67	4.65	73.67	30.81
Errors calculated	0	0	154	6
Probability of economic loss	33.24%	33.24%	21.08%	32.83%

Table 5.5: Comparing deterministic and probabilistic approaches to economic analysis

	Deterministic	Probabilistic
Net present value (millions $)	3.57	1.78
Investment efficiency	1.10	0.53
Internal rate of return (%)	33.79	24.51
Growth rate of return (%)	18.48	12.42

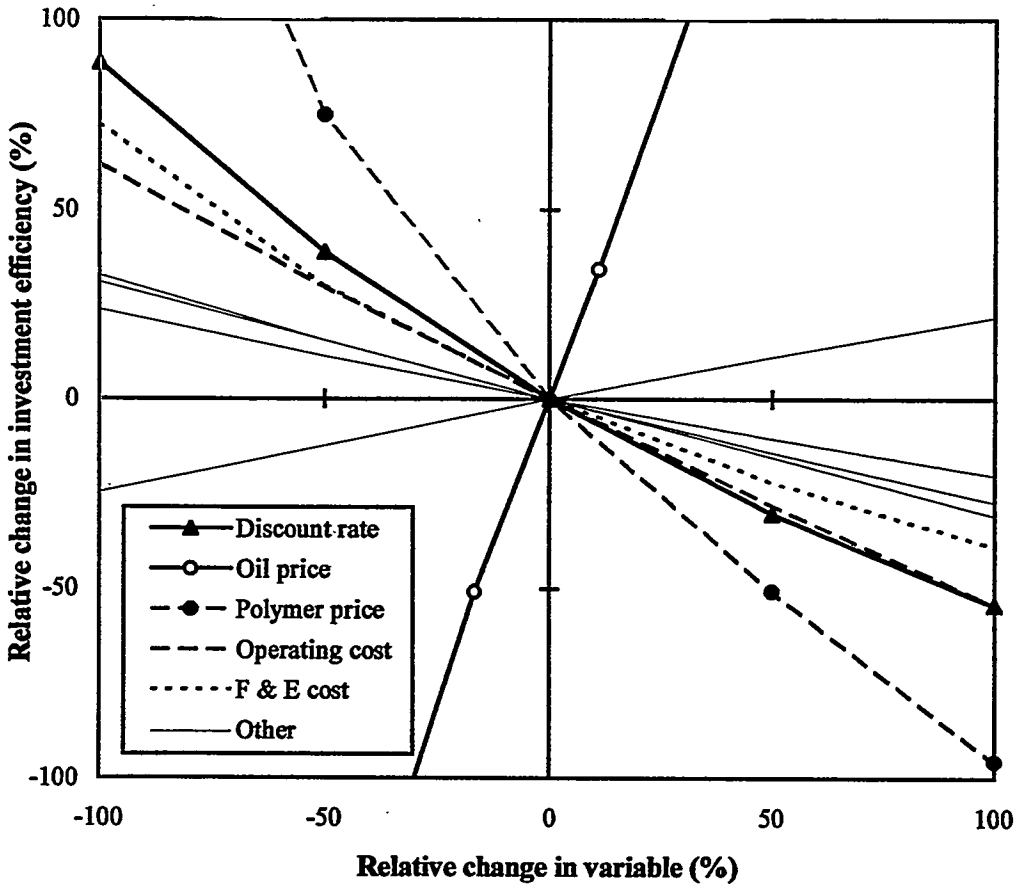


Figure 5.1: Spider diagram for the optimum design using investment efficiency as the profitability measure

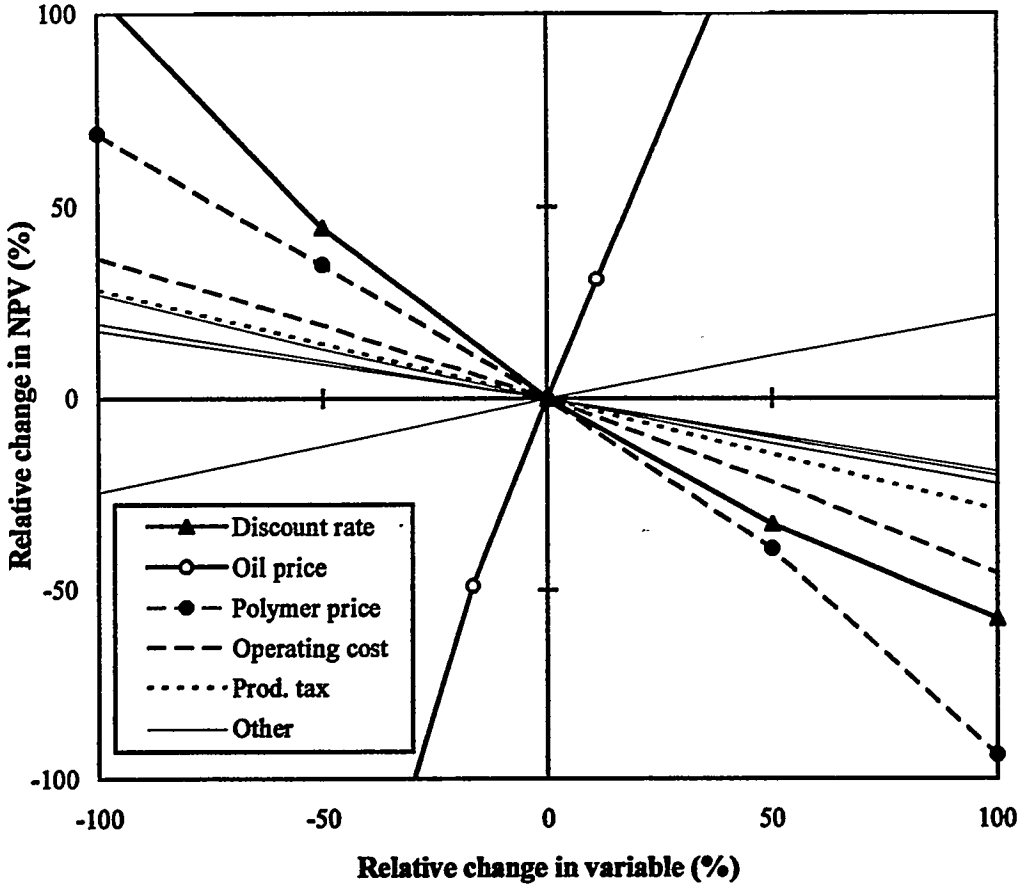


Figure 5.2: Spider diagram for the optimum design using NPV as the profitability measure

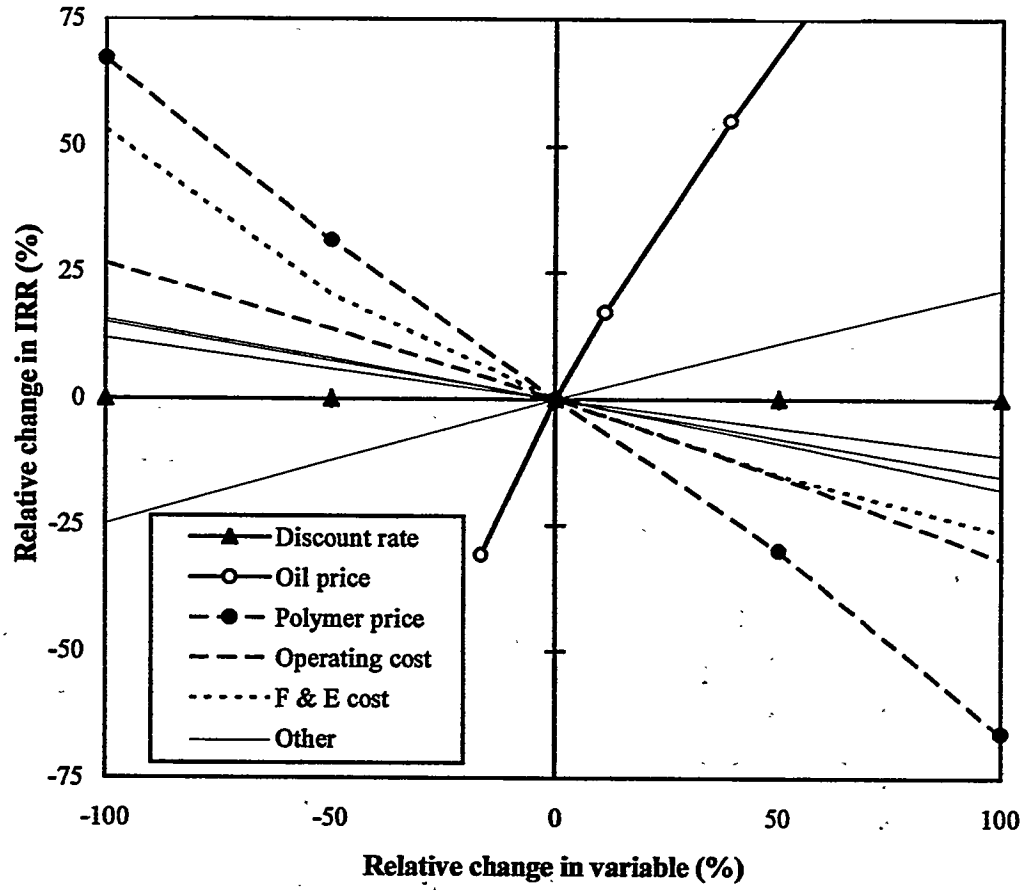


Figure 5.3: Spider diagram for the optimum design using IRR as the profitability measure

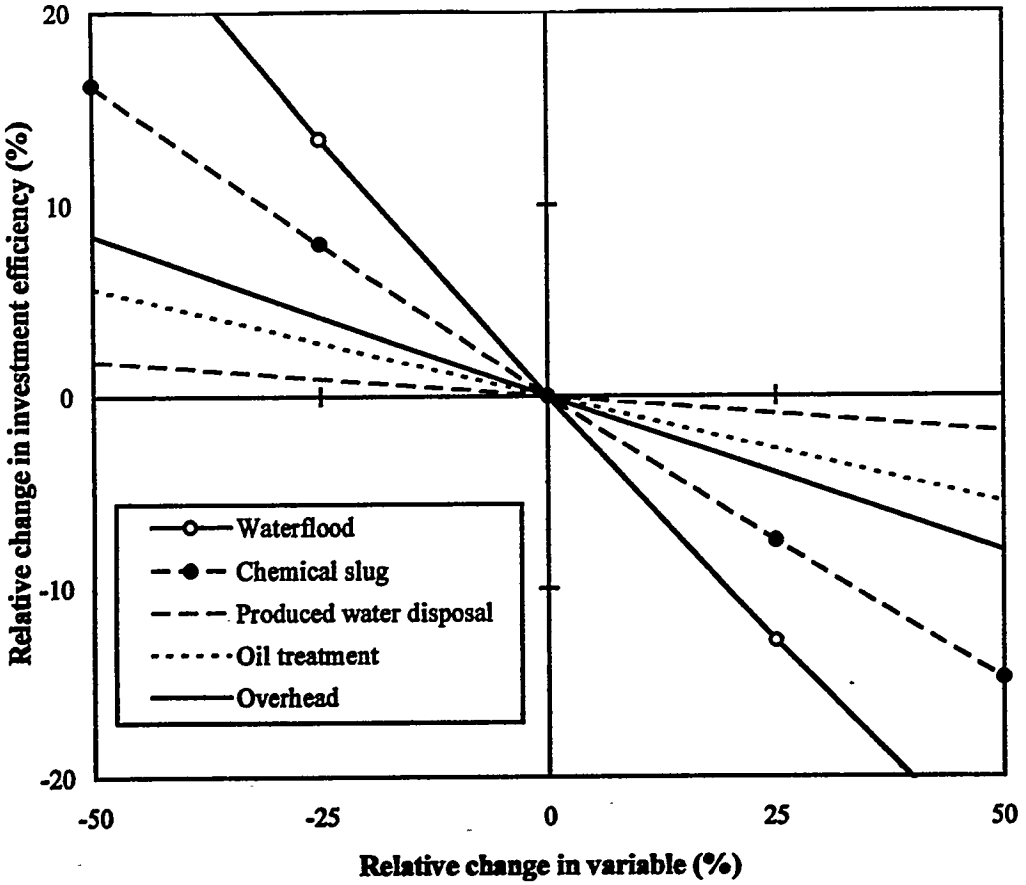


Figure 5.4: Spider diagram for operating cost components

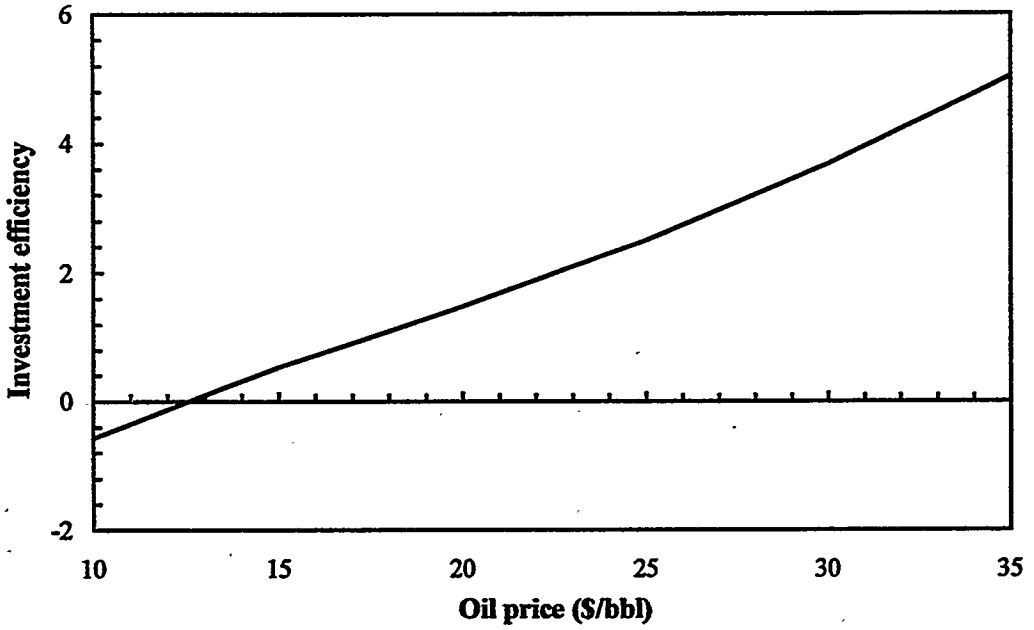


Figure 5.5: Sensitivity of investment efficiency to oil price

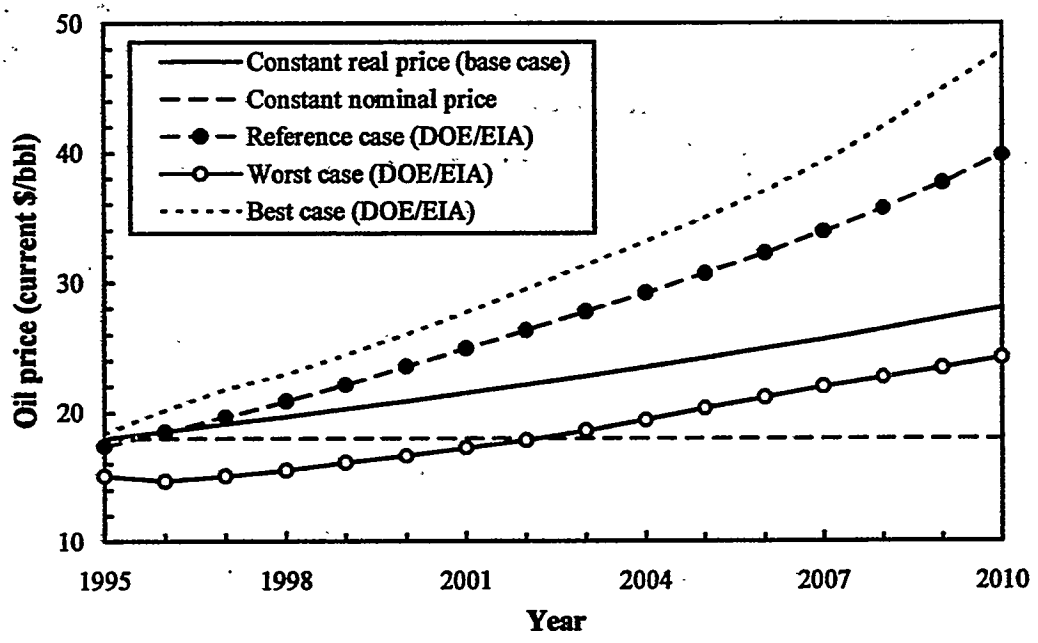


Figure 5.6: Various oil price forecasts (1995-2010)

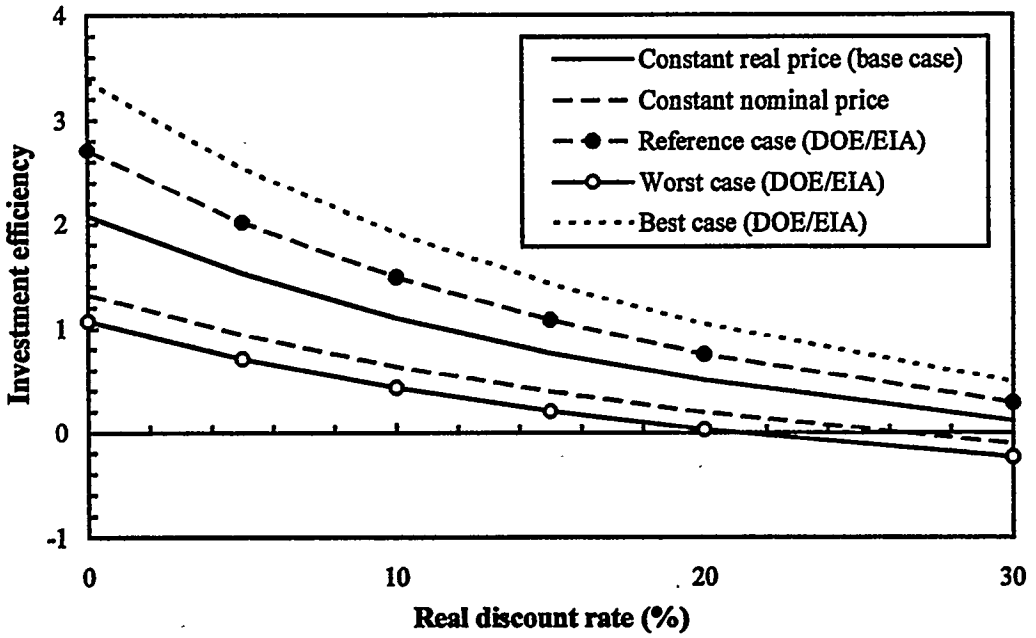


Figure 5.7: Sensitivity of investment efficiency to real discount rate using various oil price forecasts

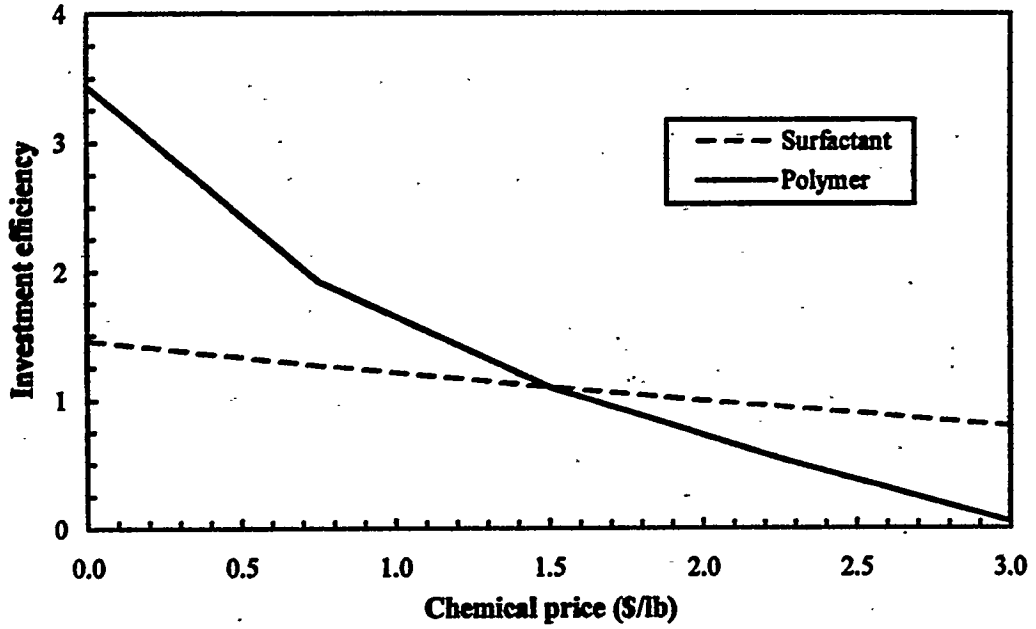


Figure 5.8: Sensitivity of investment efficiency to surfactant and polymer price

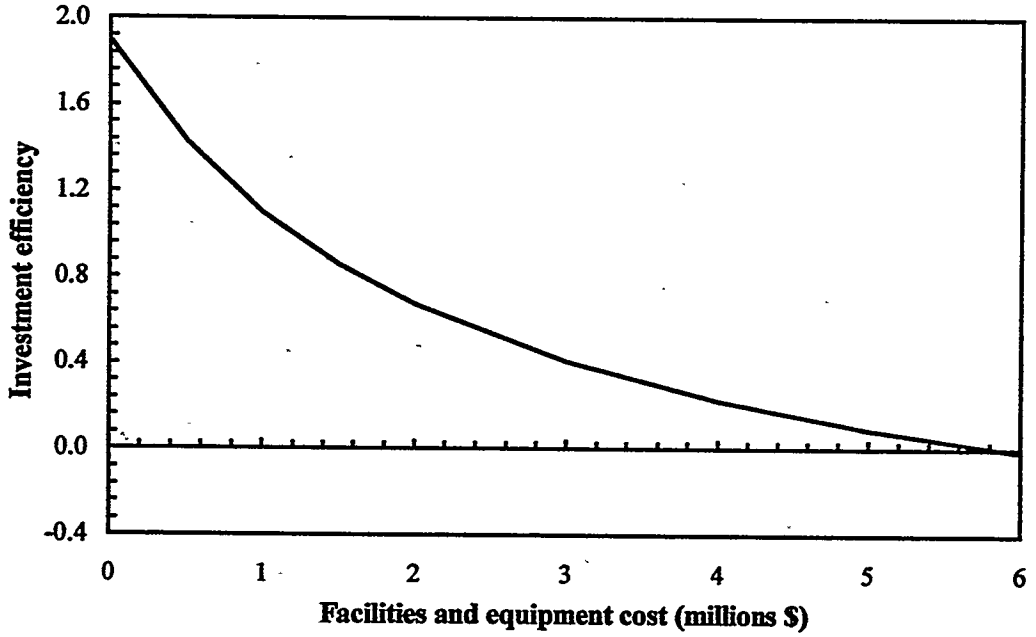


Figure 5.9: Sensitivity of investment efficiency to facilities and equipment cost

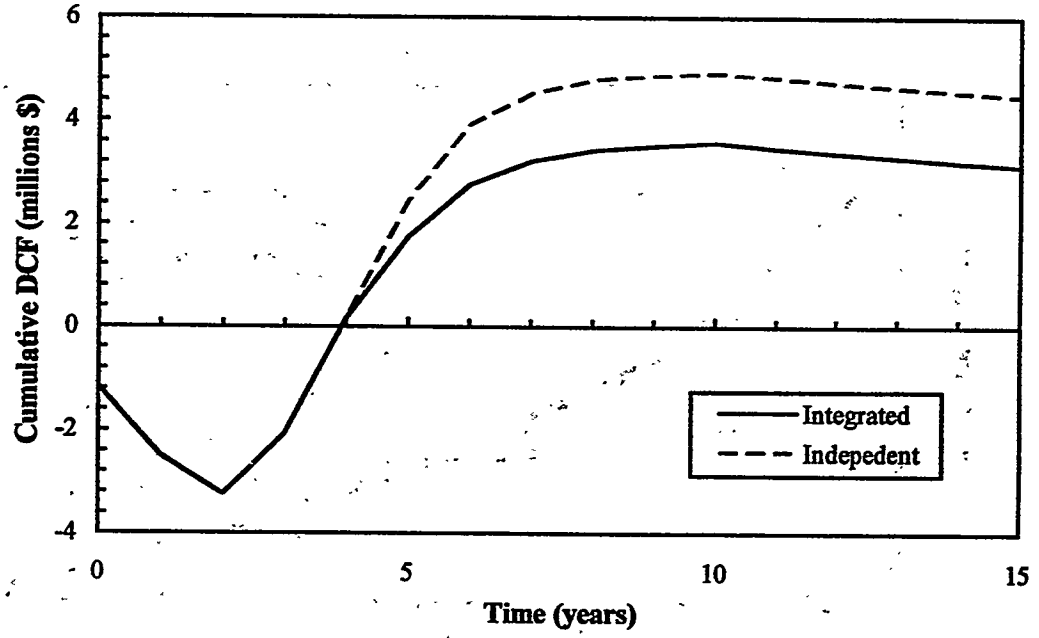


Figure 5.10: Comparing the cumulative DCF versus time for an independent producer to an integrated producer

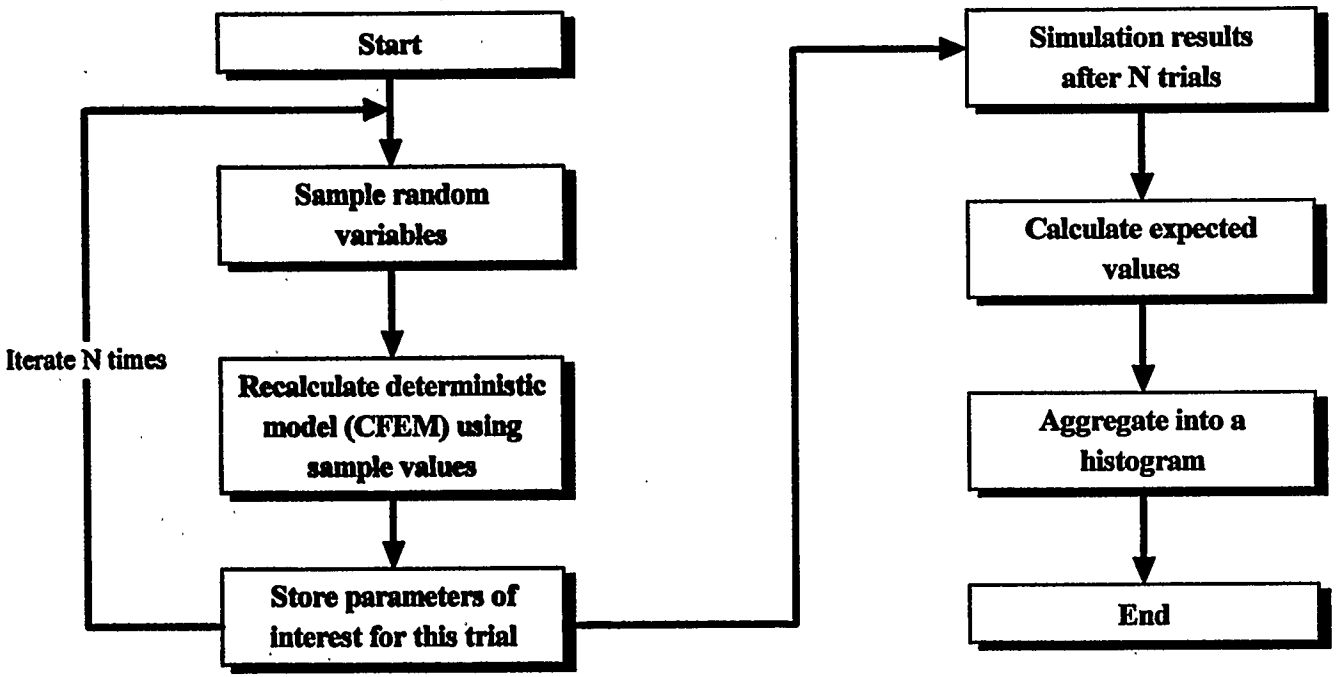


Figure 5.11: Economic risk analysis using Monte Carlo simulation

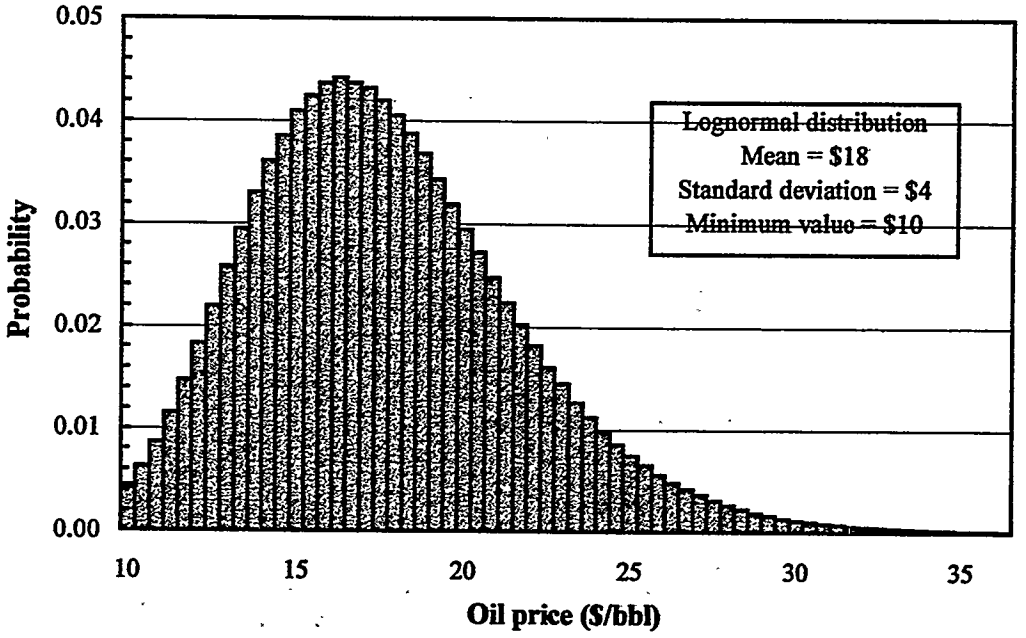


Figure 5.12: Oil price probability distribution used in the Monte Carlo simulation

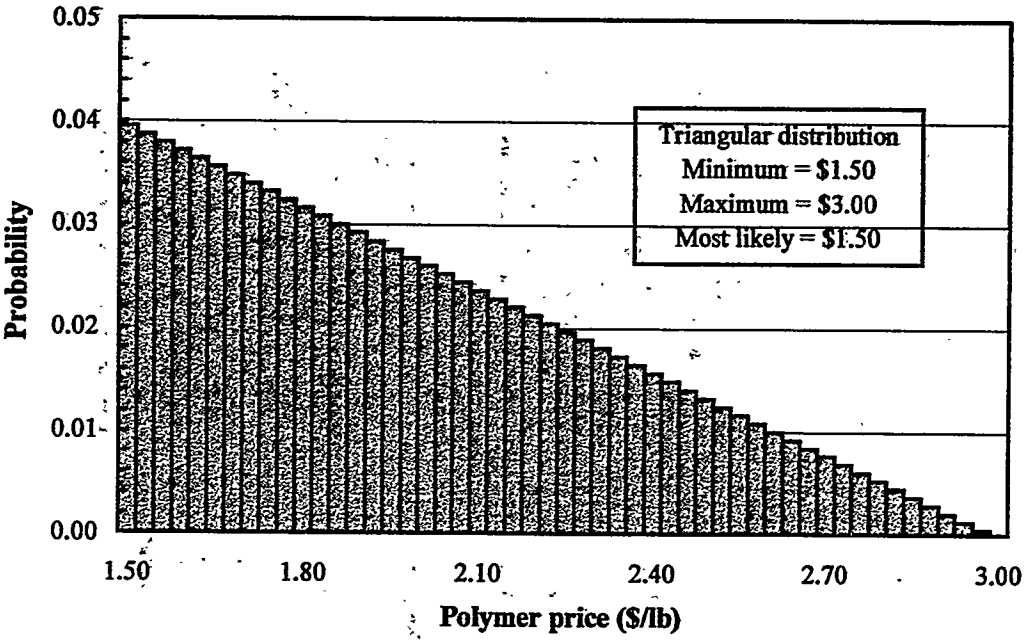


Figure 5.13: Polymer price probability distribution used in the Monte Carlo simulation

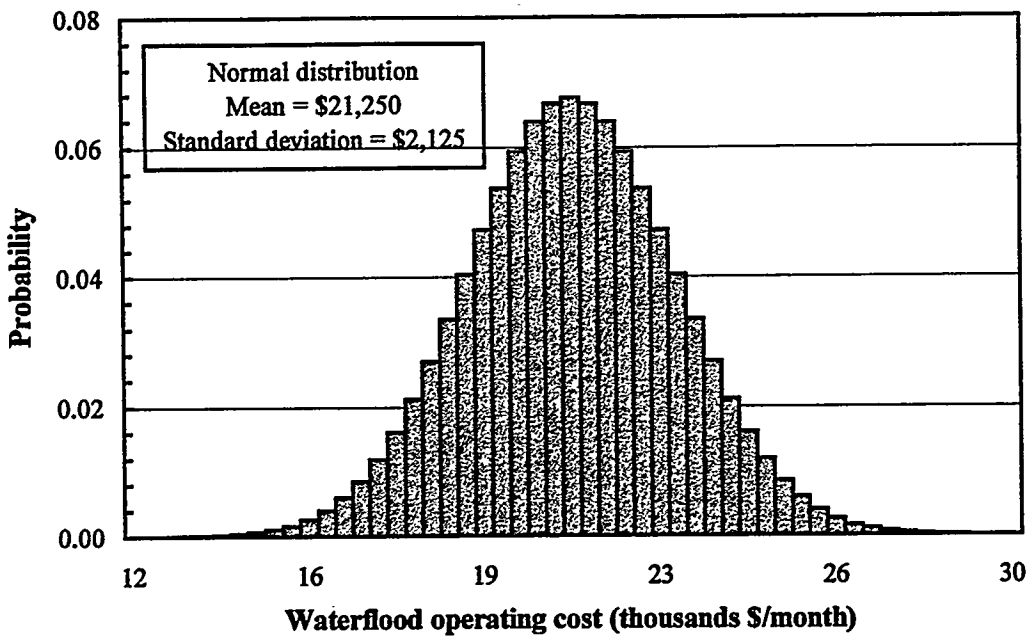


Figure 5.14: Waterflood operating cost probability distribution used in the Monte Carlo simulation

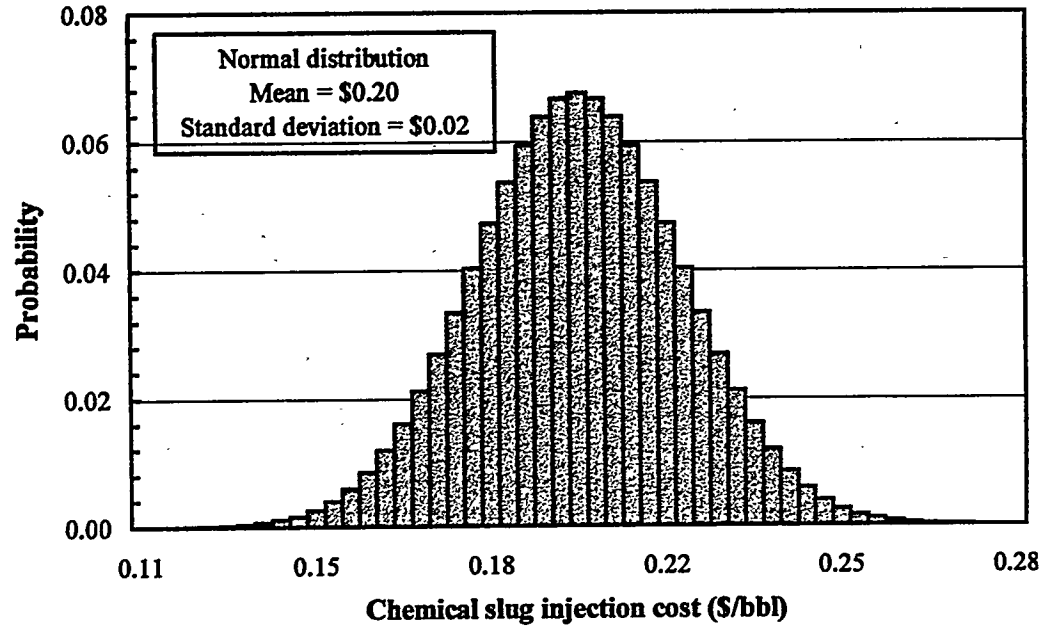


Figure 5.15: Chemical slug injection operating cost probability distribution used in the Monte Carlo simulation

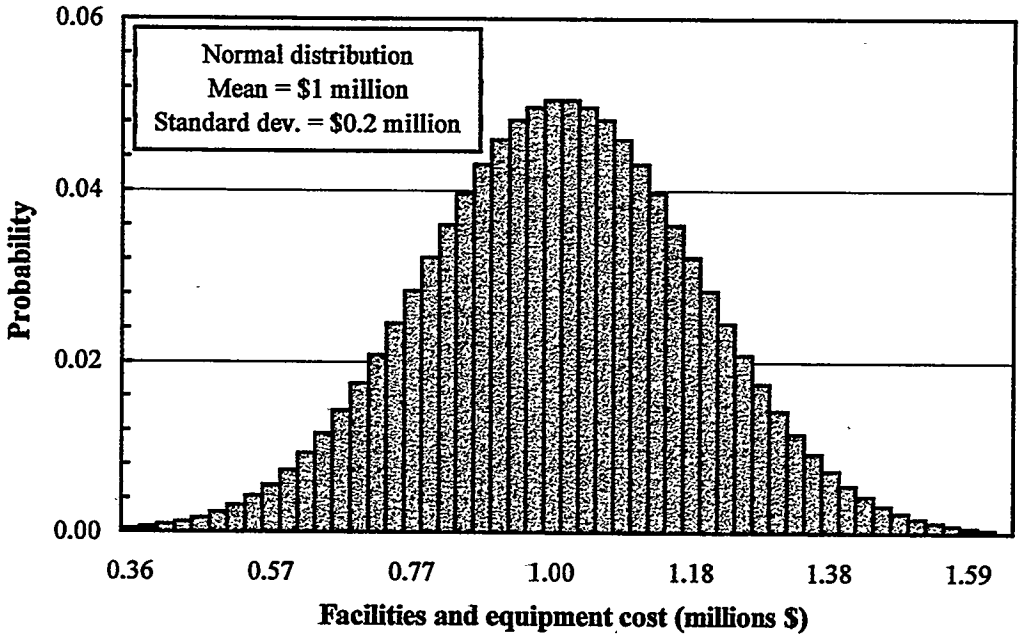


Figure 5.16: Facilities and equipment cost probability distribution used in the Monte Carlo simulation

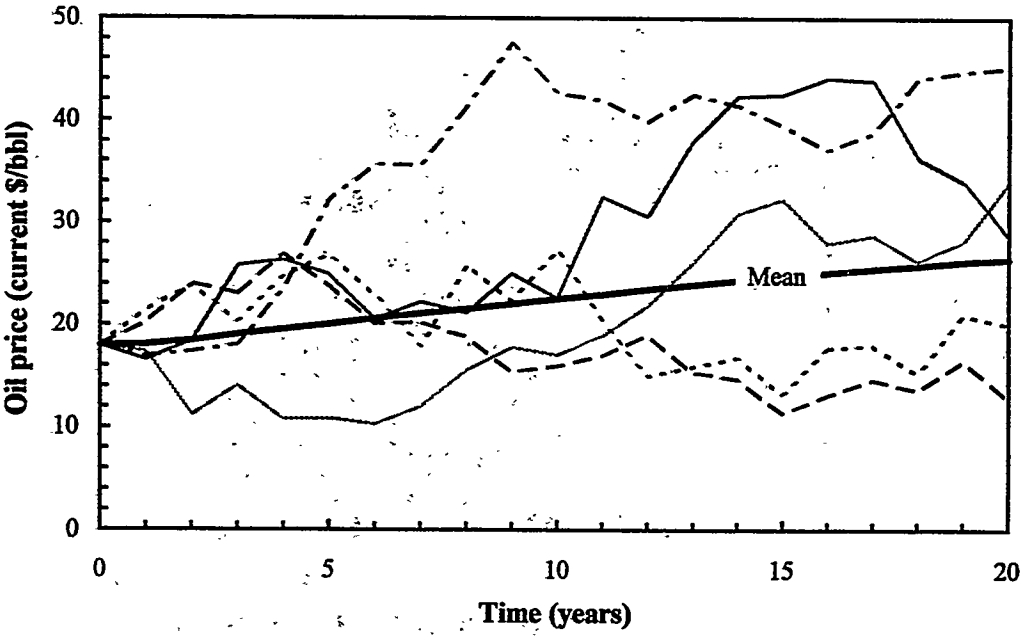


Figure 5.17: Examples of oil price forecasts for various trials from the Monte Carlo simulation

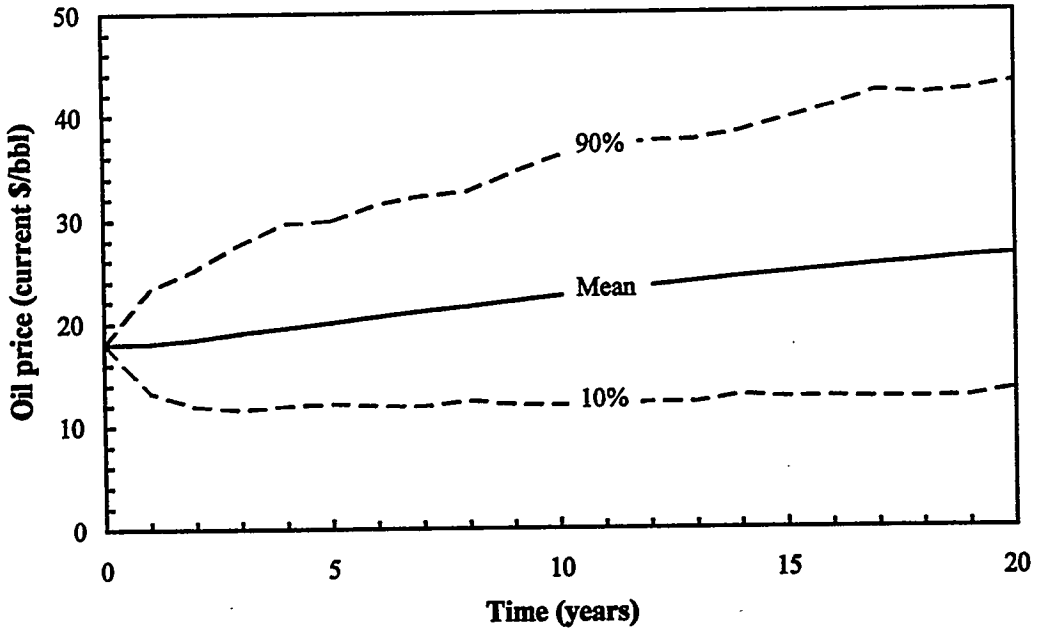


Figure 5.18: Oil price forecast generated using Monte Carlo simulation showing the mean and confidence bands

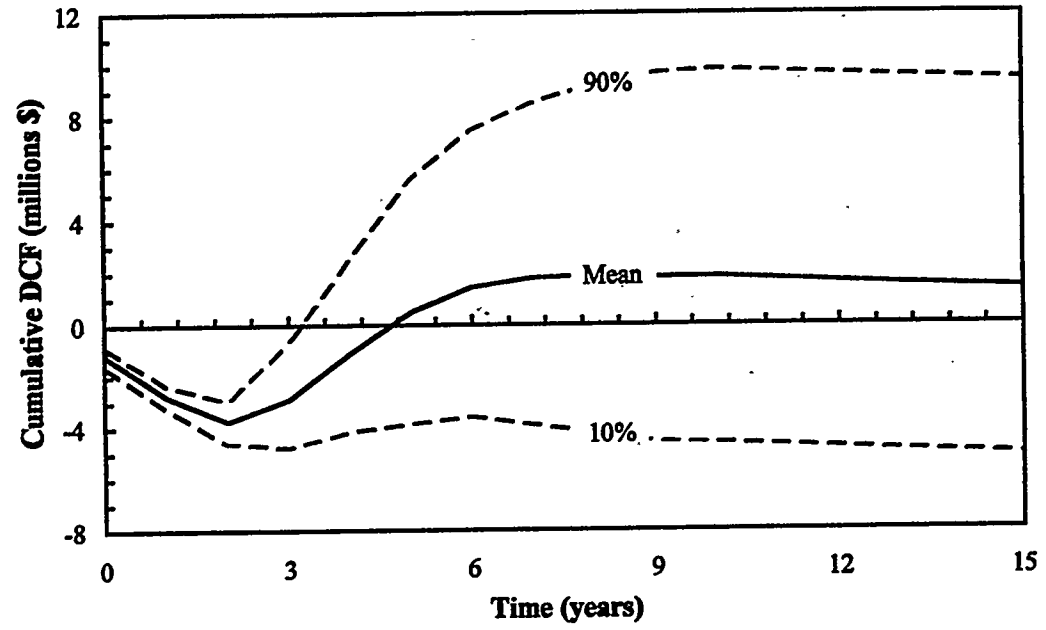


Figure 5.19: Cumulative DCF generated using Monte Carlo simulation showing the mean and confidence bands

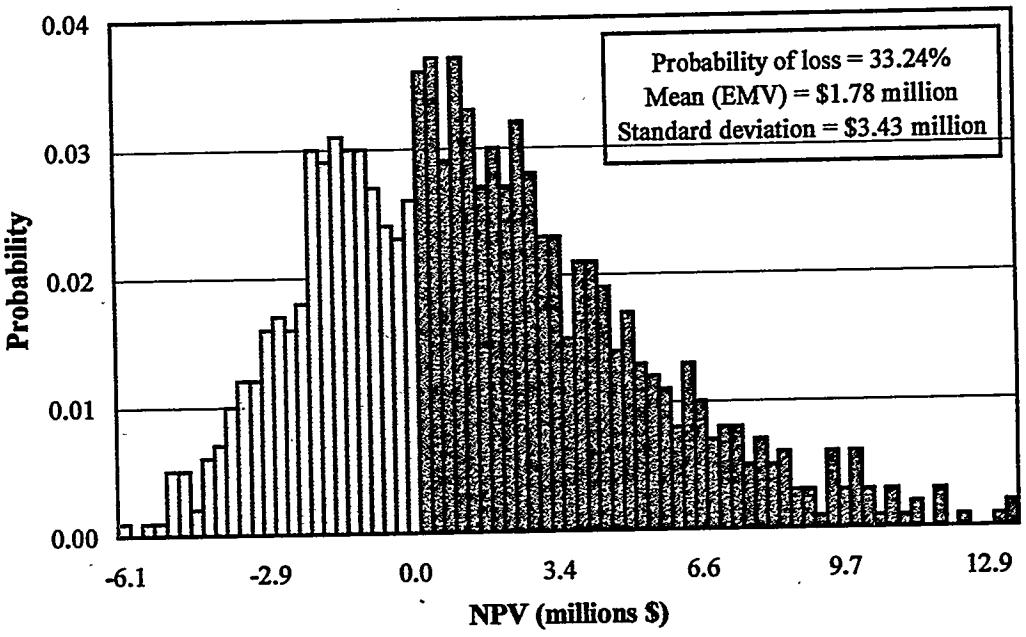


Figure 5.20: NPV distribution generated using Monte Carlo simulation

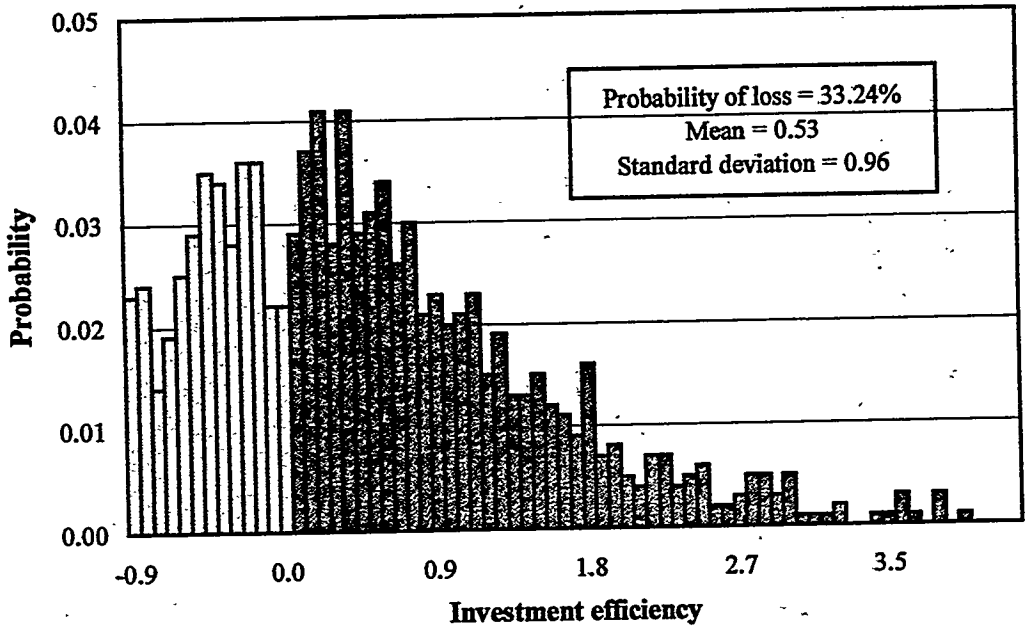


Figure 5.21: Investment efficiency distribution generated using Monte Carlo simulation

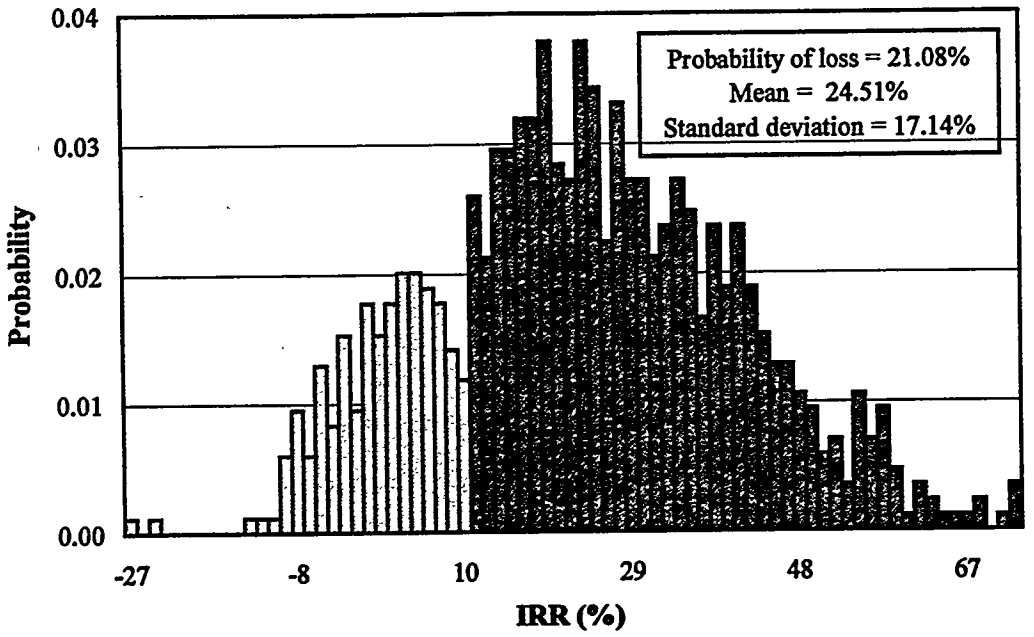


Figure 5.22: IRR distribution generated using Monte Carlo simulation

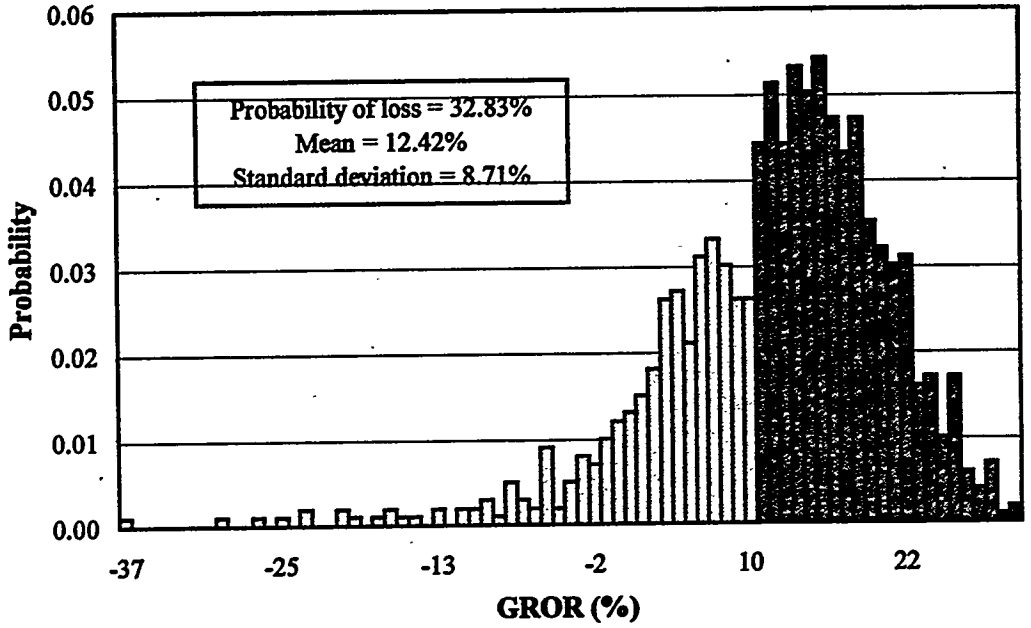


Figure 5.23: GROR distribution generated using Monte Carlo simulation

6. Conclusions and Recommendations

The objective of this study was to determine the optimum surfactant flood design, based on economic performance, for a typical U.S. onshore sandstone oil reservoir. This objective was successfully completed using realistic reservoir simulations and an economic model based on the discounted cash flow method of economic analysis.

The surfactant flood designs considered in this study took advantage of highly efficient synthetic surfactants that are active at very low concentrations and that are compatible with xanthan gum polymer. These surfactants can be readily tailored to the reservoir salinity and temperature of interest by changing the number of ethoxy and propoxy groups. A horizontal injection well was used in all the surfactant flood designs because it significantly shortens the project life and improves the injectivity. Other favorable conditions used in this study were a low surfactant CMC and a low surfactant adsorption.

This study demonstrates how the economics of surfactant flooding is sensitive to the chemical slug size and concentrations used. In Section 3, a surfactant flood consisting of a 0.6 PV chemical slug, with a 0.5 vol. % surfactant concentration and a 2000 ppm polymer concentration, was found to be marginally profitable. An optimization study of this reservoir, using a reservoir simulator and an economic model, was successful in determining a more favorable design. The optimum surfactant flood design had a 0.79 PV chemical slug, with a surfactant concentration of 0.05 vol. % and a polymer concentration of 2000 ppm, and no polymer drive. This design was highly profitable, with a IRR of 51.8%, a NPV of $4.3 million, and an investment efficiency of 1.9. The higher concentration design had the highest recovery efficiency at its economic limit (84% ROIP) of all the designs considered but is significantly less profitable than the optimum design, which recovered only about 56% ROIP at its economic limit. The large difference in the profitability of these two designs demonstrates the benefits of using an economic approach to the optimization of surfactant flooding.

In developing the CFEM, it was not critical to accurately estimate all the capital costs for a surfactant flood, because they are approximately the same for each surfactant flood design and have no effect on the optimization process. This study was concerned with relative profitability, not absolute profitability, so the attractive economics of the optimum design should not be taken too seriously. Furthermore, this study was based on a hypothetical reservoir and reservoir simulations, which may or may not give realistic production profiles for some of low concentration designs considered.

The profitability of the surfactant flood designs was most sensitive to the surfactant concentration used. As the surfactant concentration was increased, the surfactant efficiency decreased, resulting in substantially higher chemical costs per barrel of oil produced and a lower project profitability. Variations in the polymer concentration, at a constant slug size and surfactant concentration, did not have much impact on profitability. The profitability of the optimum design does not change significantly between 1500 ppm and 2500 ppm.

Investment efficiency and GROR are recommended as profitability measures for evaluating and optimizing surfactant flooding projects. These measures are favored because they include the initial negative cash flows, typical of EOR projects, as part of the investment. Using NPV as the profitability measure gives a very different optimum design than does investment efficiency, favoring higher surfactant and polymer concentrations. NPV should not be used as a ranking tool, unless the company has unlimited capital resources and is able to invest in all projects that meet the minimum required rate of return. DROI is not a suitable measure for optimization because it does not take into account the different levels of capital risk in surfactant flooding projects.

Sensitivity analysis was applied to the optimum surfactant flood design, and the strategic economic variables were found using a spider diagram. The strategic variables differed depending on which profitability measure was used. Investment efficiency was used because of its suitability as a profitability measure for chemical flooding projects. The strategic economic variables were, in

order of importance, oil price, polymer price, discount rate, and the cost of additional facilities and equipment. The surfactant price had little impact on profitability because the optimum design has a very low surfactant concentration.

The profitability of the optimum surfactant flood design was determined for an independent producer and an integrated producer. An independent producer has several tax advantages, which were equivalent to a 38% increase in the investment efficiency for the optimum design. This economic benefit and the comparatively low cost of the optimum design should make it a suitable investment opportunity for independent producers.

Monte Carlo simulation was demonstrated as a technique to quantify economic risk in a surfactant flooding project. The results of the Monte Carlo simulation indicate that the profitability of the optimum surfactant flood design is marginal, especially when the probability of economic loss is taken into account. However, when using quantitative methods to evaluate risk, there can be a tendency to place too much emphasis on the results. Monte Carlo simulation is strongly dependent on the subjective input probability distributions used and care should be taken when interpreting the results.

A comprehensive risk assessment of chemical flooding should also include uncertainties in the variables that have a strong influence on the technical performance of the chemical flood. Identifying the strategic technical variables for surfactant flooding was not part of this study, but should be included in future studies. In particular, different permeability field realizations, surfactant adsorptions, and CMC values are likely to affect the surfactant flood performance.

The optimization of surfactant flooding presented in this study only considered the composition and timing of the chemicals injected. Other controllable factors that can affect the performance of a surfactant flood are different well arrangements and well spacings. These factors should be included in future optimization studies.

As shown in this study, an economic approach to optimization can significantly improve the profitability of a surfactant flooding project. Based on specific reservoir studies of chemical flooding candidates, this approach should be combined with an assessment of technical risk to determine the most attractive surfactant flood design. The final investment decision will vary among companies and is dependent on their ability to take the economic and technical risks associated with a surfactant flooding project.

7. References

Allen, D.H.: *Economic Evaluation of Projects,* third edition, Institution of Chemical Engineers, England (1991) 105-149.

Allen, F.H. and Seba, R.D.: *Economics of Worldwide Petroleum Production,* Oil & Gas Consultants International, Inc., Tulsa, OK (1993).

Austad, T., Fjelde, I., Veggeland, K., and Taugbøl, K.: "Physicochemical Principles of Low Tension Polymer Flood," paper presented at 7th European IOR Symposium in Moscow, Russia (Oct. 27-29, 1993).

Barua, J., Prescott, T., and Haldorsen, H.H.: "Financial and Technical Decision Making for Surfactant Flooding," paper SPE 15074 presented at the 56th California Regional Meeting of the SPE, Oakland, CA (Apr. 2-4, 1986).

Baumann, R.H. and Pulsipher, A.G.: "States Pass Measures to Help Producers During Tough Times," *Oil & Gas J.* (Nov. 14, 1994) 56.

Bhuyan, D., Lake, L.W., and Pope, G.A.: "Simulation of High-pH Coreflood Experiments Using a Compositional Chemical Flood Simulator," paper SPE 21029 presented at the SPE International Symposium on Oilfield Chemistry, CA (Feb. 20-22, 1991).

Bradley, M.E. and Wood, A.R.O.: "Forecasting Oilfield Economic Performance," *JPT* (Nov. 1994) 965.

Brashear, J.P., Biglarbigi, K., and Ray, M.R.: "Impact of Recent Federal Tax and R&D Initiatives on Enhanced Oil Recovery," paper SPE 22622 presented at the 66th Annual Technical Conference and Exhibition of the SPE, Dallas, TX (Oct. 6-9, 1991).

Burke, F.M., Jr., and Starcher, M.L.: *Oil & Gas Taxation in Nontechnical Language,* Pennwell, Tulsa, OK (1993) 113-129.

"Business Expenses," Department of the Treasury: Internal Revenue Service, Publication 535, Cat. No. 15065Z (1995) 52-54.

Capen, E.C., Clapp, R.V., and Phelps, W.W.: "Growth Rate - A Rate-of-Return Measure of Investment Efficiency," *JPT* (May, 1976) 531-543.

Chapman, M.J.S.: "Discounted Cash Flow Analysis of the Alkaline Surfactant Polymer Process as an Enhanced Oil Recovery Technique," MS thesis, U. of Texas, Austin (December, 1994).

Clapp, R.V.: "An Alternative Concept of Investment for Improved Profitability Measures," paper SPE 30051 presented at the SPE Hydrocarbon Economics and Evaluation Symposium, Dallas, TX (Mar. 26-28, 1995).

"Costs and Indexes for Domestic Oil and Gas Field Equipment and Production Operations," Report DOE/EIA-0185, U.S. DOE, Energy Information Administration, Washington, DC (1994).

Dakhlia, H.: "A Simulation Study of Polymer Flooding and Surfactant Flooding Using Horizontal Wells," PhD dissertation, U. of Texas, Austin (August 1995).

Dakhlia, H., Wu, W., Lim, M.T., Delshad, M., Pope, G.A., Sepehrnoori, K.: "Simulation of Surfactant Flooding Using Horizontal Wells," paper CIM 95-82 presented at the Petroleum Society of CIM 46th Annual Technical Meeting, Banff, Alberta (May 14-17, 1995).

"Depreciation," Department of the Treasury: Internal Revenue Service, Publication 534, Cat. No. 15064O (1995) 13-25, 72.

Dougherty, E.L. and Sarkar, J.: "Current Investment Practices and Procedures: Results of a Survey of U.S. Oil and Gas Producers and Petroleum Consultants," paper SPE 25824 presented at the SPE Hydrocarbon Economics and Evaluation Symposium, Dallas, TX (Mar. 29-30, 1993).

Dreher, K.D. and Shoppman, T.D.: "Separation of Oil and Water Produced by Micellar-Solution/Polymer Flooding," *JPT* (August, 1985) 1459-1465.

Duke, R.B.: "Demulsifying the Produced Fluids from Marathon's M-1 Project," *SPE Advanced Technology Series,* vol. 2, no. 2 (April, 1994) 214.

Goodyear, S.G. and Gregory, A.T.: "Risk Assessment and Management in IOR Projects," paper SPE 28844 presented at the European Petroleum Conference, London, U.K. (Oct. 25-27, 1994).

Hartshorne, J.M. and Nikonchik, J.S.: "Micellar/Polymer Flood Shows Success in Bell Creek Field," paper SPE 13122 presented at the 59th Annual Technical Conference and Exhibition of the SPE, Houston, TX (Sept. 16-19, 1984).

Ikoku, C.U.: *Economic Analysis and Investment Decisions,* John Wiley & Sons, New York, NY (1985) 191-237.

"International Energy Outlook," Report DOE/EIA-0484, U.S. DOE, Energy Information Administration, Washington, DC (1995).

International Petroleum Encyclopedia, Pennwell, Tulsa, OK (1995) 323.

Jakobsen, S.R. and Hovland, F.: "Surfactant Flooding: Technical and Economical Conditions to Succeed," paper SPE/DOE 27824 presented at the 9th Symposium on Improved Oil Recovery, Tulsa, OK (Apr. 17-20, 1994).

Jiachao, F.J., Jiansen, Z., Shaobing, C., Chengjie, Q.: "Water/Oil Separation Characteristics of Daqing Oilfield Polymer Flooding Production Fluid," paper SPE 28540 presented at the 69th Annual Technical Conference and Exhibition of the SPE, New Orleans, LA (Sept. 25-28, 1994).

Johnson, R.E., Kenelly, R.G., and Scharwz, J.R.: "Chemical and Physical Applications in Treating Produced-Fluid Emulsions of the Bell Creek Micellar/Polymer Flood," *SPEPE* (May, 1988) 210-216.

Kalpakci, B., Arf, T.G., Grist, D.M., Hyde, S.B., Vikane, O., and Espedal, S.: "A Preliminary Evaluation of An LTPF Process for Statfjord Field, Norway," paper presented at the 7th European IOR Symposium, Moscow, Russia (Oct. 27-29, 1993).

Kalpakci, B., Arf, T.G., Barker, J.W., Krupa, A.S., Morgan, J.C., and Neira, R.D.: "The Low-Tension Polymer Flood Approach to Cost-Effective Chemical EOR," paper SPE/DOE 20220 presented at the 7th Symposium on Enhanced Oil Recovery, Tulsa, OK (Apr. 22-25, 1990).

Lim, M.T., Pope, G.A., and Sepehrnoori, K.: "Mechanistic Study of Carbon Dioxide Flooding Using Horizontal Wells," paper SPE 27807 presented at the 9th Symposium on Improved Oil Recovery, Tulsa, OK (Apr. 17-20, 1994).

Lim, M.T., Khan, S.A., Pope, G.A., and Sepehrnoori, K.: "Simulation of Carbon Dioxide Flooding Using Horizontal Wells," paper SPE 24929 presented at the 67th Annual Technical Conference and Exhibition of the SPE, Washington, DC (Oct. 4-7, 1992).

Maerker, J.M. and Gale, W.W.: "Surfactant Flood Process Design for Loudon," paper SPE/DOE 20218 presented at the SPE/DOE 7th Symposium on Enhanced Oil Recovery, Tulsa, OK (Apr. 22-25, 1990).

Mandelker, P.: "Tax Credit, Bills May Expand EOR Opportunities in U.S.," *Oil & Gas J.* (Feb. 24, 1992) 69.

Martin, F.D.: "Enhanced Oil Recovery for Independent Producers," paper SPE/DOE 24142 presented at the 8th Symposium on Enhanced Oil Recovery, Tulsa, OK (Apr. 22-24, 1992).

National Petroleum Council: *Enhanced Oil Recovery*, Washington, DC (June, 1984).

National Petroleum Council: *Marginal Wells*, Washington, DC (July, 1994).

Newendorp, P.D.: *Decision Analysis for Petroleum Exploration*, Pennwell, Tulsa, OK (1975) 58-71.

Petroleum Engineering Handbook, third edition, SPE, Richardson, TX (1992).

Rao, R.K.S.: *Financial Management, Concepts and Applications*, third edition, South-Western College, Cincinnati, OH (1995) 114.

Reppert, T.R., Bragg, J.R., Wilkinson, J.R., Snow, T.M., Maer, N.K., Jr., and Gale, W.W.: "Second Ripley Surfactant Flood Pilot Test," paper SPE/DOE 20219 presented at the SPE/DOE 7th Symposium on Enhanced Oil Recovery, Tulsa, OK (Apr. 22-25, 1990).

Saad, N., Pope, G.A., and Sepehrnoori, K.: "Simulation of Big Muddy Surfactant Pilot," *SPEJ* (Feb. 1989) 24.

Schuyler, J.R. and Hochanadel, S.M.: "Simulation Demonstrates Economics of Minnelusa Polymer Floods," *Oil & Gas J.* (May 27, 1991) 90.

Seba, R.D.: "Determining Project Profitability," *JPT* (March 1987) 263-271.

Seba, R.D.: "The Only Investment Selection Criterion You Will Ever Need," paper SPE 16310 presented at the SPE Hydrocarbon Economics and Evaluation Symposium, Dallas, TX (Mar. 2-3, 1987).

Startzman, R.A. and Wattenbarger, R.A.: "An Improved Computation Procedure for Risk Analysis Problems With Unusual Probability Functions," paper SPE 13772 presented at the SPE Hydrocarbon Economics and Evaluation Symposium, Dallas, TX (Mar. 14-15, 1985).

Stermole, F.J.: *Economic Evaluation and Investment Decision Methods*, fifth edition, Investment Evaluations Corp., Golden, CO (1984) 55, 168-170, 242.

Taber, J.J, and Seright, R.S.: "Horizontal Injection and Production Wells for EOR of Waterflooding," paper SPE 23952 presented at the SPE Permian Basin Oil and Gas Recovery Conference, Midland, TX (Mar. 18-20, 1992).

Takagi S., Pope, G.A., Sepehrnoori, K., Putz, A.G., and Dakhlia, H.: "Simulation of a Successful Polymer Flood in the Chateaurenard Field," paper SPE 24931 presented at the 67th Annual Technical Conference and Exhibition of the SPE, Washington, DC (Oct. 4-7, 1992).

"Tax Information on Corporations," Department of the Treasury: Internal Revenue Service, Publication 542, Cat. No. 15072O (1995) 7.

Thompson, R.S. and Wright, J.D.: *Oil Property Evaluation*, Thompson-Wright Associates, Golden, CO (1984).

Wellington, S.L. and Richardson, E.A.: "Low Surfactant Concentration Enhanced Waterflooding," paper SPE 30748 presented at the 70th Annual Technical Conference and Exhibition of the SPE, Dallas, TX (Oct. 22-25, 1995).

Widmeyer, R.H. and Williams, D.B.: "Performance Evaluation of the Salem Unit Surfactant/Polymer Pilot," paper SPE 14442 presented at the 60th Annual Technical Conference and Exhibition of the SPE, Las Vegas, NV (Sept. 22-25, 1985).

Wu, W.: "Optimization of Field-Scale Chemical Floodings Using Numerical Modeling," PhD dissertation, U. of Texas, Austin (May, 1996).

Yang, A.P.: "Stochastic Heterogeneity and Dispersion," Ph.D. dissertation, U. of Texas, Austin (1990).

☆U.S. GOVERNMENT PRINTING OFFICE: 1996 - 559-031/40037